Programa de Doctorado en Física y Matemáticas
Universidad de Granada

Cosmic Lighthouses at High Redshift: Intervening material in sight-lines towards GRBs and QSOs

Rubén Sánchez Ramírez

Thesis submitted for the degree of

Doctor of Philosophy

10 June 2016

Supervisors: Prof. Javier Gorosabel Urkia, Dr. Antonio de Ugarte Postigo, and Prof. Alberto J. Castro Tirado

Instituto de Astrofísica de Andalucía
Consejo Superior de Investigaciones Científicas

Para todos aquellos que caminaron a mi lado,
aún sin yo mismo entender hacia dónde me dirigía ...

In Memoriam

Javier Gorosabel Urquia (1969 - 2015)

"El polvo de las estrellas se convirtió un dia en germen de vida.
Y de él surgimos nosotros en algun momento.
Y asi vivimos, creando y recreando nuestro ambito.
Sin descanso. Trabajando pervivimos.
Y a esa dura cadena estamos todos atados."

— *Izarren Hautsa*, Mikel Laboa

"La vida son estos momentos que luego se te olvidan". Esa fue la conclusión a la que llegó Javier al final de uno de esos fantásticos días intensos y maratonianos a los que me tenía acostumbrado. Viéndolo ahora con perspectiva estaba en lo cierto, porque por más que me esfuerce en recordar y explicar lo que era el día a día con él, no puedo transmitir con justicia lo que realmente fue. La reconstrucción de esos momentos es inevitablemente incompleta.

Contaros cómo era Javier como jefe es muy sencillo: él nunca se comportó como un jefe conmigo. Nunca ordenó. Siempre me decía, lleno de orgullo, que no le hacía ni caso. Javier era para mi un líder, uno de los mejores modelos a seguir que he conocido, tanto como profesional como persona. Él no solía pedir si no daba antes. Es más, no solía pedir. Eras tú mismo quién pedía echarle una mano al ver su frenético ritmo de trabajo y como

se dejaba el alma por ti. Eras tú quien quería estar a su lado para que te contagiase esa ilusión y ansia por descubrir y aprender.

Javier entendía la dirección de una tesis doctoral como una responsabilidad suya hacia el doctorando, hacia mi, no como una oportunidad para poner a trabajar a alguien en sus proyectos. Pese a que siempre estaba involucrado en incontables estudios, solo me ofrecía la posibilidad de colaborar en aquellos que él consideraba interesantes para mi carrera científica. Pese a que las horas que he invertido en mi tesis es escandalosa, pero no más de las que dedicaba él al trabajo, apenas he hecho nada que finalmente haya caído en saco roto.

Javier nunca quiso darme las cosas hechas, disfrutaba ayudándome a buscar y entender las ideas más básicas y profundas involucradas en el problema que trabajábamos para que yo aprendiese a encontrar las soluciones (y consecuentemente más problemas) por mí mismo. Es por ello que hoy me siento preparado para resolver cualquier problema laboral o incluso personal que se me pueda presentar cuya solución no se encuentre con Google.

Javier nunca quiso imponer su visión y opinión como hipótesis de trabajo, sino que disfrutaba explorando, escuchando y discutiendo conmigo todas las posibilidades que se nos podían ocurrir. Él nunca quiso que se le viese como el científico excepcional que fue, sino como la persona humilde, alegre y accesible que también era.

Javier no solo me llevó por la ciencia que conocía, en la que era una de las personas más respetadas y valorada de la comunidad. En los últimos años, también me animó y apoyó, invirtiendo una fracción muy importante de su tiempo y recursos, a finalizar un trabajo en el que él mismo no esperaba estar involucrado. Él solo pensó en el impacto que tendría en mi carrera científica, y solo buscó como recompensa disfrutar aprendiendo conmigo esa nueva ciencia para nosotros, para al final poder serme útil en lo que pudiese, que siempre era muchísimo.

Sinceramente, me siento una persona extremadamente afortunada por haber podido aprender de mis 3 directores de tesis. He tenido el privilegio de poder buscar y recibir aquello que científicamente podía esperar de cada uno. Antonio y Alberto son dos investigadores extraordinarios y a la vez diferentes, lo que a mi punto de vista se traduce en que son complementarios, y por tanto su suma enriquecedora. Con Javier tenía las virtudes que más valoro de los dos en uno solo.

¿Cómo me siento ahora que empiezo mi etapa post-doctoral sin Javier? Huérfano. Sé que Alberto y Antonio seguirán ahí. Seguirán siendo de mi tito y mi yayo siempre. También sé que muchos de vosotros seguiréis echándome un ojo para ver cómo me va todo y me apoyaréis en lo que esté en vuestra mano. Pero es innegable que ya no voy a

poder afrontar el futuro, ya sea en ciencia o no, con la misma ilusión y confianza con que lo hubiese hecho teniéndolo a mi lado.

Gracias Javier por haberme regalado estos inolvidables años. Siempre te echaré en falta.

Resumen

Pese al gran avance que durante las últimas décadas ha habido en nuestro entendimiento del Universo, todavía quedan innumerables cuestiones tanto teóricas como observacionales pendientes de respuesta. En este sentido, la reciente construcción de telescopios de 8-10 m, junto al desarrollo de nuevos y mejores detectores, nos han permitido observar el Universo de manera mucho más profunda o, lo que es lo mismo, observarlo cuando era mucho más joven.

En lo referente a la cosmología observacional, en las últimas décadas se han hecho cartografiados del cielo en los que se detectan galaxias muy lejanas, muy jóvenes o en proceso de formación. Gracias a ello, nuestra visión del Universo a gran escala y a grandes distancias ha mejorado significativamente, aunque todavía no hemos hecho más que arañar su superficie. Debido a las limitaciones instrumentales, los cartografiados celestes que permiten la detección de la emisión de luz de galaxias lejanas y el tratamiento estadístico de los datos no son suficientes para establecer las características del Universo cuando tenía menos de 1 Ga, ya que la luz que somos capaces de captar desde sitios tan remotos en el Cosmos se limita a las fuentes más luminosas que existieron, lo que nos dice muy poco acerca de lo que era "normal" en dicho periodo.

El uso de la espectroscopía de absorción significó una revolución para la cosmología observacional. Esta técnica aprovecha fuentes muy luminosas para su uso como "linternas" que alumbran el medio entre la fuente y la Tierra. Las propiedades de dicho medio las podemos inferir no por detectar su luz, sino a través de sus sombras. Dichas linternas fueron originalmente estrellas jóvenes y masivas, que nos permitieron estudiar nuestra propia Galaxia. Sin embargo, si lo que buscamos es salir de nuestro entorno más cercano, necesitamos en este caso no sólo linternas, sino potentes "faros" situados a grandes distancias.

Afortunadamente, nuestro Universo dista mucho de ser un lugar tranquilo y en él tienen lugar fenómenos, tanto permanentes como transitorios, lo suficientemente energéticos como para generar fuentes de radiación electromagnéticas lo suficientemente luminosas

como para que actúen de "faros cósmicos" incluso desde el Universo más remoto. Los dos tipos de objetos que tradicionalmente se han venido usando como fuentes retroiluminadoras son los *cuásares* o QSOs, que son fuentes permanentes, y los estallidos de rayos gamma (GRBs), que pese a ser mucho más luminosos son eventos transitorios y por tanto sólo observables durante un breve periodo de tiempo.

Los GRBs son los fenómenos más violentos que se conocen en el Universo, y son en sí mismos fuentes con suficiente interés científico como para dedicar a ellos una parte de esta Tesis. Desde su descubrimiento casual durante la Guerra Fría, la naturaleza extrema de estos breves pero intensos estallidos de emisión gamma ha fascinado a los astrónomos. Al inicio, poco podía saberse de ellos con la instrumentación y los conocimientos de que entonces se disponía. No obstante, desde finales de los 80 comenzaron a sucederse una serie de trepidantes y apasionantes descubrimientos que culminaron con el descubrimiento de contrapartidas electromagnéticas (postluminiscencia) que seguían a las fulguraciones en gamma, y la determinación de su carácter cosmológico.

Actualmente se dispone de archivos observacionales y desarrollo teórico suficientes como para explicar la naturaleza de los GRBs. Dicho trabajo ha servido incluso para estudios cosmólogicos, como la construcción del diagrama de Hubble a alto corrimiento al rojo o *redshift*. Sin embargo, todavía siguen abiertas muchas cuestiones, tanto en la explicación de eventos atípicos, como en los detalles de los modelos que consiguen explicarlos tan sólo de un modo genérico.

En esta tesis se ha abordado, en una primera parte, el estudio multi-frecuencia de un evento que ejemplifica las limitaciones actuales en el conocimiento de la física de las postluminiscencias o *afterglows* asociados a GRBs. GRB 110715A se detectó el 15 de julio de 2011 (el nombre de los GRBs se forma a partir de la fecha del evento) y su evolución fue seguida desde múltiples observatorios, tanto espaciales como terrestres y en longitudes de onda desde radio hasta rayos gamma. Además de su extenso seguimiento, este GRB tiene la particularidad de ser el primer *afterglow* observado con las antenas del observatorio ALMA.

El análisis y modelado de los datos obtenidos para este GRB nos ha revelado detalles tanto de los procesos físicos que tienen lugar en la emisión del *afterglow*, como de la galaxia que albergó un evento de semejante violencia. En nuestro trabajo se muestra que las observaciones son consistentes con el modelo de bola de fuego, comúnmente aceptado. En él un chorro o *jet* ultra-relativista, producido durante la formación de un agujero negro en el núcleo de una estrella super-masiva, produce radiación sincrotrón al chocar con el medio circundante. Sin embargo, no ha sido posible ajustar los parámetros de dicho modelo para obtener un ajuste estadísticamente válido capaz de explicar todas

las fluctuaciones de luz observadas en las diversas bandas. Esto indica que es necesaria la inclusión de más procesos físicos y/o la modificación de los existentes para explicar observaciones con este nivel tan alto de cobertura espectral y temporal. Por otro lado, hemos podido inferir detalles de la galaxia anfitriona mediante espectroscopía de absorción usando el brillo del *afterglow* como faro cósmico. Los detalles estudiados son imposibles de extraer mediante la observación directa de la galaxia, ya que es sólo detectable al límite de la capacidad de los mayores telescopios de los que actualmente disponemos. Nuestras observaciones del espectro de líneas de absorción nos indican que se trata de una galaxia enana con un fondo de radiación ionizante más bajo de lo que normalmente se observa en otras galaxias en las que ha sucedido un GRB.

En la segunda parte de esta tesis se estudian tres GRBs, cuyo nexo de unión es que se produjeron a un redshift z>5 (cuando el Universo tenía poco más de 1 Ga). Por tanto, estos eventos han supuesto una oportunidad única para el estudio del medio interestelar e intergaláctico hasta los límites del Universo observable, y abordar cuestiones fundamentales como la evolución química o el proceso de reionización del Universo.

GRB 140304A ocurrió en una galaxia a z∼5.3. A partir del espectro óptico se detectó una gran absorción de hidrógeno, asociada a lo que se conoce como sistemas DLA (del inglés Damped Lyman-α, o Lyman-α amortiguado), siendo este caso el tercero más lejano actualmente conocido en las líneas de visión hacia GRBs. La detección de líneas metálicas en dicho sistema ha permitido estimar la metalicidad de manera suficientemente robusta como para descartar un contenido en metales atípicamente bajo, lo que marcaría la observación de la esperada evolución del contenido de metales hacia un ambiente pobre, en los cuales se espera encontrar estrellas de la llamada Población III, que fueron las primeras formadas tras el periodo de recombinación en el Universo primitivo.

El descubrimiento de GRB 130606A y su subDLA a z∼5.9 permitió establecer de nuevo una metalicidad consistente con los valores encontrados a distancias menores, aunque hay que tener en cuenta que habitualmente se observa un contenido en metales mayor en subDLAs que en DLAs. A longitudes de onda menores que la de la absorción de hidrógeno por parte de la galaxia anfitriona del GRB, se observa la fuerte absorción del medio intergaláctico debido al efecto Gunn-Peterson, ya que en esa época el medio intergaláctico terminaba de reionizarse. Gracias a ello se ha podido constatar que las medidas de la profundidad óptica son consistentes con las obtenidas mediante las líneas de visión a QSOs, las cuales son mucho más imprecisas que las obtenidas en este trabajo.

Por último, la observación de GRB 140515A a z∼6.3 ha significado la primera oportunidad para medir la fracción de hidrógeno neutro en el medio intergaláctico cuando la absorción G-P satura. Ello ha sido posible dada la baja columna de densidad de hidrógeno

neutro de la galaxia anfitriona, lo que se traduce en la observación directa de un perfil de absorción debido fundamentalmente al medio intergaláctico. Esta medida también ha permitido, por primera vez, determinar la fracción de hidrógeno neutro del medio intergaláctico a un redshift crítico para constreñir los modelos actuales de reionización del Universo.

Por tanto, en esta parte de la tesis hemos probado la utilidad de los GRBs como sondas cosmológicas a muy alto redshift, aprovechando su luminosidad y la facilidad de modelado de su emisión. También se ha mostrado la necesidad de continuar observando estos eventos para poder incrementar nuestro conocimiento acerca de las primeras etapas del Universo, ya que este método es mucho más prometedor que el uso de los QSOs porque estas fuentes decrecen rápidamente en número a dichas distancias y los GRBs pueden incluso tener como progenitores estrellas de población III.

En la última parte de esta tesis se ha utilizado una muestra de 100 QSOs, además de datos de la literatura, para abordar un problema cosmológico clásico, como es la evolución del hidrógeno neutro a lo largo del tiempo cósmico. En 1986 se llevó a cabo el primer *survey* de DLAs. Estos sistemas, detectados en absorción en la línea de visión hacia QSOs (y GRBs, como se ha mencionado), contienen la mayor parte del hidrógeno neutro del Universo. La importancia de ello radica en que a partir de estas nubes se desencadenan los procesos de formación estelar, y por tanto están íntimamente ligados a la evolución de las galaxias. Desde principios de los 90 se obtuvieron más observaciones y se analizaron conjuntamente para inferir propiedades medias a escalas cosmológicas. La validez de dichos resultados reside en el hecho de que en líneas de visión hacia QSOs, los DLAs se detectan como sistemas intervinientes, es decir, su frecuencia no está sesgada como en el caso de los DLA en las galaxias anfitrionas de GRBs. En esta tesis se ha analizado una muestra conjunta de DLAs visualmente identificados en los espectros, y se ha hecho un análisis detallado desarrollando nuevas técnicas y detectando y cuantificando fuentes de errores sistemáticos y estadísticos. Por primera vez se ha proporcionado una evidencia estadística robusta y justificada de una pequeña evolución de la cantidad de hidrógeno neutro desde z=0 a $z\sim$5 en un factor $\sim$4.

Los estudios aquí descritos sientan las bases y profundizan en las técnicas que permiten avanzar en el estudio del Universo temprano, utilizando como faros cósmicos las dos familias de objetos más luminosos que conocemos, los QSO y los GRBs.

Abstract

Despite the great progress in recent decades on our understanding of the Universe there are still countless observational and theoretical issues that are pending response. In this regard, the recent construction of 8-10 m telescopes, together with the development of newer and better detectors have allowed us to observe the Universe in a much deeper way, or in other words, observe it when it was much younger.

Regarding observational cosmology, in recent decades there have been surveys of the sky where very distant, very young, or even still forming galaxies are detected. As a result, our view of the Universe on a large scale and over long distances has significantly improved, although we have still not done much more than scratch the surface. Due to instrumental limitations, surveys that detect the emission of light from distant galaxies are not sufficient to establish the characteristics of the Universe when it was less than 1 Gyr, since the light that reaches us from such remote places in the Cosmos is limited to the brightest sources that existed at the time, which tells us very little about what was "normal" in that period.

The use of absorption spectroscopy meant a revolution for observational cosmology. This technique takes advantage of very luminous sources which are used as "flashlights" that illuminate the environment between the source and the Earth. We infer the properties of this environment not through its light, but through its "shadows". These flashlights were originally young, massive stars, which allowed us to study our own Galaxy. However, if what we seek is out of our immediate environment, we need not only flashlights, but powerful "beacons" located at great distances.

Fortunately, our Universe is far from being a quiet place and we can find phenomena, both permanent and transient, that are energetic enough to generate the necessary amount of electromagnetic radiation as to become "cosmic beacons" even on the remote Universe. The two types of objects that have been traditionally used as illuminating sources are *quasars* or QSOs, which are permanent sources, and gamma-ray bursts (GRBs), which despite being much brighter are transient and thus only observable for a short period of

time.

GRBs are the most violent phenomena known in the Universe, and are themselves sources with sufficient scientific interest as to devote to them a part of this Thesis. Since their accidental discovery during the Cold War, the nature of these brief but intense bursts of gamma emission has fascinated astronomers. Initially, little could be learned about them with the instrumentation and knowledge available at the time. However, since the late 80s a series of thrilling and exciting discoveries took place, culminating in the discovery of the electromagnetic counterparts (afterglows) that followed the gamma-ray bursts, that helped to establish their cosmological nature.

Currently, the available observational records and the development of theoretical models are helping to understand the nature of GRBs. This work has even served for cosmological studies, such as the construction of the Hubble diagram at high redshift. However, many questions still remain open, both in explaining atypical events, or in determining the details of the models that can only give general descriptions of GRBs.

This Thesis has addressed, in its first part, a multi-frequency study of an event that exemplifies the current limitations in the knowledge of the physics of the afterglows associated with GRBs. GRB 110715A was detected on July 15, 2011 (the name of the GRBs is formed from the date of the event) and its evolution was followed-up from multiple observatories, both space and ground-based, and at wavelengths ranging from radio to gamma-rays. In addition to his extensive monitoring, this GRB has the particularity of being the first afterglow observed with the antennas of the recently inaugurated ALMA observatory.

The analysis and modeling of the data obtained for this GRB has revealed details of both the physical processes taking place in the emission of the afterglow, and of the galaxy that hosted an event of such violence. In our work we show that the observations are consistent with the commonly accepted fireball model. In this model, an ultra-relativistic jet, produced during the formation of a black hole in the core of a super-massive star, produces synchrotron emission when it collides with the surrounding environment. However, it has not been possible to adjust the parameters of the model to obtain a statistically valid fit that can explain all the fluctuations observed in the different bands. This indicates that the inclusion of more physical processes and/or modification of the existing ones is necessary to explain observations with this high level of spectral and temporal coverage. On the other hand, we could infer details of the host galaxy by absorption spectroscopy using the brightness of afterglow as a cosmic lighthouse. These details are impossible to extract by directly observing the galaxy in emission, as it is only barely detectable with the largest telescopes currently available. Our observations in absorption, indicate that it

is a dwarf galaxy with an environment of lower than normal ionisation field, as compared to other GRB host galaxies.

In the second part of this Thesis we study three GRBs, linked by the fact that they all occurred at a redshift $z>5$ (when they Universe was a little over 1 Gyr old). These events provide a unique opportunity to study the interstellar and intergalactic medium to the limits of the observable Universe, and to address key issues such as the chemical evolution or the process of reionisation of the Universe.

GRB 140304A occurred in a galaxy at $z\sim5.3$. From the optical spectrum, a strong absorption of hydrogen associated with what is known as DLA (Damped Lyman-α) systems was detected, this case being the third farthest of the currently known in lines of sight to GRB. The detection of metal lines in the system has allowed us to estimate the metallicity robustly enough to rule out a low metallicity environment, which would mark the observation of the expected evolution of metal content to a poor environment in which we expect to find stars of the so-called Population III, which were first formed after the period of recombination.

The discovery of GRB 130606A and its associated subDLA at $z\sim5.9$ allowed us to establish, once again, a metallicity consistent with the values found at lower distances, although it should be noted that a greater metal content is typically observed in subDLAs as compared to DLAs. At wavelengths below that of the hydrogen absorption by the host galaxy of the GRB, we detect a strong absorption of the intergalactic medium due to the Gunn-Peterson effect, since at the time, the intergalactic medium had finished reionising. As a result we show that the optical depth measurements are consistent with those obtained from the sightlines to QSOs, which are much weaker than those obtained in this work.

Finally, the observation of GRB 140515A at $z\sim6.3$ has provided the first opportunity to measure the fraction of neutral hydrogen in the intergalactic medium when G-P absorption saturates. This has been possible due to the low column density of neutral hydrogen in the host galaxy, resulting in the direct observation of an absorption profile mainly due to the intergalactic medium. This has also allowed us, for the first time, to obtain a measure of the fraction of neutral hydrogen in the intergalactic medium at a critical redshift to constrain the current models of reionisation of the Universe.

Therefore, in this part of the thesis we tested the usefulness of GRBs as cosmological probes to very high redshift, taking advantage of their brightness and the ease of modeling their continuum. We have also shown the need to continue observing these events in order to increase our knowledge about the early stages of the Universe, as this method is much more promising than the use of QSOs because they rapidly decrease in number at large

distances, whereas GRBs may even be present as population III stars.

In the last part of this Thesis we have used a sample of 100 QSOs, together with literature data, to address a classic cosmological problem, as is the evolution of neutral hydrogen over cosmic time. In 1986 the first survey of DLAs was conducted. These systems, detected in absorption in the line of sight to QSOs (and GRBs, as seen in Part 2), contain most of the neutral hydrogen in the Universe. The importance of this is that the star formation processes are triggered from these clouds, and are therefore closely linked to the evolution of galaxies. Since the early 90's observations were obtained and analysed together to infer the average properties at cosmological scales. The validity of these results lie in the fact that in the lines of sight to QSO, the DLAs are detected as intervening systems, i.e., their frequency is not biased as in the case of the DLA in GRB host galaxies. In this Thesis we analysed a joint sample of DLAs visually identified in QSO spectra and made a detailed analysis, developing new techniques, and determining and quantifying sources of systematic and statistical errors. This has been used to provide, for the first time, a robust statistical evidence of a small amount of evolution of neutral hydrogen from z=0 to $z\sim$5 of a factor $\sim$4.

The studies presented here set the basis and deepen into the techniques that allow us to advance in the study of the early Universe, using the two families of the most luminous objects that we know as cosmic beacons, QSOs and GRBs.

Contents

THESIS INTRODUCTION

Chapter 1

The Large Scale Structure of the Universe

"In this age of specialization men who thoroughly know one field are often incompetent to discuss another. The great problems of the relations between one and another aspect of human activity have for this reason been discussed less and less in public. When we look at the past great debates on these subjects we feel jealous of those times, for we should have liked the excitement of such argument."

— Richard P. Feynman, *Caltech YMCA lunch forum, 1956*

Mankind has always looked up and admired the night sky. Civilisations have calibrated their calendars according to the sky and the stars. And they have always tried to understand what is out there, where do the stars come from, and what is our place in the Universe. When, in 1609, Galileo first aimed a telescope at the sky, we started a voyage to the deep and distant Universe, which has redefined the evolution of our World. Thanks to the most modern astronomical instrumentation, we are now in position to take the ultimate step and look back into the most remote and ancient Universe.

1.1 The Observable Universe

The Universe we observe from Earth can be defined as a mathematical *ball*, i.e., the space inside an sphere, centered on the observer, that contains galaxies formed by baryonic (ordinary) matter, dark matter, and dark energy which can be part of larger structures (groups, clusters, filaments, etc., see Figure 1.1 for an artist visualization). This means that all we see from Earth is different from what we could observe from another planet in another galaxy, so one of the challenges for the understanding on the Cosmos' history is the extrapolation from our point of view to a more global conception on the beginning and evolution of the Universe.

Figure 1.1: Artist's logarithmic scale conception of the observable Universe with the Solar System at the center, inner and outer planets, Kuiper belt, Oort cloud, Alpha Centauri, Perseus Arm, Milky Way galaxy, Andromeda galaxy, nearby galaxies, Cosmic Web, Cosmic microwave radiation and Big Bang's invisible plasma on the edge. *Credit*: Pablo Carlos Budassi.

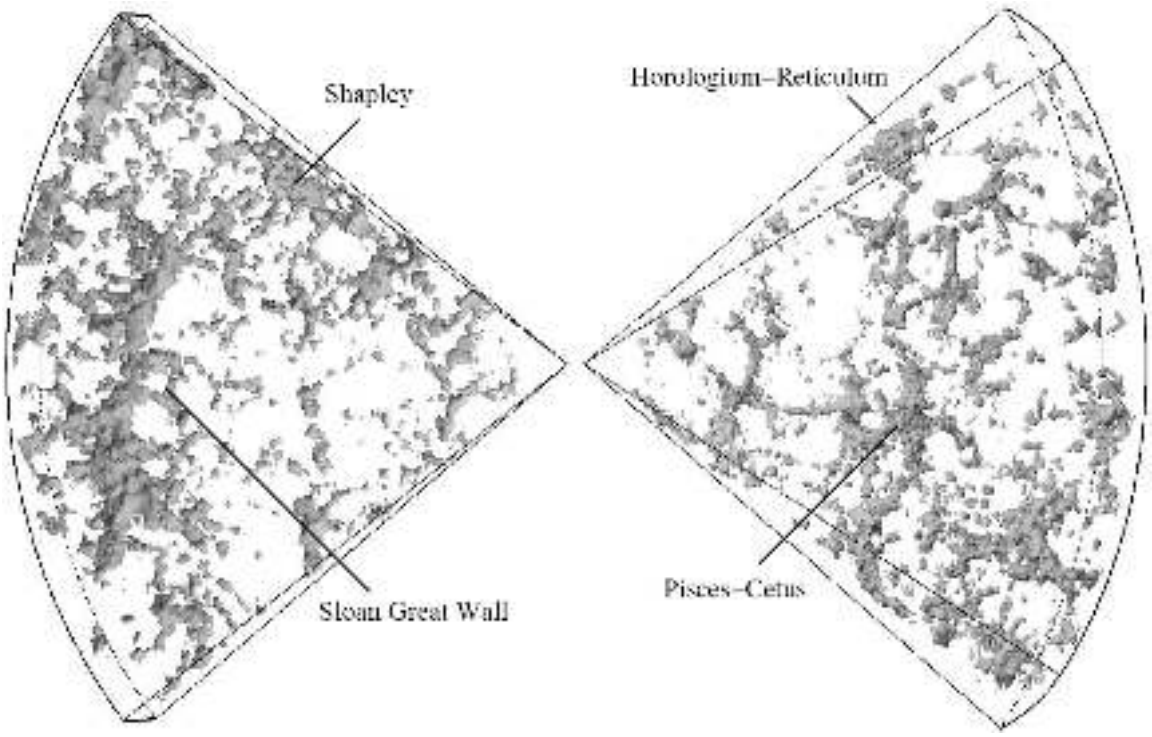

Figure 1.2: Three-dimensional DTFE (Delaunay tessellation field estimator) reconstruction of the inner parts of the 2dF Galaxy Redshift Survey. The figure reveals an impressive view of the cosmic structures in the nearby Universe. Several superclusters stand out, such as the Sloan Great Wall, once known as the largest structure in the Universe until discovery of the Huge-LQG in January 2013. This picture was featured on 7 November 2007 on Astronomy Picture of the Day (APOD) http://apod.nasa.gov/apod/ap071107.html.

The surface of last scattering is the collection of points in space at the exact distance that photons from the time of photon decoupling just reach us today. These are the photons we detect today as the cosmic microwave background radiation (CMBR). However, with future technology, it may be possible to observe the still older relic neutrino background, or even more distant events via gravitational waves.

The best estimate of the age of the Universe is 13.799 ± 0.021 billion years. It is estimated that the diameter of the observable Universe is about 28.5 gigaparsecs, placing its edge at about 46.5 billion light-years away (Planck *et al.*, 2014).

The organization of structures in the Universe appears to follow as a hierarchical model with organization up to the scale of superclusters and filaments. It begins at the stellar level. Stars are organized into galaxies, which in turn form galaxy groups, galaxy clusters, superclusters, sheets, walls and filaments, which are separated by immense voids, creating a vast foam-like structure sometimes called the "cosmic web" (e.g. Kirshner, 2002). This network is clearly visible in the 2dF Galaxy Redshift Survey. In Figure 1.2, a three-dimensional reconstruction of the inner parts of the survey is shown, revealing an impressive view of the cosmic structures in the nearby Universe. Several superclusters stand out, such as the Sloan Great Wall. In November 2013 astronomers discovered the Hercules–Corona Borealis Great Wall (Horváth *et al.*, 2014), an even bigger structure twice as large as the former. It was defined by the mapping of gamma-ray bursts.

The End of Greatness is an observational scale discovered at roughly 100 Mpc (roughly 300 million lightyears) where the lumpiness seen in the large-scale structure of the Universe is homogenised and isotropised in accordance with the Cosmological Principle (e.g. Kirshner, 2002). The superclusters and filaments seen in smaller surveys are randomized to the extent that the smooth distribution of the Universe is visually apparent. It was not until the redshift surveys of the 1990s were completed that this scale could accurately be observed.

The more accurate is our knowledge of the Universe, the better they constrain physical models that allow us to understand how Nature works. From an observational point of view, it is essential to apply valid and consistent techniques and strategies in order to achieve statistically significant results and validate theoretical models and/or discern between them.

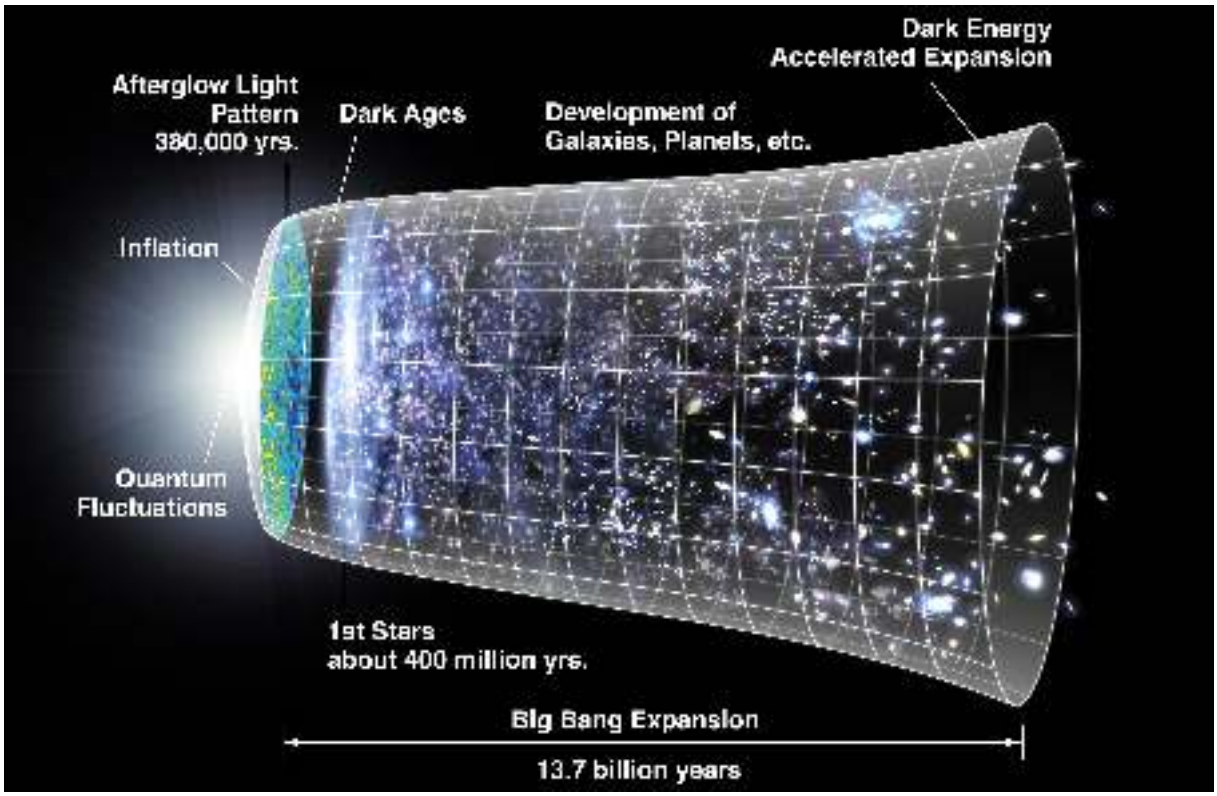

Figure 1.3: Diagram of evolution of the Universe from the Big Bang (left) to the present (right). *Credit*: NASA/WMAP Science Team.

1.2 Chronology of the Universe

All ideas concerning the very early Universe (cosmogony) are still very speculative. No experiments have yet probed energies of sufficient magnitude to provide any empiric insight into the behaviour of matter at the energy levels that prevailed during these periods. Below we present a brief summary based on current ideas:

Planck epoch – *From 0 to* 10^{-43} *seconds after the Big Bang*: This was the time when one unique fundamental force ruled the Universe. Little is understood about physics at these energy regimes, several hypothesis still propose different scenarios.

Grand unification epoch – *From* 10^{-43} *to* 10^{-36} *seconds after the Big Bang*: The grand unification epoch began when gravitation separated from the other forces of nature, which are collectively known as gauge forces. The non-gravitational physics in this epoch would be described by a so-called grand unified theory (GUT). The grand unification epoch ended when the GUT forces further separated into the strong and electroweak forces.

Electroweak epoch – *From* 10^{-36} *to* 10^{-32} *seconds after the Big Bang*: The electroweak

epoch began when the temperature of the Universe was low enough (1028 K) to separate the strong force from the electroweak force (the name for the unified forces of electromagnetism and the weak interaction). In inflationary cosmology, the electroweak epoch began when the inflationary epoch ended.

Inflationary epoch – *Unknown duration, ending at* $\sim 10^{-32}$ *seconds after the Big Bang*: Cosmic inflation was an era of accelerating expansion produced by a hypothesised field called the inflaton, which would have properties similar to the Higgs field and dark energy. While decelerating expansion would magnify deviations from homogeneity, making the Universe more chaotic, accelerating expansion would make the Universe more homogeneous. Inflation ended when the inflaton field decayed into ordinary particles in a process called "reheating", at which point the ordinary Big Bang expansion began. There are still no clear observational evidences of the validity of this theory.

Baryo-genesis – There is currently insufficient observational evidence to explain why the Universe contains far more baryons than antibaryons. After cosmic inflation ended, the Universe was filled with a quark–gluon plasma. From this point onwards the physics of the early Universe is better understood, and less speculative.

Electroweak symmetry breaking and the quark epoch – *From* 10^{-12} *to* 10^{-6} *seconds after the Big Bang*: At this time the Higgs field spontaneously acquired a vacuum expectation value, which broke the electroweak gauge symmetry. There were two consequences: The weak force and electromagnetic force, and their respective bosons (the W and Z bosons and photon), manifest differently in the present Universe, with different ranges. On the other hand, via the Higgs mechanism, all elementary particles interacting with the Higgs field became massive, having been massless at higher energy levels.

Hadron epoch – *From* 10^{-6} *to* 1 *seconds after the Big Bang*: The quark–gluon plasma that composed the Universe cooled until hadrons, including baryons such as protons and neutrons, could form. At approximately 1 second after the Big Bang, neutrinos decoupled and began travelling freely through space (this is analogue to the cosmic microwave background that was emitted much later).

Photon epoch – *From* 10 *seconds to* $380,000$ *years after the Big Bang*: After most leptons and anti-leptons were annihilated at the end of the lepton epoch the energy of the Universe became dominated by photons.

Nucleosynthetic epoch – *From* 3 *to* 20 *minutes after the Big Bang*: Protons (hydrogen ions) and neutrons began to combine into atomic nuclei in the process of nuclear fu-

sion. First, free neutrons combined with protons to form deuterium, and Deuterium rapidly fused into helium-4.

Dark ages – *From* 150 *to* 800 *million years after the Big Bang*: Hydrogen and helium neutral atoms began to form as the Universe cooled down. In the mean time, most of the photons in the Universe were interacting with electrons and protons in the photon–baryon fluid, i.e., the Universe was opaque. At the end of recombination, most of the protons in the Universe were bound up in neutral atoms. Therefore, the photons' mean free path became effectively infinite and the photons could then travel freely: the Universe became transparent, but at this point the only radiation emitted was the 21 cm spin line of neutral hydrogen. This cosmic event is usually referred to as decoupling, and its photons were known as the cosmic microwave background (CMB). Around the same time, existing pressure waves within the electron-baryon plasma – known as baryon acoustic oscillations (BAOs) – became embedded in the distribution of matter as it condensed, giving rise to a very slight preference in distribution of large scale objects.

Reionisation epoch – *From* 150 *million to* 1 *billion years after the Big Bang*: After the first stars and quasars formed from gravitational collapse, the intense UV radiation they emitted reionised the surrounding material. From this point on, most of the Universe was composed of plasma.

Formation of large scale structures – From here on, gravitational attraction lead to the formation of groups, clusters and super-clusters of galaxies.

1.3 Observing the large-scale Universe

Different methods and techniques have been used to attempt to study the Universe at its largest scales. In this section we present some of the observational methods that have been used over the last decades to obtain a glimpse of the furthermost regions of our Cosmos: The study of the emission of the brightest galaxies, the observation of quasi-stellar objects, and the investigation of the distant Universe using the most luminous transient objects as beacons.

1.3.1 Large-scale surveys in emission

Recent advances in astronomical instrumentation, such as the highly sensitive CCD detectors and the new generation of 8-10 m class telescopes, has improved the data quality

and opened a new window to investigate our Universe.

One of the most popular ways to study the Cosmic large structure, from local to very high redshifts, are the emission surveys. They consist of the mapping of certain zones of the sky, which are then used as a valid statistical approximation of the global properties. Under this assumption, the most straightforward source of bias in the results is the limit that the main hypothesis imposes, as the surveyed regions must be large enough to properly account for the anisotropies of the Universe. The other important sources of bias are purely instrumental. All these surveys are flux limited due to the sensitivity of telescopes and detectors. Therefore, nothing can be said from these maps beyond the tip of the iceberg, so we have to take into account and try to solve the limitations of this technique.

There are two ways to map the celestial sphere:

1. **Photometric surveys**: Multi-band photometry can be considered as very low resolution spectroscopy, which can be used to derive the redshift and other physical properties of each object (Baum, 1962). This is usually done by fitting galaxy SEDs of various morphological types to the magnitudes observed in several filters. Some examples of this kind of surveys are Hubble Deep Field (HDF) North (Williams *et al.*, 1996) and South (Williams *et al.*, 2000). The main advantage of this technique is that they can be very deep (up to $I \sim 28$ AB), a limit that still cannot be reached by spectroscopy. On the other hand, photometric surveys have the disadvantages of the poor spectral resolution, which translates in unavoidable degeneracies in the color-z space and difficulties to detect emission lines. Finally, it is also difficult to achieve a good compromise between resolution (the narrower and more numerous filters, the better) and SNR (the broader is the filter, the better).

2. **Spectroscopic surveys**: The analysis of the source's spectrum provides direct information on the redshift and other physical properties. Although this is the ideal method for galactic surveys, it presents several limitations, such as the observational threshold ($I \sim 24$ mag AB), limitations in the positioning of the fibers (which reduce the completeness factor as some sources cannot be observed in crowded fields), and the need of spectroscopic surveys to rely on existing photometric databases for target selection and identification purposes. Examples of this kind of survey are zCOSMOS (using VLT/VIMOS; Zucca *et al.*, 2009) and Autofib (Ellis *et al.*, 1996).

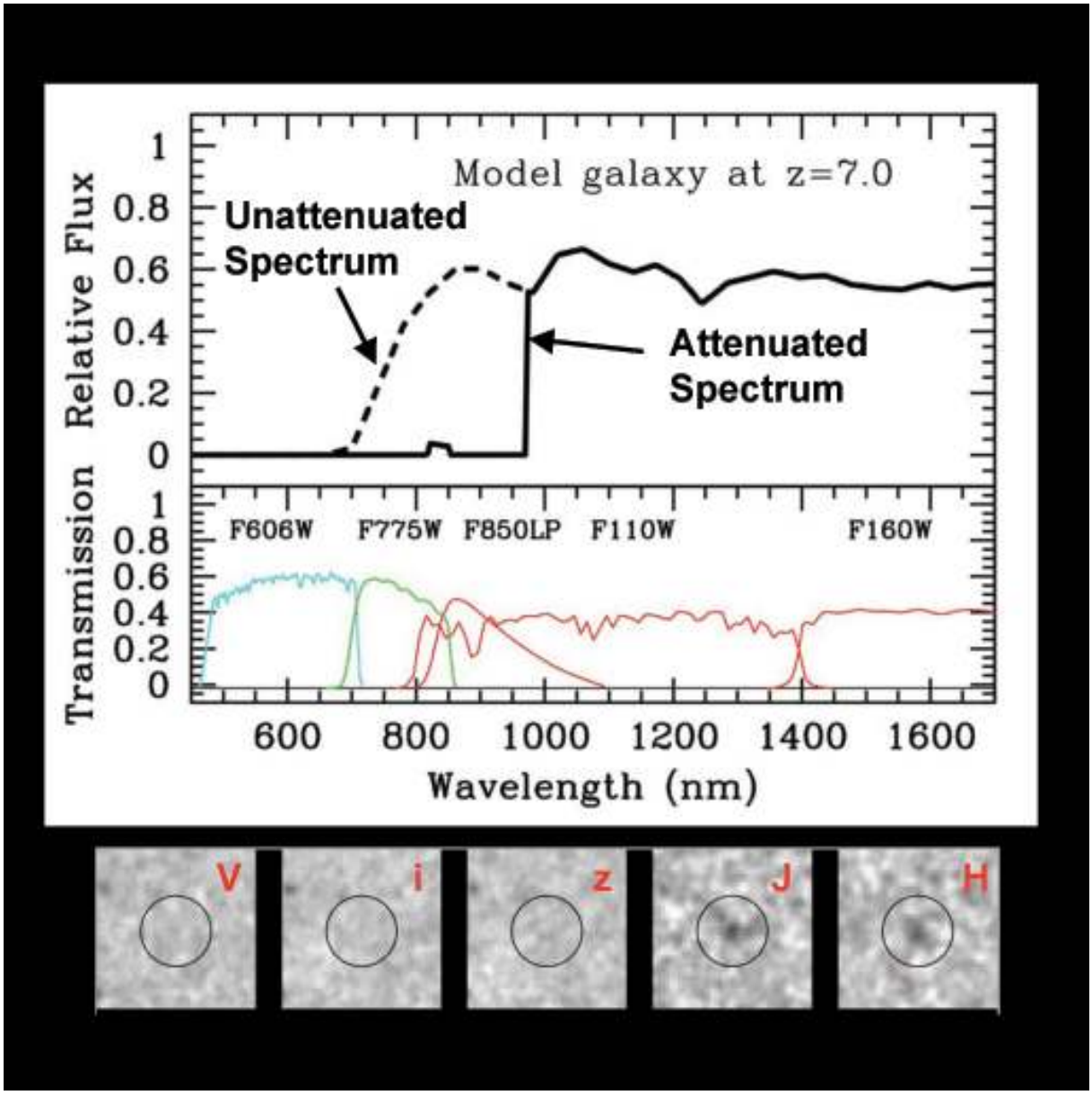

Figure 1.4: Lyman-break technique. A spectrum of a star-forming galaxy at a redshift of 7 is shown in the top panel. The presence of neutral hydrogen creates an abrupt drop in flux blueward of 970 nm. The sensitivities of several of the more relevant filters on HST are shown in the middle panel (V, i, z, J, and H bands, which have central wavelengths of 591 nm, 776 nm, 944 nm, 1119 nm, and 1604 nm, respectively). The bottom panel shows images of the redshift 7 source from the top panel, as seen through these filters. This source clearly shows up in the two longest wavelength filters J and H, but completely disappears in the three bluest wavelength filters "V," i, and z. The presence of such a distinct break is a clear indication that we have found a galaxy at very high redshift which emitted its light at very early times. *Credit*: Rychard Bouwens.

1.3.1.1 Surveys of high-redshift galaxies

In order to study the highest redshift Universe, we need to obtain the deepest possible images. Consequently, at the farthest distances we are only able to derive limited information on only the most luminous sources, which will not be representative of the actual galaxy population at these redshifts. Therefore, we have to handle with care these data-sets when interpreting their results. Currently, the most distant source detected is GN-z11 from the CANDELS survey (Oesch *et al.*, 2016), with a combined photometric and spectroscopic redshift of $z = 11.09^{+0.08}_{-0.12}$.

The main techniques currently used to detect galaxies at very high redshift are based on the observation of:

Lyman Break Galaxies (LBGs): In order to select candidates from imaging surveys, the most important technique used is the "drop-out" or Lyman-break technique: it is based on the assumption that a galaxy spectrum will be significantly absorbed by H I in both its ISM and the intervening IGM at wavelengths shorter than Lyα. Therefore, high redshift colors will be red and there will be a drop out in the bluer bands affected by the break (see Figure 1.4 and, e.g., Steidel *et al.*, 1996; Warren *et al.*, 1987). By means of this technique, Bouwens *et al.* (2011) discovered a $z \sim 10$ galaxy in the HUDF survey (Beckwith *et al.*, 2006). LBG surveys are also conducted using deep ground based imaging, covering larger areas than HST is able to. For example, Bowler *et al.* (2012) surveyed 1 deg^2, reaching a continuum level of 25 mag (AB system), and selected a sample of ∼10 highly luminous galaxies at z>6.5. Confirming LGBs spectroscopically is challenging even for 8-10m class telescopes and HST. Photometric redshifts can identify false high redshift sources due to confussion either with the 4000 Å break or due to red galactic objects (e.g. L and T dwarfs). However, at high redshift, the detection of continuum in the spectrum is usually not possible, and one has to search for emission lines arising from background noise. Often, atmospheric OH features make the detection of emission features even more difficult as they are orders of magnitude brighter and will easily outshine the galaxy emission if they are at similar wavelengths.

Lyα **emitters (LAEs):** The strongest emission line from young star-forming galaxies is Lyα. Blind searches for this emission line are usually conducted with narrow filters in a few clean (of atmospheric emission lines) wavelength windows, as z=4.5,5.7,6.5,7.0,7.3 (e.g. Iye *et al.*, 2006; Taniguchi *et al.*, 2010). A combination of both LBG and LAE techniques led to the detection of the most distant confirmed galaxy known before the discovery of GN-z11 at z=8.68 (Zitrin *et al.*, 2015).

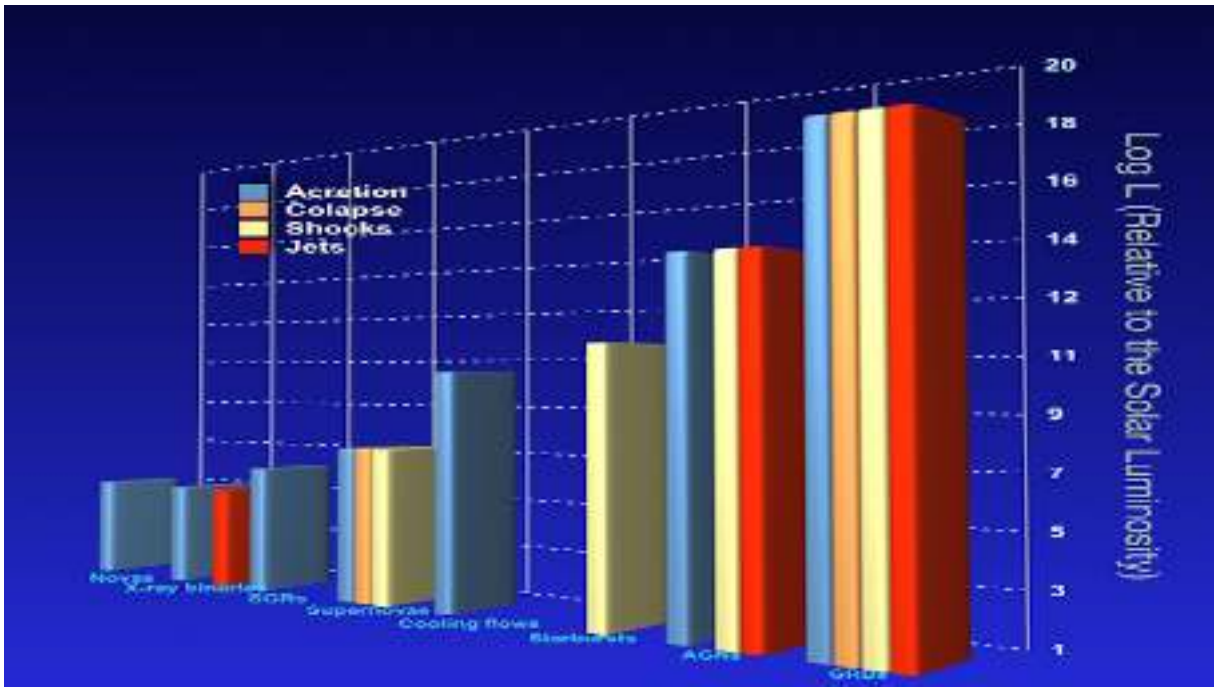

Figure 1.5: Comparison of the luminosities of the most luminous sources in the Universe, as well as the physical mechanisms that explain their emission. *Credit*: Javier Gorosabel

Gravitational lensing: If a high-redshift galaxy is located behind a massive cluster of galaxies, its flux can be magnified by a factor of a few-few tens due to gravitational lensing. There were some LBGs and LAEs surveys making use of this advantage. The cluster lensing and supernova survey with *Hubble* (CLASH Postman *et al.*, 2012) was a *Hubble Space Telescope* (HST) multicycle treasure program that deeply surveyed 25 massive clusters at $0.15 < z < 0.9$. Among other interesting results, the analysis of these data conducted to the detection of a likely very distant source at $z_P = 10.7^{+0.6}_{-0.4}$ (Coe *et al.*, 2013).

Sub-millimeter galaxies: In star forming galaxies, dust absorbs the huge UV radiation from OB stars and re-emits it in FIR and sub-millimeter wavelengths. Due to the shorter wavelength range sampled near this emission peak as redshift increases, the apparent flux at this band from $z{\sim}1$ to 10 is comparable. Consequently, this technique is highly efficient to study high-redshift galaxies (e.g. Blain *et al.*, 2000), although, by definition, it will not detect the first galaxies that formed in metal free environments.

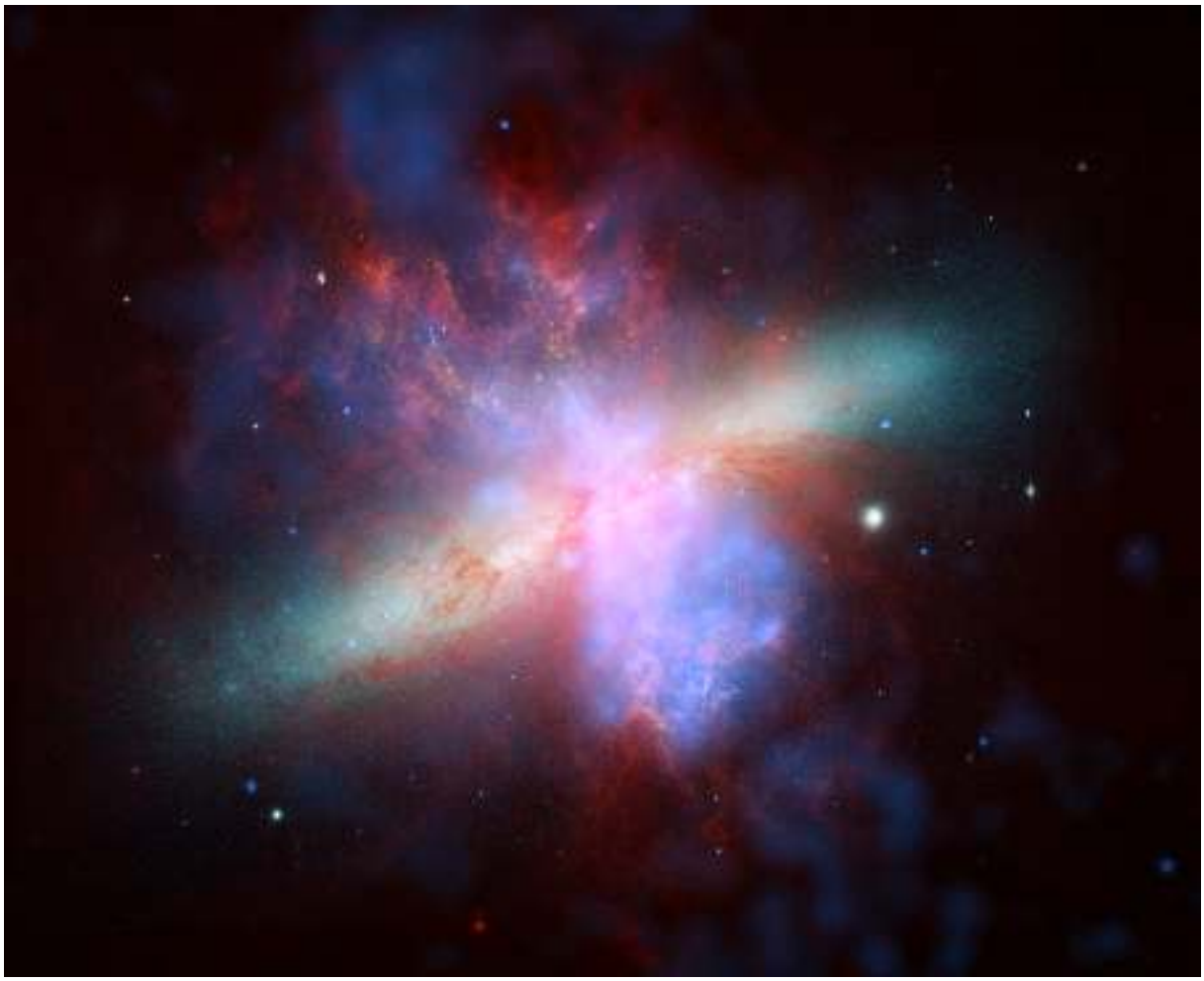

Figure 1.6: Composite image made from observation of three different satellites. Visible aspects of the galaxy were taken by the HST. Spitzer observed it in infrared, and mainly reveals dust emission (in red). Chandra photographed it in X-rays (showing mostly synchrotron emissions from fast electrons). The X-ray emission is shown in blue. *Credit:* NASA.

1.4 The most luminous sources in the Universe

It is expected, as explained in the previous section, that at the highest redshifts we only have a more complete picture of the most luminous sources. Figure 1.5 compares the most luminous sources in the Universe, some of them with a transient nature that will be explained in the next section. Let's now focus on those that have a roughly constant flux within our life's time-scale.

1.4.1 Starburst galaxies

In a starburst galaxy, an exceptionally high rate of star formation is undergoing. Consequently, the galaxy will consume all of its gas reservoir, from which the stars are forming, on a timescale much shorter than the age of the galaxy.

Starburst galaxies are defined by these three interrelated factors:

- The rate at which the galaxy is currently converting gas into stars (the star-formation rate, or SFR).
- The available quantity of gas from which stars can be formed.
- A comparison of the timescale on which star formation will consume the available gas with the age or rotation period of the galaxy.

Commonly used definitions include:

- Continued star-formation where the current SFR would exhaust the available gas reservoir in much less than the age of the Universe (the Hubble Time).
- Continued star-formation where the current SFR would exhaust the available gas reservoir in much less than the dynamical timescale of the galaxy (perhaps one rotation period in a disk type galaxy).
- The current SFR, normalised by the past-averaged SFR, is much greater than unity. This ratio is referred to as the birthrate parameter.

Starburst galaxies do not represent a specific type of galaxies, as starbursts can occur in disk and in irregular galaxies. Nevertheless, attending to their distinct observational characteristics they can be classified as:

Blue compact galaxies (BCGs): These galaxies are often low mass, low metallicity, dust-free objects. Because they contain a large number of young stars in a dust-free environment, their colour is often blue. It was initially thought that BCGs were genuinely young galaxies in the process of forming their first generation of stars, thus explaining their low metal content. However, old stellar populations have been found in most BCGs, and it is thought that efficient mixing may explain the apparent lack of dust and metals. Most BCGs show signs of recent mergers and/or close interactions. Green Pea galaxies (GPs) are small compact galaxies resembling primordial starbursts that were found by citizen scientists taking part in the Galaxy Zoo project.

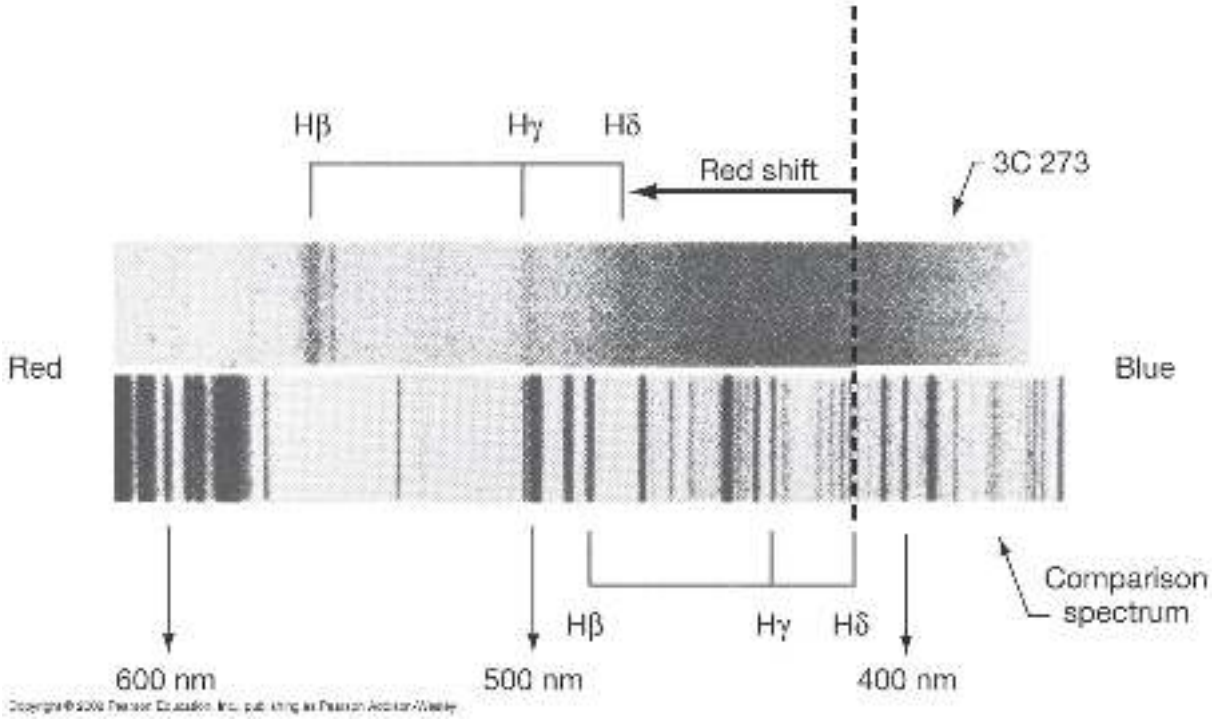

Figure 1.7: Spectrum of 3C 273. Adapted from Hazard *et al.* (1963).

Luminous infrared galaxies (LIRGs): Galaxies with luminosities above 10^{11} $L_{\odot}$. Ultra-luminous Infrared Galaxies (ULIRGs) are those with luminosities higher than 10^{13} $L_{\odot}$. There are even HLIRGs, Hyper-Luminous Infrared Galaxies, and ELIRGs, Extremely Luminous Infrared Galaxies. These galaxies are extremly dusty objects. It is still debated whether the UV radiation is produced purely by star-formation, and some astronomers believe ULIRGs to be powered (at least in part) by active galactic nuclei (AGN).

Wolf-Rayet galaxies (WR galaxies): They are galaxies where a large portion of the bright stars are Wolf-Rayet. The Wolf-Rayet phases is a relatively short-lived phase in the life of massive stars, typically 10% of the total, and as such any galaxy is likely to contain a few of these. However, because the stars are both very luminous and have very distinctive spectral features, it is possible to identify these stars in the spectra of entire galaxies and doing so allows good constraints to be placed on the properties of the starbursts in these galaxies.

1.4.2 Quasi-stellar objects – QSOs

A quasi stellar radio source (contracted to quasar) is a very powerful, luminous, and distant active galactic nuclei. It is an extremely compact region powered by accretion

of material onto a super-massive rotating black hole (SMBH) at the center of a massive galaxy. The suggestion that a black hole (BH) was involved appeared soon after their discovery (Zel'dovich & Novikov, 1964). It turned out that many quasars were not necessarily strong radio sources, so the term quasi-stellar object (QSO) started to be used frequently, as only about 10% of QSOs are radio loud.

The firsts radio surveys (such as 3C or 3rd Cambridge survey) had poor angular resolution, so many sources were unable to be associated with a particular optical source. Hazard *et al.* (1963) used the lunar occultation of 3C 273 to pin down its location, by means of the diffraction pattern produced when the source disappeared behind the moon's limb. Schmidt (1963) was then able to locate the optical counterpart and, in the position indicated by the radio observation, found two sources: a blue star and "a faint wisp or jet". The blue star, however, was not an ordinary star. Its spectrum showed strong broad emission lines that were identified with the Hydrogen Balmer series at a redshift z = 0.16. This discovery prompted Greenstein (1963) to look at the spectrum of another radio source (3C 48) and they found for this case $z = 0.3675$.

The main observational features of a quasar are:

- High luminosity
- Compact angular size
- Continuum emission from the core, ranging from radio to X-rays
- Emission lines
- Sporadic variability of the continuum and spectral line emission

The first key feature that was noticed was the emission line spectrum, which initially puzzled astronomers. The lines are very strong and broad in emission (something only seen in the hottest stars), featuring Hydrogen, Helium, Carbon, and Magnesium, amongst others. As well as broad lines there can be narrow, forbidden lines (the strongest are [O II], [O III], and [N II]).

The second key observation was regarding the optical emission of quasars are its very blue nature. The hottest main sequence stars have U–$B \simeq$ -0.5 mag, while typical AGN have U–$B \simeq$ -1 mag. This proved to be a relatively efficient way to search for quasars. A major example of this type of survey is the Palomar-Green (PG) catalogue (Green *et al.*, 1986), which was the source for the Palomar Bright Quasar Sample (BQS; Schmidt & Green, 1983).

The only model that has been successful in explaining how such amount of energy can be produced in a small region was the accretion of matter onto a black hole. Based on this idea, the basic inferred structure of a quasar would be:

- Central supermassive black hole, with masses reaching up to $10^9 M_\odot$
- Accretion disk surrounding the black hole, which is believed to be the source of the strong continuum.
- Broad line region (BLR). A region extending a few hundred light days from the black hole.
- Narrow line region (NLR). This region is farther and may be associated with the host galaxy.
- Finally, the other key feature, particularly in radio-loud quasars, is a jet.

This basic structure of a quasar (or, more generally, of an active galactic nuclei – AGN) has formed the foundation for viewing angle unification schemes. Their essence is that they explain the observed properties of different types of AGN through the variation of the line of sight angle to the system.

Because quasars are so distant and luminous, it has been difficult to study the host galaxies which contain them. Many quasar host galaxies are interacting or merging systems, as well as normal elliptical or spirals. It has been found that radio loud quasars tend to be found in elliptical and interacting galaxies, and radio quiet seem to be present in both elliptical and spiral galaxies (e.g., Wolf & Sheinis, 2008).

Nowadays, the most luminous quasar known ($4.2 \times 10^{13} L_\odot$) is SDSS J0100+2802 (Wu *et al.*, 2015), with a redshift of 6.30. The most distant QSOs is ULAS J1120+0641 (Mortlock *et al.*, 2011), at z=7.085.

In this thesis we will use QSOs as back illuminating sources to study intervening absorbers (see Chapter 2 for an introduction on the methods for doing this).

1.5 The most luminous transient sources

Some of the most luminous objects in the Universe are of transient nature, where a large quantity of energy is rapidly released to power the emission of an enormous amount of photons during a brief period of time. Some examples of such objects can be:

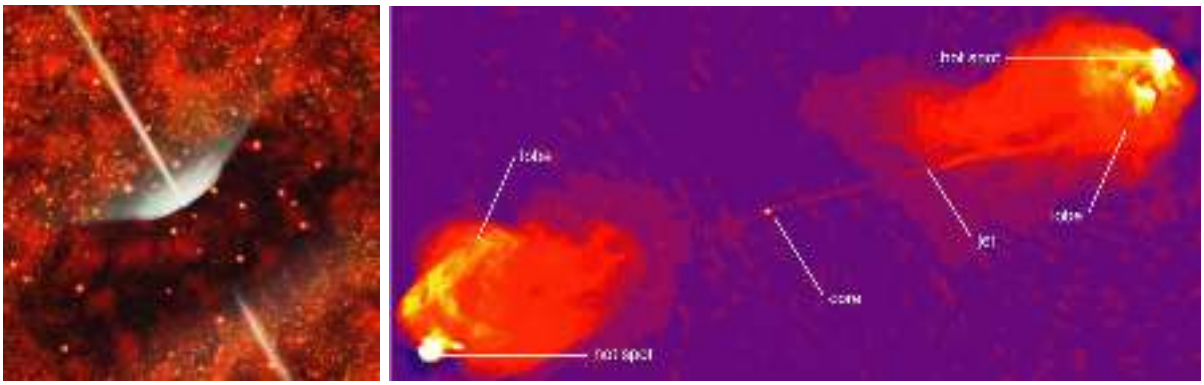

Figure 1.8: Artistic representation and radio image of a quasar. *Credit*: Pearson Education, publishing as Addison Wesley.

X-ray Binaries are binary systems which can be very luminous in X-rays. It is thought that the high energy radiation is produced by matter falling from one component (typically a MS star) onto a compact object, which can be a white dwarf, an neutron star or a black hole (Salpeter, 1964). There are hundreds of these sources in our galaxy, with $L_X \sim 10^{34}$ - 10^{38} erg s^{-1}, and they can also be detected in other galaxies.

Soft gamma repeaters (SGRs) are astronomical objects which emit dramatic but very brief bursts (typically a fraction of a second) of gamma-rays and X-rays at irregular intervals. SGR 0525-66 (PSR B0525-66) is was the first SGR ever detected, located in the Large Magellanic Cloud (Cline *et al.*, 1982, nowadays the only known located outside our galaxy). These phenomena has been interpreted as due to magnetars (Duncan & Thompson, 1992), a type of neutron star with extremely powerful magnetic fields. Kouveliotou *et al.* (1998) firmly established this association.

Supernovae (SNe) are stellar explosions that radiate as much energy as the Sun or any ordinary star is expected to emit over its entire life span, before fading from view over several weeks or months. The extremely luminous burst of radiation expels much of the star's material at a velocity of up to 30,000 km s^{-1}, driving a shock wave into the surrounding interstellar medium. This shock wave sweeps up an expanding shell of gas and dust called a supernova remnant. Their luminosity can be up to 10^{10} $L_\odot$. Supernovae can be triggered either by the sudden re-ignition of nuclear fusion in a degenerate star, or by the gravitational collapse of the core of a massive star.

Gamma-ray bursts (GRBs) are the most luminous objects in the γ wavelength range that we have ever detected in our Universe. In a few tens of seconds a GRB can become, in visible light, one million times brighter than the galaxy that contains it.

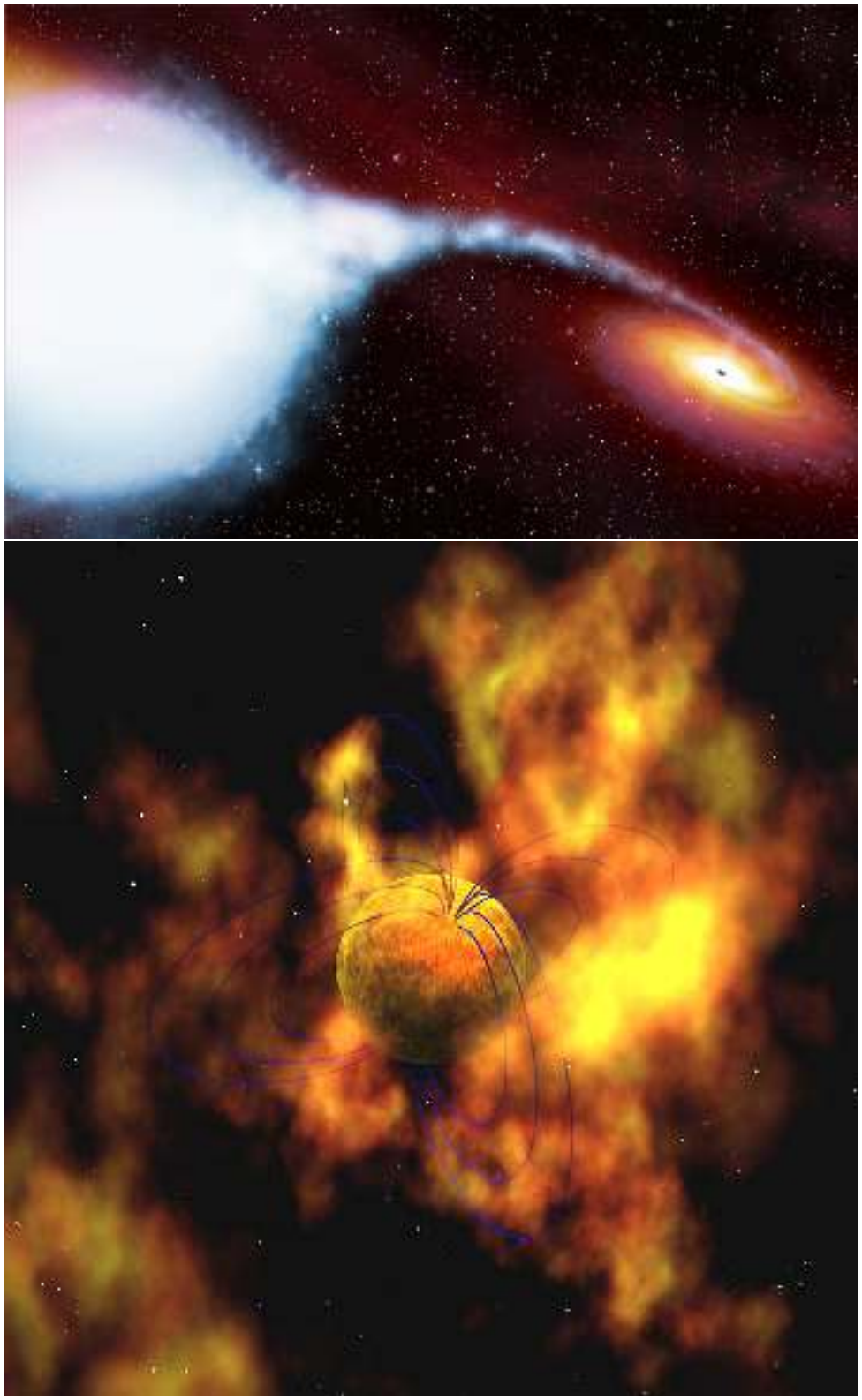

Figure 1.9: *Top:* An artist's illustration of material being gravitationally stripped off a blue supergiant variable star designated HDE 226868 onto a black hole known as Cygnus X-1 *Credit*: David A. Hardy. *Bottom:* Astronomers think soft gamma-ray repeaters are magnetars – neutron stars with a super-strong magnetic field (blue arcs in this artist's concept). *Credit*: NASA/GSFC Conceptual Image Lab.

After this, its luminosity decays rapidly and can become undetectable in just a few hours or days. In gamma-rays their emission is even more dramatic, becoming for a few seconds brighter than the rest of the Universe combined. GRBs can be 10 000 more luminous than the most luminous QSOs and a million times more luminous than the brightest SNe. Within this Thesis we will pay special attention to the study of these objects (see Chapter 3 for an introduction on GRBs) and their use (in parallel to QSOs) to illuminate the most remote corners of the Universe (see the next Chapter).

Chapter 2

The Universe in absorption

"Eventually, we reach the utmost limits of our telescopes. There, we measure shadows and search among ghostly errors of measurement for landmarks that are scarcely more substantial."

— Edwin P. Hubble, *The Realm of the Nebulae, 1936*

Traditionally, the study of the remote Universe has been performed through the observation of luminous objects, as they are easier to detect with our telescopes. However, those objects represent the most extreme environments and phenomena, which are not necessarily representative. In this chapter we show how the light emitted from those extraordinarily luminous sources in the remote Universe can be also used to study dark, cold, and calm regions that happen to lie in their sightlines, through spectroscopic studies in absorption.

2.1 Absorption systems

An absorption system is the set of lines at the same redshift, where the redshift is defined as

$$1 + z = \frac{\lambda_{obs}}{\lambda_{rest}} \tag{2.1}$$

that come from the same absorber, and that are imprinted on the spectrum of a back-illuminating source. Lines come from atom and/or molecule transitions, depending on the chemical composition of the absorption system. These systems can be often decomposed in several velocity components/subsystems, that are the result of the dynamics of the cloud and/or different clouds that are distant enough to be resolved. Figure 2.1 shows the process that forms an absorption spectrum.

In Chapter 1 we presented the most luminous sources known in the Universe, from which QSOs and GRBs are the best candidates for being used as cosmic lighthouses. Each of these beacons have their own particularities, advantages, and problems for their application in the study of their host galaxies and intervening systems.

On the one hand, quasars shine in a roughly constant way. This means that the surrounding medium is highly ionized and near the equilibrium in a Strömgrem sphere that can extend outside the host galaxy. This fact has to be taken into account in host and IGM/CGM studies, but it greatly simplifies their observations and the construction of unbiased samples to investigate statistically the physical properties of the large-scale Universe.

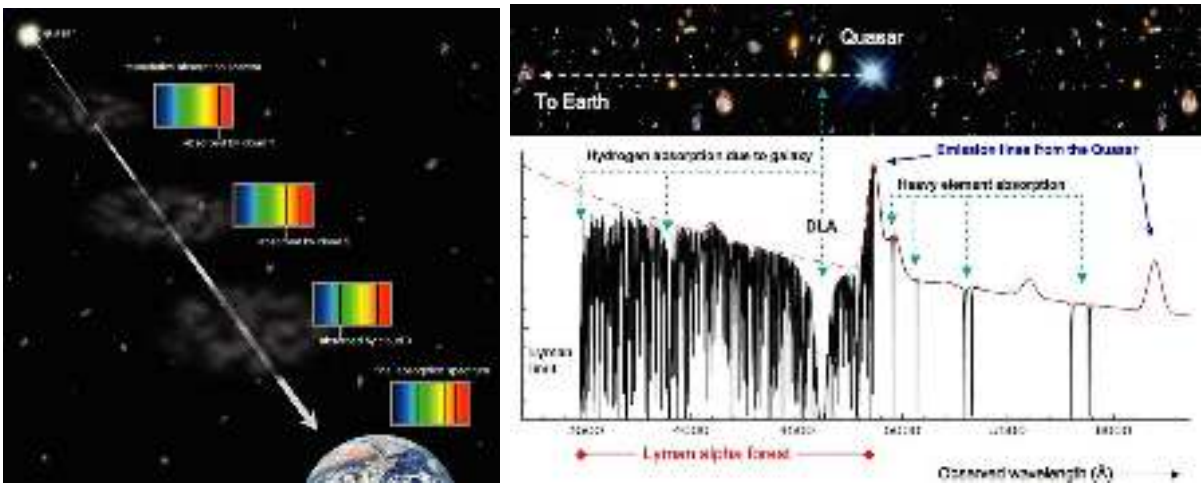

Figure 2.1: Process that forms absorption lines along the emission of a QSO. *Credit*: John Webb (left) and Pearson Education, publishing as Addison Wesley (right).

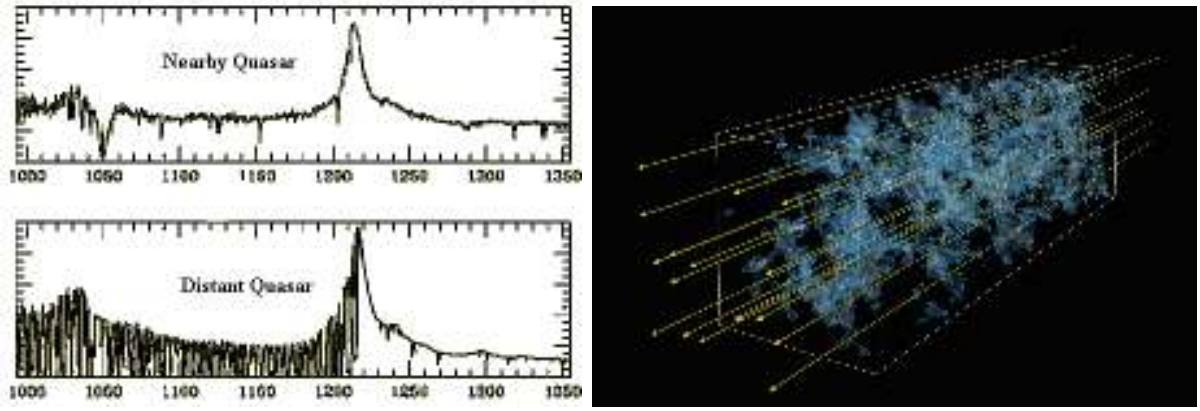

Figure 2.2: *Left*: The Lyman Alpha Forest is shown in the spectrum of the quasar on the bottom. The nearer quasar's light is not absorbed by many intervening gas clouds, so its spectrum doesn't have as many absorption features as the more distant quasar. Based on the image from Bill Keel's slide set. *Right*: Artist's impression illustrating the technique of Lyman-alpha tomography: as light from distant background galaxies (yellow arrows) travel through the Universe towards Earth, they are imprinted by the absorption signatures from hydrogen gas tracing in the foreground cosmic web. By observing a number of background galaxies in a small patch of the sky, astronomers were able to create a 3D map of the cosmic web using a technique similar to medical computer tomography (CT) scans. *Credit*: Khee-Gan Lee (MPIA) and Casey Stark (UC Berkeley).

On the other hand, GRBs shine from star-forming galaxies, tracing the material from the dying star, along its birthplace and the rest of the galaxy, to the Earth. In spite of the immense energy released by this kind of explosions, their short duration implies that their environment is not altered significantly. Consequently, we expect that the abundances measured in spectra are representative of the real conditions of the probed clouds. However, precisely because of their short duration, it is extremely difficult to observe them unless telescopes are prepared to point to them very rapidly (within minutes to hours).

The first absorption lines detected in QSO spectra were towards the line of sight of 3C 191 (Burbidge *et al.*, 1966; Stockton & Lynds, 1966). This discovery opened the door to the extragalactic absorption studies.

Attending to the origin of the absorption lines, quasars absorbers (and analogously for GRBs) can be classified as:

Associated absorption lines (AALs): Systems with $z_{\rm abs} \sim z_{\rm em}$. They are associated to the host galaxy and/or the CGM, and are classified in two types: broad absorption lines (BALs; e.g. Weymann *et al.*, 1979), with broadening of ∼10,000km s^{-1}, and narrow absorption lines (NALs; e.g. D'Odorico *et al.*, 2004), that have lower dispersions.

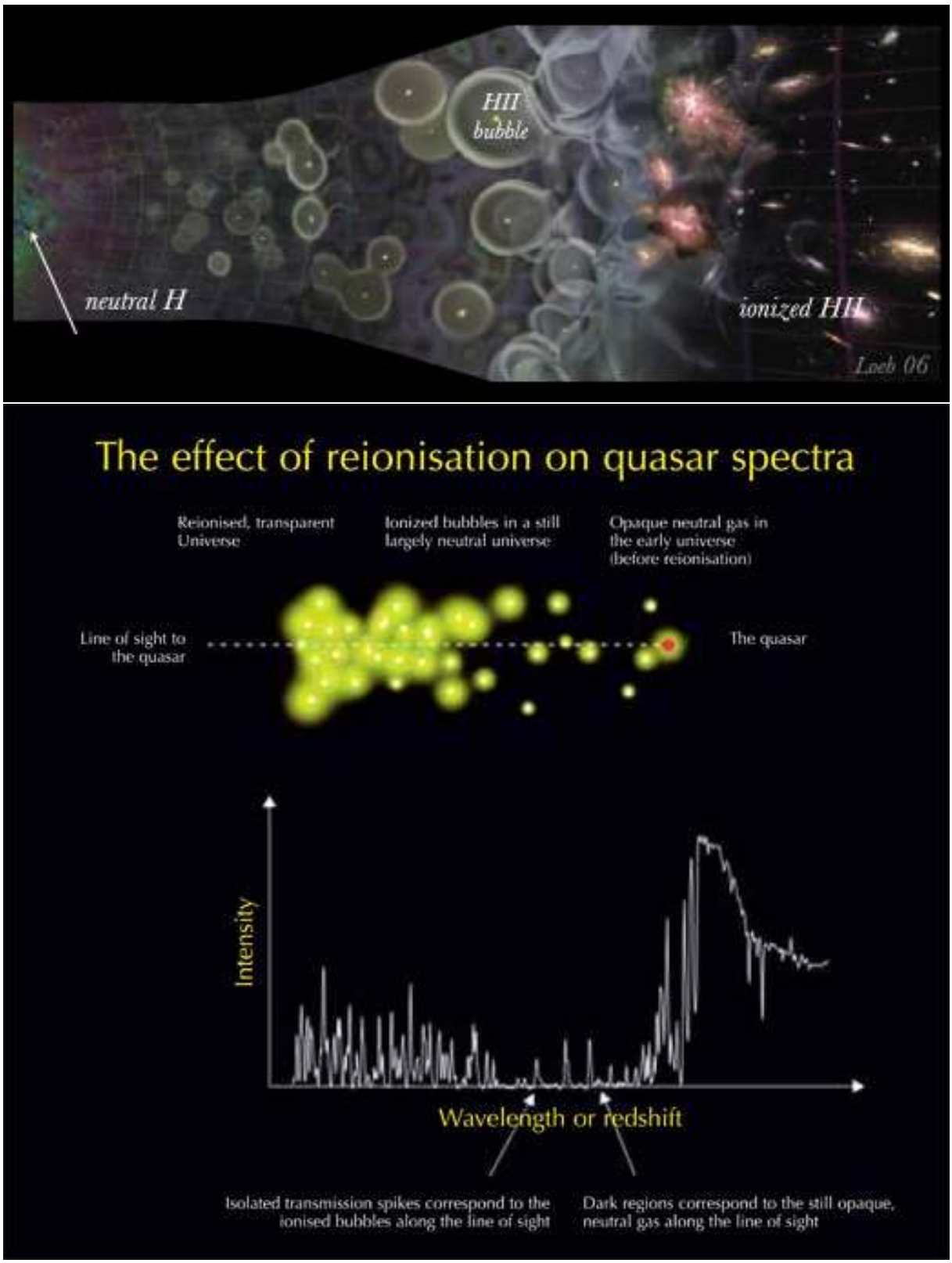

Figure 2.3: Schematic view of how the IGM state transfers into the QSO spectrum.

Intervening absorbers: Systems with $z_{\rm abs} << z_{\rm em}$. They are due to gas distributed along the line of sight to the quasar that is unrelated with it. In order to discard possible systems in the same group or cluster, it is a common practice considering as intervening absorber those with velocities v >5,000km s^{-1} with respect to the QSO emission redshift. Their classification is based on the column density of the H I absorption:

- Lyman forest ($\log N$(H I)<17.0): Lynds (1971) first suggested that the numerous absorption features present in a QSO spectrum (see Fig. 2.1) correspond to the Lyα transition (H Iλ1215) coming from absorption systems between the back-source and the Earth. This interpretation was definitely accepted with the work by Sargent *et al.* (1980). The sum of all these low density absorptions in the spectrum is the so called Lyα-forest. Theoretical simulations pointed out that the forest is formed by overdensities of H I confined by the dark matter along extended filaments (Cen *et al.*, 1994), as represented in Fig 2.2.
- Lyman limit systems (LLSs; $\log N$(H I)>17.0): These absorbers are defined as those that are dense enough so that most of the photons with $h\nu$ >13.6 eV at wavelengths λ <912 Å are captured by the absorber. Technically, these systems have an optical depth $\tau_{912} > 1$. Accordingly quasar spectra will show a discontinuity in their flux at

$$\lambda = (1 + z_{abs}) \times 912\text{Å} \tag{2.2}$$

  that can hide completely the emission under the noise level. As the absorption cross-section (σ) depends on the energy (E_γ) as

$$\sigma = 6.3 \times 10^{-18} (E_\gamma / 13.6eV)^{-3} cm^2 \tag{2.3}$$

  the transparency of the medium to an ionising photon will decrease when its energy becomes higher. It is thought that these systems are clouds in the outlayers of proto-galaxies (Prochaska, 1999).
- subDamped Lyman α systems (subDLAs; 19.0<$\log N$(H I)<20.3): These systems contain a large amount of neutral gas, which could represent ∼20% (e.g., Zafar *et al.*, 2013). They are believed to be the progenitors of massive galaxies which convert their gas mass into stars at an earlier epoch than DLAs (Kulkarni *et al.*, 2010).
- Damped Lyman α systems (DLAs; $\log N$(H I)>20.3): These systems are the main neutral hydrogen reservoirs for star formation processes (Wolfe *et al.*,

1986). They are thought to be proto-galaxies smaller than subDLAs still in the process of converting their neutral gas into stars. Their column density distribution function ($f_{\rm HI}(N, X)$) suggest they are analogous to the nearby luminous disk galaxies.

- The Gunn-Peterson effect: Gunn & Peterson (1965) predicted a feature in the spectra of quasars due to the higher presence of neutral hydrogen in the intergalactic medium at $z{\sim}6$. Further investigations were performed (e.g. Jenkins & Ostriker, 1991; Levshakov & Kegel, 1998; Songaila *et al.*, 1999) until the discovery of the trough towards SDSS J103027.10+052455.0 at z=6.28 (Becker *et al.*, 2001).

As long GRB are produced by very massive stars, their lives are consequently very short, and are good tracers of the star-forming regions in which they are born, and from which they don't have time to exit before they die. The lines of sight from the GRB to the Earth first probe the GRB surrounding medium, and then probably the star-forming region, the disk, and finally the halo of the host galaxy. When the light is outside of the host galaxy, it traces the intervening IGM and eventually other galaxies. All these systems leave their imprint on the spectrum of the afterglow. Therefore, GRB afterglows are useful tools to study the properties of galaxies that form GRBs. Comparing them to samples of star-forming galaxies, both in emission and absorption, we are able to assess questions ranging from specific issues on GRB progenitors and environments, to general cosmology.

2.2 Absorption lines

2.2.1 Voigt profiles

The intensity of an absorption line is given by

$$I(\lambda) = I_0(\lambda)(1 - e^{\tau(\lambda)}) \tag{2.4}$$

where $I_0(\lambda)$ is the intensity of the continuum and $\tau(\lambda)$ the optical depth, which depends on the number of absorbing atoms and their cross section

$$\tau(\lambda) = N\sigma(\lambda); \qquad N = \int \rho dl \tag{2.5}$$

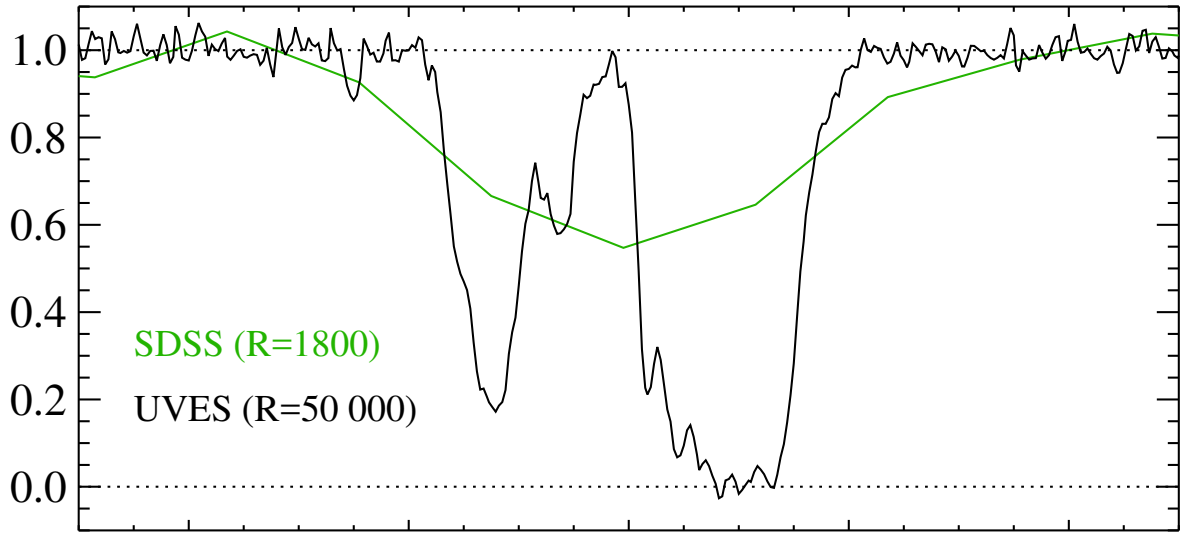

Figure 2.4: Comparison of a portion of a spectrum observed at a resolution R=1,800 and the same one at R=50,000.

The column density (N) is the integral of the number density (ρ) along the line of sight. The cross section for a given transition is assumed to be the convolution of a Gaussian profile, which describes the turbulent and thermal broadening, with a a Lorentzian profile, that accounts for the natural broadening. Using the definition of the Voigt function

$$H(a,u) = \frac{a}{\pi}\int_{-\infty}^{+\infty}\frac{e^{-y^2}}{(u-y)^2+a^2}dy \tag{2.6}$$

the optical depth is given by

$$\tau(\lambda) = 1.498\times10^{-2}\frac{Nf\lambda}{b}H(a,u) \tag{2.7}$$

with

$$\begin{cases} a = \dfrac{\lambda\Gamma}{4\pi b} \\ u = -\frac{c}{b}\left(1+\frac{v}{c}\right) - \frac{\lambda}{\lambda_0} \end{cases} \tag{2.8}$$

where b is the Doppler parameter and f and Γ are atomic parameters. Assuming that the absorption line is given by this Voigt profile, and if the instrumental resolution is high enough, it is possible to determine b and N by fitting the model to the observed spectrum. The importance of the instrumental resolution is showed in Figure 2.4. Observations with low resolution spectrographs have the disadvantage that they hide the velocity structure of the system. This leads to, e.g., the underestimation of the column density of a given

system due to the measurement of an unphysically large b (Prochaska, 2006). For the fitting of intermediate resolution spectra, a Gaussian instrumental spread function is usually assumed, which is then convolved with the Voigt profile.

2.2.2 The apparent optical depth

A very popular way to derive column densities is to use the method proposed by Savage & Sembach (1991) known as the *apparent optical depth* (AOD) method.

$$\log N_a(v) = \int N_a(v)\delta v = \int log\tau_a(v)\delta v - \log(f\lambda) + 14.576 \tag{2.9}$$

This method is commonly applied on high resolution spectra, as if the instrumental resolution is high enough, $\tau_a(v) = \tau(v)$. If features are weak and there is no hidden saturation and/or contamination, they should give the same column density value.

2.2.3 The curve of growth

When the resolution is not enough to use the methods explained before, we can measure the equivalent width (EW) of a line, which value is independent of the instrumental resolution

$$EW_{obs} \equiv \int \frac{I_0(\lambda) - I(\lambda)}{I_0(\lambda)} d\lambda = \int (1 - e^{-\tau(\lambda)}) d\lambda \tag{2.10}$$

Therefore, the EW and (N, b) are given by equations 2.10 and 2.7, and this relation is known as the "curve of grouth" (CoG). We can distinguish three zones therein:

Linear part : When the column density is low enough, the EW only depends on N, and eq. 2.10 is reduced to

$$EW_r = \frac{\pi e^2 \lambda_0}{m_e c^2} N \lambda_0 f \tag{2.11}$$

so

$$N(cm^{-2}) = 1.13 \times 10^{20} \frac{W(\mathring{A})}{\lambda_0^2(\mathring{A}) f} \tag{2.12}$$

Logarithmic part : This regime is characterised by a strong dependence with the Doppler parameter b. Therefore, in this part the CoG is degenerated and eq. 2.10

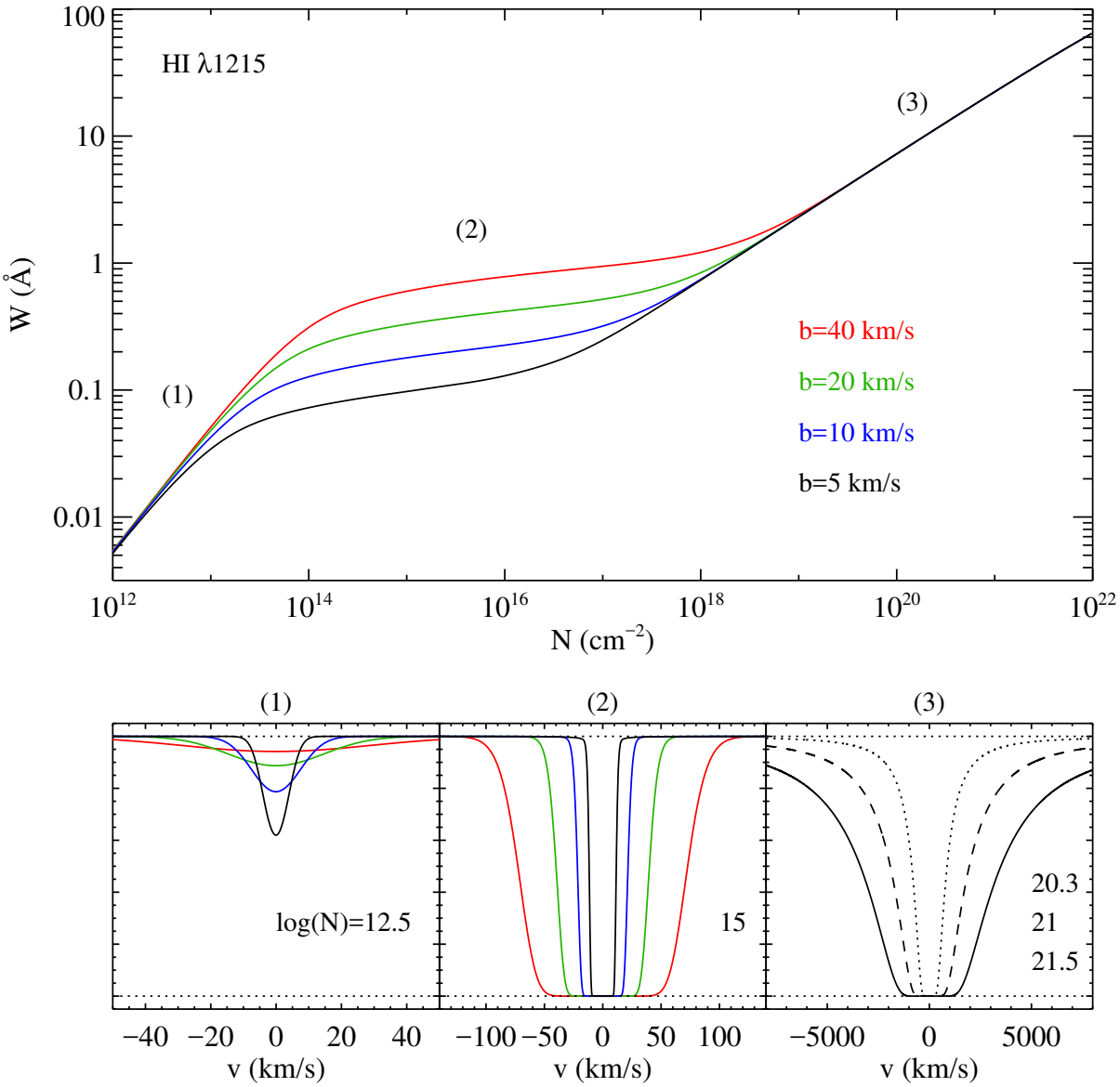

Figure 2.5: CoG for the Lyα line. Each regime is denoted by (1) linear (2) logarithmic and (3) damped.

now is

$$EW_r \sim \frac{2b\lambda_0}{c}\sqrt{\ln\frac{\sqrt{\pi}e^2 N\lambda_0 f}{m_e c b}} \tag{2.13}$$

so $EW_r \propto \sqrt{\ln N}$.

Damped part : When the column density is high enough, b becomes again a non dependent parameter for the line shape, as it is dominated by the Lorentzian component, and the EW is again proportional only to the column density

$$EW_r \sim \frac{\lambda_0^2}{c}\sqrt{\frac{e^2}{m_e c}Nf\Gamma} \tag{2.14}$$

This time $W_r \propto \sqrt{N}$.

2.3 Damped Lyman α systems

The damped Lyman alpha system definition ($\log N(\mathrm{H\,I})$>20.3) comes from historical reasons (Wolfe *et al.*, 1986). This column density limit corresponds to an equivalent width of 10 Å, which is a reasonable limit to identify damping wings from low resolution optical spectra. Moreover, this value also correspond to the limit from 21 cm observations of clouds that are able to form stars. As explained before, stars form from the collapse of molecular hydrogen, so their environment has to act as a shield to ionising photons to allow the processes to occur. Physically, it is more reasonable to fix this limit at $\log N(\mathrm{H\,I})$=19.5, as the gas remains predominantly neutral from this column density (Viegas, 1995).

The first system in absorption was discovered by Beaver *et al.* (1972); Lowrance *et al.* (1972) in the line of sight towards a QSO. Since then, several damped feature identifications were published and finally identified as due to H I (Smith *et al.*, 1979).

Damped Lyman alpha absorbers comprise the neutral gas reservoir for star formation at high redshifts (Nagamine *et al.*, 2004a,b). Stars are likely to descend from cold neutral clouds, which are the predecessors of molecular clouds and the birth sites of stars (Wolfire *et al.*, 2003). Therefore, the study of DLAs provides critical information on the formation and evolution of galaxies.

In the local Universe, neutral hydrogen is easily detected through the 21 cm transition, observed for the first time by Ewen & Purcell (1951). This technique makes possible to estimate the content of neutral gas (Zwaan *et al.*, 2005), but due to instrumental

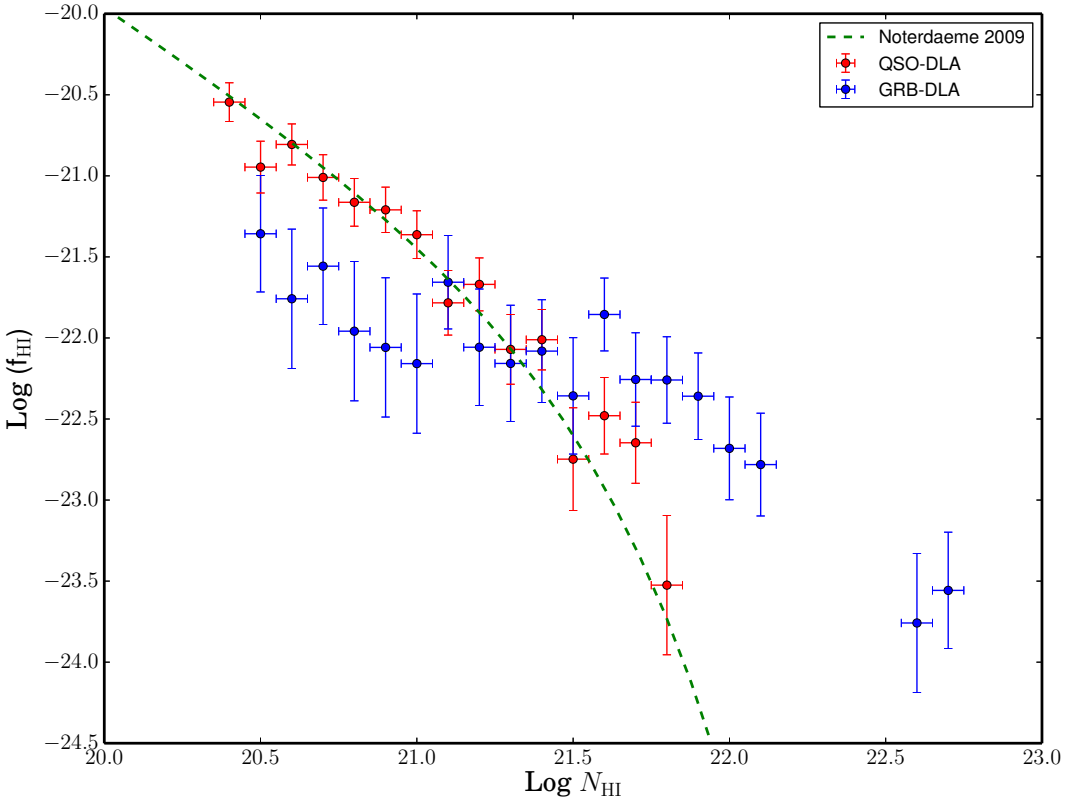

Figure 2.6: Column density distribution for our two DLA samples (QSO in red and GRB in blue). Vertical error bars are derived assuming a Poissonian distribution (95% confidence level). The model by Noterdaeme *et al.* (2009) is overplotted in green (dashed line) . Adapted from Cucchiara *et al.* (2015).

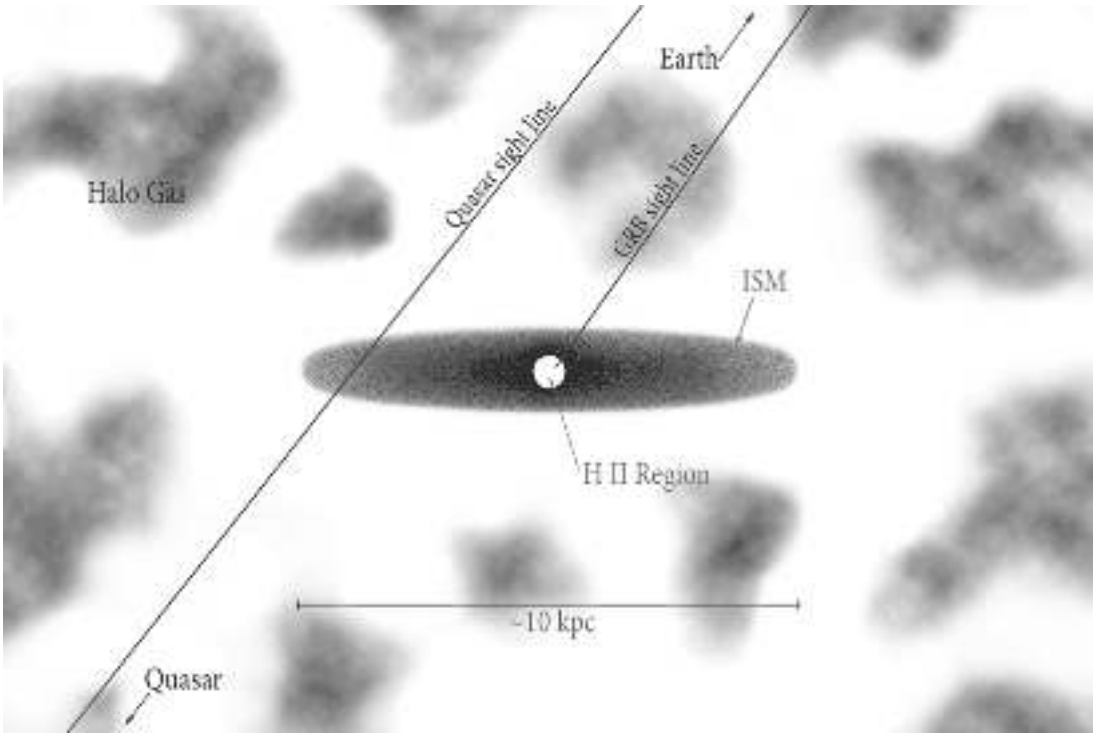

Figure 2.7: Cartoon illustrating the likely differences between QSO-DLA and GRB-DLA sight lines. Adapted from Prochaska *et al.* (2008a).

limitations, it is challenging to measure it at $z \gtrsim 0.2$ (Lah *et al.*, 2007).

As Earth's atmosphere is opaque to UV radiation, it is only possible to detect DLAs in absorption at redshifts greater than $\sim$1.6, when the Lyman alpha feature becomes observable from ground. For intermediate measurements it is therefore necessary to perform observations from space. A survey of these intermediate redshift DLAs observed from space was done for the first time by (Rao & Turnshek, 2000).

The first optical DLA survey was performed by Wolfe *et al.* (1986), and was motivated to investigate disk galaxies at high redshift, as column densities observed in radio are similar. The first estimation of the neutral gas content of the Universe ($\Omega_{\rm HI}^{\rm DLA}$) was later performed by (Lanzetta *et al.*, 1991). Since then, many DLA surveys were performed and soon researchers started to realise the statistical and systematic uncertainties that this technique presents (for more details see Part **??**, Chapter 1).

When using intervening DLAs to derive cosmological properties, apart from systematics and statistical effects we have also to take into account physical mechanisms that potentially could bias the results. Historically, the most discussed effect was the dust extinction. In surveys such as SDSS, QSOs are selected by color indices in the optical. Due to intrinsic reddening produced by dust they can show unusually red colors and can even be undetected due to extinction. Moreover, the variety of QSO continua make diffi-

cult to unambiguously determine a spectral index specific for QSOs. Pettini *et al.* (1999) pointed out that DLA samples could be biased towards low metallicity absorbers, which are less extinguished and hence more easily detected. However, the DLA search from the CORALS survey, built up with radio-selected QSOs not attending to their optical magnitude, showed that the H I content measured in optically-selected magnitude-limited samples can be underestimated at most by a factor 2 at a confidence level of $\sim 1\sigma$. Another effect that could bias a DLA survey is the gravitational lensing. Prochaska *et al.* (2005) quantified this effect to be 40 ± 20 %, but Ménard *et al.* (2008) did not find any magnification after studying a sample of almost 7000 strong Mg II absorbers.

Unsurprisingly, the most prominent feature seen in GRB afterglow spectra is the Lyα line of neutral Hydrogen (H Iλ1216). In the GRB case, it is possible to perform more accurate measurements than in QSO sigh-lines due to the clean red damping wing consequence of the nearness of the absorbing cloud to the GRB progenitor (there is no Lyα line from the IGM at the redder part of the host galaxy Lyα absorption).

Despite the fact that the current GRB-DLA sample is significantly smaller than the QSO-DLA one, there is a clear overlap of both QSO and GRB DLA distributions around $\log N(\mathrm{H\,I})$=21.5, showing GRB sight-lines a much larger number of dense systems compared with the QSO-DLA sample (see also Noterdaeme *et al.*, 2015b). As QSO-DLAs are intervening systems, we expect to find differences between QSO-DLA and GRB-DLA samples due to selection effects (see Fig. 2.7). The detection rate of absorbers in intervening QSO-DLA surveys depends on the product of the number of these systems at a given redshift and their cross section. Accounting for the cross section, it is expected that QSO-DLAs trace predominantly gas from the outer regions of the ISM. In contrast, GRB-DLA sight-lines are expected to start from the core of H II regions created by massive stars, and then probe from the inner to the outer regions of the ISM. Therefore, it is important to establish whether observed discrepancies are to these selection effects or both samples are drawn from distinct populations.

Recently, a DLA system was found towards a galaxy sightline (gal-DLA; Mawatari *et al.*, 2016, see Figure 2.8). The galaxies of these absorbers could be better studied in emission, and so this finding could open a new and interesting window in the field.

2.4 Metal abundances

The relative abundances of *metals* (in astronomy, elements heavier than He) in the ISM are related with the different nucleosynthesis processes in stars and in the collapse of massive stars. Metal enrichment of a galaxy is related to the stellar mass and their life

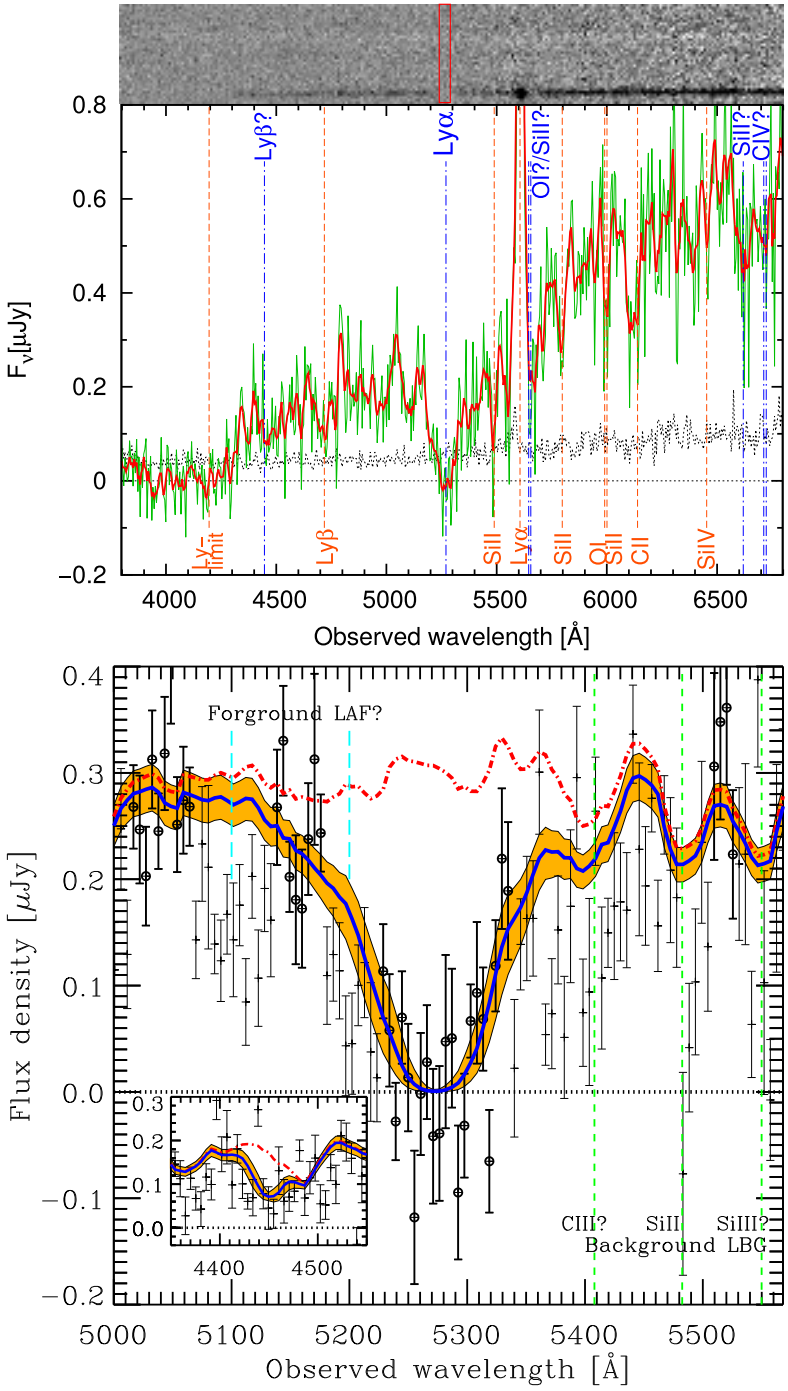

Figure 2.8: *Top panel*: Two-dimensional (top) and one-dimensional (bottom) spectra of the LBG in which the DLA can be seen. In the bottom panel, the thick red and thin green lines are the spectrum with and without a 5 pixel box-car smoothing, respectively. The vertical dot–dashed blue lines show absorption by the gal-DLA, while the dashed orange lines correspond to the emission/absorption features of the background LBG itself. *Bottom panel*: Example of the Voigt function fit for the gal-DLA spectrum. The best-fit spectrum and the acceptable fit within the 1σ confidence level is shown by the blue bold line and orange shading, respectively. The small panel embedded in the bottom left is the same but around the possible Lyβ absorption from the gal-DLA, where no flux point is used for the fit. Adapted from Mawatari *et al.* (2016)

Table 2.1: Ionisation potentials of the most frequently observed species.

Element	X	Potential I	Potential II	$\log(X/H)_\odot + 12$	Dominant ion
Hydrogen	H	13.598	–	12.00	H I
Carbon	C	11.260	24.383	8.52	C II
Nitrogen	N	14.534	29.601	7.95	N I
Oxygen	O	13.618	35.121	8.73	O I
Magnesium	Mg	7.646	15.035	7.58	Mg II
Aluminium	Al	5.986	18.829	6.49	Al II
Silicon	Si	8.152	16.346	7.56	Si II
Sulphur	S	10.360	23.338	7.20	S II
Chrome	Cr	6.767	16.486	5.69	Cr II
Iron	Fe	7.902	16.188	7.50	Fe II
Nickel	Ni	7.640	18.169	6.25	Ni II
Zinc	Zn	9.394	17.964	4.67	Zn II

cycles, so abundance patterns depend also on the ejection and mixing mechanisms. Stars from second and later starbursts in a given galaxy are produced in a ISM previously enriched by stellar winds and supernovae. Stellar winds in the form of planetary nebula mainly release He, C, N, and O, while supernovae are the responsible of the production of heavier elements. The so-called α-elements (O, Ne, Mg, Si, S, Ar, Ca and Ti) are produced by α-capture (He) during silicon fusion taking place in massive stars before the type II SN explosion. Iron-peak elements like V, Cr, Mn, Fe, Co, Zn, and Ni are produced mostly in SN Ia which come from less massive stars.

Usually, we give the abundance of an element X relative to another Y as

$$[X/Y] \equiv \log(X/Y)_{obs} - \log(X/Y)_\odot \tag{2.15}$$

where $(X/Y)_{obs}$ is the observed abundance of the elements X and Y, and $(X/Y)_\odot$ is the Solar abundance of each specie. We refer to *metallicities* when Y $\equiv$ H ([X/H]).

In DLAs, the radiation above 13.6 eV is absorbed by the neutral Hydrogen cloud, so there in the ionisation state of metals is mainly driven by this limit (see Table 2.1). Therefore, it is expected that we observe metals in the first ionisation state. As O I has a similar ionisation potential, this ion is the ideal tracer of H I.

GRB-DLAs generally show a higher α/Fe ratio than QSO-DLAs (Prochaska *et al.*, 2007), which can be due either to a nucleosynthetic origin or by dust depletion differences. The first possibility seems likely as GRBs are expected to occur in actively star forming galaxies, and the timescales to enrich the ISM significantly with Fe produced in SN Ia,

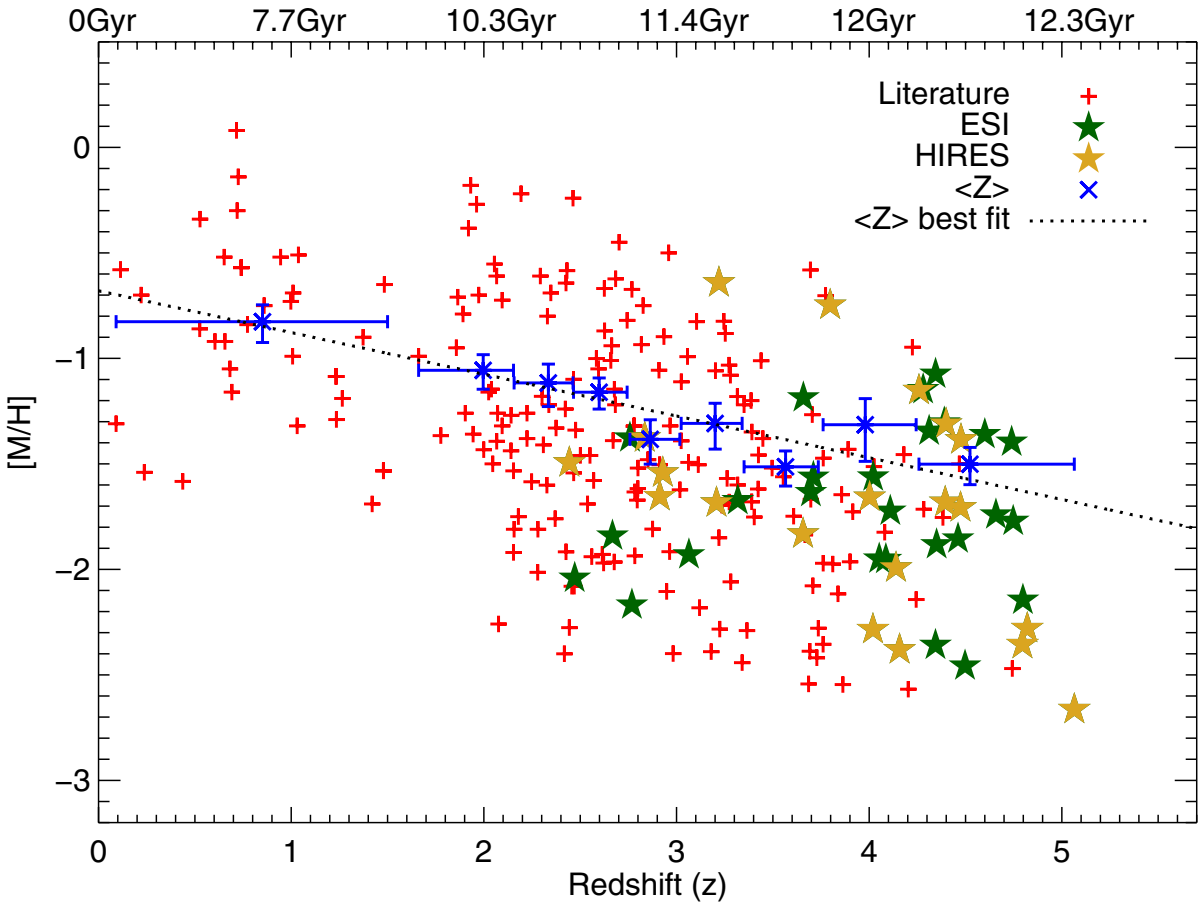

Figure 2.9: DLA metal abundance, [X/H], versus redshift. Red plus signs are from the literature. The metallicities from ESI are green stars and those from HIRES are gold stars. The nine blue crosses with error bars show the average cosmic metallicity, $< Z >$, and the black straight line is a linear fit to them. Adapted from Rafelski *et al.* (2012).

might be too short for galaxies at high redshifts.

2.5 Metallicity

A central aspect of the history of the Universe is the formation and evolution of galaxies, and their gradual build-up of metallicity (Pei & Fall, 1995). Ideally, metallicity is best measured by using the O I abundance (as it has similar cross section than H I), but the transition that we can use is often saturated, so it is not straightforward to break the (b, N) degeneracy and therefore to measure accurately the abundance. Consequently, other elements are used, though they should be analysed with care (especial attention should be payed to dust depletion; see section 2.5.3).

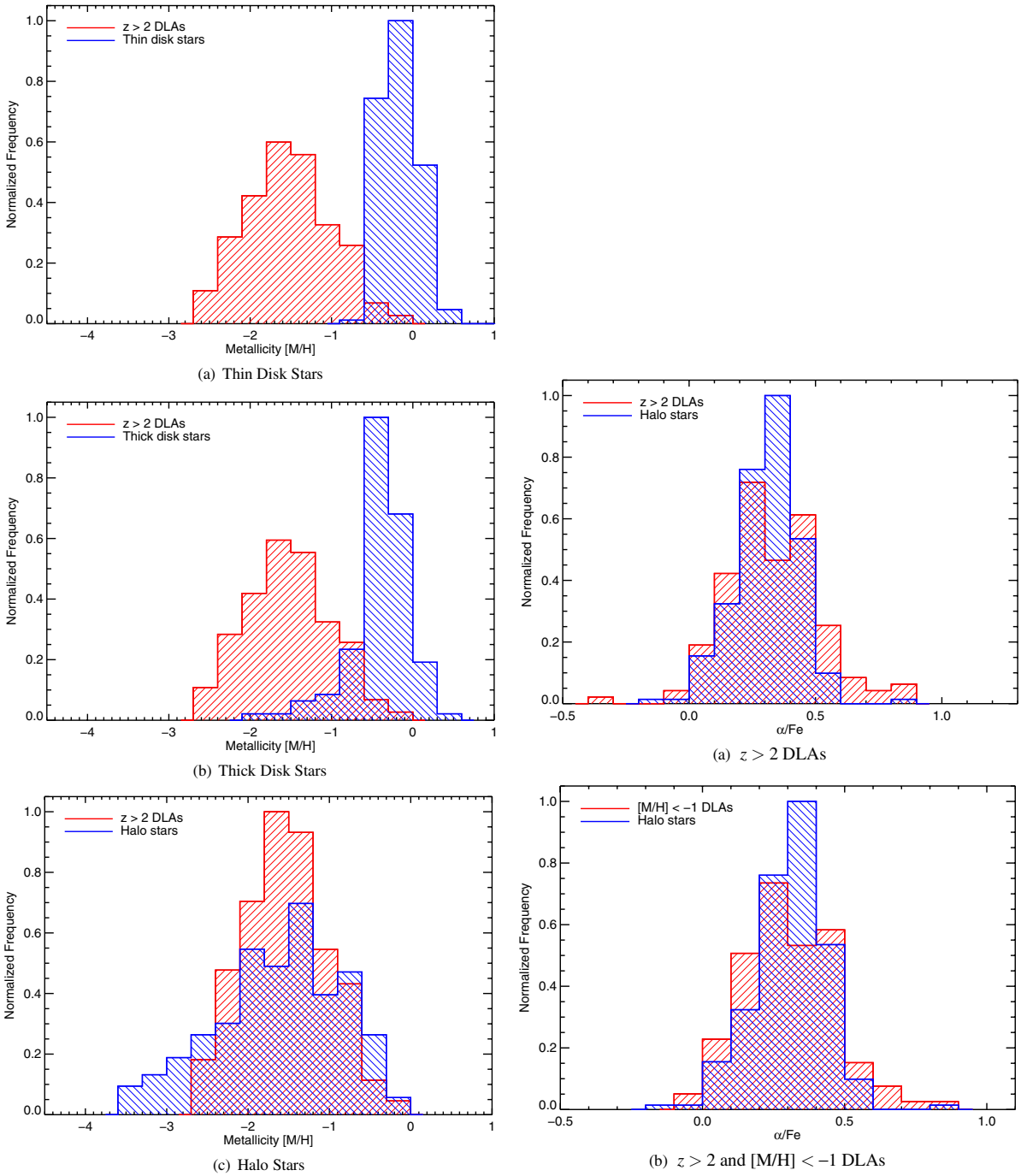

(a) Thin Disk Stars

(b) Thick Disk Stars

(c) Halo Stars

(a) $z > 2$ DLAs

(b) $z > 2$ and [M/H] < -1 DLAs

Figure 2.10: *Left*: Histograms comparing abundances of 161 DLAs at $z > 2$ with (a) 201 thin disk stars, (b) 109 thick disk stars, and (c) 207 halo stars. The red left shaded region represents the DLAs and the blue right shaded region represents the thin disk, thick disk, and halo stars. *Right*: Histogram comparing α/Fe ratios of 207 halo stars with (a) 138 DLAs at $z > 2$ and (b) 115 DLAs at $z > 2$ with [X/H] $<$ -1. Adapted from Rafelski *et al.* (2012).

Rafelski *et al.* (2012, 2014) presented a recent analysis of a high resolution QSO-DLA sample. They considered various elements to compute the metallicity and found this is the best order: O, S, Si, Zn, and Fe. They also showed that the metallicity obtained by Fe has to be corrected by a factor 0.27 ± 0.02 as consequence of the α enhancement in DLAs.

Concerning the cosmic evolution of the metal content of the Universe from QSO-DLAs, they improved the previous detection of evolution finding that

$$< Z >= (-0.22 \pm 0.03)z - (0.65 \pm 0.09) \tag{2.16}$$

out to z$\sim$4.7 with a confidence of 6.7σ. For $z\sim5$ they claim that there is a rapid decline, but due to the low counts and the large dispersions ($\sim$0.5 dex) observed at lower redshifts, this claim is still highly debated. Moreover, they still find a metallicity "floor" at [X/H]$\sim$-3 out to $z\sim5$, consistent with previous lower redshifts studies.

Finally, Rafelski *et al.* (2012) realised that the metallicity distribution and the α/Fe ratios of $z > 2$ DLAs are consistent to be drawn from the same population as halo stars (see Figure 2.10). It is therefore possible that the halo stars in our Galaxy formed from DLA gas.

The metallicity of the intervening gas towards a GRB probes instantaneous star-formation galaxies able to produce GRBs. The data collected to date show that GRBs explode generally in sub-solar metallicity environments, but are generally already metal-enriched. However, it remains unclear whether there is an evolution or not of the metallicity as a function of redshift (e.g., Cucchiara *et al.*, 2015; Fynbo *et al.*, 2006; Prochaska *et al.*, 2007; Savaglio *et al.*, 2006; Schady *et al.*, 2011; Thöne *et al.*, 2013). For QSO-DLAs, however, an anti-correlation with redshift is more evident (Rafelski *et al.*, 2012, 2014). GRB-DLAs are clearly more metal enriched. As GRBs are expected to occur in denser parts of the host galaxy, the mass-metallicity relation would give a straightforward explanation (e.g., Arabsalmani *et al.*, 2015; Fynbo *et al.*, 2008; Møller *et al.*, 2013).

On the other side, QSO-subDLAs show higher metallicities than QSO-DLAs (Péroux *et al.*, 2007; Quiret *et al.*, 2016). This clearly indicates that we can not assume that N(H I) correlates with the path length through the galaxy, and this fact could be due to subDLAs probing more massive galaxies or due to dust effects.

One possible way to explain the different metallicity distributions while assuming that QSO and GRB DLAs are drawn from the same population, is by selection effects. Following Fynbo *et al.* (2008, and references therein), GRB-DLAs are selected by the SFR ($\propto L$), while QSO-DLAs by the projected area ($\propto R^2$; Fynbo *et al.*, 1999). As $R^2 \propto L^{2t}$,

for $t = 0.5$ we would have no shift for both populations. It was found that $t = 0.4$ for $z = 0$ (Fynbo *et al.*, 1999), but it is probably lower at higher redshifts.

2.5.1 Kinematics

Absorption profiles that are not saturated provide valuable information on the kinematics of the gas (Weisheit, 1978). By using high resolution spectra, Wolfe *et al.* (1994) showed that absorption profiles of DLAs are consistent with what is expected from a rotating disk. Prochaska & Wolfe (1997) defined Δv_{90}, which is the velocity interval that contains 90% of the area under the apparent optical depth spectrum, and found that absorption profiles are systematically asymmetric and that the distribution of Δv_{90} ranges from 20 to 200 km s^{-1}. Comparing their models to the observations, they rejected the idea of DLAs being halo clouds spherically distributed, and reinforced the rapidly rotating disk hypothesis. However, Haehnelt *et al.* (1998); Ledoux *et al.* (1998) pointed out that the observed velocity dispersions can be explained by a mixture of random movements, rotation and in/out fall in different subsystems, so DLAs can be galactic building blocks consistent with standard hierarchical structure formation scenario as well (Kauffmann, 1996). Prochaska & Wolfe (2001) produced smoothed particle hydrodynamic (SPH) simulations and ruled out at high confidence that their results could explain DLA observations. Instead, these simulations support better a cold dark matter scenario (e.g., Pontzen *et al.*, 2008).

Most GRB afterglow spectra show a relatively small velocity spread (but larger than QSOs) of a few hundred km s^{-1}. Recently, Arabsalmani *et al.* (2015) analysed a sample of 16 GRBs to compare velocity dispersions, as well as the mass-metallicity relation and the gravitational well depth of their hosts, to QSO-DLA galaxies. In Figure 2.13 we can see that the observed metallicities as a function of Δv_{90} are only slightly different, showing that the clouds they probe have similar dynamical and chemical properties, and could consequently come from the same population of galaxies. Furthermore, when Arabsalmani *et al.* (2015) account for the redshift evolution the agreement is excellent. However, if other reasonable effects are taken into account, the picture turns again puzzled.

Selection effects of QSO and GRB DLA samples could explain three different effects:

- The well known differences in the H I content between QSO and GRB DLAs
- Discrepancies in the measured metallicities if there are gradients in galaxies
- Distinct paths through the gravitational well of the galaxy

The metallicity gradient was determined to be -0.022 ± 0.004 dex kpc^{-1} (Christensen

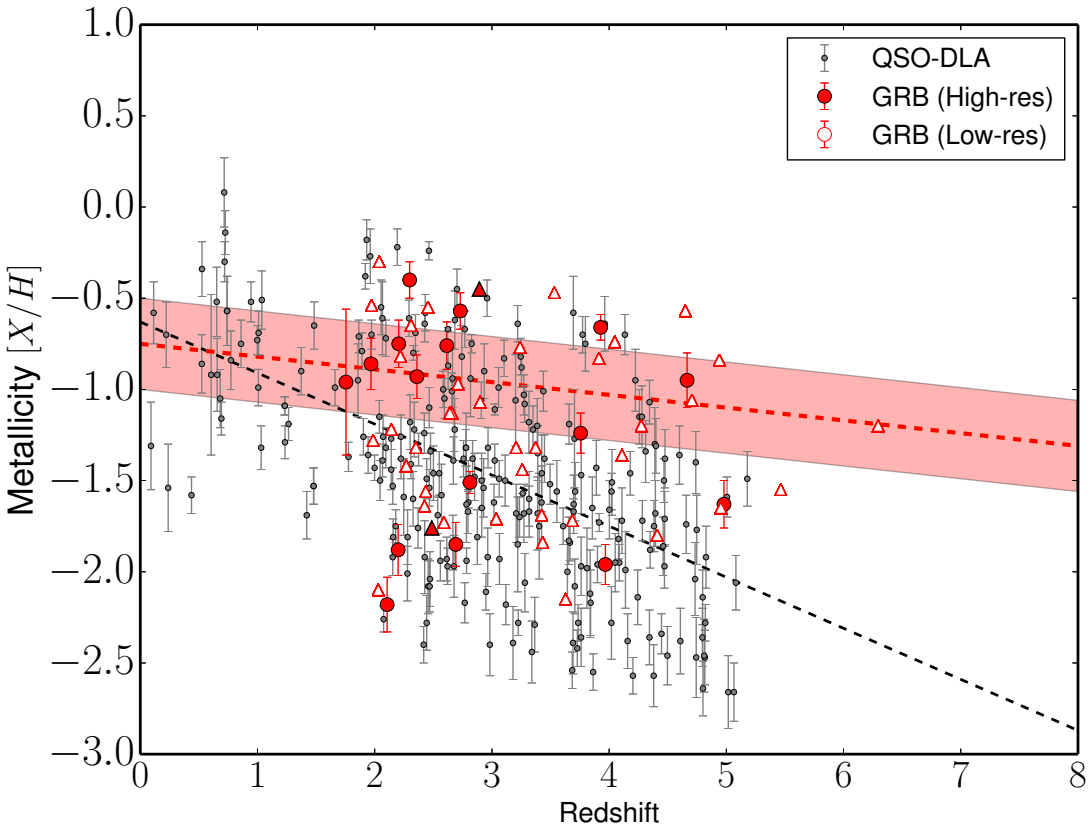

Figure 2.11: Metallicity evolution with redshift for the GRB (red) and the QSO (grey) samples. Lower limits are indicated by upward triangles, while filled/open symbols indicate if these values come from high/low resolving power instruments. A linear regression fit of the GRB-DLA data using the Schmitt survival analysis method is performed, which keeps into account the censoring within the dataset (red dashed line). The shaded area represents the 1σ error in the fitting parameters obtained using 500 bootstrap iterations. A linear fit of the QSO-DLAs metallicity is marked by the dashed black line (see text for details). Adapted from Cucchiara *et al.* (2015).

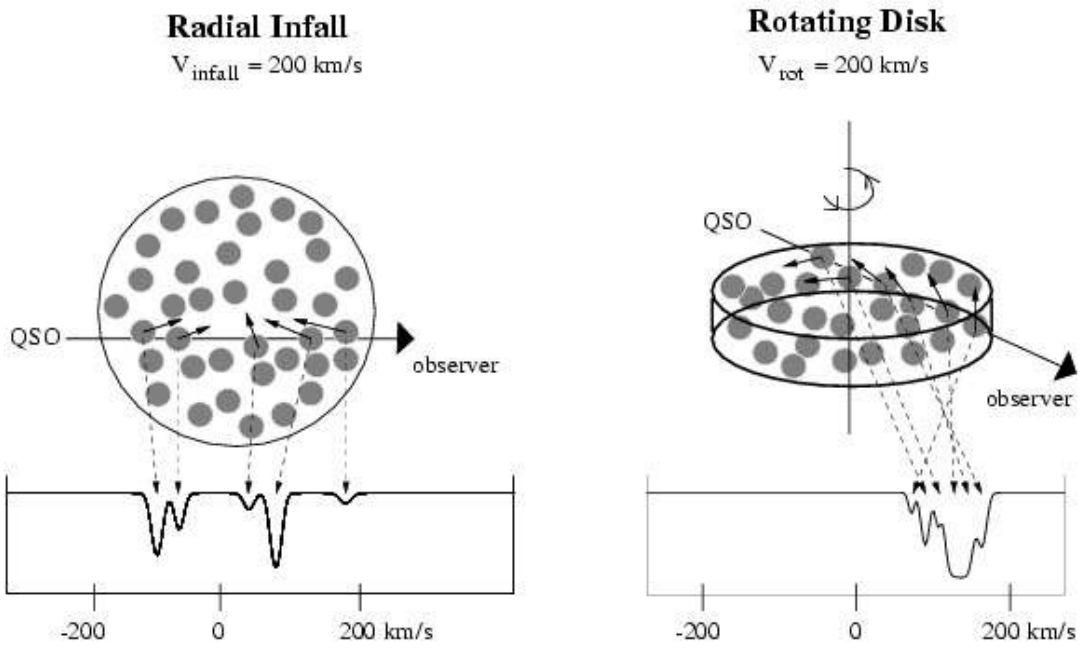

Figure 2.12: Line profiles as they would be observed against a background QSO if the velocity components would trace radial infall (*left*) or if they would come from an intersecting rotating disk (*right*).

et al., 2014). Correcting the GRB sample with the measured impact parameter (or assuming a mean value of 2.3 kpc), and assuming 2.7 kpc as the mean value for the mostly unknown QSO-DLA impact parameters, it is obtained this time discrepant distributions (see Figure 2.13. However, this shift could be explained by the different paths through the galaxy's gravitational well if the Δv_{90} is two times larger in GRB-DLAs. Accurate hydrodynamic simulations are needed to confirm this scenario (Arabsalmani *et al.*, 2015). Therefore, we are still far from the understanding of the actual scenario from which the current observations are taken.

2.5.2 Extinction

When we look in different directions of the sky, we see dark patches in the distribution of stars. These are not gaps where there are no stars, but instead are due to obscuration by interstellar dust clouds, such as the Horse-head nebula (NGC 2024) in our Galaxy. This dust does not come only from thick clouds, but also spreads diffusely throughout interstellar space.

Dust extinction is the absorption and scattering of light along the line of sight of some source. The degree of reddening can be determined by measuring the colour index

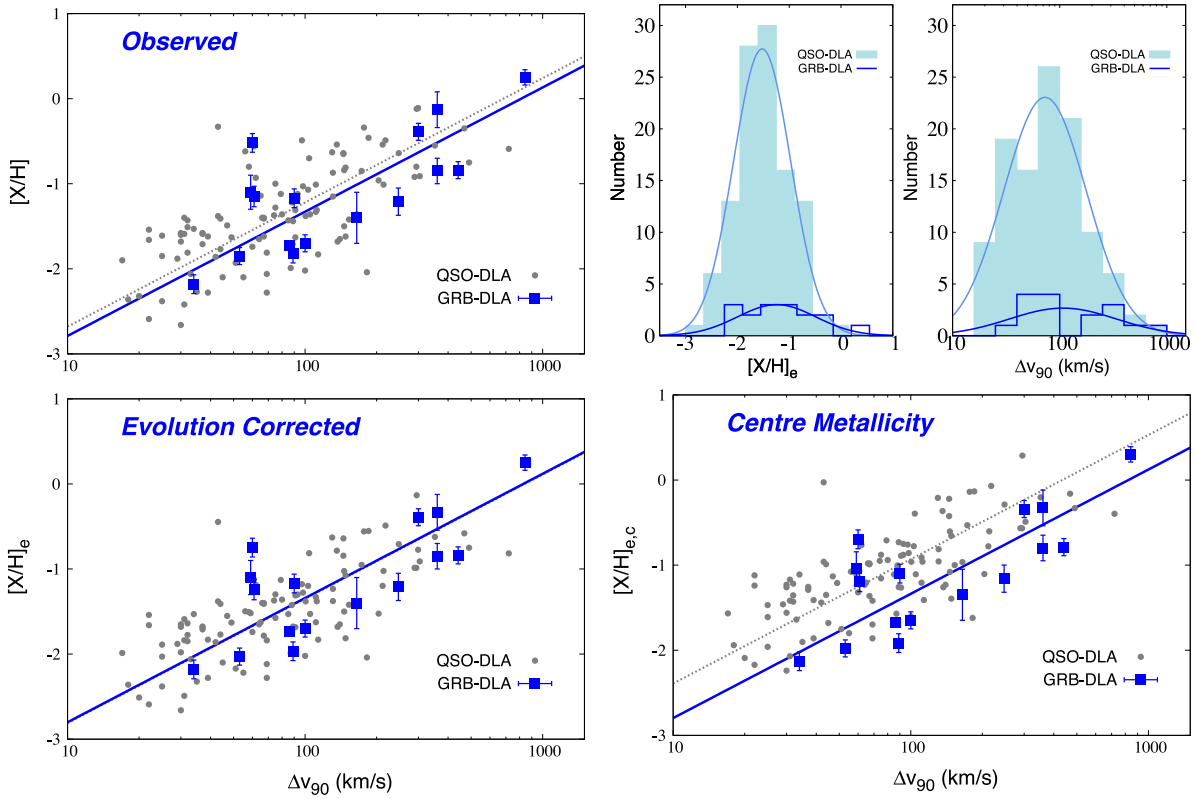

Figure 2.13: *Top left*: Observed metallicity versus velocity width for QSO-DLAs (small dots) and GRB-DLAs (blue squares). *Bottom left*: Values corrected for the redshift evolution determined for QSO-DLAs. *Bottom right*: Values corrected also for metallicity gradients. *Top right*: Histograms of metallicity and velocity widths. The light blue shades refers to QSO-DLAS and solid dark blue lines to the sample of 16 GRB-DLAs. Adapted from Arabsalmani *et al.* (2015).

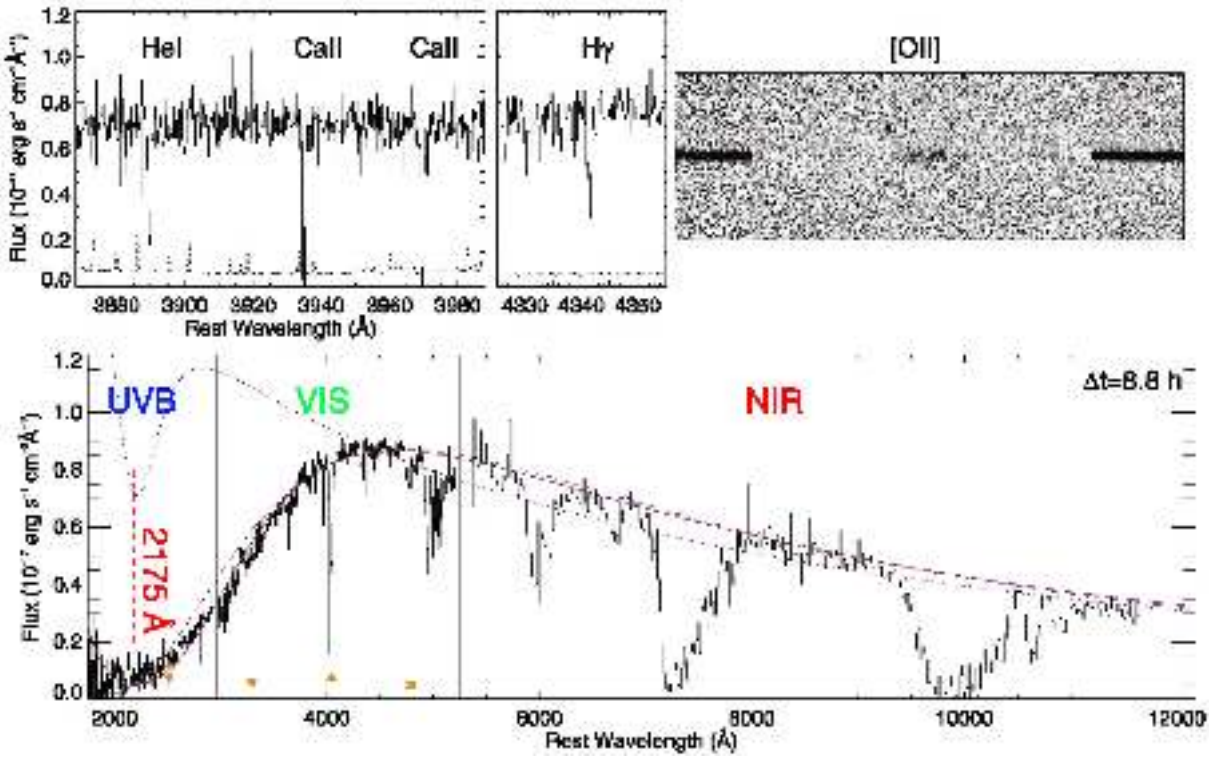

Figure 2.14: Spectroscopy of GRB 140506A and its unusual sightline. *Bottom panel*: An X-shooter spectrum taken 8.8 hr after the burst covering the range from about 2000 to 12000 Å in the rest frame of the $z = 0.889$ GRB is plotted in black and late time host photometry is overplotted in orange. *Top left*: The spectrum also shows very unusual absorption lines including absorption from excited helium as well as hydrogen Balmer lines, never seen before in any afterglow spectra. *Top right*: [O II] emission lines from the underlying host galaxy visible under the light of the afterglow. Adapted from Perley *et al.* (2016b).

$(B - V)$ of the object and comparing by its intrinsic $(B - V)_0$

$$E(B-V) = (B-V) - (B-V)_0 \tag{2.17}$$

The greater the extinction, the larger the reddening. Each line of sight has its own extinction law and is usually expressed by the variation of the extinction with wavelength (i.e., A_λ/A_V or $E(\lambda - V)/E(B - V)$). Interstellar extinction is commonly obtained by comparing spectra of reddened and unreddened stars of the same spectral type. (Cardelli *et al.*, 1989) showed that Galactic sight-lines could be characterised by a single parameter R_V, although Fitzpatrick & Massa (2007) dispute this. This R_V parameter is defined by

$$R_V = \frac{A_V}{E(B-V)} \tag{2.18}$$

which average for the MW is 3.1, and it varies from sight-line to sight-line.

Sometimes dust extinction causes certain features that can be recognised. These include the 2175 Å bump, the diffuse interstellar bands, or the 3.1 μm water ice and 10-18 μm silicate features. The mentioned 2175 Å bump is present at all R_V values of the Galaxy, and most theories attribute it to some form of carbon.

At high redshifts evidence for dust exists from DLA observations (Pettini *et al.*, 1994) and from the detection of dust thermal emission from QSOs, but it is still not clear what is the mechanism of dust production, as it cannot be the same as at low redshift.

The advantages of GRB afterglows for the study of the extinction are

- Afterglows are very bright, allowing its detection even when affected by substantial extinction
- Afterglows have simple continua, consisting of power-law segments
- Afterglows cover a wide range of frequencies, from radio to X-rays

Early studies on dark bursts suggested that these events are fairly common and the majority of these are due to dust extinction (Kann *et al.*, 2006).

Swift has allowed larger and more complete studies, showing that the fraction of dark bursts are ∼40%, and half of them are very obscured (e.g. Covino *et al.*, 2013). Detailed studies on extinction curves are presented in Covino *et al.* (2013); Japelj *et al.* (2015); Schady *et al.* (2010, 2012); Starling *et al.* (2007); Zafar *et al.* (2011). All these studies find that the best fits are in most cases similar to the curves towards the Small Magellanic Cloud (SMC), being the 2175 Å extinction bump detected only in a handful of afterglows.

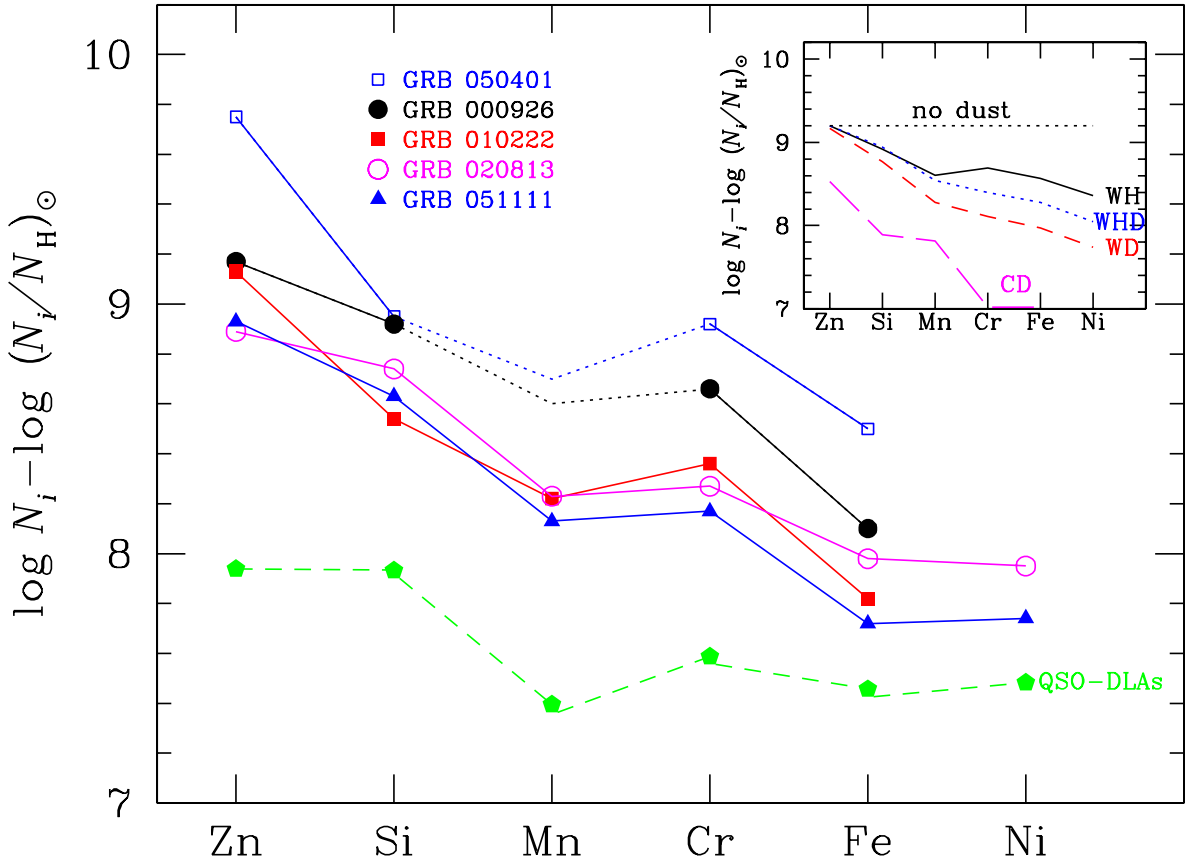

Figure 2.15: Depletion pattern in five GRB-DLAs with four or more heavy elements measured (errors are $\lesssim$0.2 dex). The dashed line at the bottom is the mean depletion pattern measured in 20 QSO-DLAs for which all six elements are detected. Metal column densities and dust depletion in GRB-DLAs are much higher than in QSO-DLAs. In the inset, the dust depletion patterns (rescaled to an arbitrary value) of the Galactic ISM are plotted for comparison; from top to bottom: warm halo, warm halo + disc, warm disc, cool disc clouds. Adapted from Savaglio (2006).

Some sightlines show evidence of extinction laws with no local analogue. The most exotic and mysterious case is the extinction pattern found towards GRB 140506A (Fynbo *et al.*, 2014). This afterglow shows several peculiarities:

- Absorption lines from excited Hydrogen and Helium
- Molecular absorption from CH^+
- Very strong dust absorption bluewards 4000 Å in rest frame.

2.5.3 Dust depletion

Refractory elements, such as Fe, Ni, Si, and Cr, can be heavily depleted into dust grains (it depends on element properties such as ionization potential and condensation temperature; Savage & Sembach, 1996), and consequently be missing from the gas-phase abundances. On the contrary, volatile elements such as Zn, S, and O do not show this behaviour. This effect was studied in DLAs for the first time by Pettini *et al.* (1994), showing that [Cr/Zn] in DLAs is usually lower than $[Cr/Zn]_{\odot}$ due to the missing Cr. Finally, the existence of a correlation between [Fe/S] and [Si/S] (Rodríguez *et al.*, 2006) made the observations difficult to explain without the dust depletion.

To estimate the level of depletion we usually compute the relative abundance of heavily depleted species towards those undergoing little depletion (e.g., De Cia *et al.*, 2013; Vladilo *et al.*, 2006). The most suitable element to compute metallicities is Zinc, as it gets very weakly depleted. However, at $z \gtrsim 3$, Zn lines are far in the red and frequently contaminated by atmospheric features. In those cases, it is better to use Sulphur, but being weak features the S II lines are not always detected. Using different metal lines and methods we can obtain the iron dust-phase column density, the dust-to-gas ratio, and the flux attenuation (Vladilo, 1998, 2002a,b; Vladilo *et al.*, 2001). The depletion patterns can also be compared with Galactic patterns to estimate the origin and the evolution of the dust-to-metal ratio (e.g., De Cia *et al.*, 2013).

Usually, depletion factors found in DLAs are lower than in our Galaxy. This is probably due to an existing correlation between metallicity and dust depletion (Ledoux *et al.*, 2003).

2.6 Molecules

Molecular absorption lines provide detailed information about the physical and chemical properties of cold and dense regions. Molecular clouds are the progenitors of stars, and they are a mix of atomic He and molecular H, with traces of CO and H_2O, at a density of 10^3 cm^{-3} (Omont, 2007). These clouds will collapse into dense accretion disks that form stars, so their understanding is crucial for the knowledge of the star forming processes and galaxy evolution.

Due to the difficulties of detecting H_2 in emission, most of the knowledge comes from CO observations, which is correlated with far infrared and Hα luminosities (e.g., Omont, 2007). However, as absorption line strengths are independent of distance, this observing strategy is more promising especially at high redshift.

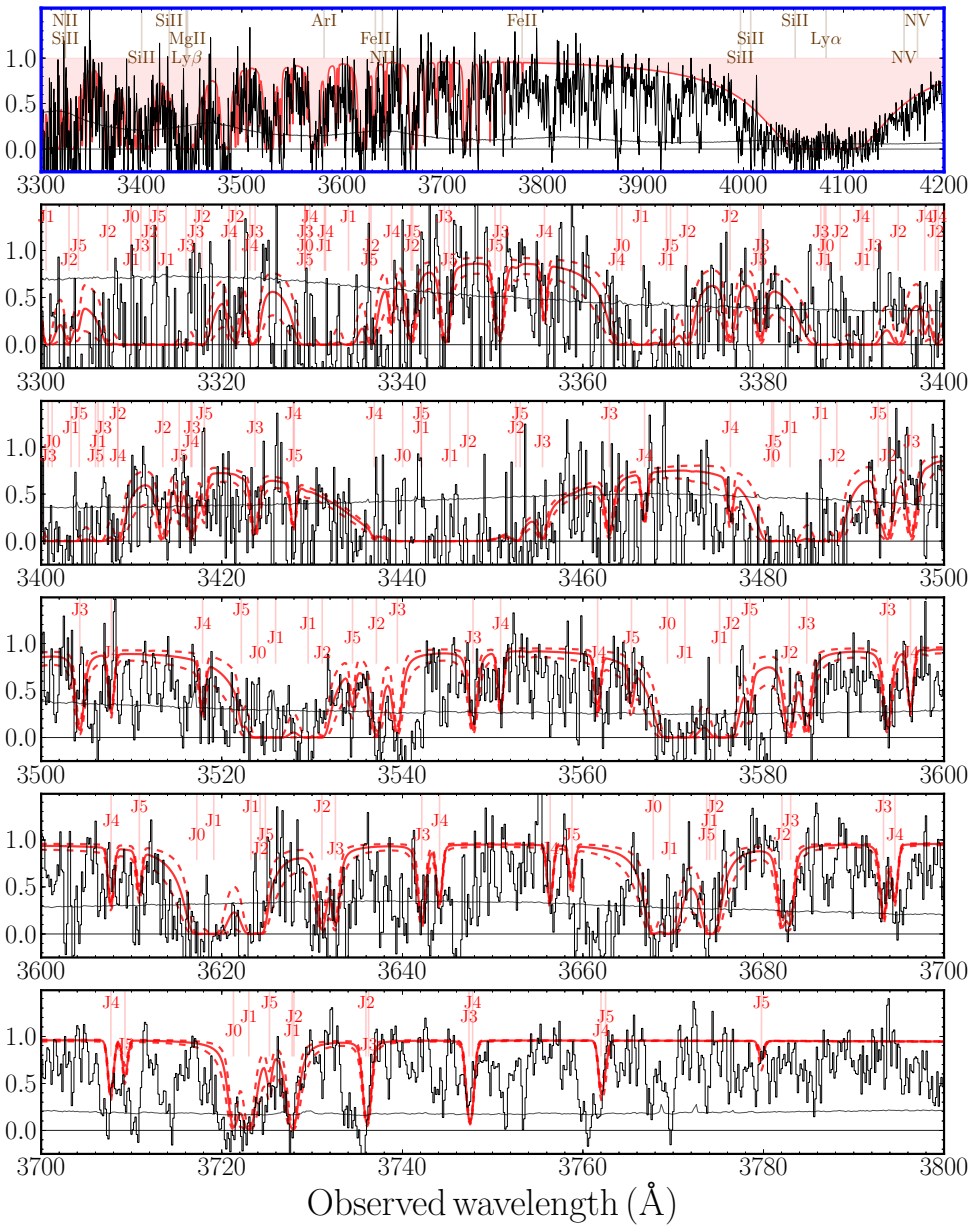

Figure 2.16: GRB spectrum between 3300 and 4200 Å illustrating the presence of H_2 absorption. The uppermost, blue-framed panel shows an overview, while the lower 5 panels show zoom-ins of 100 Åeach below 3800 Å, where most of the Lyman-Werner absorption bands are located. Light-grey lines are the normalized spectrum, while dark-grey lines indicate the error spectrum. The solid red line denote the synthetic H_2 model, with individual transitions up to J = 5 transitions marked with red labels. The dashed lines show synthetic H_2 models corresponding to the 1σ errors on the measured molecular content. In the lower panels, J0, J1, and so forth denote transitions from the J = 0, J = 1 rotational level of the vibrational ground state of the Lyman-Werner bands of H_2. Adapted from Krühler *et al.* (2013).

The first studies of high redshift molecular Hydrogen were performed by Aaronson *et al.* (1974); Carlson (1974), but the first detection was proposed by Levshakov & Varshalovich (1985) and later confirmed by Foltz *et al.* (1988). Thanks to the venue of the high resolution spectrograph UVES, mounted on one of the 8.2 m VLTs, Ledoux *et al.* (2003) performed the first systematic study of molecular Hydrogen at high redshift. The measured molecular fractions

$$f = \frac{2N(\mathrm{H_2})}{(2N(\mathrm{H_2}) + N(\mathrm{H\,I})} \tag{2.19}$$

range from $f \simeq 5 \times 10^{-7}$ to $f \simeq 0.1$, but it was surprising that only 16% of the DLAs analysed displayed H_2 features. They also showed that the presence of H_2 does not strongly depend on $N(\mathrm{H\,I})$, and the data does not point to a strong transition in the molecular fraction as a function of $N(\mathrm{H_2}) + N(\mathrm{H\,I})$. However, it was later found that high metallicity and dusty systems had the best detection rate of H_2 (Petitjean *et al.*, 2006), and recently Noterdaeme *et al.* (2015a) discovered a significant increase of $N(\mathrm{H_2})$ in DLA systems with $\log N(\mathrm{H\,I}) > 20.7$. Unlike in our Galaxy, f values in DLAs remain modest, pointing to the fact that only a small fraction of the detected H I gas could be associated with the H_2 cloud.

As GRB-DLAs probe the gas associated with star-forming regions, one would expect to easily detect H_2 signatures in the afterglow spectra. However, it was proved to be difficult. Firstly, because molecular Hydrogen rotational and vibrational transitions are blended with the Lyα forest, so high-resolution and high-SNR are required to estimate the column density. This means that there is a systematic bias in the H_2 detections towards bright afterglows. Another issue is that $N[\mathrm{H_2}]$ correlates with metallicity and dust depletion, so we also expect a bias towards these systems. As bright and very dusty afterglows are not common, there are only four detections of H_2 to date (D'Elia *et al.*, 2014; Friis *et al.*, 2015; Krühler *et al.*, 2013) and one of CH^+ (Fynbo *et al.*, 2014). In general, the fraction of H_2 over H I found along GRB lines of sight seems to be quite low.

2.7 High ionisation absorbers

Although DLAs have neutral and low ionisation species, they commonly show high ionisation features such as C IV and Si IV at a similar redshift, but with a different velocity structure, which evidences that they come from distinct clouds. Fox *et al.* (2007a,b) studied a sample DLAs and subDLAs observed at high resolution using VLT/UVES. They showed that high ionisation profiles present both narrow and broad components of

warm-photoionised and hot collisionally ionised gas, respectively. They were interpreted as highly ionised in/out flows, as the distribution of column densities are similar to the one found in LBG, where winds are directly observed (Pettini *et al.*, 2002). Surprisingly, both low and high ionisation lines have been observed in these galactic winds, showing a complex morphology with clumps, large filaments and bubbles. The main drivers for these winds are suggested to be either powered by AGN or O stars or SN explosions, being the last one the most plausible scenario.

2.8 GRB progenitor-cloud distances

One of the main problems in spectroscopy is to distinguish between distances and movement of the material, as we measure projected velocities in the line of sight. Therefore, additional information is needed in order to clarify the picture.

The GRB afterglow radiation is intense enough to have an important impact on the surrounding environment at the time of explosion. UV radiation ionises the neutral gas and destroys molecules and dust up to tens of parsecs away (e.g., Draine & Hao, 2002; Perna & Lazzati, 2002). However, neutral species such as Mg I and Ca I have been detected in afterglow spectra, pointing to that these absorption systems are rather located farther than tens of parsecs away.

The first evidence that GRBs have measurable effects on their surroundings are the detection of fine-structure and metastable transitions of existing species (O I, Si II, Fe II, Ni II) (Vreeswijk *et al.*, 2003). Silva *et al.* (1998) modelled the population of fine structure levels, and find out that three mechanism seem plausible to populate these levels:

1. Direct excitation from the Cosmic microwave background.
2. Collisional and direct excitation by IR radiation.
3. Indirect excitation by UV photons and subsequent fluorescence.

From the ratio between fine-structure and ground-state transitions it is possible to roughly estimate the distance between the GRB and the absorbing cloud if the radiation field produced by the afterglow is known. Furthermore, if variations of the fine-structure lines can be observed, it is possible to accurately establish the distance. This was achieved for the first time by Vreeswijk *et al.* (2007). They obtained series of high-resolution spectra using VLT/UVES which showed clear variations of Fe II* and Ni II*. By modelling the evolution of these transitions they found a strong evidence for the UV pumping being the responsible mechanism for the excitation.

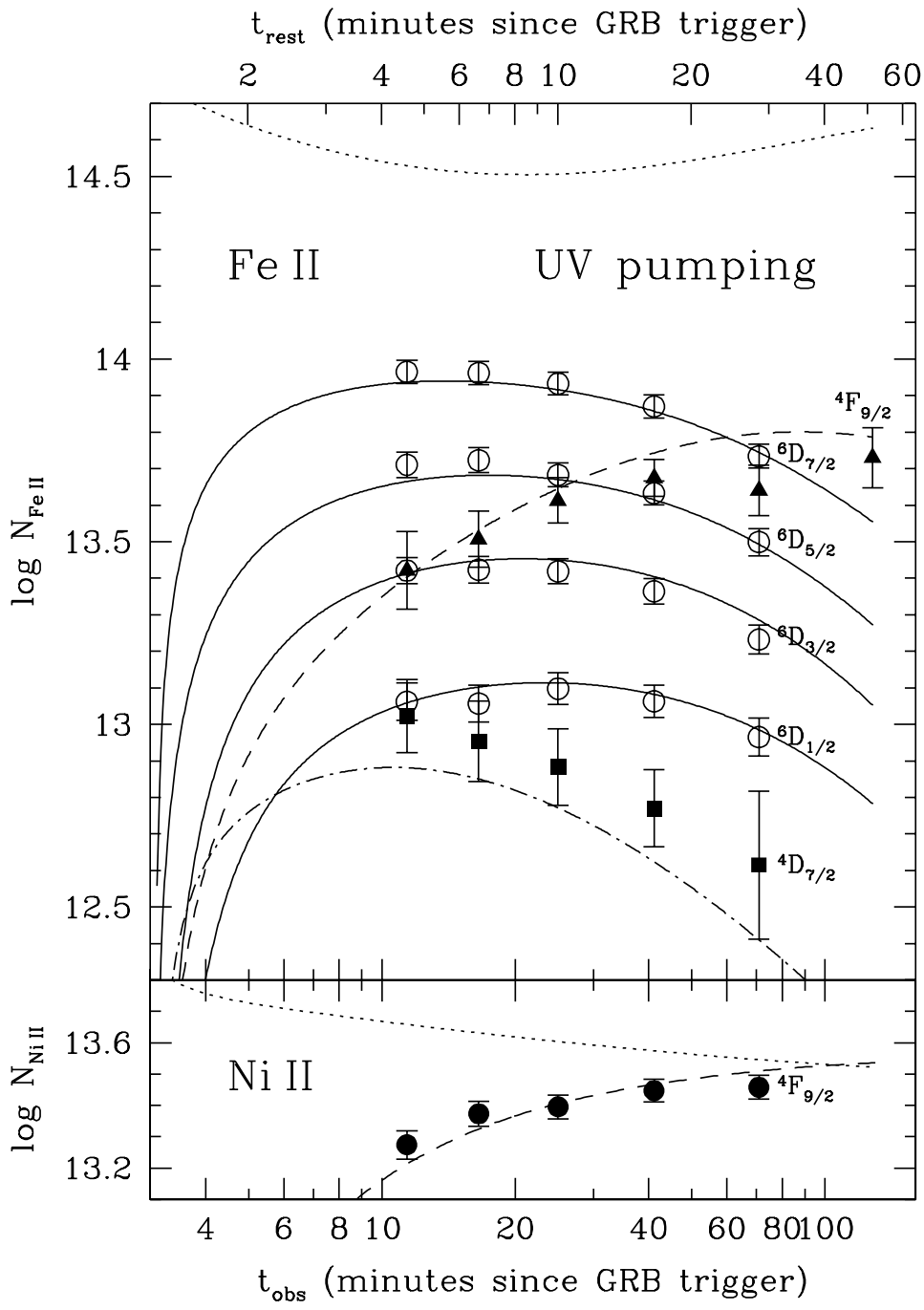

Figure 2.17: The top panel shows the observed total column densities with the UV pumping model over-plotted: solid lines for the fine-structure levels, dashed line for $^4F_{9/2}$, and dashed-dotted for $^4D_{7/2}$. The bottom panel displays the observed total column densities for Ni II $^4F_{9/2}$ (filled circles), and the best-fit Ni II model. In this Ni II fit, all parameters except for Ni II column density were fixed to the best-fit values obtained from the Fe II fit. The model prediction for the evolution of the Ni II ground state column density is indicated by the dotted line. All Fe II and Ni II column densities are very well described by the UV pumping model. Adapted from Vreeswijk *et al.* (2007).

Currently, it has been possible to use this type of analysis on ∼10 GRBs. The method has served to show that the excited gas is at least at ∼100 pc from the progenitor, being the surrounding medium ionised up to ∼20 pc. Many attempts to find the close progenitor signatures have been performed, but there are no robust identifications to date (Castro-Tirado *et al.*, 2010; Fox *et al.*, 2008).

Chapter 3

Gamma-ray bursts

"Today, every inhabitant of this planet must contemplate the day when this planet may no longer be habitable. Every man, woman and child lives under a nuclear sword of Damocles, hanging by the slenderest of threads, capable of being cut at any moment by accident or miscalculation or by madness."

— J.F. Kennedy, *UN General Assembly, 1961*

In the early 1960s, the Cold War between the East and West Blocks had rapidly escalated and the development of nuclear weapons had gotten to an unacceptable level. In an attempt to control this situation, the Limited Nuclear Test Ban Treaty was signed between USA, UK, and USSR in 1963 to forbid the further test of nuclear weapons. In order to verify the compliance with the ban, NASA launched a series of satellites called *Vela*[1]. They were equipped with γ-ray detectors to observe the radiation produced during the detonation. Up to 6 pairs of satellites were launched since the treatment was signed, and their detectors were triggered on many occasions. However, these flashes were not originated on the Earth...

[1] Vela comes from the Spanish word "velar", wich means "to guard" or "to keep watch".

3.1 An historical perspective

3.1.1 The discovery

In the years that followed, Ray Klebesadel and his team at Los Alamos National Laboratory (New Mexico, U.S.A.) searched the top secret *Vela* data for emissions not necessarily related to nuclear weapon tests. On the data of the *Vela 4A* and *Vela 4B* satellites, they saw a simultaneous γ-ray flash that ocurred on the 2nd July 1967 at 14:19 UT (a double-peaked signal shown in Fig. 3.1), which did not resemble a nuclear test and did not seem to come from the vicinity of the Earth. Several of such mysterious events were detected during the following years. Due to the restrictions of such an experiment the results were not announced until 1973, when 16 bursts detected by the *Vela* 5 and 6 satellites were published in Klebesadel *et al.* (1973), claiming the discovery of a new type of astronomical event, the Gamma-ray Burst (GRB).

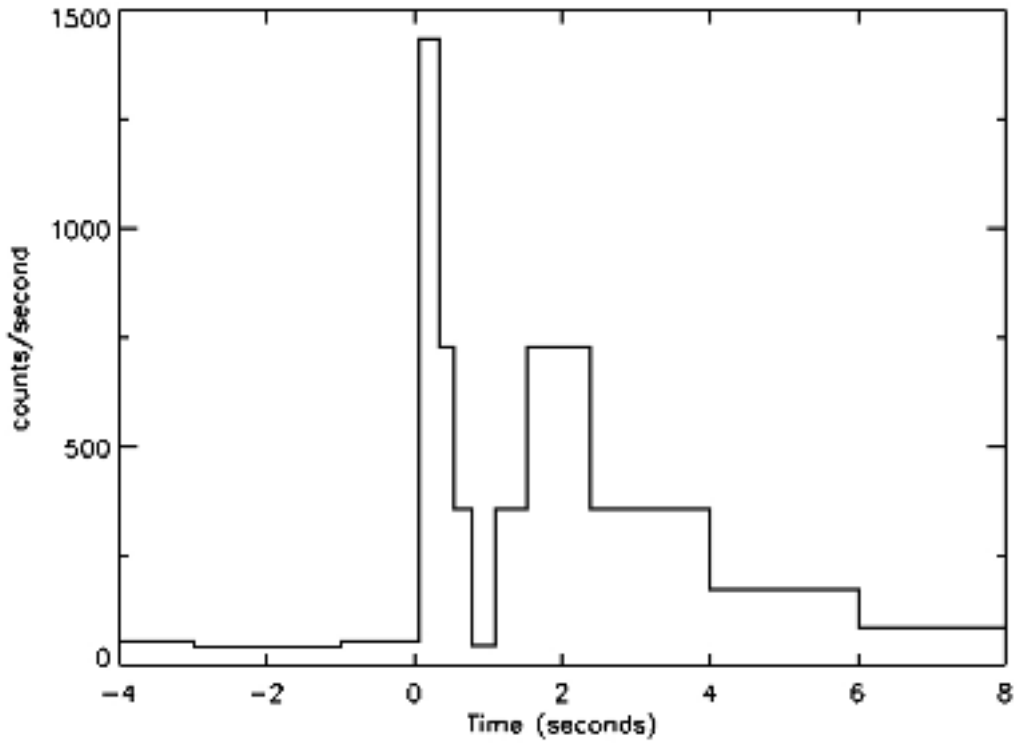

Figure 3.1: Light curve of the first GRB ever detected. Adapted from (Strong & Klebesadel, 1976).

In the following two decades, more than one hundred models were developed trying to explain the nature of these bursts. The proposed models ranged from neutron stars colliding with comets to enigmatic events that occurred at cosmological distances (see, e.g., Nemiroff, 1994). The key parameter to discern between such an amount of possibilities is the distance. However, the poor localization of the bursts that high-energy detectors offered were insufficient to detect counterparts at other wavelengths.

3.1.2 The great debate

Fishman (1981) proposed what would come to be BATSE, the Burst And Transient Source Experiment. It was a set of γ-ray scintillators covering the full sky and installed on the *Compton Gamma-Ray Observatory (CGRO)*, launched in 1991. In the mean time, the majority of the GRB community thought that these events were Galactic, most likely due to neutron stars. The claimed detections of cyclotron lines (Fenimore *et al.*, 1988; Mazets *et al.*, 1981; Murakami *et al.*, 1988) supported this scenario. To confirm this hypothesis, BATSE should show a similar distribution on the sky than neutron stars, with a larger density along the plane of the Milky Way.

Surprisingly, the first observations by BATSE pointed to a uniform distribution of GRBs on the sky, as well as the definitive analysis (Meegan *et al.*, 1992), confirming the earlier *Venera* results (Mazets *et al.*, 1981). This fact was shocking for most of the community, but it was not considered as definitive due to other results that still suggested the neutron star origin. Imitating the classical debate between Herbert Curtis and Harlow Shapley in 1920, Robert Nemiroff organized a similar event 75 years later. This time, on the one side was was Don Lamb defending the local theory, and on the other side was Bohdan Paczyński supporting the cosmological origin (Lamb, 1995; Paczynski, 1995). Like in the original debate there was not a clear winner, but the final answer would not have to wait long.

3.1.3 Unveiling the mysteries

3.1.3.1 The distance scale problem

HETE was the first mission expected to solve the fundamental mysteries of GRBs. However, due to a failure during the uncoupling manoeuvre after the launch in 1996, it was lost when it had already reached the orbit. A second unit (*HETE-2*) was finally operative in 2000.

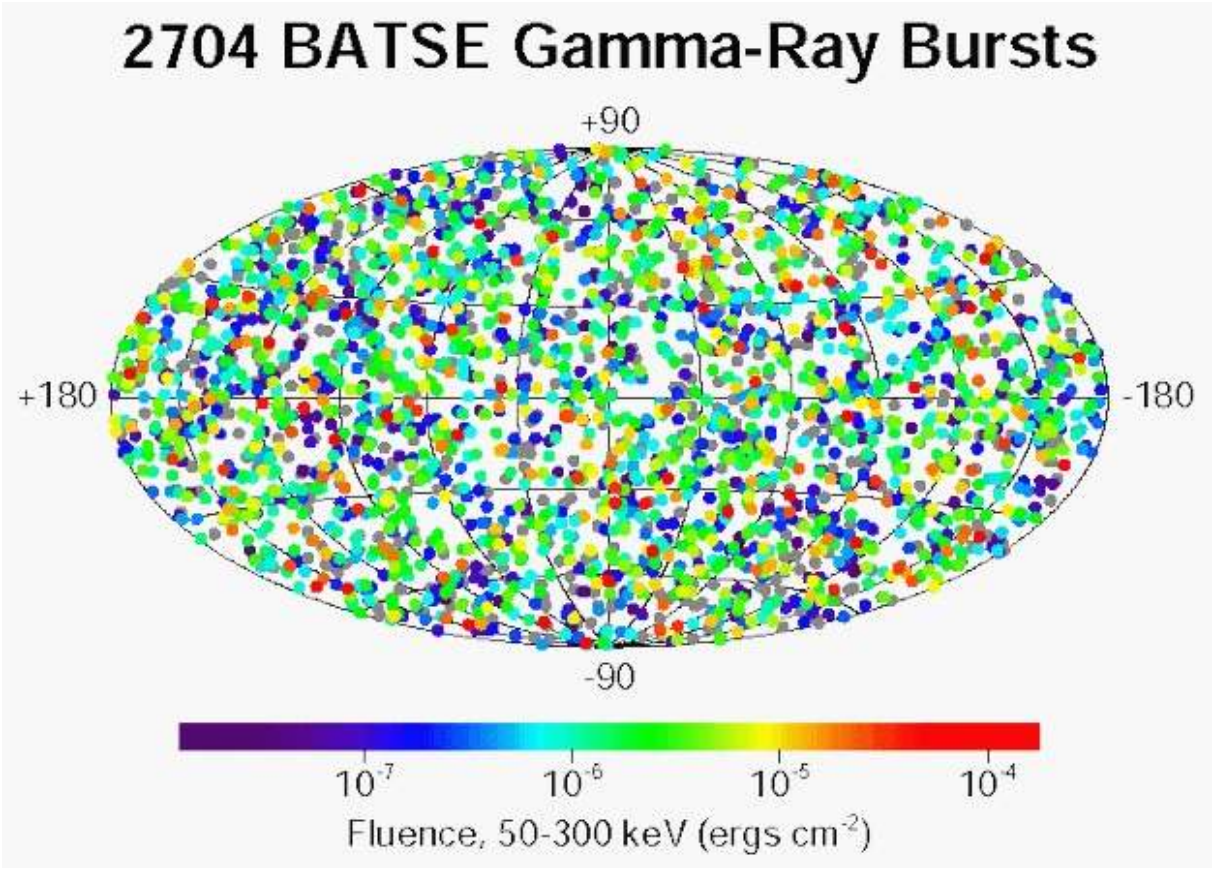

Figure 3.2: Isotropic distribution of the GRBs detected by BATSE.

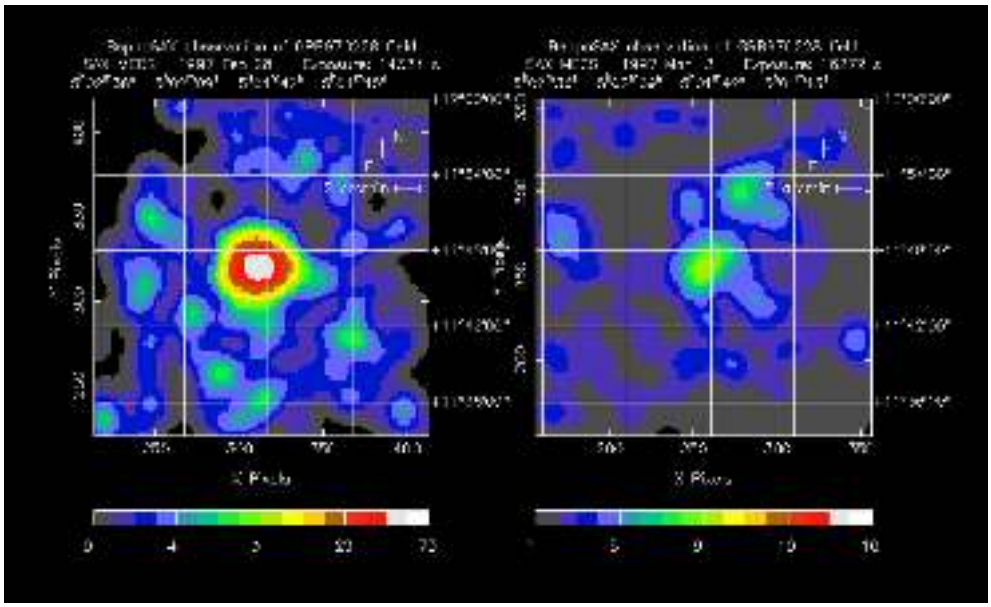

Figure 3.3: X-ray counterpart of GRB 970228 detected by *BeppoSAX*.

In the mean time, *BeppoSAX*, an Italian-Dutch satellite was launched ten years later than expected, in 1996. Although its primary science was not GRBs, it was this satellite that made a break through in the field in order to solve the GRB riddle. The main advance of this mission was that it carried an X-ray detector together with a γ-ray monitor. The X-ray counterparts were discovered for the first time with *GRANAT* for GRB 920723, so they knew that localizing these lower energy counterparts it would be possible to accurately determine the position of the burst in a short time interval, opening the door to ground-based observatories follow-ups in other wavelengths (Terekhov *et al.*, 1993).

On the 20th July 1996 the first burst was detected by both instruments on-board *BeppoSAX*, 3 months after the launch. However, the lack of experience in the data analysis delayed the communication of the result for more than a month (Piro *et al.*, 1996).

Several months later, once *BeppoSAX* team was prepared to react in a reasonable amount of time, GRB 970111 occurred and was observed by the satellite. This time, the position was circulated within 24 h after the trigger. In Calar Alto, Spain, this burst was observed by Alberto J. Castro-Tirado and his PhD student Javier Gorosabel with the 2.2m telescope. Unfortunately, no optical counterpart was detected down to a limiting magnitude of $\sim$22.6 (Castro-Tirado *et al.*, 1997). There was no success also trying to identify a radio transient either.

The next (and successful) attempt was performed in the following month. GRB 970228 was finally pinpointed by van Paradijs *et al.* (1997). The optical transient faded away and

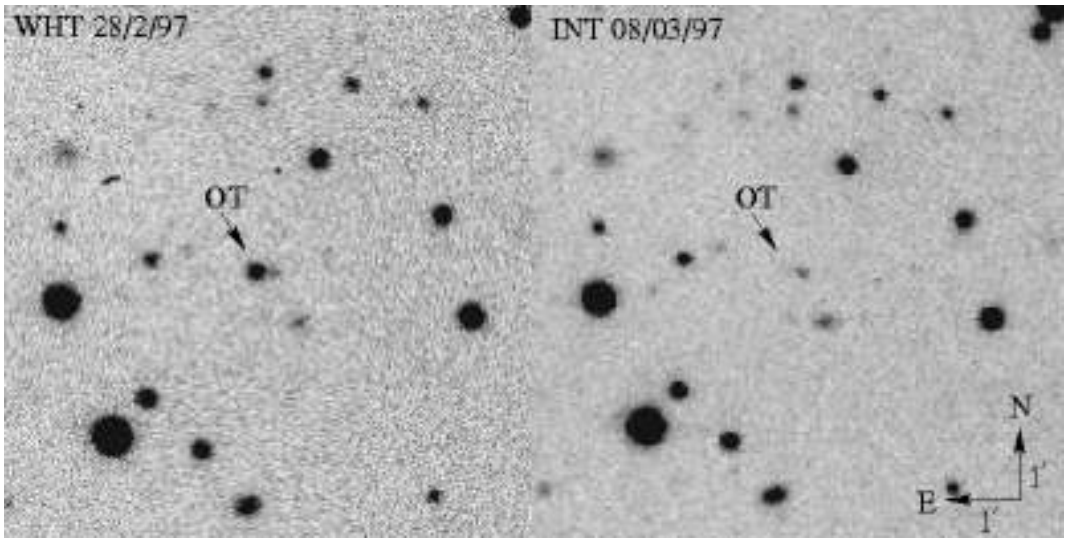

Figure 3.4: First GRB optical counterpart detected. Adapted from van Paradijs *et al.* (1997).

an underlying object appeared. It was proposed the host galaxy that would be sheltering the burst at a cosmological distance. However, to prove this hypothesis, it was mandatory to obtain a spectrum of the source.

This goal was achieved with GRB 970508, initially not an interesting burst, but which was, apart from the first radio counterpart ever detected (Frail *et al.*, 1997), the first event for which an optical telescope (2.2m CAHA) took optical spectra (Castro-Tirado *et al.*, 1998). Finally, a redshift of 0.835 was determined from the absorption lines on the 10m Keck spectrum, solving 30 years of mystery (Metzger *et al.*, 1997a,b).

3.1.3.2 The problem of energetics

Once the distance scale of GRBs was determined another problem came along. The rapid variability observed in BATSE light curves indicated that the emitting region could not be larger than ∼100 km, while the total isotropic energies released in a few seconds were of the order of 10^{52} erg. This amount of energy in such an small volume would be optically thick to pair creation and emit a thermal spectrum, which was not observed. Several effects from relativity could help to explain the problem, such as beaming, time dilation and length contraction. These ideas led to the development of the relativistic fireball model (Cavallo & Rees, 1978; Mészáros & Rees, 1993; Rees & Mészáros, 1992). Figure 3.6[1] describes a relativistic outflow from a central engine (without making any hypothesis on it). Internal shocks would explain the prompt emission while the external

[1]Adapted from http://www.theregister.co.uk/2013/11/21/scientists_spot_bigger_ever_gamma_ray_burst_from_birth_of_black_hole/

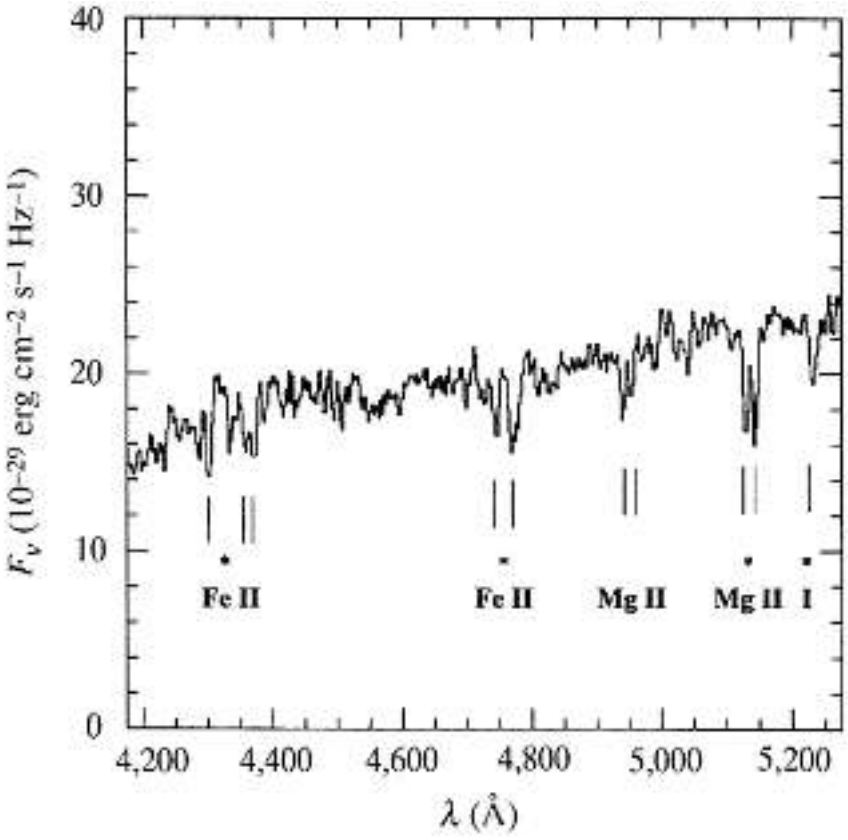

Figure 3.5: Iron and Magnesium lines in absorption at $z = 0.835$. Adapted from Metzger *et al.* (1997b).

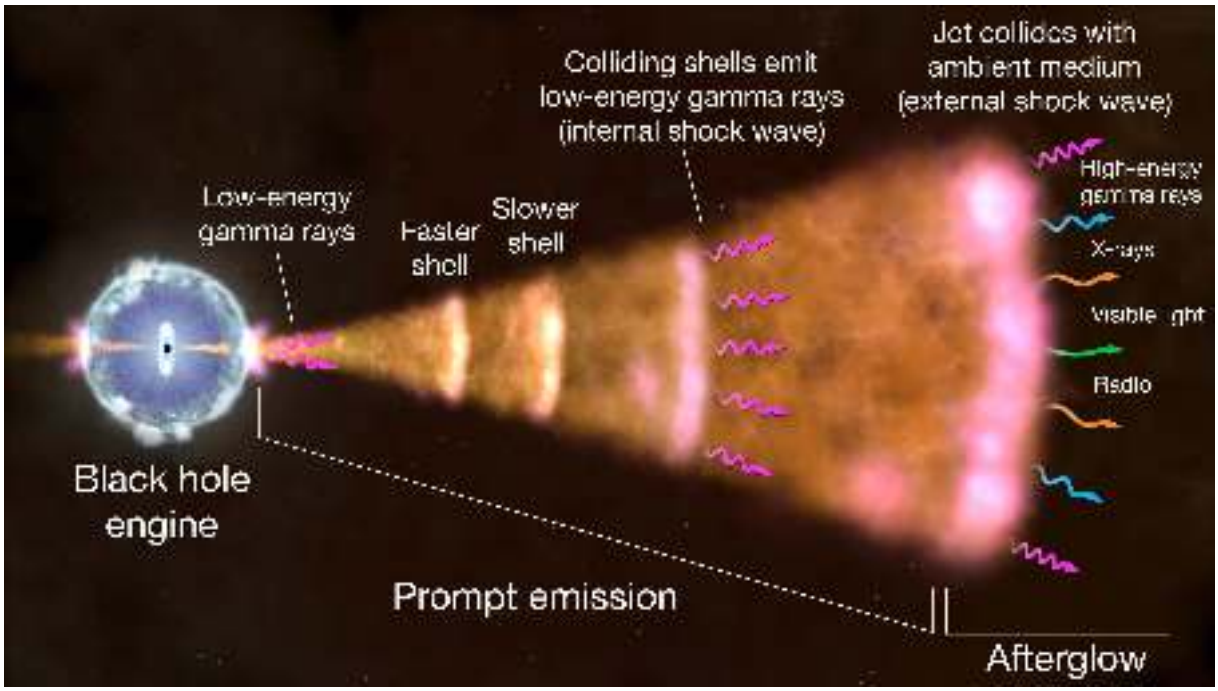

Figure 3.6: Schematic description of the GRB and the afterglow according to the fireball model. Credits: NASA's Goddard Space Flight Center

shock interacting with the ISM would be the origin of the afterglow.

Jet-like scenarios are not required, but were introduced as a likely physical context (Mészáros & Rees, 1992a; Rees & Mészáros, 1992; Rhoads, 1997; Shaviv & Dar, 1995). They started to be an essential ingredient since high-redshift events implied energies $E \gtrsim 10^{53}$ erg, beyond what reasonable models could explain. Rhoads (1997, 1999) showed that a collimated emission would decrease by 2 or 3 orders of magnitude the released energies. Observations of a collimated emission are expected to show a *jet break* in the light curve when the Lorentz factor (Γ_0) of the outflow decrease bellow $1/\theta_0$, being θ_0 the opening angle of the jet. This behavior was first suggested by Castro-Tirado *et al.* (1999); Kulkarni *et al.* (1999), and observed many times later.

The fireball model is based on an initial explosion of $E \sim 10^{52}$ erg. While the central engine is active, outflows of different bulk velocities are produced. Due to the relativistic and supersonic motion, the ejected matter form shells. Given their differential velocities, they collide producing *internal shocks*, resulting in the prompt γ-ray emission. When the ejected shells sweep up a significant amount of surrounding material, an external shock is formed by accelerated electrons which produce synchrotron emission. This emission, that cools down as time goes on and is detectable in all wavelengths, is that we know as the *afterglow*.

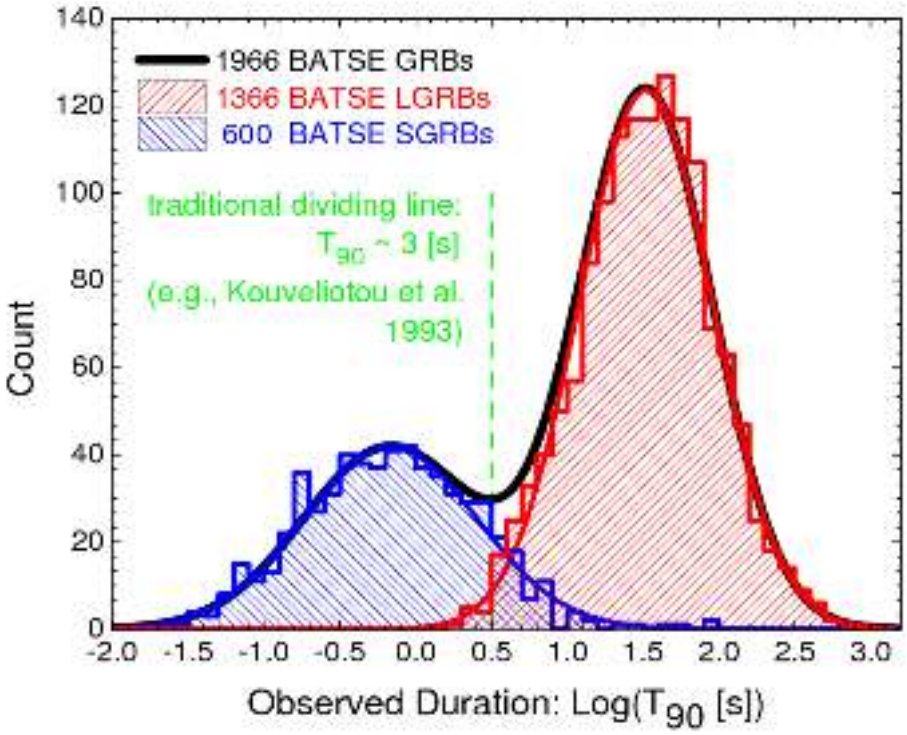

Figure 3.7: Bimodal distribution in the duration of GRBs. Adapted from (Shahmoradi, 2013)

3.1.4 The search for GRB progenitors

Kouveliotou *et al.* (1993) presented a histogram based on 222 BATSE bursts which pointed to a bimodality in the distribution (see Figure 3.7). It was interpreted as an indication of the existence of 2 GRB populations. GRBs with $T_{90} < 2$ s are called *short GRBs* (sGRBs), and have on average harder photons than longer burst, called *long GRBs* (lGRBs).

3.1.4.1 Long GRBs

Modeling the evolving SEDs of the afterglows, one can infer not only the physics of the jet, but also the structure of surrounding medium (e.g., Chevalier & Li, 1999; Sari *et al.*, 1998; Wijers & Galama, 1999). Li & Chevalier (1999) showed that a density profile $n \sim r^{-2}$ is a better representation for some burst than a constant ambient density. This result pointed to Wolf-Rayet stars as a potential progenitor for some events, such as GRB 980425.

Galama *et al.* (1998) detected a transient event on an arm of a spiral galaxy lying in the error box of GRB 980425. Its behavior was atypical in comparison with previously observed bursts. Instead of showing a fast decreasing of its brightness, it suddenly increased to decay slowly afterwards. Due to the similarity with what we expect from a

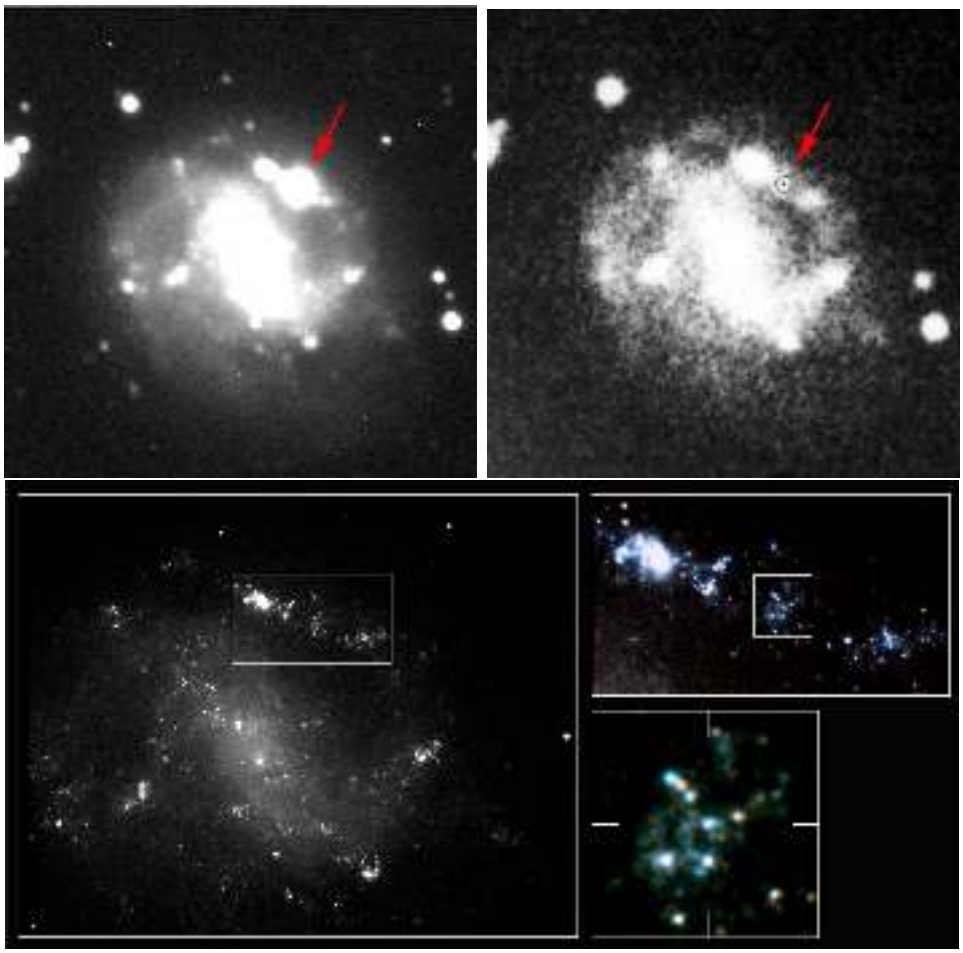

Figure 3.8: Discovery of SN 1998bw associated with GRB 980425. The upper panels show the images of the host galaxy of GRB 980425, before (right) and shortly after (left) the occurrence of SN 1998bw (Galama *et al.*, 1998). The bottom panel shows a late *HST* image of the host galaxy and SN 1998w. The 3-step zoom-in shows SN 1998bw 778 days after the explosion embedded in a large star-forming region of a spiral arm (Fynbo *et al.*, 2000).

supernova, GRB 980425 was identified also as SN 1998bw. It was also a peculiar event compared with the previous SN observations. Further studies showed that the explosion had a huge amount of radio emission (Kulkarni *et al.*, 1998), and a energy 10 times greater than a typical supernova (hypernova, Iwamoto *et al.*, 1998). This meant a strong case for the association of certain class of burst with the violent death of massive stars, in which the formation of a black hole is unavoidable.

In spite the chances of having a SN event unrelated with a GRB in the error box are extremely low, the peculiarities of GRB 980425/SN 1998bw raised the question whether this behavior is usual in GRB events. Castro-Tirado & Gorosabel (1999) first detected the expected "bumps" in the GRB 980326 light curve, which was later modeled by Bloom *et al.* (1999).

Finally, the definitive proof for the GRB-SN relation came with GRB 030329. Its spectroscopic follow-up showed the evolution from the afterglow power law to the supernova spectrum (Hjorth *et al.*, 2003; Stanek *et al.*, 2003).

3.1.4.2 Short GRBs

In spite of the great and passionate discoveries made in the 90s of long GRBs, no afterglow was detected for a short burst during this time. This had to wait until 2005, when *HETE-2* and *Swift* were able to precisely localize the X-ray counterparts of these hard and short γ-ray flashes. The first detections of sGRB afterglows were achieved by Berger *et al.* (2005); Gehrels *et al.* (2005); Hjorth *et al.* (2005). These observations pointed towards lower luminosities and distances and showed the lack of associated supernovae. This already indicated that, unlike long GRBs, they were not produced by the death of massive stars.

Short GRBs are believed to be produced due to the merger of a binary system containing very compact objects (neutron stars and/or black holes; e.g., Mészáros & Rees, 1992b; Narayan *et al.*, 1992). The merging of compact objects are expected to be powerful sources of gravitational waves, such as those that have been recently discovered by the LIGO experiment (Abbott *et al.*, 2016a,b).

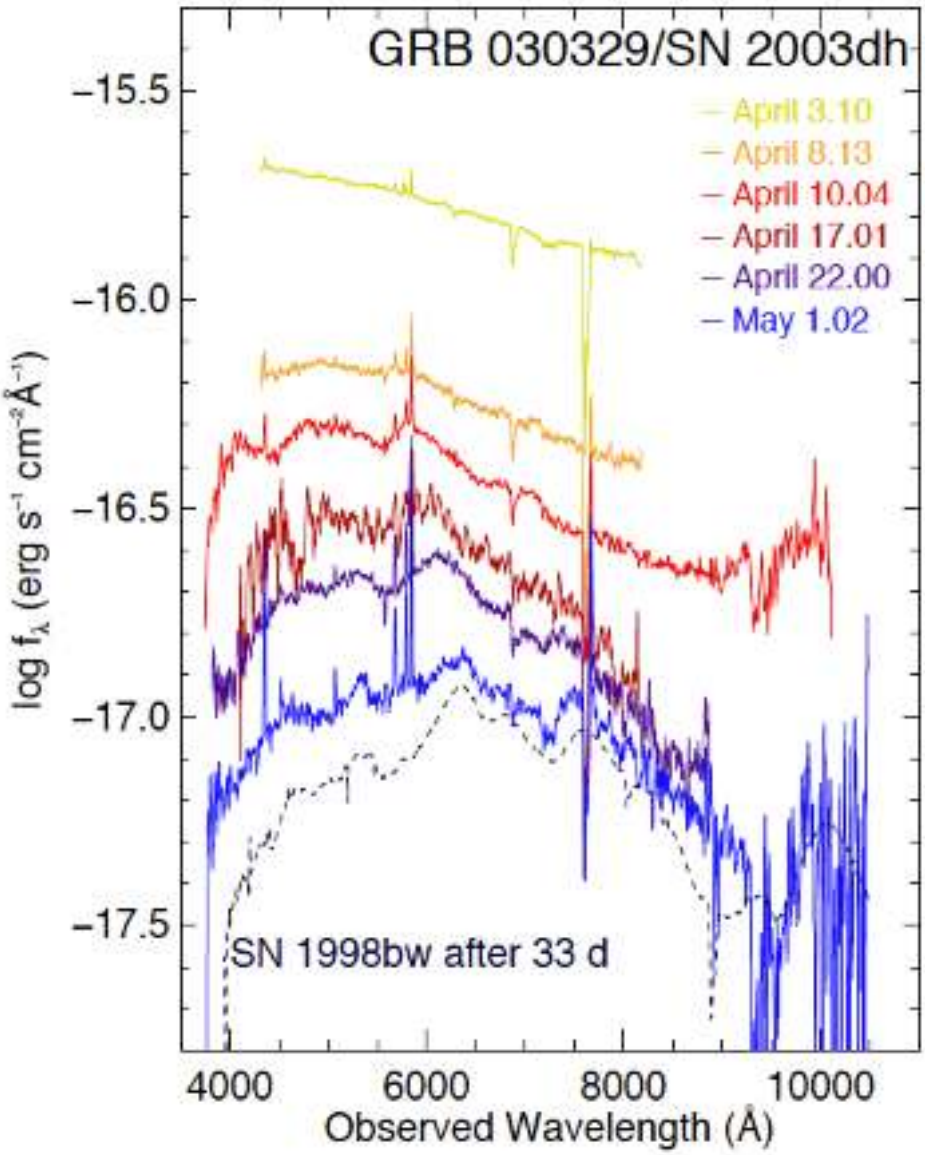

Figure 3.9: Spectral evolution of GRB 030329 from synchrotron to supernova. Adapted from Hjorth *et al.* (2003)

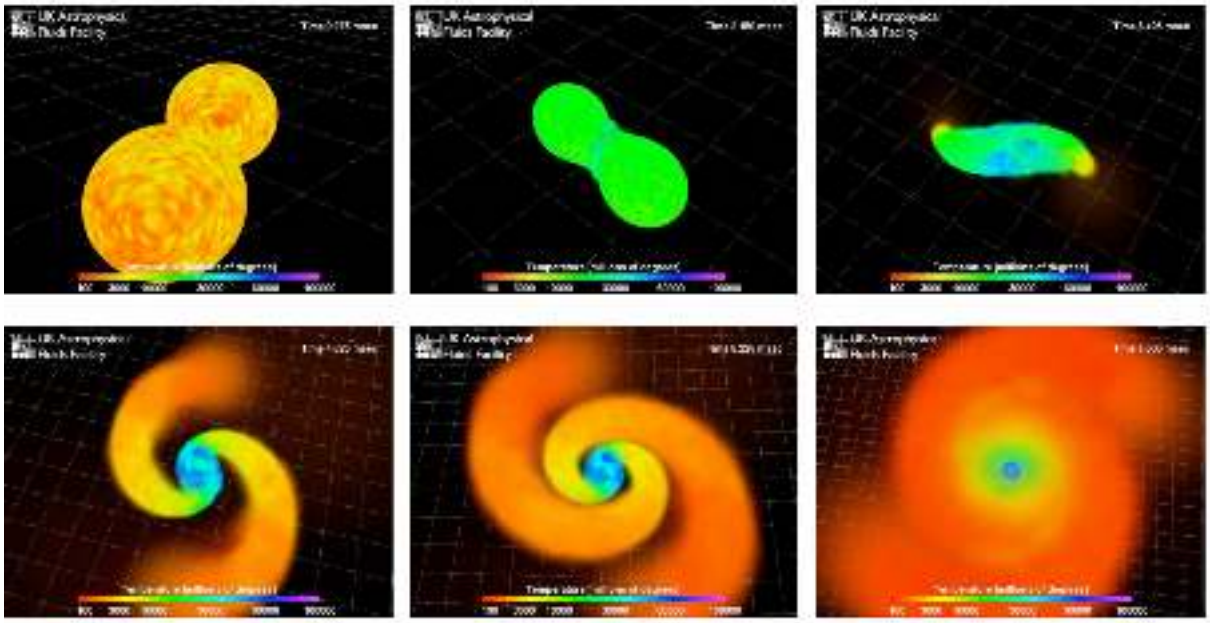

Figure 3.10: Snapshots of the simulation of the merger of two neutron stars. Initially, they are less than 10 km apart, and moving at around v=0.2c. As the two stars spiral together, they become deformed, and finally touch. When they merge, the matter reaches T $\sim 10^{11}$ K. A few percent of the matter is ejected in the form of spiral arms, which cool rapidly. The whole merger process takes only a few ms. The grid in the images has a spacing of 30 km intervals. Credit: simulation by Stephan Rosswog, visualization by Richard West, http://www.ukaff.ac.uk/movies/nsmerger/

3.2 Observational characteristics

3.2.1 Observational properties of the prompt emission

GRBs occur at a rate of a few per day on random positions of the sky. Based on the observations, there are two main phases in the GRB emission: The first one corresponds to the very early times, in which the γ-ray emission is detected (prompt phase), and the other is the afterglow phase, which is a long-lasting emission that gradually fades.

3.2.1.1 Light curves

Temporal properties of the GRB prompt emission can be summarised as the following (see Kumar & Zhang, 2015, and references therein):

- The duration T_{90} ranges from 10^{-3} s up to 10^3 s with typical peak energies between $\sim$ 1 keV and $\sim$ 10 GeV. From the BATSE sample, it was suggested that there are two GRB populations (short/hard and long/soft GRBs), limited by $T_{90} \sim 2$. However, a recent study by Horváth & Tóth (2016) with a sample of 888 *Swift* GRBs claims, in the way of other studies such as by Horváth (1998); Mukherjee *et al.* (1998), shows that the distribution is better explained by adding a third population (*intermediate* bursts). The obtained fit parameters are $T_{90} = 0.3 \pm 0.2$ s for short bursts, $T_{90} = 79 \pm 45$ s for long bursts, and $T_{90} = 12 \pm 8$ for the intermediate population. The redshift distributions of intermediate and long GRBs seem to be compatible, and different in comparison to the short events (de Ugarte Postigo *et al.*, 2011a).
- The GRB light curves are notoriously different from each other (see Fig. 3.11). The shape of the temporal evolution is unique for each burst, and it covers from smooth behaviors to highly variable curves with multiple peaks. The observed variability is high, having been measured down to scales of 10 ms.
- A fraction of GRBs have a typically softer and weaker "precursor" emission well separated from the main burst by 10-100 s.
- Power density spectrum analysis of GRB light curves reveals null periodicity.
- There is evidence that GRB light curves are the superposition of a faster and a slower component.
- The shape of individual pulses is typically asymmetric. Some bright and isolated pulses can be often modelled by a fast rising and exponential decay (FRED) function.

- There are quiescent periods during a burst.
- Light curve shapes vary with energy band.
- A "spectral lag", namely, pulses lagged behind the higher energy ones, is observed for many long GRBs. Short GRBs show lags that are consistent with zero and even, in some cases negative lags.

3.2.1.2 Spectra

The spectra of the prompt GRB phase are well fitted by an empirical smoothly-joined broken power law known as the Band function (Band *et al.*, 1993)

$$\Phi(E) = \begin{cases} AE^{\alpha}e^{-(2+\alpha)E/E_{peak}} & E \leq \frac{\alpha-\beta}{2+\alpha}E_{peak} \\ BE^{\beta} & \text{otherwise} \end{cases} \tag{3.1}$$

with α the power-law index for photon energies below the peak energy and β above it. Mean values for long bursts are α = -0.92 $\pm$ 0.42 and β = -2.27 $\pm$ 0.01. Short bursts have α = -0.4 $\pm$ 0.5 and β = -2.25 (Ghirlanda *et al.*, 2002, 2009; Nava *et al.*, 2011a,b).

The peak of the $E^2N(E)$ spectrum is called "E peak", which is given by

$$E_p = (2+\alpha)E_0 \tag{3.2}$$

Spectra for some GRBs can be fitted with a cut off power law spectrum

$$N(E) = A\left(\frac{E}{100\text{keV}}\right)^{-\widehat{\Gamma}} \exp\left(\frac{E}{E_c}\right) \tag{3.3}$$

which is essentially the Band function with α replaced by $\widehat{\Gamma}$.

A synthesised prompt emission spectrum may include three components (Tanvir *et al.*, 2013):

1. A non-thermal Band component
2. A quasi-thermal component
3. A non-thermal component that can be fit as a power law extending to high energies.

It is also interesting to note that low luminosity GRBs seem to have different prompt emission spectrum (Zhang *et al.*, 2011).

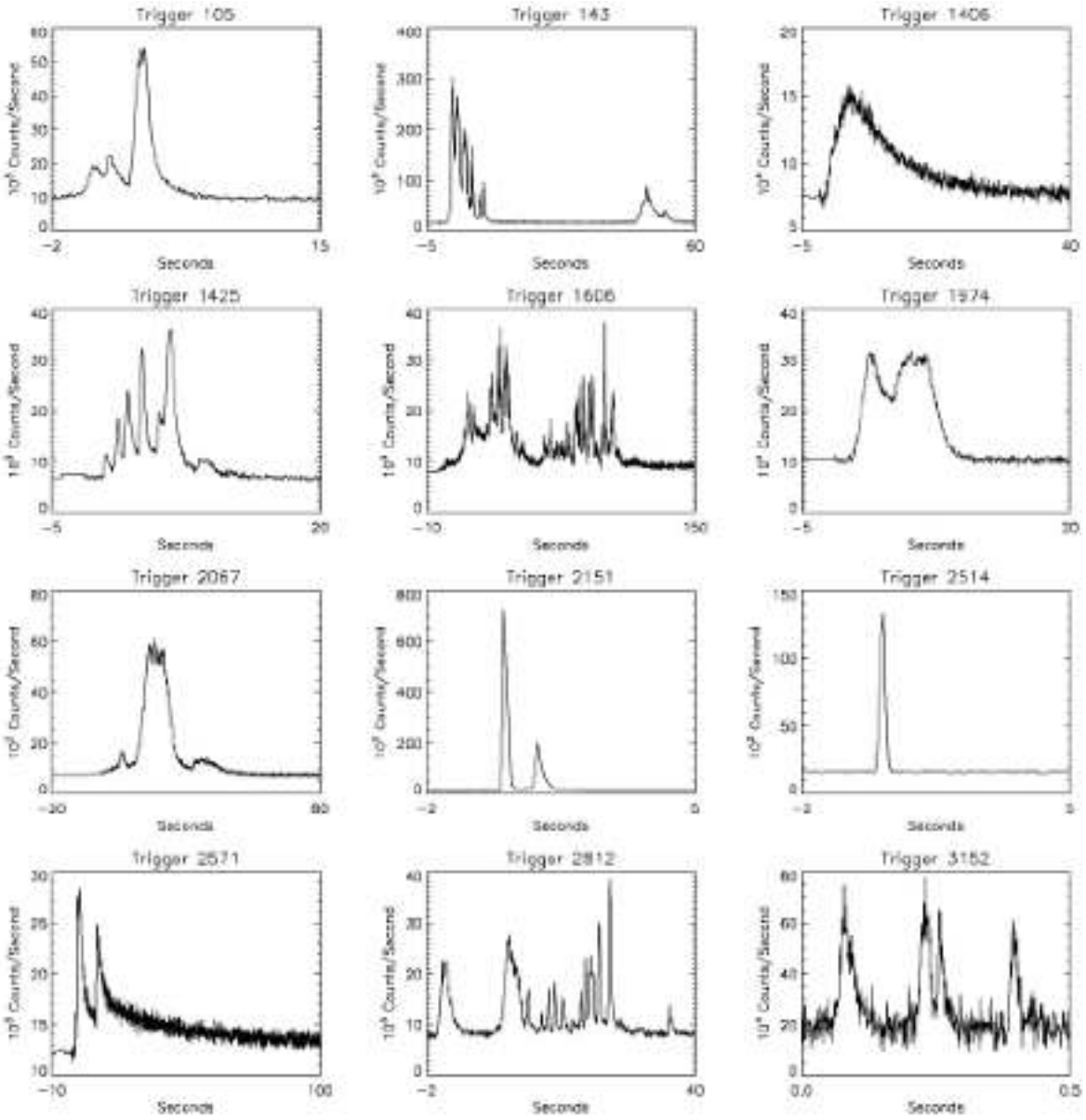

Figure 3.11: Diversity of γ-ray light curves from BATSE. Adapted from Fishman & Meegan (1995).

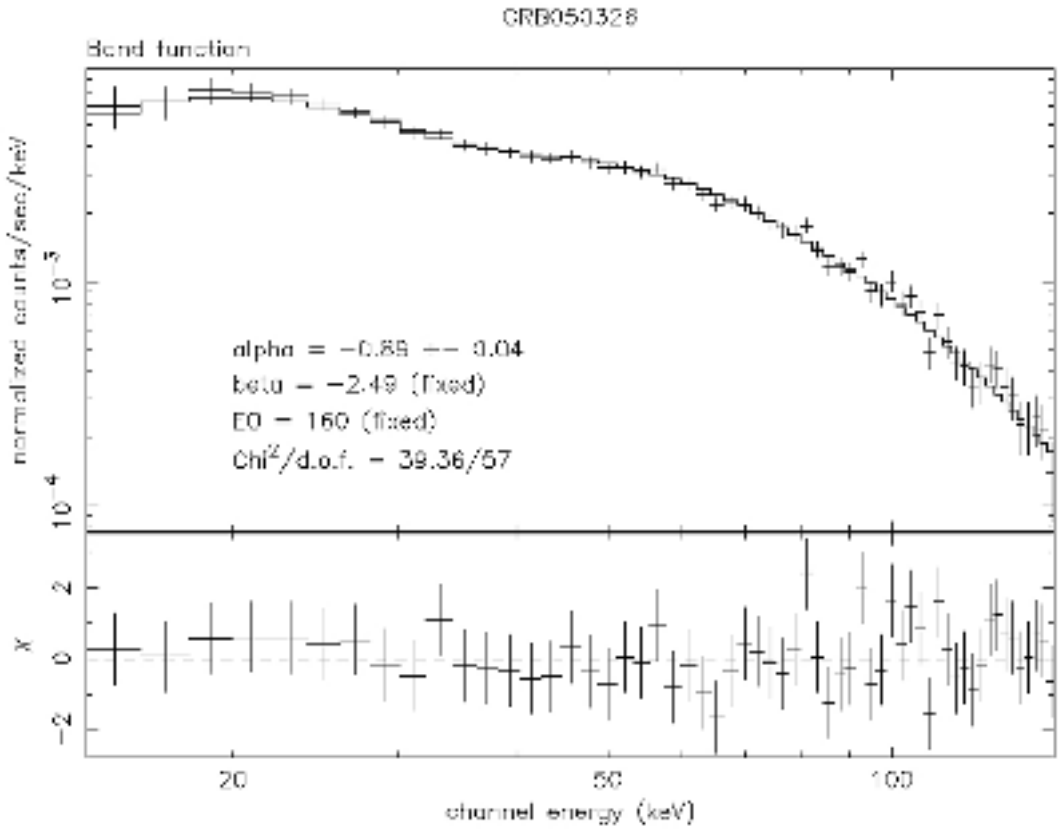

Figure 3.12: Effective areas for Swift-BAT/XRT/UVOT and Fermi-GBM/LAT. Adapted from Stamatikos (2009). *Right:* The BAT spectrum of GRB 050326. Adapted from http://swift.gsfc.nasa.gov/analysis/bat_digest.html.

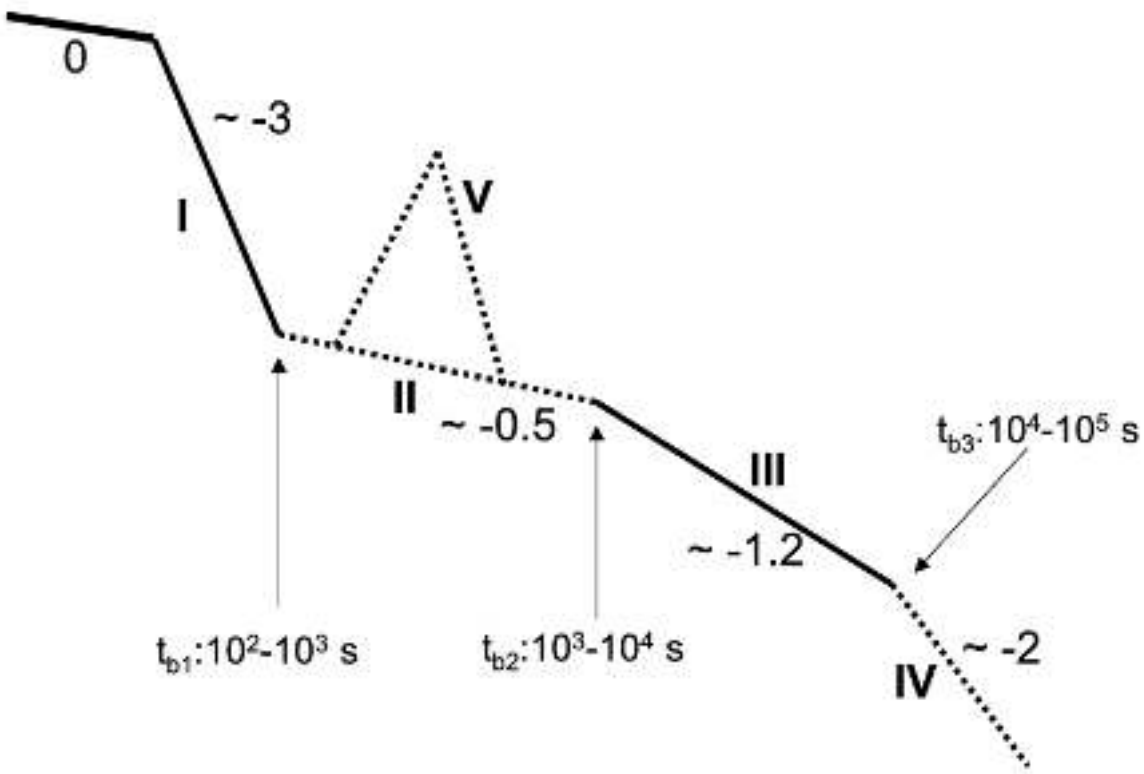

Figure 3.13: Canonical shape of GRB X-ray afterglow light curves. Adapted from Zhang *et al.* (2006)

3.2.2 Observational properties of the GRB afterglows

The main observational properties of late time afterglow radiation are (see Kumar & Zhang, 2015, and references therein):

- They exhibit a rough power law decay $F \propto t^{-\alpha}$, with $\alpha \sim 1$. This is consistent with the standard external shock model.
- A temporal break in the light curve at around one day or so, which is followed by a steeper decay ($\alpha \sim 2$). This is consistent with the theoretical prediction of a jet break.
- The radio afterglow rises and peaks at around 10 days. Then it starts to fade. It can be interpreted as the passage of ν_m or ν_a.
- The broad-band afterglow spectrum can be fitted with a broken power law. This is

expected for synchrotron radiation.

- For bursts with high quality data richer features have been observed that deviate from the simple standard model predictions. This suggests that the physics involved in the afterglow mechanisms, and/or the progenitor environments are more complex and can vary from event to event.

The *Swift* satellite was a step forward in the understanding of GRB afterglows. Its observations revealed several surprising emission components in the early X-ray afterglow not predicted by the standard model. Figure 3.13 shows the canonical X-ray light curve from XRT (Zhang *et al.*, 2006). The prompt phase is indicated by 0;

I This is the steep decay phase. The standard interpretation is that this is the tail of the prompt emission. Detailed analyses suggest that it can be due either to the high-latitude curvature effect (Zhang *et al.*, 2009), or by a rapidly expanding cocoon (Pe'er *et al.*, 2006), among other explanations.

II This is the shallow decay phase. The plausible interpretation is that it arises when energy is injected to the decelerating external shock. This model predicts achromatic breaks, so it cannot explain chromatic afterglows, so another mechanism has to be invoked. Some examples are the two-component jet and the reverse shock.

III This is known as the standard afterglow. It starts when the injection that started the previous phase finishes.

IV This steepening is the expected result of a jet break.

V This represent X-ray flares. They are usually interpreted as due to re-start of the GRB central engine. Other ideas include delayed magnetic dissipation activity and anisotropic emission in the blast wave comoving frame.

Zones marked with solid lines (I and III) are the most common, being the other shown only in a small fractions of bursts. An alternative and more simple way to describe the afterglow is differentiating two components: the "prompt" component (0 and I), probably related with the γ-ray emission, and the "afterglow" component (II, III, and IV). In any case, the afterglow modelling in the *Swift* era is much more complicated due to the complex behaviour seen in the light curves. Therefore, more detailed studies are needed to address questions such as which fraction of the afterglows can be explained within the standard external shock model, and whether are the observed discrepancies due to intrinsic differences in the central engine.

3.2.2.1 Polarisation

Polarimetric measurements are important because they are directly connected with the issue of magnetic fields and their geometry in GRBs, which remain an open question. Early attempts showed that the polarised flux is lower than 3% with a constant or smoothly variable level (e.g., Covino *et al.*, 2005). The first measurements made before and after the optical break (Gorosabel *et al.*, 2004) showed that there is no large variation (from 2.7% to 1.3%). The same weak variation is valid for the polarisation angle.

3.3 GRB-SN association

3.3.1 Photometric properties

The observer frame, optical LCs span more than 8 mags at a given observer frame post-explosion epoch. The peak SN brightness during its "bump" phase ranges from $R = 19.5$ for GRB 130702A to $R = 25$ for GRB 021211. For a GRB-SN event, there are 3 flux components in each measurement:

1. The afterglow
2. The SN
3. The host galaxy

The procedure to decompose each contribution is described in Fig. 3.15. Once the SN LC is obtained, it is usually compared to a template supernova, where the relative brightness (k) and width (stretch factor) are determined. Another approach is to fit a phenomenological model to the resultant SN LC, such as the Bazin function (Bazin *et al.*, 2011). The parameters that one can determine are the peak flux, the rise and decay times, and the width of the LC, such as Δm_{15} parameter (decrement in magnitudes from the peak to 15 days later).

Figure 3.14 shows the bolometric LCs of 12 GRB-SNe. The average peak luminosity of the sample, excluding SN 2011kl, is $\bar{L_p} = (1.03 \pm 0.36) \times 10^{43}$ erg s^{-1}. Excluding this monster event, which is $\sim 5\sigma$ more luminous than the rest average, we get $\bar{L_p} = (1.24 \pm 0.71) \times 10^{43}$ erg s^{-1}. The average peak time is $t_p = 13.16 \pm 2.61$ days and $t_p = 12.95 \pm 2.72$ days. Similarly, $\Delta m_{15} = 0.72 \pm 0.12$ and $\Delta m_{15} = 0.79 \pm 0.13$. Therefore, the inclusion or not of SN 2011kl has little effect on the derived values. There are no

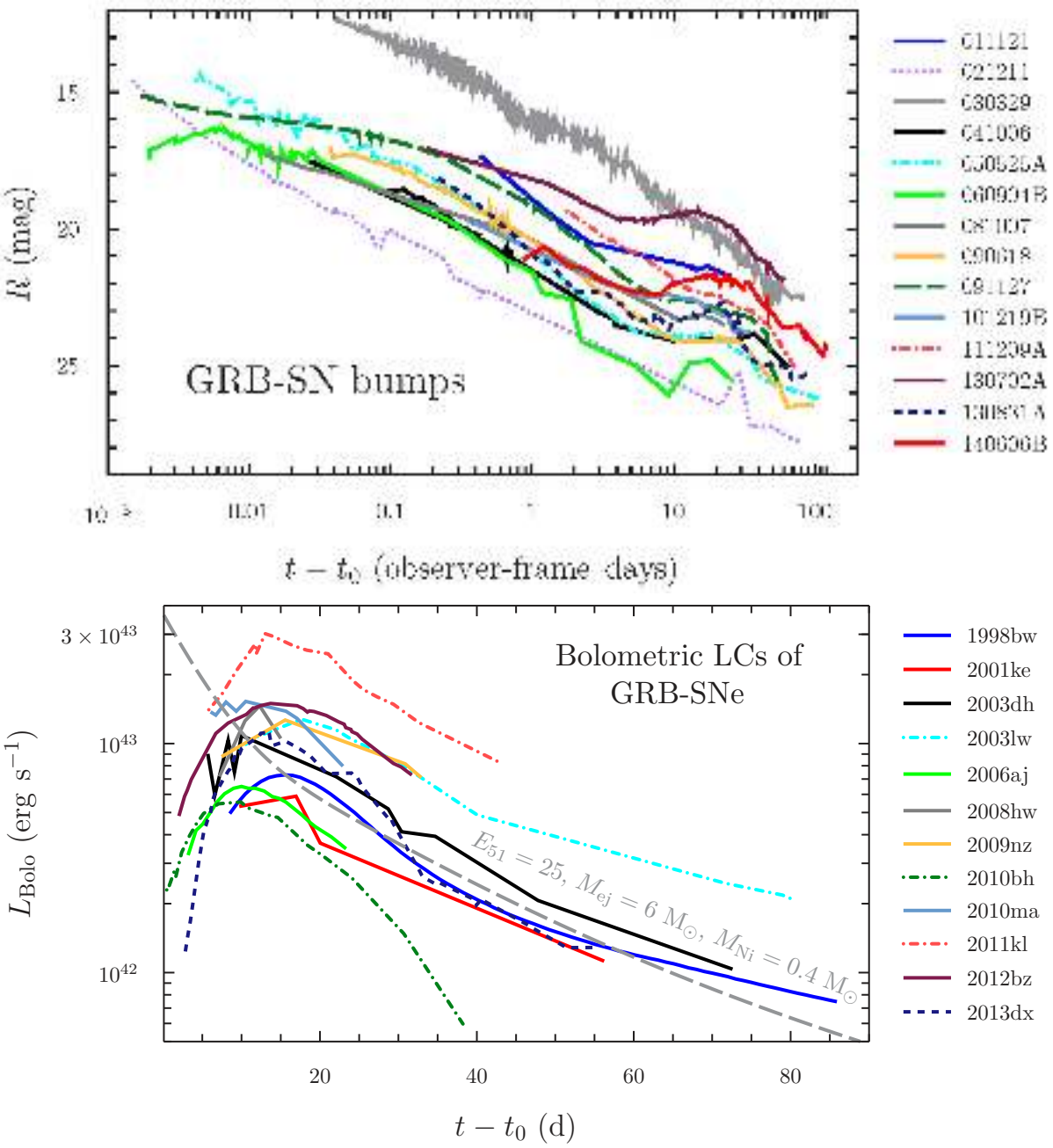

Figure 3.14: *Upper panel:* A mosaic of GRB-SNe (AG & SN). Clear SN bumps are observed for all events except SN 2003dh. *Lower panel:* Bolometric LCs of a sample of GRB-SNe. Adapted from Cano *et al.* (2016).

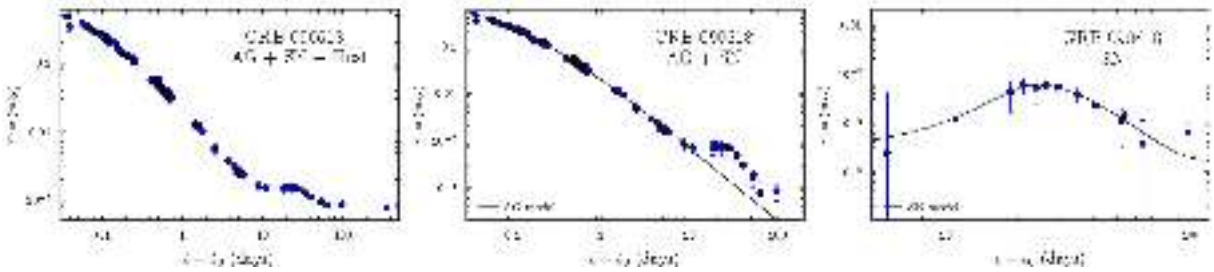

Figure 3.15: An example decomposition of the optical (R-band) LC of GRB 090618. *Left*: For a given GRB-SN event, the single-filter monochromatic flux is attributed as arising from three sources: the AG, the SN, and a constant source of flux from the host galaxy. *Middle*: Once the observations have been dereddened, the host flux is removed, either via the image-subtraction technique or mathematically subtracted away. At this point a mathematical model composed of one or more power-laws punctuated by break-times are fit to the early LC to determine the temporal behaviour of the AG. *Right*: Once the AG model has been determined, it is subtracted from the observations leaving just light from the SN. Adapted from Cano *et al.* (2016).

statistical differences in the average bolometric properties between the different GRB-SNe subtypes. As found in previous studies, relativistic SNe IcBL are roughly half as energetic as GRB-SNe, and contain approximately half ejecta mass and Niquel content therein.

3.3.2 Spectroscopic properties

Optical and NIR spectra have been obtained for a dozen GRB-SNe. Those of the highest quality show broad lines of O I, Ca II, Si II, and Fe II near maximum light. Velocities of the order of 20,000 – 40,000 km s^{-1} (for the Fe IIλ5169 transition) have been detected.

3.3.3 Phenomenological classification

Based on $E_{\gamma,\mathrm{iso}}$

- *ll*GRB-SNe: low luminosity GRB-SNe ($E_{\gamma,\mathrm{iso}} < 10^{50}$erg)
- INT-GRB-SNe: intermediate luminosity GRB-SNe ($10^{50} < E_{\gamma,\mathrm{iso}} < 10^{51}$erg)
- GRB-SNe: typical/cosmological GRB-SNe ($E_{\gamma,\mathrm{iso}} > 10^{51}$erg)

Attending the duration of the prompt emission, ultra-long-duration GRB-SNe (ULGRB-SNe) are those events with a γ-ray emission lasting several thousand seconds.

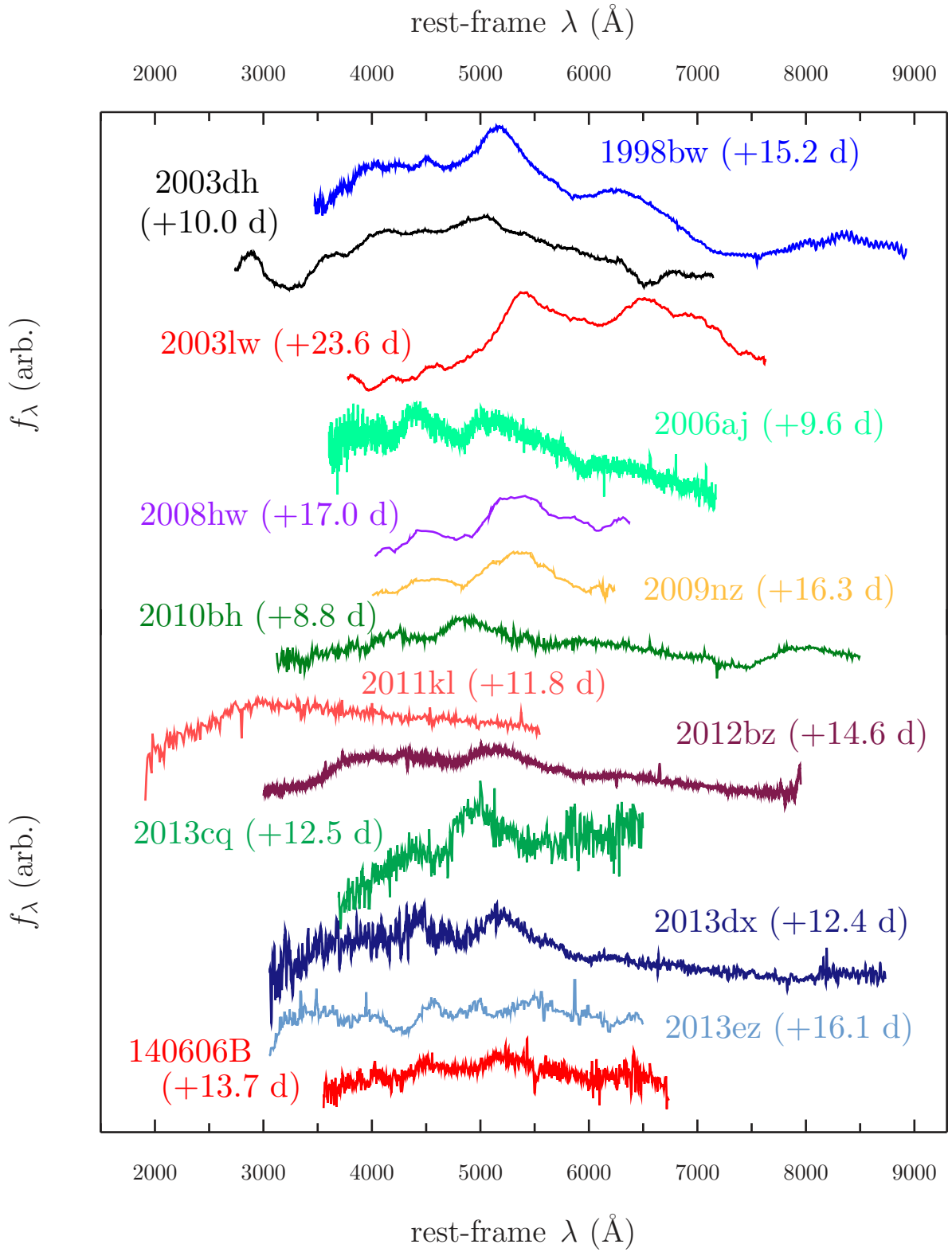

Figure 3.16: Peak/near-peak spectra of GRB-SNe. The spectra have been arbitrarily shifted in flux for comparison purposes, and to exaggerate their main features. Host emission lines have been manually removed. Adapted from (Cano *et al.*, 2016).

It is highly debated whether the γ-ray coming from *ll*GRB-SNe arises from the same mechanism than typical events or whether from a relativistic shock breakout (SBO). Bromberg *et al.* (2011); Kaneko *et al.* (2007) demonstrated that a key observable of *ll*GRBs are their single-peaked, smooth, non-variable γ-ray LCs compared to the erratic LCs of jetted-GRBs. An SBO is likely present in all lGRB events, but the energy pulse is several orders of magnitude lower ($E_{\rm SBO} = 10^{44} - 10^{47}$ erg). This means that that SBO are likely not possible to detect at redshifts higher than $\sim$0.1. Although the SBO model successfully explains the observed characteristics of GRBs 980425, 031203, 060218, and 100316D, their SBO origins are still widely debated.

Thermal black-body components in X-ray spectra have been detected for several events, which could be attributed to thermal emission arising from a cocoon that surrounds the jet, or perhaps associated to a relativistic shock breakout. The large inferred temperatures could indicate that the radiation does not come from an SBO.

3.3.4 Short GRBs and kilonova emission

The compact coalescence scenario predicts, apart from the afterglow, emission from a SN-like transient called kilonova (KN). The KN prediction is a consequence of the decompression of the neutron star material, where a compact binary coalescence provide excellent conditions for the rapid-neutron capture process (r-process; Li & Paczynski, 1998). This process occur very quickly, and is completed in less than a second, leaving behind a broad distribution of radioactive nuclei whose decay, once the ejected material becomes optically thin, powers an electromagnetic transient in a process similar to that expected to cause the GRB-SNe. There were several unfruitful searches for KN emission, getting null results until the detection of the KN associated to GRB 130603B (Tanvir *et al.*, 2013).

3.4 GRB host galaxies

3.4.1 Long GRBs

By studying the population of galaxies in which GRBs are produced and the location of GRBs inside their hosts, we can constrain the characteristics or the GRB progenitor and how it is formed (for a review see, e.g., Perley *et al.*, 2016b).

The link between lGRBs and the explosions of massive stars is well established (Hjorth & Bloom, 2012). Therefore, assuming the simplest case in which the GRB rate is inde-

pendent of everything but the overall star formation rate (SFR), it is observationally expected that GRBs stochastically sample the star formation regions. However, as previously pointed out, there are several theoretical arguments to expect that the reality may be more complex.

In order to assess this question, the population of GRB hosts has to be characterised through cosmic time. Many studies simply observe the distribution of total SFR as a function of galaxy parameters in known surveys and apply empirical laws relating properties and finding the best fit model (e.g., Trenti *et al.*, 2015). Semi-analytical models have been also developed to avoid the observational dependence, but these techniques are still limited by the uncertain physics surrounding star formation and feedback.

When constructing GRB host samples, great care has to be taken to make sure that selection biases are either minimised and/or quantified. Straightforward sources of bias are dust extinction and the instrumental threshold.

3.4.1.1 Photometric properties

The GRB host population studies in the pre-*Swift* era showed that they were very faint galaxies in comparison to other star-forming galaxies, with a lack of massive galaxies (Le Floc'h *et al.*, 2003). However, it must be taken into account that the number of small galaxies in the Universe is much larger and GRBs do not select galaxies on the way flux-limited surveys do. The same pre-*Swift* samples exhibited relatively blue colors. While not quantified in detail, the apparent absence of older or dusty systems suggested a trend to a metal-poor galaxy population. Systematic studies of larger samples of optically-reddened and optically-undetected burst (e.g., Perley *et al.*, 2013) confirmed that most obscured GRBs are hosts within luminous, massive, and reddened, precisely the systems that were missing.

Given the importance of the sample selection for minimising selection biases, several efforts were recently made, from which the most relevant are:

- **TOUGH** (Hjorth *et al.*, 2012): This sample contains 69 hosts.
- **SHOALS** (Perley *et al.*, 2016a): This sample contains 119 hosts.
- **BAT6** (Salvaterra *et al.*, 2012): This sample contains 58 hosts.

The selection criteria are quite similar, usually combining a Sun distance constraint, a foreground extinction limit, and a time requirement for the *Swift* slew. BAT6 and SHOALS also require a minimum peak flux or fluence to exclude faint burst. Finally,

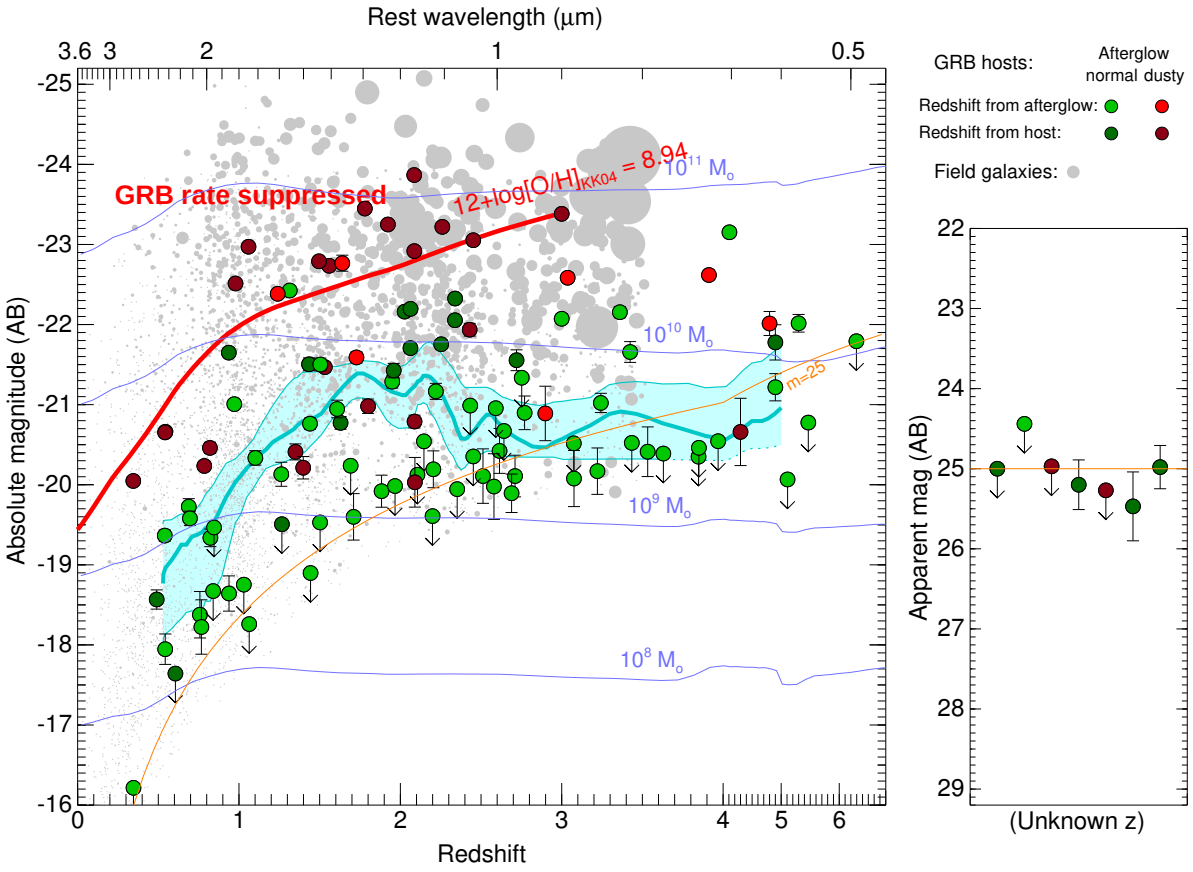

Figure 3.17: Near-infrared luminosities of GRB hosts as a function of redshift for a large and unbiased sample of 119 GRB hosts from the SHOALS sample, compared to star-forming galaxies (gray, from Kajisawa *et al.*, 2011). The horizontal blue curves indicate equivalent stellar masses. GRBs sample galaxies of all masses and redshifts, but rarely occur in the most luminous galaxies, especially at low redshift (z ¡ 1.5). The red curve shows the luminosity of a galaxy at the metallicity threshold of 12 + log[O/H] = 8.94. Adapted from Perley *et al.* (2016b).

TOUGH and BAT6 exclude bursts near celestial poles. These techniques have increased redshift completeness from the initial ∼30% of the pre-*Swift* era to 90% or more.

The K-band luminosity of low redshift GRBs from BAT6 was analysed by Vergani *et al.* (2015). They found that the deficiency of massive galaxies is still present in this unbiased sample. Furthermore, as NIR luminosity is a tracer of the galaxy stellar mass, and it is correlated with the metallicity, this can be interpreted as a metallicity bias. Recently, Perley *et al.* (2016c) found that the GRB rate increase with redshift and is uniform below a critical value of log [O/H] = 8.94, dropping by about an order of magnitude in more enriched galaxies. Schulze *et al.* (2015) also found that the distribution of UV luminosities in the TOUGH sample dominate the faint side at low and very high, but not at intermediate redshifts. This trend still needs to be confirmed.

Most luminous galaxies contain a huge amount of dust that scatter UV photons converting them into FIR/submm emission (dusty star-forming galaxies, DSFG; Casey *et al.*, 2014). Studies using large samples and sensitive instruments at long wavelengths indicate that DSFG hosts are not uncommon, but they represent a small percentage of the GRB host population.

3.4.1.2 Spectroscopic properties

Comparison between spectroscopic GRB and field samples of galaxies are subject to complex biases, but derived spectroscopic properties of GRB hosts are quite similar to what is inferred from photometric measurements (Krühler *et al.*, 2015). GRBs in very metal rich and very metal poor galaxies are uncommon but present, being the median metal content about 8.5. GRB hosts tend to be metal poorer than field-selected star-forming galaxies of the same mass, providing some evidence that metallicity is a dominant factor.

We have to keep in mind that galaxies do not have a homogeneous metallicity, and that the value measured in the host can be different from the progenitor's metal content. Niino (2011) found that both the existence of few high metallicity hosts as well as the systematically low metallicities of typical GRB hosts can be explained even if the progenitor is a moderately metal poor star.

Early samples suggested that strong Lyα emission could be common in GRB hosts (Fynbo *et al.*, 2003). However, larger and more uniform samples do not confirm this (Milvang-Jensen *et al.*, 2012).

Other authors have searched for Wolf-Rayet and other very short-lived starburst features in nearby hosts (Han *et al.*, 2010) and found some evidence pointing to a likely very young progenitor, although evidence are still weak.

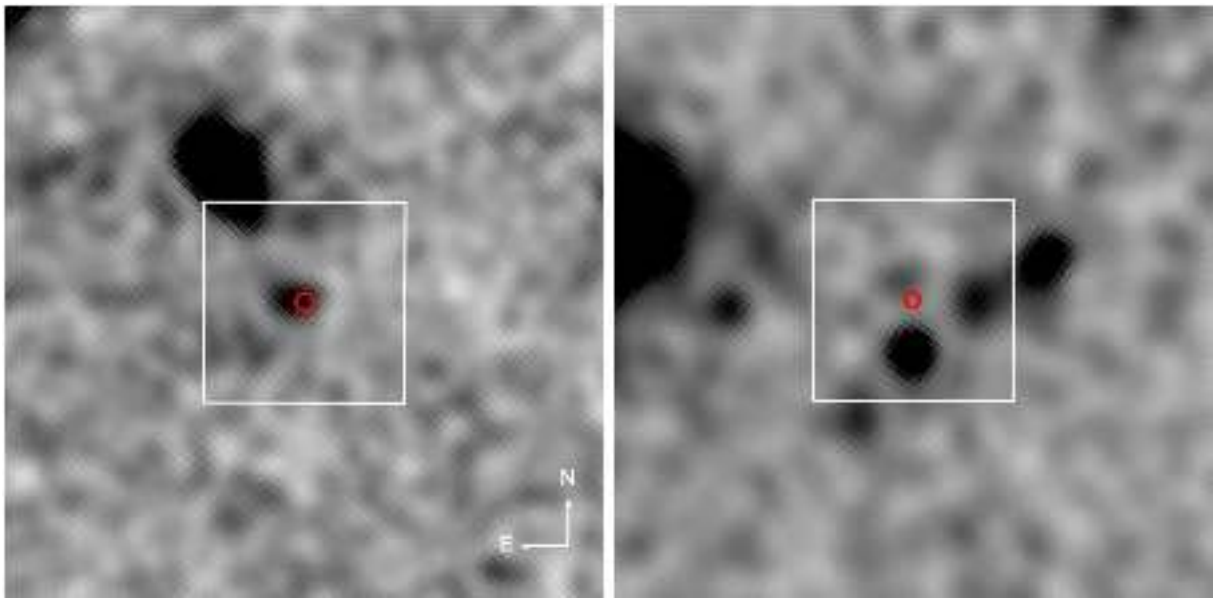

Figure 3.18: Deep HST $F140W$ filter images (lightly smoothed) of the locations of GRBs 050904 (left) and 140515A (right). Both bursts had redshifts of $z = 6.3$ and in each case the host is detected at AB magnitude ~ 28, underlying the GRB positions (indicated by red circles). These are the first GRB host galaxies found in emission at $z > 5$. The white boxes are 2 arcsec on a side. Adapted from McGuire *et al.* (2015).

3.4.1.3 GRB hosts at very high redshifts

GRBs are a great tool to study "normal" high-redshift galaxies. The GRB light first allows us to study them from the inside, as we have already shown. Once the afterglow has faded away, deep searches can lead us to the detection of the actual emission from the host. Even if these searches can be expensive in telescope time, they lead to useful results, as we know where to look: Where the GRB was produced there has to be an underlying host.

Recently, HST observations have, for the first time, detected two $z \gtrsim 6$ GRB hosts (GRB 050904 and GRB 140515A McGuire *et al.*, 2015). The luminosity of these hosts suggests they are consistent with being faint examples of the LBG found in other deep HST surveys.

3.4.2 Short GRBs

Short GRBs, produced by the merger of two compact objects, are expected to be located in a range of normal star forming and elliptical galaxies, more specifically in the outskirts which is the usual location of old merging binaries. The observation of short GRB host has indeed shown a diverse type of galaxies, with star formation rates, metallicities, sizes,

and offsets that are distinct from those of long GRB hosts, confirming that they come from different progenitors.

3.5 Cosmology with GRBs

3.5.1 Luminosity correlations of GRBs

Following (Petitjean *et al.*, 2016), the isotropic luminosity of a GRB is

$$L_{iso} = 4\pi d_L^2 P_{bolo} \tag{3.4}$$

and the isotropic energy

$$E_{iso} = \frac{4\pi d_L^2 S_{bolo}}{1+z} \tag{3.5}$$

where P_{bolo} is the bolometric peak flux, S_{bolo} the bolometric fluence, and d_L is the luminosity distance

$$d_L = (1+z)\frac{c}{H_0}\int_0^z \frac{dz'}{E(z')} \tag{3.6}$$

where $E^2(z) = \Omega_M(1+z)^3 + \Omega_X f_X(z)$, and $f_X(z)$ is given by

$$f_X(z) = \exp\left[3\int_0^z \frac{1+w(\tilde{z})}{1+\tilde{z}}d\tilde{z}\right] \tag{3.7}$$

where $w(\tilde{z})$ is the equation of state of the dark energy. Eq. 3.6 takes the form

$$d_L = (1+z)\frac{c}{H_0}\int_0^z \frac{dz'}{\Omega_M(1+z')^3 + \Omega_\Lambda} \tag{3.8}$$

in a ΛCDM cosmology.

Applying the collimation correction, the total energy is

$$E_\gamma = E_{iso} \cdot F_{beam} \tag{3.9}$$

with the beaming factor $F_{beam} = 1 - \cos\theta_{jet}$ with a jet opening angle θ_{jet}. P_{bolo} and S_{bolo}, the bolometric fluence, are usually computed from the differential energy spectrum, $\Phi(E)$

$$P_{bolo} = P \times \frac{\int_{1/(1+z)}^{10^4/(1+z)} E\Phi(E)dE}{\int_{E_{min}}^{E_{max}} E\Phi(E)dE} \tag{3.10}$$

$$S_{bolo} = S \times \frac{\int_{1/(1+z)}^{10^4/(1+z)} E\Phi(E)dE}{\int_{E_{min}}^{E_{max}} E\Phi(E)dE} \tag{3.11}$$

where P and S are the observed peak and fluence, and (E_{min}, E_{max}) the detection thresholds of the observing instrument. Usually, $\Phi(E)$ is taken to be the Band function (Band *et al.*, 1993).

The GRB bolometric and isotropic luminosity function can be described by a broken power law of the form

$$\Phi(L)dL = \Phi_0 \left[\left(\frac{L}{L_b} \right)^{\alpha_1} + \left(\frac{L}{L_b} \right)^{\alpha_2} \right]^{-1} dL \tag{3.12}$$

where the break luminosity L_b is $\sim 10^{52.2}$ erg s^{-1}. Several studies agree that the high luminosity slope is steep $\alpha_2 \sim 2.5$. The value of α_1 depends on whether one includes low luminosity GRBs ($\alpha_1 \sim 1.2$) or not ($\alpha_1 \sim 0.5$). The normalisation Φ_0 depends on the local rate of GRBs per unit volume, which is constrained to be around 1 Gpc^{-3} yr^{-1}. Low luminosity GRBs have a higher local event rate, which is inconsistent with a simple extrapolation of the high luminosity GRB luminosity function to low luminosities, and therefore they constitute a different GRB population. Its exact luminosity function form is not well constrained due to the current instrumental sensitivity limitations.

The most relevant correlations found to date are:

L_{iso} - τ_{lag}: It was first discovered by Norris *et al.* (2000), but recently challenged by a recent work by Bernardini *et al.* (2015). This correlation shows that the more luminous is a burst, the less time lag has it ($L_{iso} \propto \tau_{lag}^{-1.25}$)

E_{iso} - E_{peak}: Amati *et al.* (2002) found that E_{peak} and E_{iso} are correlated. This correlation can be interpreted from different theoretical frames, such as the synchrotron mechanism in relativistic shocks and emission from off-axis relativistic jets.

E_γ - E_{peak}: Ghirlanda *et al.* (2004a) realized that E_{peak} also correlates with E_γ tightly, showing also that can be a promising tool for constraining dark energy (Ghirlanda *et al.*, 2004b). It can be understood within the annular jet and photosphere models.

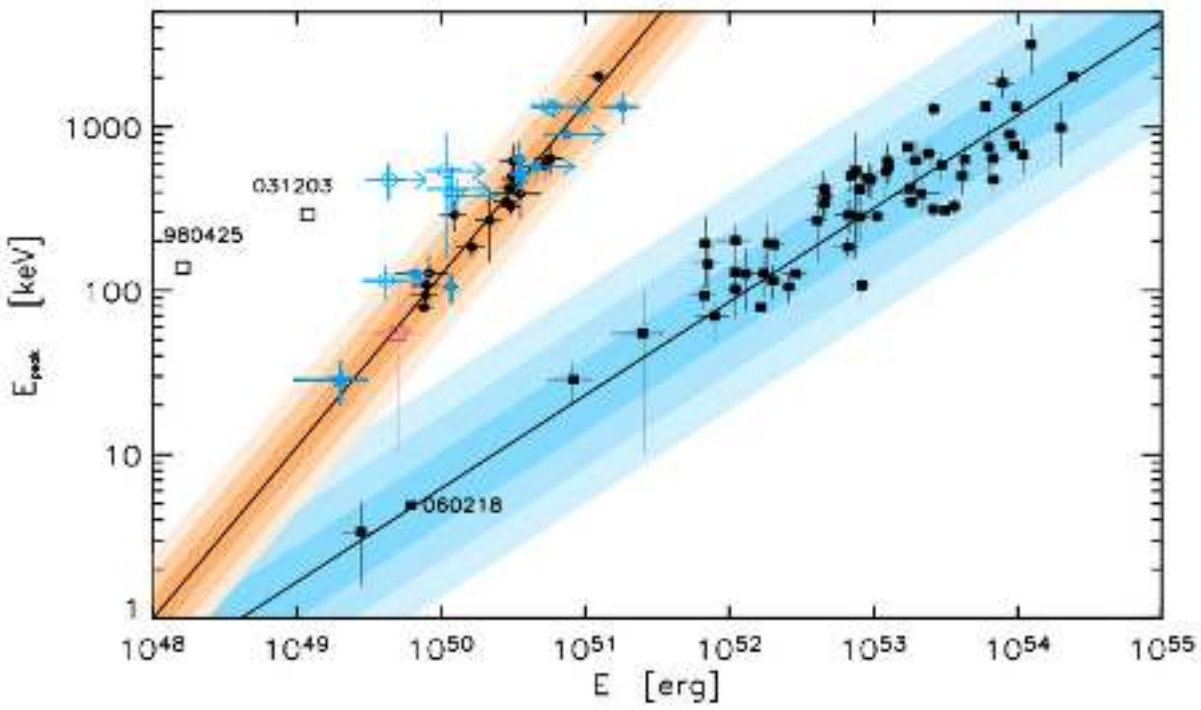

Figure 3.19: E_{peak} - E_{γ} and E_{peak} - E_{iso} correlations. Adapted from Ghirlanda *et al.* (2007).

Several works have shown that these and other correlations must be physical, but that they can also be affected by instrumental selection effects (e.g. Shahmoradi & Nemiroff, 2011). In any case, correlations are useful to constrain dark energy and cosmological parameters (e.g., Wang *et al.*, 2015, see Fig. 3.20).

3.5.2 SFR derived from GRBs

The association of long GRBs with core-collapse supernovae (Hjorth *et al.*, 2003; Stanek *et al.*, 2003) opened a new window to measure the high-z SFR. However, one crucial problem, still to be solved, is how to calibrate the SFR with the GRB event rate.

Before *Swift*, this function was determined by fitting the observed $\log N$ - $\log P$ distribution (e.g. Guetta *et al.*, 2005). The form of this function has to be assumed (usually either a broken power-law or a power-law with exponential cut-off) and the parameters are degenerate, so it is challenging to obtain. A straightforward method is proposed by Lynden-Bell (1971), developed by Efron & Petrosian (1992), and used by, e.g., Wu *et al.* (2012). Results pointed that the GRB rate traces the SFR in a wide range of redshifts. However, Yu *et al.* (2015) found for the first time that the GRB rate shows an unexpectedly low-redshift excess compared to the observed SFR (see Fig. 3.22). This behaviour

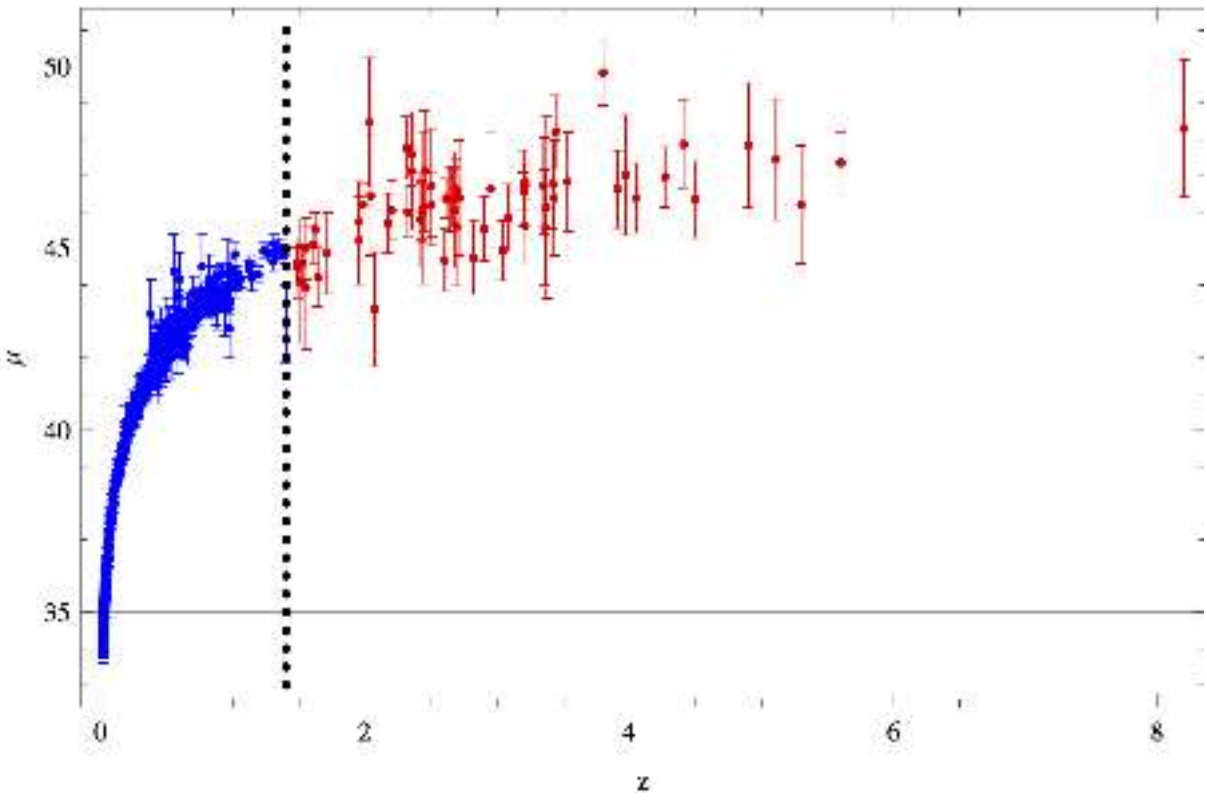

Figure 3.20: Hubble diagram of 557 SNe Ia plus 66 high-z GRBs. Adapted from Wang & Dai (2011b)

was confirmed by Petrosian *et al.* (2015). A possible explanation for this excess could be the definition of long GRB, as T_{90} is defined in the observer frame. Moreover, some GRBs shows no SN, so they may be part of other GRB population. Finally, there may exist a subclass of low luminosity GRBs which progenitor may be different to the high luminosity bursts. Therefore, more physical criteria are required to classify GRBs and use them for cosmological purposes.

Another approach for studying SFR is proposed using only high-luminosity GRBs (e.g. Wang, 2013). The expected redshift distribution of GRBs is

$$\frac{dN}{dz} = F(z)\frac{\epsilon(z)\dot{\rho}_*}{\langle f_{beam}\rangle}\frac{dV_{com}/dz}{1+z} \tag{3.13}$$

where $F(z)$ represents the ability to obtain the redshift, $\epsilon(z)$ accounts for the fraction of stars producing GRBs, and $\dot{\rho}_*$ is the SFR density. GRBs unobservable are accounted for through $\langle f_{beam}\rangle$, and $\epsilon(z) = \epsilon_0(1+z)^\delta$, with ϵ_0 an unknown constant that includes the absolute conversion from the SFR to the GRB rate in a given GRB luminosity bin. A value of $\delta \sim 0.5 - 1.2$ was inferred by Wang (2013). For a flat Universe

$$\frac{dV_{com}}{dz} = 4\pi D_{com}^2 \frac{dD_{com}}{dz} \tag{3.14}$$

with

$$D_{com}(z) = \frac{c}{H_0}\int_0^z \frac{dz'}{\sqrt{\Omega_m(1+z')^3 + \Omega_\Lambda}} \tag{3.15}$$

Figure 3.21 shows the isotropic luminosity ($L_{iso} = E_{iso}(1+z)/T_{90}$) distribution as a function of redshift. The shaded area approximates the threshold of *Swift*/BAT ($F_{lim} \sim 1.2 \times 10^{-8}$ erg cm^{-2} s^{-1}. A luminosity cut of $L_{iso} > 10^{51}$ erg s^{-1} is taken for the z-range from 0 to 4, that is used to calibrate the SFR-to-GRB conversion because SFR is well constrained at $z< 4$. The theoretical number of GRBs in the z-bin $1-4$ is

$$N_{1-4}^{th} = A\int_1^4 dz(1+z)^\delta \dot{\rho}_*(z)\frac{dV_{com}/dz}{1+z} \tag{3.16}$$

where $A = \frac{\Delta t \Delta\Omega F_0}{4\pi\langle f_{beam}\rangle}$ depends on observing time Δt, and the angular sky coverage $\Delta\Omega$. For a generic bin,

$$N_{z_1-z_2}^{th} = \langle\dot{\rho}_*\rangle_{z_1-z_2} A\int_{z_1}^{z_2} dz(1+z)^\delta \frac{dV_{com}/dz}{1+z} \tag{3.17}$$

so we can obtain the SFR as

$$\langle \dot{\rho}_* \rangle_{z_1-z_2} = \frac{N^{obs}_{z_1-z_2}}{N^{obs}_{1-4}} \frac{\int_1^4 dz (1+z)^\delta \dot{\rho}_*(z) \frac{dV_{com}/dz}{1+z}}{\int_{z_1}^{z_2} dz (1+z)^\delta \frac{dV_{com}/dz}{1+z}} \tag{3.18}$$

The SFR derived from GRBs is shown in Fig. 3.22 as filled circles. These values are significantly larger than the ones inferred from observed galaxies. This could be due by a observational bias. However, the GRB rate can be enhanced at high-z by some physical reasons.

- **Metallicity evolution**: A natural origin of this excess could be due to the lower amount of metals at high-z. The most popular model for the physical explanation of LGRBs by Woosley (1993) predicts that GRBs originate from the collapse of a high mass (>30$M_\odot$), high rotating star. Low metallicities (0.1-0.3$Z_\odot$) allow progenitors to keep more of their mass to loose by stellar winds, and therefore preserve angular momentum.

- **Evolving initial mass function**: Wang & Dai (2011a) proposed that an excess in the GRB rate can be due to the evolution of the initial mass function (IMF), which determines the number of massive stars able to produce GRBs. This function has been suggested to evolve at high redshift to produce the transition from population III to population II stars.

- **Evolving luminosity function break**: (Virgili *et al.*, 2011) found that if the break of luminosity function evolves with redshift ($\propto L_b \times (1+z)^{\sim 0.8--1.2}$), BATSE and *Swift* data can be reconciled.

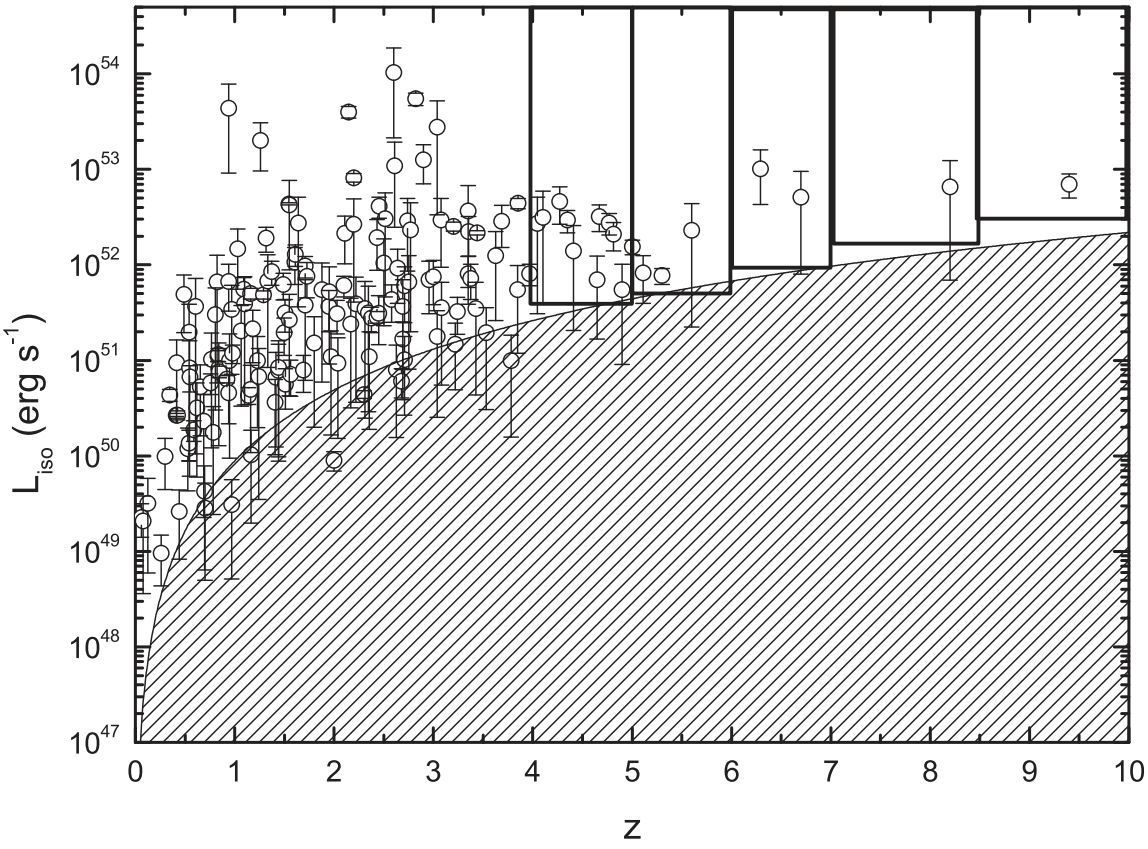

Figure 3.21: L_{iso} vs z for 157 lGRBs. The shaded area approximates the detection threshold of *Swift*. Adapted from Wang (2013).

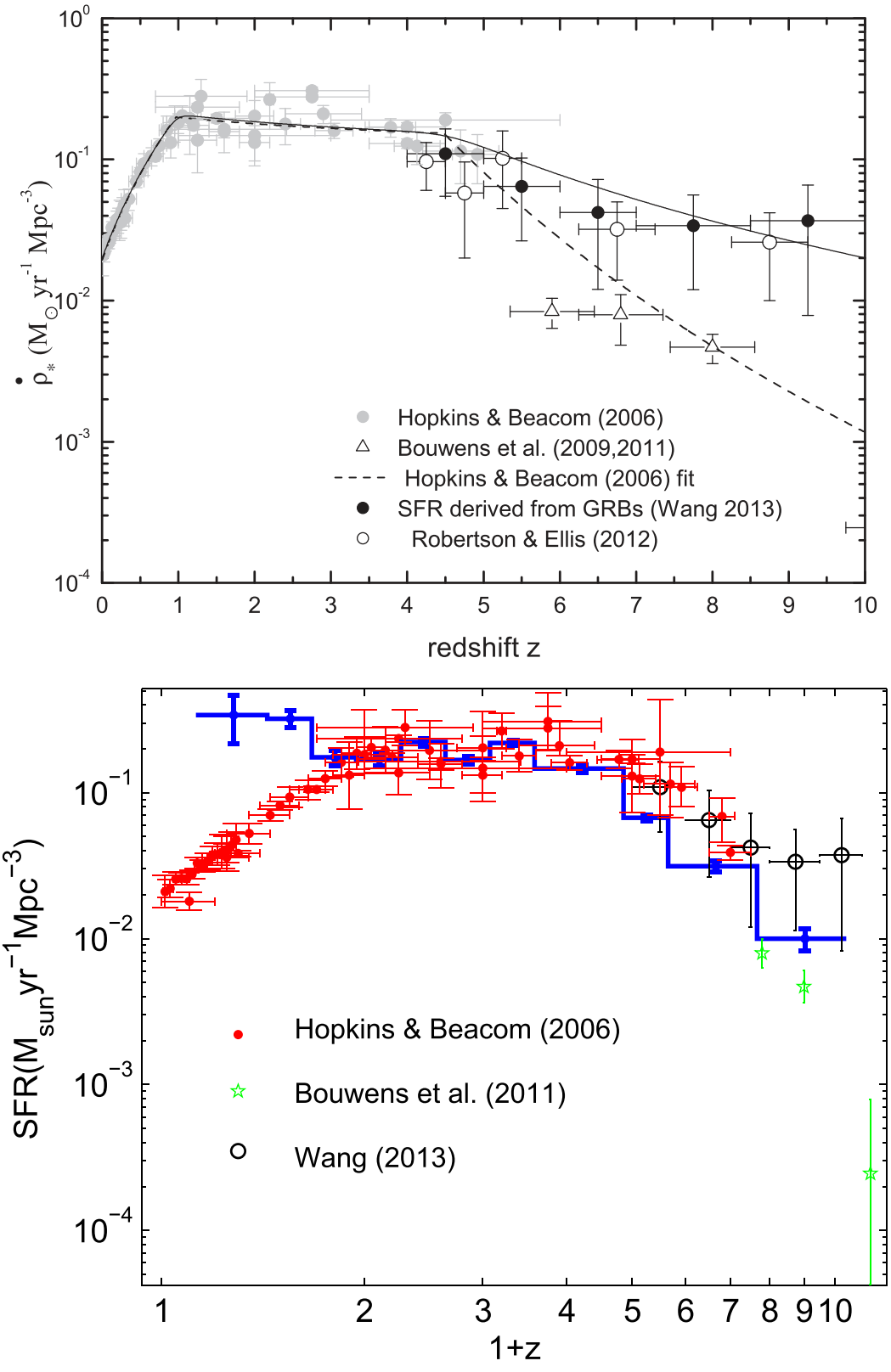

Figure 3.22: The cosmic star formation history. Adapted from Wang (2013, upper panel, which includes low luminosity GRBs) and Yu *et al.* (2015, lower panel, which includes only high luminosity GRBs).

PART I

MULTIWAVELENGTH STUDY OF GRB AFTERGLOWS

GRB 110715A: THE FIRST GAMMA-RAY BURST OBSERVED WITH ALMA

Chapter 1

Physics of Gamma-ray bursts and their afterglows

"Oppenheimer, they tell me you are writing poetry. I do not see how a man can work on the frontiers of physics and write poetry at the same time. They are in opposition. In science you want to say something that nobody knew before, in words which everyone can understand. In poetry you are bound to say... something that everybody knows already in words that nobody can understand."

— P.A.M. Dirac, *Brighter than a thousand Suns, R. Jungk, 1958*

Gamma-ray bursts (GRBs, Klebesadel *et al.*, 1973) are the most violent explosions in the Universe. They are traditionally classified into two types based on the duration (and the hardness) of their γ-emission: short and long GRBs (T_{90} $<$ 2 s with hard spectrum, and T_{90} $>$ 2 s with soft spectrum, respectively; Kouveliotou *et al.*, 1993). Counterparts of these flashes are detected from X-ray to radio bands, which are known as GRB *afterglows* and in some cases can be observed up to several months after the burst.

Currently, the most favoured model to explain the origin of GRBs is a highly magnetized relativistic jet. The prompt emission likely originates from either internal shocks in the photosphere of the jet or magnetic dissipation in a magnetically dominated jet. The afterglow emission, however, a long lasting synchrotron emission that is thought to originate from external shocks caused by the jet's interaction with the interstellar medium (ISM). In this chapter we will discuss the models that explain these emission mechanisms, which will be applied later in the study of GRB 110715A.

1.1 Synchrotron radiation

1.1.1 Single particle

The simplest model to derive the expression of the relativistic synchrotron emission is a jet that has a tangled magnetic field, i.e., its integration covers all the viewing angles. This angle is important because the radiation from each particle is strongly beamed in the direction on which the charge is travelling, since this motion is relativistic. Beamed means that the radiation appears to be concentrated in a narrow cone, and an observer will see the emission coming from a fraction $\sim 1/\gamma$ of its orbit.

First, we consider a single particle with mass m and energy

$$E = \gamma mc^2, \qquad \gamma \equiv (1-\beta^2)^{-1/2}, \qquad \beta \equiv v/c \tag{1.1}$$

moving with velocity v in a uniform magnetic field B. Equations of the motion of a particle in a magnetic field are

$$\left.\begin{array}{l} \frac{d}{dt}(\gamma m v) = \frac{q}{c}\vec{v} \\ \frac{d}{dt}(\gamma mc^2) = q\vec{v}\cdot\vec{E} = 0 \end{array}\right\} \frac{v^2}{r} = \frac{q}{\gamma mc} vB\sin\alpha_p \tag{1.2}$$

The combination of a circular and uniform motions results in helical motion. Its trajectory makes an angle α_p with the direction of B (called "pitch angle") and r is the radius of gyration around the field lines

$$r = \frac{v}{\omega_B \sin a_p}, \qquad \omega_B = \frac{qB}{\gamma mc} \tag{1.3}$$

where ω_B is the relativistic gyro-frequency (Larmor frequency) and q particle's charge.

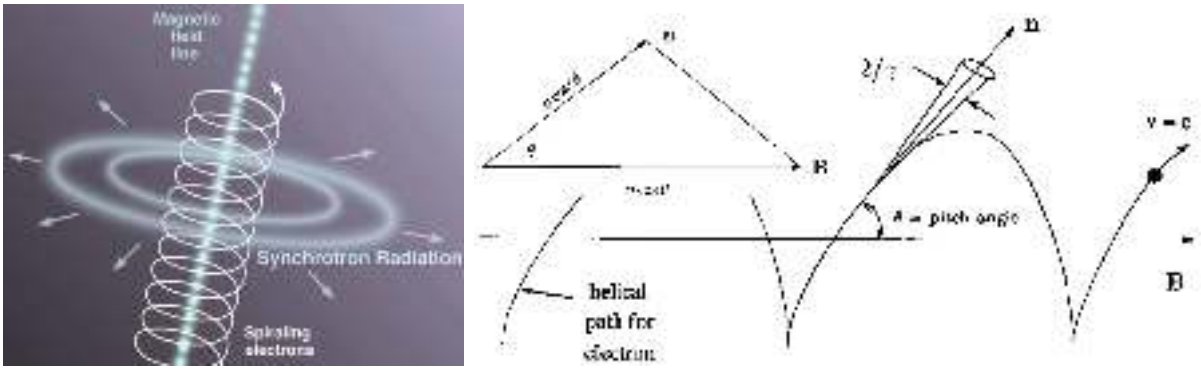

Figure 1.1: Schematic view of the synchrotron radiation by a single particle.

If the orbit were circular, then the observer would detect pulses with a period $P = 2\pi/\omega_B$. However, since the particle's guiding center is moving with velocity $v\cos\alpha_p$ along the field line, and the motion has a component projected toward the observer $v^2\cos^2\alpha_p$, there is a Doppler compression of the pulse period. They are spaced apart by a period

$$T = P\sin^2\alpha_p = \frac{2\pi}{\omega_B} \tag{1.4}$$

The relativistic aberration or *beaming* follows directly from the Lorentz transform

$$\begin{aligned} v_x &\equiv \frac{dx}{dt'}\frac{dt'}{dt} = (v'_x + v)\left(1 + \frac{\beta v'_x}{c}\right)^{-1} \\ v_y &\equiv \frac{dy}{dt'}\frac{dt'}{dt} = \frac{v'_y}{\gamma}\left(1 + \frac{\beta v'_y}{c}\right)^{-1} \end{aligned} \tag{1.5}$$

Defining as θ the angle between the direction of the emitted photon and the one of the electron, we get

$$\cos\theta = \frac{\cos\theta' + \beta}{1 + \beta\cos\theta'}, \qquad \sin\theta = \frac{\sin\theta'}{\gamma(1 + \beta\cos\theta')} \approx \frac{1}{\gamma} \approx \theta \tag{1.6}$$

since $1/\gamma << 1$. Therefore, we see the radiation confined to a very narrow beam of width $2/\gamma$.

The width of the pulse $\Delta t'$ is determined by the fraction of the gyromagnetic period P that the electron is radiating toward the observer, obtaining

$$\Delta t' = \frac{2mc}{qB\sin\alpha_p} \tag{1.7}$$

Since this pulse is subject to a Doppler compression,

$$\Delta t = \Delta t'(1 - \beta) \simeq \frac{\Delta t'}{2\gamma^2} \tag{1.8}$$

we obtain

$$\Delta t = \frac{1}{\gamma^3\omega_B\sin\alpha_p} \tag{1.9}$$

To compute the spectrum and polarisation of the synchrotron emission, we start from the expression

$$\frac{dW}{d\omega d\Omega} = \frac{q^2\omega^2}{4\pi^2 c}\left|\int \vec{n}\times(\vec{n}\times\vec{\beta}\exp[i\omega(t' - \vec{n}\cdot\vec{r}_0(t')/c]dt'\right|^2 \tag{1.10}$$

The emission can be expressed in terms of two polarisations: perpendicular and parallel to the projected direction of the magnetic field

$$\frac{dW}{d\omega d\Omega} = \frac{dW_\perp(\omega)}{d\omega d\Omega} + \frac{dW_\parallel(\omega)}{d\omega d\Omega} \tag{1.11}$$

Defining the quantities

$$\theta_\gamma^2 = 1 + \gamma^2\theta^2, \qquad \eta = \omega r\theta_\gamma^3/3c\gamma^3 \tag{1.12}$$

we get

$$\begin{aligned} \frac{dW_\perp(\omega)}{d\omega d\Omega} &= \frac{q^2\omega^2}{3\pi^2 c}\left(\frac{r\theta_\gamma^2}{\gamma^2 c}\right)^2 K_{\frac{2}{3}}^2(\eta) \\ \frac{dW_\parallel(\omega)}{d\omega d\Omega} &= \frac{q^2\omega^2\theta^2}{3\pi^2 c}\left(\frac{r\theta_\gamma}{\gamma c}\right)^2 K_{\frac{1}{3}}^2(\eta) \end{aligned} \tag{1.13}$$

where K are the modified Bessel functions. Since most radiation occurs at angles $\theta \sim 0$

$$\eta \simeq \eta(\theta = 0) = \frac{\omega}{2\omega_c}, \qquad \omega_c \equiv \frac{3}{2}\gamma^3\omega_B \sin\alpha_p \tag{1.14}$$

where ω_c is known as the characteristic frequency. Taking the element of solid angle to be $d\Omega = 2\pi \sin\alpha_p d\theta$, and defining

$$F(x) \equiv x\int_x^\infty K_{\frac{5}{3}}(z)dz, \qquad G(x) \equiv xK_{\frac{2}{3}}(x), \qquad x \equiv \frac{\omega}{\omega_c} \tag{1.15}$$

the total luminosity of the particle in each polarisation can be expressed as

$$\begin{aligned} P_\perp(\omega) &= \frac{\sqrt{3}q^3 B\sin a_p}{4\pi mc^2}[F(x) + G(x)] \\ P_\parallel(\omega) &= \frac{\sqrt{3}q^3 B\sin a_p}{4\pi mc^2}[F(x) - G(x)] \end{aligned} \tag{1.16}$$

The total emitted power is

$$P(\omega) = P_\perp(\omega) + P_\parallel(\omega) = \frac{\sqrt{3}q^3 B\sin a_p}{4\pi mc^2}F(x); \qquad P(\nu) = 2\pi P(\omega) \tag{1.17}$$

It can be derived, as a function of ω_c, that the peak frequency ω_m is

$$\omega_m = 0.29\omega_c \tag{1.18}$$

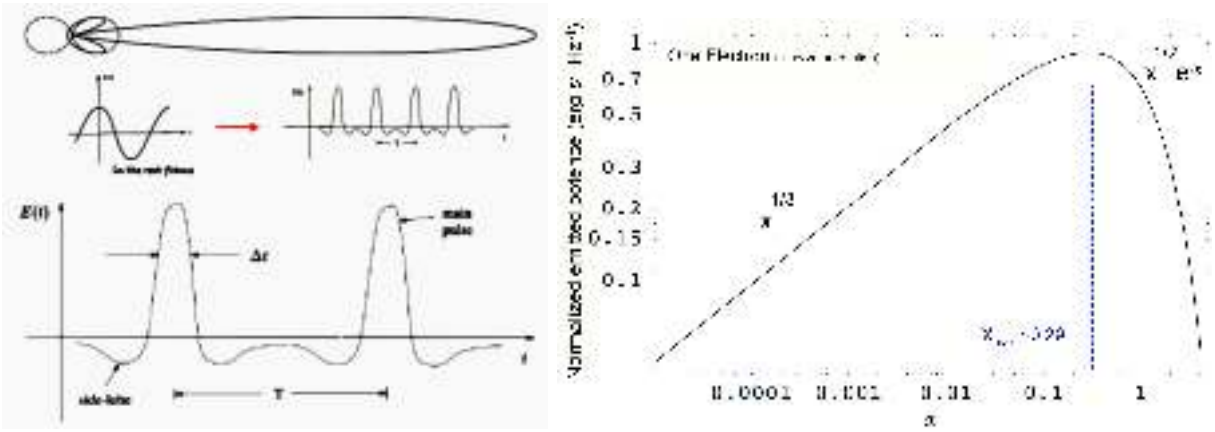

Figure 1.2: Synchrotron beaming and pulses (*left*) and spectrum (*right*) for a single particle.

and eq. 1.17 get the asymptotic forms

$$\begin{aligned} P(\omega) &\propto x^{1/3} \qquad & x << 1 \\ P(\omega) &\propto x^{1/2} \exp -x \qquad & x >> 1 \end{aligned} \tag{1.19}$$

This is illustrated in Fig. 1.2.

1.1.1.1 Population of particles

From an astronomical point of view, the observed spectrum emitted by a population of particles is much more relevant than that of a single particle. It will have a distribution of energies (and hence Lorentz factors) and pitch angles. The most common used distributions are an isotropic distribution of pitch angles ($p(\alpha_p) = \frac{1}{2}\sin\alpha_p$), and the power law distribution of Lorentz factors

$$N(\gamma)d\gamma = C\gamma^{-p}d\gamma, \qquad \gamma_m < \gamma < \gamma_M \tag{1.20}$$

It is also assumed that magnetic fields are tangled. Therefore

$$P_{tot}(\omega) = C\int_{\gamma_m}^{\gamma_M} P(\omega)\gamma^{-p}d\gamma \tag{1.21}$$

Solving the integral we get

$$P_{tot}(\omega) = \frac{\sqrt{3}q^3CB\sin\alpha_p}{2\pi mc^2(p+1)}\Gamma\left(\frac{p}{4}+\frac{19}{12}\right)\Gamma\left(\frac{p}{4}-\frac{1}{12}\right)\left(\frac{mc\omega}{3qB\sin\alpha_p}\right)^{-(p-1)/2} \tag{1.22}$$

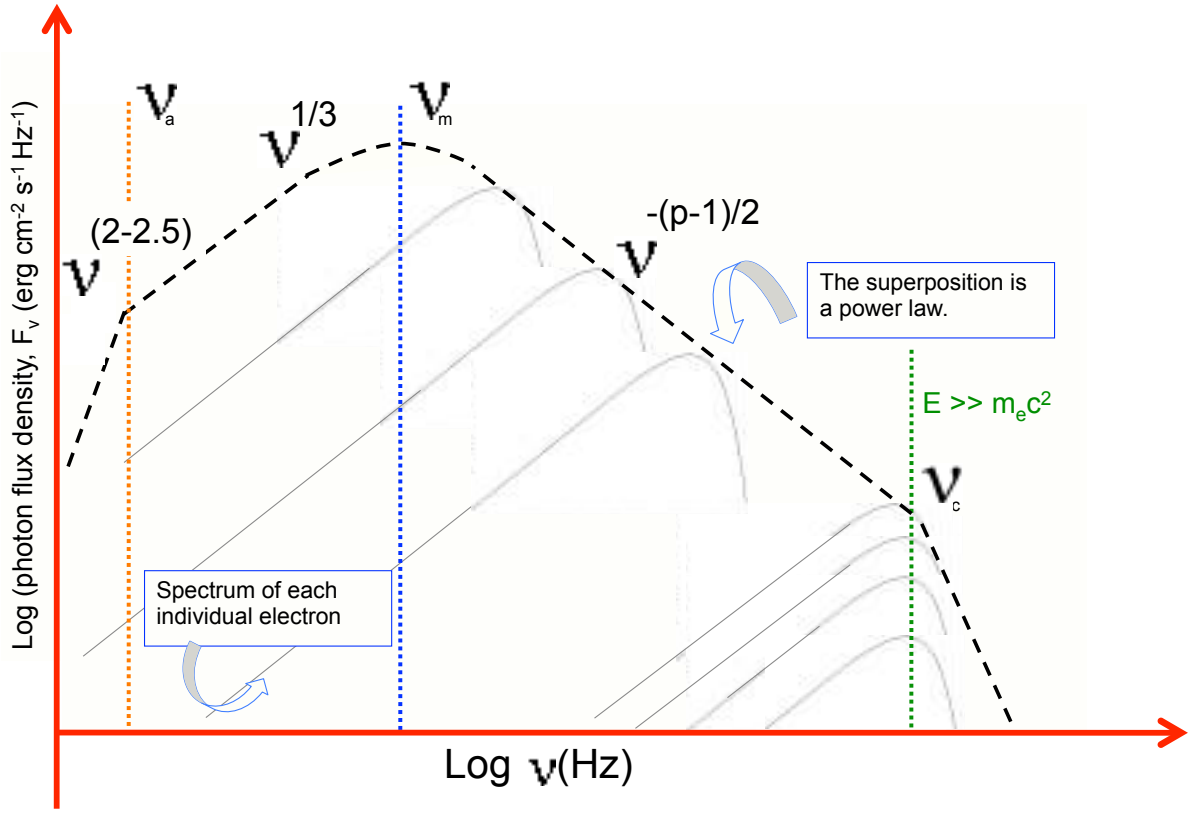

Figure 1.3: Spectrum of radiating particles with a power law distribution of energies.

In the observer frame, $P_{obs} = P_{tot}\Gamma^2$. This is a very important result, as it links an observable parameter, the power law in frequencies of the emission, to the power law slope of the particle energy distribution

$$\beta_r = (p-1)/2 \tag{1.23}$$

If the energy distribution has a cut off, the resulting emission will have a critical frequency ν_c where the power law spectrum has an exponential cut off (analogous to the single particle spectrum). This characteristic frequency usually scales like $\nu_c \propto \gamma_M B$, where γ_M is the maximum value of the γ distribution.

1.1.2 Self-absorption

If we consider radiation from a population of particles, the emitted photons will interact with the charges in the magnetic field. The absorption and stimulated emission can be

studied using the Einstein coefficients

$$\begin{aligned} j_\nu &= \frac{h\nu}{4\pi} n_1 A_{21} \phi(\nu) \\ \alpha_\nu &= \frac{h\nu}{4\pi}(n_1 B_{12} - n_2 B_{21})\phi(\nu) \end{aligned} \tag{1.24}$$

As for a given photon energy there are many possible transitions

$$\alpha_\nu = \frac{h\nu}{4\pi} \sum_{E_1} \sum_{E_2} (n(E_1)B_{12} - n(E_2)B_{21})\phi_{21}(\nu) \tag{1.25}$$

This is true because we are considering a tangled magnetic field. After some operations we get

$$\alpha_\nu = \frac{c^2}{8\pi h\nu^3} \sum_{E_2} [n(E_2 - h\nu) - n(E_2)] P(\nu, E_2) \tag{1.26}$$

where

$$P(\nu, E_2) = h\nu \sum_{E_1} A_{21}\phi_{21}(\nu) = (2h\nu^3/c^2) h\nu \sum_{E_1} B_{21}\phi_{21}(\nu) \tag{1.27}$$

Therefore, changing n(E) $\Rightarrow$ N(E)dE

$$N(E)dE = CE^{-p}dE, \qquad E_1 < E < E_2 \tag{1.28}$$

we finally obtain

$$\alpha_\nu = \frac{\sqrt{3}q^3}{8\pi m} \left(\frac{3q}{2\pi m^3 c^5}\right)^{p/2} C(B \sin\alpha_p)^{(p+2)/2} \Gamma\left(\frac{3p+2}{12}\right) \Gamma\left(\frac{3p+22}{12}\right) \nu^{-(p+4)/2} \tag{1.29}$$

Now, we can predict the observed spectrum

$$S_\nu = \frac{j_\nu}{\alpha_\nu} = \frac{P(\nu)}{4\pi\alpha_\nu} \tag{1.30}$$

in the optically thick and thin limits

optically thick: $F_\nu \propto I_\nu \propto S_\nu \propto B^{-1/2}\nu^{5/2}$

optically thin: $F_\nu \propto I_\nu \propto j_\nu \propto B^{(p+1)/2}\nu^{(1-p)/2}$

The turnover or *self-absorption* frequency is denoted by ν_a.

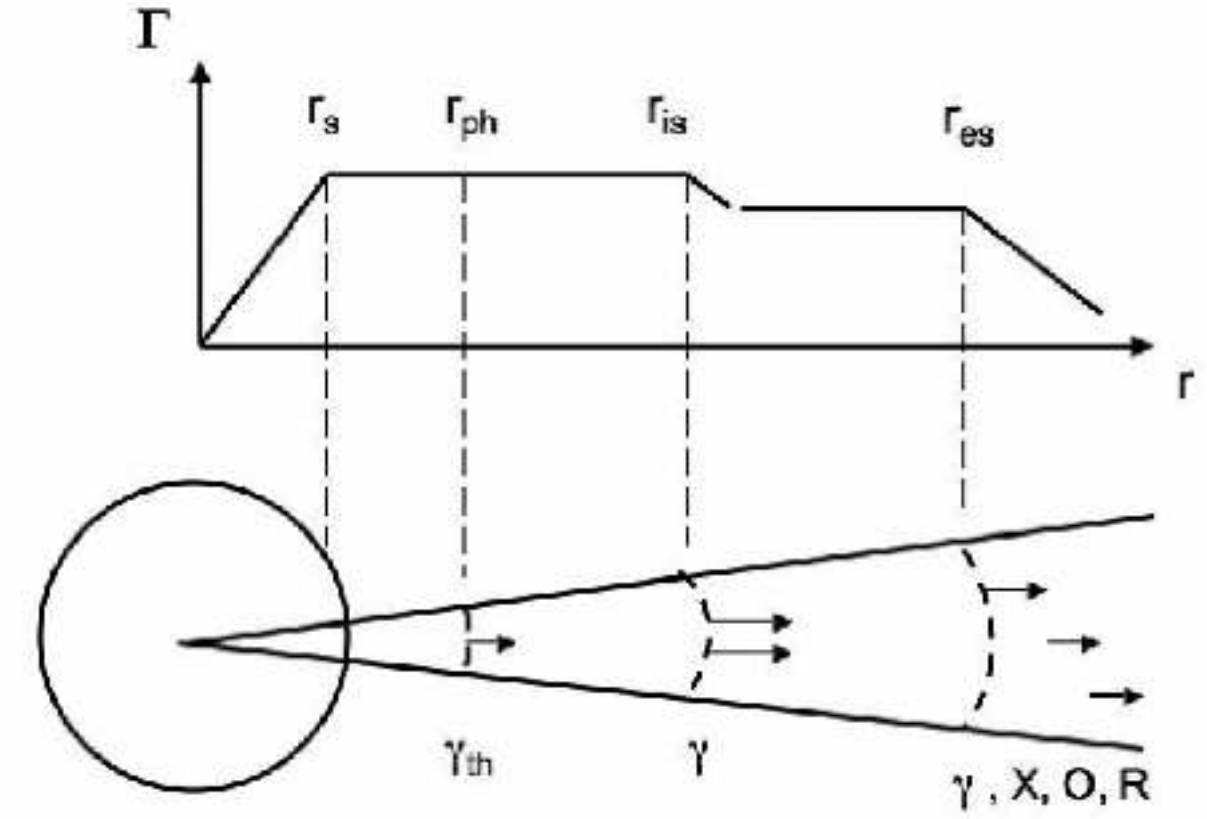

Figure 1.4: Schematic view of the evolution of the jet Lorentz factor and examples of symbolic locations of the characteristics radius.

1.2 The fireball model

As shown in the previous section, the most important parameters to characterise the synchrotron emission are p and B. Therefore, the physical model to explain GRB emission has to include processes with outputs that are consistent with the (directly) measured p. The value of B is generally given as a function of other dynamical parameters that better link the physical scenario and the observed spectral and time evolution.

The most popular model that roughly interprets GRB observations is the fireball model, introduced for the first time by Cavallo & Rees (1978). The mechanism to explain GRBs has to account for a huge energy liberation ($\sim 10^{54}$ erg) in short scale time intervals (from milliseconds to few hundred of seconds). Currently, we link these phenomena to the liberation of the gravitational energy into thermal energy when a black hole is formed (for a review, see, e.g., Mészáros *et al.*, 2015). As this thermal energy is produced explosively, a hot fireball with virial temperatures in the MeV range and composed by photons, electrons, positrons, nuclei, magnetic fields, as well as neutrinos and gravitational waves starts to expand. Thermal neutrinos (E $\sim 10^{53}$ ergFSince a few) and gravitational wave

emission ($\nu \in [10^2, 10^3]$ Hz, E $\sim 10^{53}$ erg) escape in matter of seconds or less, as the progenitor is essentially transparent to them. On the other hand, photons, $e^{\pm}$, nucleons, and magnetic fields get trapped.

A fireball can be characterised by its initial energy E_0. In the initial stage the mean energy per baryon is $\eta = E_0/M_0c^2 >> 1$, where M_0 represents the baryon loading of the fireball. The equation of motion of a blast wave sweeping up material $m(R)$ from the surrounding medium is

$$-\frac{d\Gamma}{\Gamma^2-1} = \frac{dm + \left(\frac{\Gamma}{\Gamma^2-1}\right) dU_{adi}}{M_0 + m(R) + U} \tag{1.31}$$

where the internal energy

$$dU = dU_m + dU_{adi} + dU_{rad}; \qquad dU_m = (\Gamma - 1)dm \tag{1.32}$$

In elementary treatments of the blast wave model, it is simply assumed that a fraction ϵ_e of the forward shock power is transferred to leptons, so that

$$L'_e = \epsilon_e \frac{dE'}{dt'} \tag{1.33}$$

and some mechanism, probably the first order shock Fermi process, injects electrons with a power law distribution between electrons Lorentz factors $\gamma_m \leq \gamma \leq \gamma_M$.

The initial radius of the fireball is R_{in}. Inside, the particles have a bulk Lorentz factor $\Gamma \sim 1$ and random isotropic energies with a mean Lorentz factor $\gamma \sim \eta \sim 10^2 - 10^3$. As the initial optical depth is extremely high, radial expansion is the consequence of the high super-Eddington luminosity and the thermal energy can only be converted into bulk kinetic energy. A phase of acceleration begins and the particles are confined inside an increasingly smaller angle $(R/R_{in})^{-1}$ along the radial direction. As the expansion is adiabatic, the temperature of the fireball is $T' \propto R^{-1} \propto \Gamma^{-1}$. The bulk Lorentz factor of the expanding gas increases linearly with R until it saturates at $R_{sat} \propto \Gamma_{max} R_{in}$, with $\Gamma_{max} \sim \eta$. This highly relativistic expansion of the fireball modifies its radiation: the observed photons are blueshifted while the observed timescales are shortened. Therefore, relativistic motion provides a way to reduce the rate of pair creation, and therefore explains the observed radiation above ∼1 MeV, as the opacity of the fireball to pair creation is an efficient way to suppress these photons. Beyond R_{sat} the shell coasts a constant $\Gamma = \Gamma_{max}$.

When the fireball comoving temperature is bellow $\sim$ 17 keV the $e^{\pm}$ pairs fall out of equilibrium and recombine. It occurs at the photospheric radius R_{ph}, $R_{ph} > R_{sat}$, defined as the radius where the optical depth equals to unity. However, this radiation is quasi-

thermal, in contrast with what is observed in GRBs. Moreover, the typical time scales over which the photons escape are comparable to that during which the flow becomes optically thin (milliseconds). This is too short with respect to most GRB durations.

1.2.1 Internal shocks

As explained before, if the prompt emission would come only from the fireball photons when the high initial optical depth had decreased, it is expected both a low radiative efficiency and a quasi-thermal spectrum. However, both issues are avoided if the radiation (or at least most of it) arises in shocks (e.g. Mészáros, 2006). Internal shocks explain the conversion of kinetic energy into synchrotron and inverse Compton non-thermal spectra (Rees & Mészáros, 1992, 1994).

Let's consider the relativistic shell moving with Γ_{max} after R_{sat}. It drives a shock into the surrounding ISM, which propagates with $\Gamma_{sh} = \sqrt{2}\Gamma$. These shocks take place within the relativistic ejecta when shells with different bulk Lorentz factors merge. If we call Γ_s and Γ_f the factors for the slow and fast shells, and we assume that they are of the same order, the merged bulk Lorentz factor is

$$\Gamma_m = \sqrt{\frac{m_f\Gamma_f + m_s\Gamma_s}{m_f/\Gamma_f + m_s/\Gamma_s}} \tag{1.34}$$

and the collision time will be

$$T = \frac{\Gamma_s^2\Gamma_f^2}{(\Gamma_s^2 - \Gamma_f^2)}t_{var} \tag{1.35}$$

where t_{var} is the variability time scale in the rest frame. These shocks are collisionless because the densities are so low to take place, but the magnetic fields are able to redistribute the energy between the particles. The merge will occur at a radius $R_{is} = \Gamma^2 t_{var} c$, which has to be placed at sufficiently large distances to allow the resulting radiation to escape without adiabatic looses. The efficiency of the conversion of the kinetic energy into internal energy that will be partially radiated is

$$\epsilon = \frac{1 - (m_f + m_s)\Gamma_m}{m_f\Gamma_f + m_s\Gamma_s} \tag{1.36}$$

The interaction of two shells takes place in the form of two shocks, a forward and a reverse shock (Sari & Piran, 1995). Superimposing the pulses resulting from individual two-shells interactions, synthetic bursts can be constructed (Daigne & Mochkovitch,

1998). Playing with the initial distribution of electron Lorentz factors it is possible to reproduce most of the large variety of observed GRB light curves. The separation between the peaks corresponds to periods of time during which the inner engine is quiet (Kobayashi *et al.*, 1997). With some assumptions about the energy equipartition between the electrons, protons, and magnetic fields, the Lorentz factors of the accelerated electrons can be determined. However, it gives a spectral evolution of E_p (the peak energy) that is too step. To have a better general agreement with observations, authors assume that the equipartition depends on the strength of the shock and on the post-shock density. If GRB pulses are produced by internal shocks, their temporal and spectral properties are probably governed by the hydrodynamics of the flow rather than the geometry of the emitting shells.

Even though it is generally accepted that the photons radiated during the prompt phase are due to synchrotron, inverse Compton scattering could play an important role depending on the physical conditions within the fireball. This effect can boost the energy of a photon by a factor of γ^2. For typical synchrotron photons in the $\sim$100 keV range the IC component will be in the GeV range. Such a high energy component has been observed in some GRBs.

During the last few years, several works have claimed that there is a thermal component on top of the over non thermal spectra (see Pe'er & Ryde, 2016, and references therein). This emission was predicted by the very early cosmological GRB models, but it was later abandoned because the observed spectra did not show a clear evidence of a Planck spectrum. Although the Band function provides good fits for most of GRB data, this model is not capable of capturing any feature coming from an hypothetical thermal emission. Furthermore, the fraction of GRBs in which a thermal component is detected correlates with their brightness, so for bursts observed near the detection limits the thermal component will not be detectable. Current models cannot robustly predict the strength of the thermal component. Finally, the main concern is the fact that the observed signal is often explained by more than one model. For example, a weak Planck component can be undistinguished from adiabatic losses, strong distortion due to sub-photospheric dissipation or strong magnetization.

Consequently, to make further progress, data should be fitted with physically-motivated models that can include a thermal component in addition to non-thermal emission. Several of such models already exists, but they are not frequently used.

1.2.2 External shocks

At the beginning of the fireball expansion the interstellar medium has no influence on the expanding shell, but it drives an external or termination shock when the jet starts to be decelerated by a swept up external matter at a radius

$$r_{es} \simeq \left(\frac{3E_0}{4\pi n_0 m_p c^2}\right)^{1/3} \Gamma^{-2/3}\, cm \tag{1.37}$$

This shock propagates with $\Gamma_{sh} = \sqrt{2}\Gamma$. As the shell radius increases, more ISM matter is accelerated via Fermi mechanism behind the shock and the shell is progressively influenced by the ISM. This influence becomes significant when the energy of the heated ISM is comparable to E_0. The afterglow emission begins when most of the bulk kinetic energy is transferred to the shocked external medium. The deceleration radius R_{dec} is defined as as the radius at which the initial part of the ejecta moving with $\Gamma_M = \eta$ sweeps up an amount of external gas to $E_0/(\eta c^2)$. Hence, the mass of the shocked material at the deceleration radius is

$$m_{dec} = \frac{M_0}{\eta} = \frac{4\pi}{3}\rho_{ext} R_{dec}^3 \tag{1.38}$$

Beyond this radius the shocked gas dominates the mass and energy of the expanding system.

Generally, two shocks form when the relativistic shell is slowed down by the ISM: a forward shock that propagates into the surrounding medium, and a reverse shock that propagates into the ejecta (Rees & Mészáros, 1992). At the very beginning as the forward shock builds up, its bolometric luminosity rises approximately as $L \propto t^2$, peaking when the radius reaches R_{dec}, and decays thereafter.

The dynamical evolution of the afterglow and its radiative properties are determined by E_0, ϵ_e, ϵ_B, n, and p. During the early phase of the external shock, the reverse shock is mildly relativistic and most of the energy conversion takes place in the forward shock (Sari & Piran, 1995).

1.2.3 Spectrum and light curves of the standard afterglow model

The standard afterglow model is based on the following approximations (Mészáros, 2002)

- Spherical outflow
- Line of sight scaling relations are assumed valid for the entire hemisphere

- Impulsive energy input E_0 and a single $\Gamma_0 = \eta$
- Highly relativistic expansion in the adiabatic regime
- Homogeneous external medium
- Time-independent shock acceleration parameters ϵ_e, ϵ_B, and p
- Only the forward shock radiation is considered

Most of the electrons have their energies near $E_m = \gamma_m mc^2$, $\nu_m = \nu(\gamma_m)$. Assuming that a constant fraction of the shock ϵ_e of the shock energy e goes into electrons (Sari *et al.*, 1998) then

$$\gamma_m = \epsilon_e \Gamma \frac{p-2}{p-1}\frac{m_p}{m_e} \tag{1.39}$$

The electrons gain energy by the second-order Fermi acceleration process while they lose their energy by radiating synchrotron photons. Therefore, to compute γ_M we have to equal the acceleration rate to the radiation loss rate

$$\gamma_M = 2 \times 10^8 \frac{\sqrt{\epsilon_M}}{\epsilon_B^{1/4} n_0 \sqrt{\Gamma}} \tag{1.40}$$

where ϵ_M is a constant in the order of unity. We also define the cooling Lorentz factor γ_c as the one for which the energy lost by radiation is equal to the energy lost by adiabatic cooling

$$P(\nu_c)t = \Gamma \gamma_c mc^2, \qquad \nu_c \equiv \nu(\gamma_c) \tag{1.41}$$

so

$$\gamma_c = \frac{9m_e(1+z)}{128 m_p \sigma_T \epsilon_B n_0 c \Gamma^3 t}, \qquad \sigma_T = \frac{8\pi q^4}{3m_e^2 c^4} \tag{1.42}$$

This means that an electron with initial Lorentz factor $\gamma_e > \gamma_c$ cools down to γ_c in a time t. The maximum emissivity appears at ν_c, and is given by

$$P(\nu, max) = \frac{\sigma_T mc^2}{3q}\Gamma B \tag{1.43}$$

The observed characteristic synchrotron frequency i is given by

$$\nu_i = \frac{qB\gamma_i^2 \Gamma}{2\pi m_e c(1+z)} \tag{1.44}$$

From this relation we can derive the characteristic frequencies. For example, in the adiabatic case

$$\begin{aligned}
\nu_c &= 9\times10^{12}\epsilon_B^{-3/2}n^{-1}E_{52}^{-1/2}t_d^{-1/2}(1+z)^{-1/2} && \text{Hz}\\
\nu_m &= 6\times10^{15}\left(\frac{p-2}{p-1}\right)^2\epsilon_e^2\epsilon_B^{1/2}E_{52}^{1/2}t_d^{3/2}(1+z)^{1/2} && \text{Hz}\\
\nu_a &= 2\times10^{9}\epsilon_e^{-1}\epsilon_B^{1/5}n^{3/5}E_{52}^{1/5}(1+z)^{-1} && \text{Hz}\\
F_{\nu,max} &= 1.1\times10^{5}\epsilon_B^{1/2}E_{52}n^{1/2}D_{28}^{-2} && \mu\text{Jy}
\end{aligned} \tag{1.45}$$

Two cases have to be considered:

1. $\gamma_m > \gamma_c$: All electrons cool down roughly to γ_c. This is the fast cooling case and the observed flux is given by

$$F_\nu = F_{\nu,max}\begin{cases}(\nu_a/\nu_c)^{1/3}(\nu/\nu_a)^2 & for \quad \nu<\nu_a\\ (\nu/\nu_c)^{1/3} & for \quad \nu_a\le\nu<\nu_c\\ (\nu/\nu_c)^{-1/2} & for \quad \nu_c\le\nu<\nu_m\\ (\nu_m/\nu_c)^{-1/2}(\nu/\nu_m)^{-p/2} & for \quad \nu_m\le\nu<\nu_M\end{cases} \tag{1.46}$$

   where ν_M is the frequency computed from γ_M,

$$F_{\nu,max} = N_e\frac{P_{\nu,max}}{4\pi D^2} \tag{1.47}$$

   N_e the total number of swept-up electrons in the post-shock fluid and D the distance of the source to the observer.

2. $\gamma_c > \gamma_m$: Only those electrons with $\gamma_e > \gamma_c$ can cool. This is known as the slow cooling phase, and the electrons with $\gamma_e \sim \gamma_m$ form the bulk of the population. The flux is now given by

$$F_\nu = F_{\nu,max}\begin{cases}(\nu_a/\nu_m)^{1/3}(\nu/\nu_a)^2 & for \quad \nu<\nu_a\\ (\nu/\nu_m)^{1/3} & for \quad \nu_a\le\nu<\nu_m\\ (\nu/\nu_m)^{-(p-1)/2} & for \quad \nu_m\le\nu<\nu_c\\ (\nu_c/\nu_m)^{-(p-1)/2}(\nu/\nu_c)^{-p/2} & for \quad \nu_c\le\nu<\nu_M\end{cases} \tag{1.48}$$

In the evolution, the outflow goes from initially fast to slow cooling. Fast cooling must take place during the GRB prompt emission. If not, there would be an inefficiency problem. Moreover, if the cooling time were too long the variability would be suppressed. The transition from fast to slow cooling is expected to take place during the early stages of the external shock, in the late prompt or early afterglow phase.

The light curves at a given frequency ν can be computed by considering the time t_0 of the transition between the fast and slow cooling regimes. Since at sufficiently early times $\nu_c < \nu_m$ (fast cooling) while at later times $\nu_c > \nu_m$ (slow cooling), there is a transition when $\nu_c = \nu_m$ at a time t_0

$$t_0 = \begin{cases} 210\epsilon_B^2\epsilon_e^2 E_{52} n_1 & \text{days} \quad (adiabatic) \\ 4.6\epsilon_B^{7/5}\epsilon_e^{7/5} E_{52}^{4/5}\gamma_2^{-4/5} n_1^{3/5} & \text{days} \quad (radiative) \end{cases} \tag{1.49}$$

Therefore, the corresponding $\nu_0 = \nu_c(t_0) = \nu_m(t_0)$ is

$$\nu_0 = \begin{cases} 1.8\times 10^{11}\epsilon_B^{-5/2}\epsilon_e^{-1} E_{52}^{-1} n_1^{-3/3} & \text{Hz} \quad adiabatic \\ 8.5\times 10^{12}\epsilon_B^{-19/20}\epsilon_e^{-2/5} E_{52}^{-4/5} n_1^{-11/10}\gamma_2^{4/5} & \text{Hz} \quad radiative \end{cases} \tag{1.50}$$

Ignoring synchrotron self-absorption, there are two cases to consider as well:

1. $\nu > \nu_0$: This is the *high frequency* case. Areas labelled by B, C, and D of Fig. 1.6 (top) correspond to the fast cooling case, while H is now in the slow cooling case.
2. $\nu < \nu_0$: This is the *low frequency* case. Areas labelled by F, G, and H of Fig. 1.6 (bottom) correspond to the slow cooling case, while B still remains in the fast cooling case.

In addition, if $\epsilon_e \longrightarrow 1$ the hydrodynamic evolution changes at this stage from adiabatic to radiative, while if $\epsilon_e << 1$ the evolution stays adiabatic.

1.2.4 Ingredients for more realistic afterglow models

The approximations in the standard afterglow model imply simplifications which are not valid in the real conditions of most GRBs, so it is interesting consider more complex scenarios. Some possibilities are:

- The beaming of the outflow
- The impact of the reverse chock crossing the ejecta
- Inhomogeneous external mediums
- The departure from a simple energy injection

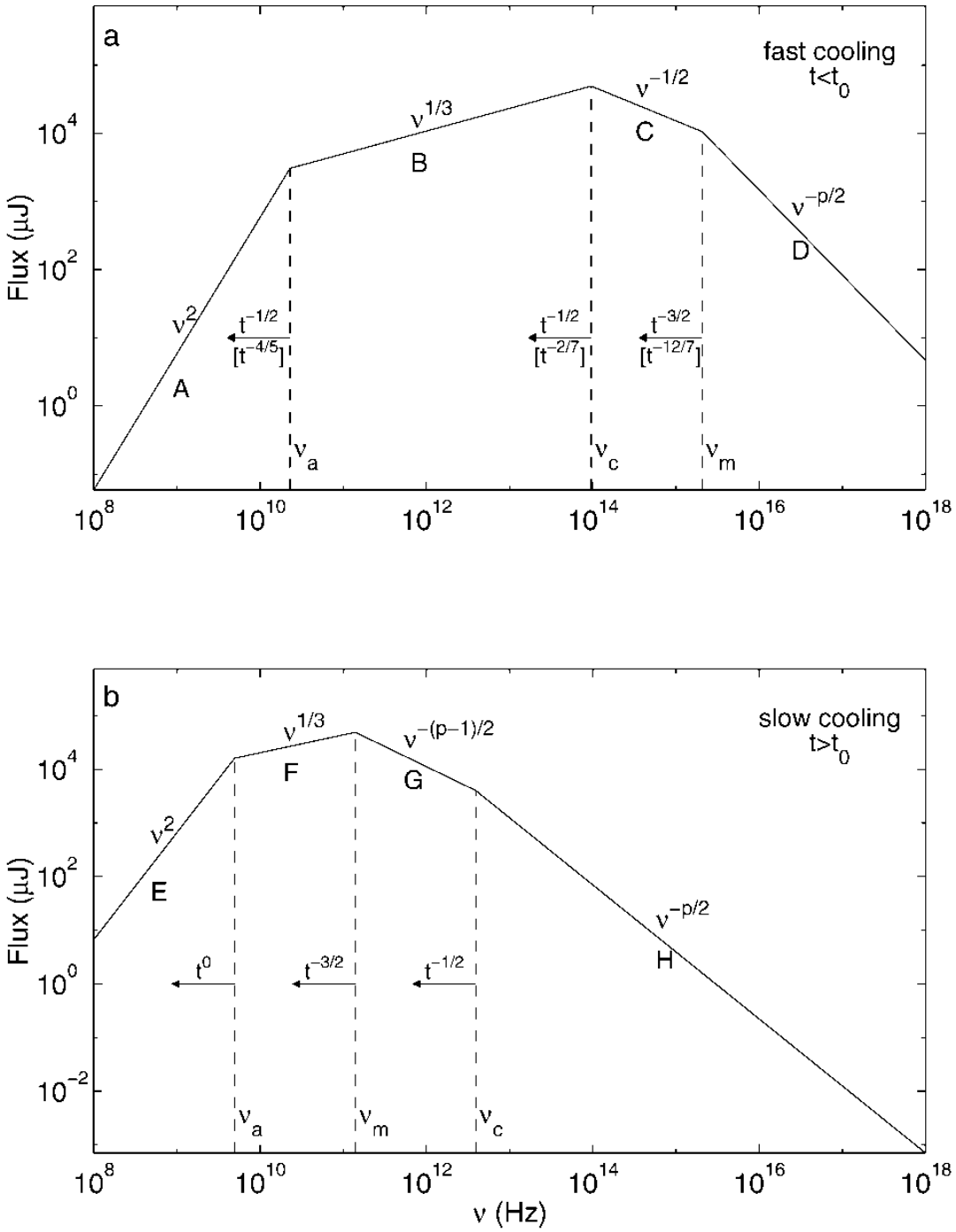

Figure 1.5: Synchrotron spectrum of a relativistic shock with a power-law electron distribution. (a) Fast cooling, which is expected at early times. The spectrum consists of four segments, identified t as A, B, C, and D. Self-absorption is important below ν_a. The frequencies, ν_m, ν_c, and ν_a, decrease with time as indicated; the scalings above the arrows correspond to an adiabatic evolution, and the scalings below, in square brackets, correspond to a fully radiative evolution. (b) Slow cooling, which is expected at late times. The evolution is always adiabatic. The four segments are identified as E, F, G, and H. Adapted from Sari *et al.* (1998).

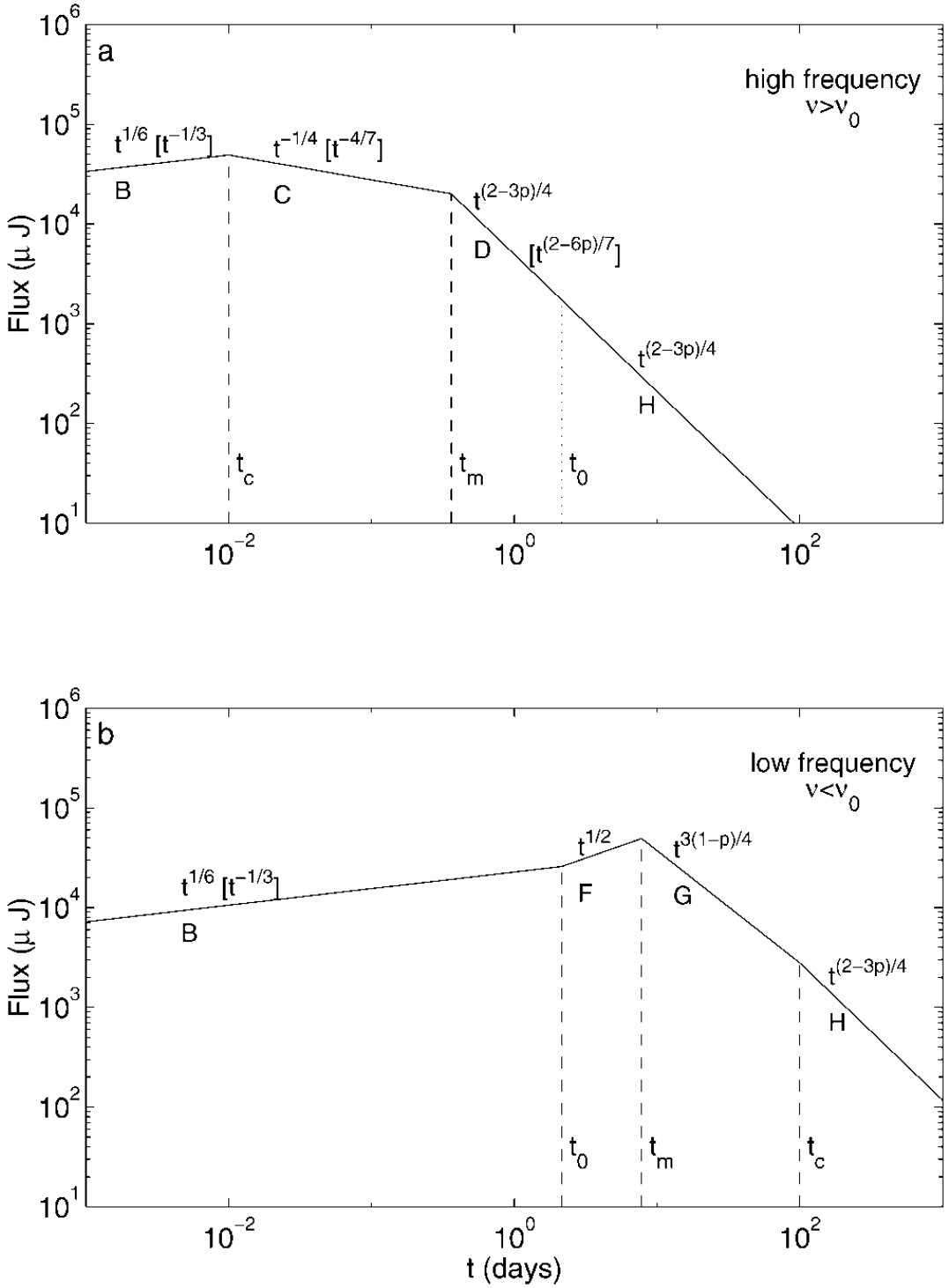

Figure 1.6: Synchrotron light curve (ignoring self-absorption). (a) High frequency case. The four segments that are separated by the critical times t_c, t_m, and t_0, correspond to the spectral segments in Fig. 1.5 with the same labels (B, C, D, and H). The observed flux varies with time as indicated; the scalings within square brackets are for radiative evolution (which is restricted to $t < t_0$), and the other scalings are for adiabatic evolution. (b) Low-frequency case. Adapted from Sari *et al.* (1998).

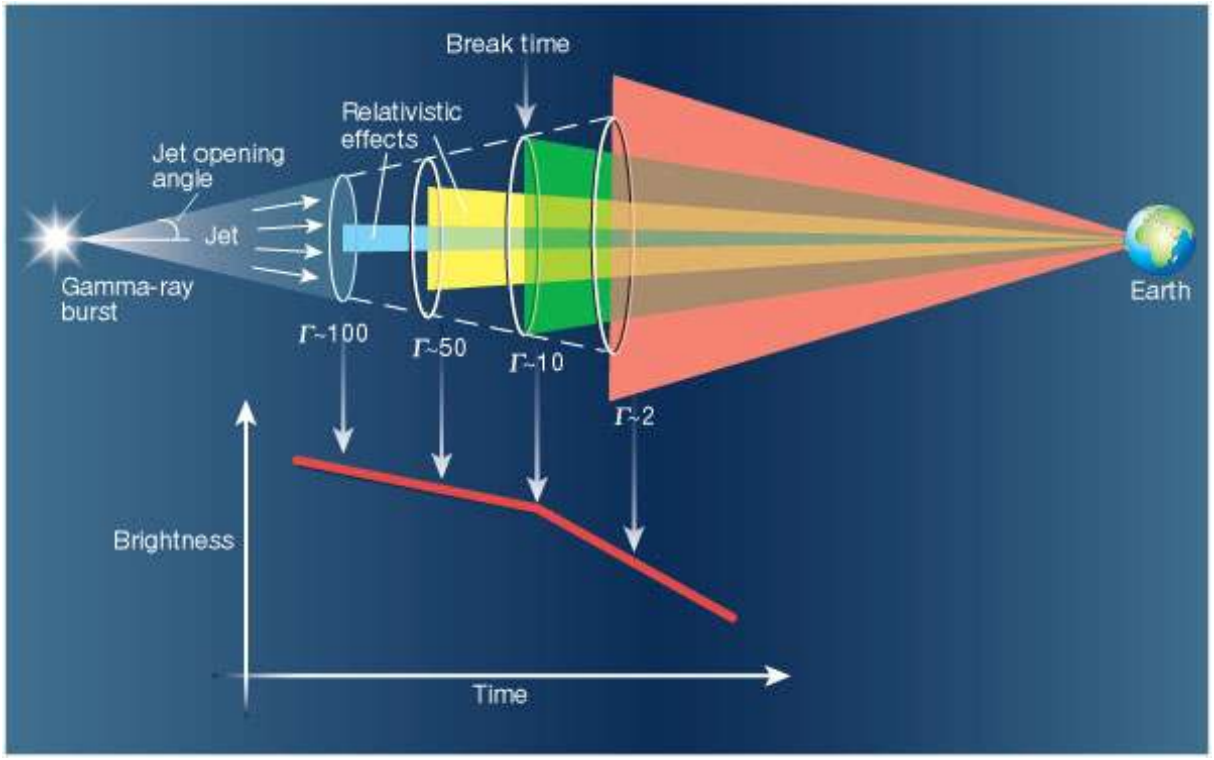

Figure 1.7: The burst launches a jet of material that moves at nearly the speed of light. Because of the effects of special relativity, an observer on Earth can initially only see a tiny fraction of that jet (light blue). As time passes and the jet runs into the surrounding material it slows down, and an observer on Earth can see more of the jet (yellow). Eventually, at the so-called break time, the entire jet becomes visible (green). Beyond this point, no new matter becomes visible and the brightness of the afterglow declines more quickly.

1.2.4.1 The beaming of the outflow

The extreme isotropic equivalent energies suggest that GRBs radiate into a narrow jet. A more direct evidence comes from long-term radio observations: several months since the GRB the afterglow becomes sub-relativistic and radiates isotropically at radio wavelengths. This allows to measure the total kinetic energy of the ejecta (Frail *et al.*, 2000; Waxman *et al.*, 1998).

An additional indirect evidence is provided by the achromatic breaks seen in afterglow light-curves (see Fig. 1.7). In the uniform or 'top hat' jet the initial energy per solid angle ϵ and Γ are uniform within the half opening angle θ_j and sharply drop outside. Due to a relativistic effect, the radiation from a blob of Γ is beamed within an angle of Γ^{-1}. During the deceleration phase Γ decreases until Γ^{-1} reaches θ_j, moment at which the hydrodynamical evolution of the jet changes.

Another interesting model proposed is the two component jet (e.g. Filgas *et al.*, 2011;

Racusin *et al.*, 2008; Starling *et al.*, 2005; van der Horst *et al.*, 2014). This model includes a narrow uniform jet of initial $\Gamma_0 > 100$ surrounded by a wider uniform jet with $\Gamma_0 \sim 10-30$. Motivation for such structure was found in the context of the cocoon in the collapsar model (Ramirez-Ruiz *et al.*, 2002) as well as in the context of a hydro-magnetically driven jet originated in the collapse of a massive star (Vlahakis *et al.*, 2003).

1.2.4.2 The impact of the reverse chock crossing the ejecta

In the standard afterglow model, a reverse shock is predicted to produce a strong optical flash and a radio flare (Mészáros & Rees, 1997; Sari & Piran, 1999; Sari *et al.*, 1999). The reverse shock heats the matter in the shell, accelerates electrons and emits a single burst. After the peak of the reverse shock no new electrons are injected and the shocked material cools adiabatically. There are two limiting cases:

- If the shell density is high, the reverse shock is Newtonian and too weak to slow down the material.
- If the shell density is low, the reverse shock is relativistic and considerably decelerates the propagation.

This picture can be modified, allowing a long-lived reverse shock, if the central engine emits slowly moving material (Genet *et al.*, 2007).

1.2.4.3 Inhomogeneous external media

The shape of the spectrum will be unaffected by the choice of density profile but it will affect the evolution of spectral breaks and therefore that of light curves. For a general density profile of the circumburst medium $n(r) \propto r^{-k}$ it can be shown that $r \propto \Gamma^{-2/(3-k)}$ (see for example Chevalier & Li, 2000, Eqn. 1). For an impulsive one-time release of energy E is constant and therefore

$$\Gamma \propto r^{-(3-k)/2} \tag{1.51}$$

$$t \propto r/\Gamma^2 \tag{1.52}$$

where t is the time in the observer's frame.

Following a similar treatment as for the standard fireball model, radiation is generated by the shock heated electrons which have Lorentz factor distribution $N(\gamma_e) \propto \gamma_e^{-p}$. The minimum Lorentz factor, γ_m, of such a distribution could be estimated by using two conservation laws:

1. Conservation of energy and

2. conservation of the total number of particles

which gives us $\gamma_m \propto \Gamma$. Similarly following standard treatment of cooling electrons the high energy cut-off of the distribution could be shown to be $\gamma_c \propto (\Gamma\ B_{co}\ t)^{-1}$ where B_{co} is the comoving magnetic field behind the shock wave. Corresponding break frequencies ν_m and ν_c, for the lower and higher energy cut-offs of the electron distribution, respectively would be:

$$\nu_m \propto \Gamma \times (\gamma_m^2\ B_{co}) \tag{1.53}$$
$$\nu_c \propto \Gamma \times (\gamma_c^2\ B_{co}) \tag{1.54}$$

where the co-moving break frequencies have been Doppler boosted by the multiplicative factor Γ - the bulk Lorentz factor of the shock wave.

From Eqn. 25 of Wijers & Galama (1999), the spectral peak would be given by:

$$F_{\nu_m} \propto \Gamma \times (N_e P_{\nu_m}) \tag{1.55}$$

where $P_{\nu_m} \propto B_{co}$ is the power emitted by each electron and N_e is the total number of radiating electrons. For the given density profile $N_e \propto r^{3-k}$.

Temporal evolution of the spectral breaks could then be obtained:

$$\nu_m \propto t^{-3/2} \tag{1.56}$$
$$\nu_c \propto t^{-\frac{4-3k}{2(4-k)}} \tag{1.57}$$
$$F_{\nu_m} \propto t^{-\frac{k}{2(4-k)}} \tag{1.58}$$

We assume that the spectral shape as given by Sari *et al.* (1998) will be unaffected by the choice of density profile. Then in the optically thin regime and for the typical afterglow parameters

$$F_\nu = F_{\nu_m} \left(\frac{\nu}{\nu_m}\right)^{-(p-1)/2} \qquad \nu_m \ll \nu \ll \nu_c \tag{1.59}$$
$$F_\nu = F_{\nu_m} \left(\frac{\nu_c}{\nu_m}\right)^{-(p-1)/2} \left(\frac{\nu}{\nu_c}\right)^{-p/2} \qquad \nu \gg \nu_c \tag{1.60}$$

Substituting for the time dependence of break frequencies from Eqn. 1.58 in Eqn. 1.60,

we get

$$F_\nu(\nu, t_\oplus) \propto \nu^{-(p-1)/2} \times t_\oplus^{-\frac{1}{4}(3p-3+\frac{2k}{4-k})} \qquad \nu_m \ll \nu \ll \nu_c \qquad (1.61)$$

$$F_\nu(\nu, t_\oplus) \propto \nu^{-p/2} \times t_\oplus^{-(3p-2)/4} \qquad \nu \gg \nu_c \qquad (1.62)$$

It is to be noted that Eqn. 1.62 is independent of k and, therefore, the light curve decay in the spectral regime $\nu_m \ll \nu \ll \nu_c$, which is appropriate for the typical X-ray afterglows, does not depend on the density profile of the circum-burst medium.

1.2.4.4 The departure from a simple energy injection

More physically realistic is the situation where the ejecta has a range of bulk Lorentz factors with larger amounts of mass and energy having lower Γ. The outer shock and contact discontinuity decelerates as the fireball sweeps up external matter. This deceleration allows slower ejecta to catch up with the forward shock, replenishing and re-energizing it, and leading to additional dissipation in the reverse shock (Rees & Mészáros, 1998).

1.2.5 The Jóhannesson *et al.* (2006) model

This models starts from the following differential equations that describe the fireball evolution

$$\begin{aligned} \frac{dr}{dt_b} &= \beta c \\ \frac{dt'}{dt_b} &= \frac{1}{\Gamma} \\ \frac{dt}{dt_b} &= \frac{1+z}{\Gamma^2(1+\beta)} \\ \frac{df}{dr} &= \frac{\Omega\rho}{M_0} r^2 \end{aligned} \qquad (1.63)$$

Here, r is the radial coordinate in the burster frame. t_b, t', and t are the burster frame time, the comoving frame time, and the observer frame time, respectively. The solid angle Ω is estimated by

$$\Omega = 2\pi \left[1 - \cos\left(\frac{\theta_0 + c_s t'}{c t_b}\right)\right] \qquad (1.64)$$

where θ_0 is the initial opening angle of the collimated outflow and c_s is the sound speed in the comoving frame, assumed to be relativistic. From the energy and momentum

conservation, the dimensionless velocity of the expanding fireball is found to be

$$\beta = \frac{\Gamma_0\beta_0 - I_2}{\Gamma_0[xF(x) + I_1] + f} \tag{1.65}$$

where

$$\begin{aligned} x &= \frac{\Gamma}{\Gamma_0} \\ \frac{dF}{dx} &= \frac{\Gamma_0}{M_0}\frac{dM}{d\Gamma} f = \frac{M_e}{M_0} \\ I_1 &= \int_x^1 F(x)dx \\ I_2 &= \int_x^1 \sqrt{\Gamma_0^2 x^2 - 1}\frac{dF}{dx}dx \end{aligned} \tag{1.66}$$

M_e is the total mass of the swept up medium. $F(x)$ is a dimensionless function to account for the distribution of Lorentz factors in instantaneous, discrete and continuous energy injections. Then, the evolution of the Lorentz factor is given by

$$\Gamma = \frac{1}{\sqrt{1-\beta^2}} = \frac{\Gamma_0[xF(x) + I_1] + f}{\sqrt{\Gamma_0[xF(x) + I_1] + f^2 - [\Gamma_0\beta_0 - I_2]^2}} \tag{1.67}$$

which is the key equation for obtaining the dynamical evolution of the fireball. Since the evolution is considered adiabatic, the dynamics is solved separately and the radiative properties computed afterwards. Several approximations are also taken into account with care. The most important one is that only the forward shock is considered in this model.

We can consider three cases for the form of $F(x)$:

Instantaneous energy injection : In the standard fireball it is assumed that the energy is released instantaneously. Fixing $x = 1$, and $F(x) = 1$

$$\Gamma = \frac{\Gamma_0 + f}{\sqrt{1 + 2\Gamma_0 f + f^2}} \tag{1.68}$$

recovering the standard result.

Discrete energy injection : It is assumed that in addition to the initial injection M_0, the central engine expels several shells with masses M_i and Lorentz factors Γ_i. Converting to dimensionless variables, $x_i = \Gamma_i/\Gamma_0$ and $m_i = M_i/M_0$, we get

$$F(x) = 1 + \sum_i m_i H(x_i - x) \tag{1.69}$$

where $H(x_i - x)$ is the Heaviside step function. Numerical calculations assume that shell collisions are instantaneous, so the effects of the interaction are not considered.

Continuous energy injection : Here it is assumed that $F(x) = x^{-s}$, with $s > 1$.

To compute the light curves and spectra, the radiation is assumed, as usual, to be synchrotron. In this model the approach of Granot & Sari (2002); Wijers & Galama (1999); Wu *et al.* (2004) is adopted. The self-absorption coefficient is computed directly, and the inverse Compton scattering is included, but neglecting the higher orders suppressed by the Klein-Nishina effect. In all calculations, the equal arriving time surfaces (EATS) of the expansion are considered. The total flux arriving at the observer time, t, is obtained by integrating over the EATS

$$F(\nu, t) = \frac{1+z}{2d_l^2} \int_0^{\theta} \int_0^{r} \frac{P'(\nu', t_{em}, \overrightarrow{r})}{\Gamma^2(1-\beta\cos\theta)^2} r^2 dr d\cos\theta \tag{1.70}$$

where

$$t_{em} = \frac{t}{1+z} + \frac{r\cos\theta}{c} \tag{1.71}$$

is the time of emission in the burst frame.

Since the dynamics of collisions are neglected, the Lorentz factor of the leading shell increases instantaneously as soon as another shell catches up with it. As the energy increases, the luminosity also does. However, as the integration is over the EATS, the increase will be gradual. Therefore, energy injection in wider and slower moving jets will create smoother bumps, and if the interaction would be considered it would further contribute to the smoothing. Finally, we note that the origin of additional shells is most likely the same as the origin of the internal shocks.

Chapter 2

GRB 110715A

Adapted from "GRB 110715A: The peculiar multiwavelength evolution of the first afterglow detected by ALMA"

— Sánchez-Ramírez et al., *MNRAS, Submitted*

In this Chapter I present the extensive follow-up campaign on GRB 110715A afterglow at 17 different wavelengths, from X-ray to radio bands, starting 81 seconds after the burst and extending up to 74 days later. We performed for the first time a GRB afterglow observation with the ALMA observatory. We find that the afterglow of GRB 110715A is particularly bright at optical and radio wavelengths. We use optical and near infrared spectroscopy to provide further information about the progenitor's environment and its host galaxy. The spectrum shows weak absorption features at a redshift $z = 0.8224$, which reveal a host galaxy environment with low ionization, column density and dynamical activity. Late deep imaging shows a very faint galaxy, consistent with the spectroscopic results. The broadband afterglow emission is modelled with synchrotron radiation using a numerical algorithm and we determine the best fit parameters using Bayesian inference in order to constrain the physical parameters of the jet and the medium in which the relativistic shock propagates. We fitted our data with a variety of models, including different density profiles and energy injections. Although the general behavior can be roughly described by these models, none of them are able to fully explain all data points simultaneously. GRB 110715A shows the complexity of reproducing extensive multi-wavelength broadband afterglow observations, as well as the need of good sampling in wavelength and time, and more complex models to accurately constrain the physics of GRB afterglows.

2.1 Introduction

Gamma-ray bursts (GRBs, Klebesadel *et al.*, 1973) are the most violent explosions in the Universe. They are characterized by a short flash of gamma-ray photons followed by a long lasting afterglow that can be observed at all wavelengths. They can be classified into two types based on the duration (and the hardness) of their γ-emission: short and long GRBs ($T_{90} < 2$ s (hard spectrum) and $T_{90} > 2$ s (soft spectrum) respectively; Kouveliotou *et al.*, 1993). Currently, the most favored model to explain the origin of GRBs is a highly magnetized relativistic jet, but more prompt polarimetric observations are needed in order to confirm this (Kopač *et al.*, 2015; Mundell *et al.*, 2013). The prompt emission likely originates from either internal shocks in the photosphere of the jet or magnetic dissipation in a magnetically dominated jet (see Zhang & Yan, 2011; Zheng *et al.*, 2012, and references therein). The afterglow emission, however, is thought to originate from external shocks caused by the jet's interaction with the interstellar medium (ISM). Multi-wavelength emission is expected to be produced by a forward shock moving into the ISM and a reverse shock moving into the expanding jet (Mészáros & Rees, 1993; Sari *et al.*, 1998, 1999). The reverse shock is supposed to be short lived, with most of the afterglow emission being generated by the forward shock.

The electrons accelerated at the shock fronts emit synchrotron radiation as they interact with the magnetic field behind the shock fronts. By modeling this emission we can determine the physical parameters of the GRB ejecta and the structure of the ISM near the progenitor along the line of sight to Earth. The most popular way to extract the parameters is by using an analytical model for the expected shape of the afterglow light curves and spectrum (Rhoads, 1997; Sari *et al.*, 1998; Wijers & Galama, 1999). The emission is split into regions in time and wavelength, where the resulting light curve and spectrum can be approximated by power laws. The slopes of these segments along with the location of the spectral breaks are then used to determine the physical parameters. An alternative method is to model the emission using a numerical code that takes as input the physical parameters of interest (Jóhannesson *et al.*, 2006; Panaitescu & Kumar, 2002). In addition to requiring fewer approximations, the numerical models allow us to study a more complex structure for the ISM and the GRB ejecta and is therefore our method of choice for this study.

To properly determine the physical properties of the GRB ejecta a wide range of accurate multi-wavelength observations are needed with as good time coverage as possible. The millimetre/sub-millimetre range is of crucial importance in constraining the afterglow models as it is where the flux density of the emission peaks during the first few days after

the GRB onset. In this range the capabilities of the new ALMA observatory bring an important leap forward, thanks to its great improvement in resolution and sensitivity in comparison with previous observatories (de Ugarte Postigo *et al.*, 2012b).

It is widely accepted that long GRBs are created by the explosive death of massive stars (Hjorth *et al.*, 2003; Woosley & Bloom, 2006), probably rapidly rotating Wolf-Rayets (for a review see, e.g., Crowther, 2007). However, it remains unclear what the specific mechanism in the core collapse process is that triggers the formation of a jet. Given the short life periods of such massive stars and their luminosity, GRB afterglows can be used as powerful tracers of star-forming galaxies over a wide range of redshifts (e.g., Kistler *et al.*, 2009; Krühler *et al.*, 2015; Robertson & Ellis, 2012; Schulze *et al.*, 2015; Vergani *et al.*, 2015). To date spectroscopically confirmed GRB redshifts range from $z = 0.0085$ (GRB 980425A Galama *et al.*, 1998; Tinney *et al.*, 1998) to $z = 8.2$ (GRB 090423A Salvaterra *et al.*, 2009; Tanvir *et al.*, 2009), and photometric redshifts have been proposed up to $z = 9.4$ (GRB 090429B Cucchiara *et al.*, 2011).

Optical/NIR spectroscopy of GRB afterglows can also be used to study the intervening matter present along the line of sight at different distance scales, ranging from regions around the progenitor to distant intervening galaxies. Its strength resides in the extremely bright afterglow, making it possible to measure atomic/molecular transitions in the host galaxy and intervening systems (e.g. D'Elia *et al.*, 2014), even when the probed galaxies are not detected by deep direct imaging. Spectroscopy has made it possible to accurately probe absorption metalliticity out to $z \geq 5$ (e.g., Hartoog *et al.*, 2015; Sparre *et al.*, 2014).

2.2 Observations

2.2.1 Gamma-ray emission

The *Swift* (Gehrels *et al.*, 2004) Burst Alert Telescope (BAT, Barthelmy *et al.*, 2005) triggered and located GRB 110715A on 15 July 2011 at T_0= 13:13:50 UT (Sonbas *et al.*, 2011). The gamma-ray light curve shows a double-peaked structure with a duration of T_{90}= 13.0 ± 4.0 s (90% confidence level) in the observer frame. Therefore we classify GRB 110715A as a long burst.

Analysis of the time-averaged spectrum gave the best fit as a power law with an exponential cutoff with the following parameters: $\Gamma_\gamma = 1.25 \pm 0.12$, S (15-150 keV) = $(1.18 \pm 0.02) \times 10^{-5}$ erg cm^{-2}, and $E_{\rm peak} = 120 \pm 21$ keV (90% confidence level, Sonbas *et al.*, 2011). GRB 110715A was also detected by *INTEGRAL*/SPI-ACS, Konus-*Wind*

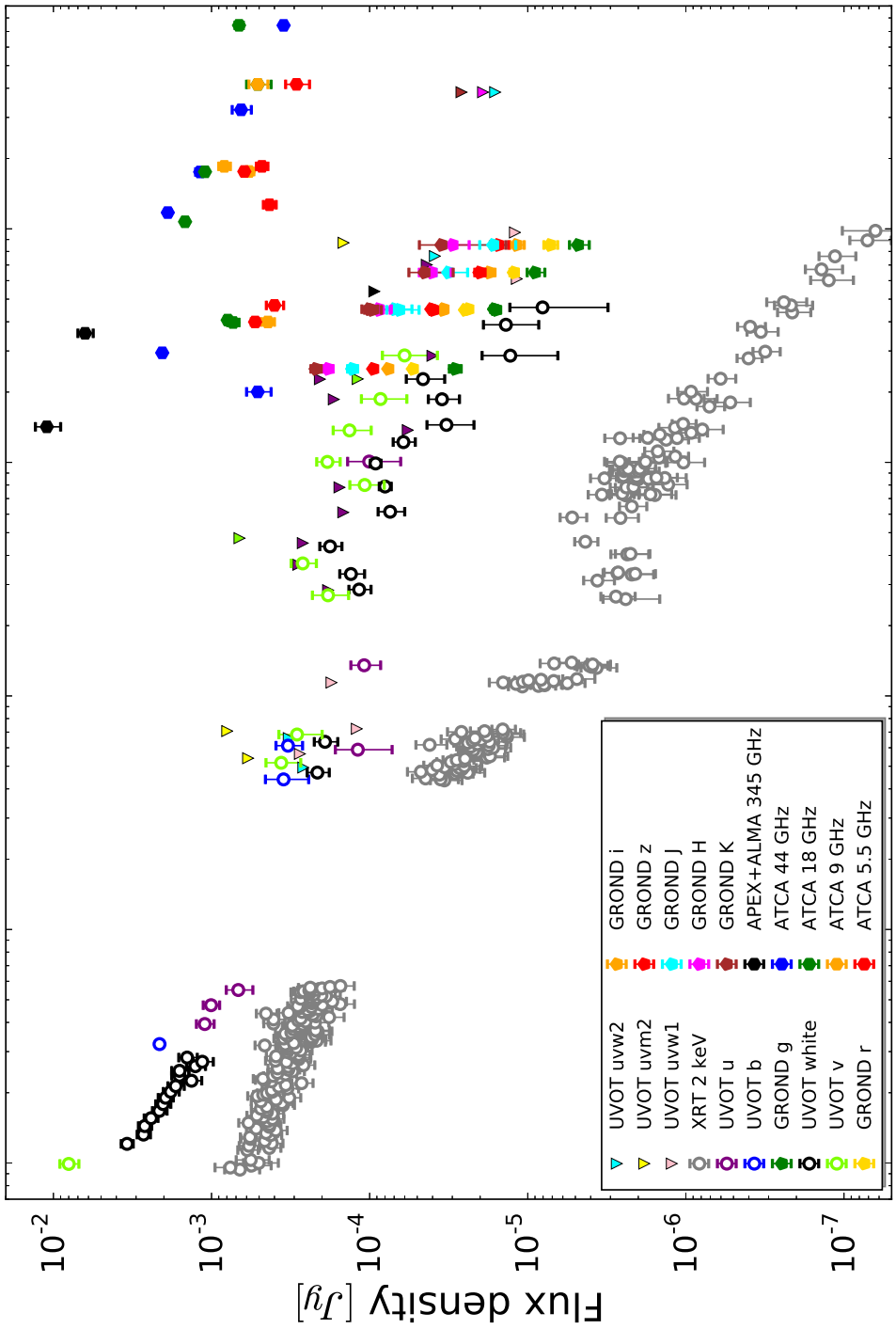

Figure 2.1: Afterglow light curve of the 17 bands observed. Upper limits are denoted by down-pointing triangles.

and *Suzaku*/WAM (see more details in Sonbas *et al.*, 2011).

2.2.2 X-ray afterglow observations

The X-Ray Telescope (XRT; Burrows *et al.*, 2005) onboard *Swift* began observing the field 90.9 seconds after the BAT trigger, localizing the X-ray afterglow at RA(J2000) = $15h\ 50m\ 44.00s$, Dec.(J2000) = -46°14′ 07.″5 with an uncertainty of 1.″4 (90% confidence level; Evans *et al.*, 2011).

The afterglow light curve used in this paper has been extracted from the Burst Analyzer [1] (Evans *et al.*, 2010), using the spectral slope to derive the flux densities at an energy of 2 keV. These observations are shown in Figure 2.1 and tabulated in Table A.1.

2.2.3 UV/Optical/NIR afterglow observations

GRB 110715A was followed-up in UV/Optical/NIR wavelengths with *Swift* (+UVOT) and the 2.2m MPG telescope (+GROND). Light curves are shown in Figure 2.1 and tabulated in Table A.1 as well.

This burst had a very bright optical counterpart in spite of the high Galactic extinction caused by its location close to the Galactic plane (Evans *et al.*, 2011). The GRB afterglow study was affected by the Galactic reddening, initially estimated to be $E(B-V) = 0.59$ mag according to the dust maps of Schlegel *et al.* (1998), and later $E(B-V) = 0.52$ mag following Schlafly & Finkbeiner (2011). We adopted the latest value. Computed effective wavelengths and extinction for each band are presented in Table 2.1.

2.2.3.1 UVOT imaging

The *Swift* Ultra-Violet/Optical Telescope (UVOT; Roming *et al.*, 2005) began settled observations of the field of GRB 110715A $100s$ after the trigger (Breeveld *et al.*, 2011). The afterglow was detected in the *white*, *u*, *b* and *v* filters at RA(J2000) = 15h 50m 44.09s, Dec.(J2000) = -46°14′ 06.″5, with a 2σ uncertainty of about 0.″62. For this analysis, we have reduced both image and event mode data grouped with binning $\Delta t/t \sim 0.2$. Before the count rates were extracted from the event lists, the astrometry was refined following the methodology in Oates *et al.* (2009). The photometry was then extracted from the event lists and image files based on the FTOOLs *uvotevtlc* and *uvotmaghist*, respectively, using a source aperture centered on the optical position and a background

[1] http://www.swift.ac.uk/burst_analyser

Table 2.1: Effective wavelengths and extinction coefficients.

Band	$\lambda_{\rm eff}$ [μm]	A_λ [a]
XRT 2 keV	0.620×10^{-3}	0.000
UVOT uvw2	0.193	4.099
UVOT uvm2	0.225	4.582
UVOT uvw1	0.260	3.623
UVOT u	0.351	2.587
UVOT b	0.441	2.021
GROND g'	0.459	2.018
UVOT *white*	0.483	2.566
UVOT v	0.545	1.628
GROND r'	0.622	1.393
GROND i'	0.764	1.042
FORS2 Ic	0.786	0.949
GROND z'	0.899	0.775
GROND J	1.239	0.455
GROND H	1.646	0.291
GROND K	2.170	0.187
APEX/ALMA 345 GHz	8.70×10^2	0.000
ATCA 44 GHz	6.81×10^3	0.000
ATCA 18 GHz	1.66×10^4	0.000
ATCA 9 GHz	3.33×10^4	0.000
ATCA 5.5 GHz	5.45×10^4	0.000

(a) $E(B-V) = 0.52$ mag (Schlafly & Finkbeiner, 2011)

region located in a source-free zone. We used a 3" source aperture to avoid contamination from neighbouring stars and applied aperture corrections to the photometry in order to be compatible with the UVOT calibration (Breeveld *et al.*, 2011). The analysis pipeline used software HEADAS 6.10 and UVOT calibration 20111031.

2.2.3.2 GROND imaging

We obtained follow-up observations of the optical/NIR afterglow of GRB 110715A with the seven-channel imager GROND (Gamma-ray burst optical/near-infrared detector; Greiner *et al.*, 2008) mounted on the 2.2m MPG@ESO telescope stationed in La Silla, Chile. The first observations were obtained 2.5 days after the trigger, after losing the first two nights due to weather. This first epoch suffers from very bad seeing, 1.″5 – 1.″9 depending on the band, but the optical/NIR afterglow was clearly detected (Updike *et al.*, 2011). Deeper follow-up under better conditions in three further epochs reveals a faint nearby source which exhibits a stellar PSF. The presence of this source was carefully accounted for during the data analysis. The GROND optical and NIR image reduction and photometry were performed by calling on standard IRAF tasks (Tody, 1993) using the custom GROND pipeline (Yoldaş *et al.*, 2008), similar to the procedure described in Krühler *et al.* (2008). Hereby, we used SExtractor (Bertin & Arnouts, 1996) for background modeling, and bright sources were masked out, which yields improved results in the case of this crowded field. A late epoch was obtained 38 days after the GRB which was supposed to be used for image subtraction purposes, but a positioning error led to the afterglow position being covered only in the NIR frames.

Afterglow magnitudes in the optical were measured against comparison stars calibrated to the SDSS catalogue (Aihara *et al.*, 2011), obtained from observing an SDSS field at similar airmass immediately after the fourth epoch, in photometric conditions. NIR magnitudes were measured against on-chip comparison stars taken from the 2MASS catalogue (Skrutskie *et al.*, 2006). The results of the photometry are displayed in Table A.1.

2.2.4 Submm afterglow observations

The Atacama pathfinder experiment telescope (APEX) observations began on July 16, 1.42 days after the burst and were performed in the 345 GHz band using the photometric mode of the Large Apex BOlometer CAmera (LABOCA; Siringo *et al.*, 2009) under good weather conditions. Data reduction was done using the BoA, CRUSH and miniCRUSH (Kovács, 2008) software packages. Using these observations we discovered a bright submm

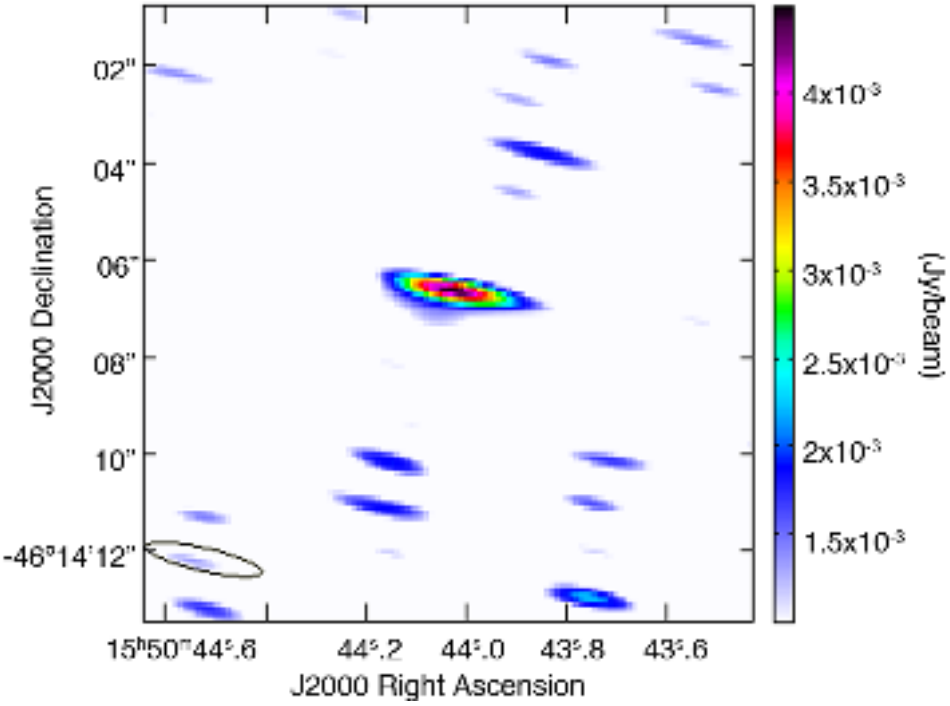

Figure 2.2: ALMA image at 345 GHz. The beam size (0.″3 × 0.″1, P.A.=76 degrees) is showed in the lower left corner.

counterpart at 10.4 ± 2.4 mJy (de Ugarte Postigo *et al.*, 2011b).

As a test of the target of opportunity programme, GRB 110715A was also observed with the Atacama Large Millimeter Array (ALMA), yielding a detection with a flux density of 4.9 ± 0.6 mJy at 345 GHz (de Ugarte Postigo *et al.*, 2012b). The ALMA observations began on July 19 at 02:50 UT (3.57 days after the burst), and they were carried out making use of only 7 antennas during 25 mins on source. We present the data in Figure 2.2.

In spite of being obtained during a test observation, with almost an order of magnitude fewer antennas than are available with the full observatory, this was the deepest observation carried out to date at 345 GHz of a GRB afterglow (de Ugarte Postigo *et al.*, 2012b). The ALMA observation also provides the most accurate coordinates available for this GRB. The centroid of the afterglow is located at RA(J2000) = $15h\ 50m\ 44.05s$ and Dec.(J2000) = -46°14′ 06.″5 with a synthesized beam size of 0.″3 × 0.″1 at a position angle of 76 degrees.

Table 2.2: X-shooter observations log.

Mean T-T_0 (hr)	Arm	Exp. time (s)	Slit width (")	Resolution [a]
12.60	UVB	618.02	1.0	4350
12.60	VIS	612.04	0.9	7450
12.60	NIR	600.00	0.9 [b]	5300

(a) Nominal values. (b) K-band blocker was not used.

2.2.5 Radio afterglow observations

Following the detection of an afterglow at submm wavelengths with APEX (de Ugarte Postigo *et al.*, 2011b), radio observations were obtained with the Australia Telescope Compact Array (Wilson *et al.*, 2011, ATCA) two and three days after the trigger. These observations resulted in further detections of the afterglow at 44 GHz (Hancock *et al.*, 2011). This GRB was monitored at 44, 18, 9, and 5 GHz for up to 75 days post-burst, where the flux remained at a sub-mJy level. The lower frequency observations were complicated by the presence of a second source within the field of view (MGPS J155058-461105). The data were reduced using standard procedures in MIRIAD (Sault *et al.*, 1995). An additional late-time visit was performed on 12 Aug 2013 at 5.5 GHz and 9 GHz, to understand the possible contribution of the host galaxy, which was found to be negligible at both bands. The flux evolution of the afterglow at the four ATCA frequencies is also shown in Figure 2.1 and tabulated in Table A.1, together with the rest of the observing bands.

2.2.6 Optical/nIR afterglow spectra

X-shooter (Vernet *et al.*, 2011), an optical/nIR intermediate resolution spectrograph mounted at the Very Large Telescope (VLT) Unit Telescope (UT) 2 in Paranal Observatory (Chile), was used to observe the GRB afterglow starting 12.7 hrs after the *Swift* trigger. The seeing was 0.″9, but observations had to be interrupted due to wind constraints (Piranomonte *et al.*, 2011). The observing log is shown in Table 2.2. We processed the spectra using version 2.0.0 of the X-shooter data reduction pipeline (Goldoni *et al.*, 2006; Modigliani *et al.*, 2010). As the observations were stopped after one exposure, the standard nodding reduction could not be performed. We thus reduced the single frames of each arm with the following steps: We performed bias subtraction, cosmic ray detection and subtraction (van Dokkum, 2001), and flat field correction on the raw frames. From these processed frames the sky emission was subtracted using the Kelson (2003) method

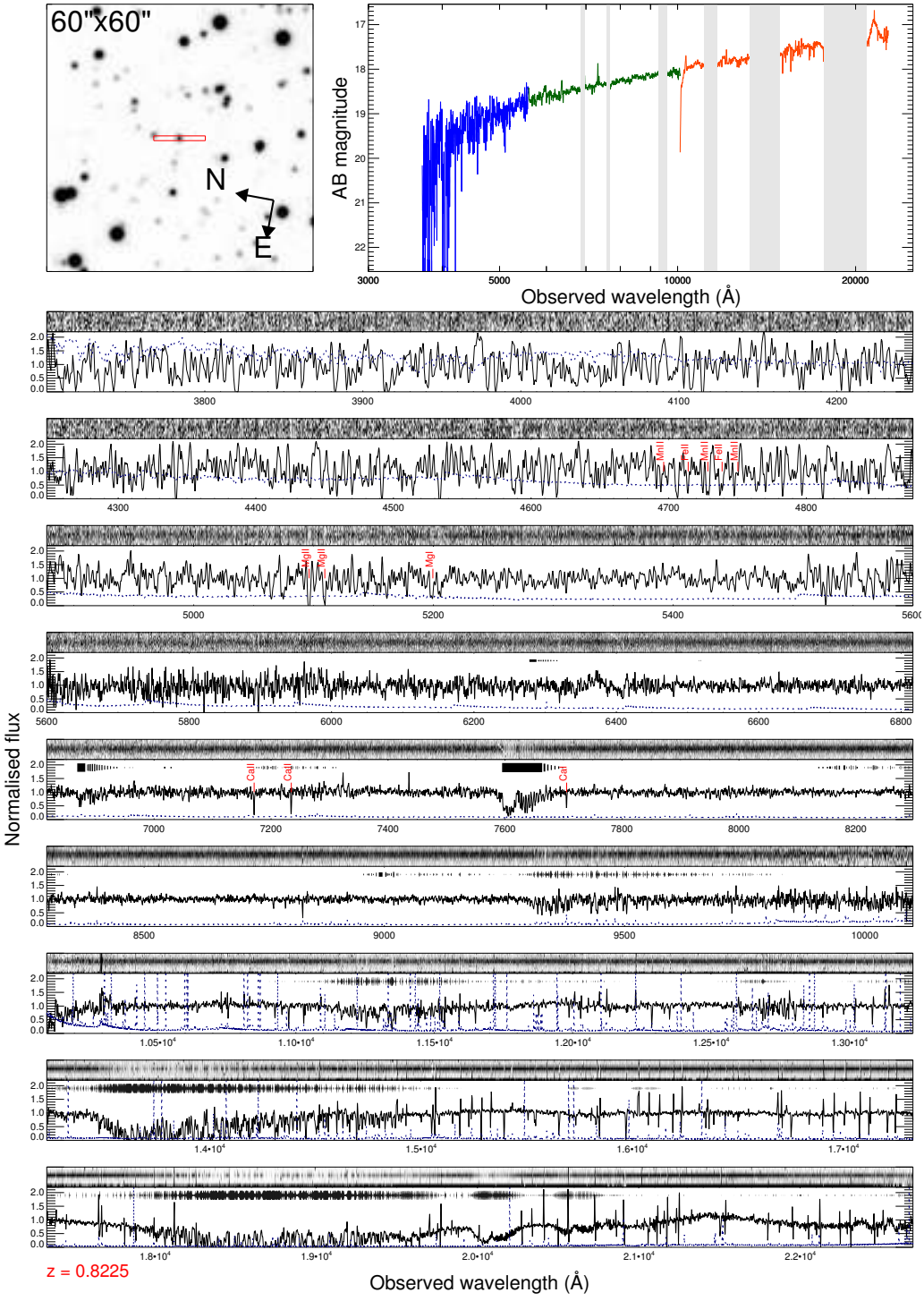

Figure 2.3: X-shooter spectra. Upper panels are the finding chart (left) and an overview of the complete flux calibrated spectra, corrected for Galactic extinction (right). In the bottom plot, we show the normalised spectra, with 3 panels per arm, starting at top with UVB and followed by VIS and NIR. Each panel includes the 2D image and 1D signal and error spectrum. Telluric absorptions are indicated by black bands above the 1D spectrum, their thickness is a measure of the absorption strength.

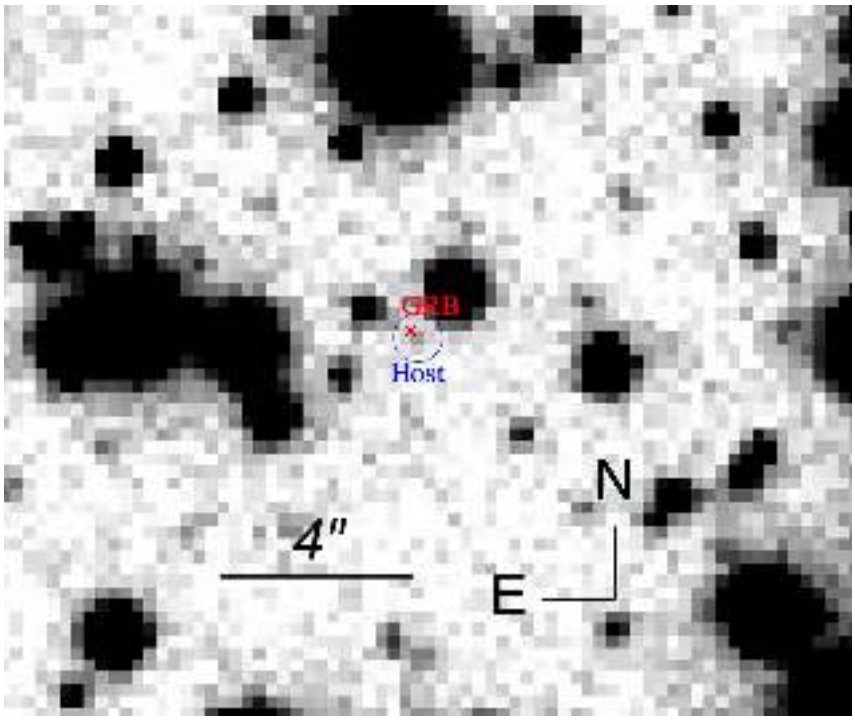

Figure 2.4: Observation of the host galaxy in the I_C-band from VLT/FORS2.

and 1D spectra were extracted directly order by order from the sky-subtracted and flat-field divided frame using optimal extraction (Horne, 1986). The resulting spectra were merged weighting them by the errors and the final merged spectra were then averaged in IDL. The spectra were flux calibrated using observations of the standard star LTT7987 taken the same night. The complete X-shooter spectrum is shown in Fig. 2.3.

2.2.7 Host galaxy imaging

606 days after the burst, the field of GRB 110715A was revisited using GROND searching for a possible host galaxy contribution. However, the data did not reveal any underlying source. We therefore derive only detection limits.

A deeper exposure was obtained on August 2013 with FORS2 at ESO's VLT, 751 days after the burst. The observation consisted of 10×240 s in I_C-band, with a seeing of $0\farcs55$, and data were reduced in a similar fashion as the GROND imaging. An object is detected close to the afterglow position at a magnitude of 26.40 ± 0.36 mag.

2.3 Results and discussion

2.3.1 The afterglow of GRB 110715A in a global context

Using the UVOT and GROND data, and adding the early R_C band observations from Nelson (2011), we construct a composite light curve by shifting all data to the R_C band (no evidence for chromatic evolution is found). This light curve extends over almost four decades in time. Comparing it to the sample of long GRB afterglow light curves taken from Kann *et al.* (2006, 2010, 2011), we find that (after correcting for the significant – 1.6 magnitudes – foreground extinction) the afterglow is among the brightest ever detected (especially after ~ 0.3 days, see Fig. 2.5 left panel), comparable to those of GRB 991208 (Castro-Tirado *et al.*, 2001) and GRB 060729 (Cano *et al.*, 2011), both at lower redshift (see section 2.3.2). It becomes fainter than 20th magnitude only after about 4.5 days. Using the GROND data, we find a best fit for the Spectral Energy Distribution (SED) of the afterglow with $\beta = 0.90 \pm 0.22$, and a small (essentially zero) $A_V = 0.09 \pm 0.18$ using SMC dust. With these data and knowledge of the redshift, we use the method of Kann *et al.* (2006) to shift the afterglow, corrected for all extinction, to $z = 1$. We find a magnitude shift of $dRc = +0.38^{+0.17}_{-0.32}$. At one day after the trigger (in the $z = 1$ frame), it is $R_C = 17.97^{+0.19}_{-0.33}$, and $R_C = 13.90^{+0.23}_{-0.35}$ at 0.001 days. This places the afterglow into the tight peak found by Kann *et al.* (2010) (their figure 6), which is formed by afterglows which are likely forward-shock dominated at early times already. This does not mean that a reverse shock component is not present. According to Kann *et al.* (2010), the early afterglow can be classified as "Limit + Slow Decay" (Kann *et al.*, 2010, their table 5). In this sense, except for the rebrightenings, the afterglow is seen to be typical.

In Figure 2.6, we compare the radio and submm emission of GRB 110715A to the samples of de Ugarte Postigo *et al.* (2012b) and Chandra & Frail (2012): in submm, the afterglow peak brightness is among the brightest observed, with similar luminosity as GRB 030329, GRB 100621A or GRB 100418A, but still an order of magnitude less luminous than the highest luminosity events (GRB 980329, GRB 090313, GRB 080129 or GRB 050904). The situation in radio is similar, with GRB 110715A being amongst the brightest events.

2.3.2 Spectral absorption lines of the optical afterglow

We detect eight absorption features in the complete X-shooter spectrum that we identify as caused by Fe II, Mg II, Mg I, Ca II, and Ca I at a common redshift of 0.8224 ± 0.0001.

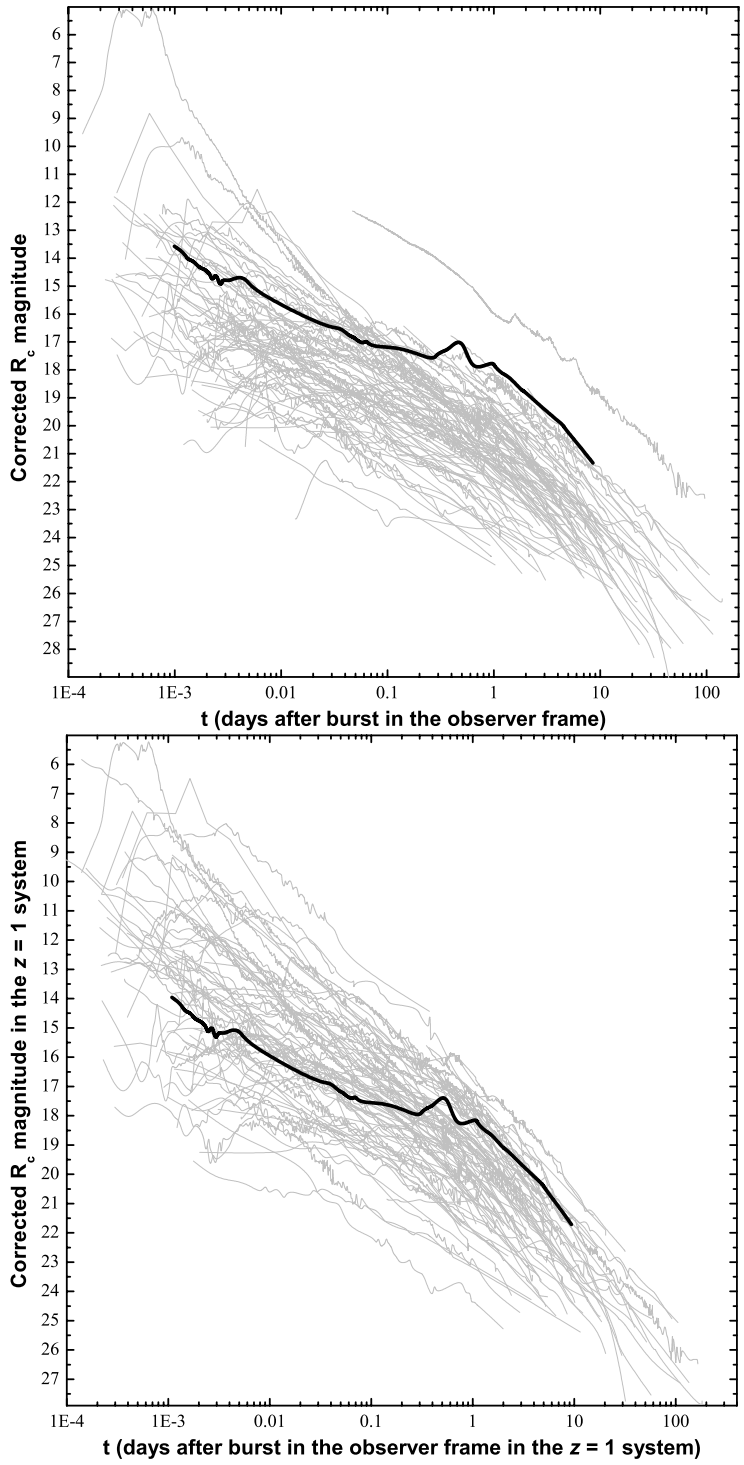

Figure 2.5: The observed R_C-band afterglow of GRB 110715A in comparison to a large sample of long GRB afterglows (left). After correction for the significant foreground extinction, it is seen to be one of the brightest afterglows ever observed. After correcting for rest-frame extinction and shifting to $z = 1$ (right), the afterglow of GRB 110715A is more common, although it remains among the more luminous detected to date at late times.

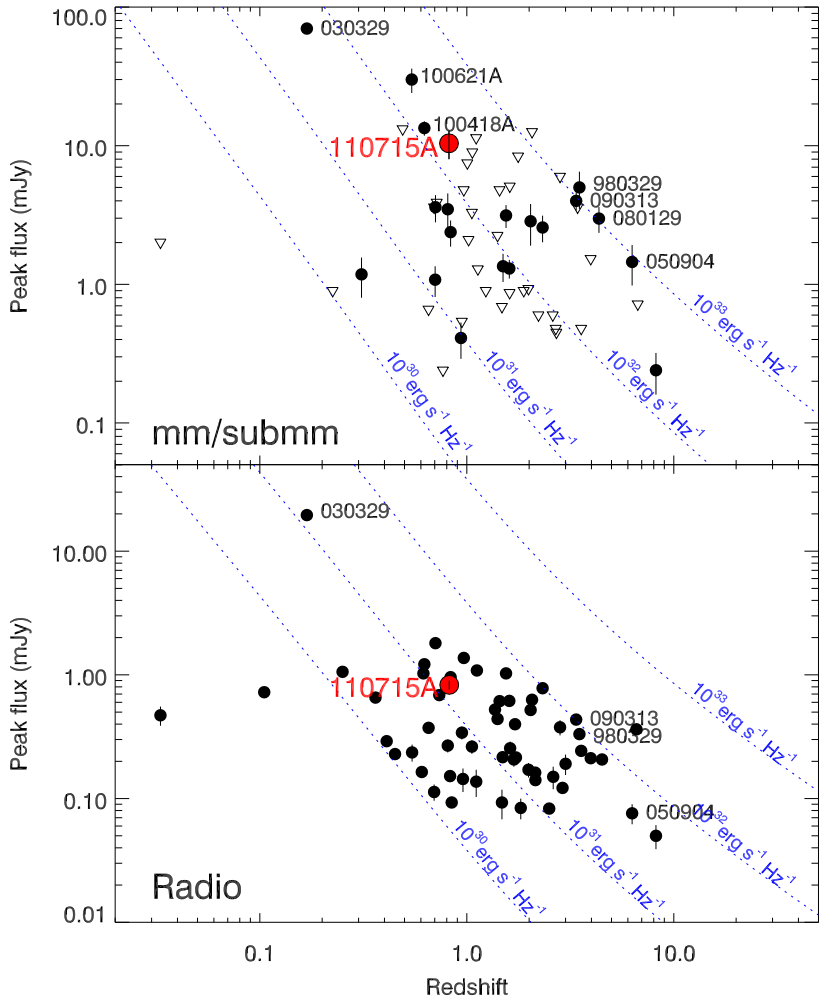

Figure 2.6: Top: mm/submm afterglow as compared with the sample of de Ugarte Postigo *et al.* (2012b). Bottom: Radio afterglow of GRB 110715A compared with the sample of Chandra & Frail (2012)

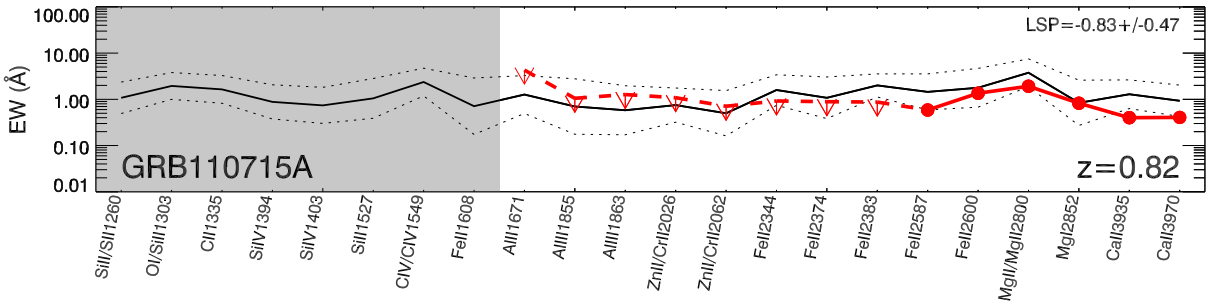

Figure 2.7: Line strength diagram of the afterglow spectrum of GRB 110715A, following the prescription of de Ugarte Postigo *et al.* (2012a).

Table 2.3: Features in the X-shooter spectra.

Feature	λ_{obs} [Å]	EW [Å]	EWc [Å] [a]
Al IIλ1671	∼3045	< 7.82	1.04 ± 0.02
Al IIIλ1855	∼3380	< 1.92	0.89 ± 0.02
Al IIIλ1863	∼3395	< 2.32	0.68 ± 0.02
Zn IIλ2026+Cr IIλ2026	∼3692	< 1.97	0.60 ± 0.02
Cr IIλ2062+Zn IIλ2063	∼3758	< 1.30	0.53 ± 0.02
Fe IIλ2261	∼4120	< 1.81	0.38 ± 0.02
Fe IIλ2344	∼4272	< 1.68	1.74 ± 0.02
Fe IIλ2374	∼4327	< 1.63	1.00 ± 0.02
Fe IIλ2383	∼4342	< 1.60	1.65 ± 0.02
Fe IIλ2587	4714.04	1.07 ± 0.47	1.33 ± 0.02
Fe IIλ2600	4737.32	2.47 ± 0.73	1.85 ± 0.03
Mg IIλ2796	5096.44	1.99 ± 0.34	1.71 ± 0.02
Mg IIλ2803	5109.09	1.50 ± 0.31	1.47 ± 0.02
Mg Iλ2853	5198.29	1.50 ± 0.40	0.78 ± 0.01
Ca IIλ3935	7171.01	0.72 ± 0.07	0.76 ± 0.02
Ca IIλ3970	7234.51	0.74 ± 0.07	0.66 ± 0.02
Ca Iλ4228	7705.26	0.37 ± 0.06	0.11 ± 0.02

(a) Equivalents widths measured on the composite GRB afterglow spectrum (Christensen *et al.*, 2011).

For recent Planck cosmological parameters ($\Omega_{\rm M} = 0.315$, $\Omega_\Lambda = 0.685$, $H_0 = 67.3$ km s^{-1} Mpc^{-1}; Planck *et al.*, 2014), this redshift corresponds to a luminosity distance of 5357.86 Mpc.

We have measured the equivalent widths of these lines and limits for several others using the self-developed code used in Fynbo *et al.* (2009) and de Ugarte Postigo *et al.* (2012a). The results are shown in table 2.3, as well as the composite afterglow spectrum by Christensen *et al.* (2011) for comparison purposes. Using the prescriptions given by de Ugarte Postigo *et al.* (2012a), we find that the neutral element population is higher than average. Detection of Ca Iλ4227, a line rarely observed in GRB afterglows (de Ugarte Postigo *et al.*, 2012a), also supports the low ionisation hypothesis of the material in the line of sight to GRB 110715A.

Following the prescription of de Ugarte Postigo *et al.* (2012a), we obtain a line strength parameter for GRB 110715A of LSP = -0.83 ± 0.47, implying that this event is in the percentile 13.4 of line strengths, and indicating a lower than average column density of material in the line of sight (86.6% of GRBs have stronger lines). This often indicates a small host galaxy (de Ugarte Postigo *et al.*, 2012a). This is consistent with the fact that there are no velocity components in the absorption features faster than 30 km s^{-1}.

2.3.3 The host galaxy

We computed the distance between the afterglow and the host galaxy core. The centroid is offset by 0.21 ± 0.03 " with respect to the ALMA position, which at the redshift of GRB 110715A corresponds to 1.56 ± 0.19 kpc. This is comparable to the typical offset of 1.2 kpc seen for long GRBs (de Ugarte Postigo *et al.*, 2012a). The host absolute magnitude (AB) would be M = -18.2 mag at a restframe wavelength of 4200 Å, which is similar to the Johnson B-band (without needing to make assumptions on the host galaxy spectral index).

The luminosity of the host galaxy is low, even relative to other GRB hosts (which tend to occur in lower-mass and lower-luminosity galaxies than average at $z \lesssim 1.5$; e.g. Perley *et al.*, 2016a), although it is by no means extreme or exceptional. For example, relative to the UV luminosity distribution of nine galaxies at roughly similar redshift ($0.5 < z < 1.1$) in the TOUGH sample (Schulze *et al.*, 2015), this host galaxy is less luminous than six or more, depending on the unknown k-correction across the Balmer break which is not known for the TOUGH sample. We also compared this magnitude to synthetic B-band magnitudes of galaxies from the larger, multi-colour SHOALS sample (Perley *et al.*, 2016c, and work in prep.). The host of GRB is about 0.6 mag less luminous than the median B magnitude of $0.5 < z < 1.1$ galaxies in this sample, and is more luminous than only five out of these 21 galaxies. Compared to a more local galaxy population, it is slightly more luminous than the LMC ($M_B \sim -17.5$) but of course much less luminous than nearby spirals such as the Milky Way or M31 ($M_B \sim -20.5$ to -21). This faint host galaxy is consistent with the faint and unresolved absorption features seen in the afterglow spectrum. Considering also its very low ionisation environment, all evidence suggest that the sight-line towards GRB 110715A is probing an small dwarf host galaxy, maybe in its initial star-forming episode due to the low background ionising radiation, which keeps an unusual abundance of Ca I.

2.3.4 Modeling of the afterglow evolution

2.3.4.1 Model and fitting description

The afterglow emission was modeled with the numerical code of Jóhannesson *et al.* (2006). This software has been used successfully to model several different afterglows, including GRB 060121 (de Ugarte Postigo *et al.*, 2006), GRB 050408 (de Ugarte Postigo *et al.*, 2007), GRB 060526 (Thöne *et al.*, 2010), and GRB 050525A (Resmi *et al.*, 2012). This model assumes the emission originates in a forward shock only, with a top-hat jet configuration.

Table 2.4: The lower and upper boundaries of the priors on parameters used in the analysis.

Parameter	Distribution	Lower	Upper
E_{iso} [10^{53} erg]	log-uniform	0.01	10000
Γ_0	log-uniform	10	2000
θ_0 [deg]	log-uniform	0.1	90
p	uniform	1.1	4.0
ϵ_i	log-uniform	0.0001	0.5
ϵ_e	log-uniform	0.0001	0.5
ϵ_B	log-uniform	0.0001	0.5
A_* [$5.015 \cdot 10^{11}$ cm^{-3}]	log-uniform	0.00001	100
n_0 [cm^{-3}]	log-uniform	0.0001	1000
t_{sh} [min]	log-uniform	0.00001	200
r_{sh}	uniform	1	50
t_1 [days]	log-uniform	0.0001	200
E_1/E_0	uniform	0	50
$A_{V,host}$ [mag]	uniform	0	1.0
$E(B-V)$ [mag]	Gaussian[(a)]		

(a) $\mu = 0.56$, $\sigma = 0.04$

The algorithm simulates that a slab of matter with mass M_0 is ejected with a Lorentz factor of Γ_0 into a cone with a half-opening angle of θ_0. The slab starts accumulating matter and slows down in the process. Energy injections (E_i) are modeled as slabs of matter moving at lower speeds than the forward shock ($\Gamma_i < \Gamma_0$) and catching up to it at later times. At the time of collision, the energy and momentum of the forward shock of the injected slab is instantaneously added to the already moving mass. The emission from any reverse shock formed in the collision is ignored. To calculate the emission, we assume that a fixed fraction of the energy of the forward shock is contained in the magnetic field and electron distribution of the forward shock. For the magnetic field, this fraction is denoted with ϵ_B. In Jóhannesson *et al.* (2006), the fraction of energy contained in the electrons was denoted with ϵ_e. This is now changed, to allow for the slope of the electron power-law distribution, p, to be less than 2. We used the formalism of Panaitescu & Kumar (2001) and denote with ϵ_i the fraction of energy contained in the electrons with the lowest energy in the distribution. The highest energy in the distribution is then limited such that the total energy of the electron distribution never exceeds a fraction ϵ_e of the forward shock energy.

To explain the data, we need a model that includes a temporary increase in flux around 0.3 days after the onset of the GRB that is observed in the light curves shown in Figure 2.1. We chose three different types of models that we expect have this behavior:

a model with a constant density interstellar medium (n_0) and a single energy injection (CM), a model with a wind density external medium ($\rho = A_* r^{-2}$) and a single energy injection (WM), and a model with a wind termination shock (with fractional change in density at the shock front denoted by r_{sh}) but no energy injection (TS).

The best fit model parameters are found using Bayesian inference using the MultiNest tool (Feroz *et al.*, 2009). MultiNest is well suited for exploring the parameter space of the non-linear afterglow model and finds parameter correlation as well as all modes in the parameter space fitting the data similarly well. In addition to the afterglow model parameters, we also determine the host dust extinction in the fit, which we assume follows an SMC-like extinction curve. It is also possible to let the Galactic dust extinction vary as a nuisance parameter. This is of special interest in our case due to the large and uncertain value along the GRB line of sight through our Galaxy.

One of the main benefits of a Bayesian analysis is the introduction of prior distributions on parameters. For this analysis we have unfortunately very little prior knowledge on their values. We therefore opted for flat priors on all parameters, but Galactic reddening, and made sure the parameter limits were large enough so that the posterior is not affected by these limits unless they are physical (see Table 2.4). Examples of such physical boundaries are the requirements that the extinction of the host be positive ($A_{V,host} > 0$) and the fractional change in density at the shock front should not decrease ($r_{sh} > 1$). We also constrain the fraction of energy in the electrons (ϵ_e) and magnetic field (ϵ_B) such that the fraction of energy contained in the rest of the jet, $\epsilon = 1 - \epsilon_e - \epsilon_B$, is larger than both ϵ_e and ϵ_B. This is to make sure the jet's energy is not dominated by that of the electrons and the magnetic field. The constraint is not hard and ϵ is usually somewhere in between ϵ_e and ϵ_B if both are large like in this analysis. There is also the hard prior that $\epsilon_e > 1.1\epsilon_i$ so the energy in the total electron distribution is always at least 10 percent greater than that contained in the electrons with the lowest value. This constraint is actually reached in all of our models, resulting in a strong correlation between ϵ_e and ϵ_i (see Appendix F).

Due to several reasons, such as the high Galactic reddening, the wavelength range on which H I absorption is located, and the difficulties to compute the effective wavelength of the UVOT *white* filter due to its band width, we performed different fits in order to identify and quantify the sources of systematic uncertainties.

2.3.4.2 The best fit

We found the best fit models to be those in which we excluded the UV bands, we set MW extinction as a nuisance parameter, and UVOT *white* band was shifted to V (see

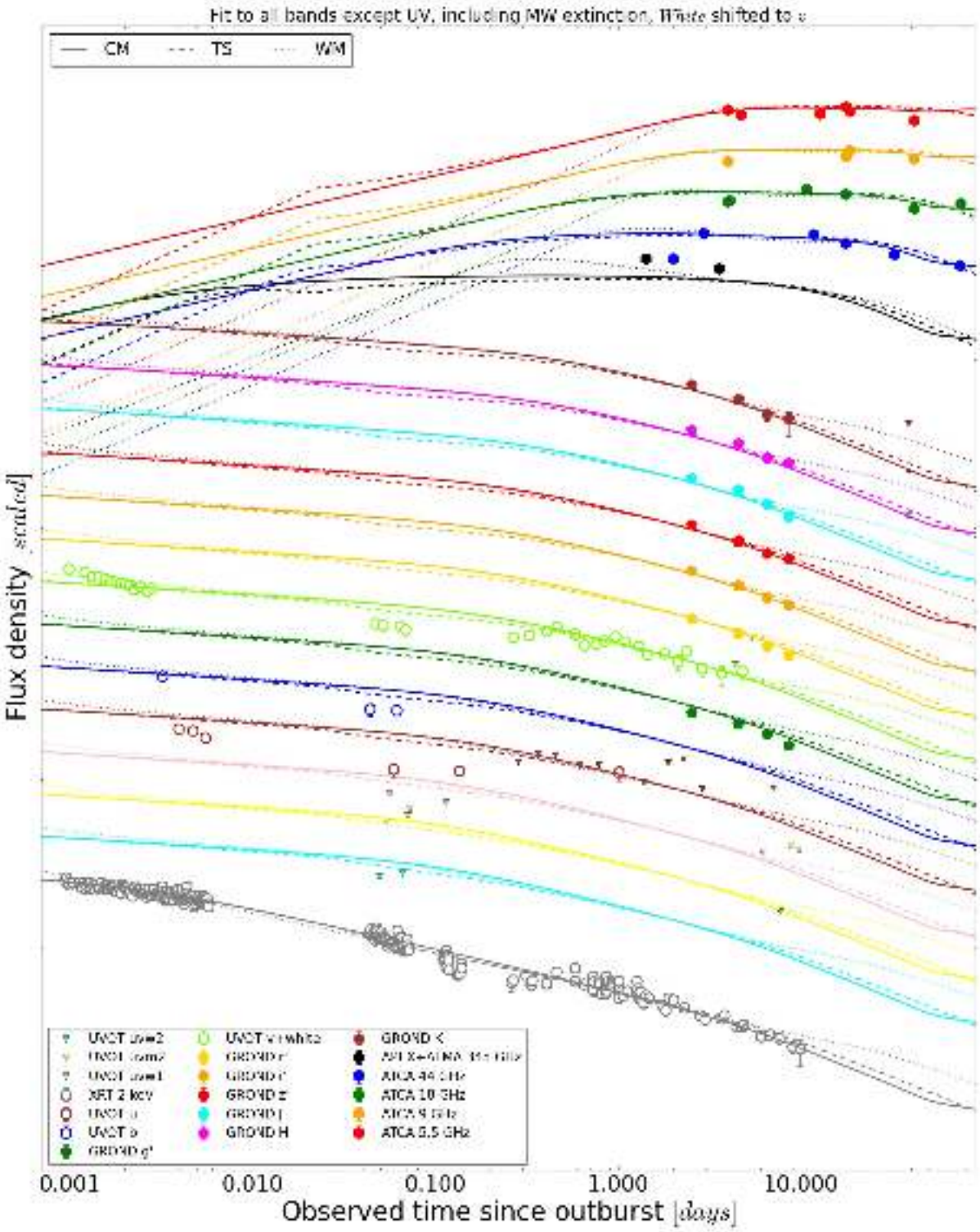

Figure 2.8: Best fits to the GRB 110715A light curves. Fluxes are independently scaled for each band for clarity. The complete set of LC plots for all performed fits can be inspected in Appendix C.

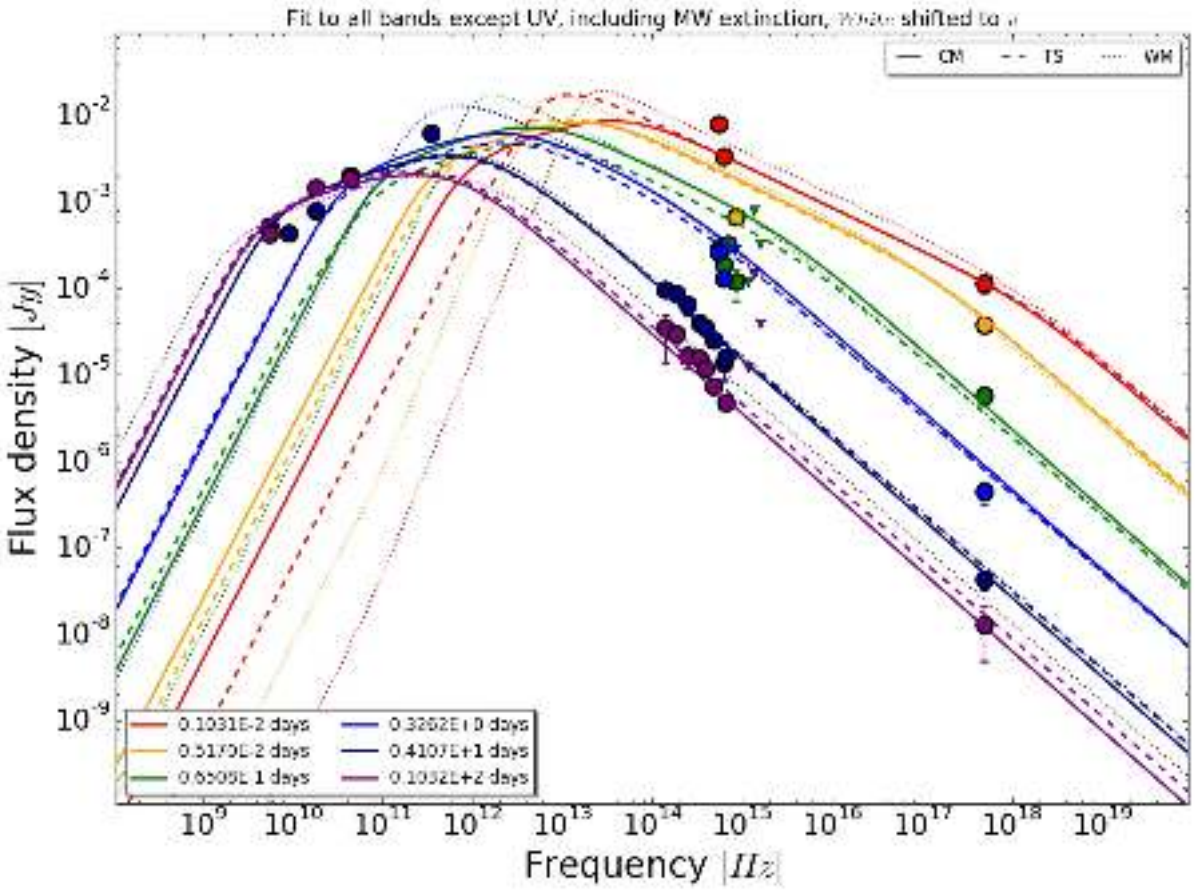

Figure 2.9: Best fits to the SED for GRB 110715A observed at several epochs. The complete set of SED plots for all performed fits can be inspected in Appendix D.

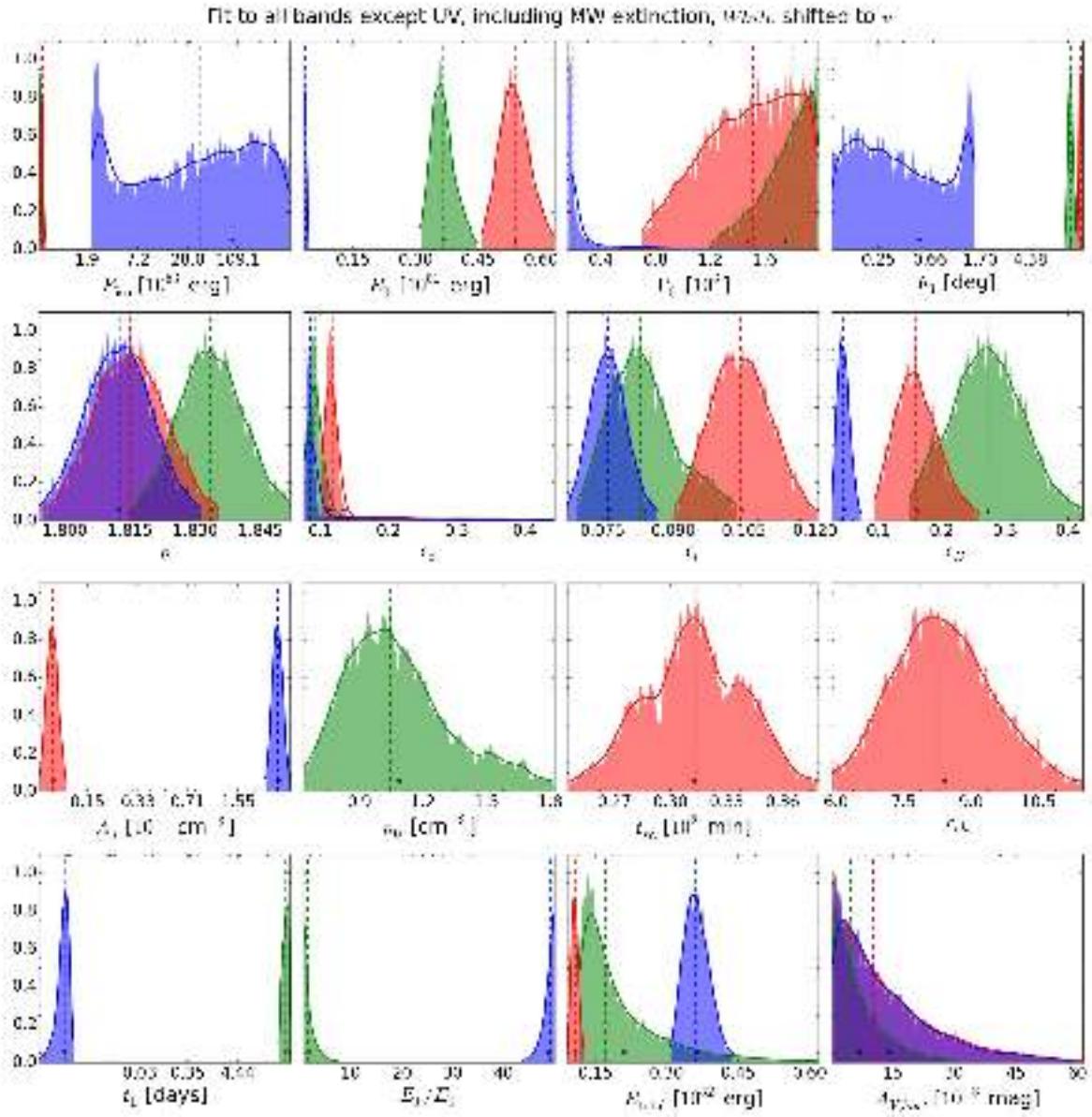

Figure 2.10: Parameter distribution for the best fits to the GRB 110715A observations. The complete set of marginal 1d plots for all performed fits can be inspected in Appendix E.

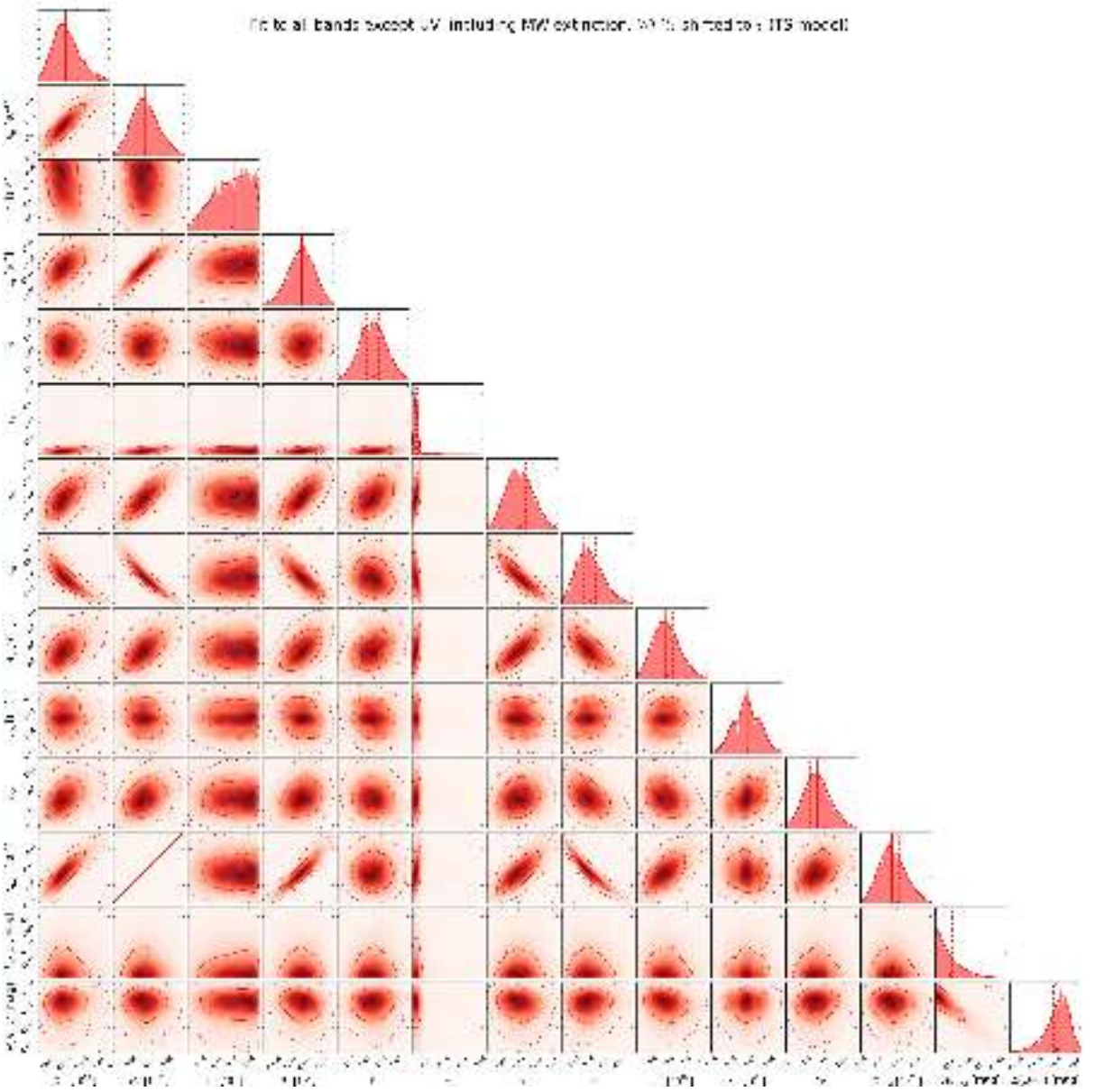

Figure 2.11: Parameter correlations for the best fit Ts model. The complete set of marginal 2d plots for all performed fits can be inspected in Appendix F.

Table 2.5: The parameter posterior mean as reported by MultiNest for the three different models of the best fit data-set.

Parameter	CM	TS	WM
$E_{\rm iso}$ [erg]	$53.63^{+0.66}_{-0.62} \times 10^{51}$	$55.10^{+0.92}_{-0.82} \times 10^{51}$	$0.38^{+0.60}_{-0.26} \times 10^{55}$
E_0 [erg]	$3.63^{+0.14}_{-0.12} \times 10^{50}$	$5.36^{+0.18}_{-0.17} \times 10^{50}$	$3.64^{+0.15}_{-0.14} \times 10^{49}$
Γ_0 1799^{+82}_{-110}	1510^{+180}_{-200}	184^{+35}_{-12}	
θ_0 [deg]	$9.44^{+0.22}_{-0.20}$	11.32 ± 0.12	$0.35^{+0.27}_{-0.13}$
p	$1.8334^{+0.0038}_{-0.0036}$	1.8148 ± 0.0041	$1.8124^{+0.0037}_{-0.0039}$
ϵ_e	$9.32^{+0.57}_{-0.41} \times 10^{-2}$	$(11.64 \pm 0.40) \times 10^{-2}$	$(8.53 \pm 0.26) \times 10^{-2}$
ϵ_i	$(8.31 \pm 0.31) \times 10^{-2}$	$(10.44 \pm 0.32) \times 10^{-2}$	$(7.62 \pm 0.19) \times 10^{-2}$
ϵ_B	$(2.72 \pm 0.28) \times 10^{-1}$	$(1.59 \pm 0.16) \times 10^{-1}$	$(4.44 \pm 0.47) \times 10^{-2}$
A_* $[5.015 \cdot 10^{11}$ cm$^{-3}]$		$0.01747^{+0.00078}_{-0.00074}$	$0.571^{+0.023}_{-0.022}$
n_0 [cm^{-3}]	$1.05^{+0.12}_{-0.10}$		
t_{sh} [min]		$3.13^{+0.13}_{-0.12} \times 10^{1}$	
r_{sh}		$8.33^{+0.56}_{-0.54}$	
t_1 [days]	$5.03^{+0.42}_{-0.44} \times 10^{1}$		$(6.79 \pm 0.91) \times 10^{-4}$
E_1/E_0	$1.34^{+0.59}_{-0.35}$		$49.01^{+0.43}_{-0.61}$
$E_{\rm total}$ [erg]	$1.72^{+0.42}_{-0.24} \times 10^{51}$	$10.72^{+0.36}_{-0.34} \times 10^{50}$	$3.62^{+0.14}_{-0.12} \times 10^{51}$
$A_{V,host}$ [mag]	$0.0048^{+0.0031}_{-0.0021}$	$0.0102^{+0.0063}_{-0.0046}$	$0.0099^{+0.0064}_{-0.0042}$
$E(B-V)$ [mag]	0.5249 ± 0.0030	$0.5277^{+0.0037}_{-0.0044}$	$0.5749^{+0.0035}_{-0.0043}$

Table 2.6 and Appendix B for a detailed statistical analysis of the results for the complete grid of fits). They are shown overlaid on the data in Figures 2.8 (light curves) and 2.9 (spectral energy distributions), as well as for all fits in Appendices C and D. An example of the plots of the parameter distributions and their correlations are shown in Figures 2.10 and 2.11 and for all fits in Appendices E and F. Bayesian evidences and χ^2s are shown in Table 2.6. This table suggests the TS fit as the most plausible model that describes the afterglow. However, none of them is either a statistically good fit or can fully explain the temporary flux increase at $\sim$0.3 days. Looking at Appendix B, we can also observe that there are no statistical arguments to reject most of the fits when compared with the best.

Despite the time of the wind termination shock for the best TS model being at the correct location and the magnitude of it being a factor of 2 greater than expected, the effect on the light curves is not strong enough to explain the data. Due to the spectral parameters required in the fit, the wind termination shock causes a flux decrease rather than an increase as the cooling break is just below the optical band. The slow decay in the early X-ray light curve in the model is caused by the injection break being above the X-ray frequency. This requires there to be a spectral evolution in the X-ray light curve that is not observed. In both cases the preferred location of the energy injection is at a different point than expected. For the best fit of the CM model it is much later and serves only to explain the latest radio points while for the WM model it happens very early to explain the shallower decay between 0.01 and 1 days. The best model also has a hard time explaining the rapid decline in the light curve observed by the GROND instrument. The earliest points are under-predicted while the later points are over-predicted. This is again something that all the models fail to reproduce. The CM model does a slightly better job, but the WM model is worst. The models have a similarly hard time at explaining the late time X-ray light curve as they don't decay rapidly enough.

Finally, the best model is unable to explain the early and late radio and submm data. The model has a hard time explaining the rapid rise of the 44 GHz data simultaneously with the decay of the 345 GHz data and the rather flat light curve at 5.5 GHz. The self-absorption break, ν_a, needs to pass through the 44 GHz band at around 2 days to explain the rapid size and it should have already passed the 345 GHz band at 1 day and the 5.5 GHz band at 2 days. It is impossible for the model to meet these criteria. In addition, the 44 GHz light curve starts decaying at around 10 days with a slope that is incompatible with post jet-break evolution and at the same time the 18 GHz band is compatible with being nearly constant. The CM model has similar issues as the TS model although it does slightly better at late times because the injection lifts the radio light curve to match the last points. There is, however, no other indication for the energy injection and it is unlikely to be the correct physical interpretation. The WM model does

the best job with the submm and radio data, but is still far from explaining the details of the observed afterglow.

Table 2.5 shows the posterior median for the parameter values and their associated 68% statistical errors. The parameter values that give the smallest χ^2 are usually located near the peak of the posterior distributions, and their distributions are mostly symmetric, with notable exceptions in the WM model where long tails can be seen for $E_{\rm iso}$, Γ_0, and θ_0. The inferred values are mostly typical for a GRB afterglow with a few exceptions. The half opening angle θ_0 in the WM model is unreasonably low and requires an extreme confinement of the outflow. It is also the worst performer of the 3 models and we therefore consider it an unreasonable model. The value of the electron power-law index p is on the lower side and lower than expected from shock-acceleration theory (Achterberg *et al.*, 2001). It is, however, well within the range of values deduced from observations of relativistic shocks (Shen *et al.*, 2006). The fraction of energy contained in the magnetic field and the electron distribution, ϵ_B, and ϵ_e, respectively is rather large. ϵ_i is also larger than usual and constrained mostly by the equipartition requirements for the electron energy distribution rather than the position of the injection peak in the synchrotron spectrum. These large values cause the afterglow to be in the fast-cooling regime for the entire duration of the afterglow and the assumption of no radiative losses is likely invalid.

Our values for the host extinction are compatible with the value being very small as found earlier using GROND data only. The statistical error is significantly smaller because we use the entire data-set, but the exact value is model dependent.

As already discussed, the Galactic line of sight extinction is important in the GRB direction. The expected uncertainty could be large too, so similarly to the host galaxy, the Galactic $E(B-V)$ was left in some fits as a free parameter. Resulting Galactic and host galaxy solutions show a clear anti-correlation, limiting our constraints of the inferred host galaxy $A_{V,host}$. In Appendix F we include the two dimensional marginal plots for the $E(B-V)$ of the Galactic extinction with the rest of the parameters when it is included in the fit. As shown, the galactic $E(B-V)$ value is model dependent, and results are somewhat bimodal, sometimes consistent with the dust maps of Schlegel *et al.* (1998), and sometimes with Schlafly & Finkbeiner (2011), the latter being the more favoured. The figures also show that the upper value found for the $E(B-V)$ parameter in this analysis is basically bound by the host extinction going to 0.

Table 2.6: Goodness of the different fits to the GRB 110715A data. A detailed analysis is given in Appendix B.

Model	Evidence	χ^2_r	$\chi^2_{r,x}$ (a)	$\chi^2_{r,o}$ (b)	$\chi^2_{r,r}$ (c)
CM/XOR/WC	-1066.52 ± 0.19	6.52	2.45	16.49	27.98
TS/XOR/WC	-951.65 ± 0.20	6.24	2.0	16.12	30.48
WM/XOR/WC	-1181.09 ± 0.19	9.78	2.61	29.6	39.61
CM/XUOR/WN	-1677.46 ± 0.20	6.92	2.46	15.75	35.57
TS/XUOR/WN	-1503.57 ± 0.20	6.79	1.92	18.22	31.42
WM/XUOR/WN	-1753.24 ± 0.20	57.02	2.25	259.83	47.46
CM/XOR/WN	-1667.78 ± 0.20	6.79	2.45	15.86	35.35
TS/XOR/WN	-1491.05 ± 0.20	6.5	1.91	17.61	31.27
WM/XOR/WN	-1730.71 ± 0.20	54.46	2.21	261.71	47.0
CM/XOR/VC	-1039.59 ± 0.20	5.69	2.49	12.62	26.91
TS/XOR/VC	-988.59 ± 0.20	5.51	2.14	11.86	31.2
WM/XOR/VC	-1145.41 ± 0.19	7.45	2.73	18.03	37.6
CM/XOR/VN	-1015.83 ± 0.21	5.73	2.47	13.0	26.79
TS/XOR/VN	-995.70 ± 0.20	5.5	2.15	11.34	32.54
WM/XOR/VN	-1129.24 ± 0.19	7.3	2.76	17.48	36.38
CM/O/VC	-201.49 ± 0.16	175.87	8.82	37.34	2997.26
TS/O/VC	-206.60 ± 0.18	71.38	19.67	70.76	800.15
WM/O/VC	-237.56 ± 0.15	727.47	277.16	228.39	8762.93
CM/R	-267.53 ± 0.16	57.98	48.6	100.81	25.24
TS/R	-252.66 ± 0.15	195.24	135.6	457.94	23.98
WM/R	-249.27 ± 0.18	467.74	190.45	1597.79	22.54
CM/XUO/VC	-555.22 ± 0.18	164.1	1.88	13.01	3000.39
TS/XUO/VC	-466.51 ± 0.21	53.66	1.73	68.71	727.94
WM/XUO/VC	-733.27 ± 0.18	183.79	2.12	14.73	3359.54
CM/XR/	-600.80 ± 0.18	8.4	2.38	25.9	25.76
TS/XR/	-558.08 ± 0.18	8.82	1.87	29.13	28.49
WM/XR/	-671.99 ± 0.18	10.69	2.29	35.22	34.55
CM/UOR/VC	-561.73 ± 0.19	20.83	18.66	26.5	30.35
TS/UOR/VC	-541.22 ± 0.19	47.79	41.7	77.02	25.68
WM/UOR/VC	-676.66 ± 0.19	23.52	25.91	11.13	35.58
CM/XUOR/VCE	-848.73 ± 0.19	9.82	3.66	21.3	28.05
TS/XUOR/VCE	-670.00 ± 0.20	13.16	2.24	39.29	29.35
WM/XUOR/VCE	-1044.04 ± 0.19	15.01	3.05	38.75	46.29
CM/XUOR/VCL	-547.08 ± 0.18	14.02	1.65	26.9	28.55
TS/XUOR/VCL	-494.77 ± 0.19	20.93	1.86	47.0	29.91
WM/XUOR/VCL	-672.83 ± 0.18	65.64	2.99	174.44	45.23

(a) χ^2 computed only with the X-ray data.
(b) χ^2 computed only with the UV, optical and nIR data.
(c) χ^2 computed only with the submm and mm data.
Fit Id = (A)/(B)/(C)(D)(E)
(A) = Model used (CM/TS/WM)
(B) = Wavelength range of the observations used for the model fitting:
X = XRT 2 keV
U = UVOT UVW2, UVM2, UVW1, and U
O = Rest of the UVOT and GROND bands
R = Radio and submm bands
(C) = UVOT White band shifted to UVOT (V) or independent (W)
(D) = Treatment of the Galactic reddening:
C = Corrected
N = Set to a nuisance parameter
(E) = Time interval used for the model fitting:
E = From $t = 0.05$ days
L = From $t = 0.5$ days

Table 2.7: Parameter posterior statistics for each performed fit ($E_{\rm iso}$, E_0, Γ_0, θ_0, and p).

Fit Id	$E_{\rm iso}[erg]$	E_0 [erg]	Γ_0	θ_0 [deg]	p
CM/XOR/WC	$5.38^{+0.29}_{-0.27} \times 10^{52}$	$3.33^{+0.29}_{-0.23} \times 10^{50}$	1783^{+89}_{-110}	$8.83^{+0.28}_{-0.23}$	$1.8542^{+0.0040}_{-0.0041}$
TS/XOR/WC	$50.47^{+0.76}_{-0.67} \times 10^{51}$	$4.56^{+0.15}_{-0.15} \times 10^{50}$	1410^{+210}_{-220}	$10.91^{+0.12}_{-0.13}$	$1.8300^{+0.0041}_{-0.0043}$
WM/XOR/WC	$1.52^{+0.96}_{-0.70} \times 10^{55}$	$4.02^{+0.15}_{-0.14} \times 10^{49}$	$152.9^{+5.1}_{-4.4}$	$0.186^{+0.067}_{-0.041}$	$1.8510^{+0.0038}_{-0.0039}$
CM/XUOR/WN	$0.114^{+0.14}_{-0.055} \times 10^{55}$	$20.88^{+0.68}_{-0.68} \times 10^{48}$	362^{+75}_{-43}	$0.49^{+0.19}_{-0.16}$	$1.8405^{+0.0035}_{-0.0036}$
TS/XUOR/WN	$48.38^{+0.56}_{-0.50} \times 10^{51}$	$4.01^{+0.11}_{-0.10} \times 10^{50}$	1360^{+230}_{-220}	$10.46^{+0.12}_{-0.13}$	$1.8127^{+0.0041}_{-0.0039}$
WM/XUOR/WN	$0.49^{+0.16}_{-0.15} \times 10^{57}$	$2.09^{+0.32}_{-0.25} \times 10^{51}$	$67.81^{+0.55}_{-0.49}$	$0.242^{+0.052}_{-0.035}$	2.0415 ± 0.0050
CM/XOR/WN	$0.86^{+1.00}_{-0.38} \times 10^{54}$	$21.13^{+0.72}_{-0.70} \times 10^{48}$	384^{+88}_{-54}	$0.57^{+0.19}_{-0.18}$	$1.8423^{+0.0035}_{-0.0036}$
TS/XOR/WN	$48.40^{+0.54}_{-0.52} \times 10^{51}$	$4.02^{+0.11}_{-0.10} \times 10^{50}$	1350^{+230}_{-220}	$10.47^{+0.13}_{-0.12}$	$1.8137^{+0.0040}_{-0.0039}$
WM/XOR/WN	$0.49^{+0.16}_{-0.15} \times 10^{57}$	$2.08^{+0.29}_{-0.25} \times 10^{51}$	$67.90^{+0.57}_{-0.52}$	$0.244^{+0.050}_{-0.036}$	$2.0402^{+0.0049}_{-0.0050}$
CM/XOR/VC	$51.07^{+0.51}_{-0.47} \times 10^{51}$	$3.92^{+0.13}_{-0.13} \times 10^{50}$	1813^{+77}_{-100}	$10.09^{+0.17}_{-0.21}$	$1.8433^{+0.0039}_{-0.0038}$
TS/XOR/VC	$54.23^{+0.99}_{-0.88} \times 10^{51}$	$5.20^{+0.19}_{-0.17} \times 10^{50}$	1510 ± 190	$11.25^{+0.12}_{-0.13}$	$1.8273^{+0.0040}_{-0.0044}$
WM/XOR/VC	$0.38^{+0.56}_{-0.26} \times 10^{55}$	$3.66^{+0.14}_{-0.13} \times 10^{49}$	184^{+39}_{-13}	$0.36^{+0.30}_{-0.13}$	$1.8311^{+0.0040}_{-0.0037}$
CM/XOR/VN	$53.63^{+0.66}_{-0.62} \times 10^{51}$	$3.63^{+0.14}_{-0.12} \times 10^{50}$	1799^{+82}_{-110}	$9.44^{+0.22}_{-0.20}$	$1.8334^{+0.0038}_{-0.0036}$
TS/XOR/VN	$55.10^{+0.92}_{-0.82} \times 10^{51}$	$5.36^{+0.18}_{-0.17} \times 10^{50}$	1510^{+180}_{-200}	11.32 ± 0.12	1.8148 ± 0.0041
WM/XOR/VN	$0.38^{+0.60}_{-0.26} \times 10^{55}$	$3.64^{+0.15}_{-0.14} \times 10^{49}$	184^{+35}_{-12}	$0.35^{+0.27}_{-0.13}$	$1.8124^{+0.0037}_{-0.0039}$
CM/O/VC	$0.087^{+0.33}_{-0.065} \times 10^{55}$	$5.34^{+0.53}_{-0.42} \times 10^{49}$	216^{+140}_{-41}	$0.89^{+0.82}_{-0.49}$	1.702 ± 0.025
TS/O/VC	$0.211^{+0.14}_{-0.096} \times 10^{57}$	$0.36^{+0.23}_{-0.14} \times 10^{52}$	279^{+22}_{-19}	$0.521^{+0.083}_{-0.079}$	$1.567^{+0.030}_{-0.034}$
WM/O/VC	$2.13^{+0.98}_{-0.79} \times 10^{56}$	$0.401^{+0.16}_{-0.070} \times 10^{51}$	311^{+23}_{-20}	$0.170^{+0.046}_{-0.032}$	2.274 ± 0.048
CM/R	$0.165^{+0.56}_{-0.094} \times 10^{55}$	$1.69^{+0.12}_{-0.11} \times 10^{50}$	270^{+220}_{-74}	1.16 ± 0.61	$1.978^{+0.021}_{-0.020}$
TS/R	$0.0195^{+0.32}_{-0.0084} \times 10^{55}$	$1.68^{+0.38}_{-0.22} \times 10^{51}$	57^{+160}_{-28}	$11.1^{+4.2}_{-8.5}$	3.03 ± 0.10
WM/R	$1.17^{+0.15}_{-0.13} \times 10^{53}$	$1.083^{+0.12}_{-0.100} \times 10^{51}$	277^{+140}_{-94}	$11.23^{+0.61}_{-0.67}$	$3.446^{+0.072}_{-0.077}$
CM/XUO/VC	$0.90^{+0.22}_{-0.13} \times 10^{53}$	$6.99^{+0.64}_{-0.55} \times 10^{49}$	590^{+310}_{-200}	$3.20^{+0.16}_{-0.20}$	$1.7667^{+0.0047}_{-0.0044}$
TS/XUO/VC	$10.81^{+0.81}_{-0.80} \times 10^{54}$	$6.29^{+0.26}_{-0.23} \times 10^{50}$	347^{+11}_{-13}	$0.868^{+0.040}_{-0.033}$	$1.9284^{+0.0056}_{-0.0055}$
WM/XUO/VC	$0.088^{+0.11}_{-0.052} \times 10^{56}$	$0.567^{+0.11}_{-0.088} \times 10^{50}$	220^{+23}_{-15}	$0.289^{+0.18}_{-0.097}$	$1.7821^{+0.0050}_{-0.0048}$
CM/XR/	$5.68^{+0.16}_{-0.14} \times 10^{52}$	$4.40^{+0.22}_{-0.20} \times 10^{50}$	1330 ± 220	$10.09^{+0.22}_{-0.21}$	$1.7821^{+0.0054}_{-0.0059}$
TS/XR/	$4.84^{+0.13}_{-0.13} \times 10^{52}$	$4.63^{+0.20}_{-0.18} \times 10^{50}$	1250^{+250}_{-230}	$11.22^{+0.11}_{-0.12}$	$1.8425^{+0.0060}_{-0.0057}$
WM/XR/	$2.15^{+0.99}_{-0.82} \times 10^{56}$	$4.32^{+0.26}_{-0.23} \times 10^{50}$	59.8 ± 1.1	$0.162^{+0.044}_{-0.029}$	$1.7529^{+0.0071}_{-0.0067}$
CM/UOR/VC	$0.142^{+0.21}_{-0.073} \times 10^{55}$	$20.00^{+0.55}_{-0.52} \times 10^{48}$	535^{+230}_{-100}	$0.43^{+0.19}_{-0.16}$	$2.174^{+0.012}_{-0.011}$
TS/UOR/VC	$3.43^{+0.17}_{-0.17} \times 10^{53}$	$3.95^{+0.21}_{-0.20} \times 10^{50}$	1030^{+290}_{-260}	$3.894^{+0.087}_{-0.092}$	$1.8073^{+0.0075}_{-0.0071}$
WM/UOR/VC	$1.40^{+0.96}_{-0.69} \times 10^{55}$	$4.14^{+0.16}_{-0.15} \times 10^{49}$	$199.8^{+13}_{-8.3}$	$0.197^{+0.080}_{-0.046}$	2.153 ± 0.011
CM/XUOR/VCE	$6.45^{+0.29}_{-0.28} \times 10^{52}$	$3.17^{+0.17}_{-0.17} \times 10^{50}$	1680^{+130}_{-160}	$8.03^{+0.16}_{-0.14}$	1.9169 ± 0.0046
TS/XUOR/VCE	$5.78^{+0.23}_{-0.19} \times 10^{52}$	$5.42^{+0.23}_{-0.22} \times 10^{50}$	970^{+300}_{-240}	$11.13^{+0.10}_{-0.12}$	$1.9064^{+0.0051}_{-0.0052}$
WM/XUOR/VCE	$1.75^{+0.97}_{-0.73} \times 10^{55}$	$4.09^{+0.14}_{-0.14} \times 10^{49}$	$141.9^{+4.2}_{-3.3}$	$0.175^{+0.053}_{-0.035}$	$1.8991^{+0.0040}_{-0.0041}$
CM/XUOR/VCL	$0.78^{+0.59}_{-0.38} \times 10^{56}$	$2.47^{+0.15}_{-0.14} \times 10^{50}$	57.4 ± 1.1	$0.205^{+0.081}_{-0.051}$	$1.8924^{+0.0050}_{-0.0053}$
TS/XUOR/VCL	$1.33^{+0.15}_{-0.12} \times 10^{53}$	$4.69^{+0.17}_{-0.17} \times 10^{50}$	$91.5^{+4.9}_{-4.8}$	$6.80^{+0.31}_{-0.34}$	$1.9140^{+0.0049}_{-0.0052}$
WM/XUOR/VCL	$0.38^{+0.18}_{-0.15} \times 10^{57}$	$4.61^{+0.48}_{-0.39} \times 10^{52}$	$28.18^{+1.0}_{-0.77}$	$1.28^{+0.39}_{-0.24}$	$2.1936^{+0.010}_{-0.0097}$

Table 2.8: Parameter posterior statistics for each performed fit (ϵ_e, ϵ_i, ϵ_B, A_*, n_0, and t_{sh}).

Fit Id	ϵ_e	ϵ_i	ϵ_B	A_* $[5.015 \cdot 10^{11}$ cm$^{-3}]$	n_0 [cm^{-3}]	t_{sh} [min]
CM/XOR/WC	$(1.88 \pm 0.14) \times 10^{-1}$	$(1.68 \pm 0.12) \times 10^{-1}$	$0.70^{+0.22}_{-0.14} \times 10^{-1}$		$2.77^{+0.32}_{-0.36}$	
TS/XOR/WC	$13.22^{+0.50}_{-0.43} \times 10^{-2}$	$(11.87 \pm 0.35) \times 10^{-2}$	$(2.08 \pm 0.20) \times 10^{-1}$	$0.01313^{+0.00055}_{-0.00053}$		$3.830^{+0.098}_{-0.16} \times 10^{1}$
WM/XOR/WC	$(10.67 \pm 0.29) \times 10^{-2}$	$(9.57 \pm 0.22) \times 10^{-2}$	$(3.30 \pm 0.28) \times 10^{-2}$	$0.658^{+0.024}_{-0.023}$		
CM/XUOR/WN	$49.63^{+0.49}_{-0.61} \times 10^{-2}$	$45.16^{+0.45}_{-0.54} \times 10^{-2}$	$(12.65 \pm 0.83) \times 10^{-3}$		4.36 ± 0.13	
TS/XUOR/WN	$(11.84 \pm 0.38) \times 10^{-2}$	$(10.66 \pm 0.31) \times 10^{-2}$	$(3.10 \pm 0.28) \times 10^{-1}$	0.00952 ± 0.00036		$44.52^{+0.64}_{-0.69}$
WM/XUOR/WN	$3.96^{+0.70}_{-0.35} \times 10^{-2}$	$(3.33 \pm 0.19) \times 10^{-2}$	$(0.34 \pm 0.10) \times 10^{-2}$	$0.287^{+0.039}_{-0.031}$		
CM/XOR/WN	$(49.51 \pm 0.66) \times 10^{-2}$	$45.04^{+0.49}_{-0.59} \times 10^{-2}$	$(12.53 \pm 0.82) \times 10^{-3}$		4.39 ± 0.13	
TS/XOR/WN	$(11.92 \pm 0.37) \times 10^{-2}$	$(10.74 \pm 0.30) \times 10^{-2}$	$(3.06 \pm 0.27) \times 10^{-1}$	$0.00969^{+0.00038}_{-0.00036}$		$44.60^{+0.64}_{-0.67}$
WM/XOR/WN	$3.94^{+0.64}_{-0.33} \times 10^{-2}$	$(3.33 \pm 0.19) \times 10^{-2}$	$0.334^{+0.14}_{-0.099} \times 10^{-2}$	$0.288^{+0.036}_{-0.032}$		
CM/XOR/VC	$(10.80 \pm 0.44) \times 10^{-2}$	$(9.69 \pm 0.39) \times 10^{-2}$	$2.29^{+0.26}_{-0.20} \times 10^{-1}$		$1.33^{+0.10}_{-0.14}$	
TS/XOR/VC	$(12.70 \pm 0.41) \times 10^{-2}$	$(11.41 \pm 0.33) \times 10^{-2}$	$(1.55 \pm 0.16) \times 10^{-1}$	$0.01662^{+0.00074}_{-0.00068}$		$3.157^{+0.14}_{-0.100} \times 10^{1}$
WM/XOR/VC	$(9.46 \pm 0.28) \times 10^{-2}$	$(8.46 \pm 0.21) \times 10^{-2}$	$(4.09 \pm 0.40) \times 10^{-2}$	$0.609^{+0.023}_{-0.022}$		
CM/XOR/VN	$9.32^{+0.57}_{-0.41} \times 10^{-2}$	$(8.31 \pm 0.31) \times 10^{-2}$	$(2.72 \pm 0.28) \times 10^{-1}$		$1.05^{+0.12}_{-0.10}$	
TS/XOR/VN	$(11.64 \pm 0.40) \times 10^{-2}$	$(10.44 \pm 0.32) \times 10^{-2}$	$(1.59 \pm 0.16) \times 10^{-1}$	$0.01747^{+0.00078}_{-0.00074}$		$3.13^{+0.13}_{-0.12} \times 10^{1}$
WM/XOR/VN	$(8.53 \pm 0.26) \times 10^{-2}$	$(7.62 \pm 0.19) \times 10^{-2}$	$(4.44 \pm 0.47) \times 10^{-2}$	$0.571^{+0.023}_{-0.022}$		
CM/O/VC	$0.324^{+0.13}_{-0.055} \times 10^{-1}$	$(2.49 \pm 0.29) \times 10^{-2}$	$2.08^{+0.32}_{-0.45} \times 10^{-1}$		$9.26^{+0.31}_{-0.43} \times 10^{2}$	
TS/O/VC	$0.39^{+0.18}_{-0.10} \times 10^{-1}$	$(2.72 \pm 0.55) \times 10^{-2}$	$(0.99 \pm 0.74) \times 10^{-4}$	$0.0217^{+0.011}_{-0.0076}$		$9.09^{+0.30}_{-0.40} \times 10^{1}$
WM/O/VC	$2.07^{+0.62}_{-0.41} \times 10^{-1}$	$1.79^{+0.51}_{-0.32} \times 10^{-1}$	$0.78^{+0.89}_{-0.55} \times 10^{-1}$	$0.0042^{+0.0026}_{-0.0013}$		
CM/R	$4.74^{+0.20}_{-0.25} \times 10^{-1}$	$(4.30 \pm 0.23) \times 10^{-1}$	$(1.07 \pm 0.19) \times 10^{-2}$		$5.99^{+0.60}_{-0.61}$	
TS/R	$1.59^{+0.35}_{-0.24} \times 10^{-1}$	$1.36^{+0.27}_{-0.18} \times 10^{-1}$	$0.39^{+0.29}_{-0.20} \times 10^{-1}$	$0.89^{+0.31}_{-0.19}$		$6.92^{+0.51}_{-0.49} \times 10^{4}$
WM/R	$(10.71 \pm 0.84) \times 10^{-2}$	$(9.55 \pm 0.68) \times 10^{-2}$	$0.40^{+0.20}_{-0.13} \times 10^{-1}$	$0.78^{+0.12}_{-0.11}$		
CM/XUO/VC	$1.19^{+0.29}_{-0.16} \times 10^{-1}$	$1.03^{+0.19}_{-0.13} \times 10^{-1}$	$2.48^{+0.72}_{-0.89} \times 10^{-1}$		$3.94^{+0.35}_{-0.31} \times 10^{2}$	
TS/XUO/VC	$0.047^{+0.14}_{-0.012} \times 10^{-1}$	$(3.05 \pm 0.14) \times 10^{-3}$	$(3.75 \pm 0.54) \times 10^{-1}$	$0.001110^{+0.00012}_{-0.000084}$		$46.68^{+0.14}_{-0.11}$
WM/XUO/VC	$4.60^{+0.21}_{-0.25} \times 10^{-1}$	$(4.18 \pm 0.23) \times 10^{-1}$	$(0.76 \pm 0.22) \times 10^{-2}$	$0.168^{+0.025}_{-0.021}$		
CM/XR/	$9.35^{+0.62}_{-0.49} \times 10^{-2}$	$(8.26 \pm 0.35) \times 10^{-2}$	$(1.32 \pm 0.17) \times 10^{-1}$		$1.71^{+0.16}_{-0.15}$	
TS/XR/	$(19.55 \pm 0.94) \times 10^{-2}$	$(17.57 \pm 0.77) \times 10^{-2}$	$(1.51 \pm 0.20) \times 10^{-1}$	$0.01085^{+0.00057}_{-0.00053}$		$4.39^{+0.10}_{-0.13} \times 10^{1}$
WM/XR/	$(5.05 \pm 0.25) \times 10^{-2}$	$(4.42 \pm 0.16) \times 10^{-2}$	$0.794^{+0.10}_{-0.094} \times 10^{-1}$	0.316 ± 0.015		
CM/UOR/VC	$(53.50 \pm 0.59) \times 10^{-2}$	$48.70^{+0.44}_{-0.50} \times 10^{-2}$	$(5.08 \pm 0.32) \times 10^{-3}$		12.78 ± 0.43	
TS/UOR/VC	$(4.69 \pm 0.14) \times 10^{-1}$	$(4.27 \pm 0.13) \times 10^{-1}$	$(7.08 \pm 0.96) \times 10^{-2}$	$0.462^{+0.029}_{-0.028}$		$46.84^{+0.28}_{-0.19} \times 10^{2}$
WM/UOR/VC	$(21.25 \pm 0.59) \times 10^{-2}$	$19.16^{+0.51}_{-0.49} \times 10^{-2}$	$(1.19 \pm 0.12) \times 10^{-2}$	$1.472^{+0.061}_{-0.059}$		
CM/XUOR/VCE	$(3.36 \pm 0.12) \times 10^{-1}$	$(3.04 \pm 0.11) \times 10^{-1}$	$(2.52 \pm 0.31) \times 10^{-2}$		$5.13^{+0.30}_{-0.29}$	
TS/XUOR/VCE	$(26.76 \pm 0.87) \times 10^{-2}$	$(24.20 \pm 0.76) \times 10^{-2}$	$(6.94 \pm 0.89) \times 10^{-2}$	$0.01323^{+0.00063}_{-0.00058}$		$3.40^{+0.11}_{-0.17} \times 10^{1}$
WM/XUOR/VCE	$(14.44 \pm 0.34) \times 10^{-2}$	$(13.01 \pm 0.28) \times 10^{-2}$	$(2.70 \pm 0.23) \times 10^{-2}$	0.774 ± 0.024		
CM/XUOR/VCL	$(2.25 \pm 0.10) \times 10^{-1}$	$(20.27 \pm 0.91) \times 10^{-2}$	$(1.48 \pm 0.27) \times 10^{-1}$		$1.94^{+0.25}_{-0.21}$	
TS/XUOR/VCL	$(20.95 \pm 0.78) \times 10^{-2}$	$(18.87 \pm 0.66) \times 10^{-2}$	$1.31^{+0.16}_{-0.14} \times 10^{-1}$	$0.00615^{+0.00040}_{-0.00039}$		$2.45^{+0.16}_{-0.17} \times 10^{1}$
WM/XUOR/VCL	$2.92^{+0.90}_{-0.32} \times 10^{-2}$	$(2.37 \pm 0.19) \times 10^{-2}$	$(1.05 \pm 0.31) \times 10^{-2}$	$0.122^{+0.021}_{-0.019}$		

Table 2.9: Parameter posterior statistics for each performed fit (r_{sh}, t_1, E_1/E_0, $E_{\rm total}$, $A_{V,host}$, and $E(B-V)$).

Fit Id	r_{sh}	t_1 [days]	E_1/E_0	$E_{\rm total}$ [erg]	$A_{V,host}$ [mag]	$E(B-V)$ [mag]
CM/XOR/WC		$0.39^{+0.16}_{-0.14} \times 10^{-1}$	$0.940^{+0.091}_{-0.085}$	$12.65^{+0.98}_{-0.77} \times 10^{50}$	$0.0716^{+0.0042}_{-0.0037}$	
TS/XOR/WC	$16.10^{+1.0}_{-0.93}$			$9.12^{+0.30}_{-0.29} \times 10^{50}$	0.1000 ± 0.0036	
WM/XOR/WC		$(0.59 \pm 0.10) \times 10^{-3}$	$49.12^{+0.40}_{-0.55}$	$4.00^{+0.14}_{-0.13} \times 10^{51}$	$0.1645^{+0.0037}_{-0.0035}$	
CM/XUOR/WN		$(5.35 \pm 0.24) \times 10^{-2}$	$32.70^{+0.58}_{-0.60}$	$14.06^{+0.36}_{-0.36} \times 10^{50}$	$0.0132^{+0.0080}_{-0.0056}$	$0.5933^{+0.0041}_{-0.0051}$
TS/XUOR/WN	$24.8^{+1.6}_{-1.5}$			$8.02^{+0.23}_{-0.20} \times 10^{50}$	$0.0203^{+0.011}_{-0.0088}$	$0.6178^{+0.0055}_{-0.0071}$
WM/XUOR/WN		$(8.88 \pm 0.78) \times 10^{-2}$	26.3 ± 1.3	$1.13^{+0.16}_{-0.12} \times 10^{53}$	$0.786^{+0.022}_{-0.023}$	$0.459^{+0.015}_{-0.014}$
CM/XOR/WN		$(5.27 \pm 0.25) \times 10^{-2}$	$32.47^{+0.57}_{-0.60}$	$14.13^{+0.38}_{-0.37} \times 10^{50}$	$0.0132^{+0.0081}_{-0.0058}$	$0.5949^{+0.0041}_{-0.0050}$
TS/XOR/WN	24.3 ± 1.5			$8.05^{+0.23}_{-0.21} \times 10^{50}$	$0.0190^{+0.011}_{-0.0082}$	$0.6190^{+0.0054}_{-0.0073}$
WM/XOR/WN		$(9.05 \pm 0.76) \times 10^{-2}$	$26.6^{+1.5}_{-1.3}$	$1.14^{+0.15}_{-0.12} \times 10^{53}$	$0.774^{+0.022}_{-0.023}$	$0.468^{+0.015}_{-0.014}$
CM/XOR/VC		$5.18^{+0.42}_{-0.44} \times 10^{1}$	$1.20^{+0.56}_{-0.34}$	$1.71^{+0.44}_{-0.25} \times 10^{51}$	$0.0140^{+0.0036}_{-0.0035}$	
TS/XOR/VC	$10.13^{+0.69}_{-0.60}$			$10.41^{+0.39}_{-0.35} \times 10^{50}$	$0.0318^{+0.0038}_{-0.0040}$	
WM/XOR/VC		$(7.99 \pm 0.93) \times 10^{-4}$	$49.11^{+0.38}_{-0.53}$	$3.64^{+0.13}_{-0.12} \times 10^{51}$	$0.1017^{+0.0038}_{-0.0035}$	
CM/XOR/VN		$5.03^{+0.42}_{-0.44} \times 10^{1}$	$1.34^{+0.59}_{-0.35}$	$1.72^{+0.42}_{-0.24} \times 10^{51}$	$0.0048^{+0.0031}_{-0.0021}$	0.5249 ± 0.0030
TS/XOR/VN	$8.33^{+0.56}_{-0.54}$			$10.72^{+0.36}_{-0.34} \times 10^{50}$	$0.0102^{+0.0063}_{-0.0046}$	$0.5277^{+0.0037}_{-0.0044}$
WM/XOR/VN		$(6.79 \pm 0.91) \times 10^{-4}$	$49.01^{+0.43}_{-0.61}$	$3.62^{+0.14}_{-0.12} \times 10^{51}$	$0.0099^{+0.0064}_{-0.0042}$	$0.5749^{+0.0035}_{-0.0043}$
CM/O/VC		$(6.63 \pm 0.98) \times 10^{-2}$	$45.9^{+1.6}_{-2.1}$	$4.95^{+0.46}_{-0.39} \times 10^{51}$	$0.287^{+0.012}_{-0.013}$	
TS/O/VC	$43.4^{+2.6}_{-3.5}$			$0.71^{+0.46}_{-0.28} \times 10^{52}$	$0.387^{+0.011}_{-0.010}$	
WM/O/VC		$0.072^{+0.17}_{-0.071} \times 10^{2}$	$16.8^{+9.6}_{-7.6}$	$1.54^{+0.88}_{-0.64} \times 10^{52}$	$0.643^{+0.011}_{-0.012}$	
CM/R		$(0.19 \pm 0.13) \times 10^{-2}$	$3.50^{+0.27}_{-0.24}$	$15.39^{+0.97}_{-0.99} \times 10^{50}$		
TS/R	$13.7^{+6.6}_{-4.5}$			$3.37^{+0.75}_{-0.44} \times 10^{51}$		
WM/R		$4.59^{+0.17}_{-0.18} \times 10^{1}$	$9.6^{+2.4}_{-2.5}$	$2.21^{+0.64}_{-0.56} \times 10^{52}$		
CM/XUO/VC		$(13.08 \pm 0.41) \times 10^{-2}$	$12.77^{+0.32}_{-0.31}$	$1.91^{+0.15}_{-0.13} \times 10^{51}$	0.100 ± 0.011	
TS/XUO/VC	$49.60^{+0.17}_{-0.25}$			$12.58^{+0.51}_{-0.46} \times 10^{50}$	0.3672 ± 0.0074	
WM/XUO/VC		$(6.96 \pm 0.43) \times 10^{-2}$	$31.2^{+1.8}_{-1.5}$	$3.67^{+0.71}_{-0.53} \times 10^{51}$	$0.0432^{+0.0042}_{-0.0043}$	
CM/XR/		$4.96^{+0.41}_{-0.42} \times 10^{1}$	$1.65^{+0.61}_{-0.34}$	$2.35^{+0.55}_{-0.31} \times 10^{51}$		
TS/XR/	$40.6^{+3.3}_{-3.5}$			$9.25^{+0.40}_{-0.37} \times 10^{50}$		
WM/XR/		$(8.79 \pm 0.79) \times 10^{-2}$	$5.03^{+0.29}_{-0.28}$	$5.21^{+0.24}_{-0.22} \times 10^{51}$		
CM/UOR/VC		$5.40^{+0.52}_{-0.44} \times 10^{-2}$	$48.83^{+0.51}_{-0.71}$	$19.82^{+0.49}_{-0.50} \times 10^{50}$	$0.2160^{+0.0062}_{-0.0060}$	
TS/UOR/VC	$10.60^{+0.41}_{-0.39}$			$7.90^{+0.41}_{-0.40} \times 10^{50}$	$0.3961^{+0.0074}_{-0.0072}$	
WM/UOR/VC		$(4.76 \pm 0.20) \times 10^{-2}$	$49.29^{+0.31}_{-0.45}$	$4.15^{+0.15}_{-0.15} \times 10^{51}$	$0.1303^{+0.0081}_{-0.0083}$	
CM/XUOR/VCE		$0.124^{+0.21}_{-0.077} \times 10^{-2}$	$1.421^{+0.086}_{-0.082}$	$15.32^{+0.69}_{-0.63} \times 10^{50}$	$0.2073^{+0.0049}_{-0.0046}$	
TS/XUOR/VCE	$46.8^{+1.3}_{-1.6}$			$10.84^{+0.46}_{-0.43} \times 10^{50}$	0.2992 ± 0.0057	
WM/XUOR/VCE		$(6.27 \pm 0.91) \times 10^{-4}$	$49.26^{+0.33}_{-0.47}$	$4.09^{+0.13}_{-0.13} \times 10^{51}$	$0.2735^{+0.0057}_{-0.0054}$	
CM/XUOR/VCL		$(0.17 \pm 0.11) \times 10^{-2}$	0.786 ± 0.058	$8.78^{+0.53}_{-0.44} \times 10^{50}$	$0.2263^{+0.0072}_{-0.0071}$	
TS/XUOR/VCL	$48.21^{+0.79}_{-1.2}$			$9.38^{+0.34}_{-0.34} \times 10^{50}$	0.2996 ± 0.0072	
WM/XUOR/VCL		$3.84^{+0.10}_{-0.11} \times 10^{1}$	$43.3^{+2.7}_{-3.4}$	$3.98^{+0.45}_{-0.45} \times 10^{54}$	$0.5734^{+0.0071}_{-0.0074}$	

2.4 Global view of all performed fits

The results for the complete grid of fits are summarised in this section. The grid consists of different cuts in wavelength and time in order to get useful additional information that clarifies some details of the physical nature of the afterglow and systematic uncertainties.

To test the constraining power of each wavelength range, we split the data into three subsets: X-rays, [UV/]optical/nIR[1], and submm/mm. These were then fitted individually and also in sets of two.

We found that the optical light curves were best fit with the TS and WM model, where the early steep decay and the bump at around 0.3 days is easily explained. The TS model was slightly better, mostly due to a better fit to the early *white+v* band data. The TS model also does a better job of predicting the XRT and radio data while the WM model is orders of magnitude off. The CM model does not do as well with the optical data, a large energy injection in combination with a low value for p does a reasonable job at explaining the late light curves, but the early *white+v* band data is not explained. The CM model also fares better with predicting the XRT and radio/sub-mm data, although it is obviously not able to reproduce them completely.

The fit to the radio data is less discriminating, the WM models are better than both the TS and CM models, but only marginally. The parameters for the WM and TS models are very similar and the energy injection and wind termination shock both happen at late times to improve the fit to the late radio points. The CM model stands out from the group with the energy injection happening at early times and is therefore the worst offender at late times. The CM model, however, is best at predicting the optical and X-ray data and roughly goes through the late time optical/nIR curves and the XRT curves. The WM and TS model under-predict those same data, with the WM model being the worst offender. Early observations would helped in constraining better modeled light curves.

No attempt was made at fitting the XRT light curve only, but when we add it to the mix with either the optical/NIR or the radio/sub-mm data things change considerably. For the former set it is now the TS model that is best, trailed by the CM and then the WM model. None of the models now explain the bump in the optical light curves, but at least the TS model explains the wiggles in the XRT light curve. The early *white+v* optical data are also not explained. In this case, the TS and WM models do a fairly good job of predicting the radio/sub-mm data, but the CM model is way off. For the latter set of XRT and radio/sub-mm we get a pretty consistent picture of the three models. The TS model is best, trailed by the CM model and finally the WM model like for the

[1]We include in the UV UVOT filters uvw1, uvw2, uvm2, and u

entire set. The resulting parameter distributions are actually fairly close to the results of the entire dataset, indicating that the additional information from the optical data does not constrain the model much. All of the models actually predict the optical data reasonably well and the full fit gives only small visible changes. This means that the large spectral lever arm added to the very fine temporal sampling of the XRT light curves is most constraining for the model.

Our final combination is the UV/radio/sub-mm and optical/NIR data together. Here the CM model shows the best fit, which fairs similarly to the WM, and significantly better fit than TS model. None of them is able to explain the bump in optical, but the early optical and early radio/sub-mm data is well explained by the TS model. All of the models approximately predict the XRT light curve but with some offset in the temporal behaviour. There is therefore little additional constraining power in the spectral information from the XRT data, but mostly from the very detailed time behavior.

In conclusion, it seems that the fine sampling in the XRT light curve with the large spectral lever arm of the radio and sub-mm data is the most constraining data for the models. We also note that the inferred physical conditions can vary up to few orders of magnitude depending on the model and the wavelength ranges considered. Therefore, observational sampling is fundamental in order to discriminate different models and constrain its physical parameters.

Due to the high Galactic dust extinction, and hence large uncertainty, we excluded the upper limits from the UV filters of UVOT as well observations using its u-band filter. None of the models are able to accurately reproduce those data points, either when included in the fit or not.

To reduce the bias from the early UVOT *white+v* band points that can be caused by a reverse shock (RS; e.g., Jelínek *et al.*, 2006; Laskar *et al.*, 2013a), we redo the analysis with all optical points before 0.005 days turned into upper limits. The parameters of the models are mostly unchanged with this exclusions of the data. A notable exception are the values of ϵ_e, ϵ_i, and ϵ_B. ϵ_B is reduced significantly while both ϵ_e and ϵ_i increase. This affects the determined host extinction which is now determined to be twice as large. The models are still unable to reproduce the data and most of the comments still apply. The contribution of a reverse shock may help to explain the early evolution in the *white* filter and/or the early sub-mm light curve, but will not help with the rest of the data. Thus the early *white* band data is not the driving cause for the models not being able to reproduce the bump.

One possibility that has often been proposed to model complex GRB light curves is the double jet model (e.g. Filgas *et al.*, 2011; Racusin *et al.*, 2008; Starling *et al.*, 2005; van der

Horst *et al.*, 2014), the early light curve being dominated by a fast moving narrow jet while a slow moving wide jet dominates at late time. This can be considered the simplest model for a two dimensional jet. To test if this is the case here, we fit the data after 0.5 days only, turning all other points into upper limits. The TS model is still the best model in this case and it is mostly able to explain the optical and X-ray bump at 0.3 days, but all the other considerations still apply and the radio/sub-mm data is still poorly modeled. We therefore conclude that a double jet model is not appropriate for this case.

2.5 Conclusions

- We present an extensive follow-up of the afterglow of GRB 110715A in 17 bands ranging from a few seconds up to 74 days after the trigger. The line of sight is affected by strong foreground Galactic extinction, which complicated the follow-up and the analysis of the data.

- GRB 110715A had a very bright afterglow at all wavelengths, although its intrinsic luminosity is not exceptional.

- Optical/nIR spectroscopy obtained with X-shooter shows weak absorption features at a redshift of $z = 0.8224$ with no resolved velocity components ($\lesssim 30$ km s^{-1}). Absorption line ratios indicate a low ionization environment, confirmed by the rare detection of Ca II.

- Deep late imaging reveals a faint host galaxy with an absolute magnitude of $M_B =$ -18.2. This is consistent with the weak absorption features detected in the spectrum.

- We attempted to model the broadband data with a fireball model based on the prescription of Jóhannesson *et al.* (2006). The best model implies a forward shock evolving through a wind environment with a termination shock. In spite of describing roughly the behavior of the afterglow, none of the models is able to get a statistically acceptable fit. This shows the need for better broadband sampling and more complex models to accurately describe the physics of GRB afterglows. There are several works that explore other possibilities, such as magneto-hydrodynamic simulations (van Eerten *et al.*, 2012), which was satisfactorily used, e.g., in Guidorzi *et al.* (2014); Ryan *et al.* (2015); Zhang *et al.* (2015), or central engine activities (Zhang *et al.*, 2014). These and other effects might be considered together in future works to get a more accurate view of the GRB afterglow physics.

- Radio and sub-mm, along with X-ray observations, have been proven to be the most constraining bands for the afterglow modeling. We were limited by sensitivity for a long time in the crucial wavelength range of sub-mm, but now that ALMA is available, we have a good chance of getting high-quality data for a larger number of GRBs. This new, current and future facilities will allow us to probe the emission mechanisms in greater detail than previously possible, and will be determinant in the evolution of the GRB afterglow models.

PART II

ABSORPTION SYSTEMS IN THE LINE OF SIGHT TO GRBS:

THE TAIL-END OF THE REIONISATION EPOCH

Chapter 1

Introduction

"It is, indeed an incredible fact that what the human mind, at its deepest and most profound, perceives as beautiful finds its realisation in external nature... What is intelligible is also beautiful."

— Subrahmanyan Chandrasekhar, *Beauty and the Quest for Beauty in Science, 1979*

One of the key frontiers in observational cosmology is to understand how the cosmic dark ages ended and the first stars and galaxies formed a few a few hundred million years after the Big Bang (e.g., Bromm *et al.*, 2009). Within ΛCDM cosmology, the first stars, the so-called Population III (Pop III), are predicted to form at $z \sim 20 - 30$ in dark matter mini-halos of mass $\sim 10^6$ $M_\odot$. The formation of the first galaxies may be delayed until more massive dark matter halos virialise (Bromm & Yoshida, 2011). Once the first sources of light appeared, the Universe rapidly transformed through the input of ionising radiation (Barkana & Loeb, 2001) and heavy chemical elements (Karlsson *et al.*, 2013). The only opportunity, at least in the coming years, to probe Pop III stars may be to catch them at the moment of their explosive death. This could involve either extremely energetic supernova or GRBs. The outlook for GRB cosmology is, therefore, bright.

1.1 The epoch of reionisation

After the recombination epoch (at z∼1200; Komatsu *et al.*, 2011), the Universe became mostly neutral, i.e., it started the so called (*dark ages* Rees, 1998). From z∼50 the first generation of dark matter halos with $\sim 10^6 M_\odot$ formed, baryons collapsed, and the first generation of stars born, the so called Population III (Pop-III) stars, by z∼20-30. These Pop-III stars are characterised by a zero metallicity and masses ranging 30-100$M_\odot$ (Abel *et al.*, 2002; Yoshida *et al.*, 2006).

The main consequence of the birth of these Pop-III stars is that, as they were a powerful UV emitters, they provided an important radiative feedback by ionising the surrounding ISM and even IGM. Consequently, the death of them also produced the first ISM chemical enrichment by super/hyper-nova, as well as the first black holes and active galactic nuclei (AGN). Furthermore, it also meant the beginning of the *cosmic reionisation* or the epoch of reionisation (EoR) (Dunkley *et al.*, 2009). Therefore, one of the key questions in modern cosmology is the understanding of the processes that led to the end of the dark ages by the first stars and galaxies (e.g. Barkana & Loeb, 2001; Bromm *et al.*, 2009). During this period two fundamental transitions are expected to occur: A change in the SFR mode from massive Pop III to Solar size Pop II/I stars, and the change of the IGM from neutral to almost fully ionised state.

The study of reionisation is important for several reasons (Becker *et al.*, 2015a):

- It is a major event in our cosmic history that impacted on almost every baryon in the Universe.
- Detailed measurements of IGM properties during reionisation will strongly constrain models of the first sources and structure formation.
- These early generations of ionising sources influenced the formation of subsequent galaxy populations.
- Uncertainties in reionisation physics lead to "nuisance" parameters that may limit our ability to extract cosmological parameters from CMB and Lyα-forest data sets.

However, while many steps towards the understanding of the reionisation processes have been achieved, there are still many fundamental questions to be answered: How does it start? How gradual and how prolonged was the process? Was radiation from early stars sufficient to sustain the transition? Do Pop III stars or QSOs have a major role in driving the process? Are there another more exotic process involved? (Salvaterra, 2015).

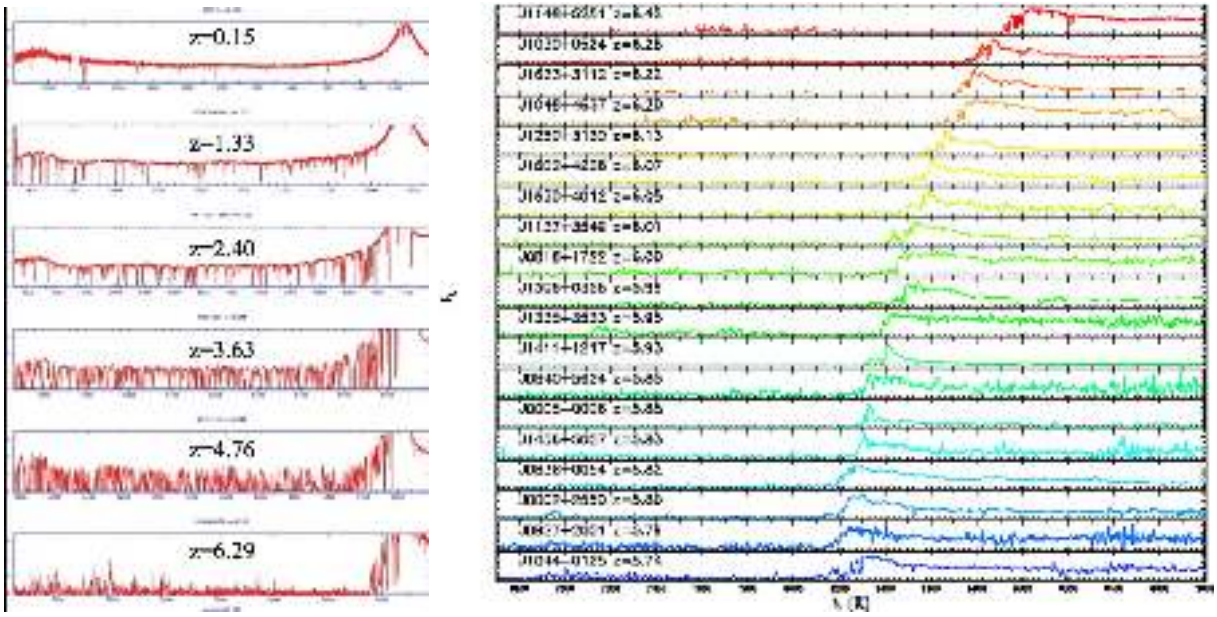

Figure 1.1: Evolution of the G-P absorption with redshift.

Historically, the exploration of the distant Universe has been performed following two ways: The use of QSO sight-lines (Fan, 2012) and LBG (Bouwens *et al.*, 2014). However, GRBs are also a newer and more promising tool to do the work.

1.1.1 The Gunn-Peterson effect

IGM measurements play an important complementary role, as the interplay between the ionising sources and the surrounding gas that determines the nature of reionisation is fundamental. Thanks to Gunn & Peterson (1965), who drew attention to the lack of prominent Lyα absorption troughs in the spectra of the newly discovered quasars, we started to realise that there is very little intervening neutral Hydrogen in intergalactic space at $z \lesssim 5$ (see Figure 1.1).

Consider light emitted by a QSO at redshift z_q passing through a uniform IGM with number density $n_{HI}(z)$. This light is observed at redshift $z < z_q$ with frequency $\nu = \nu_\alpha$ / $(1 + z)$. The total optical depth along the line of sight is then

$$\tau^{\alpha}_{GP} = \int_0^{z_q} \sigma_s[\nu(1+z)] n_{HI}(z) \frac{dl}{dz} dz \tag{1.1}$$

$$\tau^{\alpha}_{GP} \simeq 2.3 \times 10^5 \langle x_{HI} \rangle \left(\frac{\Omega_b h^2}{0.022}\right) \left(\frac{\Omega_m h^2}{0.142}\right)^{-1/2} \left(\frac{1-Y}{0.76}\right) \left(\frac{1+z}{5}\right)^{3/2} \tag{1.2}$$

where Y is the primordial Helium fraction and $\langle x_{HI} \rangle$ the average Hydrogen neutral fraction. The IGM transmittance is therefore $e^{-\tau^{\alpha}_{GP}}$, and its crucial property is that for a modest neutral fraction $\langle x_{HI} \rangle \sim 10^{-4.5}$ the Gunn-Peterson (G-P) optical depth is fully saturated, implying that the IGM is highly ionised at $z \lesssim 6$.

1.1.2 The UV background

The number of photo-ionised Hydrogen atoms per unit time, $\Delta_{HI}(z)$, is defined as

$$\Gamma_{HI}(z) = \int_{\nu_{LL}}^{\infty} \frac{4\pi J(\nu, z)}{h\nu} \sigma_{HI}(\nu) d\nu \tag{1.3}$$

where σ_{HI} is the H I photo-ionisation cross-section and ν_{LL} is the photon frequency at the Lyman Limit.

The photo-ionisation rate can be related to the neutral fraction of the IGM. Assuming ionisation equilibrium

$$n_{HI}\Gamma_{HI} = n_e n_{HII} \alpha_{HII}(T) \tag{1.4}$$

where

$$\alpha_{HII}(T) = 4.063 \times 10^{-13} \left(\frac{T}{10^4 \mathrm{K}} \right)^{-0.72} \qquad \mathrm{cm}^3\ \mathrm{s}^{-1} \tag{1.5}$$

in the case-A recombination.

Two main techniques are employed to measure the metagalactic photo-ionisation rate: The modelling of the mean transmitted flux in the Lyα-forest (Rauch *et al.*, 1997), and the QSO proximity effect (Murdoch *et al.*, 1986). The first approach typically relies on using numerical simulations of structure formation to reproduce the mean transmitted flux in the Lyα-forest. The second one estimates Γ_{HI} by quantifying the reduction in the average Lyα opacity approaching the systemic redshift of the QSO (Weymann *et al.*, 1981). The ionising radiation will ionise the nearby IGM. Ignoring peculiar velocities and spatial variations in the gas temperature

$$\tau_{\alpha}^{UVB+Q} = \frac{\tau_{\alpha}^{UVB}}{1 + \frac{\Gamma^{Q}_{HI}(r)}{\Gamma^{UVB}_{HI}}} \tag{1.6}$$

where τ_{α}^{UVB} is the typical optical depth of the Lyα-forest, $\Gamma^{Q}_{HI}(r)$ is the ionisation rate

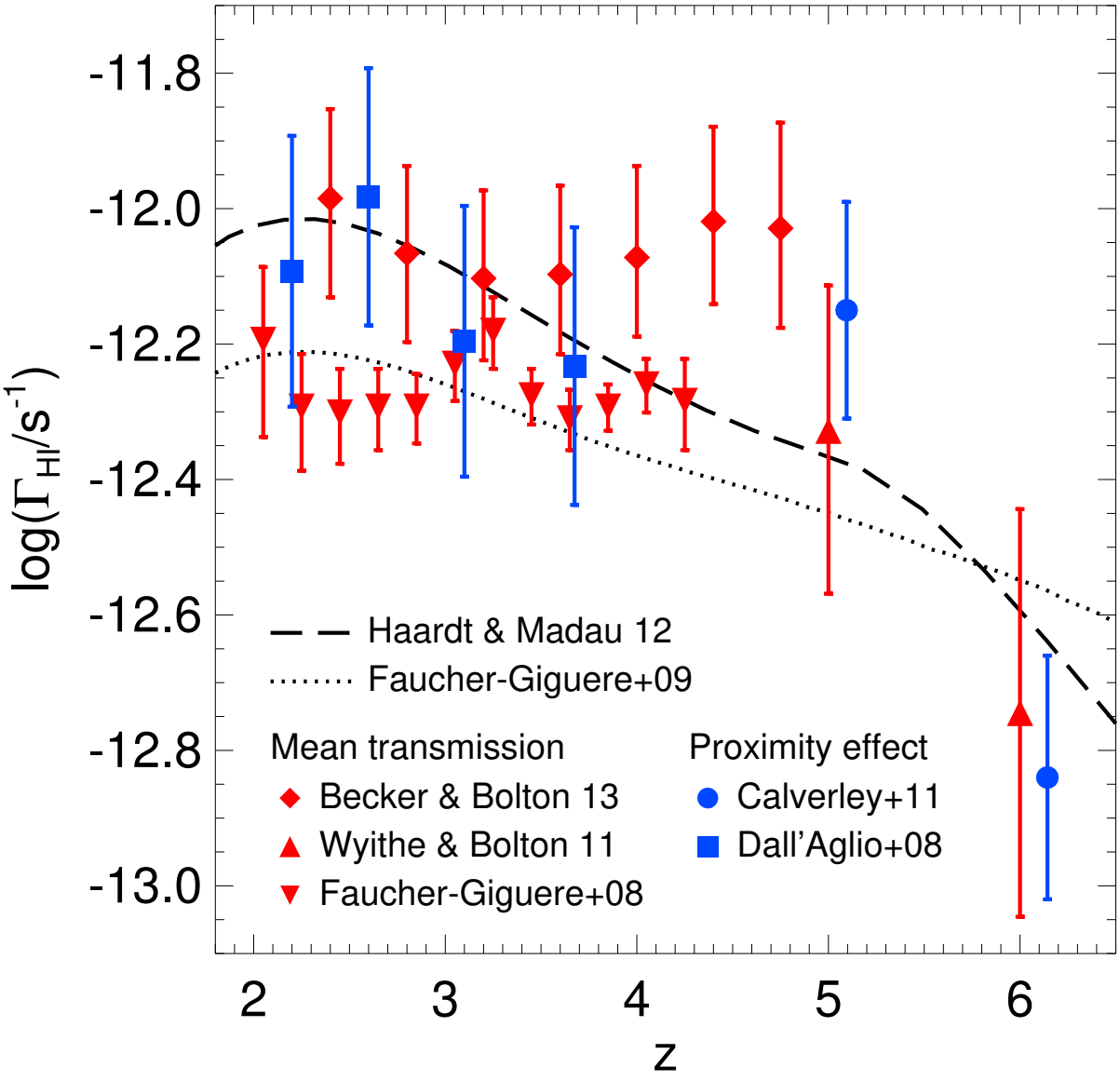

Figure 1.2: Summary of recent H I measurements obtained from the mean Lyα-forest transmission. Adapted from Becker *et al.* (2015a).

of the quasar and Γ_{HI}^{UVB} is the UVB ionisation rate. If the absolute magnitude, redshift, and SED of the QSO are known, $\Gamma_{HI}^{Q}(r)$ may be computed with eq. 1.3. Typical values are $\Gamma_{HI} \sim 10^{-12}$ s^{-1} at $2 \leq z \leq 4$, declining by a factor of 2 and 4 at $z = 5$ and $z = 6$, respectively (see Figure 1.2).

1.1.3 The mean free path at the Lyman limit

Following Becker *et al.* (2015a), let's consider the mean free path for ionising photons in an IGM populated by Poisson distributed H I absorbers, with column densities $N(\mathrm{H\,I})$ described by the column density distribution function $f(N_{HI}, z)$. The intervening effective optical depth is

$$\bar{\tau}(\nu_0, z_0, z) = \int_{z_0}^{z} dz' \int_{0}^{\infty} f(N_{HI}, z')(1 - e^{-\tau_\nu}) dN(\mathrm{H\,I}) \tag{1.7}$$

The mean free path is then the distance a photon can travel before encountering an optical depth of unity

$$\lambda_{mfp} = \frac{dl}{d\tau} = \frac{dl}{dz}\frac{dz}{d\tau} \tag{1.8}$$

Parametrising

$$f(N_{HI}, z) = N_0 N(\mathrm{H\,I})^{-\beta_N}(1+z)^{\beta_z} \tag{1.9}$$

After some operations we find

$$\lambda_{mfp}(\nu) \simeq \frac{c(\beta_N - 1)}{N_0 \sigma_{LL}^{\beta_N - 1}\Gamma(2 - \beta_N)} \left(\frac{\nu}{\nu_{LL}}\right)^{3(\beta_N - 1)} \frac{1}{H_0\sqrt{\Omega_m}(1+z)^{\beta_z + 5/2}} \tag{1.10}$$

which is an analytical approximation at $z \gtrsim 2$. In the last formula, Γ is the Gamma function. λ_{mfp} is usually given in the compact form

$$\lambda_{mfp} = \lambda_{LL}\left(\frac{\nu}{\nu_{LL}}\right)^{3(\beta_N - 1)} \tag{1.11}$$

where λ_{LL} is the mean free path at the Lyman limit.

Many surveys have attempted to infer λ_{LL} by measuring $f(N_{HI}, z)$. Unfortunately, systems with $10^{14.5} \leq N(\mathrm{H\,I}) \leq 10^{19}$ are the systems for which $N(\mathrm{H\,I})$ is most difficult to measure. Extrapolations are therefore often employed. A selection of recent measurements

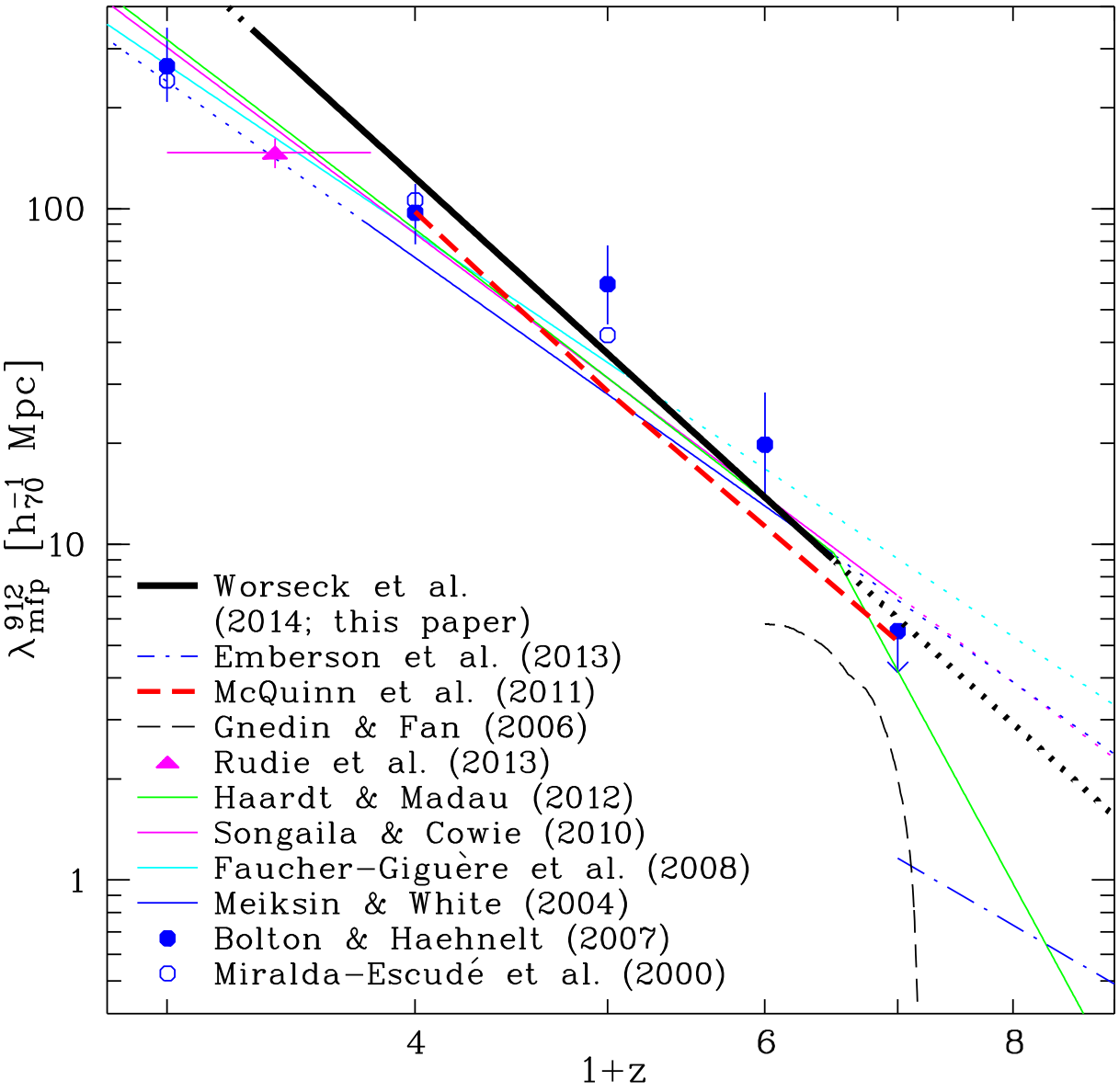

Figure 1.3: Summary of estimates for the proper mean free path at the Lyman limit, λ_{LL}. Adapted from Worseck *et al.* (2014).

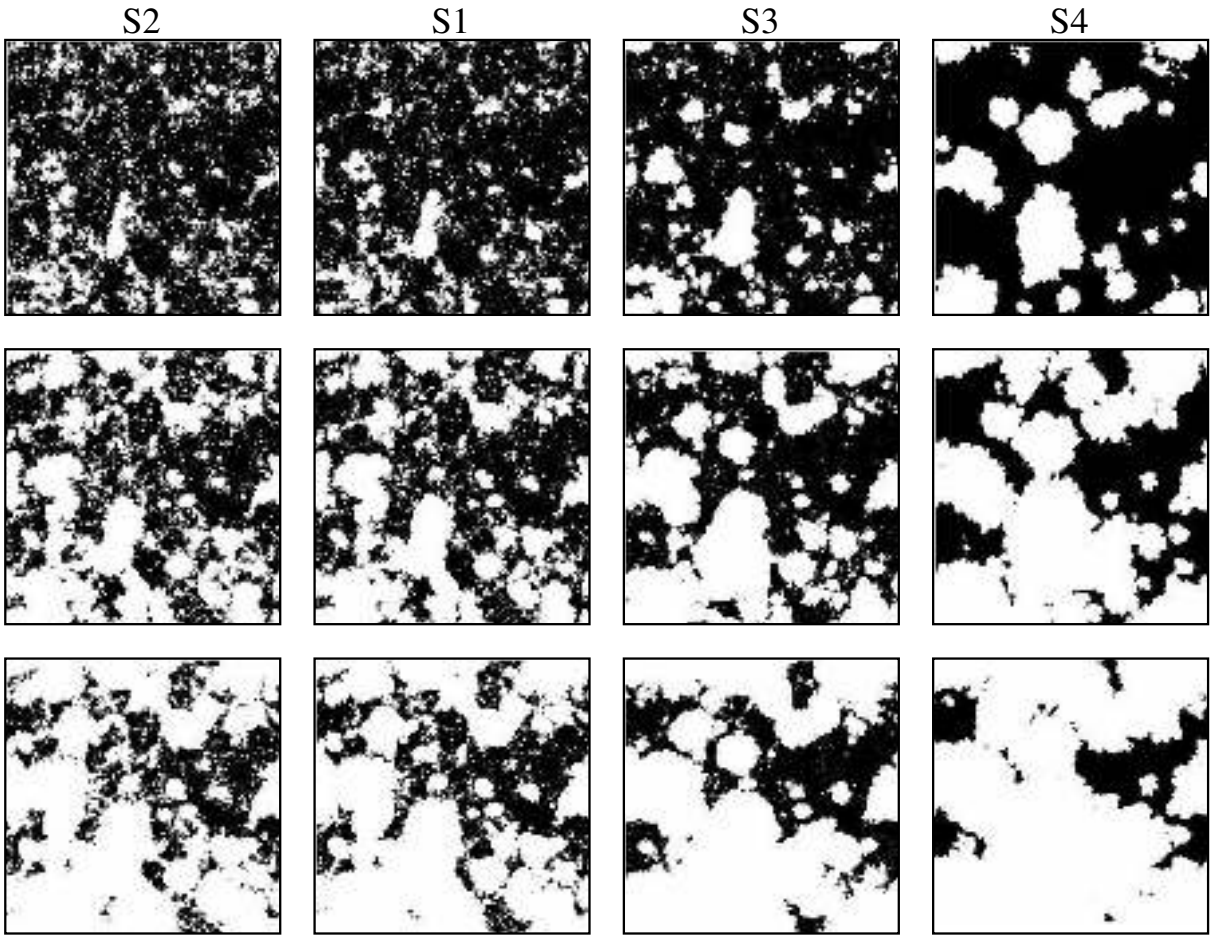

Figure 1.4: Models illustrating the size and distribution of ionised regions at different stages of reionisation. Adapted from McQuinn *et al.* (2007).

and simulation predictions are shown in Figure 1.3. A recent analysis by Worseck *et al.* (2014) gives $\lambda_{LL} = 37[(1+z)/5]^{-5.4}$ proper Mpc at $2 < z < 5$, indicating that λ_{LL} has an intrinsic evolution, directly related to the decline of the photo-ionisation rate Γ_{HI} at $z > 5$.

1.1.4 The IGM during reionisation

In the IGM is expected to coexist during a period highly ionised "bubbles" that form around high luminosity sources while the rest remain mostly neutral. At the tale-end of reionisation the IGM can be almost completely filled by ionised gas once bubbles have overlapped (see Figure 1.4). The transition between the "bubble-dominated" to the "cosmic-web-dominated" eras in the EoR has been proved to be challenging to model (Furlanetto & Oh, 2005).

This two phase medium can be characterised by two quantities: the volume filling

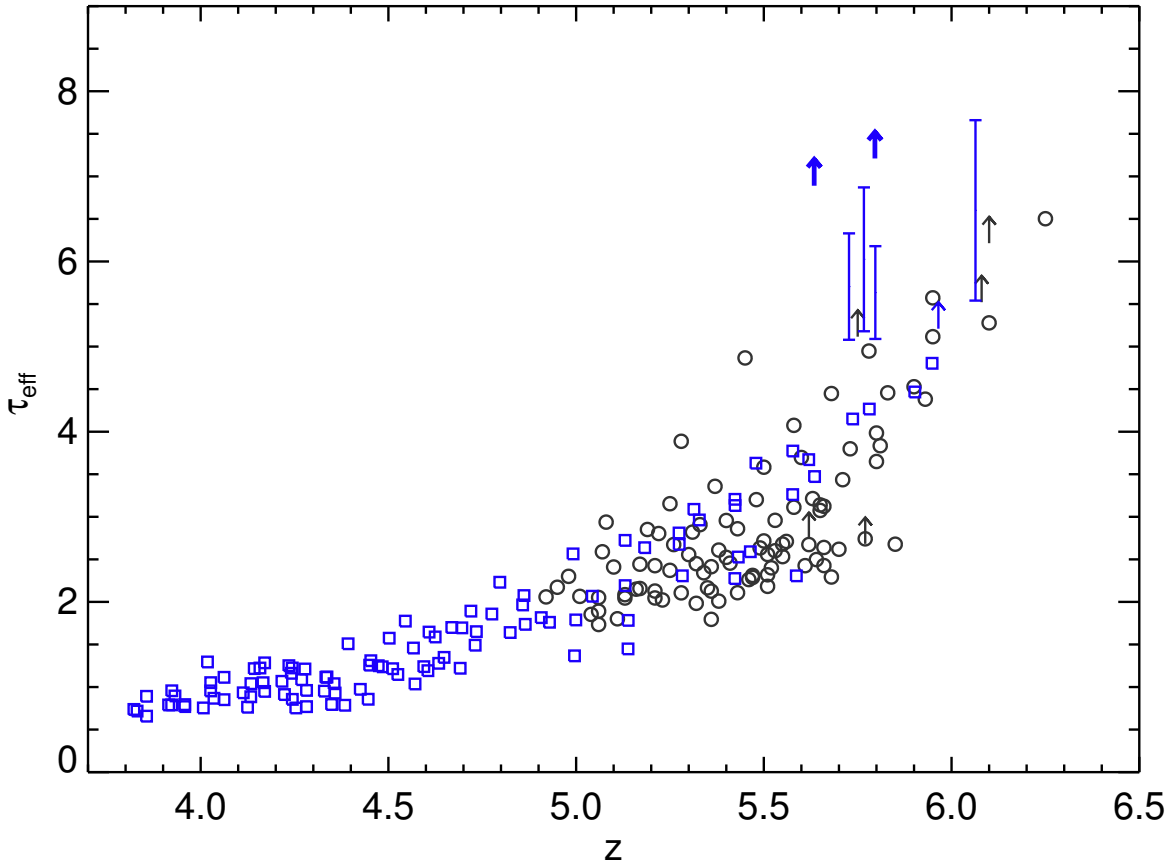

Figure 1.5: The evolution of the Lyα-forest effective optical depth with redshift. The measurements are from Fan *et al.* (2006, black circles and arrows) and Becker *et al.* (2015b, blue circles, error bars and arrows). The lower limits at $z < 5.5$ are obtained where the Lyα absorption saturates in the presence of a G-P trough. Adapted from Becker *et al.* (2015b).

factor of ionised Hydrogen and the size distribution of the ionised regions (e.g., Madau *et al.*, 1999; Miralda-Escudé *et al.*, 2000). A primary goal of EoR studies is thus to constrain these properties from observations, and then use them as inputs for models.

1.1.5 Mean Lyα-forest transmission

The first measurements we can consider to perform from optical spectra of GRB and QSO sight-lines is the redshift evolution of the average Lyα-forest transmission $\langle F \rangle$. We have to be careful with these kind of measurements as the G-P absorption saturates at $\langle x_{HI} \rangle \sim 10^{-4.5}$. However this technique can be improved and gives valuable constraints on the H neutral fraction. Figure 1.5 shows that the Universe became mostly ionised at $z \sim 6$, but it remains unclear whether the mean transmission should evolve rapidly as reionisation

completes.

Further progress has been made by using higher order Lyman series lines. These transitions have smaller cross sections relative to Lyα, and so become saturated at larger neutral fractions

$$\tau_{GP}^{\beta} = \frac{\sigma_\beta}{\sigma_\alpha}\tau_{GP}^{\alpha} = 0.16\tau_{GP}^{\alpha} \tag{1.12}$$

However, the observable ratio $\tau_{eff,\alpha}/\tau_{eff,\beta}$ depends on gas density distribution, the relation between temperature and density, and other aspects of the IGM model. Typical results show that $\tau_{eff,\alpha}/\tau_{eff,\beta}$ is ~ 3. The corresponding factor to higher lines are larger. The most important complication of this method is that the Lyβ region also contains Lyα absorption from a lower redshift systems. If we assume that both absorptions are uncorrelated

$$\langle F(\lambda)\rangle = \langle F(z_\beta)\rangle\langle F(z_\alpha)\rangle \tag{1.13}$$

1.1.6 Dark pixel fraction and dark gaps

Recent works by McGreer *et al.* (2011, 2015) has demonstrated that a conservative, almost model-independent lower bound on the filling factor of ionised regions can be placed by counting the fraction of spectral pixels that are completely absorbed. They found that $\langle x_{HI}\rangle < 0.11$ at $z = 5.6$, $\langle x_{HI}\rangle < 0.09$ at $z = 5.9$, and $\langle x_{HI}\rangle < 0.58$ at $z = 6.1$ (1σ confidence).

A related diagnostic is the size distribution of contiguous saturated regions, and the redshift evolution of the so-called "dark gaps" (e.g., Songaila & Cowie, 2002). Some measurements of the dark gap sizes and their redshift evolution are shown in Figure 1.6. The observed evolution might result in part from the presence of remaining neutral islands in the IGM.

1.1.7 Near-zones and IGM damping wings

Gas close in spectral regions to the background source, in the proximity or near-zone, are exposed to ionising radiation from the quasar itself apart from the UVB. These regions show some transmission through Lyα, and hence can be used to study $z \gtrsim 6$ IGM.

The simplest measurable property is the size of these zones. Observationally, this is usually defined as the distance from the Lyα emission over which the continuum nor-

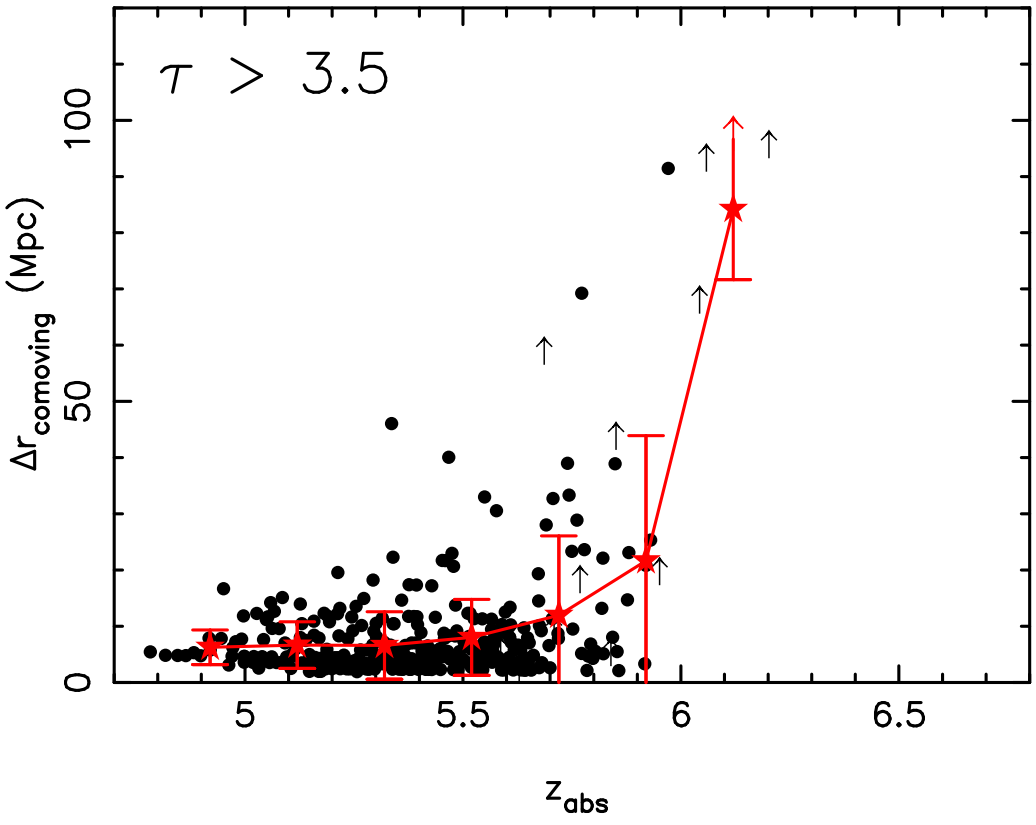

Figure 1.6: The size of dark gaps as a function of redshift measured from 12 quasar spectra obtained with Keck/ESI. The gaps are defined as contiguous regions in the observed Lyα-forest where the optical depth never goes beneath the threshold of $\tau_\alpha < 3.5$. The upward pointing arrows show lower limits on the dark gap size for observed gaps that are close to the quasar near-zone. Adapted from Fan *et al.* (2006).

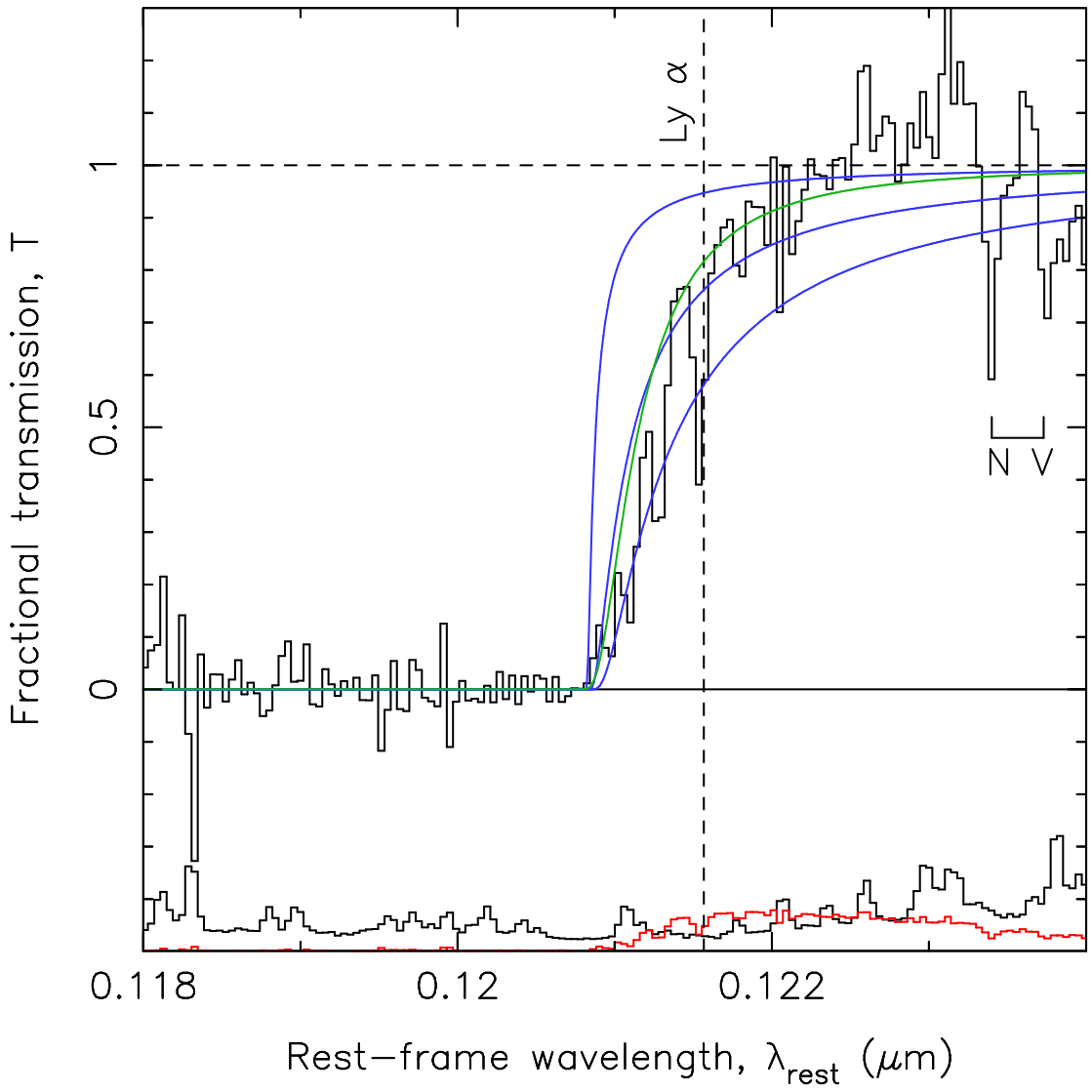

Figure 1.7: Possible damping wing feature in the spectrum of a $z = 7.1$ quasar. The black binned data shows an estimate of the transmission near the systemic redshift (dashed line) of the quasar ULAS J1120+0641. The blue lines show damping wing absorption models (assuming a fully transparent ionised zone around the quasar for simplicity), and uniform neutral fractions of 0.1, 0.5, and 1.0, with the more neutral models giving more absorption. The ionised zone is assumed to end abruptly, 2.2 Mpc in front of the quasar. The green solid line shows an alternate fit in which the IGM is highly ionised and the damping wing is instead sourced by a DLA situated 2.6 Mpc in front of the quasar. Adapted from Mortlock *et al.* (2011).

malised transmission first drops below some threshold. Fan *et al.* (2006) established it to be $F = 0.1$ after smoothing each spectrum to 20 Å spectral resolution. These sizes evolve with redshift, showing a drop from redshift 5.7 to 6.4 of a factor 2 (Carilli *et al.*, 2010). However, it is unclear whether this evolution is linked to the evolution of the photon mean free path or the presence of remaining diffuse neutral gas in the IGM. Subsequent works using also Lyβ point to preference for the presence of a IGM damping wing contribution.

Perhaps the most intriguing near-zone result comes from the spectrum of ULAS J1120+0641 at $z = 7.1$ (Mortlock *et al.*, 2011, see Figure 1.7). Toy damping wing models for a partly neutral IGM and a DLA shown in the Figure show the complexity and the variety of models that can explain the observations.

An alternative use of these near-zones is to measure the temperature of the IGM at $z \sim 6$ (Padmanabhan *et al.*, 2014). In a previous study by Raskutti *et al.* (2012) gas temperatures were inferred from the line widths in proximity zones observed in high resolution spectra at $5.8 < z < 6.4$, showing that the results are consistent with reionisation completing at $z < 6.5$ at 95% confidence level.

Similarly to QSOs, GRBs were also used to measure the neutral fraction by fitting the red damping wing. The main limitation in this case is the host absorption, which has to be negligible to obtain good constraints on x_{HI}. However, Chen *et al.* (2007) found that many GRBs have small enough N(H I) to allow a good fit of the IGM damped wing. Moreover, the study of the H I forest with SKA could offer a powerful tool to study the reionisation process if the radio afterglow is at the level of ∼10 mJy at z > 7-8, that may be possible in the case of Pop III GRBs (Ciardi *et al.*, 2015).

1.1.8 QSOs as probes for the study of the reionisation epoch

By mid-2012 only 33 QSOs were known at $z_{\rm em}$>6, most of them discovered using wide-field surveys such as Sloan Digital Sky Survey (SDSS; York *et al.*, 2000), the Canadian-French High-z Quasar Survey (CFHQS; Willott *et al.*, 2010), and the UK Infrared Deep Sky Survey (UKIDSS; Mortlock *et al.*, 2009).

Currently, the highest redshift quasar is at z=7.085 (Mortlock *et al.*, 2011).

The density of luminous quasars is a strong function of redshift (e.g., Boyle *et al.*, 2000). Compared to the evolution of SFR, QSO density peaks at higher redshifts and evolves much faster. The quasar density at z∼6 is consistent with the extrapolation of the QSO luminosity function from redshifts 3 to 5, indicating a value ∼40 times smaller than at z∼3. However, the highest redshift quasars are among the most luminous quasars at any redshift, with black hole masses ranging from 10^8 to 10^9 $M_\odot$.

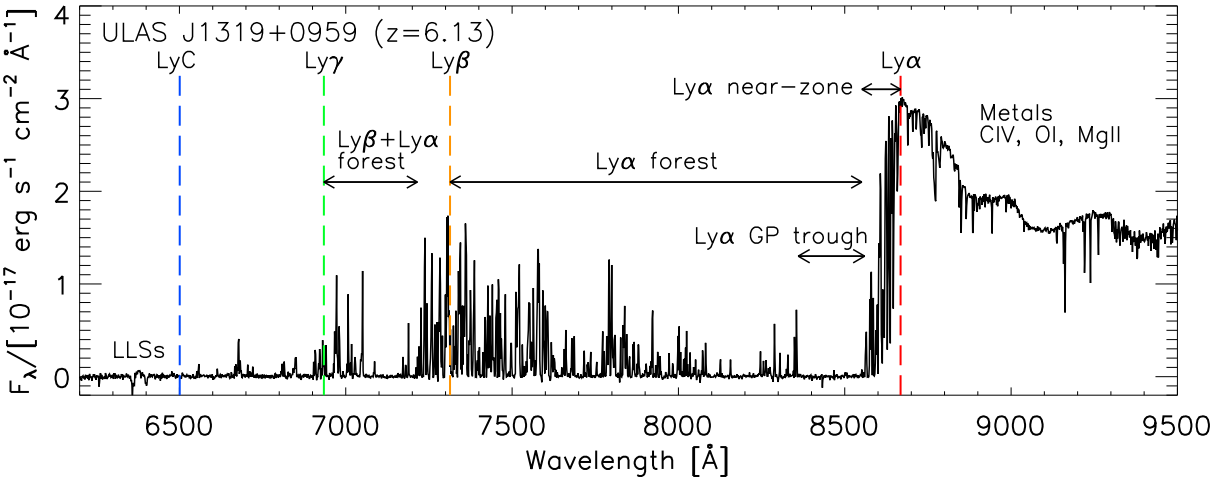

Figure 1.8: A high signal-to-noise spectrum of the quasar ULAS J1319+0959 at $z = 6.13$. The spectrum has been rebinned to 1.5 Å per pixel for presentation purposes. Adapted from (Becker *et al.*, 2015a).

The average SEDs of luminous quasars show little evolution in the UV (rest frame) out to high redshift, as well as their metallicities (e.g., De Rosa *et al.*, 2011; Fan *et al.*, 2004). This lack of evolution demonstrates that the emission line region and the accretion disk are not related with the cosmic environment.

However, observations with *Spitzer* showed some QSOs at high redshift that show no dust emission in the FIR down to a faint limit (Jiang *et al.*, 2010). Therefore, these quasars are at a very early evolutionary stage, and they are likely first generation quasars born in dust-free environment and too young to have a detectable amount of dust.

FIR to millimetre continuum observations suggest an enormous SFR (10^2 - 10^3 $M_\odot$ YR^{-1} Wang *et al.*, 2008), also supported by very strong metal emission lines. Radio-line observations of bright sub-millimetre quasars at $z\sim6$ detected strong CO emission in their host galaxies (e.g., Wang *et al.*, 2010). They found molecular masses $\sim10^{10}$ $M_\odot$ and a deviation from the black hole - bulge mass (M-σ) relation of a factor 15 above, indicating that black holes grow much faster than their host galaxy assembling.

1.1.9 GRBs as probes for the study of the reionisation epoch

A number of features render GRBs ideal probes of the epoch of first light:

1. Traditional sources to observe the high-z Universe such as QSOs and LAEs severely suffer from the effects of cosmological dimming. On the other hand, time dilation makes afterglows fade $(1 + z)$ times slower, and thus compensating for the dimming

(e.g., Ciardi & Loeb, 2000). However, some authors now suggest that this idea could be very optimistic.

2. In the hierarchical setting of cosmic structure formation, earlier times are dominated by lower-mass host systems. The massive hosts required for quasars and bright galaxies are therefore rarely found at very high redshifts (Mortlock *et al.*, 2011). On the other hand, GRBs can form in very low-mass systems.

3. Pop III GRBs would provide very clean background sources to probe the early IGM. Any proximity effect should be much more reduced than in QSOs, and thus the IGM would largely remain unperturbed.

Apart from GRB 130606A and GRB 140515A, which were studied in the context of this Thesis, the earlier high-z GRBs spectroscopically detected to date are:

GRB 050904 at $z = 6.3$ (Kawai *et al.*, 2006): The afterglow spectrum provided an upper limit on the neutral Hydrogen fraction of $x_{HI} < 0.17$ (Totani *et al.*, 2006) and a metallicity of 1.6 ± 0.3 (Thöne *et al.*, 2013).

GRB 080913 at $z = 6.7$ (Greiner *et al.*, 2009): The analysis of the red damping wing constrained $x_{HI} < 0.73$ at the 90% confidence level (Patel *et al.*, 2010).

GRB 090423 at $z = 8.2$ (Salvaterra *et al.*, 2009; Tanvir *et al.*, 2009): In spite of being the highest GRB afterglow spectroscopically confirmed, this afterglow does not look different from the others, neither for its progenitor nor the surrounding medium.

1.2 The first stars

The formation of the Pop III stars mark the fundamental transition from a simple, very homogeneous Universe, to the complex and structured one we observe a billion years after the Big Bang. The standard model of primordial star formation predicts that the firsts stars formed typically in isolation, one per mini-halo (Omukai & Nishi, 1999). This current view is that the physical conditions in the early Universe favoured an initial mass function (IMF) for the Pop III stars was top-heavy, i.e., massive stars were predominant (Abel *et al.*, 2002; Bromm & Larson, 2004; Bromm *et al.*, 2002). This is due to the lower cooling efficiency in pure H/He gas, reaching temperatures of ∼200K in contrast to ∼10K in dusty molecular clouds. Recent works have refined this paradigm and confirmed the basic prediction, that is that the first stars were typically massive (few tens of solar

masses) and few of them formed as a member of multiple systems with >100$M_\odot$, but still the final mass of Pop III stars and their final IMF remains largely uncertain (Hosokawa *et al.*, 2011; McKee & Tan, 2008; Stacy *et al.*, 2012).

Metallicity is one of the prime factors that determine the evolution of massive stars. This kind of stars in the nearby Universe are powered by the CNO cycle. As these species are absent in the primordial ISM from which the first stars formed, hydrogen starts to burn via p-p chain, which is insufficient to achieve thermal equilibrium. The main sequence evolution starts only after the star produces these elements by itself (e.g., Yoon *et al.*, 2012).

A crucial uncertainty is the physical mechanism responsible for the Pop III to II transition. Current thinking is that it was driven by chemical feedback, estimating a $Z_{crit} \sim 10^{-4} Z_\odot$. The underlying physics is really complex, resulting in some models claiming that C I and fine-structure levels of O I may drive this transition (Bromm & Loeb, 2003), and others identifying dust cooling as the key agent (Schneider *et al.*, 2006).

1.2.1 Are Pop III stars GRB progenitors?

Conditions to trigger collapsar (Woosley, 1993) events are quite stringent and often difficult to fulfill simultaneously (e.g. Belczynski *et al.*, 2007). They are summarised here

1. A central BH has to form.
2. A relativistic jet has to escape from the stellar envelope before being quenched.
3. There has to be a sufficient degree of angular momentum, close to the center, to delay the accretion of material onto the BH.

The first requirement is fulfilled because of the top-heavy nature of the primordial IMF. The binary nature of Pop III stars may allow to meet the second requirement, if the binary is sufficiently close to allow for Roche-lobe overflow and a common-envelope phase to expel the extended Hydrogen (and Helium?) outer layer (Bromm & Loeb, 2006). The hardest requirement is that they must have enough angular momentum. Almost nothing is known about this, but a first attempt has recently carried out by Stacy *et al.* (2011, 2013), showing that Pop III stars could be typically fast rotators. Thus, it is plausible that long GRBs occur in the early Universe, but we have to remember that we still cannot yet make any robust prediction on the properties of these stars.

In order to estimate the GRB rate at very high redshifts, Bromm & Loeb (2006) used

$$\frac{dN_{GRB}^{obs}}{dz} = \phi_{GRB}^{obs}(z)\frac{\Delta t_{obs}}{1+z}\frac{dV}{dz} \tag{1.14}$$

where $dN_{GRB}^{obs}dz$ is the number of GRBs within the interval dz, and $\phi_{GRB}^{obs}(z)$ the number of bursts per comoving volume

$$\phi_{GRB}^{obs}(z) = \eta_{GRB}\phi_*(z)\int_{L_{lim(z)}}^{\infty} p(L)dL \tag{1.15}$$

where η_{GRB} is the GRB formation efficiency, $\phi_*(z)$ the cosmic SFRD, $p(L)$ the GRB luminosity function, and $L_{lim(z)}$ the minimum intrinsic luminosity required to detect a burst at a given redshift with a given instrument. Numbers for the *Swift* capabilities are not promising. A robust upper limit is ~ 10 yr^{-1} sr^{-1}, but a more realistic number may be 0.1 yr^{-1} sr^{-1} (Campisi *et al.*, 2011). Anyway, we still could be lucky...

1.2.2 Observational signatures of Pop III GRBs

In the context of the study of Pop III stars, a crucial question is how can we identify GRBs originating from Pop III stars (e.g., Salvaterra, 2015; Toma *et al.*, 2016). An unambiguous way to pinpoint a Pop III progenitor is to examine whether the afterglow spectrum from its surrounding medium is devoid from iron-group elements. However, the ISM could be enriched slightly before by other stellar explosions, so it is therefore important to explore alternative strategies to identify Pop III GRBs.

In this regard, another proposed way is to focus on the total energies and durations of GRBs through X-ray and γ-ray observations of the prompt emission and their afterglows (e.g., Mészáros & Rees, 2010). However, first results imply that if only Pop III stars with $M < 100$ M$_\odot$ can produce GRBs, it would not be simple to identify such events through total energy and duration scales, and even they may be not detectable with current facilities (Nakauchi *et al.*, 2012).

There are also indirect ways to search for primordial ISM. Ma *et al.* (2015) showed that in principle the [C/O] and [Si/O] ratios could be enough to distinguish a Pop III enriched environment, although in practice detection of more species is needed. Pop II GRBs exploding in a Pop III enriched medium are expected to be rare at $z < 6$, but the probability increases to $\sim$10%. Therefore, the detection of a GRB at this redshift with a surrounding medium metallicity down to the "metallicity threshold" ([X/H] ~ 3) will be a strong candidate to be either a Pop III event or a Pop II GRB blowing up in a Pop III

enriched medium (Salvaterra, 2015).

Chapter 2

GRB140304A

Adapted from

— Jeong, Sánchez-Ramírez et al., *A&A, in preparation*

2.1 Observations

2.1.1 *Swift* observations

At 13:22:31 UT, the *Swift*/BAT triggered and located GRB 140304A. *Swift* slewed immediately to the burst. The burst's on-board localisation was RA($J2000$) = 02h 02m 40s, Dec($J2000$) = +33d 29′07"with an uncertainty of 3′(radius, 90% containment, including systematic uncertainty). The BAT light curve showed a multi-peaked structure with a total duration of about 20 sec. The peak count rate was ∼3600 counts/sec (15-350 keV), at ∼0 sec after the trigger.

The XRT began observing the field at 13:23:46.2 UT, 75.2 seconds after the BAT trigger. Using promptly downlinked data a bright, uncatalogued X-ray source is found with an enhanced position RA($J2000$) = 02h 02m 33.90s Dec($J2000$) = +33d 28′27.9"with an uncertainty of 2.2"(radius, 90% containment). This location is 89"from the BAT on-board position, within the BAT error circle. The initial flux in the 2.5 s image was 6.28 $\times$ 10^{-10} erg cm^{-2} s^{-1} (0.2-10 keV).

UVOT took a finding chart exposure of 250 seconds with the U filter starting 137 seconds after the BAT trigger. No credible afterglow candidate was found in the UVOT data, due to the redshift of the object, as we will now see.

2.1.2 Optical imaging

The optical counterpart of GRB 140304A was discovered by the MASTER II telescope, at RA($J2000$) = 02h 02m 34.13s Dec($J2000$) = +33d 28′26.6". We performed further optical follow-up of the afterglow with BOOTES 4, and Harold L. Johnson telescopes.

2.1.3 Optical spectroscopy

We took optical spectra with OSIRIS at the 10.4m Gran Telescopio de Canarias (GTC). Observations started on Mar 04, 2014, i.e. $\sim$ 7.36 h after the *Swift* trigger, using the R2500I volume-phase holographic grating (VPH), in 2 $\times$ 1200 s exposures. The 1.0"slit was positioned on the location of the host galaxy in paralactic angle. The spectra were reduced and calibrated following standard procedures using custom developed tools based in IRAF and Python. They were flux calibrated using observations of the spectrophotometic standard star HILT600, observed in the same night with a 2.52"slit. We renormalised the flux level in order to correct for any possible slit losses using the photometric value ob-

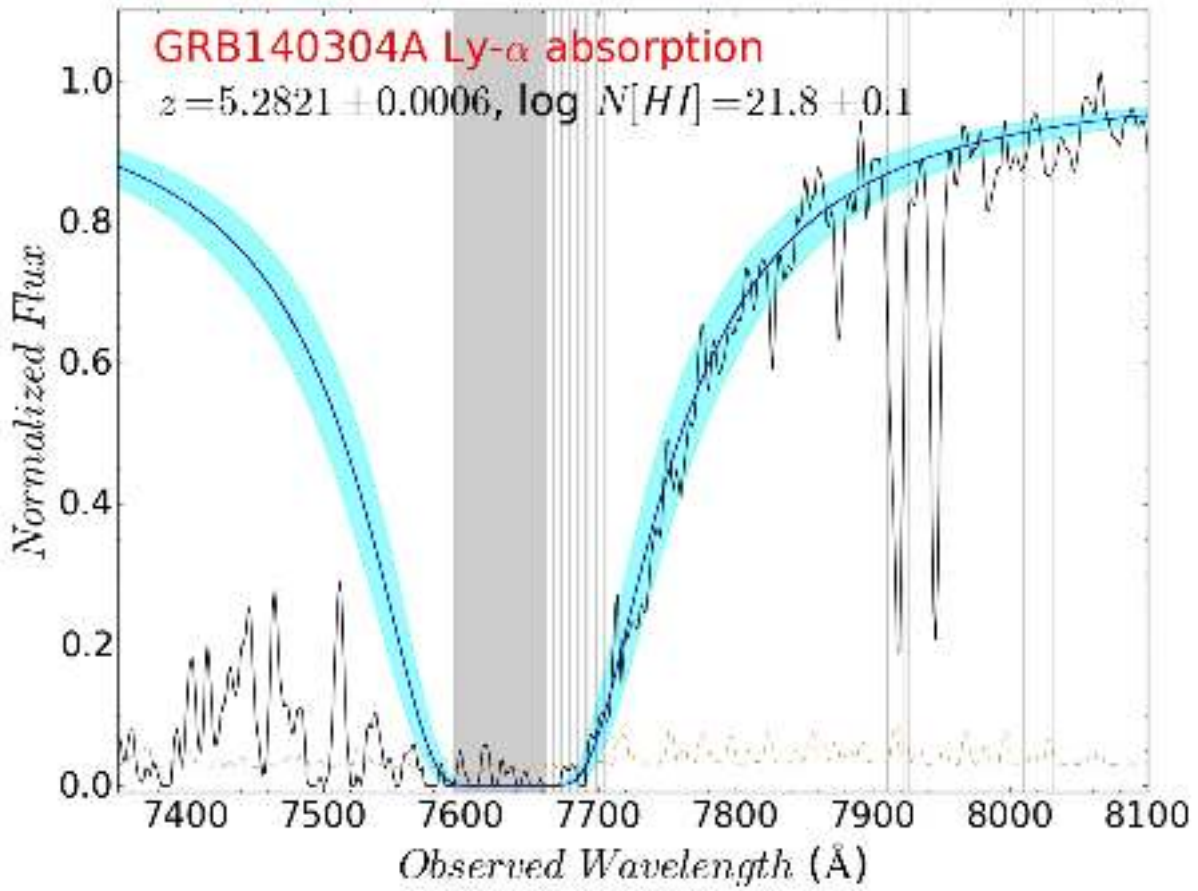

Figure 2.1: Voigt profile fit to the Lyα red damping wing absorption towards GRB 140304A. Solid cyan area represents the 68% confidence interval. Shaded areas represent regions affected by telluric absorption.

tained from the acquisition image.

2.2 Results and Discussion

2.2.1 Hydrogen abundance

Our GTC combined spectrum exhibits a clear broad Lyα absorption at $z \sim 5.283$ (Jeong *et al.*, 2014). We fitted this damped feature using the same prescription and tools as in Sánchez-Ramírez *et al.* (2016), obtaining $\log N(\mathrm{H\,I}) = 21.8 \pm 0.1$ (see Fig. 2.1). Due to the wavelength range covered by the spectrum, higher order Lyman series could not be fitted, which would reduce the chance of overestimating the Hydrogen column density (e.g. Crighton *et al.*, 2015; Sánchez-Ramírez *et al.*, 2016). However, GRB sight lines benefit from little absorption in the red damped wing. Therefore, if the continuum is well

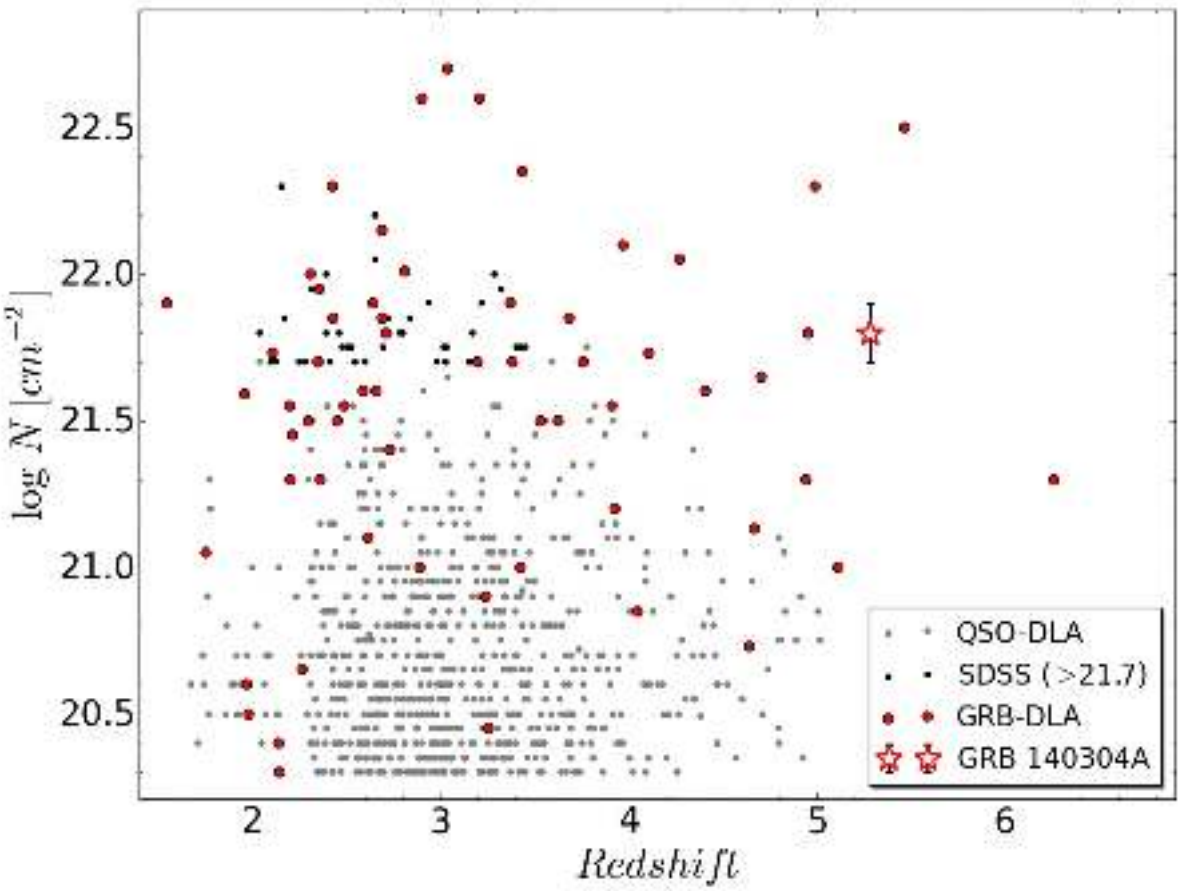

Figure 2.2: Comparison of the measured column density of the GRB 140304A DLA with the GRB-DLA compilation by Cucchiara *et al.* (2015) and the QSO-DLA one by Sánchez-Ramírez *et al.* (2016). QSO-DLA information is complemented with the log N(H I)≥21.7 DLAs from the SDSS sample (Noterdaeme *et al.*, 2012). The error bar represents the 68% confidence interval.

determined, the model fitting to this wing should provide a robust way for the N(H I) determination.

In Fig. 2.2, we place this result into context, comparing it with the GRB-DLA compilation by Cucchiara *et al.* (2015), which extend previous works by, e.g., Schady *et al.* (2011); Thöne *et al.* (2013), and QSO-DLA (Sánchez-Ramírez *et al.*, 2016) populations. We chose the latter QSO-DLA compilation (with a combined total of 742 systems, see Part 3 of this Thesis), instead of the larger SDSS sample (over 3 400 DLA systems in the statistical sample), because the SDSS DLA catalogue is strongly affected by systematics, and contains many false positives (Noterdaeme *et al.*, 2012). The compilation by Sánchez-Ramírez *et al.* (2016) uses only visually confirmed DLAs, which reduces the effect of systematics, so its distribution is more representative of the actual DLA population than the blindly selected samples. However, we include in Fig. 2.2 $\log N(\mathrm{H\,I}) \geq 21.7$ DLAs from the SDSS sample to remark the fact that the detection of these high column density systems is very rare towards QSO lines of sight. Indeed, the number of observed intervening DLAs had to be of a few thousand before one starts to detect $\log N(\mathrm{H\,I}) \gtrsim 22$ absorbers (Noterdaeme *et al.*, 2009, 2012), values easily found towards GRB sightlines (e.g., de Ugarte Postigo *et al.*, 2012a; Fynbo *et al.*, 2009; Jakobsson *et al.*, 2006; Schady *et al.*, 2011; Thöne *et al.*, 2013). Our measurement is the third farthest DLA detected to date, and further evidence that GRB and QSO DLA samples are drawn from different populations. GRB-DLAs are selected by the GRB γ-ray emission, which are thought to be produced in the cores of star forming regions, whereas QSO-DLAs are random lines of sight that pierce intervening systems, so they most likely probe the halo clouds.

2.2.2 Metal abundances

A series of absorption lines due to different species (S, Si, O, and C) are clearly detected at the same redshift as the Lyα feature, as well as at least one intervening C IV system at $z = 4.3403 \pm 0.0001$. A plot of the GTC spectrum and line identifications is provided in Fig. 2.3. We measured the equivalent widths (EWs) of the lines fitting Gaussians profiles and computing the EW of the line model. This approximation is in our case valid due to the low resolution of the GTC/OSIRIS spectrum, as the convolution of the instrumental profile with the actual Voigt profile makes the absorption remain approximately Gaussian. Furthermore, using this method we can estimate the redshift and EW of each blended feature. Results are presented in Table 2.1. With the redshifts obtained by line fitting, we are able to refine the redshift to $z = 5.2821 \pm 0.0006$. We excluded in this computation the Si IIλ1304 line, as it is blended with some unknown (probably intervening) feature and no constraint on this component can be imposed in order to perform an accurate

Table 2.1: EW measurements for the systems detected on the GRB 140304A afterglow spectrum.

Feature	Wavelength	z	EW	eEW
SIIλ1254	7875.5	5.2813	0.23	0.04
SIIλ1260	7913.4	5.2829	0.42	0.01
SiIIλ1260	7919.3	5.2831	0.85	0.03
SiII*λ1265	7945.8	5.2825	1.03	0.03
SiIIλ1304	-	-	-	-
SiII*λ1309	8224.6	5.2818	0.49	0.01
CIIλ1334	8383.5	5.2820	0.86	0.02
CII*λ1336	8390.1	5.2814	0.85	0.02
SiIVλ1394	8755.0	5.2816	0.65	0.04
SiIVλ1403	8812.1	5.2819	0.50	0.05
CIVλ1548	8267.9	4.3403	0.64	0.02
CIVλ1551	8281.6	4.3403	0.50	0.02

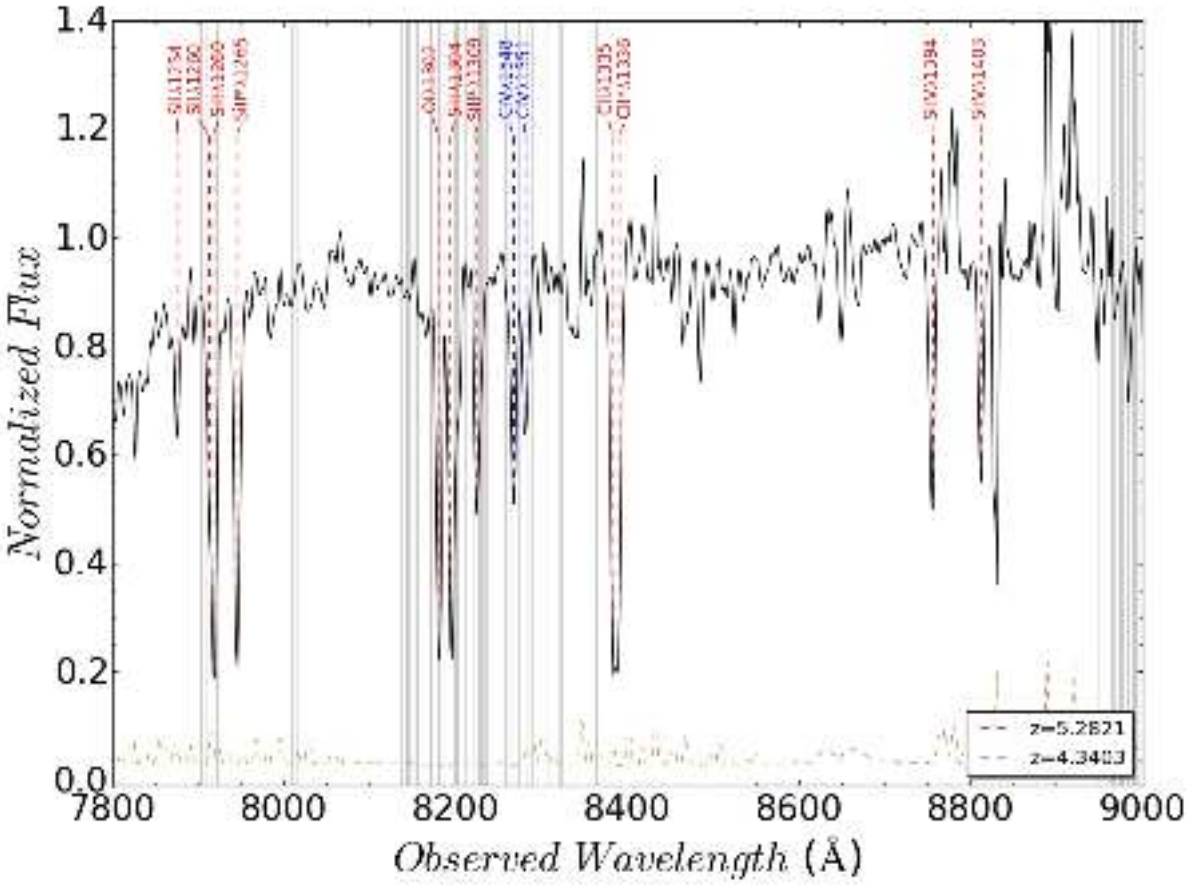

Figure 2.3: Lines detected on the GTC optical spectrum.

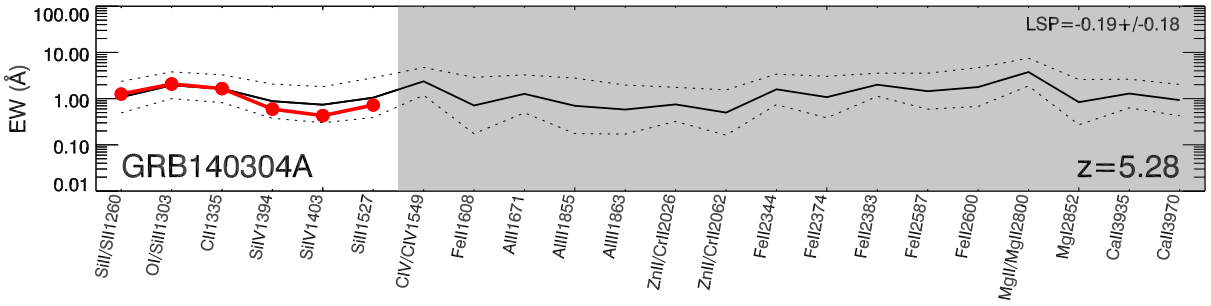

Figure 2.4: Line strength diagram of GRB 140304A, based on the prescription of de Ugarte Postigo *et al.* (2012a). The line strengths of GRB 140304A are shown in red, and compared with the sample of GRB spectra in black. The sample average strengths are shown by a black line, whereas dotted lines show the 1-sigma deviations. The shaded area corresponds to lines that were not covered by our spectrum, or strongly affected by telluric features.

Table 2.2: CoG MCMC fitting results.

Parameter	Median	95% c.i.
b_{eff}	$19.23^{+0.23}_{-0.41}$	[18.81, 20.25]
$\log N[S]$	$15.74^{+0.10}_{-0.07}$	[15.18, 16.77]
$\log N[Si^*]$	$17.12^{+0.01}_{-0.01}$	[17.06, 17.19]

deblending.

Using the prescription of de Ugarte Postigo *et al.* (2012a) we calculate the line strength parameter (LSP) of this spectrum, which can be used to compare the absorption features of this line of sight with those of a large sample of GRB afterglow spectra. We derive a LSP = -0.19±0.18, which implies features very similar to those of the sample, just slightly below the average, at a line strength percentile of 41 (41% of the sample has weaker features). In Fig. 2.4 we show a line strength diagram in which line strengths are individually compared with the sample. There we see that the absorption lines are almost on the average of the sample, with the exception of the Si IV lines which are slightly below, probably indicating a slightly lower than average ionisation field in the host galaxy of GRB 140304A.

2.2.3 Metallicity estimation

We estimate the metallicity of the GRB environment using a novel technique based on the Curve of Growth (CoG) analysis. As we cannot perform direct Voigt profile fitting on low resolution spectra, and we don't have available a weak enough line (within the linear regime) to directly measure the abundance, this method uses EW measurements

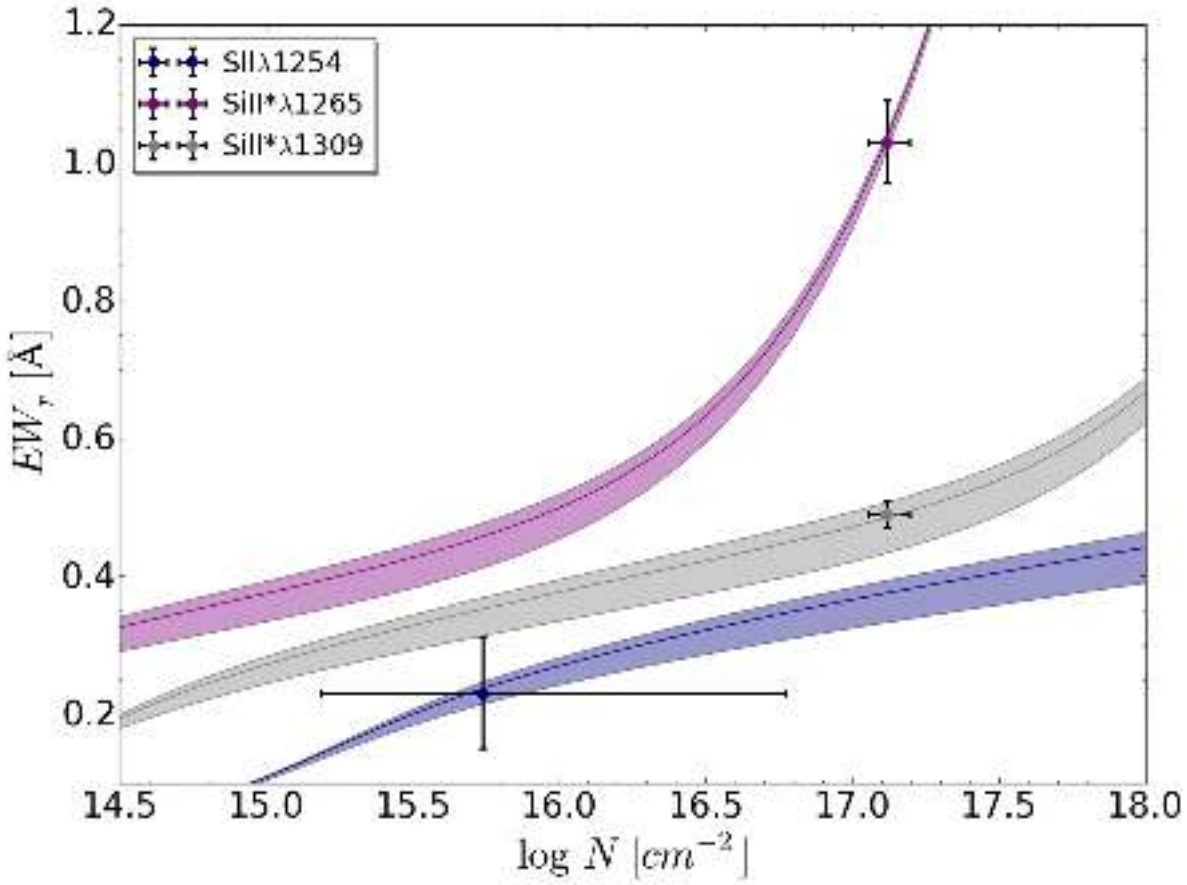

Figure 2.5: CoG analysis for the 3 features selected to estimate the metallicity of the GRB environment. Errors are represented at 95% confidence level.

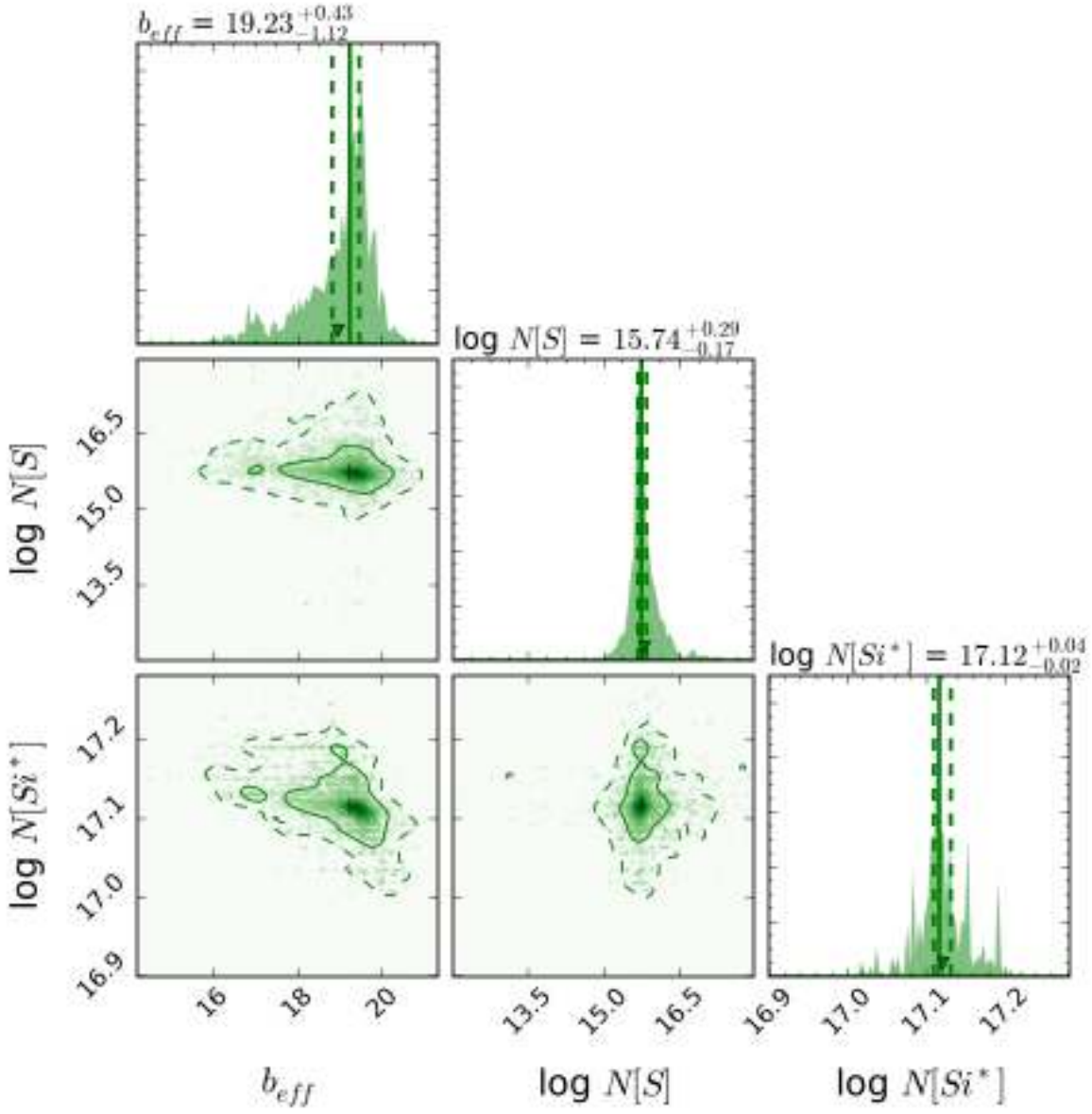

Figure 2.6: Posterior distributions of the fitted parameters. We plot the 95% confidence intervals, and dashed vertical lines limit the 68% area. Median values are marked with a cross.

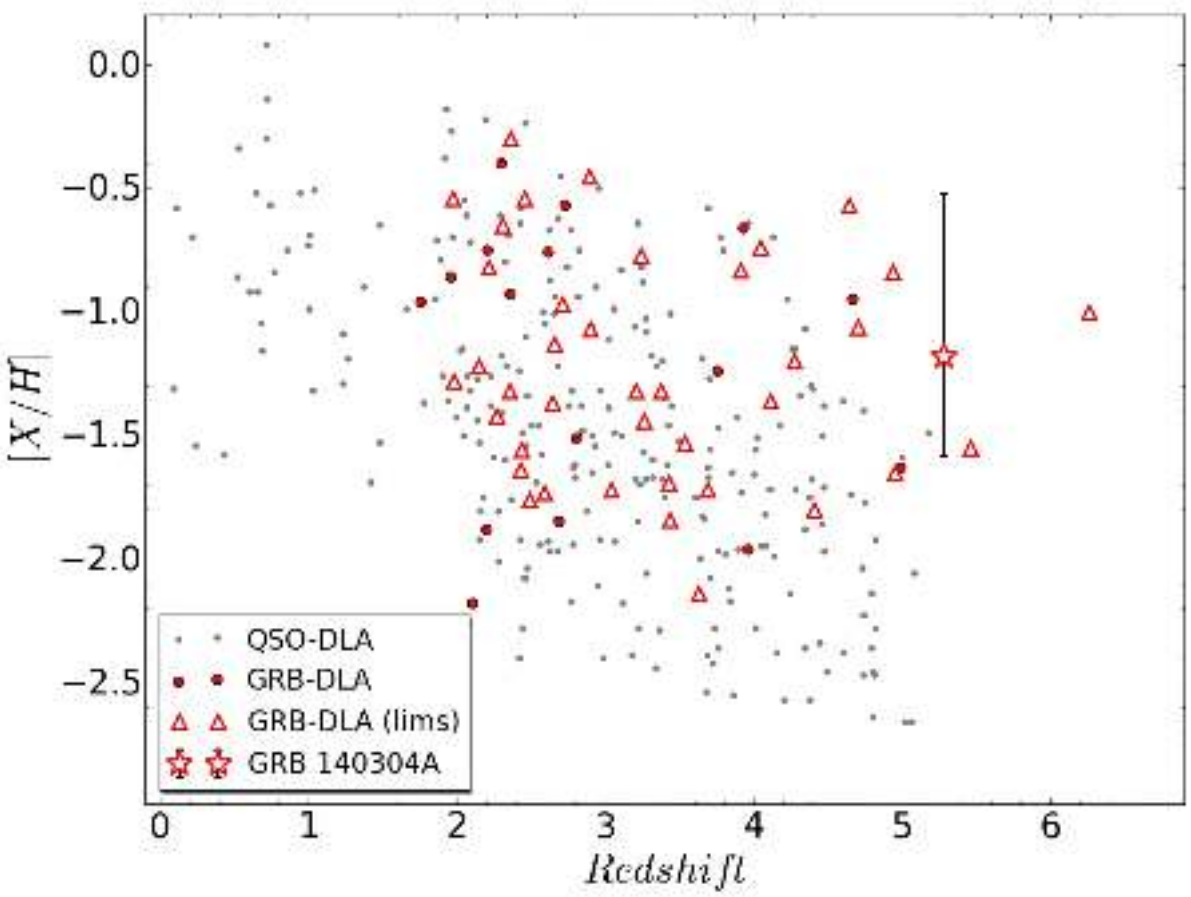

Figure 2.7: Comparison of the measured metallicity of the GRB 140304A DLA with the GRB-DLA compilation by Cucchiara *et al.* (2015); Thöne *et al.* (2013) and the QSO-DLA one by Rafelski *et al.* (2012, 2014). The error bar represents the 95% confidence interval.

as alternative to constrain b and $\log N[X]$. However, Prochaska (2006) already pointed out that this kind of analysis can underestimate severely column density determinations because in strong transitions the blending of the GRB environment absorption with near weaker systems leads to EW overestimates and unphysically high fitted b values. In order to minimise the effect of this issue, we took benefit of the observed Si II* transitions. This is because, in spite of being strong transitions, the fine-structure excited population originates from the UV radiation due to the GRB afterglow, which generally results in close component features, as only the clouds that are whithin few kpc to the GRB are excited. Furthermore, we assume that the low ionisation absorption comes from the same system than Si II*. This scenario can be supported by, e.g., the results of GRB 080310 (De Cia *et al.*, 2012), but we caution that it has not necessarily be true for this line of sight. For the metallicity estimator we chose the S IIλ1254 feature, as it is the weakest unblended line available on our spectrum.

Driven by the limitations that our feature selection imposes to the fit, as we have 3 points for 3 unknown parameters (b_{eff}, $\log N[S]$, and $\log N[Si^*]$), we decided to perform a Markov Chain Monte-Carlo analysis of the CoG of each feature by using *pymc*. This Bayesian approach can take profit of the prior knowledge we have on the parameters. We opted for uninformative flat prior distributions for the column density, limiting their values from 5 to 23. However, following de Ugarte Postigo *et al.* (2012a), we assumed that b_{eff} is log-normally distributed as they found from high resolution studies. On this way, we restrict the possibility that b_{eff} takes unrealistic values along the iterations due to contamination in a given feature (Prochaska, 2006). Due to resolution and SNR limitations, the implementation of more complex models, e.g., with a few velocity components, will not improve the results. For the fitting function (the model to fit with *pymc*), we coded up a routine that, given any value of the incoming parameters (b_{eff} and N), it computes as the output the EW of a synthetic Voigt profile generated with these parameters.

The results of the fit are displayed in Table 2.2. We performed several test to check for the convergence of the procedure, that showed positive results. Moreover, in Fig. 2.6 we see that posterior distributions are well behaved, showing only little skewness in the b_{eff} distribution. In Fig. 2.5 we represent each feature and its CoG, showing errors at 95% confidence level. This plot clearly shows that Si II*λ1265 (a strong feature with an oscillator strength value $f = 1.05$) is at the beginning of the damped regime, so the column density of the excited Silicon is accurately constrained by this line. Consequently, b_{eff} fit is mainly driven by Si II*λ1309. However, the poor constraint on EW of the S IIλ1254 line, together with the fact that it is mildly saturated, imply that Sulphur abundance cannot be determined with a similar precision as excited Silicon. Looking at Fig. 2.6, we can observe that there is only an expected mild correlation between b_{eff} and $\log N[Si^*]$,

but not for b_{eff} and $\log N[S]$, most likely due to the uncertainty in the EW measurement. This would probably explain why Si II*λ1309 is not able to be as constraining as expected to estimate b_{eff}.

Using the Sulphur abundance, which is a non-refractory element and thus will not be substantially depleted onto dust (Savage & Sembach, 1991), we obtain $[S/H] = -1.13^{+0.10}_{-0.07}$ with a 95% probability for value between $[-1.49, -0.52]$. This posterior metallicity distribution was obtained performing a Monte-Carlo simulation with the S distribution coming from the MCMC fit, and assuming normal distributions for the errors of all the other parameters except for the Solar Hydrogen abundance (Asplund *et al.*, 2009). In Fig. 2.7 we place the GRB 140403A point (star) among the GRB-DLA sample compiled by Cucchiara *et al.* (2015) and the high resolution QSO-DLA sample from Rafelski *et al.* (2012, 2014). The GRB sample is clearly dominated by limits, making it difficult to derive robust conclusions. However, this figure suggest that GRB metallicities did not substantially evolve with redshift, matching both GRB-DLA and QSO-DLA populations at low- but not at high-redshift. Our new measurement is therefore consistent with the non evolution picture of the metal content in star forming regions up to $z \sim 5$.

2.3 Conclusions

- We detect a Damped Lyman-α system at $z = 5.2821 \pm 0.0006$ on the optical spectra towards GRB 140304A. This is the third farthest DLA detected to date. The Voigt profile fitting give a column density value of $\log N(\mathrm{H\,I}) = 21.8 \pm 0.1$.
- There are several absorption lines at the same redshift as the Lyα absorption due to S, Si, O, and C, as well as at least one C IV intervening system.
- We measured the EW of the lines and compared them with the results from de Ugarte Postigo *et al.* (2012a), finding that the 41% of the sample has weaker features.
- We estimated the metal abundances of the S II and Si II* ions by using a novel technique based on the CoG method and the Bayesian inference, finding acceptable results.
- We obtained $[S/H] = -1.13^{+0.10}_{-0.07}$, a value consistent with the non evolution picture of the metal content in star forming regions up to $z{\sim}5$.

Chapter 3

GRB 130606A

Adapted from "GRB 130606A within a sub-DLA at redshift 5.91"

— Castro-Tirado, Sánchez-Ramírez et al., *A&A, submitted, arXiv:1312.5631*

3.1 Introduction

The detection of individual Population III (Pop III Bromm *et al.*, 2009) stars, either existing in the Galactic halo or at the moment of their deaths, as highly energetic supernova explosions (Mackey *et al.*, 2003) or as gamma-ray bursts (Bromm *et al.*, 2002), is one of the most challenging and profound objectives in modern observational astronomy. It is widely accepted that massive Pop III stars should be viable GRB progenitors (Bromm & Loeb, 2006) and potentially observable out to very high redshifts (Ciardi & Loeb, 2000; Lamb & Reichart, 2000). Such distant GRBs can serve as ideal background sources, with their extremely bright, featureless afterglow continuum emission, to illuminate the early intergalactic medium (IGM). At the earliest times, quasars become increasingly rare and faint to effectively play this role, but GRBs offer a potential window into the ionization and metal enrichment state of the IGM at very high redshifts.

It has been recently suggested (Cooke *et al.*, 2011a,b; Fabbian *et al.*, 2009) that very metal-poor damped Lyman-alpha (DLA) systems (regions of high column density of neutral gas at high redshifts (Wolfe *et al.*, 2005) could bear the chemical signature of the first generation of stars, born a few hundred million years after the Big Bang.

Indeed, it has been suggested that metal-free regions persist to values of $z \leq 6$, allowing Pop III stars with masses in the range 140-260 solar masses to be observed as pair-production instability supernovae (Scannapieco *et al.*, 2005), although a core-collapse (Type II) supernova is also plausible instead (Wang *et al.*, 2012). In spite of the fact that no GRB has been so far firmly associated with a Pop III collapse yet, the high z values found for several GRBs reinforces the potential of GRBs to provide bright background sources to illuminate the early intergalactic medium at a time when quasars are too rare and dim to serve this purpose.

A ∼275 s cosmic gamma-ray burst (GRB 130606A) was recorded by *Swift* and KONUS-*Wind* on 6 June 2013, 21:04:34 U.T. (T_0) (Barthelmy *et al.*, 2013; Golenetskii *et al.*, 2013), displaying a bright afterglow (the emission at other wavelengths following the gamma-rays) in X-rays, but no apparent optical transient emission (Ukwatta *et al.*, 2013) in the range of the UVOT telescope aboard *Swift*. The TELMA 0.6m diameter telescope at the BOOTES-2 station automatically responded to the alert and an optical counterpart was identified (Jelínek *et al.*, 2013), thanks to the spectral response of the detector up to 1 μm, longer than that of *Swift*/UVOT (0.17-0.65 μm).

The detection of the afterglow at BOOTES-2/TELMA prompted spectroscopic observations with the 10.4 m Gran Telescopio Canarias (GTC) starting 1.4 hr after the event, which revealed an explosion at a very high redshift ($z \sim 6$) (Castro-Tirado *et al.*, 2013c),

a value later refined to z = 5.91 (Castro-Tirado *et al.*, 2013b), when the Universe was only ∼950 million years old.

3.2 Observations

3.2.1 X-ray observations

The *Swift* X-ray Telescope (XRT) started collecting data in window timing mode (WT) ∼60 s after the initial BAT trigger on June 6 at 21:05:35 U.T., switching to photon counting mode (PC) after ∼ 500s. The position of the source was monitored up to ∼ 3 × 10^5 s post-trigger.

3.2.2 Optical/nIR Observations

3.2.2.1 Photometry

Early time prompt optical observations were carried out by the Watcher telescope starting on June 6, 21:06:49 U.T., i.e. ∼135 s after the first *Swift*/BAT trigger (T_0 = 21:04:34 UT). The BOOTES-2/TELMA observations, which resulted in the optical afterglow discovery, started on June 6, 21:17:33 U. T., i.e. ∼660 s after the first *Swift*/BAT trigger. The Watcher observations partially cover the second *Swift*/BAT peak. Additional Johnson *R* and *V*–band images were acquired with the 1.23m telescope of Calar Alto (CAHA) observatory, Spain. Late epoch optical observations were obtained with the 0.7m Abastumani Observatory, the AZT-11 (1.25m) telescope at SRI "Crimean Astrophysical Observatory", the T100 (1m) telescope at TÜBITAK National Observatory, the 1.5m OSN telescope at Observatorio de Sierra Nevada and with the 10.4m Gran Telescopio Canarias (GTC) equipped with the OSIRIS imaging spectrograph (Fig. 3.2). Optical photometry is based on isophotal corrected photometry by IRAF/PHOT31 against standard reference Landolt fields imaged at the 1.5m OSN telescope in order to provide reference stars in the field (Table 3.2).

Near-IR bservations were conducted on July 22 at the 3.5m telescope (+OMEGA 2000) at the German-Spanish Calar Alto (CAHA) Observatory, with a 5,400s overall exposure time in the *H*-band. The photometric calibration is based on the observation of the standard S889-E (Persson *et al.*, 1998) at an airmass similar to the GRB field. The photometric results of the afterglow are tabulated in Table 3.1.

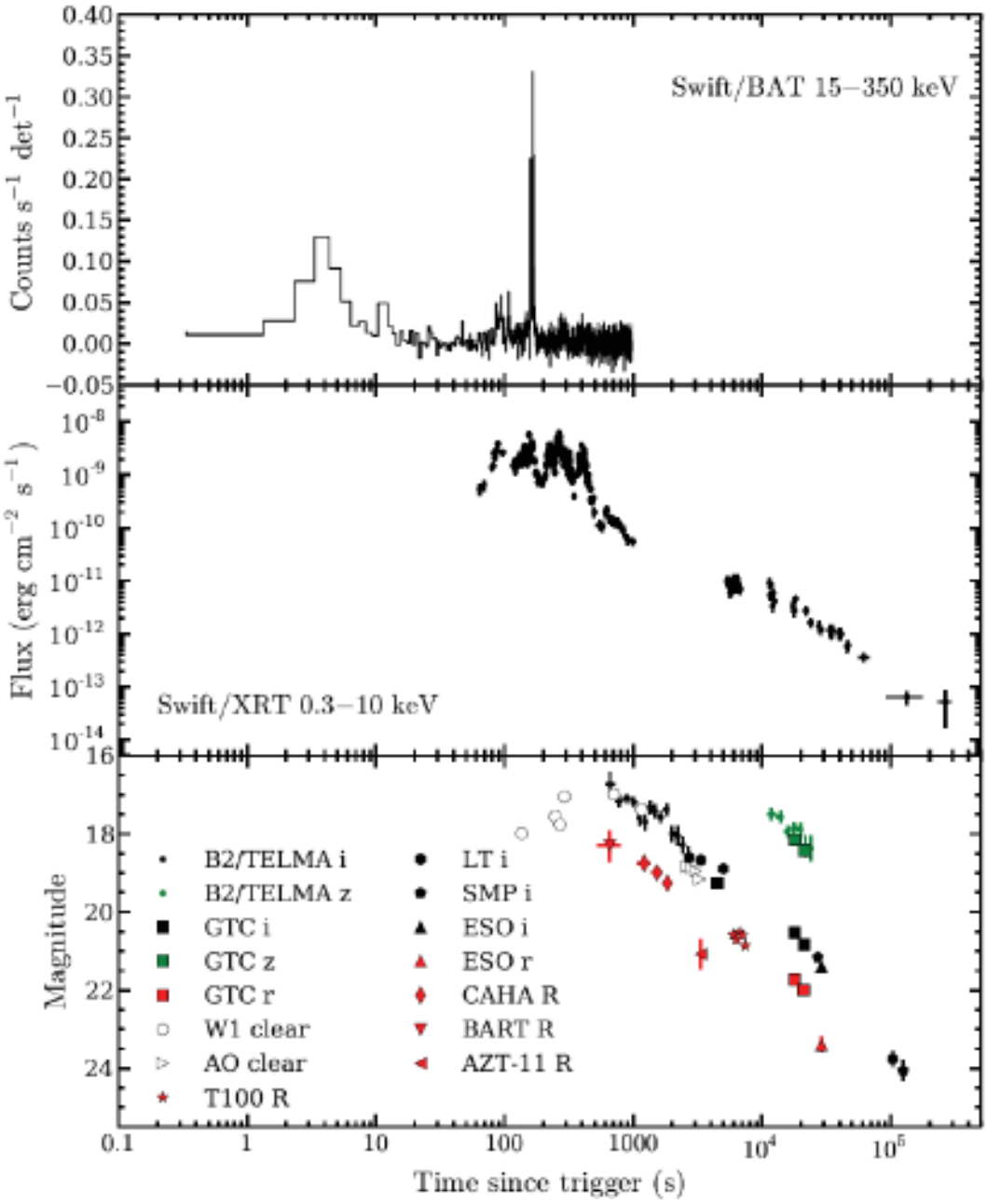

Figure 3.1: The GRB 130606A prompt gamma-ray emission and the multiwavelength afterglow evolution. The *Swift*/BAT light curve shows a double-peaked structure with an initial peak lasting ∼10 s and a brighter second peak at T_0+150 s of ∼20 s duration. The gamma-ray lightcurve is compared with the multiwavelength (X-ray, optical) GRB 130606A afterglow lightcurves. Significant temporal (and spectral) evolution is noticeable in the XRT data. The lower panel shows the rising optical afterglow lightcurve based on Watcher data, prior to the well sampled decay, based on the data gathered by BART, BOOTES-2/TELMA, 0.7m AO, T100, 1.23m CAHA, AZT-11, 1.5m OSN and 10.4m GTC (Table 3.1, complemented with other data published elsewhere; Afonso *et al.*, 2013; Butler *et al.*, 2013a,b; Virgili *et al.*, 2013a,b). 1σ error bars are plotted.

Table 3.1: Optical and near-IR observations gathered at several astronomical observatories worldwide. $VRIH$-band magnitudes are given in the Vega system whereas *clear* and Sloan-filter magnitudes are given in the AB system. Not corrected for Galactic extinction.

Start Time (JD) [a]	Magnitude	Filter	Telescope [b]
2456450.379734	17.99 ± 0.11	*clear*	0.4m Watcher
2456450.381019	17.55 ± 0.08	*clear*	0.4m Watcher
2456450.381273	17.76 ± 0.10	*clear*	0.4m Watcher
2456450.381528	17.04 ± 0.06	*clear*	0.4m Watcher
2456450.386308	16.99 ± 0.10	*clear*	0.4m Watcher
2456450.391528	17.38 ± 0.14	*clear*	0.4m Watcher
2456450.382210	>16.5	R	0.25m BART
2456450.38575	18.30 ± 0.40	R	0.25m BART
2456450.385800	16.73 ± 0.34	i'	0.6m TELMA
2456450.387112	17.16 ± 0.16	i'	0.6m TELMA
2456450.388424	17.10 ± 0.13	i'	0.6m TELMA
2456450.389742	17.18 ± 0.12	i'	0.6m TELMA
2456450.391053	17.59 ± 0.20	i'	0.6m TELMA
2456450.392371	17.70 ± 0.20	i'	0.6m TELMA
2456450.393677	17.32 ± 0.16	i'	0.6m TELMA
2456450.395124	17.42 ± 0.16	i'	0.6m TELMA
2456450.396963	17.56 ± 0.15	i'	0.6m TELMA
2456450.399062	17.38 ± 0.15	i'	0.6m TELMA
2456450.401339	17.99 ± 0.21	i'	0.6m TELMA
2456450.403521	18.04 ± 0.24	i'	0.6m TELMA
2456450.406057	18.29 ± 0.21	i'	0.6m TELMA
2456450.408959	18.61 ± 0.30	i'	0.6m TELMA
2456450.514739	17.49 ± 0.15	Z	0.6m TELMA
2456450.537466	17.56 ± 0.16	Z	0.6m TELMA
2456450.560270	17.93 ± 0.15	Z	0.6m TELMA
2456450.583792	17.84 ± 0.16	Z	0.6m TELMA
2456450.606892	17.89 ± 0.17	Z	0.6m TELMA
2456450.629280	18.32 ± 0.26	Z	0.6m TELMA
2456450.651610	18.37 ± 0.31	Z	0.6m TELMA
2456450.392159	18.75 ± 0.03	R	1.23m CAHA
2456450.395772	18.99 ± 0.04	R	1.23m CAHA
2456450.399383	19.26 ± 0.06	R	1.23m CAHA
2456450.403071	>21.5	V	1.23m CAHA
2456450.408137	18.84 ± 0.05	*clear*	0.7m AO
2456450.410694	18.86 ± 0.04	*clear*	0.7m AO
2456450.413241	18.95 ± 0.05	*clear*	0.7m AO
2456450.415799	19.16 ± 0.06	*clear*	0.7m AO
2456450.416655	21.08 ± 0.38	R	1.25m AZT-11
2456450.447046	20.58 ± 0.07	R	1.0m T100
2456450.451171	20.71 ± 0.07	R	1.0m T100
2456450.455296	20.51 ± 0.07	R	1.0m T100
2456450.459379	20.60 ± 0.08	R	1.0m T100
2456450.463463	20.86 ± 0.09	R	1.0m T100
2456450.582700	>25	g'	10.4m GTC
2456450.583935	21.73 ± 0.07	r'	10.4m GTC
2456450.120092	22.00 ± 0.07	r'	10.4m GTC
2456450.429560	19.27 ± 0.05	i'	10.4m GTC
2456450.584792	20.53 ± 0.05	i'	10.4m GTC
2456450.621551	20.83 ± 0.05	i'	10.4m GTC
2456450.585938	18.14 ± 0.08	z'	10.4m GTC
2456450.622558	18.42 ± 0.08	z'	10.4m GTC
2456451.480060	>22.1	I	1.5m OSN
2456496.462500	>21.5	H	3.5m CAHA

[a] Values measured since 21:04:34 UT June 6, epoch of the first *Swift*/BAT trigger time (Julian Date (JD) is 2556450.378171)

[b] 0.4m Watcher is at Boyden Observatory (South Africa). 0.25m BART is at Astronomical Institute at Ondrejov (Czech Republic). 0.6m TELMA is at Algarrobo Costa (Málaga, Spain). 0.7m AO is at the Abastumani Observatory (Georgia). T100 is at the TÜBITAK National Observatory (Turkey). AZT-11 is the 1.25m telecope at the SRI "Crimean Astrophysical Observatory" (Ukraine). 1.5m OSN is at Observatorio de Sierra Nevada in Granada (Spain); 3.5m CAHA is at the German-Spanish Calar Alto Observatory in Almería (Spain); GTC is the 10.4-m Gran Telescopio Canarias in Canary Islands (Spain).

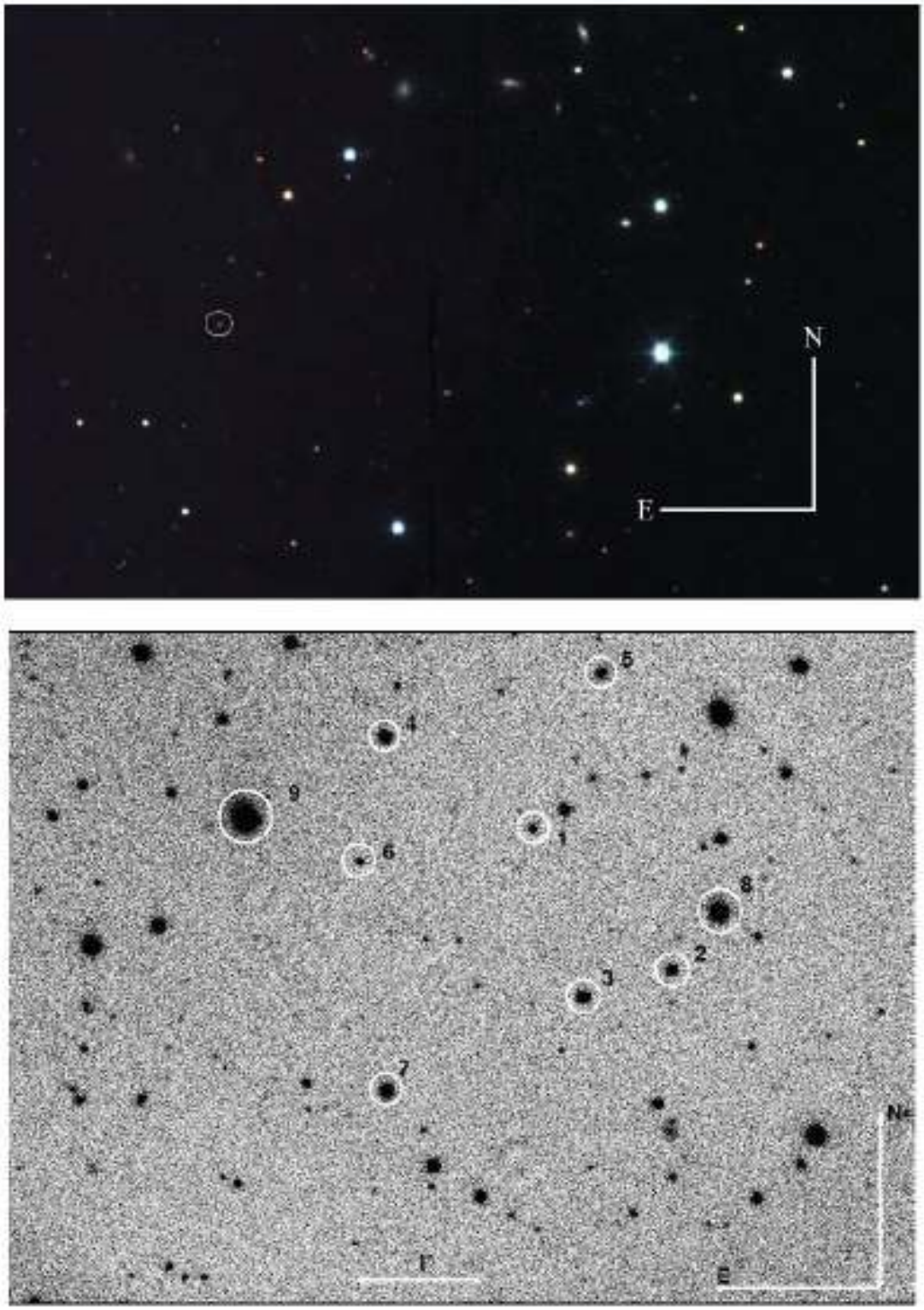

Figure 3.2: The colour composite image of the field around GRB 130606A and reference stars in the line of sight. Upper panel: The highly reddened GRB afterglow (circled) and the surrounding field, based on g' r' i' images obtained at the 10.4m GTC on June 7, 2013. The field of view is 3.8 × 2.8 arcmin^2. Lower panel: Reference stars for photometric calibration in the field around GRB 130606A (Table 3.2). The field of view (r'-band image) is 6.8 × 5.0 arcmin^2.

Table 3.2: Reference stars in the field of GRB 130606A.

N	R.A.(J2000)	Dec(J2000)	R-band mag	I-band mag	H-band mag
1	16 37 33.7	+29 48 19.0	18.04 ± 0.11	16.36 ± 0.02	14.54 ± 0.05
2	16 37 28.4	+29 47 05.6	16.97 ± 0.07	15.71 ± 0.02	13.95 ± 0.04
3	16 37 31.9	+29 46 53.6	16.41 ± 0.05	16.12 ± 0.02	15.31 ± 0.05
4	16 37 39.4	+29 49 05.6	16.22 ± 0.05	15.88 ± 0.02	15.07 ± 0.05
5	16 37 31.0	+29 49 36.4	17.65 ± 0.09	17.03 ± 0.03	−−
6	16 37 40.4	+29 48 03.4	18.62 ± 0.14	18.21 ± 0.04	17.38 ± 0.06
7	16 37 39.5	+29 46 07.7	15.99 ± 0.04	15.66 ± 0.02	−−
8	16 37 26.6	+29 47 34.5	14.57 ± 0.02	14.24 ± 0.02	13.54 ± 0.04
9	16 37 44.8	+29 48 25.3	13.11 ± 0.02	12.82 ± 0.02	−−

Table 3.3: Log of Spectroscopic data obtained at the 10.4m GTC.

Start Time (UT)	Exp Time (s)	Grism	Obs. Range (Å)	Slit width (")
06-Jun 2013-22:23:50.5	1 x 450	R1000B	3,650 – 7,750	1.2
06-Jun 2013-22:32:18.1	1 x 450	R500R	4,750 – 10,300	1.2
07-Jun 2013-02:10:09.7	2 x 1,200	R2500I	7,320 – 10,100	1.0

3.2.2.2 Spectroscopy

Starting 1.3 hr post-burst, optical spectra were obtained on 6 June 2013 with the 10.4m GTC using the R1000B and R500R grisms (1×450 s exposures) and R2500I ($2 \times 1{,}200$ s exposures) of the OSIRIS imaging spectrograph. The later one provides a nominal resolution of ~ 120 km s^{-1}. The log is given in Table 3.3. The 1" wide slit was positioned on the location of the transient source and a 2×2 binning mode was used. The GTC spectra were reduced and calibrated following standard procedures using custom tools based on IRAF and Python. Standard spectrophotometric stars used for flux calibration were Feige 92 for observations for the R1000B grism and Ross 640 for the prisms R500R and R2500I, taken the same night. All spectra were scaled in flux to correct for slit losses using the photometry of the corresponding acquisition images. The final wavelength calibration is on a vacuum scale, appropriate for the application of rest-frame UV atomic data.

3.2.3 Millimetre observations

Target-of-Opportunity millimetre observations were carried out at the Plateau de Bure Interferometer (PdBI; Guilloteau *et al.*, 1992). It was pointed at the location of GRB 130606A on two occasions in its compact 6 antenna configuration. The millimetre counterpart was

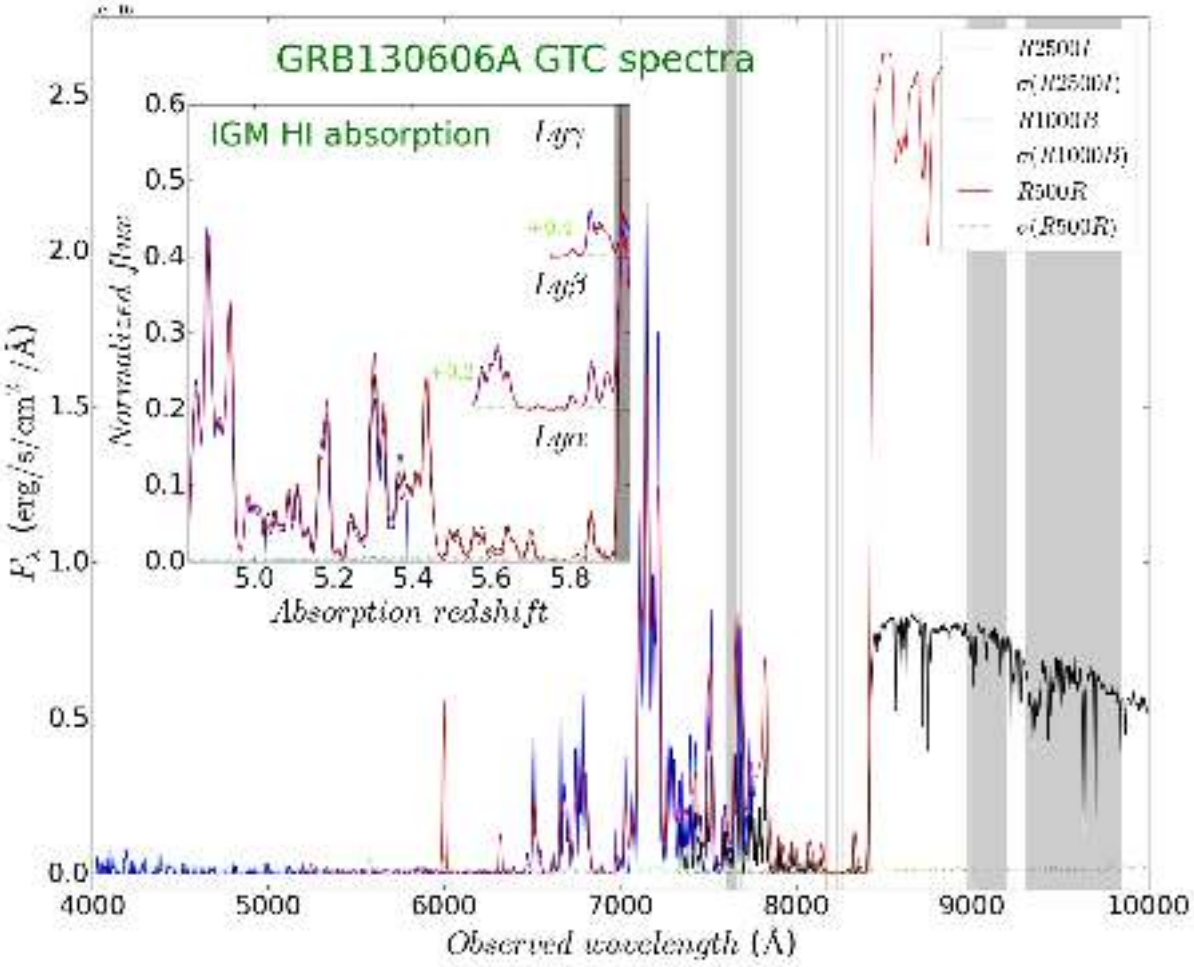

Figure 3.3: The 10.4m GTC spectra. We plot in the main panel flux-calibrated observations detailed in Table 3.3. Strong absorption by intergalactic hydrogen in the line of sight is causing the apparent low optical flux observed in the Lyman-α forest region (below 8,400 Å). In the embedded panel we show the corresponding redshift of the IGM absorption.

Table 3.4: Flux densities measured at Plateau de Bure Interferometer.

Time (days post-burst)	Flux density [mJy]	Frequency [GHz]
3.30	1.45 ± 0.15	86.7
7.50	0.03 ± 0.13	86.7

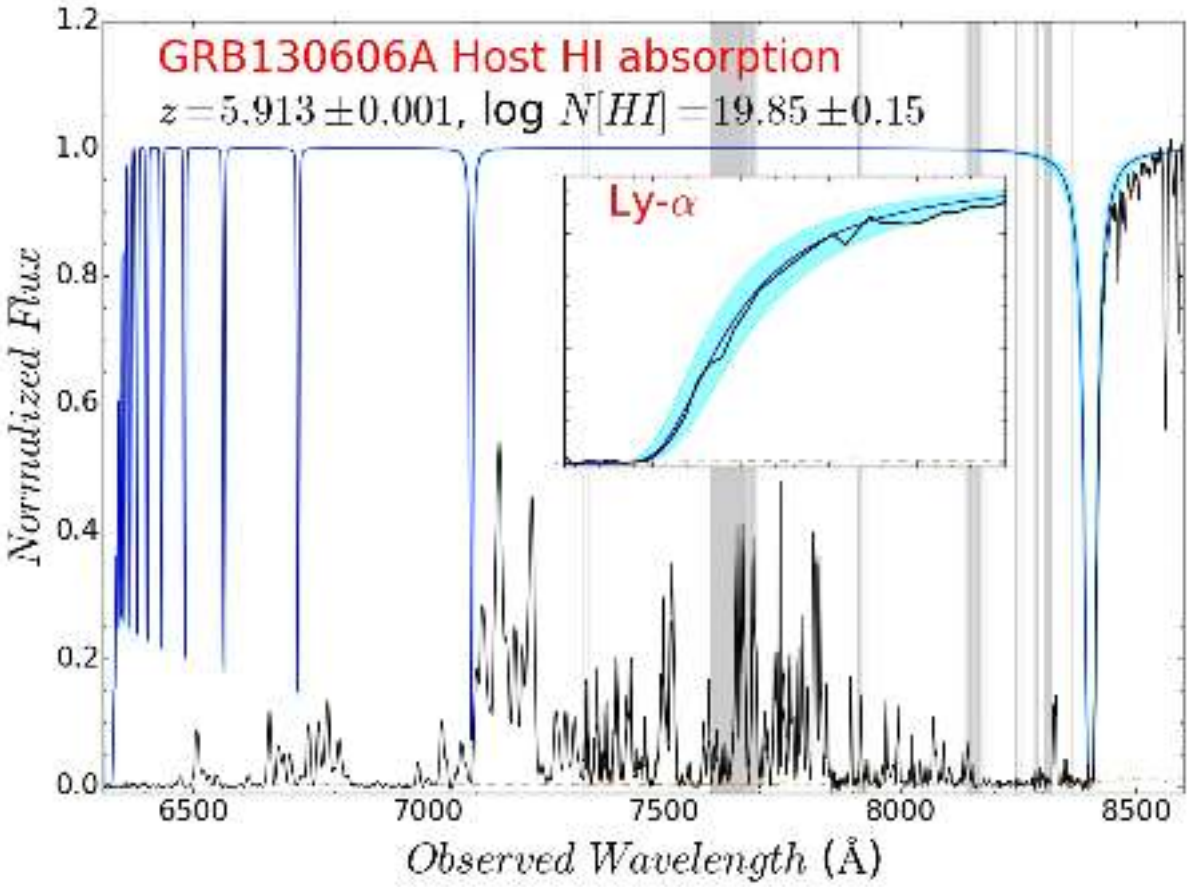

Figure 3.4: The N(H I) fit to the GTC (+ OSIRIS) spectrum of GRB 130606A. Taken on June 7, 2013, the figure shows the data (black solid line) and the best fit damped profile (solid blue line) with its 1σ confidence interval (cyan area).

detected 3.30 days after the GRB onset with a high (∼10) S/N ratio, on the phase center coordinates (J2000, R.A. = RA: 16:37:35.13; Dec: +29:47:46.5). The results of UV-plane point source fits to the phase center are given in Table 3.4.

The millimetre afterglow was detected with a flux density of ∼1.5 mJy at 3 mm, confirming the detection earlier reported at centimetre wavelengths (Laskar *et al.*, 2013b). The source became undetectable by June 14.

3.3 The GRB 130606A host galaxy

3.3.1 Hydrogen abundance

The GTC combined spectrum exhibits a huge IGM absorption which could difficult the determination of the N(H I) due to the host galaxy (e.g., Totani *et al.*, 2014). In order

Table 3.5: EW measurements for the GRB 130606A host galaxy from the afterglow spectrum.

Feature	Wavelength	z	EW	eEW
NVλ1239	8562.92	5.9122	0.417	0.001
NVλ1243	8590.33	5.9121	0.248	0.003
SiIIλ1560	8713.795	5.9134	0.407	0.003
OIλ1302	9002.57	5.9135	0.185	0.004
CIIλ1335	9225.59	5.9130	0.367	0.003
CII$^*\lambda$1336	9234.37	5.9135	0.156	0.004
SiIVλ1394	9635.38	5.9132	1.081	0.012
SiIVλ1403	9697.37	5.9130	6.04	0.04

to determine the column density of the host, we normalised the spectra with a simple power law and fitted the red damping wing of the Lyα absorption, finding $z = 5.913$ and $\log N(\mathrm{H\,I}) = 19.85 \pm 0.15$. The fit of this damped feature was performed using the same prescription and tools as in Sánchez-Ramírez *et al.* (2016) (see Fig. 2.1). Due to the huge IGM absorption we could not use higher order Lyman series lines to better constrain the host $N(\mathrm{H\,I})$. This value is in good agreement with three independent data-sets (Chornock *et al.*, 2013; Hartoog *et al.*, 2015; Totani *et al.*, 2014). The associated system is therefore technically classified as a sub-DLA.

3.3.2 Metal abundances

A series of absorption lines due to different ions (N V, Si II, Si II*, O I, C II, and C II*) are detected at the same redshift of the Lyα feature. A plot of the GTC spectrum and line identifications are provided in Fig. 3.5. We measured the equivalent widths (EWs) of the lines fitting Gaussian profiles and computing the sum over the line model. This approximation is in our case valid, as discussed in the previous chapter. Results for the host galaxy lines are presented in Table 3.5. With the redshifts obtained by the line fitting, we are able to refine the redshift up to $z = 5.9130 \pm 0.0004$.

3.3.3 Metallicity

The high signal-to-noise ratio (SNR) of the GTC spectrum permitted a search for relatively weak metal lines, and offers an improvement over some of the limits measured by Chornock *et al.* (2013).

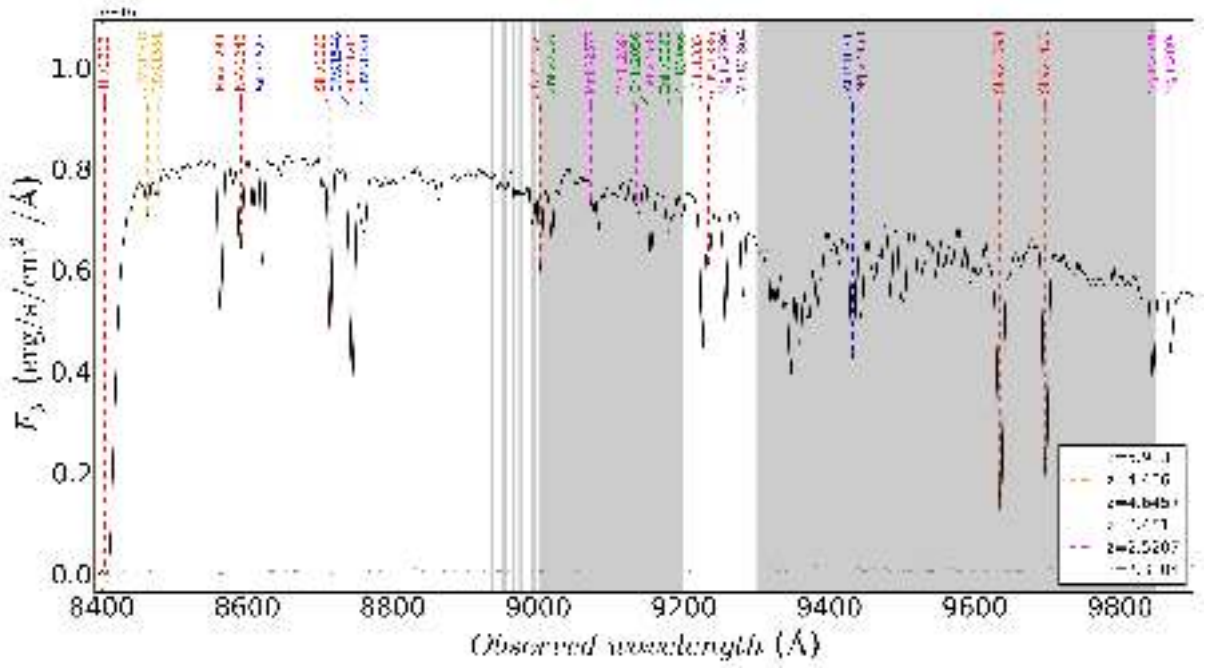

Figure 3.5: The lines identified in the R2500I 10.4m GTC spectrum ∼ 6 hr post-burst. The noise spectrum (dotted line) is also plotted. Each system is labelled as indicated in the legend.

In the case of sulphur, the triplet at 1250, 1253, 1259 Å can be used. Significant absorption is detected at the position of the weakest of these three lines (1250 Å), but the lack of absorption at 1253 Å indicates that the absorption is likely from a contaminating source. Based on the non-detection of the S IIλ1253 line, we determine an observed frame 3σ EW limit < 0.157 Å (assuming a FWHM = 3.4 Å and a S/N of 65 in the S II line region) which corresponds to 0.023 Å in the rest frame. The rest-frame EW limit yields $\log N[S] < 14.17$. Assuming a solar $[S/H]_{\odot} = 4.85$ (from Asplund *et al.*, 2009), this gives a 3σ upper limit [S/H] < -0.82, which is 0.3 dex (a factor of ∼2) deeper than the sulphur limit obtained by Chornock *et al.* (2013).

In addition to the upper limit to the sulphur abundance, we can determine lower limits to the abundances of oxygen and silicon. The limiting silicon abundance is determined from the mildly saturated Si IIλ1260 line with a rest frame EW=0.35 Å, yielding [Si/H] > -1.80, without consideration of ionization or dust depletion corrections. The oxygen abundance is determined from the O Iλ1302 Å line, which is also likely to be partly saturated despite its modest EW (0.2Å). The fact that O I does not require an ionization correction and O does not deplete, means that this is one of the best lines from which to obtain an accurate metallicity. The major uncertainty here is that it is close to a small noise feature on the red side which might lead to an overestimation of the oxygen abundance at the 0.1 dex level. Taking these factors into account, we determine [O/H]≥-

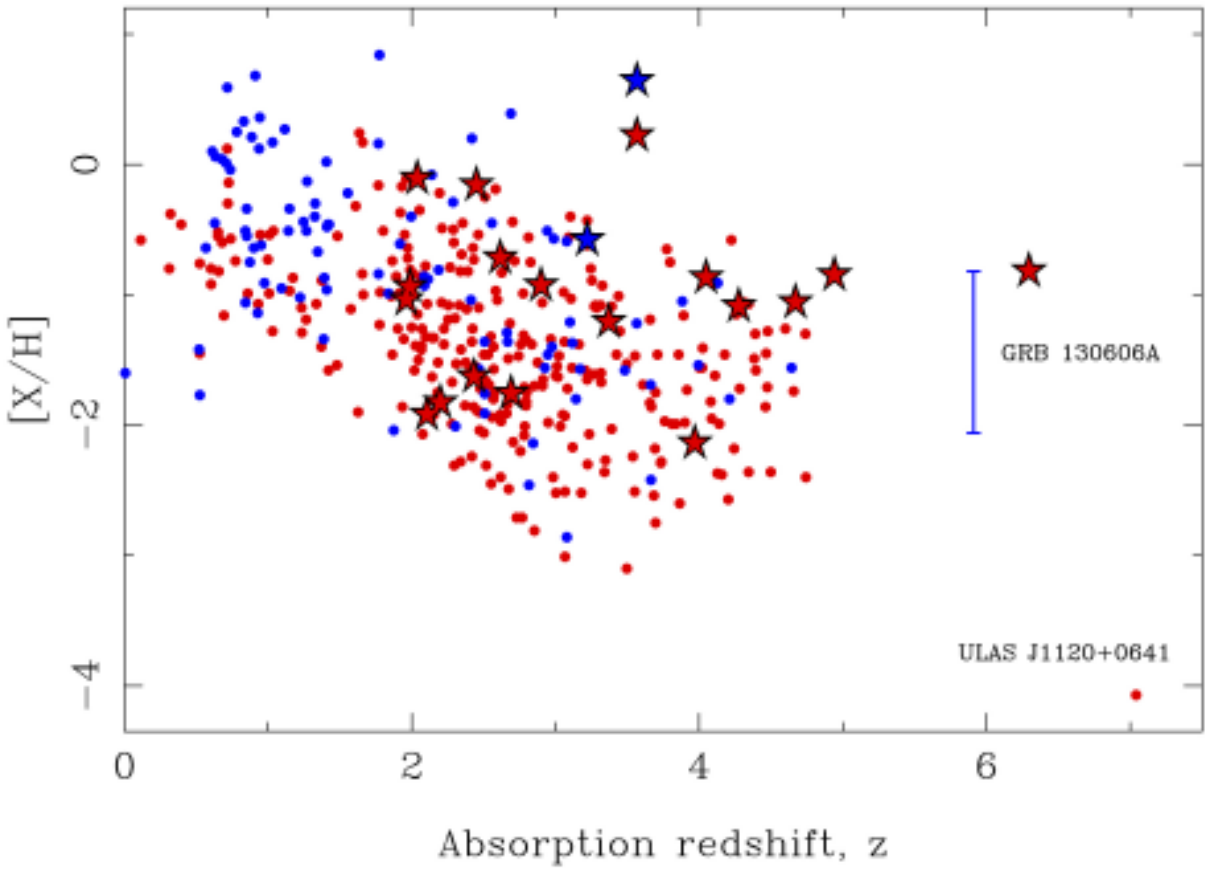

Figure 3.6: The metallicity ([X/H]) as a function of redshift is shown for a compilation of QSO-DLAs (circles; Berg *et al.*, 2015b) and GRB-DLAs (stars; Schady *et al.*, 2011; Thöne *et al.*, 2013), including the location for GRB 130606A at z = 5.9 (blue error bar) and ULAS J1120+0641 at z ∼ 7 (Simcoe *et al.*, 2012). The GRB 130606A sub-DLA is the 2nd highest redshift burst with a measured GRB-DLA metallicity and only the third GRB absorber with sub-DLA HI column density. Blue colours are used for $\log N(\mathrm{H\,I}) <$ 20.3 and red is used for $\log N(\mathrm{H\,I}) \geq$ 20.3. In order of preference for any given absorber, Zn, S, O, Si, Fe+0.4 dex is our choice of metallicity indicator, where the 0.4 offset for Fe accounts for typical dust depletion.

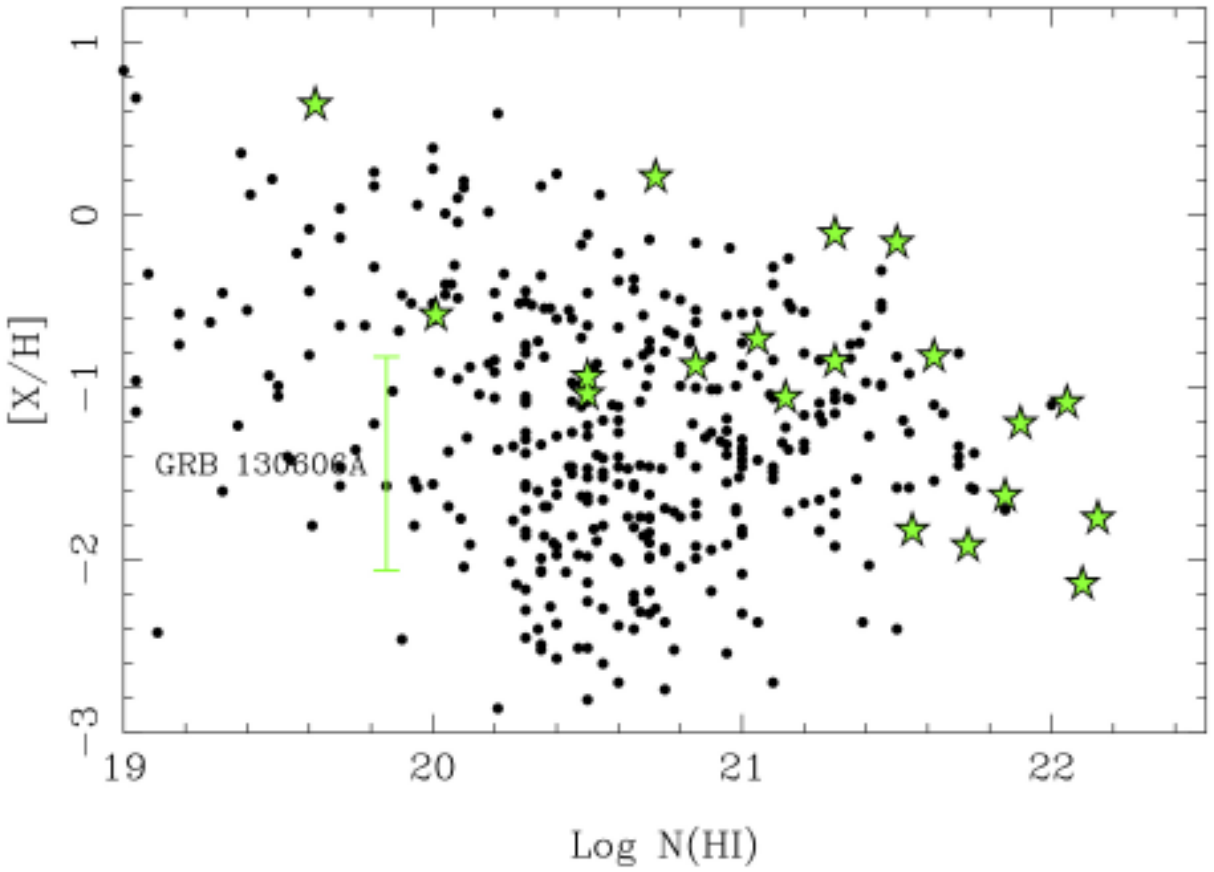

Figure 3.7: The metallicity of a GRB sample (green stars) versus N(H I) compared to a sample of DLAs (black dots). The location for GRB 130606A (green error bar) is also plotted.

Table 3.6: EW measurements for the systems detected on the GRB 130606A afterglow spectrum.

Feature	Wavelength	z	EW	eEW
SiIIλ1527	8607.85	4.6467	0.251	0.004
CIVλ1551	8754.144	4.6450	0.294	0.005
AlIIλ1671	9432.25	4.6454	0.554	0.016
CIVλ1548	8462.85	4.4662	0.086	0.004
CIVλ1551	8475.9	4.4658	0.079	0.002
ZnIIλ2026	9018.74	3.4512	0.200	0.011
ZnIIλ2063	9178.76	3.4500	0.209	0.007
CrIIλ2066	9198.15	3.4518	0.112	0.002
MnIIλ2577	9074.60	2.5215	0.162	0.003
MnIIλ2594	9132.97	2.5201	0.108	0.003
MgIIλ2796	9845.20	2.5207	0.591	0.003
MgIIλ2804	9869.96	2.5205	0.364	0.003
MgIIλ2796	9257.33	2.3105	0.538	0.003
MgIIλ2804	9281.26	2.3106	0.396	0.006
MgIλ2853	9443.95	2.3102	0.568	0.012

2.06. The Si and O limits are consistent to within 0.1 dex of the values independently derived (from different spectra) by Chornock *et al.* (2013). Combined with the upper limit from sulphur, we can constrain the metallicity within a factor of about 10, in the range from $\sim$1/7 to $\sim$1/60 of solar.

For a more comprehensive study of the abundances, we refer to Hartoog *et al.* (2015). Furthermore, we also point out that it is very likely that the gas is partially ionized: strong high-ionization lines (such as Si IV and N V) are present at the redshift of the absorber.

3.3.4 Intervening systems

The GTC optical spectra show a variety of absorption lines at different redshifts (Table 3.6). We detect 5 intervening systems at redshifts $z_1 = 4.6457 \pm 0.0004$, $z_2 = 4.4660 \pm 0.0001$, $z_3 = 4.4510 \pm 0.0005$, $z_4 = 2.5207 \pm 0.0004$, and $z_5 = 2.3104 \pm 0.0001$.

Table 3.7: IGM absorption towards GRB 140515A.

z	$\mathcal{T}$	τ_{GP}^{eff}
4.90	0.2469	1.40
5.00	0.0577	2.85
5.10	0.0574	2.86
5.20	0.0700	2.66
5.30	0.1154	2.16
5.40	0.1176	2.14
5.50	0.0249	3.69
5.60	0.0215	3.84
5.70	0.0136	4.30
5.80	0.0012	6.71

3.3.5 IGM absorption

We analysed the ionisation state of the IGM using the Gunn & Peterson (1965) optical depth, defined as $\tau_{GP}^{eff} = -\ln(\mathcal{T})$, where $\mathcal{T}$ is the average transmission in a redshift bin. Following Songaila & Cowie (2002) and Songaila (2004) we normalised the GTC spectrum by fitting a power law to the continuum, and divided it into redshift bins of 0.1 between $z = 4.9$ and $z = 5.8$. The results are presented in Fig. 3.8 and in Table 3.7.

Results are consistent with quasar measurements Fan *et al.* (2006); Songaila (2004) at similar redshifts.

It has been suggested that a better fit to the GRB 130606A is achieved when including an IGM contribution to model the Lyα red damping wing (Totani *et al.*, 2014, 2016).

3.4 Conclusions

- The host galaxy has a sub-DLA with $\log N(\mathrm{H\,I}) = 19.85 \pm 0.15$, and a metallicity content in the range from ∼1/7 to ∼1/60 of solar.

- In order to place the chemistry of the GRB sub-DLA in context with other high z absorbers, both Fig. 3.6 and Fig. 3.7 show the metallicity of a compilation of GRB host galaxy absorption systems (GRB-DLAs) compared to quasars with DLA and sub-DLAs (QSO-DLAs), combining the data reported in the literature (Berg *et al.*, 2015b; Schady *et al.*, 2011; Thöne *et al.*, 2013). The GRB 130606A sub-DLA is a rare find: the second highest redshift burst with a measured GRB-DLA metallicity

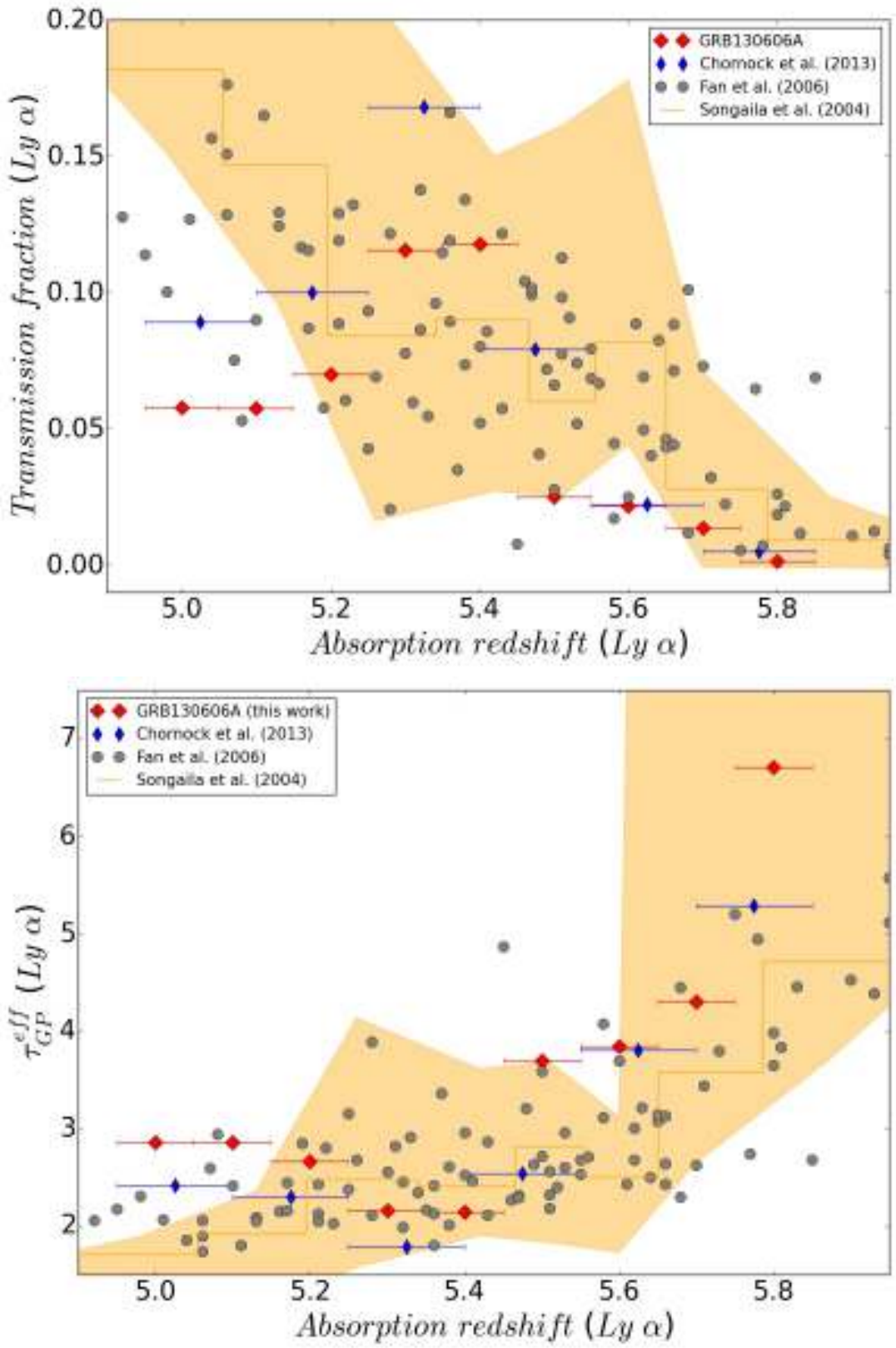

Figure 3.8: Lyα forest transmission (upper plot) and effective optical depth (bottom) in the line of sight to GRB 130606A compared with previous GRB and QSO works. The coloured area shows the optical depth found by Songaila (2004) while grey points are measurements from Fan *et al.* (2006) with sample of quasars.

and only the third GRB absorber with sub-DLA HI column density. At $z > 5$, the only other object known then with lower metallicity is the ULAS J1120+0641 DLA at z $\sim$ 7 (Simcoe *et al.*, 2012). However, the DLA towards ULAS J1120+0641 is close to the redshift of the quasar and its metallicity is determined from a stacked spectrum, both of which complicate its interpretation (Ellison *et al.*, 2010, 2011).

- We measured the G-P absorption between $z = 4.9$ and $z = 5.8$. Results are consistent with the other works on this GRB and the results from QSO sightlines.

- We note that GRB 130606A, given the non-zero metal content of the host, might have originated from a non-Pop III progenitor star, but whether its afterglow light penetrated material that was pre-enriched by Pop III nucleosynthesis at even higher redshifts (Wang *et al.*, 2012) remains uncertain. Indeed several possibilities for the death of the first stars have recently been suggested by theoretical models (Bromm, 2013). A high value of C/O is predicted to be a signature of Pop III stellar enrichment (Fabbian *et al.*, 2009). A handful of DLAs in the metallicity range -2 to -3 (1/100 to 1/1000 of the Sun's metallicity) have C/O measurements (Cooke *et al.*, 2011a; Ellison *et al.*, 2010) and all but one (towards the quasar QSO J0035-0918) have [C/O] < 0 (Cooke *et al.*, 2011a). Unfortunately, we cannot impose any constraint on this ratio as both species are likely saturated.

- Events such as GRB 130606A at $z = 5.91$, and future ones at $z > 10$, offer an exciting new window into pre-galactic metal enrichment in these very high redshift galaxies. These bright lighthouses constitute a significant step forward towards using these sources as beacons for measuring abundances at such early times. New GRB missions, equipped with on-board near-IR detectors, and coupled to state-of-the-art instruments built for the largest diameter ground-based telescopes, will allow us to study the first stars that fundamentally transformed the Universe only a few hundred million years after the Big Bang.

Chapter 4

GRB140515A

Adapted from "The high-redshift gamma-ray burst GRB 140515A. A comprehensive X-ray and optical study"

— Melandri, Bernardini, D'Avanzo, Sánchez-Ramírez et al., *A&A, 2015, 581, 86*

4.1 Introduction

A better understanding of the chemical enrichment and evolution of the high-redshift universe is one of the fundamental goals of modern Astrophysics. High redshift surveys have been performed by means of wide field surveys of bright quasars (e.g. Fan, 2012) or Lyman break galaxies (e.g. Bouwens *et al.*, 2014). The identification of high-redshift Gamma-Ray Bursts (GRBs) add a different and profitable view of the distant Universe. With respect to other probes, GRBs have many advantages: (i) they can be detected at higher redshifts; (ii) they are independent of the galaxy brightness; (iii) they do not suffer the usual biases affecting optical/NIR surveys; (iv) they reside in average cosmic regions. High-z GRBs can provide fundamental, and in some cases unique, information about the early stages of structure formation and the properties of the galaxies in which they explode. For example, GRBs may be used to trace the cosmic star formation rate (Ishida *et al.*, 2011; Kistler *et al.*, 2009; Robertson & Ellis, 2012), to pinpoint high-z galaxies and explore their metal and dust content (Elliott *et al.*, 2015; Salvaterra *et al.*, 2013; Tanvir *et al.*, 2012), and to shed light on the re-ionization history (Gallerani *et al.*, 2008; McQuinn *et al.*, 2008), to constrain the dark matter particle mass (de Souza *et al.*, 2013a) and the amount of non-Gaussianity present in the primordial density field (Maio *et al.*, 2012), and to measure the level of the local inter-galactic radiation field (Inoue *et al.*, 2010). Additionally, they could also provide direct and/or indirect evidences for the existence of the first, massive, metal-free stars, the so-called Population III stars (Campisi *et al.*, 2011; de Souza *et al.*, 2013b; Ma *et al.*, 2015; Toma *et al.*, 2011; Wang *et al.*, 2012).

Since the launch of the *Swift* satellite (Gehrels *et al.*, 2004) 8 events have been identified at redshift greater than ~ 6, and for 5 of them spectroscopic redshift was secured, including GRB 140515A, which we discuss in this chapter. Remarkably, some of them showed fairly bright early-time afterglows, even detectable by small robotic telescopes (e.g. GRB 050904; Boër *et al.*, 2006; Tagliaferri *et al.*, 2005).

4.2 Observations

4.2.1 GTC spectrum

We obtained spectroscopy of the afterglow of GRB 140515A with OSIRIS (Cepa *et al.*, 2000) at the 10.4m Gran Telescopio Canarias (de Ugarte Postigo *et al.*, 2014). The observations were obtained between 22:37:31 UT and 00:09:46 UT (mean epoch 14.184 hr after the GRB onset) with 0.6″ seeing and consisted of 3×1800 s exposures. We used

the R2500I VPH grism, which covers the range between 7330 and 10000 Å at a resolution of ∼1600 using a 1″ slit.

The data were reduced in a standard way (bias subtraction, pixel-to-pixel response correction, cosmic ray removal, wavelength calibration, 1D extraction, flux calibration, and combination of spectra) using self-made routines based on IRAF (Tody, 1993). The resulting combined GTC spectrum shows a strong continuum above ∼ 8900 Å, where the signal-to-noise ratio is ∼ 20 per pixel, or ∼ 40 per resolution element.

4.2.2 X-shooter spectrum

We observed the field of GRB 140515A with the X-shooter spectrograph mounted at the ESO/VLT using the nodding mode with 1 × 2 binning. The spectrum was acquired on 2014 May 16, starting at 00:42:43 UT (∼ 15.5 hr after the GRB onset) and consisted of 2x4x600 s exposures, for a total integration time of 4800 s on source, covering the range between ∼3000 and ∼ 24000 Å. The mid expose time is 16.3 hr (∼ 0.68 d) after the GRB trigger. The final reduced spectrum had a signal-to-noise ratio of ∼ 3 per pixel[1], with a seeing of ∼ 0.9″ (measured from combined 2D spectrum in the VIS and NIR arms). The flux calibration of X-shooter, which is problematic in general, is uncertain due to unavailable standard spectrophotometric star in the night when the observations were done and because the photometric observations, which could be used to check the quality of the calibration, have high uncertainties at this epoch.

4.3 Results

4.3.1 Lyα forest constraints on the IGM

We analysed the ionisation state of the IGM using the Gunn & Peterson (1965) optical depth, defined as $\tau_{GP}^{eff} = -\ln(\mathcal{T})$, where $\mathcal{T}$ the average transmission in a redshift bin. Following Songaila & Cowie (2002) and Songaila (2004) we normalised the GTC spectrum (as its signal-to-noise ratio, SNR, is better than the X-shooter one) by fitting a power law to the continuum, and divided it into redshift bins of 0.1 between $z = 5.2$ and $z = 6.3$. The results are presented in Fig. 4.1 and in Table 4.1.

We only see sky line residuals up to $z \sim 5.5$, above which we can just give detection limits based on the noise spectrum. Our limits are less restrictive than the ones presented

[1]The quoted difference in S/N between the GTC and X-shooter spectra is due partly to the different pixel size of the two instruments and partly to the better observing conditions of the GTC observation.

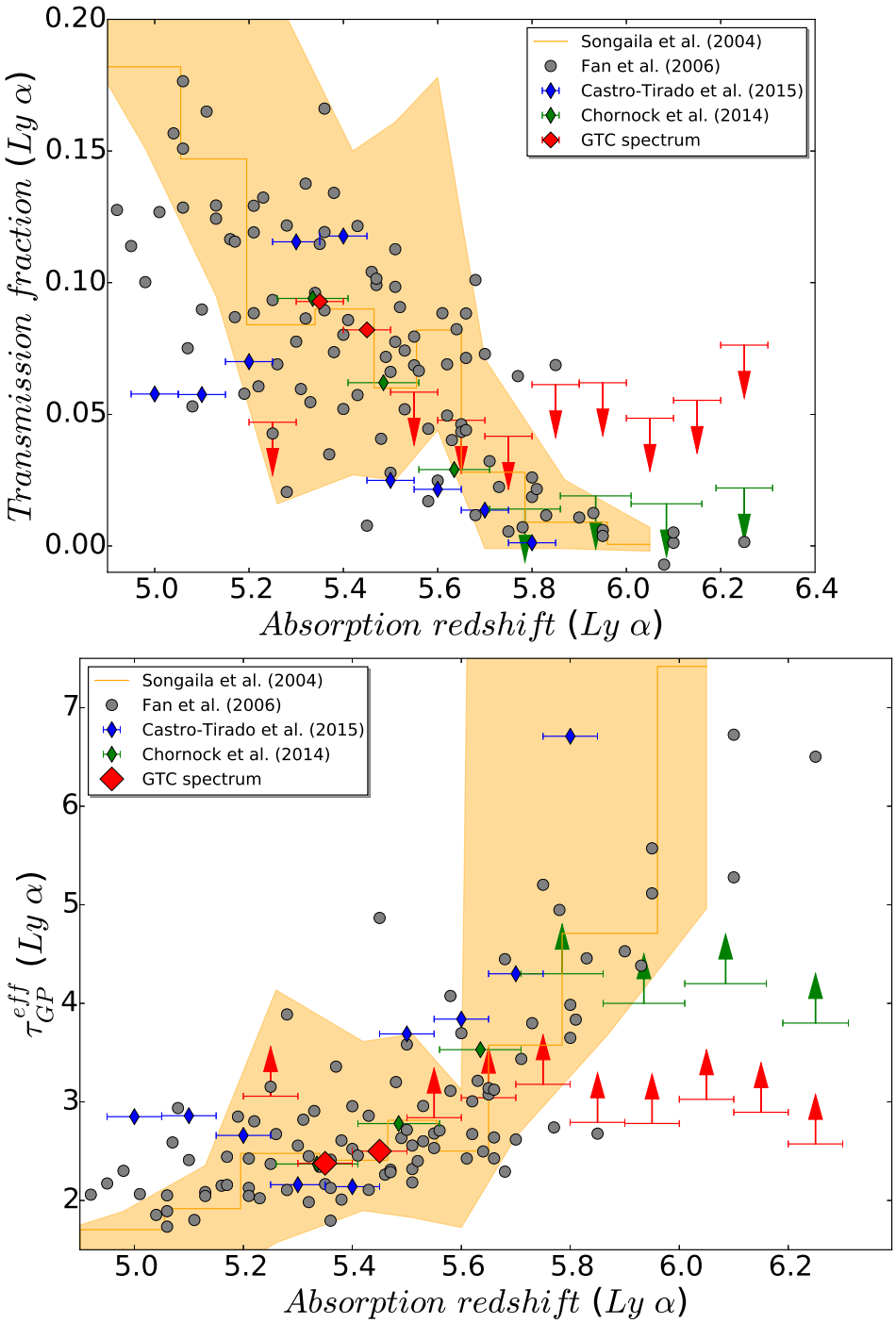

Figure 4.1: Lyα forest transmission (upper plot) and effective optical depth (bottom) in the line of sight to GRB 140515A compared with previous GRB and QSO works. The coloured area shows the optical depth found by Songaila (2004) while grey points are measurements from Fan *et al.* (2006) with sample of quasars.

Table 4.1: IGM absorption towards GRB 140515A.

z	$\mathcal{T}$	lim($\mathcal{T}$)	τ_{GP}^{eff}	lim(τ_{GP}^{eff})
5.25	–	0.0594	–	2.82
5.35	0.1174	0.0709	2.14	2.65
5.45	0.1038	0.0767	2.27	2.57
5.55	–	0.0739	–	2.61
5.65	–	0.0604	–	2.81
5.75	–	0.0527	–	2.94
5.85	–	0.0775	–	2.56
5.95	–	0.0784	–	2.55
6.05	–	0.0614	–	2.79
6.15	–	0.0700	–	2.66
6.25	–	0.0965	–	2.34

by Chornock *et al.* (2014) due to the lower SNR, but show the same behaviour (Fig. 4.1). Results coming from both GRB 140515A and GRB 130606A (Castro-Tirado *et al.*, 2013a; Chornock *et al.*, 2013; Hartoog *et al.*, 2015) are consistent with quasar measurements Fan *et al.* (2006); Songaila (2004).

4.3.2 Lyα red damping wing fitting

We tried to fit the strongest feature seen in the spectrum (at ~ 8900 $\AA$) to an absorption Lyman-α feature with a Voigt profile. Following Chornock *et al.* (2014), we first computed a Voigt model using the same constraints, obtaining inconsistent results. This could be due to the fact that they do not seem to consider the instrumental profile, whose effect on the Ly-α feature is not negligible at this resolution when $\log(N_{\rm HI}) \lesssim 19$. Looking at Fig. 4.2, we can observe the residuals of a sky line subtraction few angstroms blue-wards the wing, precisely at the zone crucial to fit a Voigt model. After a careful inspection on the 2D images of both GTC and X-shooter instruments, we concluded that there is no flux at this zone. Consequently, the wing profile is too sharp to get a satisfactory fit, suggesting that the absorption is dominated by the IGM and that the host absorption is masked.

We then built up IGM models following the prescription of Miralda-Escudé (1998), fixing the lower redshift value to $z = 6.0$ because the contribution to the wing shape below this redshift is negligible (it starts to be important closer to the host). Our best fit, with $z = 6.3298 \pm 0.0004$ and a fraction of neutral hydrogen $x_{HI} \leq 0.002$, is shown in Fig. 4.2. We caution that due to the sharpness of the wing, the few points we have because of

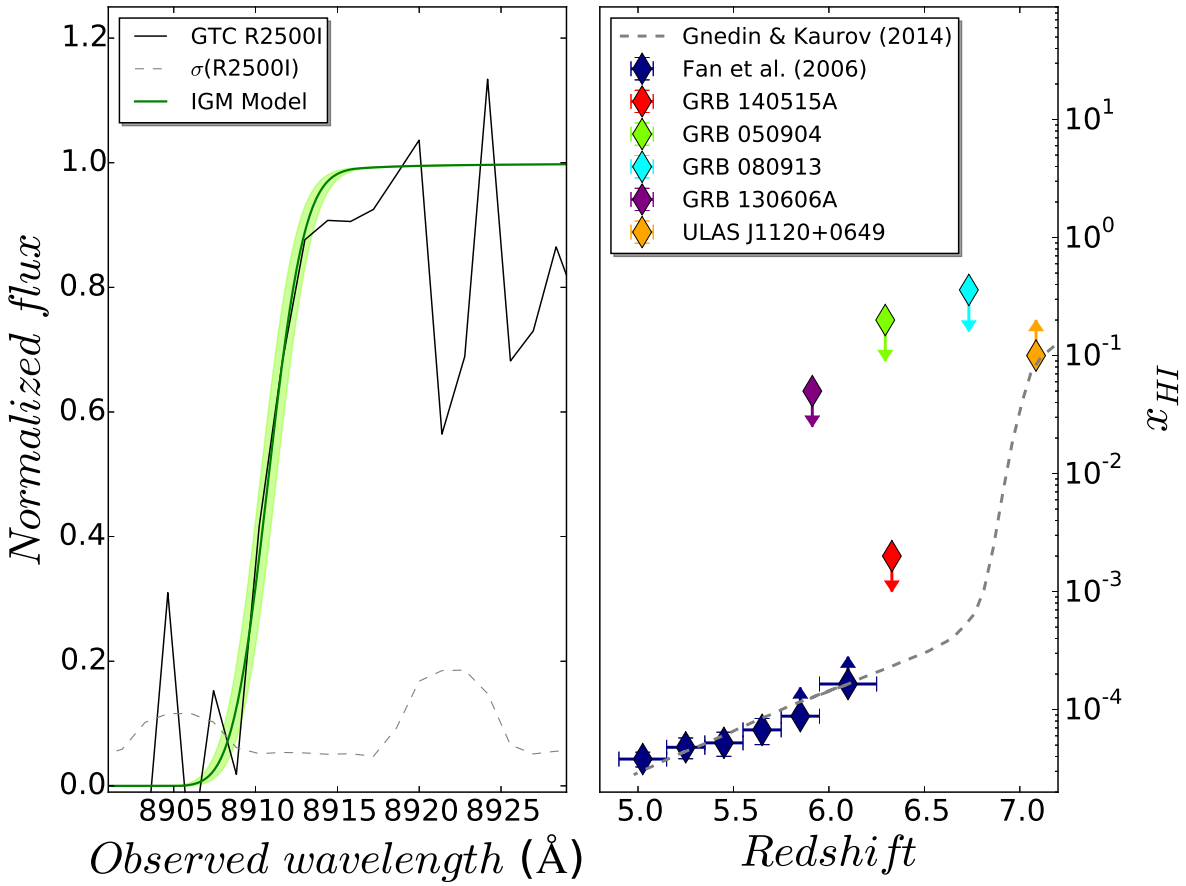

Figure 4.2: *Left*: Best IGM damping wing fit to the spectrum of GRB 140515A. *Right*: Redshift evolution of the hydrogen neutral fraction. The dotted line shows the Gnedin & Kaurov (2014) model, and points (see legend) the observational measurements of this quantity. Points with arrows are lower/upper limits.

GTC resolution, and the sky line next to the absorption, any formal constraints on these quantities would be unreliable, so the values should be interpreted as the most plausible estimations that we can obtain from the data. Moreover, especially by the fact that z cannot be determined by metal lines, hybrid models cannot offer a more accurate fit than the one showed in Fig. 4.2, so no constraints on the host HI abundance can be derived from this event (for further discussion, see Miralda-Escudé, 1998). However, due to the sharpness of the red damping wing, it is obvious that the neutral hydrogen present in the IGM cannot mask neither the presence of a DLA nor a subDLA, as their damping wings would be easily identified. Consequently, we can establish a conservative upper limit of $\log(N_{\rm HI}) \lesssim 18.5$ for the HI abundance in the host galaxy of GRB 140515A. As shown in Fig. 4.2, the fraction of neutral hydrogen derived from this analysis is in good agreement with the model by Gnedin & Kaurov (2014), and it provides a very relevant observational constraint.

Last, we estimated the 3σ upper limits on the observer-frame equivalent width (EW) for the Si IIλ1260, O Iλ1302, and C IIλ1334. We find a value of 0.67 Å, 1.06 Å, and 1.30 Å, respectively. These estimates are a factor ~ 2 more stringent of what reported by Chornock *et al.* (2014), resulting to upper limits on the gas-phase abundances of [Si/H] $\lesssim -1.4$, [O/H] $\lesssim -1.1$, and [C/H] $\lesssim -1.0$. Furthermore, these lines are weaker than the average rest-frame EWs observed for a typical GRB. In fact, the strength of those lines compared to the average GRB spectrum that can be estimated with the use of the line strength parameter (LSP, as defined in de Ugarte Postigo *et al.*, 2012a), is LSP < -3.15, < -3.89, and < -2.88, respectively. This means that these lines are very weak and that GRB 140515A exploded in a relatively low density environment. However, our limits on the metals abundances do not allow us to put a stringent limit on the metallicity of the progenitor.

4.4 Discussion

4.4.1 Pop III or enriched Pop II progenitor

GRB 140515A shows evidence of long lasting central-engine activity up to $\sim 10^4$ s after the burst event. Its redshift ($z > 6$) could suggest a Pop III star progenitor. These type of massive stars ($M \geq 100 M_{\odot}$), that formed in the early universe at low metallicity ($Z \leq 10^{-4}$), have been also proposed as progenitor of the so-called ultra-long GRBs, i.e. GRB 111209A (Gendre *et al.*, 2013), GRB 121027A (Hou *et al.*, 2014), and GRB 130925A (Willingale *et al.*, 2014).

In this scenario, the long duration is the results of the time needed for the accretion and collapse mechanisms. In the hypothesis of such a GRB progenitor one should expect to detect a very low density environment with a density profile dominated by the IGM. Another expectation for such massive collapsing stars is a long-lasting blackbody emission component in their spectra, with a typical average rest-frame temperature of $kT_{\rm BB} \sim$ 0.5 keV (Piro *et al.*, 2014). This thermal emission would be in principle detectable by BAT and/or XRT if the redshift of the event is low.

In the case of GRB 140515A observations do support the idea of a low density environment with negligible contribution from the host galaxy, but there are no hints for a particularly low value of the metallicity. Moreover, being at such a high-z we do not expect to detect the blackbody component with *Swift* instruments. Indeed we tested this possibility but we did not find any improvement of the fit with the inclusion of a blackbody component in the prompt emission spectrum. Therefore, the hypothesis that

Table 4.2: Absorption properties of the GRBs with $z \geq 5$ (for the events marked with * the redshift was estimated photometrically). References: 1) Evans et al. 2010; 2) Perley et al. 2010; 3) Jakobsson et al. 2006; 4) Covino et al. 2013; 5) Salvaterra 2015; 6) Hartoog et al. 2014; 7) Totani et al. 2006; 8) This work.

GRB	z	$\log(N_{HI})$	$\log(N_{H,X})$	A_V	Ref.
		$[cm^{-2}]$	$[10^{21}\ cm^{-2}]$	[mag]	
060522	5.11	–	< 160	–	1
071025	$\leq$5.2*	–	49 ± 19	< 0.54	1, 2
140304A	5.283	–	< 120	–	1
050814	5.3	–	< 16.8	< 0.9	3, 1
131227A	5.3	–	520^{+220}_{-190}	–	1
060927	5.467	–	< 36	< 0.17	4, 1
130606A	5.913	19.93	< 30	< 0.2	5, 6
120521C	6.0*	–	< 60	< 0.3	5
050904	6.295	21.6	63^{+34}_{-29}	0.15 ± 0.07	5,7
140515A	6.327	< 18.5	$13.5^{+12.2}_{-10.8}$	0.11 ± 0.02	8
080913	6.695	19.84	95^{+89}_{-77}	0.12 ± 0.03	5
090423	8.26	–	102^{+49}_{-54}	< 0.1	5
120923A	8.5*	–	< 720	–	5
090429B	9.4*	–	140 ± 10	0.10 ± 0.02	5

GRB 140515A originated from a Pop III star (or even from a Pop II star with environment enriched by Pop III stars) is unlikely.

4.4.2 Reionization and escape fraction of ionizing radiation

The distribution of intrinsic column densities of GRB hosts can be used to constrain the average escape fraction of ionizing radiation from the hosts (Chen *et al.*, 2007), under the assumption that GRB sightlines, taken as an ensemble, sample random lines-of-sight from star forming regions in GRB hosts. At intermediate redshifts ($z > 2$) the sample of GRB hosts from Chen *et al.* (2007) indicates that only in about 5% of all cases one expects a GRB sightline with $\log(N_{HI}) < 18.5$. With GRB 140515A being only 1 out of 7 GRBS with $z > 6$ (and only 1 out of 3 with measured HI column densities), it appears that high redshift GRB hosts may have, on average, lower HI column densities and, hence, higher escape fractions than their lower redshift counterparts.

More quantitatively, the Kolmogorov-Smirnov test for the two distributions of HI column densities - first from Chen *et al.* (2007) and the second of four $z > 5.9$ GRBs with measured N_{HI} values - shows that the two distributions are consistent with only 9%

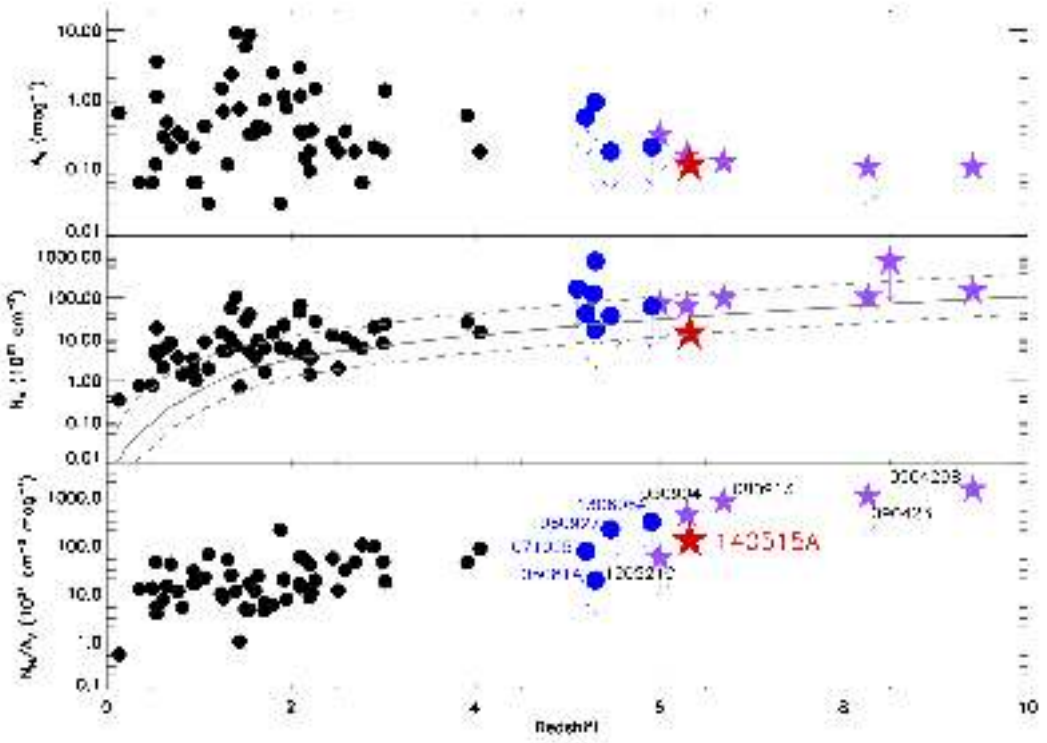

Figure 4.3: A_V, N_H, and N_H/A_V ratio as a function of redshift. Black points are from Covino et al. (2013) for events with $z \lesssim 4$, while the remaining events (blue circles, purple stars) are listed in Table 4.2. GRB 140515A is marked with a red star. The solid/dashed gray lines in the middle panel represent the effect of the intervening material along the line of sight (see Campana *et al.*, 2015; Salvaterra, 2015).

probability. That probability raises to 30% if GRB 140515A is excluded. The importance of constraining the escape fractions in reionization sources is obvious, so a larger sample of $z > 6$ GRBs with measured HI column densities would be highly desirable.

Such a sample would also serve as a direct test of reionization at $z > 6$, where constraints from high redshift quasars become scarce. A significant advantage of GRBs over quasars is in their low or negligible bias. While bright quasars, likely, do reside in the most massive, highly biased dark matter halos, GRBs hosts at high-z seem to sample the general galaxy population. Hence, constraints for the neutral hydrogen fraction obtained from the analysis of the IGM damping wing profile in the absorption spectra of GRB hosts can be expected to be more reliable than the analogous constraints from the quasar proximity zones.

In addition, constraints on the mean neutral fraction from observations of QSO proximity zones are, typically, lower limits (neutral fraction can be larger if a quasar lifetime is longer) (Bolton *et al.*, 2011; Robertson *et al.*, 2013, 2015), while constraints from GRBs are upper limits. Hence, the two observational probes are highly complementary to each other (this is demonstrated by red and orange diamonds in Fig. 4.2).

4.5 Conclusions

- We present a spectroscopic analysis of the high-z GRB 140515A.
- Our detailed spectral analysis provided a best estimate of the neutral hydrogen fraction of the IGM towards the burst of $x_{HI} \leq 0.002$ and a conservative upper limit of the HI abundance in the GRB host galaxy of $N_{\rm HI} \lesssim 10^{18.5}$ cm^{-2}. These values are slightly different from the ones estimated by Chornock et al. (2014b).
- In addition, the spectral absorption lines observed in our spectra are the weakest lines ever observed in GRB afterglows (de Ugarte Postigo *et al.*, 2012a), suggesting that GRB 140515A happened in a very low density environment. However, our upper limits on the gas-phase abundances, coupled with the fact that we cannot establish the exact metal-to-dust ratio, do not allow us to distinguish between metallicity in the range of $10^{-4} < [Z/H] < 0.1$. This makes the possible Pop III star origin for GRB 140515A uncertain and doubtful.
- For all high-z GRBs the contribution of the host galaxy was not negligible (Table 4.2). GRB 140515A is the first case when this does not happen, allowing us to give the best observational constrains on a theoretical model at $z > 6$.

PART III

ABSORPTION SYSTEMS IN THE LINE OF SIGHT TO QUASARS:

THE EVOLUTION OF NEUTRAL GAS IN DAMPED LYMAN ALPHA SYSTEMS

Chapter 1

The evolution of neutral gas in damped Lyman α systems from the XQ-100 survey

Adapted from "The evolution of neutral gas in damped Lyman α systems from the XQ-100 survey"

— Sánchez-Ramírez et al., *MNRAS, 2016, 456, 4*

In this Chapter I present a sample of 38 intervening damped Lyman α (DLA) systems identified towards 100 $z > 3.5$ quasars, observed during the XQ-100 survey. The XQ-100 DLA sample is combined with major DLA surveys in the literature. The final combined sample consists of 742 DLAs over a redshift range approximately $1.6 < z_{\rm abs} < 5.0$. We develop a novel technique for computing $\Omega_{\rm HI}^{\rm DLA}$ as a continuous function of redshift, and we thoroughly assess and quantify the sources of error therein, including fitting errors and incomplete sampling of the high column density end of the column density distribution function. There is a statistically significant redshift evolution in $\Omega_{\rm HI}^{\rm DLA}$from $z \sim 2$ to $z \sim 5$ ($\geq 3\sigma$). In order to make a complete assessment of the redshift evolution of $\Omega_{\rm HI}$, we combine our high-redshift DLA sample with absorption surveys at intermediate redshift and 21-cm emission line surveys of the local universe. Although $\Omega_{\rm HI}^{\rm DLA}$, and hence its redshift evolution, remains uncertain in the intermediate-redshift regime ($0.1 < z_{\rm abs} < 1.6$), we find that the combination of high-redshift data with 21-cm surveys of the local universe all yield a statistically significant evolution in $\Omega_{\rm HI}$from $z = 0$ to $z \sim 5$ ($\geq 3\sigma$). Despite its statistical significance, the magnitude of the evolution is small: a linear regression fit between $\Omega_{\rm HI}$ and z yields a typical slope of $\sim 0.17 \times 10^{-3}$, corresponding to a factor of ~ 4 decrease in $\Omega_{\rm HI}$ between $z \sim 5$ and $z = 0$.

1.1 Introduction

Measurements of $\Omega_{\rm HI}$, the mass density of atomic hydrogen gas scaled to the critical density, and its evolution with redshift offer cosmological constraints on several aspects of galaxy formation. The value of $\Omega_{\rm HI}$ at any epoch characterizes the instantaneous reservoir of cold, neutral gas available for star-formation integrated across the entire galaxy population. This constraint holds independently of the detailed association of individual DLAs to specific galaxy populations, i.e. $\Omega_{\rm HI}$ is a cosmic quantity (e.g. Wolfe *et al.*, 1995). It may serve, therefore, as an input to semi-analytic prescriptions for galaxy formation (e.g., Somerville & Davé, 2015). The time evolution of $\Omega_{\rm HI}$, meanwhile, tracks the global balance between the accretion of cold gas onto galaxies against the processes that consume and/or expel that gas (e.g. Davé *et al.*, 2013; Kereš *et al.*, 2012; Lilly *et al.*, 2013). As theorists continue to explore models to capture the complex processes of star-formation and feedback, $\Omega_{\rm HI}$ offers a cosmic check on their prescriptions. Indeed, there is apparent tension between previous $\Omega_{\rm HI}$ measurements and galaxy formation models that reproduce other key observables of the galactic population (Bird *et al.*, 2015; Somerville & Davé, 2015). We are hence motivated to assess $\Omega_{\rm HI}$ and the uncertainties in its estimation across cosmic time.

This cosmic evolution of $\Omega_{\rm HI}$ can be traced by combining surveys of damped Lyman alpha systems (DLAs) at moderate-to-high redshifts, with 21cm emission surveys at $z{\sim}0$. In recent years, there has been significant progress in refining measurements of $\Omega_{\rm HI}$ with both of these techniques, where large statistical samples have been crucial for addressing biases due to incompleteness. In the nearby universe the greatest uncertainty for the determination of $\Omega_{\rm HI}$ in early 21cm surveys was the faint end slope of the H I mass function (e.g. Rosenberg & Schneider, 2002; Zwaan *et al.*, 2003, 2005). The Arecibo L-band Fast ALFA (ALFALFA) survey (Giovanelli *et al.*, 2005) has now provided the $z{\sim}0$ benchmark for $\Omega_{\rm HI}$, based on over 10,000 galaxies in the local universe (Martin *et al.*, 2010). Extending the measurement of $\Omega_{\rm HI}$ to even $z \sim 0.1 - 0.2$ is extremely challenging for current 21 cm surveys. Nonetheless, stacking experiments have produced several estimates of $\Omega_{\rm HI}$ in this redshift range (Delhaize *et al.*, 2013; Lah *et al.*, 2007; Rhee *et al.*, 2013). Individual detections of 21 cm emission beyond $z = 0$ are growing, thanks to surveys such as CHILES (Fernández *et al.*, 2013) and HIGHz (Catinella & Cortese, 2015), although these surveys are not yet large or complete enough to give a statistical perspective on $\Omega_{\rm HI}$.

Fortunately, $\Omega_{\rm HI}$ in the higher redshift universe can be effectively measured in absorption, using DLA surveys. The objective of DLA surveys has largely been to assess the redshift evolution of $\Omega_{\rm HI}$, in comparison to the $z{=}0$ local benchmark. Early surveys

of DLAs focused predominantly on the redshift range $2 < z_{\rm abs} < 3.0$ (e.g. Wolfe *et al.*, 1986, 1995). The lower bound of this redshift range was set by the accessibility of the Lyα line to ground based spectrographs, and the upper bound by the limited number of bright, high redshift quasars known at the time. Although these early surveys enabled a broad-brush measurement of $\Omega_{\rm HI}$, the limited redshift range and sample sizes were insufficient to study the evolution of the cosmic gas reservoir. Subsequent ground-based surveys were motivated to extend the redshift range to earlier epochs, and reported a tentative peak in $\Omega_{\rm HI}$ at $z \sim 3$ (Storrie-Lombardi & Wolfe, 2000; Storrie-Lombardi *et al.*, 1996a). As the size of DLA samples grew, improved statistics led to an upward revision of $\Omega_{\rm HI}$ at z>3.5 and evidence for a peak at z∼3 diminished; the mass density of H I in DLAs appeared to be consistent over the range of redshifts $z\sim$ 2 – 5 (Péroux *et al.*, 2003, 2005). The apparent down-turn of $\Omega_{\rm HI}$ seen in earlier surveys seems likely to be caused by poor statistics at the survey limit (e.g. Prochaska & Herbert-Fort, 2004).

Despite these early surveys, the error bars on $\Omega_{\rm HI}$ remained substantial, and it was the advent of the Sloan Digital Sky Survey (SDSS) that led to the first truly robust measure of $\Omega_{\rm HI}$ redshift evolution. Several investigations, based on different SDSS data releases, have found a mildly decreasing $\Omega_{\rm HI}$ from z∼3.5 to 2 (e.g. Noterdaeme *et al.*, 2009, 2012; Prochaska & Herbert-Fort, 2004; Prochaska & Wolfe, 2009; Prochaska *et al.*, 2005). All of these works self-consistently show an evolution of at most a factor of two in this redshift range, an effect too subtle to be detectable in previous smaller surveys. Pushing to even higher redshifts, there again seemed to be tentative evidence of a downturn in $\Omega_{\rm HI}$ above z∼3.5 (Guimarães *et al.*, 2009; Songaila & Cowie, 2010). However, with a factor of eight increase in path length over previous compilations, Crighton *et al.* (2015) have shown that $\Omega_{\rm HI}$ evolution is statistically consistent (within the observational errors) with a power law of index 0.4 from $z = 5$ to the present day. The results of Crighton *et al.* (2015) therefore support a mild, but steady evolution in the neutral gas content of galaxies since early times.

Despite the uniform decline in $\Omega_{\rm HI}$ from high z to the present day proposed by Crighton *et al.* (2015), the value of $\Omega_{\rm HI}$ measured at $z = 5$ is formally consistent with the value measured by Rao *et al.* (2006) in the range $0.2 < z_{\rm abs} < 1.5$ (see Fig. 12 of Crighton *et al.*, 2015). A statistically plausible alternative picture to the steady decline of $\Omega_{\rm HI}$ is therefore one in which gas consumption was almost perfectly balanced by replenishment, with a statistically significant decrease (of a factor of two) only at the most recent epochs. One of the challenges in the interpretation of the data compilation presented by Crighton *et al.* (2015) is in the combination of surveys performed at different redshifts, and a homogeneous assessment of the error associated with $\Omega_{\rm HI}$.

In this work we present a new survey for DLAs in the range $1.6 < z_{\rm abs} < 4.5$ and make a novel assessment of $\Omega_{\rm HI}$ as a function of redshift. Our sample combines DLAs from our own survey, with a compilation of literature absorbers that has been carefully checked for duplicates and errors. Rather than showing our new survey results in comparison with previous surveys at different redshifts, we maximize the statistical potential of decades of work by combining previous surveys together. Moreover, by quantifying $\Omega_{\rm HI}$ within a sliding redshift window, rather than in contiguous non-overlapping bins, and with a rigorous assessment of error propagation techniques, we are able to determine a holistic perspective of the atomic gas content of galaxies up to $z = 5$.

The chapter is organized as follows. In Section 2 we describe the XQ-100 survey of 100 $z > 3.5$ quasars, and the detection of DLAs therein. The XQ-100 DLA sample is combined with various literature samples and compilations, as described in Section 3. Section 4 presents our statistical analysis, including the description of our technique to determine $\Omega_{\rm HI}$ evolution 'curves', a rigorous assessment of sources of error and the analysis of the column density distribution and line density functions.

I will use the term $\Omega_{\rm HI}^{\rm DLA}$, to mean the neutral hydrogen mass density in Damped Lyman α systems (i.e. the contribution to $\Omega_{\rm HI}$ from systems above the DLA column density threshold, $\log N({\rm H\,I}) \geq 20.3$) relative to the critical density. The total gas mass density is given by $\Omega_{\rm g}$, which requires a correction to $\Omega_{\rm HI}$ by the factor μ=1.3 to account for helium. Finally, we assume a flat ΛCDM cosmology with H_0=70.0 km s^{-1} Mpc^{-1}, Ω_m=0.3 and Ω_Λ=0.7.

1.2 The XQ-100 sample

The XQ-100 survey is an ESO Large Program (ESO ID 189.A-0424, P.I. S. Lopez) which obtained X-shooter spectra of 100 $3.5 < z < 4.7$ QSOs in the period between 10-02-2012 and 23-02-2014. X-shooter (Vernet *et al.*, 2011) is a triple-arm spectrograph which obtains moderate resolution spectra with complete wavelength coverage from $\sim 320 - 2500$ nm, permitting the simultaneous analysis of QSO absorption lines and emission features from the atmospheric cut-off to the near-IR. A full description of the XQ-100 survey characteristics, sample selection, observational set-up and data reduction is provided in Lopez et al. (in prep). We review only the basic features of the survey design and data here. In brief, the XQ-100 survey adopted slit widths of 0.9"(UVB arm) and 1.0"(VIS and NIR arms) to obtain spectra whose resolution ranged from $R \sim 5100 - 8800$. Exposure times ranged from $\sim$ 1700s to 3600s yielding a median signal-to-noise ratio (SNR) $\sim$ 30 per pixel. The data were reduced using a custom pipeline which provided a notable

improvement in the removal of the near-IR sky emission with respect to the ESO provided pipeline. All of the 1-dimensional spectra (flux and wavelength calibrated) are made publically available (see Lopez et al. in prep for details on the data reduction and public data release). Higher order data products are also made available in the public repository: spectra corrected for telluric absorption and normalized spectra derived from a variety of continuum fitting methods.

In this paper, we make use of the basic 1D products and perform our own normalization of the continuum. This decision is driven by the sensitivity of the Lyα fit in the damping wings to the continuum placement. The nomalization of the spectra and Voigt profile fits were performed using an interactive interface that permits the user to simultaneously identify and fit the absorbers, and iterate on the continuum placement. The iterative procedure is required due to both the complexity of the Lyα forest, and the challenges associated with continuum placement over the broad damped profile, particularly in the shallow wing region (Prochaska *et al.*, 2003).

The fitting procedure can be summarized as follows. First, we estimated the continuum by manually identifying regions of apparently unabsorbed continuum flux throughout the Lyα forest and around the Lyα emission. A cubic spline was used to fit these points and make an initial normalization. Next, a Voigt profile with $\log N(\mathrm{H\,I})$=19.0 is moved through the forest range looking for DLA candidates. Although the canonical threshold for DLA classification is $\log N(\mathrm{H\,I})$=20.3, the lower threshold of our scan provides a conservative initial selection for assessment. It is also useful to identify these lower column density systems to aid with fits of blended absorbers. For each potential absorption system, a simultaneous fit of all Lyman series lines up to Lyϵ was performed, with adjustments to the continuum when necessary, in order to determine the HI column density and redshift of the absorber. Metal lines associated with each potential absorber were identified (in Berg et al., MNRAS **submmited**, we present a complete assessment of the abundances in the XQ-100 DLA sample), and in cases of uncertain fits (e.g. due to blends) the redshifts from the metal lines were used to inform the fits (but the metals are not used *a priori* to fix the redshifts for all absorbers). An example of our fits is shown in Figure 1.1; a full montage of all of the fits to our DLA sample is provided in the appendices G and H.

The conservative initial search threshold of $\log N(\mathrm{H\,I})$=19.0 permits the identification of numerous absorbers whose $N(\mathrm{H\,I})$ is below the traditional DLA threshold of $\log N(\mathrm{H\,I})$=20.3, yet still exhibit damping wings that permit the accurate measurement of the HI content. These sub-DLAs have been the subject of targeted research (e.g. Zafar *et al.*, 2013) and are sometimes included explicitly (e.g. Guimarães *et al.*, 2009; Péroux

et al., 2005), or statistically (e.g. Crighton *et al.*, 2015) in the calculation of $\Omega_{\rm HI}$. Despite the ability of our dataset to identify absorbers down to at least $\log N({\rm H\,I})$=19.5, we do not include them in the present work (however, these absorbers are used to compute $f_{\rm HI}(N, X)$ and $\Omega_{\rm HI}^{\rm DLA}$ uncertainties). The motivation for this decision is one of homogeneity. Later in this work, we will combine the XQ-100 sample with other available surveys for DLAs at $z > 2$, in order to obtain the most statistically robust measure of $\Omega_{\rm HI}$ from $2 < z < 5.5$. Since many of the literature samples that we will make use of do not include sub-DLAs (often due to their more limited spectral resolution), we adopt the standard threshold of $\log N({\rm H\,I})$=20.3 for the DLA catalog presented here. However, in a separate future paper, we will present the identification of sub-DLAs, with column density completion functions and assess their contribution to both the neutral gas and metals at $z \sim 4$.

The final requirement for the DLA to be included in our XQ-100 statistical sample for the computation of $\Omega_{\rm HI}^{\rm DLA}$ is that its redshift be at least 5000 km s^{-1} from the background QSO in order to exclude the proximate DLA (PDLA) population. The PDLAs have been shown to exhibit different clustering properties (they are more prevalent than intervening systems, Ellison *et al.*, 2002; Prochaska *et al.*, 2008b; Russell *et al.*, 2006) and have also been suggested to manifest different metallicities and ionization conditions (Ellison *et al.*, 2010, 2011). These distinctions justify the exclusion of PDLAs from our statistical study of DLA gas content. These out-of-sample absorbers are flagged with a star in Table 1.1.

Our final XQ-100 DLA sample contains 38 absorbers with absorption redshifts ranging from 2.24 to 4.47. Of these DLAs, 27 are not duplicated in our combined literature sample and 22 are not in the catalog by Noterdaeme *et al.* (2012). Duplicated systems are flagged with a diamond in Table 1.1.

We compare in Figure 1.3 our fitted $N({\rm H\,I})$ values with previous estimates for some systems, where measurements have been made at a variety of spectral resolutions. Most of the DLAs in the Péroux *et al.* (2003) compilation, as well as those by Noterdaeme *et al.* (2012), are observed at $R < 2000$. The (Guimarães *et al.*, 2009) sample was observed with ESI, which has a comparable resolution to X-shooter. The 'high resolution' (HR Berg *et al.*, 2015a) data points have typical values of $R \sim 40,000$, observed with either HIRES on Keck or UVES on the VLT. There is a tendency for the XQ-100 fits to exceed those in the literature when the resolution of the latter is low. However, the agreement with high resolution measurements is generally excellent and well within the quoted uncertainties (typically 0.1 – 0.2 dex).

We also performed a further test to determine whether our XQ-100 measurements are reliable, or exhibit any systematic bias. Using the pairs of (z, $\log N({\rm H\,I})$) values of our DLA sample and the number of Lyman series lines used to fit each pair, we injected

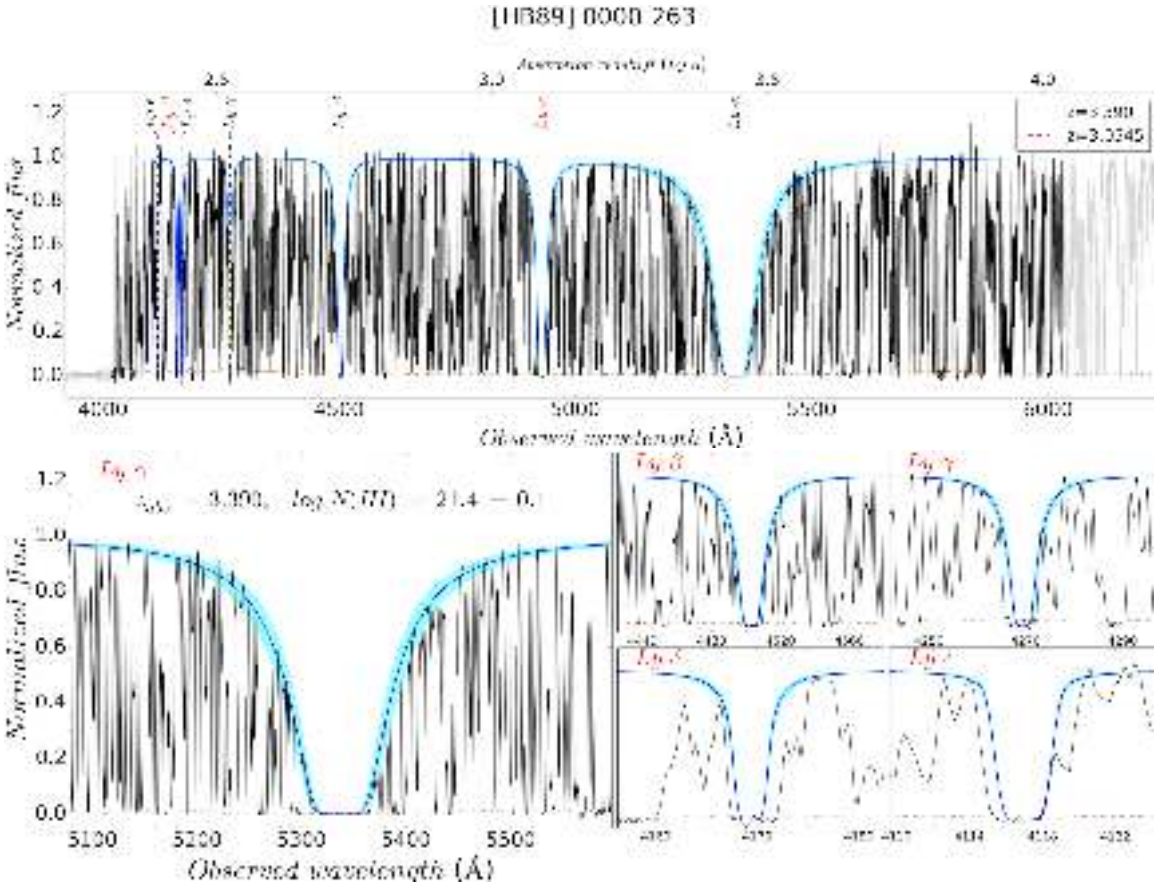

Figure 1.1: Example of normalized Lyα forest (upper panel) for the quasar [HB89] 0000-263. The part of the spectrum used for statistics is plotted in black and the rest in gray. The error spectrum is shown in brown. The model of all absorbers with $\log N(\mathrm{H\,I})\geq 19.5$ is drawn in blue with the 1σ error zone shaded in cyan. Each individual system is labeled with a specific color denoted in the legend box. However, only one of the absorbers, at $z = 3.390$, has an $N(\mathrm{H\,I})$ above the DLA threshold and is included in our catalog. The fits to the higher order lines of this DLA are shown in the lower panels.

synthetic absorbers into real XQ-100 spectra. In this way, we accurately represent the properties of the DLAs in our sample, and our ability to recover them for the noise and resolution properties of the data. We blindly measured the $\log N(\mathrm{H\,I})$ of the synthetic absorbers using the same procedure as previously employed for real systems. The comparison between the real and measured column densities are shown in Figure 1.2. The agreement at high $\log N(\mathrm{H\,I})$ is excellent. At moderate column densities, there is an increased scatter, mainly due to blending with sub-DLAs and Lyman limit systems, but most absorbers are accurately measured within 0.2 dex, and there is no systematic under or over-estimate.

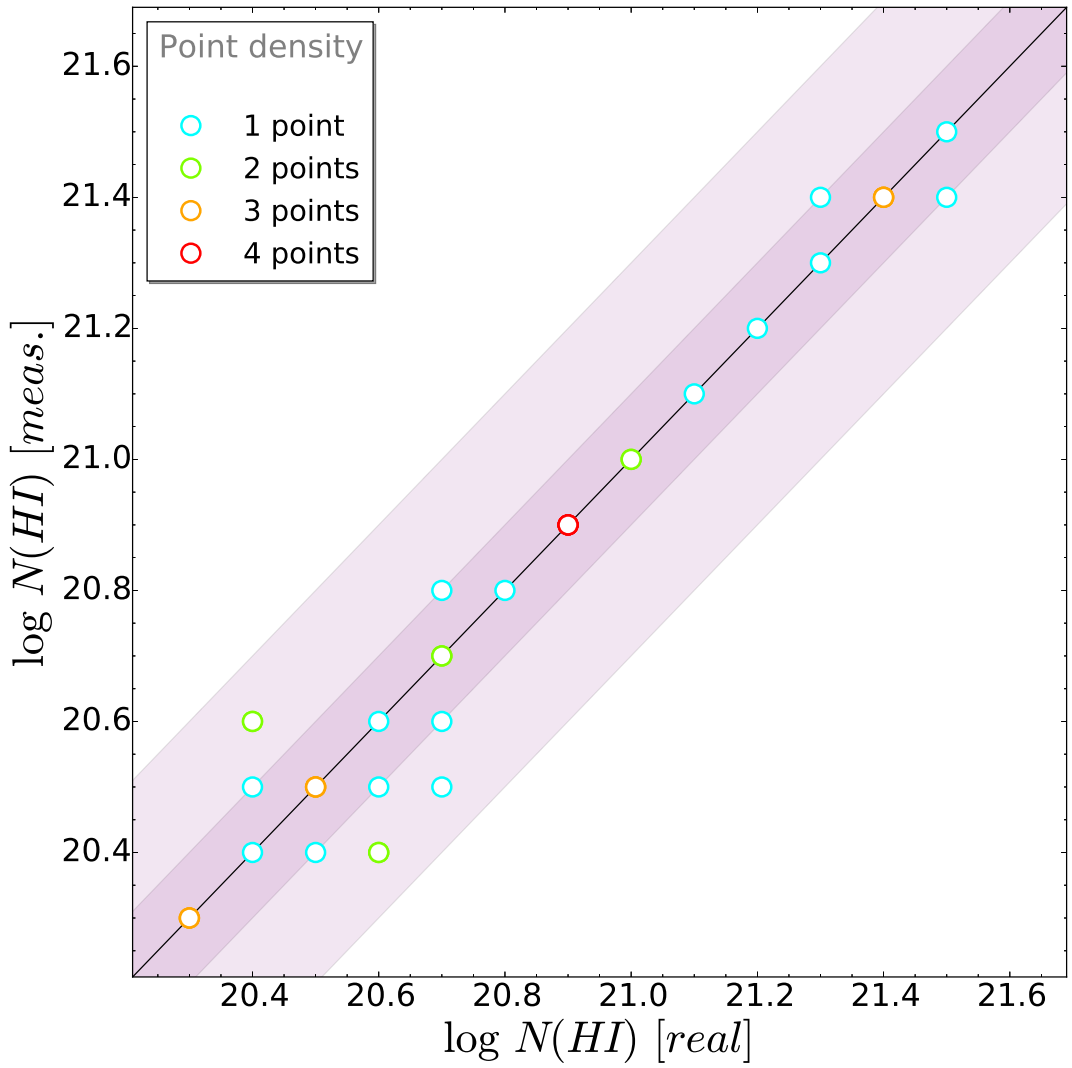

Figure 1.2: Comparison of our measurements of the synthetic DLAs inserted into XQ-100 data. The colour of the points represent the number of points that overlap due to matching $\log N(\mathrm{H\,I})$ for different redshift tests. Shaded purple regions show 0.1 dex and 0.3 dex intervals.

Table 1.1: **XQ-100 DLA catalog.**

Name	$z_{\rm em}$	$z_{\rm min}$	$z_{\rm max}$	$z_{\rm abs}$	$\log N({\rm H\,I})$	$\epsilon[\log N({\rm H\,I})]$	Lines covered
◊ [HB89] 0000-263	4.010	2.307	4.041	3.3900	21.40	0.10	Ly-α, Ly-β, Ly-γ, Ly-δ, Ly-ϵ
♠ [HB89] 0053-284	3.620	2.447	3.559				
[HB89] 0055-269	3.660	1.599	3.584				
BRI 0241-0146	4.050	2.743	3.972				
BR 0245-0608	4.240	2.891	4.147				
◊ BRI 0952-0115	4.430	2.907	4.329	4.0245	20.70	0.15	Ly-α, Ly-β, Ly-γ, Ly-δ
BR 1033-0327	4.510	2.899	4.440				
BRI 1108-0747	3.920	2.619	3.841				
[HB89] 1159+123	3.510	1.854	3.448				
BR 2212-1626	3.990	2.529	3.912				
BR 2213-6729	4.470	2.768	4.389				
BR 2248-1242	4.160	2.940	4.072				
◊ PKS B1418-064	3.690	2.356	3.611	3.4490	20.30	0.15	Ly-α, Ly-β, Ly-γ, Ly-δ, Ly-ϵ
BR J0006-6208	4.460	2.998	4.351	3.2030	20.90	0.15	Ly-α
				3.7750	21.00	0.20	Ly-α, Ly-β
BR J0030-5129	4.170	2.529	4.088				
★ PSS J0034+1639	4.29	2.9813	4.2396	4.2835	21.00	0.10	Ly-α, Ly-β, Ly-γ, Ly-δ, Ly-ϵ
★				4.2523	20.60	0.10	Ly-α, Ly-β, Ly-γ, Ly-δ, Ly-ϵ
				3.7550	20.40	0.15	Ly-α, Ly-β
SDSS J004219.74-102009.4	3.880	2.488	3.783				
BRI J0048-2442	4.150	2.587	4.000				
♠ PMN J0100-2708	3.520	2.192	3.471				
◊ BRI J0113-2803	4.300	2.784	4.227	3.1060	21.20	0.10	Ly-α
PSS J0117+1552	4.240	2.364	4.157				
PSS J0121+0347	4.130	2.546	4.041				
◊ SDSS J0124+0044	3.840	2.077	3.758	2.2610	20.70	0.15	Ly-α
◊ PSS J0132+1341	4.160	2.833	4.067	3.9360	20.40	0.15	Ly-α, Ly-β, Ly-γ, Ly-δ
◊ PSS J0133+0400	4.150	2.850	4.100	3.6920	20.70	0.10	Ly-α, Ly-β
◊				3.7725	20.70	0.10	Ly-α, Ly-β
BRI J0137-4224	3.970	2.513	3.889				
SDSS J015339.60-001104.8	4.190	2.825	4.110				
PSS J0211+1107	3.980	2.438	3.891				
PMN J0214-0518	3.990	2.554	3.895				
◊ BR J0234-1806	4.310	2.957	4.218	3.6930	20.40	0.15	Ly-α, Ly-β
PSS J0248+1802	4.420	2.858	4.350				
◊ SDSS J025518.57+004847.4	4.010	2.702	3.921	3.9145	21.50	0.10	Ly-α, Ly-β, Ly-γ, Ly-δ, Ly-ϵ
◊				3.2555	20.90	0.10	Ly-α
◊ BR J0307-4945	4.720	3.130	4.622	4.4665	20.60	0.10	Ly-α, Ly-β, Ly-γ, Ly-δ, Ly-ϵ
				3.5910	20.50	0.15	Ly-α
BR J0311-1722	4.040	2.562	3.951				
BR 0401-1711	4.230	2.858	4.141				
BR J0415-4357	4.070	2.800	3.990	3.8080	20.50	0.20	Ly-α, Ly-β, Ly-γ
◊ BR 0424-2209	4.320	2.751	4.242	2.9825	21.40	0.15	Ly-α
BR 0523-3345	4.410	2.817	4.297				
BR J0529-3526	4.410	2.817	4.329				
BR J0529-3552	4.170	2.825	4.087	3.6840	20.40	0.15	Ly-α, Ly-β
BR J0714-6455	4.460	2.776	4.374				
◊ SDSS J074711.15+273903.3	4.170	2.710	4.049	3.4235	20.90	0.10	Ly-α, Ly-β
◊				3.9010	20.60	0.15	Ly-α, Ly-β, Ly-γ, Ly-δ, Ly-ϵ
SDSS J075552.41+134551.1	3.670	2.085	3.587				
★ SDSS J080050.27+192058.9	3.96	2.7264	3.899	3.9465	20.40	0.10	Ly-α, Ly-β, Ly-γ, Ly-δ, Ly-ϵ
SDSS J081855.78+095848.0	3.670	2.406	3.580	3.3060	21.00	0.10	Ly-α, Ly-β, Ly-γ
SDSS J083322.50+095941.2	3.750	2.044	3.639				
SDSS J083510.92+065052.8	3.990	2.735	3.925				
SDSS J083941.45+031817.0	4.250	2.883	4.144				
SDSS J092041.76+072544.0	3.640	2.060	3.570	2.2380	20.90	0.15	Ly-α
SDSS J093556.91+002255.6	3.750	2.249	3.669				
SDSS J093714.48+082858.6	3.700	2.118	3.626				
SDSS J095937.11+131215.4	4.060	2.702	4.008				

Table 1.2: XQ-100 DLA catalog.

Name	$z_{\rm em}$	$z_{\rm min}$	$z_{\rm max}$	$z_{\rm abs}$	$\log N({\rm H\,I})$	$\epsilon[\log N({\rm H\,I})]$	Lines covered
SDSS J101347.29+065015.6	3.790	2.397	3.729				
♠ SDSS J101818.45+054822.8	3.520	2.299	3.441				
SDSS J102040.62+092254.2	3.640	2.093	3.564	2.5920	21.50	0.10	Ly-α
♠ SDSS J102456.61+181908.7	3.530	2.159	3.450	2.2980	21.30	0.10	Ly-α
SDSS J103221.11+092748.9	3.990	2.619	3.903				
SDSS J103446.54+110214.5	4.270	2.422	4.183				
SDSS J103730.33+213531.3	3.630	1.665	3.550				
SDSS J103732.38+070426.2	4.100	2.225	4.043				
SDSS J104234.01+195718.6	3.640	2.044	3.554				
SDSS J105340.75+010335.6	3.650	1.937	3.587				
SDSS J105434.17+021551.9	3.970	2.603	3.889				
SDSS J105705.37+191042.8	4.100	2.661	4.044	3.3735	20.30	0.10	Ly-α, Ly-β
◊ SDSS J105858.38+124554.9	4.330	2.570	4.253	3.4315	20.60	0.10	Ly-α, Ly-β
SDSS J110352.73+100403.1	3.610	2.200	3.531				
SDSS J110855.47+120953.3	3.670	2.447	3.601	3.5460	20.80	0.15	Ly-α, Ly-β, Ly-γ, Ly-δ, Ly-ϵ
◊				3.3965	20.70	0.10	Ly-α, Ly-β, Ly-γ
SDSS J111008.61+024458.0	4.120	2.364	4.062				
SDSS J111701.89+131115.4	3.620	2.208	3.546				
SDSS J112617.40-012632.6	3.610	2.225	3.558				
SDSS J112634.28-012436.9	3.740	2.430	3.687				
SDSS J113536.40+084218.9	3.830	1.780	3.755				
♠ SDSS J120210.08-005425.4	3.590	2.159	3.517				
SDSS J124837.31+130440.9	3.720	2.315	3.644				
SDSS J124957.23-015928.8	3.630	2.406	3.553				
SDSS J130452.57+023924.8	3.650	2.257	3.572				
SDSS J131242.87+084105.1	3.740	2.027	3.653	2.6600	20.50	0.10	Ly-α, Ly-β
2MASSi J1320299-052335	3.700	1.904	3.640				
SDSS J132346.05+140517.6	4.040	2.241	3.971				
BR J1330-2522	3.950	2.282	3.867				
SDSS J133150.69+101529.4	3.850	2.323	3.772				
♠ SDSS J133254.51+005250.6	3.510	2.323	3.434				
SDSS J133653.44+024338.1	3.800	1.887	3.722				
SDSS J135247.98+130311.5	3.700	2.035	3.629				
SDSS J1401+0244	4.440	2.916	4.319				
♠ SDSS J141608.39+181144.0	3.590	2.266	3.518				
♠ SDSS J144250.12+092001.5	3.530	1.780	3.458				
SDSS J144516.46+095836.0	3.520	1.599	3.487				
SDSS J150328.88+041949.0	3.660	2.118	3.615				
♠◊ SDSS J151756.18+051103.5	3.560	2.249	3.480	2.6885	21.40	0.10	Ly-α
♠ SDSS J152436.08+212309.1	3.610	2.052	3.525				
SDSS J154237.71+095558.8	3.990	2.257	3.904				
SDSS J155255.03+100538.3	3.730	2.529	3.644	3.6010	21.10	0.10	Ly-α, Ly-β, Ly-γ, Ly-δ, Ly-ϵ
SDSS J1621-0042	3.700	2.101	3.634				
◊ SDSS J163319.63+141142.0	4.330	2.438	4.277	2.8820	20.30	0.15	Ly-α
CGRaBS J1658-0739	3.740	2.537	3.671				
◊ PSS J1723+2243	4.520	3.056	4.440	3.6980	20.50	0.10	Ly-α
◊ 2MASSi J2239536-055219	4.560	2.949	4.465	4.0805	20.60	0.10	Ly-α, Ly-β, Ly-γ, Ly-δ
◊ PSS J2344+0342	4.240	2.693	4.162	3.2200	21.30	0.10	Ly-α
BR J2349-3712	4.210	2.850	4.133				

★ = PDLA, ◊ = DLA already identified in a previous survey, ♠ = Color biased sight-line.

1.3 Literature samples

Since the early work by Wolfe *et al.* (1986), numerous surveys have catalogued DLAs over a range of redshifts (e.g. Crighton *et al.*, 2015; Ellison *et al.*, 2001; Guimarães *et al.*, 2009; Lanzetta *et al.*, 1991; Neeleman *et al.*, 2016; Noterdaeme *et al.*, 2009, 2012; Péroux *et al.*, 2001; Prochaska & Herbert-Fort, 2004; Prochaska & Wolfe, 2009; Prochaska *et al.*, 2005; Rao *et al.*, 2006; Storrie-Lombardi & Wolfe, 2000; Storrie-Lombardi *et al.*, 1996c; Wolfe *et al.*, 1995) in order to trace the cosmic evolution of neutral hydrogen gas in galaxies. These surveys are extremely heterogenous and have been conducted with a variety of telescope apertures, both from space and on the ground, and at a range of spectral resolutions. There are also considerable duplications between surveys, and both the naming conventions and the presentation of the data in the literature mean that assembling a combined sample is a considerable challenge. Nonetheless, in this work we have attempted to assemble such a combined sample from the major DLA catalogs that are currently available, focusing on $z > 2$, the redshift range where ground-based surveys have most effectively contributed. We review these catalogs in turn below.

For comparison purposes, we also use Noterdaeme *et al.* (2012, hereafter N12) data in the high redshift range, Rao *et al.* (2006, hereafter R06) and Neeleman *et al.* (2016, hereafter N15) for intermediate redshifts and the 21cm samples from the local Universe by Rhee *et al.* (2013, hereafter R13), Delhaize *et al.* (2013, hereafter D13), Zwaan *et al.* (2005, hereafter Z05), and Braun (2012, hereafter B12).

1.3.1 The Peroux et al. (2003) compilation

A compilation of approximately the first decade and a half of DLA surveys is presented by Péroux *et al.* (2003), hereafter the P03 sample. The P03 sample combines the high redshift DLA survey of Péroux *et al.* (2001) with DLAs from 25 separate papers, several of which are themselves compilations from other surveys. Based on their statistical sample of 713 quasars and 114 DLAs, this sample was used by Péroux *et al.* (2003, 2005) to conclude that the total amount of neutral gas is conserved from z=2 to $z\sim$5.

In the process of duplication checking (described in more detail in Section 1.3.5) and checking the original references of the P03 compilation, we noted a number of inconsistencies with the original reference papers, such as the values of emission redshifts adopted for the computation of absorption statistics. We checked each of these inconsistencies manually, and concluded that they are likely due to typographical errors, and we have corrected them, as summarized in Table 1.3. We also identified 4 QSOs that are duplicates, but

Table 1.3: Modifications to the P03 catalog

Id	Comment
BR B0331-1622	$\equiv$ BR J0334-1612. Removed.
BR B0401-1711	$\equiv$ BR J0403-1703. Removed.
Q 0007-000	$\equiv$ Q 0007-0004. Removed.
Q 1600+0729	$\equiv$ BR J1603+0721. Removed.
Q 0101-3025	$z_{\rm em}$ changed from 4.073 to 3.164.
Q 0041-2607	$z_{\rm em}$ changed from 2.79 to 2.46.
Q 0201+3634	$z_{\rm em}$ changed from 2.49 to 2.912.
Q 2359-0216	$z_{\rm em}$ changed from 2.31 to 2.81.
MG 1559+1405	Reference not found. Removed.
MG 2254+0227	Reference not found. Removed.

with different names, within the P03 compilation; the duplicated sightlines have been removed. In two cases, we could not find the original reference for a given QSO, and were therefore unable to verify the properties of the QSO/absorber; these two sightlines were also removed from the sample. We summarize all of the modifications made to the P03 compilation in Table 1.3. We recomputed $z_{\rm max}$ to be 5000 km s^{-1} bluewards of $z_{\rm em}$, in order to be consistent with the threshold set for the XQ-100 sample.

1.3.2 The Prochaska & Wolfe (2009) SDSS DLA sample

Prochaska & Wolfe (2009, hereafter PW09) used automated search algorithms to identify DLAs in the Sloan Digital Sky Survey Data Release 5 (SDSS DR5). A SNR requirement of 4 was adopted, and DLAs are included in their statistical sample if they are at least 3000 km s^{-1} from the background QSO. DLAs have also been identified in more recent data releases, specifically the DR7 (Noterdaeme *et al.*, 2009) and DR9 (Noterdaeme *et al.*, 2012), the former of which has a public catalog of identified DLAs. However, our computation of $\Omega_{\rm HI}^{\rm DLA}$ requires additional details of the minimum and maximum redshifts of the DLA search for every sightline, which is not available for the DR7 and DR9 samples. The DR5 sample of PW09 is therefore the largest of the individual literature samples considered in this work, containing 7472 QSOs with 738 DLAs. We do, however, compare the results of our combined sample to that of Noterdaeme *et al.* (2012) later in this paper.

PW09 find that the mass density of neutral gas has decreased by a factor of about two between redshifts of 3.5 and 2.5. A similar rate of gas content decline was determined from the later SDSS data releases by Noterdaeme *et al.* (2009, 2012). However, Noterdaeme

et al. (2009) suggest that the analysis of PW09 may be biased against the detection of the lowest redshift DLAs, which could be rectified by implementing a velocity buffer to the minimum redshift used to compute DLA statistics. We implement this buffer, which has a value of 10,000 km s^{-1}, at the low redshift end of each SDSS spectrum. The new values of $z_{\rm min}$ listed in Table I.1, which describes our final combined DLA sample, include this velocity buffer. We also recomputed $z_{\rm max}$ to be 5000 km s^{-1} bluer than $z_{\rm em}$, for consistency with the XQ-100 sample.

1.3.3 The Guimaraes et al. (2009) sample

The broad Lyα wings of DLAs, and high absorber equivalent widths means that these galaxy scale absorbers can be easily detected in relatively low resolution spectra. Indeed, most surveys have been performed at typical resolutions of $R \sim$ 1000 - 2000. However, there are advantages to pursuing absorption line surveys at higher resolution, such as the ability to push down to the sub-DLA regime (e.g., O'Meara *et al.*, 2007; Zafar *et al.*, 2013) and to assess the increasing potential for contamination (blends) at higher redshifts. The trade-off is, of course, the increased exposure times necessary to reach a fixed SNR.

Guimarães *et al.* (2009, hereafter G09) presented the first systematic DLA survey for $\Omega_{\rm HI}^{\rm DLA}$measurements performed with an intermediate resolution spectrograph, namely the Echellette Spectrograph and Imager (ESI, mounted at the 10m Keck telescope, Sheinis *et al.*, 2002). ESI's resolution ($R \sim 4500$) is quite similar to that of X-shooter. However, the most notable difference between the two instruments is the wavelength coverage. Whereas X-shooter extends from the atmospheric cut-off to the K-band, ESI has no coverage below 4000 Å and a greatly reduced efficiency from $\sim$ 4000 – 4300 Å.

A total of 99 QSOs (77 considered for their statistical analysis) with emission redshifts ranging from z=4 to z=6.3 were observed by G09, leading to the detection of 100 absorbers with $\log N$(H I)>19.5, of which 40 are DLAs. DLAs at least 5000 km s^{-1} from the QSO redshift were included in the statistical sample. Based on the DLA sample, G09 find that there is a decline in $\Omega_{\rm HI}$ at $z > 3.5$. This decline is also present if the sub-DLAs (which increase the total gas mass density by about 30 per cent) are combined with the DLAs. The discrepancy with the results of Prochaska & Wolfe (2009) is suggested by G09 to come from the difficulties in establishing the damping nature of the systems with the high density Lyα forest in this very high redshift range. However, generations of previous surveys have demonstrated that low number statistics at the redshift boundary of the survey can also lead to an apparent turnover of $\Omega_{\rm HI}$. Of the 40 DLAs in the G09 sample, there are 6 duplicates with the XQ-100 sample.

Table 1.4: Data-sets included to build up our combined sample.

Id	No. QSOs	No. DLAs	No. PDLAs [1]	$\sum \Delta X_i$
XQ100	100	38	3	536
G09	68	34	0	378
GGG	154	43	0	553
PW09	4983	559	50	8529
P03	397	68	0	1494
CS	5702	742	53	10434

1.3.4 The Crighton et al. (2015) sample

The Giant Gemini GMOS (GGG) survey observed 163 $z > 4.4$ QSOs with GMOS-N and GMOS-S at the Gemini Observatory (Worseck *et al.*, 2014). Like the G09 sample, the main focus of the GGG DLA sample was the assessment of $\Omega_{\rm HI}$ at high redshifts. However, the GMOS spectra are of significantly lower resolution than the ESI spectra used by G09 and Crighton *et al.* (2015) carefully assess the contamination by both false positives (blends) and missed DLAs through a variety of blind tests and comparisons with repeated observations at higher spectral resolution. Despite potential concerns of blending and low resolution, Crighton *et al.* (2015) conclude that the required correction factors are minimal. DLAs are included in the GGG statistical sample if they are at least 5000 km s^{-1} from the background QSO.

Although Crighton *et al.* (2015) are not able to accurately identify and fit sub-DLAs, in their estimate of $\Omega_{\rm HI}$ they make a uniform correction for the contribution of these lower column density systems. We do not make this correction *a priori*, but rather use the DLA catalog of Crighton *et al.* (2015) directly in our combined sample. At $z_{\rm abs}$∼5, the $\Omega_{\rm HI}$ derived from GGG is formally consistent with the SDSS measurements of Noterdaeme *et al.* (2012) at z∼ 3. However, a power law of the form $(1+z)^{0.4}$, describing a slowly decreasing $\Omega_{\rm HI}$ towards lower redshifts is consistent with data spanning $0 < z < 5$.

1.3.5 The combined sample

The reviews provided above highlight the sensitivity of $\Omega_{\rm HI}^{\rm DLA}$ to a variety of possible systematics, including blending/contamination, SNR, robust definitions of the search path and, perhaps most importantly, sample size. Since the few, rare, high N(H I) absorbers contribute to $\Omega_{\rm HI}$ (and $\Omega_{\rm HI}^{\rm DLA}$) appreciably, large samples are required to statistically assess $\Omega_{\rm HI}$ at any given redshift. We have therefore combined the major surveys and

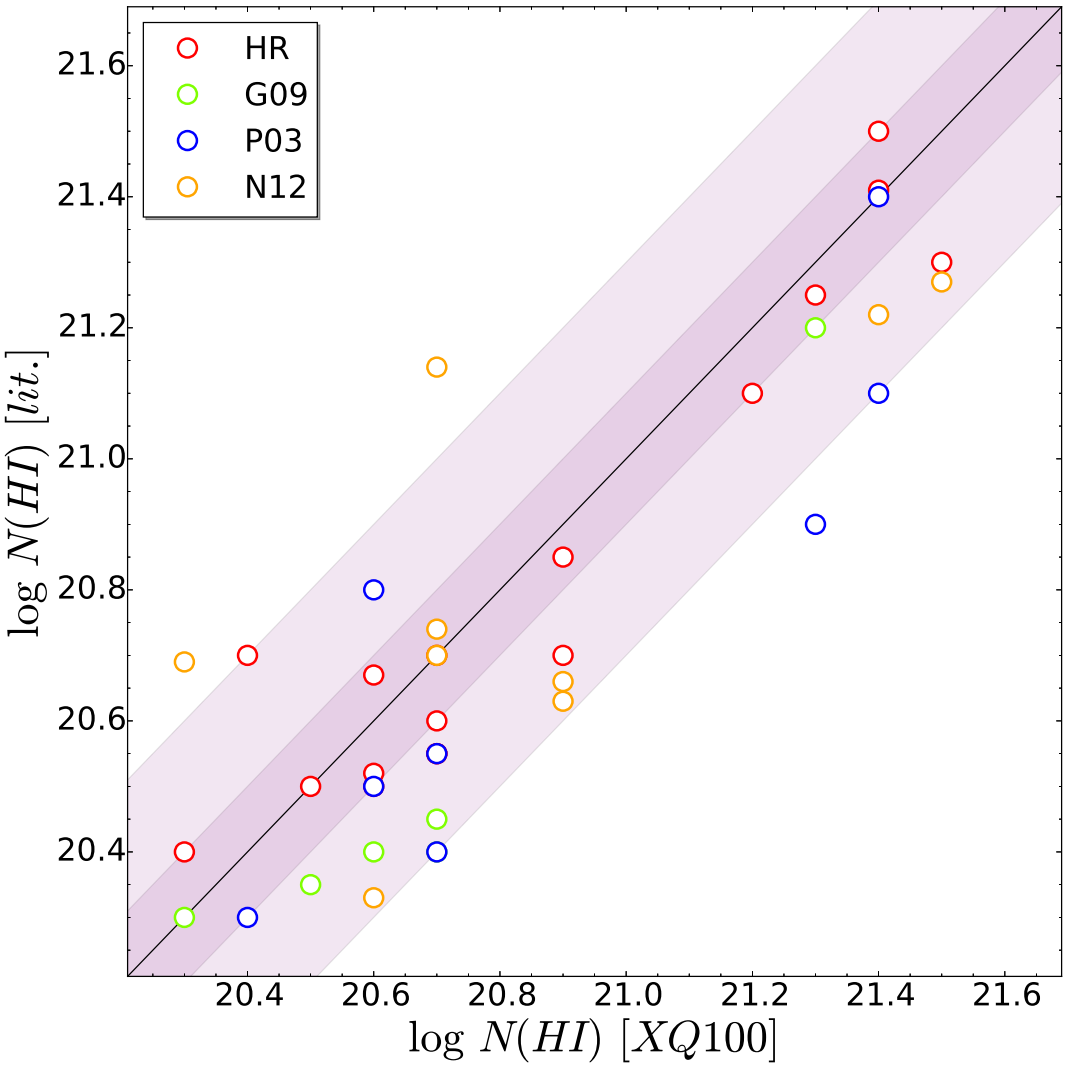

Figure 1.3: Comparison of our XQ-100 measurements with previous estimates. Shaded purple regions show 0.1 dex and 0.3 dex intervals.

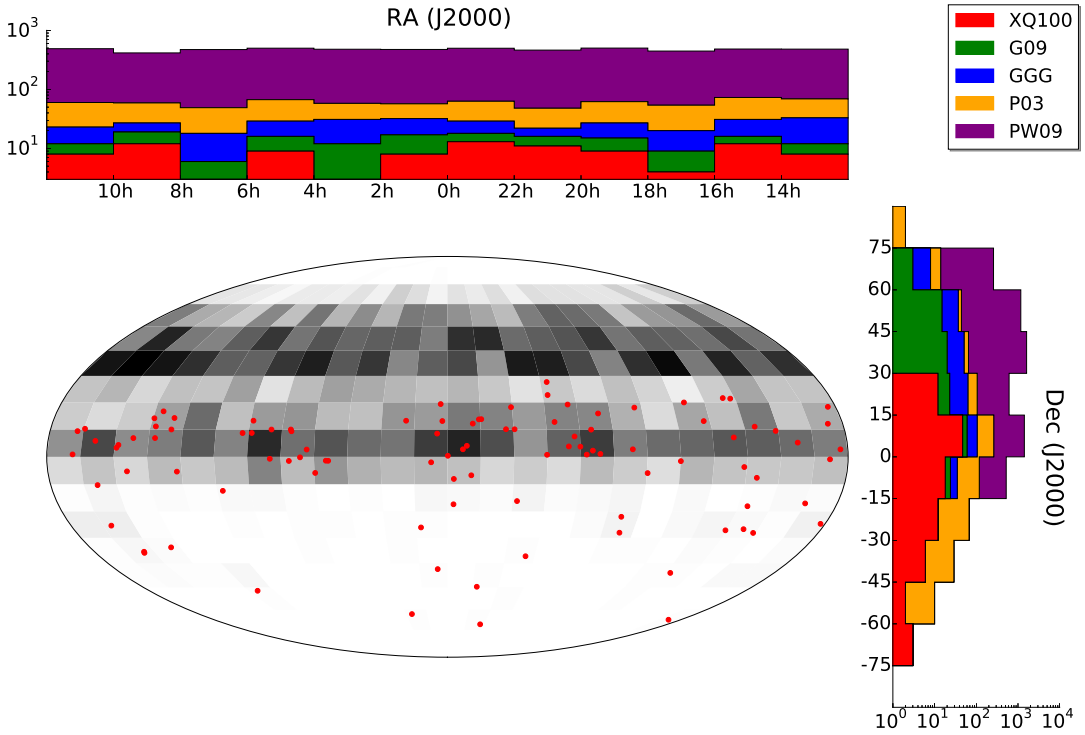

Figure 1.4: Sky position of the QSOs in the total combined sample. 1D histograms for each celestial coordinate and a 2D histogram density plot on the celestial globe are presented. The gray scale 2D histogram for the combined sample density plot represents the number of sources per surface unit (150 sq degrees), ranging from 0 (white) to 58 (black). The mean number of quasars per surface unit is 13.2. The red points over-plotted are the positions of the XQ-100 QSOs. The propensity of northern sky coverage is driven by the SDSS.

compilations described above, in order to minimize fluctuations in the determination of $\Omega_{\rm HI}$ due to inadequate sampling of the column density distribution function.

Prior to combining the literature samples and the XQ-100 sample, it is necessary to check for, and remove, duplicate DLAs. Duplication checking was achieved by obtaining the sky coordinates and redshift of all quasars in all samples from NED, SIMBAD or SDSS, since naming conventions between surveys are heterogeneous. For the join procedure, we made XQ-100 the initial base sample. The catalogs were assessed in the order listed in Table 1.4, which was adopted as an approximate ranking of spectral quality (SNR and resolution). The base sample was compared with each subsequent catalog in Table 1.4 by performing a coordinate cross-matching with a positional tolerance of 10". All matches were removed from the last table and the resulting combined (duplicate free) catalog was used as the base table for the next iteration (i.e. with the next catalog in Table 1.4).

In Table I.1 we present the final combined sample (CS) with all duplicates removed. The final combined sample contains a total of 742 DLAs, spanning a redshift from 1.673 to 5.015. A comparison of the sky positions of the combined literature sample and the XQ-100 sample is shown in Figure 1.4.

1.4 Results

1.4.1 Redshift path coverage

We begin our analysis by computing the redshift path covered by both the individual samples described in the previous section, as well as for the combined sample. Although we will ultimately use only the combined sample for our determination of $\Omega_{\rm HI}$, it is instructive to see how the various sub-samples contribute as a function of redshift.

The cumulative number of sightlines that could contain an absorber at a given redshift is defined as (Lanzetta *et al.*, 1991)

$$g(z) = \sum_i H(z^i_{max} - z)H(z - z^i_{min}) \tag{1.1}$$

where H is the Heaviside function. Then, the total redshift path surveyed is

$$\Delta z = \int_0^\infty g(z)dz = \sum_i (z^i_{max} - z^i_{min}) \tag{1.2}$$

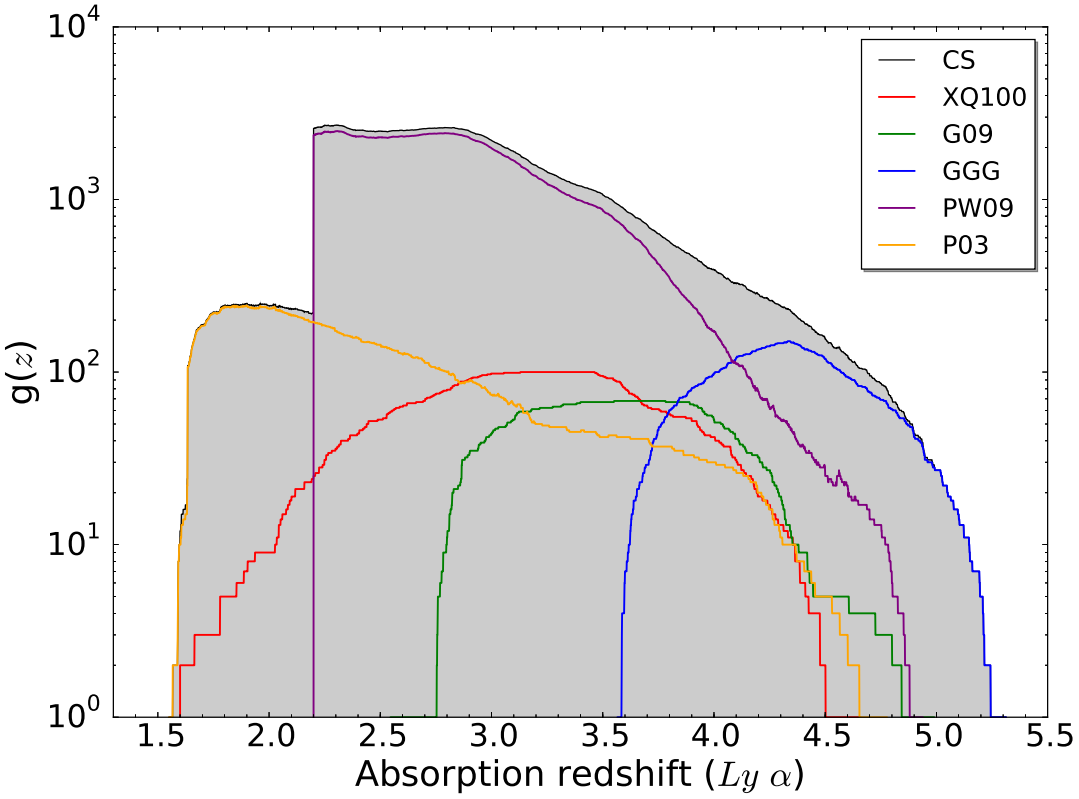

Figure 1.5: Redshift path for all samples used in this work and for the total combined sample (CS).

For the XQ-100 sample, the lower limit z^i_{min} for the i^{th} quasar was chosen as the minimum redshift where the SNR> 7.5. This SNR threshold was determined from our data as a conservative value where we start to easily identify damping wings. As described in Section 1.2, the maximum DLA search redshift, z^i_{max}, was set conservatively to be 5000 km s^{-1} bluewards of z^i_{em}.

The resulting XQ-100 $g(z)$ curve is shown in Fig. 1.5 together with the data of the other samples used in this paper. For the rest of the samples, we kept published $z_{\rm min}$ but we recomputed $z_{\rm max}$ to be 5000 km s^{-1} bluewards $z_{\rm em}$. This accounts also for possible uncertainties in the determination of emission redshifts, which are inhomogeneously computed (see, e.g., Hewett & Wild, 2010, and references therein). The 5000 km s^{-1} threshold therefore provides a safe buffer against the inclusion of PDLAs that are likely to affect our statistical sample.

Fig. 1.5 demonstrates the complementarity of the various previous surveys and the advantage of combining them all together. The XQ-100 survey probes from z=1.6 up to z=4.5, with the majority of the absorption path in the z=[3.0-3.5] range. The previous moderate resolution DLA survey by G09 extends to slightly higher redshifts than XQ-100. However, due to ESI's lack of blue sensitivity and the emission redshift distribution of this sample, there is no absorption path coverage below $z \sim 2.7$. The PW09 sample dominates at moderate redshifts, but the P03 sample and GGG samples are major contributors at the lowest and highest redshifts, respectively.

1.4.2 DLA distribution function

The differential column density distribution, that represents the number of absorbers between N and N+dN and z and z+dz, is defined (Lanzetta *et al.*, 1991) as

$$f_{HI}(N,X)dNdX = \frac{m}{\Delta N \sum_i \Delta X_i} dNdX \tag{1.3}$$

where m is the number of systems in a column density bin and the absorption distance

$$\Delta X = \int_{z_{\rm min}}^{z_{\rm max}} \frac{H_0}{H(z)}(1+z)^2 dz \tag{1.4}$$

is a quantity conveniently defined to give the distribution values in a comoving frame.

The results for the whole sample, as well as fits for the sample split in 2 or 3 different redshift bins are tabulated in Table 1.5. In Figure 1.6 we present the sample frequency and

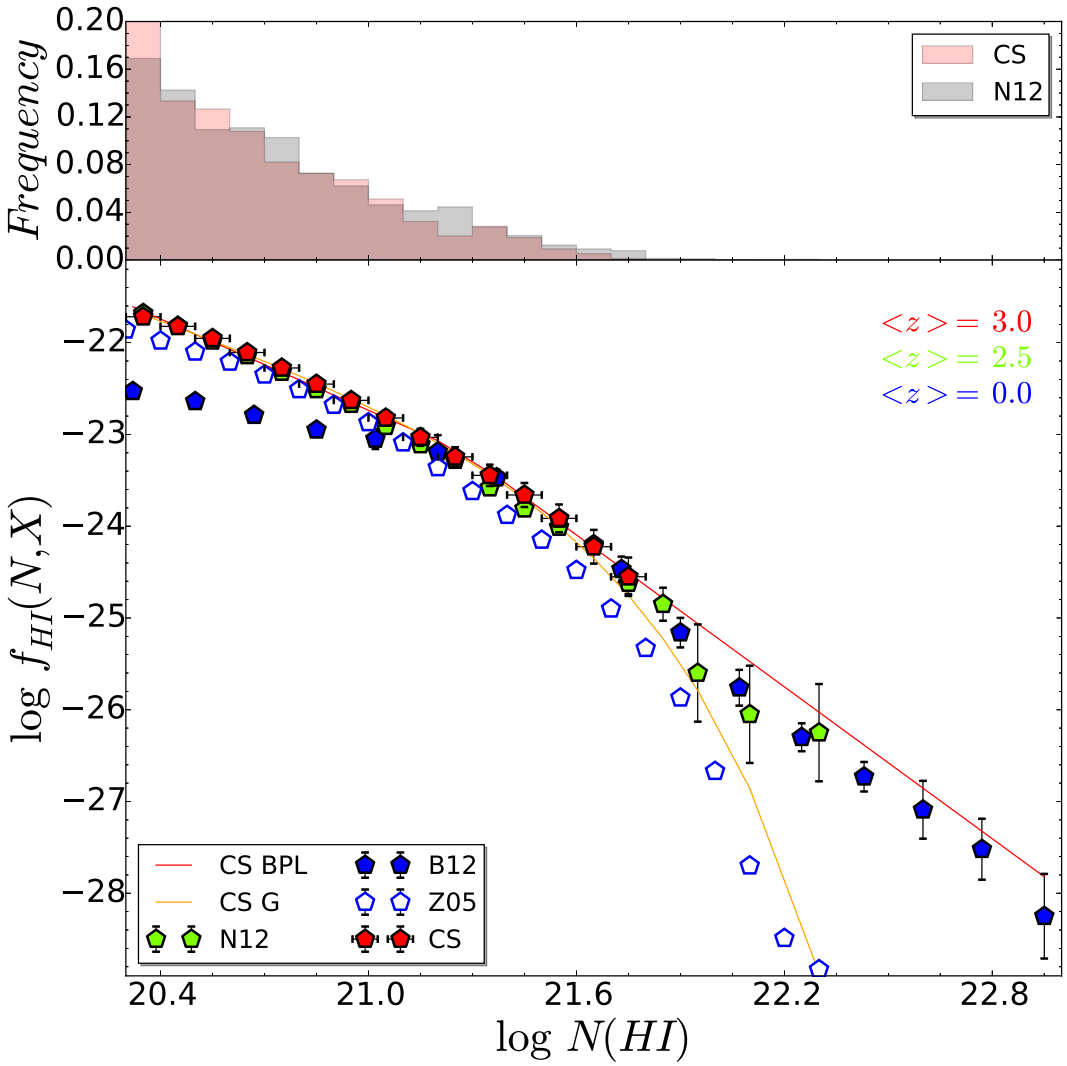

Figure 1.6: Sample frequency and distribution function for the whole combined sample compared with N12 (at similar mean redshift) and Z05+B12 representing the local universe. Model fits to a broken powerlaw (BPL, red) and a gamma function (G, orange) are also plotted.

Table 1.5: Column density distribution (binned evaluations) for the complete CS ($< z >= 2.99$), and split in 2 and 3 redshift bins

$\log N(\mathrm{H\,I})$	$\log f_{\mathrm{HI}}(N,X)$					
	z=2.99	z=2.57	z=3.47	z=2.44	z=2.95	z=3.69
20.3	-21.72 ± 0.05	-21.79 ± 0.08	-21.66 ± 0.07	-21.82 ± 0.1	-21.69 ± 0.08	-21.66 ± 0.08
20.4	-21.82 ± 0.05	-21.89 ± 0.08	-21.76 ± 0.07	-21.91 ± 0.1	-21.81 ± 0.09	-21.76 ± 0.08
20.5	-21.95 ± 0.06	-22.02 ± 0.08	-21.89 ± 0.07	-22.04 ± 0.1	-21.96 ± 0.09	-21.88 ± 0.08
20.6	-22.11 ± 0.06	-22.17 ± 0.09	-22.05 ± 0.08	-22.18 ± 0.1	-22.13 ± 0.1	-22.02 ± 0.09
20.7	-22.28 ± 0.06	-22.33 ± 0.09	-22.23 ± 0.08	-22.35 ± 0.11	-22.31 ± 0.11	-22.19 ± 0.1
20.8	-22.45 ± 0.07	-22.51 ± 0.1	-22.4 ± 0.09	-22.53 ± 0.12	-22.48 ± 0.12	-22.36 ± 0.1
20.9	-22.63 ± 0.07	-22.7 ± 0.11	-22.56 ± 0.09	-22.74 ± 0.14	-22.65 ± 0.13	-22.53 ± 0.11
21.0	-22.82 ± 0.08	-22.92 ± 0.12	-22.74 ± 0.1	-22.94 ± 0.15	-22.84 ± 0.14	-22.71 ± 0.12
21.1	-23.03 ± 0.09	-23.13 ± 0.14	-22.95 ± 0.12	-23.13 ± 0.16	-23.07 ± 0.16	-22.92 ± 0.14
21.2	-23.24 ± 0.11	-23.32 ± 0.15	-23.18 ± 0.13	-23.28 ± 0.17	-23.31 ± 0.18	-23.14 ± 0.15
21.3	-23.45 ± 0.12	-23.49 ± 0.16	-23.41 ± 0.15	-23.43 ± 0.18	-23.56 ± 0.19	-23.35 ± 0.17
21.4	-23.66 ± 0.13	-23.68 ± 0.17	-23.63 ± 0.17	-23.61 ± 0.19	-23.78 ± 0.21	-23.55 ± 0.18
21.5	-23.92 ± 0.15	-23.92 ± 0.19	-23.88 ± 0.19	-23.85 ± 0.2	-23.99 ± 0.21	-23.78 ± 0.2
21.6	-24.22 ± 0.18	-24.2 ± 0.21	-24.16 ± 0.21	-24.11 ± 0.22	-24.2 ± 0.22	-24.03 ± 0.21
21.7	-24.56 ± 0.21	—	-24.41 ± 0.22	—	—	-24.27 ± 0.22

the distribution function of the combined sample in bins of 0.1 dex. We also compare our points with the results from the SDSS/BOSS by N12, and with the samples from the local Universe by B12 and Z05. Our bias-corrected values for the combined sample[1] are in very good agreement with N12 results, although the size of our sample is not large enough to have many absorbers with column densities higher than $\log N(\mathrm{H\,I})\sim21.7$. The combined sample is also in good agreement with B12 at the high column density end ($N(\mathrm{H\,I}) > 21$), but the B12 sample has a paucity of low column density systems compared to the combined sample and N12. However, the B12 sample is limited to a small number of Local group galaxies and does not widely sample the low redshift universe. At the low column density end of the distribution function, DLA surveys are in much better agreement with Z05.

We have fitted a broken power law (e.g. Prochaska & Wolfe, 2009) to our binned data using the Nelder-Mead algorithm:

$$f_{\rm HI}(N,X) = \begin{cases} k_d \left(\frac{N}{N_d}\right)^{\alpha_{1d}} & N < N_d \\ k_d \left(\frac{N}{N_d}\right)^{\alpha_{2d}} & N \geq N_d \end{cases} \tag{1.5}$$

and a gamma function (e.g. Péroux *et al.*, 2003)

$$f_{\rm HI}(N,X) = k_g \left(\frac{N}{N_g}\right)^{\alpha_g} e^{N/N_g} \tag{1.6}$$

The coefficients from the distribution function fits are given in Table 1.7. Both expressions reproduce well our observed points, but when extrapolating to the highest column densities the broken power law describes much better the N12 and B12 distributions. The gamma function appears to significantly under-predict the frequency of the highest column density absorbers at high redshift. We note that these results are also consistent with the exponent $\alpha_2 \sim -3$ expected by Wolfe *et al.* (1995) for self-similar 'disks'.

[1]We explain the bias correction method in detail in section 1.4.3

1.4.3 Hydrogen mass density ($\Omega_{\rm HI}$) curves

The main objective of the current work is to assess the redshift evolution of the gas mass density $\Omega_{\rm HI}$, which is defined as the first moment of the distribution function

$$\Omega_{\rm HI} = \frac{H_0}{c}\frac{m_H}{\rho_c}\int_{N_{min}}^{N_{max}} N f_{HI}(N,X)dN \tag{1.7}$$

where $\rho_c = 3H_0^2/8\pi G$ is the critical density for which the spatial geometry of the universe is flat. Usually, the discrete limit

$$\int_{N_{min}}^{N_{max}} N f_{HI}(N,z)dN = \frac{\sum_j N_j}{\sum_i \Delta X_i} \tag{1.8}$$

where i refers to the QSO and j to the DLA, is taken to compute this quantity. Here, we are assuming that the sample represents properly the real population characteristics and/or the errors coming from this discretization are negligible compared with the sampling errors. We will check these assumptions in section 1.4.3.2. For the computation of $\Omega_{\rm HI}^{\rm DLA}$, log N_{min} is taken to be 20.3.

1.4.3.1 Error estimations

The error bars associated with $\Omega_{\rm HI}^{\rm DLA}$ may arise from several uncertainties. Here, we consider two main sources of uncertainty: the error associated with the fitted N(H I) of a given DLA (which includes uncertainties associated with the continuum fitting), and limited sampling of the complete column density distribution function. The relative importance of these errors, and attempts to quantify them, have been varied in the literature. It is therefore instructive to compare various methods of error estimation, in order to quantify their relative magnitude.

In some early work, (e.g. Ellison *et al.*, 2001; Storrie-Lombardi *et al.*, 1996b) a common approach to determine the error on $\Omega_{\rm HI}^{\rm DLA}$ was to assume the sampling process followed a Poisson distribution (hereafter the 'P method'). This means that we are assuming a probability function of the form $P(X) = e^{-\lambda}\frac{\lambda^x}{x!}$ for finding absorbers with column density N(H I) within the total absorption path ΔX. Under this assumption, the error on $\Omega_{\rm HI}^{\rm DLA}$

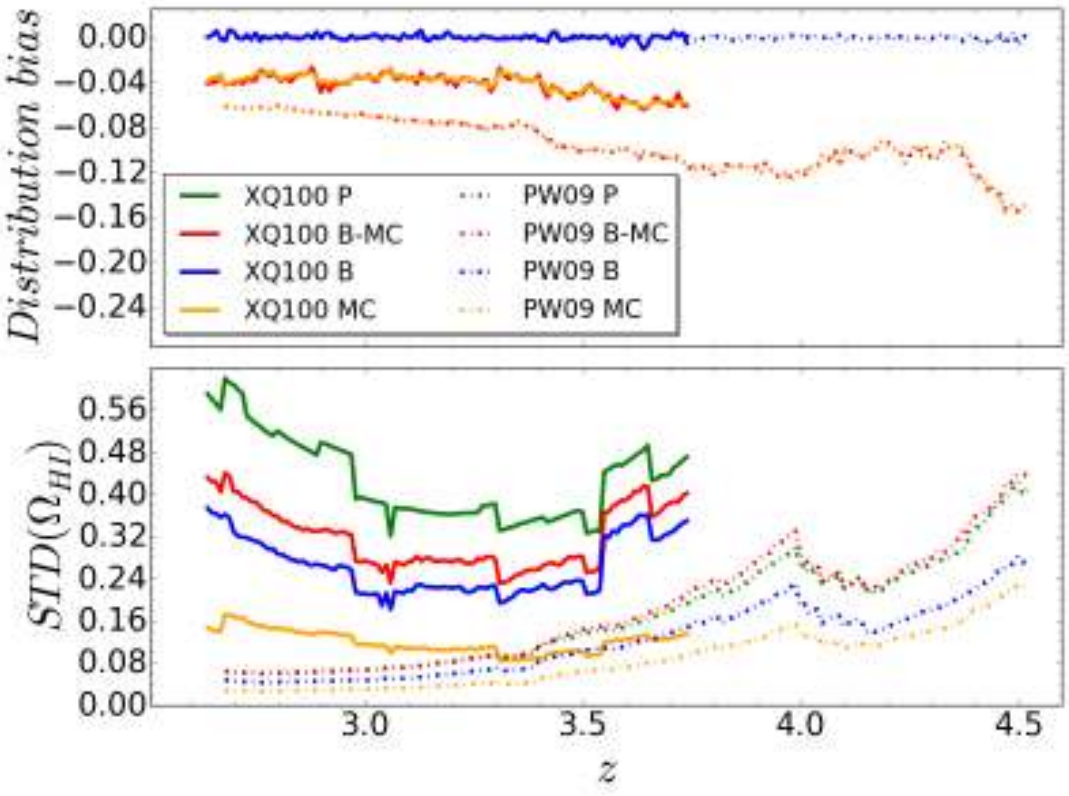

Figure 1.7: Representation of the standard deviation (lower panel) and statistical distribution bias (upper panel) as a function of redshift for the XQ-100 and PW09 samples. The y-axis represents deviations in $\Omega_{\rm HI}\times10^3$.

is propagated as

$$\Delta\Omega_{\rm HI}^{\rm DLA} = \Omega_{\rm HI}^{\rm DLA} \frac{\sqrt{\sum_{i=1}^{p} N_i^2}}{\sum_{i=1}^{p} N_i}. \tag{1.9}$$

An alternative approach is to use a bootstrap re-sampling (hereafter 'B method') of the observations in a given redshift bin (e.g. Crighton *et al.*, 2015). The bootstrap method consists of building up a large number of $\Omega_{\rm HI}^{\rm DLA}$ values ($N_{\rm re-samples} = 10,000$ in our computations) that resamples, with replacement, the observed DLA sample in a given redshift bin. If the observed DLA 'pool' is large enough, and is a good representation of the population properties, then each bootstrap realization is analogous to performing another independent DLA survey with the same total absorption path and redshift interval. Then, this large set of simulated observations provides an easy way of computing the mean $\Omega_{\rm HI}^{\rm DLA}$, its standard deviation and the distribution bias (the difference between the computed $\Omega_{\rm HI}^{\rm DLA}$ from the originally measured DLA distribution and the resampled $\Omega_{\rm HI}^{\rm DLA}$ distribution mean). Although they provide a useful estimator of the uncertainties associated with survey size and the sampling of the column density distribution function, neither the P method nor the B method account for the fit uncertainties on an individual DLA.

In order to assess the uncertainty due to errors on the N(H I) fitting, a Monte Carlo approach may be adopted (hereafter, the 'MC method'). In this approach, the $\Omega_{\rm HI}^{\rm DLA}$ for the original sample of DLAs is recomputed 10,000 times, but the value of N(H I) is perturbed on each iteration, by drawing values from within the Gaussian error distribution defined by the 1σ errors of the fit. We note the possibility of a 'boundary bias' in the application of the MC method. This bias can occur because DLAs that are barely above the limiting N(H I) threshold of 20.3 may be lost from the re-sampled distribution after they are perturbed within their error distribution. In order that this sample migration occurs equally in the other direction (absorbers just below the log N(H I) = 20.3 being boosted into the re-sampled distribution) we include in our error analysis tests all absorbers that have been identified in our sample, down to a limiting column density of log N(H I) = 19.5.

It is also possible to combine the uncertainties associated with population sampling (epitomized with the B method) and the fit uncertainties (MC method). In the 'B-MC method', the bootstrap re-sampling of the original population additionally includes the perturbation of each N(H I) within its Gaussian error distribution.

In Figure 1.7 we compare the standard deviations (lower panel) and bias distributions

(i.e. the difference between the actual $\Omega_{\rm HI}^{\rm DLA}$ computed for the original observed sample and the value derived from sampling either the population or its errors, top panel) of the various error estimation techniques. Note that the P method does not entail re-sampling, so there is no measure of bias for this technique. The error curves are computed using a fixed ΔX=2.5 (we will discuss in the following subsection different approaches to binning). Due to the different characteristics of the surveys that comprise our combined sample, such as sample size and spectral resolution, it is useful to compare the errors from the different estimation techniques for some of the separate sub-samples. In Fig. 1.7 we therefore show the error estimate comparisons for PW09 and XQ-100. The former is the largest component of our combined sample and will hence best sample the underlying N(H I) distribution. However, this sample has a relatively relaxed SNR threshold (SNR $>$ 4) and was constructed from moderate resolution spectra. Conversely, the XQ-100 sample is of modest size, but has both relatively high spectral resolution and SNR. Moreover, the wide wavelength coverage of X-shooter permits the simultaneous fitting of higher order Lyman lines. These factors are all advantageous for the reduction of N(H I) fitting uncertainties.

Fig. 1.7 reveals several interesting features of the different error estimators. The P method generally exhibits the largest standard deviations of the four techniques investigated, particularly for smaller samples. Moreover, without any re-sampling, it is difficult to explicitly test the effect of sample size, and the P method does not account at all for errors in N(H I). The technique that best captures the uncertainties in the N(H I) fit is the MC method. From the lower panel of Fig. 1.7 it can be seen that the MC errors of PW09 are smaller than XQ-100, even though the fit uncertainties are generally smaller in the latter sample. The much greater size of the PW09 sample can apparently largely compensate for the slightly poorer fit accuracy. Comparing a subset of the PW09 survey with a size matched to XQ-100 would lead to larger uncertainties in the former. An important and non negligible effect that can be seen in the upper panel of Fig. 1.7 is that any variant of the MC technique (i.e. either with or without bootstrapping) always yields a negative bias, i.e. the simulated $\Omega_{\rm HI}^{\rm DLA}$ is usually greater than the original. This is due to the error distribution which is asymmetric in linear space.

We now consider the contribution of population sampling to the error estimate, as encapsulated by the bootstrap B method. For an infinitely large survey that fully samples the underlying population, the error due to incomplete sampling becomes negligible and the error is dominated by the uncertainties in the individual N(H I) measurements. In smaller surveys, the sampling error becomes dominant. We can see this effect by comparing the large PW09 sample to the more modest sized XQ-100 sample in the lower panel of Fig. 1.7. Here, we see that the error from the sampling alone (B method) is approximately twice that of the fitting errors alone (MC method) for the XQ-100 sample. However, the

fitting errors approach the sampling errors for the much larger PW09 sample. In general, the larger the sample, the more important is the relative contribution of the fitting uncertainties, compared to population sampling alone. Therefore, where XQ-100 is dominated by the sampling uncertainties, sampling and fitting uncertainties contribute at a similar level in PW09. In contrast to the MC techniques, the top panel of Fig. 1.7 shows that the B method does not lead to a bias in the re-sampled distributions, as it considers perfect determinations of the column densities.

A combination of sampling and fitting errors seems to be required by our data, so we conclude that the best resampling technique to compute statistics is the B-MC method. However, since we have shown that the B-MC resampled distribution is biased (and could have non-negligible skewness), the standard deviation alone is an inadequate representation of the uncertainties. We have therefore computed the 68 and 95 per cent confidence intervals, using the so-called bootstrap bias corrected accelerated method (BCa, Efron, 1987) on the B-MC resampled $\Omega_{\rm HI}^{\rm DLA}$. In this non-parametric approach, the results are less affected by skewed distributions, and with this technique the bias mentioned before is also taken into account.

1.4.3.2 Binning techniques

In order to study the redshift evolution of $\Omega_{\rm HI}^{\rm DLA}$, there are two common procedures used in the literature to bin the observed data as a function of redshift. The first, and most common, is to select contiguous, and often equally spaced, z-intervals based on the characteristics of the sample (e.g., Noterdaeme *et al.*, 2012; Prochaska & Wolfe, 2009). This aproach has the advantage of being intuitive and computationally straight-forward. However, if the redshift path is very uneven, it can lead to large variations in the statistical uncertainties in $\Omega_{\rm HI}$ as a function of redshift. The alternative method is to set the redshift intervals of each $\Omega_{\rm HI}$ bin such that it uniformly samples the total absorption path (e.g., Guimarães *et al.*, 2009; Noterdaeme *et al.*, 2009). The redshift bin sizes may therefore be heterogeneous, but each bin is statistically similar. However, both of these methods adopt contiguous, non-overlapping bins to discretize the data.

In this work, we take a different approach. Instead of computing $\Omega_{\rm HI}^{\rm DLA}$ in contiguous, non-overlapping intervals, we sample the redshift distribution finely using a sliding redshift window to compute an $\Omega_{\rm HI}^{\rm DLA}(z)$ 'curve'. The computation of $\Omega_{\rm HI}^{\rm DLA}$ is still based on the summation of N(H I) between a given $z_{\rm min}$ and $z_{\rm max}$. However, we consider all $z_{\rm min}$ and $z_{\rm max}$ pairs over the full redshift range of our sample, beginning at the minimum redshift where $g(z)>0$, and incrementing $z_{\rm min}$ by 0.001. The $z_{\rm max}$ at each point in the $\Omega_{\rm HI}^{\rm DLA}$curve can be computed analogously to the two traditional methods described above: In the

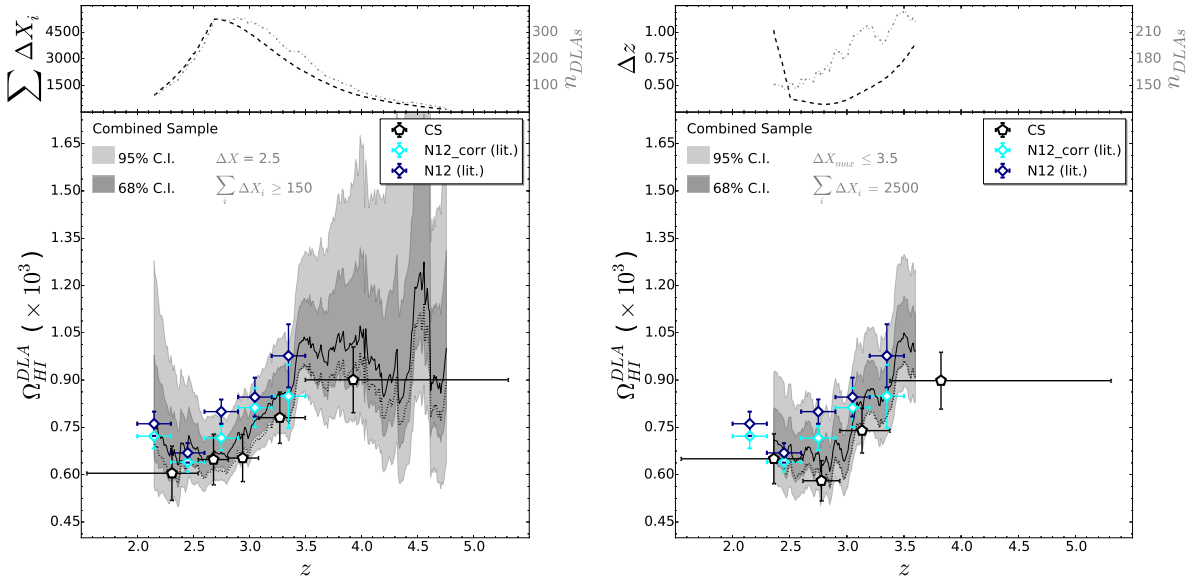

Figure 1.8: $\Omega_{\rm HI}^{\rm DLA}$curves for the combined sample using fixed comoving redshift intervals (left) and fixed total absorption path (right). 68 and 95 per cent confidence intervals derived from the BCa technique are shown in the shaded regions. Black line is the uncorrected curve. For comparison, we show the high column density correction applied to N12 results in order to have in both samples a maximum column density contribution of $\log N(\mathrm{H\,I})$=21.75, and the conventional representation of discrete bias-uncorrected $\Omega_{\rm HI}^{\rm DLA}$ points for the combined sample. Upper subpanel for each plot represents the redshift range or the total absorption path probed to build up the curve (black) and the number of DLAs used for the computations (grey).

first technique, we simply define the $z_{\rm max}$ of each $\Omega_{\rm HI}^{\rm DLA}$ curve point to be $z_{\rm max}$=$z_{\rm min}$+Δz, where Δz is determined by imposing a constant ΔX (in the example below, we use ΔX = 2.5) and using eq. 1.4. The resulting mean redshift of the interval is weighted by the $g(z)$ curve. As a result of the weighting procedure, several ($z_{\rm min}$, $z_{\rm max}$) pairs can lead to a computation of $\Omega_{\rm HI}^{\rm DLA}$ at the same mean z; when this occurs, we take the median $\Omega_{\rm HI}^{\rm DLA}$ of the duplications. Although simple in its approach, the uneven distribution of redshift coverage in our sample leads to some redshift intervals being better sampled than others. The second approach mitigates this effect by setting the $z_{\rm max}$ dynamically for each $z_{\rm min}$, so that each (z, $\Omega_{\rm HI}^{\rm DLA}$) point has the same total absorption path contributing to it (in the example below, we use $\Sigma\ \Delta X = 2500$). In this approach, we compute the z for each redshift interval by again weighting for the $g(z)$ curve in that interval. As with the first method, when multiple ($z_{\rm min}$, $z_{\rm max}$) pairs lead more than one bin to have the same mean redshift, we take the median $\Omega_{\rm HI}^{\rm DLA}$ of the duplications.

In Figure 1.8 we compare both binning methods for computing $\Omega_{\rm HI}^{\rm DLA}$ for the final combined sample, where the grey shaded regions show the 68 and 95 per cent confidence intervals determined from the BCa method described in the previous subsection. The $\Omega_{\rm HI}^{\rm DLA}$ curves are shown in the main (lower) panels and the upper panels show absorption paths/intervals (black dashed line) and number of DLAs (grey dotted line) as a function of z. The first conclusion we can draw from a comparison of the curves in Figure 1.8 is that both binning methods yield curves of $\Omega_{\rm HI}^{\rm DLA}$ that are statistically equivalent in the range $2.2 < z < 3.6$ where they can both be computed. In both cases, there is a scatter whose magnitude is inversely proportional to the number of absorbers used to compute statistics. This scatter originates from the limited sampling that draws different absorber distributions for each computed point. This effect is especially evident when high column density absorbers are included or not in a given bin. Therefore, although using a fixed total absorption path (right panel) theoretically smooths any uneven sampling, the contribution of the SDSS dominates in the redshift range where both techniques can be applied and the statistics are relatively uniform anyway. One of the most notable differences between the binning methods shown in Figure 1.8 is that a fixed total absorption path (right panel) greatly restricts the redshift range over which the curve can be computed. This is due to 'running out' of redshift path as the curve is built up towards higher z. This truncation can be mitigated by reducing the choice of $\Sigma\ \Delta X$, although in turn this is a compromise in the uncertainty. Using a fixed ΔX interval is therefore our preferred binning method.

Having constructed the $\Omega_{\rm HI}^{\rm DLA}$ curves, that we tabulate for the CS in Table 1.6 for ease of reproduction, it is interesting to compare the results to the more classical binning approach. For the combined sample, the binned-uncorrected values are shown with black symbols in Fig. 1.8, as well as the bias-uncorrected curve plotted in black. Different

redshift bins select different DLAs, which cause the small variations between both uncorrected data points and curve. Larger effects are corrected when taking into account fitting uncertainties, as we can observe when comparing the uncorrected curve with BCa confidence intervals. However, when we plot together these intervals and the N12 points (dark blue), the latter are systematically above (although still consistent within the confidence intervals) the values for the CS.

We investigate whether the values measured by N12 are higher due to a more complete sampling of the high column density end of the distribution function by those authors, i.e. whether the combined sample's incompleteness at high N(H I) may cause an underestimate of $\Omega_{\rm HI}^{\rm DLA}$. For this purpose, we also computed $\Omega_{\rm HI}^{\rm DLA}$ by integrating $f_{\rm HI}(N,X)$. In Table 1.7 we show the results of integrating up to $\log N$(H I)=21.7 (the upper limit of our DLA sample, denoted in the table by ^{max}) and to $\log N$(H I)=∞. We observe, as expected, a very good agreement between our summed $\Omega_{\rm HI}^{\rm DLA}$ (e.g. 0.97×10^{-3} for the redshift unbinned CS) and the partially integrated one (0.94×10^{-3}), being inside the derived confidence intervals for all bins. However, the difference between the partial and fully integrated values (1.16×10^{-3} for the full combined sample) indicates that our values may still be under-estimated due to our limited sample size. Our confidence intervals are actually rigorous as long as the bootstrap hypothesis is fulfilled, but we remark the fact that this technique cannot infer the information on the real population that is not contained in the combined sample. This hypothesis could be true if the contribution of the absorbers with higher column densities than $\log N$(H I)$\sim$21.7 (in our case) is negligible. However, the extrapolated broken power law fit results, supported by N12 (and B12) observations, suggest that these absorbers play an important role ($\approx 20\%$) in the value of the hydrogen gas mass density. If we impose the same maximum $\log N$(H I) = 21.7 threshold for the N12 sample as applies to the combined sample, integrating the $f_{\rm HI}(N,X)$ for the SDSS/BOSS sample yields a slightly lower value of $\Omega_{\rm HI}^{\rm DLA}$ that is now nicely consistent with the combined sample (cyan points in Fig. 1.8), confirming the equivalency of both samples over their common redshift range.

CS CURVE

z	Δz	ΔX	n_{abs}	$\Omega_{\rm HI}^{\rm DLA}$	68% C.I.		95% C.I.	
2.150	0.832	982	63	0.696	0.651	0.958	0.566	1.249
2.160	0.831	1016	66	0.681	0.640	0.935	0.559	1.231

Continued on Next Page...

Table 1.6 – Continued

z	Δz	ΔX	n_{abs}	$\Omega_{\rm HI}^{\rm DLA}$	68% C.I.		95% C.I.	
2.170	0.830	1071	68	0.659	0.620	0.908	0.542	1.190
2.180	0.828	1112	70	0.686	0.644	0.933	0.560	1.175
2.190	0.827	1174	70	0.650	0.611	0.882	0.531	1.123
2.200	0.826	1201	70	0.635	0.597	0.862	0.519	1.088
2.210	0.824	1291	76	0.633	0.602	0.843	0.529	1.069
2.220	0.822	1325	80	0.633	0.602	0.845	0.527	1.055
2.230	0.821	1400	85	0.633	0.605	0.842	0.535	1.043
2.240	0.819	1475	89	0.620	0.595	0.814	0.528	1.006
2.250	0.817	1520	91	0.608	0.582	0.793	0.517	0.968
2.260	0.815	1596	96	0.619	0.596	0.810	0.531	0.976
2.270	0.813	1645	98	0.604	0.584	0.792	0.522	0.983
2.280	0.812	1701	100	0.594	0.576	0.775	0.512	0.954
2.290	0.810	1773	105	0.585	0.567	0.760	0.508	0.925
2.300	0.808	1840	111	0.606	0.586	0.777	0.526	0.937
2.310	0.806	1895	115	0.606	0.587	0.774	0.530	0.915
2.320	0.805	1950	115	0.589	0.572	0.757	0.517	0.906
2.330	0.802	2036	119	0.604	0.588	0.767	0.529	0.911
2.340	0.801	2079	119	0.591	0.575	0.753	0.520	0.890
2.350	0.800	2128	122	0.584	0.569	0.743	0.512	0.879
2.360	0.798	2215	126	0.567	0.552	0.718	0.498	0.844
2.370	0.795	2314	133	0.568	0.553	0.712	0.500	0.837
2.380	0.795	2327	134	0.583	0.567	0.727	0.514	0.843
2.390	0.791	2446	148	0.633	0.618	0.777	0.563	0.892
2.400	0.790	2504	152	0.631	0.619	0.776	0.563	0.890
2.410	0.788	2582	158	0.633	0.619	0.772	0.565	0.875
2.420	0.787	2653	161	0.622	0.611	0.765	0.560	0.871
2.430	0.785	2705	160	0.606	0.593	0.740	0.540	0.845
2.440	0.783	2811	170	0.615	0.604	0.750	0.552	0.856
2.450	0.780	2918	183	0.631	0.621	0.766	0.570	0.867
2.460	0.778	3021	190	0.655	0.645	0.788	0.592	0.880
2.470	0.777	3069	191	0.647	0.638	0.778	0.586	0.873
2.480	0.775	3174	195	0.634	0.626	0.762	0.576	0.853

Continued on Next Page...

Table 1.6 – Continued

z	Δz	ΔX	n_{abs}	$\Omega_{\rm HI}^{\rm DLA}$	68% C.I.		95% C.I.	
2.490	0.772	3292	202	0.627	0.621	0.755	0.574	0.843
2.500	0.771	3362	204	0.619	0.612	0.741	0.566	0.831
2.510	0.768	3488	213	0.619	0.613	0.737	0.567	0.826
2.520	0.766	3610	222	0.622	0.617	0.740	0.572	0.817
2.530	0.764	3702	228	0.624	0.619	0.742	0.575	0.818
2.540	0.762	3781	234	0.612	0.609	0.722	0.566	0.793
2.550	0.760	3920	241	0.609	0.606	0.717	0.564	0.783
2.560	0.758	4015	245	0.600	0.600	0.708	0.559	0.780
2.570	0.757	4097	248	0.597	0.598	0.703	0.557	0.768
2.580	0.754	4221	252	0.586	0.586	0.691	0.547	0.754
2.590	0.752	4330	263	0.584	0.586	0.687	0.548	0.749
2.600	0.749	4482	278	0.584	0.587	0.688	0.549	0.747
2.610	0.748	4554	284	0.598	0.600	0.701	0.562	0.764
2.620	0.746	4646	294	0.600	0.603	0.703	0.563	0.764
2.630	0.743	4842	314	0.609	0.614	0.712	0.577	0.773
2.640	0.741	4917	321	0.608	0.611	0.708	0.573	0.767
2.650	0.739	5054	332	0.610	0.615	0.711	0.578	0.767
2.660	0.738	5121	337	0.610	0.615	0.708	0.579	0.768
2.670	0.735	5279	355	0.617	0.625	0.717	0.589	0.774
2.680	0.733	5375	365	0.613	0.619	0.711	0.583	0.765
2.690	0.731	5415	370	0.622	0.628	0.723	0.591	0.779
2.700	0.730	5414	371	0.615	0.622	0.715	0.586	0.772
2.710	0.728	5410	376	0.617	0.627	0.718	0.592	0.773
2.720	0.727	5405	374	0.616	0.626	0.715	0.592	0.772
2.730	0.726	5398	373	0.614	0.624	0.713	0.587	0.767
2.740	0.725	5391	375	0.616	0.625	0.716	0.588	0.770
2.750	0.723	5371	374	0.620	0.627	0.719	0.591	0.772
2.760	0.722	5361	377	0.615	0.624	0.715	0.590	0.769
2.770	0.721	5350	378	0.617	0.626	0.713	0.590	0.766
2.780	0.720	5333	377	0.615	0.624	0.713	0.590	0.769
2.790	0.718	5309	370	0.612	0.620	0.709	0.585	0.764
2.800	0.717	5289	365	0.606	0.614	0.704	0.579	0.763

Continued on Next Page...

Table 1.6 – Continued

z	Δz	ΔX	n_{abs}	$\Omega_{\rm HI}^{\rm DLA}$	68% C.I.		95% C.I.	
2.810	0.716	5276	366	0.617	0.625	0.715	0.591	0.769
2.820	0.715	5253	368	0.617	0.626	0.714	0.590	0.767
2.830	0.714	5233	368	0.624	0.635	0.726	0.600	0.782
2.840	0.712	5197	369	0.633	0.642	0.732	0.606	0.784
2.850	0.711	5176	374	0.639	0.648	0.739	0.613	0.793
2.860	0.711	5171	375	0.645	0.654	0.745	0.618	0.798
2.870	0.709	5138	377	0.651	0.662	0.754	0.627	0.806
2.880	0.708	5103	379	0.655	0.665	0.755	0.628	0.812
2.890	0.706	5062	380	0.662	0.673	0.765	0.635	0.818
2.900	0.705	5036	382	0.669	0.678	0.770	0.642	0.825
2.910	0.704	5000	382	0.678	0.689	0.781	0.652	0.836
2.920	0.703	4970	379	0.668	0.680	0.773	0.643	0.827
2.930	0.702	4938	376	0.667	0.677	0.770	0.640	0.828
2.940	0.701	4911	376	0.671	0.684	0.778	0.647	0.836
2.950	0.699	4856	373	0.675	0.684	0.779	0.647	0.839
2.960	0.698	4821	378	0.690	0.702	0.797	0.665	0.853
2.970	0.697	4787	378	0.690	0.701	0.798	0.663	0.858
2.980	0.696	4737	374	0.683	0.695	0.791	0.658	0.851
2.990	0.695	4695	365	0.674	0.683	0.781	0.646	0.843
3.000	0.694	4651	363	0.669	0.679	0.776	0.642	0.836
3.010	0.693	4612	365	0.680	0.689	0.788	0.651	0.848
3.020	0.692	4562	365	0.692	0.703	0.799	0.666	0.860
3.030	0.691	4533	365	0.699	0.711	0.812	0.674	0.872
3.040	0.689	4463	363	0.706	0.718	0.819	0.679	0.886
3.050	0.688	4412	361	0.713	0.726	0.829	0.687	0.895
3.060	0.687	4355	358	0.714	0.727	0.829	0.688	0.891
3.070	0.687	4351	358	0.714	0.726	0.828	0.686	0.892
3.080	0.686	4301	358	0.722	0.733	0.837	0.692	0.899
3.090	0.684	4213	349	0.715	0.728	0.831	0.688	0.896
3.100	0.684	4181	349	0.722	0.733	0.835	0.694	0.899
3.110	0.683	4156	348	0.724	0.735	0.839	0.695	0.901
3.120	0.682	4097	344	0.731	0.743	0.851	0.703	0.922

Continued on Next Page...

Table 1.6 – Continued

z	Δz	ΔX	n_{abs}	$\Omega_{\rm HI}^{\rm DLA}$	68% C.I.		95% C.I.	
3.130	0.681	4055	340	0.732	0.741	0.851	0.702	0.916
3.140	0.680	3990	338	0.734	0.745	0.855	0.705	0.924
3.150	0.679	3951	337	0.740	0.752	0.860	0.710	0.929
3.160	0.678	3895	337	0.749	0.760	0.872	0.718	0.944
3.170	0.677	3834	330	0.762	0.771	0.886	0.725	0.952
3.180	0.677	3816	328	0.761	0.770	0.886	0.727	0.957
3.190	0.676	3751	317	0.753	0.761	0.879	0.716	0.954
3.200	0.675	3693	309	0.740	0.749	0.864	0.707	0.935
3.210	0.674	3650	306	0.759	0.765	0.886	0.720	0.962
3.220	0.673	3594	300	0.767	0.774	0.896	0.727	0.977
3.230	0.672	3538	294	0.759	0.764	0.887	0.717	0.966
3.240	0.672	3529	295	0.762	0.770	0.894	0.722	0.975
3.250	0.671	3459	286	0.768	0.772	0.899	0.723	0.981
3.260	0.670	3402	282	0.772	0.778	0.908	0.731	0.991
3.270	0.669	3368	278	0.765	0.771	0.900	0.723	0.985
3.280	0.668	3317	275	0.771	0.775	0.909	0.725	0.993
3.290	0.667	3265	272	0.772	0.778	0.909	0.727	1.000
3.300	0.666	3211	267	0.774	0.778	0.913	0.727	1.002
3.310	0.666	3181	264	0.774	0.778	0.914	0.728	1.007
3.320	0.664	3103	260	0.768	0.771	0.899	0.722	0.979
3.330	0.664	3066	256	0.767	0.773	0.904	0.722	0.987
3.340	0.664	3054	255	0.768	0.774	0.906	0.724	0.985
3.350	0.662	2990	246	0.754	0.757	0.885	0.708	0.966
3.360	0.662	2953	243	0.756	0.756	0.886	0.709	0.970
3.370	0.661	2909	244	0.778	0.780	0.914	0.731	0.997
3.380	0.660	2873	243	0.790	0.791	0.926	0.741	1.016
3.390	0.659	2811	242	0.795	0.795	0.934	0.744	1.027
3.400	0.658	2773	240	0.807	0.810	0.948	0.758	1.037
3.410	0.658	2734	238	0.841	0.841	0.999	0.782	1.109
3.420	0.657	2675	236	0.865	0.867	1.033	0.806	1.141
3.430	0.656	2651	237	0.882	0.884	1.055	0.824	1.169
3.440	0.655	2608	240	0.901	0.902	1.071	0.841	1.187

Continued on Next Page...

Table 1.6 – Continued

z	Δz	ΔX	n_{abs}	$\Omega_{\rm HI}^{\rm DLA}$	68% C.I.		95% C.I.	
3.450	0.655	2584	240	0.927	0.930	1.108	0.862	1.228
3.460	0.654	2533	232	0.912	0.911	1.093	0.844	1.217
3.470	0.653	2487	230	0.915	0.910	1.096	0.846	1.219
3.480	0.652	2439	226	0.919	0.919	1.103	0.852	1.239
3.490	0.651	2421	227	0.928	0.926	1.116	0.856	1.247
3.500	0.650	2377	216	0.914	0.911	1.108	0.841	1.244
3.510	0.650	2346	213	0.915	0.912	1.108	0.842	1.247
3.520	0.649	2325	211	0.919	0.915	1.114	0.845	1.252
3.530	0.648	2283	205	0.902	0.897	1.094	0.827	1.231
3.540	0.647	2247	203	0.925	0.918	1.120	0.844	1.263
3.550	0.646	2206	194	0.894	0.888	1.092	0.816	1.235
3.560	0.646	2179	192	0.899	0.890	1.095	0.818	1.244
3.570	0.645	2142	189	0.895	0.888	1.096	0.813	1.243
3.580	0.644	2090	186	0.881	0.873	1.079	0.801	1.223
3.590	0.643	2070	184	0.880	0.873	1.079	0.801	1.225
3.600	0.642	2036	181	0.878	0.870	1.087	0.798	1.230
3.610	0.642	2010	174	0.861	0.849	1.062	0.777	1.226
3.620	0.641	1970	170	0.865	0.853	1.069	0.776	1.227
3.630	0.640	1937	167	0.875	0.865	1.086	0.787	1.247
3.640	0.639	1903	164	0.891	0.878	1.097	0.801	1.266
3.650	0.638	1859	160	0.871	0.861	1.089	0.787	1.249
3.660	0.638	1825	154	0.860	0.844	1.074	0.769	1.245
3.670	0.637	1820	153	0.849	0.836	1.065	0.758	1.250
3.680	0.637	1783	149	0.854	0.837	1.066	0.757	1.237
3.690	0.635	1735	144	0.852	0.835	1.074	0.756	1.256
3.700	0.635	1704	142	0.847	0.828	1.064	0.748	1.231
3.710	0.634	1682	143	0.886	0.865	1.113	0.783	1.297
3.720	0.633	1632	138	0.885	0.860	1.112	0.776	1.290
3.730	0.633	1630	138	0.887	0.866	1.118	0.783	1.304
3.740	0.632	1581	134	0.882	0.862	1.126	0.777	1.335
3.750	0.631	1563	133	0.889	0.868	1.135	0.782	1.340
3.760	0.630	1523	130	0.877	0.854	1.116	0.765	1.324

Continued on Next Page...

Table 1.6 – Continued

z	Δz	ΔX	n_{abs}	$\Omega_{\rm HI}^{\rm DLA}$	68% C.I.		95% C.I.	
3.770	0.630	1501	130	0.890	0.862	1.127	0.774	1.332
3.780	0.629	1470	127	0.902	0.878	1.152	0.793	1.362
3.790	0.629	1444	126	0.915	0.884	1.164	0.791	1.373
3.800	0.628	1427	124	0.922	0.894	1.179	0.803	1.393
3.810	0.627	1393	118	0.895	0.869	1.156	0.781	1.382
3.820	0.626	1361	115	0.899	0.872	1.161	0.781	1.378
3.830	0.626	1337	115	0.915	0.884	1.181	0.793	1.406
3.840	0.625	1316	115	0.924	0.899	1.199	0.804	1.426
3.850	0.624	1277	112	0.883	0.858	1.136	0.769	1.353
3.860	0.624	1263	111	0.874	0.848	1.132	0.760	1.374
3.870	0.623	1232	107	0.877	0.851	1.137	0.762	1.389
3.880	0.623	1228	107	0.881	0.851	1.150	0.763	1.377
3.890	0.622	1194	108	0.889	0.860	1.158	0.769	1.408
3.900	0.621	1169	106	0.898	0.866	1.157	0.775	1.418
3.910	0.621	1146	104	0.898	0.864	1.165	0.770	1.430
3.920	0.620	1133	102	0.899	0.868	1.184	0.773	1.468
3.930	0.620	1117	98	0.896	0.862	1.171	0.767	1.438
3.940	0.619	1086	92	0.891	0.853	1.164	0.760	1.455
3.950	0.618	1064	88	0.910	0.873	1.197	0.777	1.487
3.960	0.618	1051	85	0.883	0.846	1.169	0.749	1.453
3.970	0.617	1031	83	0.891	0.853	1.185	0.756	1.487
3.980	0.616	1013	83	0.898	0.861	1.189	0.760	1.484
3.990	0.616	996	83	0.938	0.901	1.243	0.793	1.534
4.000	0.615	973	80	0.917	0.874	1.222	0.767	1.526
4.010	0.614	958	77	0.905	0.863	1.223	0.757	1.543
4.020	0.614	940	74	0.904	0.865	1.228	0.752	1.574
4.030	0.613	916	73	0.888	0.848	1.173	0.733	1.427
4.040	0.612	902	73	0.908	0.864	1.205	0.761	1.482
4.050	0.612	891	71	0.866	0.830	1.156	0.730	1.412
4.060	0.611	874	68	0.826	0.787	1.107	0.687	1.386
4.070	0.610	848	65	0.799	0.761	1.056	0.667	1.300
4.080	0.610	839	65	0.807	0.774	1.086	0.680	1.362

Continued on Next Page...

Table 1.6 – Continued

z	Δz	ΔX	n_{abs}	$\Omega_{\rm HI}^{\rm DLA}$	68% C.I.		95% C.I.	
4.090	0.609	822	64	0.818	0.783	1.099	0.687	1.351
4.100	0.609	808	63	0.816	0.773	1.091	0.673	1.351
4.110	0.608	795	62	0.807	0.770	1.091	0.671	1.377
4.120	0.608	785	61	0.811	0.772	1.093	0.675	1.381
4.130	0.607	764	60	0.782	0.748	1.053	0.656	1.340
4.140	0.606	753	59	0.786	0.750	1.062	0.661	1.362
4.150	0.606	739	59	0.794	0.751	1.059	0.655	1.340
4.160	0.605	725	58	0.802	0.761	1.084	0.663	1.345
4.170	0.604	705	56	0.755	0.719	1.027	0.628	1.345
4.180	0.604	691	55	0.743	0.715	1.044	0.627	1.387
4.190	0.603	675	50	0.694	0.656	0.980	0.569	1.344
4.200	0.603	663	47	0.691	0.655	0.987	0.567	1.330
4.210	0.602	650	45	0.690	0.652	0.993	0.564	1.348
4.220	0.601	639	45	0.702	0.664	1.007	0.572	1.383
4.230	0.601	626	45	0.717	0.677	1.027	0.584	1.403
4.240	0.600	613	45	0.732	0.692	1.050	0.599	1.458
4.250	0.600	606	45	0.740	0.701	1.058	0.603	1.441
4.260	0.599	593	43	0.734	0.693	1.060	0.598	1.448
4.270	0.598	576	40	0.710	0.661	1.035	0.565	1.477
4.280	0.598	566	40	0.722	0.672	1.044	0.577	1.436
4.290	0.597	557	40	0.734	0.685	1.078	0.590	1.512
4.300	0.597	543	40	0.750	0.705	1.104	0.601	1.579
4.310	0.596	532	40	0.765	0.714	1.114	0.606	1.569
4.320	0.595	522	39	0.770	0.717	1.134	0.609	1.634
4.330	0.595	510	34	0.643	0.598	0.981	0.507	1.476
4.340	0.594	504	33	0.620	0.572	0.953	0.486	1.587
4.350	0.593	486	31	0.626	0.575	0.978	0.487	1.460
4.360	0.593	483	31	0.630	0.583	0.985	0.490	1.569
4.370	0.592	469	30	0.627	0.576	0.995	0.483	1.595
4.380	0.592	460	30	0.641	0.589	1.024	0.495	1.550
4.390	0.591	450	31	0.667	0.615	1.045	0.518	1.619
4.400	0.591	441	31	0.682	0.629	1.067	0.532	1.634

Continued on Next Page...

Table 1.6 – Continued

z	Δz	ΔX	n_{abs}	$\Omega_{\rm HI}^{\rm DLA}$	68% C.I.		95% C.I.	
4.410	0.590	435	31	0.690	0.640	1.102	0.539	1.735
4.420	0.589	422	30	0.699	0.646	1.113	0.538	1.791
4.430	0.589	414	30	0.713	0.650	1.111	0.544	1.689
4.440	0.588	403	31	0.752	0.699	1.190	0.587	1.869
4.450	0.588	397	32	0.807	0.751	1.250	0.632	1.962
4.460	0.587	385	31	0.803	0.744	1.238	0.625	1.883
4.470	0.587	376	33	0.871	0.809	1.328	0.682	1.939
4.480	0.586	368	34	0.917	0.864	1.415	0.734	2.106
4.490	0.585	356	30	0.902	0.834	1.377	0.703	1.986
4.500	0.585	350	30	0.916	0.851	1.404	0.714	2.125
4.510	0.584	340	29	0.920	0.854	1.417	0.714	2.107
4.520	0.584	333	29	0.939	0.870	1.451	0.735	2.169
4.530	0.583	321	28	0.937	0.868	1.491	0.730	2.220
4.540	0.583	315	27	0.886	0.815	1.446	0.681	2.310
4.550	0.582	308	27	0.906	0.833	1.477	0.700	2.365
4.560	0.582	302	28	0.958	0.880	1.514	0.740	2.497
4.570	0.581	289	25	0.836	0.772	1.387	0.652	2.608
4.580	0.580	283	25	0.854	0.782	1.395	0.662	2.394
4.590	0.580	275	25	0.879	0.810	1.450	0.687	2.627
4.600	0.579	269	25	0.898	0.824	1.479	0.696	2.767
4.610	0.579	262	23	0.880	0.804	1.490	0.675	2.719
4.620	0.578	251	21	0.666	0.620	0.930	0.523	1.168
4.630	0.577	243	21	0.687	0.643	0.965	0.543	1.221
4.640	0.577	234	20	0.648	0.606	0.906	0.510	1.159
4.650	0.576	229	21	0.696	0.659	0.984	0.559	1.231
4.660	0.576	220	20	0.686	0.643	0.977	0.542	1.250
4.670	0.575	217	20	0.694	0.649	0.981	0.548	1.272
4.680	0.574	206	17	0.656	0.603	0.939	0.499	1.217
4.690	0.574	200	16	0.648	0.600	0.944	0.491	1.239
4.700	0.574	195	16	0.662	0.613	0.970	0.501	1.273
4.710	0.573	186	15	0.631	0.579	0.937	0.470	1.233
4.720	0.572	180	15	0.652	0.599	0.965	0.487	1.291

Continued on Next Page...

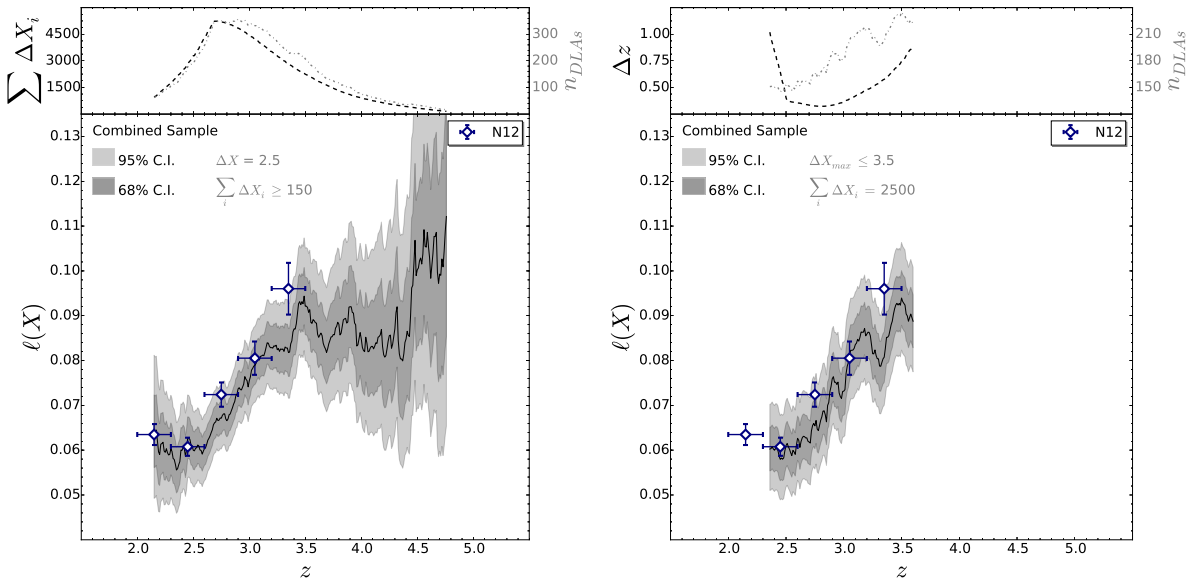

Figure 1.9: $\ell(X)$ curves for the combined sample using fixed comoving redshift intervals (left) and fixed total absorption path (right). 68 and 95 per cent confidence intervals are derived assiming a Poisson distribution. Solid line represents the value computed directly from eq. 1.11

Table 1.6 – Continued

z	Δz	ΔX	n_{abs}	$\Omega_{\rm HI}^{\rm DLA}$	68% C.I.		95% C.I.	
4.730	0.572	172	14	0.647	0.587	0.970	0.477	1.301
4.740	0.571	167	14	0.670	0.607	0.999	0.490	1.338
4.750	0.570	160	14	0.698	0.635	1.045	0.513	1.374
4.760	0.570	154	14	0.723	0.660	1.080	0.530	1.437
4.770	0.569	150	13	0.724	0.655	1.085	0.526	1.447

Table 1.6: CS curve

1.4.4 DLA incidence rate

The DLA incidence rate $\ell(X)$, or line density, is defined as the zeroth moment of $f_{\rm HI}(N, X)$

$$\ell(X)dX = \int_{N_{min}}^{N_{max}} f_{HI}(N, z)dNdX \tag{1.10}$$

Its discrete limit, commonly used to compute this quantity, is given by

$$\ell(X) = \frac{m}{\sum_i \Delta X_i} \tag{1.11}$$

i.e., it is the number of DLAs found per unit comoving redshift path.

In this analysis, for the error estimation we assumed a Poisson distribution. This is because the main variation we can expect using the B-MC technique is from the effect of the low N(H I) absorbers crossing the DLA limit from one side to the other. However, the major source of uncertainty in the column density distribution function is from the poor sampling of the highest column density absorbers. We show line density curves in Figure 1.9, built up using the same binning techniques as for $\Omega_{\rm HI}^{\rm DLA}$. Here, we can observe again an excellent agreement with the N12 results: from $z \sim 2$ to 3.5 where the samples overlap a significant increase in the line density of DLAs is seen. At higher redshifts, the limited statistics prevent us from distinguishing whether $\ell(X)$ continues to rise, or flattens, although a steep evolution is not supported by the current dataset (Crighton *et al.*, 2015).

1.5 Discussion

We have presented a new survey for DLAs based on spectra obtained for the XQ-100 survey, an X-shooter Large Program to observe 100 $z > 3.5$ QSOs (Lopez et al. A&A **submitted**). The 38 DLAs identified in the XQ-100 sample are combined with major literature samples compiled over the last $\sim$ 20 years, with close attention paid to duplications, yielding a total of 742 DLAs over a redshift range of approximately $1.6 < z < 5.0$. The total redshift path of the combined sample is ΔX = 10,434. We have described a thorough assessment of error estimators, and the relative contributions of fitting and sampling errors appropriate for our combined sample. A novel technique for binning the DLA statistics is presented, which yields continuous $\Omega_{\rm HI}^{\rm DLA}$ 'curves' rather than discretized binned values. A comparison with the limited redshift range covered by the Noterdaeme *et al.* (2012) sample of DLAs in the SDSS/BOSS indicates that, despite the large size of

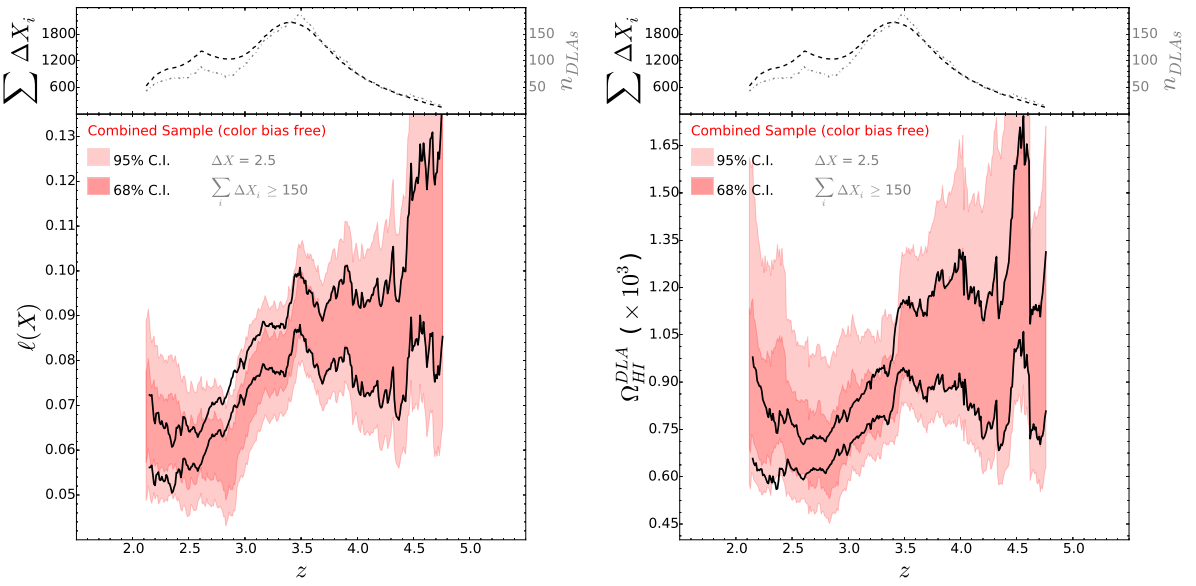

Figure 1.10: $\ell(X)$ (left) and $\Omega_{\rm HI}^{\rm DLA}$(right) curves for our color bias free sub-sample. The solid black lines represent the full CS 68% confidence limits.

our total sample, $\Omega_{\rm HI}^{\rm DLA}$ may still be under-estimated due to the absence of very high column density ($\log N({\rm H\,I}) > 21.7$) DLAs. Looking at Table 1.7, extrapolation of the whole combined sample indicates that the missing contribution of these absorbers is $\sim$20% for our sample. However, this correction could be redshift-dependent. Statistics at large column densities are too poor when splitting the sample, and this could also lead to incorrect extrapolations, as inferred from Table 1.7. Consequently, yet larger samples are needed in order to precisely constrain the impact of high column density DLAs on $\Omega_{\rm HI}$ evolution.

On the other hand, low column density DLAs are sufficiently well sampled to offer narrow $\Omega_{\rm HI}^{\rm DLA}$ confidence intervals. This means that relatively small effects in sample selection that have been previously neglected could now become important. One such example is the false positives/negatives issue, that might represent an important systematic uncertainty. Results from Crighton *et al.* (2015) and the excellent agreement within our CS and N12 distribution functions, that were obtained using different methods, suggest that still we are not able to distinguish this effect from the sampling uncertainties.

Another source of error could be due to the SDSS color-selection of QSOs (see Prochaska *et al.*, 2009; Worseck & Prochaska, 2011). In order to investigate this effect, we built up a sub-sample of our CS composed only of 'safe' quasars, i.e., we excluded 10 biased XQ-100 QSOs (flagged in Table 1.1 with spades), SDSS quasars not flagged as selected by its FIRST counterpart with $2.7<z_{\rm em}<3.6$, and the P03 sample. Results are shown in Figure 1.10. We observe that, at this sample size (3152 QSOs and 402 DLAs), there is no strong evidence of the effects of this bias in $\Omega_{\rm HI}^{\rm DLA}$. However, from the $\ell(X)$ plot we can see a

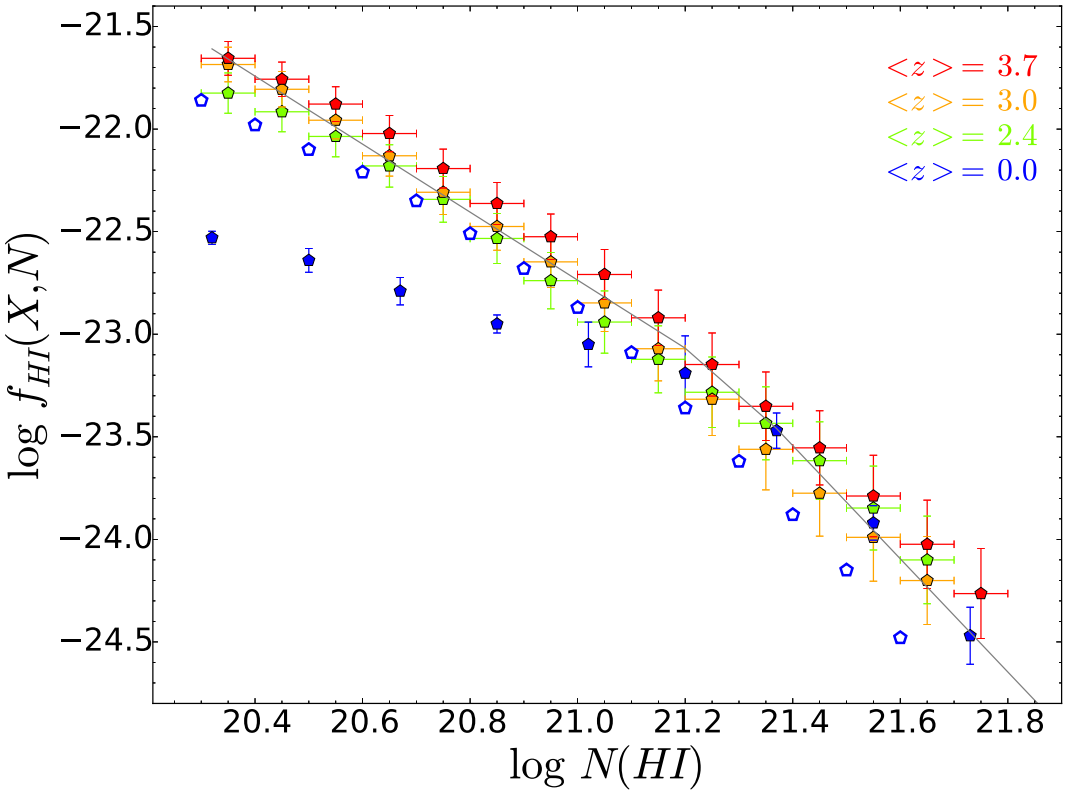

Figure 1.11: Column density distribution function of the CS 3 redshift bins compared with N12 (green points), B12 (filled blue points) and Z05 (unfilled blue points). The black line is the broken power law (BPL) fit of the whole CS.

small decrease in the incidence rate at $z\sim2.8$, consistent with what we might expect, and suggesting that this color bias could be important in larger samples.

In Fig. 1.11 we investigate whether the column density distribution function varies with redshift by comparing our $f_{\rm HI}(N,X)$ results split in 3 redshift bins with Z05 and B12 representing the local universe. Although the error bars for the 3 redshift bins of the CS overlap, there is a systematic trend for lower redshift intervals to have a lower normalization of $f_{\rm HI}(N,X)$ for moderate and low column density absorbers ($\log N({\rm H\,I}) < 20.9$). At high $N({\rm H\,I})$ there is more scatter amongst the points, due to poorer statistics, such that it is not possible to conclude if the evolution extends over the full column density range.

In Fig. 1.12 we plot the $\Omega_{\rm HI}^{\rm DLA}$ curve we derived down to $z\sim2$, together with DLA surveys conducted at lower redshift (see Neeleman *et al.*, 2016; Rao *et al.*, 2006, and references therein) and $\Omega_{\rm HI}$ from 21 cm emission surveys (the different selection techniques, sparse sampling at intermediate z, and contrast in measurement techniques mean that it is not appropriate to combine these measurements into our computation of the $\Omega_{\rm HI}^{\rm DLA}$ curve).

Table 1.7: Double power law fitting parameters and first moment of the $f_{\rm HI}(N,X)$. All values of $\Omega_{\rm HI}^{\rm DLA}$ are in units of 10^{-3}

z	$z_{\rm min}$	$z_{\rm max}$	n_{abs}	ΔX	log N_d	log k_d	α_{1d}	α_{2d}	$\Omega_{\rm HI}^{\rm DLA}{}_d^{max}$	$\Omega_{\rm HI}^{\rm DLA}{}_d^{\infty}$	$\Omega_{\rm HI}^{\rm DLA}$	$\Omega_{\rm HI}^{\rm DLA}$68% C.I.
2.99	1.550	5.313	742	10434	21.27	-23.18	-1.66	-2.77	0.94	1.16	0.97	0.93 - 1.03
2.57	1.550	2.947	318	5219	21.27	-23.26	-1.67	-2.41	0.60	1.02	0.65	0.60 - 0.71
3.47	2.947	5.313	424	5219	21.27	-23.12	-1.65	-2.74	0.83	1.05	0.85	0.80 - 0.92
2.44	1.550	2.732	208	3482	21.27	-23.26	-1.63	-2.16	0.62	1.65	0.67	0.61 - 0.74
2.95	2.732	3.207	235	3482	21.27	-23.26	-1.77	-2.64	0.63	0.86	0.64	0.58 - 0.70
3.69	3.207	5.313	300	3482	21.27	-23.08	-1.62	-2.53	0.93	1.34	0.95	0.88 - 1.05

A critical debate in the literature, that has been ongoing since the first measurements of $\Omega_{\rm HI}^{\rm DLA}$, is whether or not this quantity evolves with redshift. In order to *statistically* investigate whether the data favors (or not) an evolution of the H I content in the universe over cosmic time, we performed the following test: For each non overlapping redshift point of the CS split in 5 bins with the same ΔX, we randomly selected one value of $\Omega_{\rm HI}^{\rm DLA}$ from its probability distribution. This was repeated using the $\Omega_{\rm HI}^{\rm DLA}$ curve, in order to compare the impact of using either our new 'curve' methodology with traditional binning. In order to include intermediate redshift DLA surveys or local 21cm emission surveys in our re-samples, we draw $\Omega_{\rm HI}^{\rm DLA}$ (or $\Omega_{\rm HI}$) points assuming a Gaussian distribution within the quoted 1 σ error bars of those works. For surveys with extended redshift coverage (i.e. R06 and N15) we also re-sampled evenly across the quoted range in z, using the same Δz sampling as for the CS curve. After each re-sampling of the $\Omega_{\rm HI}^{\rm DLA}$ curve, we performed a linear regression and computed the slope and Pearson's correlation coefficient, r, which tests for the significance of a correlation between two quantities (in this case, z and $\Omega_{\rm HI}^{\rm DLA}$). We tabulate in Table 1.8 the distribution of the slopes and r for 100,000 iterations. Figure 1.13 considers only the CS, whereas Figure 1.14 include either intermediate or low redshift data.

Considering first only the CS, we observe a significant correlation for the whole sample, as shown by the red-to-yellow histograms, spanning approximately $2 < z < 5$. In Table 1.8 we can observe that the significance of the results depends on the redshift sampling of the $\Omega_{\rm HI}^{\rm DLA}$ results, since the larger the z range, the greater the degrees of freedom we have. We therefore also establish the significance of this correlation, finding $\geq 3\sigma$ **to be** independent of binning/sampling method. We note that in the z-range from 2.5 to 3.5, where our statistics are best, the slopes and r distributions are independent of the Δz chosen. From the curve analysis, the correlation is driven mostly by the data in the z-range from 2.5 to 3.5, where the median correlation coefficient is $r = 0.8$ (blue and cyan histograms). Taken together, the positive slopes and r values indicate significant redshift evolution in $\Omega_{\rm HI}^{\rm DLA}$ within these redshift ranges. However, when considering only redshifts greater than 3.5 (orange histograms), the data do not show a significant correlation, although the statistics in this high redshift regime are considerably poorer. The large confidence intervals associated with the $\Omega_{\rm HI}^{\rm DLA}$ curve at $z > 3.5$ could be masking some mild evolution.

In upper panels of Figure 1.14 we now include R06 ($0.11 < z < 1.6$, purple histograms) and N15 ($0.01 < z < 1.7$, green histograms) data. If we use the R06 statistics to represent intermediate redshift DLAs, in combination with the CS, the correlation coefficient (median $r = 0.0$) and slope (median value = 0.0) favors no evolution across the entire redshift range from $0.1 < z < 5$. Conversely, if the low value of $\Omega_{\rm HI}^{\rm DLA}$ reported by N15

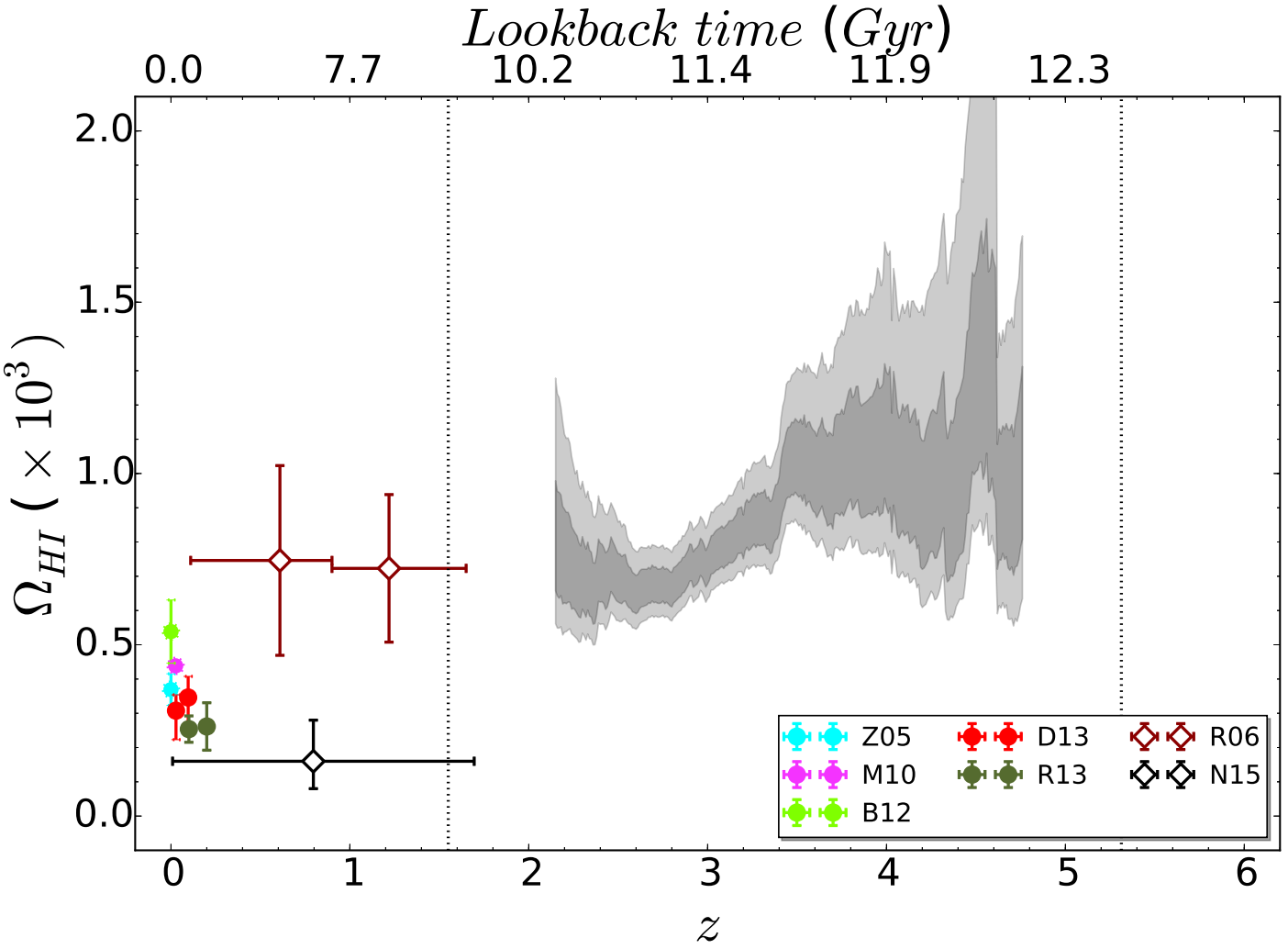

Figure 1.12: Evolution of the atomic HI gas in galaxies over the cosmic time. Data from 21cm emission line surveys (circles) and from QSO absorption systems (squares) are plotted. Empty points represents $\Omega_{\rm HI}^{\rm DLA}$ and filled $\Omega_{\rm HI}$. Vertical lines are the redshift limits of our combined sample. The data for the CS curve is tabulated in Table 1.6.

is adopted, the evolution is very significant ($\geq 6.5\sigma$, with median $r = 0.9$ and slope $= 0.24{\times}10^{-3}$). The N15 and R06 samples both have important limitations. On the one hand, the results from R06 are based on the incidence of Mg II, a pre-selection technique which may bias the high column density end of $f_{\rm HI}(N, X)$ towards higher values (see Neeleman *et al.*, 2016, and references therein). On the other hand, the N15 statistics are too poor to fully sample the column density distribution function and they had to correct their measurements assuming N12's $f_{\rm HI}(N, X)$ to include contribution by missing DLAs with $\log N({\rm H\,I})$>21.0.

Given the relatively small sample sizes of DLAs at intermediate redshifts, and the potential biases and uncertainties described above, we next test for evolution by combining the CS with $z \sim 0$ measurements of $\Omega_{\rm HI}$. However, even for the local universe, H I measurements are not absent of concerns on possible systematics, and Fig. 1.12 shows a factor of two disagreement between surveys. For example, Braun (2012) claims that current low-z measurements are strongly biased due to resolution effects, as the densest H I clouds are much smaller than the typical spatial resolution and no self-absorption correction, which is important in this case, can be computed from the data-cubes. This effect was pointed out previously by Zwaan *et al.* (2005), but with their data-set they were not able to find significant deviations. However, Braun (2012) builds up the local distribution function using high-resolution images ($\sim 100pc$) of only three galaxies, assuming that the cloud distribution is representative of the whole local Universe, which may not be accurate. We therefore repeat the evolution test, combining the CS with either R13 or B12, which show the lowest and and highest measurements of $\Omega_{\rm HI}$ respectively in the local universe. In the lower panels of Fig. 1.14 we show the distribution of slopes (left panel) and correlation coefficients (right panel) for the 100,000 resamplings when the CS is combined with either R13 (olive green histogram) or B12 (grey histogram). Although the $\Omega_{\rm HI}$ values reported by these two works differ by a factor of two, when combined with the CS both exhibit a statistically significant correlation between $\Omega_{\rm HI}$ and z; in both cases the median correlation coefficient is $r = 0.6$ with a significance $\geq 3\sigma$. The median slopes are also very similar, $\sim 0.17 \times 10^{-3}$, which correspond to a factor of ~ 4 decrease in $\Omega_{\rm HI}$ between $z = 5$ and $z = 0$.

Despite decades of effort in compiling ever larger samples, our assessment of the galactic gas reservoir in DLAs is still limited by the missing high density absorbers and the traditional $N({\rm H\,I})$ definition at $\log N({\rm H\,I}) = 20.3$. It has been argued (e.g. Péroux *et al.*, 2005) that, particularly at high redshifts, sub-DLAs ($\log N({\rm H\,I}) > 19.0$) could contribute significantly to the atomic hydrogen budget. Crighton *et al.* (2015) made a statistical 20 per cent correction for sub-DLAs in their study of $z > 3.5$ DLAs, based on results from Noterdaeme *et al.* (2009); O'Meara *et al.* (2007); Prochaska *et al.* (2010); Zafar *et al.*

(2013). The suggested redshift dependence of a sub-DLA correction means that a uniform correction to account for lower column density absorbers is not appropriate for our combined sample. Moreover, the majority of DLA surveys that comprise our combined sample were conducted at insufficient resolution to robustly identify sub-DLAs, such that a 'manual' assessment of the sub-DLA contribution to each is not possible. Although a redshift dependent sub-DLA correction could produce some changes in the $\Omega_{\rm HI}$ curve shape, existing results indicate that this factor is unlikely to dramatically change the picture that we presented in this work. In a future paper we will identify and investigate the nature of the sub-DLAs in the XQ-100 sample.

In closing, we note that the quality of the XQ-100 spectra are sufficient, both in terms of SNR and resolution, to directly determine elemental abundances for the DLAs presented here. There are numerous DLAs of interest amongst the sample, including a candidate very metal poor DLA, several PDLAs, and some cases of multiple DLAs that lie very close in velocity space along a single line of sight. All of these categories have been proposed to be chemically interesting (e.g. Cooke *et al.*, 2011b; Ellison & Lopez, 2001; Ellison *et al.*, 2010, 2011; Lopez & Ellison, 2003). In Berg et al. (in prep) we study the chemical abundances of all the XQ-100 DLAs, with a particular focus on these special cases, in the context of a large literature sample.

1.6 Conclusions

Based on the results of the XQ-100 survey, we report the detection of 38 intervening DLAs identified towards 100 $z > 3.5$ QSOs. This sample has been combined, after exhaustive checking for duplications and errors, with a literature sample of DLA surveys spanning the last $\sim$ 20 years. The final combined sample contains 742 DLAs spanning the redshift range from $z \sim 1.6$ to 5. We present statistical measures of the column density distribution function ($f_{\rm HI}(N, X)$, Fig 1.6), DLA number density ($\ell(X)$, Fig. 1.9), and the DLA HI gas content ($\Omega_{\rm HI}^{\rm DLA}$, Fig. 1.12), and present a thorough estimation of errors and potential biases (such as colour selection and incomplete sampling of the high column density end) on these quantities. The main focus of this paper is the evolution of $\Omega_{\rm HI}^{\rm DLA}$, and we present a novel technique for computing this quantity as a continuous function of redshift, with confidence intervals computed at every redshift point. In order to statistically assess whether there is evolution in $\Omega_{\rm HI}^{\rm DLA}$ over cosmic time, we perform a bootstrap re-sampling of the $\Omega_{\rm HI}^{\rm DLA}$ curve and compute the slope and correlation coefficients (r) of 100,000 iterations. For the combined sample, the most significant $\Omega_{\rm HI}^{\rm DLA}$ redshift evolution (median $r = 0.8$) is found for the interval $2.5 < z < 3.5$. However, at higher redshifts, the median slope of the

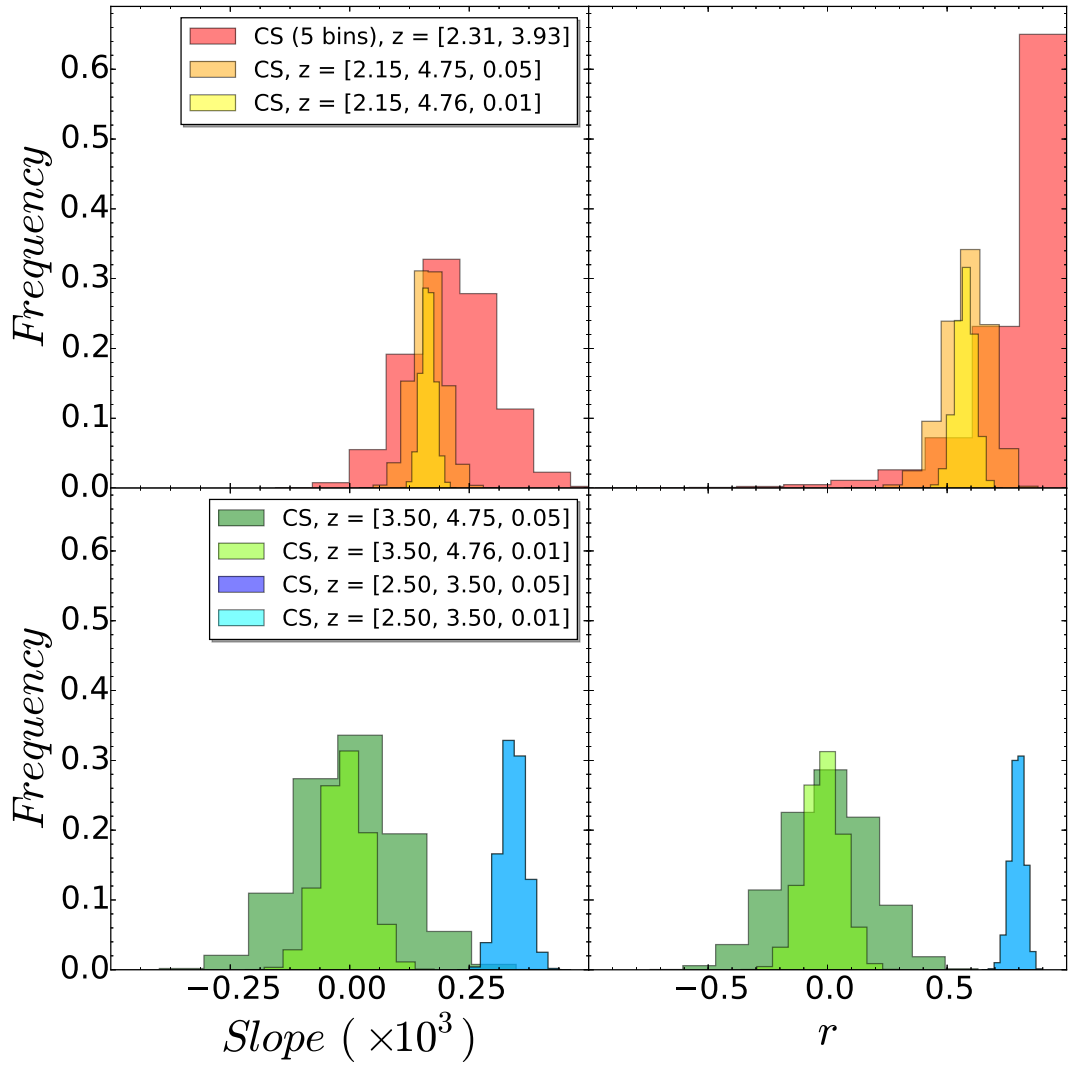

Figure 1.13: Histograms of the results of the evolution test for different redshift ranges of the CS split in 5 non overlapping bins (top panels), and the CS curve (bottom panels). Redshifts intervals in the legend have the format $[z_{\rm min},\ z_{\rm max}]$ (bins) or $[z_{\rm min},\ z_{\rm max},\ \Delta z]$ (curves). The left hand panels show the distribution of slopes from a linear regression of 100,000 re-sampled Ω curves; the right hand panels show the distributions of the Pearson correlation coefficients, r. Different colored histograms indicate different samples and redshift ranges, as given in the Figure legends.

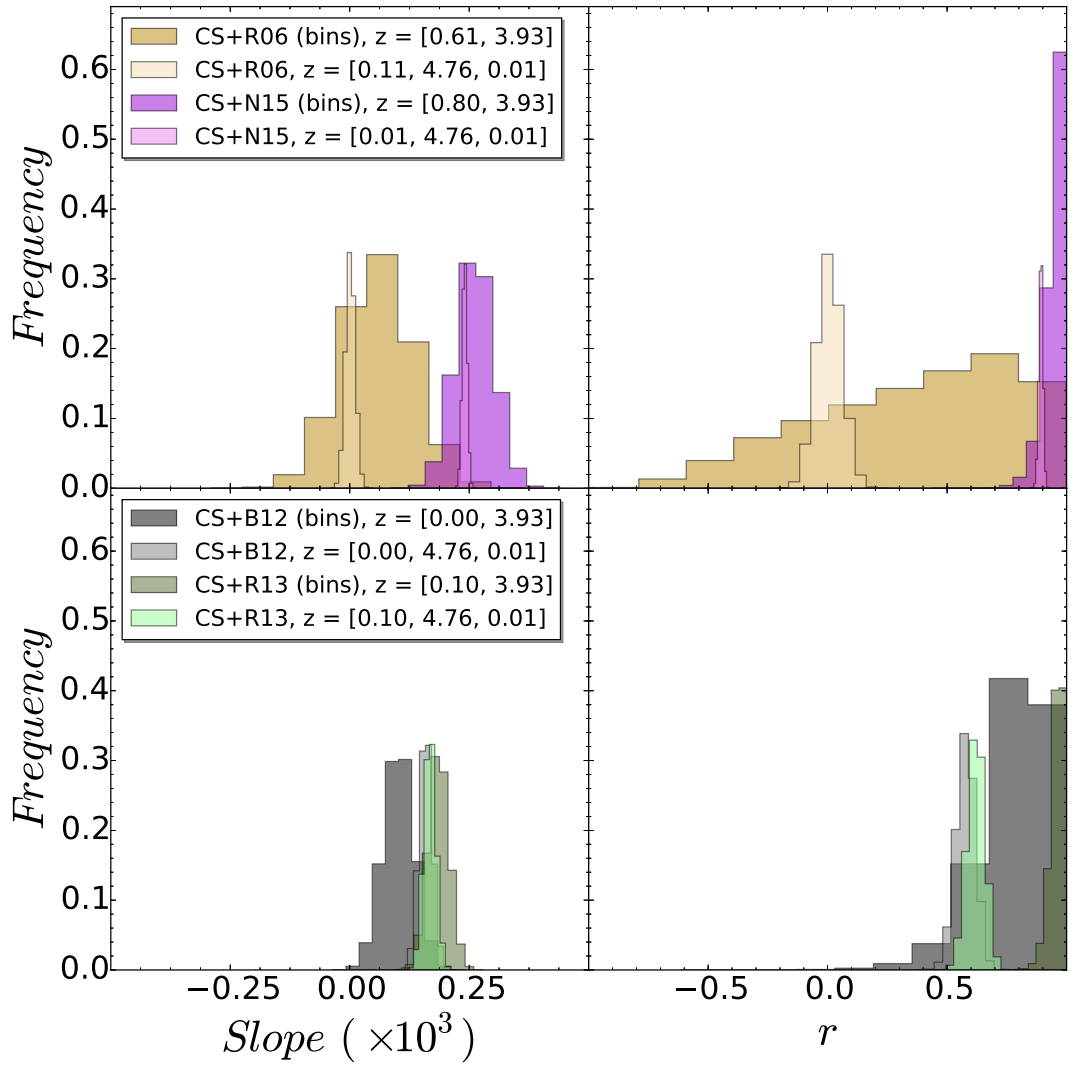

Figure 1.14: Version of Figure 1.13 with histograms of the results of the evolution test for the CS plus intermediate redshift samples (top panels), and local 21cm samples (bottom panels).

Table 1.8: Results of the evolution tests for 3 cases: non overlapping curves, $\Omega_{\rm HI}^{\rm DLA}$ curve with Δz=0.01 and its resampled version with Δz=0.05. Slopes are in units of 10^{-3}

	Non overlapping points			$\Delta z = 0.05$			$\Delta z = 0.01$		
Sample	Slope	r	σ	Slope	r	σ	Slope	r	σ
CS	0.21 ± 0.09	0.86 ± 0.19	3.0	0.16 ± 0.03	0.59 ± 0.09	5.0	0.16 ± 0.01	0.58 ± 0.04	11.0
CS ($z \geq 3.5$)	—	—	—	0.00 ± 0.11	0.00 ± 0.18	0.0	-0.01 ± 0.05	-0.01 ± 0.08	0.0
CS ($2.5 \leq z \leq 3.5$)	—	—	—	0.34 ± 0.03	0.80 ± 0.03	9.0	0.34 ± 0.03	0.80 ± 0.03	21.0
CS + R06	0.06 ± 0.07	0.42 ± 0.42	1.0	—	—	—	0.00 ± 0.01	0.0 ± 0.05	0.0
CS + N15	0.26 ± 0.04	0.95 ± 0.04	6.5	—	—	—	0.24 ± 0.01	0.89 ± 0.01	41.0
CS + B12	0.10 ± 0.03	0.80 ± 0.14	3.0	—	—	—	0.16 ± 0.01	0.58 ± 0.04	11.0
CS + R13	0.19 ± 0.02	0.96 ± 0.03	8.0	—	—	—	0.17 ± 0.01	0.62 ± 0.04	13.0

bootstrap iterations is zero and median $r = 0.0$, indicating no significant evolution, but improved statistics above $z \sim 3.5$ are still required to confirm this. Assessing evolution in $\Omega_{\rm HI}^{\rm DLA}$ down to lower redshifts is found to be highly dependent on the choice of sample used for the evolution test. Combining the CS with the intermediate redshift sample of DLAs from Rao *et al.* (2006) yields a median correlation coefficient $r = 0$, indicating that the cosmic gas density is not strongly evolving from $z \sim 0.1$ to 5. However, this picture is challenged by an alternative survey for $0 < z < 1.6$ absorbers by Neeleman *et al.* (2016) who find an $\Omega_{\rm HI}^{\rm DLA}$ value a factor of five lower than R06. Adopting the N15 value of $\Omega_{\rm HI}^{\rm DLA}$ results in a highly significant evolution of galactic gas content (median correlation coefficient $r = 0.9$). A more consistent picture is obtained when the CS is combined with $z \sim 0$ surveys. Although these surveys exhibit a factor of $\sim$ two variation in their quoted $\Omega_{\rm HI}$, both the highest (Braun, 2012) and lowest (Rhee *et al.*, 2013) yield a statistically significant ($r = 0.6$) redshift evolution when combined with the high redshift data. The median slope obtained from out bootstrap re-sampling is $\sim 0.17 \times 10^{-3}$, corresponding to a factor of ~ 4 decrease in $\Omega_{\rm HI}$ from $z = 5$ to $z = 0$. Therefore, the greatest uncertainty in $\Omega_{\rm HI}$ measurements is in the intermediate redshift regime, which is currently beyond the reach of most 21cm surveys, but still poorly sampled by DLA studies. An accurate measure of $\Omega_{\rm HI}^{\rm DLA}$ at redshifts between 0.1 and 2 is therefore clearly of the utmost importance. Upcoming surveys with the Square Kilometre Array (SKA, Staveley-Smith & Oosterloo, 2015) and its pathfinders present an exciting prospect for resolving the current uncertainty in the gas content of galaxies since $z \sim 1.5$.

THESIS CONCLUSIONS

Chapter 1

Conclusions

I have actively participated in the follow-up of large number of GRBs as part of the ARAE and HETH groups at IAA-CSIC in Spain, and as part of the X-shooter GRB collaboration, an international effort focused on GRB spectroscopy with the Very Large Telescope (VLT, in Chile). During the last 3 years, I have also been part of the XQ-100 collaboration to exploit the 100 QSOs observed with X-shooter. I spent three months working at the DARK Cosmology Centre, of the Niels Bohr Institute, at the University of Copenhagen (Denmark), and another 4 months at the University of Victoria (Canada). In both institutions I developed an important part of this thesis work, and established strong collaborations that are still ongoing. Finally, I also participated in several international conferences, workshops, and seminars where I presented my work in both orally and as posters. All this work has resulted in the publication of 32 refereed papers (plus 2 currently in press), 27 proceedings and 75 astronomical circulars. These publications have accumulated to date more than 850 citations. I have also been a reviewer for the Astrophysical Journal.

The work of this Thesis has been based on the study of GRB physics and the use of both GRBs and QSOs as beacons to study the high-redshift Universe: First, I showed the importance of very extensive follow-up to address fundamental questions that still are not answered on the nature of GRB afterglows, the exact mechanism that power them, and the properties of their progenitors. GRB afterglows were also used as probes of the very high redshift Universe, adding new measurements to the small sample that currently exists and, in particular I performed the first measurement of a pure IGM red damping wing on a GRB spectrum, using GTC/OSIRIS, which resulted in the best constraint to date on the IGM neutral fraction at $z = 6.3$. Finally, I also addressed a classical and fundamental issue in observational cosmology, which is the content and redshift evolution of the neutral Hydrogen in the Universe. I developed new techniques which were applied to new samples at $z > 3.5$, explaining statistically older discrepancies between some works and showing a small but significant evolution of $\Omega_{\rm HI}$ from the local Universe up to $z \sim 5$.

In the following sections we detail the conclusions reached in each of parts of this Thesis.

1.1 Gamma-ray burst physics

- I presented an extensive follow-up of the afterglow of GRB 110715A in 17 bands, ranging from a few seconds up to 74 days after the burst. The line of sight to the GRB is affected by strong foreground Galactic extinction, which complicated the follow-up and the analysis of the data.

- GRB 110715A had a very bright afterglow at all wavelengths, although its intrinsic luminosity is not exceptional.

- Optical/nIR spectroscopy obtained with X-shooter shows weak absorption features at a redshift of $z = 0.8224$ with no resolved velocity components ($\lesssim 30$ km s^{-1}). Absorption line ratios indicate a low ionization environment, confirmed by the rare detection of Ca I.

- Deep late imaging reveals a faint host galaxy with an absolute magnitude of $M_B =$ -18.2. This is consistent with the weak absorption features detected in the spectrum.

- We attempted to model the broadband data with a fireball model based on the prescription of Jóhannesson *et al.* (2006). The best model implies a forward shock evolving through a wind environment with a termination shock. In spite of describing roughly the behaviour of the afterglow, none of the models are able to get a statistically acceptable fit. This shows the need for good broadband sampling and more complex models to accurately describe the physics of GRB afterglows. There are several works that explore other possibilities, such as magneto-hydrodynamic simulations (van Eerten *et al.*, 2012), which was satisfactorily used, e.g., in Guidorzi *et al.* (2014); Ryan *et al.* (2015); Zhang *et al.* (2015), or central engine activities (Zhang *et al.*, 2014). These and other effects will be considered in future works to get a more accurate view of the GRB afterglow physics.

- Radio and sub-mm, along with X-ray observations, have been proven to be the most constraining bands for the afterglow modelling. We were limited by sensitivity for a long time in the crucial wavelength range of sub-mm, but now that ALMA is available, we have a good chance of getting high-quality data for a larger number of GRBs. This new, current and future facilities will allow us to probe the emission mechanisms in greater detail than previously possible, and will be the determinant in the evolution of the GRB afterglow models.

1.2 The tail-end of the reionisation era using GRBs as beacons

1.2.1 GRB 140304A:

- We detect a Damped Lyman-α system at $z = 5.2821 \pm 0.1$ on the optical spectra towards GRB 140304A. This is the third farthest DLA detected to date. The Voigt profile fitting give a column density value of $\log N(\mathrm{H\,I}) = 21.8 \pm 0.1$.

- There are several absorption lines at the same redshift as the Lyα absorption due to S, Si, O, and C, as well as at least one C IV intervening system.

- We measured the EW of the lines and compared them with the results from de Ugarte Postigo *et al.* (2012a), finding that the 41% of the sample have weaker features.

- We estimated the metal abundances of the S II and Si II* ions by using a novel technique based on the CoG method and Bayesian inference, finding acceptable results.

- We obtained $[S/H] = -1.13^{+0.10}_{-0.07}$, a value consistent with the non (or mild) evolution picture of the metal content in star forming regions up to $z\sim5$.

1.2.2 GRB 130606A:

- The host galaxy has a sub-DLA with $\log N(\mathrm{H\,I}) = 19.85 \pm 0.15$, and a metallicity content in the range from $\sim$1/7 to $\sim$1/60 of solar.

- In order to place the chemistry of the GRB sub-DLA in context with other high z absorbers, I compare the metallicity of a compilation of GRB host galaxy absorption systems (GRB-DLAs) compared to quasars with DLA and sub-DLAs (QSO-DLAs), combining the data reported in the literature (Berg *et al.*, 2015b; Schady *et al.*, 2011; Thöne *et al.*, 2013). The GRB 130606A sub-DLA is a rare find: it is the second highest redshift burst with a measured GRB-DLA metallicity and only the third GRB absorber with sub-DLA HI column density. At $z > 5$, the only other object known then with lower metallicity is the ULAS J1120+0641 DLA at z $\sim$ 7 (Simcoe *et al.*, 2012). However, the DLA towards ULAS J1120+0641 is close to the redshift of the quasar and its metallicity is determined from a stacked spectrum, both of which complicate its interpretation (Ellison *et al.*, 2010, 2011).

- We note that GRB 130606A, given the non-zero metal content of the host, might have originated from a non-Pop III progenitor star, but whether its afterglow light penetrated material that was pre-enriched by Pop III nucleosynthesis at even higher redshifts (Wang *et al.*, 2012) remains uncertain. Indeed several possibilities for the death of the first stars have recently been suggested by theoretical models (Bromm, 2013). A high value of C/O is predicted to be a signature of Pop III stellar enrichment (Fabbian *et al.*, 2009). A handful of DLAs in the metallicity range -2 to -3 (1/100 to 1/1000 of the Sun's metallicity) have C/O measurements (Cooke *et al.*, 2011a; Ellison *et al.*, 2010) and all but one (towards the quasar QSO J0035-0918) have [C/O] < 0 (Cooke *et al.*, 2011a). Unfortunately, we cannot impose any constraint on this ratio as both species are likely saturated.

- Events such as GRB 130606A at $z = 5.91$, and future ones at $z > 10$, offer an exciting new window into pre-galactic metal enrichment in these very high redshift galaxies. These bright lighthouses constitute a significant step forward towards using these sources as beacons for measuring abundances at such early times. New GRB missions, equipped with on-board near-IR detectors, and coupled to state-of-the-art instruments built for the largest diameter ground-based telescopes, will allow us to study the first stars that fundamentally transformed the Universe only a few hundred million years after the Big Bang.

1.2.3 GRB 140515A:

- We presented the multi-band spectroscopic and temporal analysis of the high-z GRB 140515A. The overall observed temporal properties of this burst, including the broad X-ray bump detected at late times, could be explained in the context of a standard afterglow model, although this requires an unusually flat index of the electron energy spectrum ($p = 1.67$).

- Another possible interpretation is to assume that an additional component (e.g. related to long-lasting central engine activity) is dominating the X-ray emission. In the latter case, the broad band observations can be explained using a more typical value of the spectral index for the injected electron spectrum ($p = 2.1$). Our modelling in this case shows that the central engine activity should cease at late times ($\sim 2 \times 10^5$ s), when the X-ray afterglow starts to dominate the emission.

- In both scenarios the cooling frequency is expected to be between the optical and the X-ray energy bands ($\nu_c \sim 2 \times 10^{16}$ Hz) and the average rest-frame circum-burst extinction ($A_V \sim 0.1$) resulted to be typical of high-z bursts.

- Our detailed spectral analysis provided a best estimate of the neutral hydrogen fraction of the IGM towards the burst of $x_{HI} \leq 0.002$ and a conservative upper limit of the HI abundance in the GRB host galaxy of $N_{\rm HI} \lesssim 10^{18.5}$ cm^{-2}. These values are slightly different from the ones estimated by Chornock *et al.* (2014).

- In addition, the spectral absorption lines observed in our spectra are the weakest lines ever observed in GRB afterglows (de Ugarte Postigo *et al.*, 2012a), suggesting that GRB 140515A happened in a very low density environment. However, our upper limits on the gas-phase abundances, coupled with the fact that we cannot establish the exact metal-to-dust ratio, do not allow us to distinguish between metallicity in the range of $10^{-4} < [Z/H] < 0.1$. This makes the possible Pop III star origin for GRB 140515A uncertain and doubtful.

- For all high-z GRBs the contribution of the host galaxy was not negligible. GRB 140515A is the first case when this does not happen, allowing us to give the best observational constrains on a theoretical model at $z > 6$.

1.3 Hydrogen content in the Universe, the XQ100 sample

- Based on the results of the XQ-100 survey, we report the detection of 38 intervening DLAs identified towards 100 $z > 3.5$ QSOs.
- This sample has been combined, after exhaustive checking for duplications and errors, with a literature sample of DLA surveys spanning the last $\sim$ 20 years. The final combined sample contains 742 DLAs spanning the redshift range from $z \sim 1.6$ to 5.
- We present statistical measures of the column density distribution function ($f_{\rm HI}(N, X)$, Fig 1.6), DLA number density ($\ell(X)$, Fig. 1.9), and the DLA HI gas content ($\Omega_{\rm HI}^{\rm DLA}$, Fig. 1.12), and present a thorough estimation of errors and potential biases (such as colour selection and incomplete sampling of the high column density end) on these quantities.
- The main focus of this Chapter is the evolution of $\Omega_{\rm HI}^{\rm DLA}$, and we present a novel technique for computing this quantity as a continuous function of redshift, with confidence intervals computed at every redshift point.
- In order to statistically assess whether there is evolution in $\Omega_{\rm HI}^{\rm DLA}$ over cosmic time, we perform a bootstrap re-sampling of the $\Omega_{\rm HI}^{\rm DLA}$ curve and compute the slope and correlation coefficients (r) of 100,000 iterations. For the combined sample, the most significant $\Omega_{\rm HI}^{\rm DLA}$ redshift evolution (median $r = 0.8$) is found for the interval $2.5 < z < 3.5$. However, at higher redshifts, the median slope of the bootstrap iterations is zero and median $r = 0.0$, indicating no significant evolution, but improved statistics above $z \sim 3.5$ are still required to confirm this.
- Assessing evolution in $\Omega_{\rm HI}^{\rm DLA}$ down to lower redshifts is found to be highly dependent on the choice of sample used for the evolution test. Combining the CS with the intermediate redshift sample of DLAs from Rao *et al.* (2006) yields a median correlation coefficient $r = 0$, indicating that the cosmic gas density is not strongly evolving from $z \sim 0.1$ to 5. However, this picture is challenged by an alternative survey for $0 < z < 1.6$ absorbers by Neeleman *et al.* (2016) who find an $\Omega_{\rm HI}^{\rm DLA}$ value a factor of five lower than R06. Adopting the N15 value of $\Omega_{\rm HI}^{\rm DLA}$ results in a highly significant evolution of galactic gas content (median correlation coefficient $r = 0.9$).
- A more consistent picture is obtained when the CS is combined with $z \sim 0$ surveys. Although these surveys exhibit a factor of $\sim$ two variation in their quoted

$\Omega_{\rm HI}$, both the highest (Braun, 2012) and lowest (Rhee *et al.*, 2013) yield a statistically significant ($r = 0.6$) redshift evolution when combined with the high redshift data. The median slope obtained from out bootstrap re-sampling is $\sim 0.17 \times 10^{-3}$, corresponding to a factor of ~ 4 decrease in $\Omega_{\rm HI}$ from $z = 5$ to $z = 0$.

- Therefore, the greatest uncertainty in $\Omega_{\rm HI}$ measurements is in the intermediate redshift regime, which is currently beyond the reach of most 21cm surveys, but still poorly sampled by DLA studies. An accurate measure of $\Omega_{\rm HI}^{\rm DLA}$ at redshifts between 0.1 and 2 is therefore clearly of the utmost importance. Upcoming surveys with the Square Kilometre Array (SKA, Staveley-Smith & Oosterloo, 2015) and its pathfinders present an exciting prospect for resolving the current uncertainty in the gas content of galaxies since $z \sim 1.5$.

APPENDICES

Appendix A

Broad-band observations of GRB 110715A

Table A.1: Broad band observations of GRB 110715A.

T - T_0 [days]	Flux [Jy]	AB [mag]	Band
0.00094	$(1.32 \pm 0.33) \times 10^{-04}$	$18.60^{+0.24}_{-0.31}$	XRT 2 keV
0.00096	$(1.52 \pm 0.37) \times 10^{-04}$	$18.44^{+0.24}_{-0.31}$	XRT 2 keV
0.00098	$(1.12 \pm 0.27) \times 10^{-04}$	$18.78^{+0.24}_{-0.31}$	XRT 2 keV
0.00100	$(1.01 \pm 0.25) \times 10^{-04}$	$18.89^{+0.24}_{-0.31}$	XRT 2 keV
0.00103	$(1.13 \pm 0.26) \times 10^{-04}$	$18.77^{+0.23}_{-0.29}$	XRT 2 keV
0.00114	$(1.19 \pm 0.17) \times 10^{-04}$	$18.71^{+0.15}_{-0.17}$	XRT 2 keV
0.00116	$(0.86 \pm 0.13) \times 10^{-04}$	$19.06^{+0.16}_{-0.18}$	XRT 2 keV
0.00119	$(1.16 \pm 0.17) \times 10^{-04}$	$18.74^{+0.15}_{-0.18}$	XRT 2 keV
0.00121	$(0.83 \pm 0.12) \times 10^{-04}$	$19.10^{+0.15}_{-0.18}$	XRT 2 keV
0.00124	$(0.92 \pm 0.14) \times 10^{-04}$	$18.99^{+0.16}_{-0.18}$	XRT 2 keV
0.00127	$(1.13 \pm 0.17) \times 10^{-04}$	$18.76^{+0.15}_{-0.18}$	XRT 2 keV
0.00129	$(1.14 \pm 0.17) \times 10^{-04}$	$18.75^{+0.15}_{-0.18}$	XRT 2 keV
0.00132	$(0.85 \pm 0.12) \times 10^{-04}$	$19.08^{+0.15}_{-0.18}$	XRT 2 keV
0.00134	$(0.90 \pm 0.14) \times 10^{-04}$	$19.01^{+0.16}_{-0.19}$	XRT 2 keV
0.00138	$(0.79 \pm 0.12) \times 10^{-04}$	$19.16^{+0.16}_{-0.18}$	XRT 2 keV
0.00140	$(1.04 \pm 0.15) \times 10^{-04}$	$18.85^{+0.15}_{-0.18}$	XRT 2 keV
0.00143	$(0.86 \pm 0.13) \times 10^{-04}$	$19.06^{+0.16}_{-0.18}$	XRT 2 keV
0.00146	$(0.86 \pm 0.12) \times 10^{-04}$	$19.06^{+0.15}_{-0.18}$	XRT 2 keV
0.00149	$(1.17 \pm 0.17) \times 10^{-04}$	$18.73^{+0.15}_{-0.18}$	XRT 2 keV
0.00151	$(0.89 \pm 0.13) \times 10^{-04}$	$19.03^{+0.15}_{-0.18}$	XRT 2 keV
0.00154	$(0.82 \pm 0.12) \times 10^{-04}$	$19.11^{+0.16}_{-0.18}$	XRT 2 keV
0.00157	$(0.94 \pm 0.14) \times 10^{-04}$	$18.97^{+0.16}_{-0.18}$	XRT 2 keV

Table A.1: continued.

T - T_0 [days]	Flux [Jy]	AB [mag]	Band
0.00160	$(1.04 \pm 0.15) \times 10^{-04}$	$18.86^{+0.16}_{-0.18}$	XRT 2 keV
0.00163	$(0.82 \pm 0.12) \times 10^{-04}$	$19.11^{+0.15}_{-0.18}$	XRT 2 keV
0.00165	$(0.89 \pm 0.13) \times 10^{-04}$	$19.02^{+0.15}_{-0.18}$	XRT 2 keV
0.00168	$(0.89 \pm 0.13) \times 10^{-04}$	$19.02^{+0.16}_{-0.18}$	XRT 2 keV
0.00171	$(0.97 \pm 0.14) \times 10^{-04}$	$18.93^{+0.15}_{-0.18}$	XRT 2 keV
0.00174	$(0.89 \pm 0.13) \times 10^{-04}$	$19.02^{+0.15}_{-0.18}$	XRT 2 keV
0.00177	$(0.71 \pm 0.10) \times 10^{-04}$	$19.28^{+0.16}_{-0.18}$	XRT 2 keV
0.00181	$(0.72 \pm 0.10) \times 10^{-04}$	$19.26^{+0.15}_{-0.18}$	XRT 2 keV
0.00184	$(0.98 \pm 0.14) \times 10^{-04}$	$18.93^{+0.15}_{-0.18}$	XRT 2 keV
0.00187	$(0.78 \pm 0.11) \times 10^{-04}$	$19.17^{+0.15}_{-0.18}$	XRT 2 keV
0.00190	$(6.45 \pm 0.99) \times 10^{-05}$	$19.38^{+0.16}_{-0.18}$	XRT 2 keV
0.00194	$(1.03 \pm 0.15) \times 10^{-04}$	$18.87^{+0.15}_{-0.18}$	XRT 2 keV
0.00196	$(0.94 \pm 0.14) \times 10^{-04}$	$18.96^{+0.15}_{-0.18}$	XRT 2 keV
0.00199	$(0.89 \pm 0.13) \times 10^{-04}$	$19.02^{+0.15}_{-0.18}$	XRT 2 keV
0.00202	$(0.83 \pm 0.12) \times 10^{-04}$	$19.11^{+0.15}_{-0.18}$	XRT 2 keV
0.00205	$(0.83 \pm 0.12) \times 10^{-04}$	$19.10^{+0.15}_{-0.18}$	XRT 2 keV
0.00208	$(0.66 \pm 0.10) \times 10^{-04}$	$19.35^{+0.15}_{-0.18}$	XRT 2 keV
0.00212	$(0.75 \pm 0.11) \times 10^{-04}$	$19.21^{+0.15}_{-0.18}$	XRT 2 keV
0.00216	$(0.68 \pm 0.10) \times 10^{-04}$	$19.32^{+0.16}_{-0.18}$	XRT 2 keV
0.00220	$(5.39 \pm 0.82) \times 10^{-05}$	$19.57^{+0.16}_{-0.18}$	XRT 2 keV
0.00224	$(0.84 \pm 0.13) \times 10^{-04}$	$19.10^{+0.16}_{-0.18}$	XRT 2 keV
0.00227	$(0.92 \pm 0.13) \times 10^{-04}$	$18.99^{+0.15}_{-0.18}$	XRT 2 keV
0.00230	$(0.95 \pm 0.14) \times 10^{-04}$	$18.96^{+0.15}_{-0.18}$	XRT 2 keV
0.00232	$(0.75 \pm 0.11) \times 10^{-04}$	$19.21^{+0.15}_{-0.18}$	XRT 2 keV
0.00236	$(0.81 \pm 0.12) \times 10^{-04}$	$19.12^{+0.15}_{-0.18}$	XRT 2 keV
0.00239	$(0.68 \pm 0.10) \times 10^{-04}$	$19.32^{+0.15}_{-0.18}$	XRT 2 keV
0.00243	$(0.77 \pm 0.11) \times 10^{-04}$	$19.19^{+0.15}_{-0.18}$	XRT 2 keV
0.00247	$(6.15 \pm 0.97) \times 10^{-05}$	$19.43^{+0.16}_{-0.19}$	XRT 2 keV
0.00251	$(0.65 \pm 0.10) \times 10^{-04}$	$19.36^{+0.16}_{-0.18}$	XRT 2 keV
0.00254	$(0.76 \pm 0.11) \times 10^{-04}$	$19.19^{+0.15}_{-0.18}$	XRT 2 keV
0.00258	$(6.54 \pm 0.99) \times 10^{-05}$	$19.36^{+0.15}_{-0.18}$	XRT 2 keV
0.00263	$(5.24 \pm 0.79) \times 10^{-05}$	$19.60^{+0.15}_{-0.18}$	XRT 2 keV
0.00267	$(6.14 \pm 0.94) \times 10^{-05}$	$19.43^{+0.16}_{-0.18}$	XRT 2 keV
0.00271	$(0.67 \pm 0.10) \times 10^{-04}$	$19.33^{+0.16}_{-0.18}$	XRT 2 keV

Table A.1: continued.

T - T_0 [days]	Flux [Jy]	AB [mag]	Band
0.00274	$(0.79 \pm 0.12) \times 10^{-04}$	$19.16^{+0.16}_{-0.18}$	XRT 2 keV
0.00278	$(5.62 \pm 0.87) \times 10^{-05}$	$19.53^{+0.16}_{-0.18}$	XRT 2 keV
0.00283	$(5.57 \pm 0.85) \times 10^{-05}$	$19.54^{+0.16}_{-0.18}$	XRT 2 keV
0.00286	$(0.78 \pm 0.11) \times 10^{-04}$	$19.17^{+0.15}_{-0.18}$	XRT 2 keV
0.00290	$(5.61 \pm 0.85) \times 10^{-05}$	$19.53^{+0.15}_{-0.18}$	XRT 2 keV
0.00295	$(6.29 \pm 0.93) \times 10^{-05}$	$19.40^{+0.15}_{-0.18}$	XRT 2 keV
0.00299	$(0.67 \pm 0.10) \times 10^{-04}$	$19.34^{+0.15}_{-0.18}$	XRT 2 keV
0.00303	$(5.45 \pm 0.82) \times 10^{-05}$	$19.56^{+0.15}_{-0.18}$	XRT 2 keV
0.00307	$(6.60 \pm 0.98) \times 10^{-05}$	$19.35^{+0.15}_{-0.18}$	XRT 2 keV
0.00311	$(5.83 \pm 0.91) \times 10^{-05}$	$19.49^{+0.16}_{-0.18}$	XRT 2 keV
0.00315	$(0.67 \pm 0.10) \times 10^{-04}$	$19.34^{+0.15}_{-0.18}$	XRT 2 keV
0.00319	$(0.92 \pm 0.13) \times 10^{-04}$	$18.99^{+0.15}_{-0.18}$	XRT 2 keV
0.00322	$(0.68 \pm 0.10) \times 10^{-04}$	$19.31^{+0.15}_{-0.18}$	XRT 2 keV
0.00326	$(6.04 \pm 0.91) \times 10^{-05}$	$19.45^{+0.15}_{-0.18}$	XRT 2 keV
0.00330	$(4.68 \pm 0.87) \times 10^{-05}$	$19.72^{+0.19}_{-0.22}$	XRT 2 keV
0.00334	$(4.32 \pm 0.80) \times 10^{-05}$	$19.81^{+0.19}_{-0.22}$	XRT 2 keV
0.00337	$(4.63 \pm 0.85) \times 10^{-05}$	$19.74^{+0.18}_{-0.22}$	XRT 2 keV
0.00341	$(0.70 \pm 0.10) \times 10^{-04}$	$19.29^{+0.16}_{-0.18}$	XRT 2 keV
0.00345	$(4.67 \pm 0.73) \times 10^{-05}$	$19.73^{+0.16}_{-0.19}$	XRT 2 keV
0.00350	$(6.61 \pm 0.98) \times 10^{-05}$	$19.35^{+0.15}_{-0.18}$	XRT 2 keV
0.00354	$(4.41 \pm 0.82) \times 10^{-05}$	$19.79^{+0.19}_{-0.23}$	XRT 2 keV
0.00358	$(0.68 \pm 0.10) \times 10^{-04}$	$19.31^{+0.15}_{-0.18}$	XRT 2 keV
0.00362	$(6.26 \pm 0.93) \times 10^{-05}$	$19.41^{+0.15}_{-0.18}$	XRT 2 keV
0.00366	$(4.26 \pm 0.79) \times 10^{-05}$	$19.83^{+0.19}_{-0.22}$	XRT 2 keV
0.00370	$(4.39 \pm 0.80) \times 10^{-05}$	$19.79^{+0.18}_{-0.22}$	XRT 2 keV
0.00374	$(6.09 \pm 0.93) \times 10^{-05}$	$19.44^{+0.16}_{-0.18}$	XRT 2 keV
0.00378	$(5.63 \pm 0.84) \times 10^{-05}$	$19.52^{+0.15}_{-0.18}$	XRT 2 keV
0.00383	$(5.72 \pm 0.85) \times 10^{-05}$	$19.51^{+0.15}_{-0.18}$	XRT 2 keV
0.00387	$(6.16 \pm 0.96) \times 10^{-05}$	$19.43^{+0.16}_{-0.18}$	XRT 2 keV
0.00391	$(5.30 \pm 0.84) \times 10^{-05}$	$19.59^{+0.16}_{-0.19}$	XRT 2 keV
0.00396	$(0.81 \pm 0.12) \times 10^{-04}$	$19.13^{+0.15}_{-0.18}$	XRT 2 keV
0.00399	$(4.43 \pm 0.80) \times 10^{-05}$	$19.78^{+0.18}_{-0.22}$	XRT 2 keV
0.00403	$(5.09 \pm 0.78) \times 10^{-05}$	$19.63^{+0.16}_{-0.18}$	XRT 2 keV
0.00408	$(5.66 \pm 0.84) \times 10^{-05}$	$19.52^{+0.15}_{-0.18}$	XRT 2 keV

Table A.1: continued.

T - T_0 [days]	Flux [Jy]	AB [mag]	Band
0.00412	$(0.81 \pm 0.12) \times 10^{-04}$	$19.13^{+0.16}_{-0.18}$	XRT 2 keV
0.00416	$(5.45 \pm 0.81) \times 10^{-05}$	$19.56^{+0.15}_{-0.18}$	XRT 2 keV
0.00421	$(3.61 \pm 0.70) \times 10^{-05}$	$20.01^{+0.19}_{-0.24}$	XRT 2 keV
0.00425	$(4.36 \pm 0.83) \times 10^{-05}$	$19.80^{+0.19}_{-0.23}$	XRT 2 keV
0.00429	$(4.61 \pm 0.88) \times 10^{-05}$	$19.74^{+0.19}_{-0.23}$	XRT 2 keV
0.00433	$(4.56 \pm 0.81) \times 10^{-05}$	$19.75^{+0.18}_{-0.21}$	XRT 2 keV
0.00436	$(0.91 \pm 0.13) \times 10^{-04}$	$19.01^{+0.15}_{-0.18}$	XRT 2 keV
0.00439	$(6.52 \pm 0.98) \times 10^{-05}$	$19.36^{+0.15}_{-0.18}$	XRT 2 keV
0.00443	$(5.33 \pm 0.81) \times 10^{-05}$	$19.58^{+0.16}_{-0.18}$	XRT 2 keV
0.00448	$(4.75 \pm 0.86) \times 10^{-05}$	$19.71^{+0.18}_{-0.22}$	XRT 2 keV
0.00452	$(4.95 \pm 0.73) \times 10^{-05}$	$19.66^{+0.15}_{-0.18}$	XRT 2 keV
0.00457	$(4.21 \pm 0.76) \times 10^{-05}$	$19.84^{+0.18}_{-0.22}$	XRT 2 keV
0.00461	$(5.57 \pm 0.85) \times 10^{-05}$	$19.54^{+0.16}_{-0.18}$	XRT 2 keV
0.00465	$(4.67 \pm 0.76) \times 10^{-05}$	$19.73^{+0.17}_{-0.19}$	XRT 2 keV
0.00470	$(5.70 \pm 0.90) \times 10^{-05}$	$19.51^{+0.16}_{-0.19}$	XRT 2 keV
0.00474	$(3.99 \pm 0.74) \times 10^{-05}$	$19.90^{+0.19}_{-0.22}$	XRT 2 keV
0.00479	$(3.07 \pm 0.57) \times 10^{-05}$	$20.18^{+0.19}_{-0.22}$	XRT 2 keV
0.00484	$(4.63 \pm 0.84) \times 10^{-05}$	$19.74^{+0.18}_{-0.22}$	XRT 2 keV
0.00488	$(4.74 \pm 0.86) \times 10^{-05}$	$19.71^{+0.18}_{-0.22}$	XRT 2 keV
0.00491	$(3.45 \pm 0.64) \times 10^{-05}$	$20.06^{+0.19}_{-0.22}$	XRT 2 keV
0.00496	$(4.48 \pm 0.81) \times 10^{-05}$	$19.77^{+0.18}_{-0.22}$	XRT 2 keV
0.00500	$(4.79 \pm 0.74) \times 10^{-05}$	$19.70^{+0.16}_{-0.18}$	XRT 2 keV
0.00505	$(5.45 \pm 0.81) \times 10^{-05}$	$19.56^{+0.15}_{-0.18}$	XRT 2 keV
0.00510	$(4.29 \pm 0.78) \times 10^{-05}$	$19.82^{+0.18}_{-0.22}$	XRT 2 keV
0.00513	$(4.77 \pm 0.89) \times 10^{-05}$	$19.70^{+0.19}_{-0.22}$	XRT 2 keV
0.00518	$(3.77 \pm 0.70) \times 10^{-05}$	$19.96^{+0.19}_{-0.22}$	XRT 2 keV
0.00522	$(4.03 \pm 0.73) \times 10^{-05}$	$19.89^{+0.18}_{-0.22}$	XRT 2 keV
0.00526	$(4.51 \pm 0.90) \times 10^{-05}$	$19.76^{+0.20}_{-0.24}$	XRT 2 keV
0.00530	$(4.82 \pm 0.76) \times 10^{-05}$	$19.69^{+0.16}_{-0.19}$	XRT 2 keV
0.00534	$(4.84 \pm 0.79) \times 10^{-05}$	$19.69^{+0.17}_{-0.19}$	XRT 2 keV
0.00539	$(5.47 \pm 0.82) \times 10^{-05}$	$19.56^{+0.15}_{-0.18}$	XRT 2 keV
0.00544	$(5.24 \pm 0.80) \times 10^{-05}$	$19.60^{+0.16}_{-0.18}$	XRT 2 keV
0.00548	$(4.81 \pm 0.89) \times 10^{-05}$	$19.69^{+0.19}_{-0.22}$	XRT 2 keV
0.00552	$(4.36 \pm 0.81) \times 10^{-05}$	$19.80^{+0.19}_{-0.22}$	XRT 2 keV

Table A.1: continued.

T - T_0 [days]	Flux [Jy]	AB [mag]	Band
0.00555	$(4.70 \pm 0.85) \times 10^{-05}$	$19.72^{+0.18}_{-0.22}$	XRT 2 keV
0.00559	$(4.00 \pm 0.74) \times 10^{-05}$	$19.90^{+0.19}_{-0.22}$	XRT 2 keV
0.00563	$(4.75 \pm 0.88) \times 10^{-05}$	$19.71^{+0.19}_{-0.22}$	XRT 2 keV
0.00567	$(3.56 \pm 0.66) \times 10^{-05}$	$20.02^{+0.19}_{-0.22}$	XRT 2 keV
0.00573	$(3.06 \pm 0.55) \times 10^{-05}$	$20.19^{+0.18}_{-0.22}$	XRT 2 keV
0.04349	$(0.67 \pm 0.15) \times 10^{-05}$	$21.83^{+0.22}_{-0.28}$	XRT 2 keV
0.04392	$(0.71 \pm 0.16) \times 10^{-05}$	$21.77^{+0.22}_{-0.28}$	XRT 2 keV
0.04433	$(0.89 \pm 0.18) \times 10^{-05}$	$21.53^{+0.21}_{-0.26}$	XRT 2 keV
0.04600	$(0.72 \pm 0.16) \times 10^{-05}$	$21.75^{+0.22}_{-0.27}$	XRT 2 keV
0.04639	$(0.57 \pm 0.13) \times 10^{-05}$	$22.00^{+0.22}_{-0.28}$	XRT 2 keV
0.04689	$(0.48 \pm 0.10) \times 10^{-05}$	$22.20^{+0.22}_{-0.27}$	XRT 2 keV
0.04731	$(0.95 \pm 0.20) \times 10^{-05}$	$21.46^{+0.21}_{-0.26}$	XRT 2 keV
0.04778	$(0.56 \pm 0.12) \times 10^{-05}$	$22.03^{+0.22}_{-0.27}$	XRT 2 keV
0.04818	$(0.81 \pm 0.17) \times 10^{-05}$	$21.63^{+0.21}_{-0.26}$	XRT 2 keV
0.04864	$(0.52 \pm 0.11) \times 10^{-05}$	$22.11^{+0.22}_{-0.28}$	XRT 2 keV
0.04915	$(0.54 \pm 0.11) \times 10^{-05}$	$22.07^{+0.21}_{-0.27}$	XRT 2 keV
0.04954	$(0.67 \pm 0.15) \times 10^{-05}$	$21.83^{+0.22}_{-0.28}$	XRT 2 keV
0.04997	$(0.50 \pm 0.11) \times 10^{-05}$	$22.14^{+0.22}_{-0.28}$	XRT 2 keV
0.05039	$(0.75 \pm 0.16) \times 10^{-05}$	$21.71^{+0.21}_{-0.26}$	XRT 2 keV
0.05088	$(5.83 \pm 0.95) \times 10^{-06}$	$21.99^{+0.16}_{-0.19}$	XRT 2 keV
0.05217	$(0.61 \pm 0.13) \times 10^{-05}$	$21.93^{+0.22}_{-0.28}$	XRT 2 keV
0.05255	$(0.51 \pm 0.11) \times 10^{-05}$	$22.13^{+0.22}_{-0.28}$	XRT 2 keV
0.05312	$(0.56 \pm 0.12) \times 10^{-05}$	$22.02^{+0.22}_{-0.27}$	XRT 2 keV
0.05385	$(0.50 \pm 0.11) \times 10^{-05}$	$22.16^{+0.22}_{-0.27}$	XRT 2 keV
0.05444	$(3.64 \pm 0.83) \times 10^{-06}$	$22.50^{+0.22}_{-0.28}$	XRT 2 keV
0.05523	$(3.46 \pm 0.78) \times 10^{-06}$	$22.55^{+0.22}_{-0.28}$	XRT 2 keV
0.05601	$(4.22 \pm 0.92) \times 10^{-06}$	$22.34^{+0.22}_{-0.27}$	XRT 2 keV
0.05668	$(4.28 \pm 0.93) \times 10^{-06}$	$22.32^{+0.21}_{-0.27}$	XRT 2 keV
0.05741	$(4.20 \pm 0.94) \times 10^{-06}$	$22.34^{+0.22}_{-0.28}$	XRT 2 keV
0.05811	$(0.45 \pm 0.10) \times 10^{-05}$	$22.27^{+0.22}_{-0.28}$	XRT 2 keV
0.05872	$(4.40 \pm 0.96) \times 10^{-06}$	$22.29^{+0.21}_{-0.27}$	XRT 2 keV
0.05922	$(3.57 \pm 0.79) \times 10^{-06}$	$22.52^{+0.22}_{-0.27}$	XRT 2 keV
0.05997	$(3.31 \pm 0.74) \times 10^{-06}$	$22.60^{+0.22}_{-0.28}$	XRT 2 keV
0.06064	$(0.46 \pm 0.10) \times 10^{-05}$	$22.25^{+0.22}_{-0.28}$	XRT 2 keV

Table A.1: continued.

T - T_0 [days]	Flux [Jy]	AB [mag]	Band
0.06121	$(3.53 \pm 0.80) \times 10^{-06}$	$22.53^{+0.22}_{-0.28}$	XRT 2 keV
0.06174	$(0.83 \pm 0.18) \times 10^{-05}$	$21.60^{+0.22}_{-0.27}$	XRT 2 keV
0.06215	$(4.16 \pm 0.94) \times 10^{-06}$	$22.35^{+0.22}_{-0.28}$	XRT 2 keV
0.06289	$(0.48 \pm 0.10) \times 10^{-05}$	$22.20^{+0.22}_{-0.28}$	XRT 2 keV
0.06354	$(3.49 \pm 0.78) \times 10^{-06}$	$22.54^{+0.22}_{-0.28}$	XRT 2 keV
0.06425	$(4.47 \pm 0.97) \times 10^{-06}$	$22.28^{+0.21}_{-0.27}$	XRT 2 keV
0.06480	$(3.95 \pm 0.88) \times 10^{-06}$	$22.41^{+0.22}_{-0.28}$	XRT 2 keV
0.06530	$(0.58 \pm 0.13) \times 10^{-05}$	$22.00^{+0.22}_{-0.28}$	XRT 2 keV
0.06583	$(4.32 \pm 0.97) \times 10^{-06}$	$22.31^{+0.22}_{-0.28}$	XRT 2 keV
0.06662	$(2.71 \pm 0.60) \times 10^{-06}$	$22.82^{+0.22}_{-0.27}$	XRT 2 keV
0.06741	$(3.62 \pm 0.77) \times 10^{-06}$	$22.50^{+0.21}_{-0.26}$	XRT 2 keV
0.06851	$(2.73 \pm 0.61) \times 10^{-06}$	$22.81^{+0.22}_{-0.27}$	XRT 2 keV
0.06946	$(2.87 \pm 0.65) \times 10^{-06}$	$22.75^{+0.22}_{-0.28}$	XRT 2 keV
0.07010	$(0.53 \pm 0.11) \times 10^{-05}$	$22.10^{+0.22}_{-0.28}$	XRT 2 keV
0.07062	$(3.75 \pm 0.86) \times 10^{-06}$	$22.46^{+0.22}_{-0.28}$	XRT 2 keV
0.07184	$(2.88 \pm 0.48) \times 10^{-06}$	$22.75^{+0.17}_{-0.20}$	XRT 2 keV
0.10980	$(2.17 \pm 0.48) \times 10^{-06}$	$23.06^{+0.22}_{-0.28}$	XRT 2 keV
0.11042	$(1.71 \pm 0.37) \times 10^{-06}$	$23.32^{+0.22}_{-0.27}$	XRT 2 keV
0.11120	$(1.56 \pm 0.35) \times 10^{-06}$	$23.42^{+0.22}_{-0.28}$	XRT 2 keV
0.11193	$(1.58 \pm 0.35) \times 10^{-06}$	$23.41^{+0.22}_{-0.28}$	XRT 2 keV
0.11261	$(2.37 \pm 0.52) \times 10^{-06}$	$22.96^{+0.22}_{-0.27}$	XRT 2 keV
0.11334	$(1.12 \pm 0.25) \times 10^{-06}$	$23.77^{+0.22}_{-0.28}$	XRT 2 keV
0.11413	$(2.87 \pm 0.63) \times 10^{-06}$	$22.76^{+0.22}_{-0.27}$	XRT 2 keV
0.11504	$(2.15 \pm 0.48) \times 10^{-06}$	$23.07^{+0.22}_{-0.28}$	XRT 2 keV
0.11581	$(1.37 \pm 0.31) \times 10^{-06}$	$23.56^{+0.22}_{-0.28}$	XRT 2 keV
0.11658	$(1.98 \pm 0.44) \times 10^{-06}$	$23.16^{+0.22}_{-0.27}$	XRT 2 keV
0.11730	$(1.65 \pm 0.37) \times 10^{-06}$	$23.36^{+0.22}_{-0.28}$	XRT 2 keV
0.11814	$(0.98 \pm 0.22) \times 10^{-06}$	$23.93^{+0.22}_{-0.28}$	XRT 2 keV
0.13186	$(0.73 \pm 0.18) \times 10^{-06}$	$24.24^{+0.25}_{-0.32}$	XRT 2 keV
0.13330	$(0.79 \pm 0.18) \times 10^{-06}$	$24.16^{+0.23}_{-0.29}$	XRT 2 keV
0.13474	$(0.82 \pm 0.19) \times 10^{-06}$	$24.12^{+0.23}_{-0.29}$	XRT 2 keV
0.13635	$(0.78 \pm 0.17) \times 10^{-06}$	$24.17^{+0.22}_{-0.28}$	XRT 2 keV
0.13772	$(1.36 \pm 0.30) \times 10^{-06}$	$23.56^{+0.22}_{-0.28}$	XRT 2 keV
0.13898	$(1.05 \pm 0.21) \times 10^{-06}$	$23.84^{+0.20}_{-0.25}$	XRT 2 keV

Table A.1: continued.

T - T_0 [days]	Flux [Jy]	AB [mag]	Band
0.25983	$(0.48 \pm 0.18) \times 10^{-06}$	$24.70^{+0.36}_{-0.54}$	XRT 2 keV
0.26627	$(0.55 \pm 0.13) \times 10^{-06}$	$24.54^{+0.24}_{-0.30}$	XRT 2 keV
0.31187	$(0.73 \pm 0.16) \times 10^{-06}$	$24.25^{+0.22}_{-0.27}$	XRT 2 keV
0.33105	$(0.44 \pm 0.12) \times 10^{-06}$	$24.79^{+0.26}_{-0.35}$	XRT 2 keV
0.33321	$(0.42 \pm 0.10) \times 10^{-06}$	$24.85^{+0.25}_{-0.32}$	XRT 2 keV
0.33549	$(0.54 \pm 0.12) \times 10^{-06}$	$24.57^{+0.23}_{-0.29}$	XRT 2 keV
0.33776	$(0.54 \pm 0.12) \times 10^{-06}$	$24.58^{+0.22}_{-0.28}$	XRT 2 keV
0.40383	$(0.47 \pm 0.12) \times 10^{-06}$	$24.72^{+0.26}_{-0.34}$	XRT 2 keV
0.40566	$(0.45 \pm 0.11) \times 10^{-06}$	$24.77^{+0.24}_{-0.31}$	XRT 2 keV
0.45723	$(0.86 \pm 0.14) \times 10^{-06}$	$24.06^{+0.17}_{-0.20}$	XRT 2 keV
0.57836	$(0.52 \pm 0.11) \times 10^{-06}$	$24.61^{+0.22}_{-0.28}$	XRT 2 keV
0.58062	$(1.05 \pm 0.20) \times 10^{-06}$	$23.85^{+0.19}_{-0.23}$	XRT 2 keV
0.64780	$(4.40 \pm 0.86) \times 10^{-07}$	$24.79^{+0.19}_{-0.24}$	XRT 2 keV
0.72256	$(0.48 \pm 0.12) \times 10^{-06}$	$24.70^{+0.25}_{-0.33}$	XRT 2 keV
0.72491	$(3.14 \pm 0.82) \times 10^{-07}$	$25.16^{+0.25}_{-0.33}$	XRT 2 keV
0.72717	$(0.68 \pm 0.14) \times 10^{-06}$	$24.32^{+0.22}_{-0.27}$	XRT 2 keV
0.72970	$(3.35 \pm 0.89) \times 10^{-07}$	$25.09^{+0.26}_{-0.34}$	XRT 2 keV
0.73196	$(0.48 \pm 0.11) \times 10^{-06}$	$24.71^{+0.24}_{-0.30}$	XRT 2 keV
0.73420	$(0.51 \pm 0.11) \times 10^{-06}$	$24.64^{+0.22}_{-0.27}$	XRT 2 keV
0.77934	$(0.44 \pm 0.11) \times 10^{-06}$	$24.79^{+0.26}_{-0.33}$	XRT 2 keV
0.78148	$(0.48 \pm 0.12) \times 10^{-06}$	$24.70^{+0.25}_{-0.33}$	XRT 2 keV
0.78472	$(4.29 \pm 0.80) \times 10^{-07}$	$24.82^{+0.19}_{-0.23}$	XRT 2 keV
0.80328	$(2.59 \pm 0.62) \times 10^{-07}$	$25.37^{+0.23}_{-0.30}$	XRT 2 keV
0.84682	$(0.40 \pm 0.10) \times 10^{-06}$	$24.89^{+0.25}_{-0.33}$	XRT 2 keV
0.84933	$(3.44 \pm 0.90) \times 10^{-07}$	$25.06^{+0.25}_{-0.33}$	XRT 2 keV
0.85203	$(0.42 \pm 0.11) \times 10^{-06}$	$24.84^{+0.25}_{-0.33}$	XRT 2 keV
0.85436	$(0.65 \pm 0.14) \times 10^{-06}$	$24.36^{+0.22}_{-0.28}$	XRT 2 keV
0.85720	$(2.72 \pm 0.72) \times 10^{-07}$	$25.31^{+0.26}_{-0.34}$	XRT 2 keV
0.86086	$(3.07 \pm 0.80) \times 10^{-07}$	$25.18^{+0.25}_{-0.33}$	XRT 2 keV
0.86342	$(0.45 \pm 0.10) \times 10^{-06}$	$24.77^{+0.22}_{-0.28}$	XRT 2 keV
0.86671	$(0.44 \pm 0.11) \times 10^{-06}$	$24.80^{+0.25}_{-0.32}$	XRT 2 keV
0.86912	$(0.41 \pm 0.10) \times 10^{-06}$	$24.87^{+0.25}_{-0.33}$	XRT 2 keV
0.87115	$(0.49 \pm 0.11) \times 10^{-06}$	$24.68^{+0.23}_{-0.30}$	XRT 2 keV
0.87428	$(0.50 \pm 0.11) \times 10^{-06}$	$24.66^{+0.23}_{-0.29}$	XRT 2 keV

Table A.1: continued.

T - T_0 [days]	Flux [Jy]	AB [mag]	Band
0.91337	$(0.42 \pm 0.11) \times 10^{-06}$	$24.83^{+0.25}_{-0.33}$	XRT 2 keV
0.91523	$(0.40 \pm 0.10) \times 10^{-06}$	$24.90^{+0.25}_{-0.33}$	XRT 2 keV
0.91831	$(4.92 \pm 0.92) \times 10^{-07}$	$24.67^{+0.19}_{-0.23}$	XRT 2 keV
0.93483	$(0.49 \pm 0.12) \times 10^{-06}$	$24.68^{+0.24}_{-0.31}$	XRT 2 keV
0.93714	$(0.46 \pm 0.11) \times 10^{-06}$	$24.74^{+0.24}_{-0.32}$	XRT 2 keV
0.94023	$(3.92 \pm 0.80) \times 10^{-07}$	$24.92^{+0.20}_{-0.25}$	XRT 2 keV
0.99305	$(3.64 \pm 0.95) \times 10^{-07}$	$25.00^{+0.25}_{-0.33}$	XRT 2 keV
0.99520	$(0.51 \pm 0.12) \times 10^{-06}$	$24.64^{+0.24}_{-0.31}$	XRT 2 keV
0.99923	$(2.07 \pm 0.55) \times 10^{-07}$	$25.61^{+0.26}_{-0.33}$	XRT 2 keV
1.00297	$(3.62 \pm 0.94) \times 10^{-07}$	$25.00^{+0.25}_{-0.33}$	XRT 2 keV
1.00541	$(3.60 \pm 0.94) \times 10^{-07}$	$25.01^{+0.25}_{-0.33}$	XRT 2 keV
1.00778	$(0.52 \pm 0.13) \times 10^{-06}$	$24.60^{+0.24}_{-0.31}$	XRT 2 keV
1.04741	$(2.96 \pm 0.78) \times 10^{-07}$	$25.22^{+0.25}_{-0.33}$	XRT 2 keV
1.05969	$(2.34 \pm 0.41) \times 10^{-07}$	$25.48^{+0.18}_{-0.21}$	XRT 2 keV
1.11522	$(3.01 \pm 0.63) \times 10^{-07}$	$25.20^{+0.21}_{-0.26}$	XRT 2 keV
1.25089	$(2.67 \pm 0.74) \times 10^{-07}$	$25.34^{+0.27}_{-0.35}$	XRT 2 keV
1.26804	$(0.52 \pm 0.13) \times 10^{-06}$	$24.61^{+0.24}_{-0.31}$	XRT 2 keV
1.27128	$(2.27 \pm 0.62) \times 10^{-07}$	$25.51^{+0.27}_{-0.35}$	XRT 2 keV
1.27480	$(3.49 \pm 0.81) \times 10^{-07}$	$25.04^{+0.23}_{-0.29}$	XRT 2 keV
1.31466	$(2.92 \pm 0.76) \times 10^{-07}$	$25.24^{+0.25}_{-0.33}$	XRT 2 keV
1.33864	$(1.85 \pm 0.38) \times 10^{-07}$	$25.73^{+0.21}_{-0.26}$	XRT 2 keV
1.38285	$(1.57 \pm 0.41) \times 10^{-07}$	$25.91^{+0.25}_{-0.33}$	XRT 2 keV
1.40841	$(2.35 \pm 0.61) \times 10^{-07}$	$25.47^{+0.25}_{-0.33}$	XRT 2 keV
1.46118	$(2.08 \pm 0.36) \times 10^{-07}$	$25.60^{+0.17}_{-0.21}$	XRT 2 keV
1.73381	$(1.42 \pm 0.28) \times 10^{-07}$	$26.02^{+0.20}_{-0.24}$	XRT 2 keV
1.80608	$(1.05 \pm 0.26) \times 10^{-07}$	$26.35^{+0.24}_{-0.32}$	XRT 2 keV
1.87122	$(1.72 \pm 0.45) \times 10^{-07}$	$25.81^{+0.25}_{-0.33}$	XRT 2 keV
1.87530	$(2.06 \pm 0.52) \times 10^{-07}$	$25.62^{+0.25}_{-0.32}$	XRT 2 keV
2.00743	$(1.85 \pm 0.39) \times 10^{-07}$	$25.73^{+0.21}_{-0.26}$	XRT 2 keV
2.28136	$(1.21 \pm 0.24) \times 10^{-07}$	$26.20^{+0.20}_{-0.24}$	XRT 2 keV
2.78891	$(0.80 \pm 0.14) \times 10^{-07}$	$26.64^{+0.18}_{-0.22}$	XRT 2 keV
2.97775	$(0.63 \pm 0.12) \times 10^{-07}$	$26.90^{+0.19}_{-0.24}$	XRT 2 keV
3.62113	$(0.67 \pm 0.14) \times 10^{-07}$	$26.83^{+0.22}_{-0.27}$	XRT 2 keV
3.80739	$(0.78 \pm 0.15) \times 10^{-07}$	$26.66^{+0.20}_{-0.24}$	XRT 2 keV

Table A.1: continued.

T - T_0 [days]	Flux [Jy]	AB [mag]	Band
4.38666	$(0.43 \pm 0.10) \times 10^{-07}$	$27.33^{+0.23}_{-0.29}$	XRT 2 keV
4.70026	$(0.43 \pm 0.11) \times 10^{-07}$	$27.31^{+0.26}_{-0.34}$	XRT 2 keV
4.84931	$(0.48 \pm 0.13) \times 10^{-07}$	$27.20^{+0.27}_{-0.36}$	XRT 2 keV
6.02367	$(2.50 \pm 0.75) \times 10^{-08}$	$27.91^{+0.29}_{-0.39}$	XRT 2 keV
6.70266	$(2.78 \pm 0.73) \times 10^{-08}$	$27.79^{+0.25}_{-0.33}$	XRT 2 keV
7.62593	$(2.28 \pm 0.59) \times 10^{-08}$	$28.01^{+0.25}_{-0.33}$	XRT 2 keV
8.92297	$(1.42 \pm 0.41) \times 10^{-08}$	$28.52^{+0.28}_{-0.38}$	XRT 2 keV
9.80520	$(1.27 \pm 0.78) \times 10^{-08}$	$28.64^{+0.52}_{-1.05}$	XRT 2 keV
0.04936	¡ 0.60×10^{-05}	¿ 21.95	UVOT uvw2
0.06599	¡ 0.74×10^{-05}	¿ 21.72	UVOT uvw2
7.64330	¡ 0.88×10^{-06}	¿ 24.03	UVOT uvw2
0.05411	¡ 0.86×10^{-05}	¿ 21.56	UVOT uvm2
0.07073	¡ 0.11×10^{-04}	¿ 21.23	UVOT uvm2
8.71353	¡ 0.21×10^{-05}	¿ 23.07	UVOT uvm2
0.05648	¡ 0.98×10^{-05}	¿ 21.42	UVOT uvw1
0.07232	¡ 0.42×10^{-05}	¿ 22.32	UVOT uvw1
0.11407	¡ 0.61×10^{-05}	¿ 21.92	UVOT uvw1
6.10495	¡ 0.41×10^{-06}	¿ 24.85	UVOT uvw1
9.64872	¡ 0.42×10^{-06}	¿ 24.82	UVOT uvw1
0.00394	$(1.02 \pm 0.13) \times 10^{-04}$	$18.88^{+0.15}_{-0.13}$	UVOT u
0.00474	$(0.93 \pm 0.11) \times 10^{-04}$	$18.98^{+0.14}_{-0.12}$	UVOT u
0.00551	$(0.63 \pm 0.11) \times 10^{-04}$	$19.41^{+0.23}_{-0.19}$	UVOT u
0.05886	$(1.10 \pm 0.42) \times 10^{-05}$	$21.30^{+0.53}_{-0.36}$	UVOT u
0.13530	$(1.00 \pm 0.21) \times 10^{-05}$	$21.40^{+0.26}_{-0.21}$	UVOT u
0.28371	¡ 0.16×10^{-04}	¿ 20.83	UVOT u
0.36449	¡ 0.26×10^{-04}	¿ 20.36	UVOT u
0.45115	¡ 0.24×10^{-04}	¿ 20.43	UVOT u
0.61076	¡ 0.13×10^{-04}	¿ 21.07	UVOT u
0.78153	¡ 0.14×10^{-04}	¿ 21.01	UVOT u
1.00808	$(0.93 \pm 0.34) \times 10^{-05}$	$21.48^{+0.50}_{-0.34}$	UVOT u
1.37423	¡ 0.53×10^{-05}	¿ 22.09	UVOT u
1.86113	¡ 0.15×10^{-04}	¿ 20.92	UVOT u
2.27112	¡ 0.19×10^{-04}	¿ 20.70	UVOT u
2.86062	¡ 0.37×10^{-05}	¿ 22.48	UVOT u

Table A.1: continued.

T - T_0 [days]	Flux [Jy]	AB [mag]	Band
7.01244	¡ 0.40×10^{-05}	¿ 22.39	UVOT u
0.00323	$(33.15 \pm 0.76) \times 10^{-05}$	17.60 ± 0.03	UVOT b
0.04392	$(0.54 \pm 0.16) \times 10^{-04}$	$19.56^{+0.39}_{-0.29}$	UVOT b
0.06123	$(5.11 \pm 0.97) \times 10^{-05}$	$19.63^{+0.23}_{-0.19}$	UVOT b
2.51402	$(4.51^{+0.40}_{-0.37}) \times 10^{-06}$	22.26 ± 0.09	GROND g'
4.49622	$(2.47^{+0.14}_{-0.13}) \times 10^{-06}$	22.92 ± 0.06	GROND g'
4.52934	$(2.55 \pm 0.13) \times 10^{-06}$	22.88 ± 0.05	GROND g'
6.50292	$(1.40^{+0.19}_{-0.17}) \times 10^{-06}$	23.53 ± 0.14	GROND g'
8.52834	$(0.75^{+0.11}_{-0.10}) \times 10^{-06}$	24.21 ± 0.15	GROND g'
606.83450	¡ 0.31×10^{-06}	¿ 25.15	GROND g'
0.00121	$(3.22 \pm 0.28) \times 10^{-04}$	$17.63^{+0.10}_{-0.09}$	UVOT white
0.00132	$(2.54 \pm 0.24) \times 10^{-04}$	$17.89^{+0.11}_{-0.10}$	UVOT white
0.00144	$(2.49 \pm 0.24) \times 10^{-04}$	$17.91^{+0.11}_{-0.10}$	UVOT white
0.00156	$(2.27 \pm 0.22) \times 10^{-04}$	$18.01^{+0.12}_{-0.10}$	UVOT white
0.00167	$(2.01 \pm 0.21) \times 10^{-04}$	$18.14^{+0.12}_{-0.11}$	UVOT white
0.00179	$(1.91 \pm 0.20) \times 10^{-04}$	$18.20^{+0.13}_{-0.11}$	UVOT white
0.00190	$(1.84 \pm 0.20) \times 10^{-04}$	$18.24^{+0.13}_{-0.11}$	UVOT white
0.00202	$(1.71 \pm 0.19) \times 10^{-04}$	$18.32^{+0.13}_{-0.12}$	UVOT white
0.00214	$(1.58 \pm 0.18) \times 10^{-04}$	$18.40^{+0.14}_{-0.12}$	UVOT white
0.00225	$(1.26 \pm 0.17) \times 10^{-04}$	$18.65^{+0.16}_{-0.14}$	UVOT white
0.00237	$(1.50 \pm 0.18) \times 10^{-04}$	$18.46^{+0.14}_{-0.13}$	UVOT white
0.00248	$(1.50 \pm 0.18) \times 10^{-04}$	$18.46^{+0.14}_{-0.13}$	UVOT white
0.00260	$(1.19 \pm 0.16) \times 10^{-04}$	$18.71^{+0.16}_{-0.14}$	UVOT white
0.00271	$(1.08 \pm 0.15) \times 10^{-04}$	$18.82^{+0.17}_{-0.15}$	UVOT white
0.00283	$(1.34 \pm 0.17) \times 10^{-04}$	$18.58^{+0.15}_{-0.14}$	UVOT white
0.04698	$(2.01 \pm 0.32) \times 10^{-05}$	$20.64^{+0.19}_{-0.16}$	UVOT white
0.06360	$(1.80 \pm 0.30) \times 10^{-05}$	$20.76^{+0.20}_{-0.17}$	UVOT white
0.28542	$(1.10 \pm 0.17) \times 10^{-05}$	$21.30^{+0.19}_{-0.16}$	UVOT white
0.33267	$(1.24 \pm 0.22) \times 10^{-05}$	$21.17^{+0.21}_{-0.18}$	UVOT white
0.43672	$(1.68 \pm 0.26) \times 10^{-05}$	$20.84^{+0.19}_{-0.16}$	UVOT white
0.61474	$(0.70 \pm 0.13) \times 10^{-05}$	$21.79^{+0.23}_{-0.19}$	UVOT white
0.78835	$(7.52 \pm 0.65) \times 10^{-06}$	$21.71^{+0.10}_{-0.09}$	UVOT white
0.98959	$(8.63 \pm 0.67) \times 10^{-06}$	$21.56^{+0.09}_{-0.08}$	UVOT white
1.22145	$(5.75 \pm 0.91) \times 10^{-06}$	$22.00^{+0.19}_{-0.16}$	UVOT white

Table A.1: continued.

T - T_0 [days]	Flux [Jy]	AB [mag]	Band
1.44721	$(0.31 \pm 0.10) \times 10^{-05}$	$22.68^{+0.43}_{-0.31}$	UVOT white
1.86317	$(3.28 \pm 0.73) \times 10^{-06}$	$22.61^{+0.27}_{-0.22}$	UVOT white
2.27295	$(0.43 \pm 0.11) \times 10^{-05}$	$22.31^{+0.35}_{-0.26}$	UVOT white
2.86442	$(1.21 \pm 0.61) \times 10^{-06}$	$23.69^{+0.77}_{-0.44}$	UVOT white
3.88343	$(1.29 \pm 0.49) \times 10^{-06}$	$23.62^{+0.53}_{-0.35}$	UVOT white
4.60764	$(0.76 \pm 0.46) \times 10^{-06}$	$24.20^{+1.02}_{-0.52}$	UVOT white
5.39492	¡ 0.87×10^{-05}	¿ 21.54	UVOT white
0.00099	$(1.79 \pm 0.24) \times 10^{-03}$	$15.77^{+0.16}_{-0.14}$	UVOT v
0.05173	$(0.81 \pm 0.20) \times 10^{-04}$	$19.13^{+0.31}_{-0.24}$	UVOT v
0.06835	$(0.64 \pm 0.19) \times 10^{-04}$	$19.38^{+0.39}_{-0.29}$	UVOT v
0.26973	$(0.41 \pm 0.10) \times 10^{-04}$	$19.87^{+0.32}_{-0.25}$	UVOT v
0.36934	$(0.59 \pm 0.10) \times 10^{-04}$	$19.47^{+0.22}_{-0.18}$	UVOT v
0.47368	¡ 0.14×10^{-03}	¿ 18.47	UVOT v
0.80018	$(2.40 \pm 0.58) \times 10^{-05}$	$20.45^{+0.30}_{-0.24}$	UVOT v
1.00463	$(4.13 \pm 0.69) \times 10^{-05}$	$19.86^{+0.20}_{-0.17}$	UVOT v
1.37053	$(2.99 \pm 0.80) \times 10^{-05}$	$20.21^{+0.34}_{-0.26}$	UVOT v
1.86764	$(1.91 \pm 0.60) \times 10^{-05}$	$20.70^{+0.42}_{-0.30}$	UVOT v
2.27620	¡ 0.26×10^{-04}	¿ 20.34	UVOT v
2.87012	$(1.34 \pm 0.51) \times 10^{-05}$	$21.08^{+0.52}_{-0.35}$	UVOT v
2.51402	$(14.76^{+0.68}_{-0.65}) \times 10^{-06}$	20.98 ± 0.05	GROND r’
4.49622	$(6.91^{+0.21}_{-0.20}) \times 10^{-06}$	21.80 ± 0.03	GROND r’
4.52934	$(6.58^{+0.22}_{-0.21}) \times 10^{-06}$	21.85 ± 0.04	GROND r’
6.50292	$(3.39^{+0.21}_{-0.20}) \times 10^{-06}$	22.57 ± 0.07	GROND r’
8.52834	$(2.00^{+0.21}_{-0.19}) \times 10^{-06}$	23.15 ± 0.11	GROND r’
606.83450	¡ 0.56×10^{-06}	¿ 24.52	GROND r’
2.51402	$(2.92 \pm 0.10) \times 10^{-05}$	20.24 ± 0.04	GROND i’
4.49622	$(13.20^{+0.46}_{-0.44}) \times 10^{-06}$	21.10 ± 0.04	GROND i’
4.52934	$(13.05^{+0.44}_{-0.43}) \times 10^{-06}$	21.11 ± 0.04	GROND i’
6.50292	$(6.72^{+0.55}_{-0.51}) \times 10^{-06}$	21.83 ± 0.09	GROND i’
8.52834	$(4.51^{+0.48}_{-0.43}) \times 10^{-06}$	22.26 ± 0.11	GROND i’
606.83450	¡ 0.10×10^{-05}	¿ 23.86	GROND i’
750.94580	$(0.70^{+0.28}_{-0.20}) \times 10^{-07}$	26.78 ± 0.36	FORS Ic
2.51402	$(4.65^{+0.19}_{-0.18}) \times 10^{-05}$	19.73 ± 0.04	GROND z’
4.49622	$(19.41^{+0.82}_{-0.79}) \times 10^{-06}$	20.68 ± 0.05	GROND z’

Table A.1: continued.

T - T_0 [days]	Flux [Jy]	AB [mag]	Band
4.52934	$(19.92^{+0.73}_{-0.70}) \times 10^{-06}$	20.65 ± 0.04	GROND z'
6.50292	$(9.88^{+0.77}_{-0.71}) \times 10^{-06}$	21.41 ± 0.08	GROND z'
8.52834	$(0.75^{+0.10}_{-0.09}) \times 10^{-05}$	21.71 ± 0.14	GROND z'
606.83450	¡ 0.15×10^{-05}	¿ 23.44	GROND z'
2.51402	$(8.47^{+0.64}_{-0.59}) \times 10^{-05}$	19.08 ± 0.08	GROND J
4.49622	$(0.43^{+0.11}_{-0.09}) \times 10^{-04}$	19.82 ± 0.24	GROND J
4.52934	$(0.46^{+0.10}_{-0.08}) \times 10^{-04}$	19.75 ± 0.22	GROND J
6.50292	$(2.09^{+0.51}_{-0.41}) \times 10^{-05}$	20.60 ± 0.24	GROND J
8.52834	$(1.09^{+0.30}_{-0.24}) \times 10^{-05}$	21.31 ± 0.27	GROND J
38.46488	¡ 0.10×10^{-04}	¿ 21.34	GROND J
606.83450	¡ 0.12×10^{-04}	¿ 21.13	GROND J
2.51402	$(1.41 \pm 0.10) \times 10^{-04}$	18.53 ± 0.08	GROND H
4.49622	$(0.67^{+0.10}_{-0.09}) \times 10^{-04}$	19.34 ± 0.15	GROND H
4.52934	$(0.67^{+0.11}_{-0.10}) \times 10^{-04}$	19.33 ± 0.17	GROND H
6.50292	$(3.10^{+0.77}_{-0.61}) \times 10^{-05}$	20.17 ± 0.24	GROND H
8.52834	$(2.29^{+0.49}_{-0.41}) \times 10^{-05}$	20.50 ± 0.21	GROND H
38.46488	¡ 0.14×10^{-04}	¿ 20.98	GROND H
606.83450	¡ 0.18×10^{-04}	¿ 20.75	GROND H
2.51402	$(1.85^{+0.14}_{-0.13}) \times 10^{-04}$	18.23 ± 0.08	GROND K
4.49622	$(0.81^{+0.10}_{-0.09}) \times 10^{-04}$	19.12 ± 0.13	GROND K
4.52934	$(0.85^{+0.10}_{-0.09}) \times 10^{-04}$	19.08 ± 0.12	GROND K
6.50292	$(0.38^{+0.13}_{-0.10}) \times 10^{-04}$	19.95 ± 0.32	GROND K
8.52834	$(0.30^{+0.18}_{-0.11}) \times 10^{-04}$	20.22 ± 0.52	GROND K
38.46488	¡ 0.22×10^{-04}	¿ 20.54	GROND K
606.83450	¡ 0.21×10^{-04}	¿ 20.58	GROND K
1.42000	$(1.10 \pm 0.20) \times 10^{-02}$	$13.80^{+0.18}_{-0.22}$	APEX 345 GHz
3.57000	$(6.30 \pm 0.70) \times 10^{-03}$	$14.40^{+0.11}_{-0.13}$	ALMA 345 GHz
2.00400	$(5.10 \pm 0.90) \times 10^{-04}$	$17.13^{+0.18}_{-0.21}$	ATCA 44 GHz
2.94500	$(20.50 \pm 0.50) \times 10^{-04}$	15.62 ± 0.03	ATCA 44 GHz
11.73800	$(18.90 \pm 0.80) \times 10^{-04}$	$15.71^{+0.04}_{-0.05}$	ATCA 44 GHz
17.52100	$(11.80 \pm 0.80) \times 10^{-04}$	$16.22^{+0.07}_{-0.08}$	ATCA 44 GHz
32.33500	$(6.50 \pm 0.90) \times 10^{-04}$	$16.87^{+0.14}_{-0.16}$	ATCA 44 GHz
74.33000	$(3.50 \pm 0.10) \times 10^{-04}$	17.54 ± 0.03	ATCA 44 GHz
3.97200	$(7.30 \pm 0.60) \times 10^{-04}$	16.74 ± 0.09	ATCA 18 GHz

Table A.1: continued.

T - T_0 [days]	Flux [Jy]	AB [mag]	Band
4.06700	$(7.90 \pm 0.40) \times 10^{-04}$	$16.66^{+0.05}_{-0.06}$	ATCA 18 GHz
10.72300	$(14.70 \pm 0.60) \times 10^{-04}$	$15.98^{+0.04}_{-0.05}$	ATCA 18 GHz
17.55100	$(11.00 \pm 0.30) \times 10^{-04}$	16.30 ± 0.03	ATCA 18 GHz
41.52600	$(5.10 \pm 0.90) \times 10^{-04}$	$17.13^{+0.18}_{-0.21}$	ATCA 18 GHz
74.36700	$(6.70 \pm 0.40) \times 10^{-04}$	$16.83^{+0.06}_{-0.07}$	ATCA 18 GHz
3.99200	$(4.40 \pm 0.40) \times 10^{-04}$	$17.29^{+0.09}_{-0.10}$	ATCA 9 GHz
17.59600	$(5.80 \pm 0.40) \times 10^{-04}$	$16.99^{+0.07}_{-0.08}$	ATCA 9 GHz
18.51700	$(8.30 \pm 0.70) \times 10^{-04}$	$16.60^{+0.09}_{-0.10}$	ATCA 9 GHz
41.55500	$(5.10 \pm 0.70) \times 10^{-04}$	$17.13^{+0.14}_{-0.16}$	ATCA 9 GHz
3.99200	$(5.30 \pm 0.30) \times 10^{-04}$	17.09 ± 0.06	ATCA 5.5 GHz
4.70000	$(4.00 \pm 0.50) \times 10^{-04}$	$17.39^{+0.13}_{-0.15}$	ATCA 5.5 GHz
12.67900	$(4.30 \pm 0.40) \times 10^{-04}$	$17.32^{+0.10}_{-0.11}$	ATCA 5.5 GHz
17.59600	$(6.20 \pm 0.30) \times 10^{-04}$	16.92 ± 0.05	ATCA 5.5 GHz
18.51700	$(4.80 \pm 0.40) \times 10^{-04}$	17.20 ± 0.09	ATCA 5.5 GHz
41.55500	$(2.90 \pm 0.50) \times 10^{-04}$	$17.74^{+0.17}_{-0.21}$	ATCA 5.5 GHz

Appendix B

Detailed goodness analysis of the fits to GRB 110715A.

B.1 Fit to all bands, except UV, MW extinction corrected

CM Model

Band	χ^2	d.o.f.	χ^2_{red}	χ^2_{frac}	$\chi^2_{frac,color}$	$\chi^2_{red,frac}$	$\chi^2_{red,frac,color}$
XRT 2 keV	655	267	2.45	28.38	100.00	0.80	100.00
UVOT uvw2	0	0	0.00	0.00	0.00	0.00	0.00
UVOT uvm2	0	0	0.00	0.00	0.00	0.00	0.00
UVOT uvw1	0	0	0.00	0.00	0.00	0.00	0.00
UVOT u	0	0	0.00	0.00	0.00	0.00	0.00
UVOT b	47	2	23.36	2.02	4.17	7.67	17.92
GROND g'	110	4	27.42	4.75	9.78	9.00	21.04
UVOT white	671	29	23.14	29.08	59.86	7.59	17.75
UVOT v	122	9	13.57	5.29	10.90	4.45	10.41
GROND r'	101	4	25.34	4.39	9.04	8.31	19.43
GROND i'	11	4	2.76	0.48	0.99	0.91	2.12
GROND z'	20	4	5.08	0.88	1.81	1.67	3.90
GROND J	9	4	2.37	0.41	0.85	0.78	1.82
GROND H	20	4	5.04	0.87	1.80	1.66	3.87
GROND K	9	4	2.27	0.39	0.81	0.74	1.74
APEX+ALMA 345 GHz	69	1	68.71	2.98	12.92	22.55	39.97
ATCA 44 GHz	120	5	23.98	5.20	22.55	7.87	13.95
ATCA 18 GHz	217	5	43.38	9.40	40.80	14.24	25.24
ATCA 9 GHz	79	3	26.49	3.44	14.95	8.69	15.41
ATCA 5.5 GHz	47	5	9.33	2.02	8.77	3.06	5.43

TS Model

Band	χ^2	d.o.f.	χ^2_{red}	χ^2_{frac}	$\chi^2_{frac,color}$	$\chi^2_{red,frac}$	$\chi^2_{red,frac,color}$
XRT 2 keV	535	267	2.00	24.19	100.00	0.57	100.00
UVOT uvw2	0	0	0.00	0.00	0.00	0.00	0.00
UVOT uvm2	0	0	0.00	0.00	0.00	0.00	0.00
UVOT uvw1	0	0	0.00	0.00	0.00	0.00	0.00
UVOT u	0	0	0.00	0.00	0.00	0.00	0.00
UVOT b	20	2	9.84	0.89	1.80	2.79	6.08
GROND g'	177	4	44.37	8.03	16.19	12.57	27.41
UVOT white	492	29	16.95	22.24	44.84	4.80	10.47
UVOT v	81	9	8.98	3.66	7.37	2.54	5.55
GROND r'	223	4	55.86	10.11	20.38	15.83	34.51
GROND i'	36	4	9.06	1.64	3.31	2.57	5.60
GROND z'	35	4	8.78	1.59	3.20	2.49	5.43
GROND J	9	4	2.14	0.39	0.78	0.61	1.32
GROND H	16	4	3.95	0.71	1.44	1.12	2.44
GROND K	8	4	1.92	0.35	0.70	0.54	1.19
APEX+ALMA 345 GHz	77	1	77.01	3.48	13.30	21.82	40.73
ATCA 44 GHz	121	5	24.24	5.48	20.93	6.87	12.82
ATCA 18 GHz	239	5	47.79	10.81	41.26	13.54	25.28
ATCA 9 GHz	87	3	29.05	3.94	15.05	8.23	15.36
ATCA 5.5 GHz	55	5	10.97	2.48	9.47	3.11	5.80

WM Model

Band	χ^2	d.o.f.	χ^2_{red}	χ^2_{frac}	$\chi^2_{frac,color}$	$\chi^2_{red,frac}$	$\chi^2_{red,frac,color}$
XRT 2 keV	698	267	2.61	20.15	100.00	0.51	100.00
UVOT uvw2	0	0	0.00	0.00	0.00	0.00	0.00
UVOT uvm2	0	0	0.00	0.00	0.00	0.00	0.00
UVOT uvw1	0	0	0.00	0.00	0.00	0.00	0.00
UVOT u	0	0	0.00	0.00	0.00	0.00	0.00
UVOT b	135	2	67.52	3.90	6.71	13.16	21.08
GROND g'	249	4	62.19	7.18	12.36	12.12	19.42
UVOT white	943	29	32.50	27.22	46.83	6.33	10.15
UVOT v	97	9	10.76	2.80	4.81	2.10	3.36
GROND r'	378	4	94.52	10.92	18.78	18.42	29.51
GROND i'	101	4	25.21	2.91	5.01	4.91	7.87
GROND z'	77	4	19.35	2.23	3.85	3.77	6.04
GROND J	13	4	3.31	0.38	0.66	0.65	1.03
GROND H	13	4	3.36	0.39	0.67	0.65	1.05
GROND K	6	4	1.62	0.19	0.32	0.32	0.51
APEX+ALMA 345 GHz	37	1	36.63	1.06	4.87	7.14	19.26
ATCA 44 GHz	253	5	50.66	7.31	33.66	9.87	26.64
ATCA 18 GHz	333	5	66.53	9.60	44.20	12.97	34.98
ATCA 9 GHz	78	3	25.87	2.24	10.31	5.04	13.61
ATCA 5.5 GHz	52	5	10.48	1.51	6.96	2.04	5.51

B.2 Fit to all bands, including MW extinction

CM Model

Band	χ^2	d.o.f.	χ^2_{red}	χ^2_{frac}	$\chi^2_{frac,color}$	$\chi^2_{red,frac}$	$\chi^2_{red,frac,color}$
XRT 2 keV	658	267	2.46	26.49	100.00	0.51	100.00
UVOT uvw2	0	0	0.00	0.00	0.00	0.00	0.00
UVOT uvm2	0	0	0.00	0.00	0.00	0.00	0.00
UVOT uvw1	0	0	0.00	0.00	0.00	0.00	0.00
UVOT u	62	5	12.49	2.51	5.43	2.58	5.53
UVOT b	37	2	18.52	1.49	3.22	3.83	8.19
GROND g'	194	4	48.53	7.82	16.88	10.04	21.47
UVOT white	262	29	9.05	10.56	22.81	1.87	4.00
UVOT v	79	9	8.80	3.19	6.89	1.82	3.89
GROND r'	279	4	69.82	11.24	24.29	14.44	30.88
GROND i'	82	4	20.52	3.30	7.14	4.24	9.08
GROND z'	78	4	19.50	3.14	6.78	4.03	8.63
GROND J	22	4	5.50	0.89	1.91	1.14	2.43
GROND H	33	4	8.22	1.32	2.86	1.70	3.64
GROND K	21	4	5.13	0.83	1.79	1.06	2.27
APEX+ALMA 345 GHz	142	1	141.66	5.70	20.96	29.29	55.55
ATCA 44 GHz	187	5	37.47	7.54	27.72	7.75	14.69
ATCA 18 GHz	140	5	28.06	5.65	20.76	5.80	11.00
ATCA 9 GHz	49	3	16.34	1.97	7.25	3.38	6.41
ATCA 5.5 GHz	157	5	31.50	6.34	23.30	6.51	12.35

TS Model

Band	χ^2	d.o.f.	χ^2_{red}	χ^2_{frac}	$\chi^2_{frac,color}$	$\chi^2_{red,frac}$	$\chi^2_{red,frac,color}$
XRT 2 keV	512	267	1.92	20.98	100.00	0.45	100.00
UVOT uvw2	0	0	0.00	0.00	0.00	0.00	0.00
UVOT uvm2	0	0	0.00	0.00	0.00	0.00	0.00
UVOT uvw1	0	0	0.00	0.00	0.00	0.00	0.00
UVOT u	102	5	20.31	4.16	7.64	4.75	8.89
UVOT b	18	2	9.20	0.75	1.38	2.15	4.03
GROND g'	227	4	56.79	9.32	17.08	13.29	24.86
UVOT white	431	29	14.85	17.66	32.37	3.47	6.50
UVOT v	78	9	8.64	3.19	5.85	2.02	3.78
GROND r'	320	4	80.00	13.12	24.06	18.72	35.02
GROND i'	69	4	17.18	2.82	5.17	4.02	7.52
GROND z'	57	4	14.15	2.32	4.26	3.31	6.19
GROND J	8	4	2.09	0.34	0.63	0.49	0.91
GROND H	14	4	3.39	0.56	1.02	0.79	1.49
GROND K	7	4	1.83	0.30	0.55	0.43	0.80
APEX+ALMA 345 GHz	82	1	81.71	3.35	13.69	19.12	41.46
ATCA 44 GHz	125	5	24.91	5.11	20.86	5.83	12.64
ATCA 18 GHz	242	5	48.40	9.92	40.53	11.32	24.56
ATCA 9 GHz	92	3	30.73	3.78	15.44	7.19	15.60
ATCA 5.5 GHz	57	5	11.31	2.32	9.47	2.65	5.74

WM Model

Band	χ^2	d.o.f.	χ^2_{red}	χ^2_{frac}	$\chi^2_{frac,color}$	$\chi^2_{red,frac}$	$\chi^2_{red,frac,color}$
XRT 2 keV	601	267	2.25	2.94	100.00	0.05	100.00
UVOT uvw2	0	0	0.00	0.00	0.00	0.00	0.00
UVOT uvm2	0	0	0.00	0.00	0.00	0.00	0.00
UVOT uvw1	0	0	0.00	0.00	0.00	0.00	0.00
UVOT u	978	5	195.54	4.78	5.15	3.92	4.18
UVOT b	3887	2	1943.45	18.99	20.49	38.99	41.59
GROND g'	1695	4	423.65	8.28	8.93	8.50	9.07
UVOT white	4407	29	151.98	21.53	23.24	3.05	3.25
UVOT v	300	9	33.29	1.46	1.58	0.67	0.71
GROND r'	3671	4	917.77	17.93	19.35	18.41	19.64
GROND i'	2200	4	550.06	10.75	11.60	11.03	11.77
GROND z'	1533	4	383.16	7.49	8.08	7.69	8.20
GROND J	121	4	30.34	0.59	0.64	0.61	0.65
GROND H	89	4	22.25	0.43	0.47	0.45	0.48
GROND K	87	4	21.79	0.43	0.46	0.44	0.47
APEX+ALMA 345 GHz	140	1	139.88	0.68	15.51	2.81	45.20
ATCA 44 GHz	244	5	48.77	1.19	27.05	0.98	15.76
ATCA 18 GHz	171	5	34.19	0.84	18.96	0.69	11.05
ATCA 9 GHz	129	3	43.09	0.63	14.34	0.86	13.93
ATCA 5.5 GHz	218	5	43.54	1.06	24.14	0.87	14.07

B.3 Fit to all bands except UV, including MW extinction

CM Model

Band	χ^2	d.o.f.	χ^2_{red}	χ^2_{frac}	$\chi^2_{frac,color}$	$\chi^2_{red,frac}$	$\chi^2_{red,frac,color}$
XRT 2 keV	655	267	2.45	27.24	100.00	0.52	100.00
UVOT uvw2	0	0	0.00	0.00	0.00	0.00	0.00
UVOT uvm2	0	0	0.00	0.00	0.00	0.00	0.00
UVOT uvw1	0	0	0.00	0.00	0.00	0.00	0.00
UVOT u	0	0	0.00	0.00	0.00	0.00	0.00
UVOT b	43	2	21.42	1.78	3.97	4.56	10.01
GROND g'	191	4	47.73	7.94	17.71	10.16	22.31
UVOT white	255	29	8.80	10.61	23.67	1.87	4.11
UVOT v	81	9	9.05	3.38	7.55	1.93	4.23
GROND r'	274	4	68.46	11.38	25.39	14.57	31.99
GROND i'	81	4	20.22	3.36	7.50	4.30	9.45
GROND z'	77	4	19.36	3.22	7.18	4.12	9.05
GROND J	22	4	5.52	0.92	2.05	1.18	2.58
GROND H	33	4	8.28	1.38	3.07	1.76	3.87
GROND K	21	4	5.16	0.86	1.91	1.10	2.41
APEX+ALMA 345 GHz	140	1	140.20	5.83	20.87	29.84	55.34
ATCA 44 GHz	183	5	36.50	7.59	27.17	7.77	14.41
ATCA 18 GHz	144	5	28.75	5.98	21.40	6.12	11.35
ATCA 9 GHz	51	3	17.11	2.13	7.64	3.64	6.75
ATCA 5.5 GHz	154	5	30.78	6.40	22.91	6.55	12.15

TS Model

Band	χ^2	d.o.f.	χ^2_{red}	χ^2_{frac}	$\chi^2_{frac,color}$	$\chi^2_{red,frac}$	$\chi^2_{red,frac,color}$
XRT 2 keV	510	267	1.91	22.15	100.00	0.48	100.00
UVOT uvw2	0	0	0.00	0.00	0.00	0.00	0.00
UVOT uvm2	0	0	0.00	0.00	0.00	0.00	0.00
UVOT uvw1	0	0	0.00	0.00	0.00	0.00	0.00
UVOT u	0	0	0.00	0.00	0.00	0.00	0.00
UVOT b	19	2	9.46	0.82	1.58	2.38	4.73
GROND g'	219	4	54.82	9.53	18.32	13.78	27.41
UVOT white	432	29	14.90	18.78	36.10	3.75	7.45
UVOT v	78	9	8.71	3.41	6.55	2.19	4.35
GROND r'	304	4	75.94	13.20	25.37	19.09	37.97
GROND i'	63	4	15.64	2.72	5.23	3.93	7.82
GROND z'	52	4	13.11	2.28	4.38	3.29	6.55
GROND J	8	4	2.08	0.36	0.69	0.52	1.04
GROND H	14	4	3.49	0.61	1.17	0.88	1.75
GROND K	7	4	1.85	0.32	0.62	0.47	0.93
APEX+ALMA 345 GHz	81	1	81.41	3.54	13.70	20.47	41.57
ATCA 44 GHz	126	5	25.13	5.46	21.15	6.32	12.83
ATCA 18 GHz	243	5	48.61	10.56	40.92	12.22	24.82
ATCA 9 GHz	89	3	29.75	3.88	15.03	7.48	15.19
ATCA 5.5 GHz	55	5	10.93	2.38	9.20	2.75	5.58

WM Model

Band	χ^2	d.o.f.	χ^2_{red}	χ^2_{frac}	$\chi^2_{frac,color}$	$\chi^2_{red,frac}$	$\chi^2_{red,frac,color}$
XRT 2 keV	590	267	2.21	3.06	100.00	0.05	100.00
UVOT uvw2	0	0	0.00	0.00	0.00	0.00	0.00
UVOT uvm2	0	0	0.00	0.00	0.00	0.00	0.00
UVOT uvw1	0	0	0.00	0.00	0.00	0.00	0.00
UVOT u	0	0	0.00	0.00	0.00	0.00	0.00
UVOT b	3813	2	1906.53	19.78	21.43	40.30	43.13
GROND g'	1670	4	417.56	8.66	9.39	8.83	9.45
UVOT white	4361	29	150.38	22.62	24.51	3.18	3.40
UVOT v	305	9	33.94	1.58	1.72	0.72	0.77
GROND r'	3632	4	908.09	18.84	20.41	19.20	20.55
GROND i'	2184	4	546.00	11.33	12.27	11.54	12.35
GROND z'	1527	4	381.78	7.92	8.58	8.07	8.64
GROND J	122	4	30.57	0.63	0.69	0.65	0.69
GROND H	91	4	22.68	0.47	0.51	0.48	0.51
GROND K	90	4	22.48	0.47	0.51	0.48	0.51
APEX+ALMA 345 GHz	142	1	142.01	0.74	15.90	3.00	46.06
ATCA 44 GHz	263	5	52.69	1.37	29.51	1.11	17.09
ATCA 18 GHz	167	5	33.32	0.86	18.66	0.70	10.81
ATCA 9 GHz	121	3	40.36	0.63	13.56	0.85	13.09
ATCA 5.5 GHz	200	5	39.96	1.04	22.37	0.84	12.96

B.4 Fit to all bands except UV, MW extinction corrected, White shifted to V

CM Model

Band	χ^2	d.o.f.	χ^2_{red}	χ^2_{frac}	$\chi^2_{frac,color}$	$\chi^2_{red,frac}$	$\chi^2_{red,frac,color}$
XRT 2 keV	666	267	2.49	33.34	100.00	0.91	100.00
UVOT uvw2	0	0	0.00	0.00	0.00	0.00	0.00
UVOT uvm2	0	0	0.00	0.00	0.00	0.00	0.00
UVOT uvw1	0	0	0.00	0.00	0.00	0.00	0.00
UVOT u	0	0	0.00	0.00	0.00	0.00	0.00
UVOT b	62	2	30.81	3.08	7.51	11.20	29.12
GROND g'	70	4	17.44	3.49	8.50	6.34	16.48
UVOT v+white	518	35	14.80	25.93	63.14	5.38	13.99
GROND r'	42	4	10.47	2.10	5.11	3.81	9.90
GROND i'	26	4	6.44	1.29	3.14	2.34	6.09
GROND z'	39	4	9.87	1.98	4.81	3.59	9.33
GROND J	15	4	3.78	0.76	1.84	1.37	3.57
GROND H	32	4	8.01	1.60	3.90	2.91	7.57
GROND K	17	4	4.18	0.84	2.04	1.52	3.95
APEX+ALMA 345 GHz	68	1	67.83	3.40	13.27	24.66	40.67
ATCA 44 GHz	119	5	23.84	5.97	23.32	8.67	14.30
ATCA 18 GHz	206	5	41.13	10.29	40.22	14.95	24.66
ATCA 9 GHz	77	3	25.64	3.85	15.04	9.32	15.37
ATCA 5.5 GHz	42	5	8.34	2.09	8.16	3.03	5.00

TS Model

Band	χ^2	d.o.f.	χ^2_{red}	χ^2_{frac}	$\chi^2_{frac,color}$	$\chi^2_{red,frac}$	$\chi^2_{red,frac,color}$
XRT 2 keV	570	267	2.14	29.48	100.00	0.68	100.00
UVOT uvw2	0	0	0.00	0.00	0.00	0.00	0.00
UVOT uvm2	0	0	0.00	0.00	0.00	0.00	0.00
UVOT uvw1	0	0	0.00	0.00	0.00	0.00	0.00
UVOT u	0	0	0.00	0.00	0.00	0.00	0.00
UVOT b	27	2	13.58	1.40	3.52	4.32	11.64
GROND g'	130	4	32.51	6.72	16.86	10.35	27.87
UVOT v+white	375	35	10.70	19.36	48.56	3.41	9.17
GROND r'	137	4	34.37	7.11	17.83	10.95	29.47
GROND i'	22	4	5.55	1.15	2.88	1.77	4.76
GROND z'	31	4	7.69	1.59	3.99	2.45	6.59
GROND J	12	4	3.12	0.64	1.62	0.99	2.67
GROND H	24	4	6.02	1.24	3.12	1.92	5.16
GROND K	12	4	3.12	0.65	1.62	1.00	2.68
APEX+ALMA 345 GHz	80	1	79.95	4.13	13.49	25.46	40.96
ATCA 44 GHz	128	5	25.65	6.63	21.63	8.17	13.14
ATCA 18 GHz	231	5	46.13	11.92	38.90	14.69	23.63
ATCA 9 GHz	95	3	31.65	4.91	16.02	10.08	16.21
ATCA 5.5 GHz	59	5	11.82	3.05	9.97	3.76	6.05

WM Model

Band	χ^2	d.o.f.	χ^2_{red}	χ^2_{frac}	$\chi^2_{frac,color}$	$\chi^2_{red,frac}$	$\chi^2_{red,frac,color}$
XRT 2 keV	729	267	2.73	27.88	100.00	0.63	100.00
UVOT uvw2	0	0	0.00	0.00	0.00	0.00	0.00
UVOT uvm2	0	0	0.00	0.00	0.00	0.00	0.00
UVOT uvw1	0	0	0.00	0.00	0.00	0.00	0.00
UVOT u	0	0	0.00	0.00	0.00	0.00	0.00
UVOT b	168	2	83.84	6.41	14.31	19.21	33.45
GROND g'	194	4	48.52	7.42	16.56	11.11	19.36
UVOT v+white	381	35	10.88	14.55	32.48	2.49	4.34
GROND r'	266	4	66.57	10.18	22.72	15.25	26.56
GROND i'	64	4	15.90	2.43	5.43	3.64	6.34
GROND z'	55	4	13.82	2.11	4.72	3.17	5.51
GROND J	15	4	3.78	0.58	1.29	0.86	1.51
GROND H	20	4	5.00	0.77	1.71	1.15	2.00
GROND K	9	4	2.33	0.36	0.79	0.53	0.93
APEX+ALMA 345 GHz	37	1	37.06	1.42	5.19	8.49	20.23
ATCA 44 GHz	222	5	44.50	8.51	31.14	10.19	24.29
ATCA 18 GHz	319	5	63.81	12.20	44.65	14.62	34.83
ATCA 9 GHz	80	3	26.61	3.05	11.17	6.10	14.53
ATCA 5.5 GHz	56	5	11.20	2.14	7.84	2.57	6.12

B.5 Fit to all bands except UV, including MW extinction, White shifted to V

CM Model

Band	χ^2	d.o.f.	χ^2_{red}	χ^2_{frac}	$\chi^2_{frac,color}$	$\chi^2_{red,frac}$	$\chi^2_{red,frac,color}$
XRT 2 keV	659	267	2.47	29.81	100.00	0.75	100.00
UVOT uvw2	0	0	0.00	0.00	0.00	0.00	0.00
UVOT uvm2	0	0	0.00	0.00	0.00	0.00	0.00
UVOT uvw1	0	0	0.00	0.00	0.00	0.00	0.00
UVOT u	197	5	39.40	8.91	18.91	12.02	24.97
UVOT b	80	2	40.01	3.62	7.68	12.21	25.36
GROND g'	54	4	13.44	2.43	5.16	4.10	8.52
UVOT v+white	510	35	14.56	23.07	48.93	4.45	9.23
GROND r'	24	4	5.94	1.07	2.28	1.81	3.76
GROND i'	43	4	10.67	1.93	4.10	3.26	6.76
GROND z'	56	4	14.12	2.56	5.42	4.31	8.95
GROND J	19	4	4.63	0.84	1.78	1.41	2.94
GROND H	39	4	9.66	1.75	3.71	2.95	6.12
GROND K	21	4	5.32	0.96	2.04	1.62	3.37
APEX+ALMA 345 GHz	68	1	68.27	3.09	13.41	20.84	40.78
ATCA 44 GHz	114	5	22.89	5.18	22.48	6.99	13.67
ATCA 18 GHz	205	5	41.02	9.28	40.29	12.52	24.50
ATCA 9 GHz	82	3	27.44	3.72	16.17	8.37	16.39
ATCA 5.5 GHz	39	5	7.79	1.76	7.65	2.38	4.65

TS Model

Band	χ^2	d.o.f.	χ^2_{red}	χ^2_{frac}	$\chi^2_{frac,color}$	$\chi^2_{red,frac}$	$\chi^2_{red,frac,color}$
XRT 2 keV	574	267	2.15	27.68	100.00	0.62	100.00
UVOT uvw2	0	0	0.00	0.00	0.00	0.00	0.00
UVOT uvm2	0	0	0.00	0.00	0.00	0.00	0.00
UVOT uvw1	0	0	0.00	0.00	0.00	0.00	0.00
UVOT u	145	5	29.02	6.99	16.45	8.38	20.65
UVOT b	35	2	17.38	1.68	3.94	5.02	12.36
GROND g'	97	4	24.18	4.66	10.97	6.98	17.20
UVOT v+white	367	35	10.50	17.71	41.66	3.03	7.47
GROND r'	87	4	21.63	4.17	9.81	6.24	15.38
GROND i'	32	4	7.93	1.53	3.60	2.29	5.64
GROND z'	46	4	11.39	2.20	5.16	3.29	8.10
GROND J	19	4	4.64	0.89	2.10	1.34	3.30
GROND H	35	4	8.80	1.70	3.99	2.54	6.26
GROND K	20	4	5.12	0.99	2.32	1.48	3.64
APEX+ALMA 345 GHz	83	1	83.49	4.02	13.50	24.10	40.98
ATCA 44 GHz	140	5	28.08	6.77	22.71	8.10	13.78
ATCA 18 GHz	233	5	46.57	11.22	37.66	13.44	22.85
ATCA 9 GHz	100	3	33.28	4.81	16.15	9.61	16.33
ATCA 5.5 GHz	62	5	12.34	2.97	9.98	3.56	6.05

WM Model

Band	χ^2	d.o.f.	χ^2_{red}	χ^2_{frac}	$\chi^2_{frac,color}$	$\chi^2_{red,frac}$	$\chi^2_{red,frac,color}$
XRT 2 keV	736	267	2.76	26.34	100.00	0.57	100.00
UVOT uvw2	0	0	0.00	0.00	0.00	0.00	0.00
UVOT uvm2	0	0	0.00	0.00	0.00	0.00	0.00
UVOT uvw1	0	0	0.00	0.00	0.00	0.00	0.00
UVOT u	231	5	46.16	8.26	16.88	9.50	15.37
UVOT b	219	2	109.27	7.82	15.99	22.48	36.39
GROND g'	159	4	39.64	5.67	11.60	8.16	13.20
UVOT v+white	382	35	10.92	13.67	27.95	2.25	3.64
GROND r'	202	4	50.44	7.22	14.76	10.38	16.80
GROND i'	56	4	13.97	2.00	4.09	2.87	4.65
GROND z'	56	4	13.98	2.00	4.09	2.88	4.66
GROND J	19	4	4.85	0.69	1.42	1.00	1.61
GROND H	29	4	7.21	1.03	2.11	1.48	2.40
GROND K	15	4	3.81	0.55	1.12	0.78	1.27
APEX+ALMA 345 GHz	43	1	42.76	1.53	6.19	8.80	23.37
ATCA 44 GHz	201	5	40.29	7.21	29.14	8.29	22.02
ATCA 18 GHz	310	5	61.96	11.08	44.81	12.75	33.85
ATCA 9 GHz	79	3	26.37	2.83	11.44	5.43	14.41
ATCA 5.5 GHz	58	5	11.63	2.08	8.41	2.39	6.36

B.6 Fit to optical/nIR bands except UV, MW extinction corrected, White shifted to V

CM Model

Band	χ^2	d.o.f.	χ^2_{red}	χ^2_{frac}	$\chi^2_{frac,color}$	$\chi^2_{red,frac}$	$\chi^2_{red,frac,color}$
XRT 2 keV	2355	267	8.82	3.82	100.00	0.07	100.00
UVOT uvw2	0	0	0.00	0.00	0.00	0.00	0.00
UVOT uvm2	0	0	0.00	0.00	0.00	0.00	0.00
UVOT uvw1	0	0	0.00	0.00	0.00	0.00	0.00
UVOT u	0	0	0.00	0.00	0.00	0.00	0.00
UVOT b	530	2	265.07	0.86	21.84	2.04	38.74
GROND g'	441	4	110.25	0.71	18.17	0.85	16.11
UVOT v+white	249	35	7.11	0.40	10.26	0.05	1.04
GROND r'	719	4	179.71	1.16	29.62	1.39	26.27
GROND i'	286	4	71.48	0.46	11.78	0.55	10.45
GROND z'	179	4	44.73	0.29	7.37	0.34	6.54
GROND J	10	4	2.60	0.02	0.43	0.02	0.38
GROND H	3	4	0.71	0.00	0.12	0.01	0.10
GROND K	10	4	2.53	0.02	0.42	0.02	0.37
APEX+ALMA 345 GHz	96	1	96.32	0.16	0.17	0.74	0.78
ATCA 44 GHz	10694	5	2138.87	17.32	18.78	16.50	17.43
ATCA 18 GHz	14475	5	2894.94	23.45	25.42	22.33	23.59
ATCA 9 GHz	6049	3	2016.36	9.80	10.62	15.55	16.43
ATCA 5.5 GHz	25633	5	5126.67	41.52	45.01	39.54	41.77

TS Model

Band	χ^2	d.o.f.	χ^2_{red}	χ^2_{frac}	$\chi^2_{frac,color}$	$\chi^2_{red,frac}$	$\chi^2_{red,frac,color}$
XRT 2 keV	5253	267	19.67	20.97	100.00	0.42	100.00
UVOT uvw2	0	0	0.00	0.00	0.00	0.00	0.00
UVOT uvm2	0	0	0.00	0.00	0.00	0.00	0.00
UVOT uvw1	0	0	0.00	0.00	0.00	0.00	0.00
UVOT u	0	0	0.00	0.00	0.00	0.00	0.00
UVOT b	1147	2	573.70	4.58	24.95	12.12	42.94
GROND g'	727	4	181.64	2.90	15.80	3.84	13.60
UVOT v+white	455	35	12.99	1.81	9.88	0.27	0.97
GROND r'	1274	4	318.59	5.09	27.71	6.73	23.85
GROND i'	597	4	149.35	2.38	12.99	3.16	11.18
GROND z'	364	4	91.08	1.45	7.92	1.92	6.82
GROND J	23	4	5.87	0.09	0.51	0.12	0.44
GROND H	5	4	1.19	0.02	0.10	0.03	0.09
GROND K	6	4	1.55	0.02	0.13	0.03	0.12
APEX+ALMA 345 GHz	365	1	364.97	1.46	2.40	7.71	10.81
ATCA 44 GHz	9519	5	1903.88	37.99	62.62	40.23	56.37
ATCA 18 GHz	4747	5	949.36	18.95	31.22	20.06	28.11
ATCA 9 GHz	335	3	111.79	1.34	2.21	2.36	3.31
ATCA 5.5 GHz	236	5	47.27	0.94	1.55	1.00	1.40

WM Model

Band	χ^2	d.o.f.	χ^2_{red}	χ^2_{frac}	$\chi^2_{frac,color}$	$\chi^2_{red,frac}$	$\chi^2_{red,frac,color}$
XRT 2 keV	74001	267	277.16	28.98	100.00	0.66	100.00
UVOT uvw2	0	0	0.00	0.00	0.00	0.00	0.00
UVOT uvm2	0	0	0.00	0.00	0.00	0.00	0.00
UVOT uvw1	0	0	0.00	0.00	0.00	0.00	0.00
UVOT u	0	0	0.00	0.00	0.00	0.00	0.00
UVOT b	3703	2	1851.64	1.45	24.95	4.43	44.92
GROND g'	1921	4	480.34	0.75	12.94	1.15	11.65
UVOT v+white	2328	35	66.52	0.91	15.68	0.16	1.61
GROND r'	3630	4	907.45	1.42	24.45	2.17	22.02
GROND i'	1999	4	499.75	0.78	13.47	1.20	12.12
GROND z'	1186	4	296.41	0.46	7.99	0.71	7.19
GROND J	57	4	14.30	0.02	0.39	0.03	0.35
GROND H	13	4	3.19	0.00	0.09	0.01	0.08
GROND K	8	4	2.06	0.00	0.06	0.00	0.05
APEX+ALMA 345 GHz	3424	1	3424.35	1.34	2.06	8.19	9.16
ATCA 44 GHz	72236	5	14447.16	28.29	43.39	34.57	38.64
ATCA 18 GHz	60029	5	12005.82	23.51	36.05	28.73	32.11
ATCA 9 GHz	10142	3	3380.58	3.97	6.09	8.09	9.04
ATCA 5.5 GHz	20665	5	4132.95	8.09	12.41	9.89	11.05

B.7 Fit to radio/submm bands

CM Model

Band	χ^2	d.o.f.	χ^2_{red}	χ^2_{frac}	$\chi^2_{frac,color}$	$\chi^2_{red,frac}$	$\chi^2_{red,frac,color}$
XRT 2 keV	12976	267	48.60	62.34	100.00	2.86	100.00
UVOT uvw2	0	0	0.00	0.00	0.00	0.00	0.00
UVOT uvm2	0	0	0.00	0.00	0.00	0.00	0.00
UVOT uvw1	0	0	0.00	0.00	0.00	0.00	0.00
UVOT u	630	5	125.94	3.03	8.56	7.41	8.42
UVOT b	1824	2	912.06	8.76	24.79	53.64	60.98
GROND g'	311	4	77.74	1.49	4.23	4.57	5.20
UVOT white	3411	29	117.61	16.39	46.35	6.92	7.86
UVOT v	242	9	26.85	1.16	3.28	1.58	1.80
GROND r'	542	4	135.53	2.60	7.37	7.97	9.06
GROND i'	206	4	51.58	0.99	2.80	3.03	3.45
GROND z'	150	4	37.48	0.72	2.04	2.20	2.51
GROND J	17	4	4.19	0.08	0.23	0.25	0.28
GROND H	8	4	2.09	0.04	0.11	0.12	0.14
GROND K	18	4	4.60	0.09	0.25	0.27	0.31
APEX+ALMA 345 GHz	66	1	66.18	0.32	13.80	3.89	42.45
ATCA 44 GHz	103	5	20.67	0.50	21.55	1.22	13.26
ATCA 18 GHz	182	5	36.50	0.88	38.05	2.15	23.40
ATCA 9 GHz	53	3	17.68	0.25	11.06	1.04	11.34
ATCA 5.5 GHz	74	5	14.90	0.36	15.53	0.88	9.56

TS Model

Band	χ^2	d.o.f.	χ^2_{red}	χ^2_{frac}	$\chi^2_{frac,color}$	$\chi^2_{red,frac}$	$\chi^2_{red,frac,color}$
XRT 2 keV	36206	267	135.60	51.66	100.00	1.62	100.00
UVOT uvw2	0	0	0.00	0.00	0.00	0.00	0.00
UVOT uvm2	0	0	0.00	0.00	0.00	0.00	0.00
UVOT uvw1	0	0	0.00	0.00	0.00	0.00	0.00
UVOT u	378	5	75.54	0.54	1.13	0.90	0.93
UVOT b	597	2	298.45	0.85	1.79	3.57	3.68
GROND g'	3250	4	812.47	4.64	9.72	9.71	10.02
UVOT white	1594	29	54.97	2.27	4.77	0.66	0.68
UVOT v	285	9	31.62	0.41	0.85	0.38	0.39
GROND r'	9461	4	2365.14	13.50	28.30	28.27	29.18
GROND i'	9176	4	2294.10	13.09	27.45	27.42	28.31
GROND z'	6690	4	1672.58	9.55	20.01	19.99	20.64
GROND J	671	4	167.86	0.96	2.01	2.01	2.07
GROND H	784	4	195.88	1.12	2.34	2.34	2.42
GROND K	545	4	136.14	0.78	1.63	1.63	1.68
APEX+ALMA 345 GHz	35	1	35.17	0.05	7.72	0.42	28.04
ATCA 44 GHz	117	5	23.32	0.17	25.59	0.28	18.59
ATCA 18 GHz	157	5	31.40	0.22	34.46	0.38	25.03
ATCA 9 GHz	46	3	15.49	0.07	10.20	0.19	12.35
ATCA 5.5 GHz	100	5	20.07	0.14	22.03	0.24	16.00

WM Model

Band	χ^2	d.o.f.	χ^2_{red}	χ^2_{frac}	$\chi^2_{frac,color}$	$\chi^2_{red,frac}$	$\chi^2_{red,frac,color}$
XRT 2 keV	50851	267	190.45	30.28	100.00	0.66	100.00
UVOT uvw2	0	0	0.00	0.00	0.00	0.00	0.00
UVOT uvm2	0	0	0.00	0.00	0.00	0.00	0.00
UVOT uvw1	0	0	0.00	0.00	0.00	0.00	0.00
UVOT u	836	5	167.20	0.50	0.72	0.58	0.58
UVOT b	3104	2	1552.22	1.85	2.66	5.35	5.41
GROND g'	12176	4	3043.99	7.25	10.44	10.49	10.60
UVOT white	5015	29	172.94	2.99	4.30	0.60	0.60
UVOT v	784	9	87.12	0.47	0.67	0.30	0.30
GROND r'	34104	4	8526.12	20.31	29.24	29.38	29.70
GROND i'	31013	4	7753.35	18.47	26.59	26.71	27.01
GROND z'	22759	4	5689.77	13.55	19.51	19.60	19.82
GROND J	2265	4	566.20	1.35	1.94	1.95	1.97
GROND H	2608	4	651.95	1.55	2.24	2.25	2.27
GROND K	1973	4	493.27	1.18	1.69	1.70	1.72
APEX+ALMA 345 GHz	44	1	43.81	0.03	10.23	0.15	34.25
ATCA 44 GHz	98	5	19.57	0.06	22.85	0.07	15.29
ATCA 18 GHz	164	5	32.75	0.10	38.24	0.11	25.60
ATCA 9 GHz	54	3	18.12	0.03	12.70	0.06	14.16
ATCA 5.5 GHz	68	5	13.69	0.04	15.98	0.05	10.70

B.8 Fit to X-rays + optical/nIR bands, MW extinction corrected, White shifted to V

CM Model

Band	χ^2	d.o.f.	χ^2_{red}	χ^2_{frac}	$\chi^2_{frac,color}$	$\chi^2_{red,frac}$	$\chi^2_{red,frac,color}$
XRT 2 keV	502	267	1.88	0.86	100.00	0.02	100.00
UVOT uvw2	0	0	0.00	0.00	0.00	0.00	0.00
UVOT uvm2	0	0	0.00	0.00	0.00	0.00	0.00
UVOT uvw1	0	0	0.00	0.00	0.00	0.00	0.00
UVOT u	128	5	25.59	0.22	14.05	0.21	16.16
UVOT b	40	2	20.07	0.07	4.41	0.16	12.68
GROND g'	180	4	44.99	0.31	19.77	0.36	28.42
UVOT v+white	329	35	9.41	0.56	36.17	0.08	5.94
GROND r'	188	4	47.02	0.32	20.66	0.38	29.70
GROND i'	22	4	5.62	0.04	2.47	0.05	3.55
GROND z'	10	4	2.57	0.02	1.13	0.02	1.62
GROND J	2	4	0.48	0.00	0.21	0.00	0.31
GROND H	9	4	2.25	0.02	0.99	0.02	1.42
GROND K	1	4	0.31	0.00	0.14	0.00	0.19
APEX+ALMA 345 GHz	19	1	19.50	0.03	0.03	0.16	0.16
ATCA 44 GHz	10132	5	2026.37	17.34	17.77	16.35	16.56
ATCA 18 GHz	14694	5	2938.89	25.15	25.78	23.71	24.02
ATCA 9 GHz	6143	3	2047.80	10.52	10.78	16.52	16.74
ATCA 5.5 GHz	26018	5	5203.66	44.54	45.64	41.98	42.53

TS Model

Band	χ^2	d.o.f.	χ^2_{red}	χ^2_{frac}	$\chi^2_{frac,color}$	$\chi^2_{red,frac}$	$\chi^2_{red,frac,color}$
XRT 2 keV	462	267	1.73	2.42	100.00	0.04	100.00
UVOT uvw2	0	0	0.00	0.00	0.00	0.00	0.00
UVOT uvm2	0	0	0.00	0.00	0.00	0.00	0.00
UVOT uvw1	0	0	0.00	0.00	0.00	0.00	0.00
UVOT u	506	5	101.25	2.65	10.53	2.35	7.42
UVOT b	1202	2	600.88	6.29	24.99	13.94	44.06
GROND g'	636	4	158.97	3.33	13.22	3.69	11.66
UVOT v+white	513	35	14.66	2.69	10.67	0.34	1.08
GROND r'	1137	4	284.19	5.95	23.63	6.59	20.84
GROND i'	497	4	124.18	2.60	10.33	2.88	9.10
GROND z'	303	4	75.75	1.59	6.30	1.76	5.55
GROND J	13	4	3.20	0.07	0.27	0.07	0.23
GROND H	1	4	0.32	0.01	0.03	0.01	0.02
GROND K	2	4	0.52	0.01	0.04	0.01	0.04
APEX+ALMA 345 GHz	119	1	118.95	0.62	0.86	2.76	4.04
ATCA 44 GHz	7987	5	1597.42	41.81	57.75	37.05	54.23
ATCA 18 GHz	3489	5	697.81	18.26	25.23	16.19	23.69
ATCA 9 GHz	631	3	210.46	3.31	4.56	4.88	7.15
ATCA 5.5 GHz	1604	5	320.87	8.40	11.60	7.44	10.89

WM Model

Band	χ^2	d.o.f.	χ^2_{red}	χ^2_{frac}	$\chi^2_{frac,color}$	$\chi^2_{red,frac}$	$\chi^2_{red,frac,color}$
XRT 2 keV	567	267	2.12	0.87	100.00	0.01	100.00
UVOT uvw2	0	0	0.00	0.00	0.00	0.00	0.00
UVOT uvm2	0	0	0.00	0.00	0.00	0.00	0.00
UVOT uvw1	0	0	0.00	0.00	0.00	0.00	0.00
UVOT u	50	5	9.96	0.08	4.83	0.07	5.50
UVOT b	45	2	22.43	0.07	4.35	0.15	12.38
GROND g'	146	4	36.49	0.22	14.16	0.25	20.15
UVOT v+white	385	35	11.01	0.59	37.37	0.08	6.08
GROND r'	171	4	42.87	0.26	16.64	0.29	23.67
GROND i'	58	4	14.50	0.09	5.62	0.10	8.00
GROND z'	66	4	16.62	0.10	6.45	0.11	9.18
GROND J	27	4	6.77	0.04	2.63	0.05	3.74
GROND H	47	4	11.85	0.07	4.60	0.08	6.54
GROND K	35	4	8.63	0.05	3.35	0.06	4.76
APEX+ALMA 345 GHz	1353	1	1352.59	2.07	2.12	9.29	9.41
ATCA 44 GHz	25033	5	5006.56	38.26	39.22	34.38	34.82
ATCA 18 GHz	25496	5	5099.26	38.97	39.94	35.02	35.47
ATCA 9 GHz	3972	3	1324.00	6.07	6.22	9.09	9.21
ATCA 5.5 GHz	7978	5	1595.52	12.19	12.50	10.96	11.10

B.9 Fit to X-rays + radio/submm bands

CM Model

Band	χ^2	d.o.f.	χ^2_{red}	χ^2_{frac}	$\chi^2_{frac,color}$	$\chi^2_{red,frac}$	$\chi^2_{red,frac,color}$
XRT 2 keV	636	267	2.38	21.09	100.00	0.48	100.00
UVOT uvw2	0	0	0.00	0.00	0.00	0.00	0.00
UVOT uvm2	0	0	0.00	0.00	0.00	0.00	0.00
UVOT uvw1	0	0	0.00	0.00	0.00	0.00	0.00
UVOT u	186	5	37.16	6.16	9.83	7.51	11.35
UVOT b	78	2	39.14	2.60	4.14	7.91	11.95
GROND g'	8	4	2.02	0.27	0.43	0.41	0.62
UVOT white	647	29	22.32	21.46	34.24	4.51	6.82
UVOT v	115	9	12.74	3.80	6.06	2.58	3.89
GROND r'	63	4	15.63	2.07	3.31	3.16	4.77
GROND i'	278	4	69.46	9.21	14.70	14.04	21.22
GROND z'	274	4	68.43	9.08	14.48	13.83	20.90
GROND J	59	4	14.77	1.96	3.13	2.99	4.51
GROND H	106	4	26.40	3.50	5.59	5.34	8.06
GROND K	77	4	19.36	2.57	4.10	3.91	5.91
APEX+ALMA 345 GHz	71	1	71.29	2.36	14.57	14.41	43.25
ATCA 44 GHz	106	5	21.14	3.50	21.60	4.27	12.83
ATCA 18 GHz	202	5	40.39	6.70	41.26	8.16	24.50
ATCA 9 GHz	74	3	24.78	2.47	15.19	5.01	15.04
ATCA 5.5 GHz	36	5	7.22	1.20	7.38	1.46	4.38

TS Model

Band	χ^2	d.o.f.	χ^2_{red}	χ^2_{frac}	$\chi^2_{frac,color}$	$\chi^2_{red,frac}$	$\chi^2_{red,frac,color}$
XRT 2 keV	499	267	1.87	15.75	100.00	0.30	100.00
UVOT uvw2	0	0	0.00	0.00	0.00	0.00	0.00
UVOT uvm2	0	0	0.00	0.00	0.00	0.00	0.00
UVOT uvw1	0	0	0.00	0.00	0.00	0.00	0.00
UVOT u	73	5	14.54	2.30	3.42	2.31	3.26
UVOT b	58	2	29.19	1.84	2.75	4.64	6.55
GROND g'	393	4	98.26	12.41	18.48	15.63	22.06
UVOT white	398	29	13.73	12.57	18.72	2.18	3.08
UVOT v	82	9	9.06	2.57	3.83	1.44	2.03
GROND r'	681	4	170.13	21.49	32.00	27.05	38.19
GROND i'	241	4	60.26	7.61	11.33	9.58	13.53
GROND z'	175	4	43.70	5.52	8.22	6.95	9.81
GROND J	10	4	2.40	0.30	0.45	0.38	0.54
GROND H	7	4	1.73	0.22	0.33	0.28	0.39
GROND K	10	4	2.50	0.32	0.47	0.40	0.56
APEX+ALMA 345 GHz	80	1	79.75	2.52	14.73	12.68	43.94
ATCA 44 GHz	107	5	21.45	3.39	19.81	3.41	11.82
ATCA 18 GHz	229	5	45.73	7.22	42.24	7.27	25.20
ATCA 9 GHz	71	3	23.61	2.24	13.09	3.75	13.01
ATCA 5.5 GHz	55	5	10.96	1.73	10.12	1.74	6.04

WM Model

Band	χ^2	d.o.f.	χ^2_{red}	χ^2_{frac}	$\chi^2_{frac,color}$	$\chi^2_{red,frac}$	$\chi^2_{red,frac,color}$
XRT 2 keV	612	267	2.29	15.93	100.00	0.33	100.00
UVOT uvw2	0	0	0.00	0.00	0.00	0.00	0.00
UVOT uvm2	0	0	0.00	0.00	0.00	0.00	0.00
UVOT uvw1	0	0	0.00	0.00	0.00	0.00	0.00
UVOT u	291	5	58.15	7.57	11.31	8.37	11.62
UVOT b	404	2	202.15	10.53	15.72	29.08	40.40
GROND g'	72	4	17.93	1.87	2.79	2.58	3.58
UVOT white	984	29	33.93	25.63	38.27	4.88	6.78
UVOT v	121	9	13.49	3.16	4.72	1.94	2.70
GROND r'	112	4	27.95	2.91	4.35	4.02	5.59
GROND i'	181	4	45.36	4.73	7.06	6.52	9.06
GROND z'	188	4	46.93	4.89	7.30	6.75	9.38
GROND J	59	4	14.85	1.55	2.31	2.14	2.97
GROND H	91	4	22.84	2.38	3.55	3.29	4.56
GROND K	67	4	16.82	1.75	2.62	2.42	3.36
APEX+ALMA 345 GHz	61	1	60.92	1.59	9.28	8.76	31.65
ATCA 44 GHz	169	5	33.82	4.40	25.76	4.86	17.57
ATCA 18 GHz	246	5	49.18	6.40	37.46	7.07	25.55
ATCA 9 GHz	93	3	31.08	2.43	14.20	4.47	16.15
ATCA 5.5 GHz	87	5	17.46	2.27	13.30	2.51	9.07

B.10 Fit to optical/nIR + radio/submm band, MW extinction corrected, White shifted to V

CM Model

Band	χ^2	d.o.f.	χ^2_{red}	χ^2_{frac}	$\chi^2_{frac,color}$	$\chi^2_{red,frac}$	$\chi^2_{red,frac,color}$
XRT 2 keV	4983	267	18.66	67.20	100.00	2.62	100.00
UVOT uvw2	0	0	0.00	0.00	0.00	0.00	0.00
UVOT uvm2	0	0	0.00	0.00	0.00	0.00	0.00
UVOT uvw1	0	0	0.00	0.00	0.00	0.00	0.00
UVOT u	213	5	42.66	2.88	11.50	6.00	8.67
UVOT b	349	2	174.64	4.71	18.83	24.56	35.47
GROND g'	246	4	61.39	3.31	13.23	8.63	12.47
UVOT v+white	217	35	6.21	2.93	11.72	0.87	1.26
GROND r'	460	4	115.11	6.21	24.82	16.19	23.38
GROND i'	172	4	43.11	2.33	9.29	6.06	8.76
GROND z'	144	4	36.10	1.95	7.78	5.08	7.33
GROND J	16	4	3.97	0.21	0.86	0.56	0.81
GROND H	11	4	2.82	0.15	0.61	0.40	0.57
GROND K	25	4	6.31	0.34	1.36	0.89	1.28
APEX+ALMA 345 GHz	98	1	98.38	1.33	17.06	13.84	49.18
ATCA 44 GHz	149	5	29.85	2.01	25.88	4.20	14.92
ATCA 18 GHz	123	5	24.60	1.66	21.32	3.46	12.29
ATCA 9 GHz	45	3	15.02	0.61	7.81	2.11	7.51
ATCA 5.5 GHz	161	5	32.21	2.17	27.93	4.53	16.10

TS Model

Band	χ^2	d.o.f.	χ^2_{red}	χ^2_{frac}	$\chi^2_{frac,color}$	$\chi^2_{red,frac}$	$\chi^2_{red,frac,color}$
XRT 2 keV	11133	267	41.70	65.44	100.00	2.67	100.00
UVOT uvw2	0	0	0.00	0.00	0.00	0.00	0.00
UVOT uvm2	0	0	0.00	0.00	0.00	0.00	0.00
UVOT uvw1	0	0	0.00	0.00	0.00	0.00	0.00
UVOT u	404	5	80.78	2.37	7.49	5.17	5.93
UVOT b	990	2	494.75	5.82	18.35	31.66	36.31
GROND g'	662	4	165.55	3.89	12.28	10.59	12.15
UVOT v+white	960	35	27.43	5.64	17.81	1.76	2.01
GROND r'	1257	4	314.20	7.39	23.31	20.10	23.06
GROND i'	626	4	156.40	3.68	11.60	10.01	11.48
GROND z'	425	4	106.30	2.50	7.89	6.80	7.80
GROND J	29	4	7.26	0.17	0.54	0.46	0.53
GROND H	14	4	3.45	0.08	0.26	0.22	0.25
GROND K	25	4	6.27	0.15	0.47	0.40	0.46
APEX+ALMA 345 GHz	69	1	69.09	0.41	14.16	4.42	43.53
ATCA 44 GHz	124	5	24.76	0.73	25.38	1.58	15.60
ATCA 18 GHz	184	5	36.81	1.08	37.72	2.36	23.19
ATCA 9 GHz	44	3	14.67	0.26	9.02	0.94	9.24
ATCA 5.5 GHz	67	5	13.39	0.39	13.72	0.86	8.44

WM Model

Band	χ^2	d.o.f.	χ^2_{red}	χ^2_{frac}	$\chi^2_{frac,color}$	$\chi^2_{red,frac}$	$\chi^2_{red,frac,color}$
XRT 2 keV	6917	267	25.91	82.62	100.00	7.23	100.00
UVOT uvw2	0	0	0.00	0.00	0.00	0.00	0.00
UVOT uvm2	0	0	0.00	0.00	0.00	0.00	0.00
UVOT uvw1	0	0	0.00	0.00	0.00	0.00	0.00
UVOT u	129	5	25.72	1.54	16.51	7.18	15.37
UVOT b	53	2	26.41	0.63	6.78	7.37	15.78
GROND g'	123	4	30.82	1.47	15.83	8.60	18.41
UVOT v+white	154	35	4.40	1.84	19.78	1.23	2.63
GROND r'	194	4	48.49	2.32	24.90	13.53	28.97
GROND i'	50	4	12.40	0.59	6.37	3.46	7.41
GROND z'	49	4	12.21	0.58	6.27	3.41	7.29
GROND J	11	4	2.71	0.13	1.39	0.76	1.62
GROND H	9	4	2.30	0.11	1.18	0.64	1.37
GROND K	8	4	1.92	0.09	0.99	0.54	1.15
APEX+ALMA 345 GHz	29	1	29.16	0.35	4.31	8.14	17.66
ATCA 44 GHz	243	5	48.58	2.90	35.93	13.56	29.43
ATCA 18 GHz	289	5	57.84	3.45	42.78	16.14	35.04
ATCA 9 GHz	49	3	16.38	0.59	7.27	4.57	9.92
ATCA 5.5 GHz	66	5	13.13	0.78	9.71	3.66	7.95

B.11 Fit to all bands without early optical data, MW extinction corrected, White shifted to V

CM Model

Band	χ^2	d.o.f.	χ^2_{red}	χ^2_{frac}	$\chi^2_{frac,color}$	$\chi^2_{red,frac}$	$\chi^2_{red,frac,color}$
XRT 2 keV	567	155	3.66	25.46	100.00	0.80	100.00
UVOT uvw2	0	0	0.00	0.00	0.00	0.00	0.00
UVOT uvm2	0	0	0.00	0.00	0.00	0.00	0.00
UVOT uvw1	0	0	0.00	0.00	0.00	0.00	0.00
UVOT u	93	3	30.99	4.17	8.24	6.81	11.57
UVOT b	26	1	25.60	1.15	2.27	5.62	9.56
GROND g'	246	4	61.56	11.05	21.82	13.52	22.99
UVOT v+white	204	21	9.73	9.16	18.10	2.14	3.63
GROND r'	375	4	93.84	16.84	33.25	20.61	35.04
GROND i'	97	4	24.35	4.37	8.63	5.35	9.09
GROND z'	70	4	17.54	3.15	6.22	3.85	6.55
GROND J	7	4	1.80	0.32	0.64	0.40	0.67
GROND H	5	4	1.18	0.21	0.42	0.26	0.44
GROND K	5	4	1.20	0.21	0.42	0.26	0.45
APEX+ALMA 345 GHz	87	1	86.82	3.90	16.29	19.07	47.23
ATCA 44 GHz	147	5	29.33	6.58	27.52	6.44	15.96
ATCA 18 GHz	161	5	32.29	7.24	30.30	7.09	17.56
ATCA 9 GHz	58	3	19.49	2.62	10.97	4.28	10.60
ATCA 5.5 GHz	79	5	15.90	3.57	14.92	3.49	8.65

TS Model

Band	χ^2	d.o.f.	χ^2_{red}	χ^2_{frac}	$\chi^2_{frac,color}$	$\chi^2_{red,frac}$	$\chi^2_{red,frac,color}$
XRT 2 keV	347	155	2.24	11.60	100.00	0.33	100.00
UVOT uvw2	0	0	0.00	0.00	0.00	0.00	0.00
UVOT uvm2	0	0	0.00	0.00	0.00	0.00	0.00
UVOT uvw1	0	0	0.00	0.00	0.00	0.00	0.00
UVOT u	64	3	21.33	2.14	3.07	3.12	4.20
UVOT b	8	1	8.25	0.28	0.40	1.21	1.63
GROND g'	445	4	111.18	14.89	21.36	16.27	21.90
UVOT v+white	121	21	5.76	4.05	5.81	0.84	1.14
GROND r'	817	4	204.19	27.35	39.23	29.89	40.23
GROND i'	342	4	85.57	11.46	16.44	12.53	16.86
GROND z'	247	4	61.74	8.27	11.86	9.04	12.16
GROND J	13	4	3.27	0.44	0.63	0.48	0.64
GROND H	7	4	1.68	0.22	0.32	0.25	0.33
GROND K	18	4	4.61	0.62	0.89	0.67	0.91
APEX+ALMA 345 GHz	67	1	67.08	2.25	12.03	9.82	38.69
ATCA 44 GHz	108	5	21.53	3.60	19.31	3.15	12.42
ATCA 18 GHz	260	5	52.08	8.72	46.70	7.62	30.04
ATCA 9 GHz	61	3	20.44	2.05	11.00	2.99	11.79
ATCA 5.5 GHz	61	5	12.23	2.05	10.96	1.79	7.05

WM Model

Band	χ^2	d.o.f.	χ^2_{red}	χ^2_{frac}	$\chi^2_{frac,color}$	$\chi^2_{red,frac}$	$\chi^2_{red,frac,color}$
XRT 2 keV	473	155	3.05	13.89	100.00	0.43	100.00
UVOT uvw2	0	0	0.00	0.00	0.00	0.00	0.00
UVOT uvm2	0	0	0.00	0.00	0.00	0.00	0.00
UVOT uvw1	0	0	0.00	0.00	0.00	0.00	0.00
UVOT u	137	3	45.64	4.02	6.67	6.47	9.24
UVOT b	52	1	51.52	1.51	2.51	7.31	10.43
GROND g'	377	4	94.30	11.07	18.36	13.38	19.09
UVOT v+white	344	21	16.38	10.10	16.75	2.32	3.32
GROND r'	669	4	167.21	19.64	32.57	23.72	33.86
GROND i'	249	4	62.23	7.31	12.12	8.83	12.60
GROND z'	183	4	45.82	5.38	8.92	6.50	9.28
GROND J	17	4	4.29	0.50	0.84	0.61	0.87
GROND H	12	4	2.90	0.34	0.56	0.41	0.59
GROND K	14	4	3.60	0.42	0.70	0.51	0.73
APEX+ALMA 345 GHz	28	1	27.82	0.82	3.16	3.95	13.37
ATCA 44 GHz	334	5	66.84	9.81	38.00	9.48	32.13
ATCA 18 GHz	401	5	80.28	11.78	45.64	11.39	38.59
ATCA 9 GHz	74	3	24.73	2.18	8.44	3.51	11.89
ATCA 5.5 GHz	42	5	8.38	1.23	4.76	1.19	4.03

B.12 Fit to all bands after 0.5 days, MW extinction corrected, White shifted to V

CM Model

Band	χ^2	d.o.f.	χ^2_{red}	χ^2_{frac}	$\chi^2_{frac,color}$	$\chi^2_{red,frac}$	$\chi^2_{red,frac,color}$
XRT 2 keV	108	65	1.65	6.13	100.00	0.38	100.00
UVOT uvw2	0	0	0.00	0.00	0.00	0.00	0.00
UVOT uvm2	0	0	0.00	0.00	0.00	0.00	0.00
UVOT uvw1	0	0	0.00	0.00	0.00	0.00	0.00
UVOT u	0	0	0.00	0.02	0.02	0.00	0.00
UVOT b	0	0	0.00	0.00	0.00	0.00	0.00
GROND g'	302	4	75.46	17.22	27.37	17.24	28.30
UVOT v+white	52	13	4.01	2.97	4.72	0.92	1.50
GROND r'	480	4	119.96	27.37	43.50	27.40	44.98
GROND i'	150	4	37.58	8.57	13.63	8.58	14.09
GROND z'	102	4	25.48	5.81	9.24	5.82	9.55
GROND J	8	4	1.97	0.45	0.71	0.45	0.74
GROND H	3	4	0.63	0.14	0.23	0.14	0.24
GROND K	6	4	1.59	0.36	0.58	0.36	0.60
APEX+ALMA 345 GHz	67	1	67.20	3.83	12.39	15.35	39.65
ATCA 44 GHz	137	5	27.34	7.80	25.20	6.25	16.13
ATCA 18 GHz	212	5	42.46	12.11	39.14	9.70	25.05
ATCA 9 GHz	54	3	18.09	3.10	10.00	4.13	10.67
ATCA 5.5 GHz	72	5	14.39	4.11	13.27	3.29	8.49

TS Model

Band	χ^2	d.o.f.	χ^2_{red}	χ^2_{frac}	$\chi^2_{frac,color}$	$\chi^2_{red,frac}$	$\chi^2_{red,frac,color}$
XRT 2 keV	121	65	1.86	4.62	100.00	0.29	100.00
UVOT uvw2	0	0	0.00	0.00	0.00	0.00	0.00
UVOT uvm2	0	0	0.00	0.00	0.00	0.00	0.00
UVOT uvw1	0	0	0.00	0.00	0.00	0.00	0.00
UVOT u	0	0	0.00	0.01	0.02	0.00	0.00
UVOT b	0	0	0.00	0.00	0.00	0.00	0.00
GROND g'	439	4	109.86	16.80	22.80	17.07	23.32
UVOT v+white	61	13	4.71	2.34	3.18	0.73	1.00
GROND r'	802	4	200.52	30.66	41.62	31.15	42.56
GROND i'	339	4	84.77	12.96	17.60	13.17	17.99
GROND z'	242	4	60.61	9.27	12.58	9.42	12.87
GROND J	15	4	3.81	0.58	0.79	0.59	0.81
GROND H	7	4	1.86	0.28	0.39	0.29	0.39
GROND K	20	4	4.96	0.76	1.03	0.77	1.05
APEX+ALMA 345 GHz	60	1	59.86	2.29	10.53	9.30	35.05
ATCA 44 GHz	117	5	23.39	4.47	20.58	3.63	13.70
ATCA 18 GHz	270	5	53.92	10.30	47.44	8.38	31.57
ATCA 9 GHz	69	3	23.15	2.65	12.22	3.60	13.55
ATCA 5.5 GHz	52	5	10.48	2.00	9.22	1.63	6.14

WM Model

Band	χ^2	d.o.f.	χ^2_{red}	χ^2_{frac}	$\chi^2_{frac,color}$	$\chi^2_{red,frac}$	$\chi^2_{red,frac,color}$
XRT 2 keV	194	65	2.99	2.37	100.00	0.15	100.00
UVOT uvw2	0	0	0.00	0.00	0.00	0.00	0.00
UVOT uvm2	0	0	0.00	0.00	0.00	0.00	0.00
UVOT uvw1	0	0	0.00	0.00	0.00	0.00	0.00
UVOT u	8	0	0.00	0.09	0.11	0.00	0.00
UVOT b	0	0	0.00	0.00	0.00	0.00	0.00
GROND g'	1349	4	337.14	16.43	18.86	16.90	19.79
UVOT v+white	478	13	36.74	5.82	6.68	1.84	2.16
GROND r'	2666	4	666.47	32.49	37.28	33.41	39.13
GROND i'	1502	4	375.38	18.30	20.99	18.82	22.04
GROND z'	982	4	245.55	11.97	13.73	12.31	14.42
GROND J	79	4	19.82	0.97	1.11	0.99	1.16
GROND H	44	4	10.92	0.53	0.61	0.55	0.64
GROND K	45	4	11.35	0.55	0.63	0.57	0.67
APEX+ALMA 345 GHz	125	1	125.49	1.53	14.60	6.29	43.54
ATCA 44 GHz	218	5	43.62	2.66	25.38	2.19	15.13
ATCA 18 GHz	188	5	37.64	2.29	21.90	1.89	13.06
ATCA 9 GHz	120	3	39.92	1.46	13.93	2.00	13.85
ATCA 5.5 GHz	208	5	41.57	2.53	24.19	2.08	14.42

Appendix C

Light curve modelling to GRB 110715A data.

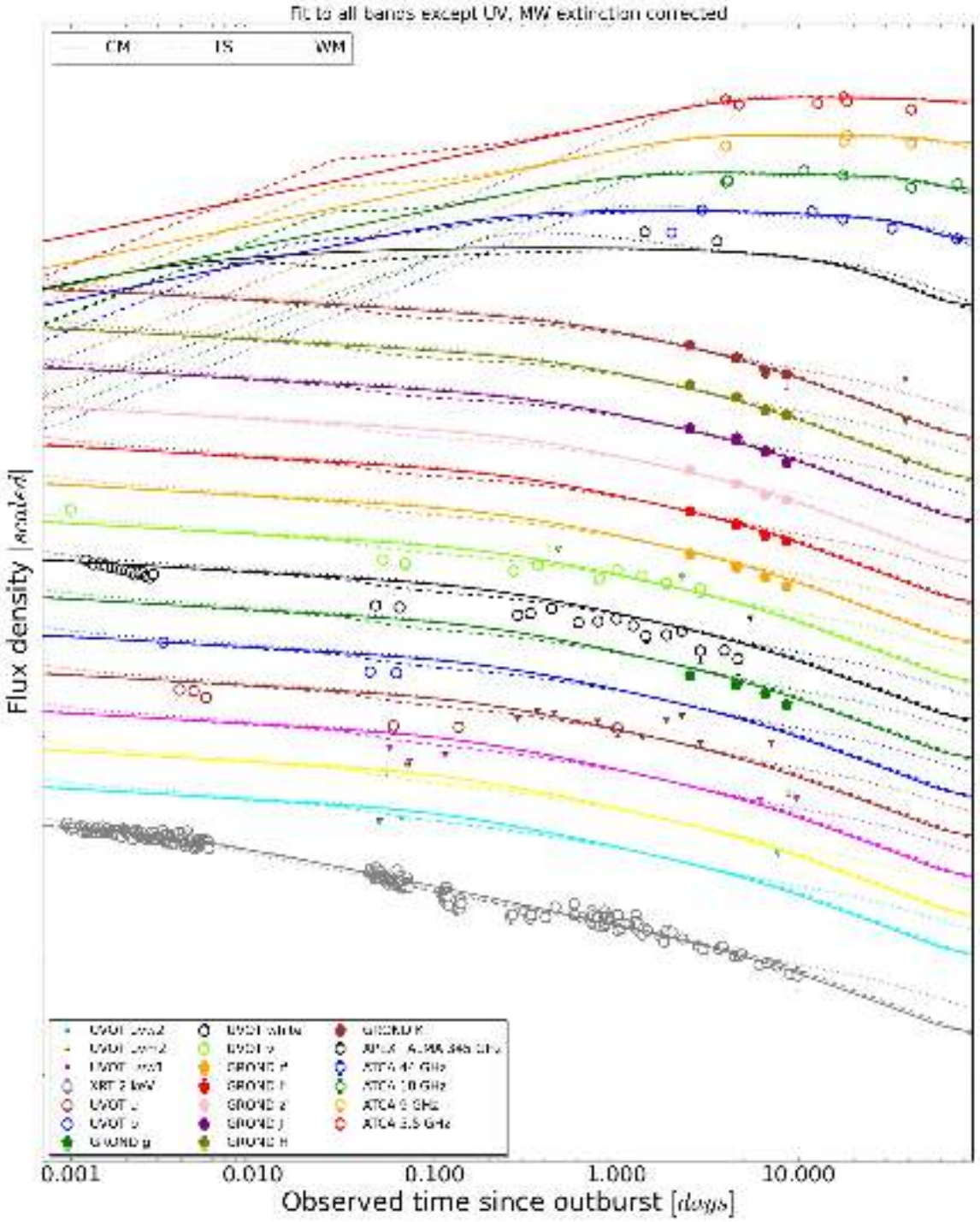
fit to all bands except UV, MW extinction corrected
CM
IS
WM
Flux density [scaled]
0.001
0.010
0.100
1.000
10.000
Observed time since outburst [days]

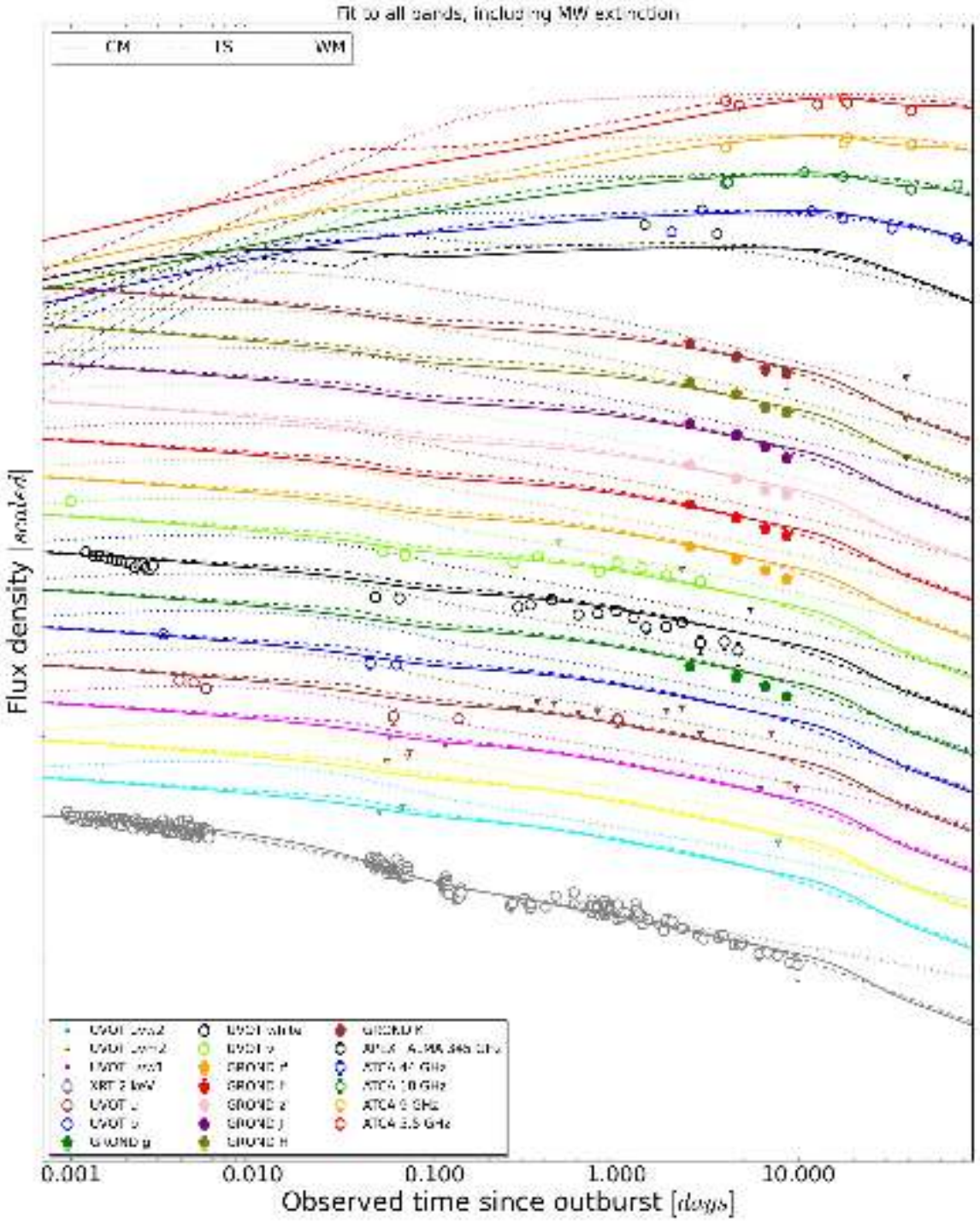
Fit to all bands, including MW extinction
CM
IS
WM
Flux density [scaled]
0.001
0.010
0.100
1.000
10.000
Observed time since outburst [days]

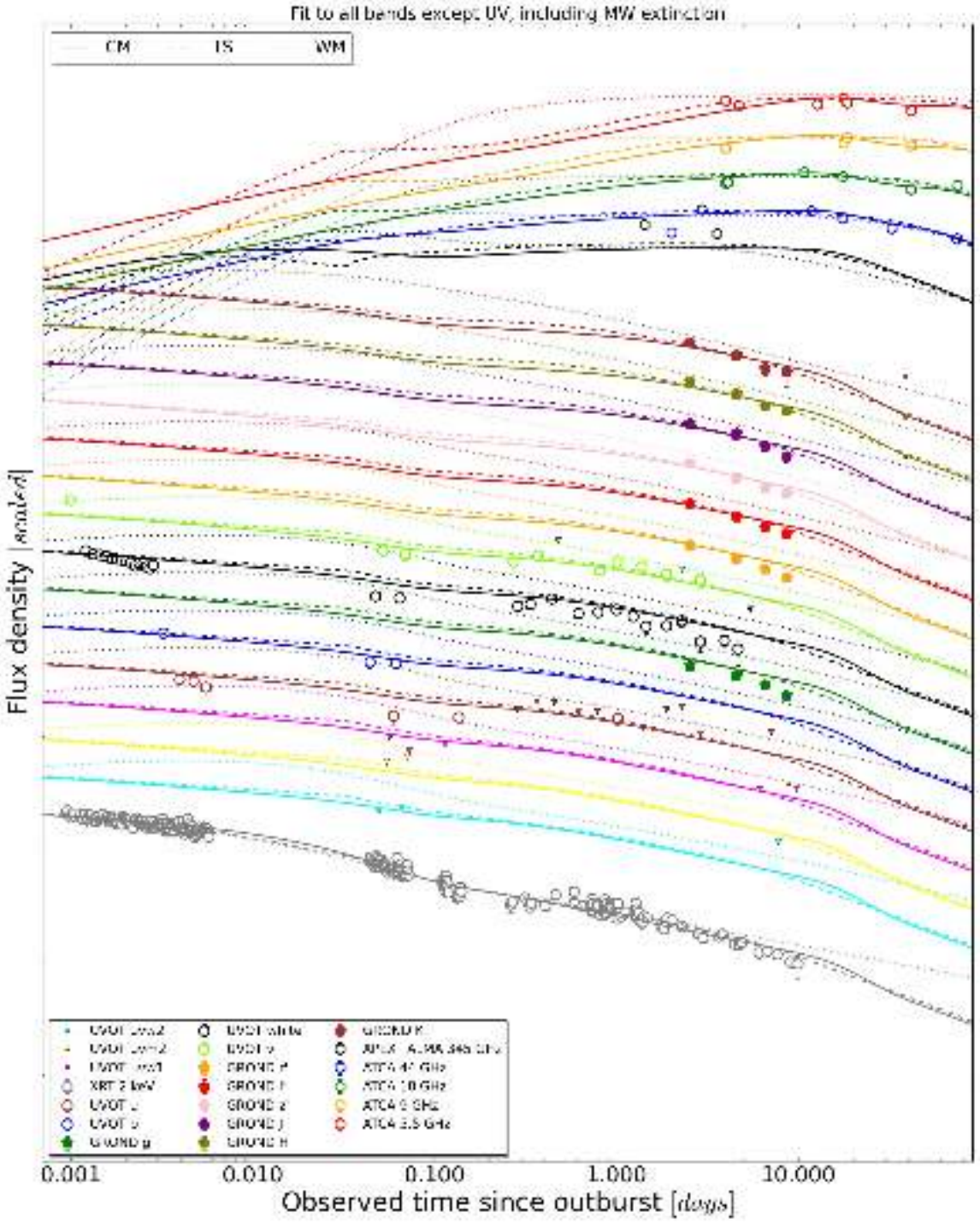
Fit to all bands except UV, including MW extinction
CM
IS
WM
Flux density [arbitrary]
0.001
0.010
0.100
1.000
10.000
Observed time since outburst [days]

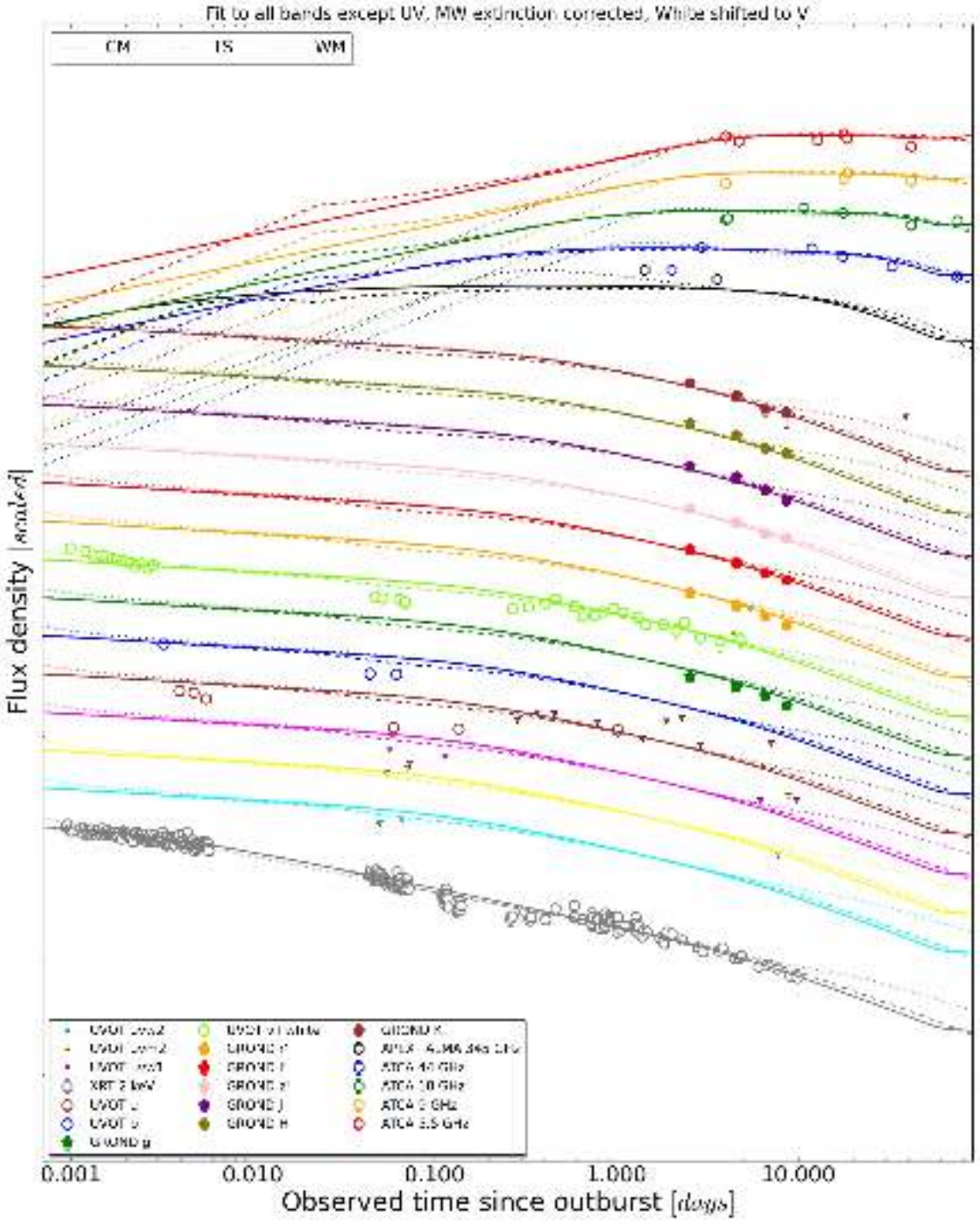
Fit to all bands except UV, MW extinction corrected, White shifted to V
CM
IS
WM
Flux density [scaled]
0.001
0.010
0.100
1.000
10.000
Observed time since outburst [days]

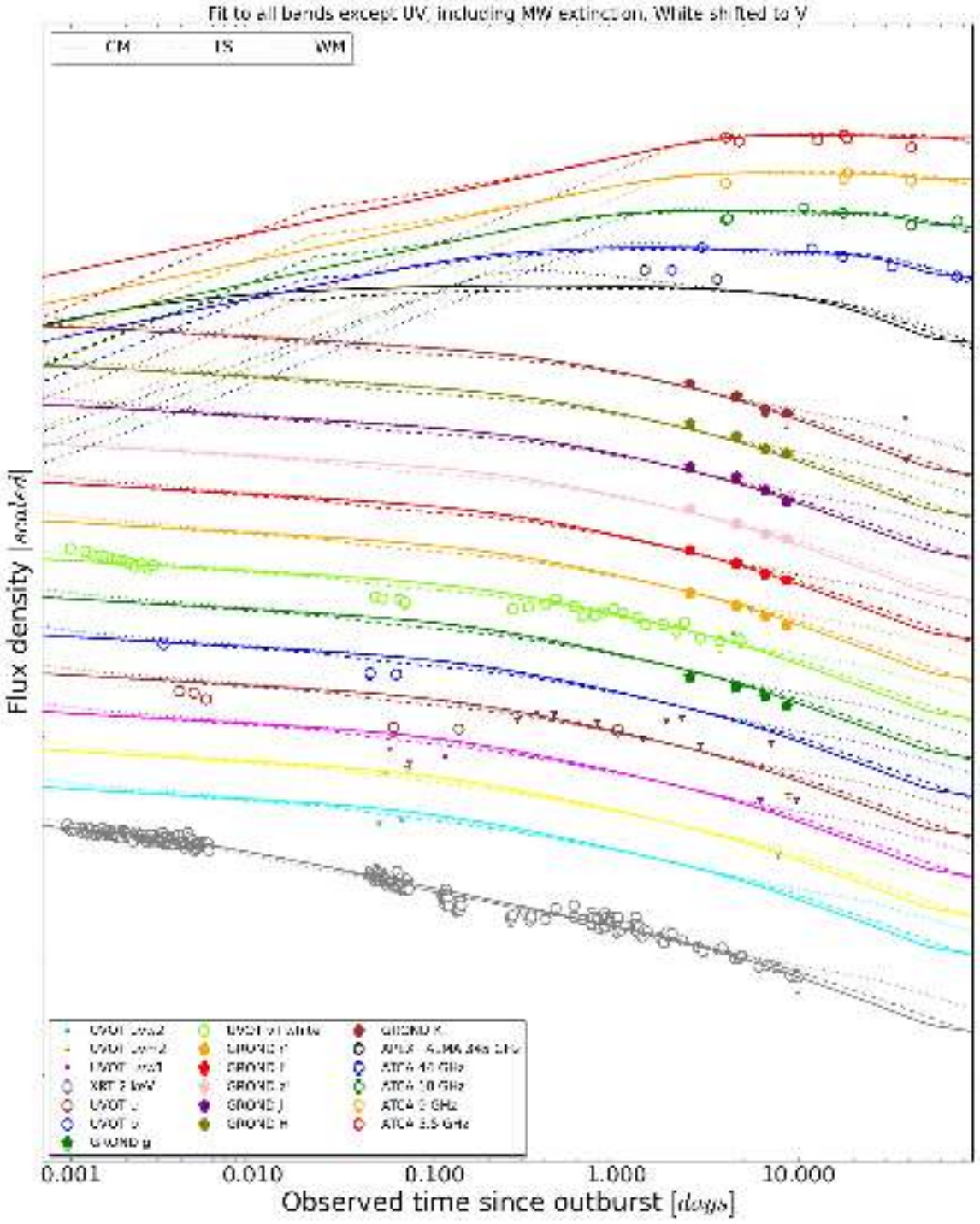
Fit to all bands except UV, including MW extinction, White shifted to V
CM
IS
WM
Flux density [scaled]
0.001
0.010
0.100
1.000
10.000
Observed time since outburst [days]

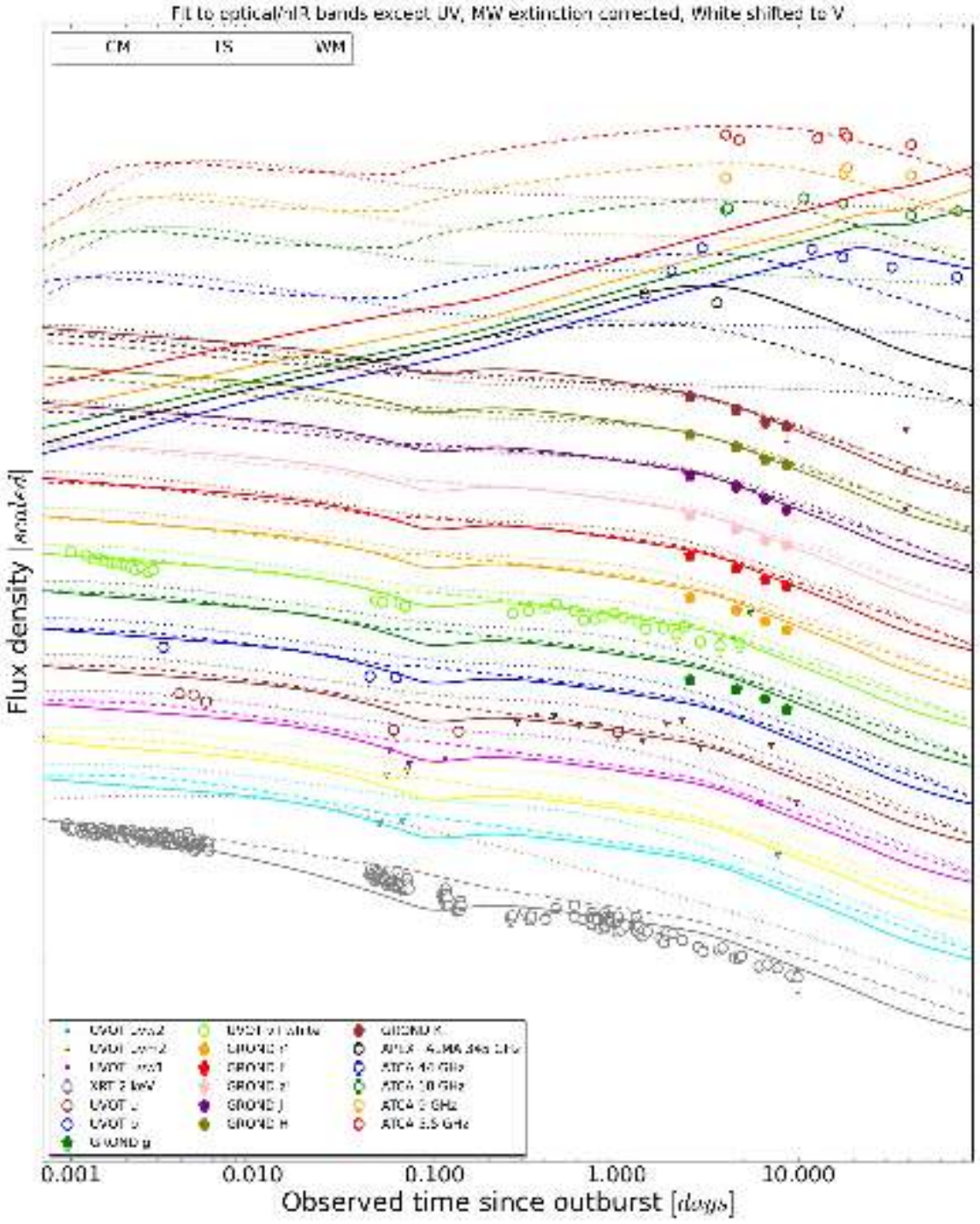
Fit to optical/nIR bands except UV, MW extinction corrected, White shifted to V
CM
IS
WM
Flux density [scaled]
0.001
0.010
0.100
1.000
10.000
Observed time since outburst [days]

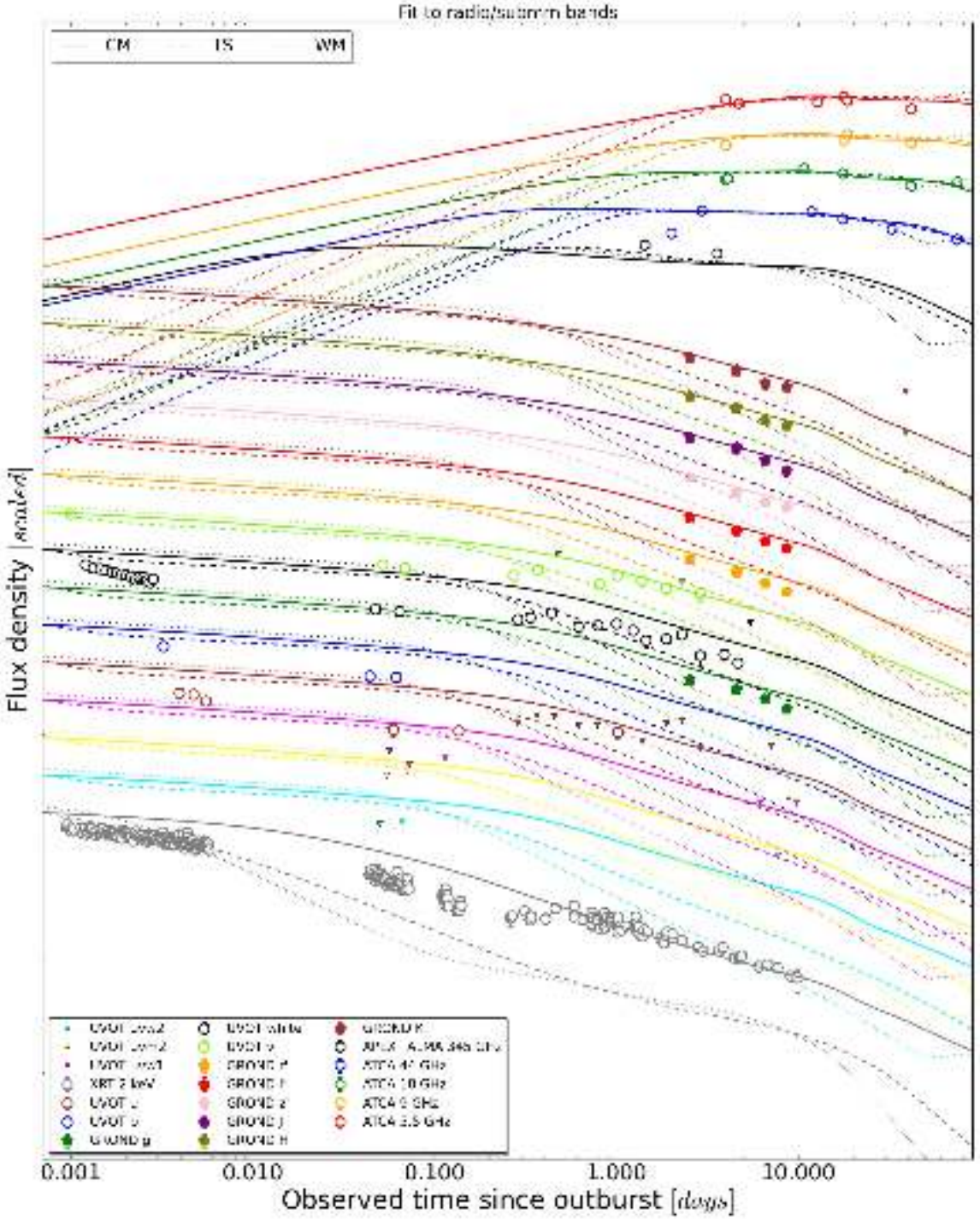
Fit to radio/submm bands
CM
IS
WM
Flux density [scaled]
0.001
0.010
0.100
1.000
10.000
Observed time since outburst [days]

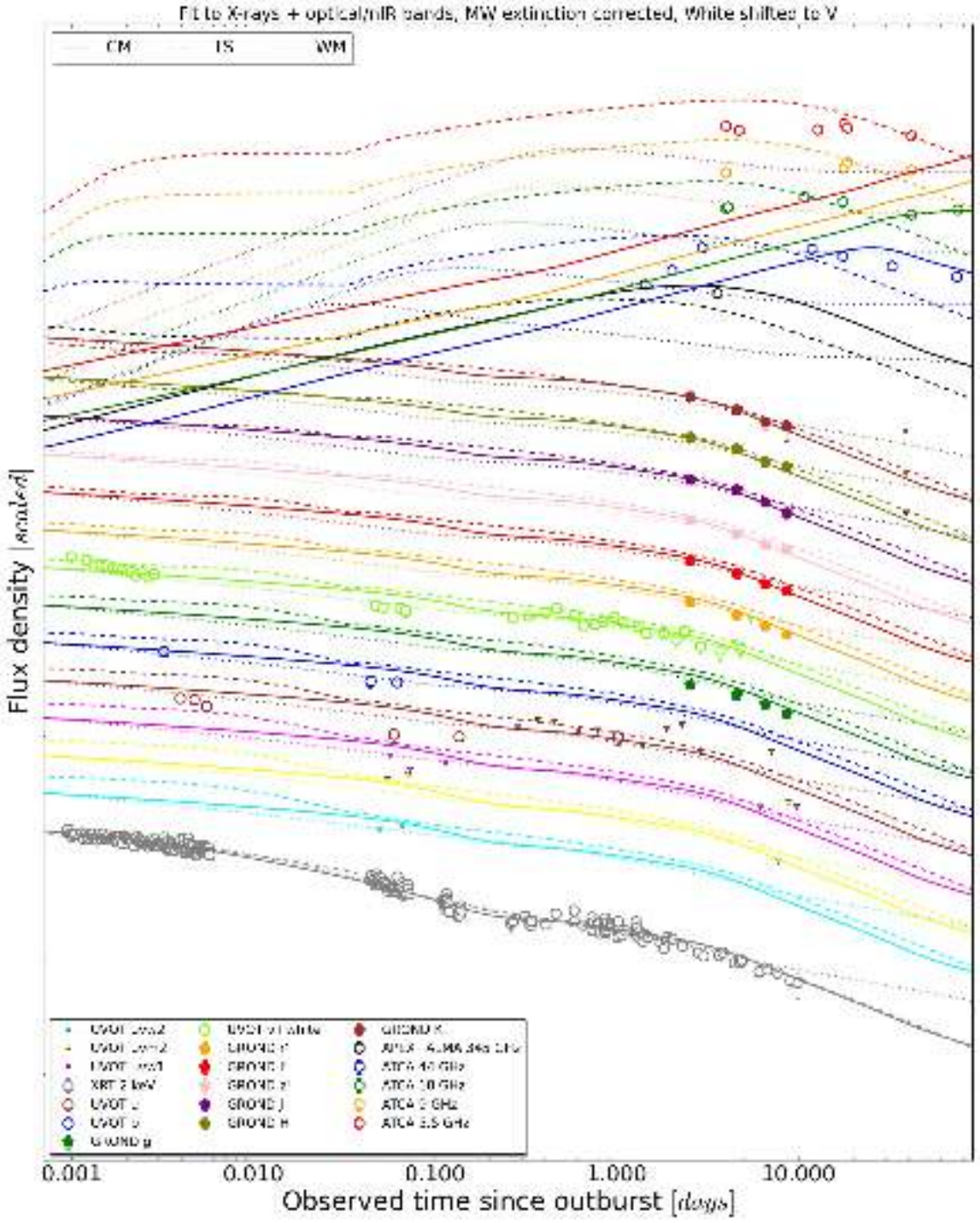
Fit to X-rays + optical/nIR bands, MW extinction corrected, White shifted to V
CM
IS
WM
Flux density [scaled]
0.001
0.010
0.100
1.000
10.000
Observed time since outburst [days]

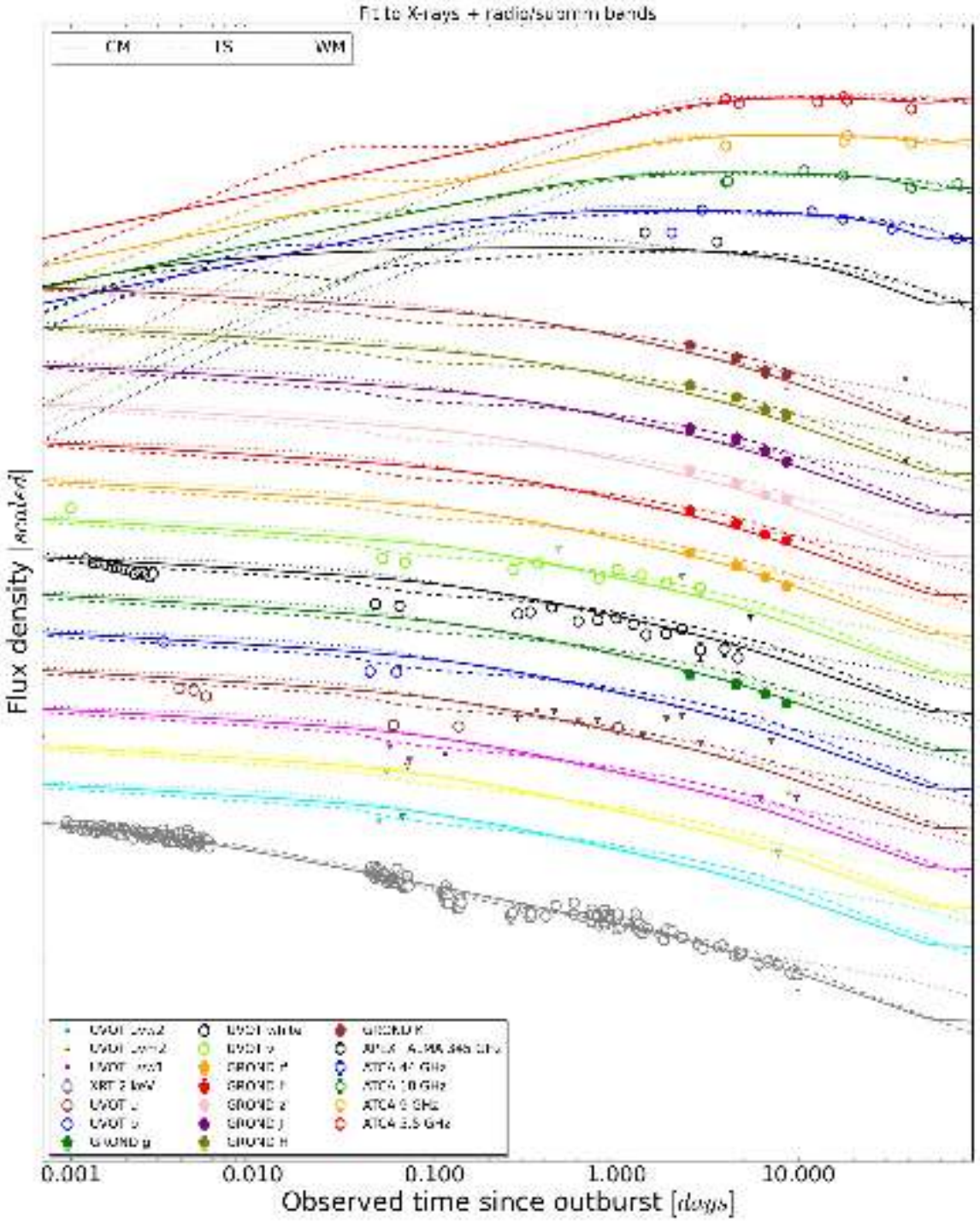
Fit to X-rays + radio/submm bands
CM
IS
WM
Flux density [arbitrary]
0.001
0.010
0.100
1.000
10.000
Observed time since outburst [days]

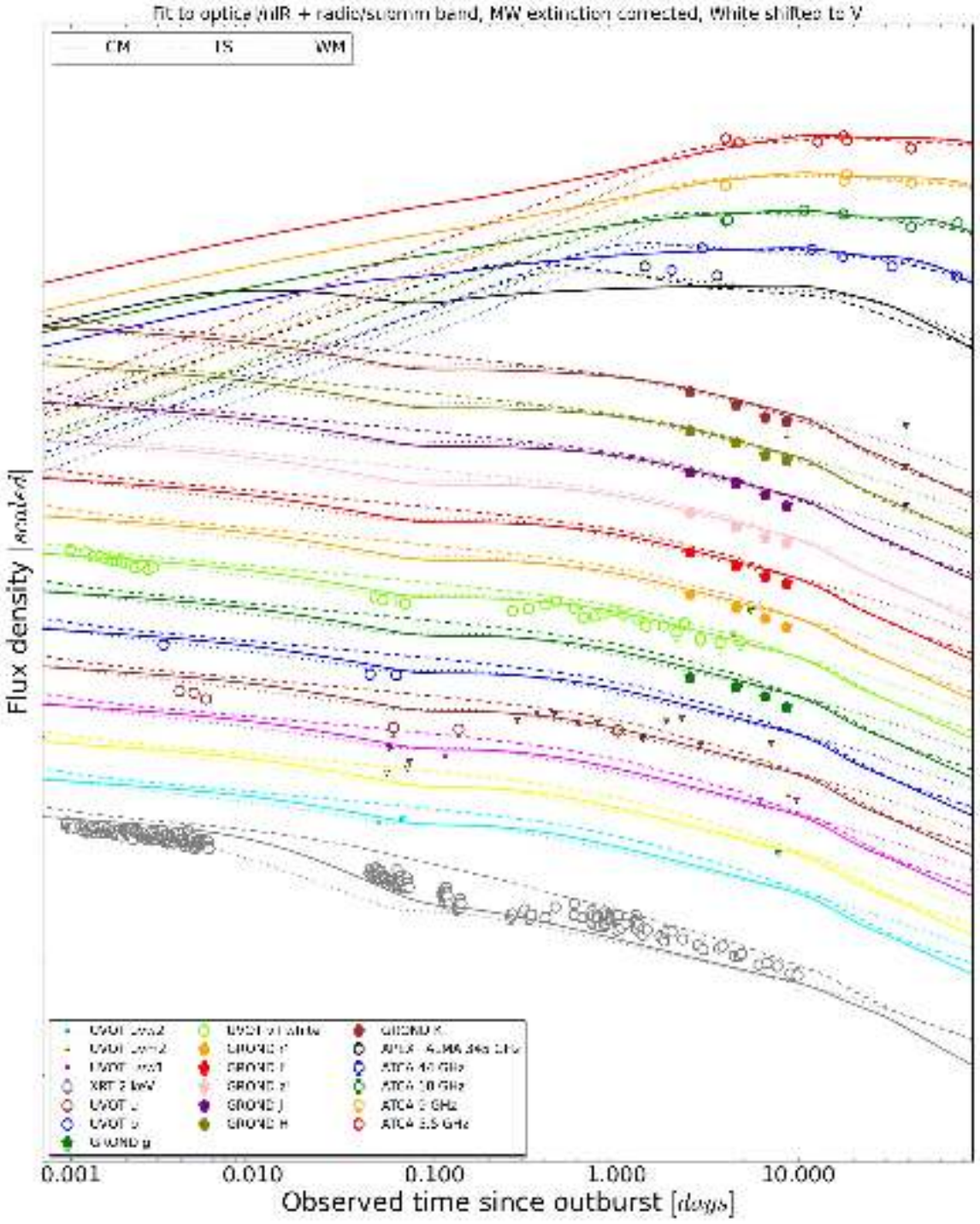
fit to optical/nIR + radio/submm band, MW extinction corrected, White shifted to V
CM
IS
WM
Flux density [scaled]
0.001
0.010
0.100
1.000
10.000
Observed time since outburst [days]

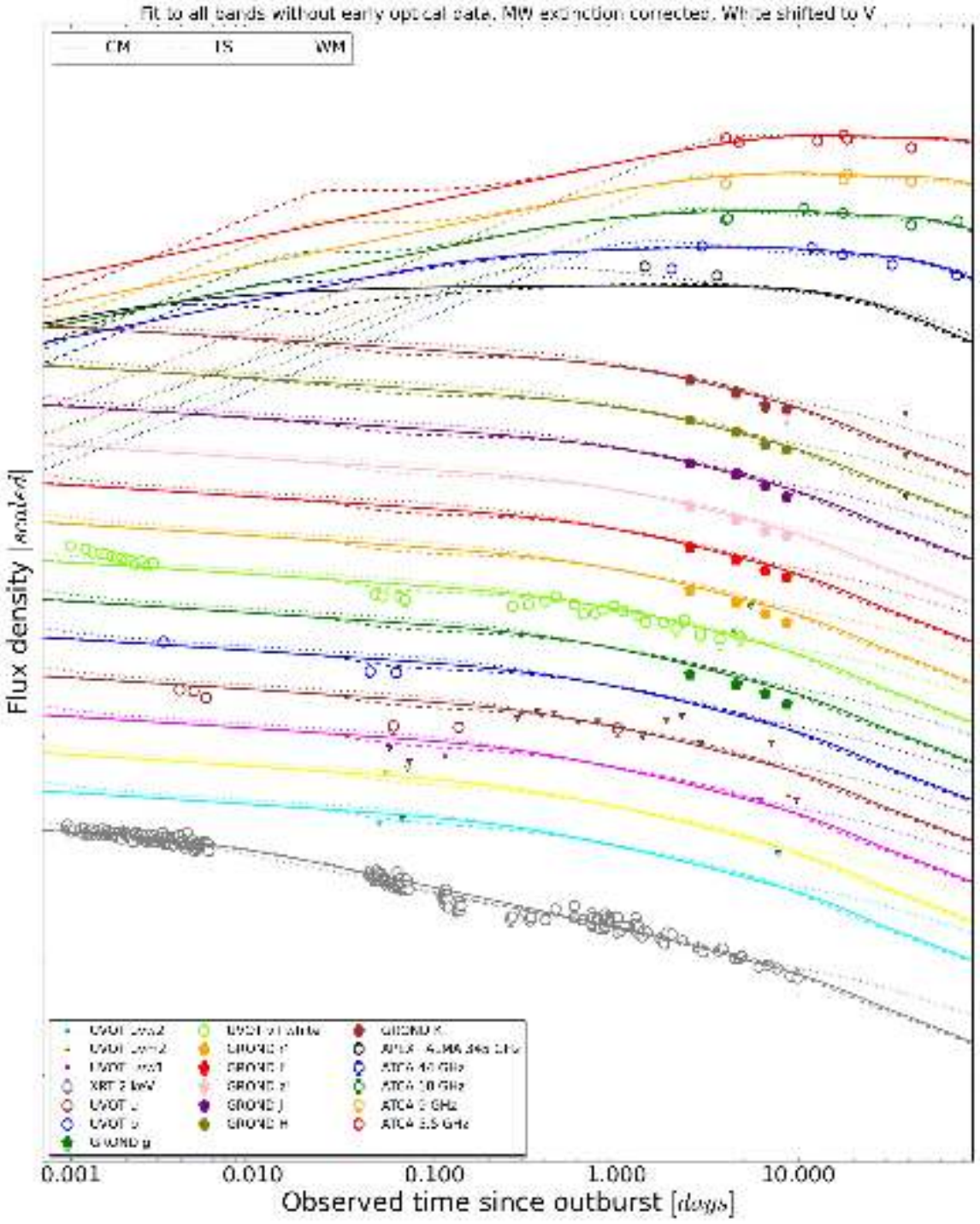
Fit to all bands without early optical data, MW extinction corrected, White shifted to V
CM
IS
WM
Flux density [scaled]
0.001
0.010
0.100
1.000
10.000
Observed time since outburst [days]

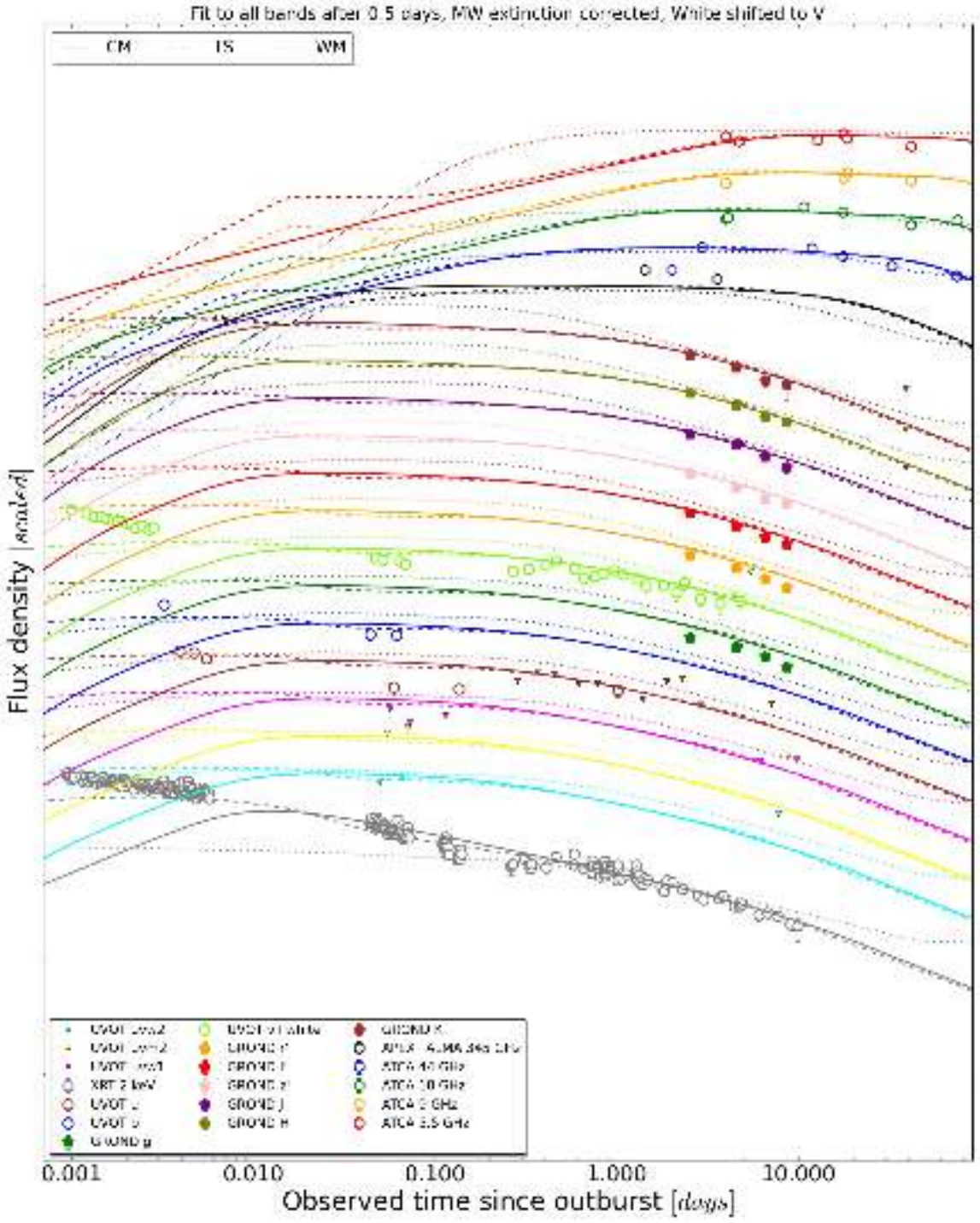
Fit to all bands after 0.5 days, MW extinction corrected, White shifted to V
CM
IS
WM
Flux density [scaled]
0.001
0.010
0.100
1.000
10.000
Observed time since outburst [days]

Appendix D

Spectral energy distribution models of GRB 110715A.

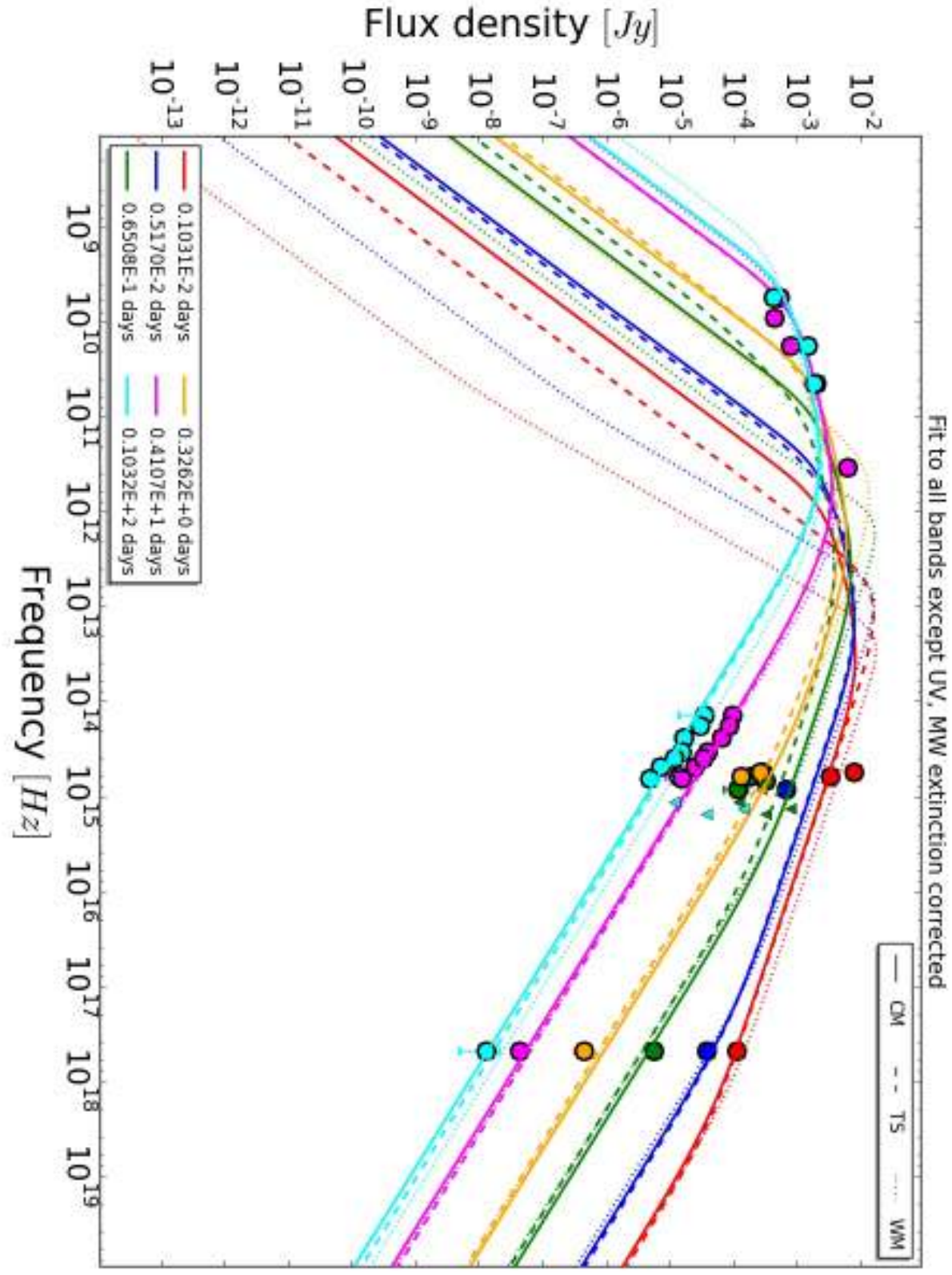
Flux density $[Jy]$
Frequency $[Hz]$
Fit to all bands except UV, MW extinction corrected
CM
TS
VM
0.1031E-2 days
0.5170E-2 days
0.6508E-1 days
0.3262E+0 days
0.4107E+1 days
0.1032E+2 days

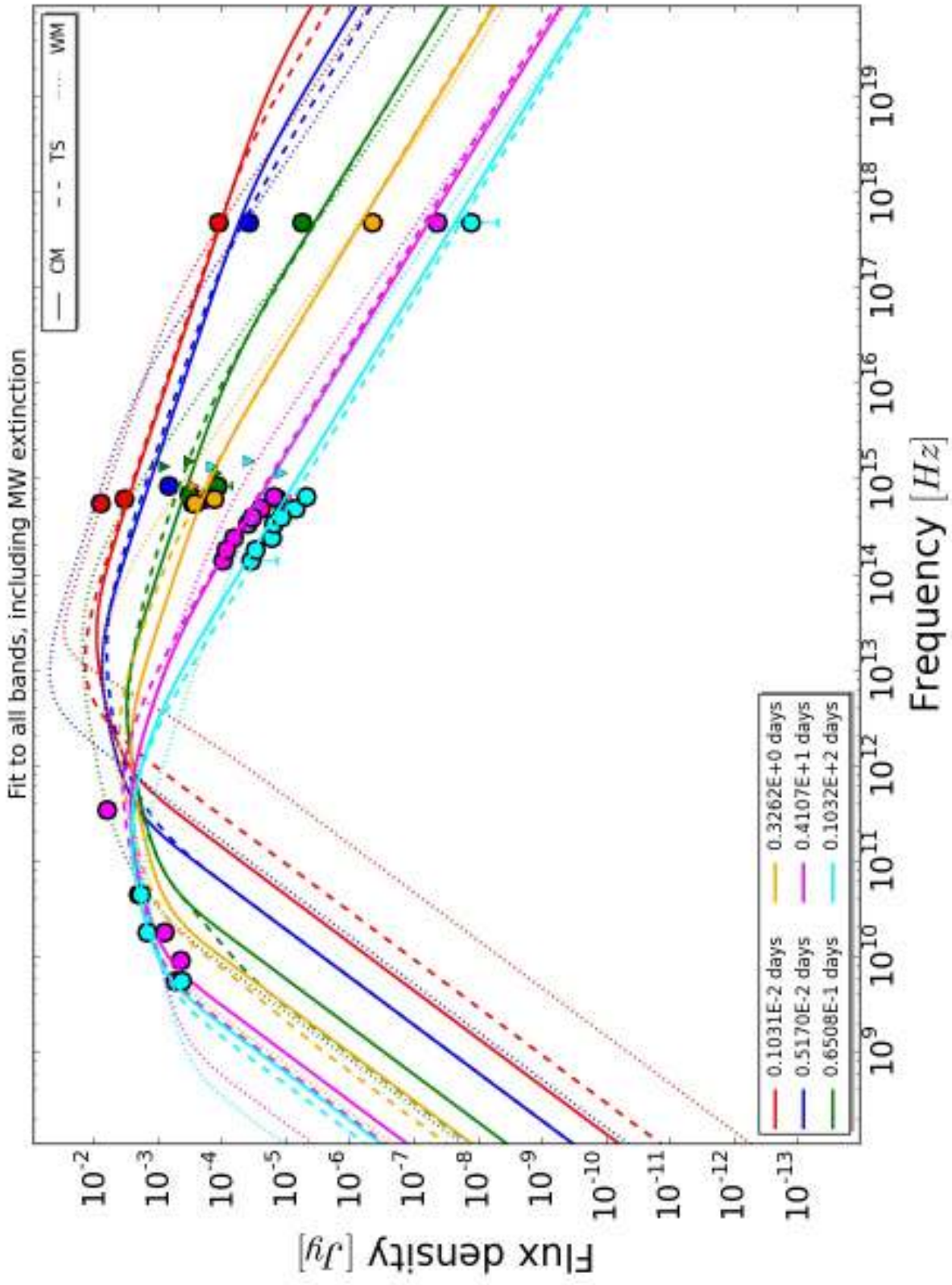
Fit to all bands, including MW extinction
CM
TS
WM
0.1031E-2 days
0.5170E-2 days
0.6508E-1 days
0.3262E+0 days
0.4107E+1 days
0.1032E+2 days
Flux density $[\mu_y]$
Frequency $[Hz]$

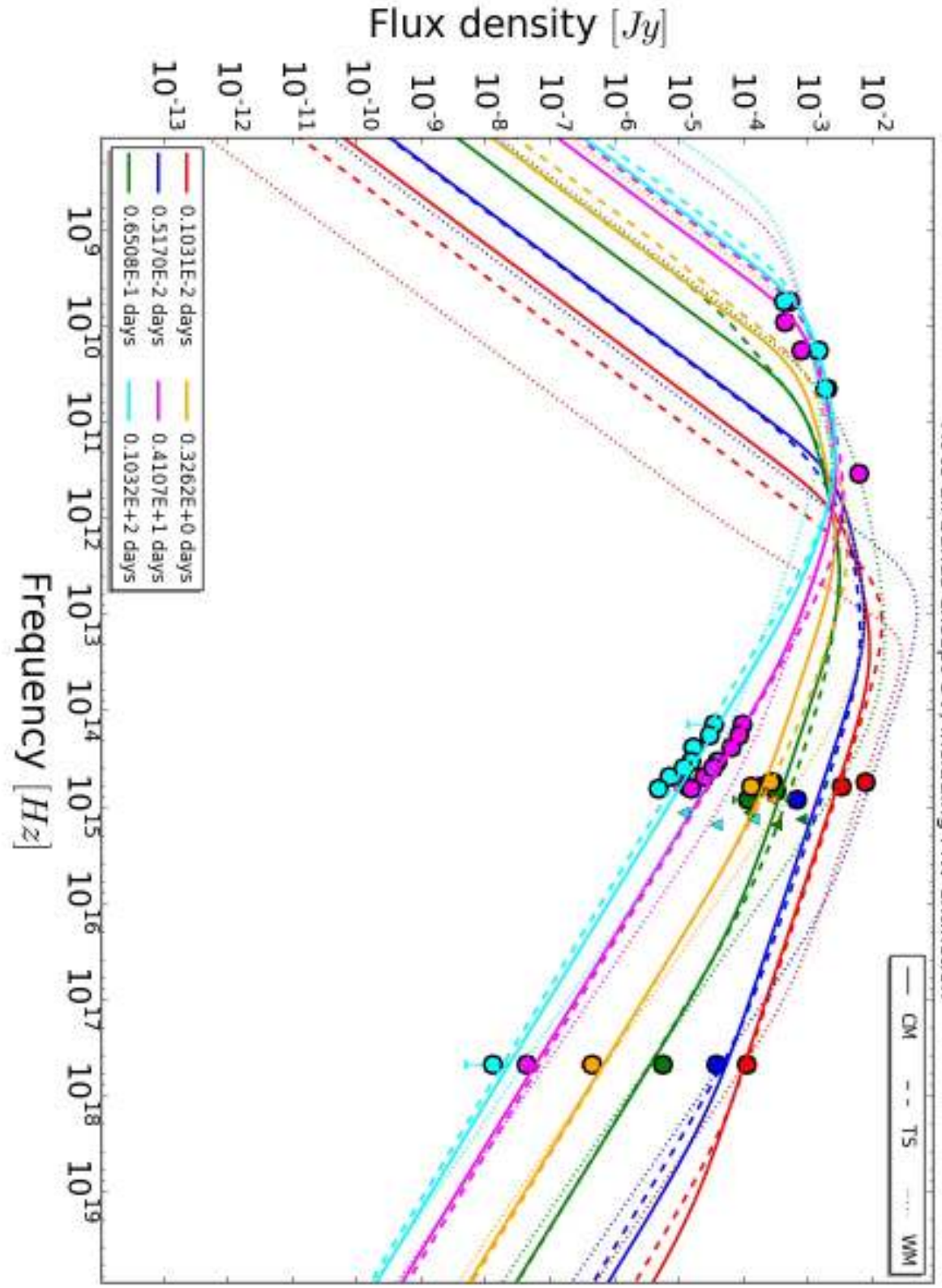
Flux density $[Jy]$
Frequency $[Hz]$
Fit to all bands except UV, including MW extinction
CM
TS
VM
0.1031E-2 days
0.5170E-2 days
0.6508E-1 days
0.3262E+0 days
0.4107E+1 days
0.1032E+2 days

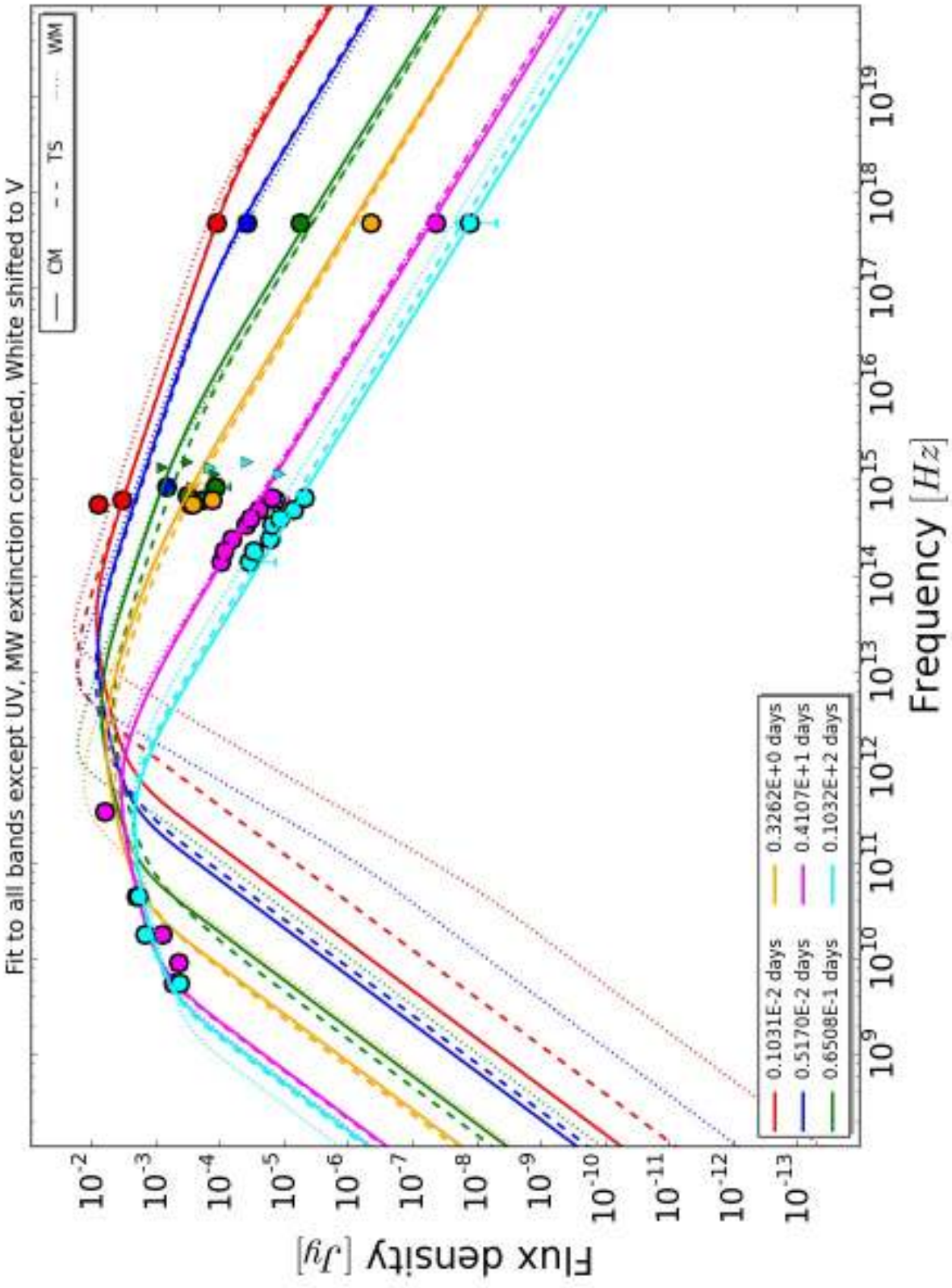
Fit to all bands except UV, MW extinction corrected, White shifted to V
CM
TS
WM
0.1031E-2 days
0.5170E-2 days
0.6508E-1 days
0.3262E+0 days
0.4107E+1 days
0.1032E+2 days
Flux density [Jy]
Frequency [Hz]

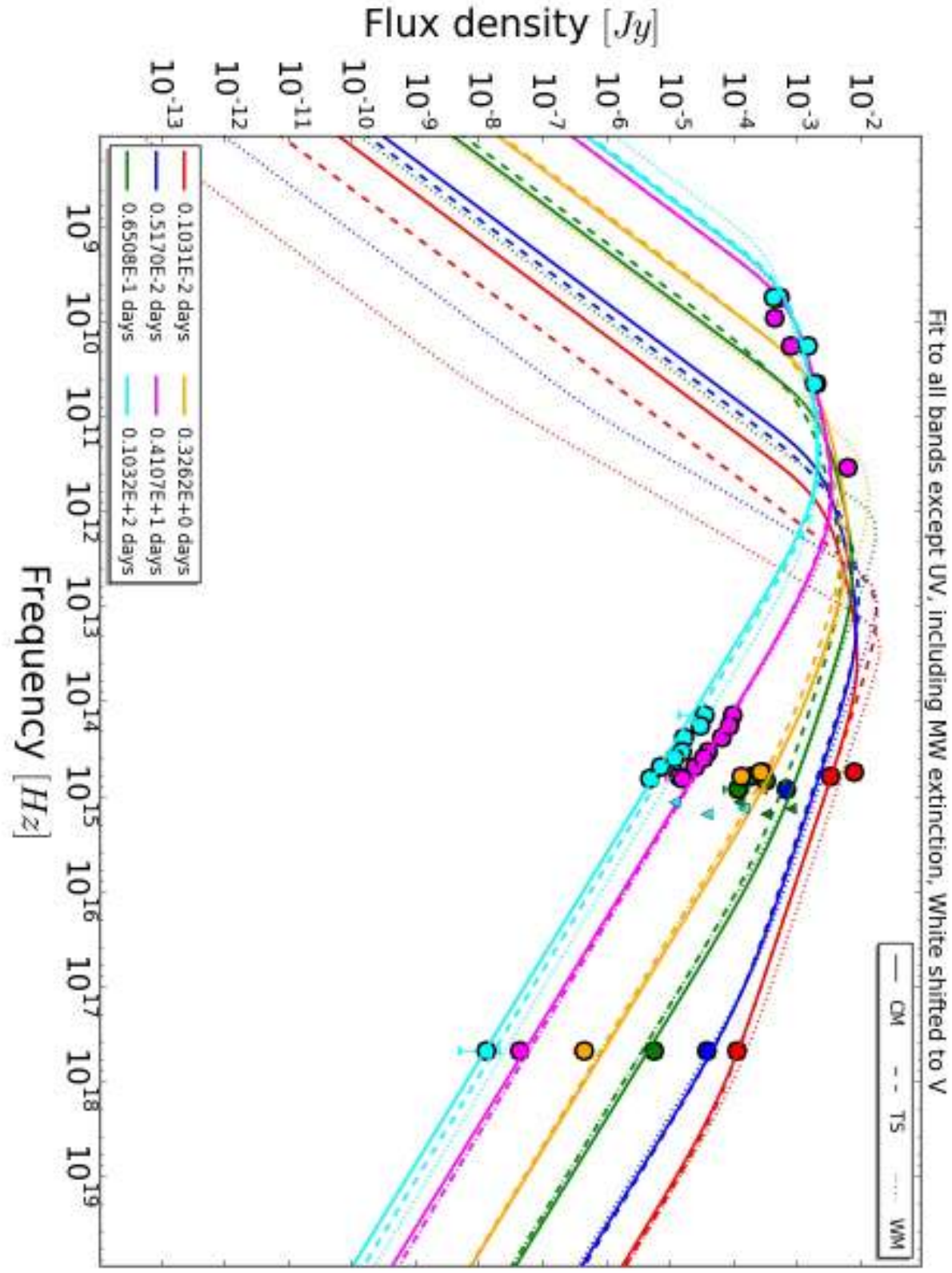
Fit to all bands except UV, including MW extinction, White shifted to V
CM
TS
VM
Flux density $[Jy]$
Frequency $[Hz]$
0.1031E-2 days
0.5170E-2 days
0.6508E-1 days
0.3262E+0 days
0.4107E+1 days
0.1032E+2 days

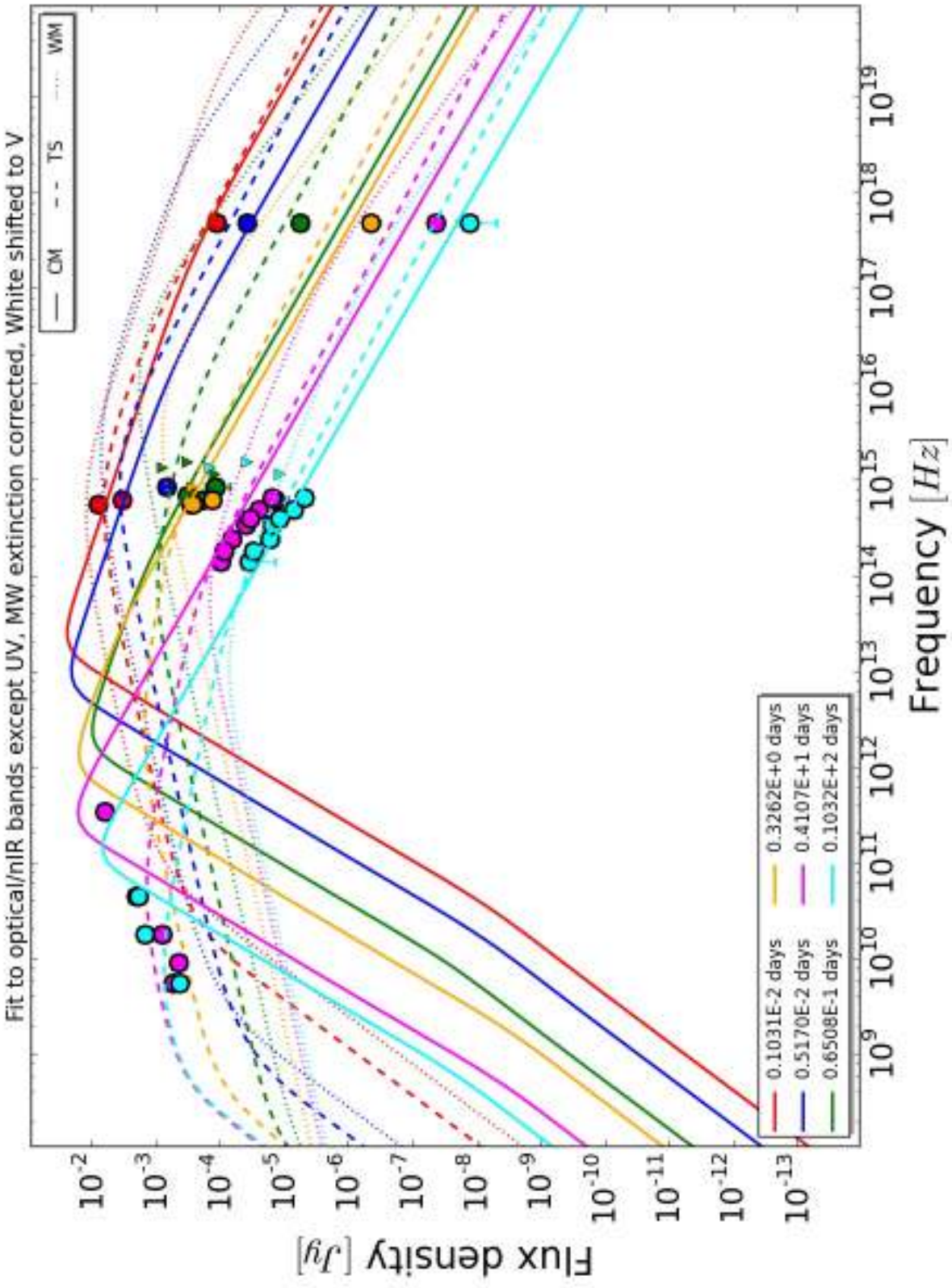
Fit to optical/nIR bands except UV, MW extinction corrected, White shifted to V
CM
TS
WM
0.1031E-2 days
0.5170E-2 days
0.6508E-1 days
0.3262E+0 days
0.4107E+1 days
0.1032E+2 days
Flux density [Jy]
Frequency [Hz]

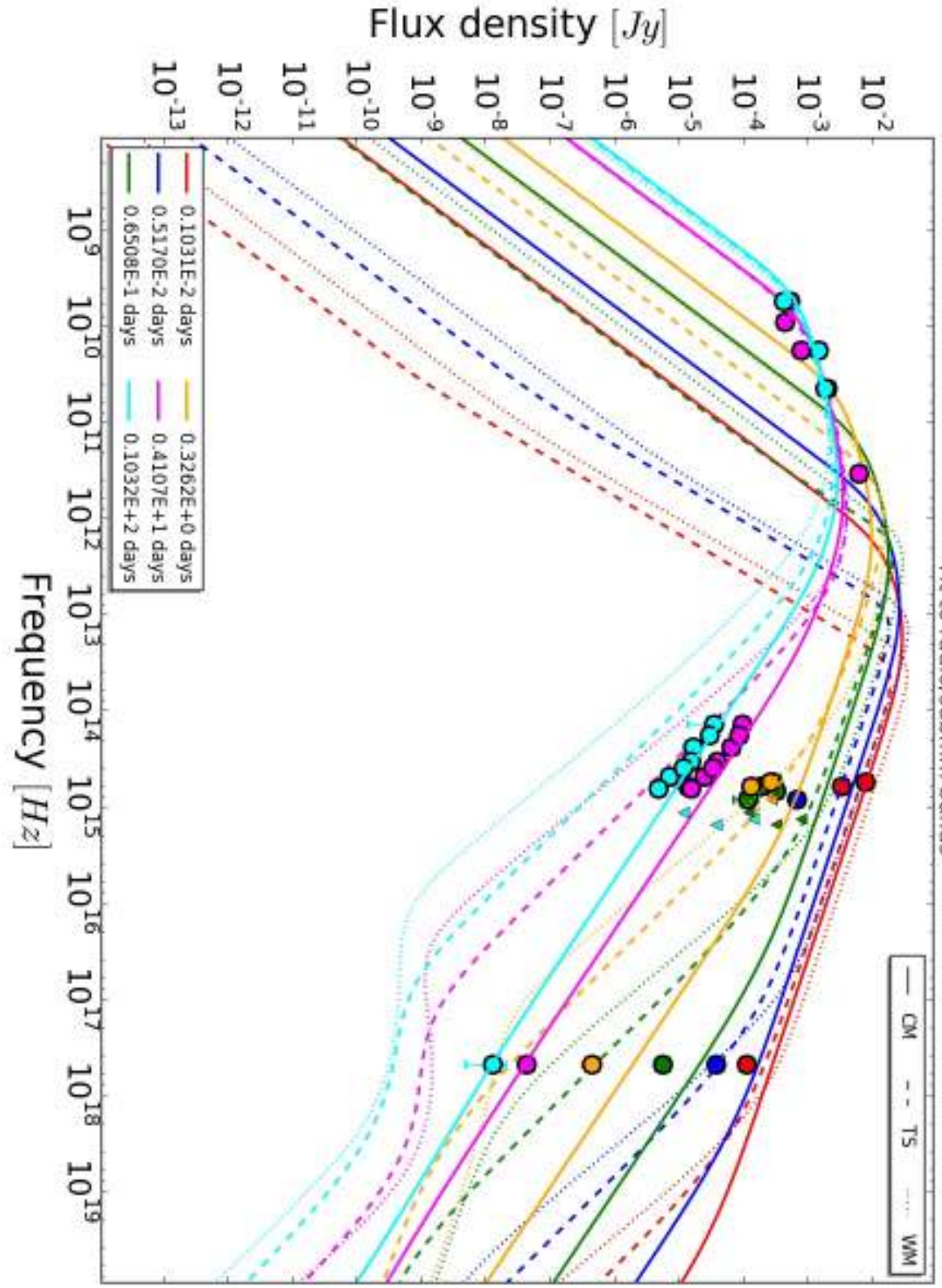
Flux density $[Jy]$
Frequency $[Hz]$
Fit to radio/submm bands
CM
TS
VM
0.1031E-2 days
0.5170E-2 days
0.6508E-1 days
0.3262E+0 days
0.4107E+1 days
0.1032E+2 days

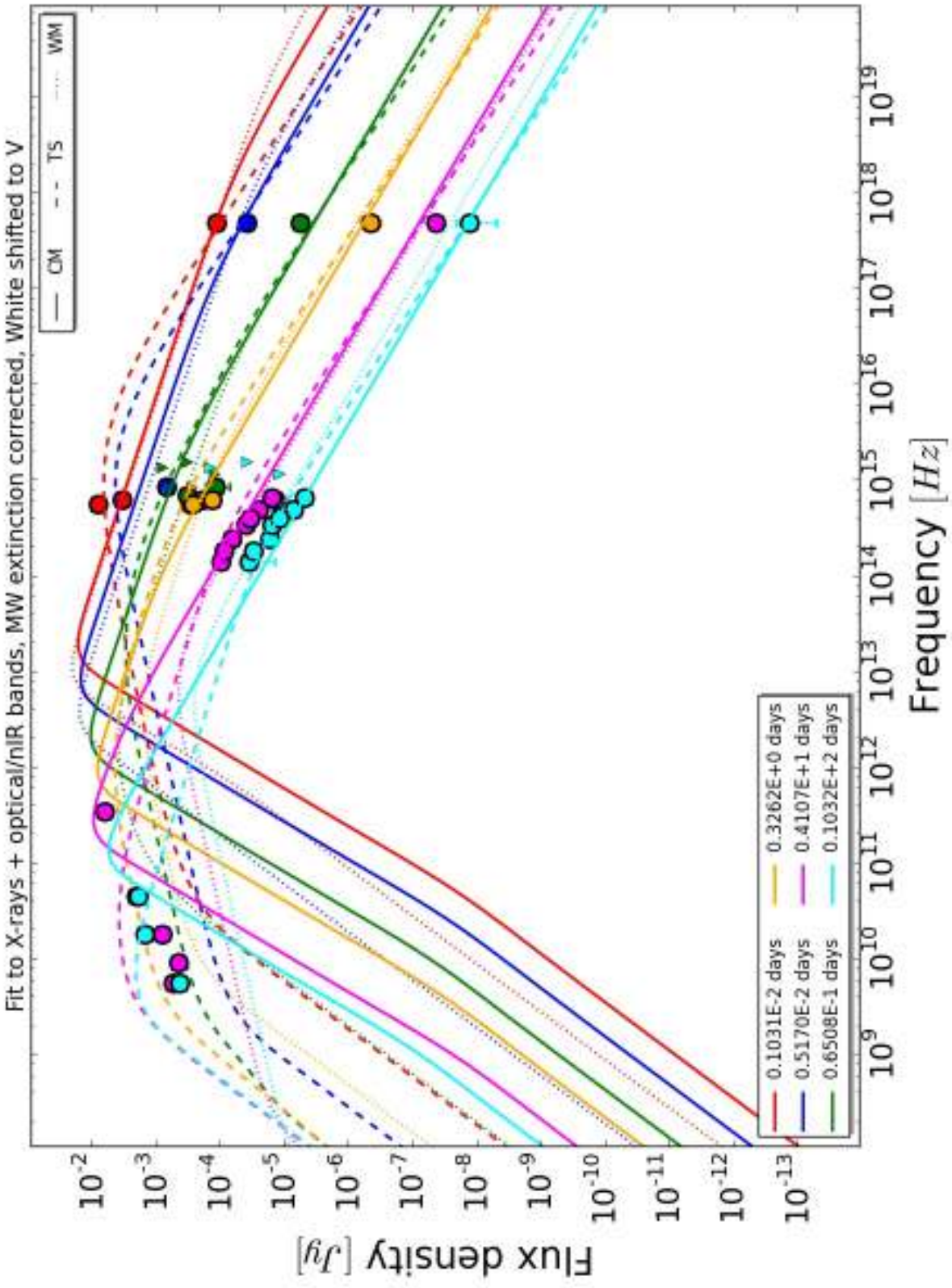
Fit to X-rays + optical/nIR bands, MW extinction corrected, White shifted to V
CM
TS
WM
0.1031E-2 days
0.5170E-2 days
0.6508E-1 days
0.3262E+0 days
0.4107E+1 days
0.1032E+2 days
Flux density [Jy]
Frequency [Hz]

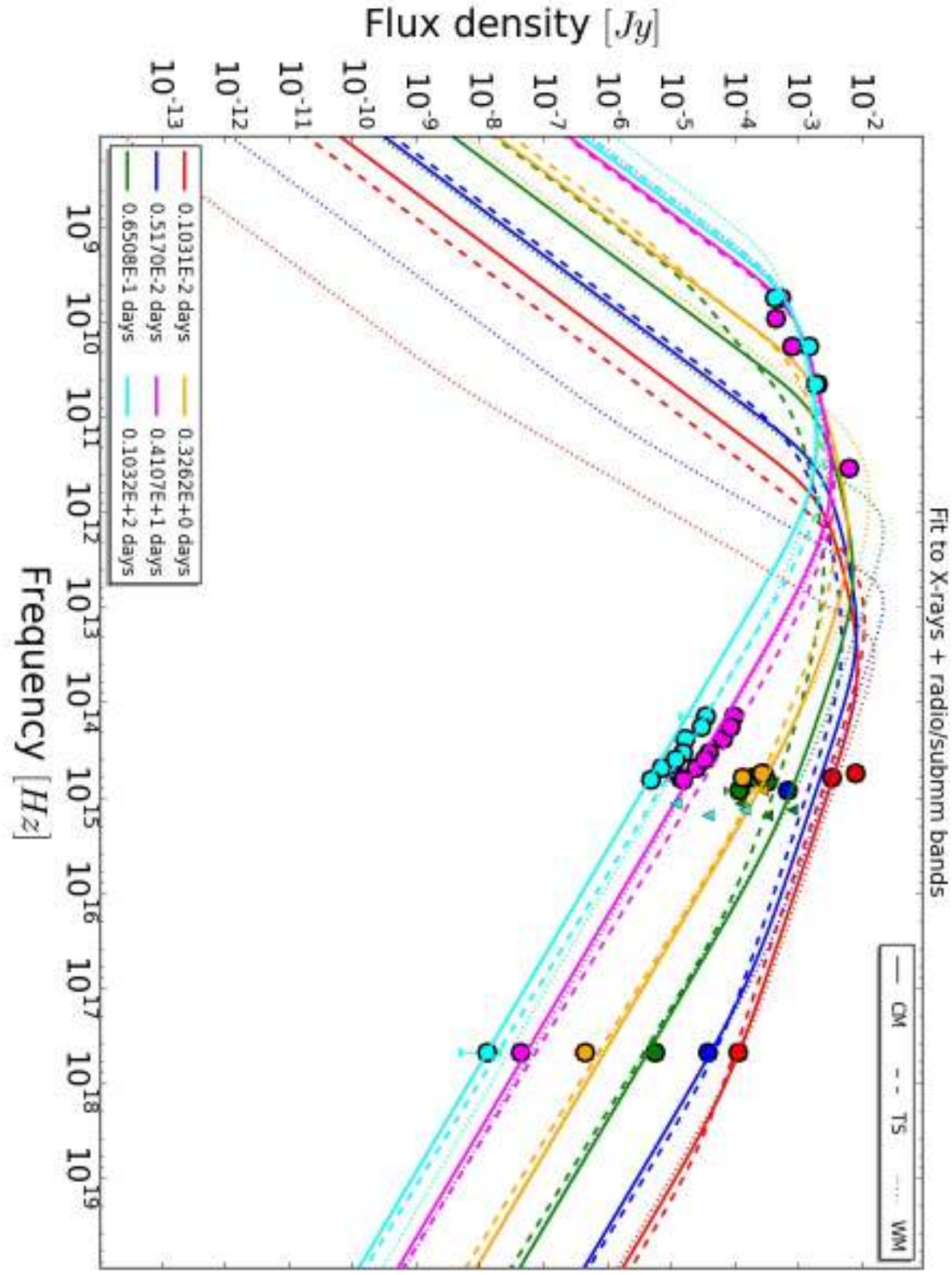
Flux density $[Jy]$
Frequency $[Hz]$
Fit to X-rays + radio/submm bands
CM
TS
VM
0.1031E-2 days
0.5170E-2 days
0.6508E-1 days
0.3262E+0 days
0.4107E+1 days
0.1032E+2 days

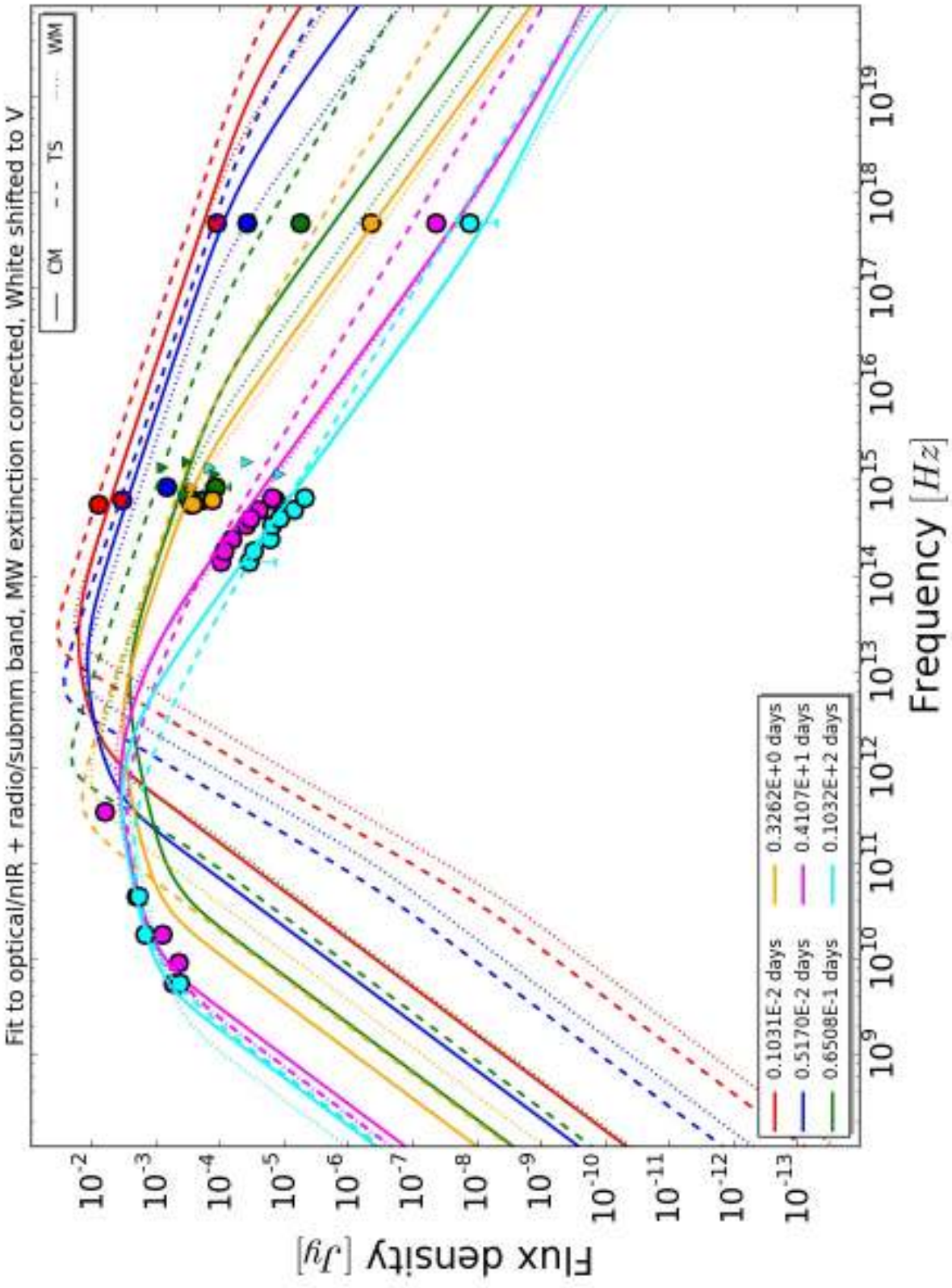
Fit to optical/nIR + radio/submm band, MW extinction corrected, White shifted to V
CM
TS
WM
0.1031E-2 days
0.5170E-2 days
0.6508E-1 days
0.3262E+0 days
0.4107E+1 days
0.1032E+2 days
Flux density [Jy]
Frequency [Hz]

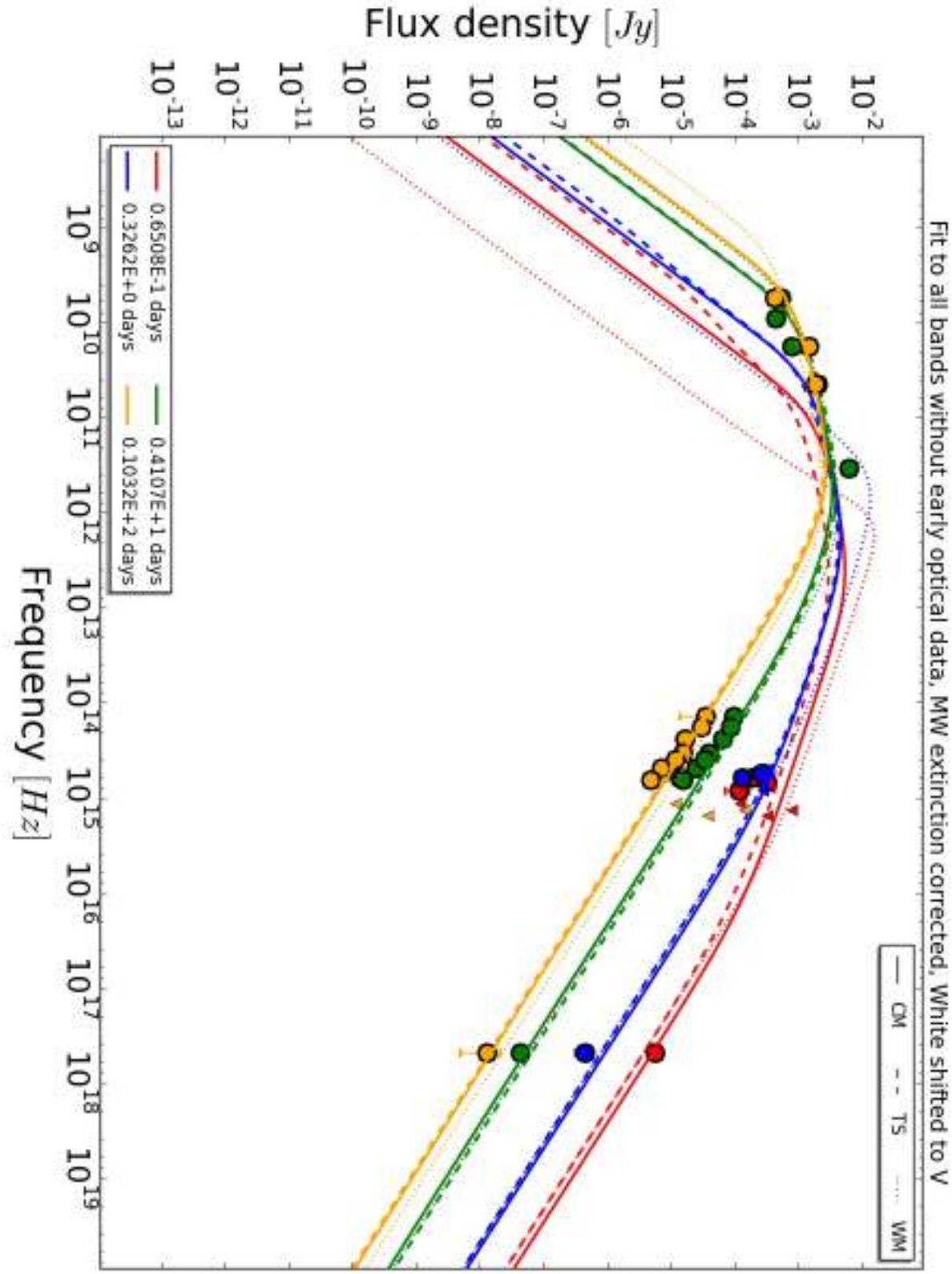
Fit to all bands without early optical data, MW extinction corrected, White shifted to V
CM
TS
VM
Flux density $[Jy]$
Frequency $[Hz]$
0.6508E-1 days
0.3262E+0 days
0.4107E+1 days
0.1032E+2 days

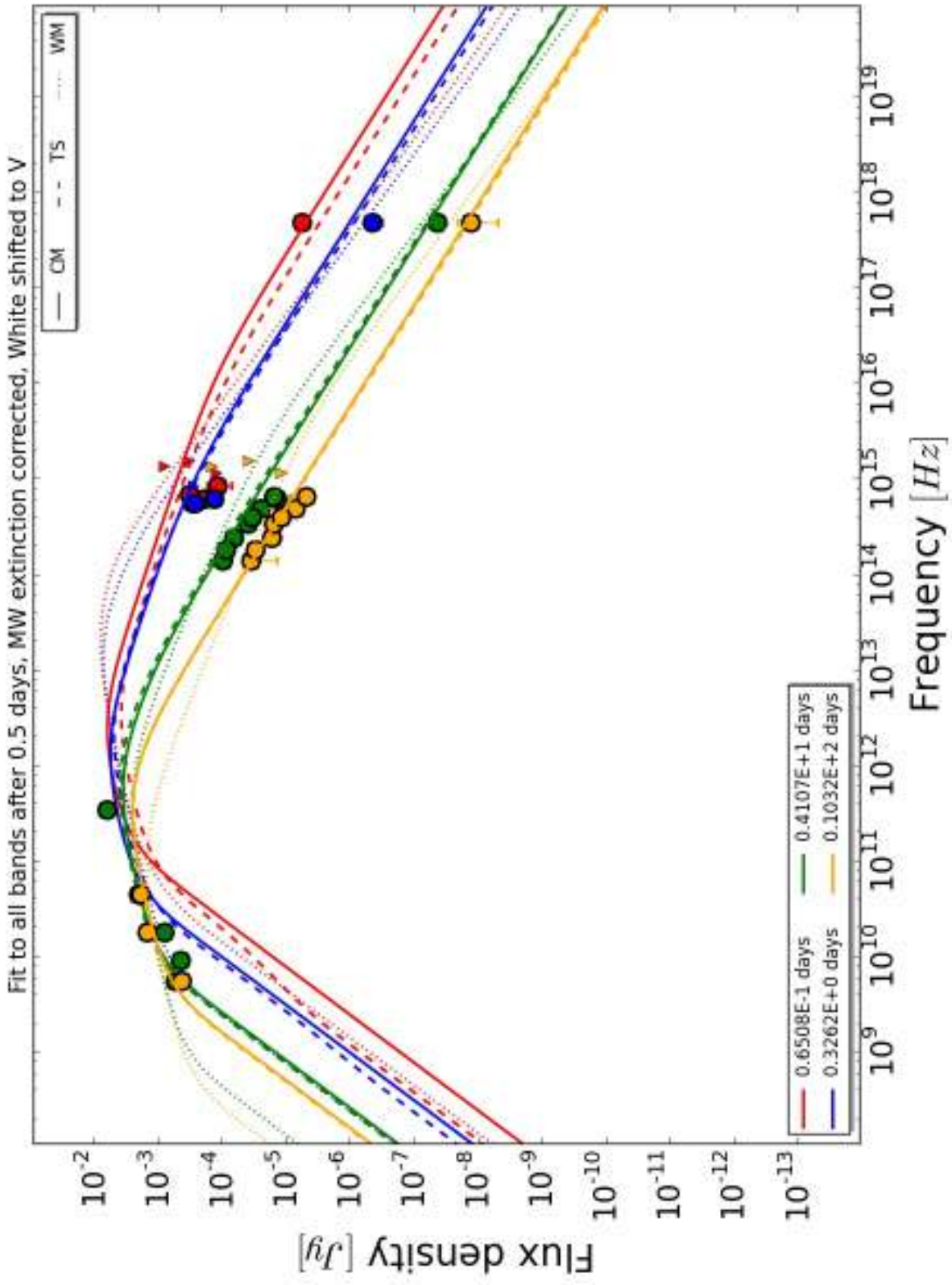
Fit to all bands after 0.5 days, MW extinction corrected, White shifted to V
CM
TS
WM
0.65508E-1 days
0.3262E+0 days
0.4107E+1 days
0.1032E+2 days
Flux density [μy]
Frequency [Hz]

Appendix E

Marginal 1D plots of GRB 110715A model fits.

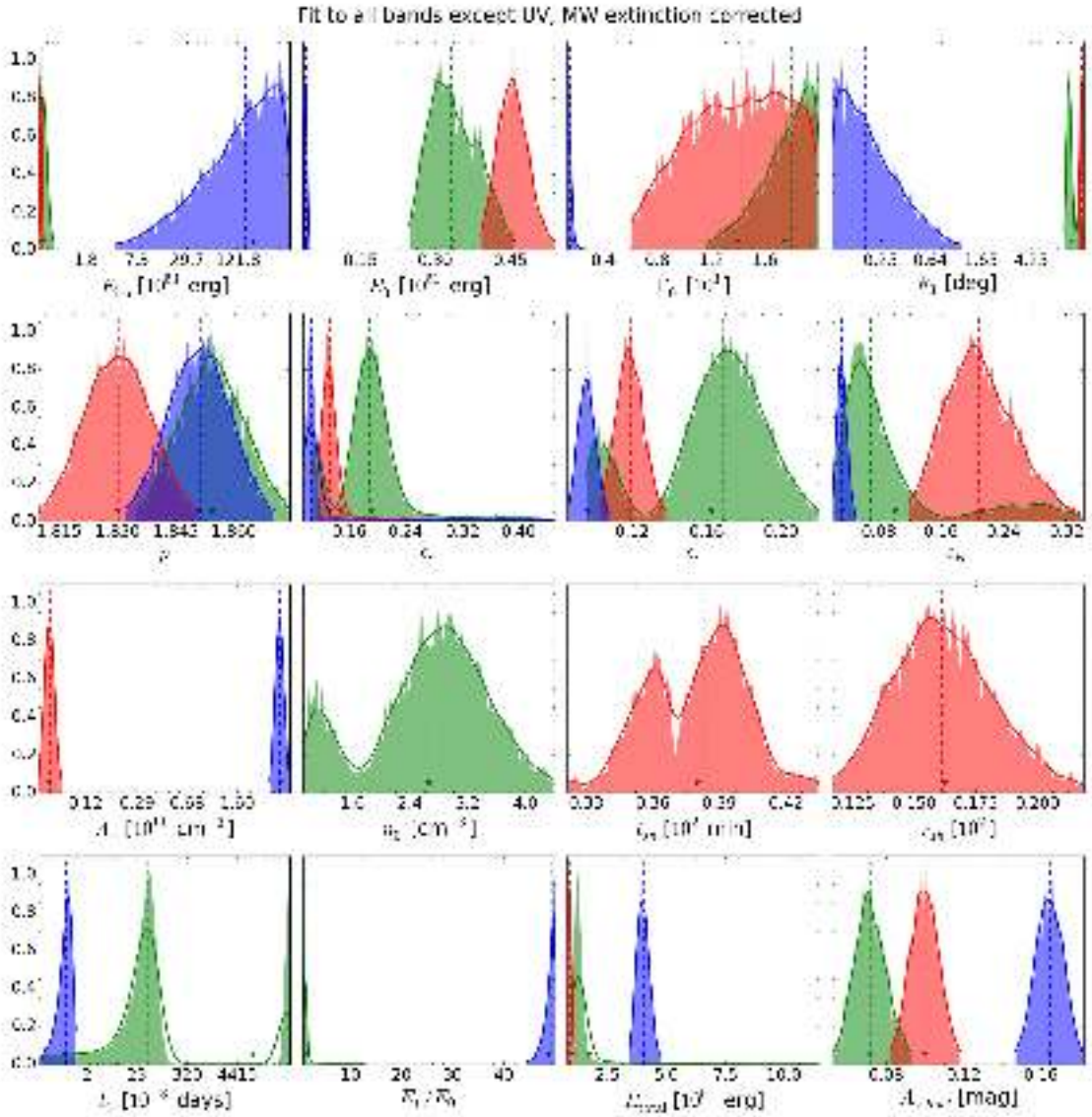
Fit to all bands except UV, MW extinction corrected

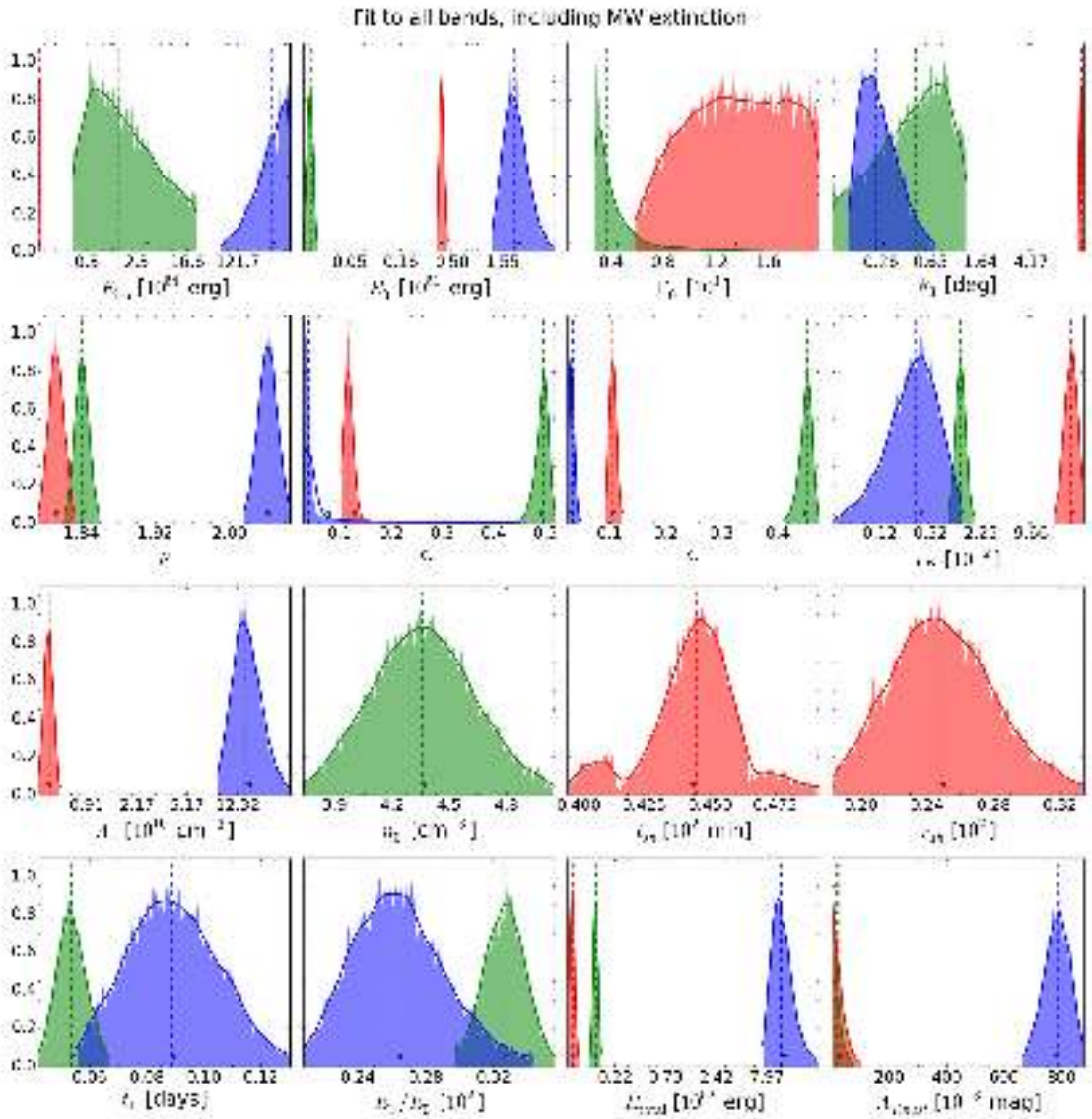
Fit to all bands, including MW extinction

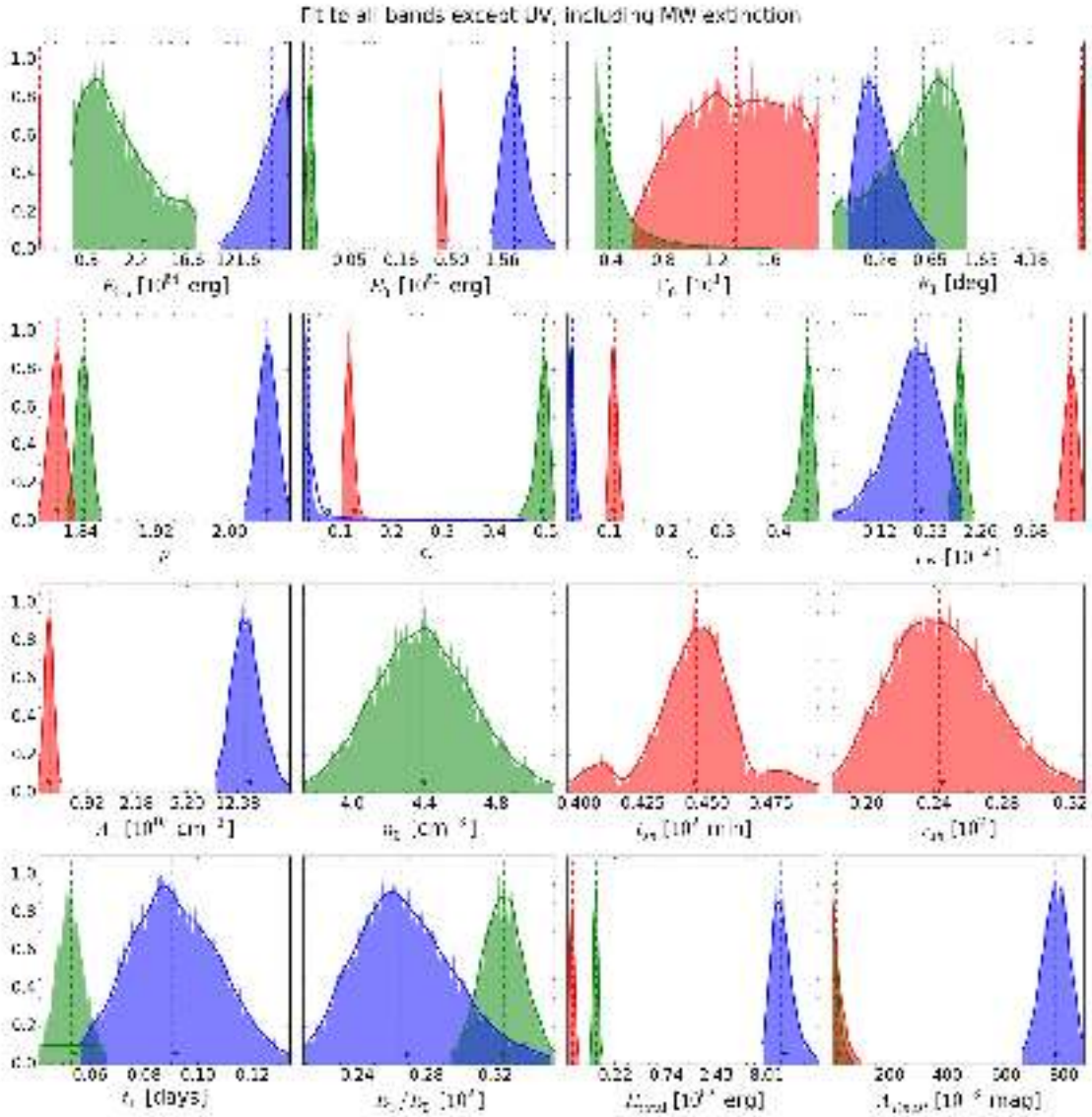
Fit to all bands except UV, including MW extinction

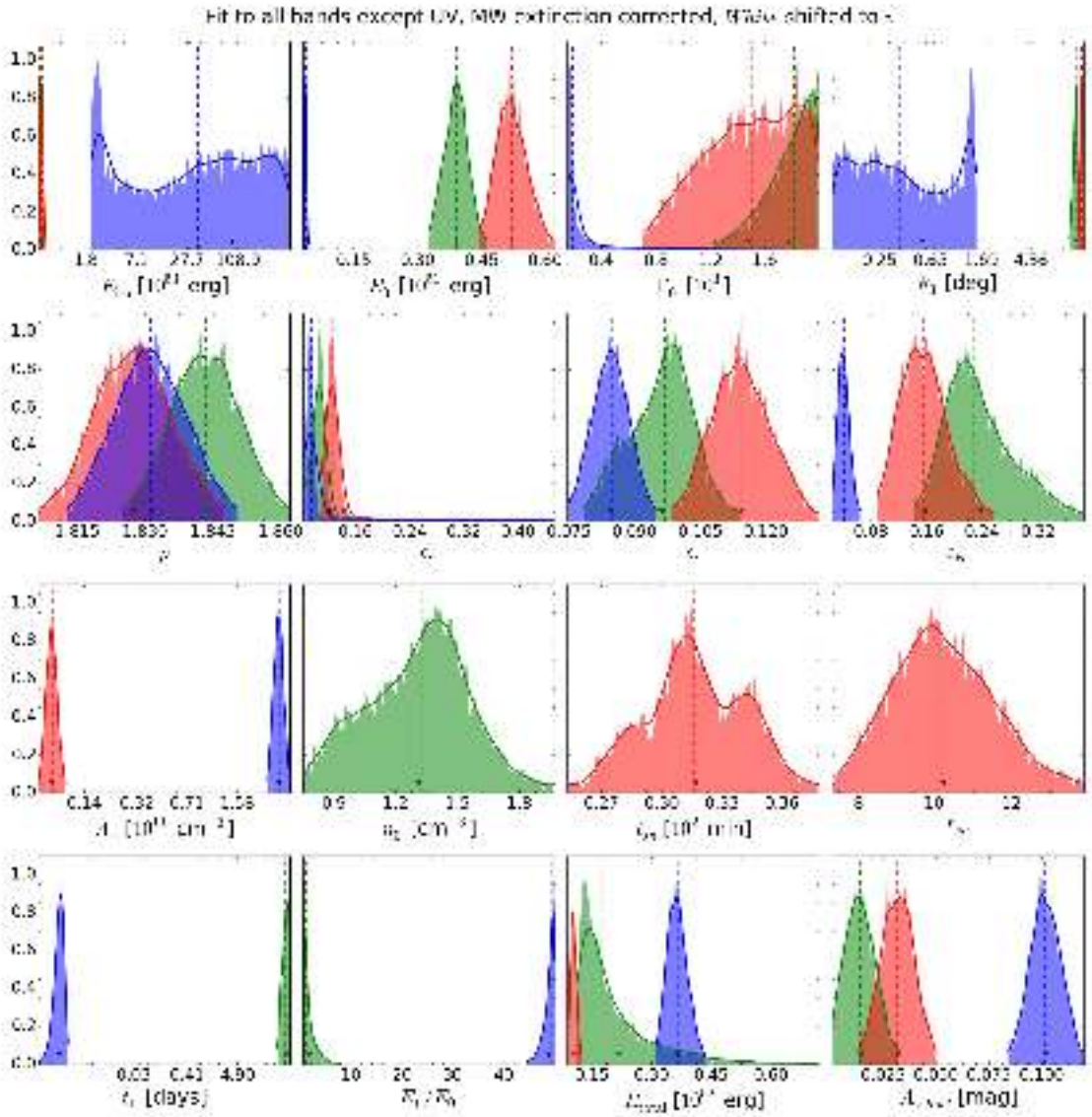

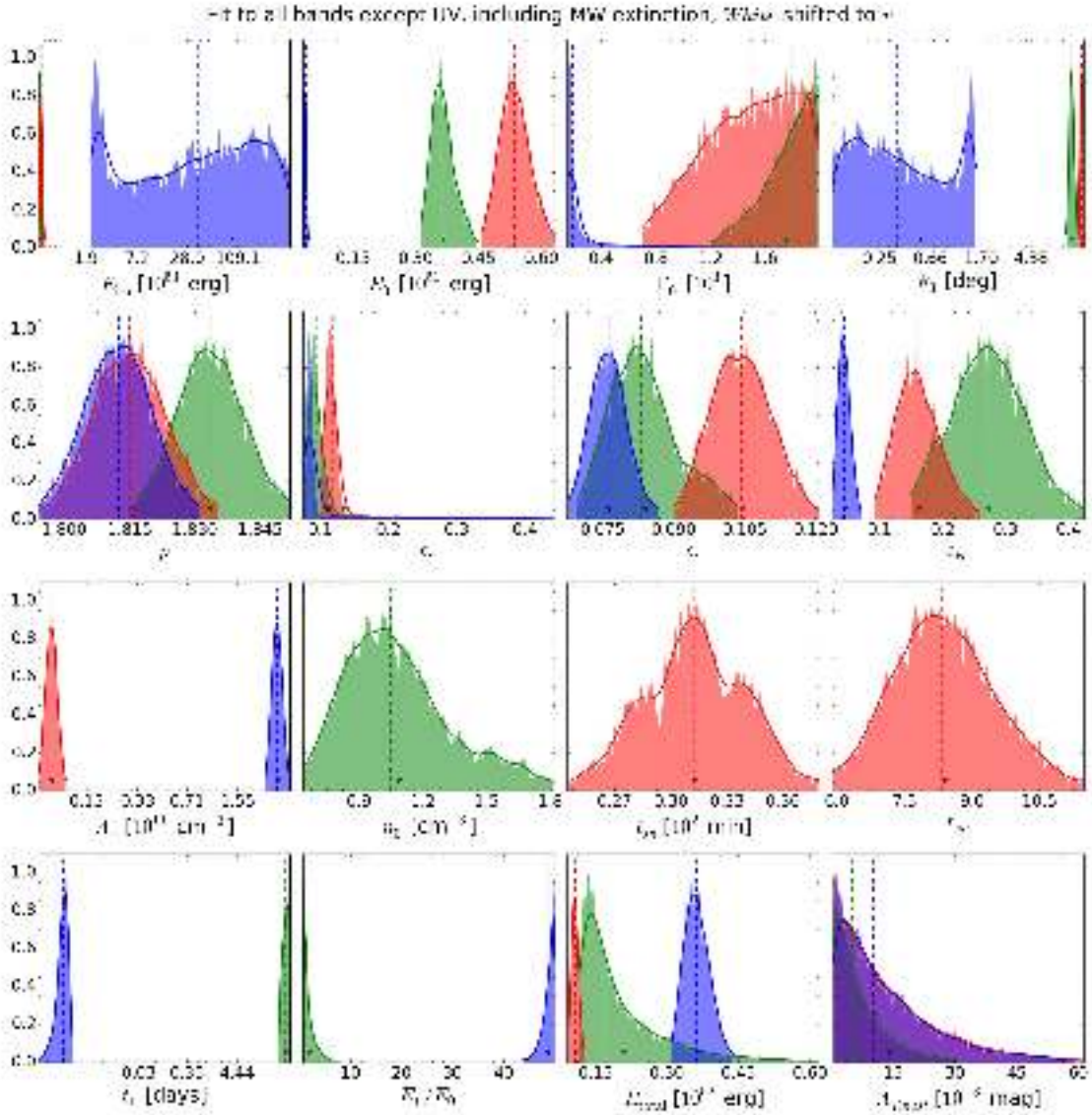

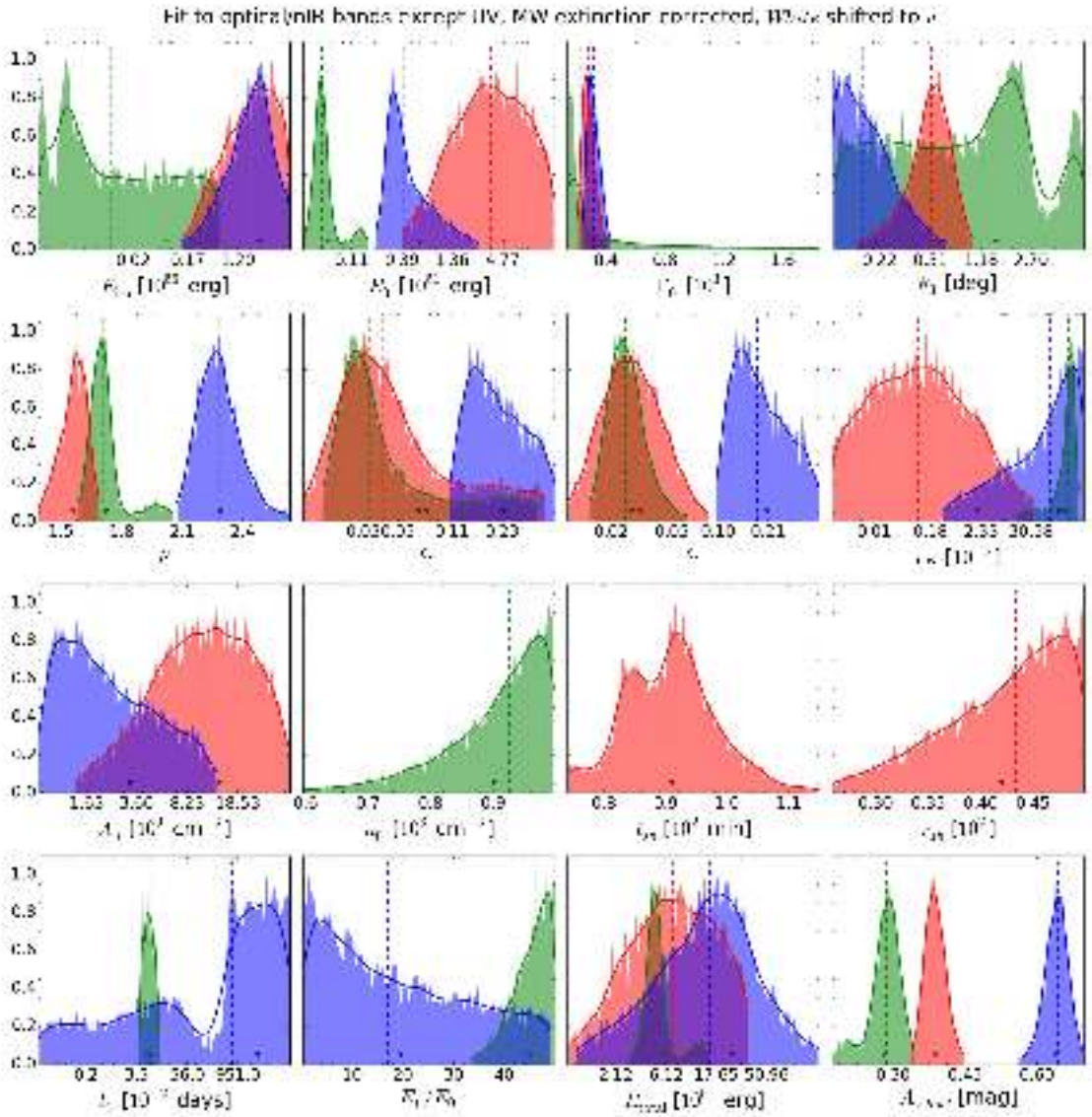

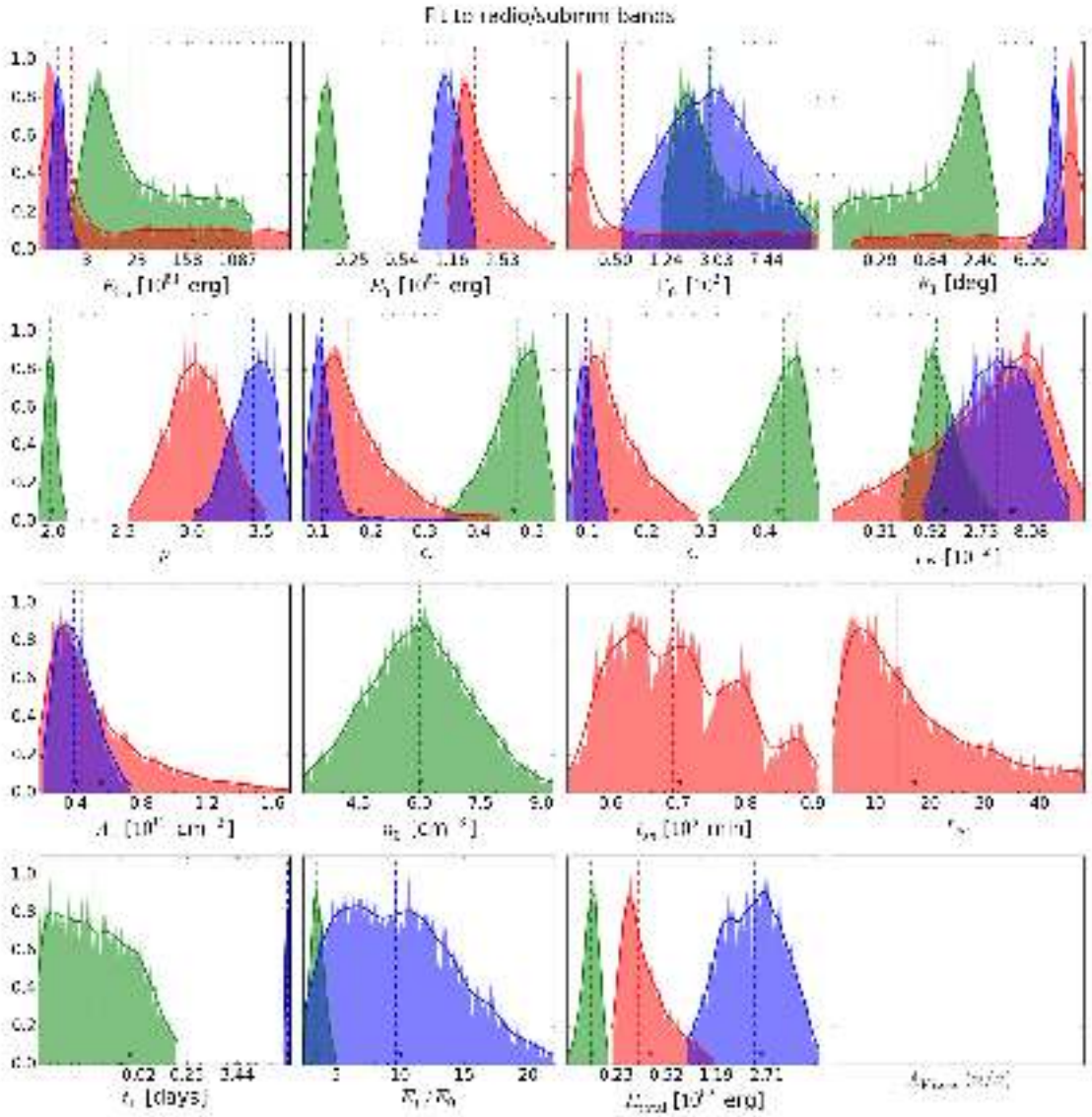
FLs to radio/submm bands

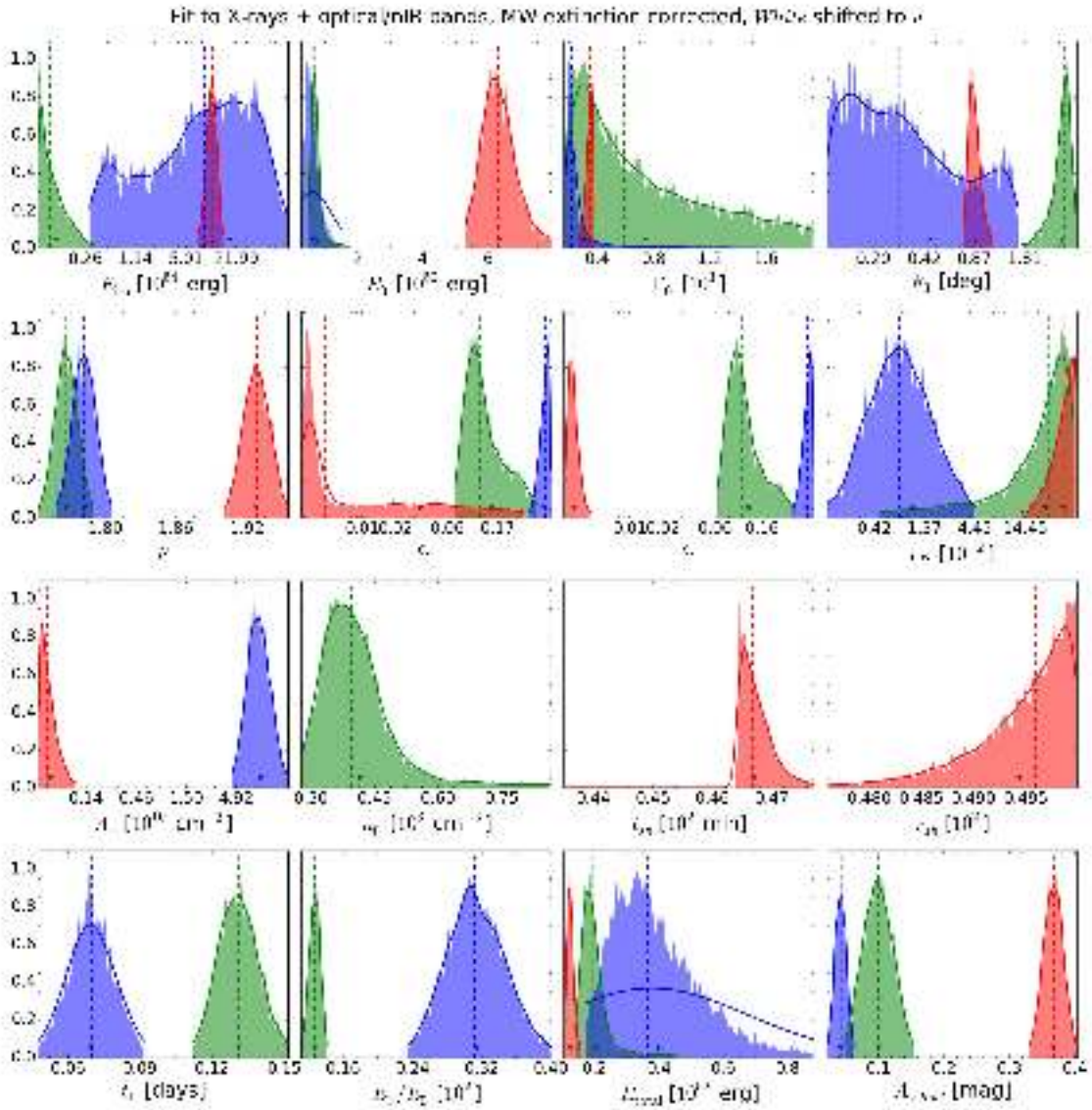

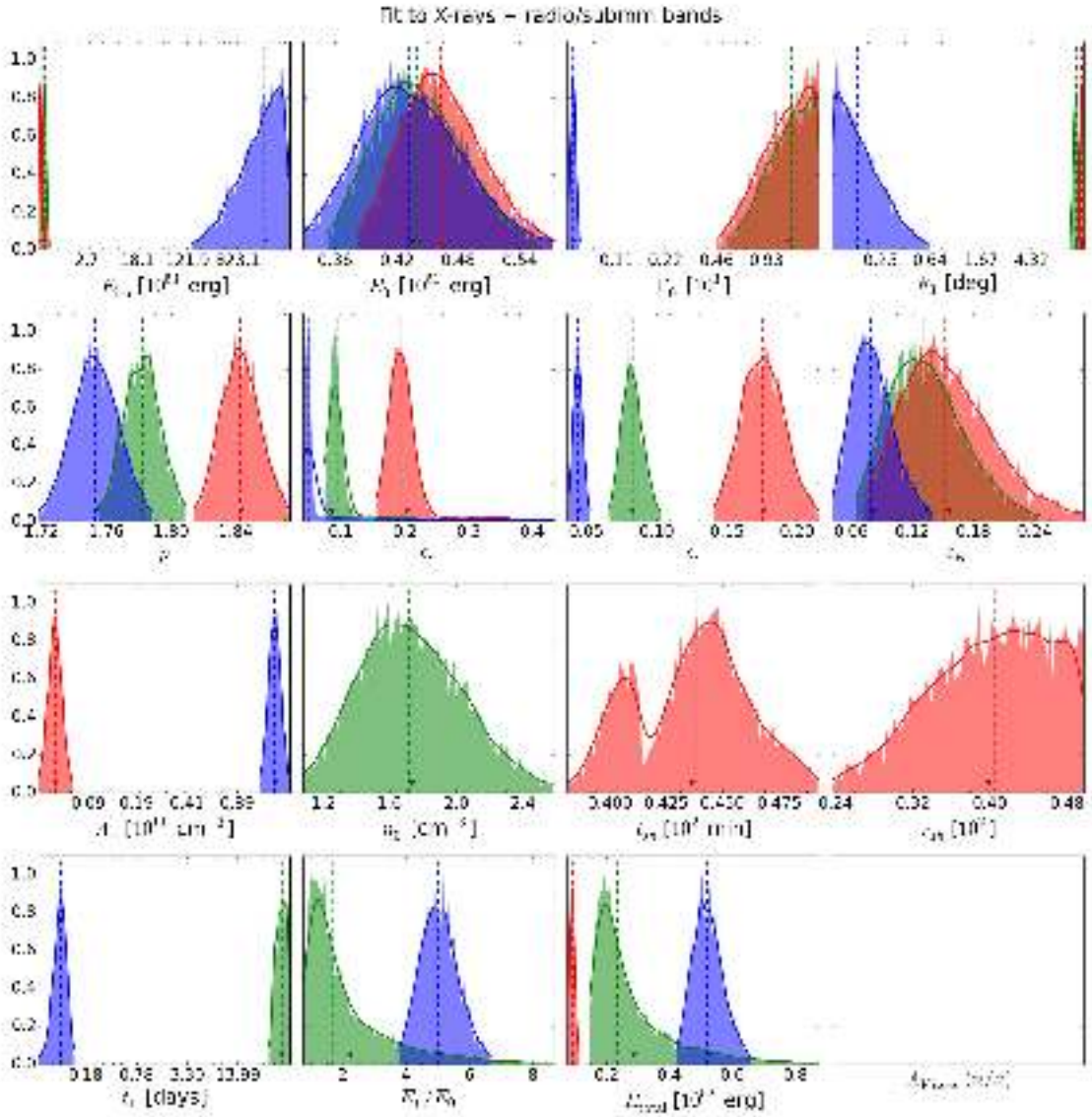
fit to X-rays + radio/submm bands

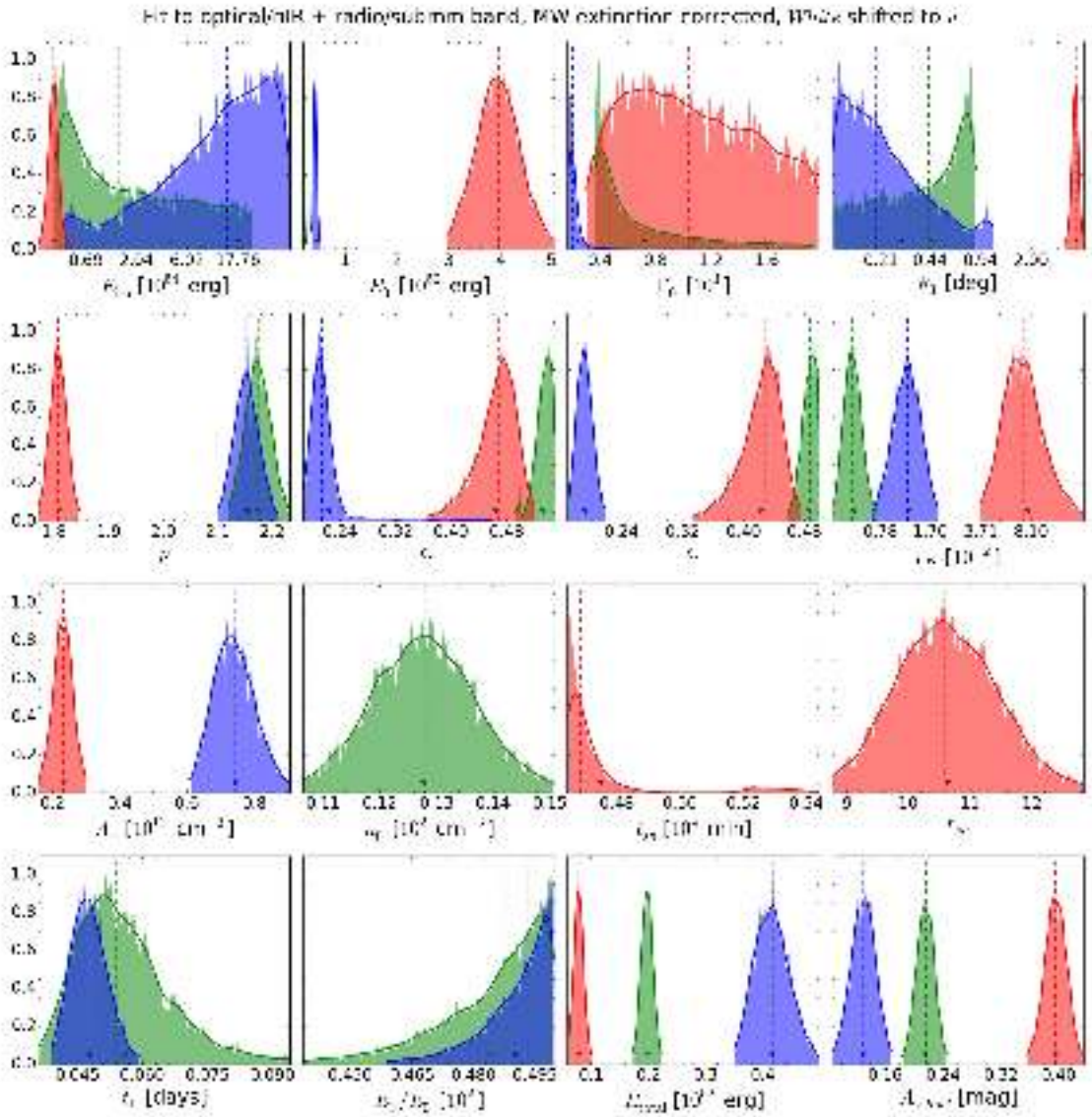

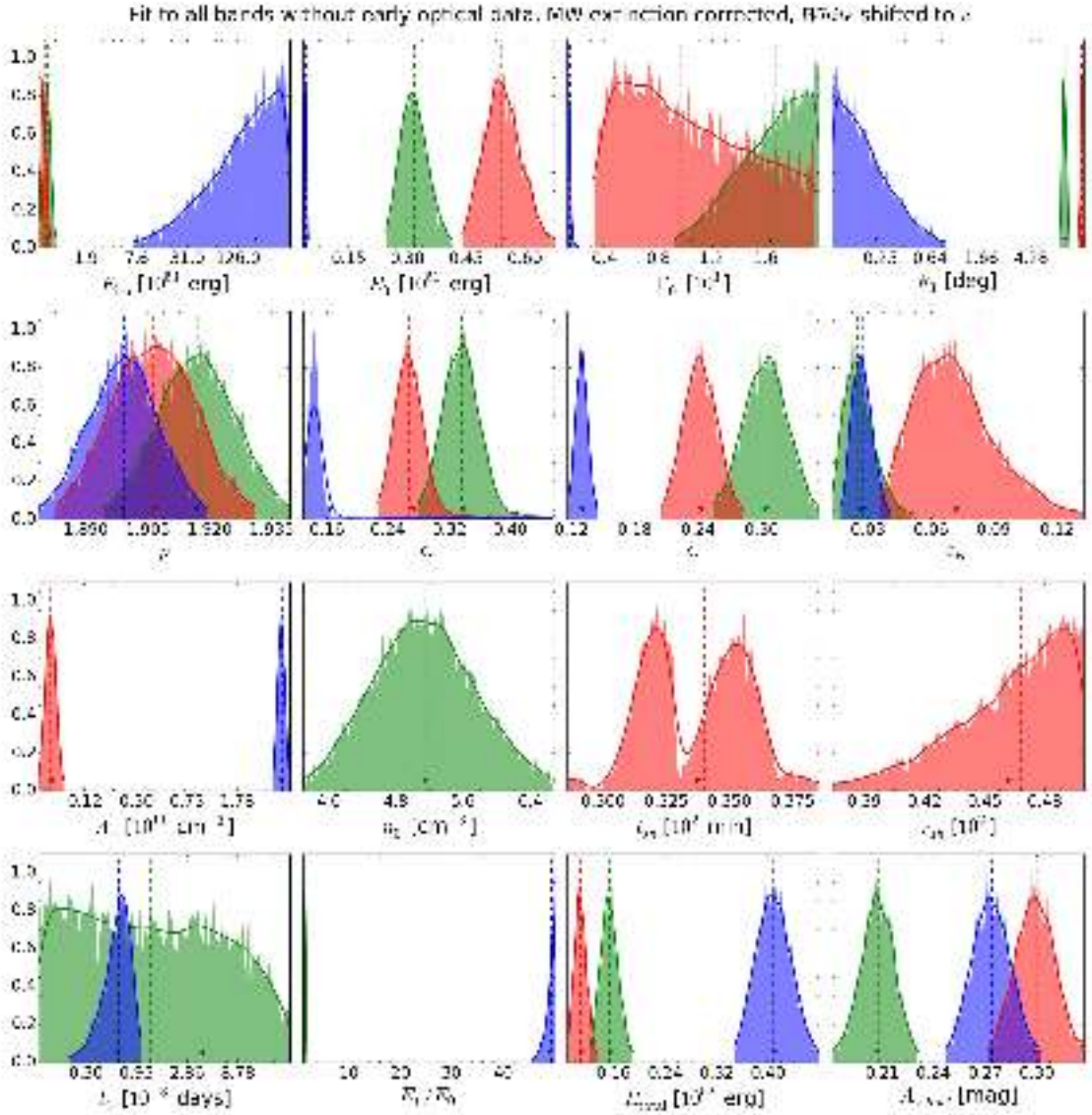
Fit to all bands without early optical data. MW extinction corrected, R-V shifted to z
1.0
0.8
0.6
0.4
0.2
0.0
1.890 1.905 1.920 1.935
0.15 0.30 0.45 0.60
0.10 0.24 0.32 0.40
0.12 0.18 0.24 0.30
0.00 0.06 0.09 0.12
0.12 0.30 0.75 1.75
4.0 4.8 5.6 6.4
0.300 0.325 0.350 0.375
0.39 0.42 0.45 0.48
0.30 0.83 2.30 6.38
10 20 30 40
0.18 0.24 0.32 0.40
0.21 0.24 0.27 0.30

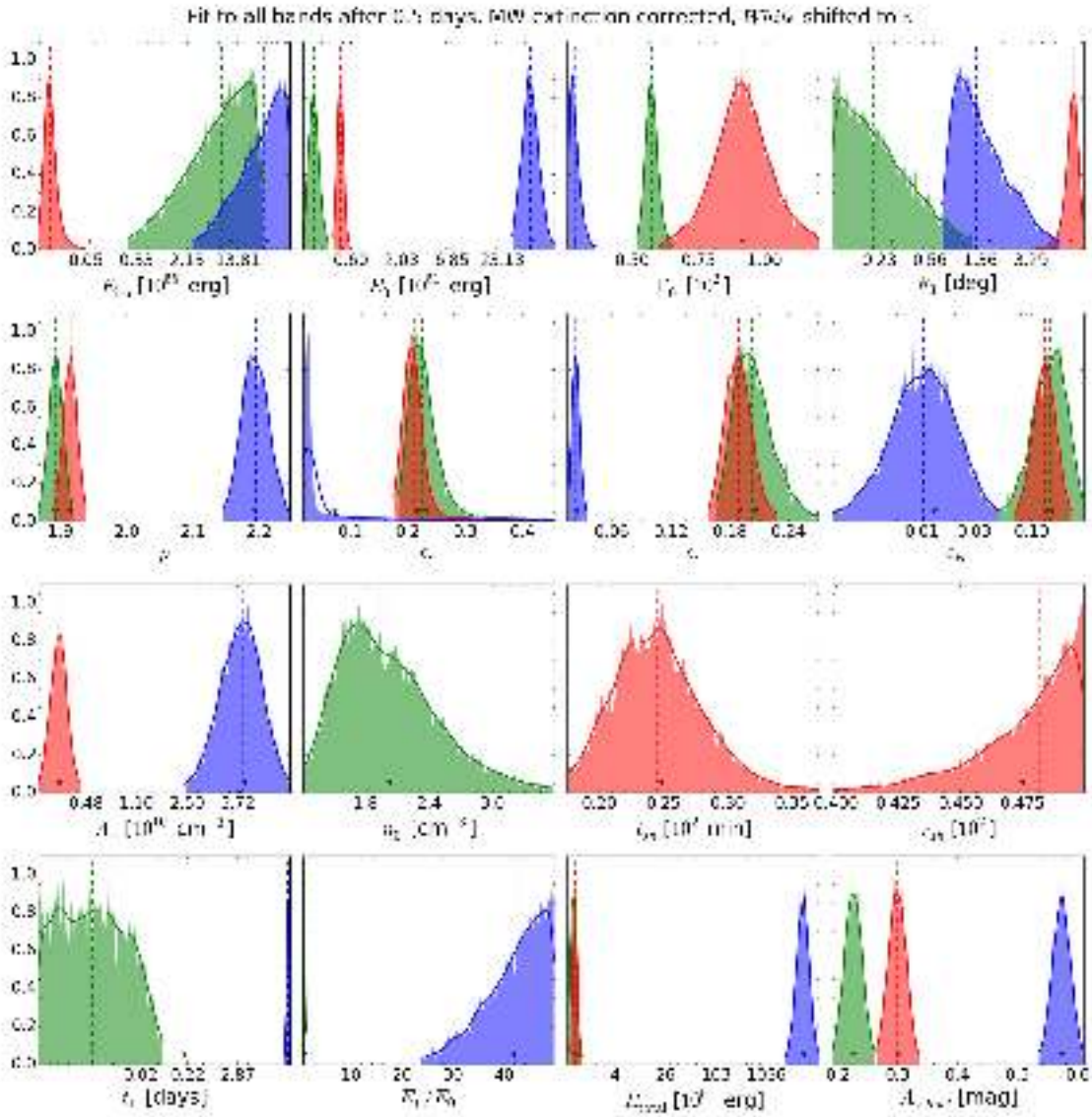
Fit to all bands after 0.5 days. MW extinction corrected, RWs shifted to z
1.0
0.8
0.6
0.4
0.2
0.0
0.65 0.88 2.15 13.81
0.80 3.03 9.85 25.13
0.30 0.73 1.30
0.23 0.56 1.26 2.70
θ_3 [deg]
1.9 2.0 2.1 2.2
0.1 0.2 0.3 0.4
0.00 0.12 0.18 0.24
0.01 0.03 0.10
0.48 1.10 2.00 3.72
1.8 2.4 3.0
0.20 0.25 0.30 0.35
0.400 0.425 0.450 0.475
0.02 0.22 2.87
10 20 30 40
4 20 100 1000
0.2 0.3 0.4 0.5 0.6

Appendix F

Marginal 2D plots of GRB 110715A model fits.

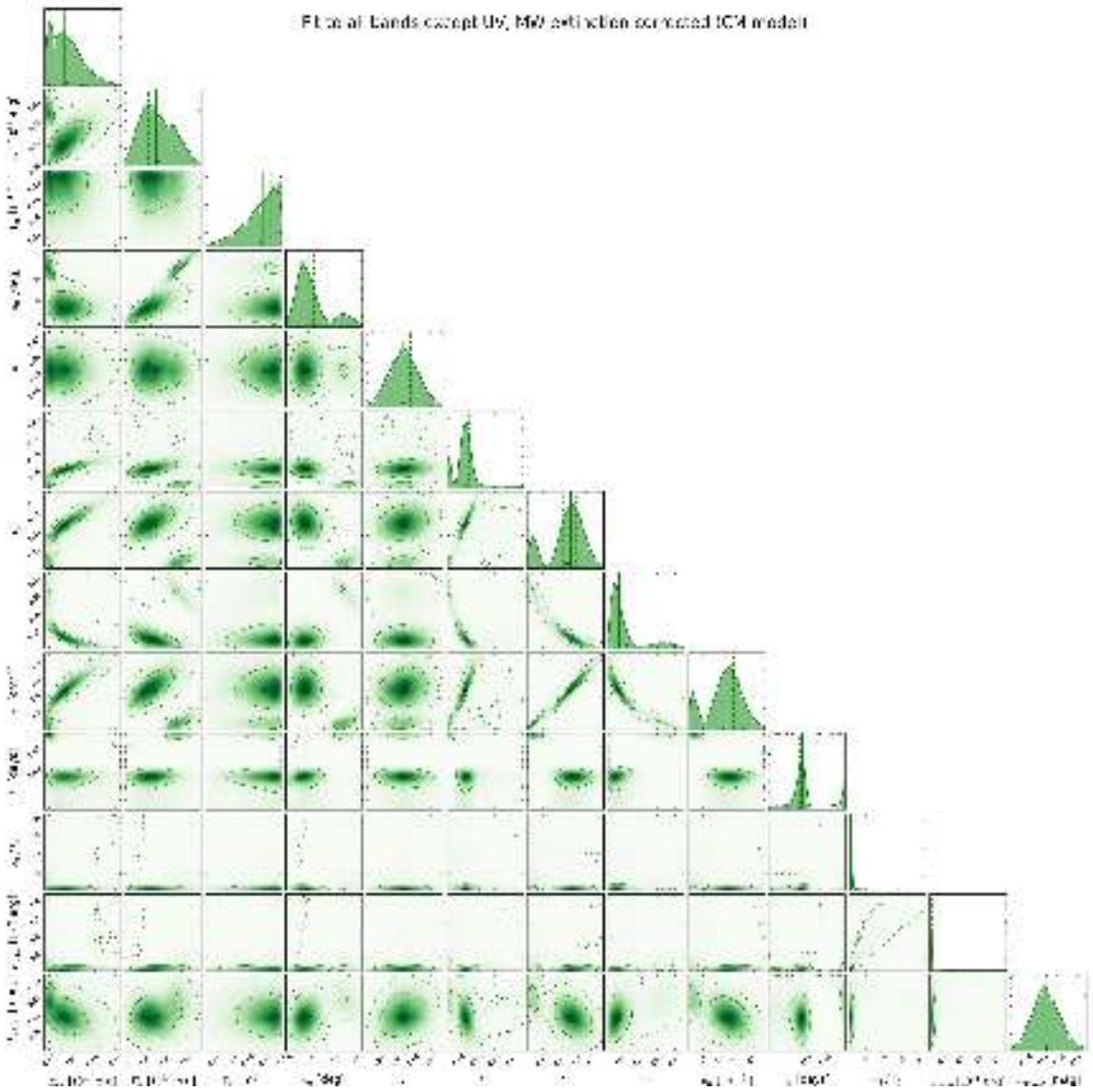

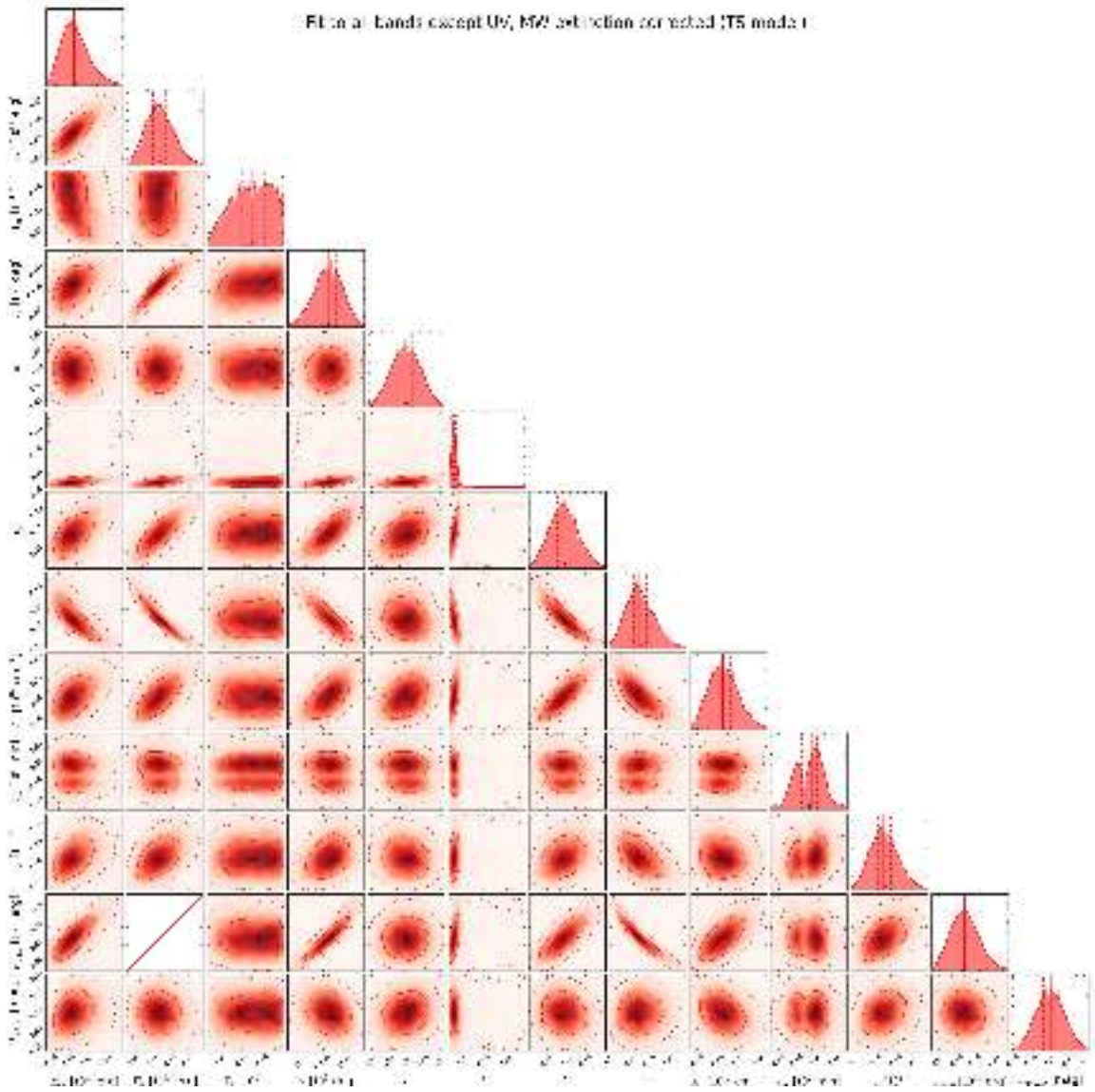

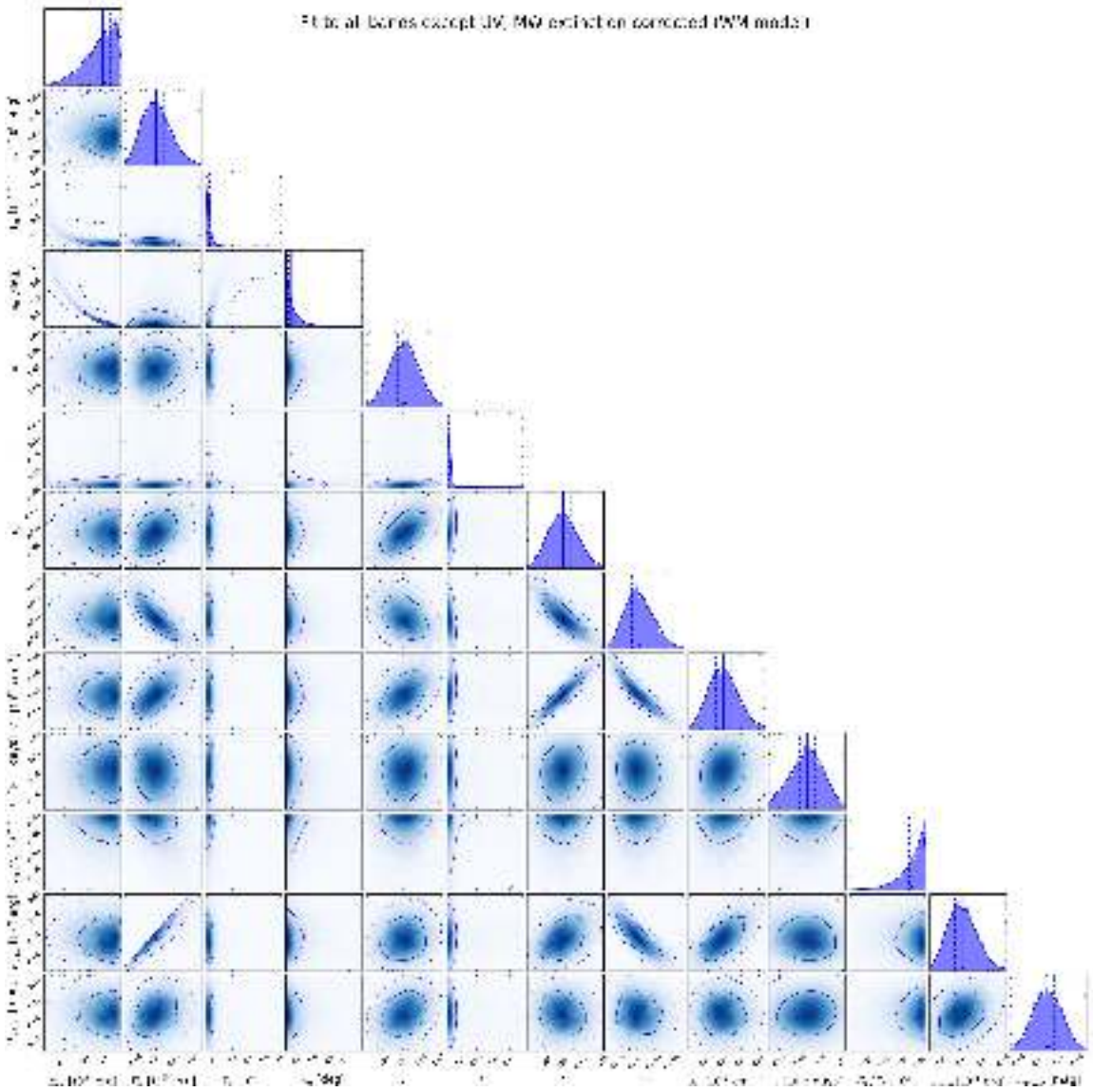

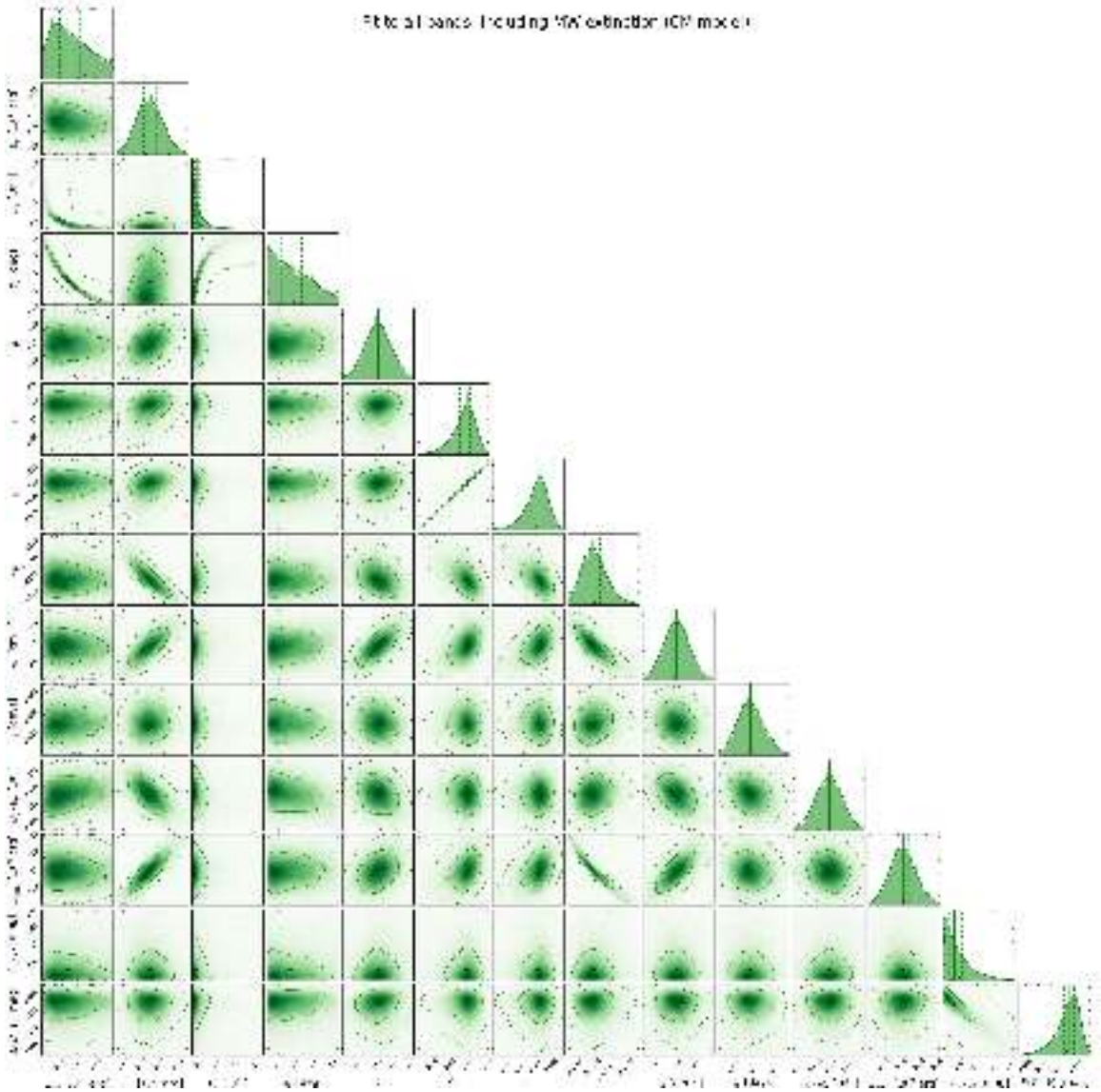

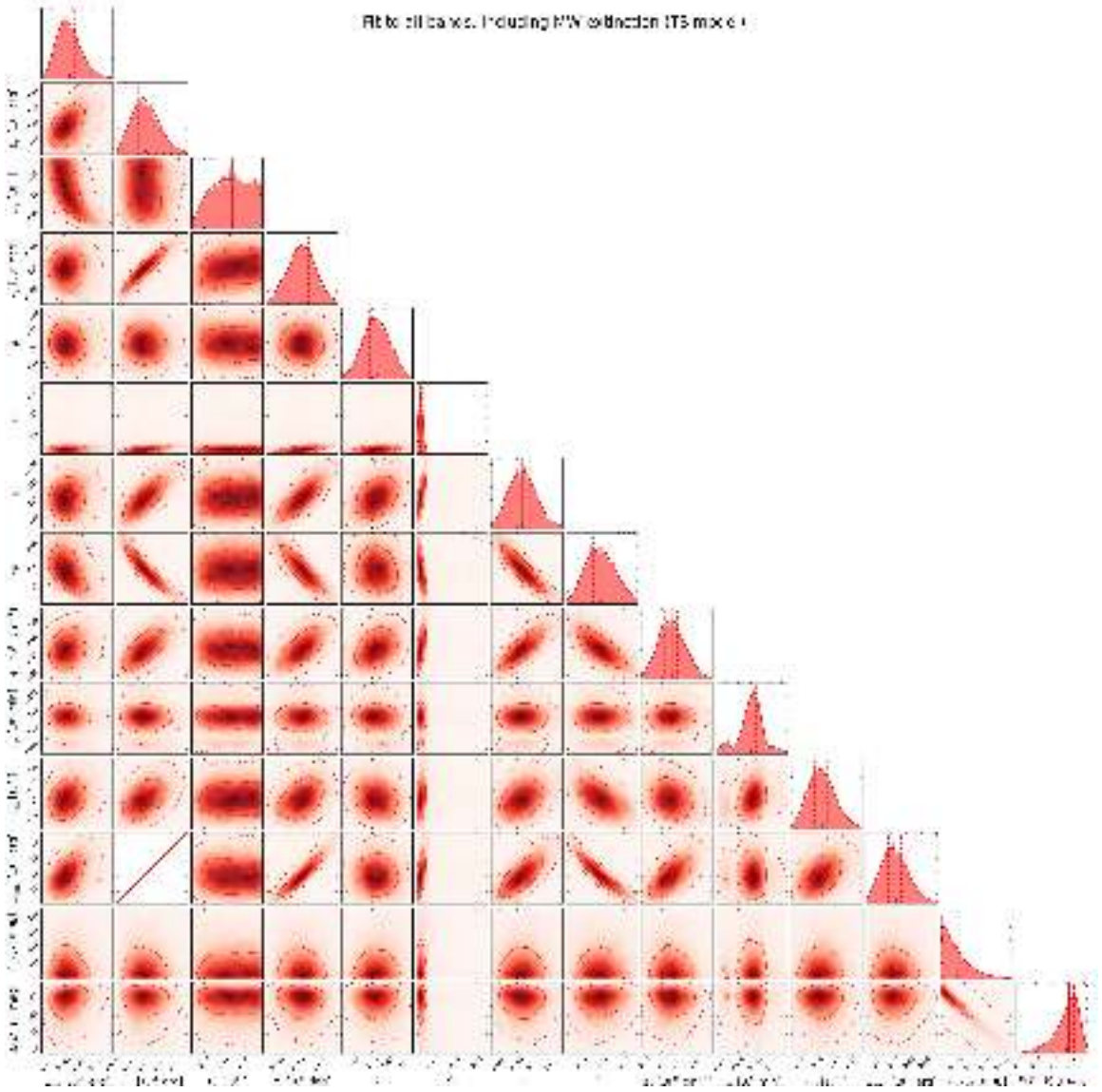

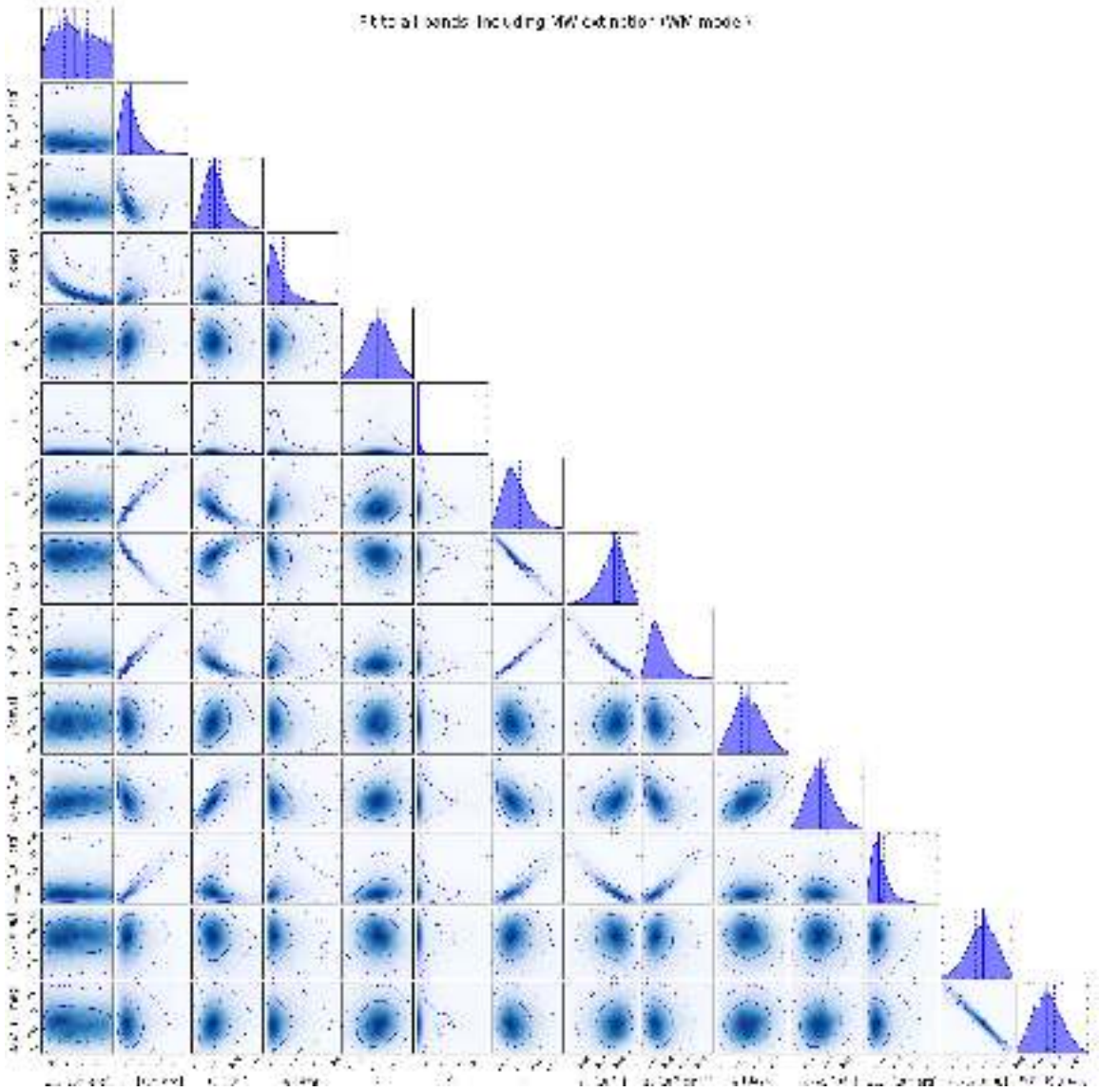

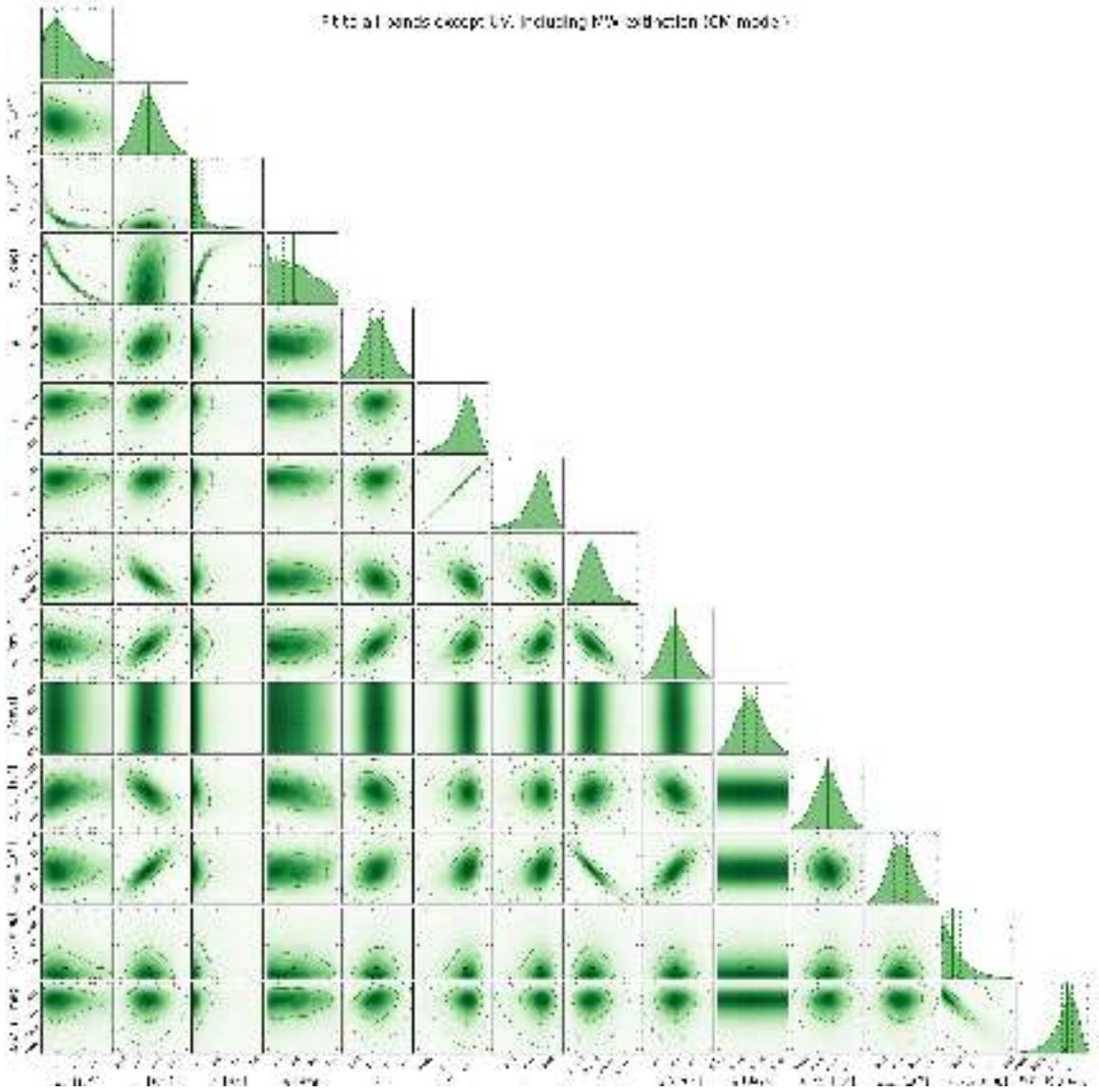

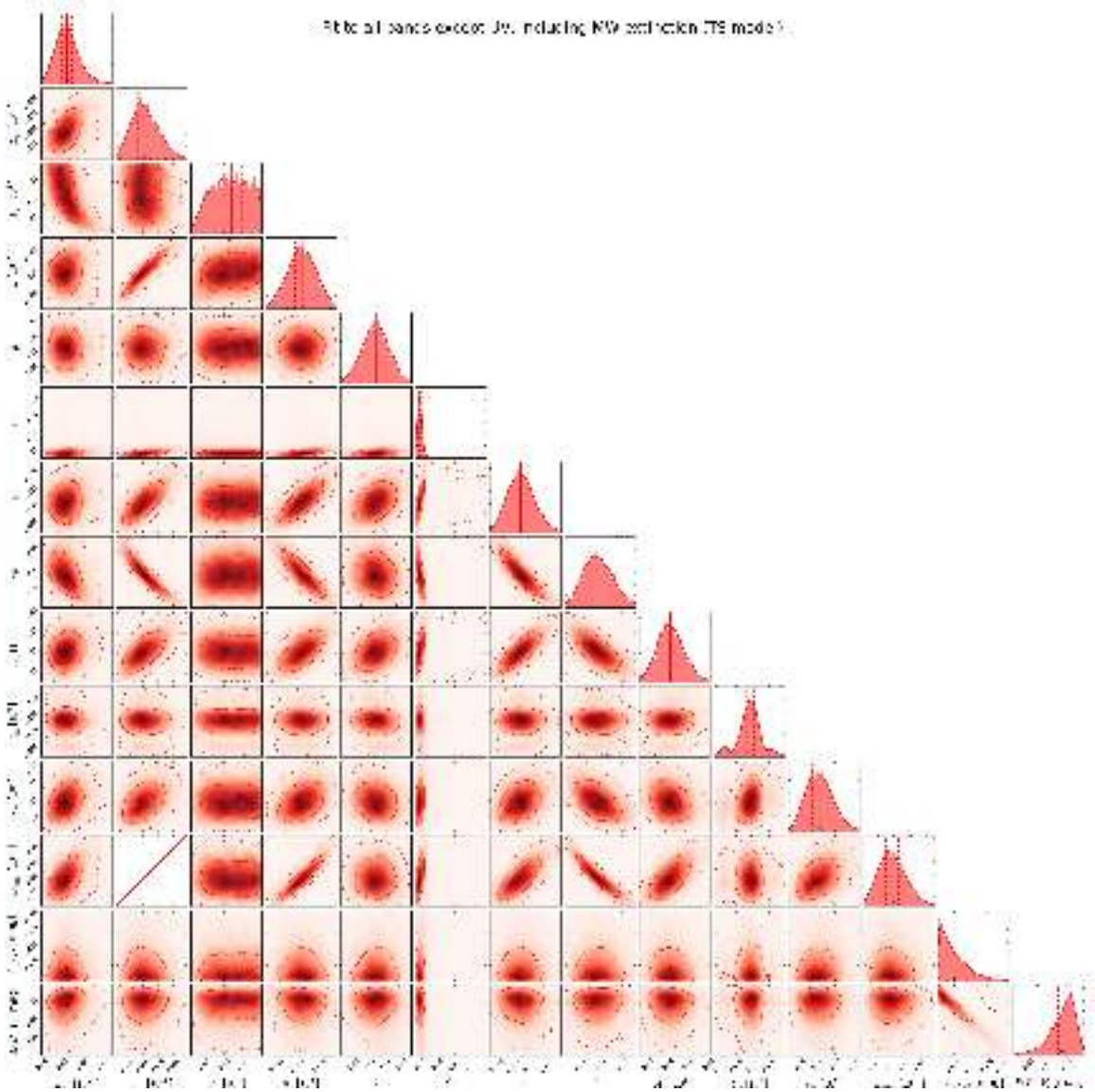

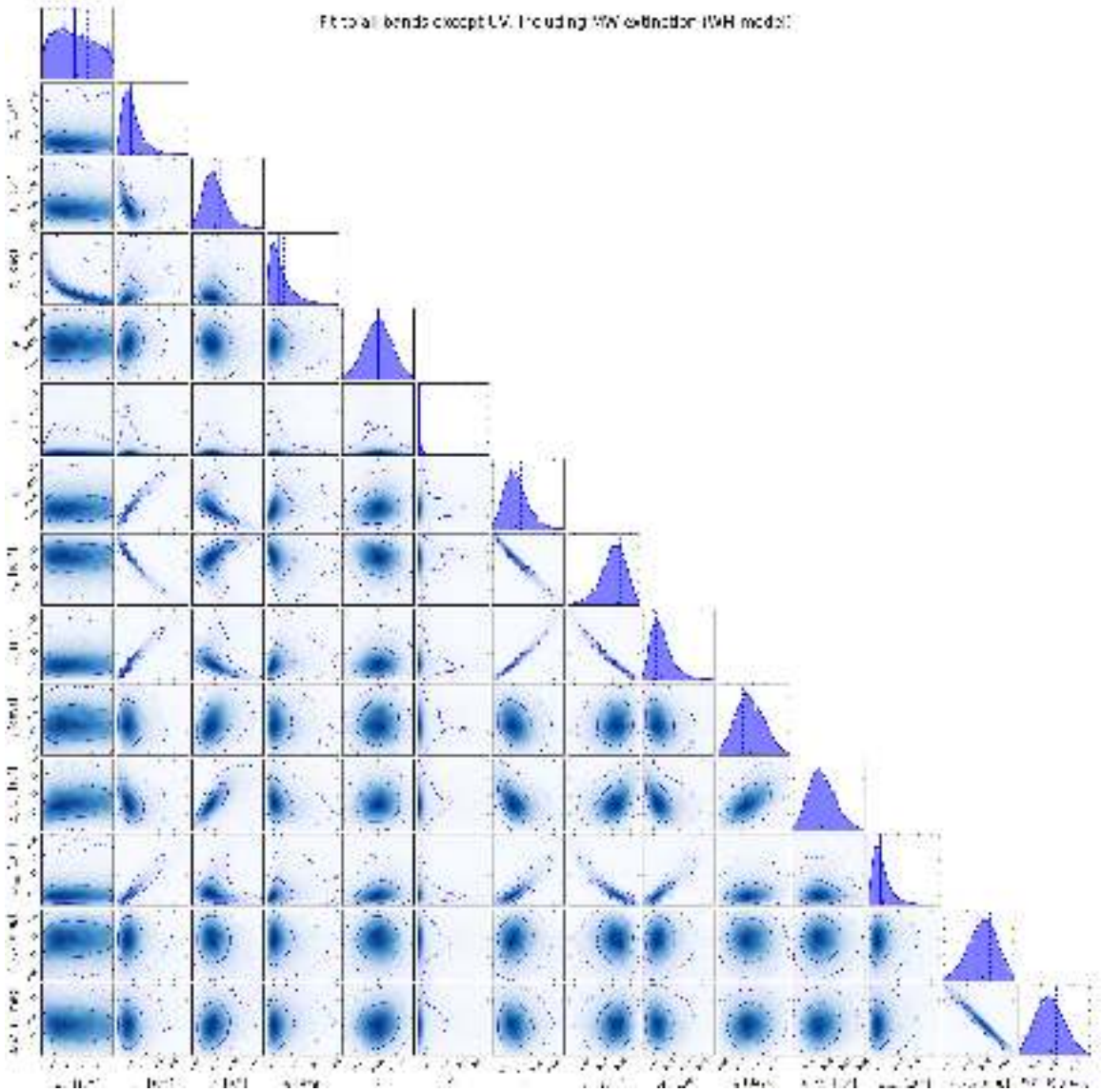

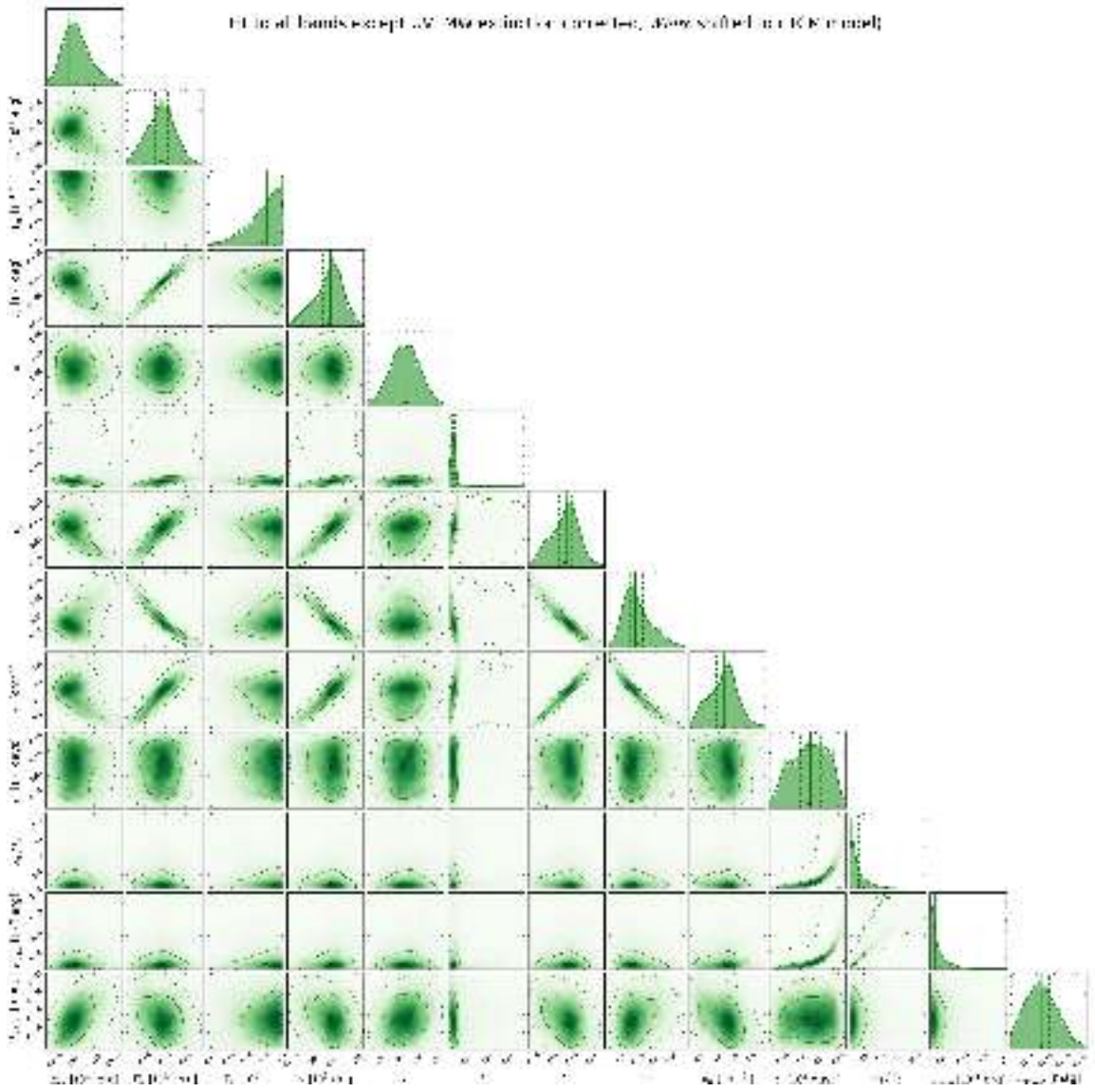

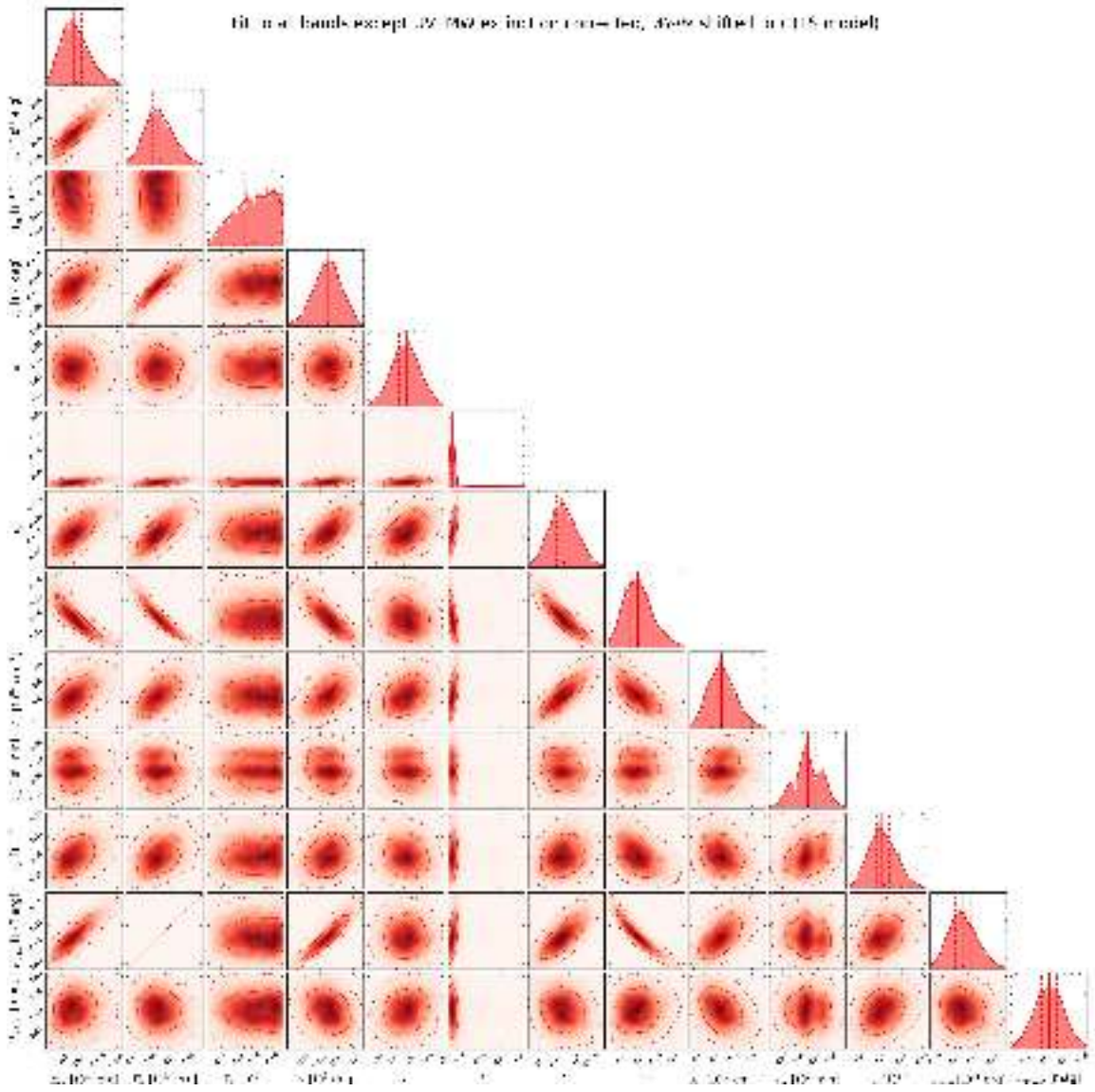

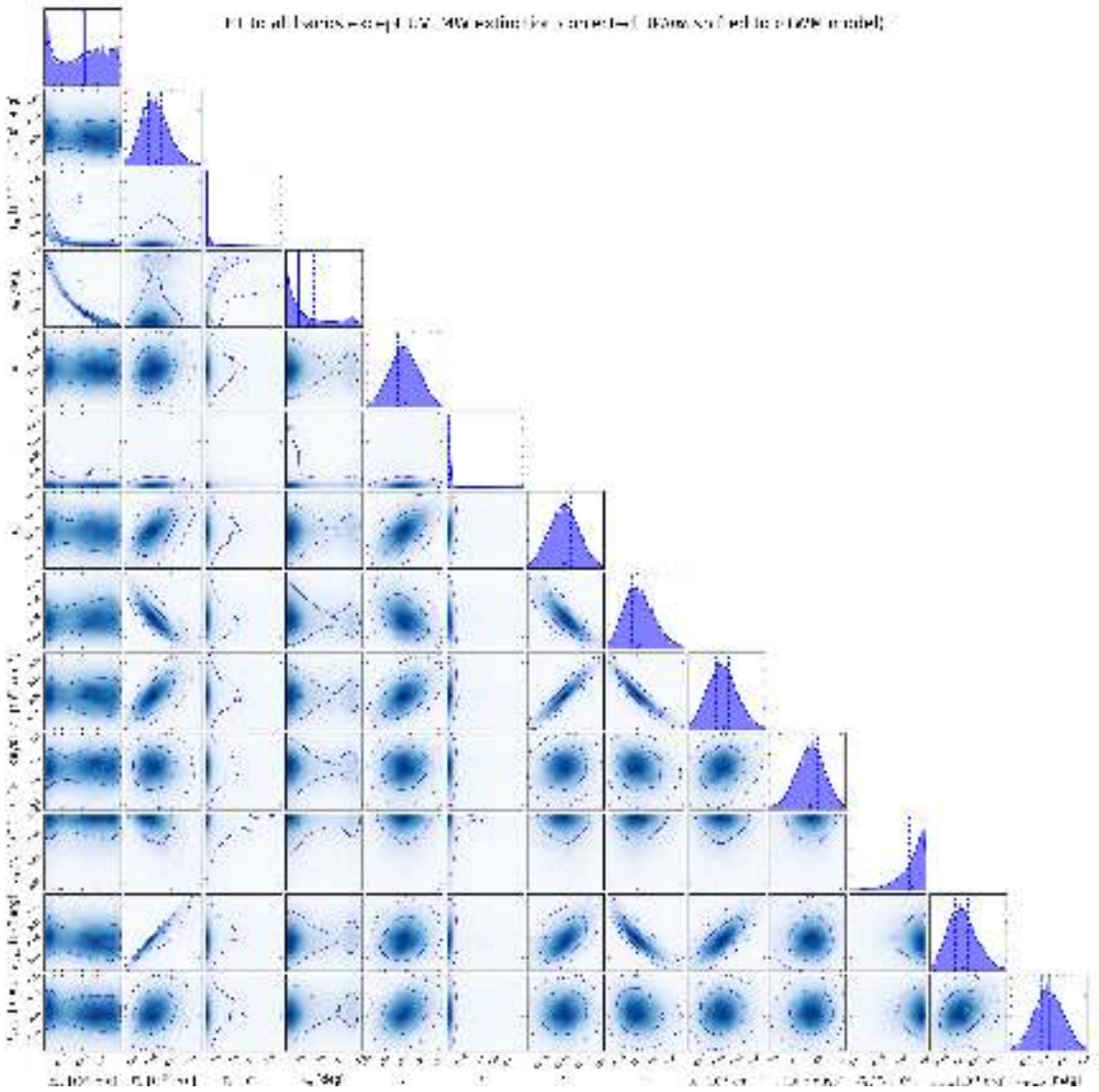

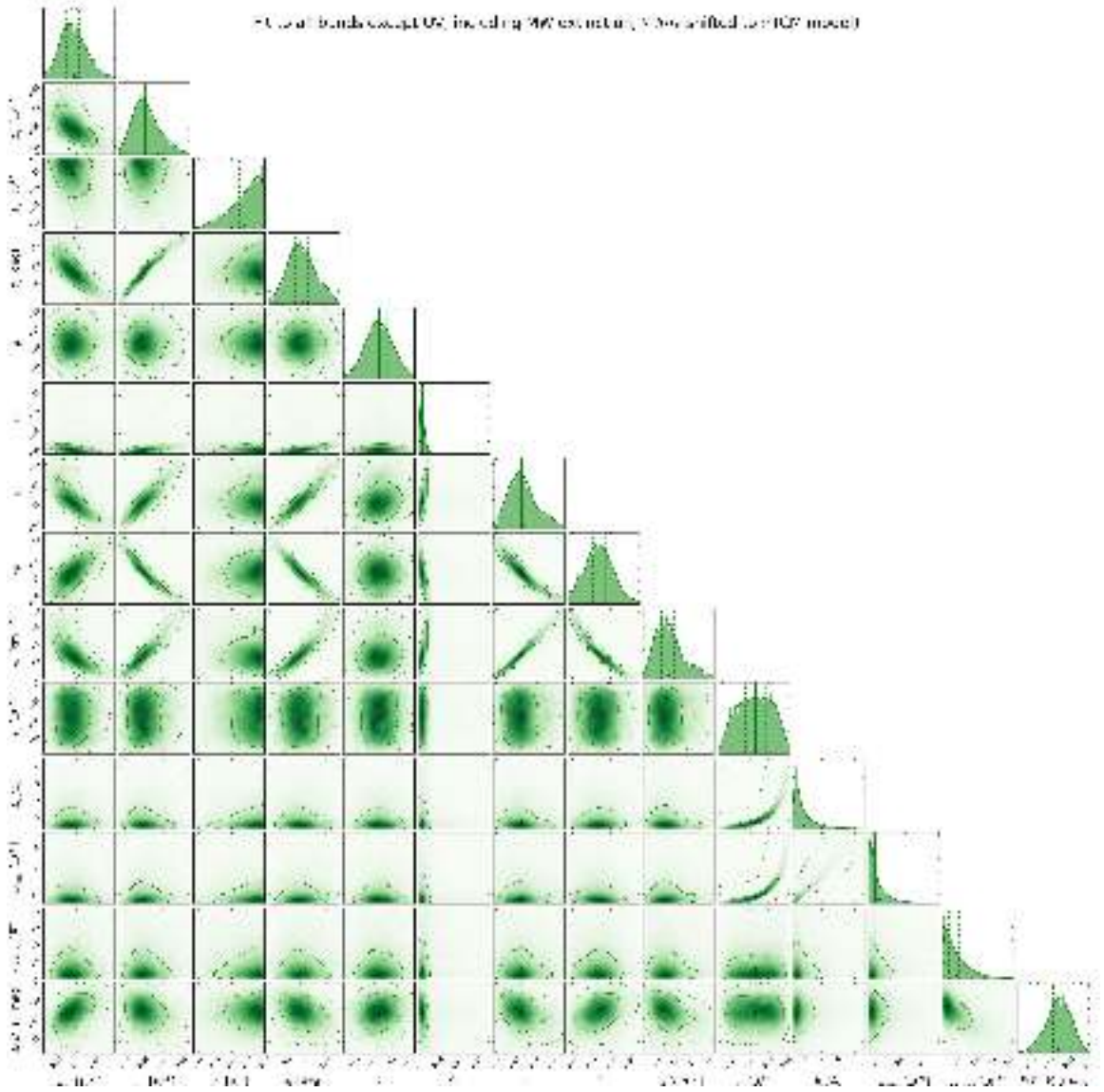

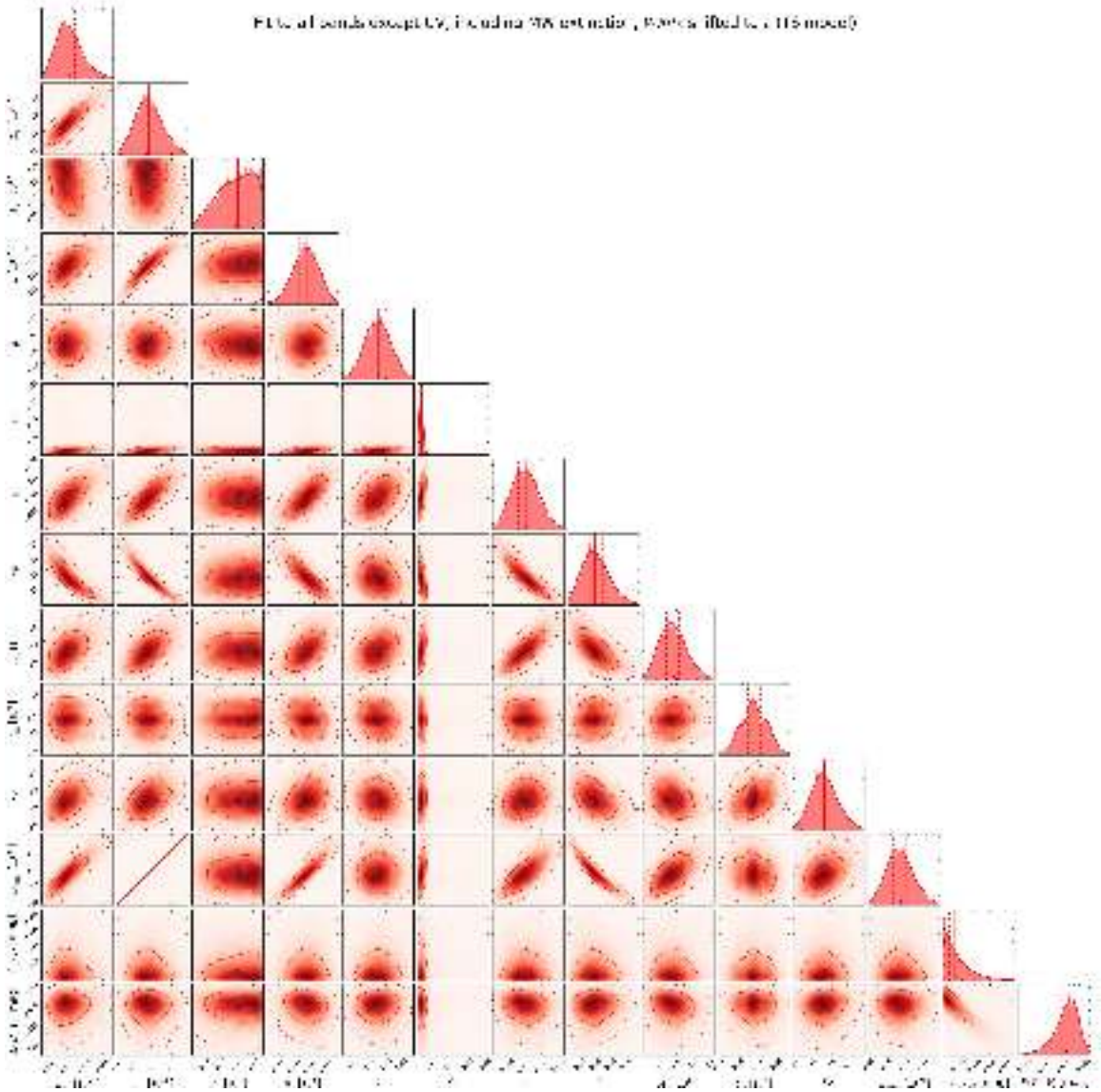

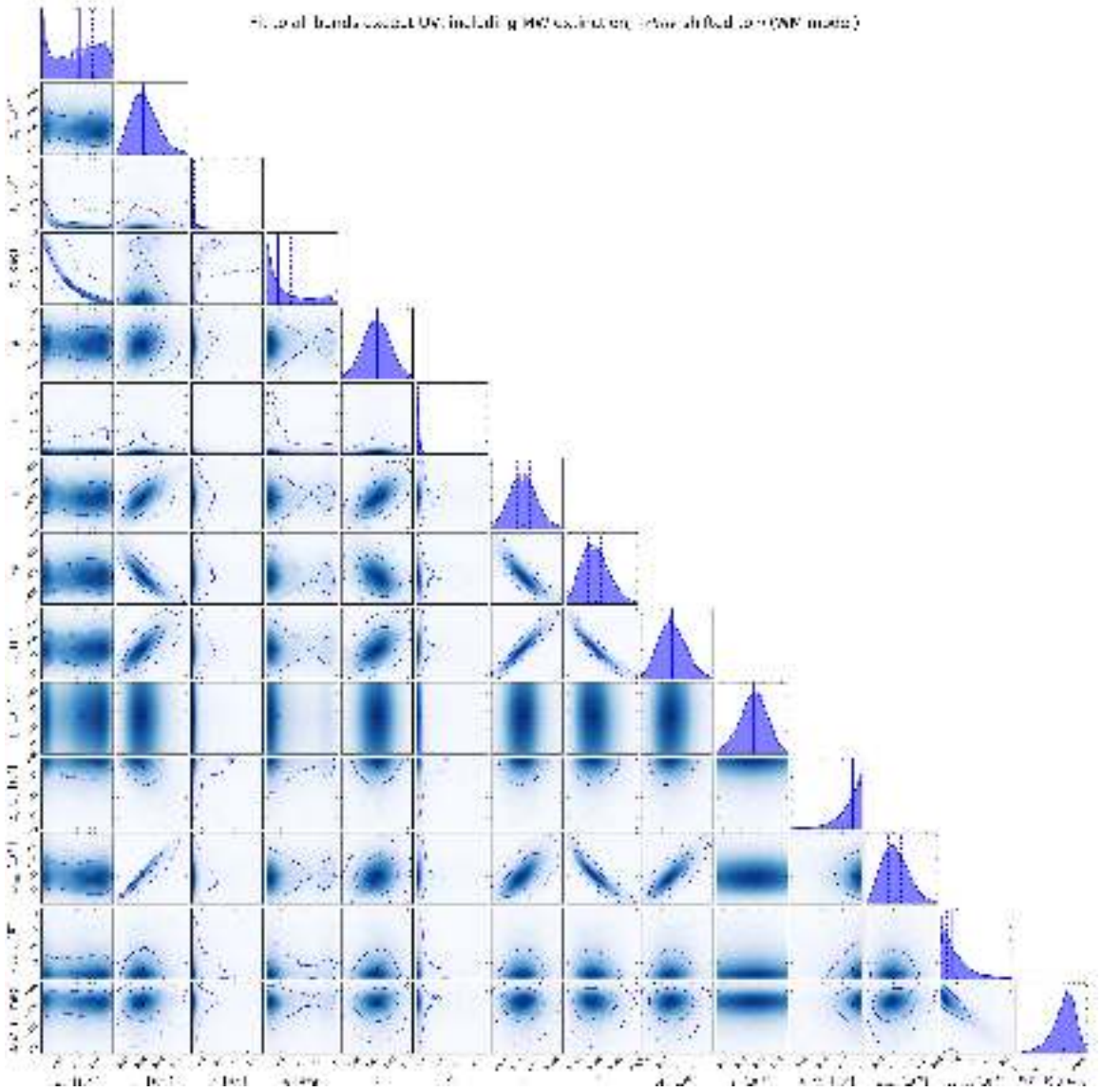

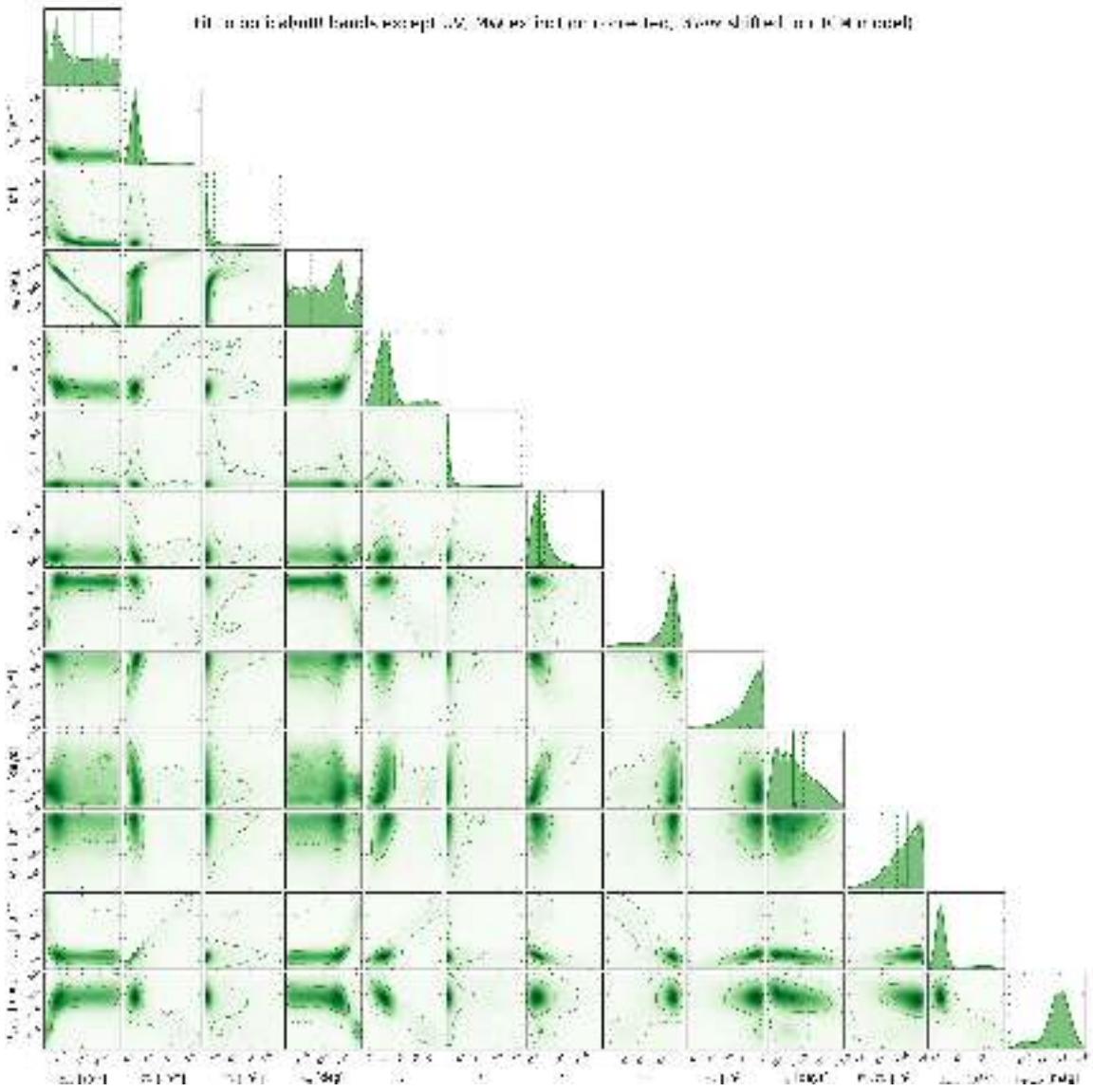

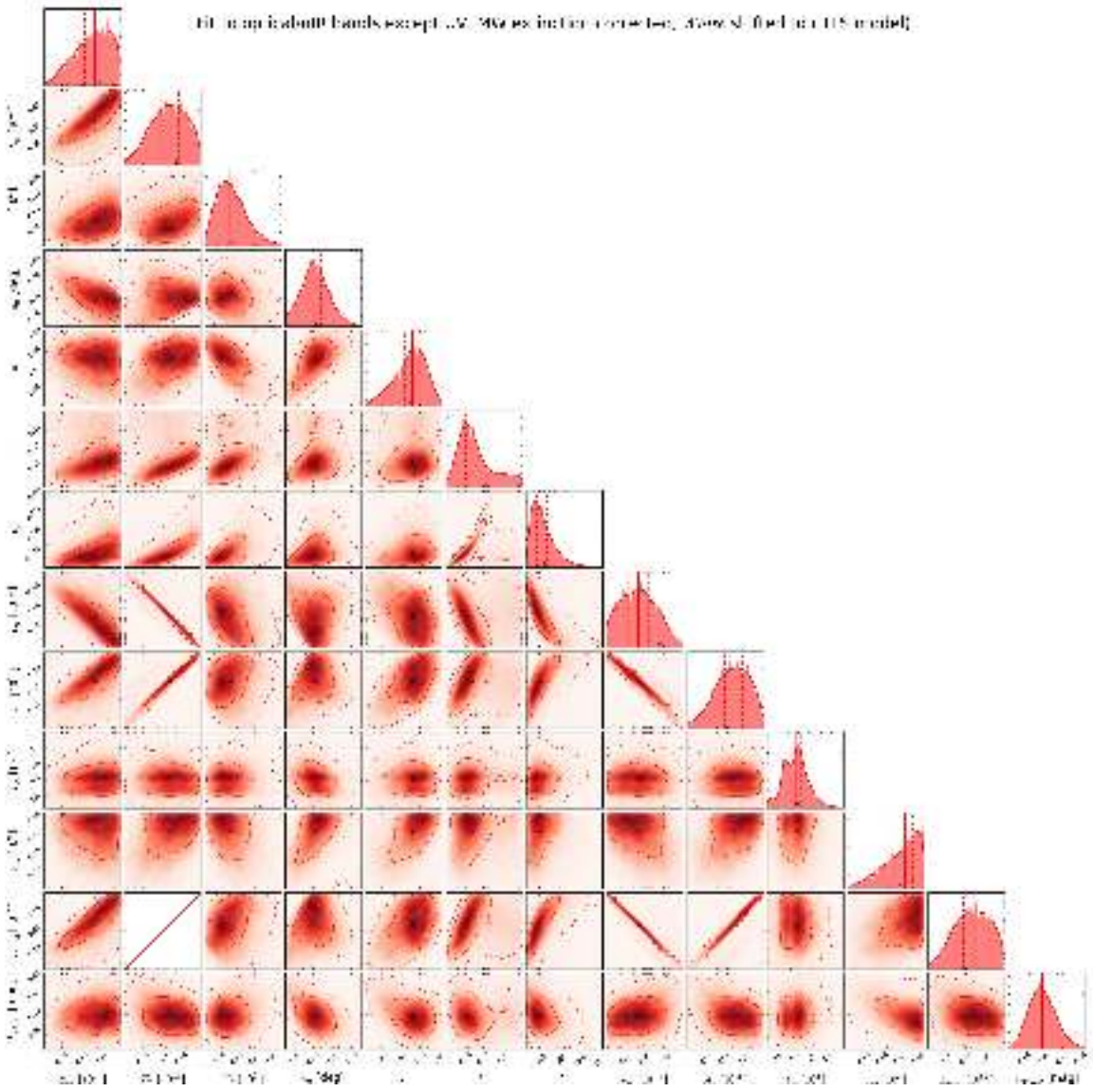

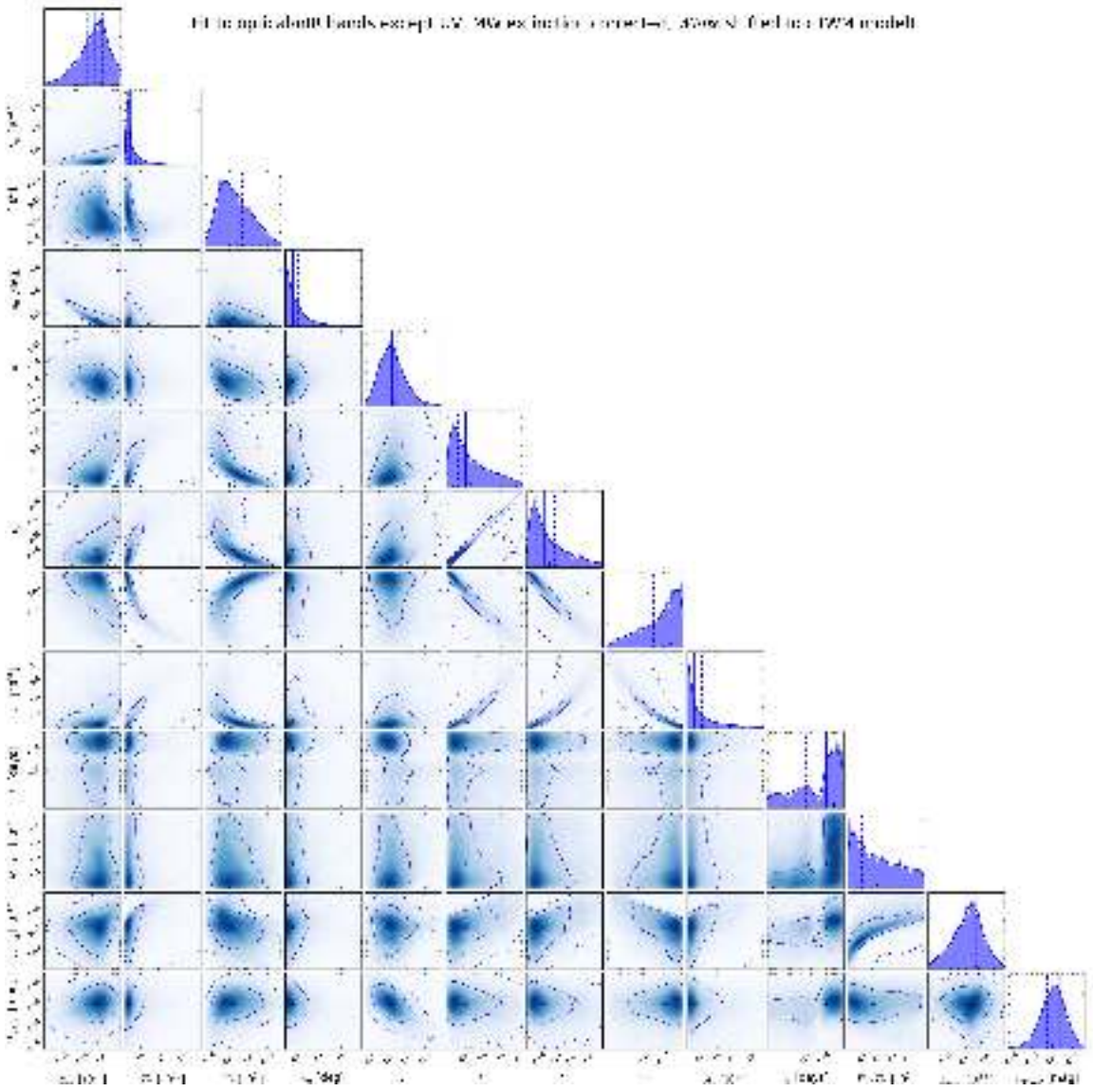

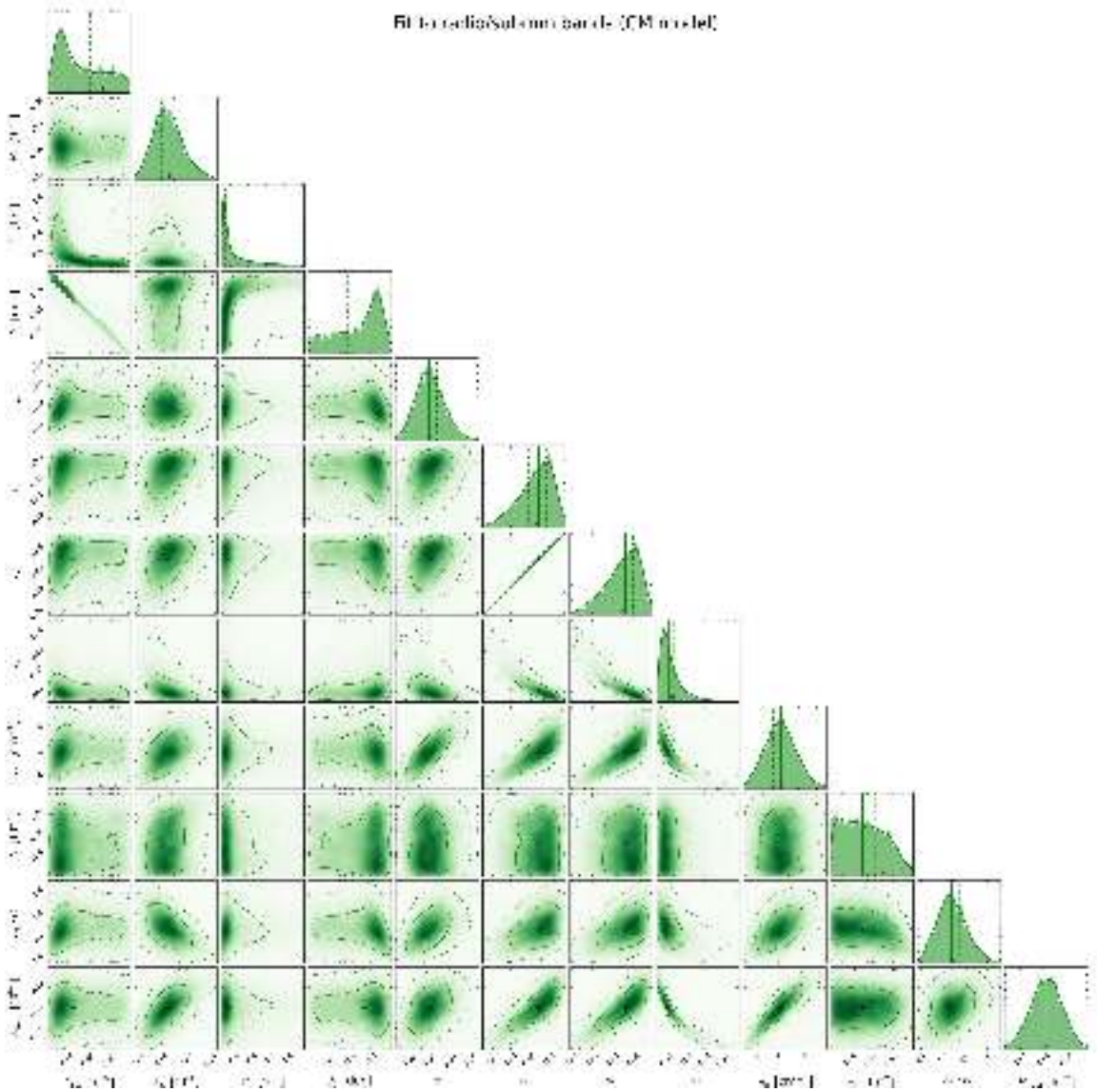

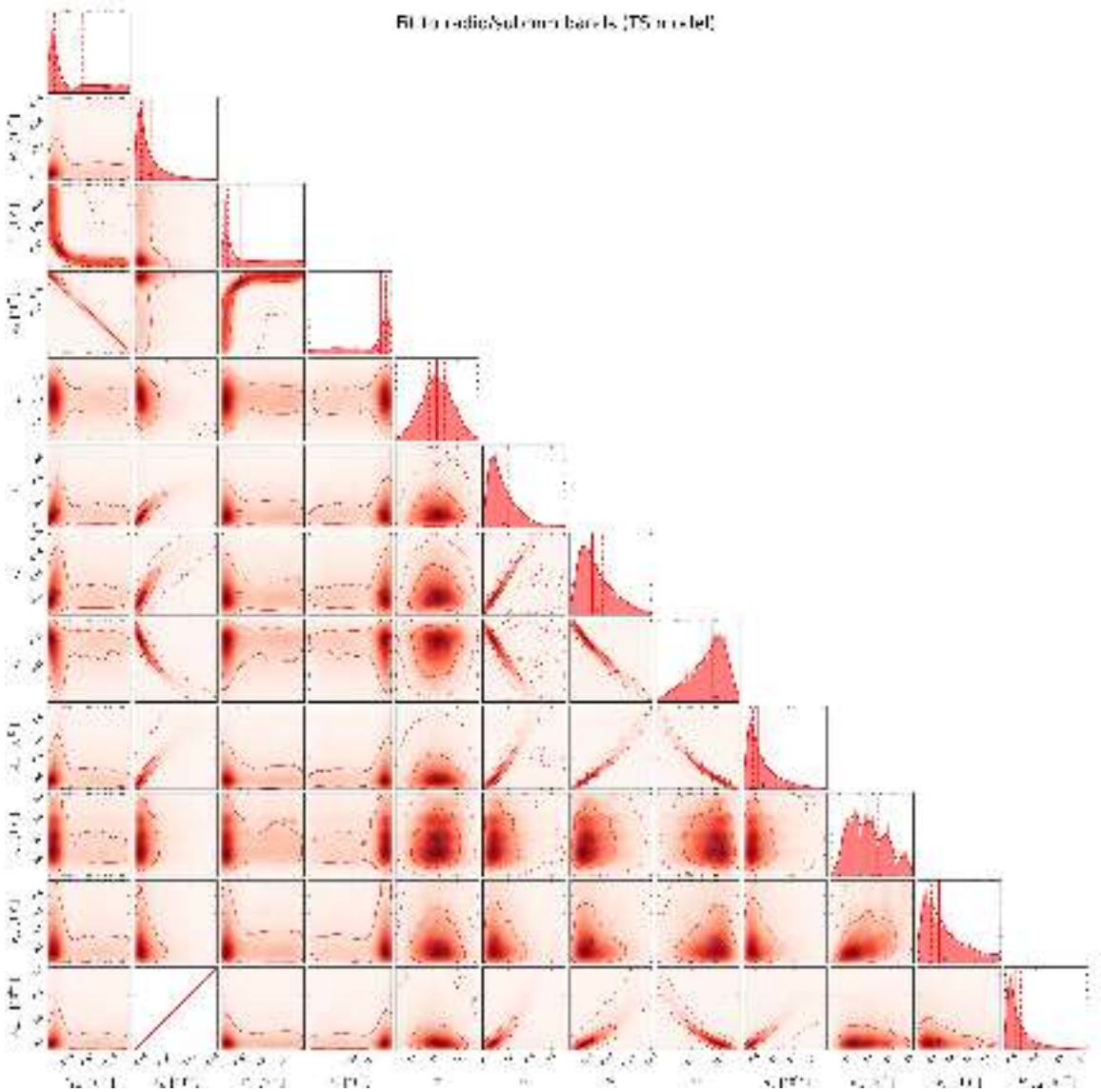

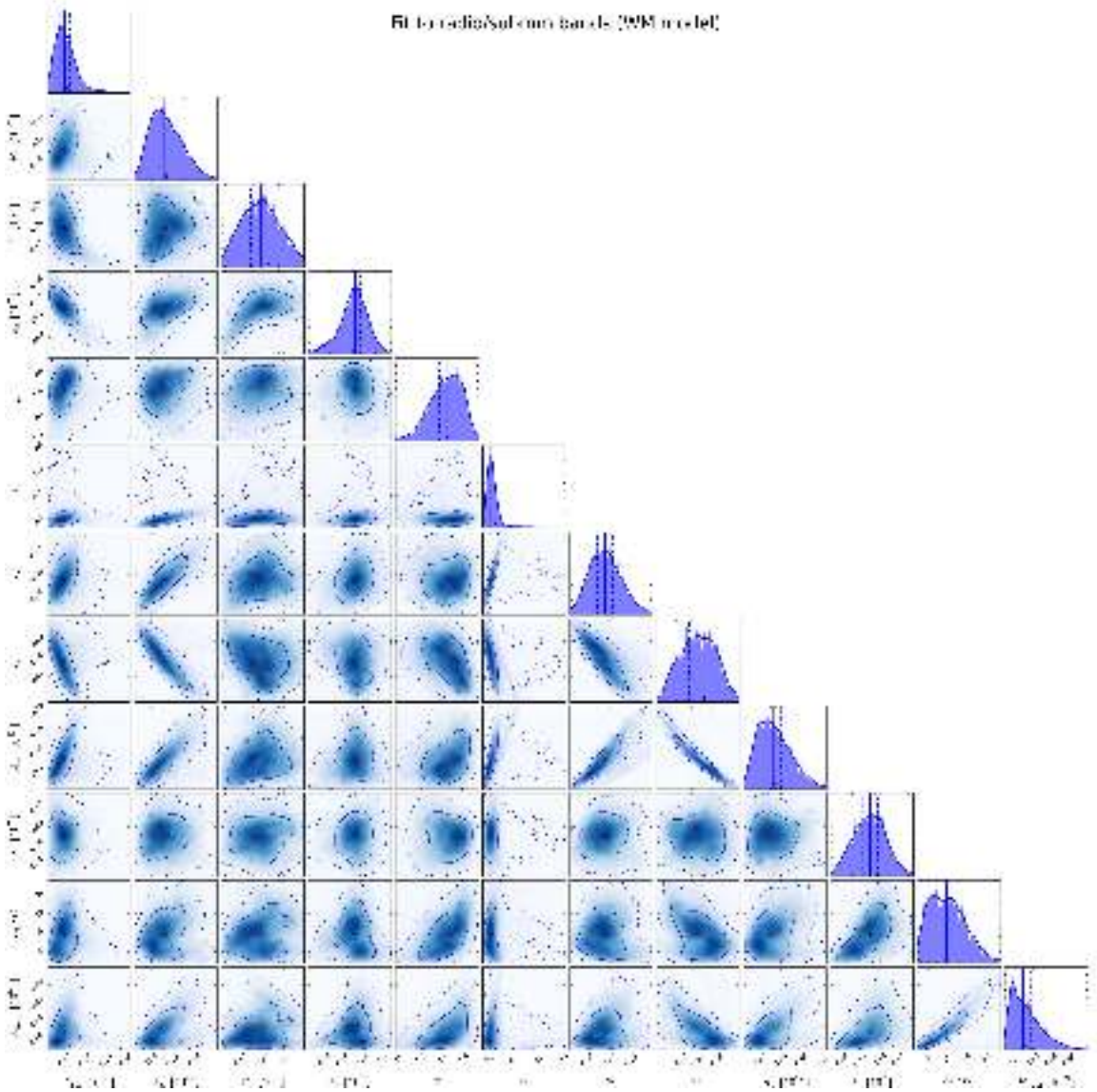

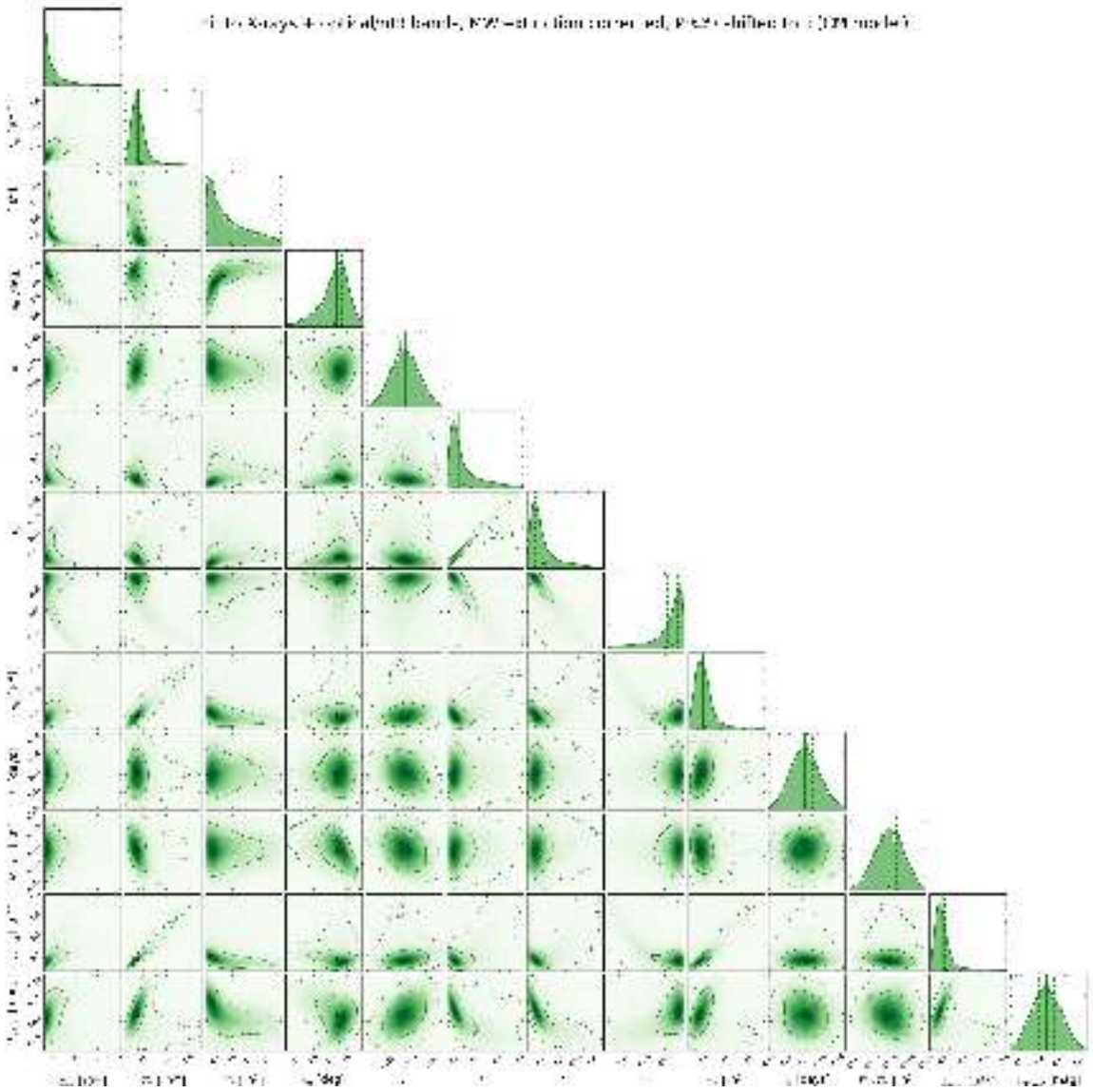

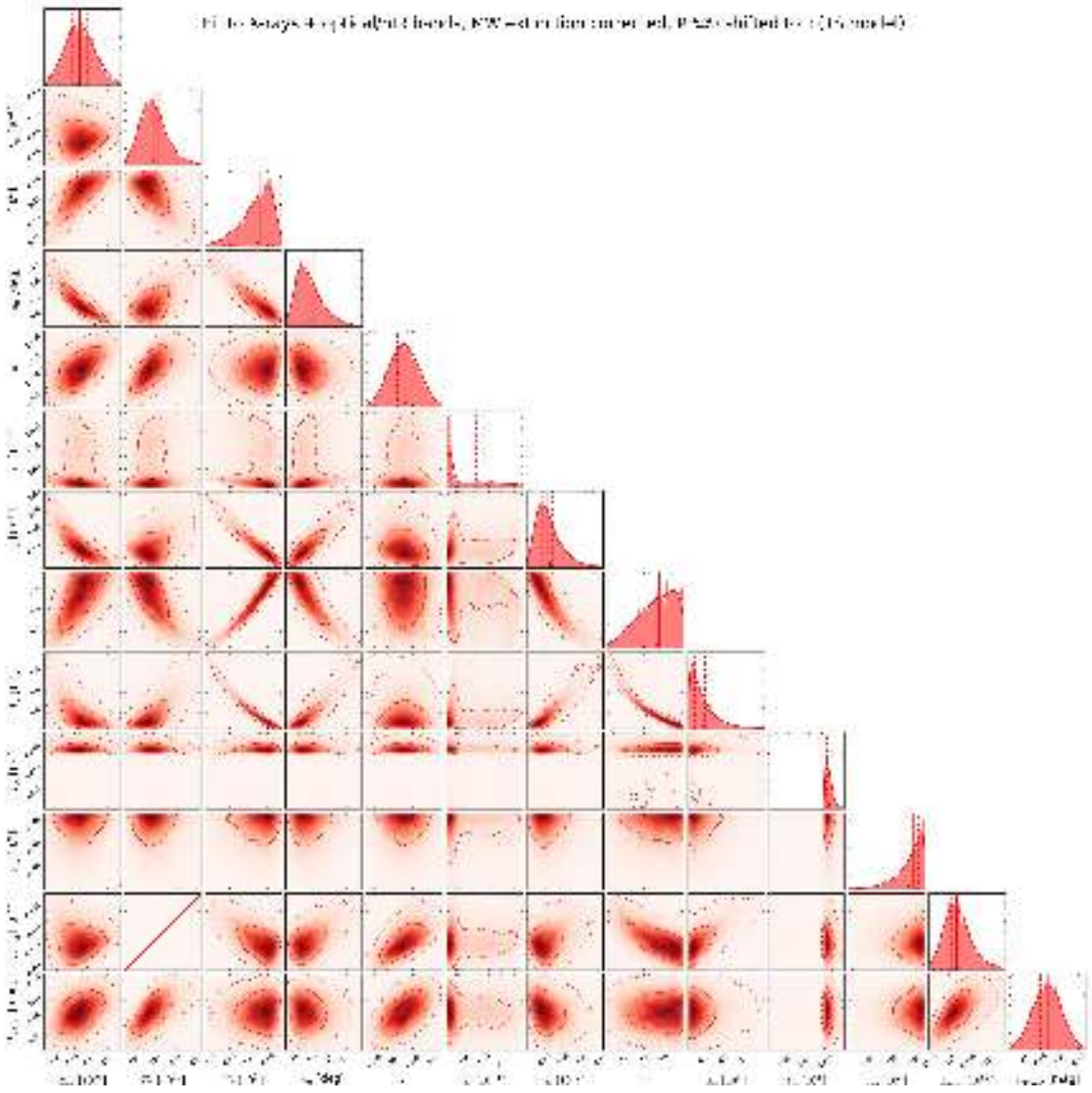

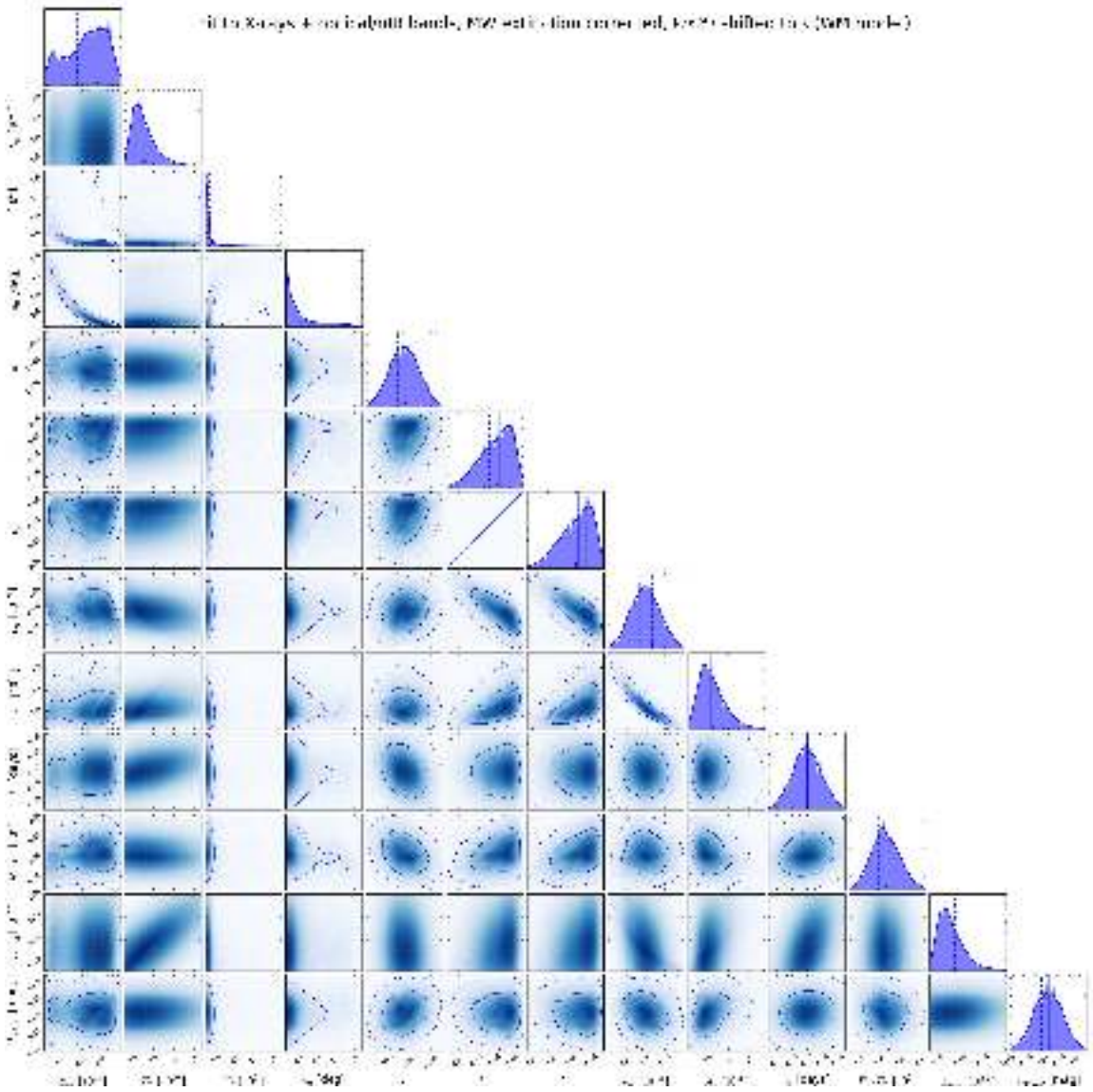

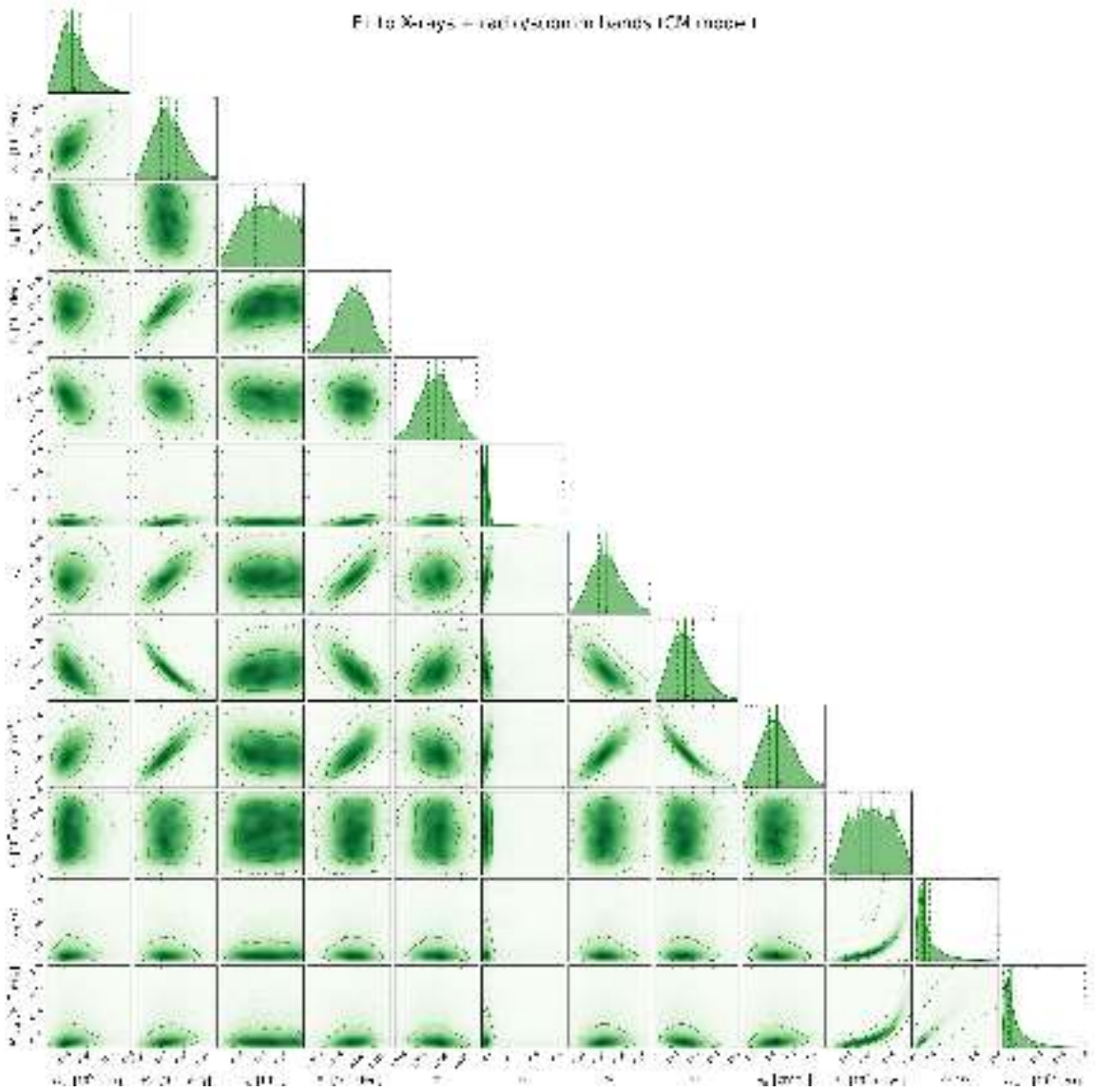

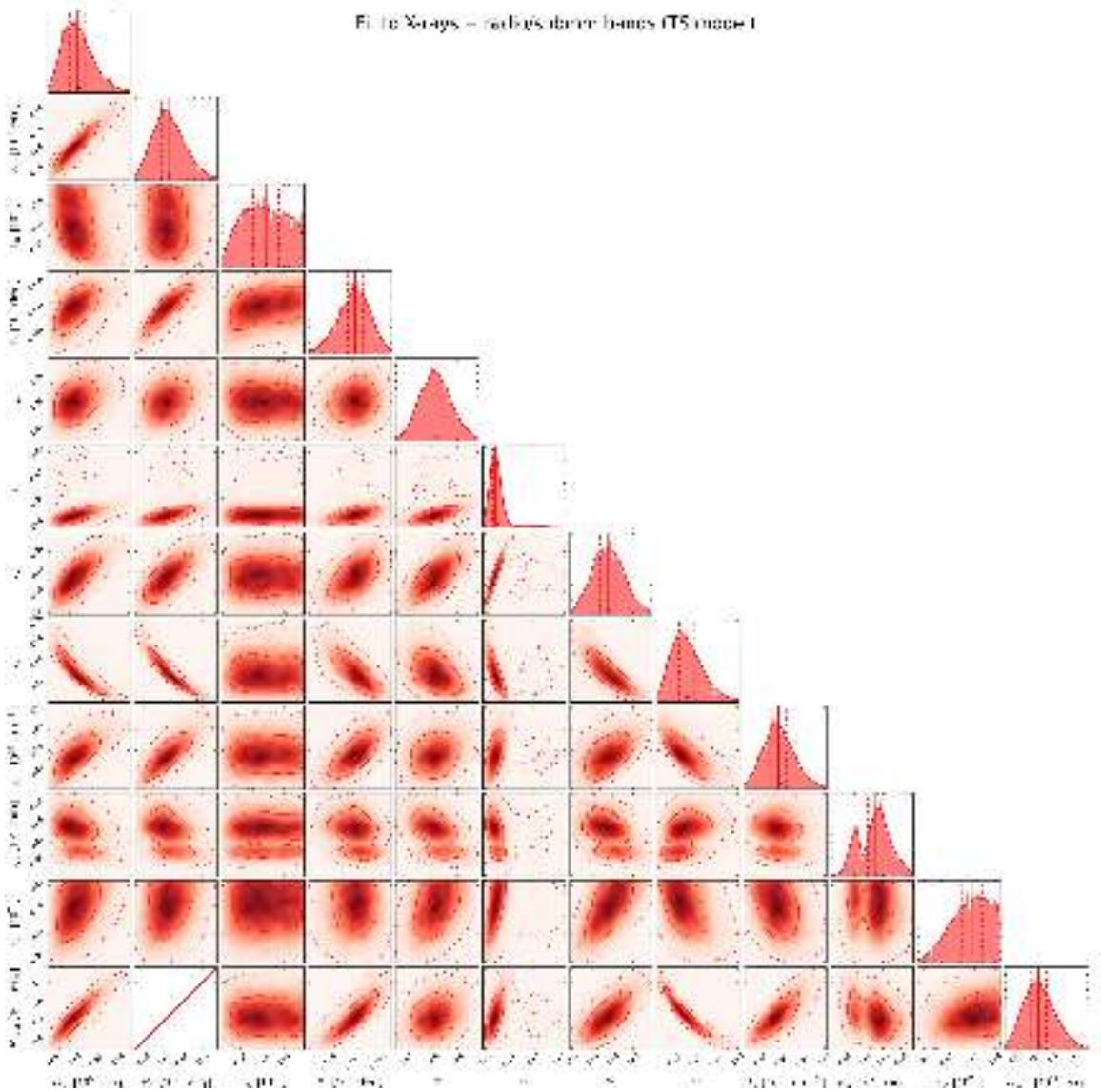

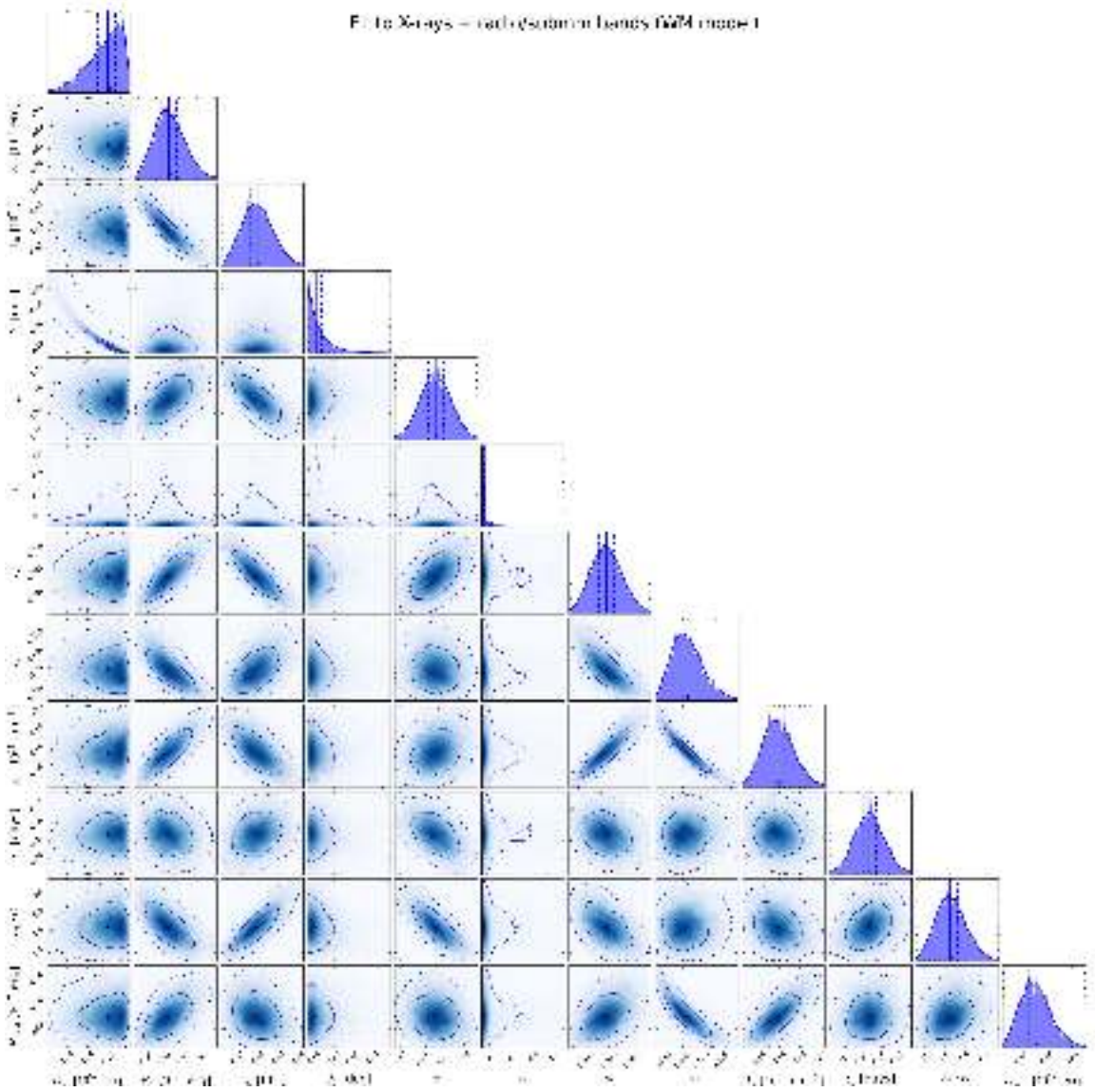

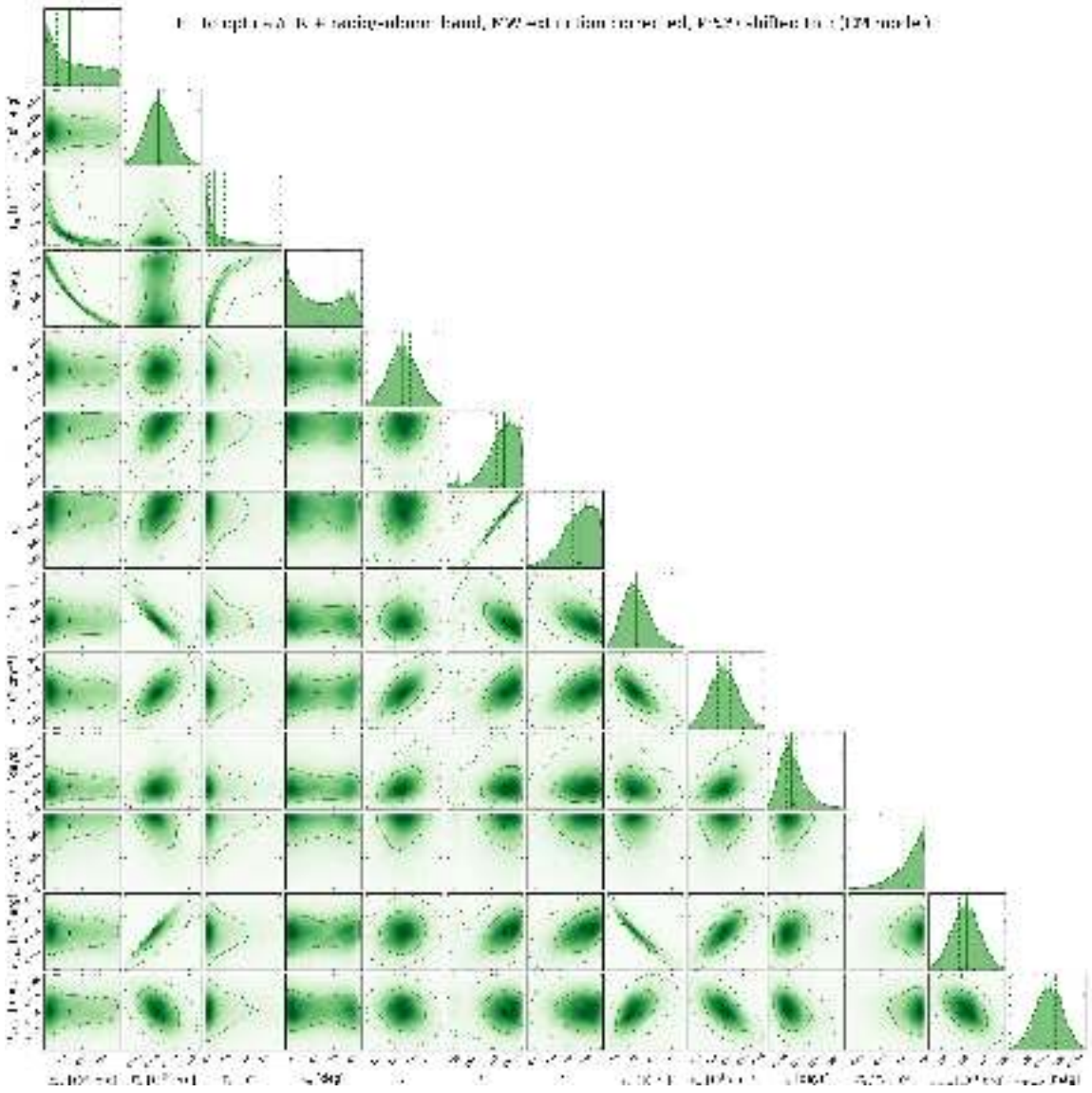

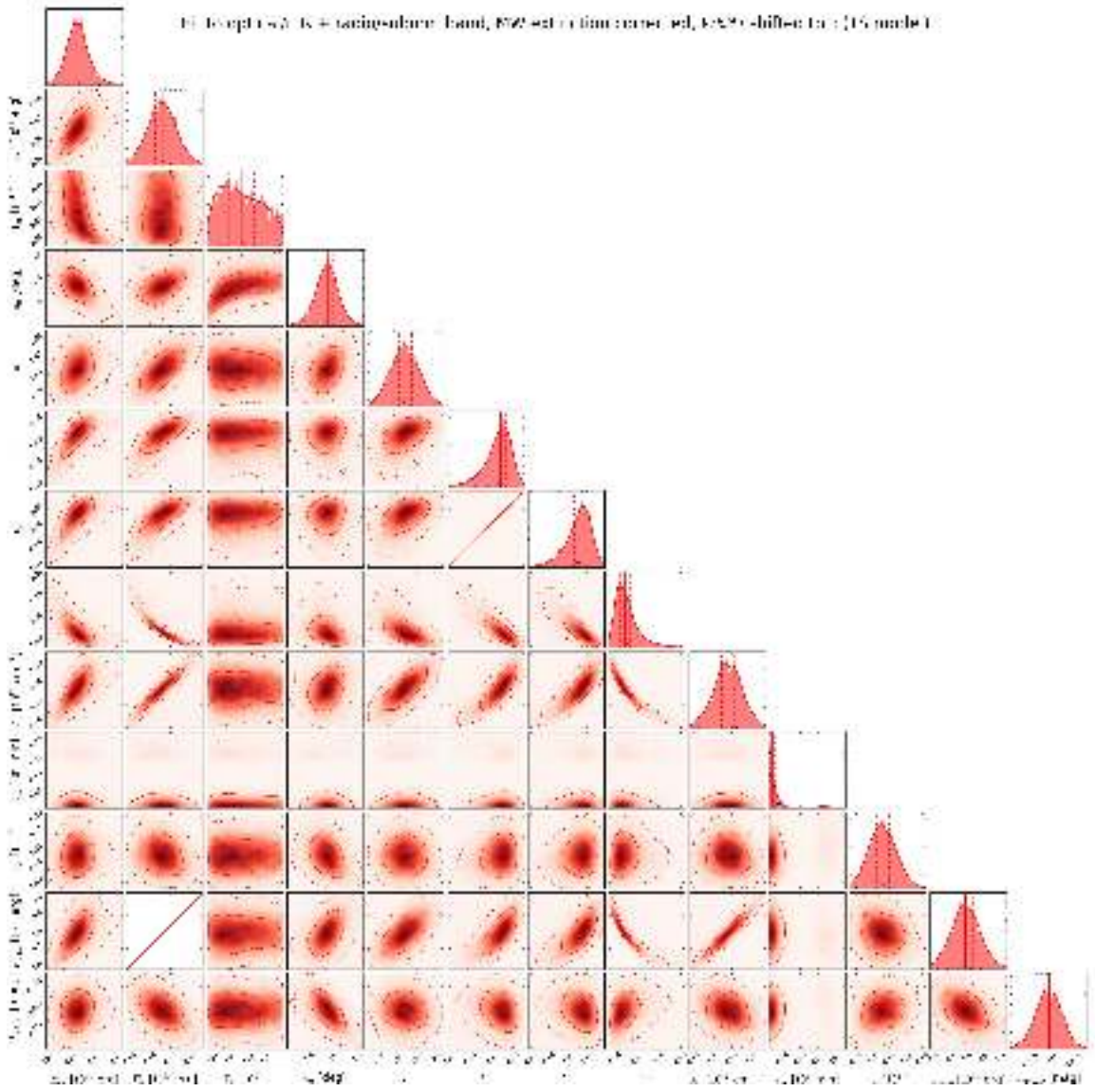

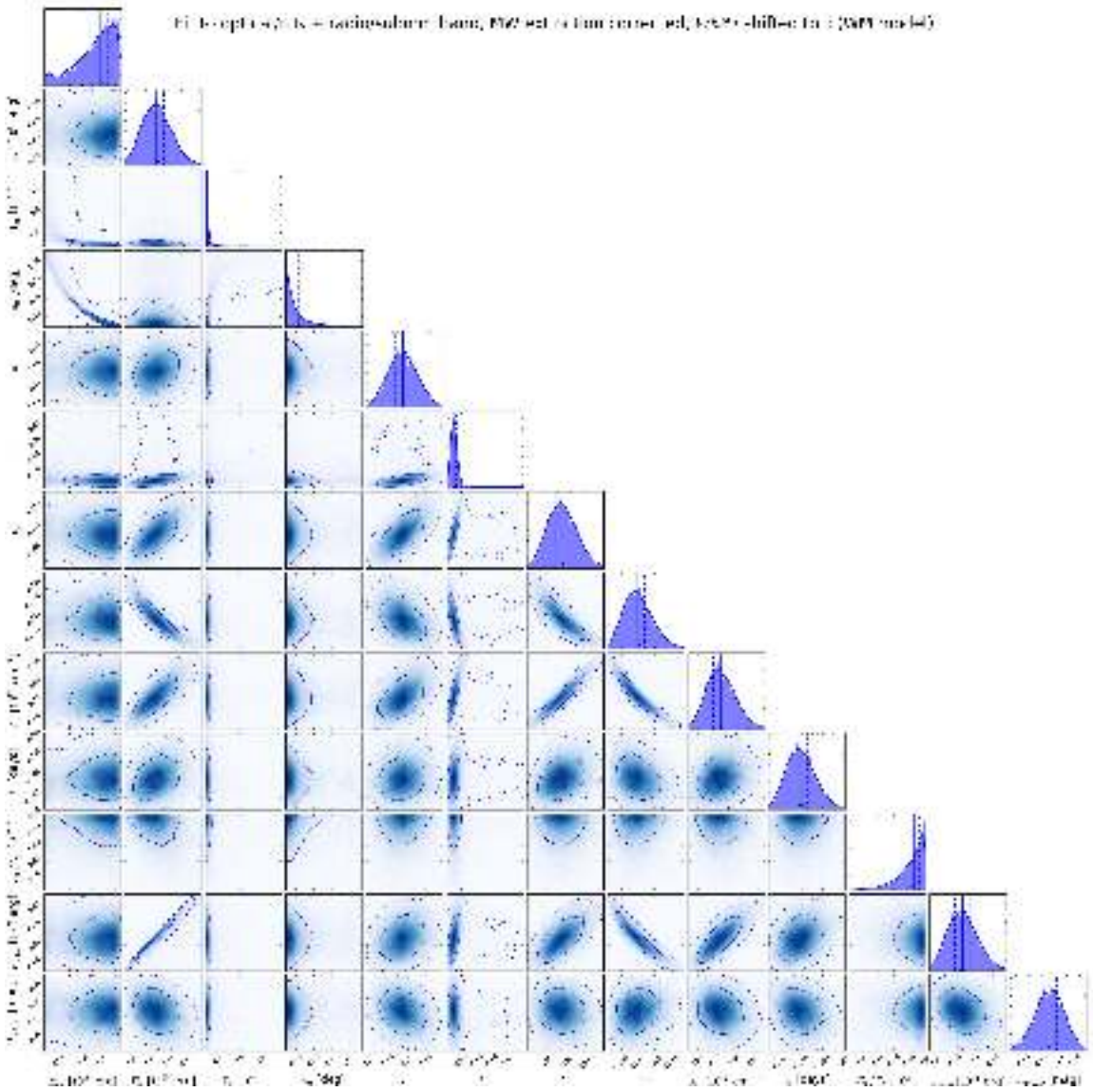

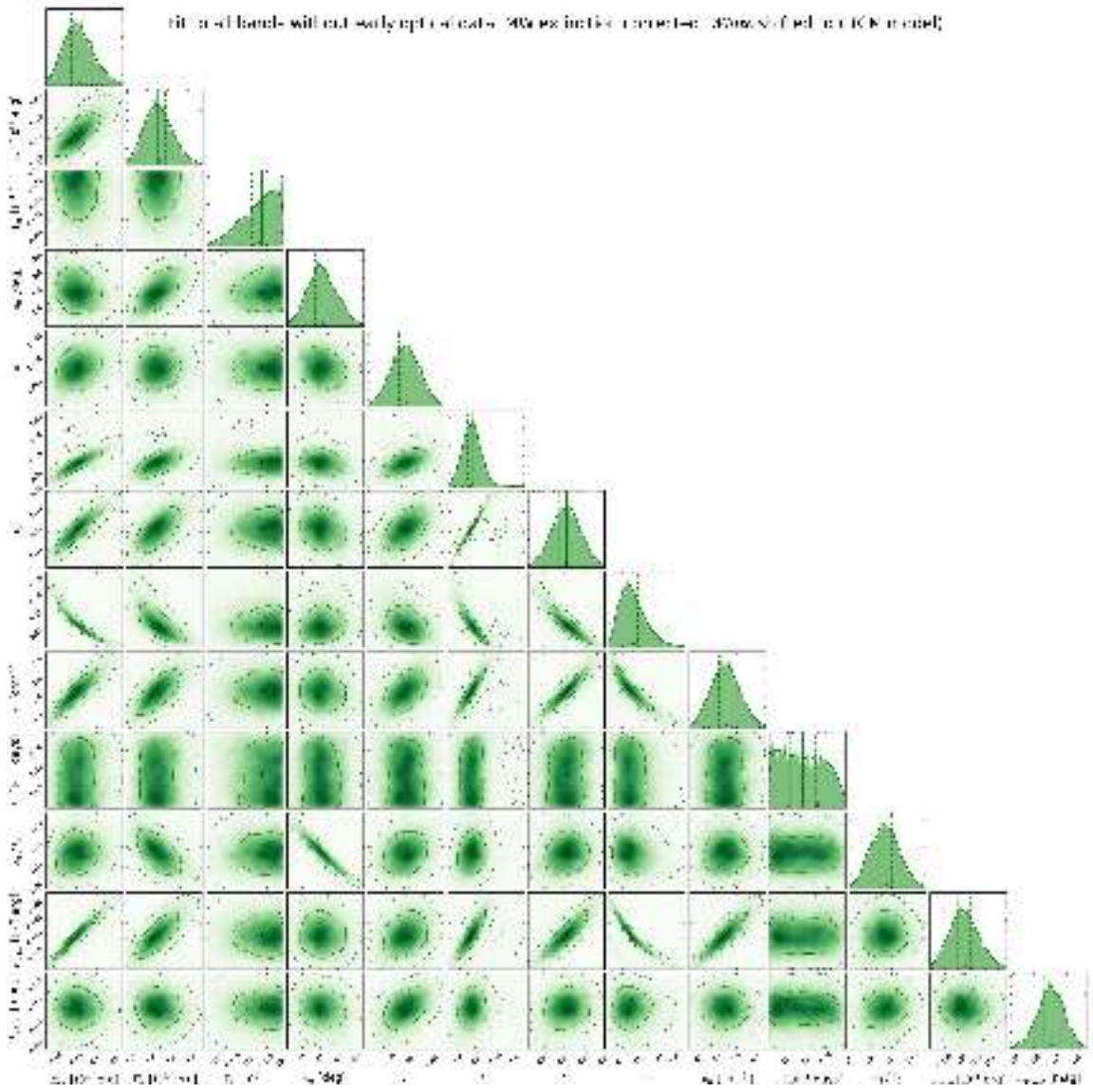

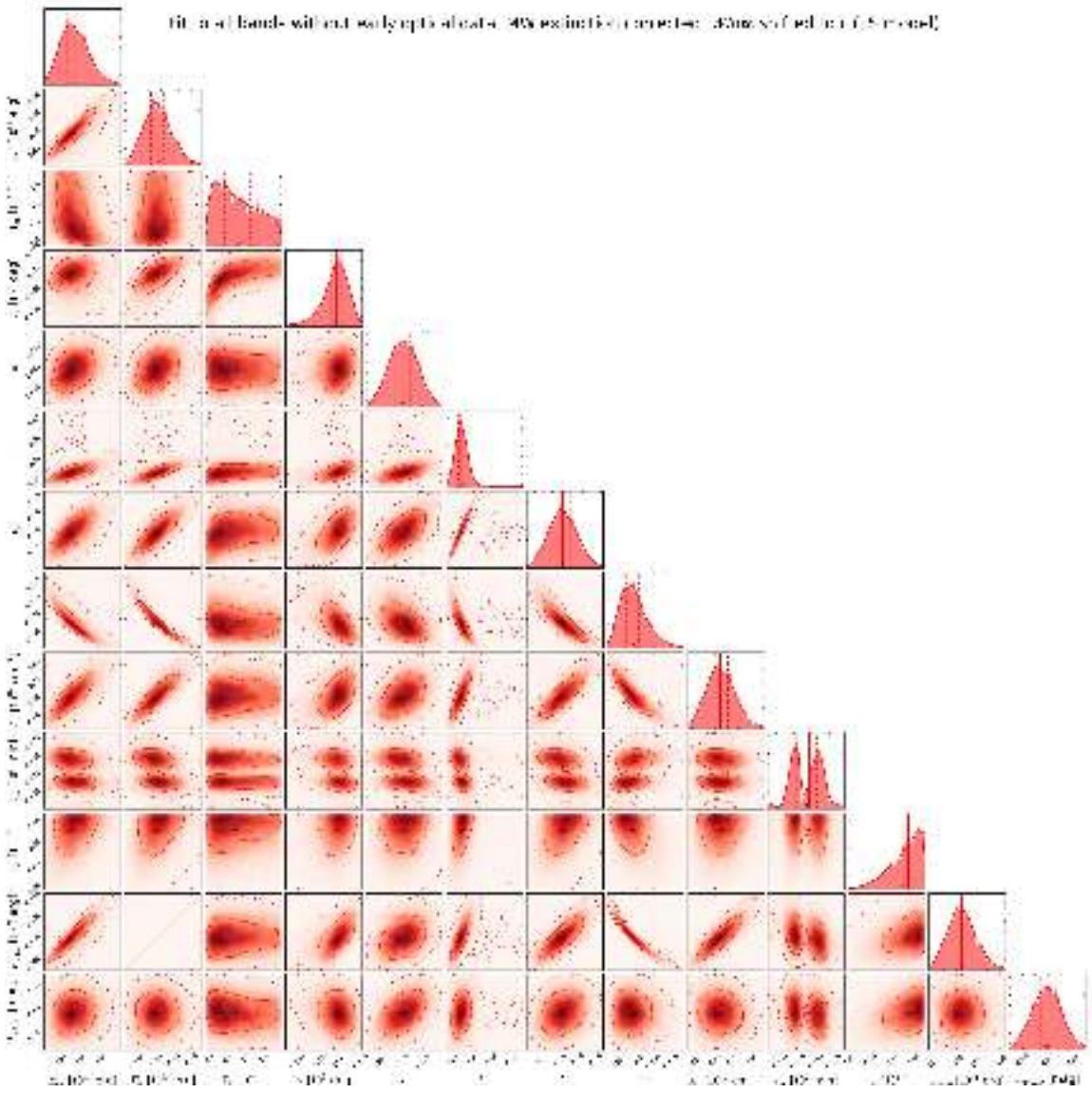

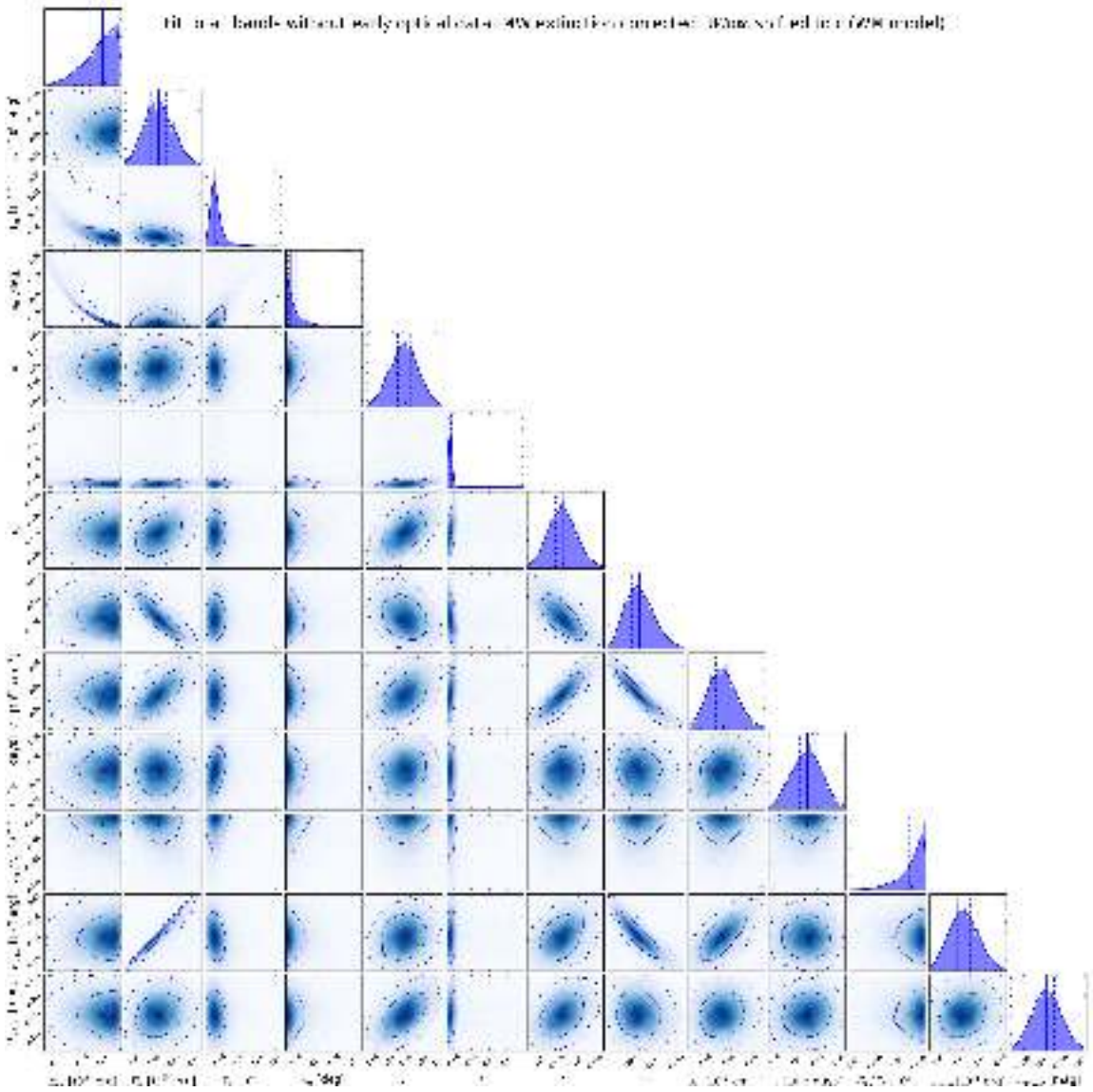

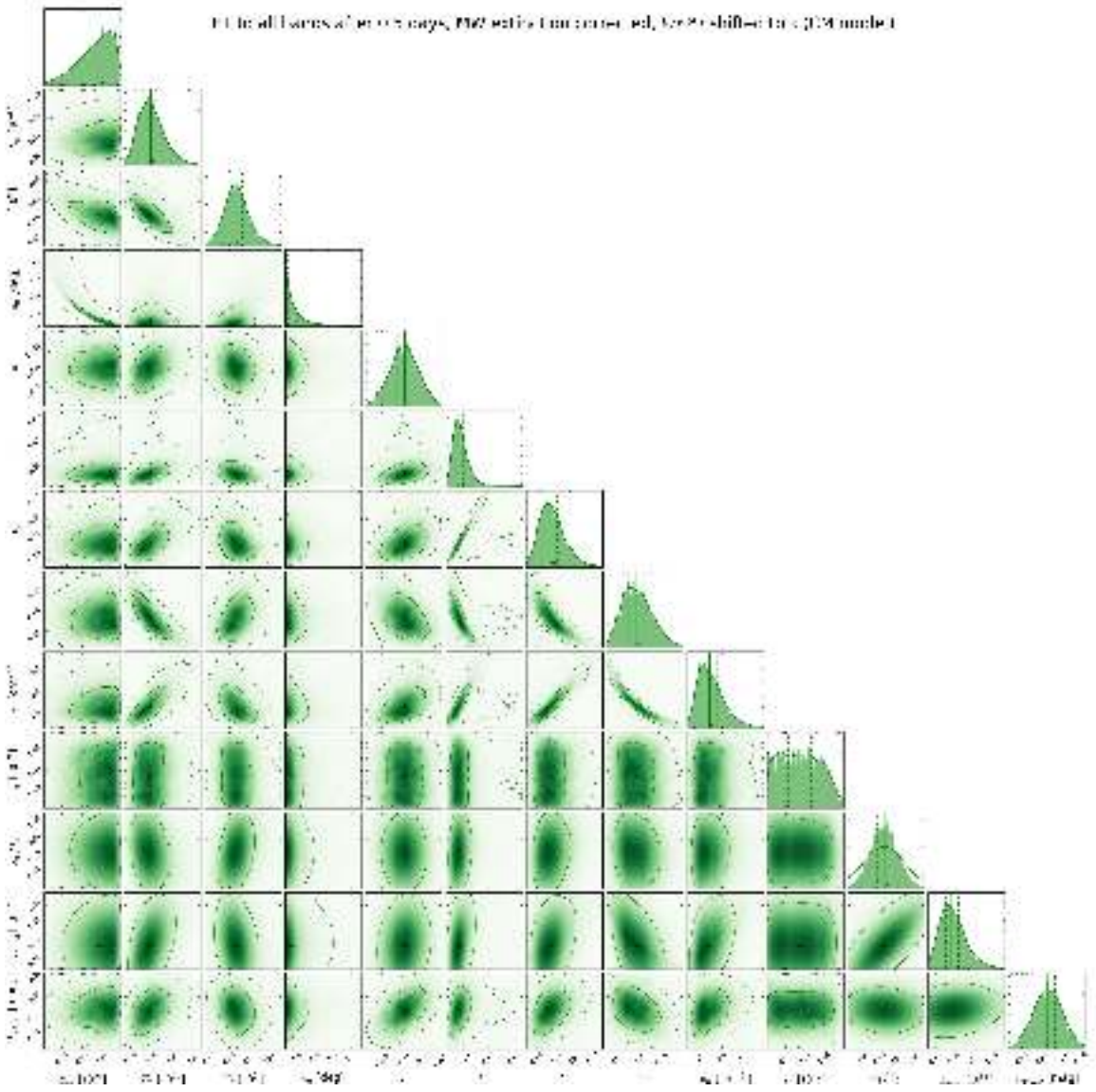

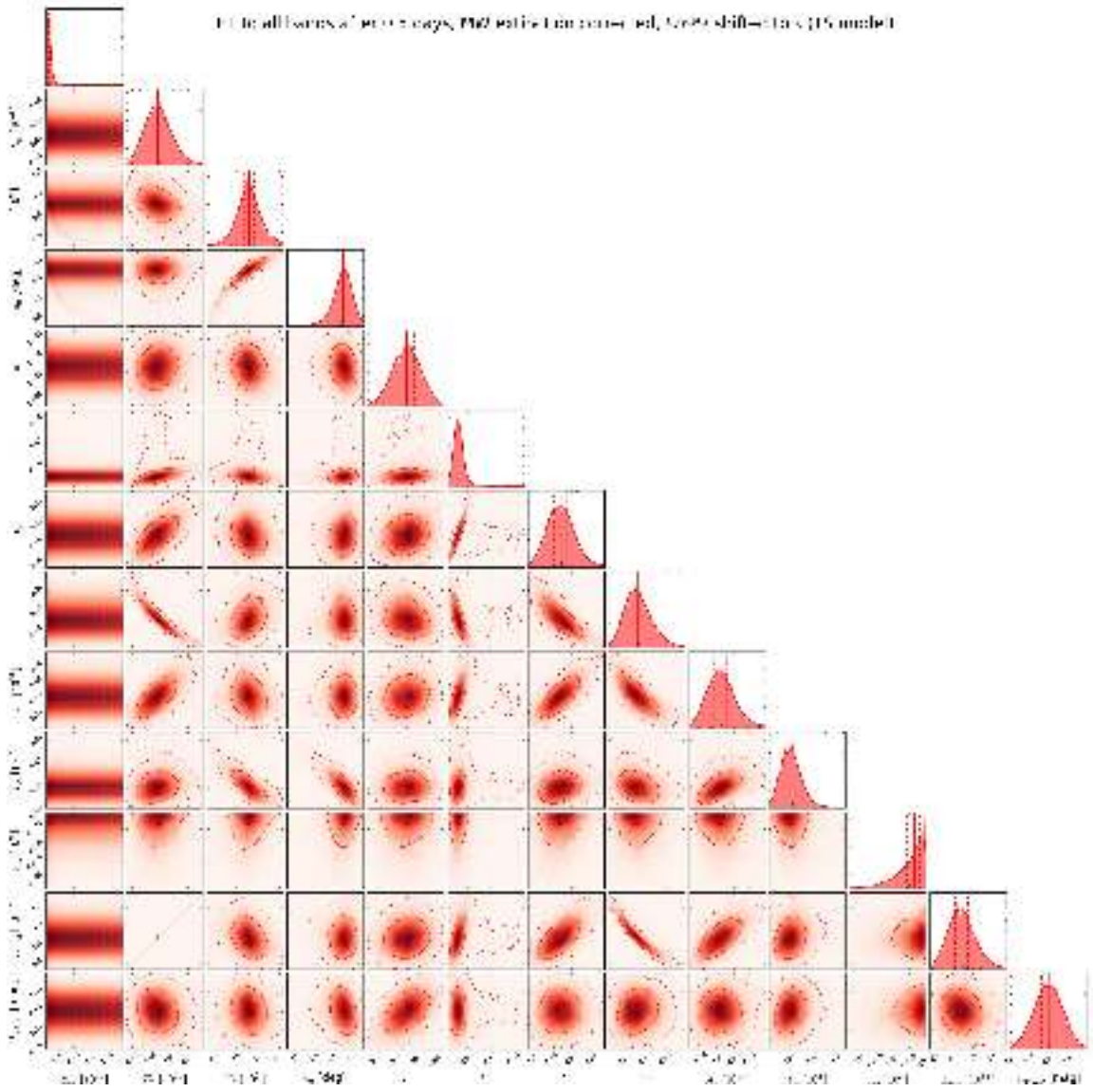

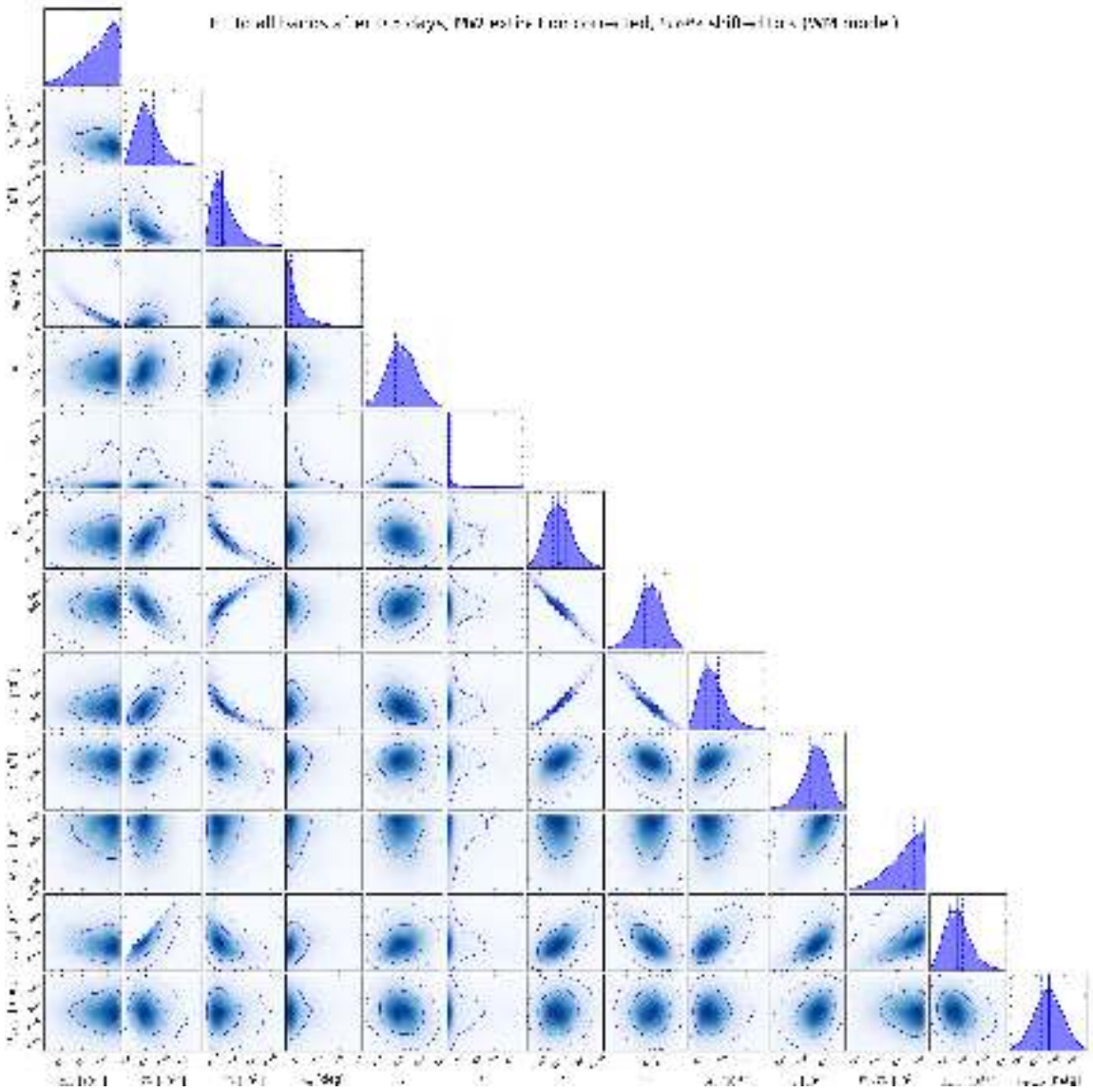

Appendix G

QSO Lyα forest models for $\log N(\mathrm{H\,I}) \geq 19.5$

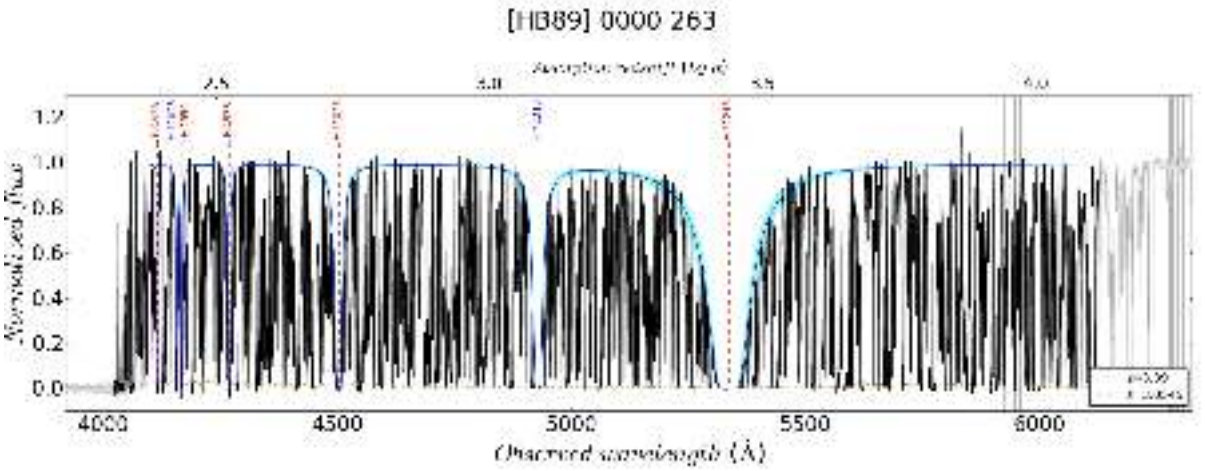

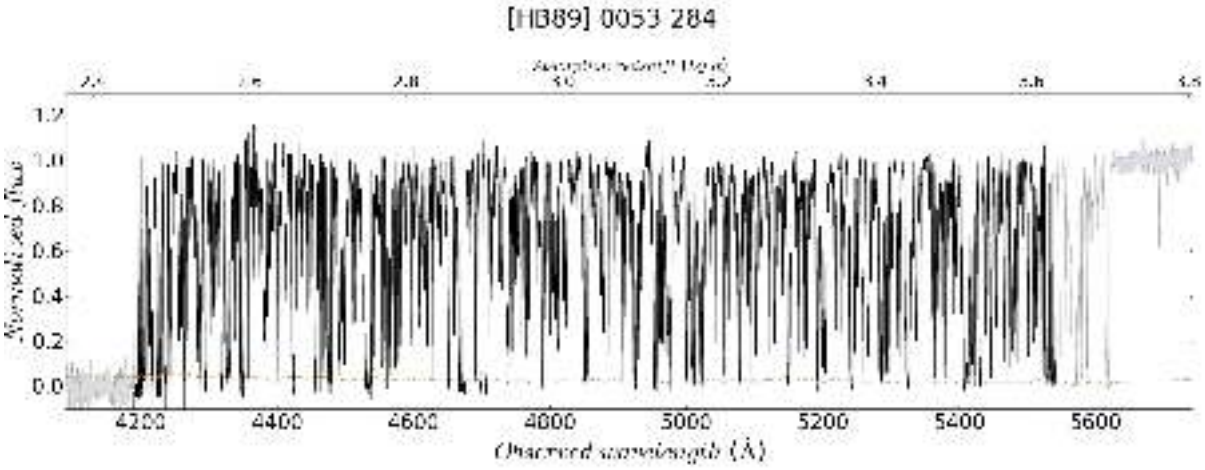

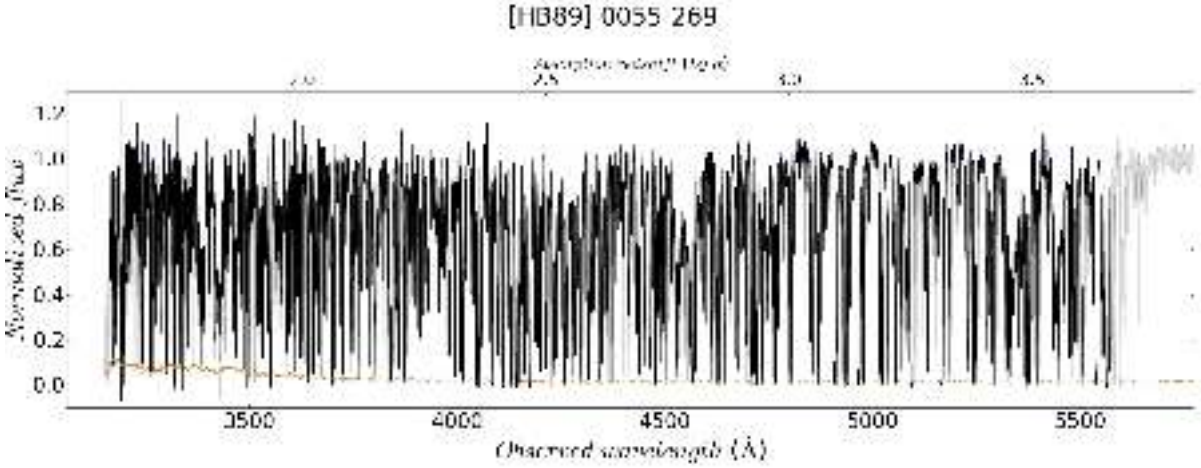
[HB89] 0055 269
Normalized flux
Observed wavelength (Å)

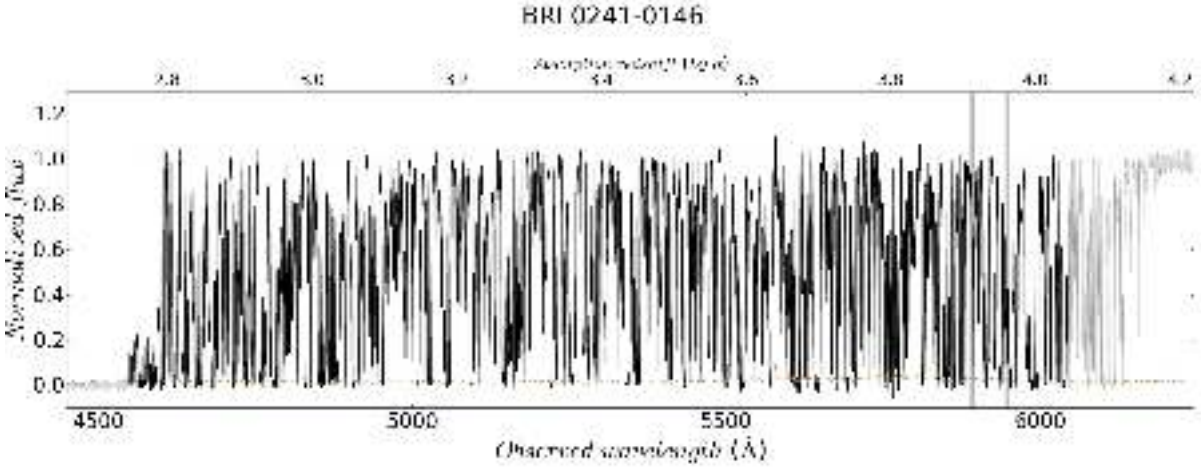
BRI 0241-0146
Normalized flux
Observed wavelength (Å)

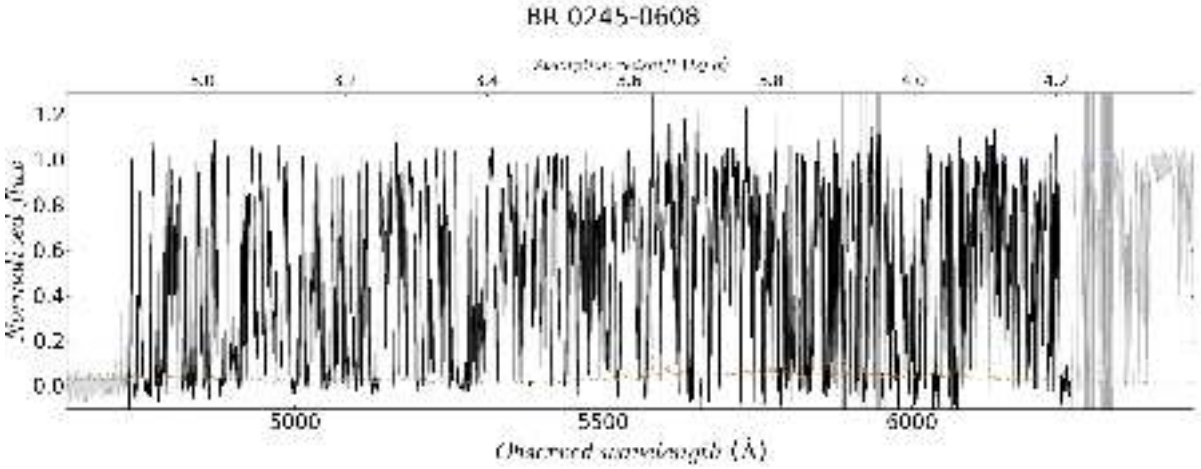
BR 0245-0608
Normalized flux
Observed wavelength (Å)

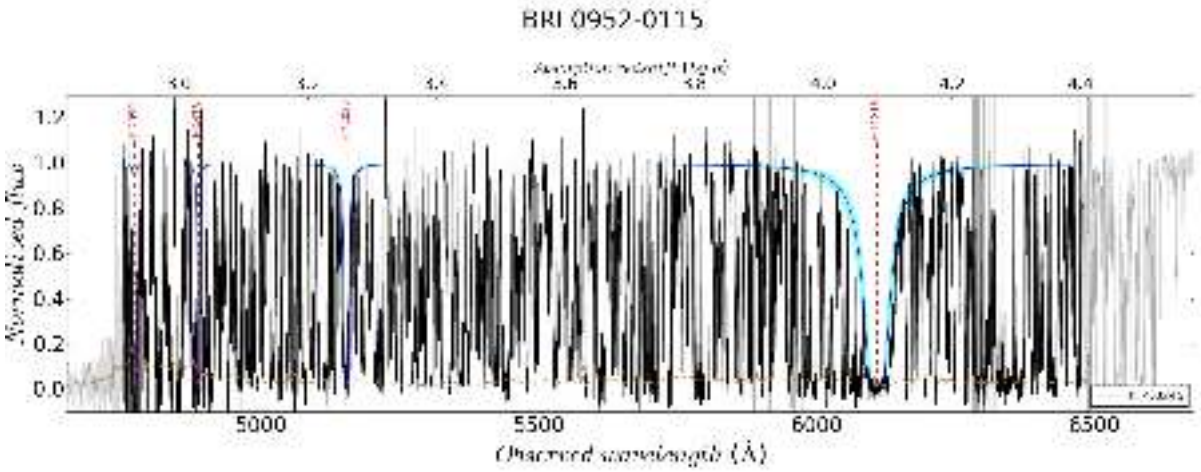
BRI 0952-0115
Normalized flux
0.0
0.2
0.4
0.6
0.8
1.0
1.2
5000
5500
6000
6500
Observed wavelength (Å)

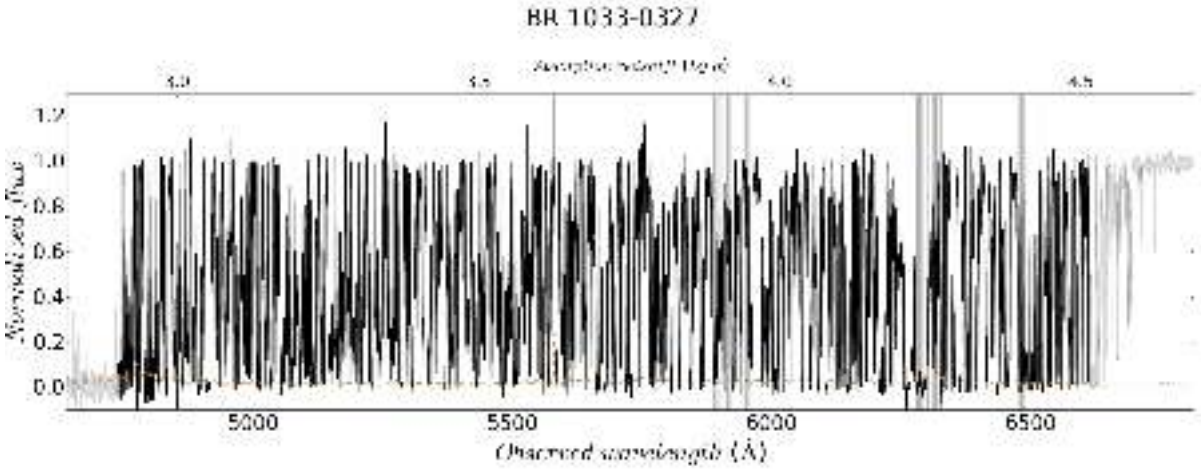
BR 1033-0327
Normalized flux
0.0
0.2
0.4
0.6
0.8
1.0
1.2
5000
5500
6000
6500
Observed wavelength (Å)

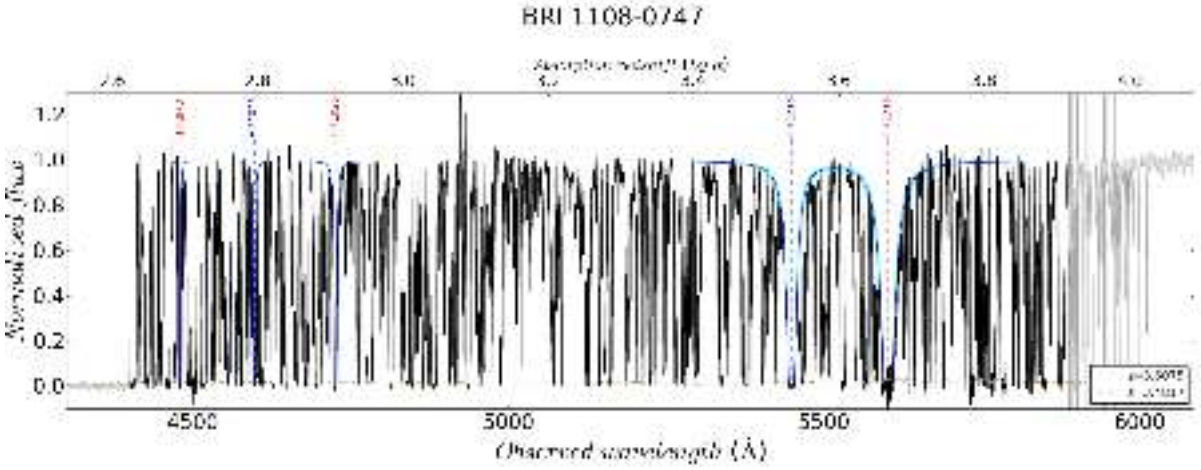
BRI 1108-0747
Normalized flux
0.0
0.2
0.4
0.6
0.8
1.0
1.2
4500
5000
5500
6000
Observed wavelength (Å)

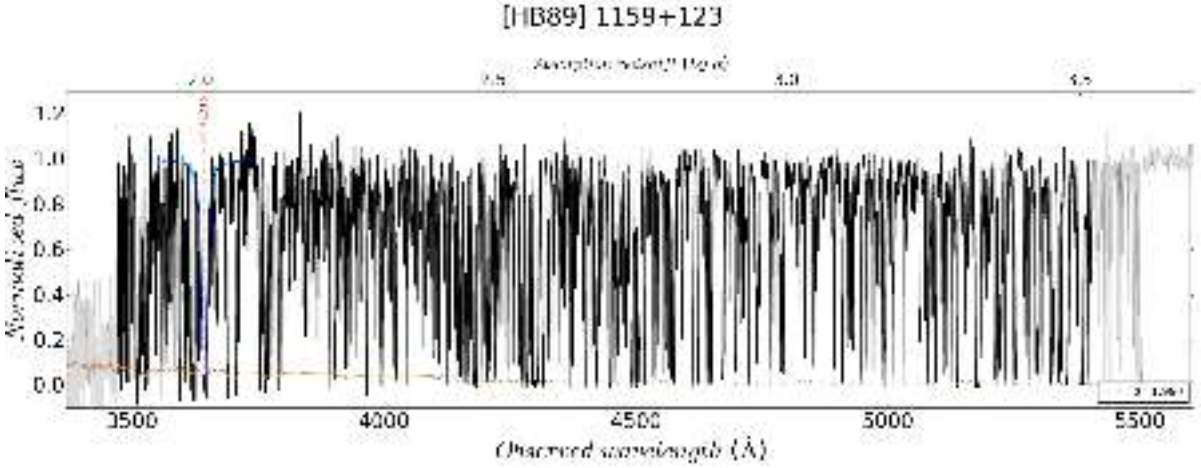
[HB89] 1159+123
Normalized flux
Observed wavelength (Å)

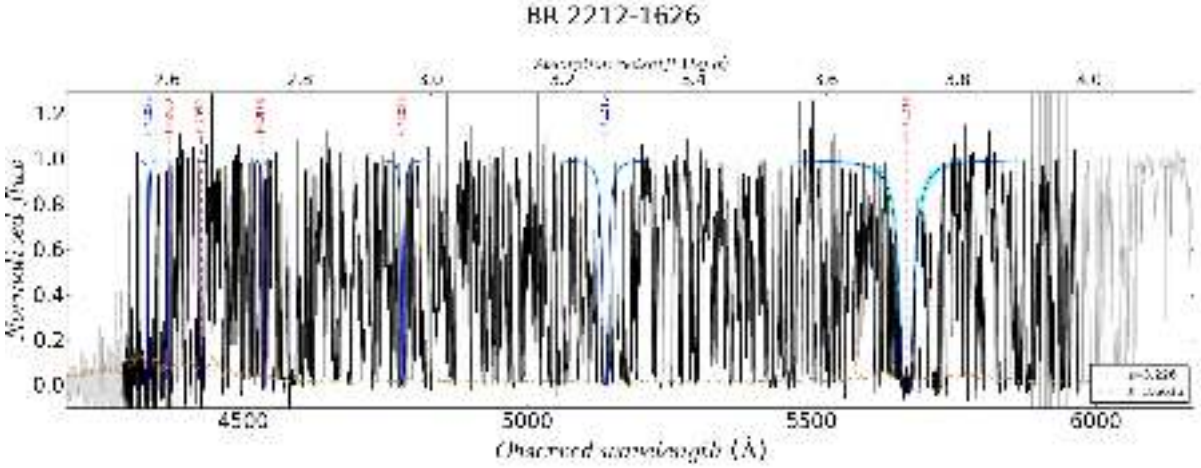
BR 2212-1626
Normalized flux
Observed wavelength (Å)

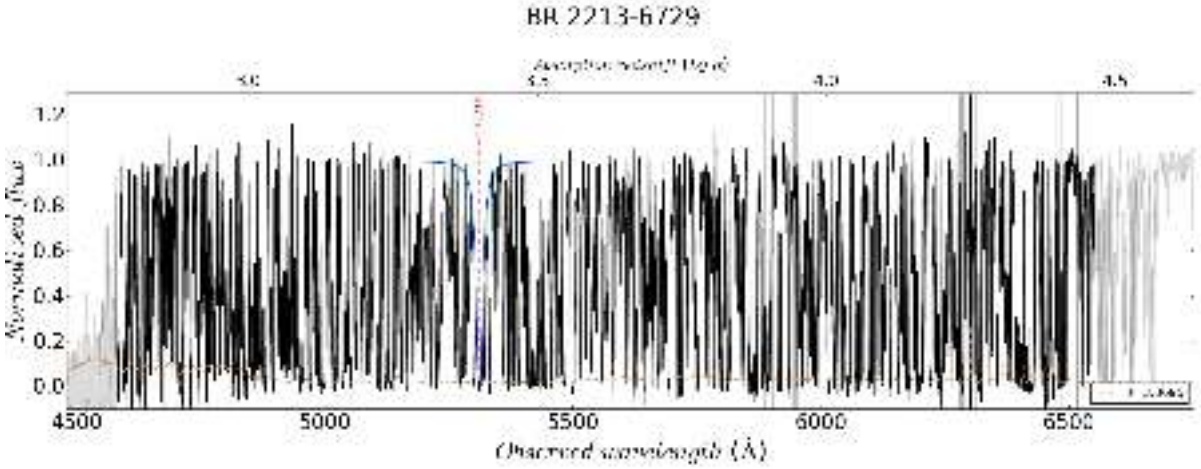
BR 2213-6729
Normalized flux
Observed wavelength (Å)

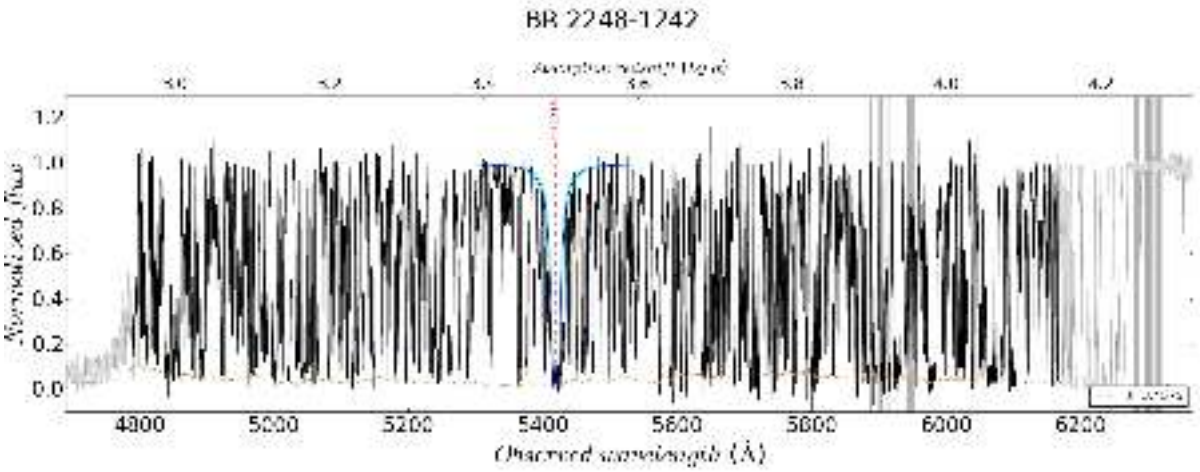
BR 2248-1242
4800
5000
5200
5400
5600
5800
6000
6200

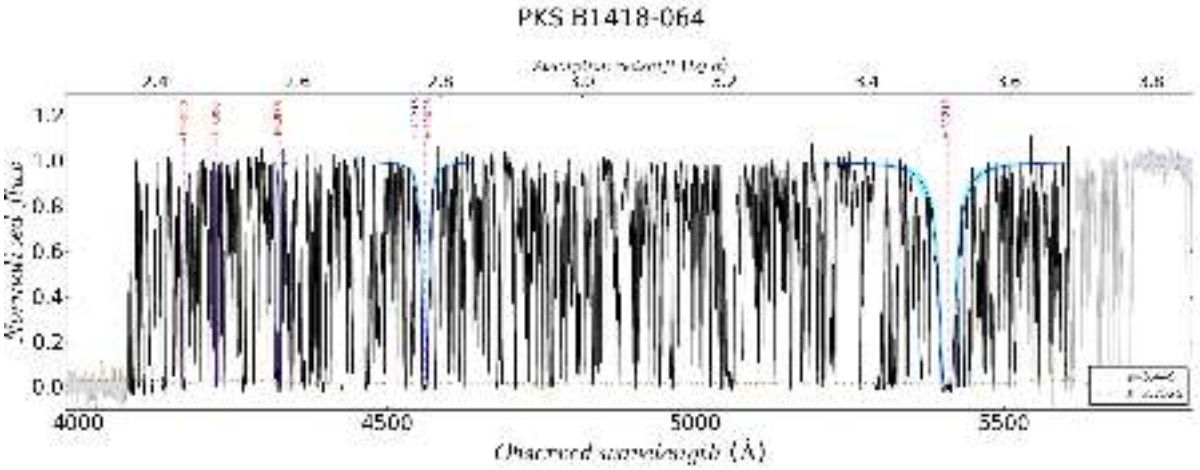
PKS B1418-064
4000
4500
5000
5500

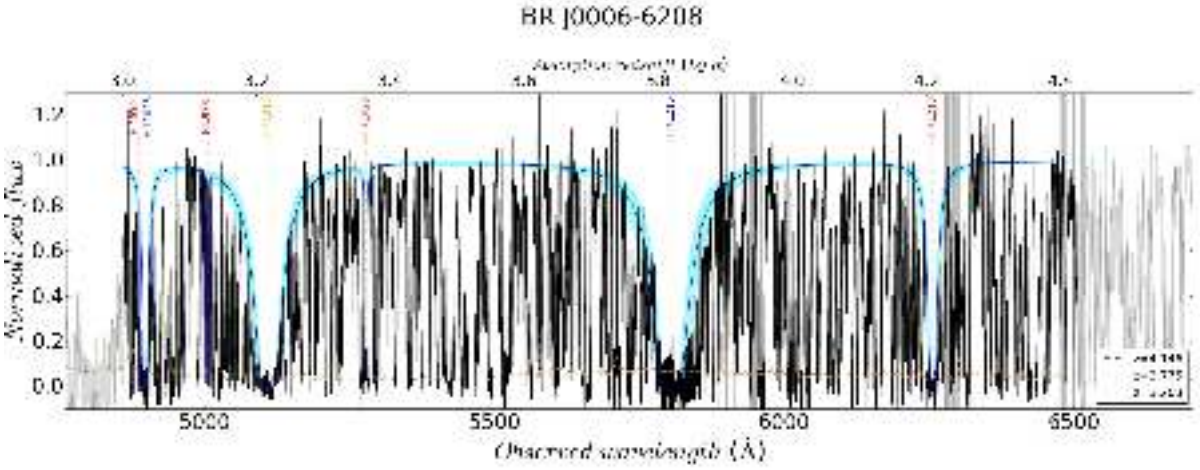
BR J0006-6208
5000
5500
6000
6500

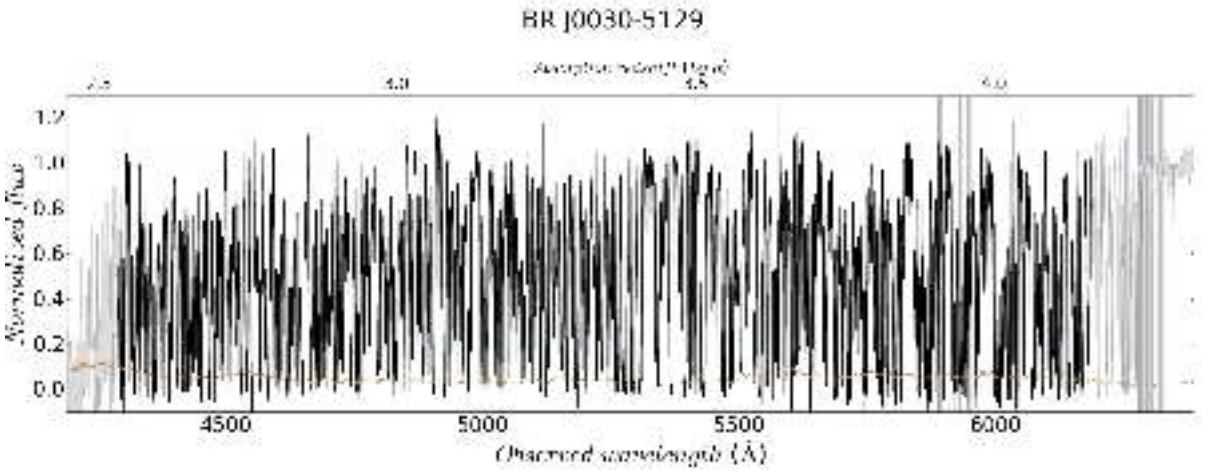
BR J0030-5129
Normalized flux
Observed wavelength (Å)
4500
5000
5500
6000

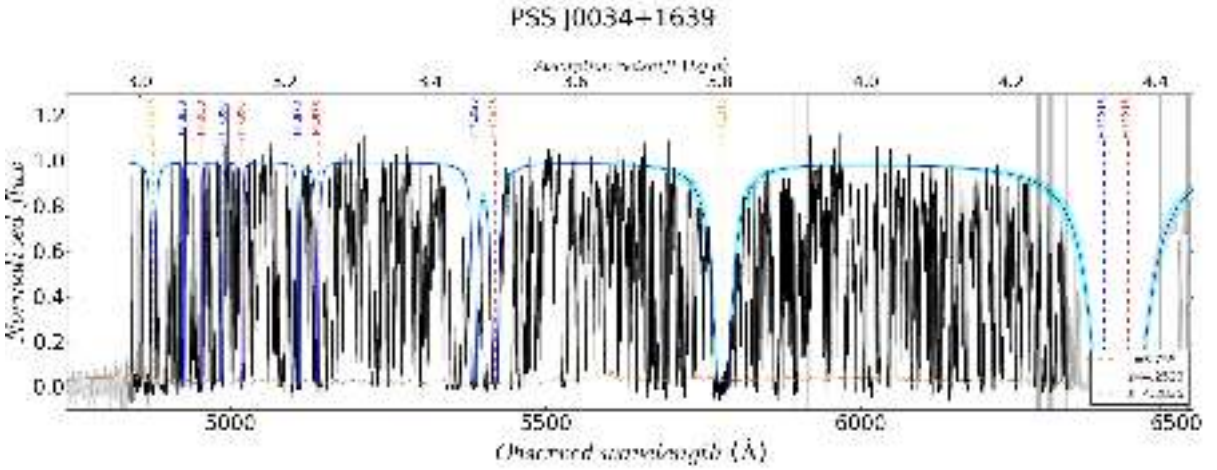
PSS J0034+1639
Normalized flux
Observed wavelength (Å)
5000
5500
6000
6500

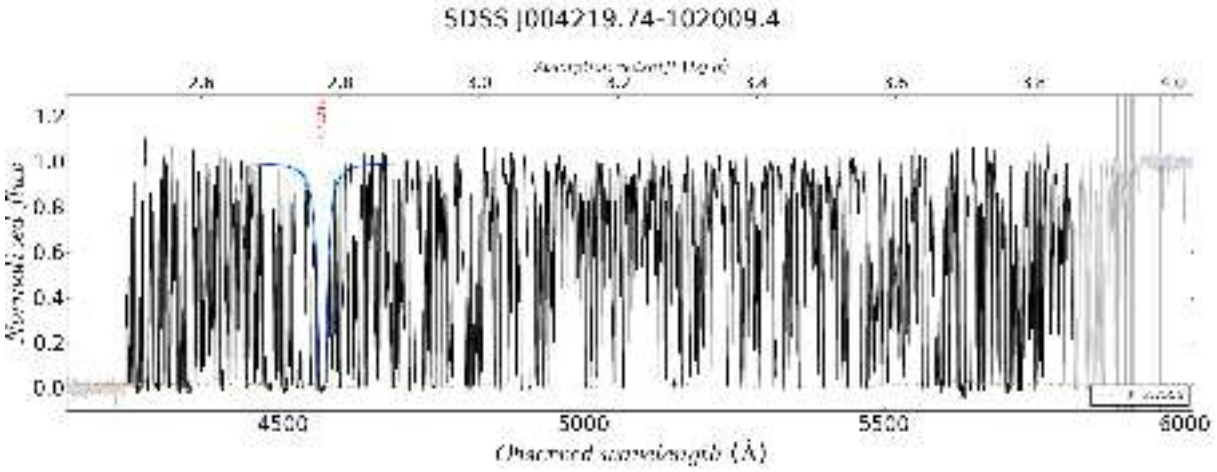
SDSS J004219.74-102009.4
Normalized flux
Observed wavelength (Å)
4500
5000
5500
6000

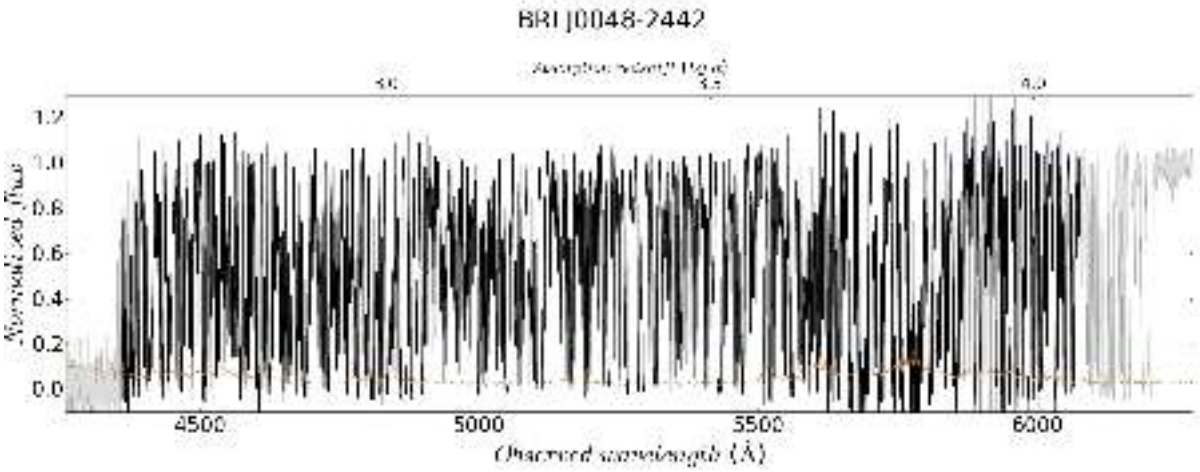
BRI J0048-2442
4500
5000
5500
6000

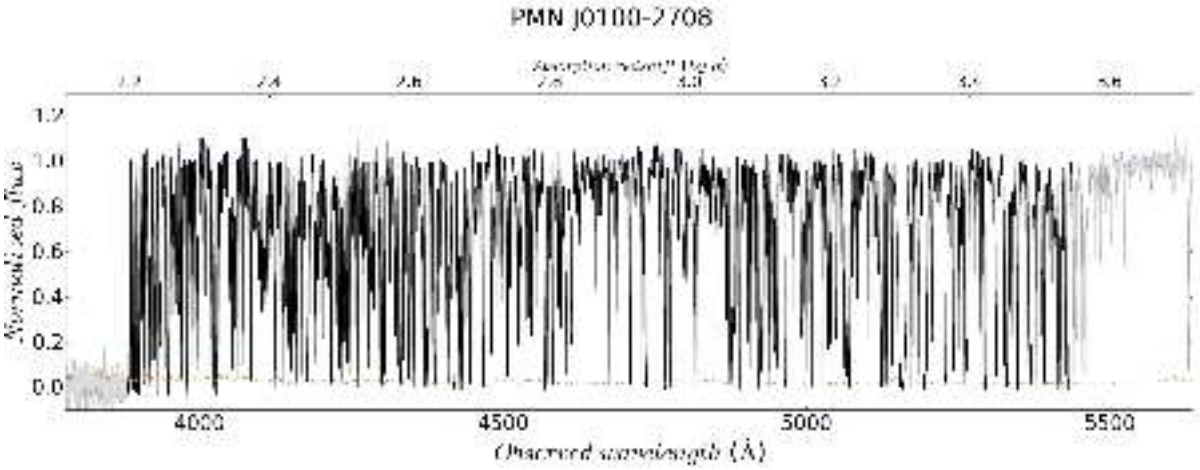
PMN J0100-2708
4000
4500
5000
5500

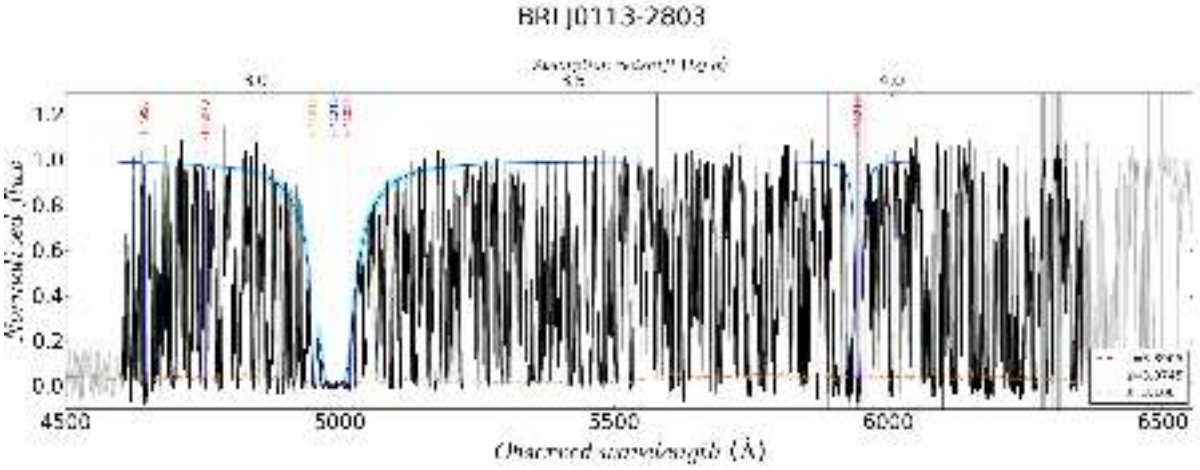
BRI J0113-2803
4500
5000
5500
6000
6500

PSS J0117+1552

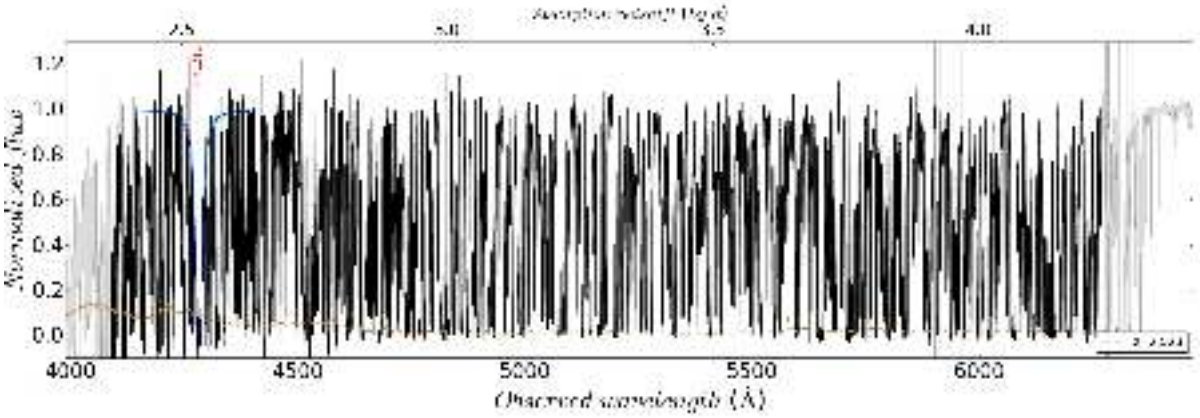

PSS J0121+0347

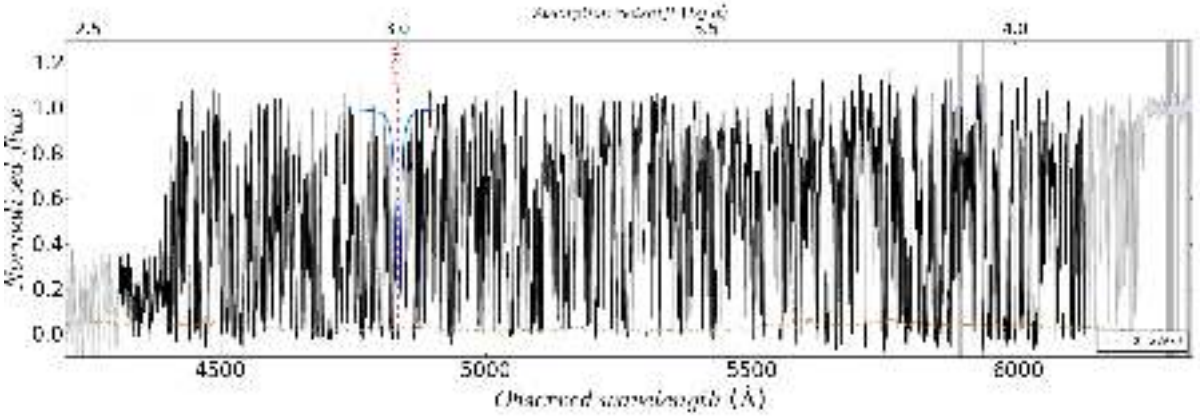

SDSS J0124+0044

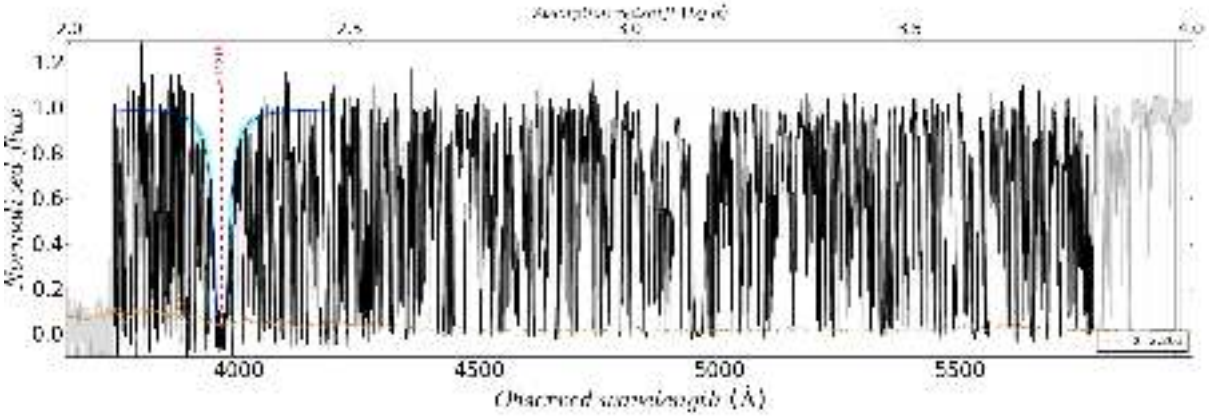

PSS J0132+1341

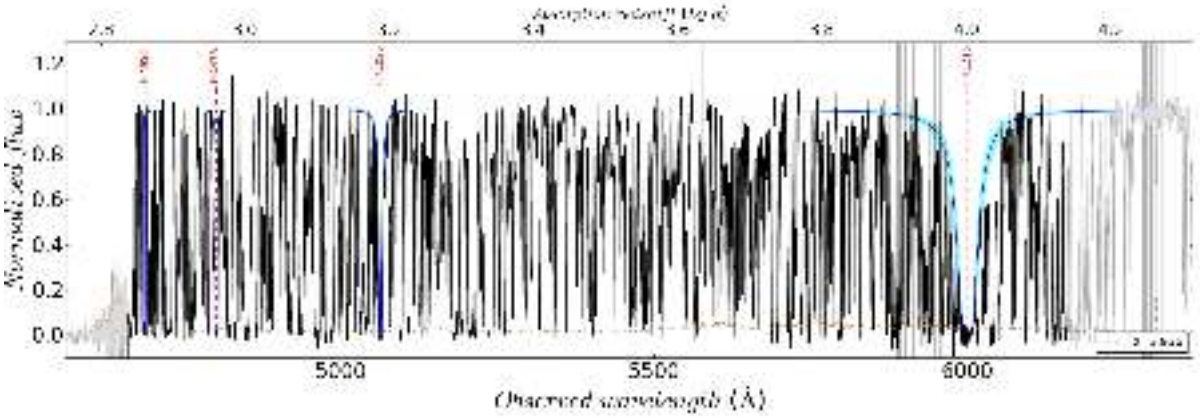

PSS J0133+0400

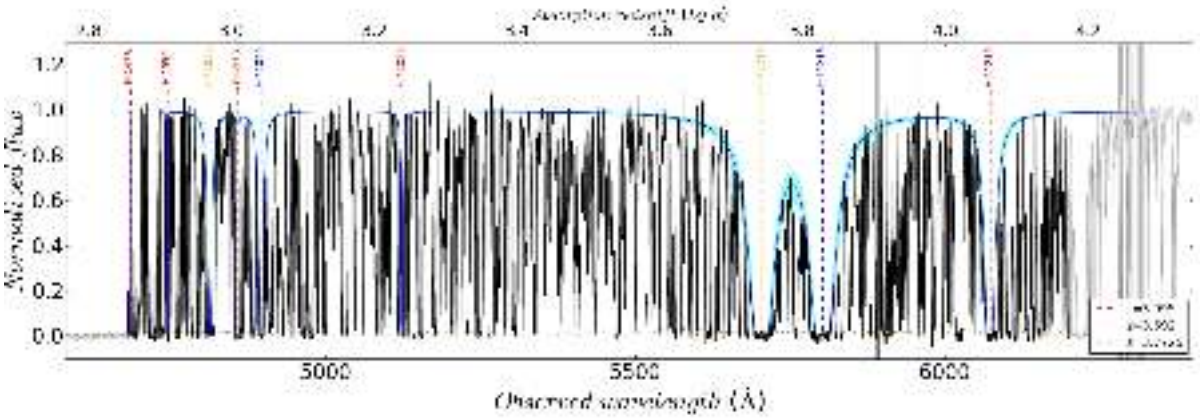

BRI J0137-4224

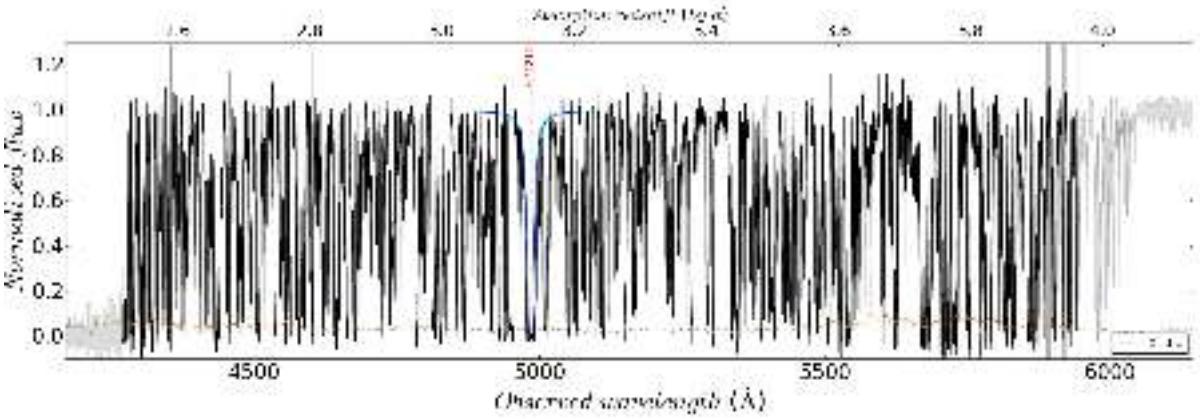

SDSS J015339.60-001104.8

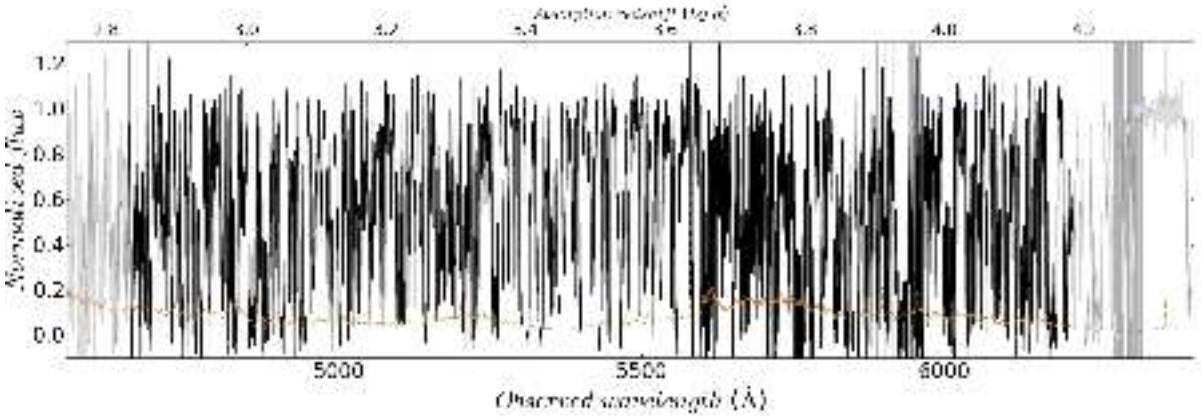

PSS J0211+1107

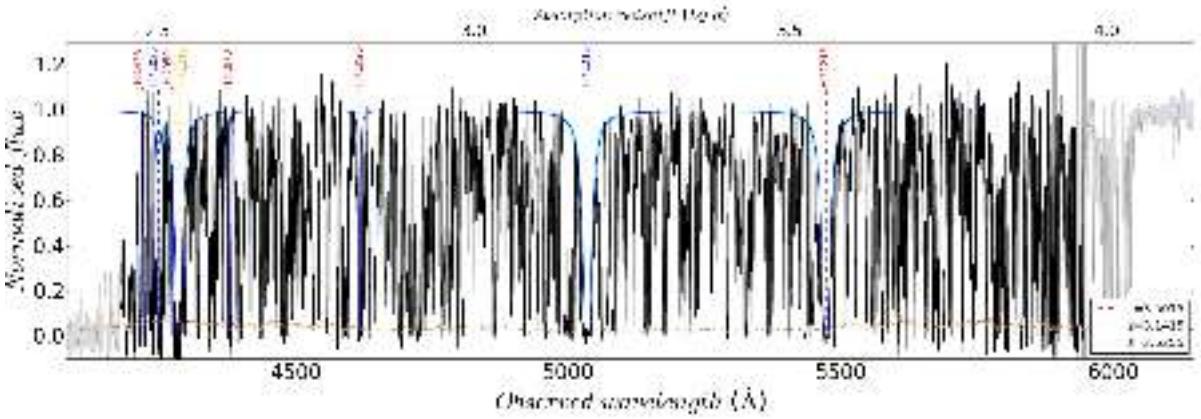

PMN J0214-0518

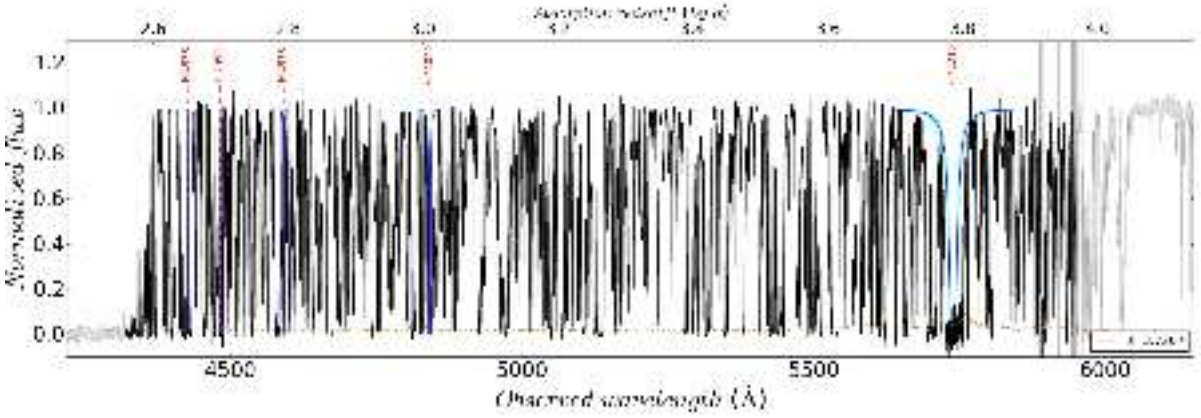

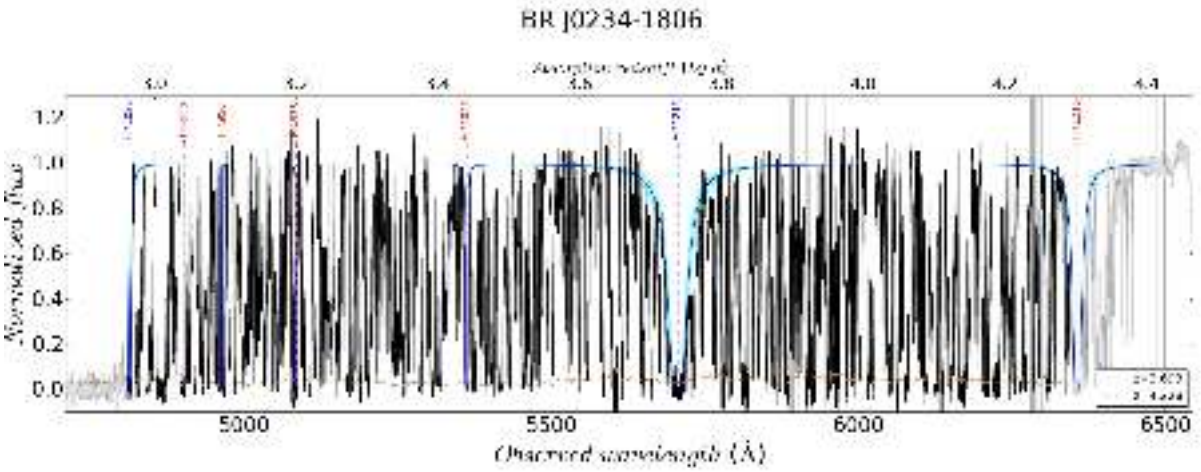
BR J0234-1806
5000
5500
6000
6500

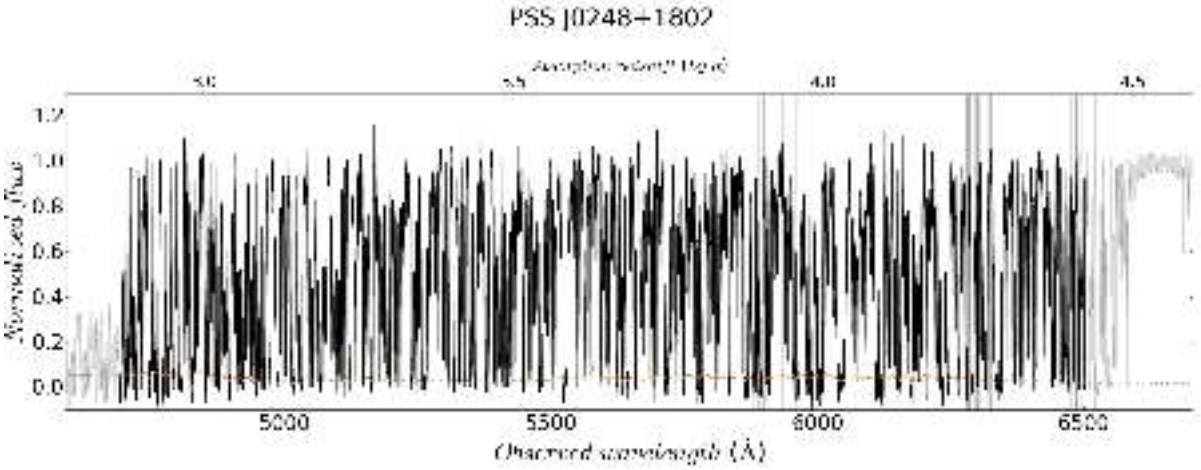
PSS J0248+1802
5000
5500
6000
6500

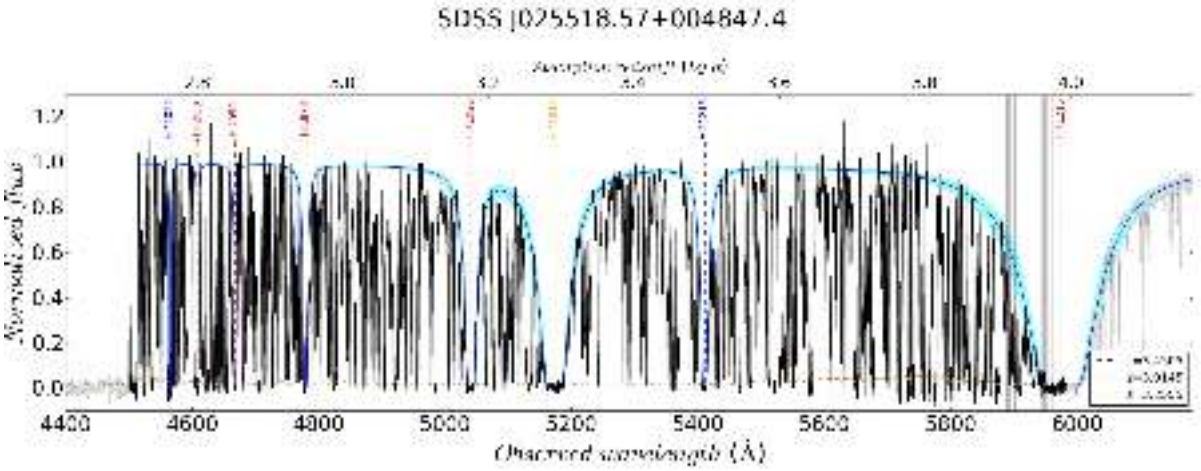
SDSS J025518.57+004847.4
4400
4600
4800
5000
5200
5400
5600
5800
6000

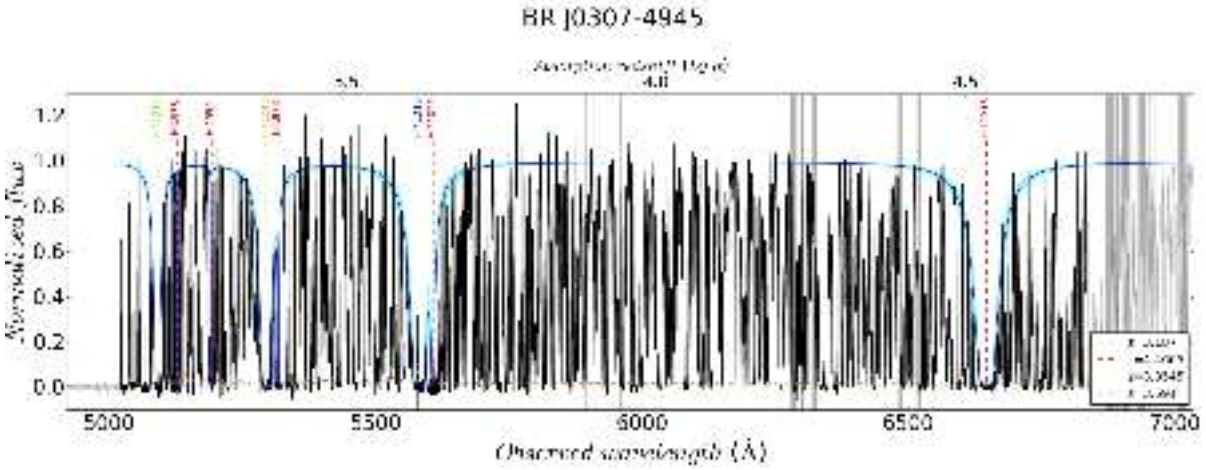
BR J0307-4945
5.5
4.0
4.5
1.2
1.0
0.8
0.6
0.4
0.2
0.0
5000
5500
6000
6500
7000
Observed wavelength (Å)

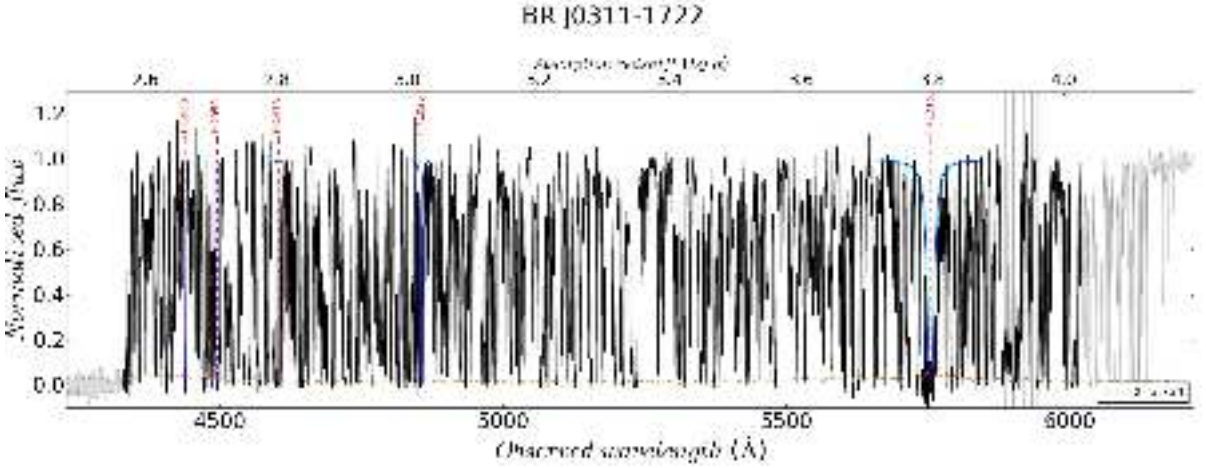
BR J0311-1722
3.6
3.8
4.0
5.2
5.4
5.6
5.8
6.0
1.2
1.0
0.8
0.6
0.4
0.2
0.0
4500
5000
5500
6000
Observed wavelength (Å)

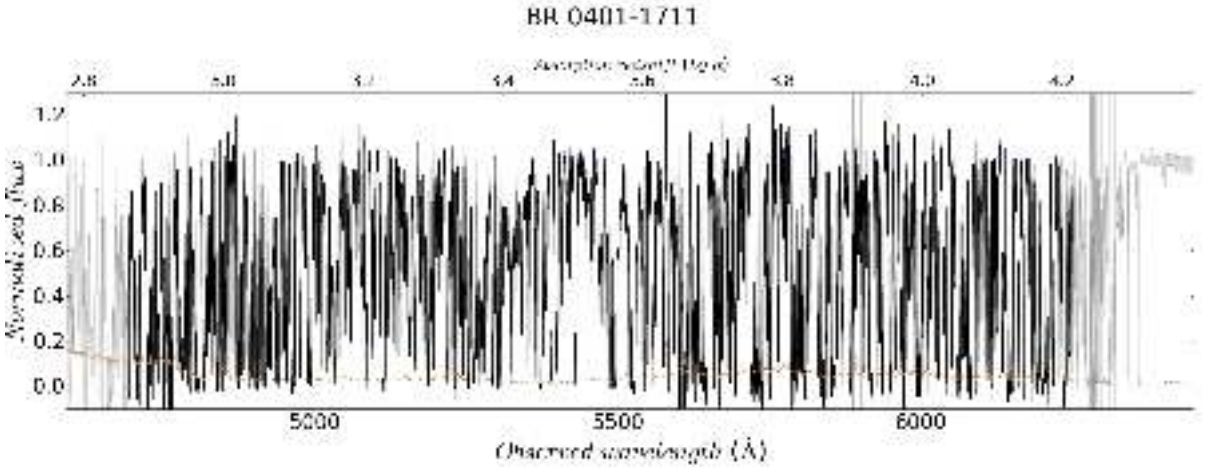
BR 0401-1711
3.6
3.8
5.2
5.4
5.6
5.8
6.0
6.2
1.2
1.0
0.8
0.6
0.4
0.2
0.0
5000
5500
6000
Observed wavelength (Å)

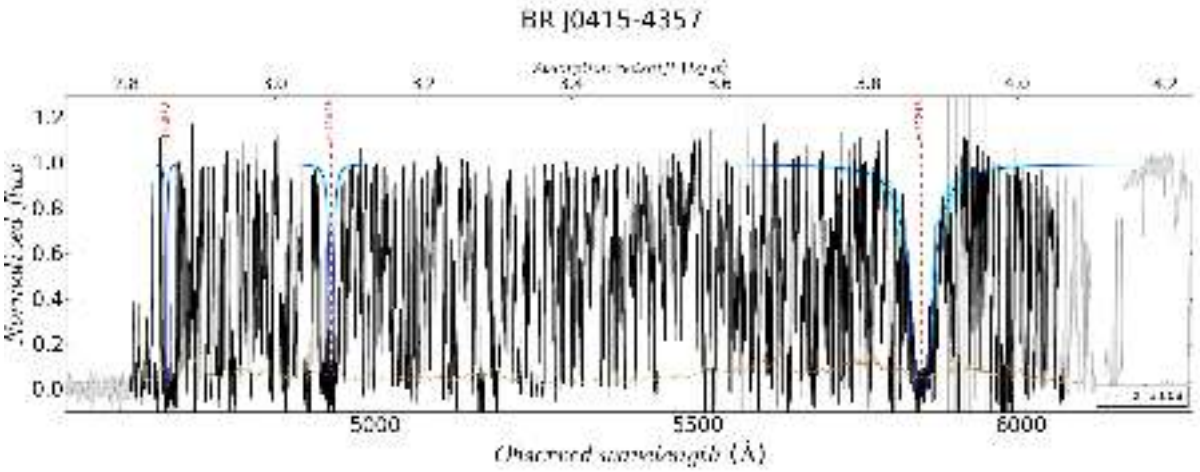
BR J0415-4357
5000
5500
6000

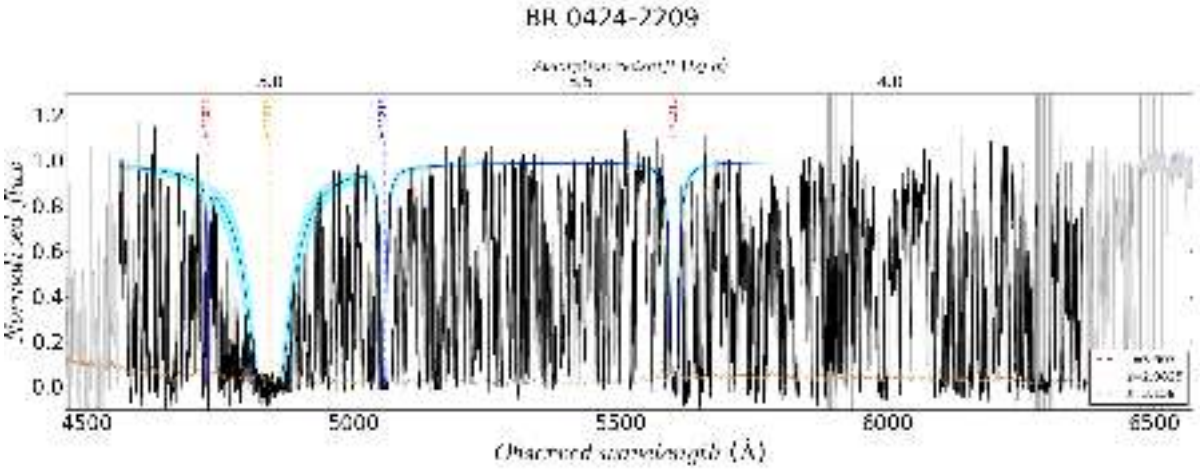
BR 0424-2209
4500
5000
5500
6000
6500

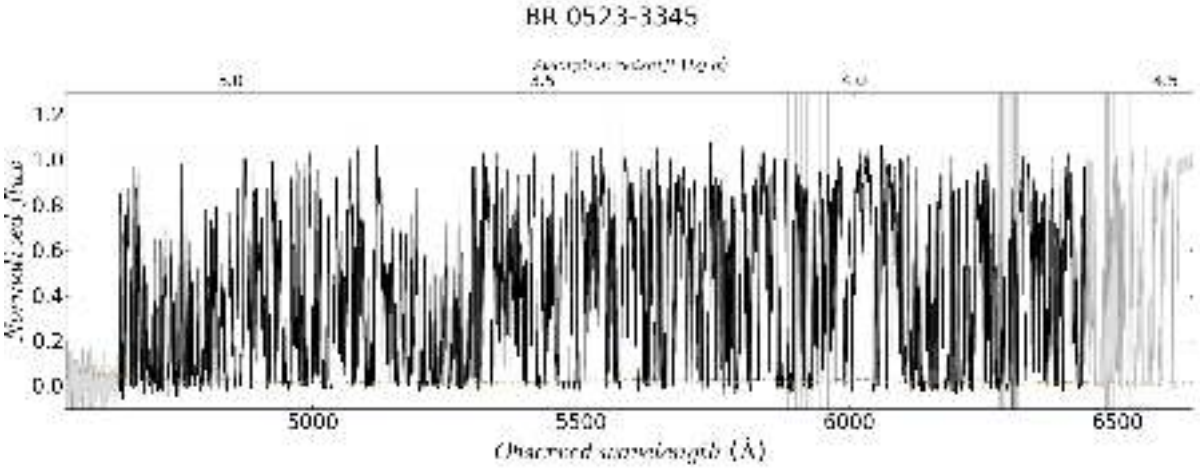
BR 0523-3345
5000
5500
6000
6500

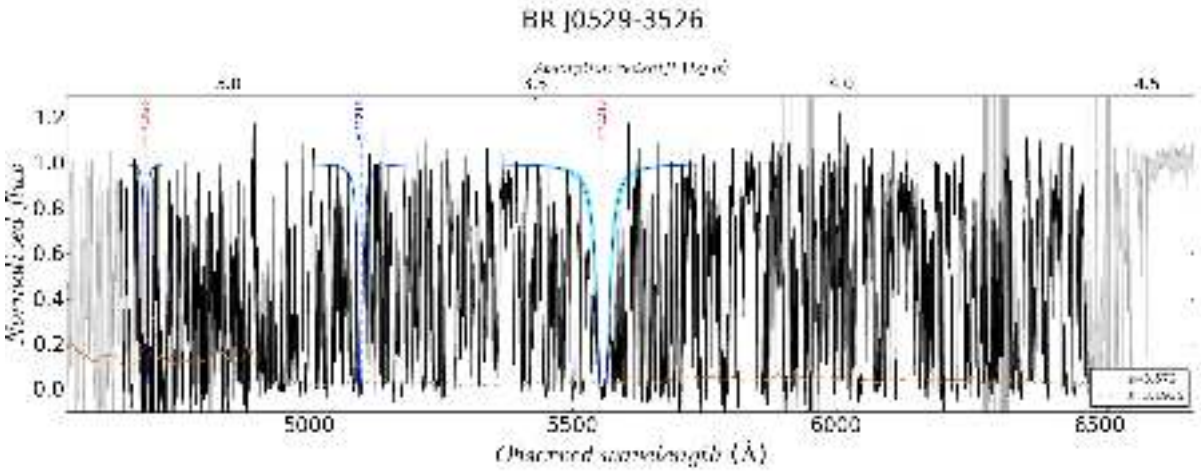
BR J0529-3526
Normalized flux
Observed wavelength (Å)
5000
5500
6000
6500

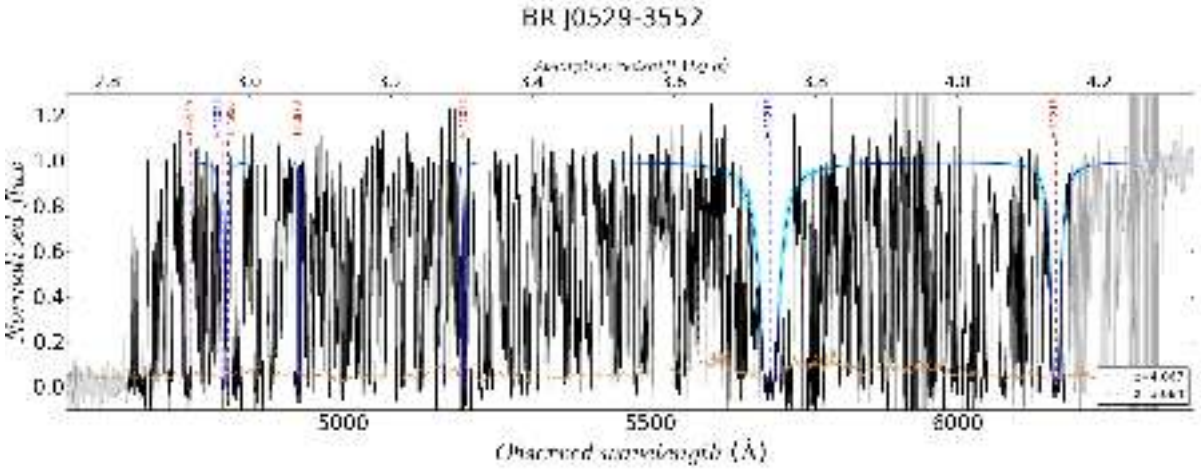
BR J0529-3552
Normalized flux
Observed wavelength (Å)
5000
5500
6000

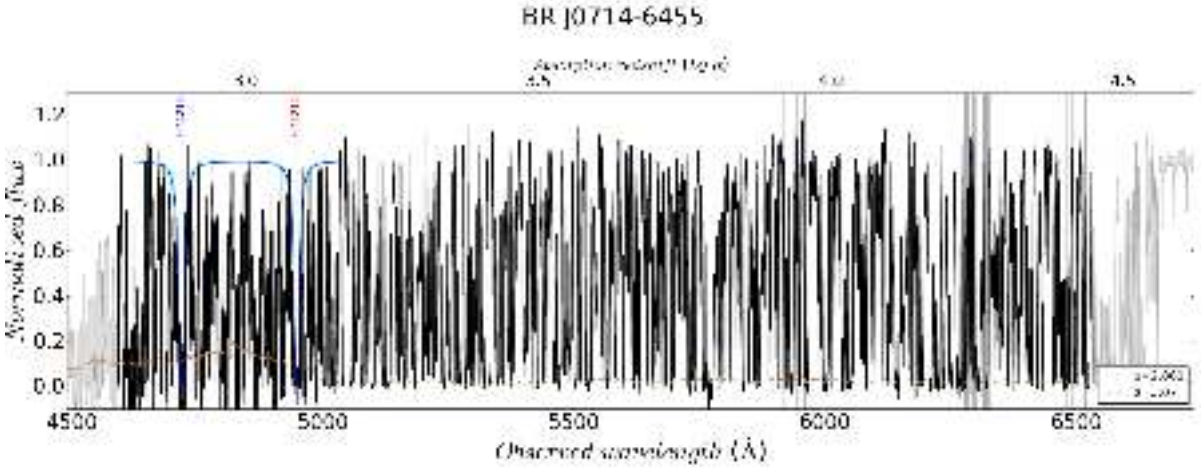
BR J0714-6455
Normalized flux
Observed wavelength (Å)
4500
5000
5500
6000
6500

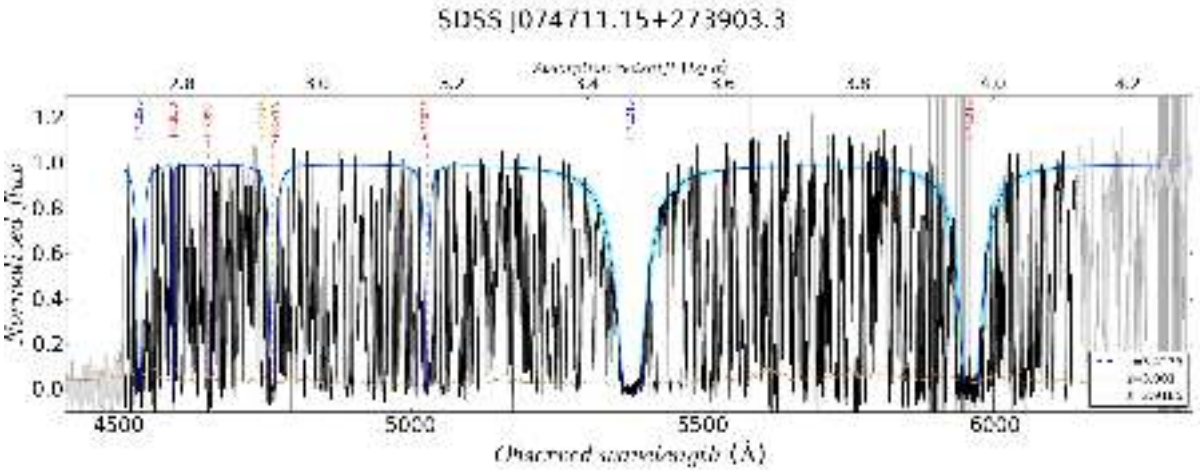
SDSS J074711.15+273903.3
Normalized flux
4500
5000
5500
6000
Observed wavelength (Å)

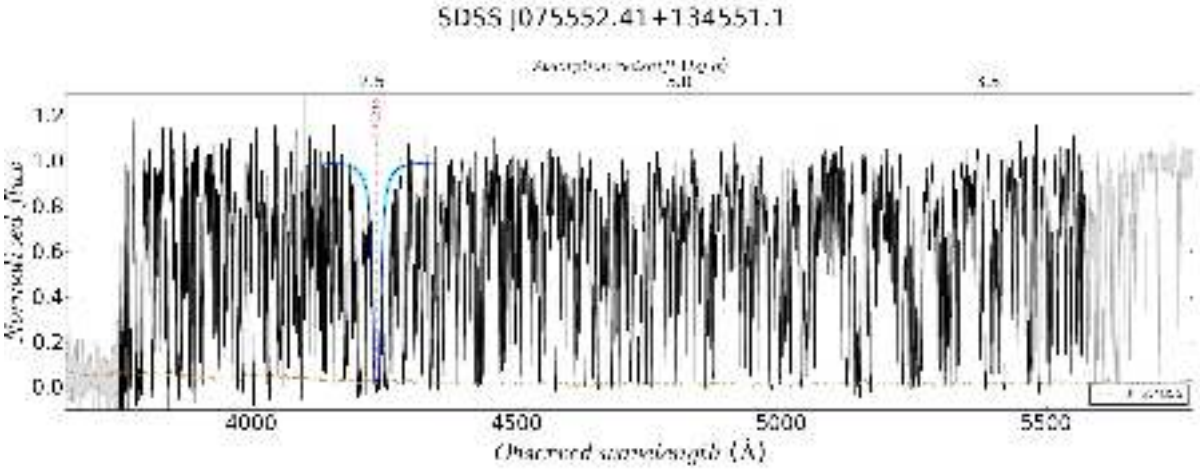
SDSS J075552.41+134551.1
Normalized flux
4000
4500
5000
5500
Observed wavelength (Å)

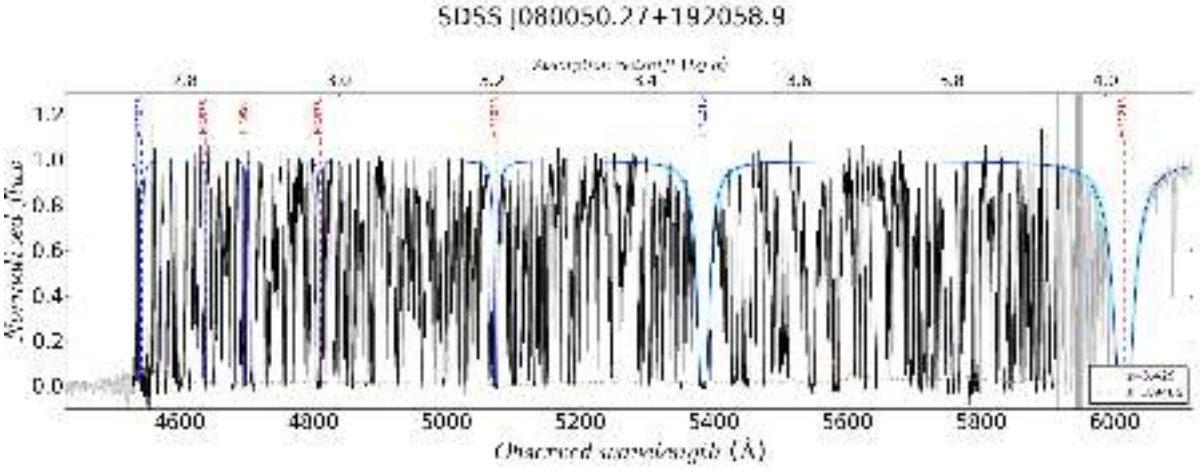
SDSS J080050.27+192058.9
Normalized flux
4600
4800
5000
5200
5400
5600
5800
6000
Observed wavelength (Å)

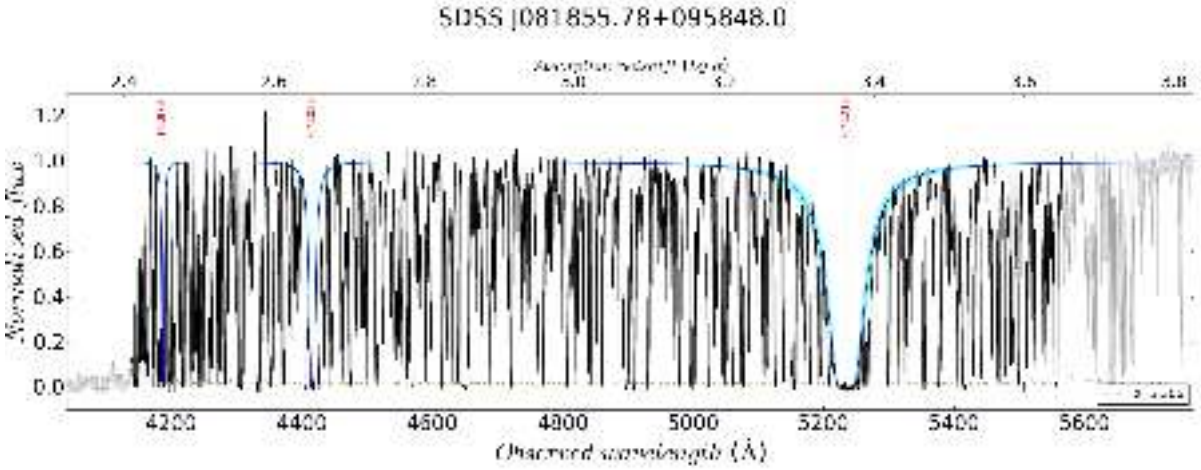
SDSS J081855.78+095848.0
Normalized flux
Observed wavelength (Å)

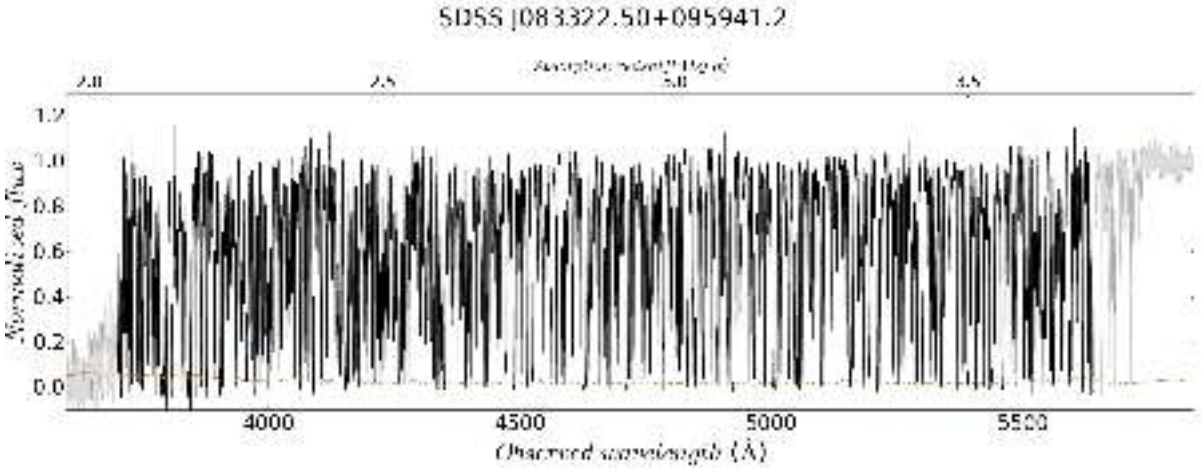
SDSS J083322.50+095941.2
Normalized flux
Observed wavelength (Å)

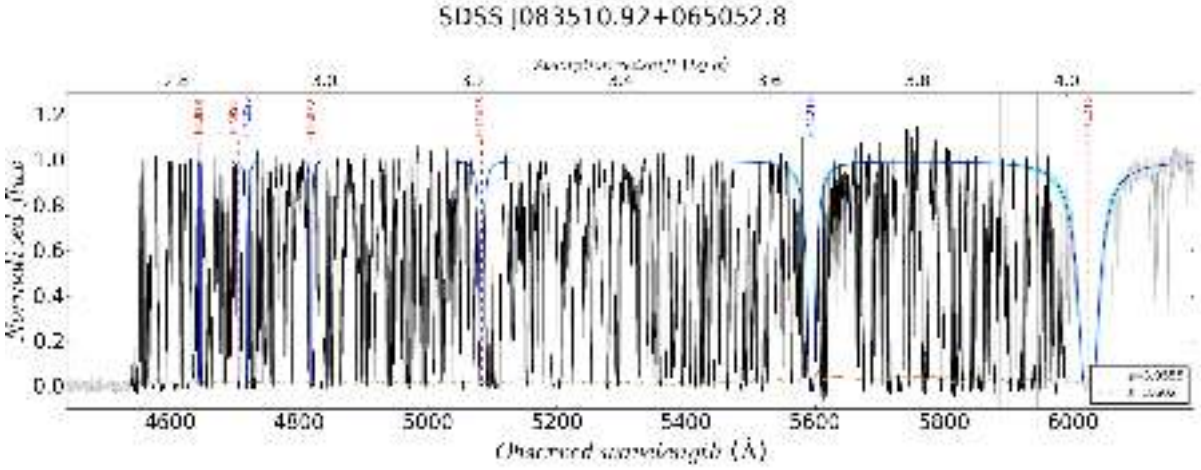
SDSS J083510.92+065052.8
Normalized flux
Observed wavelength (Å)

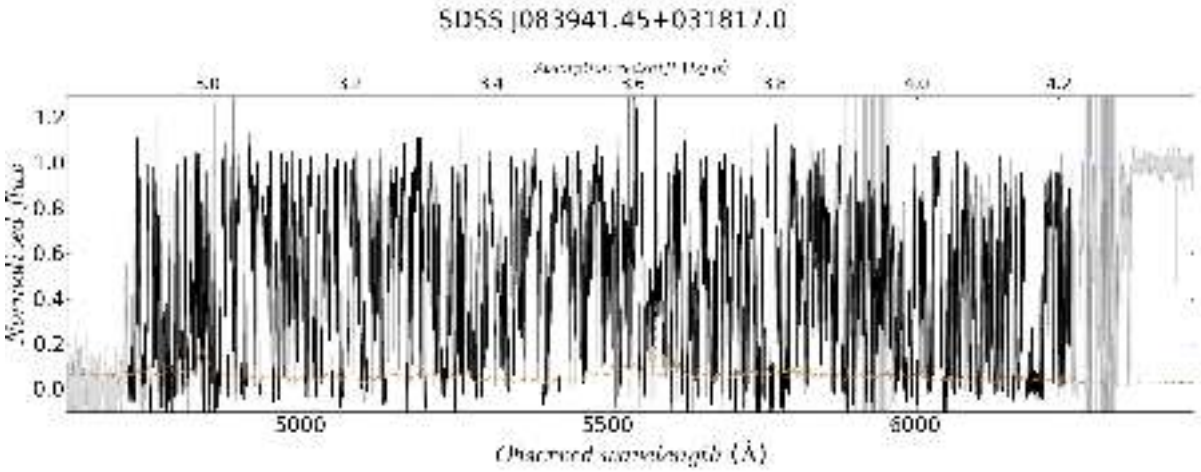
SDSS J083941.45+031817.0
5000
5500
6000

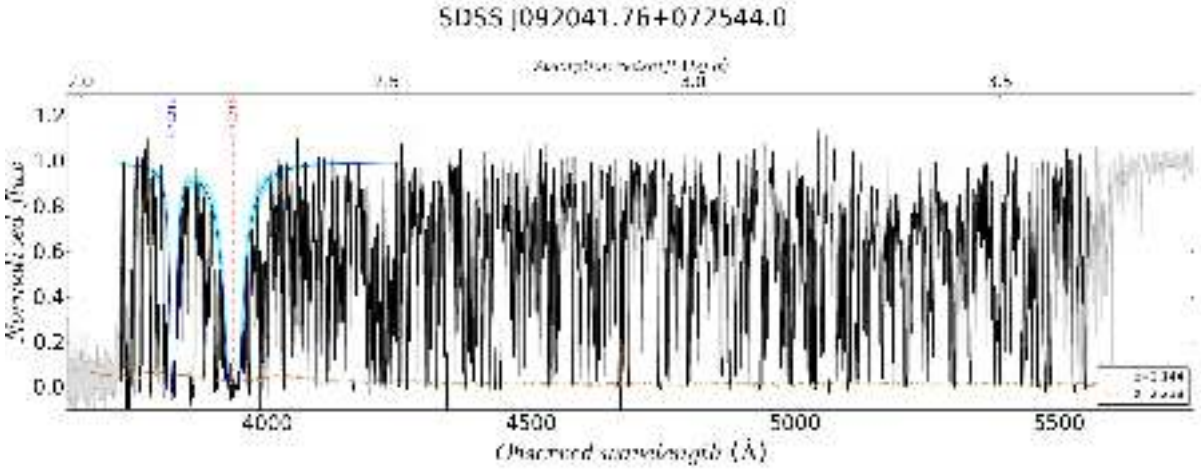
SDSS J092041.76+072544.0
4000
4500
5000
5500

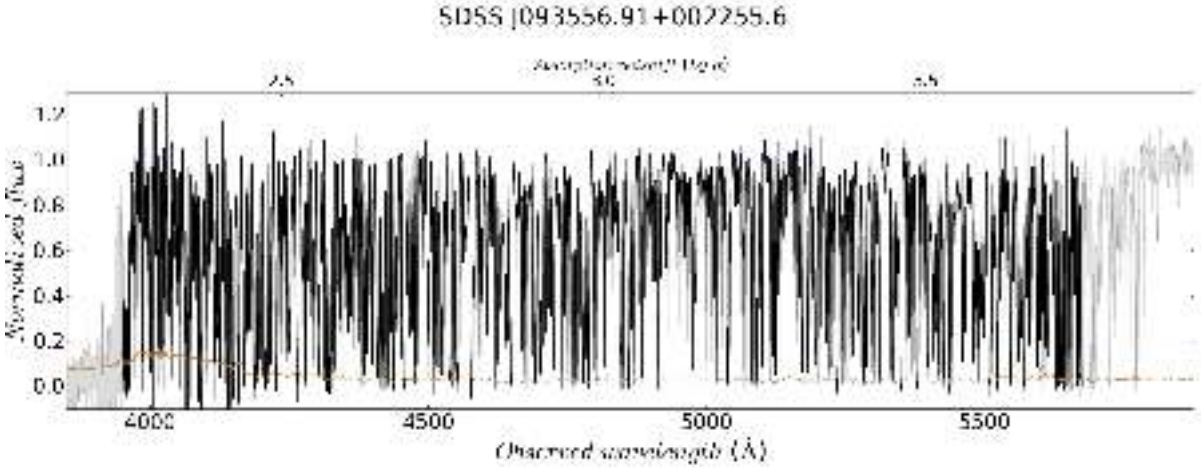
SDSS J093556.91+002255.6
4000
4500
5000
5500

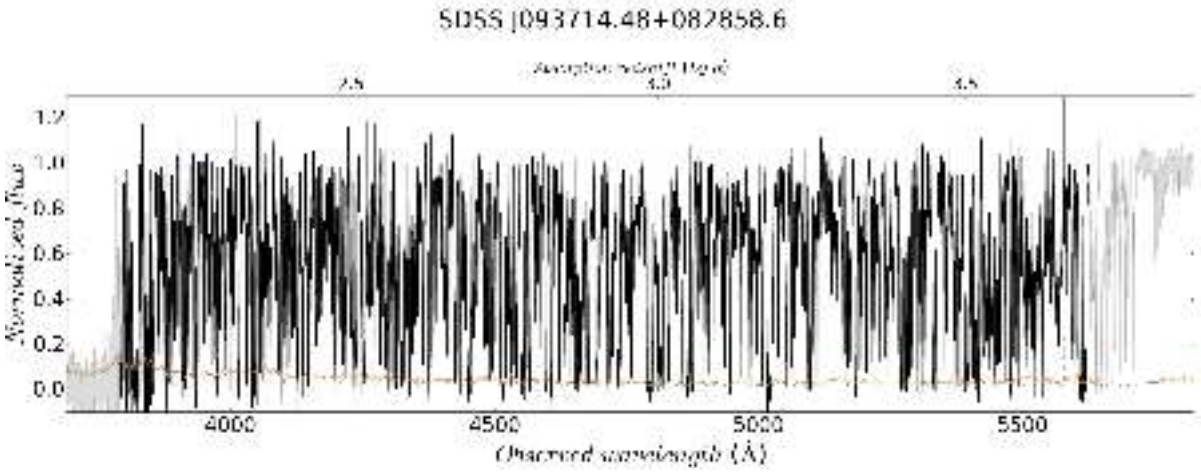
SDSS J093714.48+082858.6
Normalized flux
Observed wavelength (Å)

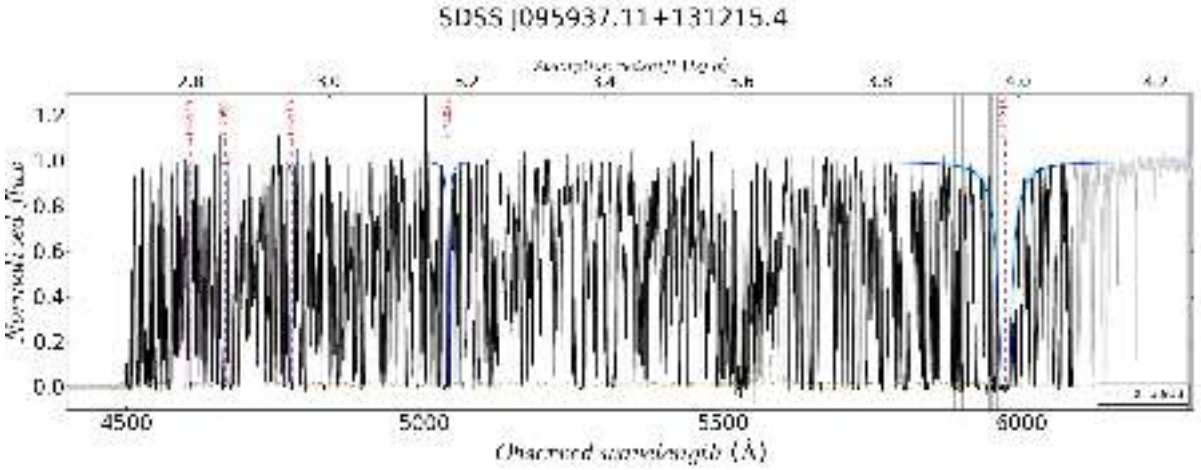
SDSS J095937.11+131215.4
Normalized flux
Observed wavelength (Å)

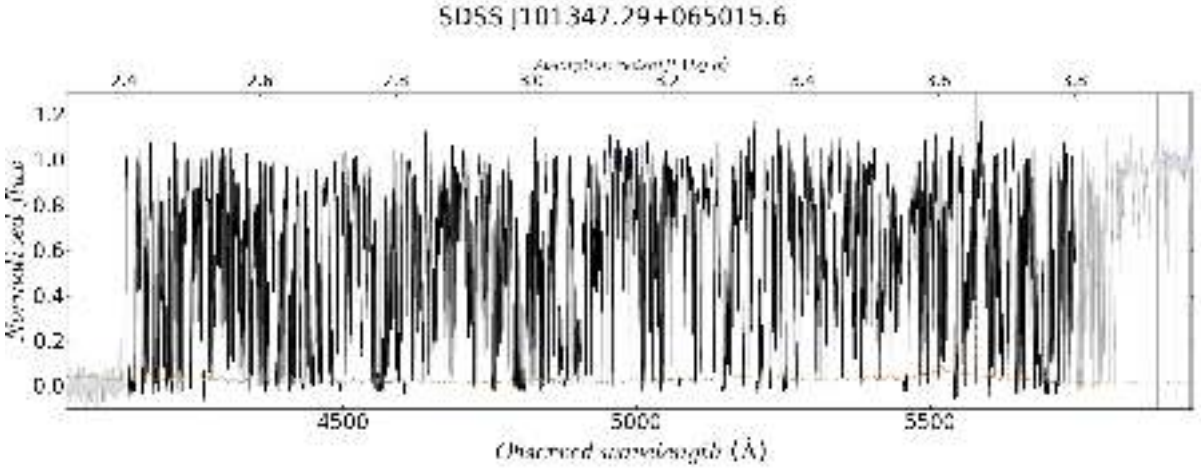
SDSS J101347.29+065015.6
Normalized flux
Observed wavelength (Å)

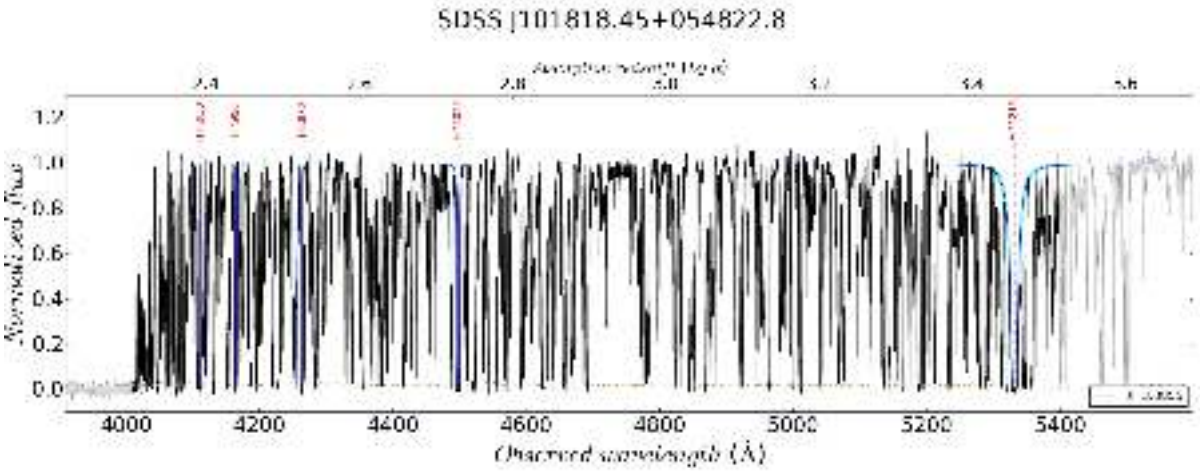
SDSS J101818.45+054822.8
Normalized flux
Observed wavelength (Å)

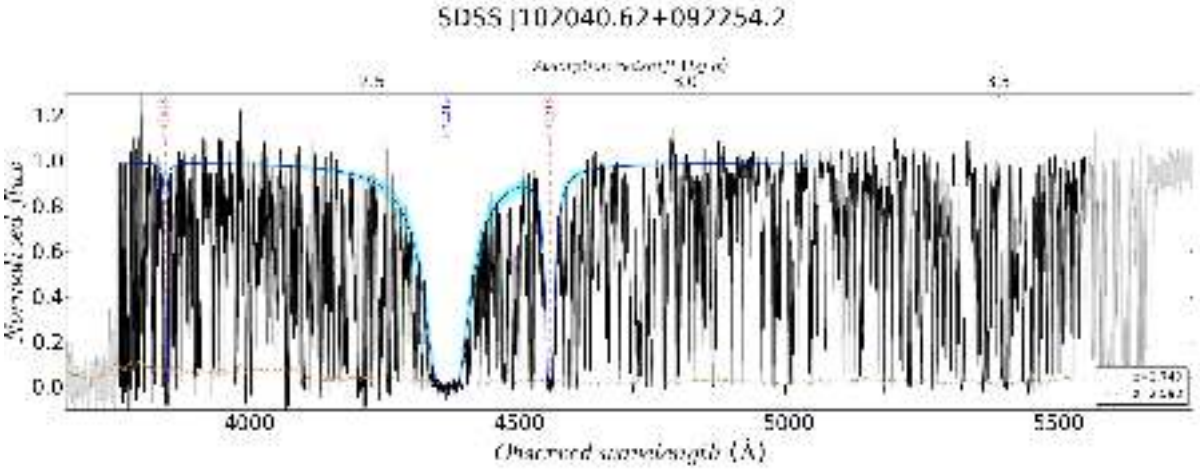
SDSS J102040.62+092254.2
Normalized flux
Observed wavelength (Å)

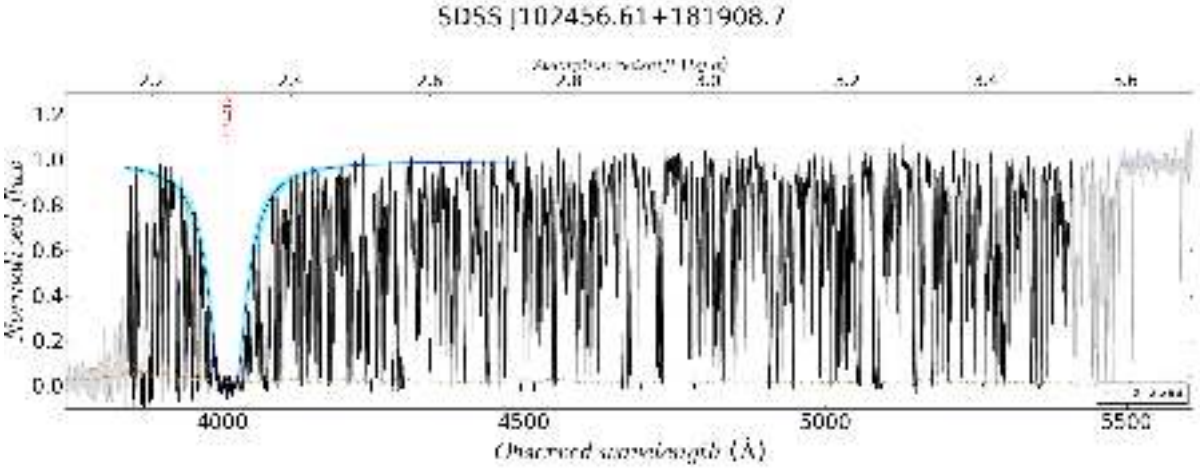
SDSS J102456.61+181908.7
Normalized flux
Observed wavelength (Å)

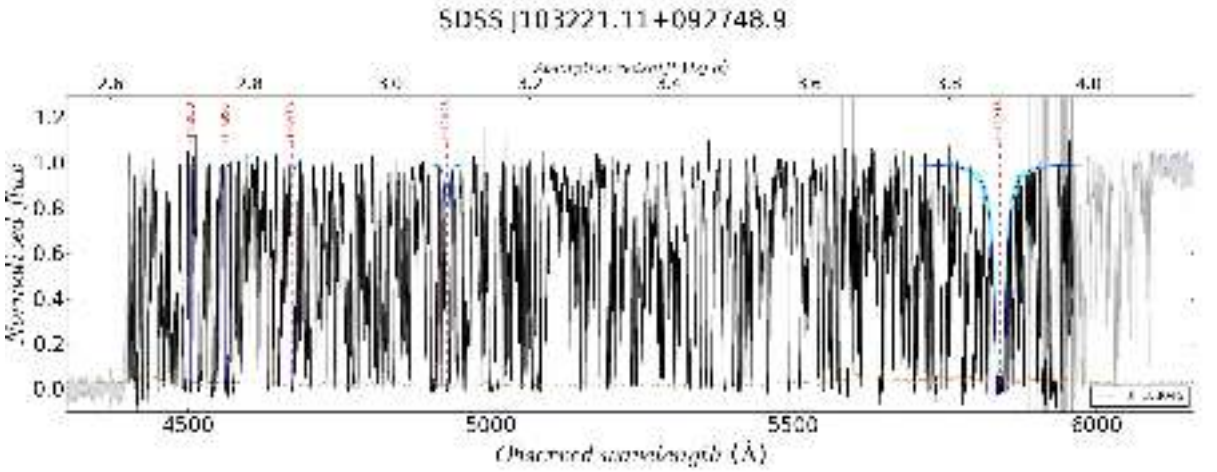
SDSS J103221.11+092748.9
Normalized flux
Observed wavelength (Å)

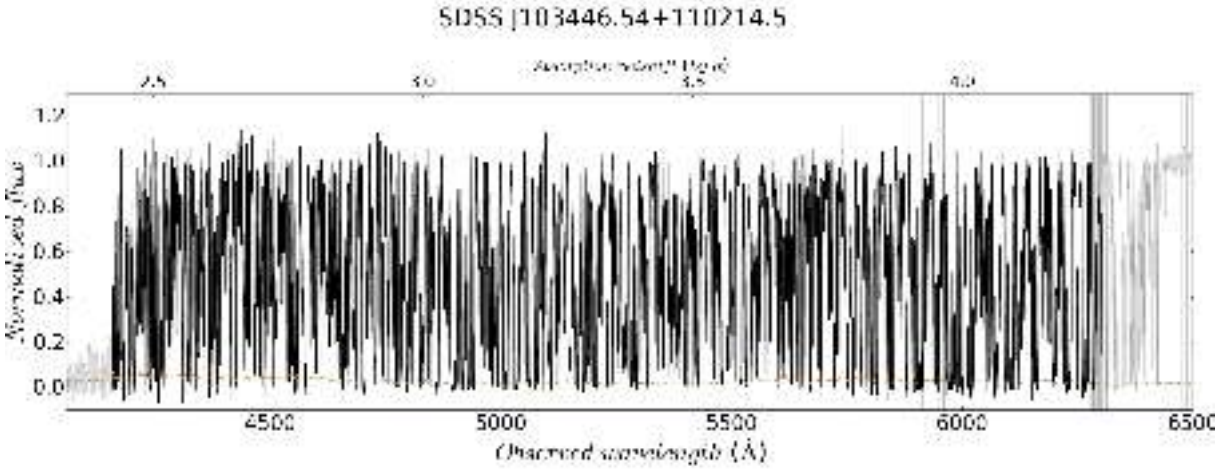
SDSS J103446.54+110214.5
Normalized flux
Observed wavelength (Å)

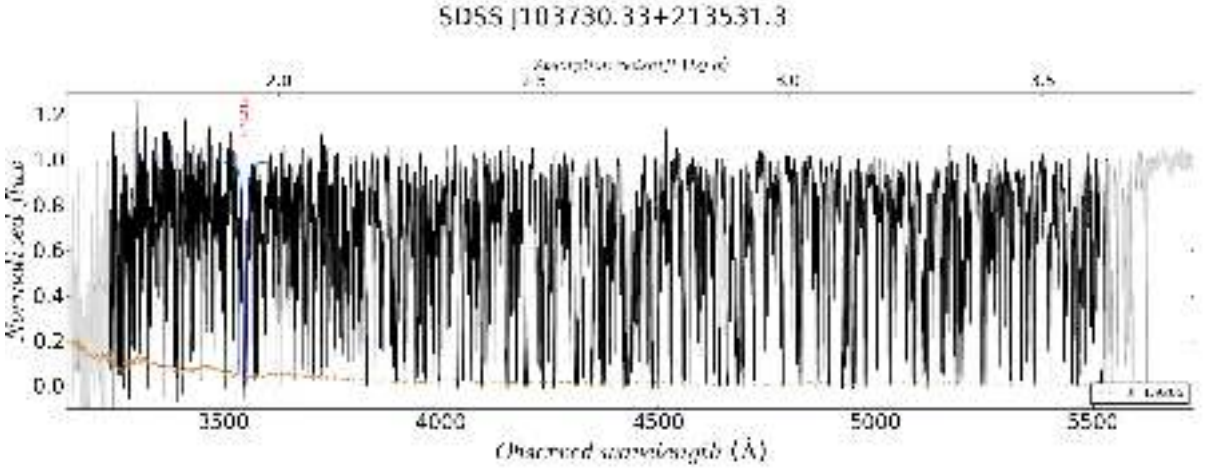
SDSS J103730.33+213531.3
Normalized flux
Observed wavelength (Å)

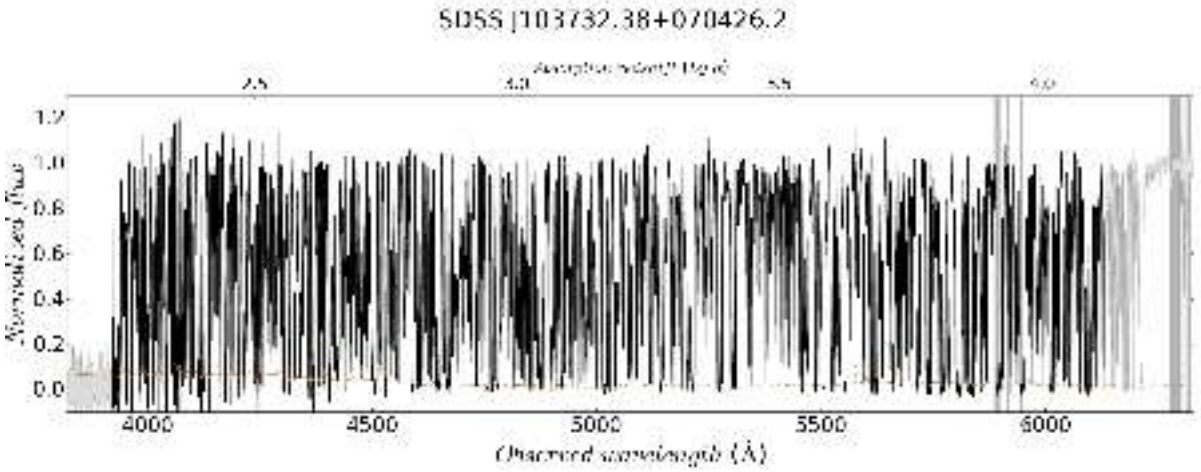
SDSS J103732.38+070426.2
4000
4500
5000
5500
6000

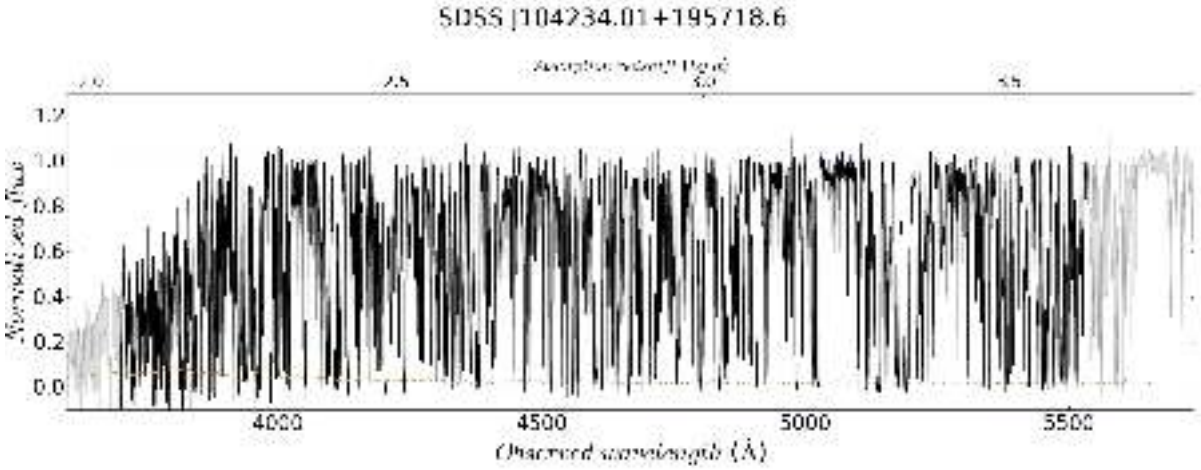
SDSS J104234.01+195718.6
4000
4500
5000
5500

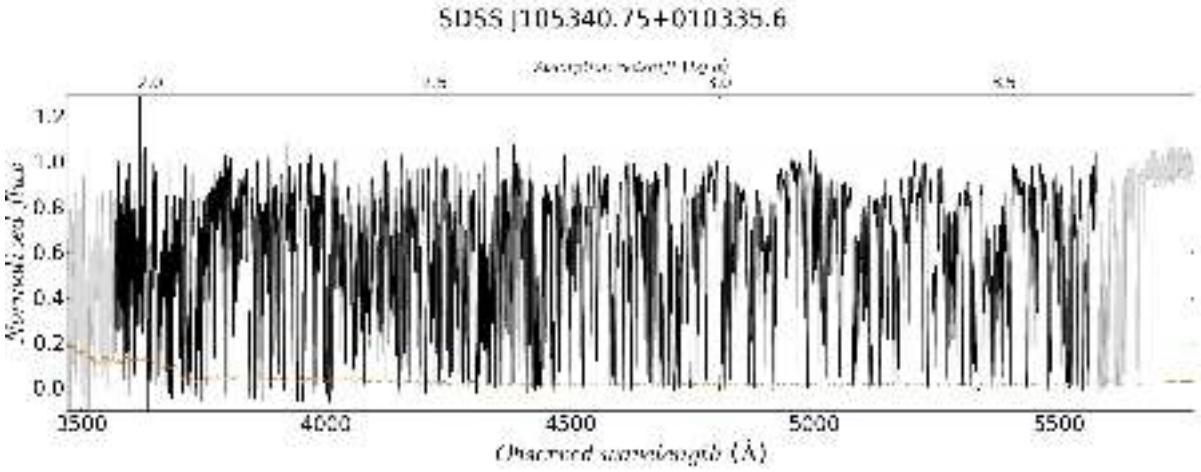
SDSS J105340.75+010335.6
3500
4000
4500
5000
5500

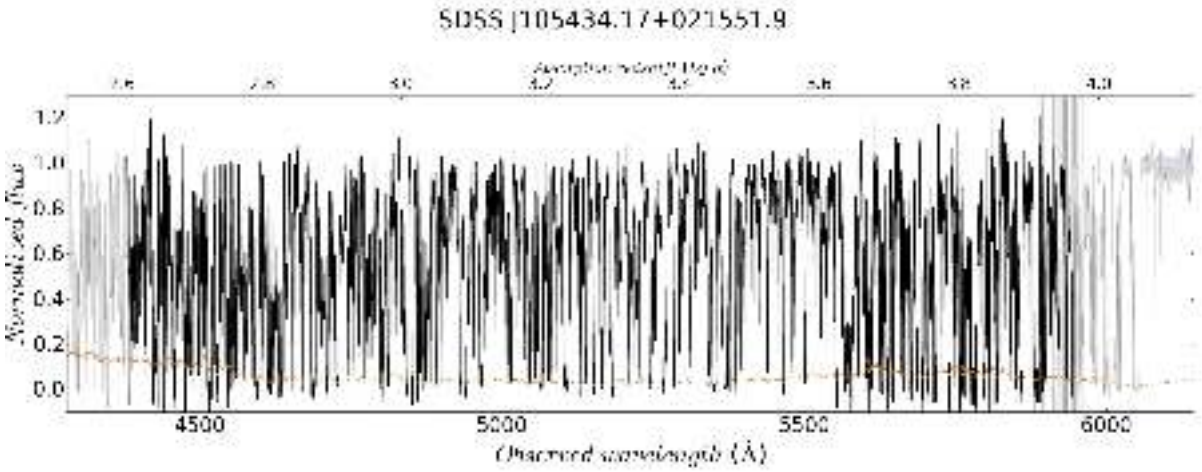
SDSS J105434.17+021551.9
Normalized flux
Observed wavelength (Å)
4500
5000
5500
6000

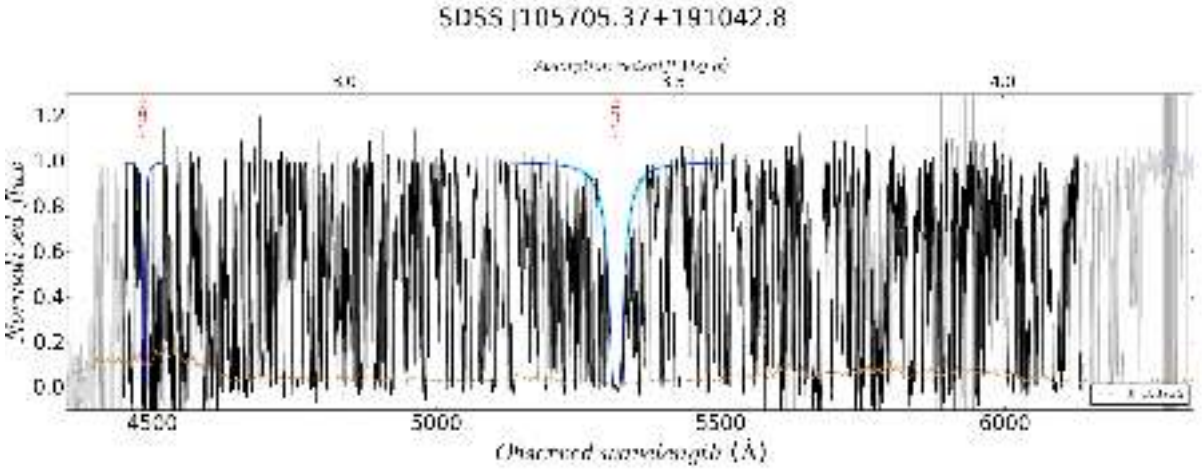
SDSS J105705.37+191042.8
Normalized flux
Observed wavelength (Å)
4500
5000
5500
6000

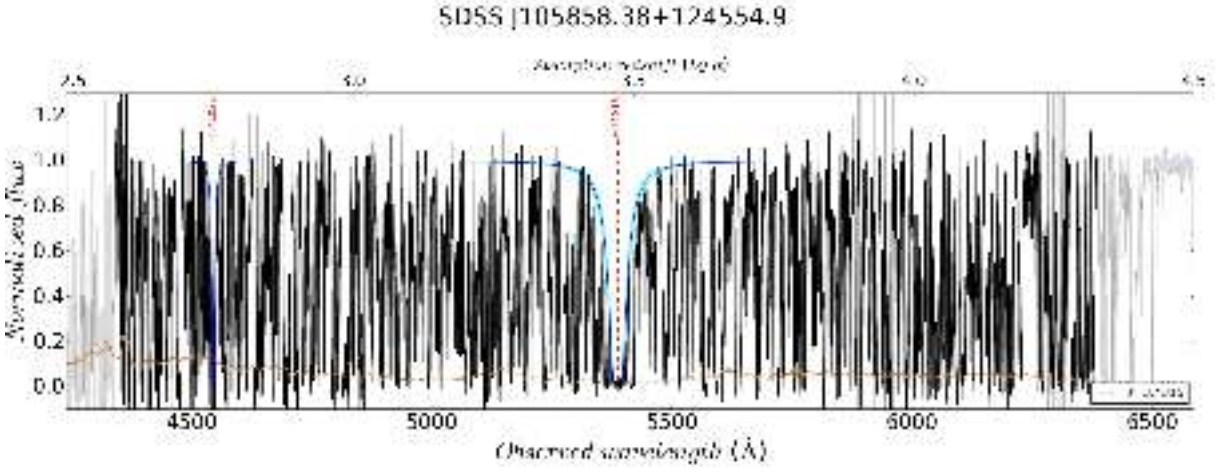
SDSS J105858.38+124554.9
Normalized flux
Observed wavelength (Å)
4500
5000
5500
6000
6500

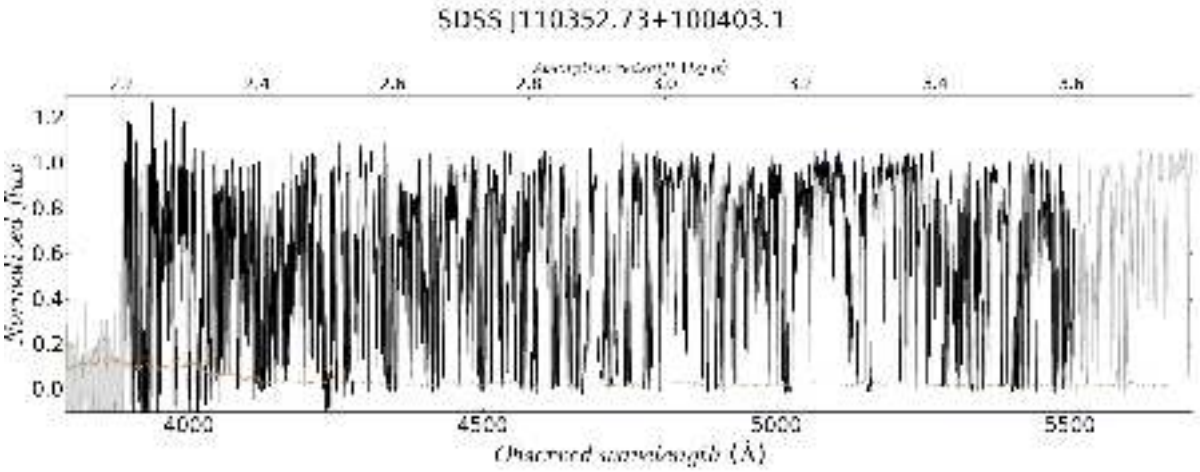
SDSS J110352.73+100403.1
Normalized flux
Observed wavelength (Å)

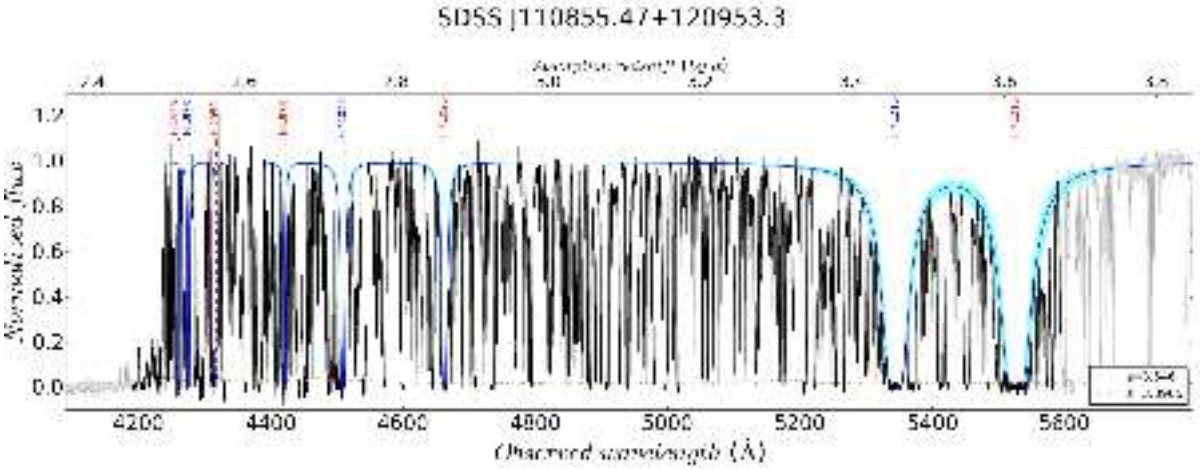
SDSS J110855.47+120953.3
Normalized flux
Observed wavelength (Å)

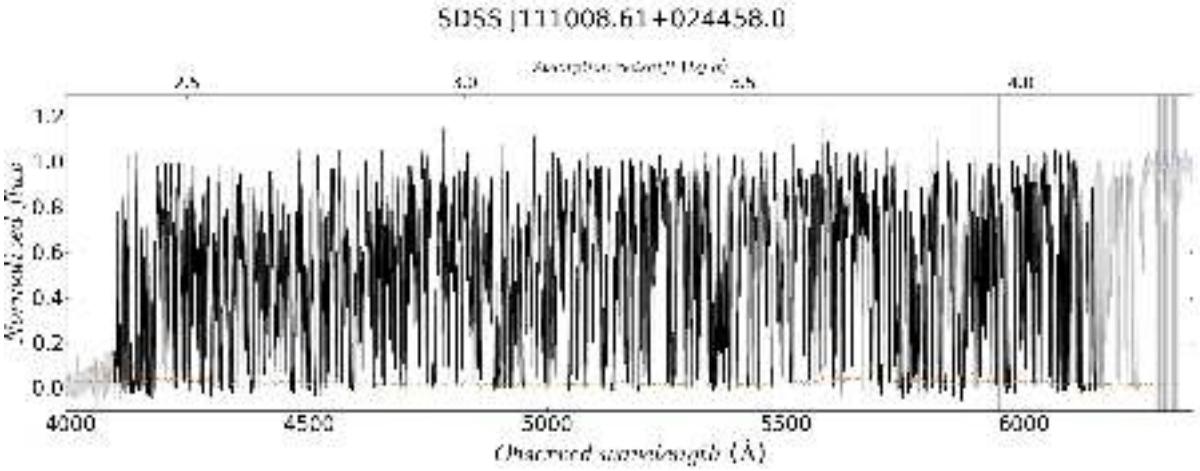
SDSS J111008.61+024458.0
Normalized flux
Observed wavelength (Å)

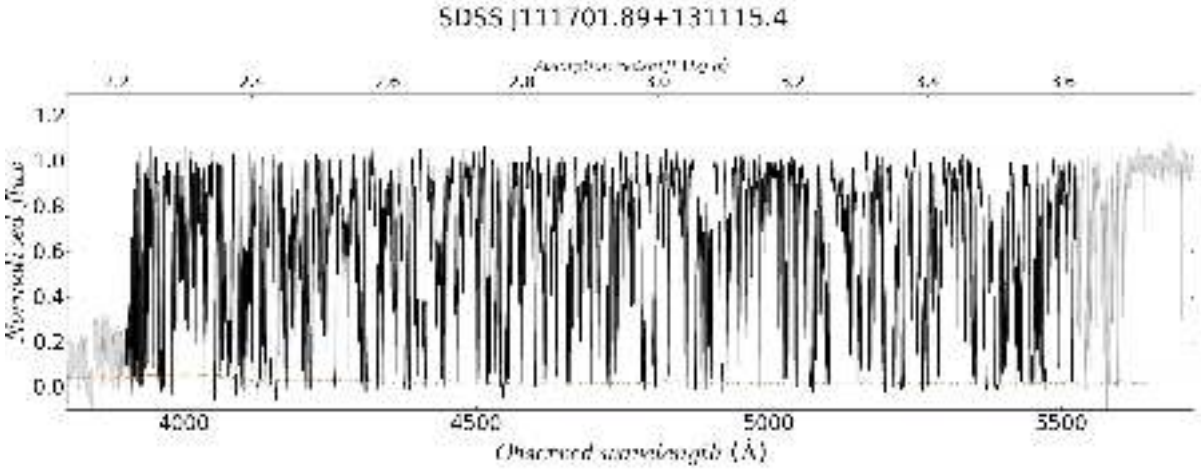
SDSS J111701.89+131115.4
Normalized flux
Observed wavelength (Å)
4000
4500
5000
5500

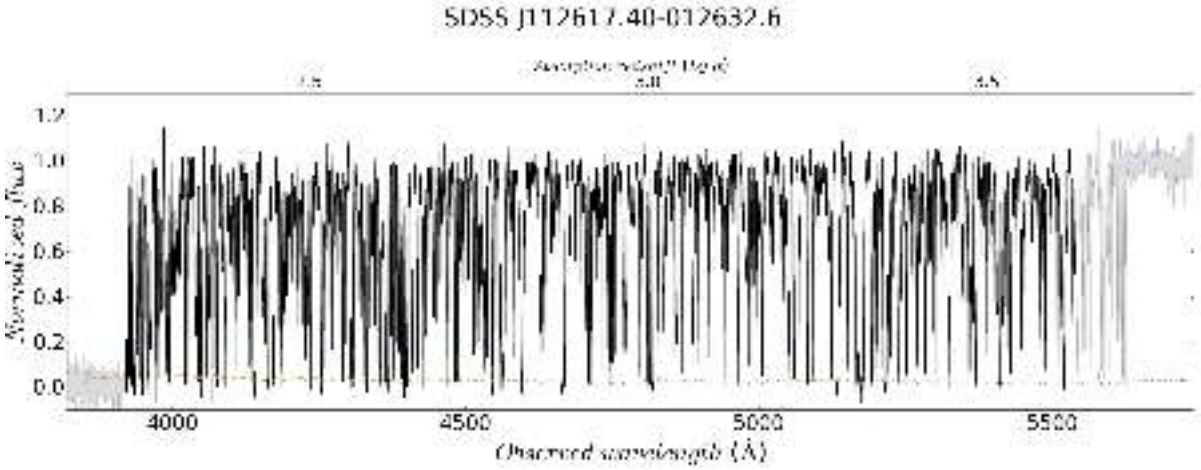
SDSS J112617.40-012632.6
Normalized flux
Observed wavelength (Å)
4000
4500
5000
5500

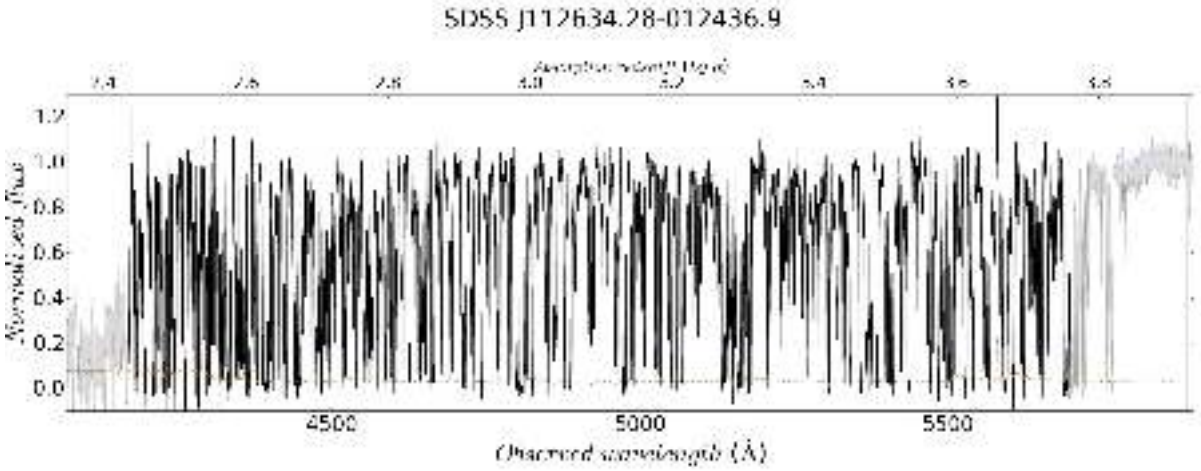
SDSS J112634.28-012436.9
Normalized flux
Observed wavelength (Å)
4500
5000
5500

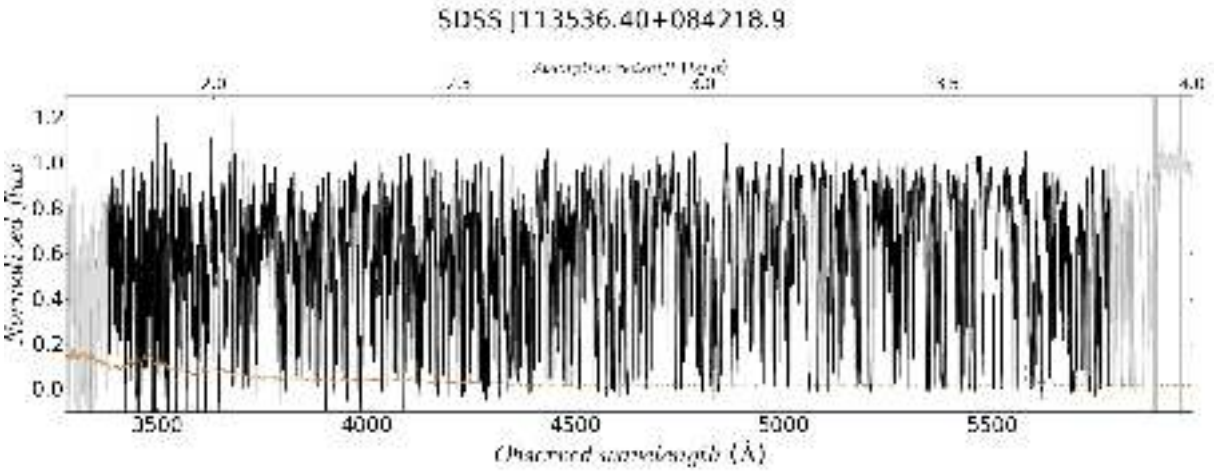
SDSS J113536.40+084218.9
Normalized flux
3500
4000
4500
5000
5500
Observed wavelength (Å)

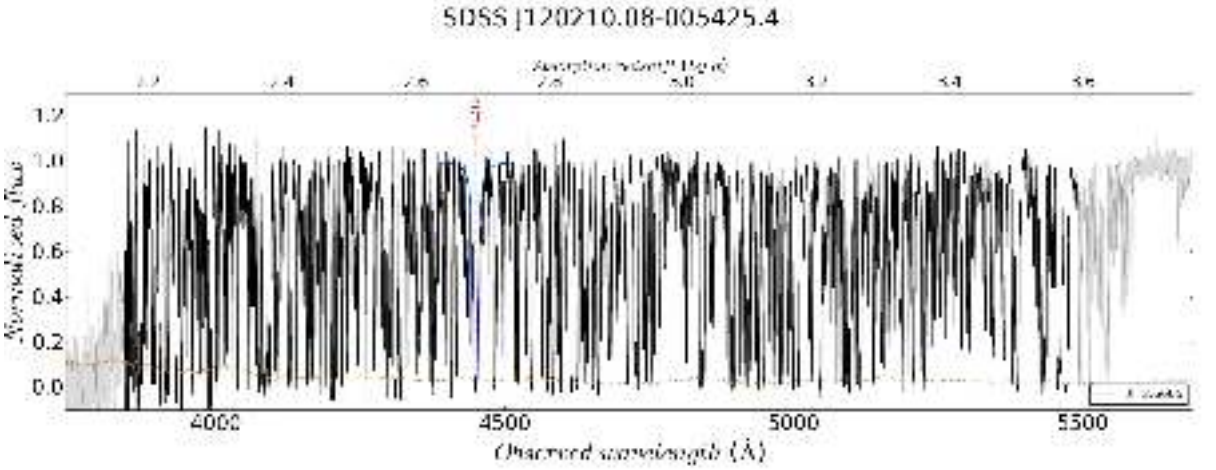
SDSS J120210.08-005425.4
Normalized flux
4000
4500
5000
5500
Observed wavelength (Å)

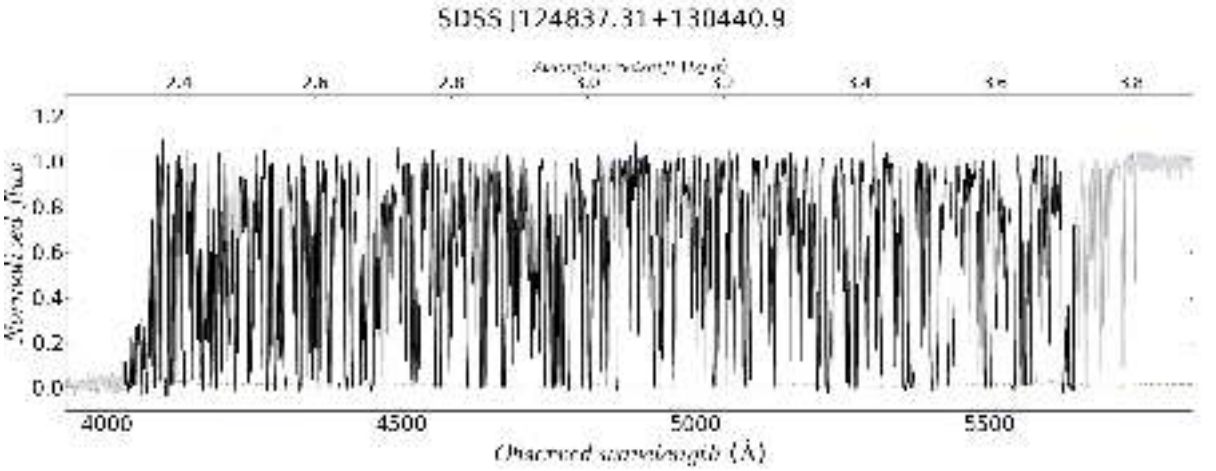
SDSS J124837.31+130440.9
Normalized flux
4000
4500
5000
5500
Observed wavelength (Å)

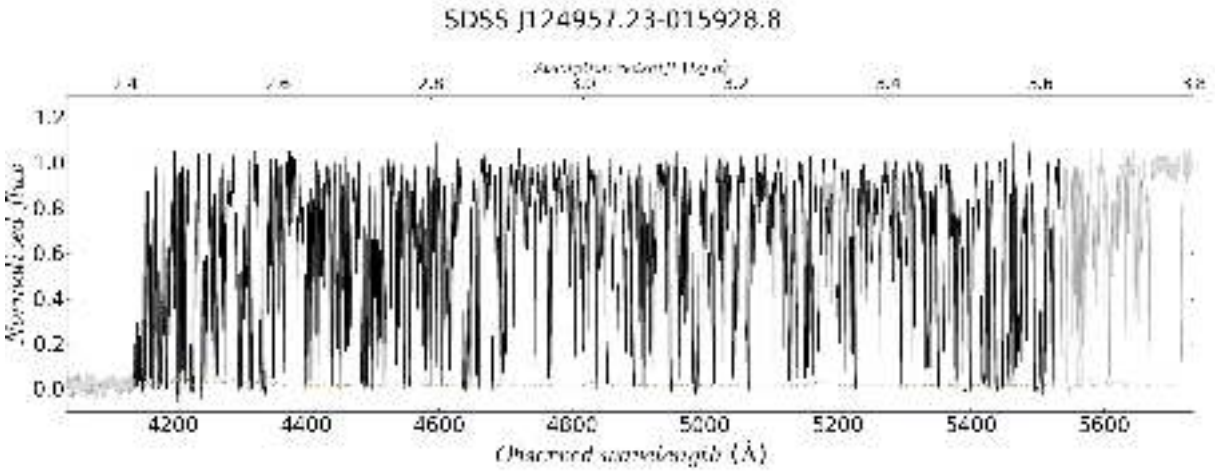
SDSS J124957.23-015928.8
Normalized Flux
Observed wavelength (Å)

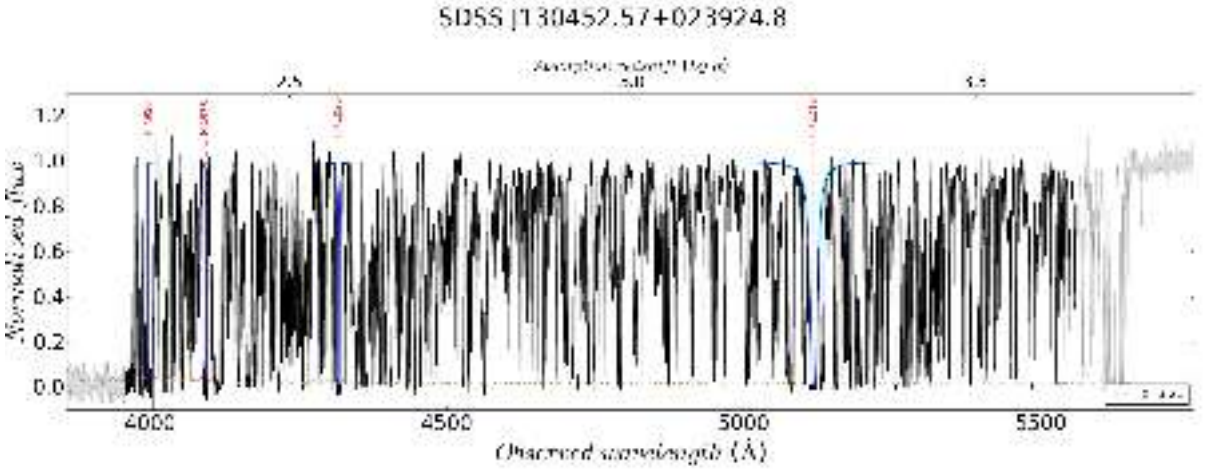
SDSS J130452.57+023924.8
Normalized Flux
Observed wavelength (Å)

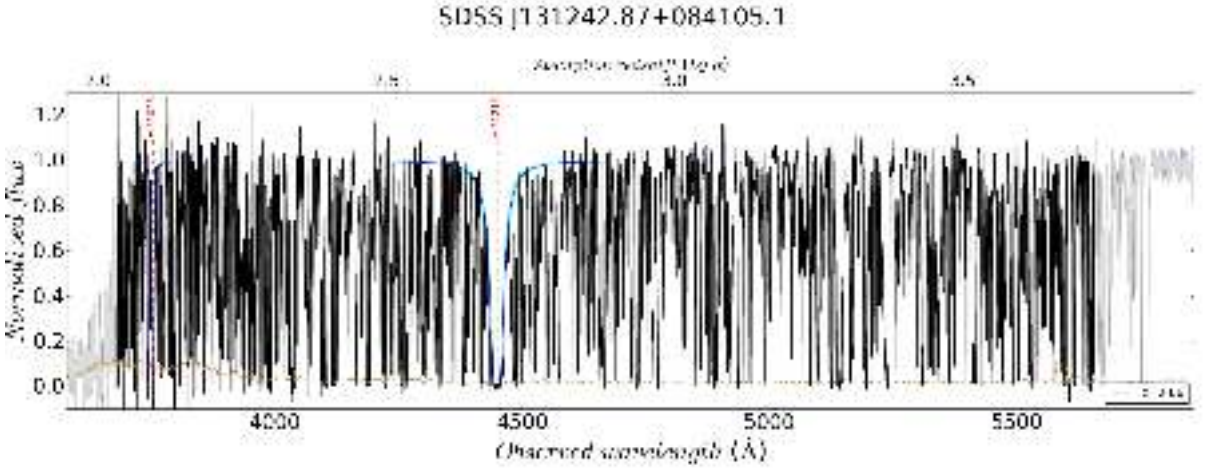
SDSS J131242.87+084105.1
Normalized Flux
Observed wavelength (Å)

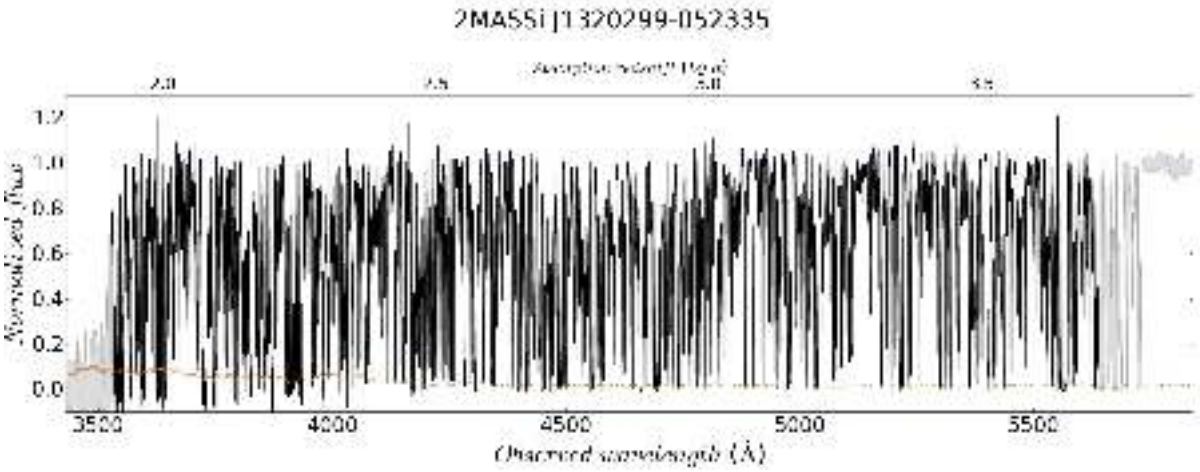
2MASSi J1320299-052335
3500
4000
4500
5000
5500
Observed wavelength (Å)

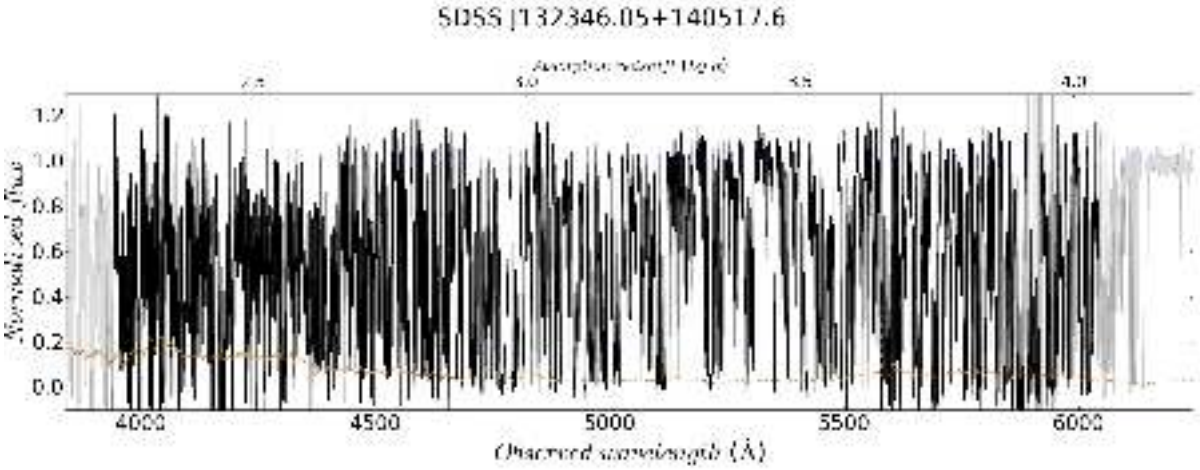
SDSS J132346.05+140517.6
4000
4500
5000
5500
6000
Observed wavelength (Å)

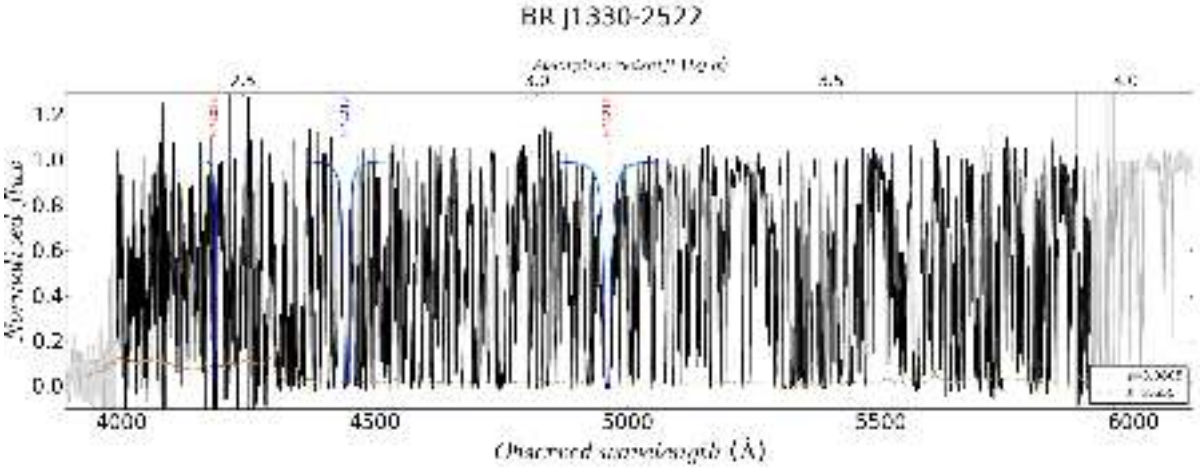
BR J1330-2522
4000
4500
5000
5500
6000
Observed wavelength (Å)

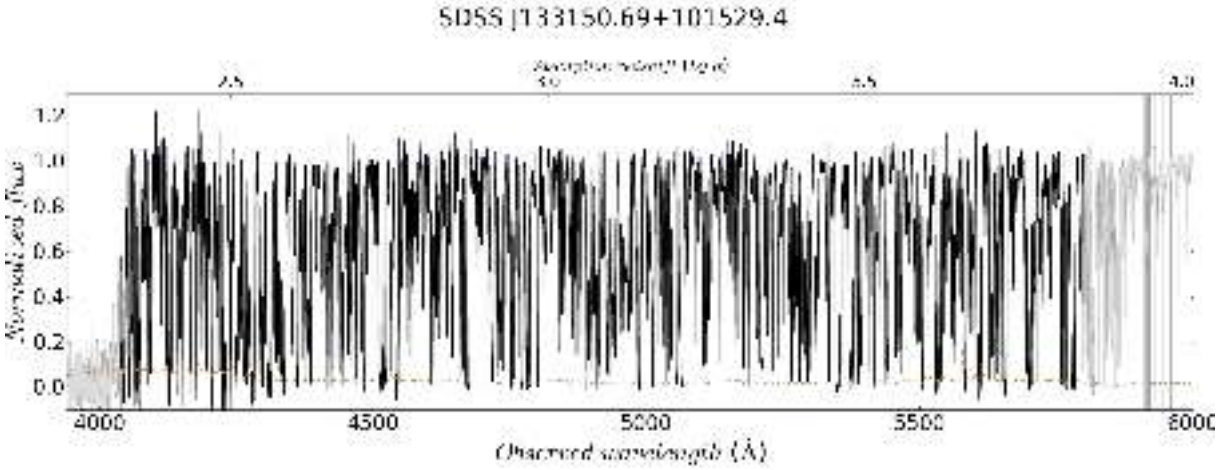
SDSS J133150.69+101529.4
Normalized flux
Observed wavelength (Å)

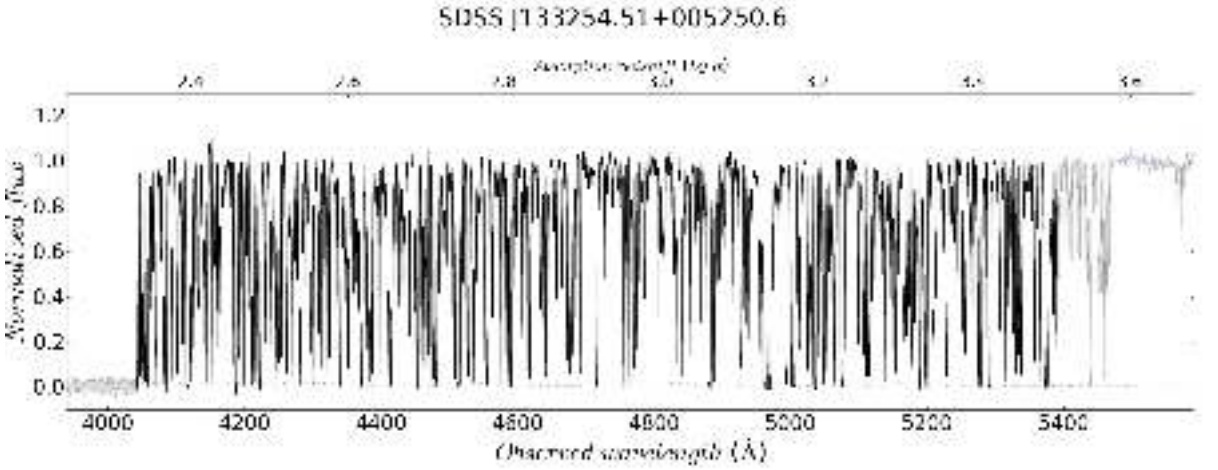
SDSS J133254.51+005250.6
Normalized flux
Observed wavelength (Å)

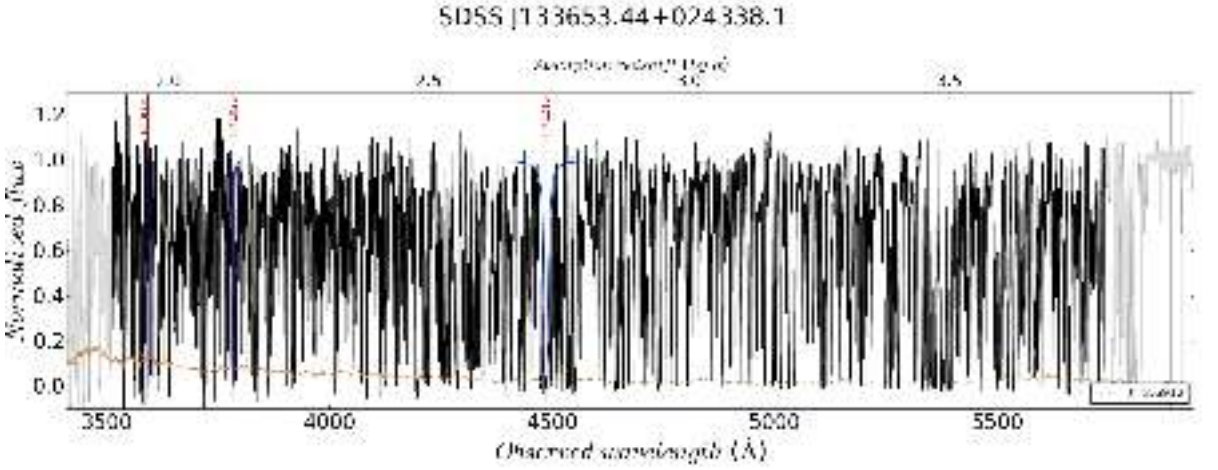
SDSS J133653.44+024338.1
Normalized flux
Observed wavelength (Å)

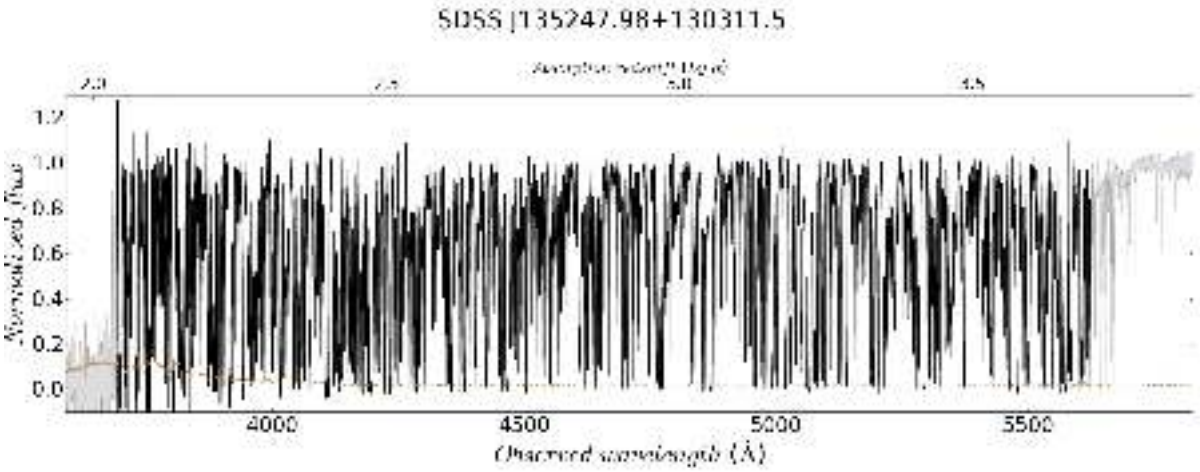
SDSS J135247.98+130311.5
Normalized flux
Observed wavelength (Å)

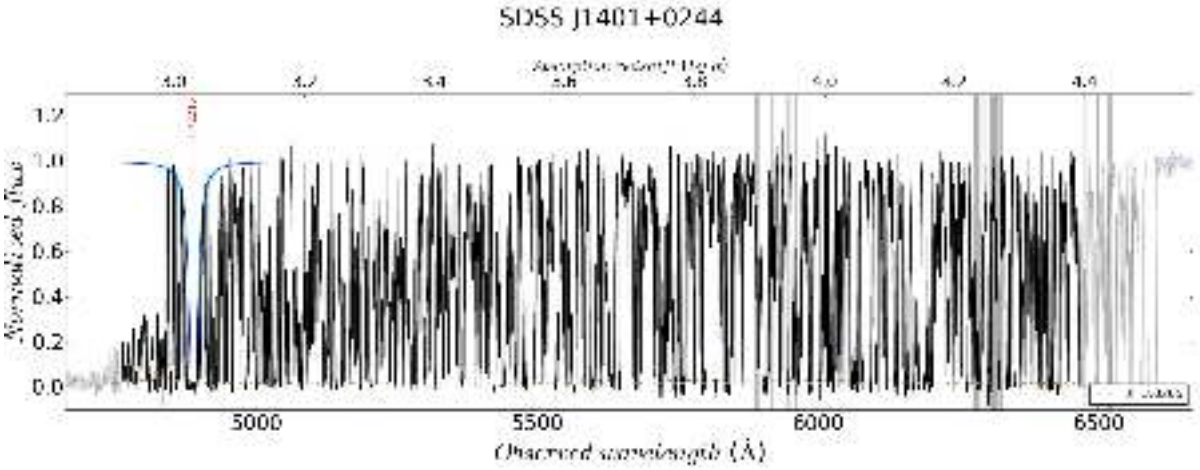
SDSS J1401+0244
Normalized flux
Observed wavelength (Å)

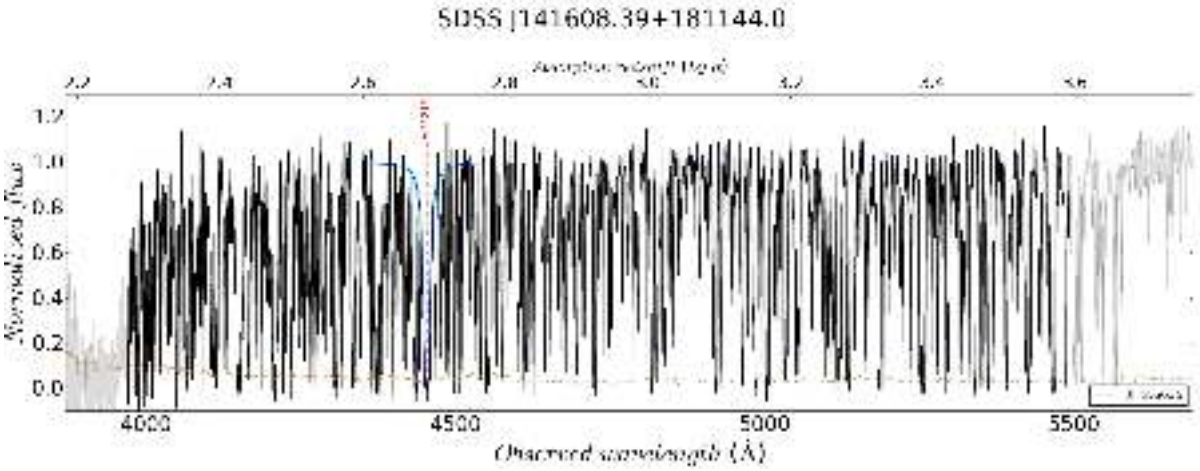
SDSS J141608.39+181144.0
Normalized flux
Observed wavelength (Å)

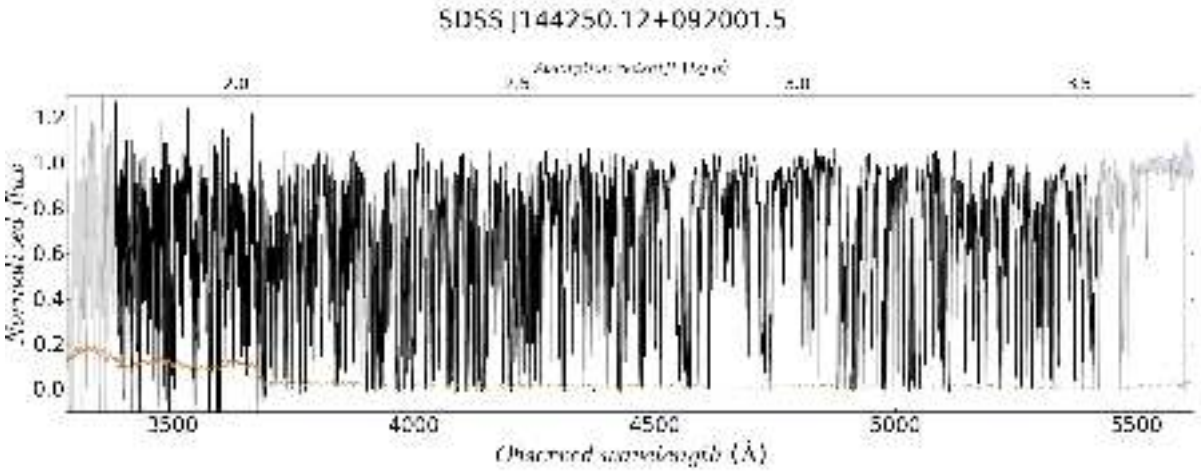
SDSS J144250.12+092001.5
Normalized Flux
Observed wavelength (Å)

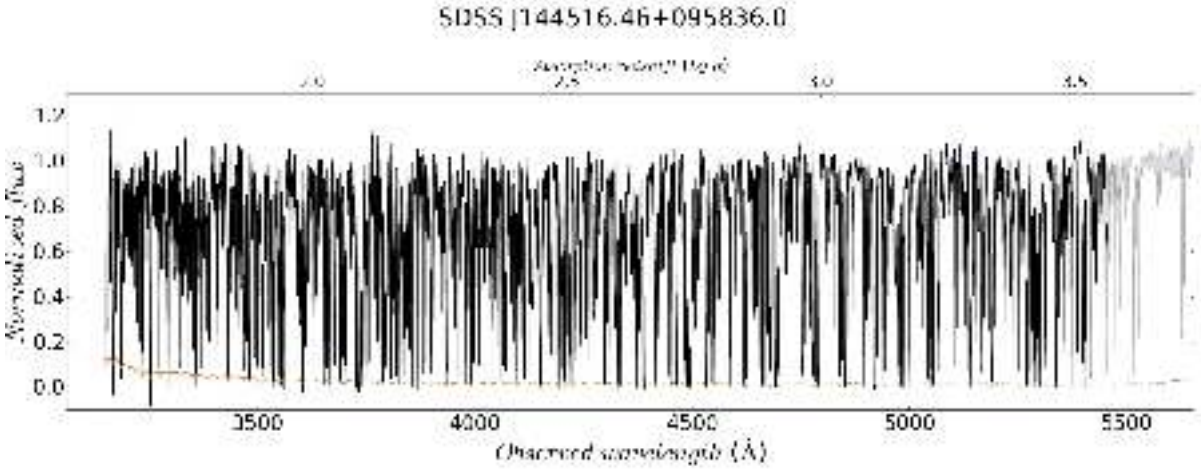
SDSS J144516.46+095836.0
Normalized Flux
Observed wavelength (Å)

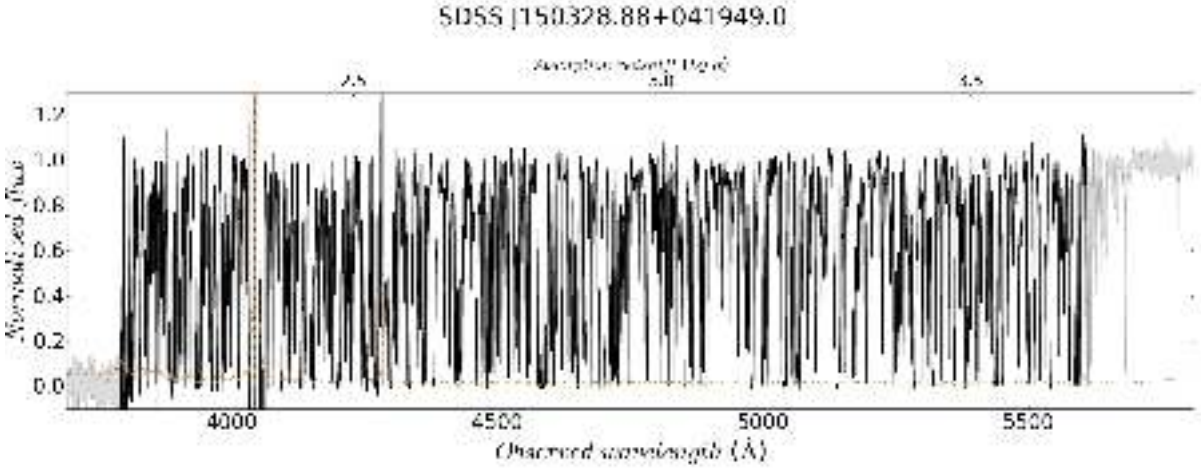
SDSS J150328.88+041949.0
Normalized Flux
Observed wavelength (Å)

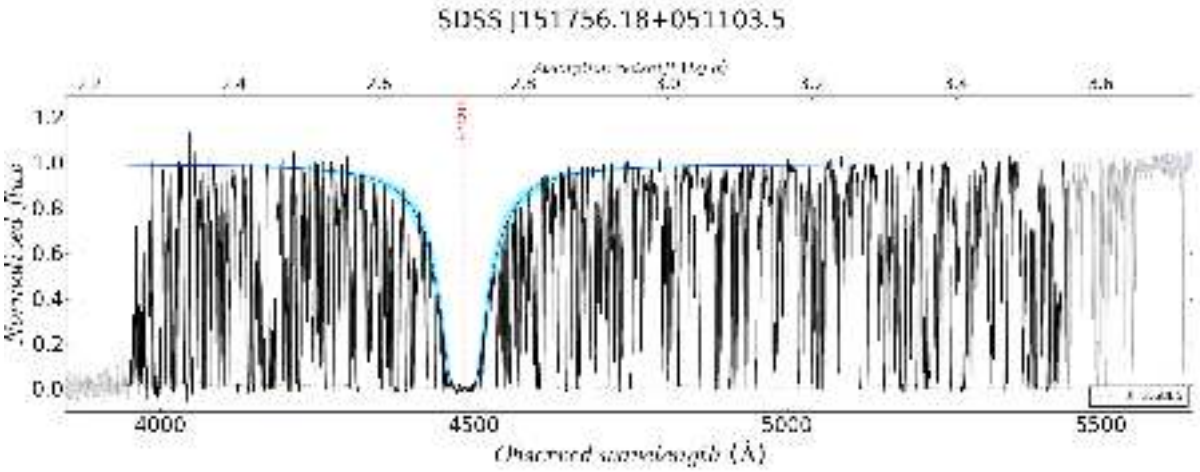
SDSS J151756.18+051103.5
4000
4500
5000
5500
Observed wavelength (Å)

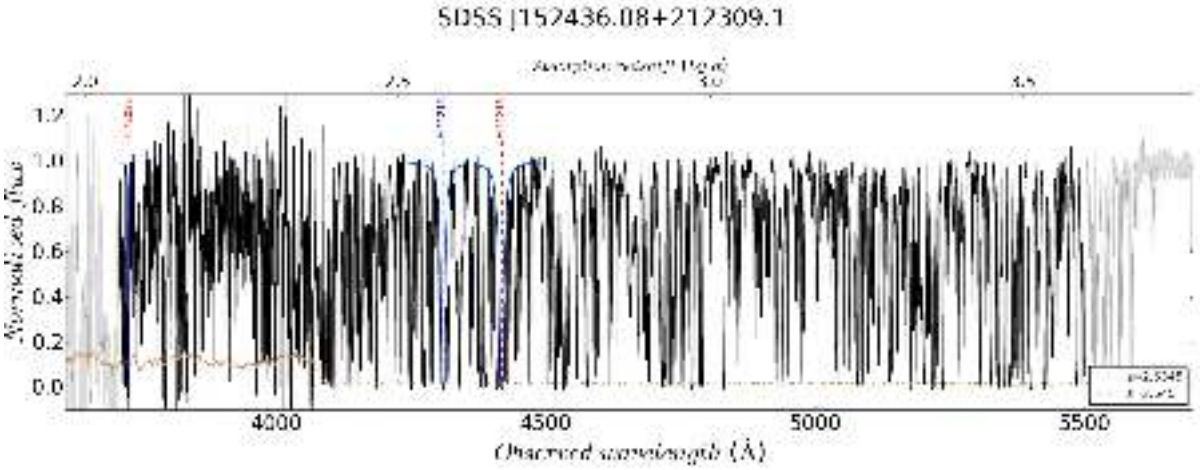
SDSS J152436.08+212309.1
4000
4500
5000
5500
Observed wavelength (Å)

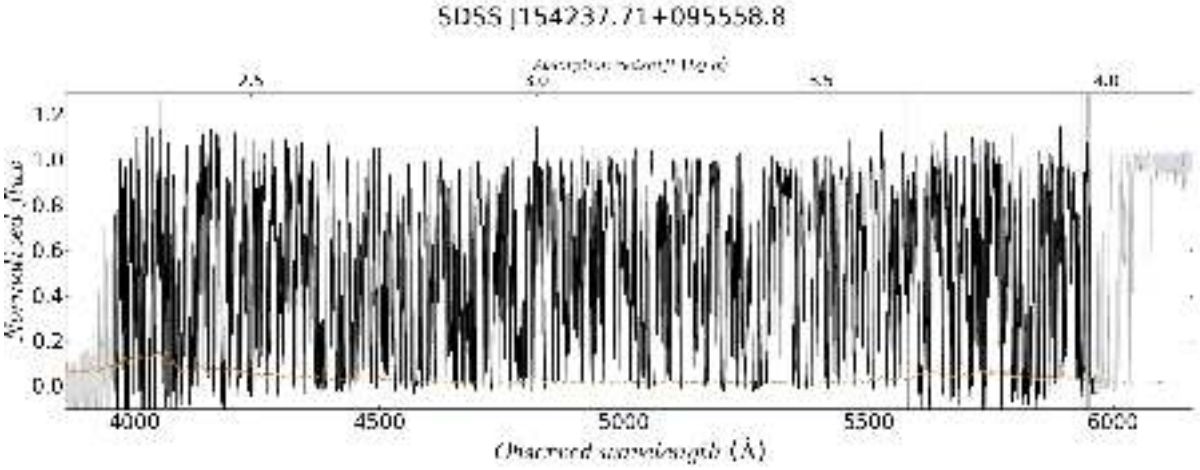
SDSS J154237.71+095558.8
4000
4500
5000
5500
6000
Observed wavelength (Å)

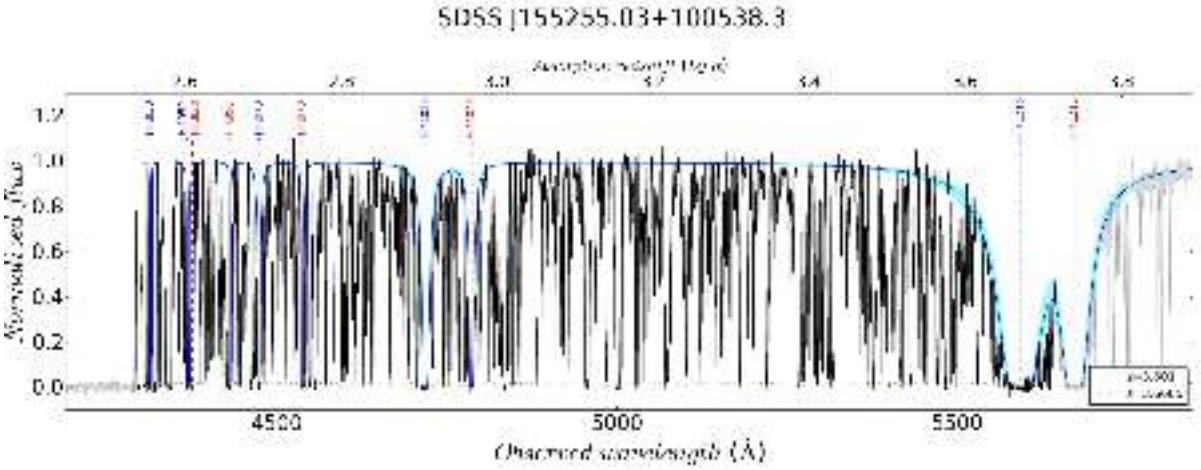
SDSS J155255.03+100538.3
Normalized flux
Observed wavelength (Å)
4500
5000
5500

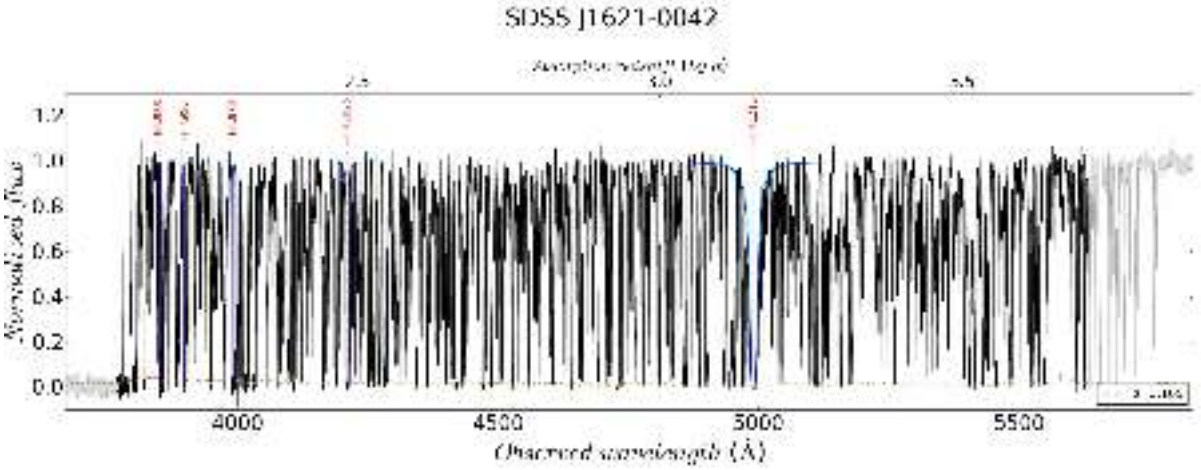
SDSS J1621-0042
Normalized flux
Observed wavelength (Å)
4000
4500
5000
5500

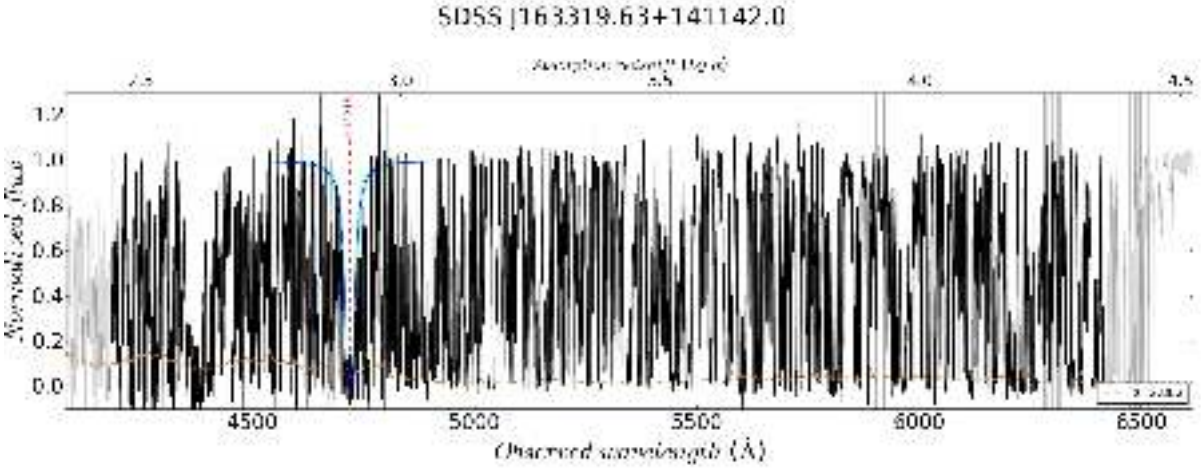
SDSS J163319.63+141142.0
Normalized flux
Observed wavelength (Å)
4500
5000
5500
6000
6500

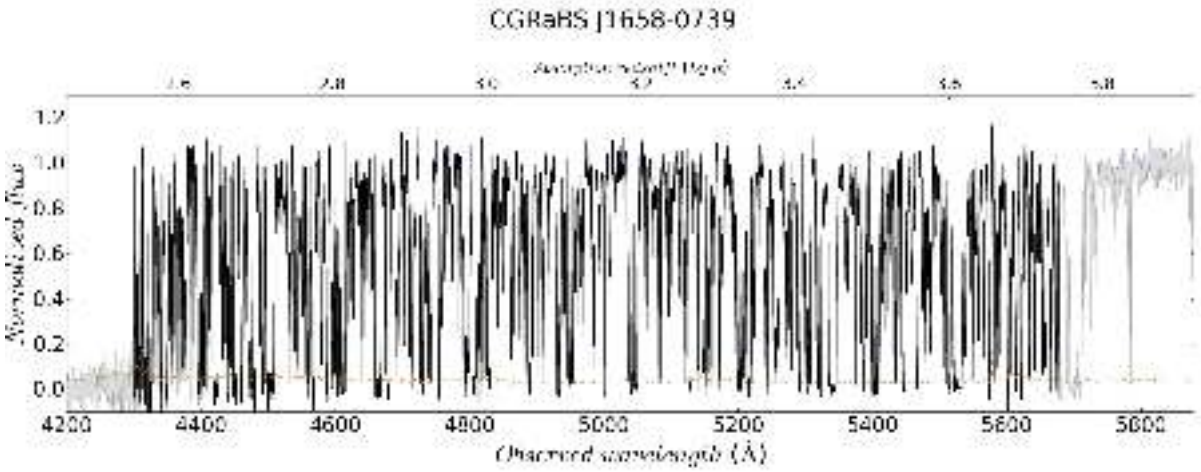
CGRaBS J1658-0739
Normalized flux
4200
4400
4600
4800
5000
5200
5400
5600
5800
Observed wavelength (Å)

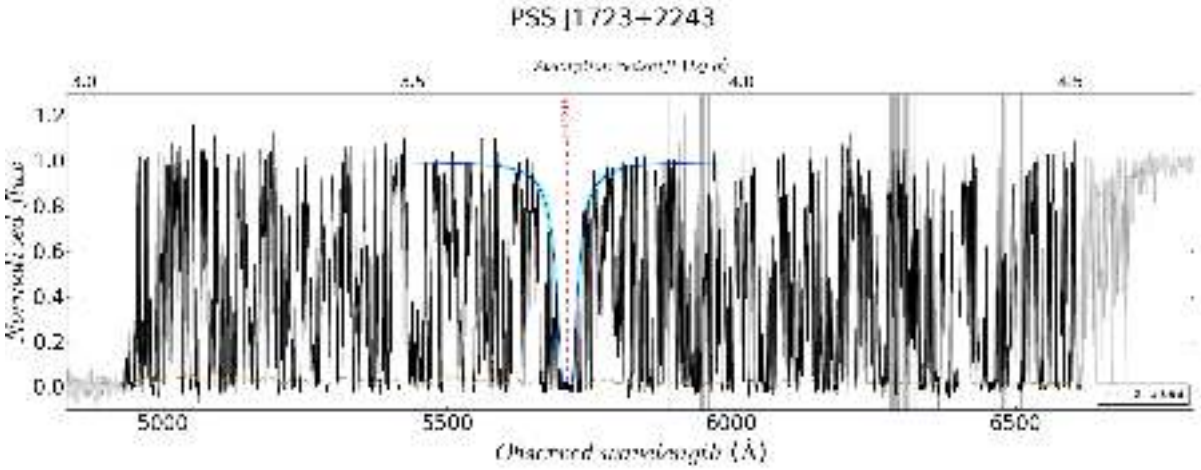
PSS J1723+2243
Normalized flux
5000
5500
6000
6500
Observed wavelength (Å)

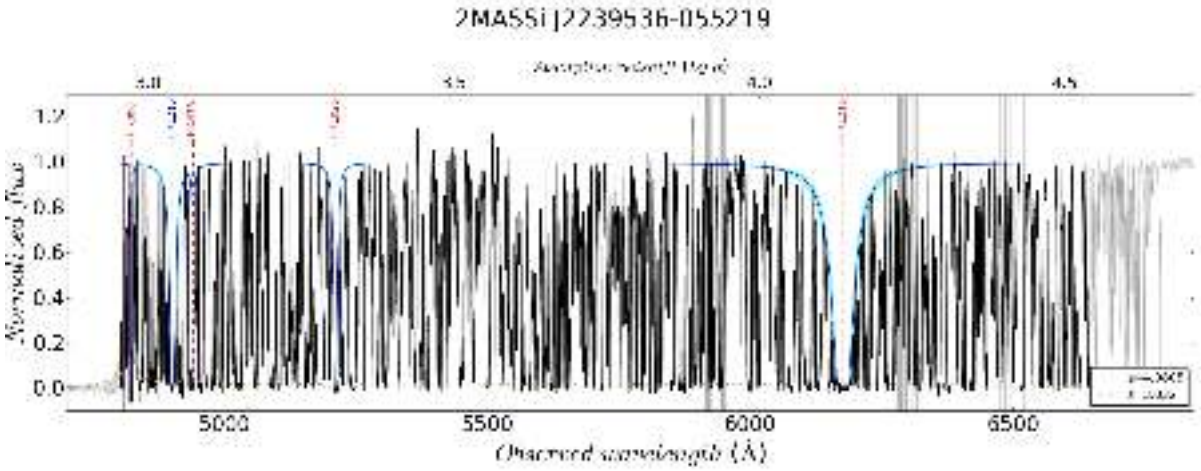
2MASSi J2239536-055219
Normalized flux
5000
5500
6000
6500
Observed wavelength (Å)

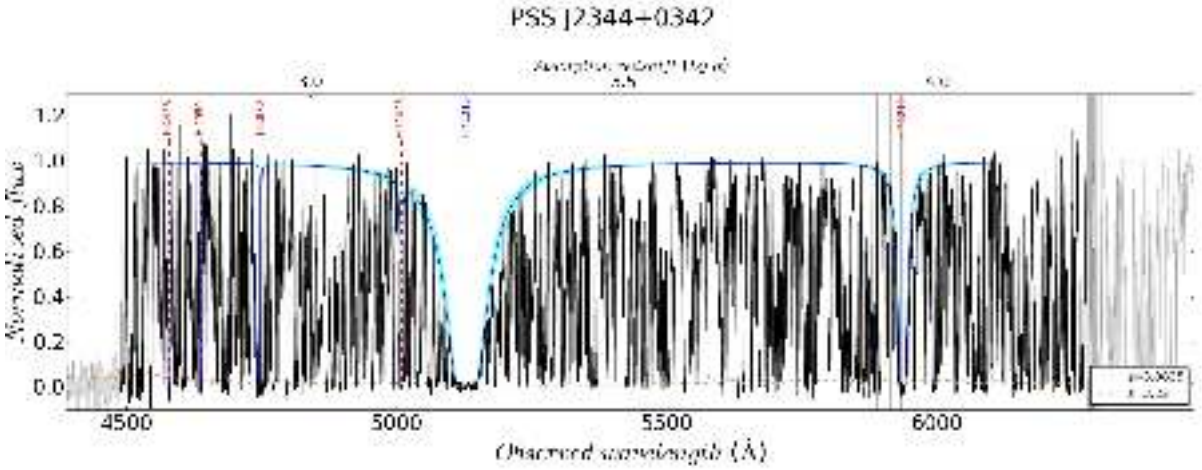
PSS J2344+0342
Normalized flux
Observed wavelength (Å)
4500
5000
5500
6000

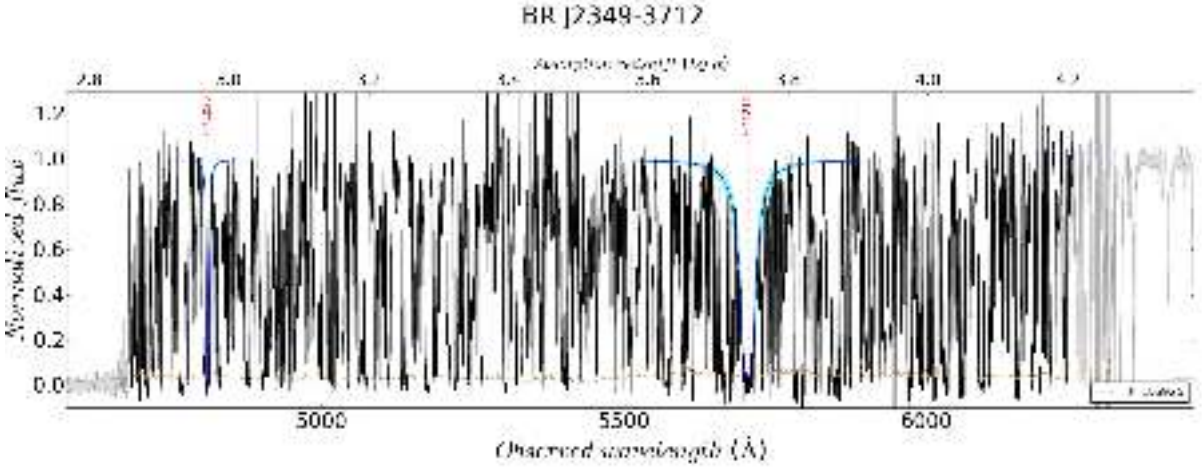
BR J2349-3712
Normalized flux
Observed wavelength (Å)
5000
5500
6000

Appendix H

XQ-100 DLA fits

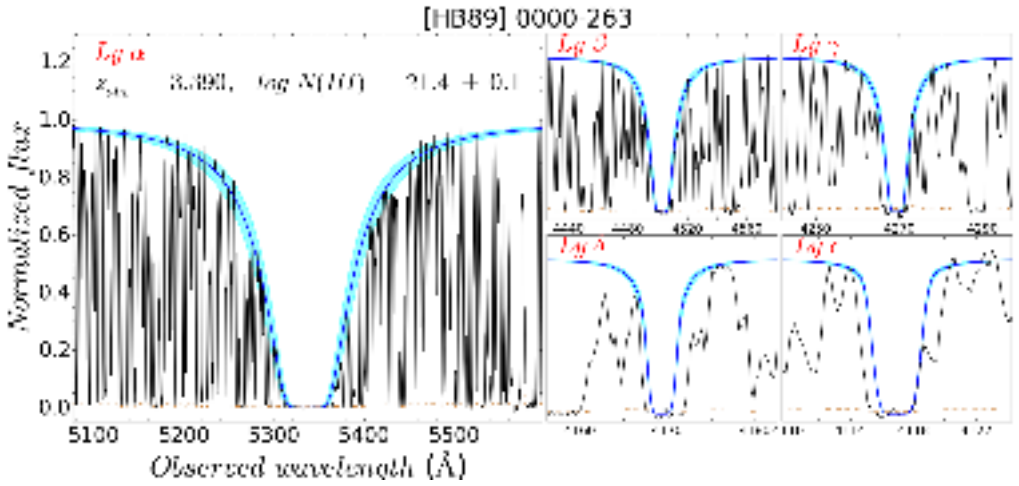

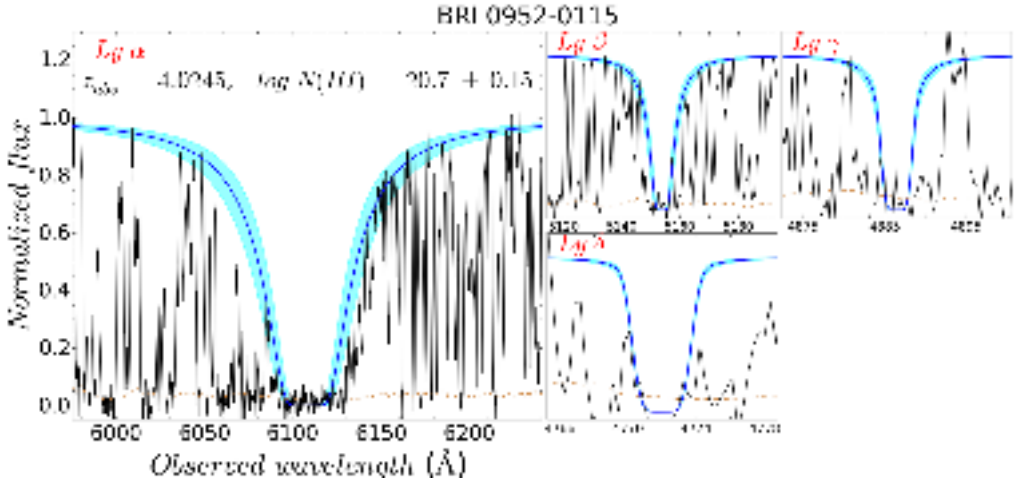

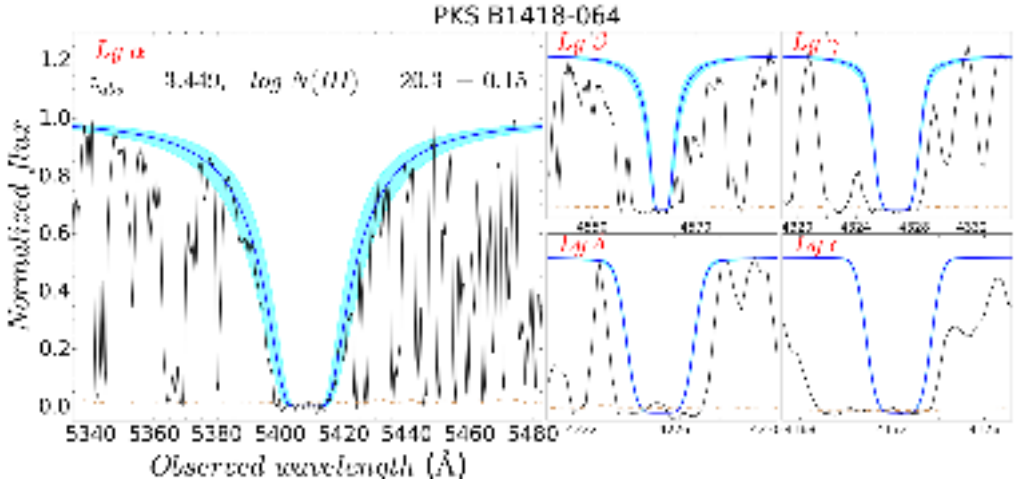
PKS B1418-064
Lyα
Lyβ
Lyγ
Lyδ
Lyε
Normalised flux
Observed wavelength (Å)

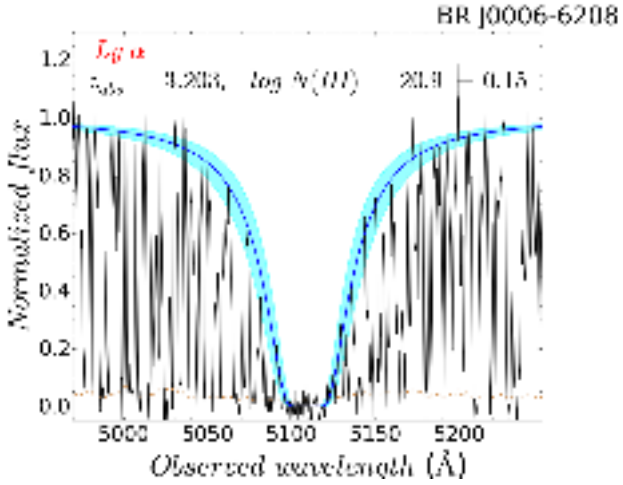
BR J0006-6208
Lyα
Normalised flux
Observed wavelength (Å)

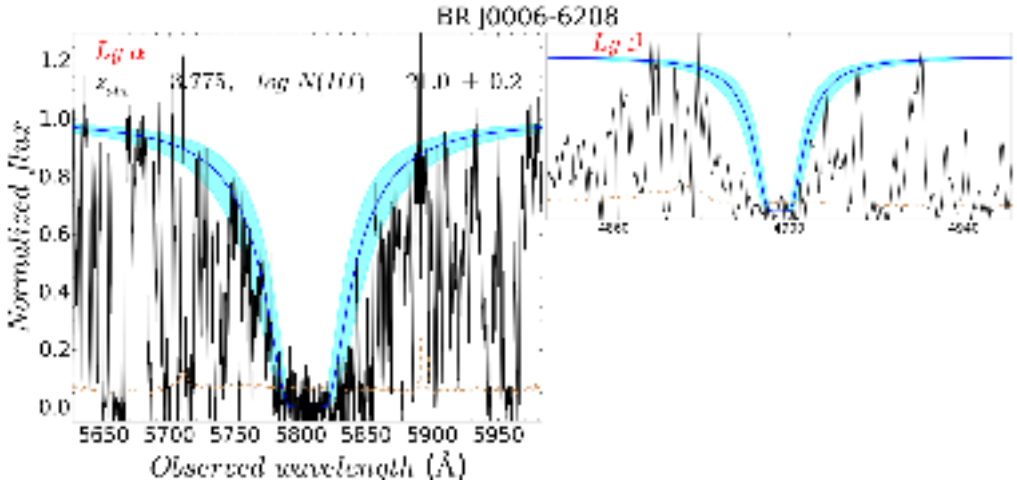
BR J0006-6208
Lyα
Lyβ
Normalised flux
Observed wavelength (Å)

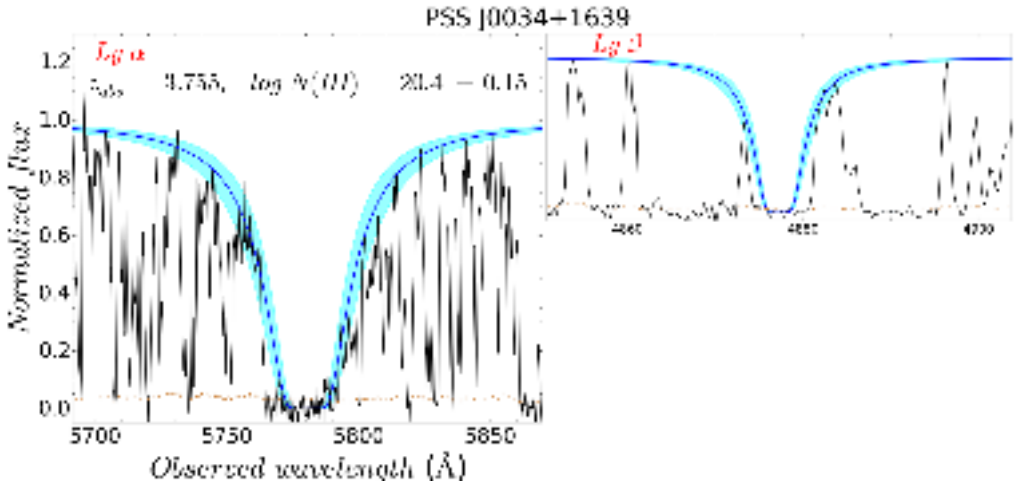
PSS J0034+1639
Lyα
Lyβ
Normalised flux
Observed wavelength (Å)

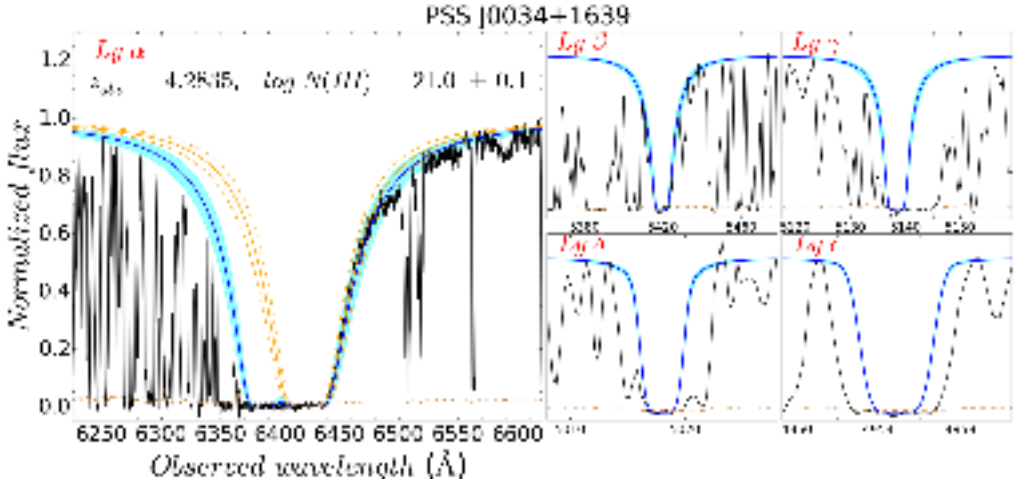
PSS J0034+1639
Lyα
Lyβ
Lyγ
Lyδ
Lyε
Normalised flux
Observed wavelength (Å)

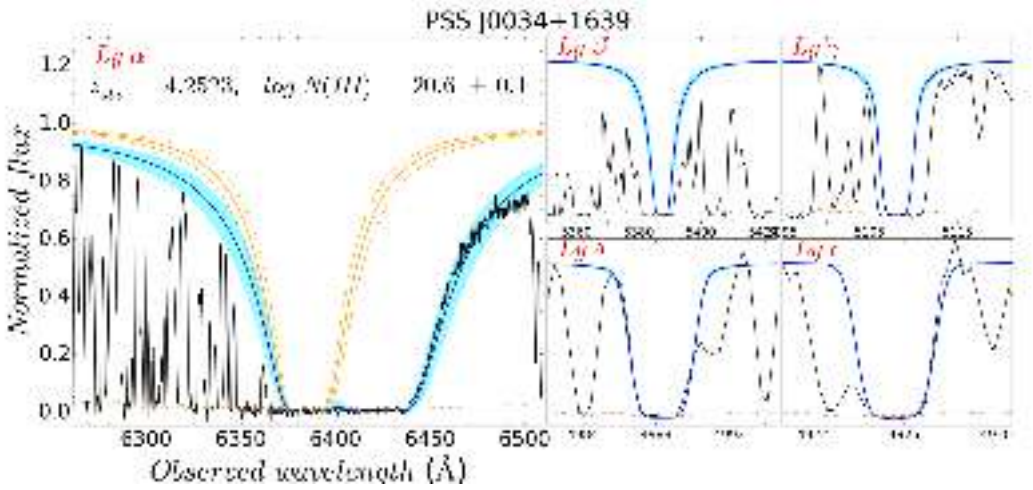
PSS J0034+1639
Lyα
Lyβ
Lyγ
Lyδ
Lyε
Normalised flux
Observed wavelength (Å)

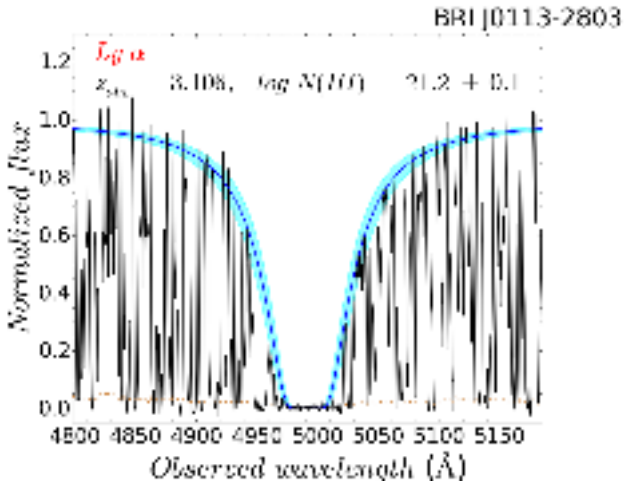
BRI J0113-2803
Lyα
3.108, log N(HI) 21.2 ± 0.1
Normalised flux
Observed wavelength (Å)

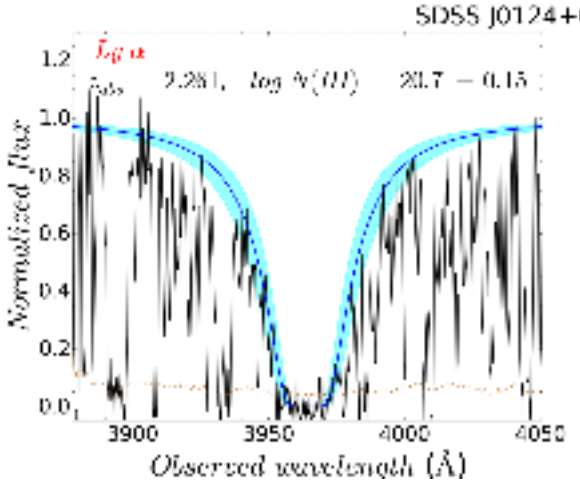
SDSS J0124+0044
Lyα
2.281, log N(HI) 20.7 ± 0.15
Normalised flux
Observed wavelength (Å)

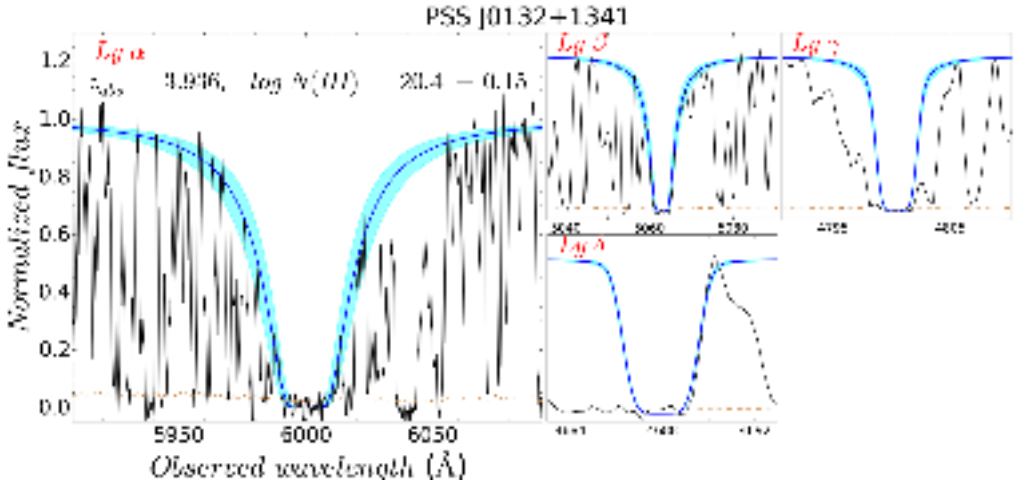
PSS J0132+1341
Lyα
3.936, log N(HI) 20.4 ± 0.15
Lyβ
Lyγ
Lyδ
Normalised flux
Observed wavelength (Å)

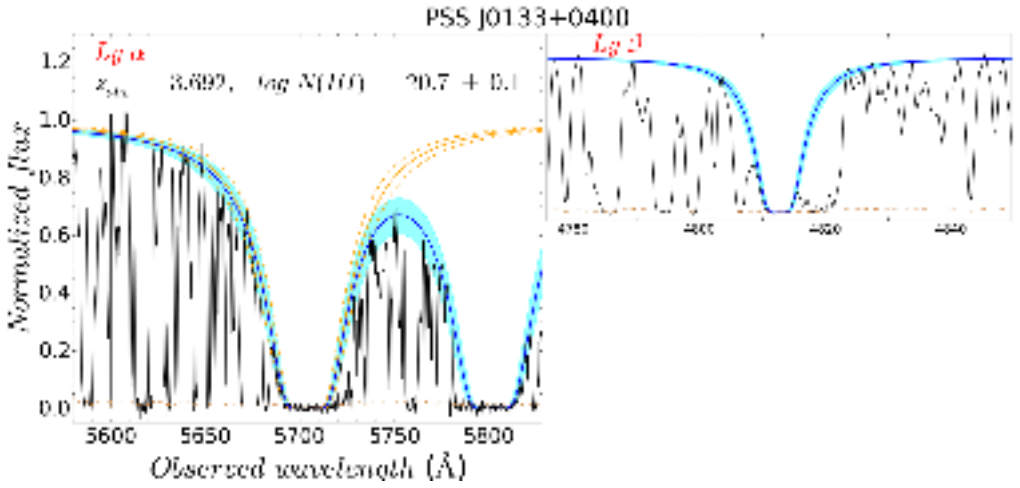
PSS J0133+0400
Lyα
Lyβ
Normalised flux
Observed wavelength (Å)

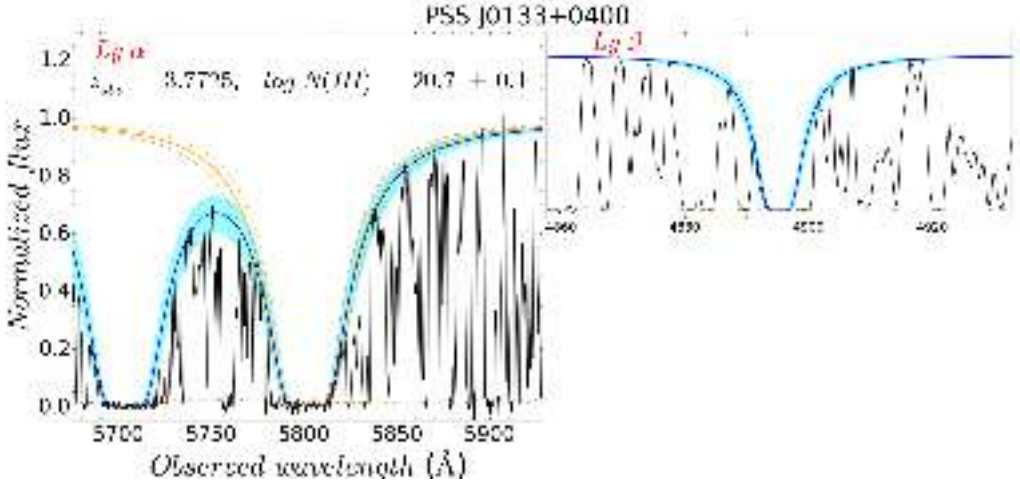
PSS J0133+0400
Lyα
Lyβ
Normalised flux
Observed wavelength (Å)

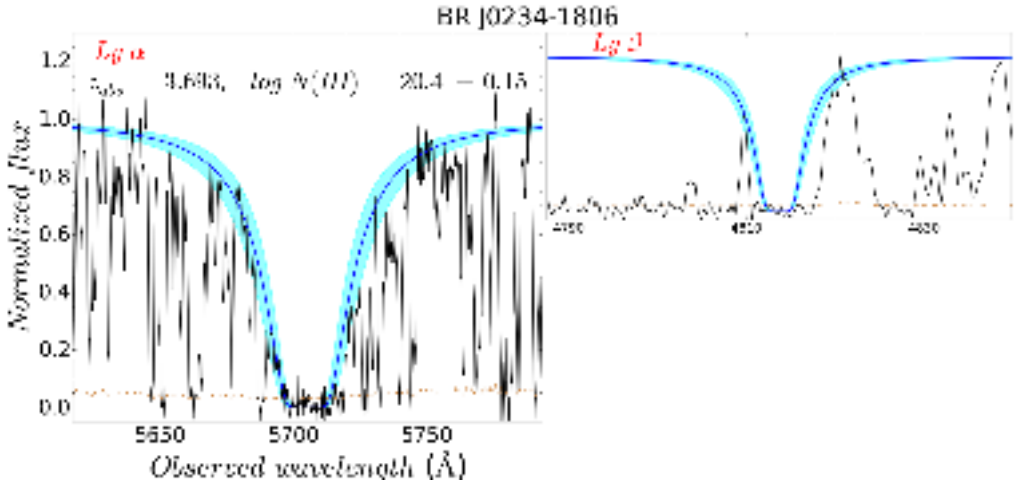
BR J0234-1806
Lyα
Lyβ
Normalised flux
Observed wavelength (Å)

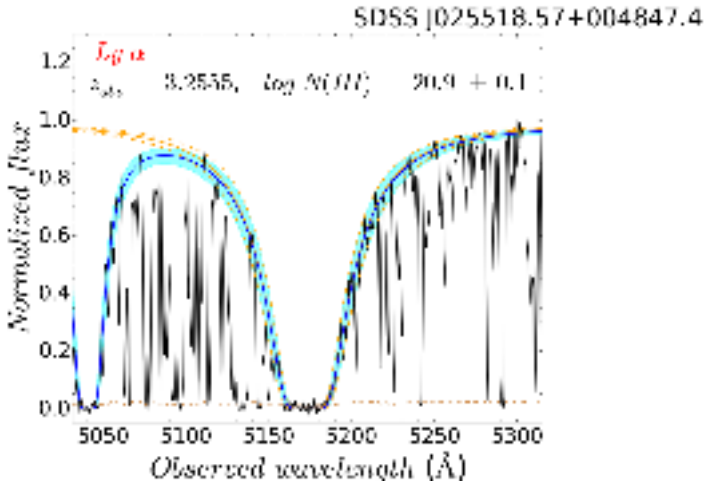
SDSS J025518.57+004847.4
Normalised flux
Observed wavelength (Å)

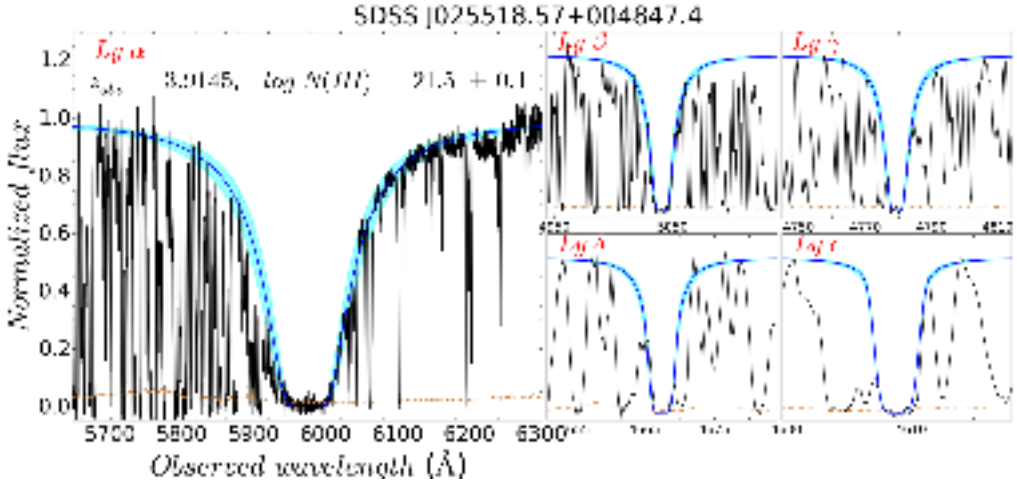
SDSS J025518.57+004847.4
Normalised flux
Observed wavelength (Å)

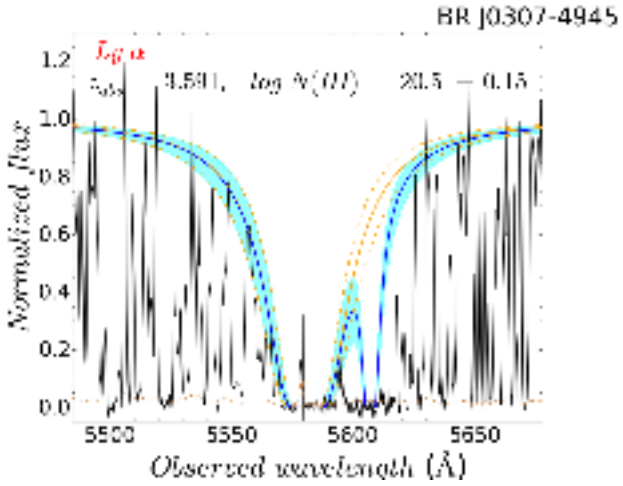
BR J0307-4945
Normalised flux
Observed wavelength (Å)

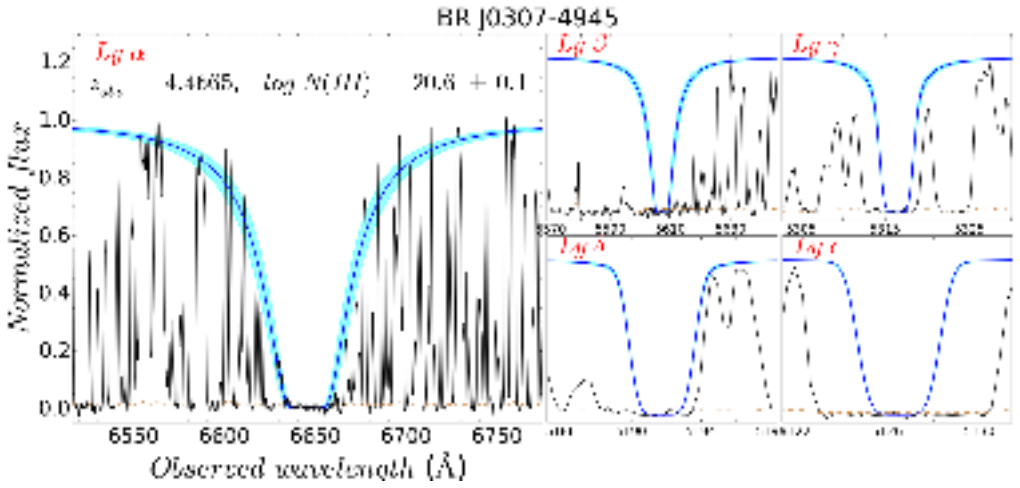
BR J0307-4945
Lyβ α
4.4665, log N(HI) 20.6 ± 0.1
Lyβ 2
Lyβ 3
Lyβ 5
Lyβ 6
Normalised flux
Observed wavelength (Å)

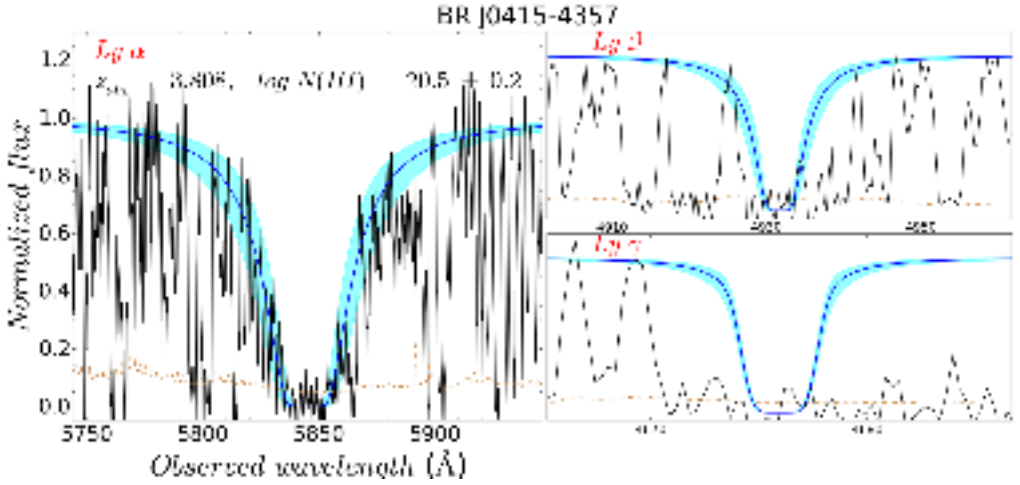
BR J0415-4357
Lyβ α
3.808, log N(HI) 20.5 ± 0.2
Lyβ 2
Lyβ 3
Normalised flux
Observed wavelength (Å)

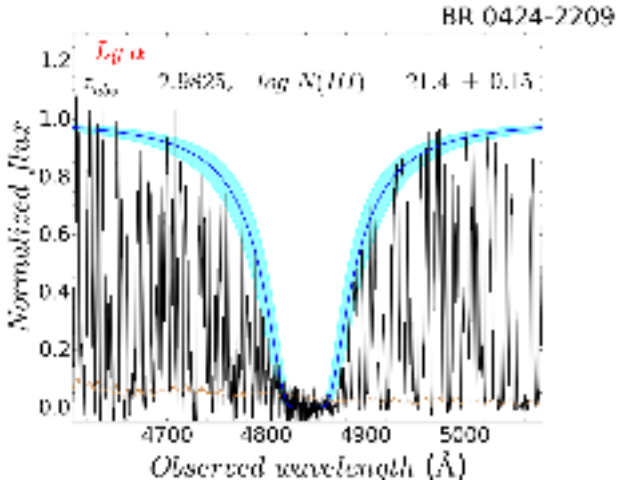
BR 0424-2209
Lyβ α
2.5825, log N(HI) 21.4 ± 0.15
Normalised flux
Observed wavelength (Å)

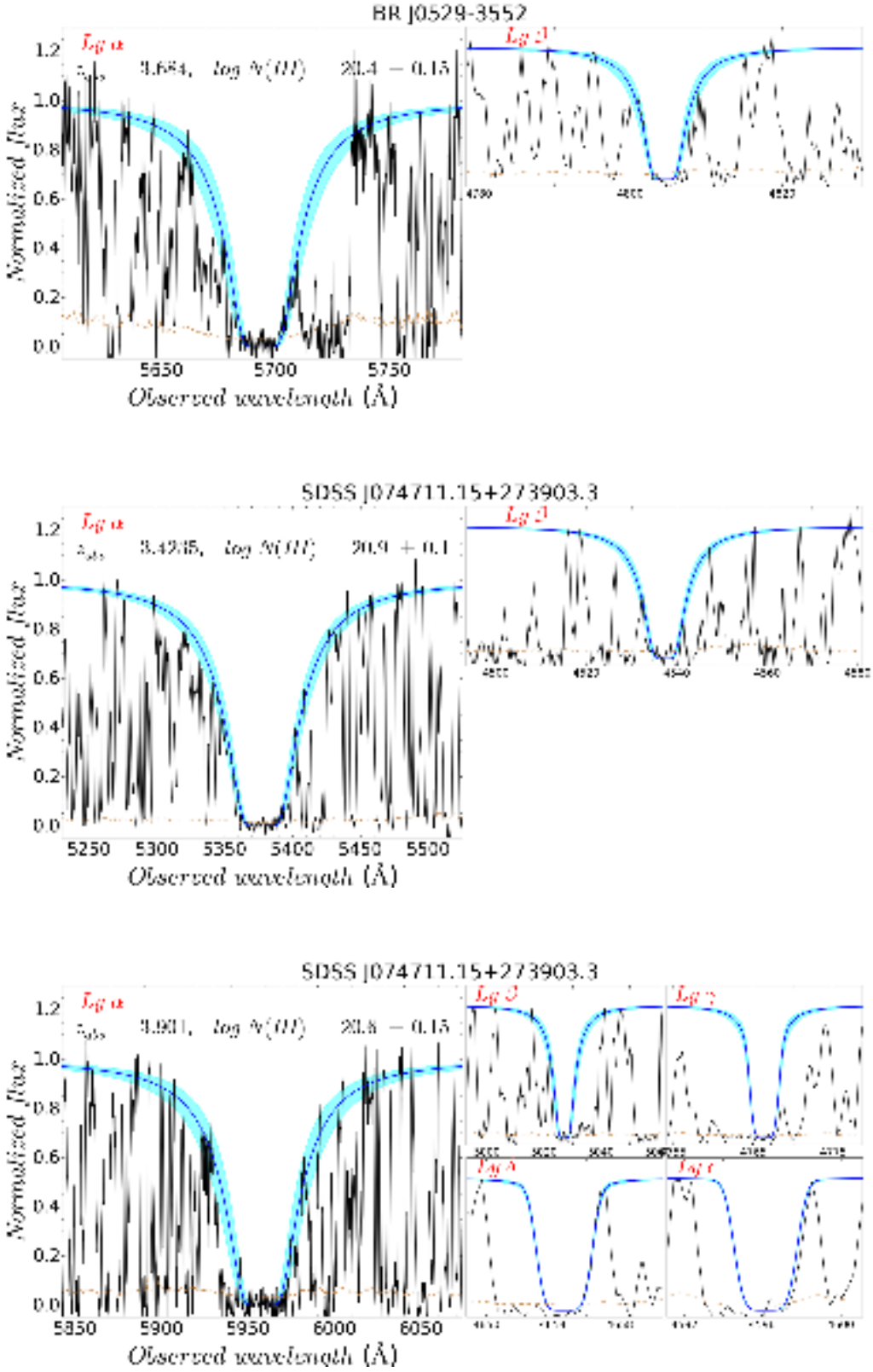
BR J0529-3552
Lg α
3.684, log N(HI) 20.4 − 0.15
Lg 2
Lg 3
Normalised flux
Observed wavelength (Å)
SDSS J074711.15+273903.3
Lg α
3.4285, log N(HI) 20.9 + 0.1
Lg 3
Normalised flux
Observed wavelength (Å)
SDSS J074711.15+273903.3
Lg α
3.931, log N(HI) 20.8 − 0.15
Lg 3
Lg 2
Lg 5
Lg 4
Normalised flux
Observed wavelength (Å)

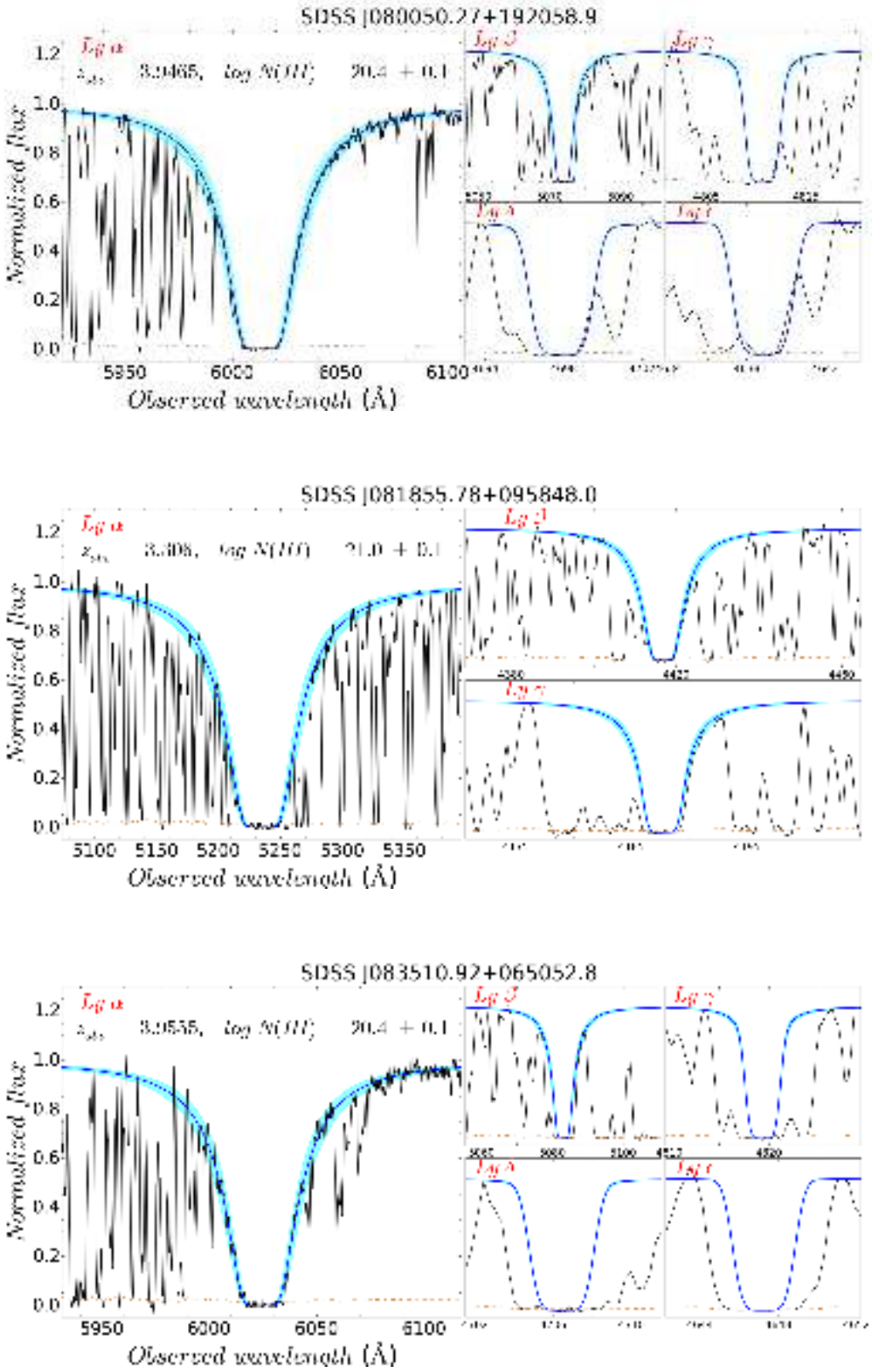
SDSS J080050.27+192058.9
Lyβ α
3.0465, log N(HI) 20.4 ± 0.1
Lyβ 2
Lyβ 3
Lyβ 4
Lyβ 5
Normalised flux
Observed wavelength (Å)
SDSS J081855.78+095848.0
Lyβ α
3.308, log N(HI) 21.0 ± 0.1
Lyβ 2
Lyβ 3
Normalised flux
Observed wavelength (Å)
SDSS J083510.92+065052.8
Lyβ α
3.0555, log N(HI) 20.4 ± 0.1
Lyβ 2
Lyβ 3
Lyβ 4
Lyβ 5
Normalised flux
Observed wavelength (Å)

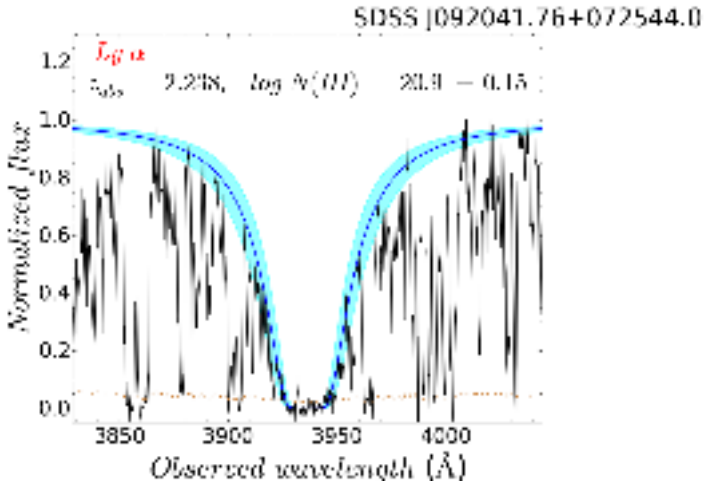
SDSS J092041.76+072544.0
Lyα
Normalised flux
Observed wavelength (Å)

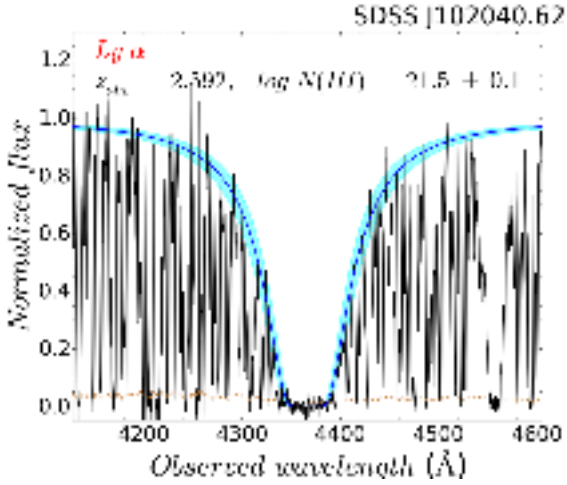
SDSS J102040.62+092254.2
Lyα
Normalised flux
Observed wavelength (Å)

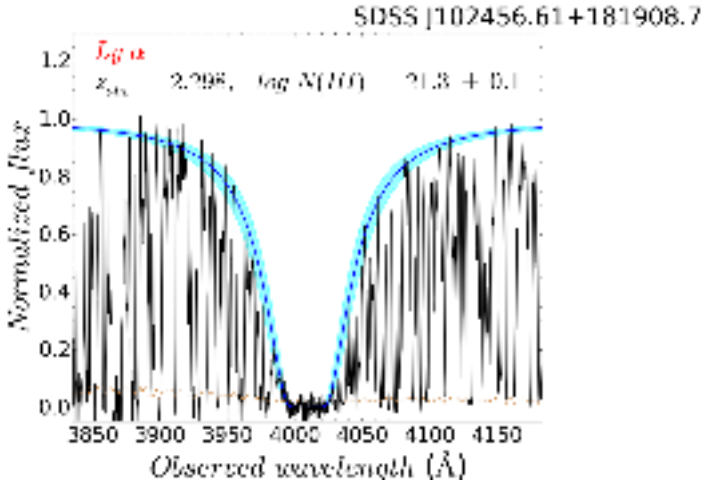
SDSS J102456.61+181908.7
Lyα
Normalised flux
Observed wavelength (Å)

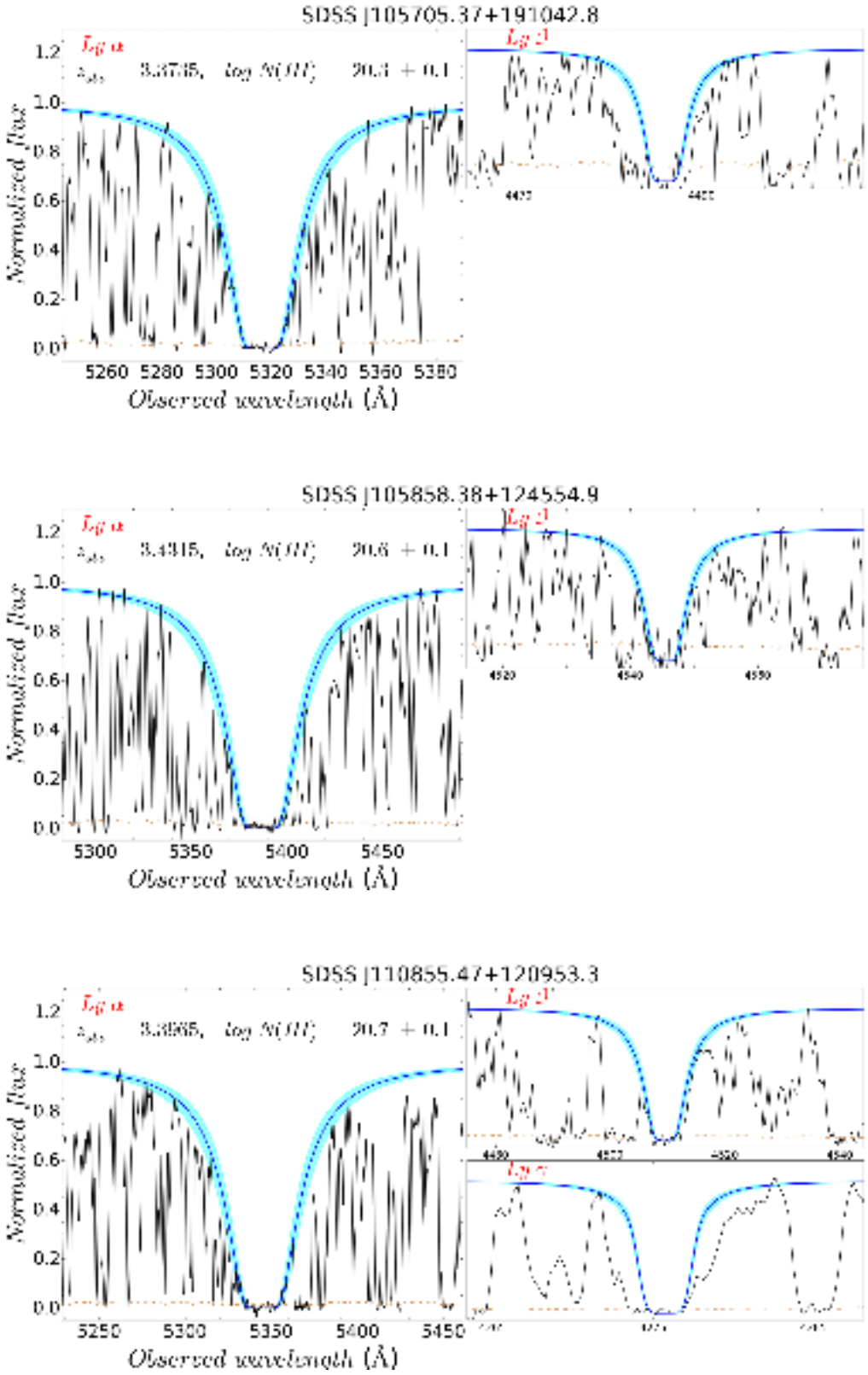
SDSS J105705.37+191042.8
Lyα
3.3785, log N(HI) 20.3 ± 0.1
Lyβ
Normalised flux
Observed wavelength (Å)
SDSS J105858.38+124554.9
Lyα
3.4315, log N(HI) 20.6 ± 0.1
Lyβ
Normalised flux
Observed wavelength (Å)
SDSS J110855.47+120953.3
Lyα
3.3965, log N(HI) 20.7 ± 0.1
Lyβ
Lyγ
Normalised flux
Observed wavelength (Å)

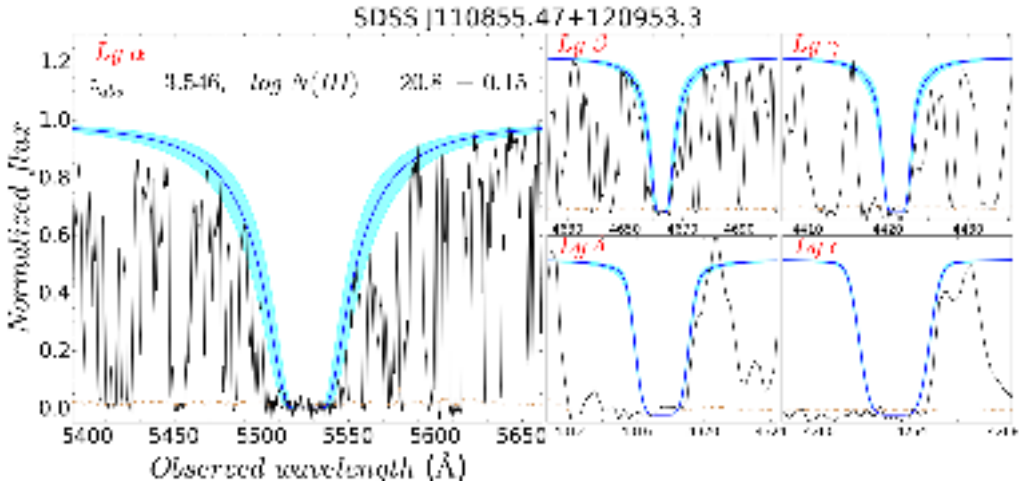
SDSS J110855.47+120953.3
Lyβ α
Lyβ 2
Lyβ 3
Lyβ 4
Lyβ 5
Normalised flux
Observed wavelength (Å)

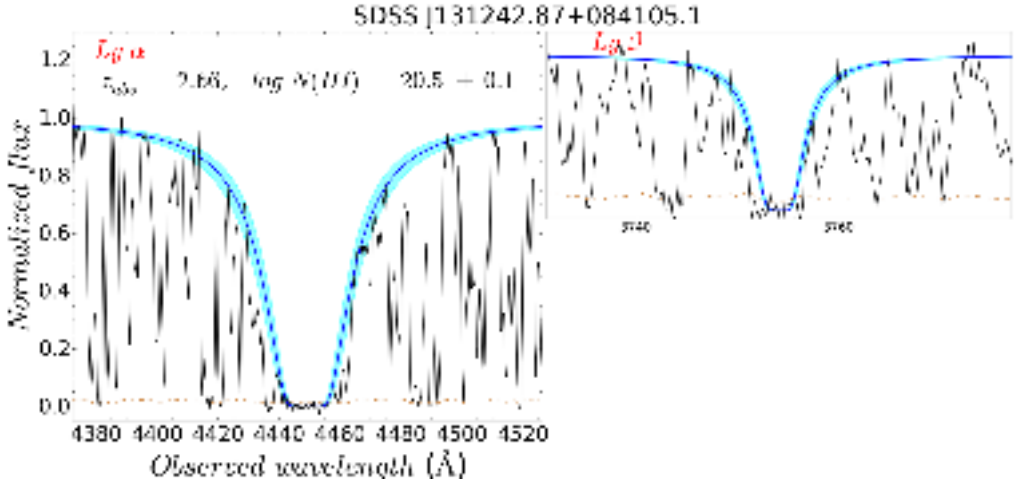
SDSS J131242.87+084105.1
Lyβ α
Lyβ 2
Normalised flux
Observed wavelength (Å)

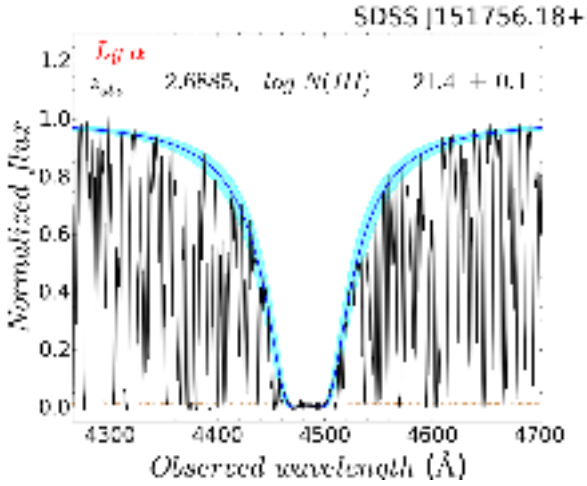
SDSS J151756.18+051103.5
Lyβ α
Normalised flux
Observed wavelength (Å)

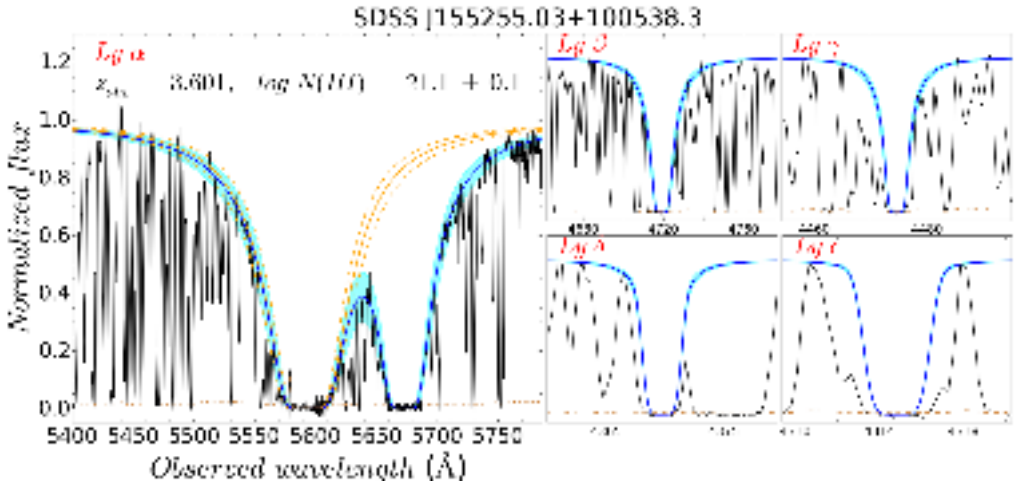
SDSS J155255.03+100538.3
Lyβ
Lyβ
Lyγ
Lyδ
Normalised flux
Observed wavelength (Å)

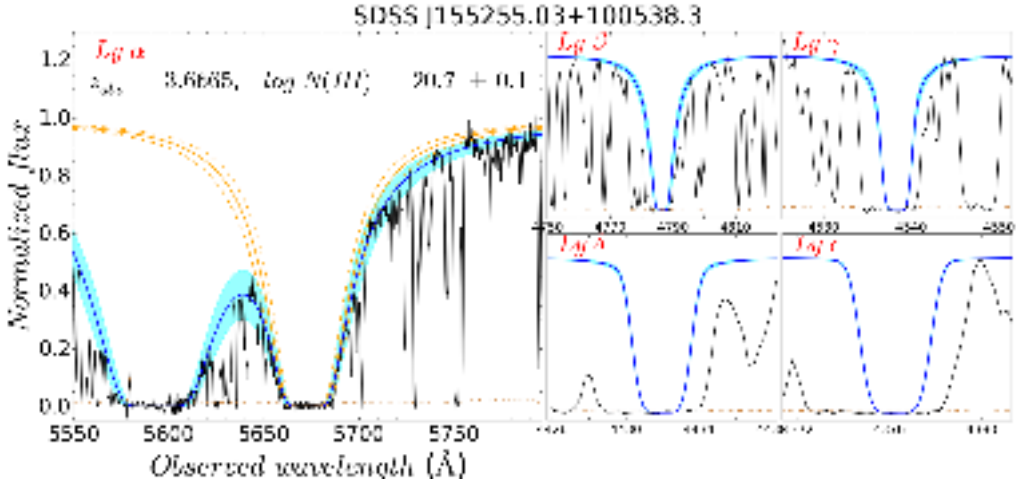
SDSS J155255.03+100538.3
Lyβ
Lyβ
Lyγ
Lyδ
Normalised flux
Observed wavelength (Å)

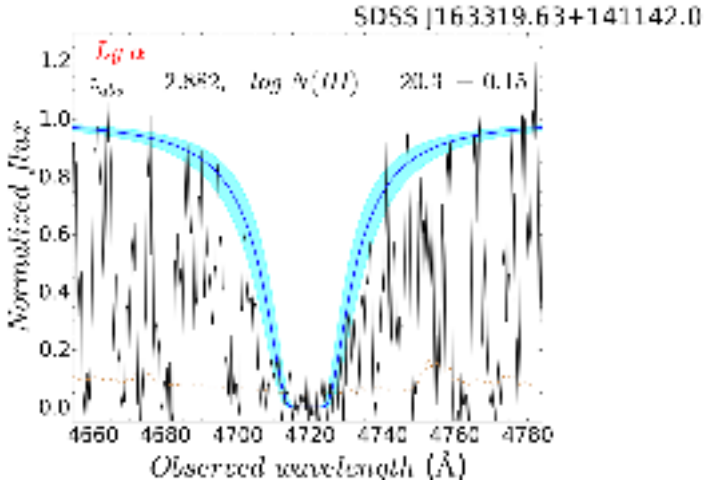
SDSS J163319.63+141142.0
Lyβ
Normalised flux
Observed wavelength (Å)

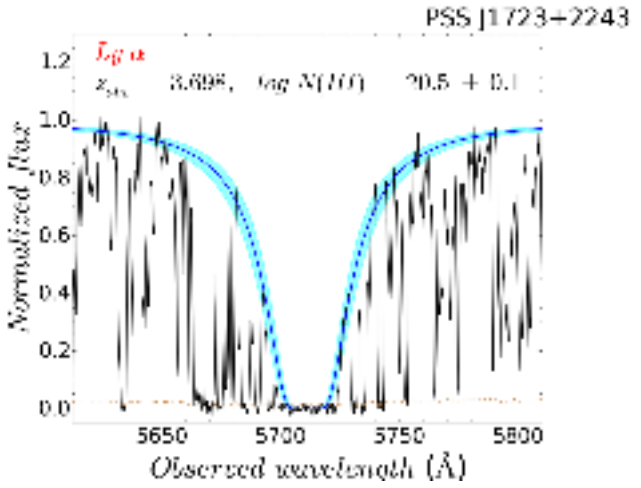
PSS J1723+2243
Lyα α
Normalised flux
Observed wavelength (Å)

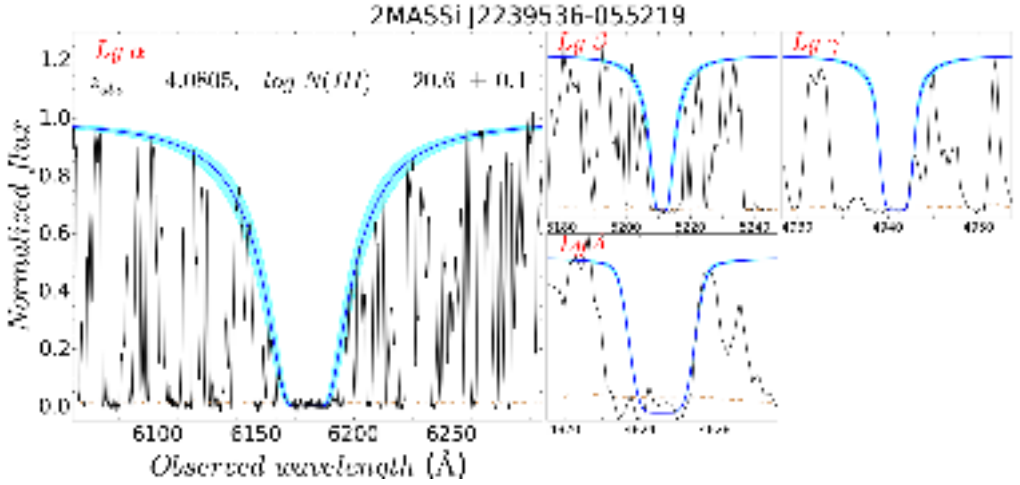
2MASSi J2239536-055219
Lyα α
Lyα 2
Lyα 3
Normalised flux
Observed wavelength (Å)

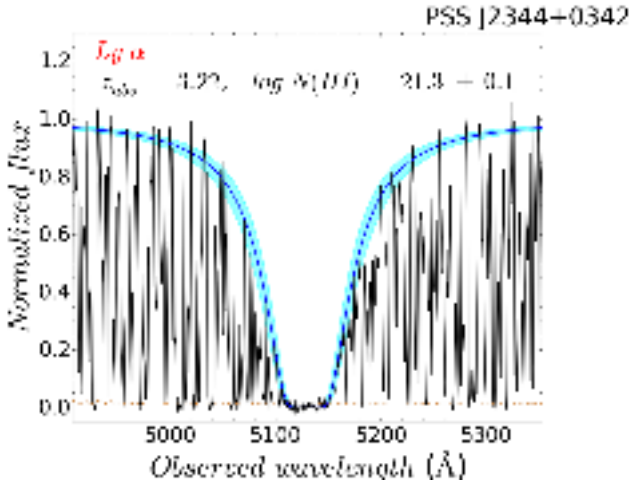
PSS J2344+0342
Lyα α
Normalised flux
Observed wavelength (Å)

Appendix I

Appendix I: QSO-DLA Combined Sample

Combined Sample

Name	RA	Dec	$z_{\rm em}$	$z_{\rm min}$	$z_{\rm max}$	$z_{\rm abs}$	$\log N({\rm H\,I})$	$\epsilon[\log N({\rm H\,I})]$
FBQS J0000-1021	0.21084	-10.3655	2.640	2.307	2.604			
[HB89] 2359+068	0.41920	7.1650	3.238	1.632	3.203			
SDSS J000143.41+152021.4	0.43088	15.3393	2.638	2.307	2.602			
[HB89] 2359+003	0.44475	0.6663	2.897	1.714	2.857			
LBQS 2359-0216B	0.45833	-1.9945	2.810	1.747	2.779	2.0951	20.70	0.20
						2.1537	20.30	0.20
FBQS J0002+0021	0.58799	0.3637	3.057	2.307	3.016			
SDSS J000300.34+160027.6	0.75146	16.0077	3.675	3.428	3.629			
SDSS J000303.34-105150.6	0.76396	-10.8641	3.647	3.187	3.564			
[HB89] 0000-263	0.84546	-26.0547	4.125	2.307	4.074	3.3900	21.40	0.10
PSS J0003+2730	0.84625	27.5064	4.240	2.718	4.188			
[HB89] 0001+087	0.92751	8.9924	3.241	2.024	3.199			
SDSS J000413.63-085529.5	1.05684	-8.9249	2.424	2.307	2.389			
SDSS J000424.16-085047.9	1.10070	-8.8467	2.433	2.307	2.399			
[HB89] 0004+171	1.69735	17.4705	2.898	2.002	2.851			
BR J0006-6208	1.71504	-62.1344	4.440	2.998	4.386	3.2030	20.90	0.15
						3.7750	21.00	0.20
SDSS J000657.53+141546.7	1.73973	14.2630	3.250	1.899	3.207			
SDSS J000730.82+160732.5	1.87846	16.1257	3.501	3.278	3.456			
PSS J0007+2417	1.91125	24.2900	4.050	2.758	4.000	3.4970	20.95	0.10
						3.7060	20.65	0.15
						3.8390	20.65	0.10
SDSS J000807.27-103942.7	2.03036	-10.6619	2.459	2.307	2.424			
LBQS 0006+0230	2.23903	2.7934	2.090	1.787	2.059			
LBQS 0006+0200	2.38077	2.2851	2.350	1.634	2.317			
SDSS J000950.50+141002.0	2.46046	14.1672	3.151	2.456	3.110			
PKS 0007+016	2.49443	1.9653	2.900	1.882	2.861			
LBQS 0007-0004	2.56871	0.2077	2.290	1.670	2.260			
SDSS J001022.14-003701.1	2.59227	-0.6170	3.152	2.507	3.110			
SDSS J001115.23+144601.8	2.81348	14.7672	4.970	4.037	4.870			
SDSS J001205.03+144122.2	3.02097	14.6895	2.522	2.307	2.486			
LBQS 0009-0138	3.04500	-1.3686	1.990	1.634	1.960			
LBQS 0009+0219	3.08167	2.6100	2.660	1.784	2.623			
LBQS 0009-0215	3.08819	-1.9826	2.110	1.634	2.079			
SDSS J001240.56+135236.7	3.16905	13.8769	3.187	2.490	3.145	3.0217	20.55	0.15
SDSS J001255.36-091425.7	3.23069	-9.2405	3.004	2.594	2.964			
LBQS 0010-0012	3.27563	0.0755	2.150	1.634	2.119	2.0233	20.80	0.20
SDSS J001328.20+135828.0	3.36754	13.9744	3.575	2.635	3.530	3.2808	21.55	0.15
PSS J0014+3032	3.67917	30.5343	4.470	2.866	4.415			
SDSS J001502.25+001212.5	3.75943	0.2035	2.852	2.470	2.769			
SDSS J001512.45+155248.3	3.80190	15.8801	3.211	2.337	3.169			
SDSS J001549.08+001731.9	3.95452	0.2922	3.066	2.920	3.025			
LBQS 0013-0029	4.01001	-0.2070	2.080	1.634	2.049	1.9730	20.70	0.20
SDSS J001617.03-100419.2	4.07101	-10.0720	2.444	2.307	2.410			
SDSS J001641.17+010045.2	4.17156	1.0126	3.038	2.642	2.998			

Continued on Next Page...

Table I.1 – Continued

Name	RA	Dec	z_{em}	z_{min}	z_{max}	z_{abs}	$\log N(\mathrm{H\,I})$	$\epsilon[\log N(\mathrm{H\,I})]$
[HB89] 0014+813	4.28531	81.5856	3.380	1.928	3.340			
LBQS 0014-0256	4.33840	-2.6557	1.850	1.729	1.821			
LBQS 0015+0239	4.54739	2.9443	2.470	1.784	2.435			
SDSS J001813.88+142455.6	4.55788	14.4155	4.232	3.351	4.179			
SDSS J001820.71+141851.5	4.58632	14.3143	3.937	2.799	3.887			
SDSS J001918.43+150611.3	4.82681	15.1032	4.153	3.719	4.101	3.9710	20.40	0.20
LBQS 0016+0045	4.83047	1.0312	2.310	1.651	2.277			
SDSS J001950.05-004040.7	4.95859	-0.6780	4.327	3.310	4.274			
SDSS J002120.04+155125.6	5.33354	15.8571	3.696	2.898	3.649			
LBQS 0018-0220	5.36399	-2.0593	2.560	1.634	2.524			
LBQS 0018+0047	5.36618	1.0723	1.830	1.655	1.802			
SDSS J002130.68+140953.5	5.37787	14.1649	2.413	2.307	2.379			
SDSS J002146.71-004847.9	5.44466	-0.8133	2.502	2.307	2.467			
BR 0019-1522	5.53332	-15.0944	4.528	2.970	4.473	3.4370	20.92	0.20
LBQS 0020+0217	5.85353	2.5662	1.800	1.665	1.772			
SDSS J002337.54+003127.4	5.90645	0.5243	2.407	2.307	2.373			
LBQS 0022+0150	6.14719	2.1133	2.770	1.791	2.732			
LBQS 0023+0010	6.40541	0.4568	1.900	1.657	1.871			
SDSS J002609.07-003749.3	6.53780	-0.6304	2.382	2.311	2.348			
SDSS J002627.28+152446.2	6.61367	15.4129	3.591	3.232	3.545			
SDSS J002636.27+151247.0	6.65115	15.2131	3.226	2.565	3.184			
LBQS 0025-0151	6.89083	-1.5811	2.080	1.634	2.049			
SDSS J002820.38+153358.5	7.08493	15.5663	2.402	2.307	2.368			
LBQS 0026+0158	7.18445	2.2561	1.890	1.727	1.861			
SDSS J002937.33+001412.7	7.40557	0.2369	2.561	2.307	2.526			
SDSS J002946.37-093540.8	7.44323	-9.5947	3.614	3.179	3.568			
LBQS 0027+0149	7.46724	2.1016	2.330	1.694	2.297			
LBQS 0027+0103	7.53378	1.3366	2.290	1.634	2.257	1.9375	20.60	0.20
PSS J0030+1702	7.56829	17.0445	4.282	2.763	4.229			
BR J0030-5129	7.64321	-51.4962	4.173	2.529	4.122			
LBQS 0028+0236	7.68827	2.8913	2.000	1.634	1.970			
LBQS 0028-0148	7.74708	-1.5303	2.080	1.840	2.049			
SDSS J003126.79+150739.5	7.86167	15.1276	4.283	3.410	4.230			
LBQS 0029+0017	7.89823	0.5726	2.230	1.725	2.198			
LBQS 0029-0152	7.90202	-1.6061	2.390	2.013	2.356			
SDSS J003146.62+145519.4	7.94425	14.9221	3.365	2.489	3.321			
SDSS J003203.29-084405.0	8.01373	-8.7348	3.253	2.443	3.211			
SDSS J003250.12-105357.6	8.20885	-10.8994	2.447	2.344	2.353			
PSS J0034+1639	8.72842	16.6554	4.292	2.981	4.240	3.7550	20.40	0.15
SDSS J003501.88-091817.6	8.75785	-9.3049	2.424	2.307	2.390	2.3376	20.55	0.15
SDSS J003503.76+001641.6	8.76572	0.2782	2.671	2.307	2.634			
SDSS J0035+0040	8.85535	0.6675	4.747	3.309	4.690			
SDSS J003545.86+002305.7	8.94111	0.3850	3.226	2.383	3.183			
SDSS J003742.04+154938.1	9.42518	15.8273	2.707	2.335	2.670			
SDSS J003939.96+152720.3	9.91652	15.4557	2.867	2.471	2.829			
UM 264	10.07589	-1.6228	2.340	1.654	2.303			
SDSS J004054.65-091526.8	10.22772	-9.2574	4.980	4.046	4.880			
SDSS J004142.52-085704.6	10.42718	-8.9513	3.612	3.143	3.566			
SDSS J004143.15-005855.1	10.42985	-0.9820	2.544	2.307	2.509			
LBQS 0039-2630	10.51727	-26.2344	1.810	1.634	1.782			
SDSS J004205.22-103957.5	10.52176	-10.6660	2.489	2.440	2.454			
SDSS J004219.74-102009.4	10.58228	-10.3360	3.863	2.488	3.815			
SDSS J004240.65+141529.6	10.66940	14.2582	3.722	2.684	3.675			
LBQS 0040-2917	10.78500	-29.0150	2.090	1.634	2.056			
PKS 0040-005	10.84763	-0.2646	2.798	2.409	2.760			
LBQS 0041-2638	10.92836	-26.3696	3.045	1.657	3.005			
LBQS 0041-2707	10.96597	-26.8576	2.790	1.668	2.748			
LBQS 0041-2607	10.99494	-25.8541	2.460	1.634	2.426			
LBQS 0041-2658	11.02438	-26.7014	2.460	1.634	2.422			
LBQS 0041-2859	11.03264	-28.7195	2.130	1.589	2.103			
LBQS 0042-2627	11.14151	-26.1891	3.298	2.113	3.253			
[WHO91] 0042-269	11.21774	-26.6695	3.330	2.215	3.287			
LBQS 0042-3053	11.25831	-30.6173	1.970	1.634	1.944			
LBQS 0042-2930	11.28542	-29.2422	2.390	1.591	2.354	1.9310	20.50	0.20
LBQS 0042-2657	11.33162	-26.6809	2.900	2.226	2.859			
LBQS 0043-2937	11.36878	-29.3437	2.230	1.656	2.198			
LBQS 0045-3002	11.87796	-29.7751	2.020	1.603	1.991			
SDSS J004732.71+002111.4	11.88639	0.3532	2.879	2.495	2.796			
UM 667	11.95880	-3.4253	3.138	1.961	3.094			
SDSS J004806.04+004623.6	12.02524	0.7732	2.358	2.307	2.325			
UM 278	12.02524	-1.0560	2.527	2.307	2.492			
[HB89] 0046-293 NED01	12.12300	-29.0559	4.014	2.882	3.964			

Continued on Next Page...

Table I.1 – Continued

Name	RA	Dec	z_{em}	z_{min}	z_{max}	z_{abs}	$\log N(\mathrm{H\,I})$	$\epsilon[\log N(\mathrm{H\,I})]$
BRI J0048-2442	12.14404	-24.7017	4.083	2.587	4.033			
SDSS J004852.41-002430.7	12.21841	-0.4086	2.696	2.338	2.613			
[LWT91] 0047-2326	12.36562	-23.1610	3.422	2.291	3.378			
SDSS J0050-0053	12.52645	-0.8887	4.332	2.590	4.278			
SDSS J005010.53+153909.6	12.54392	15.6527	2.954	2.585	2.872			
LBQS 0047-2759	12.56625	-27.7211	2.130	1.649	2.099			
LBQS 0047-3050	12.58373	-30.5725	2.970	1.930	2.933			
LBQS 0047-2538	12.60356	-25.3762	1.970	1.591	1.939			
SDSS J005043.09-094314.7	12.67956	-9.7208	2.899	2.517	2.860			
LBQS 0048-2545	12.75840	-25.4800	2.080	1.634	2.051			
LBQS 0048-0119	12.76013	-1.0456	1.880	1.634	1.849			
LBQS 0049-2820	12.86338	-28.0761	2.260	1.638	2.223	2.0713	20.50	0.20
LBQS 0049-0104	12.90971	-0.8033	2.100	1.715	2.065			
LBQS 0049-0012	12.98853	0.0652	1.950	1.634	1.916			
LBQS 0049+0045	13.01000	1.0248	2.270	1.644	2.238			
SDSS J005206.08-110837.9	13.02534	-11.1439	3.249	2.426	3.207			
SDSS J005225.44+004251.0	13.10602	0.7142	2.920	2.307	2.881			
SDSS J005229.50-110310.0	13.12297	-11.0527	2.438	2.307	2.404			
UM 288	13.14050	1.6779	2.310	1.681	2.276			
LBQS 0050-2523	13.18625	-25.1144	2.160	1.592	2.127			
SDSS J005319.20+134708.8	13.33002	13.7858	2.923	2.522	2.884	2.6285	20.75	0.15
SDSS J005419.98+002727.9	13.58328	0.4578	2.519	2.307	2.484			
LBQS 0051-0226	13.60179	-2.1776	2.530	1.634	2.491			
LBQS 0052-0058	13.72851	-0.7122	2.210	1.634	2.180			
SDSS J005508.97-085914.8	13.78744	-8.9874	2.476	2.307	2.441			
LBQS 0053-0134	14.06098	-1.3078	2.060	1.634	2.031			
[HB89] 0053-284	14.10446	-28.1425	3.635	2.447	3.589			
LBQS 0054+0200	14.18598	2.2750	1.870	1.634	1.844			
SDSS J005653.25-094121.7	14.22191	-9.6894	3.244	2.837	3.201			
SDSS J005700.18+143737.7	14.25082	14.6272	2.643	2.307	2.607			
[HB89] 0054-006	14.32084	-0.4092	2.760	1.854	2.724			
LBQS 0055-2744	14.39545	-27.4744	2.200	1.567	2.163			
LBQS 0055+0141	14.40445	1.9646	2.230	1.651	2.200			
LBQS 0055-0200	14.45244	-1.7398	1.980	1.782	1.953			
[HB89] 0055-269	14.49135	-26.7206	3.661	1.600	3.615			
SDSS J005814.30+011530.3	14.55966	1.2584	2.495	2.307	2.460			
LBQS 0055+0025	14.60313	0.6871	1.910	1.634	1.885			
LBQS 0056+0125	14.82340	1.7018	3.160	2.197	3.119	2.7750	21.00	0.20
LBQS 0056-0241	14.83463	-2.4280	2.230	1.779	2.194			
SDSS J005922.65+000301.4	14.84438	0.0504	4.154	3.784	4.103			
[VV2006] J145833.4+681321	14.97594	68.2225	4.291	2.990	4.238			
PMN J0100-2708	15.05104	-27.1477	3.546	2.192	3.501			
LBQS 0057-0225	15.06875	-2.1536	2.010	1.715	1.979			
LBQS 0058-2604	15.13165	-25.8096	2.470	1.606	2.437			
LBQS 0058-0227	15.18627	-2.1880	2.230	1.712	2.194			
LBQS 0058+0155	15.22565	2.1935	1.950	1.634	1.924			
[WHO91] 0058-292	15.26916	-28.9669	3.070	1.778	3.030	2.6711	21.20	0.20
LBQS 0059-0207	15.42597	-1.8641	2.290	1.653	2.257			
LBQS 0059-2625	15.47005	-26.1496	2.100	1.614	2.069			
LBQS 0059+0035	15.61464	0.8602	2.533	2.307	2.498			
LBQS 0100-3105	15.76132	-30.8271	2.640	1.687	2.605	2.1310	20.50	0.20
LBQS 0100+0146	15.78476	2.0387	1.910	1.692	1.880			
[HB89] 0100+130	15.79708	13.2717	2.690	1.640	2.653	2.3093	21.40	0.20
LBQS 0101-2548	15.88873	-25.5400	1.970	1.596	1.943			
LBQS 0101-3025	15.98043	-30.1634	3.164	1.937	3.116			
LBQS 0102-0240	16.22542	-2.4014	1.840	1.731	1.818			
UM 669	16.32002	-18.7784	3.040	2.044	2.995	2.3693	21.00	0.20
LBQS 0102-0214	16.32121	-1.9742	1.980	1.649	1.949	1.7431	20.60	0.20
LBQS 0103-0140	16.41762	-1.4157	2.210	1.634	2.174			
LBQS 0103-2901	16.48548	-28.7581	2.870	1.922	2.831			
PSS J0106+2601	16.50333	26.0174	4.309	2.764	4.256	3.9600	20.50	0.20
SDSS J010619.24+004823.3	16.58017	0.8065	4.449	3.598	4.358			
LBQS 0104+0030	16.70014	0.7744	1.870	1.667	1.845			
PC 0104+0215	16.70685	2.5171	4.171	2.881	4.119			
SDSS J010657.94-085500.1	16.74144	-8.9167	2.346	2.307	2.312			
LBQS 0105-2649	16.92472	-26.5582	2.460	1.667	2.428			
SDSS J010758.75-101916.7	16.99482	-10.3213	2.555	2.307	2.519			
SDSS J010815.26+000708.5	17.06359	0.1191	2.355	2.307	2.322			
SDSS J010822.69+001147.9	17.09455	0.1967	3.708	2.879	3.661			
LBQS 0106-0230	17.15057	-2.2422	2.280	1.634	2.246			
LBQS 0106+0119	17.16155	1.5834	2.100	1.871	2.068			
SDSS J010858.02+005114.5	17.24176	0.8541	2.952	2.553	2.913	2.7570	20.60	0.15

Continued on Next Page...

Table I.1 – Continued

Name	RA	Dec	z_{em}	z_{min}	z_{max}	z_{abs}	log N(H I)	ϵ[log N(H I)]
						2.9010	20.95	0.15
FBQS J0109-0928	17.27473	-9.4805	2.582	2.307	2.546			
LBQS 0107+0022	17.47655	0.6370	1.970	1.634	1.938			
LBQS 0108+0028	17.65869	0.7483	2.010	1.733	1.975			
LBQS 0109+0213	18.07045	2.4966	2.350	1.734	2.317			
SDSS J011237.34+001929.7	18.15564	0.3249	2.697	2.645	2.660			
LBQS 0110-0107	18.16766	-0.8676	1.890	1.643	1.860			
BRI J0113-2803	18.43488	-28.0548	4.314	2.784	4.261	3.1060	21.20	0.10
SDSS J011351.96-093551.0	18.46652	-9.5976	3.669	2.643	3.622			
[VCV96] BR 0111-28	18.46876	-28.2354	4.300	2.709	4.247	3.1043	21.00	0.20
[VCV96] Q 0112-27	18.72010	-27.2358	2.894	1.784	2.855			
[HB89] 0112+030	18.72167	3.2492	2.810	1.813	2.785	2.4227	21.00	0.20
[VCV96] Q 0112-30	18.76958	-30.4206	2.990	1.881	2.945	2.4191	20.50	0.20
						2.7023	20.30	0.20
SDSS J011532.42-105300.2	18.88508	-10.8834	2.960	2.786	2.921			
SDSS J011545.58-091457.3	18.93994	-9.2493	2.512	2.307	2.477			
SDSS J011546.19-100145.8	18.94252	-10.0294	2.507	2.307	2.472			
UM 670	19.34737	-8.6923	3.163	1.838	3.118			
PSS J0117+1552	19.37987	15.8712	4.243	2.364	4.191			
[VCV96] Q 0115-30	19.39167	-29.7747	3.249	1.733	3.207			
PSS J0118+0320	19.50000	3.3333	4.232	2.901	4.180			
SDSS J011847.34+004654.9	19.69732	0.7819	2.664	2.307	2.627			
SDSS J012019.99+000735.5	20.08331	0.1266	4.101	3.230	4.050			
SDSS J012020.36+132433.6	20.08488	13.4093	2.567	2.307	2.532			
PSS J0121+0347	20.35898	3.7851	4.125	2.545	4.074			
2MASSi J0121560+144824	20.48342	14.8067	2.865	2.307	2.826			
SDSS J012211.11+150914.3	20.54633	15.1540	4.460	3.471	4.049	3.5194	20.45	0.20
SDSS J012230.61+133437.8	20.62758	13.5772	3.013	2.307	2.973	2.3486	20.30	0.15
SDSS J0124+0044	21.01571	0.7424	3.837	2.077	3.789	2.2610	20.70	0.15
SDSS J012412.45-010049.9	21.05195	-1.0138	2.830	2.307	2.792			
SDSS J012509.42-104300.8	21.28927	-10.7169	4.498	3.639	4.406			
SDSS J012530.85-102739.8	21.37857	-10.4611	3.351	2.347	3.308			
SDSS J012606.60+142825.9	21.52752	14.4739	2.775	2.732	2.737			
[HB89] 0123+257	21.67830	25.9837	2.370	1.644	2.338			
SDSS J012656.34+153642.9	21.73479	15.6119	3.267	2.382	3.224			
SDSS J012700.68-004559.1	21.75287	-0.7664	4.084	2.546	4.033	3.7280	20.85	0.10
SDSS J012747.80+140543.2	21.94919	14.0954	2.488	2.307	2.453	2.4416	20.30	0.15
SDSS J012906.01+145907.1	22.27508	14.9853	3.864	3.049	3.816	3.2355	20.85	0.20
PSS J0131+0633	22.80083	6.5611	4.430	3.008	4.376			
PSS J0132+1341	23.04104	13.6943	4.152	2.833	4.101	3.9360	20.40	0.15
SDSS J013242.76-094301.5	23.17820	-9.7171	4.264	3.278	4.212			
FBQS J0132+0026	23.20576	0.4409	3.183	2.307	3.141			
SDSS J013317.78+144300.4	23.32414	14.7168	3.231	2.563	3.189			
PSS J0133+0400	23.41800	4.0166	4.185	2.850	4.134	3.6920	20.70	0.10
						3.7725	20.70	0.10
[HB89] 0131+013	23.45347	1.6046	3.792	3.116	3.744			
PSS J0134+3307	23.58958	33.1323	4.536	2.976	4.481	3.7600	20.60	0.10
UM 672	23.66100	-19.5353	3.130	1.714	3.089			
BRI J0137-4224	24.35171	-42.4047	3.971	2.512	3.922			
SDSS J013724.43-082419.8	24.35180	-8.4055	2.566	2.307	2.531			
SDSS J013729.94+002243.1	24.37478	0.3786	2.744	2.374	2.662			
SDSS J013854.66+142848.8	24.72781	14.4803	3.126	2.830	3.085			
SDSS J013858.67-101624.4	24.74452	-10.2735	3.241	2.530	3.198			
SDSS J013900.78-084720.5	24.75329	-8.7891	3.135	2.328	3.093			
SDSS J013901.40-082443.9	24.75586	-8.4122	3.016	2.307	2.976	2.6773	20.70	0.15
UM 121	24.76010	6.2604	2.350	1.749	2.317			
[HB89] 0136+176	24.92491	17.8854	2.730	1.632	2.679			
SDSS J014049.18-083942.5	25.20495	-8.6618	3.716	3.249	3.633			
FBQS J0141-0024	25.34600	-0.4061	2.598	2.307	2.562			
SDSS J014214.73+002324.3	25.56147	0.3901	3.373	2.427	3.330			
SDSS J014347.87+002736.3	25.94956	0.4601	2.423	2.307	2.389			
SDSS J014406.90-080701.5	26.02876	-8.1171	2.508	2.406	2.473			
[HB89] 0142-100	26.31921	-9.7548	2.731	2.349	2.694			
SDSS J014518.72+134300.2	26.32801	13.7167	2.490	2.307	2.455			
SDSS J014529.65-084133.3	26.37355	-8.6926	2.483	2.315	2.448			
UM 366	26.46342	-1.3419	3.141	1.673	3.097			
SDSS J014609.33-092918.2	26.53889	-9.4884	4.148	3.625	4.097			
UM 368	26.58323	-0.7747	3.172	2.307	3.130			
SDSS J014850.64-090712.8	27.21108	-9.1203	3.313	2.307	3.270			
SDSS J014937.97+142548.6	27.40823	14.4302	3.305	2.639	3.262			
SDSS J015006.46-080203.5	27.52697	-8.0343	2.592	2.307	2.556			
SDSS J015009.45-082510.7	27.53941	-8.4197	2.763	2.404	2.725			

Continued on Next Page...

Table I.1 – Continued

Name	RA	Dec	z_{em}	z_{min}	z_{max}	z_{abs}	$\log N(\mathrm{H\,I})$	$\epsilon[\log N(\mathrm{H\,I})]$
SDSS J015017.71+002902.3	27.57380	0.4840	2.979	2.586	2.897			
SDSS J0150+0041	27.70346	0.6906	3.703	3.238	3.621			
MG3 J015105+2516	27.77597	25.2913	3.100	1.825	3.059			
UM 674	27.77793	-9.5334	2.850	1.797	2.810			
PSS J0152+0735	28.04625	7.5973	4.051	1.890	4.000	3.8400	20.70	0.20
[HB89] 0149+335	28.14407	33.8425	2.430	1.640	2.396	2.1413	20.50	0.20
SDSS J015313.81-085820.5	28.30760	-8.9724	2.468	2.307	2.433			
SDSS J015339.60-001104.8	28.41505	-0.1847	4.195	2.825	4.144			
SDSS J015514.43+141241.4	28.81019	14.2115	3.824	3.346	3.742	3.6579	20.60	0.15
UM 148	29.15011	4.7578	2.993	1.673	2.951			
SDSS J015741.56-010629.5	29.42320	-1.1082	3.564	2.456	3.519			
SDSS J015819.76-001222.0	29.58237	-0.2061	3.285	2.307	3.242			
SDSS J015925.07-001755.3	29.85448	-0.2987	3.281	2.356	3.238			
SDSS J015935.48+000401.2	29.89784	0.0670	3.275	2.921	3.232			
UM 154	30.49892	3.8451	2.470	1.644	2.436			
SDSS J020316.37-074832.1	30.81821	-7.8089	3.303	2.436	3.260			
SDSS J020446.86+125650.0	31.19529	12.9472	3.086	2.409	3.045			
[HB89] 0201+365	31.23165	36.8217	2.912	1.632	2.879	1.7680	20.50	0.20
						2.4614	20.40	0.20
SDSS J020608.14-085923.1	31.53392	-8.9898	2.361	2.307	2.327			
SDSS J020651.46-094141.3	31.71443	-9.6948	3.132	2.785	3.091			
PSS J0209+0517	32.43588	5.2871	4.194	2.943	4.142	3.6660	20.50	0.10
						3.8620	20.30	0.15
UM 402	32.46129	-0.0851	2.850	2.307	2.812			
SDSS J020951.92-082904.8	32.46635	-8.4847	3.040	2.696	2.999			
SDSS J0210-0018	32.67984	-0.3051	4.700	3.177	4.643			
SDSS J0211-0009	32.76133	-0.1529	4.874	3.402	4.815			
PSS J0211+1107	32.83346	11.1212	3.973	2.439	3.924			
SDSS J021129.16+124110.7	32.87154	12.6863	2.954	2.307	2.914	2.5947	20.60	0.15
SDSS J021150.72+120949.7	32.96138	12.1639	3.067	2.686	3.026			
SDSS J021206.14-091438.5	33.02559	-9.2440	2.418	2.307	2.384			
SDSS J021232.19-100422.1	33.13417	-10.0728	2.497	2.350	2.355			
SDSS J021318.98-090458.2	33.32910	-9.0829	3.794	2.820	3.746			
PMN J0214-0518	33.62208	-5.2958	3.977	2.554	3.928			
SDSS J021540.92-092536.7	33.92056	-9.4269	3.059	2.440	3.018			
SDSS J021646.94-092107.2	34.19560	-9.3520	3.716	3.249	3.633			
SDSS J021720.47+005935.6	34.33530	0.9933	2.788	2.400	2.750			
SDSS J021740.96-085447.9	34.42070	-8.9133	2.571	2.307	2.489			
[HB89] 0216+080	34.73890	8.2910	3.000	1.731	2.953	2.2930	20.50	0.20
SDSS J022103.53-074948.8	35.26472	-7.8303	2.575	2.307	2.539			
SDSS J022143.18-001803.8	35.42996	-0.3011	2.645	2.307	2.609			
SDSS J022437.10-083426.6	36.15460	-8.5741	3.136	2.713	3.094			
SDSS J022518.35-001332.2	36.32651	-0.2256	3.627	2.661	3.581			
SDSS J022559.77-073938.7	36.49908	-7.6608	2.993	2.598	2.911			
SDSS J022632.49-003841.4	36.63546	-0.6448	2.351	2.307	2.318			
SDSS J022827.64-010050.3	37.11518	-1.0140	3.165	2.466	3.123			
SDSS J022844.08+000217.0	37.18372	0.0381	2.721	2.353	2.639			
SDSS J022922.88-075833.1	37.34535	-7.9759	3.774	3.592	3.726			
SDSS J023137.65-072854.4	37.90688	-7.4818	5.420	4.417	5.313	4.8860	20.75	0.20
SDSS J023139.52+001758.4	37.91472	0.2996	2.375	2.307	2.341			
[HB89] 0229+131	37.94123	13.3819	2.070	1.767	2.039			
SDSS J023230.42-072644.2	38.12678	-7.4456	2.551	2.512	2.516			
SDSS J023308.30-002605.0	38.28465	-0.4347	2.484	2.307	2.449			
SDSS J023359.71+004938.5	38.49884	0.8274	2.522	2.307	2.487			
SDSS J023408.97-075107.6	38.53740	-7.8521	2.540	2.307	2.505	2.3189	20.95	0.15
SDSS J023423.47-075939.6	38.59784	-7.9943	2.541	2.456	2.506			
BR J0234-1806	38.72975	-18.1024	4.305	2.957	4.252	3.6930	20.40	0.15
SDSS J023903.43-003850.8	39.76430	-0.6475	3.078	2.307	3.037	3.0192	20.35	0.15
SDSS J023923.47-081005.1	39.84782	-8.1681	4.023	3.176	3.973			
SDSS J023924.48-090138.6	39.85201	-9.0274	2.472	2.307	2.437			
SDSS J023933.23-071125.5	39.88848	-7.1905	3.225	2.512	3.183			
SDSS J024154.42-004757.5	40.47678	-0.7994	2.384	2.307	2.351			
UM 677	40.48557	-15.2450	2.786	1.928	2.744			
SDSS J024337.16-002340.1	40.90488	-0.3945	2.349	2.307	2.315			
SDSS J024338.46+004433.5	40.91026	0.7427	2.421	2.307	2.386			
BRI 0241-0146	41.00765	-1.5678	4.055	2.743	4.005			
SDSS J024447.78-081606.1	41.19914	-8.2683	4.046	2.883	3.996			
SDSS J024555.83-084025.7	41.48264	-8.6738	2.572	2.307	2.536			
SDSS J024614.54+005427.3	41.56059	0.9076	3.009	2.307	2.969			
BR 0245-0608	41.98522	-5.9329	4.233	2.891	4.181			
PSS J0248+1802	42.22625	18.0472	4.439	2.858	4.385			
SDSS J024933.40-083454.4	42.38922	-8.5818	2.492	2.307	2.457			

Continued on Next Page...

Table I.1 – Continued

Name	RA	Dec	z_{em}	z_{min}	z_{max}	z_{abs}	$\log N(\mathrm{H\,I})$	$\epsilon[\log N(\mathrm{H\,I})]$
SDSS J025021.76-075749.9	42.59069	-7.9639	3.344	2.311	3.301			
UM 678	42.91830	-22.0074	3.210	2.044	3.160			
UM 679	42.95007	-18.2414	3.210	1.871	3.163			
SDSS J025151.19-073708.0	42.96337	-7.6189	3.078	2.307	3.037			
SDSS J025345.19-004706.0	43.43837	-0.7851	2.451	2.307	2.417			
SDSS J025345.38-003809.6	43.43914	-0.6360	2.972	2.579	2.889			
SDSS J025512.28-071107.9	43.80122	-7.1856	2.820	2.437	2.782	2.6120	20.45	0.15
LBQS 0252+0136	43.81350	1.8079	2.470	1.634	2.430			
SDSS J025518.57+004847.4	43.82741	0.8132	4.003	2.702	3.953	3.2555	20.90	0.10
						3.9145	21.50	0.10
LBQS 0254+0000	44.18621	0.2128	2.250	1.634	2.215			
SDSS J025647.05-085041.3	44.19605	-8.8448	4.230	3.713	4.148			
SDSS J025754.18+000506.4	44.47579	0.0851	2.680	2.572	2.643			
LBQS 0256-0000	44.77349	0.1894	3.365	2.307	3.322			
LBQS 0256-0031	44.86882	-0.3333	2.000	1.634	1.965			
LBQS 0258+0210	45.19178	2.3792	2.520	1.634	2.489			
SDSS J030047.61-074902.8	45.19842	-7.8175	2.939	2.621	2.900			
BR J0301-5537	45.33979	-55.6199	4.133	2.825	4.082	3.2200	20.30	0.20
SDSS J030307.91-064457.6	45.78298	-6.7493	3.041	2.353	3.000			
LBQS 0301-0035	45.92103	-0.3894	3.231	2.307	3.188			
LBQS 0302-0019	46.20774	-0.1371	3.295	2.307	3.252			
BR J0307-4945	46.84533	-49.7633	4.716	3.130	4.659	3.5910	20.50	0.15
						4.4665	20.60	0.10
LBQS 0305+0127	47.01414	1.6555	2.150	1.634	2.118			
LBQS 0307-0058	47.51256	-0.7794	2.110	1.634	2.075			
SDSS J031013.11-065806.2	47.55466	-6.9684	3.041	2.359	3.001			
UM 682	47.61711	-19.1621	2.756	1.673	2.714			
SDSS J031028.87-005326.1	47.62030	-0.8906	2.460	2.307	2.425			
SDSS J031036.84+005521.5	47.65354	0.9227	3.782	2.825	3.734			
SDSS J0310-0014	47.65404	-0.2492	4.658	3.087	4.601	3.4200	20.50	0.20
BR J0311-1722	47.81333	-17.3798	4.034	2.562	3.984			
LBQS 0308+0129	47.85770	1.6836	2.340	1.739	2.302			
[HB89] 0308+190	47.92750	19.2278	2.839	1.673	2.797			
SDSS J031213.97-062658.8	48.05826	-6.4497	4.033	2.923	3.982			
SDSS J031348.33-010433.0	48.45143	-1.0758	2.468	2.307	2.433			
SDSS J031452.06+001346.3	48.71695	0.2295	3.202	2.436	3.160			
SDSS J031522.08-080043.7	48.84206	-8.0122	2.894	2.307	2.855			
SDSS J031609.83+004043.0	49.04099	0.6786	2.920	2.336	2.881			
SDSS J031712.23-075850.3	49.30098	-7.9807	2.899	2.307	2.860			
[HB89] 0316-203	49.60507	-20.2052	2.869	1.747	2.826			
SDSS J031845.17-001845.3	49.68822	-0.3126	3.223	2.342	3.181			
SDSS J031906.71-010928.6	49.77797	-1.1580	3.139	2.752	3.098			
SDSS J0322-0558	50.60872	-5.9736	3.957	3.491	3.907			
BR J0324-2918	51.18456	-29.3059	4.622	2.900	4.566			
SDSS J032608.12-003340.0	51.53385	-0.5611	4.158	3.108	4.107			
SDSS J032740.66-065147.3	51.91946	-6.8632	3.015	2.355	2.975			
SDSS J033029.75-005918.1	52.62397	-0.9884	2.747	2.407	2.665			
[HB89] 0329-255	52.78717	-25.4120	2.689	1.661	2.662			
SDSS J033119.66-074143.1	52.83194	-7.6953	4.734	3.838	4.638			
SDSS J033224.95-062116.0	53.10396	-6.3545	2.760	2.390	2.722			
SDSS J033406.98-063406.4	53.52910	-6.5685	3.966	3.001	3.917			
BR 0331-1622	53.55604	-16.2014	4.380	2.868	4.326	3.5600	20.60	0.20
UM 683	54.11208	-20.3278	3.132	2.057	3.089			
SDSS J033721.73-070901.7	54.34057	-7.1505	2.641	2.428	2.604			
SDSS J033829.30+002156.2	54.62211	0.3656	5.040	4.096	4.939			
SDSS J033854.77-000520.9	54.72824	-0.0892	3.050	2.307	3.009			
PKS 0336-017	54.75413	-1.5549	3.200	2.109	3.155	3.0619	21.20	0.20
SDSS J033957.96-065220.7	54.99152	-6.8724	2.833	2.511	2.795			
SDSS J034024.57-051909.2	55.10243	-5.3193	2.340	2.307	2.307			
SDSS J034300.87-062229.9	55.75367	-6.3750	3.623	3.207	3.576			
SDSS J034402.85-065300.6	56.01188	-6.8835	3.957	2.820	3.908			
SDSS J034435.96-001527.5	56.14985	-0.2577	2.345	2.307	2.312			
SDSS J034502.22-063622.7	56.25927	-6.6063	2.484	2.307	2.450			
[HB89] 0345+015	57.00952	1.6551	3.638	2.699	3.592			
SDSS J034930.23-063925.1	57.37603	-6.6570	2.541	2.358	2.506			
[HB89] 0347-383	57.43201	-38.1754	3.230	2.044	3.186	3.0244	20.80	0.20
[HB89] 0351-390	58.33039	-38.9323	3.010	1.632	2.970			
SDSS J035329.87-004327.2	58.37448	-0.7242	3.677	2.951	3.631			
BR 0351-1034	58.44544	-10.4220	4.351	3.090	4.297			
UM 684	58.52330	-27.4056	2.823	1.673	2.781			
BR 0353-3820	58.77037	-38.1952	4.545	3.030	4.490			
SDSS J040241.42-064137.9	60.67260	-6.6939	2.432	2.307	2.398			

Continued on Next Page...

Table I.1 – Continued

Name	RA	Dec	z_{em}	z_{min}	z_{max}	z_{abs}	$\log N(\mathrm{H\,I})$	$\epsilon[\log N(\mathrm{H\,I})]$
BR 0401-1711	60.98613	-17.0562	4.227	2.858	4.175			
BR J0415-4357	63.81321	-43.9647	4.073	2.800	4.023	3.8080	20.50	0.20
BR 0418-5723	64.96225	-57.2703	4.461	2.820	4.406			
[HB89] 0420-388 NED01	65.56163	-38.7479	3.123	2.094	3.082			
[HB89] 0420+003	65.67466	0.5056	2.918	1.673	2.879			
BR 0424-2209	66.54304	-22.0381	4.329	2.751	4.276	2.9825	21.40	0.15
H 0428-1342	67.66154	-13.5962	3.244	1.965	3.200			
H 0449-1325	72.92738	-13.3425	3.097	2.006	3.056	2.0520	20.40	0.20
PSS J0452+0355	73.21458	3.9325	4.395	3.115	4.341			
[HB89] 0457+024	74.96688	2.4920	2.380	1.645	2.346			
[HB89] 0458-020	75.30337	-1.9873	2.290	1.960	2.257	2.0399	21.70	0.20
[HB89] 0504+030	76.90194	3.1312	2.460	1.803	2.425			
BR 0523-3345	81.27575	-33.7182	4.385	2.817	4.332			
BR J0529-3526	82.31621	-35.4343	4.418	2.817	4.364			
BR J0529-3552	82.33671	-35.8761	4.172	2.825	4.121	3.6840	20.40	0.15
[HB89] 0528-250	82.53318	-25.0583	2.779	1.961	2.741	2.1404	21.00	0.20
[HB89] 0552+398	88.87836	39.8137	2.360	1.644	2.325			
[HB89] 0636+680	100.51774	67.9766	3.178	2.019	3.132			
[HB89] 0642+449	101.63344	44.8546	3.408	2.192	3.362			
BR J0714-6455	108.63071	-64.9196	4.464	2.776	4.410			
SDSS J072117.43+415114.6	110.32267	41.8541	2.467	2.307	2.432			
SDSS J072321.95+382440.9	110.84148	38.4114	3.099	2.915	3.017			
SDSS J072534.23+431335.0	111.39266	43.2264	2.449	2.307	2.415			
SDSS J072554.52+392243.3	111.47717	39.3787	3.248	2.463	3.205			
SDSS J072559.05+432303.8	111.49606	43.3844	4.019	3.055	3.969			
SDSS J072609.12+385114.4	111.53801	38.8540	2.474	2.307	2.439			
SDSS J072737.89+411424.6	111.90791	41.2402	4.283	3.742	4.230			
SDSS J072949.00+365729.3	112.45422	36.9582	2.490	2.334	2.455			
SDSS J073002.80+434003.0	112.51173	43.6675	2.937	2.307	2.898			
SDSS J073006.47+381400.3	112.52699	38.2334	3.086	2.936	3.045			
SDSS J073103.12+445949.4	112.76302	44.9971	4.998	4.061	4.898			
SDSS J073146.99+364346.3	112.94583	36.7295	4.033	2.994	3.983	3.5913	20.80	0.20
SDSS J073149.50+285448.6	112.95631	28.9136	3.676	2.625	3.629	2.6859	20.55	0.15
SDSS J073231.41+385027.2	113.13089	38.8409	3.052	2.745	3.011			
SDSS J073232.79+435500.4	113.13663	43.9168	3.435	2.483	3.391			
B2 0730+27A	113.33538	27.3510	2.937	2.332	2.898			
[HB89] 0731+653	114.08875	65.2200	3.038	2.019	2.993			
SDSS J073634.60+402603.5	114.14417	40.4343	3.977	3.096	3.928			
SDSS J073706.77+430904.0	114.27823	43.1511	3.013	2.605	2.973			
SDSS J073718.16+323631.4	114.32568	32.6088	3.017	2.307	2.977	2.8924	20.30	0.15
SDSS J073728.62+284655.0	114.36926	28.7820	2.567	2.307	2.532			
SDSS J073735.50+280927.5	114.39793	28.1577	3.004	2.307	2.964	2.8797	20.30	0.15
SDSS J073746.98+242458.1	114.44575	24.4162	3.590	3.135	3.507			
SDSS J073748.60+263205.0	114.45254	26.5347	4.589	3.568	4.533			
SDSS J073813.18+271038.2	114.55495	27.1773	2.442	2.307	2.407			
SDSS J073816.91+314437.0	114.57047	31.7436	2.013	2.533	2.629			
SDSS J073820.28+412716.0	114.58455	41.4544	3.033	2.307	2.993			
SDSS J073912.62+410254.1	114.80261	41.0484	2.994	2.442	2.954			
SDSS J073912.74+282856.0	114.80312	28.4822	3.242	2.807	3.199			
SDSS J073932.63+294249.5	114.88600	29.7138	2.494	2.312	2.459			
SDSS J073934.66+231450.6	114.89445	23.2474	2.869	2.496	2.787			
SDSS J073947.17+445236.7	114.94656	44.8769	3.575	2.650	3.529			
SDSS J073952.95+221307.4	114.97065	22.2187	3.739	2.812	3.692			
SDSS J074005.66+242609.6	115.02363	24.4360	3.778	3.347	3.730			
SDSS J074026.97+224034.5	115.11241	22.6763	3.666	2.986	3.619			
SDSS J074034.41+441002.8	115.14341	44.1675	2.412	2.307	2.378			
SDSS J074037.08+491845.1	115.15453	49.3126	3.767	3.083	3.719			
SDSS J074131.39+212432.9	115.38080	21.4092	2.662	2.307	2.625			
SDSS J074134.46+381559.3	115.39363	38.2665	2.372	2.307	2.338			
SDSS J074141.91+311810.7	115.42467	31.3030	2.415	2.307	2.381			
SDSS J074144.48+335637.0	115.43535	33.9436	3.819	3.005	3.771			
SDSS J074145.00+215932.8	115.43753	21.9925	3.036	2.623	2.996			
SDSS J074154.59+341252.1	115.47749	34.2145	3.909	2.843	3.860			
SDSS J074247.94+422844.6	115.69978	42.4791	3.799	3.619	3.751			
SDSS J074318.01+472514.0	115.82508	47.4206	3.070	2.371	3.029	2.9590	20.85	0.15
SDSS J074354.28+464130.2	115.97620	46.6917	4.367	4.186	4.314			
SDSS J074359.72+481952.7	115.99886	48.3313	2.440	2.307	2.406			
SDSS J074429.82+251037.4	116.12426	25.1771	2.458	2.307	2.423			
SDSS J074437.52+205900.1	116.15635	20.9834	2.680	2.307	2.643	2.5341	20.80	0.15
SDSS J074442.12+375521.5	116.17553	37.9226	2.389	2.307	2.356			
SDSS J074444.14+502959.1	116.18392	50.4998	3.033	2.699	2.993			
SDSS J074500.40+193618.8	116.25170	19.6052	3.388	2.530	3.344			

Continued on Next Page...

Table I.1 – Continued

Name	RA	Dec	z_{em}	z_{min}	z_{max}	z_{abs}	$\log N(\mathrm{H\,I})$	$\epsilon[\log N(\mathrm{H\,I})]$
SDSS J074500.46+341731.0	116.25196	34.2920	3.711	2.614	3.664	2.9946	20.30	0.15
						3.2283	21.10	0.15
SDSS J074503.25+214727.2	116.26356	21.7909	3.081	2.307	3.040			
SDSS J074517.73+223157.7	116.32392	22.5327	3.517	3.069	3.435			
SDSS J074520.21+415725.3	116.33422	41.9571	2.855	2.307	2.816			
2MASSi J0745217+473436	116.34078	47.5767	3.221	2.307	3.179	3.0179	20.40	0.15
SDSS J074545.97+471014.3	116.44155	47.1707	2.948	2.544	2.908			
SDSS J074549.94+373225.2	116.45813	37.5403	3.003	2.858	2.963			
B2 0743+25	116.60781	25.8173	2.979	2.353	2.940			
SDSS J074626.95+322929.4	116.61233	32.4915	3.047	2.348	3.006			
SDSS J074628.65+344248.3	116.61941	34.7134	2.743	2.360	2.706			
SDSS J074640.16+344624.7	116.66737	34.7735	4.009	2.903	3.959			
SDSS J074643.26+210854.9	116.68027	21.1486	3.482	3.024	3.437			
SDSS J074644.53+395749.7	116.68560	39.9638	3.769	2.872	3.721			
SDSS J074711.15+273903.3	116.79647	27.6509	4.133	2.710	4.082	3.4235	20.90	0.10
						3.9010	20.60	0.15
SDSS J074713.25+175948.2	116.80524	17.9967	3.747	3.269	3.699	3.5739	20.45	0.20
SDSS J074724.99+482236.0	116.85414	48.3767	2.380	2.307	2.346			
SDSS J074732.63+244747.0	116.88599	24.7964	3.112	2.415	3.071			
SDSS J074743.65+500027.6	116.93196	50.0077	3.377	2.681	3.334			
SDSS J074746.77+345819.3	116.94489	34.9721	3.153	2.307	3.111			
SDSS J074749.74+443417.0	116.95729	44.5714	4.435	3.107	4.381	4.0190	21.10	0.15
SDSS J074758.56+293315.9	116.99402	29.5544	3.145	3.055	3.104			
SDSS J074759.97+190019.4	116.99991	19.0054	3.344	2.976	3.300			
SDSS J074815.54+225838.0	117.06477	22.9772	3.148	2.752	3.106			
SDSS J074823.85+332051.2	117.09941	33.3476	2.983	2.575	2.944			
SDSS J074834.05+474224.2	117.14189	47.7068	2.490	2.307	2.455			
SDSS J074851.16+343359.1	117.21319	34.5664	3.330	2.331	3.287			
SDSS J074856.03+222953.3	117.23348	22.4981	3.623	2.870	3.576	2.9818	20.40	0.20
SDSS J074859.02+382231.9	117.24594	38.3756	2.583	2.307	2.547			
SDSS J074914.13+305605.8	117.30889	30.9350	3.436	2.396	3.391			
SDSS J074916.67+264740.8	117.31948	26.7947	3.380	2.357	3.336	2.8809	20.45	0.15
SDSS J074926.83+414631.5	117.36180	41.7754	3.739	2.951	3.692			
FBQS J074927.9+415242	117.36628	41.8784	3.111	2.307	3.070			
SDSS J074931.89+153055.8	117.38292	15.5155	2.536	2.307	2.501			
SDSS J074934.44+172305.8	117.39352	17.3850	3.244	2.524	3.202			
SDSS J074939.01+433217.6	117.41257	43.5382	3.142	2.307	3.100			
SDSS J075003.88+415923.0	117.51618	41.9897	2.403	2.364	2.369			
SDSS J075006.62+491834.1	117.52760	49.3095	3.582	2.799	3.536			
SDSS J075017.49+405825.3	117.57290	40.9737	3.863	2.883	3.815			
SDSS J075018.22+263002.0	117.57593	26.5006	2.436	2.307	2.354			
SDSS J075020.46+173729.0	117.58526	17.6247	2.417	2.363	2.382			
SDSS J075032.56+444526.1	117.63568	44.7573	3.358	3.030	3.314			
SDSS J075037.01+313848.1	117.65423	31.6467	2.399	2.307	2.365			
SDSS J075047.95+144322.1	117.69983	14.7228	3.133	2.307	3.092			
SDSS J075051.53+370920.0	117.71472	37.1556	3.229	2.415	3.186			
SDSS J075052.91+372044.0	117.72049	37.3456	2.562	2.307	2.526			
SDSS J075103.95+424211.5	117.76647	42.7032	4.163	2.973	4.111			
SDSS J075104.41+385404.0	117.76839	38.9011	2.502	2.307	2.467			
SDSS J075113.04+312038.0	117.80434	31.3439	3.761	2.931	3.713	3.2237	20.45	0.15
						3.3840	20.45	0.20
SDSS J075117.58+513739.1	117.82328	51.6275	2.658	2.430	2.575			
SDSS J075154.08+264352.5	117.97538	26.7313	3.800	3.058	3.752			
SDSS J075154.63+163652.4	117.97763	16.6146	3.368	2.385	3.324			
SDSS J075155.09+451619.7	117.97959	45.2721	3.340	2.461	3.297	2.6812	20.55	0.20
						2.9291	20.35	0.20
						3.0457	20.45	0.20
SDSS J075158.64+424522.9	117.99438	42.7564	2.453	2.307	2.418			
SDSS J075207.23+243201.9	118.03013	24.5339	2.433	2.307	2.399			
SDSS J075214.14+221356.9	118.05892	22.2325	2.941	2.537	2.901	2.6575	21.40	0.15
SDSS J075238.60+280515.9	118.16086	28.0878	3.409	2.986	3.365			
SDSS J075254.75+280337.0	118.22816	28.0603	2.382	2.307	2.348			
B3 0749+426	118.26391	42.5252	3.589	2.324	3.543			
SDSS J075303.87+284715.5	118.26616	28.7877	2.682	2.342	2.646	2.3925	20.45	0.20
SDSS J075313.81+330327.6	118.30758	33.0577	3.962	3.014	3.913			
SDSS J075320.67+433832.8	118.33616	43.6425	3.806	3.011	3.758			
2MASSi J0753261+403039	118.35885	40.5107	2.935	2.307	2.896			
SDSS J075327.45+272957.1	118.36441	27.4992	3.348	2.413	3.305			
SDSS J075334.52+512343.3	118.39387	51.3954	2.427	2.307	2.392			
SDSS J075347.41+281805.1	118.44757	28.3014	4.031	3.063	3.981			
SDSS J075354.94+193639.4	118.47895	19.6110	3.826	3.045	3.778			
SDSS J075357.85+424100.3	118.49104	42.6835	3.203	2.601	3.161			

Continued on Next Page...

Table I.1 – Continued

Name	RA	Dec	z_{em}	z_{min}	z_{max}	z_{abs}	$\log N(\mathrm{H\,I})$	$\epsilon[\log N(\mathrm{H\,I})]$
SDSS J075442.10+323240.0	118.67544	32.5444	2.342	2.307	2.309			
SDSS J075443.02+234941.2	118.67928	23.8281	3.424	2.584	3.380			
SDSS J075509.98+233210.0	118.79159	23.5361	3.657	2.967	3.610			
SDSS J075510.30+202351.7	118.79293	20.3977	2.878	2.307	2.839			
SDSS J075515.93+154216.6	118.81639	15.7046	3.298	3.237	3.255			
SDSS J075521.96+432424.0	118.84151	43.4067	3.167	2.436	3.125			
SDSS J075526.94+360151.1	118.86228	36.0309	2.382	2.307	2.348			
SDSS J075535.60+405802.9	118.89839	40.9675	2.417	2.307	2.383			
SDSS J075540.14+183500.7	118.91728	18.5836	3.198	2.481	3.156			
PC 0751+5623	118.93329	56.2522	4.281	3.526	4.228			
SDSS J075545.60+405643.5	118.94002	40.9455	2.343	2.307	2.310			
SDSS J075550.45+510621.2	118.96023	51.1059	2.816	2.307	2.778			
SDSS J075552.41+134551.1	118.96840	13.7642	3.663	2.085	3.617			
SDSS J075552.49+491738.2	118.96876	49.2939	3.605	3.148	3.559			
SDSS J0756+4104	119.07559	41.0691	5.090	3.551	5.029			
SDSS J075620.42+354126.2	119.08512	35.6906	3.021	2.351	2.981			
SDSS J075630.59+483228.7	119.12749	48.5413	2.365	2.307	2.332			
SDSS J075635.22+434124.8	119.14678	43.6902	2.354	2.307	2.321			
SDSS J075636.73+164850.7	119.15306	16.8141	2.867	2.471	2.828			
SDSS J075647.86+390830.5	119.19947	39.1418	3.054	2.655	3.013			
SDSS J075658.38+193253.3	119.24328	19.5482	3.349	2.625	3.305			
SDSS J075710.36+362301.5	119.29320	36.3838	2.994	2.307	2.954			
SDSS J075715.33+213333.7	119.31391	21.5594	2.974	2.581	2.891			
SDSS J075724.01+265846.9	119.35007	26.9797	2.402	2.307	2.368			
SDSS J075732.89+441424.6	119.38705	44.2402	4.170	3.088	4.118			
SDSS J075741.13+153838.7	119.42142	15.6441	2.675	2.619	2.638			
SDSS J075757.12+191021.5	119.48801	19.1727	2.908	2.344	2.869			
SDSS J075819.70+202300.9	119.58211	20.3836	3.748	2.677	3.700			
SDSS J075847.84+483210.3	119.69936	48.5362	4.476	3.583	4.421			
SDSS J075859.81+165811.8	119.74923	16.9700	3.442	2.514	3.398			
SDSS J075901.28+284703.4	119.75537	28.7843	2.855	2.461	2.816			
SDSS J075907.57+180054.7	119.78158	18.0152	4.820	3.911	4.723	4.6570	20.95	0.20
SDSS J075910.07+383642.8	119.79199	38.6119	3.989	2.774	3.939			
SDSS J075929.44+201105.0	119.87267	20.1847	3.142	2.400	3.100			
SDSS J075947.38+410636.9	119.94747	41.1103	3.781	2.970	3.733			
SDSS J075948.31+510538.8	119.95135	51.0942	2.365	2.307	2.331			
SDSS J075951.83+312941.1	119.96599	31.4948	3.166	2.307	3.125	3.0335	20.50	0.15
SDSS J080005.95+213137.6	120.02482	21.5271	3.996	3.523	3.946			
SDSS J080014.89+272036.0	120.06209	27.3434	3.786	2.747	3.738			
SDSS J080018.82+522725.2	120.07845	52.4570	3.190	2.783	3.149			
SDSS J080023.01+305101.1	120.09595	30.8504	4.676	3.789	4.581	4.0960	21.05	0.20
SDSS J080025.10+441723.1	120.10462	44.2898	3.555	2.347	3.509			
SDSS J080037.12+290723.6	120.15469	29.1232	3.804	3.024	3.756			
SDSS J080050.27+192058.9	120.20950	19.3497	3.948	2.726	3.899			
SDSS J080055.45+212547.9	120.23107	21.4300	2.493	2.307	2.458			
SDSS J080105.01+345006.7	120.27090	34.8352	2.858	2.528	2.819			
2MASSi J0801178+521034	120.32414	52.1763	3.235	2.307	2.353			
SDSS J080131.31+223055.5	120.38049	22.5154	2.401	2.307	2.367			
SDSS J080132.02+192317.5	120.38342	19.3882	2.542	2.307	2.507			
B3 0758+475	120.40701	47.4245	3.273	2.625	3.231	3.2228	20.70	0.15
SDSS J080144.54+273549.5	120.43559	27.5971	3.121	2.307	3.079	2.9462	20.65	0.15
SDSS J080205.33+185714.8	120.52222	18.9541	2.416	2.307	2.381			
SDSS J080240.49+245732.6	120.66871	24.9591	2.878	2.307	2.840			
SDSS J080245.86+531456.2	120.69112	53.2490	3.829	3.049	3.780			
B2 0759+29	120.70175	29.2929	2.379	2.307	2.345			
SDSS J080300.49+500331.6	120.75208	50.0588	3.775	3.587	3.727			
SDSS J080305.83+503215.1	120.77432	50.5376	3.244	3.020	3.202			
SDSS J080318.73+422037.0	120.82806	42.3436	3.398	2.480	3.354			
SDSS J080333.64+281443.5	120.89018	28.2455	3.707	2.910	3.660			
SDSS J080336.37+432757.3	120.90157	43.4659	2.899	2.499	2.860			
SDSS J080342.39+355448.4	120.92665	35.9135	3.308	2.367	3.265			
SDSS J080349.50+512319.9	120.95633	51.3889	2.885	2.307	2.847			
SDSS J080356.98+251042.5	120.98745	25.1785	2.641	2.307	2.605			
SDSS J080357.85+222700.2	120.99105	22.4501	2.478	2.307	2.443			
SDSS J080400.30+302046.5	121.00134	30.3463	3.446	3.006	3.364			
SDSS J080425.95+183339.6	121.10814	18.5610	2.538	2.337	2.502			
SDSS J080428.58+433641.2	121.11914	43.6115	3.814	3.338	3.732			
SDSS J080430.56+542041.1	121.12738	54.3448	3.760	2.399	3.712			
SDSS J080500.28+332302.5	121.25118	33.3840	2.346	2.307	2.313			
SDSS J080506.67+551607.3	121.27780	55.2687	2.374	2.307	2.340			
SDSS J080523.32+214921.1	121.34719	21.8225	3.491	2.603	3.446			
SDSS J080542.63+233426.8	121.42765	23.5741	3.354	2.614	3.310			

Continued on Next Page...

Table I.1 – Continued

Name	RA	Dec	z_{em}	z_{min}	z_{max}	z_{abs}	$\log N(\mathrm{H\,I})$	$\epsilon[\log N(\mathrm{H\,I})]$
SDSS J080553.02+302937.3	121.47094	30.4937	3.443	2.635	3.399			
SDSS J080556.13+242042.5	121.48390	24.3452	2.449	2.307	2.414			
SDSS J080601.38+382149.9	121.50578	38.3639	3.563	2.700	3.518			
SDSS J080620.47+504124.4	121.58531	50.6901	2.432	2.307	2.398			
SDSS J080622.42+262232.0	121.59346	26.3756	2.389	2.307	2.355			
SDSS J080622.90+251857.6	121.59543	25.3160	2.437	2.307	2.403			
SDSS J080624.43+270359.5	121.60181	27.0665	2.435	2.307	2.401			
SDSS J080624.60+180456.8	121.60252	18.0825	2.445	2.307	2.411			
SDSS J080702.73+232932.1	121.76139	23.4923	2.410	2.307	2.346			
SDSS J080715.11+132805.1	121.81299	13.4681	4.880	3.961	4.782			
SDSS J080721.42+490143.0	121.83928	49.0286	3.123	2.362	3.082			
SDSS J080723.51+544221.2	121.84798	54.7059	4.004	3.036	3.954	3.1778	20.80	0.20
SDSS J080725.41+174345.6	121.85590	17.7294	3.139	2.394	3.097			
SDSS J080732.60+524037.5	121.88590	52.6771	2.913	2.556	2.874			
SDSS J080735.16+413935.4	121.89655	41.6598	3.897	3.412	3.814			
SDSS J080743.58+060903.4	121.93160	6.1510	3.246	2.585	3.204			
SDSS J080744.89+234825.6	121.93705	23.8071	3.745	3.301	3.697			
SDSS J080749.05+451550.2	121.95438	45.2640	3.200	2.374	3.158			
[HB89] 0805+046	121.98974	4.5429	2.880	1.838	2.834			
SDSS J080806.61+281547.7	122.02757	28.2633	2.883	2.335	2.844			
SDSS J080822.02+364612.5	122.09180	36.7702	3.120	2.483	3.079			
SDSS J080838.42+294724.4	122.16009	29.7901	3.243	2.528	3.200			
SDSS J080849.42+521515.3	122.20597	52.2543	4.510	3.181	4.455	3.1140	20.60	0.10
SDSS J080853.86+070940.5	122.22444	7.1613	3.842	2.808	3.794			
SDSS J080856.17+455006.6	122.23413	45.8352	3.154	2.497	3.112			
SDSS J080906.87+172955.1	122.27867	17.4987	2.954	2.307	2.915			
SDSS J080908.50+201455.8	122.28542	20.2488	2.435	2.307	2.400			
SDSS J080909.87+424213.4	122.29115	42.7037	2.674	2.307	2.637			
SDSS J080912.68+311602.1	122.30289	31.2673	2.796	2.307	2.758			
SDSS J080913.45+314518.9	122.30607	31.7553	3.140	2.307	3.098			
SDSS J080916.98+053941.9	122.32078	5.6617	2.537	2.307	2.501			
SDSS J080918.16+453136.7	122.32569	45.5269	2.513	2.307	2.477			
SDSS J080923.45+253613.5	122.34772	25.6038	2.458	2.307	2.424			
SDSS J080926.52+354243.3	122.36052	35.7120	3.140	2.335	3.099	2.9604	20.40	0.15
SDSS J080930.27+352148.4	122.37617	35.3635	3.187	2.761	3.145			
SDSS J080942.99+534706.1	122.42915	53.7850	3.994	3.004	3.944	3.3640	20.50	0.20
SDSS J080953.55+421419.2	122.47317	42.2387	2.979	2.642	2.939			
SDSS J080954.34+233844.5	122.47645	23.6457	3.632	2.595	3.586	3.2431	20.80	0.15
SDSS J080956.02+502000.9	122.48345	50.3336	3.281	2.394	3.238			
SDSS J081001.75+051936.4	122.50734	5.3268	3.935	3.430	3.885			
SDSS J081009.94+384757.0	122.54142	38.7991	3.946	3.177	3.897			
SDSS J081014.62+204021.4	122.56095	20.6726	2.484	2.307	2.450			
SDSS J081029.10+360042.9	122.62127	36.0119	2.531	2.307	2.496			
SDSS J081032.22+414044.1	122.63429	41.6789	2.400	2.307	2.366			
SDSS J081039.79+345730.9	122.66581	34.9586	3.772	2.670	3.724			
SDSS J081044.73+372231.2	122.68644	37.3754	3.341	2.568	3.297			
SDSS J081054.88+460357.8	122.72872	46.0661	4.074	2.811	4.023	2.9560	20.55	0.25
SDSS J081103.27+281621.0	122.76366	28.2725	3.369	2.325	3.325			
SDSS J081109.57+245804.0	122.78989	24.9678	3.158	2.976	3.075			
SDSS J081110.32+283814.1	122.79301	28.6373	2.953	2.307	2.913	2.4331	20.65	0.20
SDSS J081114.32+393633.2	122.80971	39.6093	3.073	2.920	3.033			
SDSS J081125.46+233349.1	122.85611	23.5636	3.097	2.307	3.056			
SDSS J081131.91+224636.9	122.88300	22.7769	3.366	2.375	3.322			
SDSS J081220.23+323939.5	123.08431	32.6610	2.417	2.307	2.383			
FBQS J081240.6+320808	123.16950	32.1357	2.704	2.325	2.667	2.6264	21.30	0.15
SDSS J081241.12+442129.0	123.17136	44.3581	4.338	3.435	4.285			
SDSS J081242.93+322404.0	123.17890	32.4011	3.454	3.020	3.409	3.1737	21.10	0.15
SDSS J081246.93+230858.4	123.19558	23.1496	3.275	2.307	3.232			
SDSS J081251.94+200723.5	123.21646	20.1232	2.958	2.564	2.918			
SDSS J081256.05+563746.8	123.23357	56.6297	3.317	2.456	3.274			
[HB89] 0809+558	123.27863	55.6793	2.403	2.307	2.369			
SDSS J081326.77+230013.4	123.36159	23.0037	3.574	3.113	3.529	3.4125	21.10	0.20
SDSS J081333.32+350810.8	123.38887	35.1363	4.923	4.385	4.864			
SDSS J081339.42+251004.7	123.41429	25.1680	2.886	2.307	2.847			
SDSS J081418.40+233843.1	123.57670	23.6453	3.685	3.312	3.639			
SDSS J081427.60+514516.4	123.61503	51.7546	3.732	2.980	3.685	3.1791	20.40	0.20
SDSS J081435.17+502946.4	123.64657	50.4962	3.885	2.741	3.836	3.7076	21.35	0.15
SDSS J081450.47+370949.8	123.71031	37.1638	3.464	2.742	3.420			
SDSS J081453.45+195018.6	123.72272	19.8385	3.135	2.725	3.052			
SDSS J081502.70+062221.4	123.76126	6.3726	3.113	2.817	3.072			
SDSS J081503.13+230304.7	123.76305	23.0513	2.402	2.307	2.368			
SDSS J081506.82+551604.8	123.77846	55.2680	3.002	2.694	2.962			

Continued on Next Page...

Table I.1 – Continued

Name	RA	Dec	z_{em}	z_{min}	z_{max}	z_{abs}	$\log N(\mathrm{H\,I})$	$\epsilon[\log N(\mathrm{H\,I})]$
SDSS J081510.32+465855.0	123.79301	46.9820	3.664	2.544	3.618			
SDSS J081512.48+363711.1	123.80202	36.6198	3.178	2.828	3.136			
SDSS J081518.31+060604.2	123.82633	6.1012	2.529	2.458	2.494			
SDSS J081518.56+291153.9	123.82738	29.1983	4.255	3.165	4.203			
SDSS J081522.86+343047.1	123.84531	34.5131	3.498	2.526	3.453	2.6783	20.95	0.15
SDSS J081532.62+070323.4	123.88595	7.0565	3.143	3.072	3.102			
[HB89] 0812+332	123.89235	33.0914	2.426	2.307	2.392			
SDSS J081534.27+560524.2	123.89281	56.0901	3.202	2.551	3.160			
SDSS J081534.90+244350.6	123.89543	24.7307	3.158	2.307	3.116			
SDSS J081537.40+223534.0	123.90587	22.5928	3.216	2.633	3.174			
SDSS J081538.22+362321.1	123.90925	36.3892	3.619	2.763	3.573			
SDSS J081543.16+370036.9	123.92986	37.0103	3.190	2.538	3.148			
SDSS J081552.76+271018.7	123.96986	27.1719	3.202	2.347	3.160			
SDSS J081605.19+032232.6	124.02163	3.3757	2.775	2.388	2.737			
SDSS J081618.99+482328.4	124.07914	48.3912	3.582	2.644	3.537	2.7066	20.40	0.15
						3.4358	20.80	0.15
SDSS J081621.32+470300.1	124.08887	47.0500	3.305	2.489	3.262			
SDSS J081633.21+305446.1	124.13844	30.9128	3.886	2.836	3.838			
SDSS J081643.53+264634.1	124.18139	26.7762	2.638	2.307	2.601			
SDSS J081643.72+301614.4	124.18221	30.2707	2.630	2.307	2.593			
SDSS J081648.98+391223.6	124.20410	39.2066	2.385	2.307	2.351			
SDSS J081653.37+054146.3	124.22239	5.6962	2.766	2.380	2.728			
SDSS J081703.36+234640.1	124.26400	23.7778	3.079	2.698	3.038			
SDSS J081707.05+230425.4	124.27940	23.0738	2.424	2.307	2.390			
SDSS J081708.87+383036.0	124.28697	38.5100	3.747	3.063	3.699			
SDSS J081735.95+372858.8	124.39980	37.4830	2.510	2.307	2.475			
SDSS J081754.52+413225.3	124.47718	41.5404	3.536	2.572	3.491			
SDSS J081803.63+321152.6	124.51516	32.1980	2.433	2.307	2.399			
SDSS J081806.87+071920.2	124.52866	7.3223	4.625	3.746	4.531			
SDSS J081809.56+321912.8	124.53984	32.3202	3.786	2.698	3.738			
SDSS J081810.03+443148.8	124.54180	44.5302	3.877	2.841	3.828			
SDSS J081811.49+053713.9	124.54792	5.6205	2.511	2.307	2.476			
SDSS J081812.91+333354.0	124.55384	33.5650	3.509	2.551	3.464			
SDSS J081813.05+263136.9	124.55440	26.5269	4.180	3.442	4.128	3.5651	20.80	0.20
SDSS J081823.95+375620.1	124.59983	37.9389	2.912	2.861	2.873			
SDSS J081838.09+062314.5	124.65874	6.3874	3.218	2.884	3.176			
SDSS J081844.34+355243.9	124.68476	35.8789	3.933	3.003	3.884			
SDSS J081850.01+490817.0	124.70843	49.1381	2.954	2.307	2.915			
SDSS J081851.32+285703.2	124.71385	28.9509	3.686	3.207	3.639	3.2320	20.45	0.20
SDSS J081855.78+095848.0	124.73242	9.9800	3.656	2.406	3.610	3.3060	21.00	0.10
SDSS J081901.26+225627.9	124.75529	22.9411	2.491	2.307	2.456			
SDSS J081909.05+355057.8	124.78771	35.8494	3.144	2.751	3.102			
SDSS J081910.16+501159.5	124.79234	50.1999	2.556	2.307	2.520			
SDSS J081915.23+275311.2	124.81347	27.8865	3.292	2.577	3.249			
SDSS J081932.35+260635.9	124.88482	26.1100	3.169	2.408	3.127			
SDSS J081957.31+314847.8	124.98883	31.8133	2.426	2.307	2.392			
SDSS J081957.38+305237.8	124.98913	30.8772	2.574	2.307	2.538			
SDSS J082000.18+532114.3	125.00080	53.3540	3.075	2.307	3.034			
SDSS J082008.73+075913.0	125.03638	7.9870	2.903	2.822	2.864			
SDSS J082011.04+451330.5	125.04607	45.2251	3.350	2.412	3.307			
SDSS J082012.75+344325.8	125.05316	34.7238	3.492	2.634	3.447	2.9145	20.35	0.15
						3.0037	21.15	0.15
SDSS J082021.74+320737.6	125.09060	32.1271	2.428	2.307	2.394			
SDSS J082033.97+432751.8	125.14159	43.4644	2.407	2.307	2.373			
SDSS J082038.69+522706.3	125.16126	52.4518	2.462	2.307	2.427			
SDSS J082038.86+310026.6	125.16193	31.0074	2.563	2.307	2.528			
SDSS J082039.66+372137.3	125.16527	37.3604	4.270	3.805	4.217			
SDSS J082045.59+080326.2	125.18997	8.0573	2.910	2.307	2.871			
SDSS J082050.72+431146.1	125.21135	43.1962	2.496	2.307	2.461			
SDSS J082058.37+081948.0	125.24322	8.3300	2.517	2.307	2.482			
SDSS J082059.34+561021.9	125.24730	56.1728	3.659	3.305	3.612			
SDSS J082104.92+535146.5	125.27052	53.8629	2.898	2.307	2.859			
SDSS J082107.33+562111.3	125.28055	56.3532	3.618	3.160	3.535			
2MASSi J0821075+310750	125.28172	31.1309	2.619	2.307	2.583			
SDSS J082122.22+081947.1	125.34261	8.3298	3.109	2.917	3.026			
[HB89] 0819-032	125.41682	-3.3868	2.350	1.704	2.319			
SDSS J082150.30+441218.6	125.45962	44.2052	2.425	2.321	2.391			
SDSS J082159.58+402236.4	125.49827	40.3768	3.775	2.973	3.728	3.6126	20.45	0.15
SDSS J082204.67+393722.8	125.51950	39.6230	3.028	2.307	2.988			
SDSS J082209.16+313956.7	125.53818	31.6658	2.362	2.307	2.328			
SDSS J082212.34+160436.9	125.55146	16.0769	4.510	3.649	4.418			
SDSS J082214.29+275200.9	125.55955	27.8669	3.273	2.584	3.231			

Continued on Next Page...

Table I.1 – Continued

Name	RA	Dec	z_{em}	z_{min}	z_{max}	z_{abs}	$\log N(\mathrm{H\,I})$	$\epsilon[\log N(\mathrm{H\,I})]$
SDSS J082214.48+251902.5	125.56036	25.3174	2.739	2.356	2.702			
SDSS J082221.22+214410.5	125.58843	21.7363	2.944	2.307	2.904			
SDSS J082225.16+331716.7	125.60487	33.2880	2.771	2.384	2.733			
SDSS J082234.68+543421.1	125.64452	54.5725	3.562	3.111	3.480			
SDSS J082236.84+274624.1	125.65351	27.7734	2.449	2.307	2.415			
SDSS J082257.04+070104.3	125.73769	7.0179	2.954	2.307	2.914			
SDSS J082308.63+225655.2	125.78598	22.9487	3.056	2.641	3.016			
SDSS J082313.06+535024.0	125.80445	53.8400	2.555	2.307	2.520			
SDSS J082316.57+224204.6	125.81906	22.7013	3.214	2.492	3.172			
SDSS J082320.88+472020.2	125.83702	47.3390	2.620	2.307	2.583			
SDSS J082322.36+221741.8	125.84318	22.2950	2.875	2.307	2.836			
SDSS J082328.61+061146.0	125.86925	6.1961	2.783	2.397	2.746			
SDSS J082340.47+342753.0	125.91865	34.4647	4.248	3.093	4.195			
[HB89] 0820+296	125.92138	29.4745	2.370	1.644	2.333			
SDSS J082341.92+202531.8	125.92469	20.4255	2.526	2.417	2.491			
SDSS J082358.28+413739.2	125.99290	41.6276	2.886	2.499	2.847			
SDSS J082401.62+313113.6	126.00677	31.5205	3.215	2.404	3.173	2.8351	20.55	0.20
SDSS J082405.90+311235.3	126.02462	31.2098	2.387	2.307	2.353			
SDSS J082409.97+042318.4	126.04158	4.3884	3.763	2.848	3.715			
SDSS J082422.65+443509.1	126.09441	44.5859	2.549	2.307	2.514			
SDSS J082426.97+072325.9	126.11240	7.3905	2.877	2.307	2.838	2.3488	20.40	0.15
SDSS J082428.02+234107.9	126.11676	23.6855	2.578	2.307	2.542			
SDSS J082435.59+073243.4	126.14833	7.5454	2.500	2.307	2.465			
SDSS J082454.02+130217.0	126.22510	13.0381	5.207	4.237	5.103	4.8300	20.85	0.20
SDSS J082503.02+361520.0	126.26262	36.2556	3.875	3.522	3.826			
SDSS J082503.56+071344.0	126.26485	7.2289	2.524	2.309	2.488			
SDSS J082508.95+313040.1	126.28733	31.5112	2.432	2.307	2.398			
SDSS J082520.02+570523.7	126.33343	57.0899	3.453	2.570	3.408			
SDSS J082527.26+310019.6	126.36360	31.0055	2.485	2.307	2.450			
SDSS J082531.88+263619.2	126.38284	26.6054	2.564	2.307	2.528			
SDSS J082535.18+512706.3	126.39662	51.4518	3.512	2.461	3.467	3.3180	20.85	0.15
SDSS J082538.66+294649.0	126.41112	29.7803	3.065	2.663	3.024			
SDSS J082540.12+354414.2	126.41720	35.7373	3.846	2.742	3.797	3.6562	21.10	0.20
SDSS J082544.61+333208.8	126.43593	33.5358	2.935	2.307	2.895	2.4854	20.70	0.15
SDSS J082612.54+451355.6	126.55228	45.2321	3.817	2.798	3.769	3.4595	21.35	0.15
						3.7062	20.50	0.15
SDSS J082617.20+210514.0	126.57169	21.0873	2.656	2.307	2.619			
SDSS J082619.70+314847.9	126.58212	31.8133	3.094	2.307	3.053	2.9122	20.30	0.15
SDSS J082625.22+261252.7	126.60511	26.2146	2.495	2.307	2.413			
SDSS J082631.20+483320.7	126.63000	48.5558	2.438	2.347	2.403			
SDSS J082632.78+544540.0	126.63660	54.7611	3.134	2.518	3.092			
SDSS J082638.58+515233.1	126.66078	51.8759	2.844	2.307	2.805			
SDSS J082645.88+071647.0	126.69120	7.2797	3.137	2.307	3.096			
SDSS J082708.26+355532.5	126.78444	35.9257	2.490	2.320	2.455			
SDSS J082725.02+284736.4	126.85428	28.7934	3.078	2.381	3.037	2.9083	20.50	0.15
SDSS J082726.33+230238.7	126.85975	23.0441	3.030	2.618	2.990			
SDSS J082801.65+411937.2	127.00691	41.3270	2.546	2.307	2.510			
SDSS J082813.47+065326.2	127.05614	6.8906	3.002	2.605	2.919			
SDSS J082815.42+214313.9	127.06428	21.7205	2.390	2.307	2.356			
SDSS J082819.63+393617.1	127.08183	39.6048	2.958	2.620	2.919			
SDSS J082854.70+431220.1	127.22797	43.2056	3.169	2.314	3.127			
SDSS J082855.82+490251.5	127.23266	49.0476	3.120	2.439	3.079			
SDSS J082857.47+205243.7	127.23950	20.8788	2.611	2.307	2.575			
SDSS J082859.97+500451.3	127.24991	50.0809	2.467	2.310	2.385			
SDSS J082900.83+282804.2	127.25350	28.4678	2.633	2.307	2.597			
SDSS J082902.69+440511.2	127.26127	44.0865	3.057	2.655	3.016			
SDSS J082906.63+242322.9	127.27765	24.3897	2.416	2.307	2.382			
SDSS J082917.89+353116.1	127.32457	35.5211	3.029	2.620	2.989			
SDSS J082918.45+442614.8	127.32692	44.4375	3.679	2.672	3.632			
SDSS J082939.30+070844.7	127.41379	7.1458	3.985	3.186	3.935	3.3165	20.40	0.20
SDSS J083009.05+335726.7	127.53774	33.9574	2.632	2.307	2.595			
SDSS J083021.74+444000.9	127.59060	44.6669	3.606	3.207	3.560			
SDSS J083030.66+463111.7	127.62775	46.5199	3.266	2.598	3.223			
SDSS J083045.98+293308.9	127.69162	29.5525	3.106	2.526	3.064			
SDSS J083047.06+511025.7	127.69613	51.1738	2.968	2.410	2.928			
SDSS J083047.20+221557.6	127.69668	22.2660	3.199	2.545	3.157			
SDSS J083049.77+043822.7	127.70741	4.6397	2.479	2.307	2.445			
SDSS J083051.75+323327.7	127.71564	32.5577	2.370	2.307	2.336			
SDSS J083052.88+380907.3	127.72040	38.1521	3.149	2.381	3.107			
SDSS J083053.71+390300.2	127.72385	39.0500	3.244	2.528	3.202			
SDSS J083055.56+324342.1	127.73153	32.7284	2.432	2.307	2.398			
SDSS J083102.55+335803.1	127.76067	33.9676	2.429	2.307	2.394			

Continued on Next Page...

Table I.1 – Continued

Name	RA	Dec	z_{em}	z_{min}	z_{max}	z_{abs}	$\log N(\mathrm{H\,I})$	$\epsilon[\log N(\mathrm{H\,I})]$
SDSS J083103.00+523533.5	127.76255	52.5927	4.444	3.341	4.390	3.8677	20.45	0.15
SDSS J083119.74+482018.5	127.83230	48.3385	2.345	2.307	2.312			
SDSS J083122.57+404623.3	127.84407	40.7732	4.885	3.865	4.826	4.3404	20.70	0.20
SDSS J083212.37+530327.3	128.05155	53.0576	4.050	3.071	4.000	3.5403	20.40	0.15
SDSS J083219.41+230541.4	128.08089	23.0949	2.402	2.307	2.368			
SDSS J083223.60+455418.9	128.09839	45.9053	2.469	2.307	2.435			
SDSS J083224.52+273041.5	128.10220	27.5115	3.867	2.846	3.818			
SDSS J083226.80+264124.6	128.11168	26.6902	2.383	2.307	2.349			
SDSS J083231.61+211534.6	128.13174	21.2596	2.482	2.307	2.448			
SDSS J083234.67+315418.9	128.14450	31.9053	3.064	2.703	3.024			
SDSS J083234.75+285205.8	128.14483	28.8683	2.362	2.307	2.329			
SDSS J083236.53+302255.7	128.15223	30.3821	3.218	2.496	3.175	2.6648	20.80	0.20
SDSS J083257.77+262032.7	128.24075	26.3424	2.425	2.307	2.391			
SDSS J083301.64+353133.8	128.25691	35.5260	2.719	2.675	2.682			
[HB89] 0830+115	128.30986	11.3934	2.979	1.797	2.936			
SDSS J083317.40+245851.1	128.32250	24.9809	3.448	2.356	3.404			
SDSS J083320.53+203910.6	128.33557	20.6530	3.050	2.402	3.010			
SDSS J083322.50+095941.2	128.34381	9.9948	3.716	2.044	3.669			
SDSS J083323.84+230119.8	128.34934	23.0222	2.383	2.307	2.350			
SDSS J083326.81+081552.0	128.36175	8.2645	2.572	2.307	2.537			
SDSS J083328.06+081317.5	128.36695	8.2215	3.326	2.357	3.283	2.9453	20.60	0.15
SDSS J083330.56+233909.1	128.37736	23.6526	2.423	2.315	2.389			
SDSS J083335.10+463601.9	128.39629	46.6005	2.506	2.376	2.471			
SDSS J083341.64+303348.8	128.42353	30.5636	3.778	2.574	3.730			
SDSS J083349.99+043200.0	128.45832	4.5334	3.562	2.687	3.516	3.3021	20.45	0.15
SDSS J083355.70+354614.2	128.48212	35.7706	3.311	2.597	3.268			
SDSS J083400.05+430148.1	128.50021	43.0300	2.403	2.307	2.369			
SDSS J083400.49+394216.9	128.50204	39.7047	3.212	2.577	3.170			
[HB89] 0831+128	128.53597	12.6435	2.748	1.961	2.706			
SDSS J083429.43+214024.6	128.62267	21.6735	4.497	3.633	4.442	3.7107	20.65	0.20
						4.3899	20.70	0.20
SDSS J083431.60+362015.8	128.63170	36.3377	2.396	2.307	2.362			
SDSS J083436.20+481715.9	128.65089	48.2878	2.900	2.348	2.861			
SDSS J083450.61+383337.0	128.71088	38.5603	3.403	2.694	3.359			
SDSS J083510.92+065052.8	128.79551	6.8480	4.007	2.735	3.957	3.9555	20.40	0.10
SDSS J083513.15+070729.3	128.80481	7.1248	4.053	3.061	4.003			
SDSS J083535.69+212240.1	128.89872	21.3778	3.116	2.709	3.034			
SDSS J083546.51+351300.8	128.94382	35.2169	3.299	2.873	3.216			
SDSS J083606.80+374044.1	129.02834	37.6789	3.509	2.563	3.464			
SDSS J083608.07+354948.8	129.03367	35.8302	3.643	2.935	3.597			
SDSS J083609.20+462020.9	129.03837	46.3392	3.063	2.652	3.022			
SDSS J083612.35+451458.4	129.05146	45.2496	2.529	2.307	2.494			
SDSS J083620.98+562038.5	129.08743	56.3441	3.190	2.761	3.148			
[HB89] 0834-201	129.16340	-20.2832	2.750	1.632	2.704	1.7150	20.40	0.20
SDSS J083642.82+493934.4	129.17846	49.6596	2.968	2.567	2.928			
SDSS J083653.08+275039.1	129.22120	27.8442	3.191	2.785	3.149			
SDSS J083655.80+064104.6	129.23254	6.6846	4.435	3.586	4.344			
SDSS J083658.08+273846.2	129.24200	27.6462	3.183	2.406	3.142			
SDSS J083659.83+351019.3	129.24933	35.1720	3.319	2.940	3.276			
SDSS J083700.82+350550.1	129.25345	35.0973	3.311	2.337	3.267			
SDSS J083802.33+485412.9	129.50980	48.9036	3.193	2.307	3.151			
SDSS J083803.75+242643.2	129.51563	24.4453	2.917	2.307	2.878			
SDSS J083805.17+484735.9	129.52161	48.7933	3.280	2.531	3.237			
SDSS J083808.93+091640.2	129.53722	9.2779	2.580	2.307	2.544			
SDSS J083826.94+222759.0	129.61225	22.4664	3.426	2.569	3.382			
SDSS J083827.56+323515.3	129.61485	32.5876	3.245	2.571	3.202			
SDSS J083834.31+414838.6	129.64298	41.8108	2.480	2.307	2.445			
SDSS J083839.16+285852.7	129.66321	28.9813	4.363	2.954	4.309			
SDSS J083841.55+390217.1	129.67317	39.0381	4.345	3.521	4.292			
SDSS J083848.67+411703.9	129.70284	41.2844	2.852	2.307	2.814			
SDSS J083903.73+555603.8	129.76559	55.9344	2.629	2.312	2.593			
SDSS J083914.14+485125.7	129.80892	48.8572	2.967	2.307	2.928			
SDSS J083920.53+352459.3	129.83553	35.4165	4.784	3.880	4.688			
SDSS J083922.09+334839.5	129.84207	33.8110	3.388	2.536	3.344			
SDSS J083922.13+343721.1	129.84224	34.6225	3.305	2.910	3.261			
SDSS J083923.09+250805.5	129.84624	25.1349	3.494	2.757	3.449			
SDSS J083928.73+211404.7	129.86972	21.2347	2.692	2.314	2.655			
[HB89] 0836+113	129.88756	11.2011	2.700	1.740	2.670	2.4660	20.60	0.20
SDSS J083941.45+031817.0	129.92271	3.3047	4.230	2.883	4.178			
SDSS J083941.95+322402.5	129.92482	32.4007	3.366	2.920	3.322			
SDSS J083946.21+511202.8	129.94258	51.2008	4.390	3.857	4.308			
SDSS J083955.83+224215.9	129.98263	22.7044	3.031	2.397	2.991			

Continued on Next Page...

Table I.1 – Continued

Name	RA	Dec	z_{em}	z_{min}	z_{max}	z_{abs}	$\log N(\mathrm{H\,I})$	$\epsilon[\log N(\mathrm{H\,I})]$
SDSS J084011.64+360855.2	130.04853	36.1487	2.369	2.307	2.335			
SDSS J084014.68+441909.9	130.06122	44.3194	2.504	2.307	2.469			
SDSS J084015.41+333659.2	130.06422	33.6165	2.416	2.307	2.382			
SDSS J084027.32+070037.0	130.11389	7.0103	3.198	2.557	3.156			
SDSS J084039.27+525504.8	130.16364	52.9180	3.091	2.397	3.050	2.8622	20.30	0.15
SDSS J084042.19+370552.5	130.17583	37.0979	2.905	2.614	2.866			
SDSS J084044.18+341101.6	130.18412	34.1838	3.889	3.421	3.840			
SDSS J084045.40+090809.4	130.18921	9.1360	4.519	4.168	4.463			
SDSS J084047.39+293427.7	130.19748	29.5744	2.666	2.307	2.630			
SDSS J084048.96+273754.6	130.20403	27.6319	2.423	2.307	2.389			
SDSS J084049.25+030927.8	130.20523	3.1578	2.450	2.307	2.415			
SDSS J084051.22+404806.7	130.21345	40.8019	4.417	3.404	4.363	4.0073	20.85	0.20
SDSS J084100.66+300553.0	130.25276	30.0981	2.397	2.307	2.363			
SDSS J084101.38+311941.2	130.25577	31.3281	2.896	2.307	2.857			
SDSS J084104.49+420818.9	130.26874	42.1386	2.758	2.610	2.720			
SDSS J084107.23+333921.7	130.28017	33.6561	3.066	2.955	3.026			
SDSS J084112.55+065129.3	130.30231	6.8582	2.399	2.348	2.365			
SDSS J084128.24+485422.6	130.36770	48.9063	2.812	2.307	2.774			
SDSS J084130.25+290310.5	130.37608	29.0529	2.768	2.408	2.730			
SDSS J084131.73+040616.7	130.38221	4.1047	3.114	2.692	3.072	3.0456	21.35	0.20
SDSS J084136.18+541047.0	130.40080	54.1798	3.012	2.307	2.972			
SDSS J084146.06+483804.3	130.44194	48.6345	2.372	2.307	2.338			
SDSS J084156.54+423825.7	130.48561	42.6405	2.870	2.700	2.831			
SDSS J084203.35+063752.2	130.51396	6.6312	3.692	2.550	3.645			
SDSS J084205.65+462510.3	130.52360	46.4195	3.478	2.623	3.433			
SDSS J084212.40+391323.5	130.55168	39.2232	2.888	2.312	2.849			
SDSS J084214.26+270259.0	130.55944	27.0497	2.994	2.643	2.954			
SDSS J084215.87+474248.8	130.56618	47.7136	2.704	2.325	2.667			
SDSS J084231.26+275837.5	130.63029	27.9771	3.189	2.370	3.147			
SDSS J084233.27+365129.9	130.63865	36.8583	3.773	2.918	3.726			
SDSS J084241.41+464140.3	130.67262	46.6945	3.965	3.458	3.916			
SDSS J084243.55+043249.3	130.68146	4.5470	2.724	2.562	2.687			
SDSS J084245.32+325314.2	130.68887	32.8873	2.399	2.307	2.365			
SDSS J084249.02+235204.7	130.70429	23.8680	3.316	2.503	3.273			
SDSS J084253.46+431912.8	130.72276	43.3202	3.039	2.625	2.998			
SDSS J084255.60+331822.5	130.73170	33.3063	2.590	2.307	2.554			
SDSS J084255.92+223431.9	130.73304	22.5755	2.715	2.335	2.678			
SDSS J084258.83+361444.1	130.74514	36.2456	2.490	2.307	2.407			
SDSS J084307.19+403626.7	130.77998	40.6074	3.852	3.093	3.804	3.3883	20.50	0.20
SDSS J084309.66+241559.2	130.79027	24.2665	2.864	2.683	2.825			
SDSS J084311.13+042619.5	130.79638	4.4388	2.526	2.307	2.491			
SDSS J084312.64+075029.3	130.80268	7.8415	3.266	2.844	3.183			
SDSS J084314.15+025946.5	130.80900	2.9963	2.909	2.347	2.870			
SDSS J084337.74+503518.6	130.90731	50.5885	2.415	2.307	2.381			
[HB89] 0840+447	130.90912	44.5708	3.210	2.311	3.168			
SDSS J084340.94+490900.9	130.92064	49.1503	3.026	2.406	2.986			
SDSS J084346.45+290811.6	130.94357	29.1366	3.146	2.755	3.104			
[HB89] 0840+450	130.95286	44.8741	2.582	2.307	2.500			
SDSS J084355.61+560610.4	130.98173	56.1029	2.392	2.307	2.358			
SDSS J084407.29+515311.0	131.03041	51.8865	3.199	2.493	3.157	2.7753	21.45	0.15
SDSS J084408.29+423226.9	131.03457	42.5408	2.991	2.596	2.909			
SDSS J084410.16+421323.0	131.04237	42.2231	3.809	2.873	3.761			
SDSS J084416.82+394300.6	131.07011	39.7169	2.476	2.307	2.441			
SDSS J084421.61+333805.7	131.09005	33.6349	2.948	2.307	2.908			
SDSS J084426.10+421646.5	131.10878	42.2796	3.006	2.599	2.965	2.8206	20.85	0.15
SDSS J084434.15+224305.1	131.14230	22.7181	3.122	2.357	3.081			
SDSS J084437.13+311048.3	131.15474	31.1801	3.011	2.688	2.971			
SDSS J084438.62+462425.3	131.16099	46.4070	3.785	2.990	3.737	3.3345	20.85	0.15
SDSS J084441.44+314327.2	131.17269	31.7243	3.042	2.643	2.960			
SDSS J084451.72+051827.7	131.21552	5.3077	4.465	4.195	4.410			
SDSS J084455.22+251840.8	131.23009	25.3114	3.753	2.848	3.706			
SDSS J084455.69+033337.2	131.23209	3.5604	3.786	2.879	3.738			
SDSS J084502.73+081214.2	131.26138	8.2040	2.349	2.307	2.315			
SDSS J084509.34+321956.7	131.28895	32.3324	3.073	2.374	3.032			
SDSS J084519.18+424621.0	131.32997	42.7725	2.876	2.599	2.837			
SDSS J084530.36+341344.8	131.37655	34.2291	2.414	2.307	2.380			
SDSS J084532.62+304920.4	131.38594	30.8223	3.625	2.843	3.578			
SDSS J084533.04-000919.7	131.38770	-0.1555	3.231	2.514	3.189			
SDSS J084539.97+305641.9	131.41656	30.9450	2.419	2.307	2.385			
SDSS J084543.38+525641.5	131.43081	52.9449	2.714	2.368	2.677			
SDSS J084552.27+504524.2	131.46782	50.7568	2.895	2.503	2.856	2.7734	20.30	0.25
SDSS J084616.80+242707.7	131.57002	24.4521	2.668	2.307	2.631			

Continued on Next Page...

Table I.1 – Continued

Name	RA	Dec	z_{em}	z_{min}	z_{max}	z_{abs}	$\log N(\mathrm{H\,I})$	$\epsilon[\log N(\mathrm{H\,I})]$
SDSS J084621.71+004025.2	131.59046	0.6737	3.017	2.391	2.977			
SDSS J084627.84+080051.7	131.61602	8.0144	5.028	4.086	4.927			
SDSS J084629.48+090521.9	131.62285	9.0894	2.694	2.316	2.657			
SDSS J084631.52+241108.3	131.63137	24.1857	4.742	3.845	4.646			
SDSS J084654.27+300012.8	131.72614	30.0036	3.650	3.211	3.604			
FBQS J084715.1+383110	131.81320	38.5194	3.182	2.307	3.140			
SDSS J084752.61+531048.0	131.96926	53.1800	2.368	2.307	2.335			
SDSS J084758.11+454202.3	131.99214	45.7006	2.577	2.347	2.541			
SDSS J084806.96+333151.2	132.02904	33.5309	2.470	2.307	2.435			
SDSS J084807.49+362325.9	132.03122	36.3906	2.355	2.307	2.322			
SDSS J084809.25+275454.5	132.03858	27.9152	2.470	2.307	2.435			
SDSS J084811.52-001417.9	132.04801	-0.2383	4.124	3.062	4.073			
SDSS J084826.41+051838.8	132.11007	5.3108	2.492	2.380	2.457			
SDSS J084830.94+394443.7	132.12894	39.7455	3.567	2.521	3.521			
SDSS J084838.58+374541.7	132.16079	37.7616	2.619	2.307	2.582			
SDSS J084838.84+441828.7	132.16185	44.3080	3.749	3.263	3.701			
SDSS J084842.16+025626.5	132.17568	2.9407	2.975	2.606	2.935			
SDSS J084847.98+464717.3	132.19995	46.7882	2.788	2.613	2.705			
SDSS J084852.70+380229.5	132.21962	38.0415	3.129	2.449	3.088	3.0509	20.45	0.15
SDSS J084904.09+072600.6	132.26708	7.4335	3.397	2.520	3.353	3.1443	21.15	0.15
SDSS J084909.58+323322.9	132.28992	32.5564	2.915	2.518	2.876			
SDSS J084917.22+030605.8	132.32179	3.1016	3.081	2.662	3.040			
SDSS J084917.71+302406.1	132.32383	30.4017	2.483	2.307	2.448			
SDSS J084932.42+402247.2	132.38512	40.3798	3.713	3.247	3.631			
[HB89] 0846+152	132.40892	15.1060	2.640	1.831	2.599			
SDSS J084939.88+235129.1	132.41620	23.8581	3.239	2.341	3.196			
SDSS J084948.98+275638.7	132.45410	27.9441	2.853	2.307	2.814			
[HB89] 0847+100	132.45823	9.8427	2.806	2.307	2.767			
SDSS J084951.45+383548.5	132.46442	38.5968	2.429	2.307	2.395			
SDSS J084952.38+342356.6	132.46828	34.3991	3.266	2.517	3.223			
SDSS J084957.67+543529.7	132.49037	54.5916	3.834	3.356	3.752			
SDSS J084959.62+430111.4	132.49843	43.0199	3.656	3.195	3.574			
SDSS J085000.95+283602.1	132.50399	28.6006	2.546	2.307	2.511			
SDSS J085006.08+072959.0	132.52535	7.4997	2.684	2.308	2.648			
SDSS J085011.23+364015.9	132.54681	36.6711	2.355	2.307	2.322			
SDSS J085028.32+453713.7	132.61803	45.6205	3.921	3.192	3.871			
SDSS J085039.05+222319.9	132.66274	22.3889	3.194	2.779	3.112			
SDSS J085045.44+563618.7	132.68935	56.6052	2.464	2.307	2.430			
[HB89] 0848+155	132.71587	15.3709	2.010	1.735	1.980			
SDSS J085058.39+064627.7	132.74338	6.7744	2.821	2.307	2.783			
SDSS J085115.10+463215.6	132.81296	46.5377	2.762	2.377	2.724			
SDSS J085124.67+262938.1	132.85281	26.4939	3.069	2.307	3.028	2.3604	21.15	0.15
SDSS J085126.96+292304.3	132.86236	29.3846	2.487	2.307	2.452			
SDSS J085142.90+561732.0	132.92880	56.2922	2.508	2.307	2.473			
SDSS J085143.72+233208.9	132.93220	23.5358	4.499	4.177	4.444			
SDSS J085149.01+371645.5	132.95421	37.2793	3.011	2.341	2.971			
SDSS J085150.75+412349.3	132.96148	41.3971	2.395	2.307	2.361			
SDSS J085150.96+282738.3	132.96235	28.4607	3.551	2.685	3.505			
SDSS J085151.26+020755.9	132.96359	2.1322	4.292	4.164	4.210			
SDSS J085151.54+045200.4	132.96479	4.8668	3.510	3.063	3.428			
SDSS J085155.78+300618.0	132.98242	30.1050	3.601	2.697	3.555			
SDSS J085213.83+241718.7	133.05765	24.2886	2.497	2.307	2.462			
SDSS J085216.23+325247.2	133.06763	32.8798	3.737	3.404	3.689			
SDSS J085227.27+504510.7	133.11366	50.7530	4.216	2.939	4.164			
SDSS J085228.72+565349.3	133.11970	56.8971	2.897	2.553	2.858			
SDSS J085237.93+263758.5	133.15808	26.6329	3.290	2.583	3.247			
SDSS J085245.09+010239.3	133.18790	1.0443	2.503	2.307	2.468			
SDSS J085246.05+295501.4	133.19191	29.9171	2.430	2.307	2.395			
SDSS J085248.14+314648.1	133.20061	31.7800	2.381	2.331	2.347			
SDSS J085257.12+243103.1	133.23802	24.5175	3.617	2.729	3.571	2.7904	20.80	0.20
						2.8177	21.15	0.20
[HB89] 0850+283	133.26612	28.1198	2.976	2.605	2.936			
SDSS J085304.15+523649.1	133.26734	52.6136	2.395	2.317	2.361			
SDSS J085304.35+093000.8	133.26814	9.5002	3.105	2.695	3.064			
SDSS J085305.81+450826.8	133.27423	45.1408	2.510	2.307	2.475			
SDSS J085309.70+232454.3	133.29044	23.4151	2.524	2.307	2.489			
SDSS J085316.55+445616.5	133.31898	44.9380	2.530	2.307	2.495			
SDSS J085323.22+415121.3	133.34678	41.8559	3.388	2.464	3.344			
SDSS J085329.31+243541.7	133.37216	24.5949	2.806	2.667	2.768			
SDSS J085330.69+254250.0	133.37791	25.7139	2.425	2.307	2.391			
SDSS J085346.24+000839.4	133.44271	0.1443	2.606	2.426	2.570			
SDSS J085406.12+423810.7	133.52551	42.6363	2.387	2.307	2.353			

Continued on Next Page...

Table I.1 – Continued

Name	RA	Dec	z_{em}	z_{min}	z_{max}	z_{abs}	$\log N(\mathrm{H\,I})$	$\epsilon[\log N(\mathrm{H\,I})]$
SDSS J085410.84+412938.5	133.54518	41.4941	3.451	2.586	3.407			
SDSS J085417.60+532735.2	133.57339	53.4598	2.418	2.307	2.384			
SDSS J085427.66+444255.0	133.61529	44.7153	3.547	2.797	3.501			
SDSS J085430.17+004213.6	133.62573	0.7038	4.084	3.275	4.033	3.6905	20.35	0.20
SDSS J085430.37+205650.8	133.62655	20.9475	5.179	4.214	5.076	4.4250	21.05	0.20
SDSS J085441.49+465203.1	133.67294	46.8676	2.513	2.307	2.477			
SDSS J085503.81+293248.9	133.76587	29.5469	3.389	2.417	3.345			
SDSS J085505.92+241351.6	133.77470	24.2310	2.413	2.307	2.379			
SDSS J085528.98+225733.6	133.87076	22.9593	2.884	2.805	2.845			
SDSS J085529.34+240326.4	133.87230	24.0573	3.048	2.656	3.007			
SDSS J085531.08+322728.4	133.87954	32.4579	3.267	2.591	3.224			
SDSS J085534.39+510632.7	133.89336	51.1091	3.260	2.307	3.217			
SDSS J085546.23+082051.2	133.94266	8.3476	4.285	3.135	4.233	3.7422	21.05	0.15
SDSS J085606.89+393924.0	134.02873	39.6567	4.105	3.247	4.054			
SDSS J085609.46+374928.8	134.03949	37.8247	2.570	2.307	2.535			
SDSS J085611.69+411516.8	134.04872	41.2547	3.683	2.605	3.637			
SDSS J085619.18+235531.8	134.07995	23.9255	2.544	2.307	2.509			
SDSS J085624.92+102017.0	134.10383	10.3381	3.702	2.708	3.655			
SDSS J085630.42+310759.4	134.12678	31.1332	3.506	2.580	3.461			
SDSS J085637.69+100855.5	134.15709	10.1487	4.550	4.100	4.494			
SDSS J085643.38+321242.2	134.18078	32.2118	3.228	2.390	3.186			
SDSS J085647.17+293700.5	134.19657	29.6168	2.422	2.307	2.388			
SDSS J085651.37+435812.1	134.21406	43.9700	3.530	2.390	3.485			
SDSS J085652.27+355812.1	134.21782	35.9700	2.880	2.341	2.841			
SDSS J085707.02+102312.2	134.27929	10.3867	3.739	3.270	3.656			
SDSS J085707.94+321031.9	134.28310	32.1756	4.796	3.890	4.699			
SDSS J085728.90+251456.5	134.37043	25.2490	2.559	2.307	2.524			
SDSS J085729.48+420054.6	134.37285	42.0152	3.532	2.617	3.487	2.6865	21.15	0.15
						3.0347	20.35	0.20
SDSS J085731.90+365446.5	134.38296	36.9130	2.903	2.533	2.864			
SDSS J085734.26+273141.9	134.39279	27.5283	2.482	2.307	2.400			
SDSS J085734.56+545901.6	134.39401	54.9838	2.982	2.374	2.943			
SDSS J085737.17+294132.4	134.40492	29.6924	3.104	2.307	3.063			
SDSS J085739.12+090131.2	134.41303	9.0253	3.088	2.669	3.047			
SDSS J085743.65+292710.4	134.43192	29.4529	2.453	2.307	2.419			
SDSS J085753.05+470439.2	134.47107	47.0776	3.257	2.821	3.214			
SDSS J085753.39+010511.1	134.47251	1.0864	3.308	2.503	3.264			
SDSS J085754.40+313026.9	134.47670	31.5075	3.301	2.570	3.258			
SDSS J085805.31+530038.5	134.52215	53.0107	3.896	2.890	3.847			
SDSS J085816.82+080437.7	134.57009	8.0772	3.409	2.988	3.365			
SDSS J085817.57+322349.7	134.57322	32.3971	3.506	2.537	3.461			
SDSS J085822.66+345706.2	134.59442	34.9517	3.871	3.389	3.789			
SDSS J085824.79+265903.0	134.60332	26.9842	2.461	2.307	2.426			
SDSS J085825.70+005006.6	134.60711	0.8352	2.855	2.307	2.816			
SDSS J085832.39+481821.6	134.63500	48.3060	2.393	2.307	2.359			
SDSS J085833.02+401203.1	134.63759	40.2009	3.013	2.307	2.973			
SDSS J085837.95+052141.7	134.65816	5.3616	3.529	2.641	3.483			
SDSS J085848.35+310127.9	134.70180	31.0243	2.970	2.593	2.930			
SDSS J085848.91+483539.0	134.70385	48.5942	3.225	2.812	3.183			
SDSS J085848.96+180109.9	134.70401	18.0194	2.620	1.682	2.580			
SDSS J085853.98+312639.4	134.72493	31.4443	3.105	2.698	3.064			
SDSS J085909.25+382303.8	134.78855	38.3844	2.783	2.397	2.745			
SDSS J085909.77+371301.8	134.79077	37.2172	3.195	2.312	3.153			
SDSS J085919.78+360051.2	134.83236	36.0143	2.865	2.470	2.827			
SDSS J085921.88+274408.5	134.84119	27.7357	2.529	2.311	2.493			
SDSS J085922.02+051356.9	134.84178	5.2325	3.644	2.822	3.598			
SDSS J085952.36+350724.7	134.96820	35.1235	2.372	2.307	2.338			
SDSS J085956.85+250810.8	134.98689	25.1364	3.248	2.442	3.206			
SDSS J085957.55+242443.4	134.98982	24.4121	3.349	2.616	3.306			
SDSS J085959.14+020519.7	134.99644	2.0888	2.981	2.307	2.941			
SDSS J090000.06+445031.4	135.00029	44.8421	2.447	2.307	2.413			
SDSS J090007.89+233452.7	135.03289	23.5813	3.603	3.148	3.521			
SDSS J090017.60+490001.9	135.07338	49.0005	3.208	2.356	3.166			
SDSS J090028.66+481900.8	135.11946	48.3169	3.616	3.185	3.570			
SDSS J090029.53+430053.7	135.12308	43.0149	4.379	3.829	4.325	4.2639	20.50	0.25
SDSS J090030.78+010446.4	135.12829	1.0796	3.595	2.867	3.549			
FBQS J090033.4+421546	135.13969	42.2631	3.295	2.329	3.252	3.2459	20.30	0.15
SDSS J090034.57+251957.7	135.14406	25.3327	2.819	2.441	2.781			
SDSS J090036.80+321129.5	135.15335	32.1915	2.970	2.307	2.931			
SDSS J090037.93+303040.9	135.15807	30.5114	3.306	2.879	3.223			
SDSS J090058.91+085011.9	135.24549	8.8367	3.585	3.115	3.539			
SDSS J090059.22+324622.5	135.24679	32.7729	3.007	2.597	2.967			

Continued on Next Page...

Table I.1 – Continued

Name	RA	Dec	z_{em}	z_{min}	z_{max}	z_{abs}	$\log N(\mathrm{H\,I})$	$\epsilon[\log N(\mathrm{H\,I})]$
SDSS J090100.61+472536.2	135.25252	47.4267	4.598	3.723	4.505			
SDSS J090102.93+354928.5	135.26225	35.8246	3.116	2.307	3.074			
SDSS J090110.39+325652.1	135.29330	32.9478	3.951	3.461	3.869			
SDSS J090112.41+465553.3	135.30180	46.9315	2.490	2.307	2.456			
SDSS J090123.95+255238.7	135.34982	25.8774	3.563	2.643	3.518			
SDSS J090134.30+284048.5	135.39295	28.6802	3.642	2.644	3.596			
SDSS J090136.03+555126.1	135.40017	55.8573	2.943	2.307	2.904			
SDSS J090140.67+441402.8	135.41947	44.2341	2.354	2.307	2.320			
SDSS J090141.98+093213.2	135.42494	9.5370	3.572	3.163	3.527			
SDSS J090148.24+043702.1	135.45103	4.6173	2.754	2.605	2.716			
SDSS J090150.16+325001.3	135.45904	32.8337	3.522	2.738	3.476			
SDSS J090203.84+005926.7	135.51603	0.9908	3.234	2.474	3.192			
SDSS J090216.54+363845.2	135.56896	36.6459	3.447	3.049	3.403			
SDSS J090218.51+050317.4	135.57715	5.0549	2.967	2.307	2.927			
SDSS J090234.53+284118.5	135.64389	28.6885	3.566	2.465	3.520			
SDSS J090234.76+432154.4	135.64487	43.3651	4.196	3.669	4.144			
FBQS J090239.8+395726	135.66623	39.9574	3.091	2.307	3.050			
SDSS J090243.55+374909.1	135.68149	37.8192	3.269	2.333	3.227			
SDSS J090244.64+091011.8	135.68603	9.1700	3.459	3.016	3.414			
SDSS J090245.76+085115.8	135.69069	8.8544	5.226	4.253	5.122			
SDSS J090250.50+400331.5	135.71043	40.0588	2.430	2.307	2.396			
SDSS J090253.43+062824.2	135.72264	6.4734	3.375	2.659	3.331			
SDSS J090253.68+092149.9	135.72369	9.3639	3.857	3.376	3.775			
SDSS J090300.70+300901.1	135.75292	30.1503	3.884	2.924	3.836			
SDSS J090301.24+535315.6	135.75522	53.8877	2.441	2.307	2.406			
SDSS J090305.80+424426.9	135.77422	42.7408	2.637	2.307	2.601			
SDSS J090320.46+254810.0	135.83527	25.8028	3.006	2.307	2.966			
SDSS J090333.55+262836.3	135.88982	26.4768	3.223	2.320	3.181			
SDSS J090351.07+535101.1	135.96284	53.8503	2.855	2.461	2.817			
SDSS J090359.24+341358.6	135.99688	34.2330	2.625	2.307	2.589			
SDSS J090406.21+482057.3	136.02591	48.3493	3.630	2.655	3.584			
SDSS J090425.10+102932.5	136.10459	10.4924	4.153	3.286	4.102			
SDSS J090425.43+335302.7	136.10597	33.8841	4.050	3.550	3.968			
SDSS J090430.48+343108.9	136.12708	34.5191	3.408	2.972	3.326			
SDSS J090440.63+535038.8	136.16936	53.8441	4.271	3.082	4.218			
SDSS J090440.73+240923.6	136.16972	24.1566	2.510	2.307	2.475			
SDSS J090442.50+415905.9	136.17712	41.9850	4.092	3.298	4.041			
SDSS J090443.29+370311.2	136.18037	37.0531	2.629	2.307	2.592			
SDSS J090446.59+351040.0	136.19416	35.1778	2.492	2.307	2.457			
SDSS J090453.76+381030.8	136.22404	38.1752	2.392	2.307	2.358			
SDSS J090454.24+441554.1	136.22601	44.2651	3.843	3.155	3.795			
SDSS J090508.88+305757.3	136.28702	30.9659	3.027	2.307	2.987			
SDSS J090518.02+410757.6	136.32513	41.1327	2.954	2.553	2.915			
SDSS J090527.46+485049.9	136.36443	48.8472	2.689	2.311	2.652			
SDSS J090536.07+355551.6	136.40027	35.9310	2.839	2.307	2.800			
SDSS J090540.81+331549.8	136.42008	33.2638	3.382	2.570	3.338			
SDSS J090546.61+352748.5	136.44422	35.4635	2.876	2.508	2.794			
SDSS J090549.05+041010.1	136.45442	4.1695	3.153	2.484	3.111			
[HB89] 0903+155	136.46656	15.3802	2.680	1.659	2.645			
SDSS J090556.77+462727.7	136.48658	46.4577	2.508	2.307	2.473			
SDSS J090558.22+082101.8	136.49259	8.3505	2.681	2.324	2.644	2.5627	20.75	0.15
SDSS J090602.63+314255.5	136.51099	31.7154	3.544	2.449	3.498			
SDSS J090607.06+395319.6	136.52943	39.8888	3.688	3.280	3.641			
SDSS J090621.07+490720.9	136.58780	49.1225	3.176	3.024	3.094			
SDSS J090627.48+005250.3	136.61453	0.8807	2.740	2.375	2.703			
SDSS J090634.84+023433.8	136.64519	2.5761	4.516	3.654	4.424			
SDSS J090642.28+501444.9	136.67618	50.2458	2.343	2.307	2.310			
SDSS J090649.62+420308.5	136.70678	42.0524	2.825	2.307	2.787			
SDSS J090655.02+303621.3	136.72926	30.6059	2.815	2.431	2.777			
SDSS J090703.74+041101.9	136.76560	4.1839	2.602	2.307	2.566			
SDSS J090703.91+410748.3	136.76634	41.1301	2.671	2.307	2.634			
SDSS J090709.89+250620.7	136.79122	25.1058	3.319	2.347	3.276			
SDSS J090715.97+485343.1	136.81659	48.8953	2.527	2.307	2.491			
SDSS J090727.58+445142.9	136.86493	44.8619	2.522	2.307	2.486			
SDSS J090746.77-001856.5	136.94490	-0.3157	2.488	2.307	2.453			
SDSS J090748.42+064044.4	136.95177	6.6790	2.523	2.381	2.487			
SDSS J090752.81+312913.1	136.97005	31.4870	3.752	3.281	3.670	3.5560	20.55	0.15
SDSS J090803.95+314159.5	137.01647	31.6999	3.958	3.539	3.908			
SDSS J090810.35+023818.7	137.04315	2.6385	3.686	2.954	3.639	2.9604	20.95	0.20
						3.4071	21.25	0.15
SDSS J090813.43+070956.7	137.05596	7.1658	2.349	2.307	2.316			
SDSS J090832.28+065853.8	137.13453	6.9816	3.073	2.312	3.033			

Continued on Next Page...

Table I.1 – Continued

Name	RA	Dec	z_{em}	z_{min}	z_{max}	z_{abs}	$\log N(\mathrm{H\,I})$	$\epsilon[\log N(\mathrm{H\,I})]$
SDSS J090842.27+081949.8	137.17617	8.3305	3.137	2.436	3.095			
SDSS J090855.33+333637.4	137.23058	33.6104	4.591	4.038	4.509			
SDSS J090908.17+071432.5	137.28410	7.2424	2.898	2.307	2.859			
SDSS J090915.91+035442.7	137.31631	3.9119	3.200	1.811	3.158			
SDSS J090930.42+070050.7	137.37676	7.0141	3.276	2.584	3.233			
SDSS J090930.69+071602.2	137.37788	7.2673	3.722	2.838	3.674			
SDSS J090931.70+261239.8	137.38213	26.2111	3.214	2.522	3.172			
SDSS J090938.71+041525.8	137.41130	4.2572	2.450	2.307	2.416			
SDSS J090940.66+330347.6	137.41946	33.0632	3.783	2.738	3.736	3.6588	20.60	0.15
SDSS J090950.53+245846.0	137.46056	24.9795	2.352	2.307	2.319			
SDSS J090958.03+263311.3	137.49184	26.5531	3.212	2.497	3.170			
SDSS J091001.34+520522.7	137.50563	52.0896	2.507	2.307	2.472			
SDSS J091002.76+422023.5	137.51152	42.3399	3.067	2.398	3.026			
SDSS J091009.05+535355.3	137.53771	53.8987	3.018	2.620	2.978	2.8942	20.50	0.15
SDSS J091016.79+575331.0	137.57000	57.8920	4.011	3.595	3.961	3.9480	20.45	0.15
SDSS J091024.34+042748.7	137.60145	4.4635	2.564	2.307	2.528			
SDSS J091030.73+320853.6	137.62805	32.1482	4.071	3.111	4.020			
SDSS J091033.43+453418.3	137.63929	45.5718	2.795	2.307	2.757			
SDSS J091038.11+463936.3	137.65884	46.6601	2.763	2.397	2.725			
FBQS J091044.9+261253	137.68710	26.2149	2.942	2.552	2.860			
SDSS J091046.67+102629.9	137.69449	10.4417	2.917	2.605	2.878			
SDSS J091053.57+563119.9	137.72327	56.5222	2.362	2.317	2.329			
SDSS J091054.79+023704.5	137.72830	2.6179	3.295	2.371	3.252			
B2 0908+25A	137.73015	25.6560	2.752	2.368	2.714			
SDSS J091056.60+084451.9	137.73588	8.7478	3.059	2.383	3.018			
SDSS J091058.07+080640.7	137.74197	8.1113	2.960	2.568	2.878			
SDSS J091105.50+482207.4	137.77296	48.3687	3.672	3.278	3.625			
SDSS J091105.99+411213.3	137.77500	41.2037	2.917	2.307	2.877			
SDSS J091114.18+110443.0	137.80912	11.0786	3.570	2.809	3.525			
SDSS J091123.19+322318.1	137.84667	32.3884	3.605	2.712	3.559			
SDSS J091127.61+055054.0	137.86517	5.8484	2.793	2.307	2.755			
SDSS J091127.74+260539.6	137.86562	26.0943	2.978	2.307	2.939			
SDSS J091129.00+501624.4	137.87086	50.2735	2.962	2.307	2.922			
SDSS J091135.20+482841.3	137.89669	48.4782	3.918	3.683	3.868			
SDSS J091140.27+290717.6	137.91783	29.1216	3.602	2.549	3.556			
SDSS J091155.27+322405.6	137.98031	32.4016	3.433	2.358	3.388			
SDSS J091157.26+261921.1	137.98860	26.3225	3.321	2.442	3.278			
SDSS J091202.49+533436.0	138.01040	53.5767	2.380	2.307	2.346			
SDSS J091206.54+553436.0	138.02729	55.5767	3.198	2.536	3.156			
SDSS J091206.78+331109.3	138.02826	33.1859	3.328	2.402	3.285			
SDSS J091210.34+054742.0	138.04312	5.7950	3.241	2.313	3.198	3.1236	20.35	0.15
SDSS J091222.78+482153.4	138.09493	48.3649	2.428	2.307	2.393			
SDSS J091223.01+562128.5	138.09590	56.3579	2.982	2.307	2.942	2.8894	20.55	0.15
SDSS J091223.32+401530.2	138.09718	40.2584	2.504	2.307	2.469			
SDSS J091226.78+013358.5	138.11164	1.5663	2.413	2.364	2.379			
SDSS J091234.73+254441.3	138.14475	25.7448	2.348	2.307	2.315			
SDSS J091244.23+073055.4	138.18430	7.5154	3.128	2.467	3.086			
SDSS J091247.59-004717.3	138.19833	-0.7882	2.859	2.464	2.821			
SDSS J091249.15+075205.0	138.20483	7.8681	3.618	2.853	3.572	3.2087	20.60	0.20
SDSS J091257.32+023909.7	138.23885	2.6527	2.401	2.307	2.367			
SDSS J091300.60+250446.5	138.25251	25.0796	2.443	2.307	2.409			
SDSS J091308.52+283744.4	138.28552	28.6290	3.658	2.761	3.611	3.4667	20.60	0.20
SDSS J091314.63+442700.5	138.31099	44.4502	2.342	2.307	2.309			
SDSS J091316.34+545946.0	138.31813	54.9961	2.375	2.307	2.341			
SDSS J091316.55+591921.6	138.31899	59.3227	5.122	4.165	5.020	4.7940	20.45	0.20
SDSS J091337.35+314859.9	138.40563	31.8167	3.001	2.600	2.961			
SDSS J091338.96+291254.6	138.41237	29.2152	3.224	2.509	3.181			
SDSS J091344.98+091407.7	138.43749	9.2355	2.900	2.507	2.861			
SDSS J091349.73+513743.9	138.45722	51.6289	2.626	2.307	2.590			
SDSS J091406.11+320628.2	138.52547	32.1078	2.661	2.307	2.579			
SDSS J091410.73+015408.9	138.54473	1.9025	3.134	2.421	3.093			
SDSS J091424.10+295151.0	138.60045	29.8642	2.486	2.307	2.451			
SDSS J091434.91+362059.4	138.64549	36.3499	2.416	2.307	2.382			
SDSS J091445.89+301738.3	138.69123	30.2940	4.270	3.441	4.217	3.8038	21.05	0.20
SDSS J091454.45+093044.0	138.72691	9.5122	2.976	2.596	2.936			
SDSS J091456.30+493936.8	138.73461	49.6602	2.412	2.307	2.378			
SDSS J091504.58+360651.0	138.76910	36.1142	2.685	2.307	2.641	2.5216	20.60	0.15
SDSS J091510.01+475658.7	138.79172	47.9497	3.337	2.307	3.293			
SDSS J091510.75+442655.9	138.79484	44.4489	3.945	2.913	3.895			
SDSS J091516.26+071750.8	138.81779	7.2975	2.389	2.307	2.355			
SDSS J091517.71+443628.7	138.82382	44.6080	2.375	2.307	2.341			
SDSS J091530.43+042259.8	138.87684	4.3833	2.648	2.307	2.612			

Continued on Next Page...

Table I.1 – Continued

Name	RA	Dec	z_{em}	z_{min}	z_{max}	z_{abs}	$\log N(\mathrm{H\,I})$	$\epsilon[\log N(\mathrm{H\,I})]$
SDSS J091533.96+071900.1	138.89153	7.3167	3.789	3.318	3.742			
SDSS J091540.08+440113.7	138.91703	44.0205	2.673	2.346	2.636			
SDSS J091543.63+492416.6	138.93184	49.4047	5.199	4.230	5.096			
SDSS J091544.85+471049.7	138.93692	47.1805	3.273	2.384	3.230	2.7992	20.50	0.15
SDSS J091546.67+054942.7	138.94451	5.8285	2.968	2.307	2.928			
SDSS J091547.51+310635.1	138.94800	31.1098	3.290	2.631	3.247			
SDSS J091548.20+393155.0	138.95090	39.5320	3.053	2.661	3.013			
SDSS J091548.90+302542.6	138.95375	30.4286	3.193	2.368	3.151	3.0676	20.45	0.15
SDSS J091603.39+330931.8	139.01415	33.1588	3.153	2.743	3.071	2.9762	20.30	0.20
SDSS J091604.06+253555.4	139.01692	25.5987	2.623	2.307	2.587			
SDSS J091611.02+331130.5	139.04593	33.1918	3.112	2.309	3.071			
[HB89] 0913+072	139.05818	7.0401	2.780	1.866	2.739	2.6187	20.30	0.20
SDSS J091622.88+073114.7	139.09537	7.5208	2.350	2.307	2.316			
SDSS J091627.00+350756.9	139.11251	35.1325	2.933	2.560	2.893			
SDSS J091635.39+370545.4	139.14747	37.0960	2.713	2.338	2.676			
SDSS J091637.55+004733.9	139.15648	0.7928	3.717	3.313	3.670			
SDSS J091701.45+303808.4	139.25608	30.6357	3.023	2.371	2.983	2.5459	20.45	0.15
SDSS J091705.79+060354.8	139.27414	6.0652	2.398	2.307	2.364			
SDSS J091719.98+441030.7	139.33326	44.1752	2.963	2.562	2.923			
SDSS J091724.02+273959.6	139.35010	27.6666	2.511	2.307	2.476			
SDSS J091727.49+591747.7	139.36460	59.2966	2.388	2.307	2.354	2.3293	20.35	0.15
SDSS J091738.90+082053.9	139.41212	8.3483	3.253	2.582	3.210			
SDSS J091745.56+283458.1	139.43986	28.5828	3.355	2.397	3.312			
SDSS J091759.82+040208.8	139.49929	4.0358	2.378	2.307	2.345			
SDSS J091800.65+512143.5	139.50275	51.3621	3.453	2.707	3.408			
SDSS J091804.33+481240.5	139.51808	48.2113	2.409	2.307	2.375			
SDSS J091814.39+321631.5	139.55998	32.2754	2.468	2.354	2.433			
SDSS J091820.34+082508.1	139.58479	8.4189	3.149	2.500	3.107			
SDSS J091822.14+330306.2	139.59229	33.0517	3.095	2.690	3.013			
SDSS J091830.41+334824.4	139.62675	33.8068	3.911	3.419	3.862			
SDSS J091845.27+484806.2	139.68865	48.8017	2.840	2.447	2.802			
SDSS J091845.77+453658.9	139.69075	45.6164	2.733	2.357	2.695			
SDSS J091848.38+090353.7	139.70162	9.0649	3.567	3.137	3.484			
SDSS J091857.67+533220.0	139.74032	53.5389	3.012	2.873	2.972			
SDSS J091858.96+544327.8	139.74570	54.7244	2.367	2.307	2.333			
SDSS J091902.87+373041.9	139.76198	37.5117	3.276	2.840	3.233			
SDSS J091903.18+404344.5	139.76328	40.7290	4.008	3.240	3.958			
SDSS J091908.74+330458.1	139.78645	33.0828	2.523	2.307	2.487			
SDSS J091940.03+442600.8	139.91681	44.4336	3.925	3.463	3.876			
SDSS J091940.82+094929.2	139.92011	9.8248	2.967	2.600	2.927			
SDSS J091942.82+340301.3	139.92842	34.0504	2.447	2.307	2.412			
SDSS J091946.06+112229.0	139.94193	11.3748	2.722	2.353	2.639			
SDSS J091954.32+082626.8	139.97634	8.4408	3.496	2.644	3.451			
SDSS J091955.42+551205.6	139.98097	55.2016	2.508	2.325	2.473	2.3870	20.40	0.15
SDSS J092003.12+464503.5	140.01300	46.7510	2.467	2.307	2.433			
SDSS J092014.47+022803.7	140.06033	2.4677	2.943	2.307	2.903	2.3515	20.70	0.15
SDSS J092019.38+315735.7	140.08077	31.9599	2.625	2.307	2.588			
SDSS J092028.41+294757.2	140.11834	29.7992	2.955	2.307	2.915			
SDSS J092035.80+002330.5	140.14917	0.3919	2.491	2.307	2.456			
SDSS J092038.48+564235.8	140.16038	56.7100	4.169	3.657	4.086			
SDSS J092041.76+072544.0	140.17401	7.4289	3.646	2.060	3.600	2.2380	20.90	0.15
SDSS J092050.90+462851.4	140.21212	46.4809	2.458	2.307	2.423			
SDSS J092057.11+525917.9	140.23798	52.9883	3.067	2.366	3.027			
SDSS J092101.83+353827.7	140.25763	35.6410	2.709	2.328	2.672			
SDSS J092103.64+014700.2	140.26520	1.7834	2.592	2.307	2.556			
SDSS J092104.30+034150.5	140.26795	3.6974	3.140	2.503	3.099			
FBQS J092104.4+302031	140.26818	30.3418	3.350	2.308	3.307			
SDSS J092123.27+565056.5	140.34698	56.8491	3.674	3.195	3.627			
SDSS J092126.70+003858.6	140.36130	0.6496	2.470	2.307	2.436			
SDSS J092143.50+063643.5	140.43128	6.6121	3.716	3.246	3.669			
SDSS J092146.69+284712.2	140.44458	28.7867	3.109	2.923	3.068			
SDSS J092155.63+423300.3	140.48182	42.5501	3.817	2.819	3.769			
SDSS J092156.27+305157.1	140.48450	30.8659	3.062	2.307	3.022			
SDSS J092210.25+045751.9	140.54275	4.9644	4.045	2.980	3.994			
SDSS J092216.81+265358.9	140.57007	26.8997	5.042	4.098	4.941			
SDSS J092222.86+314612.2	140.59528	31.7701	4.052	3.060	4.002	3.0675	20.35	0.20
SDSS J092235.44+284642.0	140.64768	28.7784	2.414	2.307	2.380			
SDSS J092247.83+532146.5	140.69934	53.3630	3.000	2.435	2.960			
SDSS J092256.19+561849.1	140.73417	56.3137	4.198	3.024	4.034			
SDSS J092314.08+081940.1	140.80871	8.3278	2.541	2.307	2.506			
SDSS J092316.44+332116.3	140.81854	33.3546	2.360	2.307	2.326			
SDSS J092322.86+033821.5	140.84526	3.6393	3.006	2.366	2.966			

Continued on Next Page...

Table I.1 – Continued

Name	RA	Dec	z_{em}	z_{min}	z_{max}	z_{abs}	$\log N(\mathrm{H\,I})$	$\epsilon[\log N(\mathrm{H\,I})]$
SDSS J092325.25+453222.1	140.85521	45.5395	3.452	2.307	3.408			
SDSS J092329.99+301107.6	140.87485	30.1854	3.079	2.704	3.038			
SDSS J092331.31+020048.8	140.88048	2.0136	2.564	2.409	2.529			
SDSS J092339.85+284127.1	140.91605	28.6909	3.493	3.120	3.448			
SDSS J092354.84+574721.3	140.97853	57.7893	2.557	2.307	2.521			
SDSS J092359.58+495439.4	140.99832	49.9110	2.465	2.307	2.430			
SDSS J092404.36-000707.8	141.01818	-0.1189	2.447	2.307	2.412			
SDSS J092410.75+285709.5	141.04481	28.9527	2.580	2.307	2.544			
SDSS J092417.32+060053.6	141.07219	6.0149	2.916	2.307	2.877			
SDSS J092419.08+353938.4	141.07951	35.6607	2.809	2.307	2.771			
SDSS J092428.26+111237.2	141.11780	11.2104	3.824	2.812	3.776	3.4474	20.55	0.20
SDSS J092429.67+423542.8	141.12363	42.5952	3.183	2.535	3.142			
SDSS J092435.14+444838.8	141.14643	44.8108	3.381	2.933	3.337			
SDSS J092444.66-000924.0	141.18612	-0.1567	2.870	2.488	2.788			
SDSS J0924+4852	141.19734	48.8786	3.020	2.307	2.980			
SDSS J092450.33+064633.9	141.20972	6.7761	2.490	2.307	2.455			
SDSS J092456.66+305354.8	141.23613	30.8986	3.417	2.411	3.373			
SDSS J092459.91+095103.4	141.24964	9.8510	3.453	2.998	3.409	3.3401	20.90	0.20
SDSS J092507.53+521102.4	141.28145	52.1841	2.995	2.599	2.912			
SDSS J092514.04+522112.6	141.30856	52.3535	2.869	2.473	2.831			
SDSS J092550.67+385951.3	141.46115	38.9976	3.103	2.421	3.062			
SDSS J092554.73+290114.5	141.47807	29.0207	3.129	2.415	3.087			
SDSS J092555.04+490338.2	141.47937	49.0606	2.343	2.307	2.310			
SDSS J092559.34+364713.3	141.49728	36.7871	3.883	3.482	3.800			
SDSS J092625.70+344843.1	141.60712	34.8120	2.615	2.307	2.579			
SDSS J092633.42+415958.0	141.63929	41.9995	3.282	2.906	3.239			
SDSS J092633.70+332546.4	141.64043	33.4296	3.279	2.690	3.236			
SDSS J092636.33+305505.0	141.65133	30.9181	4.198	2.951	4.146			
SDSS J092644.24+101409.3	141.68436	10.2359	2.482	2.307	2.447			
SDSS J092646.25+471124.0	141.69277	47.1900	3.477	2.349	3.432			
SDSS J092656.94+602504.2	141.73729	60.4179	2.956	2.307	2.916			
SDSS J092700.60+513047.2	141.75256	51.5131	2.930	2.307	2.891			
SDSS J092712.95+342249.1	141.80399	34.3803	2.408	2.307	2.374			
SDSS J092714.70+030827.2	141.81129	3.1409	3.143	2.732	3.102			
SDSS J092721.19+074639.0	141.83832	7.7775	2.539	2.307	2.504	2.3101	20.70	0.15
SDSS J092726.55+383629.0	141.86056	38.6081	2.587	2.307	2.552			
SDSS J092735.73+354407.8	141.89888	35.7355	2.567	2.421	2.531			
SDSS J092737.13+025110.6	141.90473	2.8530	2.608	2.307	2.572			
SDSS J092739.76+275115.3	141.91572	27.8543	2.733	2.378	2.695			
SDSS J092801.72+432105.3	142.00717	43.3515	2.811	2.434	2.729			
SDSS J092803.34+095143.4	142.01396	9.8621	2.344	2.307	2.310			
SDSS J092814.93+093955.2	142.06222	9.6654	3.655	2.794	3.608	2.9101	20.70	0.20
SDSS J092818.96+024823.7	142.07901	2.8066	2.954	2.347	2.915			
SDSS J092830.97+052432.3	142.12909	5.4090	2.413	2.307	2.379			
SDSS J092833.90+313831.3	142.14128	31.6421	2.559	2.307	2.524			
SDSS J092837.80+353405.3	142.15755	35.5682	2.549	2.307	2.514			
SDSS J092839.01+473804.0	142.16255	47.6345	3.052	2.738	3.012			
SDSS J092844.29+261224.5	142.18457	26.2068	3.028	2.621	2.988			
SDSS J092849.24+504930.5	142.20519	50.8252	2.347	2.307	2.314			
SDSS J092905.45+340434.4	142.27273	34.0762	3.463	3.006	3.419			
SDSS J092907.27+441334.6	142.28033	44.2263	2.411	2.307	2.377			
SDSS J092914.49+282529.0	142.31039	28.4248	3.404	2.357	3.360	2.7688	20.80	0.15
						3.2636	21.10	0.15
SDSS J092915.49+351013.7	142.31456	35.1705	2.862	2.307	2.824			
SDSS J092917.51+300230.0	142.32298	30.0417	3.020	2.673	2.937			
SDSS J092918.04+413444.2	142.32521	41.5790	3.110	2.430	3.069			
SDSS J092926.85+090850.2	142.36189	9.1473	3.734	3.336	3.686			
SDSS J092928.79+275418.6	142.36997	27.9052	2.445	2.307	2.411			
SDSS J092946.83+000158.1	142.44515	0.0328	3.060	2.645	3.020			
SDSS J092958.40+040032.7	142.49338	4.0091	3.152	2.757	3.111			
SDSS J093008.51+364621.3	142.53548	36.7726	2.407	2.307	2.373			
SDSS J093019.52+063441.0	142.58138	6.5781	3.076	2.690	3.036			
SDSS J093019.58+423803.9	142.58160	42.6345	3.736	2.954	3.689	3.2972	21.00	0.15
SDSS J093026.24+361328.6	142.60936	36.2246	2.921	2.557	2.881			
SDSS J093032.42+472021.8	142.63512	47.3394	3.147	2.489	3.105			
SDSS J093051.93+602301.1	142.71640	60.3837	3.719	2.949	3.672	3.0011	20.80	0.15
						3.6370	20.55	0.15
SDSS J093056.35+330959.3	142.73481	33.1665	3.167	2.504	3.125			
SDSS J093058.84+083321.5	142.74518	8.5560	2.985	2.366	2.945	2.9362	20.40	0.15
SDSS J093059.75+560229.4	142.74896	56.0415	2.978	2.307	2.938			
SDSS J093102.78+581759.1	142.76164	58.2998	2.706	2.540	2.669			
SDSS J093104.95+433639.8	142.77064	43.6111	3.050	2.635	3.009	2.6463	20.35	0.15

Continued on Next Page...

Table I.1 – Continued

Name	RA	Dec	z_{em}	z_{min}	z_{max}	z_{abs}	log N(H I)	ϵ[log N(H I)]
SDSS J093110.35+304653.7	142.79315	30.7816	3.845	3.099	3.796			
SDSS J093111.12+443736.5	142.79638	44.6268	3.652	2.868	3.606			
SDSS J093130.75+282719.9	142.87817	28.4555	3.153	2.527	3.111			
SDSS J093139.19+423037.3	142.91335	42.5104	2.493	2.307	2.458			
SDSS J093140.47+005353.0	142.91866	0.8981	2.643	2.307	2.606			
SDSS J093152.42+463343.6	142.96845	46.5621	3.608	2.531	3.562			
SDSS J093153.12-000051.0	142.97135	-0.0142	3.211	2.307	3.169			
SDSS J093156.23+043123.7	142.98433	4.5233	3.116	2.307	3.075			
SDSS J093157.62+041944.9	142.99013	4.3292	3.134	2.307	3.093			
SDSS J093203.81+121326.1	143.01588	12.2239	3.489	3.071	3.444			
SDSS J093205.20+311529.0	143.02169	31.2581	2.433	2.341	2.399			
SDSS J093207.46+365745.5	143.03109	36.9627	2.898	2.307	2.859			
SDSS J093210.17+280425.5	143.04238	28.0738	2.354	2.307	2.321			
SDSS J093213.01+370344.4	143.05421	37.0624	2.846	2.307	2.807			
SDSS J093222.89+294153.1	143.09539	29.6981	2.932	2.307	2.893			
SDSS J093223.19+523115.6	143.09667	52.5210	3.559	2.622	3.513			
SDSS J093250.99+090733.9	143.21249	9.1261	2.654	2.307	2.618	2.3424	21.05	0.20
SDSS J093308.64-000834.1	143.28601	-0.1428	2.543	2.356	2.508			
SDSS J093309.04+392038.4	143.28770	39.3440	3.668	2.759	3.621			
SDSS J093317.33+424034.9	143.32225	42.6764	2.712	2.332	2.675			
SDSS J093322.33+120112.7	143.34308	12.0202	2.396	2.307	2.362			
SDSS J093323.46+295902.3	143.34776	29.9840	3.234	2.375	3.191			
SDSS J093323.58+101025.6	143.34829	10.1738	3.579	2.800	3.533			
SDSS J093330.76+620144.8	143.37822	62.0291	2.986	2.844	2.946			
SDSS J093333.85+051839.9	143.39108	5.3111	4.490	4.277	4.408			
FBQS J0933+2845	143.40541	28.7590	3.410	2.173	3.366	3.2400	20.50	0.20
SDSS J093342.51+121628.2	143.42716	12.2745	2.513	2.307	2.478			
SDSS J093355.72+084043.0	143.48221	8.6786	2.629	2.476	2.592			
SDSS J093359.54+351830.6	143.49812	35.3085	3.158	2.307	3.116			
SDSS J093402.94+293629.4	143.51228	29.6082	3.170	2.783	3.128			
FBQS J0934+3153	143.51653	31.8921	2.423	2.307	2.389			
SDSS J093418.28+355508.3	143.57617	35.9190	2.450	2.307	2.367			
SDSS J093424.38+520517.3	143.60164	52.0882	2.654	2.307	2.618			
SDSS J093430.84+095036.0	143.62854	9.8433	2.620	2.307	2.584			
SDSS J093431.32+025625.1	143.63054	2.9403	3.229	2.873	3.187	3.0542	20.75	0.15
SDSS J093434.73+543109.3	143.64475	54.5193	2.840	2.307	2.801			
SDSS J093441.08+604539.1	143.67121	60.7609	3.278	2.477	3.235			
SDSS J093445.59+275958.0	143.69000	27.9994	3.155	2.732	3.113			
SDSS J093449.34+321340.3	143.70563	32.2279	2.942	2.645	2.903			
SDSS J093515.64+392154.7	143.81520	39.3652	2.962	2.307	2.922			
SDSS J093523.31+411518.5	143.84717	41.2552	4.806	3.899	4.709			
SDSS J093523.89+284248.0	143.84956	28.7134	2.637	2.307	2.601			
SDSS J093525.85+292827.9	143.85772	29.4744	2.740	2.370	2.657			
SDSS J093529.10+073737.8	143.87130	7.6272	3.178	2.772	3.136			
SDSS J093530.74+461832.9	143.87817	46.3092	2.430	2.352	2.395			
SDSS J093530.78+510208.6	143.87826	51.0357	3.344	2.307	3.301			
[HB89] 0932+367	143.88267	36.5549	2.858	2.307	2.819			
SDSS J093534.19+033133.2	143.89249	3.5259	3.809	2.916	3.761			
SDSS J093535.38+483254.6	143.89742	48.5485	2.353	2.307	2.319			
SDSS J093540.42+521336.3	143.91844	52.2268	3.211	2.533	3.169	3.1055	20.45	0.15
SDSS J093548.47+050225.9	143.95200	5.0405	2.511	2.341	2.476			
SDSS J093548.50+363121.9	143.95211	36.5228	2.977	2.584	2.895			
SDSS J093551.31+444644.7	143.96383	44.7791	3.074	2.665	3.034			
SDSS J093554.45+525616.4	143.97690	52.9379	4.004	3.509	3.922			
SDSS J093555.11+033618.2	143.97965	3.6051	2.584	2.307	2.548			
SDSS J093556.91+002255.6	143.98715	0.3821	3.747	2.249	3.700			
SDSS J093607.34+120119.7	144.03061	12.0221	2.848	2.453	2.809	2.7843	20.45	0.20
SDSS J093621.85+394247.7	144.09106	39.7133	3.319	2.951	3.276			
SDSS J093632.03+343350.5	144.13350	34.5640	2.860	2.510	2.821			
SDSS J093632.65+092749.0	144.13608	9.4636	2.354	2.307	2.321			
SDSS J093643.51+292713.6	144.18131	29.4538	2.926	2.307	2.886			
SDSS J093657.13+581118.9	144.23804	58.1886	2.536	2.307	2.501			
SDSS J093657.52+500558.4	144.23971	50.0996	2.892	2.494	2.853			
SDSS J093704.58+531315.9	144.26911	53.2211	2.876	2.493	2.794			
SDSS J093708.76+622005.5	144.28657	62.3349	2.523	2.329	2.487			
SDSS J093714.48+082858.6	144.31038	8.4829	3.703	2.118	3.656			
SDSS J093715.38+041737.6	144.31412	4.2938	3.126	2.307	3.085			
SDSS J093722.84+025712.5	144.34521	2.9535	3.165	2.740	3.124			
SDSS J093724.55+444602.6	144.35232	44.7674	2.761	2.406	2.723	2.6347	20.30	0.20
SDSS J093728.12+415922.5	144.36722	41.9896	2.682	2.307	2.645			
SDSS J093735.37+533224.2	144.39741	53.5401	3.382	2.426	3.338	3.1726	20.90	0.15
SDSS J093742.13+503708.7	144.42554	50.6191	3.599	2.890	3.554	3.4873	21.20	0.15

Continued on Next Page...

Table I.1 – Continued

Name	RA	Dec	z_{em}	z_{min}	z_{max}	z_{abs}	$\log N(\mathrm{H\,I})$	$\epsilon[\log N(\mathrm{H\,I})]$
SDSS J093746.47+114038.3	144.44366	11.6773	4.356	3.541	4.303			
[HB89] 0933+733	144.45333	73.0328	2.530	1.651	2.493			
SDSS J093751.91+292343.9	144.46632	29.3955	2.561	2.307	2.525			
SDSS J093753.26+381625.3	144.47195	38.2737	3.191	2.307	3.149			
SDSS J093753.73+024000.3	144.47391	2.6667	3.159	2.351	3.118			
SDSS J093754.11+555613.5	144.47548	55.9371	2.459	2.351	2.424			
SDSS J093800.62+100954.4	144.50264	10.1652	3.529	2.657	3.484			
SDSS J093816.91+034649.0	144.57050	3.7803	3.425	2.307	3.380			
SDSS J093819.55+044533.4	144.58147	4.7593	3.675	2.881	3.628			
SDSS J093823.57+334610.3	144.59822	33.7696	2.721	2.404	2.684			
SDSS J093825.53+310810.8	144.60642	31.1364	2.386	2.307	2.352			
SDSS J093833.51+445603.4	144.63964	44.9343	3.704	2.347	3.657			
SDSS J093841.30+554830.0	144.67210	55.8083	2.659	2.568	2.623			
SDSS J093842.21+042803.0	144.67592	4.4675	2.583	2.443	2.547			
SDSS J093845.65+014522.0	144.69023	1.7561	2.483	2.404	2.448			
SDSS J093846.82+302418.5	144.69511	30.4052	2.459	2.307	2.424			
SDSS J093852.90+394030.6	144.72043	39.6752	2.480	2.307	2.445			
SDSS J093853.06+465000.3	144.72112	46.8334	3.004	2.659	2.964			
SDSS J093916.87+535111.4	144.82035	53.8531	3.144	2.307	3.102			
SDSS J093917.57+272713.1	144.82323	27.4537	4.406	3.130	4.351	3.8657	20.70	0.20
SDSS J093947.07+273705.0	144.94617	27.6181	3.252	2.583	3.209			
SDSS J093949.43+335548.3	144.95596	33.9301	4.106	3.685	4.055			
SDSS J093958.42+410913.0	144.99348	41.1536	3.693	2.907	3.646			
2MASSi J0939588+360921	144.99547	36.1561	2.579	2.307	2.543			
SDSS J094003.02+511602.7	145.01260	51.2674	3.601	2.865	3.555			
SDSS J094005.33+322403.4	145.02226	32.4010	3.197	2.323	3.155			
SDSS J094005.98+105919.8	145.02499	10.9888	3.399	2.969	3.355			
SDSS J094008.07+415046.1	145.03367	41.8461	3.322	2.350	3.279			
SDSS J094008.44+023209.0	145.03519	2.5358	3.210	2.612	3.168			
SDSS J094013.69+285816.2	145.05705	28.9712	3.248	2.307	3.206			
[HB89] 0937+121	145.16125	11.9317	2.739	2.356	2.702			
SDSS J094041.88+413752.0	145.17454	41.6311	2.897	2.560	2.858			
SDSS J094050.44+461730.5	145.21020	46.2918	3.430	2.533	3.385			
SDSS J094054.56+054903.5	145.22735	5.8177	3.235	2.331	3.193			
SDSS J094056.01+584830.2	145.23340	58.8084	4.664	3.779	4.570			
SDSS J094100.98+562843.5	145.25412	56.4788	3.000	2.402	2.960	2.4362	20.40	0.20
SDSS J094102.50+560706.5	145.26048	56.1185	3.786	2.851	3.738			
SDSS J094103.25+423641.3	145.26356	42.6115	3.047	2.338	3.007			
SDSS J0941+5947	145.28483	59.7905	4.820	3.322	4.762			
[HB89] 0938+119	145.30649	11.7590	3.196	2.345	3.154			
SDSS J094118.94+325132.4	145.32896	32.8590	2.353	2.307	2.320			
SDSS J094121.66+572259.0	145.34028	57.3831	3.197	2.806	3.155			
SDSS J094139.82+352305.2	145.41592	35.3848	3.378	3.024	3.334			
SDSS J094140.17+325703.2	145.41739	32.9509	3.452	2.533	3.408			
SDSS J094149.45+293343.3	145.45605	29.5620	3.437	3.001	3.393			
SDSS J094150.90+275635.6	145.46210	27.9432	3.798	2.840	3.750			
SDSS J094151.38+315346.4	145.46413	31.8962	2.530	2.307	2.494	2.4296	20.60	0.20
SDSS J094151.49+350445.4	145.46456	35.0793	3.138	2.359	3.096			
SDSS J094159.06-001552.3	145.49612	-0.2646	2.546	2.307	2.510			
SDSS J094202.04+042244.5	145.50852	4.3790	3.276	2.307	3.233			
SDSS J094203.04+540518.9	145.51270	54.0886	2.347	2.307	2.314			
SDSS J094212.55+081737.2	145.55234	8.2937	3.148	2.369	3.106			
SDSS J094229.02+073239.7	145.62095	7.5444	3.311	2.552	3.268			
SDSS J094246.23+522002.5	145.69274	52.3341	2.866	2.307	2.827			
SDSS J094254.47+313153.8	145.72699	31.5316	2.390	2.307	2.356			
SDSS J094259.05+432845.7	145.74609	43.4794	2.509	2.320	2.474			
SDSS J094305.87+284629.4	145.77449	28.7749	3.666	2.974	3.620			
SDSS J094312.02+575604.3	145.80012	57.9346	2.438	2.360	2.403			
SDSS J094314.40+065357.0	145.81002	6.8992	3.238	2.517	3.196			
SDSS J094323.92+074856.0	145.84970	7.8156	3.416	2.648	3.372			
SDSS J094329.70+433659.2	145.87379	43.6165	2.464	2.307	2.429			
SDSS J094330.06+535000.7	145.87530	53.8336	3.881	3.398	3.799			
SDSS J094331.49+363931.1	145.88122	36.6587	2.471	2.307	2.436			
SDSS J094331.85+042749.5	145.88274	4.4638	3.660	2.710	3.613			
SDSS J094334.38+051039.9	145.89326	5.1778	3.267	2.505	3.224			
SDSS J094337.28+280135.9	145.90538	28.0267	3.113	2.415	3.072			
SDSS J094340.00+544550.2	145.91670	54.7640	2.995	2.331	2.955			
SDSS J094350.73+425305.5	145.96150	42.8849	3.709	2.763	3.661	3.1763	20.55	0.20
SDSS J094352.56+430810.4	145.96904	43.1362	2.352	2.307	2.319			
SDSS J094353.80+432058.3	145.97419	43.3496	2.947	2.542	2.907			
SDSS J094356.76+363007.4	145.98654	36.5021	3.866	2.902	3.817			
SDSS J094403.55+373454.4	146.01481	37.5818	2.402	2.307	2.368			

Continued on Next Page...

Table I.1 – Continued

Name	RA	Dec	z_{em}	z_{min}	z_{max}	z_{abs}	$\log N(\mathrm{H\,I})$	$\epsilon[\log N(\mathrm{H\,I})]$
SDSS J094408.81+434427.0	146.03675	43.7408	4.591	4.364	4.535			
SDSS J094409.52+100656.6	146.03968	10.1157	4.776	3.873	4.680			
SDSS J094413.16+631758.1	146.05486	63.2995	3.178	2.307	3.136			
SDSS J094419.82+374609.3	146.08260	37.7693	3.712	3.230	3.665			
SDSS J094431.21+005700.0	146.13005	0.9500	2.531	2.364	2.496			
SDSS J094439.69+561944.2	146.16543	56.3289	3.983	3.490	3.901			
[HB89] 0941+261	146.17633	25.9120	2.913	1.731	2.867			
SDSS J094444.09+110654.3	146.18372	11.1151	3.870	3.041	3.821	3.6961	20.45	0.15
SDSS J094444.96+373414.3	146.18738	37.5707	2.969	2.307	2.929			
SDSS J094450.50+344726.3	146.21043	34.7906	2.430	2.307	2.396			
SDSS J094453.81+504300.8	146.22423	50.7169	3.789	2.706	3.741	3.0131	20.40	0.15
						3.3677	20.40	0.15
SDSS J094453.89+372840.2	146.22455	37.4778	3.340	2.486	3.296			
SDSS J094508.02+504057.6	146.28345	50.6827	3.736	2.505	3.688	2.9144	20.30	0.15
SDSS J094508.11+370104.5	146.28381	37.0179	2.930	2.582	2.891			
SDSS J094523.31+592917.3	146.34715	59.4882	3.583	2.715	3.537			
SDSS J094525.95+024330.6	146.35817	2.7252	2.603	2.522	2.567			
SDSS J094529.55+283542.9	146.37317	28.5953	3.178	2.321	3.136			
SDSS J094531.78+033757.7	146.38244	3.6327	2.963	2.355	2.924			
SDSS J094541.28+093116.4	146.42205	9.5212	2.343	2.307	2.309			
SDSS J094543.40+394958.4	146.43086	39.8329	3.946	3.460	3.896			
SDSS J094556.04+601232.8	146.48354	60.2091	2.510	2.307	2.474			
SDSS J094558.95+383711.2	146.49566	38.6198	3.224	2.531	3.181			
FBQS J094602.2+274407	146.50965	27.7353	2.382	2.307	2.348			
SDSS J094613.12+294527.2	146.55467	29.7576	3.171	2.307	3.129			
SDSS J094631.60+345012.8	146.63169	34.8369	3.610	3.301	3.564			
SDSS J094632.82+125147.0	146.63676	12.8631	3.300	2.370	3.257			
SDSS J094642.42+330754.7	146.67679	33.1319	2.477	2.307	2.442			
SDSS J094648.42+063038.2	146.70177	6.5106	2.960	2.864	2.920			
SDSS J094648.86+352458.1	146.70360	35.4161	3.761	3.377	3.713			
SDSS J094652.81+282134.3	146.72005	28.3596	3.845	3.004	3.796			
SDSS J094656.16+330625.7	146.73403	33.1072	2.484	2.307	2.449			
SDSS J094706.49+080752.9	146.77705	8.1314	3.319	2.536	3.275			
SDSS J094707.81+481613.7	146.78255	48.2705	2.439	2.307	2.404			
SDSS J094711.53+390502.3	146.79807	39.0840	3.803	2.881	3.755			
SDSS J094712.20+114230.1	146.80085	11.7084	2.585	2.307	2.549			
SDSS J094741.14+471540.1	146.92146	47.2612	3.063	2.364	3.023			
SDSS J094743.32+420837.9	146.93056	42.1439	2.559	2.307	2.523			
SDSS J094745.26-004113.2	146.93862	-0.6870	2.829	2.510	2.746			
SDSS J094755.14+323107.9	146.97978	32.5189	3.364	2.569	3.320			
SDSS J094759.41+632803.1	146.99757	63.4675	2.617	2.307	2.581	2.4960	20.90	0.15
SDSS J094802.47+430714.0	147.01039	43.1206	3.705	2.662	3.658	3.4858	20.80	0.20
SDSS J094804.42+572603.0	147.01844	57.4342	2.353	2.307	2.320			
SDSS J094812.71+103141.3	147.05296	10.5282	3.137	2.714	3.096			
SDSS J094815.73+093953.3	147.06558	9.6648	2.435	2.307	2.401			
SDSS J094851.42+493538.8	147.21426	49.5941	3.026	2.627	2.944			
SDSS J094902.82+414050.2	147.26178	41.6806	2.775	2.388	2.737	2.5787	20.40	0.15
SDSS J094906.65+002605.1	147.27772	0.4348	2.452	2.353	2.417			
SDSS J094913.08+294353.4	147.30454	29.7315	3.767	2.932	3.719			
SDSS J094925.37+364238.9	147.35574	36.7108	2.392	2.307	2.358			
SDSS J094927.88+111518.2	147.36618	11.2551	3.824	2.811	3.776			
SDSS J094930.39+521400.7	147.37665	52.2336	3.375	2.928	3.332	3.0619	21.00	0.15
SDSS J094932.26+033531.7	147.38446	3.5922	4.049	2.860	3.999			
SDSS J094942.61+043750.0	147.42755	4.6306	3.640	2.778	3.593			
SDSS J094945.21+304916.8	147.43841	30.8213	3.658	3.010	3.612			
SDSS J094953.87+482315.1	147.47448	48.3875	2.647	2.307	2.611			
SDSS J095001.01+294456.1	147.50426	29.7489	2.943	2.539	2.903			
SDSS J095006.68+614349.3	147.52787	61.7304	3.166	2.410	3.124			
SDSS J095013.70+525335.1	147.55714	52.8931	2.581	2.413	2.593			
SDSS J095014.04+580136.5	147.55855	58.0268	3.973	2.759	3.923	3.2640	20.50	0.10
SDSS J095018.68+040307.4	147.57787	4.0521	2.977	2.415	2.937			
SDSS J095037.09+501925.5	147.65458	50.3237	3.821	2.990	3.773			
SDSS J095043.84+320538.3	147.68269	32.0940	3.514	2.653	3.469			
SDSS J095050.36+044431.0	147.70985	4.7420	2.494	2.307	2.459			
SDSS J095050.82+113139.8	147.71178	11.5277	2.487	2.307	2.452			
SDSS J095056.19+424719.2	147.73414	42.7887	3.319	2.916	3.276	3.1246	20.35	0.15
SDSS J095106.33+541149.5	147.77642	54.1971	2.680	2.307	2.644			
SDSS J095107.17+352255.4	147.77988	35.3821	3.000	2.430	2.960			
SDSS J095107.40+374237.4	147.78085	37.7104	2.541	2.307	2.506			
SDSS J095108.76+314705.8	147.78653	31.7850	2.936	2.741	2.897			
SDSS J095112.84+025527.2	147.80351	2.9242	2.373	2.307	2.339			
SDSS J095114.35+565107.1	147.80980	56.8520	3.788	2.667	3.740			

Continued on Next Page...

Table I.1 – Continued

Name	RA	Dec	z_{em}	z_{min}	z_{max}	z_{abs}	$\log N(\mathrm{H\,I})$	$\epsilon[\log N(\mathrm{H\,I})]$
SDSS J095141.73+611403.6	147.92393	61.2343	3.761	3.276	3.714	3.6212	20.65	0.20
SDSS J095143.97+365012.0	147.93322	36.8367	2.988	2.364	2.948			
SDSS J095156.29+011341.8	147.98458	1.2283	2.364	2.307	2.331			
SDSS J095156.55+123502.5	147.98564	12.5840	3.603	2.653	3.557			
SDSS J095209.89+121835.0	148.04125	12.3097	2.772	2.386	2.734			
SDSS J095217.51+534854.6	148.07298	53.8152	2.449	2.311	2.415			
SDSS J095220.25+315548.5	148.08440	31.9302	2.481	2.307	2.446			
SDSS J095234.22+321958.1	148.14262	32.3329	2.890	2.322	2.851			
SDSS J095237.26+600554.0	148.15528	60.0983	2.649	2.307	2.613			
SDSS J0952+0114	148.22432	1.2394	3.021	2.447	2.981			
SDSS J095256.41+332939.0	148.23506	33.4942	3.396	2.484	3.352	3.3471	20.70	0.20
SDSS J095300.07+294137.3	148.25032	29.6937	3.166	2.435	3.124			
SDSS J095329.97+100400.6	148.37490	10.0668	2.807	2.307	2.769			
SDSS J095330.36+353223.1	148.37652	35.5398	2.376	2.307	2.342			
SDSS J0953+0037	148.39566	0.6234	2.605	2.484	2.569			
SDSS J095336.17+422707.6	148.40074	42.4521	2.970	2.320	2.930			
SDSS J095349.60+320548.4	148.45669	32.0968	2.742	2.359	2.704			
BR 0951-0450	148.48205	-5.0718	4.350	2.866	4.296	3.8560	20.70	0.20
						4.2020	20.35	0.15
SDSS J095406.40+290208.0	148.52671	29.0356	3.246	2.307	3.203			
SDSS J095412.20+371026.3	148.55087	37.1740	3.057	2.437	3.017			
SDSS J095414.12+061522.6	148.55886	6.2563	2.348	2.307	2.315			
SDSS J095414.77+610455.2	148.56157	61.0820	2.617	2.307	2.581			
SDSS J095423.99+420225.0	148.59999	42.0403	3.200	2.519	3.158			
SDSS J095434.93+091519.6	148.64558	9.2554	3.381	2.351	3.337	2.4418	21.05	0.25
SDSS J095456.01+050428.3	148.73340	5.0746	2.385	2.320	2.352			
BRI 0952-0115	148.75039	-1.5018	4.418	2.907	4.364	4.0245	20.70	0.15
SDSS J095511.32+594030.6	148.79719	59.6752	4.340	3.070	4.287	3.5420	20.30	0.10
FBQS J0955+3335	148.90808	33.5844	2.477	2.307	2.442			
SDSS J095539.73+024250.1	148.91558	2.7140	2.487	2.307	2.452			
SDSS J095542.12+411655.2	148.92551	41.2820	3.432	2.616	3.388	3.2767	20.30	0.20
SDSS J095546.35+432244.7	148.94316	43.3791	3.240	2.519	3.197			
SDSS J095602.89+420226.5	149.01208	42.0407	3.586	2.644	3.540			
SDSS J095604.39+345357.4	149.01831	34.8993	3.050	2.648	3.009			
SDSS J095604.43+344415.5	149.01848	34.7377	3.428	2.556	3.383			
SDSS J095604.70+041752.8	149.01961	4.2980	2.340	2.307	2.307			
SDSS J095607.17+103410.7	149.02989	10.5697	2.408	2.338	2.374			
SDSS J095612.86+543312.9	149.05362	54.5536	2.385	2.344	2.352			
SDSS J095616.81+060341.0	149.07008	6.0614	3.550	3.118	3.468			
SDSS J095617.30+053912.0	149.07211	5.6533	2.551	2.337	2.515			
SDSS J095618.11+310352.2	149.07548	31.0645	3.237	2.404	3.194	3.0942	20.30	0.15
SDSS J095620.59+311354.3	149.08581	31.2318	3.144	2.307	3.102			
SDSS J095624.74+355604.4	149.10309	35.9346	2.802	2.307	2.764			
SDSS J095625.16+473442.5	149.10488	47.5785	4.457	3.010	4.004	3.4030	20.90	0.20
						3.8900	21.10	0.20
SDSS J095630.01+085754.7	149.12507	8.9652	3.175	2.316	3.134			
SDSS J095632.03+321612.6	149.13349	32.2702	4.632	3.752	4.538			
SDSS J095647.07+361127.0	149.19617	36.1909	2.688	2.311	2.651			
SDSS J095651.39+595807.7	149.21418	59.9688	3.216	2.307	3.174			
SDSS J095707.67+061059.5	149.28200	6.1832	5.167	4.203	5.064			
SBS 0953+549	149.31113	54.6715	2.587	2.307	2.552			
SDSS J095724.95+060903.7	149.35397	6.1510	3.259	2.600	3.217			
SDSS J095726.94+042139.0	149.36229	4.3608	3.147	2.327	3.106			
SDSS J095735.37+353520.6	149.39738	35.5891	3.277	2.311	3.234			
SDSS J095741.87+331504.3	149.42447	33.2512	2.996	2.616	2.914			
SDSS J095744.46+330820.7	149.43527	33.1391	4.283	2.969	4.230	3.2800	20.50	0.10
						4.1790	20.60	0.10
SDSS J095751.47+302103.4	149.46448	30.3510	3.002	2.338	2.962			
SDSS J095755.63-002027.5	149.48184	-0.3410	3.753	2.966	3.705			
SDSS J095817.81+494618.3	149.57422	49.7718	2.355	2.307	2.322			
SDSS J095826.23+561228.0	149.60936	56.2078	3.499	2.623	3.454			
SDSS J095829.46+422256.8	149.62280	42.3825	2.618	2.307	2.582			
SDSS J095832.57+094017.2	149.63573	9.6715	3.024	2.643	2.984			
SDSS J095833.60+035144.3	149.64004	3.8623	3.680	2.741	3.633			
SDSS J095835.98+015157.0	149.64995	1.8659	2.934	2.565	2.851			
SDSS J095837.29+440548.8	149.65542	44.0969	2.366	2.307	2.332			
SDSS J095837.68+570332.8	149.65704	57.0592	2.483	2.307	2.449			
SDSS J095845.40+341319.4	149.68919	34.2221	2.551	2.307	2.516			
[HB89] 0956+122	149.71749	12.0458	3.298	2.307	3.255			
SDSS J095858.14+362318.9	149.74226	36.3886	2.678	2.314	2.595			
SDSS J095858.67+020138.8	149.74456	2.0275	2.454	2.307	2.419			
SDSS J095905.12+103325.0	149.77138	10.5570	4.019	3.671	3.936			

Continued on Next Page...

Table I.1 – Continued

Name	RA	Dec	z_{em}	z_{min}	z_{max}	z_{abs}	$\log N(\mathrm{H\,I})$	$\epsilon[\log N(\mathrm{H\,I})]$
SDSS J095907.95+360602.0	149.78314	36.1006	3.274	2.594	3.231			
SDSS J095920.86+392534.6	149.83697	39.4263	2.697	2.328	2.660			
SDSS J095922.98+531531.4	149.84576	53.2587	2.554	2.308	2.519			
SDSS J095930.68+094435.3	149.87787	9.7431	2.702	2.414	2.665			
SDSS J095931.60+005619.1	149.88172	0.9386	2.395	2.333	2.362			
SDSS J095937.11+131215.4	149.90466	13.2043	4.092	2.702	4.042			
SDSS J095939.58+045540.6	149.91494	4.9280	3.043	2.346	3.002			
SDSS J095955.12+551531.8	149.97970	55.2589	3.097	2.317	3.056			
SDSS J100012.26+102151.8	150.05110	10.3644	3.638	2.841	3.592			
SDSS J100014.13+020054.4	150.05887	2.0152	2.497	2.364	2.462			
SDSS J100016.09+450153.1	150.06705	45.0314	3.317	3.188	3.274			
SDSS J100023.21+361658.7	150.09673	36.2830	2.682	2.348	2.645			
SDSS J100023.69+333506.6	150.09873	33.5852	3.507	2.710	3.462	3.4478	20.35	0.15
SDSS J100028.41+612929.1	150.11842	61.4914	2.968	2.307	2.929			
SDSS J100041.10+405939.1	150.17127	40.9942	3.800	2.509	3.752			
SDSS J100053.22+632200.0	150.22182	63.3667	2.383	2.307	2.349			
SDSS J100054.61+315940.4	150.22758	31.9946	3.306	2.611	3.262			
SDSS J100054.98+541144.2	150.22912	54.1956	3.210	2.490	3.167	3.1142	20.40	0.15
SDSS J100104.32+463023.9	150.26803	46.5067	2.803	2.414	2.765			
SDSS J100106.13+312834.7	150.27558	31.4763	2.680	2.307	2.643			
SDSS J100113.63-001234.4	150.30680	-0.2096	2.459	2.333	2.424			
SDSS J100122.48+485300.8	150.34371	48.8836	3.235	2.836	3.193	3.0261	20.40	0.20
SDSS J100125.06+072329.1	150.35444	7.3914	3.138	2.426	3.097			
SDSS J100143.57+621942.1	150.43158	62.3284	2.525	2.307	2.489			
SDSS J100143.71+295526.3	150.43215	29.9240	3.115	2.697	3.074			
SDSS J100148.11+461946.2	150.45049	46.3295	2.958	2.387	2.918			
SDSS J100151.45+034301.4	150.46440	3.7171	3.201	2.507	3.159	3.0774	20.30	0.20
SDSS J100151.58-001626.9	150.46495	-0.2742	3.674	2.884	3.627			
SDSS J100159.83+044134.5	150.49930	4.6929	3.120	2.328	3.079			
SDSS J100201.37+095054.8	150.50574	9.8486	3.927	2.982	3.878			
SDSS J100205.68+462411.9	150.52370	46.4033	3.133	2.394	3.092			
SDSS J100212.57+440743.5	150.55240	44.1288	2.823	2.432	2.785			
SDSS J100238.25+013746.5	150.65939	1.6296	2.506	2.307	2.471			
SDSS J100244.72+293801.4	150.68636	29.6337	2.461	2.307	2.427			
SDSS J100245.84+450112.6	150.69105	45.0202	3.161	2.517	3.119			
SDSS J100247.15+005211.5	150.69650	0.8699	2.582	2.307	2.546			
SDSS J100248.37+363624.0	150.70159	36.6067	2.688	2.311	2.652			
SDSS J100251.20+223135.1	150.71335	22.5264	4.761	3.861	4.665			
SDSS J100255.50+345246.6	150.73129	34.8796	3.466	2.568	3.422			
SDSS J100302.60+404813.1	150.76075	40.8036	2.368	2.307	2.334			
SDSS J100305.51+104141.2	150.77299	10.6948	2.453	2.307	2.419			
SDSS J100312.36+390936.0	150.80153	39.1600	3.249	2.400	3.207			
SDSS J100312.62+402505.6	150.80263	40.4182	3.271	2.858	3.189			
SDSS J100318.98+521506.3	150.82912	52.2518	3.325	2.348	3.282			
SDSS J100321.11+552059.4	150.83800	55.3499	3.068	2.358	3.027	2.5019	20.60	0.20
SDSS J100325.12+325307.0	150.85471	32.8853	2.511	2.307	2.476	2.3308	21.70	0.15
SDSS J100330.05+475331.2	150.87522	47.8920	2.580	2.422	2.498			
SDSS J100341.50+040654.1	150.92293	4.1151	2.636	2.307	2.600			
SDSS J100352.84+473653.4	150.97015	47.6148	2.934	2.531	2.895			
SDSS J100357.24+345902.6	150.98854	34.9841	2.407	2.307	2.373			
SDSS J100402.92+475620.7	151.01217	47.9391	2.782	2.395	2.744			
SDSS J100409.35+120256.5	151.03897	12.0490	2.880	2.606	2.842	2.8006	20.60	0.20
SDSS J100412.42+292121.5	151.05178	29.3560	3.694	2.654	3.647			
SDSS J100416.12+434739.0	151.06719	43.7942	4.872	3.954	4.774	4.4720	20.40	0.20
SDSS J100423.26-004042.8	151.09698	-0.6786	2.732	2.350	2.695			
SDSS J100428.43+001825.6	151.11847	0.3071	3.045	2.307	3.004	2.5400	21.00	0.15
						2.6850	21.35	0.15
SDSS J100430.52+071103.2	151.12717	7.1842	2.981	2.573	2.941			
SDSS J100438.11+380201.4	151.15880	38.0337	2.823	2.432	2.785			
SDSS J100444.30+202520.0	151.18463	20.4222	5.084	4.133	4.983			
SDSS J100450.03+364617.7	151.20848	36.7716	2.433	2.307	2.399			
SDSS J100455.36+103619.8	151.23072	10.6055	3.138	2.512	3.097			
SDSS J100459.13+470057.9	151.24642	47.0161	2.578	2.307	2.542			
SDSS J100459.54+130411.4	151.24809	13.0699	2.365	2.307	2.331			
SDSS J100506.58+294237.0	151.27744	29.7103	3.313	2.496	3.270	2.9160	21.20	0.20
						3.2274	21.10	0.20
SDSS J100509.70+604902.3	151.29047	60.8173	2.962	2.569	2.922			
SDSS J100513.60+004028.4	151.30674	0.6745	2.554	2.307	2.519			
SDSS J100514.04+402030.6	151.30853	40.3419	3.336	2.491	3.293			
SDSS J100515.98+480533.2	151.31662	48.0926	2.372	2.307	2.338			
SDSS J100517.60+615417.2	151.32337	61.9048	2.740	2.357	2.703			
SDSS J100518.65+322541.2	151.32775	32.4281	2.577	2.307	2.541			

Continued on Next Page...

Table I.1 – Continued

Name	RA	Dec	z_{em}	z_{min}	z_{max}	z_{abs}	$\log N(\mathrm{H\,I})$	$\epsilon[\log N(\mathrm{H\,I})]$
SDSS J100521.46+453401.0	151.33946	45.5670	3.137	2.311	3.096			
SDSS J100536.41+085607.3	151.40174	8.9354	2.719	2.339	2.682			
SDSS J100543.72+325917.8	151.43219	32.9883	3.882	2.616	3.833			
SDSS J100544.53+520903.1	151.43555	52.1509	3.159	2.307	3.117			
SDSS J100546.72+295329.8	151.44470	29.8916	3.505	3.168	3.460			
SDSS J100547.72+091751.9	151.44887	9.2978	2.430	2.307	2.396			
SDSS J100549.47+103139.3	151.45618	10.5276	3.537	3.087	3.491			
SDSS J100553.33+001927.1	151.47225	0.3242	2.500	2.307	2.465			
SDSS J100555.81+330350.0	151.48258	33.0639	3.646	2.867	3.600			
SDSS J100602.59+035753.8	151.51082	3.9650	2.581	2.307	2.545			
SDSS J100603.79+554934.3	151.51584	55.8262	3.757	2.951	3.709			
SDSS J100609.65+103340.2	151.54023	10.5612	2.373	2.307	2.339			
2MASSi J1006105+370513	151.54397	37.0872	3.201	2.307	3.159			
SDSS J100646.23+544401.0	151.69264	54.7336	2.425	2.307	2.391			
SDSS J100653.01+512101.5	151.72091	51.3504	2.665	2.320	2.628	2.3458	20.30	0.15
SDSS J100655.80+050324.7	151.73254	5.0569	3.088	2.822	3.047	2.9345	20.50	0.15
SDSS J100714.86+314621.5	151.81194	31.7727	3.331	2.349	3.288			
SDSS J100716.85+400356.3	151.82023	40.0656	2.728	2.347	2.691			
SDSS J100730.66+305654.2	151.87777	30.9484	2.956	2.374	2.917			
SDSS J100734.07+413912.9	151.89197	41.6536	3.140	2.400	3.099			
[HB89] 1004+141	151.92291	13.9416	2.707	1.786	2.672			
SDSS J100743.09+320347.9	151.92957	32.0633	2.380	2.307	2.346			
SDSS J100745.89+472321.1	151.94127	47.3892	3.408	2.542	3.364			
SDSS J100746.57+525516.9	151.94407	52.9214	2.492	2.307	2.457			
SDSS J100751.71+124846.5	151.96550	12.8129	3.109	2.751	3.067			
SDSS J100753.63+561230.8	151.97350	56.2086	2.370	2.307	2.336			
SDSS J100757.18+061836.1	151.98829	6.3100	4.235	3.717	4.153			
SDSS J100809.67+614445.1	152.04033	61.7459	2.754	2.565	2.717			
SDSS J100828.42+093329.3	152.11845	9.5582	2.873	2.307	2.835			
SDSS J100838.97+494143.3	152.16240	49.6954	3.597	2.684	3.551			
FBQS J100841.2+362319	152.17186	36.3887	3.126	2.307	3.084	2.7997	20.55	0.15
SDSS J100844.54+581730.1	152.18559	58.2917	2.813	2.422	2.775			
SDSS J100852.61+475552.5	152.21923	47.9312	2.846	2.663	2.807			
SDSS J100855.76-005816.4	152.23237	-0.9712	3.097	2.416	3.056			
SDSS J100857.35+031243.9	152.23899	3.2122	2.623	2.557	2.587			
SDSS J100914.14+044835.5	152.30894	4.8099	2.398	2.307	2.364			
SDSS J100923.31+451724.1	152.34718	45.2901	2.595	2.307	2.559			
SDSS J100927.41+111811.9	152.36424	11.3033	3.219	2.798	3.177			
SDSS J100928.88+505605.3	152.37040	50.9348	3.742	3.329	3.660			
SDSS J100934.38+330121.2	152.39327	33.0226	3.243	2.532	3.201			
SDSS J100956.05+391718.3	152.48355	39.2884	3.833	2.831	3.785			
SDSS J101003.95+332625.6	152.51649	33.4405	2.986	2.307	2.946			
SDSS J101010.89+064556.2	152.54542	6.7656	2.966	2.573	2.884			
SDSS J101021.08+360043.5	152.58786	36.0121	2.625	2.313	2.589			
SDSS J101037.04+092948.2	152.65439	9.4967	3.365	2.933	3.282			
SDSS J101049.63+132746.8	152.70683	13.4630	4.136	3.297	4.084			
SDSS J101054.91+452216.6	152.72882	45.3713	3.118	2.403	3.077			
SDSS J101104.79+562003.9	152.76997	56.3344	2.629	2.307	2.593			
SDSS J101107.98+553407.0	152.78327	55.5686	3.340	2.896	3.297			
SDSS J101108.70+435618.4	152.78631	43.9385	3.070	2.668	3.029			
SDSS J101110.75+423937.1	152.79481	42.6603	3.560	2.541	3.514			
SDSS J101111.21+341548.5	152.79675	34.2635	2.411	2.307	2.377			
SDSS J101119.20+305709.4	152.83003	30.9526	2.379	2.307	2.345			
SDSS J101120.39+031244.5	152.83500	3.2124	2.457	2.307	2.423			
SDSS J101120.80+405104.2	152.83671	40.8512	3.880	3.406	3.831			
SDSS J101122.59+470042.1	152.84414	47.0117	2.928	2.307	2.889			
SDSS J101131.64+102038.9	152.88187	10.3442	3.126	2.471	3.084			
SDSS J101203.96+385202.3	153.01652	38.8673	2.778	2.391	2.740			
SDSS J101204.04+531331.7	153.01685	53.2255	2.990	2.368	2.950			
SDSS J101212.95+501321.4	153.05396	50.2226	2.362	2.307	2.329			
LBQS 1009-0252	153.06583	-3.1172	2.750	1.651	2.708			
SDSS J101216.79+005746.4	153.07003	0.9629	2.447	2.307	2.412			
SDSS J101224.64+393559.3	153.10270	39.5998	2.615	2.307	2.578			
SDSS J101246.48+500534.1	153.19370	50.0928	3.532	3.067	3.486			
SDSS J101249.66+090151.9	153.20693	9.0311	2.995	2.705	2.913			
SDSS J101252.58+474708.5	153.21910	47.7857	2.604	2.307	2.568			
SDSS J101257.52+025933.1	153.23969	2.9926	2.434	2.307	2.400			
SDSS J101301.05+041159.6	153.25439	4.1999	3.546	3.081	3.500			
FBQS J101302.2+352605	153.25959	35.4349	2.649	2.307	2.612			
SDSS J101303.73+434606.3	153.26557	43.7684	2.930	2.583	2.890			
SDSS J101304.31+321248.7	153.26797	32.2135	3.724	2.948	3.677			
SDSS J101310.39+053630.1	153.29331	5.6084	3.852	2.949	3.804			

Continued on Next Page...

Table I.1 – Continued

Name	RA	Dec	z_{em}	z_{min}	z_{max}	z_{abs}	$\log N(\mathrm{H\,I})$	$\epsilon[\log N(\mathrm{H\,I})]$
SDSS J101329.40+443829.9	153.37256	44.6417	2.994	2.353	2.955			
SDSS J101336.33+424026.4	153.40141	42.6740	5.038	4.420	4.977	4.7997	20.40	0.25
SDSS J101336.37+561536.3	153.40157	56.2601	3.614	2.675	3.568			
SDSS J101345.50+330718.7	153.43962	33.1219	3.655	2.908	3.609			
SDSS J101346.55+112231.7	153.44398	11.3755	3.259	2.307	3.216			
SDSS J101347.29+065015.6	153.44707	6.8377	3.808	2.397	3.760			
SDSS J101414.01+350127.9	153.55841	35.0244	3.228	2.353	3.186			
LBQS 1011-0144	153.55901	-1.9881	2.240	1.669	2.204			
SDSS J101419.93+594550.5	153.58306	59.7640	3.047	2.397	3.006			
SDSS J101420.52+325931.9	153.58553	32.9922	2.393	2.307	2.311			
SDSS J101425.64+322309.6	153.60688	32.3860	2.501	2.449	2.466			
SDSS J101429.72+610354.6	153.62388	61.0652	4.162	3.003	4.110			
SDSS J101446.63+083500.9	153.69433	8.5836	2.509	2.307	2.474			
2MASSi J1014471+430030	153.69660	43.0084	3.125	2.307	3.084	2.9582	20.50	0.15
SDSS J101448.30+045920.3	153.70128	4.9890	2.475	2.321	2.440			
SDSS J101459.26+320941.8	153.74696	32.1616	2.896	2.354	2.857			
LBQS 1012-0206	153.77732	-2.3548	2.140	1.634	2.104			
SDSS J101518.80+562852.7	153.82836	56.4813	2.367	2.307	2.333			
SDSS J101524.99+553801.8	153.85414	55.6339	3.237	2.805	3.195			
SDSS J101526.33+392107.1	153.85971	39.3520	3.575	2.672	3.529			
SDSS J101539.17+542148.6	153.91325	54.3635	3.787	2.853	3.739			
SDSS J101539.35+111815.9	153.91398	11.3044	2.915	2.307	2.876			
SDSS J101542.04+430455.6	153.92518	43.0821	2.420	2.307	2.386			
SDSS J101547.38+512615.8	153.94744	51.4377	2.766	2.381	2.728			
SDSS J101549.00+002019.9	153.95419	0.3389	4.380	3.123	4.326			
SDSS J101601.50+404052.8	154.00626	40.6814	2.963	2.557	2.924			
SDSS J101617.67+405912.2	154.07364	40.9868	2.364	2.313	2.331			
SDSS J101622.48+071508.7	154.09369	7.2524	3.293	2.598	3.250			
SDSS J101626.91+060108.2	154.11215	6.0190	2.842	2.489	2.803			
LBQS 1014+0023	154.14995	0.1475	2.290	1.634	2.257			
PKS 1014+208	154.18468	20.6298	3.110	1.945	3.069			
SDSS J101648.22+431338.7	154.20095	43.2274	3.218	2.368	3.176			
SDSS J101656.72+620446.9	154.23636	62.0797	3.254	2.410	3.212			
SDSS J101700.09+342310.8	154.25040	34.3863	3.223	2.446	3.181			
SDSS J101725.88+611627.5	154.35786	61.2743	2.807	2.307	2.769	2.7681	20.60	0.10
SDSS J101741.94+035150.2	154.42477	3.8640	2.662	2.375	2.626			
SDSS J101755.14+652802.2	154.47983	65.4673	2.741	2.389	2.704			
SDSS J101806.27+310627.2	154.52617	31.1076	3.629	2.562	3.582			
SDSS J101818.45+054822.8	154.57689	5.8063	3.515	2.299	3.470			
SDSS J101821.67+064434.4	154.59031	6.7429	3.397	2.503	3.353			
SDSS J101822.86+070534.8	154.59526	7.0930	3.752	3.266	3.705			
SDSS J101829.31+095918.7	154.62217	9.9885	3.162	2.776	3.120			
SDSS J101832.18+383035.7	154.63411	38.5099	3.837	3.052	3.789			
SDSS J101844.40+452504.6	154.68504	45.4179	4.432	3.509	4.378	3.6865	20.85	0.20
SDSS J101846.35+384052.3	154.69315	38.6812	2.476	2.307	2.441			
SDSS J101852.96+375643.0	154.72070	37.9453	2.422	2.307	2.388			
SDSS J101853.24+355222.3	154.72186	35.8729	2.384	2.307	2.350			
LBQS 1016-0039	154.74984	-0.9056	2.180	1.649	2.144			
SDSS J101902.01+473714.5	154.75841	47.6207	2.945	2.349	2.905	2.7436	20.90	0.15
SDSS J101908.10+030526.9	154.78380	3.0908	2.418	2.307	2.384			
SDSS J101908.25+025432.0	154.78443	2.9089	3.390	2.375	3.346			
SDSS J101909.49+061822.9	154.78956	6.3064	3.367	2.935	3.323			
SDSS J101917.25+464319.3	154.82195	46.7221	3.736	3.334	3.688			
SDSS J101917.58+363429.2	154.82329	36.5748	2.959	2.353	2.919			
SDSS J101935.32+473250.3	154.89719	47.5473	2.439	2.307	2.404			
2MASSi J1019479+354145	154.95001	35.6962	2.685	2.308	2.648	2.4984	20.35	0.15
SDSS J101952.58+375011.0	154.96903	37.8364	2.430	2.307	2.396			
SDSS J101954.53+082515.0	154.97725	8.4209	3.010	2.307	2.970	2.3172	20.40	0.15
SDSS J101956.96+455728.9	154.98734	45.9581	2.424	2.307	2.389			
SDSS J102001.19+392557.4	155.00498	39.4326	2.955	2.597	2.916	2.6609	20.55	0.25
						2.8969	20.45	0.20
SDSS J102001.33+031515.6	155.00557	3.2543	3.025	2.626	2.984			
[HB89] 1017+109	155.04164	10.6674	3.167	2.307	3.125			
SDSS J102015.63+093223.2	155.06517	9.5398	3.684	2.693	3.637	3.0653	21.05	0.20
SDSS J102023.78+105351.7	155.09909	10.8977	3.085	2.377	3.045	2.8762	20.45	0.15
SDSS J102025.27+334633.4	155.10533	33.7760	2.930	2.307	2.891			
SDSS J102025.69+514419.0	155.10705	51.7386	2.529	2.307	2.493			
SDSS J102036.37+335644.6	155.15156	33.9457	3.230	2.570	3.188	2.9332	20.90	0.20
SDSS J102037.15+383031.5	155.15483	38.5088	3.482	2.624	3.437	3.2583	20.40	0.20
SDSS J102040.62+092254.2	155.16926	9.3817	3.640	2.093	3.594	2.5920	21.50	0.10
LBQS 1018-0005	155.24822	-0.3407	2.600	2.307	2.564			
SDSS J102106.78+303137.5	155.27828	30.5271	3.062	2.672	3.021			

Continued on Next Page...

Table I.1 – Continued

Name	RA	Dec	z_{em}	z_{min}	z_{max}	z_{abs}	$\log N(\mathrm{H\,I})$	$\epsilon[\log N(\mathrm{H\,I})]$
SDSS J102109.59+371042.9	155.29000	37.1786	3.684	3.263	3.637			
SDSS J102115.70+360521.7	155.31544	36.0894	2.540	2.307	2.504			
SDSS J102116.82+052332.5	155.32013	5.3924	3.687	3.292	3.640			
SDSS J102135.83+580244.8	155.39940	58.0458	2.706	2.325	2.668			
SDSS J102240.88+044356.8	155.67037	4.7325	3.081	2.323	3.040	2.7416	20.40	0.15
SDSS J102243.05+304927.0	155.67939	30.8242	2.724	2.343	2.687			
SDSS J102256.63+372018.3	155.73600	37.3384	3.971	2.525	3.921			
SDSS J102301.01+070918.2	155.75424	7.1551	3.795	2.817	3.747	3.3781	20.45	0.20
SDSS J102304.39+361052.6	155.76830	36.1813	3.582	3.206	3.537			
SDSS J102320.39+521437.8	155.83503	52.2438	2.424	2.307	2.390			
SDSS J102325.31+514251.0	155.85549	51.7142	3.447	2.307	3.403			
LBQS 1020+0028	155.87479	0.2194	1.900	1.680	1.872			
SDSS J102332.07+633508.0	155.88364	63.5856	4.872	3.954	4.774	4.2590	20.70	0.20
SDSS J102334.42+334735.8	155.89344	33.7933	2.393	2.307	2.359			
SDSS J102340.74+615052.0	155.91981	61.8478	2.930	2.618	2.890			
SDSS J102343.13+553132.3	155.92974	55.5257	4.455	4.262	4.400			
SDSS J102348.95+365423.2	155.95397	36.9065	3.347	2.499	3.304			
SDSS J102350.92+044509.1	155.96222	4.7525	2.362	2.307	2.328			
SDSS J102408.14+490307.5	156.03398	49.0521	4.006	3.626	3.956			
SDSS J102424.56+585755.9	156.10236	58.9656	2.954	2.563	2.872			
[HB89] 1021-006	156.12328	-0.8821	2.554	2.307	2.519			
SDSS J102436.60+332046.7	156.15251	33.3463	3.304	2.635	3.261			
SDSS J102447.59+400525.5	156.19830	40.0904	2.388	2.307	2.354			
SDSS J102456.61+181908.7	156.23590	18.3191	3.524	2.159	3.479	2.2980	21.30	0.10
SDSS J102458.02+103716.4	156.24177	10.6212	3.189	2.774	3.106			
SDSS J102509.63+045246.7	156.29016	4.8797	3.244	2.307	3.201			
SDSS J102514.54+581749.7	156.31060	58.2972	2.518	2.307	2.483			
SDSS J102524.92+605420.8	156.35387	60.9059	2.516	2.346	2.481			
SDSS J102525.49+505519.9	156.35625	50.9222	2.428	2.307	2.394			
SDSS J102529.33+631520.0	156.37221	63.2556	2.519	2.429	2.484			
SDSS J102541.39+120506.7	156.42246	12.0852	3.580	3.126	3.497			
SDSS J102552.89+040503.2	156.47039	4.0842	3.073	2.428	3.032			
SDSS J102600.07+112441.8	156.50033	11.4116	3.047	2.307	3.006			
SDSS J102600.84+454616.8	156.50354	45.7713	3.044	2.307	3.004			
SDSS J102602.88+473921.2	156.51202	47.6559	2.679	2.307	2.642			
SDSS J102611.35+341459.9	156.54730	34.2500	3.399	2.481	3.355	2.9194	20.30	0.20
SDSS J102618.80+461445.2	156.57835	46.2459	3.335	2.665	3.292			
SDSS J102619.09+613628.8	156.57956	61.6080	3.844	2.813	3.796	3.7855	20.35	0.15
SDSS J102622.87+471907.2	156.59541	47.3186	4.932	4.005	4.833			
SDSS J102623.61+254259.5	156.59842	25.7165	5.254	4.277	5.150			
SDSS J102627.88+014034.2	156.61617	1.6762	2.988	2.675	2.948			
SDSS J102635.23+625536.7	156.64680	62.9269	3.325	2.898	3.282			
LBQS 1024+0030	156.65397	0.2584	2.170	1.717	2.135			
SDSS J102642.13+333557.0	156.67558	33.5992	3.179	2.396	3.137			
B2 1023+37	156.68892	36.9738	3.202	2.521	3.160			
SDSS J102646.02+353145.4	156.69179	35.5293	3.654	2.385	3.607			
SDSS J102647.67+643319.9	156.69865	64.5556	2.787	2.504	2.749			
SDSS J102649.59+582101.7	156.70670	58.3505	2.794	2.581	2.756	2.5866	20.60	0.15
SDSS J102656.59+382843.8	156.73582	38.4789	4.180	2.756	4.128			
SDSS J102708.89+562806.8	156.78710	56.4685	2.507	2.307	2.472			
2MASSi J1027147+354317	156.81158	35.7215	3.108	2.307	3.067			
SDSS J102715.63+345804.1	156.81514	34.9678	2.481	2.307	2.447			
SDSS J102715.98+351918.8	156.81662	35.3219	3.146	2.736	3.063	2.7904	21.50	0.15
SDSS J102720.64+553525.2	156.83601	55.5904	3.027	2.366	2.987			
SDSS J102749.21+623305.0	156.95511	62.5514	2.873	2.590	2.834			
SDSS J102750.14+121020.6	156.95895	12.1724	3.450	3.064	3.406			
SDSS J102752.51+390054.7	156.96882	39.0152	3.155	2.495	3.113	3.0326	20.55	0.15
SDSS J102753.88+661219.5	156.97455	66.2055	2.375	2.307	2.341			
SDSS J102805.89+362327.3	157.02457	36.3909	2.880	2.307	2.842			
SDSS J102806.06+502126.1	157.02528	50.3573	3.476	2.662	3.431			
SDSS J102809.70+110435.5	157.04044	11.0765	3.160	2.736	3.118			
SDSS J102815.47+321317.0	157.06450	32.2214	2.773	2.628	2.735			
SDSS J102817.24+050403.1	157.07185	5.0675	2.937	2.657	2.897			
SDSS J102819.76+105052.4	157.08235	10.8479	3.050	2.447	3.009			
SDSS J102822.71+070605.9	157.09467	7.1017	2.873	2.526	2.834			
LBQS 1025-0030	157.13372	-0.7686	2.859	2.307	2.821			
SDSS J102832.67+465750.0	157.13622	46.9639	2.498	2.307	2.463			
BZQ J1028-0844	157.16167	-8.7441	4.276	2.533	4.223			
SDSS J102846.09-010203.0	157.19207	-1.0342	3.744	3.345	3.696			
SDSS J102847.56+530556.6	157.19821	53.0990	2.808	2.430	2.770			
SDSS J102900.79+622341.9	157.25332	62.3950	2.469	2.307	2.435			
SDSS J102907.12+141817.8	157.27969	14.3050	3.512	3.065	3.430			

Continued on Next Page...

Table I.1 – Continued

Name	RA	Dec	z_{em}	z_{min}	z_{max}	z_{abs}	$\log N(\mathrm{H\,I})$	$\epsilon[\log N(\mathrm{H\,I})]$
SDSS J102908.25+471742.2	157.28445	47.2951	3.034	2.307	2.994	2.5196	21.00	0.15
SDSS J102908.79+455139.3	157.28664	45.8610	3.223	2.338	3.181			
SDSS J102909.56+544536.0	157.28985	54.7600	3.143	2.307	3.102			
SDSS J102916.43+094643.4	157.31850	9.7788	2.944	2.372	2.904			
SDSS J102921.85+621034.4	157.34114	62.1762	2.481	2.409	2.446			
SDSS J102924.16+423812.2	157.35070	42.6367	3.277	2.307	3.234			
SDSS J102925.49+393707.4	157.35626	39.6187	3.406	2.539	3.362			
SDSS J102929.42+621231.1	157.37263	62.2086	3.263	2.499	3.220			
SDSS J102942.12+135624.2	157.42552	13.9401	3.140	2.307	3.098	2.9938	20.60	0.20
SDSS J102953.92+404011.9	157.47470	40.6700	3.175	2.339	3.133	2.5957	20.70	0.15
SDSS J102958.68+651210.3	157.49457	65.2029	2.478	2.307	2.443			
SDSS J103007.90+130229.0	157.53294	13.0414	3.584	3.115	3.538			
SDSS J103018.35+552324.3	157.57649	55.3901	3.022	2.639	2.981			
SDSS J103019.46+654106.6	157.58112	65.6852	3.575	3.107	3.529			
SDSS J103024.72+452303.1	157.60305	45.3842	3.671	2.797	3.624			
SDSS J103032.12+134919.1	157.63387	13.8220	3.019	2.667	2.937			
SDSS J103035.66+445033.4	157.64861	44.8426	2.854	2.564	2.815	2.7283	20.80	0.20
						2.7493	21.25	0.20
SDSS J103037.56+345259.8	157.65653	34.8833	2.552	2.307	2.517			
SDSS J103045.31+650828.6	157.68885	65.1413	2.877	2.480	2.838			
SDSS J103046.36+024147.1	157.69319	2.6964	2.925	2.720	2.886			
SDSS J103048.24+391234.3	157.70103	39.2095	3.721	2.756	3.674			
SDSS J103051.47+471548.3	157.71451	47.2634	3.063	2.307	3.022			
SDSS J103054.29+354427.3	157.72622	35.7409	3.721	2.973	3.674			
SDSS J103055.95+432037.7	157.73315	43.3438	3.700	2.958	3.653			
SDSS J103057.33+473136.4	157.73892	47.5268	2.928	2.307	2.888			
SDSS J103108.24+375801.2	157.78438	37.9670	2.585	2.333	2.549			
SDSS J103114.20+051718.2	157.80918	5.2884	2.427	2.307	2.393			
SDSS J103126.13+405532.5	157.85890	40.9257	3.006	2.437	2.966	2.5707	20.40	0.20
SDSS J103134.04+562050.8	157.89189	56.3475	3.214	2.800	3.172			
SDSS J103147.64+575858.0	157.94852	57.9828	2.879	2.481	2.840			
SDSS J103152.64+362504.1	157.96937	36.4178	3.328	2.495	3.284			
SDSS J103201.03+595030.5	158.00431	59.8418	2.346	2.307	2.312			
SDSS J103202.72+081116.3	158.01134	8.1879	3.256	2.820	3.213	3.0738	21.15	0.15
SDSS J103212.88+120612.8	158.05370	12.1036	3.189	2.307	3.147			
SDSS J103217.25+070350.3	158.07190	7.0640	3.031	2.307	2.991			
SDSS J103220.01+345302.1	158.08341	34.8839	2.411	2.307	2.377			
SDSS J103221.11+092748.9	158.08797	9.4636	3.985	2.620	3.936			
SDSS J103231.72+513543.6	158.13221	51.5955	3.208	2.782	3.166			
SDSS J103239.90+132824.6	158.16629	13.4735	2.548	2.307	2.512			
SDSS J103240.53+501210.9	158.16891	50.2030	3.822	2.836	3.774			
SDSS J103240.88+072942.9	158.17034	7.4953	3.637	2.650	3.591	2.8959	20.50	0.20
						3.0374	21.65	0.20
SDSS J103245.34+014924.6	158.18895	1.8235	2.428	2.307	2.393			
SDSS J103249.88+054118.3	158.20786	5.6884	2.851	2.307	2.812			
SDSS J103255.68+112155.1	158.23204	11.3653	3.672	2.970	3.626	3.3952	21.05	0.20
SDSS J103259.92+095630.7	158.24970	9.9419	3.261	2.860	3.218			
SDSS J103300.95+462311.5	158.25401	46.3865	2.644	2.307	2.608			
SDSS J103305.85+393633.0	158.27438	39.6092	3.666	2.844	3.619			
SDSS J103310.70+540646.9	158.29462	54.1130	2.959	2.307	2.920			
SDSS J103311.77+603146.6	158.29911	60.5296	2.493	2.307	2.458			
SDSS J103312.89+601342.2	158.30376	60.2284	2.515	2.307	2.480			
SDSS J103314.58+345112.0	158.31076	34.8533	3.813	3.073	3.765			
SDSS J103339.05+555321.8	158.41273	55.8894	2.478	2.307	2.443			
SDSS J103339.81+072214.9	158.41588	7.3708	2.906	2.506	2.867			
SDSS J103340.39+361302.1	158.41831	36.2173	3.204	2.967	3.161			
SDSS J103341.43+135428.1	158.42266	13.9078	3.096	3.186	4.019			
SDSS J103356.20+355745.1	158.48422	35.9625	4.035	2.972	3.984			
SDSS J103359.96+583457.7	158.49989	58.5827	3.114	2.481	3.073			
SDSS J103401.75+624214.0	158.50732	62.7039	3.863	3.431	3.815			
SDSS J103403.87+380248.4	158.51615	38.0468	3.560	2.571	3.515			
SDSS J103407.74+452830.6	158.53226	45.4752	2.433	2.307	2.350			
SDSS J103417.09+450855.4	158.57123	45.1487	3.066	2.356	3.025	2.9422	20.60	0.20
SDSS J103418.65+203300.2	158.57772	20.5501	4.998	4.061	4.898			
SDSS J103425.91+625803.7	158.60799	62.9677	2.992	2.413	2.952			
SDSS J103446.54+110214.5	158.69393	11.0374	4.269	2.422	4.217			
SDSS J103456.31+035859.3	158.73464	3.9832	3.369	2.406	3.326			
SDSS J103459.13+323701.6	158.74641	32.6171	2.888	2.490	2.849			
SDSS J103500.87+073734.2	158.75367	7.6262	2.474	2.307	2.439			
SDSS J103502.72+373912.4	158.76137	37.6534	2.462	2.307	2.427			
SDSS J103508.02+571255.7	158.78342	57.2155	2.587	2.307	2.552			
SDSS J103513.17+141623.5	158.80490	14.2732	2.461	2.307	2.426			

Continued on Next Page...

Table I.1 – Continued

Name	RA	Dec	z_{em}	z_{min}	z_{max}	z_{abs}	$\log N(\mathrm{H\,I})$	$\epsilon[\log N(\mathrm{H\,I})]$
SDSS J103514.22+544040.1	158.80927	54.6778	2.988	2.307	2.949	2.6840	20.50	0.20
SDSS J103515.95+105623.8	158.81648	10.9400	3.373	2.965	3.329	3.1908	20.95	0.15
SDSS J103527.92+140224.2	158.86634	14.0401	3.512	2.636	3.467			
SDSS J103528.34+531340.7	158.86813	53.2280	3.226	2.793	3.184			
SDSS J103531.16+594747.0	158.87985	59.7964	2.987	2.307	2.947			
SDSS J103532.58+423018.9	158.88574	42.5053	2.441	2.308	2.406			
SDSS J103545.78+614019.5	158.94075	61.6721	2.853	2.664	2.814			
SDSS J103546.02+110546.4	158.94179	11.0962	2.360	2.307	2.327			
SDSS J103556.29+443312.8	158.98460	44.5536	2.909	2.307	2.870			
SDSS J103601.03+500831.7	159.00431	50.1422	4.480	3.624	4.389			
SDSS J103601.11+084948.4	159.00467	8.8301	3.679	2.806	3.633			
SDSS J103608.97+065443.9	159.03741	6.9122	2.438	2.307	2.404			
SDSS J103612.94+001100.0	159.05393	0.1833	2.986	2.579	2.946			
SDSS J103615.84+375434.4	159.06604	37.9096	3.155	2.507	3.114			
SDSS J103621.01+490155.2	159.08758	49.0320	2.816	2.472	2.778			
BR 1033-0327	159.09874	-3.7219	4.531	2.899	4.476			
[HB89] 1033+137	159.11200	13.4477	3.096	2.307	3.055			
SDSS J103628.15+585832.0	159.11732	58.9756	3.933	3.241	3.884			
SDSS J103635.94+591800.4	159.14978	59.3001	3.662	3.201	3.580			
SDSS J103637.07+075005.9	159.15449	7.8350	3.092	2.687	3.009			
SDSS J103638.39+484116.8	159.15998	48.6880	2.361	2.307	2.328			
SDSS J103642.20+400204.6	159.17586	40.0346	2.933	2.549	2.851			
SDSS J103647.18+093252.4	159.19659	9.5479	2.950	2.635	2.910			
SDSS J103653.24+490351.3	159.22187	49.0643	2.829	2.474	2.791	2.6021	20.40	0.15
SDSS J103702.51+451748.8	159.26046	45.2969	4.094	3.251	4.043			
SDSS J103710.44+343935.7	159.29353	34.6599	2.378	2.307	2.344			
SDSS J103711.04+313433.5	159.29604	31.5760	4.916	3.992	4.817			
SDSS J103713.05+110251.7	159.30439	11.0477	3.276	2.349	3.233			
SDSS J103715.11-000248.7	159.31299	-0.0469	3.677	2.895	3.631			
SDSS J103724.40+013933.9	159.35167	1.6594	3.089	2.714	3.048			
SDSS J103725.42+392112.2	159.35596	39.3534	3.295	2.307	3.252	3.0725	20.65	0.15
						3.1213	20.30	0.15
SDSS J103730.33+213531.3	159.37640	21.5921	3.626	1.665	3.580			
SDSS J103732.38+070426.2	159.38495	7.0740	4.127	2.225	4.076			
SDSS J103750.59+081425.0	159.46083	8.2403	2.830	2.437	2.791			
SDSS J103751.05+091034.9	159.46275	9.1764	3.580	2.681	3.534	2.8427	21.20	0.15
SDSS J103753.56+340706.1	159.47319	34.1184	3.224	2.553	3.182			
SDSS J103800.49+582343.0	159.50209	58.3953	2.697	2.318	2.660			
SDSS J103808.24+473135.2	159.53437	47.5265	2.976	2.355	2.936			
SDSS J103815.27+630302.1	159.56369	63.0506	2.566	2.520	2.530			
SDSS J103821.23+094322.9	159.58850	9.7231	3.625	3.186	3.542			
SDSS J103848.11+004753.3	159.70049	0.7982	3.768	2.750	3.720	2.8199	21.00	0.15
SDSS J103854.10+543814.4	159.72546	54.6373	3.796	2.776	3.748			
SDSS J103857.36+502707.6	159.73906	50.4521	3.131	2.544	3.089	2.7952	20.50	0.15
SDSS J103919.28+344504.5	159.83035	34.7513	4.390	2.881	4.336			
SDSS J103919.59+604001.6	159.83171	60.6671	3.901	3.033	3.852			
SDSS J103924.05+304059.5	159.85024	30.6832	2.705	2.365	2.668			
SDSS J103941.50+341319.6	159.92294	34.2221	4.184	3.052	4.132			
SDSS J103944.49+295912.4	159.93538	29.9868	3.607	2.688	3.561			
SDSS J103945.90+084834.6	159.94127	8.8096	4.293	3.453	4.240			
SDSS J103951.00+331107.4	159.96252	33.1854	3.194	2.499	3.152			
SDSS J103956.17+480128.9	159.98408	48.0247	3.433	2.583	3.389			
SDSS J104000.46+333830.7	160.00195	33.6419	2.634	2.356	2.598			
SDSS J104002.01+314149.8	160.00843	31.6972	3.001	2.408	2.961			
SDSS J104002.51+310449.7	160.01047	31.0805	3.550	2.666	3.505	3.2178	20.55	0.20
SDSS J104004.02+322150.5	160.01676	32.3640	2.609	2.307	2.573			
SDSS J104007.57+062508.7	160.03157	6.4191	2.395	2.307	2.361			
SDSS J104008.10+651429.2	160.03375	65.2415	4.538	4.354	4.482			
SDSS J104018.51+572448.1	160.07717	57.4134	3.409	2.390	3.365			
SDSS J104018.81+320814.9	160.07839	32.1375	2.718	2.380	2.681			
SDSS J104040.13-001540.8	160.16724	-0.2614	4.298	3.084	4.245	3.5454	20.70	0.15
SDSS J104041.09+162233.8	160.17123	16.3761	4.809	3.901	4.712			
SDSS J104046.44+005950.8	160.19353	0.9975	3.046	2.994	3.006			
SDSS J104051.23+613814.8	160.21348	61.6375	2.384	2.307	2.350			
SDSS J104056.01+453209.0	160.23340	45.5359	4.234	3.355	4.182			
SDSS J104057.67+514505.9	160.24033	51.7516	4.045	2.903	3.995			
SDSS J104105.07+431945.3	160.27115	43.3293	3.121	2.307	3.080			
SDSS J104106.04+144417.3	160.27521	14.7382	3.014	2.645	2.973			
SDSS J104110.69+491750.6	160.29456	49.2974	2.797	2.614	2.715	2.6649	21.05	0.20
SDSS J104121.10+334901.6	160.33796	33.8171	4.108	3.032	4.057	3.4412	21.30	0.20
SDSS J104125.40+402107.1	160.35587	40.3520	3.077	2.307	3.036			
SDSS J104127.46+023920.5	160.36447	2.6557	3.606	2.830	3.560	3.3100	20.40	0.15

Continued on Next Page...

Table I.1 – Continued

Name	RA	Dec	z_{em}	z_{min}	z_{max}	z_{abs}	$\log N(\mathrm{H\,I})$	$\epsilon[\log N(\mathrm{H\,I})]$
SDSS J104128.31+302815.9	160.36798	30.4711	3.219	3.056	3.177			
[HB89] 1038+528 NED02	160.45374	52.5654	2.300	1.677	2.262			
SDSS J104156.30+534246.7	160.48460	53.7130	2.801	2.412	2.763			
SDSS J104157.03+010917.6	160.48768	1.1549	2.986	2.834	2.946	2.8944	21.05	0.15
SDSS J104206.72+293826.9	160.52804	29.6408	2.564	2.379	2.528			
SDSS J104210.86+300259.4	160.54529	30.0498	2.531	2.478	2.495			
FBQS J104229.1+381111	160.62158	38.1865	2.632	2.307	2.595			
SDSS J104233.41+423218.3	160.63923	42.5384	2.898	2.307	2.859			
SDSS J104234.01+195718.6	160.64172	19.9552	3.630	2.044	3.584			
SDSS J104238.00+561802.0	160.65835	56.3006	3.693	2.643	3.646			
SDSS J104242.40+310713.1	160.67672	31.1203	4.688	3.517	4.631	4.0849	21.00	0.15
SDSS J104245.47+365642.2	160.68950	36.9451	2.855	2.522	2.772			
[HB89] 1040+015 NED02	160.71802	1.2935	2.441	2.307	2.407			
SDSS J104253.43-001300.9	160.72267	-0.2169	2.960	2.307	2.920			
SDSS J104255.96+512936.3	160.73319	51.4934	3.386	2.424	3.342			
SDSS J104257.52+310103.3	160.73971	31.0176	3.710	2.657	3.663			
SDSS J104300.06+343359.0	160.75027	34.5664	3.178	2.458	3.136			
SDSS J104302.42+312434.0	160.76013	31.4095	3.816	2.999	3.768	3.4010	20.85	0.15
SDSS J104304.87+464953.4	160.77035	46.8315	2.894	2.496	2.855			
SDSS J104313.68+143435.7	160.80702	14.5766	3.365	2.426	3.321			
SDSS J104318.41+352226.7	160.82672	35.3741	3.481	2.708	3.436			
SDSS J104318.88+004747.2	160.82868	0.7965	2.552	2.388	2.517			
SDSS J104319.65+321709.3	160.83190	32.2859	2.655	2.316	2.618			
SDSS J104321.55+624127.2	160.83983	62.6909	2.354	2.307	2.320			
SDSS J104325.55+404849.5	160.85650	40.8137	4.923	3.998	4.824			
SDSS J104328.08+430620.6	160.86702	43.1057	3.096	3.023	3.055			
SDSS J104328.57+295943.7	160.86907	29.9955	2.530	2.307	2.495			
SDSS J104328.84+111412.0	160.87020	11.2367	2.576	2.307	2.540			
SDSS J104344.95+494516.6	160.93732	49.7546	2.477	2.403	2.442			
SDSS J104351.19+650647.6	160.96334	65.1132	4.516	3.654	4.424			
SDSS J104357.80+043825.1	160.99087	4.6403	2.415	2.307	2.380			
SDSS J104406.33+295900.9	161.02643	29.9836	2.983	2.346	2.943			
SDSS J104407.32+094214.6	161.03052	9.7041	3.781	2.794	3.733			
SDSS J104422.46+290751.1	161.09362	29.1309	3.375	2.996	3.332			
SDSS J104431.36+344021.3	161.13067	34.6726	3.215	2.602	3.173	2.7016	20.75	0.15
SDSS J104437.05+650645.0	161.15444	65.1125	3.648	2.580	3.602			
SDSS J104441.76+053353.2	161.17403	5.5648	2.753	2.390	2.715			
SDSS J104448.78+423509.3	161.20329	42.5859	4.101	3.070	4.050			
SDSS J104451.88+431938.7	161.21619	43.3274	2.393	2.307	2.359			
SDSS J104458.99+343727.1	161.24581	34.6242	2.940	2.307	2.901			
SDSS J104500.37+324653.7	161.25158	32.7816	2.536	2.307	2.500			
SDSS J104501.02+351303.9	161.25430	35.2178	3.314	2.572	3.271			
SDSS J104501.43+504046.0	161.25602	50.6794	4.000	3.206	3.950	3.9492	20.35	0.20
SDSS J104507.48+375025.1	161.28119	37.8403	2.967	2.597	2.927	2.9166	20.70	0.20
SDSS J104514.61+593707.3	161.31089	59.6187	2.470	2.307	2.435			
SDSS J104520.94+124535.5	161.33728	12.7599	2.993	2.585	2.953			
SDSS J104523.43+314231.6	161.34784	31.7088	3.244	2.344	3.201			
SDSS J104524.48+492822.0	161.35203	49.4728	2.895	2.523	2.856			
SDSS J104536.41+304146.1	161.40173	30.6962	3.145	2.507	3.104			
SDSS J104538.43+310323.7	161.41015	31.0566	2.817	2.307	2.778			
SDSS J104539.84+372734.2	161.41603	37.4595	3.280	2.899	3.237			
FBQS J1045+3440	161.42093	34.6787	2.351	2.307	2.318			
SDSS J104541.27+494507.8	161.42199	49.7522	2.873	2.477	2.834			
SDSS J104543.55+654321.3	161.43152	65.7226	2.971	2.651	2.931			
SDSS J104601.37+532753.4	161.50577	53.4648	3.092	2.408	3.051			
SDSS J104605.87+534408.8	161.52455	53.7358	3.695	2.822	3.648			
SDSS J104612.99+584719.0	161.55406	58.7887	3.037	2.623	2.996			
SDSS J104619.33+610900.0	161.58061	61.1500	3.296	2.576	3.253			
SDSS J104619.38+314716.7	161.58079	31.7880	2.418	2.307	2.384			
SDSS J104623.29+363024.2	161.59705	36.5067	3.250	2.549	3.207			
SDSS J104628.45+545540.2	161.61857	54.9279	3.426	2.565	3.381	2.8820	20.30	0.15
SDSS J104635.24+095539.5	161.64686	9.9277	4.358	3.168	4.304			
SDSS J104639.42+584047.8	161.66428	58.6800	3.180	2.307	3.138			
SDSS J104642.83+053107.0	161.67850	5.5186	2.699	2.333	2.616			
SDSS J104705.45+514406.7	161.77275	51.7352	2.932	2.309	2.893			
SDSS J104707.35+464910.4	161.78069	46.8195	2.808	2.307	2.770			
SDSS J104713.38+095711.3	161.80580	9.9532	2.680	2.307	2.643			
SDSS J104734.98+010157.0	161.89577	1.0325	3.724	2.911	3.677	3.2219	20.70	0.15
SDSS J104743.08+434404.8	161.92953	43.7347	3.285	2.356	3.243			
SDSS J104801.31+072952.8	162.00549	7.4980	4.080	3.563	4.029			
SDSS J104809.18+570241.9	162.03832	57.0450	3.242	2.377	3.200			
SDSS J104810.31+315554.1	162.04298	31.9317	3.740	2.830	3.693			

Continued on Next Page...

Table I.1 – Continued

Name	RA	Dec	z_{em}	z_{min}	z_{max}	z_{abs}	$\log N(\mathrm{H\,I})$	$\epsilon[\log N(\mathrm{H\,I})]$
SDSS J104810.80+575526.8	162.04504	57.9241	3.171	2.802	3.129			
SDSS J104814.84+545600.2	162.06185	54.9334	2.668	2.307	2.585			
SDSS J104815.59+033443.4	162.06497	3.5787	3.126	2.704	3.085			
SDSS J104822.61+474238.2	162.09426	47.7106	3.422	2.506	3.378			
SDSS J104826.03+391110.4	162.10848	39.1862	2.795	2.406	2.757			
SDSS J104837.40-002813.6	162.15584	-0.4705	4.007	2.924	3.957	3.8880	20.65	0.20
SDSS J104838.23+343645.4	162.15931	34.6126	3.240	2.875	3.158			
SDSS J104845.21+133152.2	162.18840	13.5312	3.104	2.307	3.063	2.9199	20.55	0.15
SDSS J104847.81+525925.0	162.19924	52.9903	3.325	2.510	3.282			
SDSS J104849.05+443915.7	162.20441	44.6544	3.908	3.086	3.859			
SDSS J104852.50+465610.5	162.21876	46.9363	2.766	2.381	2.729			
SDSS J104859.57+624940.0	162.24825	62.8278	2.751	2.368	2.714			
SDSS J104904.47+495511.6	162.26865	49.9199	2.500	2.414	2.465			
SDSS J104909.82+373759.0	162.29095	37.6330	2.987	2.307	2.947	2.5064	21.10	0.15
SDSS J104910.56+055756.5	162.29403	5.9657	2.895	2.307	2.856			
SDSS J104910.60+624428.4	162.29418	62.7412	2.759	2.378	2.721			
SDSS J104911.19+120748.1	162.29667	12.1301	3.158	2.526	3.117			
SDSS J104932.93+464152.8	162.38721	46.6980	3.644	3.297	3.597			
SDSS J104941.09+133255.6	162.42124	13.5488	2.764	2.379	2.727			
SDSS J105002.03+522243.9	162.50847	52.3789	2.978	2.307	2.939			
SDSS J105020.40+262002.3	162.58505	26.3340	4.892	3.971	4.794			
SDSS J105036.46+580424.6	162.65196	58.0735	5.151	4.190	5.048			
SDSS J105043.24+435834.9	162.68020	43.9764	2.911	2.307	2.872			
SDSS J105044.27+060958.3	162.68448	6.1662	3.267	2.867	3.224			
SDSS J105049.27+441144.7	162.70534	44.1958	4.271	3.284	4.218			
SDSS J105049.37+354520.5	162.70574	35.7557	3.315	2.356	3.272			
SDSS J105058.28+614406.0	162.74284	61.7350	2.797	2.420	2.714			
SDSS J105106.66+521111.6	162.77776	52.1866	2.690	2.312	2.653			
SDSS J105108.29+335030.4	162.78455	33.8418	3.537	2.584	3.492			
SDSS J105108.75+140744.3	162.78649	14.1290	3.320	2.893	3.238			
SDSS J105121.36+612038.0	162.83902	61.3439	3.689	2.596	3.642			
SDSS J105123.03+354534.3	162.84599	35.7595	4.899	3.928	4.840	4.3454	20.55	0.20
						4.8208	20.40	0.20
SDSS J105128.75+344546.3	162.86983	34.7629	3.226	2.572	3.184			
SDSS J105133.59+295119.3	162.89000	29.8554	3.822	3.401	3.773			
SDSS J105135.24+532348.4	162.89684	53.3968	3.444	3.085	3.400	3.3439	20.90	0.20
SDSS J105146.05+592213.9	162.94189	59.3705	2.925	2.536	2.842			
SDSS J105150.61+405943.3	162.96088	40.9954	3.053	2.665	3.012			
SDSS J105200.42+140846.9	163.00177	14.1464	3.203	2.387	3.161			
SDSS J105202.52+413153.1	163.01051	41.5314	2.509	2.307	2.474			
SDSS J105213.95+021920.5	163.05815	2.3224	2.580	2.307	2.544			
SDSS J105232.30+075935.1	163.13463	7.9931	2.894	2.307	2.855			
SDSS J105236.08+504306.6	163.15037	50.7185	3.782	3.365	3.734			
SDSS J105237.75+342447.1	163.15730	34.4131	3.587	3.209	3.541			
SDSS J105238.60+470156.9	163.16087	47.0325	3.408	3.240	3.364	3.2774	20.35	0.15
SDSS J105242.50+651231.4	163.17713	65.2087	3.016	2.307	2.976			
SDSS J105245.47+391547.3	163.18950	39.2632	3.932	2.889	3.883			
SDSS J105250.10+063249.5	163.20880	6.5471	3.482	2.765	3.437			
SDSS J105254.59-000625.7	163.22750	-0.1072	4.162	3.174	4.110			
SDSS J105258.08+112759.2	163.24204	11.4665	3.164	2.482	3.123			
SDSS J105302.81+433112.0	163.26174	43.5200	3.248	2.389	3.206			
SDSS J105310.61+045624.5	163.29423	4.9402	2.539	2.307	2.504			
SDSS J105311.39+123516.6	163.29750	12.5880	2.926	2.307	2.887			
SDSS J105311.53+294808.2	163.29807	29.8023	3.795	2.585	3.747			
SDSS J105315.89+400756.4	163.31624	40.1324	2.482	2.307	2.447			
SDSS J105320.40+063747.9	163.33502	6.6300	3.310	2.654	3.267			
SDSS J105320.42-001649.5	163.33511	-0.2805	4.303	3.208	4.250			
SDSS J105322.98+580412.1	163.34578	58.0700	5.250	4.273	5.146			
SDSS J105329.73+524758.3	163.37388	52.7996	2.535	2.307	2.500			
SDSS J105336.02+000735.6	163.40014	0.1266	2.600	2.307	2.564			
SDSS J105336.27+353251.7	163.40116	35.5477	3.299	2.597	3.256			
SDSS J105340.75+010335.6	163.41982	1.0599	3.663	1.937	3.617			
SDSS J105357.47+143236.6	163.48947	14.5435	3.052	2.637	3.012			
SDSS J105358.66+500421.4	163.49447	50.0726	3.425	2.712	3.380			
SDSS J105400.53+461841.2	163.50221	46.3115	2.437	2.307	2.403			
SBS 1051+528	163.56496	52.6315	2.382	2.307	2.348			
SDSS J105423.31+130803.0	163.59716	13.1342	3.453	2.492	3.409			
SDSS J105428.89+521747.6	163.62041	52.2966	3.120	2.412	3.079	2.4555	20.55	0.15
SDSS J105434.17+021551.9	163.64239	2.2644	3.971	2.603	3.922			
SDSS J105440.86+651133.0	163.67036	65.1925	3.801	2.704	3.753			
SDSS J105441.62+610726.5	163.67347	61.1240	2.588	2.307	2.552			
SDSS J105445.43+163337.4	163.68931	16.5604	5.154	4.192	5.051			

Continued on Next Page...

Table I.1 – Continued

Name	RA	Dec	z_{em}	z_{min}	z_{max}	z_{abs}	log N(H I)	ϵ[log N(H I)]
SDSS J105505.30+415848.6	163.77210	41.9802	2.666	2.307	2.629			
SDSS J105511.70-002022.7	163.79880	-0.3397	3.622	2.594	3.576			
SDSS J105516.62+145416.9	163.81929	14.9047	2.836	2.307	2.797			
SDSS J105516.85+531829.8	163.82025	53.3083	3.282	2.378	3.239			
SDSS J105524.56+580957.3	163.85235	58.1659	2.416	2.307	2.382			
SDSS J105533.27+353215.6	163.88863	35.5377	2.681	2.307	2.644			
SDSS J105537.00+400905.3	163.90421	40.1515	2.435	2.307	2.401			
SDSS J105551.81+343031.6	163.96588	34.5088	3.685	3.008	3.638			
SDSS J105602.36+003222.0	164.00991	0.5395	4.036	3.034	3.986			
SDSS J105622.94+384440.2	164.09561	38.7445	3.384	2.436	3.340			
SDSS J105623.88+125414.3	164.09953	12.9040	3.667	2.924	3.621			
SDSS J105629.61+494340.6	164.12341	49.7280	3.801	3.448	3.753			
SDSS J105635.52+405236.1	164.14804	40.8767	3.452	2.602	3.407			
SDSS J105640.29+075629.0	164.16790	7.9414	3.620	3.205	3.574	3.4605	20.35	0.20
SDSS J105642.55+380548.7	164.17733	38.0969	3.024	2.613	2.984			
SDSS J105651.30+413809.5	164.21377	41.6360	2.678	2.549	2.641			
SDSS J105701.33+021933.4	164.25558	2.3260	2.950	2.653	2.910			
SDSS J105705.37+191042.8	164.27240	19.1786	4.128	2.661	4.077	3.3735	20.30	0.10
SDSS J105706.98+452059.1	164.27912	45.3498	3.486	2.751	3.441			
SDSS J105709.91+381859.5	164.29133	38.3165	2.960	2.314	2.920			
SDSS J105714.82+440323.8	164.31176	44.0566	3.280	2.371	3.237			
SDSS J105726.62+032448.0	164.36093	3.4134	2.832	2.440	2.794			
SDSS J105730.50+120411.3	164.37712	12.0698	3.054	2.658	3.014			
SDSS J105731.19+552845.0	164.38002	55.4792	3.206	2.817	3.164			
SDSS J105744.45+062914.3	164.43523	6.4873	3.143	2.307	3.101	2.5000	20.50	0.15
SDSS J105747.55+395146.1	164.44817	39.8628	2.452	2.307	2.418			
2MASSi J1057562+455553	164.48452	45.9314	4.126	2.776	4.075			
SDSS J105757.49+363302.1	164.48960	36.5506	2.812	2.422	2.774			
SDSS J105802.88+075930.1	164.51202	7.9917	2.563	2.307	2.528			
SDSS J105806.16+600826.8	164.52571	60.1408	2.936	2.315	2.897			
SDSS J105808.47+003930.5	164.53532	0.6585	2.815	2.307	2.777			
SDSS J105810.05+551205.5	164.54192	55.2016	3.302	3.186	3.259			
SDSS J105813.57+462836.3	164.55661	46.4768	3.209	2.778	3.167			
SDSS J105830.03+333859.3	164.62513	33.6498	3.833	2.882	3.785	3.2923	20.85	0.15
SDSS J105831.18+303733.2	164.62994	30.6259	3.223	2.520	3.181			
SDSS J105833.80+443153.1	164.64087	44.5314	4.063	3.221	4.012			
SDSS J105834.49+585438.9	164.64375	58.9108	3.175	2.806	3.133			
SDSS J105841.03+385731.2	164.67098	38.9587	2.833	2.441	2.795			
SDSS J105848.97+445456.1	164.70408	44.9156	2.368	2.307	2.334			
SDSS J105856.88+374557.0	164.73705	37.7659	2.977	2.329	2.937			
SDSS J105857.08+110128.6	164.73788	11.0246	4.338	3.315	4.285			
SDSS J105858.38+124554.9	164.74326	12.7653	4.341	2.570	4.288	3.4315	20.60	0.10
SDSS J105904.58+454822.9	164.76912	45.8064	4.896	4.513	4.837			
SDSS J105904.68+121024.0	164.76954	12.1733	2.502	2.307	2.467			
SDSS J105911.88+410151.2	164.79950	41.0309	3.206	2.532	3.164			
SDSS J105916.79+073837.1	164.82001	7.6437	2.884	2.307	2.845			
SDSS J105921.31+080207.6	164.83882	8.0355	3.139	2.420	3.097			
SDSS J105922.31+663806.1	164.84296	66.6351	3.075	2.387	3.035			
SDSS J105926.40+130643.9	164.86004	13.1122	4.109	3.275	4.058			
SDSS J105941.47+385353.0	164.92282	38.8981	3.526	3.102	3.481	3.3380	20.70	0.20
SDSS J105949.30+121225.1	164.95546	12.2070	2.870	2.474	2.831			
SDSS J105952.59+375616.7	164.96911	37.9380	2.637	2.327	2.601			
SDSS J110000.82+434454.8	165.00345	43.7486	3.445	2.770	3.401			
SDSS J110000.93+454749.7	165.00389	45.7972	3.072	2.346	3.031			
SDSS J110001.49+301215.1	165.00623	30.2042	3.350	2.734	3.307			
SDSS J110016.31+054210.1	165.06797	5.7028	2.982	2.319	2.942			
SDSS J110025.36+592316.2	165.10571	59.3879	3.350	3.209	3.306			
SDSS J110027.79+354221.5	165.11582	35.7060	2.479	2.347	2.445			
SDSS J110032.94+530819.5	165.13728	53.1388	2.372	2.307	2.338			
SDSS J110045.23+112239.1	165.18848	11.3775	4.728	3.833	4.632	4.3950	21.60	0.20
SDSS J110058.35+301931.8	165.24318	30.3255	2.537	2.307	2.502			
SDSS J110104.63+141849.3	165.26932	14.3137	3.214	2.384	3.172			
SDSS J110105.42-000155.3	165.27261	-0.0321	2.467	2.307	2.433			
SDSS J110114.88+432332.1	165.31202	43.3923	3.056	2.307	3.015			
SDSS J110122.50+144716.6	165.34377	14.7880	3.225	2.806	3.183			
SDSS J110134.36+053133.8	165.39317	5.5261	5.045	4.100	4.944	4.3470	21.40	0.20
SDSS J110138.04+383335.3	165.40863	38.5598	2.933	2.530	2.893			
SDSS J1101+1053	165.48225	10.8840	3.031	2.347	2.991			
SDSS J110156.74+304001.5	165.48647	30.6671	3.245	2.307	3.203			
SDSS J110206.66+112104.9	165.52779	11.3514	2.351	2.307	2.318			
SDSS J110217.80+070939.6	165.57421	7.1610	3.372	2.633	3.328			
SDSS J110227.22+312157.4	165.61346	31.3660	2.383	2.307	2.349			

Continued on Next Page...

Table I.1 – Continued

Name	RA	Dec	z_{em}	z_{min}	z_{max}	z_{abs}	$\log N(\mathrm{H\,I})$	$\epsilon[\log N(\mathrm{H\,I})]$
SDSS J110228.21+483721.3	165.61760	48.6226	3.167	2.517	3.125			
SDSS J110236.79+460101.2	165.65329	46.0170	3.846	2.682	3.797			
SDSS J110243.40-002320.7	165.68087	-0.3891	2.494	2.456	2.459			
SDSS J110246.16+085201.6	165.69237	8.8671	2.632	2.307	2.596			
SDSS J110250.04+605625.7	165.70852	60.9405	2.363	2.307	2.330			
SDSS J110255.31+555229.0	165.73050	55.8748	3.739	2.947	3.692			
SDSS J110307.96+340959.0	165.78320	34.1664	2.419	2.307	2.385			
SDSS J110323.57+405004.2	165.84823	40.8345	2.982	2.307	2.942			
SDSS J110340.93+131741.5	165.92055	13.2949	3.387	2.476	3.343			
SDSS J110344.53+023209.9	165.93558	2.5361	2.514	2.307	2.479			
SDSS J110347.56+654548.6	165.94825	65.7635	2.689	2.318	2.652			
SDSS J110352.73+100403.1	165.96976	10.0676	3.607	2.200	3.561			
SDSS J110353.34+080348.6	165.97227	8.0635	2.569	2.312	2.533			
SDSS J110401.04+581621.3	166.00440	58.2726	3.874	3.081	3.825			
SDSS J110401.42+132134.6	166.00593	13.3596	2.573	2.307	2.537			
SDSS J110406.82+135506.4	166.02843	13.9185	3.652	2.597	3.606			
SDSS J110411.62+024655.3	166.04845	2.7820	2.533	2.307	2.498			
SDSS J110412.85+115925.2	166.05358	11.9903	2.576	2.307	2.541			
SDSS J110413.44+451642.6	166.05604	45.2785	3.417	3.032	3.373			
SDSS J110426.65+404621.2	166.11105	40.7726	2.560	2.307	2.525			
SDSS J110427.08+054848.3	166.11287	5.8134	3.006	2.307	2.966			
SDSS J110427.87+504952.7	166.11615	50.8313	2.465	2.307	2.430			
SDSS J110434.61-000128.7	166.14424	-0.0247	2.396	2.323	2.362			
SDSS J110441.73+470625.7	166.17391	47.1071	2.984	2.597	2.909			
SDSS J110443.31+434857.4	166.18047	43.8160	2.709	2.604	2.627			
SDSS J110445.38+573643.9	166.18912	57.6122	2.644	2.307	2.607			
SDSS J110453.42+422603.4	166.22262	42.4343	3.249	2.816	3.206			
SDSS J110459.13+604829.3	166.24641	60.8082	3.188	2.390	3.147			
SDSS J110503.72+132910.6	166.26552	13.4863	2.395	2.307	2.361			
SDSS J110518.49+083820.9	166.32708	8.6392	3.066	2.815	3.025			
2MASSi J1105250+354257	166.35443	35.7159	2.346	2.307	2.312			
SDSS J110530.39+495553.3	166.37664	49.9315	3.878	2.941	3.829	3.0090	20.70	0.15
SDSS J110555.07+110359.1	166.47950	11.0664	3.484	2.626	3.440			
SDSS J110556.97+084645.5	166.48742	8.7793	3.243	2.847	3.200			
SDSS J110557.06+361448.4	166.48781	36.2468	2.984	2.355	2.944			
SDSS J110559.50+482847.0	166.49796	48.4798	2.422	2.307	2.388			
SDSS J110603.01+482304.6	166.51260	48.3846	2.372	2.307	2.338			
SDSS J110604.20+344504.2	166.51753	34.7512	2.399	2.307	2.365			
SDSS J110605.97+061202.9	166.52491	6.2008	2.448	2.307	2.414			
SDSS J110612.85+573617.4	166.55354	57.6049	3.055	2.703	3.014			
SDSS J110616.68+135458.5	166.56952	13.9163	3.846	3.413	3.764			
SDSS J110622.99+013055.5	166.59581	1.5154	3.709	2.996	3.662			
SDSS J110623.51-004326.0	166.59799	-0.7239	2.443	2.307	2.360			
SDSS J110638.41+403615.3	166.66009	40.6043	2.967	2.573	2.928			
SDSS J110642.26+145713.2	166.67612	14.9537	2.991	2.307	2.952			
SDSS J110657.17+575122.9	166.73829	57.8564	2.721	2.340	2.683			
SDSS J110657.82+081643.3	166.74096	8.2787	4.270	3.093	4.217	3.2240	20.30	0.20
SDSS J110716.29+061659.5	166.81789	6.2832	2.698	2.320	2.661			
SDSS J110727.40+574203.0	166.86420	57.7009	3.029	2.617	2.989			
SDSS J110741.92+555728.4	166.92468	55.9579	3.352	2.914	3.308			
SDSS J110743.78+113937.5	166.93244	11.6604	3.453	3.013	3.371			
SDSS J110750.42+035340.6	166.96009	3.8946	3.812	3.018	3.764			
SDSS J110752.39+045201.9	166.96831	4.8672	2.406	2.307	2.372			
SDSS J110808.77+623130.4	167.03659	62.5251	2.576	2.353	2.541			
SDSS J110811.29+595640.7	167.04711	59.9446	3.024	2.444	2.984			
SDSS J110813.85-005944.5	167.05774	-0.9957	4.017	2.959	3.967	3.0965	20.95	0.15
SDSS J110814.82+012058.4	167.06178	1.3496	3.282	2.565	3.239			
SDSS J110818.16+095931.4	167.07574	9.9921	3.320	2.504	3.277			
SDSS J110819.15-005823.9	167.07980	-0.9733	4.566	3.586	4.510			
SDSS J110819.93+081140.1	167.08307	8.1945	2.405	2.307	2.371			
SDSS J110830.18+403042.5	167.12579	40.5118	3.143	2.433	3.101			
SDSS J110834.54+411900.9	167.14392	41.3169	2.444	2.307	2.409			
SDSS J110845.19+071135.4	167.18831	7.1932	2.971	2.564	2.931			
SDSS J110849.70+501302.7	167.20713	50.2174	2.791	2.403	2.753			
SDSS J110850.84+110736.3	167.21188	11.1268	2.470	2.307	2.435			
SDSS J110855.47+120953.3	167.23113	12.1648	3.678	2.447	3.632	3.3965	20.70	0.10
						3.5460	20.80	0.15
SDSS J110859.28+031127.9	167.24708	3.1911	3.459	2.709	3.414			
SDSS J110914.19+034450.7	167.30917	3.7474	3.538	3.097	3.456			
SDSS J110926.75+531658.1	167.36151	53.2828	2.957	2.311	2.918			
SDSS J110927.18+554120.5	167.36328	55.6890	3.472	2.597	3.427			
SDSS J110929.81+582945.5	167.37425	58.4960	3.264	2.470	3.222			

Continued on Next Page...

Table I.1 – Continued

Name	RA	Dec	z_{em}	z_{min}	z_{max}	z_{abs}	$\log N(\mathrm{H\,I})$	$\epsilon[\log N(\mathrm{H\,I})]$
SDSS J110935.38+533624.7	167.39744	53.6069	2.590	2.307	2.555			
SDSS J110936.43+343031.0	167.40181	34.5086	3.154	2.765	3.112			
SDSS J110936.93+362558.9	167.40391	36.4331	2.550	2.307	2.515			
SDSS J110938.70+543241.4	167.41128	54.5448	2.430	2.307	2.395			
SDSS J110939.02+481632.0	167.41269	48.2756	2.406	2.346	2.371			
SDSS J110939.20+423556.2	167.41336	42.5989	2.503	2.307	2.468			
SDSS J110939.50+080009.4	167.41461	8.0026	3.340	2.581	3.296			
SDSS J110952.32+554224.9	167.46804	55.7069	3.177	2.786	3.135			
SDSS J110954.12+460642.2	167.47552	46.1118	2.610	2.347	2.574			
SDSS J111005.58+553533.0	167.52332	55.5925	3.546	2.784	3.501			
SDSS J111008.17+094804.5	167.53411	9.8012	3.416	2.964	3.372			
SDSS J111008.61+024458.0	167.53592	2.7495	4.146	2.364	4.095			
SDSS J111020.05+392724.5	167.58359	39.4568	2.423	2.307	2.389			
SDSS J111021.83+142001.8	167.59100	14.3338	4.157	3.676	4.105			
SDSS J111033.39+113259.9	167.63914	11.5500	2.897	2.307	2.858			
SDSS J111033.42+311602.8	167.63929	31.2675	3.821	3.399	3.773			
SDSS J111034.69+480037.1	167.64463	48.0103	3.920	2.913	3.871			
SDSS J111034.84+472352.2	167.64524	47.3979	2.729	2.347	2.692			
SDSS J111038.45+421715.6	167.66026	42.2877	2.571	2.336	2.489			
SDSS J111038.63+483115.6	167.66101	48.5210	2.955	2.307	2.915			
SDSS J111043.29+520331.3	167.68038	52.0587	3.043	2.629	3.003			
SDSS J111046.46+521709.1	167.69360	52.2859	2.493	2.307	2.458			
SDSS J111047.12+312732.4	167.69636	31.4590	4.128	3.604	4.077			
SDSS J111054.81+455056.1	167.72841	45.8489	2.822	2.307	2.784			
SDSS J111055.21+430510.0	167.73008	43.0861	3.821	3.344	3.739			
SDSS J111055.84+381055.1	167.73268	38.1820	2.524	2.367	2.489			
SDSS J111109.65+144238.2	167.79024	14.7106	3.092	2.307	3.051	2.6004	21.35	0.15
BRI 1108-0747	167.80682	-8.0673	3.922	2.620	3.873			
SDSS J111119.10+133603.8	167.82961	13.6011	3.481	2.307	3.436	3.2014	21.20	0.15
SDSS J111125.99+071459.5	167.85834	7.2499	2.891	2.307	2.852	2.6812	20.60	0.15
SDSS J111126.65+350921.4	167.86107	35.1560	4.119	3.029	4.067	4.0523	21.00	0.20
SDSS J111130.77+583438.1	167.87822	58.5773	3.382	2.990	3.339			
SDSS J111137.71+073305.9	167.90717	7.5517	3.466	2.585	3.422			
SDSS J111140.91+421859.2	167.92047	42.3165	3.353	2.701	3.310			
2MASSi J1111516+133236	167.96504	13.5433	2.433	2.307	2.398	2.3828	20.30	0.15
SDSS J111156.04+140049.3	167.98351	14.0137	3.858	2.706	3.809	3.2531	20.50	0.15
SDSS J111204.51+132717.2	168.01881	13.4548	2.919	2.568	2.880			
SDSS J111213.94+572548.0	168.05814	57.4300	2.498	2.307	2.463			
SDSS J111218.34+030224.7	168.07646	3.0402	3.349	2.613	3.305			
SDSS J111224.18+004630.3	168.10077	0.7751	4.039	3.055	3.989	3.7942	20.45	0.15
						3.9581	20.55	0.20
SDSS J111226.04+352551.3	168.10854	35.4310	2.787	2.400	2.749			
SDSS J111227.29+525520.7	168.11378	52.9224	3.188	2.402	3.146			
SDSS J111231.00+032040.8	168.12917	3.3447	3.291	2.322	3.248			
SDSS J111233.48+060618.9	168.13954	6.1053	3.292	2.906	3.249			
SDSS J111237.64+151429.7	168.15687	15.2416	3.147	2.318	3.105			
SDSS J111240.68+113331.0	168.16954	11.5586	2.761	2.375	2.723			
SDSS J111246.30+004957.3	168.19292	0.8326	3.944	2.720	3.895			
SDSS J111252.25+375910.2	168.21772	37.9862	3.977	2.959	3.927	3.8206	21.55	0.20
2MASSi J1112524+152123	168.21856	15.3565	2.786	2.399	2.749			
SDSS J111301.24+650234.1	168.25523	65.0428	2.445	2.346	2.410			
SDSS J111311.99+453314.3	168.29996	45.5540	3.046	2.374	3.006			
SDSS J111316.06+305526.3	168.31697	30.9240	2.378	2.307	2.344			
SDSS J111320.04+121548.8	168.33353	12.2636	3.176	2.307	3.134			
SDSS J111336.10+494034.7	168.40043	49.6763	2.466	2.307	2.431			
SDSS J111337.46+030053.9	168.40612	3.0150	2.490	2.307	2.455			
SDSS J111338.28+122658.9	168.40953	12.4497	3.057	2.642	3.017			
SDSS J111342.81+383244.2	168.42841	38.5456	3.371	2.481	3.328			
SDSS J111401.47-005321.0	168.50614	-0.8892	4.603	3.514	4.547			
SDSS J111404.27+454352.5	168.51786	45.7313	2.443	2.332	2.409			
SDSS J111417.52+554420.9	168.57307	55.7392	2.544	2.307	2.509			
SDSS J111423.42+354939.6	168.59760	35.8277	3.180	2.344	3.139	2.7461	20.90	0.15
SDSS J111434.62+492109.8	168.64427	49.3528	3.209	2.806	3.167			
SDSS J111437.20+651248.2	168.65501	65.2134	2.386	2.307	2.352			
SDSS J111442.16+053432.0	168.67569	5.5756	3.342	2.561	3.299			
SDSS J111448.07+085417.3	168.70030	8.9048	3.618	2.871	3.572			
SDSS J111450.19+452027.7	168.70916	45.3411	3.247	2.397	3.205	3.0456	20.95	0.15
SDSS J111451.11+393756.1	168.71297	39.6323	3.640	3.164	3.594			
SDSS J111454.86+584940.6	168.72860	58.8280	3.565	2.841	3.520			
SDSS J111503.42+624000.1	168.76431	62.6667	2.934	2.551	2.894			
SDSS J111510.64+520333.8	168.79438	52.0594	2.926	2.735	2.887			
SDSS J111511.65+144512.0	168.79856	14.7534	4.288	3.365	4.235			

Continued on Next Page...

Table I.1 – Continued

Name	RA	Dec	z_{em}	z_{min}	z_{max}	z_{abs}	$\log N(\mathrm{H\,I})$	$\epsilon[\log N(\mathrm{H\,I})]$
SDSS J111517.52+522617.7	168.82301	52.4383	2.995	2.410	2.956			
SDSS J111517.97+345330.2	168.82489	34.8917	3.515	2.814	3.469			
SDSS J111518.47+143539.6	168.82697	14.5944	2.720	2.339	2.682			
SDSS J111523.24+082918.4	168.84684	8.4885	4.710	3.818	4.615			
SDSS J111532.67+052054.3	168.88617	5.3484	3.188	3.046	3.146			
SDSS J111547.43+035437.7	168.94767	3.9105	2.835	2.442	2.796	2.7566	20.80	0.15
SDSS J111606.39+135808.0	169.02667	13.9689	3.034	2.356	2.993			
SDSS J111606.54+150324.2	169.02729	15.0567	2.355	2.307	2.321			
SDSS J111610.68+411814.4	169.04451	41.3040	2.980	2.409	2.941			
SDSS J111611.73+411821.5	169.04889	41.3060	2.983	2.307	2.943	2.6619	20.35	0.20
SDSS J111614.40+645335.1	169.06002	64.8931	3.016	2.641	2.976			
SDSS J111619.68+594555.7	169.08206	59.7655	3.582	2.859	3.536			
SDSS J111624.48+653804.2	169.10201	65.6345	2.892	2.473	2.830			
SDSS J111629.76+032407.2	169.12403	3.4020	2.462	2.307	2.428			
SDSS J111638.32+345705.2	169.15971	34.9515	3.204	2.812	3.162			
SDSS J111638.79+613014.6	169.16167	61.5041	2.775	2.388	2.737			
SDSS J111639.39+575935.0	169.16413	57.9931	2.587	2.319	2.551			
SDSS J111641.22+601224.3	169.17180	60.2068	2.626	2.307	2.590			
SDSS J111642.81+420324.9	169.17840	42.0569	2.526	2.307	2.491			
SDSS J111649.95+433727.3	169.20816	43.6243	2.614	2.307	2.578			
SDSS J111651.96+022512.3	169.21653	2.4201	2.565	2.307	2.529			
SDSS J111654.83+553117.8	169.22848	55.5216	3.277	2.585	3.234			
SDSS J111701.89+131115.4	169.25791	13.1876	3.622	2.208	3.576			
SDSS J111702.74+414800.9	169.26145	41.8003	2.899	2.529	2.860			
BRI 1114-0822	169.36273	-8.6494	4.495	3.190	4.440	4.2576	20.30	0.20
SDSS J111728.75+490216.4	169.36983	49.0379	2.451	2.307	2.369			
SDSS J111740.32+101253.7	169.41804	10.2149	3.293	2.532	3.250	2.9736	20.70	0.15
SDSS J111741.26+261039.2	169.42194	26.1776	4.626	3.747	4.532			
SDSS J111812.90+441122.3	169.55380	44.1895	4.017	2.890	3.967	3.0274	20.60	0.15
SDSS J111814.87+595511.3	169.56204	59.9198	2.920	2.325	2.881			
SDSS J111815.28+311953.2	169.56371	31.3315	3.126	2.712	3.084			
SDSS J111820.46+044125.2	169.58527	4.6903	3.451	2.720	3.407	3.1777	20.50	0.20
SDSS J111822.76+020236.3	169.59486	2.0434	3.930	3.205	3.881			
SDSS J111822.84+384839.3	169.59517	38.8109	3.491	2.705	3.447			
SDSS J111832.88+053919.9	169.63702	5.6555	2.396	2.307	2.362			
SDSS J111832.96+441956.9	169.63737	44.3325	3.214	2.520	3.172			
SDSS J111856.15+370255.9	169.73399	37.0489	4.030	2.893	3.980			
SDSS J111858.54+000654.6	169.74396	0.1152	2.436	2.307	2.401			
SBS 1116+603	169.80977	60.0826	2.646	2.307	2.610			
SDSS J111918.78+574737.6	169.82826	57.7938	2.997	2.588	2.957			
SDSS J111919.05+555214.5	169.82940	55.8707	3.352	3.008	3.309			
SDSS J111920.64+345248.1	169.83601	34.8800	4.992	4.056	4.892			
SDSS J111922.36+090656.9	169.84321	9.1158	3.819	3.326	3.771			
SDSS J111928.37+130251.0	169.86825	13.0475	2.401	2.307	2.367			
SDSS J111931.11+604921.8	169.87963	60.8227	2.645	2.307	2.608			
SDSS J111947.07+462229.2	169.94613	46.3748	3.573	3.131	3.528			
SDSS J112003.16+395231.6	170.01319	39.8755	2.729	2.347	2.692			
SDSS J112006.49+135559.1	170.02707	13.9331	4.059	3.558	3.976			
SDSS J112013.27+372843.9	170.05533	37.4789	3.255	2.466	3.212			
SDSS J112030.20+471910.2	170.12585	47.3195	3.629	2.597	3.583	3.2833	21.10	0.15
SDSS J112039.84+352517.3	170.16603	35.4215	3.053	2.327	3.013			
SDSS J112048.73+403549.3	170.20308	40.5970	2.909	2.519	2.869			
SDSS J112053.15+463335.3	170.22153	46.5598	2.497	2.307	2.462			
SDSS J112101.95+402516.5	170.25813	40.4213	3.156	2.730	3.114			
SDSS J112107.99+513005.4	170.28333	51.5015	3.931	2.799	3.882			
SDSS J112115.52+395427.4	170.31468	39.9076	3.244	2.349	3.201	2.7333	21.00	0.20
SDSS J112120.04+354920.7	170.33354	35.8224	3.054	2.362	3.014			
SDSS J112121.63+153201.4	170.34014	15.5337	3.047	2.367	3.006			
SDSS J112152.06+375615.5	170.46692	37.9376	3.554	2.796	3.508	2.9040	20.95	0.20
SDSS J112154.99+035516.5	170.47914	3.9213	3.172	2.774	3.130			
SDSS J112156.80+393251.5	170.48669	39.5477	3.581	2.789	3.535			
SDSS J112202.95+303947.6	170.51233	30.6632	2.435	2.307	2.400			
SDSS J112203.33+143522.0	170.51391	14.5895	3.093	2.412	3.052			
SDSS J112207.75+315618.8	170.53232	31.9386	4.221	3.266	4.169			
SDSS J112226.41+401642.8	170.61009	40.2786	2.944	2.542	2.905			
SDSS J112251.99+153536.1	170.71664	15.5934	3.175	2.779	3.133			
SDSS J112253.50+005329.7	170.72292	0.8916	4.586	3.713	4.493			
SDSS J112302.14+600737.7	170.75893	60.1272	3.158	3.070	3.116			
SDSS J112328.23+592755.1	170.86766	59.4653	3.068	2.869	3.027			
SDSS J112340.17+135415.0	170.91740	13.9042	3.092	2.673	3.051			
SDSS J112358.52+114842.1	170.99386	11.8117	2.506	2.307	2.423			
SDSS J112404.52+040418.1	171.01887	4.0717	3.841	2.863	3.793			

Continued on Next Page...

Table I.1 – Continued

Name	RA	Dec	z_{em}	z_{min}	z_{max}	z_{abs}	$\log N(\mathrm{H\,I})$	$\epsilon[\log N(\mathrm{H\,I})]$
SDSS J112412.79+504405.6	171.05331	50.7349	2.446	2.307	2.411			
SDSS J112413.00+055521.0	171.05420	5.9225	2.442	2.406	2.407			
SDSS J112426.11+311602.5	171.10880	31.2674	2.462	2.307	2.428			
SDSS J112440.81+550233.6	171.17007	55.0427	2.932	2.542	2.850			
SDSS J112446.07+353615.6	171.19199	35.6043	2.820	2.449	2.782			
SDSS J112504.16+584920.1	171.26739	58.8223	2.351	2.307	2.317			
SDSS J112513.25+450346.2	171.30523	45.0629	2.404	2.307	2.370			
SDSS J112529.09+412234.3	171.37124	41.3762	3.252	2.817	3.210			
SDSS J112530.47+575722.7	171.37700	57.9563	3.682	2.708	3.635			
SDSS J112534.93+380149.3	171.39558	38.0304	4.606	3.730	4.513			
SDSS J112534.99+322530.6	171.39583	32.4252	3.405	2.677	3.361			
SDSS J112545.17+021149.8	171.43824	2.1972	3.357	2.400	3.313			
SDSS J112549.95+511332.8	171.45816	51.2258	2.484	2.307	2.449			
SDSS J112553.54+474650.1	171.47317	47.7806	3.882	3.096	3.833			
[HB89] 1123+264	171.47380	26.1722	2.350	1.645	2.317			
SDSS J112554.71+571841.4	171.47798	57.3115	2.969	2.576	2.887	2.6771	20.30	0.20
SDSS J112601.69+022935.8	171.50708	2.4933	2.511	2.307	2.476			
SDSS J112607.54+602946.4	171.53142	60.4962	2.818	2.307	2.779			
SDSS J112617.40-012632.6	171.57254	-1.4424	3.634	2.225	3.588			
SDSS J112620.73+392541.4	171.58638	39.4282	2.762	2.377	2.724			
SDSS J112624.70+112117.8	171.60295	11.3550	3.444	2.700	3.400			
SDSS J112630.22+394758.4	171.62595	39.7996	3.133	2.356	3.091			
SDSS J112634.28-012436.9	171.64286	-1.4103	3.765	2.430	3.718			
SDSS J112646.97+110842.7	171.69572	11.1452	4.231	3.405	4.179	3.8027	20.40	0.20
SDSS J112648.62+055628.1	171.70259	5.9412	3.188	2.528	3.146	3.1462	20.80	0.20
SDSS J112655.14+603655.8	171.72984	60.6155	3.781	2.849	3.733			
SDSS J112706.62+395621.3	171.77761	39.9393	3.094	2.307	3.053			
SDSS J112726.75+320036.2	171.86151	32.0101	2.350	2.307	2.316			
SDSS J112731.57+154856.9	171.88155	15.8158	2.787	2.414	2.749	2.4356	21.15	0.20
SDSS J112733.69+343008.8	171.89041	34.5025	4.068	3.591	4.017			
[HB89] 1124+571	171.91723	56.8374	2.890	1.762	2.851			
SDSS J112743.63+594338.6	171.93184	59.7274	2.415	2.307	2.381			
SDSS J112749.45+051140.5	171.95605	5.1946	3.711	2.833	3.664			
SDSS J112753.57+450011.7	171.97322	45.0033	2.474	2.307	2.439			
SDSS J112813.79+594213.4	172.05749	59.7037	4.332	3.818	4.250			
SDSS J112822.79+110034.0	172.09501	11.0095	2.859	2.529	2.820			
SDSS J112823.64+362612.2	172.09851	36.4368	2.515	2.307	2.480			
SDSS J112825.48+345519.7	172.10620	34.9221	3.070	2.367	3.029			
SDSS J112831.69+321556.7	172.13207	32.2658	3.578	2.800	3.532			
SDSS J112840.90+421629.9	172.17044	42.2750	2.739	2.356	2.701			
SDSS J112846.23+441902.3	172.19266	44.3173	3.488	2.632	3.443			
SDSS J112847.90+342343.8	172.19963	34.3955	3.155	2.794	3.114			
SDSS J112857.84+575909.8	172.24099	57.9861	4.992	4.056	4.892			
FBQS J112857.8+362250	172.24108	36.3806	2.900	2.307	2.861			
SDSS J112906.69+414558.1	172.27790	41.7662	2.965	2.559	2.925			
SDSS J112915.61+135620.0	172.31508	13.9389	3.679	3.226	3.633			
SDSS J112924.66+464119.2	172.35276	46.6887	2.467	2.307	2.432			
SDSS J112930.74+441941.4	172.37811	44.3282	3.073	2.428	3.032			
SDSS J112933.75+615648.4	172.39064	61.9468	3.753	2.913	3.706			
SDSS J112933.93+581529.3	172.39138	58.2582	2.717	2.337	2.680			
SDSS J112933.99+400805.0	172.39164	40.1347	3.177	2.307	3.135			
[HB89] 1127+078	172.39580	7.5243	2.660	1.644	2.621			
SDSS J112938.73+131232.2	172.41140	13.2090	3.607	2.590	3.561			
SDSS J112950.14+320714.1	172.45897	32.1206	2.433	2.307	2.399			
SDSS J112951.01+445717.2	172.46255	44.9548	2.491	2.307	2.456			
SDSS J112953.02+651559.8	172.47095	65.2666	3.091	2.307	3.050			
SDSS J112956.27+360142.9	172.48449	36.0286	2.369	2.307	2.335			
SDSS J112957.82+373244.7	172.49096	37.5458	2.980	2.572	2.940			
SDSS J113000.23+344625.9	172.50096	34.7739	3.607	2.701	3.561			
SDSS J113002.34+115438.3	172.50979	11.9107	3.394	2.442	3.350			
SDSS J113008.19+535419.8	172.53415	53.9055	3.049	2.307	3.009			
SDSS J113037.64+480533.6	172.65685	48.0927	3.059	2.873	3.018			
[HB89] 1128+105	172.65952	10.2469	2.650	2.040	2.610			
SDSS J113107.64+495131.2	172.78185	49.8587	3.934	3.445	3.852			
SDSS J113120.08+383156.2	172.83368	38.5323	4.013	3.127	3.963	3.8735	21.45	0.20
SDSS J113126.70+572416.6	172.86132	57.4046	3.233	2.307	3.191			
SDSS J113130.41+604420.7	172.87672	60.7391	2.907	2.307	2.868			
SDSS J113130.79+345554.0	172.87833	34.9317	2.606	2.307	2.570			
SDSS J113132.65+012745.4	172.88609	1.4626	2.418	2.359	2.383			
SDSS J113141.61+095849.6	172.92343	9.9804	2.486	2.430	2.451			
SDSS J113150.70+533558.7	172.96125	53.5996	2.903	2.582	2.864			
SDSS J113151.94+463851.1	172.96644	46.6475	3.274	2.310	3.231			

Continued on Next Page...

Table I.1 – Continued

Name	RA	Dec	z_{em}	z_{min}	z_{max}	z_{abs}	$\log N(\mathrm{H\,I})$	$\epsilon[\log N(\mathrm{H\,I})]$
SDSS J113232.81+510733.5	173.13674	51.1260	2.532	2.307	2.497			
SDSS J113236.07+154850.2	173.15031	15.8140	2.487	2.307	2.452			
SDSS J113237.10+330541.8	173.15464	33.0950	3.184	2.867	3.142			
SDSS J113243.72+093152.3	173.18222	9.5312	4.024	3.177	3.973	3.8572	21.15	0.20
SDSS J113246.50+120901.6	173.19378	12.1505	5.180	4.214	5.077	5.0150	20.75	0.20
SDSS J113307.63+522835.5	173.28181	52.4765	3.736	3.268	3.654	3.2747	21.05	0.15
SDSS J113308.50+315647.7	173.28544	31.9466	2.609	2.307	2.527			
SDSS J113310.45+053958.7	173.29358	5.6663	3.033	2.350	2.993			
FBQS J113324.7+323449	173.35327	32.5804	2.536	2.307	2.500			
SDSS J113330.17+144758.9	173.37575	14.7997	3.244	2.823	3.161			
SDSS J113330.91+380638.1	173.37881	38.1106	3.631	3.157	3.585			
SDSS J113334.22+130553.1	173.39261	13.0981	3.659	2.397	3.612	2.5974	20.50	0.15
SDSS J113341.26+345921.9	173.42194	34.9894	2.350	2.307	2.316			
SDSS J113348.04-001121.9	173.45017	-0.1895	3.600	3.304	3.517			
SDSS J113354.89+022420.8	173.47873	2.4058	3.987	2.941	3.937	3.9150	20.65	0.15
SDSS J113358.04+432103.2	173.49184	43.3509	2.532	2.307	2.496			
SDSS J113400.06+620451.8	173.50030	62.0811	3.618	2.850	3.572			
SDSS J113402.13-024842.3	173.50890	-2.8118	2.752	2.475	2.715			
SDSS J113403.19+625624.6	173.51334	62.9402	3.207	2.531	3.165			
SDSS J113409.31+442620.9	173.53882	44.4392	2.837	2.307	2.798			
LBQS 1131-0043	173.55381	-0.9965	2.160	1.653	2.128			
SDSS J113413.86+153843.4	173.55777	15.6454	2.528	2.307	2.493			
SDSS J113415.89+040007.9	173.56623	4.0022	2.987	2.416	2.948			
SDSS J113418.96+574204.6	173.57902	57.7013	3.522	2.467	3.476			
SDSS J113429.26+405327.3	173.62208	40.8911	3.002	2.347	2.962			
SDSS J113430.42+635505.4	173.62684	63.9182	3.035	2.390	2.994			
SDSS J113432.77+312326.8	173.63658	31.3908	2.486	2.307	2.451	2.4497	20.80	0.15
SDSS J113434.30+564610.7	173.64296	56.7696	2.367	2.307	2.333			
SDSS J113441.76+553317.3	173.67404	55.5548	2.932	2.529	2.892			
SDSS J113444.21+340933.8	173.68424	34.1594	3.142	2.307	3.100	2.6278	20.30	0.15
SDSS J113511.20+592445.7	173.79669	59.4127	3.381	2.515	3.337			
LBQS 1132-0054	173.81236	-1.1870	2.760	1.717	2.718			
SDSS J113525.49+484644.5	173.85624	48.7790	3.167	2.470	3.125			
SDSS J113529.76+515039.6	173.87404	51.8444	2.369	2.307	2.335			
SDSS J113536.40+084218.9	173.90168	8.7053	3.834	1.780	3.786			
SDSS J113537.99+650646.8	173.90829	65.1130	2.444	2.309	2.410			
SDSS J113548.67+513558.8	173.95282	51.5997	3.126	2.814	3.085			
SDSS J113550.37-024527.3	173.95991	-2.7576	3.641	3.194	3.595			
2MASSi J1135506+460705	173.96120	46.1181	2.498	2.307	2.463			
SDSS J113555.72+390050.2	173.98218	39.0140	2.350	2.307	2.316			
SDSS J113559.41+422004.4	173.99756	42.3346	2.973	2.307	2.933			
SDSS J113559.93+002422.7	173.99978	0.4063	4.057	3.117	4.006	3.6845	20.50	0.25
SDSS J113600.10+422553.9	174.00043	42.4316	4.169	3.730	4.117			
SDSS J113621.04+005021.2	174.08772	0.8392	3.428	2.338	3.384			
SDSS J113627.36+634652.2	174.11404	63.7812	2.473	2.307	2.439			
SDSS J113627.81+541504.4	174.11592	54.2512	3.236	2.457	3.194			
SDSS J113634.73+022050.0	174.14472	2.3472	2.639	2.307	2.602			
UM 438	174.14535	-0.9586	2.509	2.307	2.474			
SDSS J113657.23+433402.9	174.23850	43.5675	3.673	2.793	3.627	3.2246	20.35	0.20
SDSS J113703.19+104312.1	174.26330	10.7200	4.530	4.132	4.475			
SDSS J113708.49+344452.1	174.28540	34.7478	3.889	2.961	3.840			
SDSS J1137+6237	174.34051	62.6187	3.783	2.667	3.735			
SDSS J113722.84+544155.2	174.34518	54.6987	2.752	2.368	2.714			
SDSS J113725.31+443506.0	174.35550	44.5850	3.186	2.402	3.144	2.9735	21.20	0.20
SDSS J113729.42+375224.2	174.37262	37.8734	4.172	3.375	4.120			
SDSS J113738.74+501142.6	174.41144	50.1952	3.978	2.878	3.928			
SDSS J113747.64+391941.5	174.44852	39.3282	2.395	2.307	2.361			
SDSS J113757.98+320241.4	174.49162	32.0448	2.607	2.307	2.571			
LBQS 1135-0255	174.50157	-3.1966	2.402	2.307	2.368			
SDSS J113805.24+130332.6	174.52184	13.0591	3.855	3.041	3.806			
SDSS J113806.05+594058.1	174.52524	59.6828	3.209	2.620	3.166			
SDSS J113814.97+352124.8	174.56240	35.3569	2.455	2.307	2.421			
SDSS J113823.94+154058.0	174.59977	15.6828	3.075	2.307	3.034			
SDSS J113833.60+514832.0	174.64003	51.8089	3.076	2.751	2.994			
SDSS J113836.41+085221.0	174.65174	8.8725	3.200	2.409	3.158			
SDSS J113838.26-020607.2	174.65947	-2.1020	3.343	2.430	3.300			
SDSS J113838.54+525418.2	174.66063	52.9051	2.750	2.366	2.712			
SDSS J113838.64+314540.7	174.66102	31.7613	3.227	2.809	3.145	3.0925	20.45	0.15
SDSS J113844.68+652746.3	174.68617	65.4629	2.960	2.618	2.920			
SDSS J113846.58+135129.1	174.69410	13.8581	4.327	3.832	4.274			
SDSS J113854.76+374901.0	174.72821	37.8169	3.470	3.013	3.426			
SDSS J113900.78+551135.7	174.75326	55.1933	2.425	2.307	2.391			

Continued on Next Page...

Table I.1 – Continued

Name	RA	Dec	z_{em}	z_{min}	z_{max}	z_{abs}	$\log N(\mathrm{H\,I})$	$\epsilon[\log N(\mathrm{H\,I})]$
SDSS J113902.13+152606.3	174.75892	15.4351	3.542	3.092	3.459			
SDSS J113903.04+484423.7	174.76270	48.7399	3.002	2.593	2.962			
SDSS J113903.11+335502.7	174.76300	33.9174	3.935	2.752	3.886			
[HB89] 1136+122	174.83004	11.9686	2.900	1.781	2.862			
SDSS J113924.91-023754.7	174.85385	-2.6319	3.193	2.473	3.151			
SDSS J113931.15+313621.1	174.87981	31.6059	3.926	3.438	3.844			
SDSS J113934.96+053827.0	174.89567	5.6409	2.397	2.307	2.363			
SDSS J113946.43+433945.3	174.94346	43.6626	3.282	2.511	3.239			
SDSS J113956.79+144703.6	174.98665	14.7844	3.922	3.435	3.839			
SDSS J114002.40+401914.2	175.01004	40.3206	2.360	2.307	2.326			
SDSS J114004.79+124254.1	175.01998	12.7150	2.482	2.307	2.447			
SDSS J114008.67+620530.0	175.03615	62.0917	4.509	3.113	4.454			
SDSS J114012.93+314512.1	175.05389	31.7534	3.600	3.203	3.554			
SDSS J114013.07+515944.9	175.05448	51.9958	2.902	2.507	2.863			
SDSS J114015.20+150430.7	175.06337	15.0752	3.309	2.446	3.266			
SDSS J114015.98+155928.9	175.06659	15.9914	4.039	2.930	3.989			
SDSS J114023.06+372815.1	175.09605	37.4709	2.580	2.307	2.544			
SDSS J114026.37+451042.4	175.10990	45.1785	2.790	2.403	2.753	2.5082	20.80	0.15
SDSS J114027.13+133231.2	175.11307	13.5420	3.092	2.673	3.051			
LBQS 1138-0107	175.17620	-1.4022	2.760	1.953	2.718			
SDSS J114044.41+054608.3	175.18504	5.7690	3.020	2.375	2.980	2.8851	20.35	0.15
SDSS J114053.97+484331.9	175.22492	48.7255	3.363	2.329	3.320			
SDSS J114112.29+004759.0	175.30121	0.7997	2.893	2.307	2.854			
SDSS J114121.49+123434.8	175.33958	12.5763	2.889	2.802	2.850			
SDSS J114202.29+312944.7	175.50958	31.4958	3.757	2.568	3.710			
SDSS J114203.12+090400.3	175.51305	9.0668	3.673	3.293	3.627			
SDSS J114206.80+561356.0	175.52835	56.2322	3.375	2.644	3.331			
SDSS J114207.40+644524.2	175.53084	64.7567	3.145	2.352	3.103			
SDSS J114209.26+115232.6	175.53861	11.8757	3.849	3.047	3.801			
LBQS 1139-0139	175.54118	-1.9403	1.930	1.634	1.884			
LBQS 1139-0037	175.54828	-0.8956	1.910	1.634	1.881			
SDSS J114218.85+572824.4	175.57856	57.4735	2.891	2.307	2.852			
SDSS J114220.26-001216.3	175.58442	-0.2045	2.486	2.307	2.451			
SDSS J114225.30+110217.3	175.60547	11.0382	4.596	3.722	4.503			
SDSS J114228.65+154420.2	175.61941	15.7390	2.574	2.307	2.539			
SDSS J114242.61+494050.9	175.67758	49.6808	2.645	2.307	2.608			
SDSS J114251.51+572937.6	175.71467	57.4938	2.342	2.307	2.308			
SDSS J114302.24+144838.6	175.75937	14.8107	2.368	2.307	2.335			
SDSS J114307.21+475101.7	175.78008	47.8505	2.589	2.307	2.553			
2MASSi J1143089+345223	175.78702	34.8729	3.147	2.307	3.106			
SDSS J114311.60+651513.4	175.79836	65.2537	2.393	2.307	2.359			
SDSS J114316.98+132400.8	175.82077	13.4002	2.514	2.307	2.479			
SDSS J114317.13+142431.0	175.82140	14.4086	3.774	2.802	3.726			
SDSS J114319.98+043951.4	175.83327	4.6643	2.522	2.307	2.487			
SDSS J114323.44+132542.0	175.84768	13.4284	2.515	2.307	2.480			
SDSS J114332.19+110521.3	175.88414	11.0893	3.033	2.417	2.993	2.8751	20.45	0.15
SDSS J114346.19+642350.2	175.94247	64.3973	3.203	2.610	3.161			
SDSS J114350.30+362911.3	175.95962	36.4865	2.346	2.307	2.313			
SDSS J114354.81+541623.1	175.97841	54.2731	2.871	2.489	2.789			
SDSS J114355.07+492230.8	175.97946	49.3753	3.315	2.909	3.272			
SDSS J114356.35+093438.4	175.98484	9.5773	2.346	2.307	2.312			
SDSS J114358.52+052444.9	175.99385	5.4125	2.561	2.307	2.525			
SDSS J114400.45+125832.5	176.00192	12.9757	3.869	2.728	3.821			
SDSS J114406.43+563041.3	176.02683	56.5115	3.273	2.588	3.230	2.9984	20.90	0.20
SDSS J114408.22+490134.0	176.03428	49.0262	3.600	3.204	3.554			
SDSS J114412.76+315800.8	176.05323	31.9669	3.235	2.337	3.193			
SDSS J114423.36+362531.5	176.09736	36.4254	2.834	2.444	2.796			
SDSS J114426.64+501403.5	176.11102	50.2343	2.889	2.504	2.806	2.6695	21.25	0.15
[HB89] 1142+102	176.15272	9.9847	3.150	2.346	3.109			
LBQS 1142+0138	176.16795	1.3622	2.428	2.307	2.394			
SDSS J114504.93+624624.2	176.27065	62.7734	2.523	2.307	2.487			
SDSS J114508.83+441657.8	176.28681	44.2827	3.017	2.307	2.977			
SDSS J114514.05+520154.0	176.30856	52.0317	3.566	3.113	3.520	3.3447	20.35	0.15
SDSS J114514.18+394715.9	176.30911	39.7878	4.061	2.787	4.010			
SDSS J114517.64-022202.3	176.32351	-2.3673	3.096	2.307	3.055			
SDSS J114527.32+360232.8	176.36388	36.0425	2.601	2.307	2.565			
SDSS J114527.88+545151.3	176.36621	54.8643	3.082	2.356	3.041			
SDSS J114529.04+365712.6	176.37105	36.9535	3.049	2.885	3.009			
SDSS J114534.27+493559.0	176.39280	49.5997	2.984	2.307	2.944			
[HB89] 1143+099	176.39395	9.7056	2.600	1.676	2.567			
SDSS J114548.38+393746.6	176.45160	39.6296	3.105	2.698	3.022			
LBQS 1143+0142	176.46529	1.4352	2.280	1.634	2.248			

Continued on Next Page...

Table I.1 – Continued

Name	RA	Dec	z_{em}	z_{min}	z_{max}	z_{abs}	$\log N(\mathrm{H\,I})$	$\epsilon[\log N(\mathrm{H\,I})]$
SDSS J114623.61+145523.6	176.59838	14.9232	2.556	2.307	2.520			
SDSS J114624.22+420914.3	176.60092	42.1540	3.730	2.812	3.683	3.6729	20.65	0.15
SDSS J114632.58+512422.0	176.63579	51.4061	3.197	2.506	3.155	2.8827	20.80	0.20
[HB89] 1144+115	176.64424	11.2722	2.510	1.682	2.471			
SDSS J114644.02+053812.3	176.68346	5.6368	2.358	2.307	2.325			
SDSS J114646.72+015603.8	176.69468	1.9344	2.651	2.307	2.614			
SDSS J114653.63+442706.7	176.72347	44.4519	2.700	2.321	2.663			
SDSS J114657.79+403708.6	176.74084	40.6191	4.996	4.059	4.896			
SDSS J114658.57+111618.9	176.74408	11.2719	2.512	2.345	2.477			
LBQS 1144+0140	176.74984	1.3979	2.593	2.307	2.558			
SDSS J114704.00+130403.3	176.76670	13.0676	2.360	2.307	2.326			
SDSS J114709.25+132118.3	176.78859	13.3551	3.359	2.344	3.316			
SDSS J114710.35+441232.3	176.79313	44.2090	2.810	2.420	2.772			
SDSS J114713.01+362702.4	176.80424	36.4507	3.794	2.637	3.746			
SDSS J114743.24-015527.5	176.93019	-1.9243	3.148	2.358	3.106			
LBQS 1145-0039	176.93989	-0.9359	1.940	1.634	1.912			
LBQS 1145+0121	176.96945	1.0752	2.080	1.721	2.045			
SDSS J114801.57+144443.5	177.00658	14.7454	3.238	2.514	3.196			
SDSS J114816.19+374355.3	177.06748	37.7321	3.246	2.524	3.203			
SDSS J114826.16+302019.3	177.10902	30.3387	5.128	4.170	5.026			
SDSS J114830.99+610608.4	177.12916	61.1024	3.147	2.307	3.106			
SDSS J114840.87+471623.0	177.17031	47.2731	3.001	2.327	2.961			
LBQS 1146+0207	177.25144	1.8547	2.060	1.634	2.025			
SDSS J114900.89+112025.6	177.25375	11.3405	3.623	2.662	3.577			
SDSS J114904.15+673920.3	177.26732	67.6557	3.023	2.341	2.983			
SDSS J114908.23+501424.9	177.28433	50.2403	3.033	2.657	2.951			
SDSS J114914.88+281308.7	177.31203	28.2191	4.556	3.688	4.463			
SDSS J114925.40+362228.6	177.35586	36.3746	3.608	2.599	3.562			
SDSS J114930.83+325714.0	177.37849	32.9539	3.007	2.307	2.967			
[HB89] 1147+084	177.39271	8.1386	2.610	1.854	2.577			
SDSS J114946.92+565048.0	177.44551	56.8467	3.468	3.200	3.423			
SDSS J114950.07-032816.7	177.45864	-3.4713	3.221	2.828	3.179			
SDSS J115002.38+394041.5	177.50993	39.6782	3.134	2.711	3.093	2.8375	20.50	0.20
						2.9014	20.40	0.20
						3.0853	20.80	0.20
B3 1147+438	177.56918	43.5350	3.020	2.035	2.980			
SDSS J115021.93+500615.2	177.59138	50.1043	2.823	2.307	2.785			
SDSS J115023.00+160437.6	177.59586	16.0771	2.968	2.562	2.928			
SDSS J115041.97+583549.1	177.67491	58.5970	2.587	2.321	2.354			
LBQS 1148-0007	177.68279	-0.3984	1.977	1.634	1.947			
SDSS J115044.42+681322.0	177.68513	68.2228	2.791	2.472	2.753			
SDSS J115045.61+424001.1	177.69005	42.6670	3.894	3.067	3.845			
SDSS J115046.97+133257.6	177.69574	13.5494	3.259	2.504	3.217			
SDSS J115052.64+135835.3	177.71935	13.9765	2.708	2.328	2.671			
SDSS J115102.80+525501.3	177.76170	52.9171	3.002	2.387	2.962			
SDSS J115105.43+103941.1	177.77267	10.6614	3.902	2.815	3.853			
LBQS 1148+0055	177.81411	0.6409	1.890	1.667	1.858			
SDSS J115122.14+020426.3	177.84226	2.0740	2.401	2.307	2.319			
SDSS J115130.48+353624.9	177.87703	35.6069	3.582	2.503	3.536	2.5768	20.65	0.20
						2.5985	20.90	0.15
SDSS J115145.26+151651.8	177.93861	15.2811	2.997	2.307	2.957			
SDSS J115153.86+150944.9	177.97446	15.1625	3.078	2.388	3.037			
SDSS J115158.34+055244.3	177.99311	5.8790	3.240	2.343	3.198	2.9287	20.70	0.15
SDSS J115200.54+451741.4	178.00227	45.2948	2.379	2.307	2.345			
SDSS J115236.67+363009.6	178.15280	36.5027	3.257	2.316	3.214			
SDSS J115247.46+373700.4	178.19779	37.6168	3.074	2.307	3.033	2.4299	20.65	0.15
SDSS J115249.17+094646.3	178.20489	9.7795	3.967	2.926	3.917	3.6300	21.30	0.25
SDSS J115250.29+493220.4	178.20957	49.5390	2.362	2.307	2.328			
SDSS J115254.79+002010.5	178.22832	0.3363	2.359	2.307	2.325			
SDSS J115254.96+150707.7	178.22904	15.1188	3.329	2.436	3.286			
SDSS J115255.49+122112.9	178.23125	12.3536	3.407	2.958	3.363			
SDSS J115257.53+530234.3	178.23972	53.0429	3.525	3.078	3.443			
SDSS J115258.19+144922.3	178.24248	14.8229	2.540	2.307	2.505			
SDSS J115304.62+035951.5	178.26928	3.9977	3.432	3.028	3.388			
SDSS J115305.16+423230.6	178.27152	42.5419	3.480	2.605	3.436			
SDSS J115305.23+394351.5	178.27184	39.7310	3.514	2.610	3.469			
SDSS J115311.50+344751.2	178.29800	34.7975	2.892	2.493	2.853			
SDSS J115314.05+424552.8	178.30858	42.7647	3.299	2.341	3.256			
SDSS J115321.16+123054.0	178.33818	12.5150	2.388	2.307	2.354			
SDSS J115321.68+101112.9	178.34035	10.1870	4.127	3.025	4.076	3.4688	20.55	0.20
						3.7957	21.50	0.20
SDSS J115322.89+145107.9	178.34540	14.8522	3.314	2.541	3.270			

Continued on Next Page...

Table I.1 – Continued

Name	RA	Dec	z_{em}	z_{min}	z_{max}	z_{abs}	$\log N(\mathrm{H\,I})$	$\epsilon[\log N(\mathrm{H\,I})]$
SDSS J115333.99+031353.2	178.39163	3.2315	2.509	2.307	2.474			
SDSS J115337.56+320046.2	178.40654	32.0129	2.407	2.307	2.373			
SDSS J115350.78+351409.9	178.46162	35.2361	3.368	2.655	3.324			
SDSS J115354.22+523730.0	178.47595	52.6250	3.072	2.778	3.031			
SDSS J115355.86+470430.6	178.48276	47.0752	2.402	2.307	2.368			
SDSS J115357.97+632531.2	178.49155	63.4253	3.820	2.801	3.772			
SDSS J115401.10+155919.5	178.50462	15.9888	2.343	2.307	2.310			
SDSS J115405.89+310538.8	178.52457	31.0941	2.378	2.307	2.345			
SDSS J115407.43+353315.3	178.53099	35.5543	4.061	2.969	4.011			
[HB89] 1151+068	178.54629	6.5771	2.760	1.650	2.723	1.7737	21.30	0.20
SDSS J115424.73+134145.7	178.60306	13.6960	5.060	4.113	4.959			
SDSS J115446.13+422220.8	178.69224	42.3725	2.790	2.449	2.708			
SDSS J115457.71+390617.2	178.74048	39.1048	2.491	2.307	2.456			
SDSS J115509.53+542237.2	178.78973	54.3770	3.245	2.811	3.202			
SDSS J115524.96+364339.1	178.85403	36.7276	3.060	2.350	3.019			
SDSS J115526.34+351052.6	178.85978	35.1813	2.837	2.307	2.799	2.7583	20.70	0.20
SDSS J115534.46+511904.8	178.89364	51.3180	3.442	2.987	3.397			
SDSS J115538.60+053050.5	178.91086	5.5141	3.475	2.444	3.430	2.6083	20.35	0.20
						3.3268	21.05	0.10
SDSS J115541.17+615145.4	178.92160	61.8627	2.347	2.307	2.313			
SDSS J115543.61+014420.7	178.93174	1.7391	2.627	2.307	2.590			
SDSS J115547.83+022716.1	178.94930	2.4545	4.360	4.153	4.307			
SDSS J115554.60+564040.9	178.97753	56.6780	2.621	2.307	2.584			
FBQS J115607.8+373414	179.03274	37.5708	2.450	2.307	2.415			
SDSS J115620.92+330700.7	179.08720	33.1169	3.571	2.753	3.525			
SDSS J115621.05+313222.9	179.08772	31.5397	2.898	2.706	2.859			
SDSS J115624.76+375322.1	179.10318	37.8895	3.777	2.746	3.729			
SDSS J115631.40+133714.9	179.13084	13.6208	3.332	2.440	3.289			
SDSS J115632.32+471925.4	179.13470	47.3237	3.167	2.526	3.126			
SDSS J115655.69+310727.6	179.23209	31.1244	2.963	2.307	2.924			
SDSS J115659.59+551308.1	179.24830	55.2190	3.095	2.473	3.054	2.4910	20.55	0.20
SDSS J115702.46+604035.4	179.26030	60.6765	3.460	3.396	3.416			
SDSS J115703.18+115106.2	179.26328	11.8517	2.984	2.307	2.944			
SDSS J115704.48+601217.7	179.26868	60.2049	3.518	2.756	3.473			
SDSS J115705.67+520828.3	179.27366	52.1412	3.372	2.939	3.290			
SDSS J115706.90+312313.1	179.27878	31.3870	2.417	2.307	2.383			
SDSS J115737.24+141345.7	179.40519	14.2294	3.023	2.349	2.983			
SDSS J115809.39+634252.8	179.53914	63.7147	4.479	3.623	4.388			
SDSS J115813.02+650303.7	179.55429	65.0511	2.783	2.396	2.745			
SDSS J115830.96+631004.2	179.62904	63.1678	2.917	2.368	2.877			
SDSS J115832.30+544509.6	179.63461	54.7527	3.938	2.737	3.888	3.0625	21.25	0.20
SDSS J115842.48+371649.4	179.67705	37.2804	3.184	2.325	3.143	2.4857	20.70	0.15
SDSS J115843.66+314355.8	179.68193	31.7322	2.956	2.552	2.917			
SDSS J115848.62+560433.3	179.70261	56.0759	2.975	2.307	2.935			
SDSS J115848.94+141823.0	179.70392	14.3064	3.352	2.594	3.308			
SDSS J115852.58+115124.7	179.71911	11.8569	3.260	2.865	3.217			
SDSS J115904.29+022214.2	179.76795	2.3706	2.725	2.378	2.688			
2MASSi J1159065+133738	179.77719	13.6272	4.081	2.823	4.030			
SDSS J115906.62+342648.2	179.77762	34.4467	3.124	2.760	3.083			
SDSS J115909.66+453920.5	179.79027	45.6557	2.904	2.725	2.821			
SDSS J115911.52+313427.3	179.79804	31.5743	3.055	2.307	3.014			
SDSS J115915.36+425451.9	179.81403	42.9144	3.113	2.421	3.072			
SDSS J115921.85+144708.4	179.84110	14.7857	4.120	3.768	4.069			
SDSS J115922.76+393616.8	179.84485	39.6047	3.784	3.016	3.736			
SDSS J115935.63+042420.0	179.89850	4.4056	3.448	2.525	3.404			
SDSS J115947.10+413659.1	179.94626	41.6164	2.944	2.307	2.905			
SDSS J115950.14+041056.2	179.95895	4.1823	2.968	2.562	2.929			
SDSS J115959.71+410152.9	179.99880	41.0314	2.788	2.400	2.750			
2MASSi J1200062+312630	180.02606	31.4419	2.989	2.307	2.949			
SDSS J120011.66+140815.4	180.04861	14.1376	2.576	2.307	2.540			
SDSS J120016.65+034926.1	180.06938	3.8240	3.167	2.405	3.125			
SDSS J120018.82+105759.3	180.07845	10.9665	3.750	3.282	3.668			
SDSS J120021.14+361926.1	180.08811	36.3239	4.373	3.296	4.320			
SDSS J120034.70+623618.7	180.14465	62.6052	3.849	2.805	3.800			
SDSS J120036.72+461850.2	180.15306	46.3140	4.741	3.844	4.645	4.4760	20.60	0.20
SDSS J120039.81+401556.1	180.16591	40.2656	3.364	2.358	3.320	3.2199	20.65	0.15
SDSS J120054.79+355005.6	180.22832	35.8349	3.666	2.958	3.620			
SDSS J120055.61+181732.9	180.23174	18.2925	4.995	4.058	4.895			
SDSS J120059.68+400913.1	180.24871	40.1536	3.352	2.614	3.308			
SDSS J120102.01+073648.1	180.25840	7.6134	4.472	3.617	4.381			
SDSS J120110.31+211758.5	180.29298	21.2996	4.579	3.707	4.486	3.8070	21.35	0.20
SDSS J120111.28+424705.2	180.29704	42.7848	3.044	2.700	3.003			

Continued on Next Page...

Table I.1 – Continued

Name	RA	Dec	z_{em}	z_{min}	z_{max}	z_{abs}	$\log N(\mathrm{H\,I})$	$\epsilon[\log N(\mathrm{H\,I})]$
SDSS J120117.46+622522.5	180.32280	62.4229	2.841	2.461	2.758			
SDSS J120131.56+053510.1	180.38153	5.5861	4.840	3.927	4.743			
SDSS J120132.10+573636.7	180.38377	57.6102	3.422	3.021	3.377			
SDSS J120134.65+514650.5	180.39439	51.7807	2.405	2.307	2.371			
SDSS J120138.56+010336.1	180.41068	1.0601	3.847	3.051	3.799			
SDSS J120144.36+011611.5	180.43487	1.2699	3.233	2.307	3.191	2.6844	21.00	0.15
SDSS J120144.96+095352.1	180.43736	9.8978	3.570	3.204	3.524			
[HB89] 1159+123	180.44963	12.1084	3.522	1.854	3.477			
SDSS J120152.41+350136.3	180.46839	35.0268	2.548	2.307	2.513			
[VCV96] Q 1159+00	180.51565	0.2216	2.586	1.671	2.550			
SDSS J120204.05+383040.4	180.51691	38.5112	3.035	2.328	2.995			
SDSS J120206.80+370919.5	180.52834	37.1554	2.479	2.307	2.444			
SDSS J120207.78+323538.8	180.53243	32.5941	5.298	4.314	5.193	4.7980	20.75	0.20
SDSS J120210.08-005425.4	180.54200	-0.9071	3.592	2.159	3.547			
2MASSi J1202168+122005	180.56995	12.3349	2.548	2.307	2.512			
SDSS J120223.39+504515.8	180.59749	50.7544	2.626	2.307	2.590			
SDSS J120223.95+325059.4	180.59982	32.8498	3.674	2.503	3.627			
SDSS J120233.38+580501.8	180.63900	58.0838	3.424	2.408	3.380			
SDSS J120242.91+414701.6	180.67884	41.7838	3.314	2.365	3.271	3.1867	20.75	0.15
SDSS J120245.00+145229.8	180.68754	14.8750	3.366	2.307	2.349			
SDSS J120304.64+324817.0	180.76937	32.8047	3.174	2.819	3.132			
SDSS J120308.69+552245.8	180.78623	55.3794	3.355	2.972	3.311			
SDSS J120312.50+683005.5	180.80209	68.5016	2.376	2.307	2.342			
SDSS J120315.72-011123.6	180.81552	-1.1899	2.612	2.307	2.576			
SDSS J120324.07+564449.1	180.85030	56.7470	2.616	2.464	2.580			
2MASSi J1203312+152254	180.88038	15.3819	2.977	2.307	2.937			
SDSS J120336.57+535953.0	180.90245	53.9981	3.725	2.768	3.678			
SDSS J120344.95+445915.9	180.93732	44.9878	3.616	3.207	3.569			
SDSS J120347.17+523348.3	180.94658	52.5635	3.509	2.735	3.464	2.9623	20.50	0.15
SDSS J120350.77+403944.6	180.96160	40.6624	2.409	2.307	2.375			
SDSS J120359.07+341114.2	180.99614	34.1873	3.748	2.761	3.701	3.6743	20.60	0.15
						3.6868	20.60	0.15
SDSS J120403.49-013107.3	181.01457	-1.5187	2.963	2.570	2.881			
SDSS J120408.47+383353.5	181.03530	38.5649	3.389	3.010	3.345			
SDSS J120415.12-033429.3	181.06345	-3.5748	3.814	3.017	3.766			
SDSS J1204+0221:[PH2009] BG	181.06954	2.3531	2.529	2.307	2.494			
SDSS J120426.35+535804.3	181.10986	53.9679	2.389	2.307	2.355			
4C +52.25	181.15333	52.4783	2.734	2.352	2.697			
SDSS J120439.42+663549.7	181.16434	66.5971	4.059	3.139	4.008			
SDSS J120441.73-002149.6	181.17382	-0.3638	5.094	4.142	4.992			
SDSS J120444.09+515201.0	181.18375	51.8670	2.382	2.307	2.349			
SDSS J120449.77+020635.6	181.20738	2.1099	2.776	2.463	2.693			
SDSS J120455.83+564516.3	181.23265	56.7546	3.044	2.332	3.003			
SDSS J120500.55+055020.3	181.25232	5.8390	3.342	2.920	3.298			
SDSS J120501.98+585522.2	181.25828	58.9228	3.182	3.053	3.140			
SDSS J120503.15+425958.0	181.26315	42.9995	2.961	2.307	2.921			
2MASSi J1205231-074232	181.34637	-7.7091	4.694	3.160	4.637	4.3830	20.49	0.20
SDSS J120523.48+403514.7	181.34786	40.5874	3.960	3.535	3.911			
SDSS J120525.27+502355.8	181.35532	50.3988	3.429	3.333	3.384			
SDSS J120532.23-004848.2	181.38432	-0.8134	2.969	2.307	2.930			
SDSS J120539.54+014356.5	181.41479	1.7324	3.856	2.890	3.807	3.2855	20.70	0.15
						3.3302	20.80	0.15
SDSS J120549.05+395506.9	181.45441	39.9186	2.458	2.359	2.424			
SDSS J120551.50+500609.9	181.46462	50.1028	3.441	3.037	3.397			
SDSS J120610.60+371747.5	181.54418	37.2966	4.317	3.107	4.264			
SDSS J120611.29+464532.5	181.54706	46.7591	3.877	2.878	3.828			
SDSS J120612.32+542906.0	181.55138	54.4850	3.200	2.784	3.118			
SDSS J120626.18+375428.2	181.60911	37.9079	3.177	2.527	3.135			
SDSS J120633.18+445040.1	181.63830	44.8445	3.092	2.687	3.010			
SDSS J120638.69+130126.1	181.66123	13.0239	3.053	2.307	3.012			
SDSS J120639.09+392932.2	181.66292	39.4923	2.446	2.314	2.411			
SDSS J120639.85+025308.2	181.66608	2.8856	2.516	2.307	2.481			
SDSS J120640.06+060147.3	181.66694	6.0298	2.389	2.307	2.355			
SDSS J120644.21+564314.1	181.68421	56.7206	3.231	2.592	3.189			
SDSS J120645.67+090645.3	181.69032	9.1126	3.930	3.431	3.881			
SDSS J120652.82+570601.9	181.72011	57.1005	2.539	2.307	2.503			
SDSS J120704.93+414507.3	181.77055	41.7520	3.154	2.307	3.113			
SDSS J120706.99+350922.2	181.77915	35.1562	3.094	2.307	3.053			
SDSS J120709.34+354307.8	181.78894	35.7188	3.244	2.847	3.201			
SDSS J120719.82+094833.5	181.83261	9.8093	3.071	2.674	3.030			
SDSS J120725.27+321530.4	181.85535	32.2585	4.621	3.743	4.527			
SDSS J120729.75+042909.9	181.87397	4.4861	2.418	2.307	2.384			

Continued on Next Page...

Table I.1 – Continued

Name	RA	Dec	z_{em}	z_{min}	z_{max}	z_{abs}	$\log N(\mathrm{H\,I})$	$\epsilon[\log N(\mathrm{H\,I})]$
SDSS J120729.77+111523.4	181.87407	11.2565	3.904	3.449	3.822			
SDSS J120730.84+153338.1	181.87855	15.5606	4.452	3.600	4.361			
SDSS J120800.96+635010.0	182.00406	63.8361	4.014	3.044	3.964	3.8439	21.00	0.15
SDSS J120802.65+630328.7	182.01105	63.0580	2.561	2.307	2.525	2.4433	20.70	0.15
SDSS J120802.74+623232.6	182.01146	62.5424	2.414	2.371	2.380			
SDSS J120806.87+345124.7	182.02865	34.8569	2.447	2.307	2.412			
SDSS J120810.28+590827.2	182.04292	59.1409	2.455	2.307	2.421			
[VCV96] Q 1205-30	182.05292	-30.5184	3.036	2.045	2.996			
SDSS J120816.92+393317.7	182.07052	39.5549	2.838	2.307	2.800	2.5147	20.70	0.15
SDSS J120820.45+643809.2	182.08522	64.6359	2.414	2.307	2.380			
LBQS 1205+0918	182.08757	9.0251	2.080	1.634	2.046	1.6730	20.60	0.20
SDSS J120827.93+614325.6	182.11640	61.7238	4.074	3.054	4.023			
SDSS J120830.82+060934.3	182.12845	6.1596	3.061	2.719	3.020			
SDSS J120833.24+633348.5	182.13852	63.5635	2.899	2.504	2.860			
SDSS J120834.84+002047.7	182.14518	0.3466	2.709	2.350	2.627			
[VCV96] Q 1206+123	182.15634	12.0869	2.554	2.307	2.518			
SDSS J120847.63+004321.6	182.19848	0.7227	2.720	2.351	2.683	2.6080	20.45	0.15
SDSS J120847.91+501353.5	182.19966	50.2315	2.458	2.307	2.424			
LBQS 1206+1500	182.20234	14.7271	2.600	1.793	2.568			
LBQS 1206+1727	182.25438	17.1852	2.360	1.634	2.321			
SDSS J120910.71+113545.2	182.29464	11.5959	3.122	2.414	3.080			
SDSS J120916.56+110348.8	182.31904	11.0636	2.446	2.307	2.411			
[HB89] 1206+119	182.32474	11.6418	3.105	2.307	3.064			
SDSS J120922.81+125748.2	182.34506	12.9634	3.553	2.606	3.507			
SDSS J120934.53+553745.5	182.39393	55.6293	3.572	2.542	3.527			
SDSS J120945.71+601758.5	182.44049	60.2996	2.962	2.307	2.922			
SDSS J120949.74+453400.4	182.45727	45.5668	3.591	2.421	3.545	2.7078	20.50	0.20
SDSS J120952.72+183147.2	182.46972	18.5298	5.127	4.170	5.025			
SDSS J120952.82+544531.7	182.47012	54.7588	2.368	2.307	2.334			
SDSS J120957.55+390834.3	182.48982	39.1429	3.272	2.507	3.230	3.0973	20.80	0.15
SDSS J121001.72+392150.8	182.50719	39.3641	2.962	2.560	2.922	2.8032	21.40	0.15
SDSS J121003.29+512707.0	182.51373	51.4520	3.271	2.884	3.228			
[HB89] 1207+399	182.54257	39.6600	2.454	2.307	2.420			
SDSS J121019.96+442652.3	182.58319	44.4479	3.370	3.082	3.326			
SDSS J121021.68+464618.7	182.59037	46.7719	3.487	3.208	3.442			
SDSS J121028.63+330440.0	182.61933	33.0778	3.321	2.379	3.278			
SDSS J121031.44+414329.7	182.63101	41.7249	2.440	2.307	2.405			
SDSS J121032.88+341302.2	182.63702	34.2173	3.200	2.543	3.158			
SDSS J121037.74+360941.6	182.65728	36.1616	2.477	2.324	2.442			
SDSS J121039.40+160839.2	182.66422	16.1442	2.355	2.307	2.322			
SDSS J121040.36+350911.3	182.66819	35.1531	2.919	2.307	2.880			
SDSS J121054.01+140928.2	182.72508	14.1579	2.959	2.307	2.920			
SDSS J121057.12+122700.9	182.73803	12.4503	2.370	2.307	2.336			
SDSS J121115.54+474651.6	182.81478	47.7810	2.421	2.307	2.386			
SDSS J121117.59+042222.2	182.82332	4.3729	2.541	2.307	2.506	2.3762	20.70	0.15
SDSS J121122.63+565259.7	182.84430	56.8833	2.520	2.307	2.485			
SDSS J121126.69+610723.1	182.86125	61.1231	3.639	2.707	3.593			
SDSS J121129.84+130023.0	182.87438	13.0064	2.955	2.311	2.915			
SDSS J121134.04+484235.9	182.89186	48.7100	4.544	3.678	4.452			
SDSS J121134.77+454918.2	182.89489	45.8217	2.947	2.343	2.907	2.7607	20.95	0.15
[HB89] 1209+093	182.89564	9.0391	3.292	2.346	3.249	2.5843	21.35	0.15
LBQS 1209+1046	182.91915	10.5006	2.200	1.634	2.163			
SDSS J121142.89-014643.1	182.92875	-1.7787	3.229	2.510	3.186			
SDSS J121143.52+013011.2	182.93137	1.5031	2.590	2.307	2.554			
SDSS J121146.93+122419.0	182.94557	12.4053	3.869	3.422	3.820			
SDSS J121153.64+343654.1	182.97353	34.6151	2.451	2.307	2.416			
SDSS J121157.22+590851.2	182.98852	59.1476	2.441	2.307	2.406			
SDSS J121159.91+364733.1	182.99965	36.7925	3.719	2.752	3.671			
SDSS J121209.54+034749.8	183.03977	3.7972	4.037	3.057	3.986			
SDSS J121213.13+114857.2	183.05474	11.8159	3.369	3.308	3.325			
SDSS J121221.56+534127.8	183.08983	53.6911	3.097	2.331	3.056			
SDSS J121225.31+114436.1	183.10549	11.7434	3.373	3.305	3.329			
SDSS J121230.40+024653.6	183.12667	2.7816	2.540	2.388	2.505			
LBQS 1209+1524	183.13355	15.1238	3.060	1.634	3.021			
SDSS J121238.39+675920.5	183.15998	67.9891	2.573	2.307	2.537			
SDSS J121240.94+592125.3	183.17064	59.3570	2.845	2.708	2.806			
SDSS J121255.68+475335.7	183.23200	47.8933	3.061	2.349	3.020			
SDSS J121257.98+532029.2	183.24162	53.3415	3.127	2.515	3.085			
SDSS J121258.27+474953.6	183.24280	47.8316	3.575	2.940	3.529			
LBQS 1210+1731	183.26259	17.2398	2.540	1.634	2.502	1.8920	20.60	0.20
SDSS J121303.25+120838.9	183.26359	12.1442	3.384	3.220	3.340			
SDSS J121309.24+365409.9	183.28852	36.9028	3.033	2.378	2.993			

Continued on Next Page...

Table I.1 – Continued

Name	RA	Dec	z_{em}	z_{min}	z_{max}	z_{abs}	$\log N(\mathrm{H\,I})$	$\epsilon[\log N(\mathrm{H\,I})]$
SDSS J121310.72+120715.1	183.29468	12.1209	3.469	3.102	3.424			
SDSS J121320.97+050601.7	183.33738	5.1005	2.434	2.307	2.400			
SDSS J121324.58+423538.5	183.35244	42.5941	3.766	2.758	3.719			
SDSS J121332.56+575814.6	183.38569	57.9708	3.005	2.372	2.965			
SDSS J121339.75+354556.8	183.41568	35.7658	3.571	2.653	3.525			
SDSS J121351.69+084948.1	183.46540	8.8300	3.075	2.775	3.035			
SDSS J121419.05+594430.9	183.57941	59.7419	3.181	2.471	3.140			
SDSS J121419.44+100433.8	183.58104	10.0761	2.427	2.307	2.392			
SDSS J121420.12+404305.8	183.58384	40.7183	2.394	2.307	2.360			
SDSS J121421.76+513332.9	183.59069	51.5592	3.311	2.560	3.268			
SDSS J121422.02+665707.5	183.59175	66.9521	4.650	3.767	4.556			
SDSS J121430.10+132522.3	183.62543	13.4229	3.081	2.662	3.040			
SDSS J121437.93+095542.8	183.65804	9.9286	3.863	3.099	3.815			
SDSS J121438.69+421105.9	183.66122	42.1850	3.365	2.533	3.322			
LBQS 1212+1551	183.71915	15.5821	1.950	1.665	1.918			
SDSS J121454.10+554121.0	183.72549	55.6891	3.071	2.411	3.031			
LBQS 1212+1045	183.75682	10.4773	1.950	1.634	1.922			
SDSS J121502.11-010832.2	183.75882	-1.1423	2.357	2.307	2.324			
SDSS J121504.99+134135.4	183.77081	13.6932	3.310	2.712	3.267	2.9723	20.35	0.20
LBQS 1212+0854	183.78348	8.6379	2.350	1.634	2.319			
SDSS J121522.75+525102.8	183.84482	52.8508	2.458	2.372	2.424			
SDSS J121524.60+091804.8	183.85252	9.3013	2.875	2.339	2.837			
SDSS J121528.60+413336.9	183.86919	41.5603	2.975	2.582	2.893			
SDSS J121529.35-033659.9	183.87231	-3.6167	2.444	2.403	2.410			
SDSS J121537.77+545937.1	183.90744	54.9937	4.082	3.274	4.032			
LBQS 1213+1015	183.91175	9.9792	2.513	2.307	2.478			
SDSS J121538.87+621844.3	183.91202	62.3123	3.953	3.465	3.871	3.7445	21.25	0.15
LBQS 1213+0922	183.91528	9.1021	2.723	2.342	2.686			
SDSS J121548.90+642228.5	183.95378	64.3746	3.232	2.307	3.190	2.5364	20.85	0.15
UM 485	183.95752	-0.5755	2.707	2.328	2.670			
SDSS J121601.78+370754.5	184.00744	37.1318	2.771	2.416	2.734			
SDSS J121606.40+604241.3	184.02672	60.7115	2.468	2.307	2.434			
SDSS J121607.58+415653.9	184.03159	41.9483	4.552	4.364	4.470			
SDSS J121614.04+444441.6	184.05853	44.7449	3.123	3.082	3.082			
SDSS J121617.68+465509.9	184.07371	46.9194	3.779	3.335	3.732			
SDSS J121618.60+430353.9	184.07753	43.0650	2.857	2.462	2.818			
SDSS J121619.12+392415.1	184.07970	39.4042	3.313	3.241	3.269			
SDSS J121625.94+153747.9	184.10814	15.6300	3.509	2.801	3.463			
2MASX J12163754+3243301	184.16209	32.7244	3.258	3.062	3.215			
SDSS J121643.74+624051.4	184.18226	62.6810	4.008	3.555	3.958			
SDSS J121644.54+041841.5	184.18561	4.3115	3.173	2.473	3.131			
SDSS J121655.58+633743.0	184.23161	63.6286	3.168	2.422	3.126	2.9917	20.60	0.15
SDSS J121706.49+124245.4	184.27709	12.7126	3.234	2.498	3.192			
SDSS J121711.02+583526.2	184.29591	58.5906	2.552	2.307	2.516			
[HB89] 1214+348	184.31337	34.5939	2.638	2.307	2.601			
FBQS J121732.5+330538	184.38558	33.0939	2.610	1.640	2.574	1.9989	21.00	0.20
SDSS J121746.79+014354.3	184.44497	1.7318	2.666	2.307	2.629			
SDSS J121747.06-025003.8	184.44609	-2.8344	2.408	2.307	2.374			
SDSS J121752.44+085319.3	184.46855	8.8887	3.545	3.117	3.499	3.3896	21.35	0.20
SDSS J121758.74+154250.5	184.49478	15.7141	3.339	2.663	3.296	3.1228	20.85	0.15
LBQS 1215+1244	184.54147	12.4708	2.080	1.634	2.048			
SDSS J121815.43+492638.5	184.56432	49.4441	2.591	2.307	2.555			
LBQS 1215+1202	184.56498	11.7644	2.830	1.634	2.788			
LBQS 1216+1517	184.64050	15.0186	1.830	1.723	1.802			
SDSS J121841.78+015223.7	184.67409	1.8733	2.354	2.307	2.320			
SDSS J121846.20+491845.9	184.69256	49.3128	2.997	2.318	2.957			
LBQS 1216+1754	184.69421	17.6381	1.810	1.634	1.781			
SDSS J121852.36+355239.6	184.71817	35.8777	3.630	2.581	3.584			
SDSS J121904.04+044410.8	184.76684	4.7364	3.175	2.804	3.133			
SDSS J121904.63+023217.3	184.76934	2.5381	2.471	2.307	2.437			
SDSS J121913.19+043809.1	184.80498	4.6359	2.739	2.356	2.701			
SDSS J121913.57+522433.0	184.80659	52.4092	2.424	2.307	2.390			
SDSS J121916.76+623026.1	184.81985	62.5073	3.056	2.649	3.015			
SDSS J121920.26+010736.1	184.83445	1.1267	2.800	2.484	2.762			
LBQS 1216+1656	184.83502	16.6582	2.830	1.659	2.791			
SDSS J121922.19+002905.4	184.84249	0.4849	2.626	2.307	2.590			
LBQS 1216+0947	184.86122	9.5174	2.310	1.645	2.279			
SDSS J121928.92+160357.1	184.87052	16.0659	3.152	2.732	3.110	3.0054	20.30	0.20
SBS 1217+499	184.87824	49.6812	2.698	2.319	2.661			
SDSS J121933.25+003226.4	184.88858	0.5407	2.879	2.307	2.840			
SDSS J121935.27+121030.2	184.89700	12.1751	2.982	2.348	2.942	2.8704	20.80	0.20
SDSS J121941.10-025654.5	184.92126	-2.9485	3.227	2.437	3.184			

Continued on Next Page...

Table I.1 – Continued

Name	RA	Dec	z_{em}	z_{min}	z_{max}	z_{abs}	$\log N(\mathrm{H\,I})$	$\epsilon[\log N(\mathrm{H\,I})]$
SDSS J121944.79+461015.3	184.93663	46.1709	2.484	2.307	2.449			
SDSS J121951.65+361216.7	184.96524	36.2047	3.044	2.401	3.003	2.4749	20.35	0.20
SDSS J121957.82-012614.3	184.99095	-1.4373	2.634	2.307	2.598			
SDSS J122003.95+565826.9	185.01651	56.9742	2.991	2.307	2.951			
SDSS J122008.93+343642.3	185.03723	34.6118	4.316	3.818	4.263			
SDSS J122012.52+495952.4	185.05220	49.9979	2.660	2.307	2.623	2.4301	20.70	0.20
SDSS J122015.50+460802.4	185.06461	46.1340	2.465	2.307	2.431			
SDSS J122016.05+315253.0	185.06693	31.8814	4.900	3.978	4.802			
SDSS J122017.06+454941.0	185.07111	45.8281	3.293	2.869	3.211			
SDSS J122021.39+092135.7	185.08915	9.3600	4.133	3.127	4.082	3.3048	20.40	0.20
SDSS J122040.23+092326.8	185.16765	9.3908	3.146	2.307	3.105			
SDSS J122044.52+055106.9	185.18554	5.8519	3.101	2.756	3.060	2.7894	20.30	0.20
SDSS J122046.80+441236.7	185.19501	44.2102	3.241	2.821	3.159	3.1356	20.35	0.15
SDSS J122055.02+060409.2	185.22928	6.0692	2.664	2.307	2.628			
SDSS J122058.14+330246.7	185.24228	33.0463	2.712	2.333	2.675			
SDSS J122104.20+030331.2	185.26754	3.0587	3.140	2.307	3.099			
SDSS J122115.30+391932.9	185.31379	39.3258	3.543	2.553	3.498			
SDSS J122118.35-031542.6	185.32649	-3.2618	3.140	2.461	3.099			
SDSS J122125.35+575246.3	185.35564	57.8796	2.934	2.307	2.895			
LBQS 1219+1140	185.42812	11.4034	2.180	1.634	2.147			
SDSS J122143.05+542757.8	185.42944	54.4661	3.960	3.486	3.910			
SDSS J122146.42+444528.0	185.44342	44.7578	5.203	4.234	5.100	4.9310	20.35	0.20
SDSS J122155.25+543956.9	185.48024	54.6658	3.183	2.356	3.141			
SDSS J122158.06+142409.8	185.49196	14.4027	2.400	2.350	2.366			
SDSS J122201.38+611803.3	185.50575	61.3009	3.209	2.617	3.167			
SDSS J122209.56+494736.0	185.53988	49.7934	3.374	2.508	3.331			
SDSS J122212.01+580709.9	185.55008	58.1194	2.540	2.307	2.504			
SDSS J122225.97+670717.5	185.60828	67.1215	2.905	2.735	2.866			
SDSS J122237.21+544300.9	185.65505	54.7169	3.661	2.773	3.614			
SDSS J122237.96+195842.9	185.65818	19.9786	5.120	4.164	5.018			
SDSS J122240.82+591715.2	185.67013	59.2876	3.243	2.853	3.161			
SDSS J122247.85+624609.7	185.69942	62.7694	3.242	2.335	3.200			
SDSS J122250.57+425808.0	185.71074	42.9689	3.248	2.813	3.206			
SDSS J122301.02+422057.1	185.75426	42.3492	2.448	2.307	2.413			
SDSS J122307.52+103448.1	185.78134	10.5801	2.761	2.397	2.723	2.7194	20.35	0.20
SDSS J122319.91+423950.9	185.83300	42.6641	3.886	3.423	3.837			
SDSS J122321.26+441929.8	185.83860	44.3250	3.391	2.577	3.347			
SDSS J122330.30+534850.1	185.87630	53.8139	3.277	3.203	3.234			
SDSS J122343.15+503753.4	185.92987	50.6315	3.488	2.307	3.443			
SDSS J122356.81+145823.4	185.98674	14.9732	3.246	2.307	3.203			
SDSS J122359.35+112800.0	185.99731	11.4667	4.113	3.278	4.062			
SDSS J122405.78+610859.2	186.02415	61.1498	3.302	2.606	3.259			
SDSS J122411.54+525216.1	186.04812	52.8712	3.054	2.432	3.014			
SDSS J122423.67+152312.1	186.09866	15.3867	3.974	3.505	3.925			
SDSS J122437.01+434244.0	186.15424	43.7122	2.850	2.809	2.812			
SDSS J122439.54+505054.9	186.16478	50.8486	3.436	2.737	3.392			
SDSS J122453.80-022557.4	186.22419	-2.4327	3.196	2.771	3.154			
SDSS J122458.03+102300.5	186.24181	10.3835	3.251	2.831	3.169			
SDSS J122458.08+472644.0	186.24203	47.4456	2.939	2.581	2.899			
LBQS 1222+1053	186.25101	10.6157	2.300	1.641	2.263			
SDSS J122500.64+491127.3	186.25270	49.1909	2.953	2.549	2.914			
SDSS J122518.64+483116.0	186.32769	48.5211	3.090	2.307	3.049			
SDSS J122518.82+563817.6	186.32850	56.6382	2.568	2.307	2.532			
LBQS 1223+1059	186.41934	10.7113	2.320	1.643	2.288			
SDSS J122541.88+453801.1	186.42452	45.6337	3.527	3.079	3.445			
SDSS J122545.92+555529.1	186.44140	55.9247	2.377	2.307	2.343			
SDSS J122551.05+500114.0	186.46275	50.0206	2.656	2.318	2.620			
SDSS J122600.45+493726.8	186.50188	49.6241	3.701	2.895	3.654			
SDSS J122600.68+005923.5	186.50285	0.9899	4.259	3.329	4.206			
SDSS J122602.10+132114.5	186.50876	13.3540	3.532	2.449	3.487			
SDSS J122602.90+032547.3	186.51211	3.4298	2.969	2.307	2.930	2.5095	20.65	0.15
LBQS 1223+1753	186.52999	17.6139	2.920	1.945	2.879	2.4658	21.50	0.20
LBQS 1223+1723	186.62508	17.1118	2.420	1.659	2.386			
SDSS J122639.69+103708.3	186.66544	10.6190	3.283	2.870	3.240			
SDSS J122646.65+575054.4	186.69445	57.8485	2.944	2.568	2.904			
SDSS J122649.06+140143.2	186.70446	14.0287	2.902	2.503	2.863			
SDSS J122654.38-005430.4	186.72663	-0.9085	2.610	2.307	2.527			
SDSS J122656.61+650204.3	186.73590	65.0345	2.998	2.598	2.958			
SDSS J122657.96+000938.3	186.74155	0.1607	4.140	3.097	4.088			
LBQS 1224+1244	186.80492	12.4678	2.140	1.634	2.110			
SDSS J122721.29+435327.9	186.83874	43.8911	3.082	2.433	3.041			
SDSS J122729.87-003410.6	186.87449	-0.5697	2.962	2.307	2.923			

Continued on Next Page...

Table I.1 – Continued

Name	RA	Dec	z_{em}	z_{min}	z_{max}	z_{abs}	$\log N(\mathrm{H\,I})$	$\epsilon[\log N(\mathrm{H\,I})]$
SDSS J122730.37-010446.0	186.87657	-1.0795	2.870	2.307	2.831			
SDSS J122733.57+571914.3	186.88993	57.3207	2.486	2.307	2.451			
SDSS J122736.72+435933.6	186.90303	43.9927	3.144	2.916	3.103			
SDSS J122736.73+640957.9	186.90308	64.1661	2.557	2.307	2.522			
SDSS J122741.25+570856.5	186.92202	57.1490	2.407	2.307	2.373			
SDSS J122752.11+353026.5	186.96714	35.5074	3.170	2.507	3.128			
SDSS J122813.71+664918.5	187.05716	66.8218	2.919	2.307	2.879			
SDSS J122821.25+472809.0	187.08856	47.4692	3.418	2.396	3.374			
LBQS 1225+1512	187.09254	14.9318	2.010	1.797	1.977			
SDSS J122825.77+672859.0	187.10741	67.4831	2.497	2.307	2.462			
SDSS J122826.33+130106.2	187.10973	13.0184	3.230	2.549	3.187			
LBQS 1225+1610	187.12073	15.9063	2.230	1.663	2.200			
SDSS J122829.98+520241.8	187.12495	52.0450	3.032	2.416	2.992			
SDSS J122836.05+510746.1	187.15022	51.1295	2.442	2.307	2.408			
LBQS 1226+1035	187.15370	10.3117	2.320	1.634	2.287			
SDSS J122838.50+503137.6	187.16047	50.5271	3.057	2.320	3.016			
SDSS J122844.16+642605.5	187.18403	64.4349	2.432	2.307	2.397	2.3090	20.95	0.20
SDSS J122844.82+152402.3	187.18679	15.4007	3.721	2.994	3.674			
SDSS J122848.21-010414.4	187.20091	-1.0707	2.655	2.307	2.619			
SDSS J122848.50+640354.2	187.20212	64.0651	3.007	2.307	2.967			
LBQS 1226+1115	187.24200	10.9820	1.980	1.634	1.950			
SDSS J122900.86+422243.1	187.25361	42.3787	3.842	2.794	3.794	3.4524	20.60	0.15
SDSS J122904.74+413115.1	187.26978	41.5209	3.068	2.670	3.027			
SDSS J122905.38+625326.4	187.27249	62.8907	3.027	2.307	2.987			
LBQS 1226+1639	187.28965	16.3773	2.250	1.634	2.216			
SDSS J122910.53+641737.9	187.29389	64.2939	3.203	2.382	3.161			
SDSS J122911.10+533027.1	187.29628	53.5075	2.994	2.381	2.954			
SDSS J122924.11-020914.6	187.35050	-2.1541	3.624	2.880	3.578			
SDSS J122927.19+391718.7	187.36330	39.2885	3.598	2.324	3.552			
SDSS J122932.06+540837.3	187.38362	54.1437	2.900	2.507	2.861			
SDSS J122934.78+103520.4	187.39493	10.5890	3.838	3.021	3.789			
SDSS J122944.93+004253.0	187.43722	0.7147	2.884	2.599	2.845			
LBQS 1227+1215	187.47937	11.9859	2.170	1.624	2.138			
SDSS J123000.85+153254.1	187.50357	15.5484	3.243	2.861	3.201			
SDSS J123005.86+142956.1	187.52444	14.4989	3.255	2.385	3.213			
SDSS J123011.99+102237.6	187.54997	10.3771	3.553	2.611	3.507			
SDSS J123038.67+054013.3	187.66116	5.6704	2.530	2.307	2.495			
SDSS J123053.16-025352.0	187.72151	-2.8978	2.837	2.443	2.798			
SDSS J123054.81+495426.9	187.72842	49.9075	3.703	2.956	3.656			
LBQS 1228+1808	187.73737	17.8610	2.640	1.780	2.607			
SDSS J123058.54+383601.7	187.74395	38.6005	2.368	2.307	2.335			
SDSS J123116.08+411337.3	187.81702	41.2270	3.838	3.009	3.789			
SDSS J123118.78+553644.5	187.82829	55.6124	3.169	2.320	3.128			
[HB89] 1228+077	187.83567	7.4313	2.390	1.691	2.354			
SDSS J123131.88-015350.6	187.88285	-1.8974	3.896	3.001	3.847	3.6702	20.30	0.15
SDSS J123132.37+013813.9	187.88490	1.6372	3.229	2.307	3.186			
SDSS J123139.12+010229.2	187.91303	1.0415	2.883	2.321	2.844			
SDSS J123139.17+031257.3	187.91325	3.2159	2.517	2.382	2.434			
SDSS J123141.33-034007.6	187.92224	-3.6688	2.426	2.314	2.392			
SDSS J123146.70+424309.1	187.94462	42.7192	3.106	2.456	3.065			
LBQS 1229+1414	187.94510	13.9578	2.900	1.764	2.862			
LBQS 1229+1531	187.95997	15.2465	2.270	1.634	2.237			
SDSS J123153.18-031155.1	187.97161	-3.1987	2.713	2.362	2.676			
SDSS J123158.85-013520.5	187.99523	-1.5891	2.942	2.546	2.902			
SDSS J123159.60+123816.7	187.99836	12.6380	2.539	2.307	2.503			
SDSS J123208.19+360355.1	188.03416	36.0653	3.034	2.667	2.994			
SDSS J123220.70+382840.8	188.08626	38.4780	2.400	2.344	2.366			
SDSS J123224.35+481626.3	188.10149	48.2740	3.142	2.731	3.060			
SDSS J123229.73+473654.3	188.12391	47.6151	3.068	2.743	3.027			
SDSS J123230.55+043837.0	188.12733	4.6436	3.111	2.405	3.070			
SDSS J123231.51+160244.3	188.13132	16.0457	3.835	3.039	3.787			
SDSS J123239.29+525250.9	188.16375	52.8808	4.294	3.149	4.241			
LBQS 1230+1042	188.16388	10.4345	2.420	2.307	2.386			
SDSS J123239.52-003611.1	188.16467	-0.6031	2.555	2.307	2.519			
LBQS 1230+1318	188.22698	13.0354	2.290	1.634	2.257			
SDSS J123255.28+540920.9	188.23039	54.1558	2.344	2.307	2.311			
SDSS J123259.50+502120.8	188.24798	50.3558	2.718	2.338	2.681			
SDSS J123303.01+325302.5	188.26256	32.8841	2.358	2.307	2.324			
LBQS 1230+1627B	188.29349	16.1814	2.700	1.634	2.663			
SDSS J123311.84+375747.5	188.29935	37.9632	3.444	2.694	3.399			
SDSS J123315.94+313218.4	188.31644	31.5385	3.219	2.787	3.177			
SDSS J123318.16+110032.3	188.32571	11.0090	2.875	2.307	2.836	2.7931	20.80	0.15

Continued on Next Page...

Table I.1 – Continued

Name	RA	Dec	z_{em}	z_{min}	z_{max}	z_{abs}	$\log N(\mathrm{H\,I})$	$\epsilon[\log N(\mathrm{H\,I})]$
SDSS J123327.60+354948.9	188.36500	35.8303	2.457	2.307	2.422			
SDSS J123328.95+502032.4	188.37067	50.3424	3.205	2.519	3.163			
LBQS 1230+0941	188.37341	9.4217	1.840	1.641	1.812			
SDSS J123330.01+492250.3	188.37507	49.3807	2.772	2.672	2.734			
SDSS J123333.47+062234.2	188.38950	6.3762	5.300	4.316	5.195			
SDSS J123337.68+414608.3	188.40702	41.7690	2.487	2.307	2.452			
SDSS J123338.00+155251.1	188.40836	15.8809	2.976	2.582	2.893	2.8765	20.50	0.15
SDSS J123345.33+505837.9	188.43894	50.9772	3.030	2.387	2.990			
SDSS J123347.21-014853.8	188.44675	-1.8150	4.253	3.218	4.200			
SDSS J123352.74+475003.8	188.46978	47.8344	3.779	3.015	3.732			
SDSS J123404.48-024041.4	188.51868	-2.6782	3.201	2.785	3.119			
SDSS J123404.81+041512.7	188.52006	4.2535	2.353	2.307	2.319			
SDSS J123405.18+420508.3	188.52163	42.0857	3.289	2.503	3.246	3.0466	20.85	0.20
SDSS J123412.73+373210.6	188.55308	37.5363	3.107	2.720	3.066			
SDSS J123426.65+615432.0	188.61106	61.9089	2.518	2.387	2.482			
SDSS J123429.99+501045.6	188.62497	50.1794	2.545	2.307	2.463			
SDSS J123431.72+645556.5	188.63222	64.9324	3.036	2.307	2.995			
LBQS 1232+0815	188.65647	7.9787	2.570	1.789	2.534	2.3376	20.90	0.20
SDSS J123450.00+375530.3	188.70834	37.9251	3.138	2.352	3.096			
SDSS J123452.55+361146.6	188.71898	36.1963	4.879	4.649	4.820			
LBQS 1232+1139	188.73529	11.3878	2.870	1.848	2.831			
SDSS J123503.01+441118.2	188.76258	44.1884	2.857	2.307	2.818			
SDSS J123506.31+401510.7	188.77628	40.2530	3.086	2.307	3.045			
LBQS 1232-0051	188.79410	-1.1294	2.780	1.782	2.745			
SDSS J123515.83+630113.2	188.81597	63.0204	2.383	2.307	2.350			
SDSS J123517.70+133018.4	188.82378	13.5051	3.115	2.458	3.074			
SDSS J123518.55+441928.5	188.82733	44.3246	3.280	2.443	3.237			
SDSS J123525.82+014945.6	188.85762	1.8294	4.031	2.965	3.980			
SDSS J123528.68+451929.5	188.86955	45.3249	3.841	2.740	3.793			
SDSS J123535.36+400125.3	188.89734	40.0237	2.451	2.307	2.417			
SDSS J123539.00+331920.3	188.91255	33.3223	3.227	2.866	3.184			
SBS 1233+594	188.95598	59.1742	2.824	2.307	2.786			
SDSS J123556.85+550826.7	188.98690	55.1408	3.655	3.214	3.608			
SDSS J123557.10+504753.4	188.98796	50.7982	3.531	2.629	3.486			
SDSS J123558.04+384505.7	188.99185	38.7516	2.467	2.320	2.432			
SDSS J123610.15+615607.1	189.04234	61.9353	3.385	2.779	3.341			
SDSS J123612.82+651339.1	189.05349	65.2275	3.239	2.307	3.196	2.6406	20.50	0.15
SDSS J123625.75+360744.1	189.10733	36.1289	4.009	3.535	3.959			
SDSS J123637.44+615814.4	189.15606	61.9707	2.520	2.307	2.485			
SDSS J123638.55+381043.2	189.16065	38.1787	3.505	2.627	3.460			
SDSS J123639.28+543249.6	189.16367	54.5471	3.566	2.706	3.520	3.0406	20.35	0.15
SDSS J123641.45+655442.1	189.17276	65.9117	3.387	2.307	3.343			
2MASSi J1236513+453334	189.21368	45.5596	2.560	2.307	2.478			
SDSS J123654.46+134127.5	189.22694	13.6910	3.149	2.761	3.107			
SDSS J123659.89+004212.1	189.24957	0.7034	2.368	2.307	2.335			
SDSS J123706.10+382357.8	189.27544	38.3994	2.473	2.307	2.438			
SDSS J123706.53+361516.8	189.27722	36.2547	4.106	3.234	4.055	3.6714	20.40	0.20
LBQS 1234+0122	189.35216	1.1043	2.030	1.634	1.996			
SDSS J123729.74+005433.5	189.37395	0.9093	3.283	2.394	3.240			
SDSS J123731.68+574907.9	189.38207	57.8189	3.123	2.438	3.082	2.7324	20.35	0.20
LBQS 1235+1453	189.40176	14.6112	2.681	2.316	2.598			
SDSS J123741.14+475353.3	189.42144	47.8982	2.585	2.307	2.549			
SDSS J1237+6301	189.42951	63.0291	3.425	2.593	3.381			
SDSS J123746.04+663017.2	189.44191	66.5048	2.450	2.307	2.415			
LBQS 1235+1807A	189.44274	17.8489	2.410	1.782	2.371			
SDSS J123746.76+533342.8	189.44485	53.5619	4.069	3.638	3.987			
SDSS J123748.99+012606.9	189.45413	1.4353	3.145	2.341	3.103			
SDSS J123749.39+654855.0	189.45583	65.8153	2.463	2.307	2.428			
SDSS J123817.64+405632.5	189.57351	40.9424	3.604	3.163	3.558			
SDSS J123821.66+010518.6	189.59027	1.0885	3.151	2.390	3.110			
SDSS J123831.45+443258.1	189.63107	44.5495	3.268	2.584	3.226			
SDSS J123834.69+551742.8	189.64463	55.2952	2.465	2.307	2.430			
SDSS J123840.93+343703.3	189.67057	34.6176	2.572	2.307	2.536	2.4714	20.80	0.15
SDSS J123848.34+393045.3	189.70146	39.5126	2.516	2.307	2.481			
LBQS 1236-0043	189.73375	-0.9919	1.840	1.690	1.815			
SDSS J123906.82+322147.3	189.77842	32.3631	3.936	3.191	3.886			
LBQS 1236-0207	189.86674	-2.3921	2.250	1.729	2.213			
SDSS J123930.24+501512.2	189.87601	50.2534	2.380	2.307	2.346			
SDSS J123936.33+361404.2	189.90142	36.2345	3.114	2.943	3.073			
SDSS J123937.17+674020.7	189.90490	67.6725	4.400	3.866	4.318	4.2545	20.30	0.25
SDSS J123937.55+343701.8	189.90650	34.6172	2.463	2.307	2.429			
SDSS J123946.76+650832.4	189.94485	65.1424	3.126	2.403	3.085			

Continued on Next Page...

Table I.1 – Continued

Name	RA	Dec	z_{em}	z_{min}	z_{max}	z_{abs}	$\log N(\mathrm{H\,I})$	$\epsilon[\log N(\mathrm{H\,I})]$
SDSS J124002.65+443206.1	190.01107	44.5350	3.029	2.681	2.989			
LBQS 1237+1515	190.01548	14.9852	2.040	1.634	2.009			
LBQS 1237+1508	190.04106	14.8617	2.070	1.634	2.035			
LBQS 1237+0107	190.04482	0.8581	1.810	1.733	1.780			
SDSS J1240+1455	190.08714	14.9266	3.107	2.309	3.066	3.0241	20.45	0.15
LBQS 1237+1212	190.08754	11.9277	2.310	1.634	2.281			
SDSS J124028.46+453356.5	190.11862	45.5657	3.250	2.653	3.208			
SDSS J124051.74+392327.0	190.21561	39.3908	2.845	2.451	2.806			
SDSS J124101.26+090829.7	190.25528	9.1416	3.096	2.694	3.055			
SDSS J124103.84+421405.1	190.26601	42.2348	3.192	2.763	3.150			
SDSS J124138.32+461717.0	190.40971	46.2881	2.770	2.384	2.732	2.6668	20.70	0.15
SDSS J124138.96+043719.2	190.41234	4.6220	3.754	3.310	3.706			
SDSS J124140.91+443932.8	190.42050	44.6591	3.175	2.812	3.134			
SDSS J124146.19+022806.3	190.44248	2.4685	2.884	2.307	2.845			
SDSS J124155.37+561322.9	190.48074	56.2230	2.925	2.307	2.886			
SDSS J124157.54+633241.6	190.48978	63.5449	2.624	2.307	2.588			
SDSS J124158.18+123059.3	190.49245	12.5165	2.971	2.564	2.931			
SDSS J124200.49+341454.3	190.50206	34.2484	2.943	2.307	2.903			
SDSS J124204.27+625712.1	190.51782	62.9534	3.321	2.904	3.278			
SDSS J124205.02+111250.8	190.52096	11.2141	2.827	2.522	2.789			
LBQS 1239+1435	190.52548	14.3225	1.930	1.634	1.900			
SDSS J124206.94+624438.0	190.52892	62.7439	3.042	2.867	3.002			
SDSS J124207.40-021727.7	190.53087	-2.2911	3.065	2.307	3.024			
B2 1239+37	190.54088	37.3349	3.819	2.836	3.771			
LBQS 1239+0249	190.58366	2.5493	2.220	1.719	2.184			
SDSS J124229.16+414938.6	190.62151	41.8274	3.083	2.406	3.042			
SDSS J124230.58+542257.3	190.62744	54.3826	4.730	4.495	4.672			
SDSS J124235.04+490536.0	190.64602	49.0934	2.837	2.444	2.799			
SDSS J124247.91+521306.8	190.69963	52.2186	5.036	4.093	4.935			
LBQS 1240+1516	190.72237	14.9977	2.280	1.634	2.247	1.7380	20.70	0.20
SDSS J124300.34+113554.6	190.75147	11.5985	2.940	2.585	2.901			
SDSS J124302.42+521009.8	190.76010	52.1694	2.557	2.307	2.521	2.5043	20.30	0.10
SDSS J124306.55+530522.0	190.77733	53.0895	3.566	2.371	3.521			
LBQS 1240+1504	190.80392	14.8034	1.850	1.634	1.823			
SDSS J124334.51+445141.3	190.89382	44.8615	2.365	2.307	2.332			
SDSS J124345.37-010322.3	190.93910	-1.0562	2.430	2.307	2.396			
SDSS J124351.48+453257.2	190.96453	45.5492	3.201	2.834	3.159			
SDSS J124359.55+633606.7	190.99818	63.6019	3.000	2.591	2.960			
SDSS J124400.04+553406.8	191.00023	55.5686	4.660	3.776	4.566			
SDSS J124426.82+671021.9	191.11181	67.1727	3.122	2.700	3.081			
SDSS J124451.43+141802.0	191.21436	14.3006	2.528	2.307	2.492			
SDSS J124454.77+645245.6	191.22824	64.8794	2.455	2.307	2.420			
SDSS J124456.12+601946.3	191.23389	60.3295	2.806	2.488	2.768			
SDSS J124456.98+620142.9	191.23747	62.0286	3.057	2.307	3.017			
SDSS J124504.98+510433.5	191.27077	51.0760	2.514	2.364	2.479			
SDSS J124508.06+532429.1	191.28363	53.4081	2.763	2.390	2.725			
SDSS J124515.46+382247.5	191.31446	38.3799	4.963	4.031	4.864	4.4470	20.80	0.20
LBQS 1242+0213	191.31859	1.9448	1.990	1.634	1.958			
LBQS 1242+1732	191.34863	17.2711	1.830	1.696	1.805			
LBQS 1242+0006	191.35250	-0.1606	2.080	1.634	2.045			
LBQS 1242+1737	191.36171	17.3481	1.860	1.634	1.828			
SDSS J124543.83+385430.3	191.43266	38.9084	2.543	2.307	2.507			
SDSS J124547.76+414334.7	191.44901	41.7263	2.906	2.307	2.867			
LBQS 1243+0121	191.46437	1.0847	2.809	2.432	2.727			
SDSS J124602.04+042658.4	191.50855	4.4496	2.439	2.307	2.405			
SDSS J124628.83+400839.5	191.62016	40.1443	2.368	2.307	2.334			
LBQS 1244+1129	191.66822	11.2175	3.148	2.307	3.106	3.0981	20.45	0.15
SDSS J124645.15+644036.0	191.68821	64.6767	3.622	3.432	3.539			
LBQS 1244+1642	191.69664	16.4373	2.870	1.848	2.826			
SDSS J124655.27+604330.6	191.73038	60.7252	3.331	2.467	3.287			
SDSS J124659.55+421735.4	191.74813	42.2932	3.149	2.446	3.108			
SDSS J124712.95+673009.9	191.80405	67.5028	3.112	2.307	3.070			
SDSS J124718.01+042714.5	191.82509	4.4541	3.718	3.333	3.671			
[HB89] 1244+347	191.84375	34.4575	2.480	1.640	2.446	1.8593	20.50	0.20
SDSS J124747.51+485417.2	191.94799	48.9048	2.930	2.541	2.848			
SDSS J124748.44+042627.0	191.95187	4.4409	2.783	2.397	2.745			
SDSS J124753.19-014712.2	191.97165	-1.7867	3.672	2.688	3.626			
SDSS J124812.40+554600.1	192.05168	55.7667	3.165	2.470	3.123			
SDSS J124820.21+311043.2	192.08423	31.1787	4.346	3.088	4.293	3.6970	20.35	0.10
SDSS J124830.64+491400.2	192.12768	49.2334	3.073	2.898	3.032			
SDSS J124831.65+580928.8	192.13191	58.1580	2.593	2.307	2.557			
SDSS J124834.71+463917.2	192.14466	46.6548	3.237	2.348	3.195			

Continued on Next Page...

Table I.1 – Continued

Name	RA	Dec	z_{em}	z_{min}	z_{max}	z_{abs}	$\log N(\mathrm{H\,I})$	$\epsilon[\log N(\mathrm{H\,I})]$
SDSS J124836.80+474034.7	192.15338	47.6763	2.701	2.322	2.664			
SDSS J124837.31+130440.9	192.15548	13.0780	3.721	2.315	3.674			
LBQS 1246-0059	192.16701	-1.2600	2.450	1.669	2.415			
SDSS J124845.63+520247.1	192.19016	52.0464	2.344	2.307	2.311			
SDSS J124847.29+492008.2	192.19708	49.3356	3.837	2.740	3.788			
LBQS 1246+0032	192.24861	0.2626	2.310	1.651	2.273			
SDSS J124924.36+592932.2	192.35151	59.4923	2.609	2.307	2.573			
LBQS 1246-0217	192.35361	-2.5610	2.110	1.634	2.075	1.7790	21.20	0.20
SDSS J124935.53+132941.1	192.39807	13.4948	2.642	2.307	2.606			
SDSS J124942.12+334953.8	192.42552	33.8316	4.897	3.314	4.838			
SDSS J124943.67+152707.0	192.43197	15.4520	3.995	3.132	3.945			
SDSS J124957.23-015928.8	192.48850	-1.9913	3.629	2.406	3.583			
SDSS J125013.96+114105.7	192.55818	11.6849	2.406	2.307	2.372			
SDSS J125025.40+183458.1	192.60588	18.5828	4.557	3.689	4.464			
SDSS J125032.99+484630.8	192.63747	48.7752	2.587	2.400	2.551			
SDSS J125041.31+031619.2	192.67213	3.2720	3.550	3.116	3.468			
SDSS J125049.57+475011.7	192.70658	47.8366	3.136	2.713	3.095			
SDSS J125050.39+144805.0	192.71000	14.8014	4.052	3.013	4.001			
SDSS J125118.67+130825.3	192.82783	13.1404	3.398	2.658	3.354			
SDSS J125125.36+412000.4	192.85568	41.3335	3.173	2.344	3.132	2.7304	21.00	0.20
SDSS J125131.72+661627.1	192.88218	66.2742	3.019	2.607	2.979	2.7773	20.45	0.15
SDSS J125143.16+000725.8	192.92987	0.1239	2.955	2.307	2.916			
SDSS J125200.35+450005.2	193.00150	45.0015	2.439	2.307	2.404			
SDSS J125206.16+553603.0	193.02568	55.6009	2.529	2.410	2.494			
SDSS J125226.88+455747.3	193.11201	45.9632	3.237	2.828	3.194			
SDSS J125227.28+001001.9	193.11368	0.1672	3.555	2.858	3.510			
SDSS J125241.54-002040.5	193.17313	-0.3446	2.891	2.506	2.809			
SDSS J125304.33+550108.3	193.26806	55.0190	2.899	2.307	2.860	2.7245	20.55	0.20
SDSS J125305.01+453333.6	193.27091	45.5594	2.448	2.307	2.414			
SDSS J125306.73+130604.9	193.27806	13.1014	3.625	2.544	3.579	2.9818	20.50	0.15
SDSS J125316.09+114720.6	193.31705	11.7891	3.284	2.307	3.242	2.9441	20.35	0.15
SDSS J125319.10+454152.8	193.32961	45.6980	3.526	3.037	3.369			
B3 1251+468	193.33505	46.5639	2.452	2.307	2.418			
SDSS J125328.10+494751.0	193.36711	49.7975	3.575	2.362	3.529	2.9160	20.65	0.15
SDSS J125329.98+000730.1	193.37495	0.1250	2.694	2.345	2.657			
SDSS J125333.31+050705.2	193.38882	5.1181	3.102	2.709	3.061			
SDSS J125336.35-022807.7	193.40147	-2.4688	4.007	2.868	3.957			
SDSS J125345.48+051611.2	193.43954	5.2698	2.396	2.307	2.362			
SDSS J125353.35+104603.1	193.47230	10.7675	4.918	3.993	4.819			
SDSS J1253+6817	193.47378	68.2873	3.473	2.446	3.428			
SDSS J125356.90+111355.3	193.48711	11.2320	3.009	2.648	2.969	2.8095	20.65	0.20
SDSS J125418.97+534852.3	193.57905	53.8145	2.478	2.307	2.444			
SDSS J125426.69+412715.4	193.61125	41.4543	3.317	2.939	3.274			
SDSS J125430.36+450935.3	193.62655	45.1598	2.608	2.307	2.572			
SDSS J125438.40+043010.9	193.66002	4.5030	2.466	2.307	2.431			
SDSS J125444.69+140046.7	193.68625	14.0130	3.820	2.983	3.772			
UM 524	193.72833	1.0022	2.389	2.307	2.355			
SDSS J125525.66+030518.4	193.85696	3.0885	2.530	2.307	2.448			
SDSS J125526.36+613121.2	193.85986	61.5226	2.970	2.823	2.930			
SDSS J125526.52+334821.4	193.86052	33.8060	3.402	3.027	3.358			
SDSS J125537.33+520220.9	193.90556	52.0392	2.518	2.307	2.483			
SDSS J125620.41+144216.5	194.08507	14.7046	2.500	2.307	2.465			
SDSS J125623.55+503350.1	194.09821	50.5639	2.567	2.307	2.531			
SDSS J125630.27+054439.1	194.12613	5.7442	3.258	2.880	3.215			
SDSS J125644.97+510710.1	194.18744	51.1195	2.588	2.542	2.552			
SDSS J125648.84+042051.0	194.20354	4.3475	2.655	2.307	2.619			
SDSS J125650.35+041323.9	194.20981	4.2233	3.139	2.738	3.098	3.0232	20.95	0.20
SDSS J125659.47+301439.0	194.24783	30.2442	2.946	2.307	2.906	2.8809	20.70	0.15
SDSS J125659.79-033813.8	194.24914	-3.6372	2.974	2.596	2.935			
SDSS J125704.11+341920.8	194.26714	34.3225	3.133	2.496	3.092			
SDSS J125705.89+530213.2	194.27458	53.0370	2.892	2.803	2.853			
SDSS J125716.01+481948.4	194.31675	48.3301	4.591	4.094	4.536			
SDSS J125718.02+374729.9	194.32513	37.7916	4.733	3.837	4.637			
SDSS J125720.18+490158.4	194.33411	49.0329	2.388	2.307	2.354			
SDSS J125726.27+345410.7	194.35950	34.9030	3.167	2.307	3.126			
SDSS J125743.51+341520.9	194.43133	34.2558	3.787	3.027	3.739	3.3393	20.40	0.20
SDSS J125743.93+535942.1	194.43308	53.9950	2.376	2.307	2.343			
SDSS J125759.21-011130.2	194.49675	-1.1918	4.112	2.999	4.061	4.0215	20.30	0.15
SDSS J125759.76+120103.9	194.49902	12.0177	3.122	2.715	3.040			
SDSS J125824.56-033140.6	194.60236	-3.5280	2.376	2.328	2.342			
SDSS J125825.08+044129.3	194.60450	4.6915	2.427	2.307	2.393			
SDSS J125826.44+403029.0	194.61019	40.5081	2.759	2.374	2.721			

Continued on Next Page...

Table I.1 – Continued

Name	RA	Dec	z_{em}	z_{min}	z_{max}	z_{abs}	$\log N(\mathrm{H\,I})$	$\epsilon[\log N(\mathrm{H\,I})]$
SDSS J125832.14+290903.0	194.63395	29.1508	3.483	2.584	3.438	3.1736	21.35	0.15
						3.3515	20.55	0.15
SDSS J125837.61-013033.6	194.65674	-1.5094	2.837	2.507	2.799			
SDSS J125838.94+633332.9	194.66232	63.5592	2.931	2.529	2.892			
SDSS J125841.50+623912.4	194.67295	62.6534	3.325	2.356	3.281			
SDSS J125847.60+543811.7	194.69835	54.6366	3.807	2.901	3.759			
SDSS J125850.56+622851.6	194.71067	62.4811	2.781	2.394	2.744	2.6568	20.60	0.15
SDSS J125853.64+435541.4	194.72354	43.9282	2.560	2.307	2.524			
SDSS J125854.73+340557.9	194.72809	34.0994	2.857	2.307	2.818			
SDSS J125903.25+621211.6	194.76356	62.2032	3.240	2.820	3.158			
SDSS J125906.79+342529.9	194.77831	34.4250	2.760	2.419	2.722			
SDSS J125914.83+672011.8	194.81185	67.3366	2.442	2.307	2.408			
SDSS J125938.09+675039.5	194.90880	67.8443	2.494	2.327	2.460			
SDSS J125948.77+635536.9	194.95325	63.9269	3.114	2.484	3.073			
SDSS J125954.26-022153.9	194.97612	-2.3650	2.351	2.307	2.317			
SDSS J130002.16+011823.0	195.00902	1.3064	4.619	3.741	4.525			
SDSS J130011.30+405434.6	195.04711	40.9096	2.949	2.326	2.910			
SDSS J130022.57+490929.0	195.09408	49.1581	2.434	2.307	2.400			
SDSS J130024.29+290147.5	195.10123	29.0299	3.946	3.033	3.896			
SDSS J130035.29-003928.2	195.14705	-0.6579	3.626	3.169	3.544			
SDSS J130039.20+413331.2	195.16336	41.5587	3.234	2.459	3.192			
SDSS J130047.83+475439.3	195.19932	47.9109	3.941	3.170	3.892			
SDSS J130055.01+454535.9	195.22922	45.7600	4.041	3.064	3.991			
SDSS J130055.67+055620.5	195.23198	5.9391	2.434	2.307	2.400			
SDSS J130108.90+022152.3	195.28715	2.3645	2.641	2.486	2.605			
SDSS J130110.95+252738.3	195.29567	25.4607	4.666	3.781	4.572			
SDSS J130118.31+445350.2	195.32632	44.8973	3.669	2.738	3.622			
SDSS J130124.46-015407.4	195.35193	-1.9021	3.013	2.707	2.973			
SDSS J130129.43+045613.6	195.37266	4.9371	3.264	2.880	3.221			
SDSS J130134.24+323608.4	195.39270	32.6023	3.216	2.307	3.173			
SDSS J130137.24+124605.0	195.40519	12.7681	4.104	3.034	4.053			
SDSS J130149.12+454526.3	195.45467	45.7573	2.979	2.403	2.939			
SDSS J130149.48+044023.4	195.45618	4.6732	4.071	3.570	3.989			
SDSS J130149.86-033031.3	195.45776	-3.5087	2.393	2.307	2.360			
SDSS J130150.33+535432.3	195.45972	53.9090	3.673	2.756	3.626			
SDSS J130152.55+221012.1	195.46899	22.1700	4.805	3.898	4.708	4.2130	20.50	0.20
SDSS J130152.57-030729.3	195.46906	-3.1248	3.071	2.307	3.030			
SDSS J130208.16-033710.5	195.53404	-3.6196	3.718	3.061	3.671	3.4668	20.95	0.15
SDSS J130209.30+134519.9	195.53877	13.7555	3.298	2.926	3.255			
SDSS J130215.71+550553.5	195.56553	55.0982	4.461	3.608	4.370			
SDSS J130221.80-004638.1	195.59085	-0.7773	2.704	2.520	2.667			
[HB89] 1300+345	195.59169	34.2835	2.899	2.308	2.860			
SDSS J130222.86+284411.3	195.59531	28.7365	2.540	2.307	2.504			
SDSS J130227.52+445617.7	195.61468	44.9383	3.619	2.546	3.573			
SDSS J130234.33+572103.7	195.64307	57.3510	3.112	2.705	3.029			
SDSS J130238.90-013732.8	195.66212	-1.6258	2.499	2.307	2.464			
SDSS J130240.16+025457.6	195.66734	2.9160	2.415	2.307	2.380			
SDSS J130245.79+300232.8	195.69084	30.0424	3.477	2.738	3.432			
SDSS J130245.89+652028.0	195.69123	65.3411	3.068	2.652	3.027			
B2 1300+39	195.70065	39.5006	2.443	2.307	2.408			
SDSS J130255.09+465522.0	195.72957	46.9228	3.161	2.337	3.119			
SDSS J130259.60+433504.5	195.74835	43.5846	3.909	3.031	3.860	3.3097	21.55	0.15
						3.3462	20.35	0.25
						3.7554	21.05	0.15
SDSS J130304.24+450929.3	195.76770	45.1582	3.045	2.692	3.004			
SDSS J130309.57+595123.3	195.78989	59.8565	2.355	2.307	2.322			
SDSS J130326.77+603045.0	195.86160	60.5125	3.176	2.307	3.134			
SDSS J130334.92+575118.9	195.89551	57.8552	2.588	2.307	2.552			
SDSS J130348.94+002010.4	195.95392	0.3362	3.647	3.210	3.565			
SDSS J130355.12+445925.1	195.97971	44.9903	4.020	3.515	3.970			
SDSS J130420.71-020302.9	196.08633	-2.0508	3.086	2.430	3.045			
SDSS J130421.40+634114.4	196.08925	63.6873	2.638	2.323	2.601			
SDSS J130421.54+031138.1	196.08978	3.1939	2.552	2.308	2.470			
SDSS J130423.24+340438.0	196.09685	34.0772	2.559	2.307	2.524			
SDSS J130424.00-003757.1	196.10001	-0.6325	3.029	2.355	2.988			
SDSS J130426.14+120245.5	196.10896	12.0460	2.977	2.307	2.938	2.9139	20.55	0.15
						2.9284	20.35	0.15
SDSS J130439.03+341213.7	196.16265	34.2038	3.154	2.571	3.113			
SDSS J130448.83+121736.8	196.20350	12.2936	3.120	2.460	3.078			
SDSS J130452.57+023924.8	196.21906	2.6569	3.648	2.257	3.602			
SDSS J130456.80+654516.5	196.23670	65.7546	2.619	2.307	2.583			
SDSS J130458.40+384941.4	196.24335	38.8282	3.176	2.750	3.134	3.1143	20.30	0.15

Continued on Next Page...

Table I.1 – Continued

Name	RA	Dec	z_{em}	z_{min}	z_{max}	z_{abs}	$\log N(\mathrm{H\,I})$	$\epsilon[\log N(\mathrm{H\,I})]$
SDSS J130501.20+343927.5	196.25504	34.6577	2.943	2.577	2.904			
SDSS J130501.32+472824.1	196.25555	47.4734	3.560	2.790	3.514			
SDSS J130502.28+052151.1	196.25951	5.3642	4.086	3.208	4.035	3.6415	20.30	0.20
						3.6790	21.10	0.20
SDSS J130502.66+112302.4	196.26110	11.3840	3.197	2.774	3.155			
SDSS J130508.36+140418.6	196.28485	14.0718	2.387	2.307	2.353			
SDSS J130509.55+412540.5	196.28980	41.4279	3.025	2.384	2.985			
SDSS J130511.63-014244.8	196.29849	-1.7125	3.640	2.965	3.594			
SDSS J130520.01+572950.7	196.33343	57.4974	3.043	2.693	3.003			
SDSS J130529.96+581724.8	196.37486	58.2902	3.000	2.663	2.960			
SDSS J130532.94+325518.1	196.38731	32.9217	2.468	2.307	2.386			
SDSS J130534.02+611754.0	196.39175	61.2983	2.353	2.307	2.319			
SDSS J130544.59+152604.9	196.43582	15.4347	3.140	2.783	3.099	2.9759	20.40	0.15
SDSS J130548.92+290228.1	196.45387	29.0411	2.585	2.307	2.550	2.3855	20.30	0.20
SDSS J130600.05+293335.8	196.50021	29.5600	4.090	3.212	4.039			
SDSS J130618.60+151017.8	196.57753	15.1716	2.388	2.307	2.354			
SDSS J130619.38+023658.9	196.58079	2.6164	4.860	3.944	4.762			
SDSS J130621.12+414234.8	196.58802	41.7097	2.941	2.772	2.901			
SDSS J130629.95+474132.3	196.62479	47.6923	2.523	2.307	2.488			
SDSS J130630.95-002451.9	196.62896	-0.4144	3.055	2.307	3.015			
SDSS J130631.02+133732.2	196.62927	13.6256	2.480	2.307	2.445			
SDSS J130634.60+523250.2	196.64421	52.5473	2.569	2.307	2.533			
SDSS J130643.05-013552.6	196.67941	-1.5980	2.942	2.307	2.903	2.7730	20.60	0.15
SDSS J130709.85+644817.7	196.79117	64.8049	2.431	2.307	2.397			
SDSS J130710.25+123021.6	196.79272	12.5060	3.210	2.307	3.168			
SDSS J130719.29+115218.8	196.83041	11.8719	2.895	2.564	2.856	2.7739	20.50	0.20
SDSS J130723.68+582950.1	196.84872	58.4973	3.079	2.669	3.038			
SDSS J130723.77+390858.7	196.84907	39.1497	3.254	2.332	3.212			
SDSS J130738.83+150752.0	196.91180	15.1311	4.082	3.285	4.031			
SDSS J130746.50+005055.9	196.94376	0.8489	2.460	2.307	2.426			
SDSS J130749.87+580451.5	196.95782	58.0810	2.744	2.557	2.706			
SDSS J130750.24-020340.7	196.95938	-2.0613	2.769	2.384	2.732			
SDSS J130756.73+042215.5	196.98639	4.3710	3.022	2.307	2.982			
SDSS J130800.35+630240.5	197.00148	63.0446	3.119	2.510	3.078			
SDSS J130807.61+154519.4	197.03174	15.7554	2.428	2.307	2.394			
SDSS J130828.42+584000.5	197.11845	58.6668	3.092	2.387	3.051			
SDSS J130900.50+504101.5	197.25209	50.6838	2.805	2.439	2.767			
SDSS J130907.92+025432.6	197.28304	2.9091	2.940	2.307	2.901			
SDSS J130917.12+165758.5	197.32138	16.9662	4.714	3.821	4.619	3.9370	21.10	0.20
SDSS J130918.11+402918.4	197.32550	40.4885	3.420	2.599	3.376	3.0109	21.35	0.20
SDSS J130928.82+473131.9	197.37012	47.5255	3.015	2.307	2.975	2.8876	20.95	0.15
SDSS J130931.03+051745.3	197.37931	5.2959	3.077	2.384	3.036			
SDSS J130932.96+634318.5	197.38735	63.7218	3.142	2.731	3.059			
SDSS J130934.18-033318.4	197.39246	-3.5551	2.781	2.658	2.743			
SDSS J130940.60+031826.7	197.41921	3.3074	2.755	2.480	2.718			
SDSS J130940.65+571057.5	197.41940	57.1827	3.450	2.582	3.405			
SDSS J130941.51+404757.1	197.42296	40.7992	2.910	2.338	2.871			
SDSS J130942.14-022652.2	197.42564	-2.4479	2.579	2.307	2.543			
SDSS J130948.55+534634.7	197.45238	53.7763	2.436	2.307	2.402			
SDSS J130949.70+124354.5	197.45713	12.7318	2.420	2.307	2.386			
SDSS J130950.07+591423.3	197.45865	59.2398	3.012	2.616	2.972			
SDSS J131003.34+535348.2	197.51398	53.8967	3.278	2.866	3.235			
SDSS J131007.14+143503.9	197.52978	14.5845	3.757	3.095	3.709			
SDSS J131018.11+060152.9	197.57547	6.0314	4.227	3.125	4.174			
BR J1310-1740	197.61092	-17.6746	4.185	2.508	4.133			
SDSS J131034.74+041648.5	197.64477	4.2801	2.399	2.307	2.365			
SDSS J131052.50-005533.2	197.71879	-0.9259	4.152	2.830	4.101			
SDSS J131052.54+613503.1	197.71897	61.5842	2.953	2.307	2.913			
SDSS J131054.23+510839.0	197.72599	51.1442	3.042	2.693	3.001			
SBS 1308+512	197.77299	51.0106	3.148	2.307	3.107			
LBQS 1308-0214	197.81212	-2.5126	2.880	2.307	2.841			
SDSS J131116.42+593505.6	197.81844	59.5849	2.577	2.307	2.542			
LBQS 1308-0104	197.83020	-1.3419	2.590	1.634	2.549			
SDSS J131123.09+453159.4	197.84623	45.5332	2.403	2.307	2.369			
LBQS 1308+0105	197.86816	0.8249	2.809	2.307	2.771			
SDSS J131140.25+560416.9	197.91776	56.0714	3.676	2.905	3.629	3.2457	20.80	0.15
SDSS J131142.63+555737.7	197.92766	55.9605	3.754	3.283	3.672			
SDSS J131152.08+472135.2	197.96702	47.3598	2.423	2.307	2.389			
SDSS J131213.83+000002.9	198.05767	0.0008	2.679	2.350	2.597			
SDSS J131215.22+423900.8	198.06362	42.6502	2.567	2.307	2.531			
SDSS J131227.68+151849.0	198.11536	15.3136	3.653	2.772	3.606			
SDSS J131234.08+230716.3	198.14202	23.1212	4.960	4.029	4.861			

Continued on Next Page...

Table I.1 – Continued

Name	RA	Dec	z_{em}	z_{min}	z_{max}	z_{abs}	$\log N(\mathrm{H\,I})$	$\epsilon[\log N(\mathrm{H\,I})]$
SDSS J131242.87+084105.1	198.17863	8.6847	3.731	2.027	3.684	2.6600	20.50	0.10
SDSS J131252.22+422818.7	198.21752	42.4721	3.134	2.313	3.092			
SDSS J131256.89+042827.3	198.23708	4.4742	2.403	2.307	2.369			
SDSS J131300.90+604309.5	198.25376	60.7193	3.553	2.576	3.508			
SDSS J131304.10+114923.0	198.26712	11.8231	2.448	2.307	2.413			
SDSS J131321.14+143441.0	198.33812	14.5781	3.614	2.908	3.568			
SDSS J131346.72+393604.7	198.44470	39.6013	3.439	2.514	3.395			
SDSS J131412.28+511512.5	198.55119	51.2535	2.567	2.307	2.531			
SDSS J131415.48+111820.4	198.56453	11.3057	3.374	2.706	3.330			
SDSS J131420.35+471321.2	198.58481	47.2226	3.105	2.784	3.064			
SDSS J131429.00+494149.0	198.62086	49.6970	3.813	2.835	3.765	3.0261	20.55	0.15
SDSS J131429.24+621300.1	198.62191	62.2166	3.138	2.731	3.096			
SDSS J131432.95+520212.3	198.63731	52.0368	2.493	2.307	2.458			
[HB89] 1312+043	198.69440	4.1026	2.350	1.813	2.319			
SDSS J131504.49+500239.5	198.76875	50.0443	3.288	2.864	3.206			
SDSS J131511.59+472517.1	198.79830	47.4214	2.375	2.307	2.341			
SDSS J131518.07+570012.6	198.82533	57.0035	2.591	2.307	2.555			
SDSS J131520.31+523629.4	198.83468	52.6082	3.200	2.384	3.158			
SDSS J1315+4856	198.90239	48.9414	3.618	3.211	3.572			
SDSS J131538.36+025311.8	198.90986	2.8866	2.955	2.307	2.916			
SDSS J131549.22+133845.7	198.95509	13.6461	3.776	3.303	3.693			
SDSS J131550.42+463537.3	198.96009	46.5937	2.980	2.307	2.941			
SDSS J131610.70+124150.3	199.04463	12.6973	2.351	2.307	2.317			
SDSS J131618.38+045400.9	199.07661	4.9003	3.976	3.494	3.926			
SDSS J131623.99-015834.9	199.09999	-1.9764	3.004	2.372	2.964			
SDSS J131625.40+124411.8	199.10585	12.7366	3.094	2.415	3.053			
LBQS 1313+0107	199.12693	0.8571	2.403	2.307	2.369			
SDSS J131640.04+105856.8	199.16685	10.9825	3.383	2.951	3.340			
SDSS J131642.99+043058.0	199.17917	4.5161	3.824	3.062	3.776			
SDSS J131643.59+130927.6	199.18166	13.1577	3.795	2.316	3.747			
SDSS J131703.31+621940.0	199.26384	62.3278	3.987	3.108	3.937			
LBQS 1314+0116	199.30924	1.0036	2.698	2.333	2.616	2.5381	21.55	0.15
SDSS J131715.49+051802.5	199.31459	5.3007	2.539	2.307	2.504			
SDSS J131728.65+060046.5	199.36939	6.0129	2.609	2.307	2.573			
SDSS J131743.12+353131.8	199.42971	35.5255	4.369	2.998	4.315			
SDSS J131745.83+563148.0	199.44098	56.5300	3.158	2.533	3.117			
SDSS J131757.98+044922.9	199.49161	4.8230	2.680	2.307	2.643			
[HB89] 1315+473	199.50783	47.1078	2.594	2.307	2.558			
SDSS J131806.83+134858.2	199.52849	13.8162	3.043	2.307	3.002			
SDSS J131815.18+424556.4	199.56327	42.7657	2.454	2.307	2.419			
SDSS J131821.04+413254.2	199.58769	41.5484	3.479	2.794	3.434	2.9474	20.55	0.20
SDSS J131848.56+280616.0	199.70236	28.1045	3.354	2.908	3.311			
SDSS J131849.25+494606.5	199.70526	49.7685	3.126	2.321	3.085			
SDSS J131904.22+051606.8	199.76762	5.2686	3.453	2.636	3.408			
SDSS J131907.48+621721.3	199.78119	62.2893	3.074	2.315	3.033			
SDSS J131912.15+290501.3	199.80064	29.0837	4.044	3.205	3.994			
SDSS J131912.39+534720.5	199.80167	53.7891	3.091	2.686	3.009			
SDSS J131914.20+520200.0	199.80919	52.0334	3.899	2.307	3.850			
SDSS J131917.78+441201.3	199.82412	44.2004	3.909	3.087	3.860			
SDSS J131926.27+143439.9	199.85948	14.5778	2.541	2.307	2.506			
SDSS J131927.57+445656.5	199.86488	44.9490	2.978	2.307	2.938			
SDSS J131929.50+571307.8	199.87296	57.2188	2.577	2.307	2.541			
SDSS J131938.89+530353.3	199.91212	53.0648	3.087	2.307	3.046			
SDSS J131946.79-024926.4	199.94499	-2.8240	3.065	2.411	3.024			
SDSS J132005.97+131015.3	200.02488	13.1709	3.352	2.534	3.308	2.6727	20.30	0.20
						3.0040	20.60	0.15
SDSS J132009.70+505058.4	200.04045	50.8496	3.818	3.032	3.770	3.2062	20.30	0.20
SDSS J132012.88+132409.4	200.05370	13.4026	2.870	2.593	2.831			
SDSS J132022.29+423308.9	200.09290	42.5525	2.403	2.307	2.369			
SDSS J132027.63+320109.9	200.11515	32.0194	3.215	2.384	3.173			
2MASSi J1320299-052335	200.12458	-5.3931	3.717	1.904	3.670			
SDSS J132045.49+025016.0	200.18956	2.8378	3.025	2.367	2.985			
[HB89] 1318-113	200.28908	-11.6588	2.308	1.896	2.273			
SDSS J132110.16+502202.4	200.29237	50.3674	3.702	3.319	3.620			
SDSS J132115.66+495546.3	200.31525	49.9295	2.442	2.307	2.408			
SDSS J132120.27+153611.3	200.33449	15.6032	2.593	2.307	2.557			
SDSS J132124.64+393829.9	200.35269	39.6417	2.381	2.307	2.347			
LBQS 1318-0150	200.36618	-2.1063	2.010	1.651	1.980			
SDSS J132145.91+380045.1	200.44132	38.0125	3.717	3.317	3.670			
SDSS J132156.47+115714.9	200.48531	11.9542	3.329	2.604	3.286			
SDSS J132201.50+492237.6	200.50631	49.3771	2.942	2.323	2.903	2.5441	20.80	0.15
						2.5786	21.20	0.15

Continued on Next Page...

Table I.1 – Continued

Name	RA	Dec	z_{em}	z_{min}	z_{max}	z_{abs}	$\log N(\mathrm{H\,I})$	$\epsilon[\log N(\mathrm{H\,I})]$
SDSS J132205.63+494352.0	200.52350	49.7311	3.234	2.858	3.191			
SDSS J132225.48+412220.2	200.60619	41.3723	2.394	2.307	2.360			
SDSS J132228.10+394804.4	200.61711	39.8012	2.915	2.760	2.876			
SDSS J132235.12+584124.6	200.64635	58.6902	2.851	2.307	2.812			
SDSS J132240.25+322754.2	200.66774	32.4651	2.539	2.307	2.504			
SDSS J132245.74+553138.1	200.69060	55.5273	3.785	3.442	3.737			
SDSS J132249.36+571100.7	200.70570	57.1835	2.463	2.307	2.428			
FBQS J132255.6+391207	200.73193	39.2022	2.985	2.307	2.945			
SDSS J132259.97+395529.9	200.74988	39.9250	2.898	2.307	2.859			
SDSS J132300.27+113855.0	200.75116	11.6486	3.110	2.307	3.069			
SDSS J132312.83+414933.0	200.80349	41.8259	2.447	2.307	2.412			
LBQS 1320+0048	200.81042	0.5475	1.960	1.655	1.925			
SDSS J132322.75+513730.6	200.84481	51.6252	2.910	2.332	2.871			
SDSS J132332.02+533812.7	200.88345	53.6369	2.424	2.307	2.390			
SDSS J132336.47+282350.1	200.90197	28.3973	3.424	2.523	3.380			
SDSS J132346.05+140517.6	200.94189	14.0882	4.054	2.241	4.004			
SDSS J132359.76+451518.3	200.99901	45.2551	2.360	2.307	2.326			
SDSS J132406.42+470543.2	201.02678	47.0954	2.449	2.307	2.415			
SDSS J132417.33+440300.0	201.07222	44.0500	3.286	2.358	3.243			
SDSS J132420.83+422554.5	201.08682	42.4318	4.036	2.922	3.986			
SDSS J132423.25+623342.0	201.09692	62.5617	3.634	3.176	3.552			
SDSS J132435.71+485533.8	201.14880	48.9261	2.434	2.307	2.400			
SDSS J132505.15+493430.5	201.27150	49.5752	3.575	2.810	3.529			
SDSS J132512.49+112329.7	201.30206	11.3916	4.400	3.017	4.346			
SDSS J132521.27+524513.0	201.33866	52.7537	3.953	3.445	3.903			
SDSS J132521.64+033335.7	201.34020	3.5599	4.012	2.884	3.962			
SDSS J132552.17+663405.7	201.46741	66.5683	2.511	2.307	2.476			
SDSS J132554.11+125546.5	201.47550	12.9296	4.140	3.132	4.089	3.5497	20.40	0.20
SDSS J132600.07+612822.5	201.50031	61.4729	2.966	2.583	2.926			
SDSS J132601.21-014128.6	201.50506	-1.6913	2.865	2.307	2.827			
SDSS J132605.10+491448.4	201.52125	49.2468	3.234	2.387	3.192			
SDSS J132611.85+074358.4	201.54945	7.7329	4.123	2.866	4.072			
LBQS 1323-0248	201.56319	-3.0660	2.120	1.661	2.090			
SDSS J132626.21+042654.3	201.60921	4.4484	2.788	2.400	2.750			
SDSS J132632.31+035127.9	201.63466	3.8578	3.273	2.905	3.230			
SDSS J132633.64+531753.7	201.64021	53.2983	3.649	3.438	3.603			
SDSS J132634.07+055911.5	201.64197	5.9865	3.012	2.603	2.972			
LBQS 1324-0212	201.65897	-2.4668	1.890	1.634	1.857			
SDSS J132649.16+381152.2	201.70484	38.1979	3.429	2.990	3.384			
SDSS J132659.23+541349.7	201.74683	54.2305	3.142	2.317	3.101			
SDSS J132700.15+443356.2	201.75066	44.5656	2.992	2.369	2.952			
SDSS J132703.21+031311.2	201.76342	3.2198	2.827	2.448	2.745			
SDSS J132703.26+341321.7	201.76360	34.2227	2.557	2.307	2.521			
SDSS J132706.22+381539.8	201.77593	38.2611	3.038	2.625	2.998			
SDSS J132707.05+313838.6	201.77941	31.6441	2.806	2.307	2.768			
SDSS J132708.44+022001.6	201.78518	2.3338	2.552	2.307	2.517			
SDSS J132725.57+294530.3	201.85659	29.7584	3.131	2.429	3.090			
SDSS J132729.74+484500.9	201.87395	48.7503	3.140	2.495	3.099	2.6082	20.35	0.20
LBQS 1325+0027	201.96020	0.1991	2.524	2.307	2.442			
SDSS J132753.04+334000.0	201.97100	33.6667	3.516	3.054	3.471			
SDSS J132820.18+301245.0	202.08409	30.2125	3.366	2.920	3.322			
SDSS J132827.06+581836.8	202.11282	58.3103	3.140	2.730	3.058			
SDSS J132833.20+442720.9	202.13838	44.4558	2.440	2.351	2.406			
SDSS J132833.99+051546.4	202.14167	5.2629	2.422	2.307	2.388			
SDSS J132837.10+275611.2	202.15462	27.9365	3.688	2.611	3.641			
SDSS J132839.57+435953.0	202.16488	43.9981	3.046	2.631	3.005	2.8803	20.75	0.15
SDSS J132844.32-022409.2	202.18470	-2.4026	3.640	2.763	3.593	2.8913	20.35	0.20
SDSS J132845.00+510225.8	202.18754	51.0405	3.410	2.461	3.365			
SDSS J132905.54+600445.2	202.27311	60.0792	3.677	2.653	3.630			
SDSS J132914.15+553740.2	202.30898	55.6278	3.171	2.397	3.130			
SDSS J132914.32+410727.9	202.30968	41.1244	3.891	3.065	3.842			
SDSS J132924.79+044915.5	202.35332	4.8210	2.820	2.442	2.738			
SDSS J132930.65+521114.2	202.37771	52.1873	3.100	2.533	3.059			
SDSS J132938.94+401708.5	202.41229	40.2857	3.716	2.752	3.669			
SDSS J132945.03+283902.5	202.43765	28.6507	2.912	2.512	2.873	2.8334	20.85	0.15
SDSS J133000.93+651947.9	202.50390	65.3300	3.274	2.407	3.231	2.9513	20.80	0.15
SDSS J133002.50+510303.6	202.51046	51.0510	2.925	2.536	2.843			
SDSS J133022.76+281333.1	202.59486	28.2259	3.320	2.592	3.277			
SDSS J133027.05+280134.5	202.61274	28.0263	3.765	2.963	3.717			
SDSS J133027.55+541237.9	202.61483	54.2106	3.235	2.597	3.193			
SDSS J133029.38+495427.4	202.62245	49.9076	2.839	2.307	2.801			
SDSS J133030.25+492718.6	202.62608	49.4552	3.830	3.028	3.782			

Continued on Next Page...

Table I.1 – Continued

Name	RA	Dec	z_{em}	z_{min}	z_{max}	z_{abs}	$\log N(\mathrm{H\,I})$	$\epsilon[\log N(\mathrm{H\,I})]$
SDSS J133031.21+515036.3	202.63007	51.8434	3.170	2.524	3.128			
SDSS J133042.51-011927.4	202.67715	-1.3243	3.443	2.587	3.399			
SDSS J133044.99+044430.5	202.68747	4.7418	2.956	2.552	2.917			
SDSS J133045.19+623412.5	202.68838	62.5701	3.517	2.815	3.472			
LBQS 1328+0223	202.70186	2.1308	2.150	1.937	2.122			
SDSS J133048.68+034032.0	202.70285	3.6756	2.822	2.307	2.784	2.3226	21.50	0.15
SDSS J133050.47+465204.2	202.71031	46.8678	2.935	2.533	2.896			
BR J1330-2522	202.71658	-25.3719	3.948	2.282	3.899			
SDSS J133052.96+525513.5	202.72070	52.9204	2.520	2.318	2.485			
SDSS J133055.02-030535.0	202.72926	-3.0931	2.964	2.390	2.925			
SDSS J133110.22+281616.8	202.79260	28.2714	2.662	2.307	2.626			
SDSS J133115.56-023407.5	202.81487	-2.5688	2.421	2.327	2.386			
SDSS J133117.96+510425.2	202.82486	51.0737	3.210	2.554	3.168			
SDSS J133122.92+410859.5	202.84555	41.1499	2.475	2.307	2.441			
SDSS J133124.73+665812.5	202.85307	66.9702	2.675	2.345	2.639			
SDSS J133125.63+283641.1	202.85681	28.6114	3.415	2.496	3.371			
BRI 1328-0433	202.87861	-4.8143	4.217	2.240	4.165			
SDSS J133138.49+004221.1	202.91042	0.7059	2.429	2.307	2.395			
SDSS J133139.90+312757.7	202.91645	31.4660	3.022	2.307	2.981			
SDSS J133144.06+050954.3	202.93360	5.1651	2.610	2.307	2.574			
SDSS J133146.20+483826.3	202.94254	48.6406	3.734	2.815	3.686	3.2402	20.95	0.20
SDSS J133147.31+640129.1	202.94719	64.0248	2.612	2.307	2.576			
SDSS J133150.37+511046.3	202.95991	51.1795	2.387	2.307	2.353			
SDSS J133150.69+101529.4	202.96125	10.2582	3.852	2.323	3.804			
LBQS 1329+0231	203.01060	2.2645	2.442	2.307	2.407			
SDSS J133202.81+531044.8	203.01175	53.1791	3.307	2.470	3.264			
SDSS J133203.86+553105.0	203.01613	55.5181	4.737	3.841	4.641			
SDSS J133204.68+535922.6	203.01952	53.9896	3.100	2.307	2.360			
SDSS J133207.83+420537.3	203.03265	42.0937	3.106	2.961	3.065			
SDSS J133211.89+031556.2	203.04958	3.2656	4.662	4.153	4.606			
LBQS 1329+0018	203.06266	0.0479	2.350	1.661	2.318			
SDSS J133219.65+622715.9	203.08191	62.4545	3.180	2.317	3.138			
SDSS J133223.26+503431.3	203.09695	50.5754	3.807	2.623	3.759	2.6948	21.35	0.20
SDSS J133229.38+492637.9	203.12243	49.4439	2.368	2.307	2.335			
SDSS J133249.91+384021.4	203.20799	38.6726	3.189	2.475	3.147			
SDSS J133250.08+465108.6	203.20871	46.8524	4.844	3.931	4.747	4.3030	20.55	0.20
SDSS J133254.38+663059.3	203.22667	66.5165	2.642	2.355	2.605			
SDSS J133254.51+005250.6	203.22715	0.8807	3.508	2.323	3.463			
SDSS J133305.56+381552.1	203.27321	38.2645	4.139	3.186	4.088			
SDSS J133313.15+570403.8	203.30486	57.0677	2.961	2.347	2.921			
SDSS J133321.26+291010.8	203.33860	29.1697	2.656	2.307	2.620			
SDSS J133325.06+472935.3	203.35443	47.4932	2.620	2.307	2.584			
SDSS J133326.31+463143.3	203.35965	46.5287	3.708	2.778	3.661	3.0550	20.60	0.25
						3.1683	20.40	0.20
SDSS J133342.56+123352.7	203.42738	12.5647	3.271	2.307	3.228			
SDSS J133350.44+312022.3	203.46021	31.3395	2.666	2.307	2.629			
SDSS J133357.40+495327.6	203.48925	49.8910	4.161	3.222	4.110	3.7567	20.65	0.15
SDSS J133401.41+461937.5	203.50590	46.3271	2.512	2.307	2.477			
SDSS J133412.56+122020.7	203.55235	12.3391	5.130	4.172	5.028			
SDSS J133422.38-012520.1	203.59327	-1.4223	3.827	3.333	3.779			
SDSS J133422.63+475033.5	203.59431	47.8427	4.950	4.388	4.890			
SDSS J133424.33+054750.8	203.60140	5.7975	3.862	3.396	3.813			
SDSS J133431.66+412949.6	203.63194	41.4971	3.011	2.341	2.971			
SDSS J133433.88+035545.1	203.64119	3.9292	2.582	2.307	2.546			
SDSS J133435.80+114740.1	203.64918	11.7945	2.605	2.343	2.569			
SDSS J133446.72+571254.4	203.69468	57.2151	3.021	2.610	2.980			
SDSS J133448.70+521317.9	203.70294	52.2217	3.605	2.537	3.559			
SDSS J133448.87+515743.6	203.70365	51.9621	3.252	2.817	3.210			
SDSS J133458.25+283520.8	203.74273	28.5891	3.077	2.687	3.037			
SDSS J133512.84+440417.3	203.80355	44.0715	3.088	2.952	3.047			
[HB89] 1333+459	203.84151	45.7106	2.452	2.307	2.418			
SDSS J133523.37+490635.0	203.84739	49.1097	2.812	2.307	2.774			
SDSS J133523.81+463742.1	203.84924	46.6284	2.474	2.307	2.439			
SDSS J133533.55+304654.0	203.88985	30.7817	2.840	2.447	2.802			
SDSS J133541.38+483530.0	203.92246	48.5917	2.742	2.406	2.705			
SDSS J133546.19+280550.9	203.94250	28.0975	2.972	2.567	2.932			
SDSS J133548.85+610750.0	203.95358	61.1306	2.375	2.307	2.341			
SDSS J133553.00+522947.0	203.97085	52.4964	2.505	2.307	2.469			
SDSS J133600.50+383921.6	204.00210	38.6560	3.079	2.663	3.038			
SDSS J133602.42+541825.1	204.01012	54.3070	2.531	2.307	2.495			
SDSS J133606.00+281323.7	204.02500	28.2233	2.384	2.307	2.350			
SDSS J133608.53+391116.7	204.03556	39.1880	2.730	2.347	2.692			

Continued on Next Page...

Table I.1 – Continued

Name	RA	Dec	z_{em}	z_{min}	z_{max}	z_{abs}	$\log N(\mathrm{H\,I})$	$\epsilon[\log N(\mathrm{H\,I})]$
SDSS J133615.04+420050.0	204.06268	42.0139	3.891	2.823	3.842			
SDSS J133624.95+602715.9	204.10404	60.4544	2.469	2.307	2.434			
SDSS J133628.66+602001.8	204.11947	60.3338	3.265	3.063	3.222			
LBQS 1334+0212	204.19401	1.9616	2.378	2.307	2.344			
LBQS 1334-0033	204.19644	-0.8159	2.800	2.307	2.762			
SDSS J133652.27+114657.2	204.21783	11.7826	2.689	2.311	2.652			
SDSS J133653.44+024338.1	204.22267	2.7273	3.801	1.887	3.753			
SDSS J133701.39-024630.2	204.25581	-2.7751	3.064	2.661	2.981	2.6874	20.60	0.15
SDSS J133718.67+452237.4	204.32782	45.3771	3.122	3.037	3.081			
SDSS J133724.69+315254.5	204.35291	31.8818	3.183	2.347	3.141			
SDSS J133728.32+042919.7	204.36801	4.4888	3.924	3.523	3.875			
SDSS J133728.61+023427.8	204.36922	2.5744	2.968	2.371	2.928			
SDSS J133728.81+415539.8	204.37006	41.9277	5.018	4.078	4.918	4.3480	20.55	0.20
SDSS J133730.55+123937.7	204.37731	12.6605	2.537	2.307	2.502			
SDSS J133749.09+040129.7	204.45458	4.0249	2.423	2.370	2.389			
SDSS J133749.39+672514.8	204.45584	67.4208	2.854	2.307	2.815			
SDSS J133754.41+451239.1	204.47672	45.2109	2.758	2.374	2.721			
SDSS J133757.87+021820.9	204.49114	2.3058	3.333	2.362	3.290			
SDSS J133802.28+502625.6	204.50952	50.4404	2.448	2.307	2.414			
BRI 1335-0417	204.51409	-4.5431	4.396	3.080	4.342			
SDSS J133813.37+490311.5	204.55579	49.0532	3.753	3.282	3.671			
SDSS J133828.47+395922.5	204.61866	39.9896	2.340	2.307	2.307			
SDSS J133842.65-032517.6	204.67773	-3.4216	2.342	2.307	2.308			
SDSS J133844.35+513756.8	204.68484	51.6324	3.405	2.728	3.361			
LBQS 1336+0210	204.68518	1.9177	1.960	1.634	1.932			
SDSS J133854.68+493453.7	204.72787	49.5816	3.379	2.328	3.335			
SDSS J133858.81+275711.6	204.74505	27.9532	3.325	2.920	3.282			
SDSS J133912.94+515403.7	204.80396	51.9010	4.080	2.783	4.029			
SDSS J133919.33+283908.8	204.83060	28.6525	2.528	2.307	2.493			
SDSS J133922.30+462749.2	204.84294	46.4637	3.371	2.449	3.327	3.0177	20.60	0.15
SDSS J133923.22+581354.1	204.84676	58.2317	2.383	2.307	2.349			
SDSS J133923.33+521847.5	204.84723	52.3132	3.228	2.842	3.146			
SDSS J133923.77+632858.4	204.84910	63.4829	2.558	2.348	2.523			
SDSS J133932.73+322942.9	204.88639	32.4953	2.361	2.307	2.327			
SDSS J133941.95+054822.1	204.92481	5.8062	2.980	2.307	2.940	2.5849	20.45	0.15
[HB89] 1337+113	205.01060	11.1084	2.925	2.349	2.886	2.7956	20.80	0.15
SDSS J134014.90+515228.7	205.06209	51.8747	3.129	2.706	3.088			
SDSS J134015.03+392630.7	205.06265	39.4419	5.048	4.103	4.947	4.8270	21.05	0.20
SDSS J134022.94+375443.8	205.09563	37.9122	3.100	1.737	3.059			
SDSS J134023.22+400935.1	205.09679	40.1598	2.741	2.380	2.703			
SDSS J134027.39+660348.2	205.11423	66.0634	2.392	2.307	2.358			
[HB89] 1338+101	205.11997	9.9306	2.450	1.724	2.412			
SDSS J134029.38+111618.8	205.12244	11.2719	3.108	2.537	3.067			
SDSS J134040.24+281328.1	205.16768	28.2245	5.349	4.357	5.243			
SDSS J134059.06+000504.5	205.24612	0.0846	2.600	2.307	2.564			
SDSS J134100.13+580724.2	205.25056	58.1234	3.491	2.566	3.301			
SDSS J134102.46+440615.2	205.26029	44.1042	2.419	2.307	2.385			
SDSS J134107.26-030342.2	205.28028	-3.0617	3.222	2.599	3.180	2.7556	20.40	0.15
SDSS J134110.27+470014.4	205.29284	47.0040	2.914	2.513	2.874			
SDSS J134112.37-011545.6	205.30155	-1.2627	2.767	2.395	2.685			
SDSS J134114.95+010906.5	205.31232	1.1519	2.442	2.307	2.408			
SDSS J134132.36+661910.2	205.38489	66.3195	2.633	2.307	2.597			
SDSS J134134.19+014157.7	205.39250	1.6994	4.696	3.806	4.601			
SDSS J134141.45+461110.3	205.42274	46.1862	5.003	4.065	4.903			
SDSS J134148.11+410009.8	205.45048	41.0027	3.742	2.690	3.695	3.2353	20.35	0.15
						3.5949	21.70	0.15
SDSS J134154.01+351005.6	205.47509	35.1683	5.252	4.275	5.148			
SDSS J134155.92+415127.0	205.48300	41.8575	2.401	2.307	2.367			
SDSS J134158.14+541233.6	205.49233	54.2093	2.521	2.307	2.485			
SDSS J134158.44+025448.3	205.49355	2.9134	2.521	2.307	2.486			
SDSS J134159.13+115123.0	205.49638	11.8564	2.635	2.307	2.599			
SBS 1340+605	205.54994	60.2570	2.399	2.307	2.365			
SDSS J134215.68+443724.7	205.56535	44.6235	3.332	2.385	3.289			
SDSS J134224.31+511012.4	205.60131	51.1701	2.603	2.307	2.567			
[HB89] 1340+099	205.62287	9.7461	2.942	1.894	2.897			
SDSS J134231.87+573135.1	205.63285	57.5264	2.459	2.307	2.425			
SDSS J134234.61+494825.8	205.64424	49.8072	2.684	2.307	2.647			
SDSS J134243.37+534649.5	205.68074	53.7804	2.588	2.307	2.552			
SDSS J134243.47+583849.9	205.68116	58.6472	4.850	4.394	4.792			
SDSS J134248.64+514406.4	205.70267	51.7351	3.037	2.307	2.997			
SDSS J134301.30+325422.7	205.75543	32.9063	2.926	2.307	2.887			
SDSS J134313.79+505028.1	205.80747	50.8412	3.132	2.484	3.091			

Continued on Next Page...

Table I.1 – Continued

Name	RA	Dec	z_{em}	z_{min}	z_{max}	z_{abs}	$\log N(\mathrm{H\,I})$	$\epsilon[\log N(\mathrm{H\,I})]$
SDSS J134319.83+542053.1	205.83264	54.3481	2.406	2.307	2.372			
SBS 1341+576	205.86971	57.3631	3.034	2.307	2.994			
SDSS J134329.90+320800.2	205.87463	32.1334	3.157	2.794	3.115	3.0377	20.40	0.15
SDSS J134334.31+433643.6	205.89300	43.6121	2.623	2.307	2.587			
SDSS J134345.50+121647.0	205.93963	12.2797	2.345	2.307	2.312			
SDSS J134403.06+314915.0	206.01280	31.8209	3.511	2.591	3.466			
SDSS J134412.79+285216.2	206.05332	28.8712	2.403	2.307	2.369			
SDSS J134416.87-032316.5	206.07031	-3.3879	3.256	2.416	3.213	3.1900	21.00	0.15
SDSS J134428.34+532830.6	206.11812	53.4752	3.309	2.462	3.266			
SDSS J134430.46+044658.9	206.12692	4.7831	2.480	2.307	2.445			
SDSS J134440.06+283100.6	206.16695	28.5169	3.765	2.946	3.717			
SDSS J134451.99+281113.9	206.21664	28.1872	2.405	2.346	2.371			
SDSS J134453.51+294519.6	206.22297	29.7554	4.712	4.442	4.655			
SDSS J134537.93+410600.6	206.40805	41.1002	3.490	2.675	3.445			
SDSS J134544.01+475209.1	206.43341	47.8692	2.912	2.541	2.830			
SDSS J134546.67+495701.0	206.44453	49.9503	2.973	2.307	2.933			
SDSS J134633.51+582509.1	206.63967	58.4192	4.001	2.988	3.951			
LBQS 1344+0137	206.65246	1.3705	1.920	1.634	1.886			
SDSS J134637.93+564915.6	206.65810	56.8210	3.460	2.724	3.415			
SDSS J134645.18+111851.8	206.68828	11.3144	3.384	2.611	3.340			
SDSS J134649.81+385419.7	206.70755	38.9055	2.839	2.514	2.757			
SDSS J134705.47+435156.4	206.77281	43.8657	3.172	2.785	3.090			
SDSS J134708.33+525522.5	206.78472	52.9230	3.198	2.581	3.156	2.7291	20.55	0.20
SDSS J134714.14+015901.4	206.80894	1.9837	3.709	3.292	3.662			
SDSS J134723.08+002158.8	206.84622	0.3663	4.308	3.124	4.255			
SDSS J134723.35+012317.6	206.84732	1.3882	2.647	2.359	2.611			
SDSS J134731.31+395750.0	206.88048	39.9639	2.391	2.324	2.358			
SDSS J134743.29+495621.3	206.93041	49.9393	4.563	3.694	4.470			
LBQS 1345-0137	206.95517	-1.8734	1.930	1.634	1.900			
SDSS J134752.70+655657.1	206.96963	65.9492	2.341	2.307	2.307			
SDSS J134755.67+003935.0	206.98200	0.6597	3.813	3.061	3.765			
SDSS J134757.49+371050.8	206.98958	37.1808	3.084	2.444	3.043			
SDSS J134759.60+021308.4	206.99836	2.2190	3.317	2.931	3.273	3.2070	20.50	0.15
SDSS J134800.16-022216.7	207.00071	-2.3713	3.407	3.024	3.362	3.0414	20.90	0.25
SDSS J134800.75+024553.3	207.00318	2.7648	3.017	2.936	2.977			
SDSS J134808.79+003723.1	207.03665	0.6231	3.626	3.168	3.543			
SDSS J134811.21+641348.2	207.04675	64.2301	3.838	3.110	3.790	3.5550	21.50	0.15
LBQS 1345-0120	207.06942	-1.5861	2.947	2.307	2.908			
SDSS J134816.80+520317.4	207.07007	52.0548	2.576	2.307	2.540			
SDSS J134819.87+181925.8	207.08283	18.3238	4.954	4.024	4.855			
SDSS J134820.86+243707.9	207.08694	24.6189	3.200	2.548	3.158			
[HB89] 1346-036	207.18365	-3.8903	2.360	1.653	2.327			
SDSS J134848.98+401503.6	207.20410	40.2510	2.977	2.307	2.937			
SDSS J134850.23+262504.1	207.20931	26.4179	2.915	2.514	2.876			
SDSS J134858.83+105314.7	207.24514	10.8874	2.471	2.366	2.437			
BRI 1346-0322	207.31967	-3.6208	3.992	2.650	3.942	3.7343	20.72	0.20
SDSS J134919.67+380448.4	207.33198	38.0801	2.997	2.356	2.957			
SDSS J134939.77+124230.7	207.41575	12.7085	4.185	3.373	4.133	3.4920	20.40	0.20
						3.7443	20.30	0.20
SDSS J134945.16+434131.1	207.43819	43.6920	2.354	2.307	2.321			
SDSS J134945.24+051504.1	207.43854	5.2512	3.276	2.386	3.234			
SDSS J134948.52+401143.7	207.45220	40.1955	3.330	2.589	3.287			
[HB89] 1347+112	207.47222	11.0211	2.700	1.920	2.663	2.4709	20.30	0.20
SDSS J135004.53+034953.9	207.51889	3.8316	3.043	2.672	3.003			
SDSS J135004.87+360045.5	207.52033	36.0127	3.575	2.706	3.530			
SDSS J135005.36+661423.8	207.52243	66.2400	2.991	2.351	2.951	2.3650	20.70	0.20
SDSS J135044.20+595205.3	207.68422	59.8682	2.963	2.557	2.923	2.7558	20.75	0.15
SBS 1348+575	207.68615	57.2786	2.905	2.307	2.866			
SDSS J135057.60+122054.4	207.74005	12.3484	3.782	3.619	3.734			
SDSS J135057.86-004355.2	207.74110	-0.7320	4.438	4.266	4.383			
SDSS J135057.97+002612.0	207.74161	0.4367	3.702	3.268	3.655			
SDSS J135058.12+261855.2	207.74219	26.3154	2.613	2.307	2.576			
SDSS J135131.17+455434.5	207.87988	45.9096	2.924	2.328	2.885			
SDSS J135150.18+392316.4	207.95909	39.3879	3.198	2.338	3.156			
SDSS J135203.25+024643.5	208.01357	2.7788	2.554	2.307	2.518			
SDSS J135211.82+533053.7	208.04926	53.5149	3.347	2.429	3.304			
SDSS J135213.31+581536.7	208.05549	58.2602	3.114	2.419	3.073			
SDSS J135218.48+122408.5	208.07703	12.4024	3.440	2.692	3.396			
SDSS J135229.60+455446.2	208.12337	45.9128	4.260	3.720	4.207			
SDSS J135230.48+531108.7	208.12705	53.1857	4.216	3.208	4.164	3.3204	20.95	0.20
SDSS J135231.82-031611.6	208.13260	-3.2699	2.726	2.344	2.689			
SDSS J135234.24+102207.1	208.14272	10.3686	2.552	2.307	2.517			

Continued on Next Page...

Table I.1 – Continued

Name	RA	Dec	z_{em}	z_{min}	z_{max}	z_{abs}	log N(H I)	ϵ[log N(H I)]
SDSS J135247.98+130311.5	208.19992	13.0532	3.706	2.035	3.659			
SDSS J135251.05+042055.6	208.21273	4.3488	3.049	2.420	3.008			
SDSS J135256.87+021528.5	208.23696	2.2579	2.571	2.427	2.536			
SDSS J135301.24+633255.4	208.25522	63.5487	3.164	2.479	3.122			
SDSS J135305.17-025018.2	208.27159	-2.8384	2.415	2.307	2.381	2.3624	20.30	0.20
SDSS J135310.11+242259.6	208.29213	24.3833	3.113	2.394	3.072			
SDSS J135310.75+482243.3	208.29485	48.3787	3.814	2.622	3.766			
SDSS J135317.10+532825.4	208.32129	53.4738	2.915	2.307	2.876	2.8353	20.80	0.15
SDSS J135325.61-023443.5	208.35674	-2.5788	3.125	2.703	3.084	2.9527	20.40	0.15
SDSS J135326.01+572552.7	208.35841	57.4313	3.464	2.675	3.419			
SDSS J135326.27-002400.9	208.35949	-0.4003	2.416	2.307	2.382			
SDSS J135334.75-031022.2	208.39482	-3.1728	2.974	2.359	2.934	2.5600	20.35	0.15
SDSS J135347.77+602407.6	208.44906	60.4021	2.537	2.356	2.501			
[HB89] 1351-018	208.52873	-2.1009	3.715	2.739	3.668			
SDSS J135411.13+040103.3	208.54639	4.0176	2.396	2.307	2.362			
SDSS J135411.19+582833.4	208.54663	58.4760	2.390	2.307	2.356			
SDSS J135426.21+414759.9	208.60924	41.8000	3.034	2.799	2.994			
SDSS J135440.16+015827.5	208.66737	1.9743	3.294	2.470	3.251	2.5624	20.80	0.15
SDSS J135445.65+002050.2	208.69024	0.3473	2.503	2.307	2.468			
[HB89] 1352+108	208.70240	10.6030	3.142	2.307	3.100			
SDSS J135515.89+343303.9	208.81622	34.5511	3.755	2.860	3.707			
SDSS J135520.35+592510.3	208.83483	59.4195	2.612	2.307	2.576			
SDSS J135535.04+041526.1	208.89600	4.2573	2.927	2.543	2.888			
SDSS J135552.48+564732.3	208.96871	56.7923	2.409	2.307	2.375			
SDSS J135552.86+382317.5	208.97029	38.3882	2.400	2.307	2.366			
SDSS J135554.55+450421.0	208.97731	45.0725	4.095	3.245	4.044			
SDSS J135557.54+581318.0	208.98977	58.2217	3.375	2.523	3.331	3.2919	20.50	0.15
SDSS J135604.28+471058.7	209.01786	47.1830	3.384	2.668	3.340			
SDSS J135607.30+392205.4	209.03046	39.3682	2.420	2.307	2.386			
SDSS J135607.49+581236.0	209.03125	58.2100	3.320	2.916	3.277	3.1451	21.10	0.20
SDSS J135612.51+495725.1	209.05217	49.9570	3.271	2.519	3.228			
SDSS J135619.90+591705.3	209.08293	59.2848	3.295	2.353	3.252			
SDSS J135659.38+543318.8	209.24742	54.5552	3.686	3.209	3.639			
SDSS J135707.51+614234.7	209.28133	61.7097	3.258	2.422	3.216			
SDSS J135712.76+504952.7	209.30317	50.8313	3.031	2.307	2.591			
SDSS J135718.05+502458.3	209.32524	50.4162	3.044	2.366	3.003			
SDSS J135744.56+393223.7	209.43570	39.5399	2.477	2.307	2.442			
SDSS J135750.92+345023.5	209.46220	34.8399	2.922	2.324	2.882			
SDSS J135803.97+034936.0	209.51657	3.8267	2.894	2.307	2.855	2.8535	20.40	0.15
SDSS J135808.61+621946.6	209.53588	62.3296	3.051	2.636	3.010	2.8463	20.95	0.20
SDSS J135815.62+334700.7	209.56509	33.7835	3.168	2.741	3.126			
SDSS J135818.98+431925.4	209.57913	43.3237	2.464	2.307	2.429			
SDSS J135823.50+602507.2	209.59796	60.4187	2.341	2.307	2.308			
SDSS J135827.55+511930.4	209.61481	51.3252	3.304	3.207	3.261			
SDSS J135828.74+005811.3	209.61976	0.9698	3.923	2.806	3.873	3.0202	20.30	0.15
SDSS J135831.78+050522.8	209.63248	5.0896	2.448	2.307	2.413			
SDSS J135837.94+353436.8	209.65812	35.5769	3.271	2.307	3.228			
SDSS J135842.91+652236.6	209.67886	65.3769	3.173	2.457	3.131	3.0690	20.30	0.15
SDSS J135843.12+472735.0	209.67971	47.4598	3.602	2.670	3.556	3.2565	20.30	0.15
SDSS J135845.63+103643.9	209.69014	10.6122	2.562	2.307	2.526			
SDSS J135854.28+470833.1	209.72622	47.1425	3.015	2.604	2.975			
SDSS J135904.92+342143.8	209.77053	34.3622	2.962	2.307	2.923			
SDSS J135915.25+362237.6	209.81355	36.3771	3.217	2.806	3.175			
SDSS J135917.69-015145.9	209.82372	-1.8628	3.097	2.682	3.056			
SDSS J135930.83+373609.4	209.87848	37.6026	3.618	3.174	3.572			
SDSS J135936.21+483923.1	209.90090	48.6564	2.364	2.307	2.330			
SDSS J135936.43+552258.0	209.90180	55.3828	2.996	2.599	2.956			
SDSS J135944.47+430416.2	209.93531	43.0712	3.438	3.240	3.393			
SDSS J135945.41+451823.4	209.93925	45.3065	3.058	2.484	3.017			
SDSS J135946.43+350438.3	209.94348	35.0773	4.226	3.311	4.174	3.5206	20.40	0.20
SDSS J140006.88+412142.5	210.02871	41.3618	2.760	2.388	2.678			
2MASSi J1400138+385418	210.05771	38.9050	3.277	2.359	3.234			
SDSS J140020.76+504101.3	210.08650	50.6837	2.347	2.307	2.314			
SDSS J140022.78+395030.8	210.09495	39.8419	3.751	2.581	3.704	3.2932	20.30	0.15
SDSS J140023.43+543205.4	210.09765	54.5348	3.069	2.706	3.028			
SDSS J140028.81+643030.9	210.12015	64.5086	2.360	2.307	2.326			
SDSS J140029.01+411243.4	210.12088	41.2121	2.550	2.307	2.515			
SDSS J140031.61+044628.2	210.13171	4.7745	3.245	3.077	3.202			
SDSS J140032.45+040000.1	210.13522	4.0000	3.556	3.157	3.511			
SDSS J140034.29+465413.6	210.14290	46.9038	2.807	2.307	2.769			
[HB89] 1358+115	210.16250	11.3396	2.590	1.677	2.550			
SDSS J140041.15+370319.8	210.17149	37.0555	2.582	2.307	2.546			

Continued on Next Page...

Table I.1 – Continued

Name	RA	Dec	z_{em}	z_{min}	z_{max}	z_{abs}	$\log N(\mathrm{H\,I})$	$\epsilon[\log N(\mathrm{H\,I})]$
SDSS J140042.36+383023.8	210.17651	38.5066	2.643	2.307	2.607			
SDSS J140045.53+545231.8	210.18974	54.8755	2.946	2.307	2.906			
SDSS J140046.21+452807.7	210.19255	45.4688	3.633	2.808	3.587			
SDSS J140053.59+410129.7	210.22330	41.0249	3.096	2.931	3.055			
SDSS J140056.11+354553.1	210.23381	35.7648	2.964	2.402	2.924			
SDSS J140101.13+131833.7	210.25475	13.3094	2.580	2.307	2.544			
SDSS J140103.13+053914.2	210.26308	5.6540	3.709	3.239	3.662			
SDSS J140107.66+362510.8	210.28194	36.4197	3.221	2.359	3.179			
SDSS J140114.28-004537.1	210.30956	-0.7603	2.522	2.307	2.487			
SDSS J140124.04+511345.3	210.35021	51.2293	3.213	2.353	3.171			
SDSS J140126.14+520834.6	210.35897	52.1430	2.972	2.307	2.933			
SDSS J140132.76+411150.4	210.38653	41.1974	4.026	2.866	3.976			
SDSS J140135.98+515711.8	210.39995	51.9533	4.122	3.283	4.071			
SDSS J1401+0244	210.44389	2.7430	4.408	2.915	4.354			
SDSS J140154.35+365519.9	210.47647	36.9222	3.022	2.311	2.982			
SDSS J140200.88+011751.6	210.50370	1.2977	2.948	2.338	2.909	2.4310	20.30	0.15
SDSS J140208.47+485209.6	210.53531	48.8694	3.059	2.398	3.019	3.0140	20.30	0.20
SDSS J140213.64+352908.5	210.55685	35.4857	2.359	2.307	2.325			
SDSS J140224.15+003002.2	210.60065	0.5006	2.418	2.307	2.383			
SDSS J140226.71+050353.7	210.61130	5.0649	2.968	2.307	2.928			
SDSS J140237.22+493259.9	210.65512	49.5500	3.109	2.307	3.068			
SDSS J140243.97+590958.9	210.68325	59.1664	4.135	3.303	4.084	3.7789	21.75	0.20
SDSS J140246.24+445013.2	210.69270	44.8370	4.045	3.256	3.995			
SDSS J140248.07+014634.1	210.70033	1.7761	4.161	2.961	4.109	3.2773	20.95	0.15
SDSS J140252.00+550430.5	210.71671	55.0752	2.441	2.307	2.357			
SDSS J140306.48+645532.3	210.77703	64.9257	2.466	2.307	2.432			
SDSS J140308.27+433802.7	210.78449	43.6341	3.652	3.284	3.605			
UM 629	210.84748	-0.1019	2.462	2.307	2.427			
[HB89] 1400+095	210.86043	9.3455	2.980	2.022	2.930			
SDSS J140336.66+395916.6	210.90277	39.9880	3.060	2.675	3.019			
SDSS J140337.05+403205.9	210.90441	40.5350	4.052	3.552	3.970			
SDSS J140345.52+555128.5	210.93969	55.8579	3.177	2.309	3.135			
SDSS J140354.57+543246.8	210.97739	54.5463	3.258	2.645	3.215			
SDSS J140355.68+412617.2	210.98202	41.4381	3.862	2.866	3.813			
SDSS J140359.38+355806.2	210.99744	35.9684	2.504	2.345	2.469			
SDSS J140400.34+443906.0	211.00144	44.6517	3.546	2.855	3.501			
SDSS J140404.23+124859.0	211.01764	12.8164	3.187	2.518	3.145			
SDSS J140404.63+031403.9	211.01934	3.2344	4.924	3.998	4.825			
SDSS J140405.37+365607.6	211.02240	36.9355	2.666	2.307	2.630			
SDSS J140409.73+350702.0	211.04058	35.1172	2.475	2.307	2.440			
SDSS J140423.04+400511.0	211.09601	40.0864	3.950	3.443	3.901			
SDSS J140425.15+391504.5	211.10482	39.2513	3.622	2.615	3.576			
SDSS J140428.54+400257.4	211.11895	40.0493	2.935	2.532	2.896			
SDSS J140432.99+072846.9	211.13747	7.4797	2.866	2.307	2.827			
SDSS J140433.54+424512.5	211.13977	42.7535	4.212	3.370	4.160			
SDSS J140437.93-022137.4	211.15808	-2.3604	2.933	2.307	2.894			
SDSS J140438.26+402039.8	211.15943	40.3444	3.631	3.173	3.548	3.3620	20.65	0.15
SDSS J140439.87+580509.0	211.16615	58.0859	2.371	2.307	2.337			
UM 632	211.19123	-1.5061	2.507	2.307	2.472			
[HB89] 1402+044	211.25467	4.2599	3.215	2.533	3.173	2.7076	20.90	0.15
SDSS J140503.29+334149.8	211.26371	33.6972	4.467	3.613	4.376			
SDSS J140504.25+031026.7	211.26773	3.1741	2.403	2.307	2.369			
SDSS J140512.59+522114.3	211.30253	52.3540	3.843	2.885	3.794	2.9804	20.70	0.15
SDSS J140521.67+050744.4	211.34032	5.1290	2.991	2.307	2.951			
SDSS J140523.53+370500.9	211.34806	37.0836	2.886	2.501	2.803			
SDSS J140525.49+552837.4	211.35623	55.4771	3.206	2.413	3.164			
SDSS J140525.63+404356.0	211.35681	40.7322	2.483	2.352	2.448			
SDSS J140529.01+063514.0	211.37089	6.5872	3.879	2.913	3.830			
SDSS J140542.95+345550.4	211.42898	34.9307	3.065	2.654	3.025			
SDSS J140543.72+650142.0	211.43220	65.0284	2.977	2.604	2.937			
SDSS J140554.06-000036.8	211.47530	-0.0103	3.550	3.099	3.468			
SDSS J140600.95+072518.4	211.50398	7.4218	3.034	2.307	2.993			
SDSS J140602.16+590443.2	211.50905	59.0787	2.366	2.307	2.333			
SDSS J140602.63+391235.8	211.51098	39.2100	2.888	2.494	2.849			
SDSS J140606.68+352707.8	211.52788	35.4522	3.405	3.067	3.361			
SDSS J140620.41+135958.9	211.58505	13.9997	3.201	2.843	3.159			
SDSS J140633.01+513017.3	211.63755	51.5048	3.040	2.417	2.999			
SDSS J140637.31-030331.5	211.65547	-3.0588	2.443	2.307	2.409			
SDSS J140637.60+141530.0	211.65670	14.2584	2.926	2.307	2.887			
SDSS J140641.51+585214.0	211.67299	58.8706	3.083	2.706	3.042	2.9864	21.05	0.15
SDSS J140641.79+054453.0	211.67415	5.7481	3.043	2.429	3.002			
SDSS J140650.01+411301.2	211.70842	41.2170	2.393	2.307	2.359			

Continued on Next Page...

Table I.1 – Continued

Name	RA	Dec	z_{em}	z_{min}	z_{max}	z_{abs}	$\log N(\mathrm{H\,I})$	$\epsilon[\log N(\mathrm{H\,I})]$
SDSS J140653.84+343337.3	211.72436	34.5604	2.567	2.307	2.531			
SDSS J140655.66+631523.7	211.73193	63.2566	2.533	2.380	2.497			
SDSS J140702.57+552217.3	211.76075	55.3715	3.191	2.831	3.109			
SDSS J140705.25+065054.7	211.77192	6.8486	3.037	2.637	2.997			
SDSS J140709.34+012420.0	211.78894	1.4056	3.326	2.572	3.282	2.7113	20.60	0.20
SDSS J140711.70+431230.7	211.79877	43.2086	2.584	2.307	2.548			
SDSS J140728.18+373619.4	211.86746	37.6054	3.359	2.455	3.315			
SDSS J140729.39+011218.2	211.87246	1.2051	3.062	2.329	3.022			
SDSS J140742.21+590135.3	211.92595	59.0265	2.401	2.307	2.366			
SDSS J140744.05+355448.0	211.93356	35.9134	3.657	2.916	3.611			
SDSS J140747.22+645419.9	211.94670	64.9055	3.081	2.307	3.040			
SDSS J140754.53+001312.1	211.97722	0.2200	3.713	3.285	3.666			
SDSS J140755.06+465750.8	211.97944	46.9641	2.479	2.307	2.444			
SDSS J140802.98+535154.2	212.01245	53.8651	4.037	2.913	3.986			
SDSS J140815.58+060023.2	212.06495	6.0065	2.580	2.307	2.544			
SDSS J140817.26+401155.3	212.07196	40.1987	3.175	2.748	3.133			
[HB89] 1406+123	212.16218	12.1194	2.940	2.018	2.903			
SDSS J140838.93+350331.1	212.16223	35.0587	3.639	3.463	3.592			
SDSS J140841.77-021502.5	212.17407	-2.2507	3.315	2.631	3.272			
SDSS J140850.91+020522.6	212.21215	2.0896	4.008	2.837	3.957			
SBS 1407+586	212.22595	58.4129	3.120	2.307	3.079	2.3802	20.85	0.20
SDSS J140904.15+541023.6	212.26729	54.1733	2.483	2.307	2.448			
SDSS J140906.47+385350.2	212.27698	38.8973	3.435	2.695	3.391	2.8255	20.70	0.20
SDSS J140906.90+353112.3	212.27878	35.5201	3.048	2.667	3.008			
SDSS J140909.22+060548.4	212.28846	6.0968	3.115	2.803	3.073			
SDSS J140909.74+071226.1	212.29062	7.2073	2.734	2.352	2.697			
SDSS J140923.36+485101.0	212.34736	48.8503	2.520	2.320	2.485			
SDSS J140927.30-021828.5	212.36376	-2.3079	3.433	3.314	3.389			
SDSS J140931.62+531146.7	212.38178	53.1963	3.781	2.761	3.734			
SDSS J140934.37+422737.1	212.39321	42.4603	3.025	2.325	2.985			
SDSS J140938.23-012511.2	212.40932	-1.4198	2.425	2.307	2.391			
SDSS J141001.07+653703.1	212.50451	65.6175	2.539	2.307	2.503			
SDSS J141007.73+530719.4	212.53221	53.1221	3.110	2.689	3.069			
SDSS J141009.65+624834.1	212.54022	62.8095	2.447	2.307	2.413			
SDSS J141020.77+531316.9	212.58658	53.2214	3.223	2.307	3.180			
UM 642	212.61008	-0.8360	2.371	2.307	2.337			
SDSS J141030.60+511113.5	212.62753	51.1871	3.206	2.352	3.164	2.9344	20.80	0.15
						2.9642	20.85	0.20
SBS 1408+550	212.67503	54.7720	2.485	2.307	2.450			
FIRST J1410+3409	212.69112	34.1562	4.351	3.026	4.297			
SDSS J141052.99-023256.9	212.72082	-2.5492	2.517	2.307	2.482			
SDSS J141053.53+373301.9	212.72305	37.5506	3.595	2.677	3.549			
SDSS J141059.61+472733.3	212.74842	47.4593	2.901	2.349	2.862			
SDSS J141059.92+141811.7	212.74971	14.3033	3.140	2.332	3.099			
SDSS J141104.13+521755.4	212.76722	52.2988	2.883	2.496	2.844			
SDSS J141116.65+344049.9	212.81939	34.6805	3.250	2.823	3.207			
SDSS J141123.17+360210.5	212.84656	36.0363	3.070	2.405	3.029	2.8369	20.55	0.20
SDSS J141147.68+142153.8	212.94868	14.3650	3.544	2.533	3.499			
SDSS J141155.91+403031.8	212.98298	40.5089	3.330	2.508	3.286			
SDSS J141204.61+554724.9	213.01922	55.7903	2.394	2.307	2.360			
SDSS J141209.96+062406.9	213.04154	6.4019	4.411	3.566	4.321			
[HB89] 1409+095	213.07205	9.2735	2.860	1.979	2.800	2.4561	20.50	0.20
SDSS J141244.10+334426.7	213.18378	33.7408	3.461	3.020	3.379			
SDSS J141251.99+511124.7	213.21664	51.1902	3.197	2.519	3.155			
SDSS J141254.37+541410.8	213.22658	54.2364	4.329	3.418	4.275			
SDSS J141254.79+355948.3	213.22833	35.9968	2.459	2.307	2.424			
2MASSi J1413136+411636	213.30674	41.2772	2.616	2.307	2.580			
SDSS J141315.21+640526.2	213.31344	64.0906	3.084	2.401	3.043			
SDSS J141318.86+371927.8	213.32859	37.3244	2.709	2.329	2.672			
SDSS J141318.86+450522.9	213.32861	45.0897	3.120	2.542	3.079			
[HB89] 1410+096	213.33774	9.3680	3.210	2.099	3.169			
SDSS J141322.43+523249.7	213.34347	52.5472	3.707	3.242	3.625			
SDSS J141327.46+523851.8	213.36442	52.6477	3.153	3.062	3.112			
SDSS J141332.35-004909.5	213.38482	-0.8193	4.138	3.629	4.056			
SDSS J141332.53+495041.4	213.38556	49.8449	2.642	2.331	2.606			
FBQS J141334.4+421201	213.39332	42.2005	2.817	2.439	2.735			
SDSS J141342.62+040536.1	213.42761	4.0934	2.436	2.307	2.401			
SDSS J141359.00+064359.5	213.49587	6.7332	3.477	2.701	3.432			
SDSS J141404.15+395543.5	213.51733	39.9288	3.213	2.320	3.171			
SDSS J141420.77+562933.0	213.58656	56.4925	2.390	2.307	2.356			
SDSS J141421.80+060520.5	213.59088	6.0891	2.604	2.387	2.568			
SDSS J141422.55+140126.0	213.59400	14.0239	2.775	2.388	2.737			

Continued on Next Page...

Table I.1 – Continued

Name	RA	Dec	z_{em}	z_{min}	z_{max}	z_{abs}	$\log N(\mathrm{H\,I})$	$\epsilon[\log N(\mathrm{H\,I})]$
SDSS J141431.47+342809.2	213.63116	34.4693	2.996	2.659	2.914			
SDSS J141436.72+464838.2	213.65305	46.8106	2.350	2.307	2.316			
SDSS J141513.99+365412.2	213.80833	36.9034	2.915	2.527	2.832			
SDSS J141521.04+035354.5	213.83767	3.8985	3.243	2.384	3.201			
FBQS J141528.4+370621	213.86861	37.1059	2.370	2.307	2.336			
SDSS J141546.88+465342.4	213.94535	46.8951	3.267	2.537	3.224			
SDSS J141552.49+125730.8	213.96873	12.9586	2.444	2.307	2.409			
SDSS J141555.35+424158.8	213.98064	42.6997	2.585	2.315	2.549			
SDSS J141607.28+383153.6	214.03037	38.5316	3.524	3.264	3.479			
SDSS J141608.39+181144.0	214.03497	18.1956	3.593	2.266	3.547			
SDSS J141608.43+064431.8	214.03517	6.7422	3.148	2.307	3.107			
SDSS J141610.25+494730.4	214.04273	49.7918	3.107	2.704	3.025			
SDSS J141618.64+410656.8	214.07770	41.1158	2.380	2.314	2.347			
SDSS J141624.12+623019.3	214.10050	62.5054	3.075	2.368	3.034			
SDSS J141631.70+025309.8	214.13211	2.8861	2.468	2.307	2.433			
SDSS J141633.37+074513.7	214.13906	7.7538	2.631	2.317	2.595			
SDSS J141637.07+135436.1	214.15450	13.9101	2.378	2.307	2.344			
SDSS J141657.93+123431.6	214.24138	12.5755	2.614	2.307	2.578			
SDSS J141738.53+534251.0	214.41060	53.7142	2.583	2.307	2.547			
SDSS J141744.05+044948.1	214.43355	4.8301	2.659	2.322	2.622			
SDSS J141802.90+501656.4	214.51211	50.2824	2.453	2.314	2.419			
[HB89] 1415+093	214.53643	9.1272	2.510	2.307	2.475			
SDSS J141811.40-021724.0	214.54752	-2.2900	3.332	2.631	3.289			
SDSS J141812.81+453132.1	214.55339	45.5256	2.599	2.307	2.563			
SDSS J141815.63+351204.5	214.56514	35.2012	3.125	3.081	3.084			
SDSS J141817.90+033727.3	214.57462	3.6243	2.393	2.307	2.359			
SDSS J141819.22+044135.0	214.58009	4.6931	2.500	2.307	2.465			
SDSS J141822.89+585806.4	214.59545	58.9684	2.785	2.398	2.747			
SDSS J141827.31+553631.1	214.61384	55.6086	3.668	2.690	3.621			
SDSS J141830.86+612500.5	214.62863	61.4168	3.218	2.478	3.176			
SDSS J141831.70+444937.5	214.63210	44.8271	4.323	2.974	4.270			
SDSS J141831.72+065711.2	214.63219	6.9531	2.401	2.307	2.367			
SDSS J141837.13+441503.5	214.65475	44.2510	2.932	2.307	2.893			
SDSS J141849.09+123144.6	214.70455	12.5291	3.200	3.040	3.158			
SDSS J141857.11+635524.4	214.73803	63.9235	3.116	2.479	3.075			
SDSS J141904.08+495033.1	214.76703	49.8426	2.997	2.308	2.957			
SDSS J141914.18-015012.6	214.80912	-1.8369	4.590	3.717	4.497			
SDSS J141919.45+574513.9	214.83106	57.7539	3.339	2.673	3.296			
SDSS J141925.48+074953.5	214.85618	7.8315	2.382	2.307	2.348			
SDSS J141950.54+082948.2	214.96062	8.4967	3.034	2.307	2.994			
SDSS J141956.80+423630.3	214.98669	42.6084	2.341	2.307	2.307			
SDSS J142007.73+484843.2	215.03221	48.8120	3.252	2.581	3.209			
SDSS J142008.21+463126.2	215.03423	46.5240	3.206	2.836	3.123			
SDSS J142014.98+404252.4	215.06246	40.7146	3.860	3.367	3.811			
SDSS J142024.68+140122.1	215.10284	14.0228	2.392	2.307	2.358			
SDSS J142025.75+615510.0	215.10731	61.9194	4.448	3.597	4.357	4.1120	20.60	0.20
SDSS J142028.83+054425.3	215.12016	5.7404	2.430	2.307	2.396			
SDSS J142030.09+344127.2	215.12539	34.6909	3.975	3.192	3.926			
SDSS J142033.15-020551.9	215.13815	-2.0978	3.307	2.566	3.264			
SDSS J142033.25-003233.3	215.13858	-0.5426	2.682	2.315	2.645			
SDSS J142034.42+064358.8	215.14344	6.7330	3.397	2.946	3.353			
SDSS J142036.06+471432.4	215.15029	47.2424	3.233	2.481	3.190			
SDSS J142045.34+084332.0	215.18895	8.7256	3.235	2.801	3.193			
SDSS J142103.83+343332.0	215.26596	34.5589	4.815	4.242	4.757			
PKS B1418-064	215.28232	-6.7323	3.688	2.356	3.642	3.4490	20.30	0.15
SDSS J142120.80+394720.4	215.33673	39.7890	3.035	2.397	2.995			
SDSS J142123.97+463318.0	215.34996	46.5550	3.365	2.307	3.321			
SDSS J142129.39+522752.0	215.37248	52.4644	3.205	2.339	3.163			
SDSS J142141.51+133722.7	215.42300	13.6230	2.989	2.366	2.949			
SDSS J142144.98+351315.4	215.43745	35.2210	4.599	3.724	4.506			
SDSS J142158.70+061654.1	215.49463	6.2817	3.891	2.988	3.842			
SDSS J142200.93+074028.9	215.50388	7.6747	2.526	2.334	2.491			
SDSS J142203.06+134018.1	215.51277	13.6717	3.772	2.684	3.724			
SDSS J142209.11+005436.2	215.53798	0.9101	3.671	2.691	3.625			
SDSS J142216.59+073730.4	215.56915	7.6251	3.234	2.575	3.191			
SDSS J142225.66+121900.4	215.60696	12.3168	3.046	2.707	3.006			
SDSS J142231.09+091954.2	215.62958	9.3317	3.548	2.746	3.502			
SDSS J142233.84+462034.5	215.64104	46.3429	3.321	2.923	3.278			
SDSS J142239.88+420220.3	215.66618	42.0390	3.236	2.948	3.194			
SDSS J142241.39+541715.3	215.67246	54.2876	2.660	2.307	2.623			
SDSS J142241.42+391815.4	215.67275	39.3044	3.505	2.756	3.459			
SDSS J142242.13+461310.2	215.67557	46.2195	3.727	2.569	3.680	2.9023	21.10	0.15

Continued on Next Page...

Table I.1 – Continued

Name	RA	Dec	z_{em}	z_{min}	z_{max}	z_{abs}	$\log N(\mathrm{H\,I})$	$\epsilon[\log N(\mathrm{H\,I})]$
SDSS J142243.02+441721.2	215.67927	44.2893	3.545	2.526	3.500	3.3621	20.50	0.15
SDSS J142244.45+382330.6	215.68521	38.3919	3.728	3.259	3.646			
SDSS J142253.02+235534.4	215.72095	23.9262	2.961	2.307	2.922			
SDSS J142257.66+375807.3	215.74029	37.9687	3.181	3.002	3.139			
SDSS J142259.77+380523.5	215.74907	38.0899	2.361	2.307	2.327			
SDSS J142301.64+075803.7	215.75685	7.9677	3.218	2.899	3.176			
SDSS J142306.46+590420.2	215.77694	59.0723	3.221	2.512	3.179			
SDSS J142325.92+130300.6	215.85801	13.0502	5.048	4.103	4.947			
SDSS J142328.65+481801.2	215.86942	48.3004	3.007	2.340	2.967			
SDSS J142329.50+402412.9	215.87296	40.4036	3.054	2.429	3.013			
SDSS J142329.98+004138.4	215.87492	0.6940	3.779	2.977	3.731			
SDSS J142333.40+455051.2	215.88919	45.8476	3.283	2.537	3.240			
SDSS J142338.57+052834.0	215.91075	5.4761	3.790	2.958	3.742			
SDSS J142340.27+331435.9	215.91782	33.2433	2.875	2.307	2.836			
SDSS J142346.63+564143.9	215.94431	56.6955	3.060	2.357	3.019			
SDSS J142346.90+563444.8	215.94544	56.5791	3.190	2.479	3.148	3.0224	20.30	0.15
SDSS J142347.22+613848.3	215.94677	61.6468	2.897	2.307	2.858	2.6071	20.95	0.15
						2.7148	20.80	0.15
SDSS J142352.24+404604.4	215.96768	40.7679	3.342	2.898	3.299			
SDSS J142355.40+460733.6	215.98086	46.1260	3.202	2.836	3.119			
SDSS J142357.35+371642.2	215.98898	37.2784	3.396	2.507	3.352			
SDSS J142359.69-022933.8	215.99874	-2.4927	3.679	3.216	3.596			
SDSS J142403.82+091351.7	216.01595	9.2311	2.872	2.307	2.833			
SDSS J142430.13+361036.0	216.12557	36.1767	2.445	2.307	2.410			
SDSS J142440.39+515527.3	216.16831	51.9243	3.922	3.435	3.873			
SDSS J142446.29+054717.3	216.19291	5.7881	2.394	2.307	2.360	2.3078	20.40	0.15
SDSS J142451.40+574540.6	216.21424	57.7613	2.806	2.499	2.768			
SDSS J142502.12+233437.9	216.25887	23.5772	3.612	2.447	3.566	3.1868	21.00	0.15
SDSS J142514.69+434909.4	216.31123	43.8193	2.585	2.307	2.550			
SDSS J142522.79+394337.9	216.34510	39.7273	3.359	2.628	3.315			
SDSS J142526.09+082718.4	216.35875	8.4551	4.955	4.025	4.856			
SDSS J142537.71+545834.2	216.40713	54.9762	3.373	3.042	3.330			
SDSS J142539.09+453504.0	216.41291	45.5845	4.028	3.606	3.978			
SBS 1424+543	216.43052	54.1054	3.248	2.307	3.206			
SDSS J142545.42+491654.0	216.43929	49.2817	4.227	3.753	4.175			
SDSS J142555.22+373900.7	216.48011	37.6502	2.731	2.349	2.694			
SDSS J142613.05+535129.1	216.55442	53.8581	3.235	2.375	3.192			
SDSS J142618.25+053439.2	216.57608	5.5776	3.035	2.636	2.995			
SDSS J142619.76+025949.7	216.58237	2.9971	2.894	2.630	2.855			
SDSS J142623.15+351154.9	216.59649	35.1986	3.477	3.176	3.433			
SDSS J142644.91+042653.4	216.68713	4.4482	2.622	2.307	2.586			
SDSS J142647.80+002739.9	216.69920	0.4611	3.713	3.246	3.630			
SDSS J142651.02+380906.1	216.71259	38.1517	3.009	2.449	2.969			
SDSS J142656.04+394604.8	216.73351	39.7680	2.459	2.307	2.424			
SBS 1425+606	216.73407	60.4308	3.192	2.307	3.150	2.8267	20.30	0.10
SDSS J142704.23-030745.6	216.76765	-3.1294	3.320	2.994	3.277			
SDSS J142704.63+065410.6	216.76931	6.9030	3.175	2.332	3.133			
SDSS J142705.86+330817.9	216.77443	33.1383	4.703	3.812	4.608			
SDSS J142709.41+342847.7	216.78921	34.4799	3.172	2.810	3.130			
SDSS J142709.81+001450.2	216.79090	0.2473	2.908	2.307	2.869			
SDSS J142714.57+465913.7	216.81072	46.9872	3.206	2.487	3.164			
SDSS J142715.33-012631.2	216.81389	-1.4420	2.521	2.307	2.486			
SDSS J142727.98+461914.2	216.86661	46.3206	3.205	2.440	3.163	2.6256	20.50	0.20
SDSS J142743.12+123440.0	216.92969	12.5778	2.415	2.310	2.381			
SDSS J142745.71+550410.2	216.94047	55.0695	3.155	2.886	3.114			
SDSS J142746.83+441718.8	216.94514	44.2886	2.498	2.307	2.463			
SDSS J142749.56-012941.3	216.95652	-1.4948	3.434	2.699	3.390	3.0018	20.35	0.15
SDSS J142755.85-002951.0	216.98273	-0.4975	3.365	2.331	3.322			
SDSS J142836.58+065647.1	217.15244	6.9464	3.034	2.307	2.993			
SDSS J142840.38-012755.2	217.16827	-1.4653	2.603	2.307	2.567			
SDSS J142848.50+504710.2	217.20211	50.7862	3.374	2.960	3.330	2.9872	20.60	0.20
SDSS J142858.01+344149.9	217.24172	34.6972	3.076	2.725	3.035			
SDSS J142903.03-014519.3	217.26264	-1.7554	3.399	2.471	3.355			
SDSS J142915.19+343820.3	217.31332	34.6390	2.351	2.307	2.318			
SDSS J142921.87+320624.6	217.34114	32.1068	3.097	2.307	3.056			
SDSS J142933.00+631412.4	217.38755	63.2368	2.753	2.678	2.716			
SDSS J142938.90+644826.5	217.41216	64.8074	2.533	2.438	2.451			
SDSS J142946.07+121612.8	217.44199	12.2702	3.197	2.768	3.156			
SDSS J142947.70+114316.7	217.44878	11.7213	2.408	2.307	2.374			
SDSS J142951.86+631631.9	217.46614	63.2755	2.404	2.307	2.370			
SDSS J142954.00+450335.3	217.47501	45.0598	2.433	2.307	2.398			
SDSS J142957.09-011757.1	217.48790	-1.2992	3.111	2.925	3.070			

Continued on Next Page...

Table I.1 – Continued

Name	RA	Dec	z_{em}	z_{min}	z_{max}	z_{abs}	$\log N(\mathrm{H\,I})$	$\epsilon[\log N(\mathrm{H\,I})]$
SDSS J143002.55+565647.5	217.51071	56.9466	2.526	2.307	2.491			
SDSS J143005.32+451042.2	217.52220	45.1784	3.108	2.368	3.067			
SDSS J143007.33+483052.9	217.53063	48.5147	3.987	3.516	3.937			
SDSS J143009.54+550535.0	217.53980	55.0931	3.722	3.367	3.675			
SDSS J143012.35+430333.0	217.55150	43.0592	2.736	2.353	2.698			
SDSS J143031.61+282831.5	217.63176	28.4754	4.306	2.811	4.253			
LBQS 1428+0202	217.67016	1.8278	2.110	1.634	2.075			
SDSS J143044.40+560627.3	217.68504	56.1076	3.288	2.909	3.245			
SDSS J143048.84+481102.7	217.70350	48.1841	2.499	2.334	2.464			
SDSS J143049.38+651050.5	217.70585	65.1807	2.743	2.359	2.705			
SDSS J143051.26+071833.2	217.71360	7.3092	3.123	2.715	3.041			
SDSS J143052.63+094654.8	217.71933	9.7819	2.587	2.525	2.551			
SDSS J143057.15+625113.0	217.73821	62.8536	2.509	2.307	2.474			
SDSS J143108.97+381000.7	217.78738	38.1669	3.211	2.341	3.169			
SDSS J143111.46+334230.2	217.79779	33.7084	2.343	2.307	2.309			
SDSS J143118.10+572428.6	217.82546	57.4079	3.231	2.347	3.189			
SDSS J143119.22+521242.2	217.83012	52.2117	2.556	2.488	2.520			
SDSS J143133.97+460132.2	217.89159	46.0256	2.639	2.326	2.602			
SDSS J143147.40+124519.5	217.94753	12.7554	2.362	2.307	2.328			
SDSS J143153.23+531400.3	217.97182	53.2334	2.615	2.307	2.579			
SDSS J143157.92+121722.1	217.99134	12.2895	3.424	2.510	3.379			
SDSS J143159.30-015609.3	217.99709	-1.9359	3.325	2.356	3.282			
SDSS J143211.03+480210.5	218.04599	48.0363	2.458	2.307	2.424			
[HB89] 1429+118	218.05360	11.6648	2.990	2.307	2.950			
SDSS J143222.86+423350.0	218.09527	42.5639	2.787	2.400	2.749			
SDSS J143224.77+394024.4	218.10321	39.6735	4.292	3.105	4.239	3.2740	21.00	0.15
LBQS 1429-0053	218.12190	-1.1045	2.080	1.719	2.047			
SDSS J143231.97+395042.8	218.13324	39.8452	3.055	2.654	2.973			
SDSS J143232.70+401153.7	218.13627	40.1983	2.996	2.399	2.956	2.6566	20.45	0.15
SDSS J143236.18+234914.4	218.15076	23.8207	2.945	2.325	2.905	2.8115	20.40	0.15
SDSS J143239.76+031153.5	218.16570	3.1982	2.513	2.328	2.477			
SDSS J143244.93+525150.4	218.18724	52.8640	3.094	2.689	3.012			
SDSS J143245.60+231122.1	218.19002	23.1895	2.507	2.307	2.472			
SDSS J143247.06+462154.0	218.19613	46.3650	3.357	2.664	3.314			
SDSS J143248.81+501048.7	218.20338	50.1802	2.464	2.307	2.429			
SDSS J143254.86+405335.5	218.22862	40.8932	3.279	3.115	3.237			
SDSS J143256.63+494844.1	218.23598	49.8123	2.543	2.307	2.507			
SDSS J143300.89+103027.7	218.25372	10.5077	4.141	3.327	4.090			
SDSS J143302.89+043343.7	218.26205	4.5621	3.201	2.557	3.159			
SDSS J143304.34+640214.8	218.26809	64.0375	3.775	3.302	3.692			
SDSS J143306.61+404628.0	218.27757	40.7745	2.458	2.307	2.424			
SDSS J143307.40+003319.0	218.28085	0.5553	2.743	2.359	2.706			
SDSS J143310.60+604055.2	218.29422	60.6820	3.759	2.832	3.712			
SDSS J143318.83-013744.5	218.32849	-1.6291	3.955	3.086	3.905			
SDSS J143319.52+492954.3	218.33136	49.4984	3.576	2.564	3.530	2.9111	21.60	0.15
SDSS J143327.40+482354.1	218.36418	48.3984	3.924	2.763	3.875			
SDSS J143352.21+022713.9	218.46754	2.4539	4.729	3.834	4.633			
SDSS J143355.02+503832.4	218.47929	50.6424	2.471	2.307	2.437	2.3567	20.30	0.15
SDSS J143359.69+550425.3	218.49875	55.0737	3.265	2.618	3.222			
SDSS J143402.92+484400.9	218.51220	48.7336	3.707	3.225	3.660			
SDSS J143406.28+440741.8	218.52617	44.1283	3.067	2.404	3.026			
SDSS J143408.31+232229.9	218.53464	23.3750	3.970	3.171	3.920	3.4111	20.70	0.20
SDSS J143415.64+601037.7	218.56522	60.1772	2.490	2.307	2.455			
SDSS J143428.02+442924.6	218.61677	44.4902	2.498	2.307	2.463			
SDSS J143428.62+453627.5	218.61930	45.6077	2.648	2.307	2.612			
SDSS J143431.21+062736.7	218.63008	6.4602	3.344	2.611	3.301			
SDSS J143433.77+402758.4	218.64073	40.4662	2.977	2.324	2.937			
SDSS J143440.93+584305.7	218.67060	58.7183	3.342	3.226	3.298			
SDSS J143443.11-021113.8	218.67964	-2.1872	3.650	2.635	3.604			
SDSS J143447.89+422048.0	218.69957	42.3467	3.206	2.375	3.164			
SDSS J143449.63+594556.6	218.70681	59.7658	2.906	2.307	2.867			
SDSS J143450.08+621158.9	218.70869	62.1997	4.027	3.155	3.977			
SDSS J143455.38+035030.8	218.73076	3.8419	2.853	2.307	2.815			
SDSS J143500.46+050614.5	218.75192	5.1040	2.483	2.307	2.448			
SBS 1433+542	218.75225	53.9983	2.636	2.307	2.599	2.3428	21.05	0.10
SDSS J143502.84-013411.1	218.76186	-1.5698	3.220	2.356	3.178			
SDSS J143506.16+240144.8	218.77570	24.0291	2.810	2.433	2.727			
SDSS J143506.45+335526.0	218.77689	33.9239	3.940	2.900	3.891			
SDSS J143523.42+305722.0	218.84761	30.9561	4.350	2.942	4.297			
SDSS J143534.64+032529.5	218.89436	3.4249	2.862	2.496	2.823			
SDSS J143536.83+010956.9	218.90347	1.1658	2.971	2.323	2.931			
SDSS J143537.40+405649.0	218.90587	40.9470	3.137	2.359	3.096			

Continued on Next Page...

Table I.1 – Continued

Name	RA	Dec	z_{em}	z_{min}	z_{max}	z_{abs}	log N(H I)	ϵ[log N(H I)]
LBQS 1433+0223	218.91544	2.1791	2.140	1.634	2.111			
SDSS J143543.71+342906.4	218.93217	34.4851	2.547	2.307	2.512			
SDSS J143545.62+115345.7	218.94013	11.8960	2.442	2.307	2.408			
SDSS J143551.83+434132.4	218.96599	43.6923	3.189	2.499	3.147			
SDSS J143557.16+490518.3	218.98820	49.0884	3.923	3.130	3.874			
SDSS J143605.00+213239.2	219.02087	21.5442	5.227	4.254	5.123	4.5270	20.60	0.20
SDSS J143620.40+330746.8	219.08503	33.1297	3.209	2.781	3.167			
SDSS J143621.28+484607.4	219.08868	48.7687	2.395	2.307	2.361			
LBQS 1433-0025	219.11859	-0.6445	2.040	1.634	2.012			
SDSS J143629.94+063508.0	219.12477	6.5856	4.828	3.917	4.731			
SDSS J143707.56+042817.0	219.28152	4.4714	2.859	2.320	2.821			
SDSS J143708.07+062735.9	219.28364	6.4600	3.778	2.729	3.730			
SDSS J143718.08+051800.5	219.32538	5.3002	2.907	2.507	2.868			
SDSS J143734.45+603858.1	219.39356	60.6495	2.535	2.316	2.500			
SDSS J143740.08+342619.0	219.41704	34.4386	3.030	2.632	2.990			
SDSS J143745.77+401203.6	219.44076	40.2010	3.080	2.928	3.039			
SDSS J143751.82+232313.3	219.46594	23.3870	5.320	4.332	5.215	4.8010	21.10	0.20
SDSS J143755.26+071257.6	219.48025	7.2160	2.356	2.307	2.322			
SDSS J143819.76-000241.0	219.58235	-0.0447	2.850	2.307	2.811			
SDSS J143820.46+541639.0	219.58529	54.2775	2.536	2.399	2.500			
SDSS J143827.56+344210.0	219.61487	34.7028	3.648	2.667	3.602			
SDSS J143828.50+441812.0	219.61877	44.3034	2.100	1.769	2.069			
SDSS J143832.29+481815.4	219.63457	48.3043	3.828	2.864	3.780	3.5559	20.35	0.20
SDSS J143835.95+431459.2	219.64983	43.2498	4.686	3.798	4.591	4.3980	20.80	0.20
SDSS J143840.20+543752.4	219.66752	54.6312	3.157	3.001	3.115			
SDSS J143850.48+055622.6	219.71038	5.9396	4.437	3.587	4.346			
SDSS J143900.33+055228.9	219.75142	5.8747	3.346	2.666	3.303			
SDSS J143901.35+504241.0	219.75566	50.7114	2.642	2.307	2.606			
SDSS J143903.98+523836.2	219.76662	52.6434	2.467	2.307	2.432			
SDSS J143912.04+111740.5	219.80018	11.2946	2.583	2.313	2.547			
SDSS J143914.73+384401.9	219.81143	38.7339	3.065	2.325	3.024			
SDSS J143917.17+095838.8	219.82158	9.9775	2.993	2.628	2.953			
SDSS J143926.32+115528.4	219.85969	11.9246	3.043	2.397	3.003			
SDSS J143931.00+013701.1	219.87918	1.6170	2.522	2.307	2.487			
SDSS J143931.17+470317.7	219.87990	47.0549	2.431	2.307	2.397			
SDSS J143943.05+491214.4	219.92942	49.2040	3.072	2.307	3.031			
SDSS J143944.38+405534.6	219.93498	40.9263	3.692	2.731	3.645			
SDSS J143948.06+042112.8	219.95029	4.3536	2.857	2.307	2.819			
SDSS J143952.59+415051.6	219.96917	41.8477	3.711	2.882	3.664			
SDSS J143954.64+334658.9	219.97769	33.7831	3.425	2.481	3.381			
SDSS J144014.66+472528.0	220.06109	47.4245	2.704	2.525	2.667			
SDSS J144032.04+403932.9	220.13352	40.6592	2.876	2.495	2.837	2.5982	21.40	0.15
SDSS J144033.05+104304.1	220.13773	10.7178	2.968	2.656	2.929			
SDSS J144038.37+621511.5	220.15991	62.2532	2.988	2.380	2.948	2.7882	20.35	0.15
SDSS J144039.54+404730.7	220.16476	40.7919	3.213	2.307	3.171			
SDSS J144046.51+512654.3	220.19382	51.4484	3.692	2.853	3.645			
SDSS J144051.89+063709.6	220.21623	6.6193	3.386	2.495	3.342	2.5090	21.35	0.20
						2.8229	20.30	0.20
SDSS J144055.55+091607.4	220.23149	9.2687	2.365	2.307	2.332			
SDSS J144059.63+420404.1	220.24846	42.0678	3.027	2.846	2.987			
SDSS J144101.18+555222.9	220.25496	55.8731	3.457	2.588	3.412	2.9052	20.30	0.20
						2.9379	20.95	0.20
						3.2032	20.60	0.15
SDSS J144102.20+474611.9	220.25921	47.7700	3.753	3.282	3.670			
SDSS J144105.32+581408.9	220.27217	58.2358	3.309	2.543	3.266			
SDSS J144106.07+481109.8	220.27531	48.1861	3.018	2.325	2.978			
SDSS J144112.80+585839.8	220.30338	58.9777	2.899	2.307	2.860			
SDSS J144113.27-013745.3	220.30531	-1.6293	2.708	2.449	2.671			
SDSS J144114.64+345605.1	220.31101	34.9348	3.047	2.477	3.006			
SDSS J144117.46+035910.5	220.32276	3.9863	4.289	3.050	4.236			
SDSS J144127.65+475048.7	220.36525	47.8469	3.198	2.384	3.156			
SDSS J144144.76+472003.1	220.43652	47.3342	3.627	2.658	3.580	3.3746	20.35	0.20
SDSS J144147.52+541538.1	220.44803	54.2606	3.467	2.720	3.422	3.3305	20.35	0.15
SDSS J144153.51+454246.5	220.47304	45.7129	3.037	2.647	2.996	2.7925	20.45	0.20
LBQS 1439+0047	220.50749	0.5802	1.860	1.649	1.828			
SDSS J144204.05+042602.4	220.51691	4.4340	2.510	2.307	2.475	2.3937	20.85	0.20
SDSS J144204.90+470145.3	220.52043	47.0293	3.820	3.329	3.772	3.6152	20.80	0.20
SDSS J144213.09+391856.0	220.55457	39.3156	3.627	2.597	3.580			
SDSS J144217.82+464809.6	220.57428	46.8027	2.614	2.307	2.347			
SDSS J144218.09+484101.8	220.57540	48.6839	2.419	2.307	2.385			
SDSS J144225.30+625600.9	220.60543	62.9336	3.246	2.400	3.203	3.0624	20.35	0.15
SDSS J144228.49+470604.6	220.61872	47.1013	2.473	2.307	2.439			

Continued on Next Page...

Table I.1 – Continued

Name	RA	Dec	z_{em}	z_{min}	z_{max}	z_{abs}	$\log N(\mathrm{H\,I})$	$\epsilon[\log N(\mathrm{H\,I})]$
SDSS J144234.85+442833.5	220.64522	44.4760	3.582	2.817	3.536	2.9148	20.90	0.20
SDSS J144237.42+304921.4	220.65595	30.8226	4.794	4.713	4.736			
SDSS J144239.55+020418.9	220.66480	2.0719	2.821	2.430	2.782			
SDSS J144241.74+100533.9	220.67395	10.0928	2.889	2.307	2.850			
SDSS J144250.12+092001.5	220.70884	9.3338	3.532	1.780	3.487			
SDSS J144258.86+423206.4	220.74531	42.5351	3.622	2.927	3.576			
LBQS 1440-0024	220.74962	-0.6236	1.810	1.634	1.786			
SDSS J144306.66+563112.7	220.77786	56.5202	2.463	2.307	2.428			
SDSS J144311.58+354646.3	220.79829	35.7796	2.942	2.307	2.902			
SDSS J144319.63+011917.1	220.83185	1.3214	2.694	2.500	2.657			
SDSS J144324.20+381319.8	220.85087	38.2222	4.007	3.520	3.957			
SDSS J144331.17+272436.7	220.87988	27.4102	4.406	3.095	4.352	4.2230	20.90	0.15
SDSS J144335.15+334859.8	220.89650	33.8166	3.637	2.639	3.591			
SDSS J144340.69+585653.2	220.91960	58.9481	4.278	3.756	4.195			
SDSS J144346.26+564545.9	220.94279	56.7627	2.732	2.503	2.695			
SDSS J144346.67+462509.2	220.94454	46.4192	2.373	2.333	2.339			
SDSS J144404.61+345735.3	221.01925	34.9598	3.386	2.965	3.343			
SDSS J144404.86+375714.6	221.02027	37.9541	3.358	2.474	3.314			
SDSS J144407.63-010152.7	221.03180	-1.0313	4.530	3.666	4.438			
SDSS J144418.22+350022.8	221.07592	35.0063	2.976	2.880	2.937			
SDSS J144420.79+380000.5	221.08664	38.0002	4.303	3.292	4.250	3.7630	20.55	0.25
						3.9432	20.70	0.20
SDSS J1444-0123	221.11931	-1.3956	4.179	3.315	4.127			
SDSS J144429.39+124906.6	221.12248	12.8185	2.996	2.600	2.913			
SDSS J144436.68+105549.8	221.15286	10.9305	3.236	2.828	3.194			
SDSS J144436.92+042904.1	221.15387	4.4845	2.397	2.307	2.363			
SDSS J144447.14+413940.2	221.19644	41.6612	3.145	2.942	3.104			
SDSS J144448.37+382248.5	221.20159	38.3802	2.438	2.356	2.404			
SDSS J144452.44+052758.7	221.21852	5.4663	3.419	3.000	3.375			
SDSS J144452.77+505403.0	221.21992	50.9008	3.372	2.413	3.328			
SDSS J144456.24+474455.2	221.23441	47.7487	2.467	2.307	2.433			
SDSS J144456.56+113512.2	221.23571	11.5868	3.379	2.613	3.335	2.6737	21.15	0.20
SDSS J144504.58+405848.3	221.26915	40.9801	3.142	2.751	3.100	2.8822	20.90	0.25
SDSS J144516.46+095836.0	221.31860	9.9767	3.562	1.600	3.517			
SDSS J144524.49+070932.1	221.35206	7.1589	3.045	2.307	3.005			
SDSS J144542.75+490248.9	221.42817	49.0469	3.876	2.661	3.827	3.0495	20.65	0.15
SDSS J144544.90+373328.9	221.43711	37.5581	2.956	2.307	2.916			
SDSS J144549.95+003047.1	221.45813	0.5131	2.691	2.549	2.654			
SDSS J144553.60+395124.8	221.47336	39.8569	2.669	2.383	2.632			
SDSS J144554.08+052438.0	221.47535	5.4106	2.558	2.413	2.522			
SDSS J144559.71+372317.1	221.49880	37.3881	3.741	2.949	3.694			
SDSS J144606.64+070200.1	221.52768	7.0334	2.500	2.307	2.465			
SDSS J144609.35-021700.8	221.53897	-2.2836	3.563	2.916	3.517			
SDSS J144612.33+113409.3	221.55139	11.5693	3.257	2.937	3.214			
SDSS J144617.35-010131.1	221.57232	-1.0253	4.147	3.058	4.095	3.7098	20.30	0.20
						4.0859	20.40	0.15
SDSS J144622.54+111810.7	221.59396	11.3030	3.266	2.554	3.224			
SDSS J144622.99+434308.7	221.59586	43.7191	3.169	2.342	3.127			
SDSS J144631.99+441812.6	221.63333	44.3035	3.096	3.015	3.055			
SDSS J144634.35+012019.9	221.64316	1.3389	3.201	2.432	3.159			
SDSS J144644.75+342610.2	221.68647	34.4362	3.001	2.307	2.961			
SDSS J144651.04+400436.0	221.71268	40.0767	2.528	2.307	2.493			
LBQS 1444+0126	221.72104	1.2322	2.210	1.717	2.174			
SDSS J144659.83+412935.4	221.74936	41.4932	2.980	2.307	2.940	2.5702	20.35	0.15
SDSS J144713.03-012158.5	221.80435	-1.3663	4.028	3.514	3.978			
LBQS 1444-0112	221.82282	-1.4118	2.150	1.651	2.121			
SDSS J144717.97+040112.4	221.82490	4.0201	4.580	3.708	4.487			
SDSS J144724.65+333852.5	221.85273	33.6479	2.494	2.307	2.459			
SDSS J144733.46+465723.6	221.88943	46.9566	3.587	2.782	3.541			
SDSS J144741.45+510824.7	221.92276	51.1402	3.513	2.613	3.468			
SDSS J144742.93-015919.7	221.92892	-1.9888	3.104	2.749	3.063			
SDSS J144751.02+412640.3	221.96263	41.4445	3.092	3.041	3.052			
SDSS J144752.45+582420.2	221.96859	58.4057	2.983	2.307	2.356			
SDSS J144758.43-005055.3	221.99349	-0.8487	3.836	3.071	3.787			
SDSS J144805.84+440806.4	222.02434	44.1351	3.284	2.581	3.242	2.5968	21.25	0.15
SDSS J144818.61+400830.4	222.07758	40.1418	3.673	2.694	3.626			
SDSS J144841.49+484123.8	222.17295	48.6899	2.484	2.307	2.449			
SDSS J144844.58+363103.2	222.18575	36.5176	3.306	3.091	3.263			
SDSS J144850.34+401234.1	222.20979	40.2095	3.057	2.900	3.016			
SDSS J144852.25+105956.7	222.21774	10.9991	2.997	2.370	2.957			
SDSS J144853.41+473821.2	222.22255	47.6392	2.894	2.566	2.855			
SDSS J144855.25+020448.7	222.23022	2.0802	2.480	2.319	2.445			

Continued on Next Page...

Table I.1 – Continued

Name	RA	Dec	z_{em}	z_{min}	z_{max}	z_{abs}	$\log N(\mathrm{H\,I})$	$\epsilon[\log N(\mathrm{H\,I})]$
SDSS J144903.01+633541.8	222.26259	63.5950	2.380	2.307	2.346			
SDSS J144907.50-025722.6	222.28126	-2.9563	3.793	2.815	3.746			
SDSS J144929.30+124344.0	222.37209	12.7289	3.220	2.850	3.178			
SDSS J144934.43+323129.2	222.39347	32.5248	3.575	2.861	3.529	3.4572	20.75	0.15
SDSS J144943.54+490730.0	222.43152	49.1250	2.994	2.585	2.954			
SDSS J144946.61+442551.6	222.44423	44.4310	2.444	2.383	2.410			
SDSS J144954.48+531554.7	222.47705	53.2652	3.099	2.681	3.058	3.0104	20.35	0.15
SDSS J145005.38+114248.2	222.52244	11.7134	3.388	2.495	3.344			
SDSS J145017.66+340557.0	222.57362	34.0992	3.116	2.707	3.075			
SDSS J145019.25-011740.3	222.58022	-1.2945	3.456	2.750	3.411	3.1901	21.00	0.15
SDSS J145034.49+411651.6	222.64374	41.2810	2.974	2.317	2.934	2.8450	20.30	0.15
SDSS J145101.97+060229.7	222.75824	6.0416	3.666	2.860	3.619			
SDSS J145107.93+025615.6	222.78307	2.9377	4.483	3.626	4.392			
SDSS J145114.31+380628.1	222.80975	38.1079	2.534	2.388	2.498			
SDSS J145117.20+020616.9	222.82169	2.1047	2.859	2.817	2.820			
SDSS J145120.55+382606.4	222.83565	38.4351	2.513	2.335	2.478			
SDSS J145144.43+444019.4	222.93516	44.6721	3.824	3.053	3.775			
SDSS J145201.55+410443.9	223.00649	41.0789	4.118	2.840	4.067			
SDSS J145214.96+382632.6	223.06236	38.4424	3.534	2.414	3.489	2.6569	20.40	0.20
SDSS J145227.20+381701.2	223.11334	38.2837	3.104	2.684	3.063			
SDSS J145229.37+595156.3	223.12242	59.8657	4.029	2.954	3.979			
SDSS J145232.93+495329.8	223.13722	49.8916	3.889	3.072	3.840			
SDSS J145239.17+542808.6	223.16325	54.4691	2.838	2.307	2.799			
SDSS J145243.61+015430.7	223.18177	1.9085	3.908	2.882	3.859	3.2529	21.45	0.15
SDSS J145247.72+115620.1	223.19884	11.9389	4.026	3.238	3.975			
SDSS J145249.77+402654.9	223.20739	40.4486	2.901	2.307	2.862			
SDSS J145301.68+502238.0	223.25703	50.3772	2.400	2.307	2.366			
SDSS J145312.03+324932.7	223.30014	32.8258	3.188	2.759	3.146			
SDSS J145329.53+002357.3	223.37306	0.3993	2.542	2.307	2.506	2.4440	20.40	0.15
SDSS J145345.02+502821.8	223.43762	50.4727	2.525	2.307	2.490			
SDSS J145350.38+610108.9	223.45993	61.0192	4.112	3.275	4.061			
SDSS J145350.48+025252.2	223.46038	2.8812	2.520	2.307	2.484			
SDSS J145352.72+561220.0	223.46970	56.2056	2.745	2.391	2.707			
SDSS J145353.56+032450.8	223.47318	3.4141	2.405	2.307	2.370			
SDSS J145403.78+402603.1	223.51577	40.4342	3.333	3.175	3.289			
SDSS J145405.01+002822.8	223.52091	0.4730	2.653	2.307	2.617			
SDSS J145408.95+511443.7	223.53732	51.2455	3.644	2.464	3.598	3.4084	20.50	0.15
SDSS J145416.81+395501.8	223.57008	39.9172	2.863	2.490	2.824			
[HB89] 1451+123	223.57743	12.1816	3.260	2.158	3.207	2.4780	20.40	0.20
SDSS J145428.52+571441.3	223.61885	57.2448	3.241	3.054	3.159			
SDSS J145429.57+402319.8	223.62322	40.3889	3.108	2.476	3.067			
SDSS J145429.65+004121.1	223.62357	0.6892	2.657	2.307	2.620			
SDSS J145431.53+585053.0	223.63140	58.8481	2.646	2.307	2.609			
SDSS J145437.08+374134.5	223.65450	37.6929	3.195	2.408	3.153			
SBS 1453+506	223.70037	50.4853	2.348	2.307	2.315			
SDSS J145453.53+032456.8	223.72307	3.4158	2.367	2.307	2.334			
SDSS J145455.51-022243.6	223.73130	-2.3788	2.497	2.309	2.462			
SDSS J145457.05+590614.4	223.73772	59.1040	2.455	2.326	2.420			
SDSS J145512.99+453338.5	223.80416	45.5607	4.249	3.730	4.197			
SDSS J145519.13+350901.7	223.82973	35.1505	3.146	2.763	3.104			
SDSS J145525.75+373958.2	223.85731	37.6662	3.744	3.279	3.697			
SDSS J145525.94+485701.5	223.85810	48.9504	3.499	2.769	3.454			
SDSS J145527.92+552647.1	223.86638	55.4464	4.260	3.205	4.208			
SDSS J145535.24+041938.1	223.89685	4.3273	3.052	2.427	3.012			
SDSS J145543.11+491703.3	223.92967	49.2843	3.837	3.429	3.788			
SDSS J145554.12+443137.6	223.97557	44.5271	2.671	2.307	2.634			
SBS 1454+525	223.97629	52.3079	2.347	2.307	2.314			
SDSS J145555.80+501915.1	223.98254	50.3209	2.478	2.404	2.443			
SDSS J145603.82+123650.5	224.01593	12.6141	2.343	2.307	2.309			
SDSS J145624.66+040741.0	224.10277	4.1281	2.899	2.307	2.860	2.6732	20.35	0.20
SDSS J145628.97+200727.1	224.12074	20.1242	4.249	2.878	4.197			
SDSS J145635.26+502136.2	224.14694	50.3601	2.658	2.307	2.622			
SDSS J145635.72+001150.5	224.14885	0.1974	2.390	2.307	2.357			
SDSS J145640.98-021819.3	224.17077	-2.3054	2.963	2.584	2.923			
SDSS J145702.95+600034.4	224.26234	60.0096	2.944	2.566	2.904			
SDSS J145705.33+474830.8	224.27226	47.8086	2.495	2.307	2.460			
SDSS J145706.33+001745.8	224.27639	0.2961	2.525	2.307	2.490			
SDSS J145722.13+345304.8	224.34224	34.8847	3.329	2.467	3.286			
SDSS J145754.03+003639.0	224.47516	0.6108	2.760	2.375	2.723			
SDSS J145759.63+623321.2	224.49848	62.5559	3.068	2.313	2.357			
SDSS J145801.55+460516.6	224.50650	46.0879	2.571	2.342	2.535			
SDSS J145804.06+340438.0	224.51692	34.0772	3.750	2.970	3.703			

Continued on Next Page...

Table I.1 – Continued

Name	RA	Dec	z_{em}	z_{min}	z_{max}	z_{abs}	$\log N(\mathrm{H\,I})$	$\epsilon[\log N(\mathrm{H\,I})]$
SDSS J145806.00+332723.0	224.52500	33.4564	4.848	4.433	4.790			
[HB89] 1455+123	224.53156	12.1606	3.080	1.830	3.033			
SDSS J145817.52-004115.7	224.57300	-0.6877	2.618	2.307	2.582			
SDSS J145829.13+333408.0	224.62141	33.5689	3.957	2.984	3.908	3.0039	20.70	0.20
SDSS J145836.82+430657.5	224.65343	43.1160	2.585	2.307	2.549			
SDSS J145907.18+002401.2	224.77996	0.4004	3.011	2.307	2.971			
SDSS J145910.13+425213.2	224.79223	42.8703	2.967	2.574	2.885			
FBQS J145924.2+340113	224.85105	34.0203	2.790	2.307	2.752			
SDSS J145926.41-021259.6	224.86006	-2.2166	3.020	2.610	2.980			
SDSS J145927.03+325357.9	224.86271	32.8996	3.324	2.697	3.281			
SDSS J145952.05+321320.3	224.96689	32.2223	3.022	2.307	2.982			
SDSS J150000.19+333038.1	225.00081	33.5106	2.408	2.307	2.374			
SDSS J150007.66+582937.4	225.03195	58.4937	4.224	3.031	4.172	3.9150	20.50	0.10
SDSS J150026.20+330054.4	225.10917	33.0151	2.550	2.307	2.515			
SDSS J150027.89+434200.8	225.11623	43.7002	4.641	3.760	4.547			
SDSS J150056.04+382332.1	225.23353	38.3922	2.996	2.309	2.956			
SDSS J150058.13+362332.1	225.24222	36.3923	2.483	2.307	2.448			
SDSS J150116.10+525556.8	225.31713	52.9325	3.818	3.341	3.736			
SDSS J150131.76+395548.0	225.38236	39.9300	2.591	2.307	2.555			
SDSS J150133.79+605705.8	225.39082	60.9516	2.741	2.357	2.703			
SDSS J150137.63+321437.2	225.40683	32.2437	3.529	3.088	3.483	3.3928	20.65	0.15
SDSS J150147.25+480335.8	225.44691	48.0600	2.781	2.394	2.743			
SDSS J150147.63+553342.9	225.44849	55.5619	2.583	2.307	2.548			
SDSS J150217.11+355459.0	225.57132	35.9164	3.345	2.435	3.302			
SDSS J150226.18+453852.6	225.60911	45.6480	2.891	2.307	2.852			
SDSS J150226.88+483711.4	225.61204	48.6199	3.209	2.503	3.167	2.5700	20.35	0.15
SDSS J150238.38+030228.2	225.65995	3.0412	3.359	2.417	3.315			
SDSS J150245.37+081305.1	225.68905	8.2181	3.943	2.390	3.894	2.7968	20.80	0.20
[HB89] 1501+450	225.69673	44.8953	2.505	2.371	2.470			
SDSS J150321.87+323742.1	225.84113	32.6284	2.592	2.331	2.556	2.3971	20.75	0.15
SDSS J150328.88+041949.0	225.87037	4.3303	3.692	2.118	3.646			
SDSS J150332.17+364118.0	225.88408	36.6883	3.263	2.841	3.181			
SDSS J150345.94+043421.3	225.94143	4.5726	3.059	2.357	3.018	2.6184	20.40	0.15
SDSS J150406.12+360626.7	226.02551	36.1074	2.549	2.307	2.514			
SDSS J150425.53-000803.2	226.10639	-0.1343	2.840	2.446	2.802			
SDSS J150427.84+394147.7	226.11601	39.6966	2.514	2.307	2.479			
SDSS J150444.90+481222.6	226.18713	48.2063	2.992	2.308	2.952			
SDSS J150513.36+363656.7	226.30568	36.6158	2.435	2.307	2.400			
[HB89] 1503+118	226.34890	11.6901	2.780	1.957	2.740			
SDSS J150527.79+331123.5	226.36582	33.1899	2.908	2.307	2.869			
SDSS J150532.00+421803.4	226.38337	42.3010	3.107	2.326	3.066			
SDSS J150533.24+411946.3	226.38853	41.3295	3.400	2.538	3.326			
SDSS J150538.81+561259.2	226.41174	56.2165	2.423	2.307	2.389			
SBS 1504+515	226.44010	51.3778	2.791	2.307	2.753			
SDSS J150546.47+562756.9	226.44370	56.4658	3.087	2.307	3.046			
SDSS J150549.13-014338.3	226.45473	-1.7273	2.929	2.527	2.890			
SDSS J150605.35+340635.2	226.52233	34.1098	3.981	2.847	3.931	3.7239	21.05	0.15
SDSS J150606.82+041513.1	226.52846	4.2537	2.680	2.307	2.644			
SDSS J150611.23+001823.5	226.54679	0.3066	2.838	2.445	2.799			
SDSS J150613.10+002854.8	226.55463	0.4819	3.369	2.350	3.325			
SDSS J150620.48+460642.4	226.58535	46.1118	3.504	2.428	3.459	3.2686	20.35	0.15
SDSS J150628.59+315545.4	226.61917	31.9293	3.836	3.009	3.787			
SDSS J150629.87+515512.6	226.62448	51.9202	3.579	3.119	3.534			
SDSS J150634.64+351937.0	226.64436	35.3270	3.382	2.952	3.339			
SDSS J150635.62+450259.5	226.64843	45.0499	3.908	3.424	3.825			
SDSS J150643.80+533134.4	226.68256	53.5262	3.790	2.799	3.742			
SDSS J150654.54+522004.6	226.72729	52.3346	4.180	3.275	4.128	3.2230	20.70	0.10
SDSS J150702.12+335215.7	226.75885	33.8710	2.477	2.349	2.442			
SDSS J150726.31+440649.2	226.85968	44.1137	3.113	2.307	3.072	3.0643	20.75	0.15
SDSS J150728.03+351013.9	226.86681	35.1705	2.868	2.486	2.786			
SDSS J150734.93+364527.2	226.89557	36.7576	2.624	2.307	2.588			
SDSS J150753.31+334206.0	226.97216	33.7017	3.276	2.883	3.233			
SDSS J150800.30+582707.4	227.00126	58.4521	3.305	2.441	3.262			
SDSS J150802.28+430645.4	227.00956	43.1126	4.681	3.793	4.586			
SDSS J150803.99+344007.2	227.01664	34.6687	3.276	2.308	3.234			
SDSS J150817.57+432635.7	227.07321	43.4433	4.028	3.189	3.978			
SDSS J150837.68+562759.7	227.15706	56.4666	2.701	2.536	2.618			
SDSS J150851.94+515627.7	227.21644	51.9410	3.799	3.361	3.751	3.5868	20.90	0.15
SDSS J150852.00+494553.7	227.21668	49.7649	2.877	2.307	2.838			
SDSS J150914.86+372813.2	227.31193	37.4704	2.755	2.601	2.717			
SDSS J150925.53+341851.8	227.35639	34.3144	3.181	2.323	3.139			
SDSS J150925.63+505609.3	227.35682	50.9359	2.365	2.307	2.332			

Continued on Next Page...

Table I.1 – Continued

Name	RA	Dec	z_{em}	z_{min}	z_{max}	z_{abs}	log N(H I)	ϵ[log N(H I)]
SBS 1507+511	227.38430	50.9643	2.343	2.307	2.310			
SDSS J150934.84+370837.8	227.39520	37.1439	3.214	2.307	3.171			
SDSS J150936.49+451243.3	227.40206	45.2120	2.409	2.307	2.375			
SDSS J150937.77+543618.9	227.40743	54.6053	2.990	2.307	2.951			
SDSS J150937.92+343049.2	227.40795	34.5137	3.296	2.577	3.253			
SDSS J150944.08+561605.2	227.43368	56.2681	3.174	2.482	3.132			
SDSS J150949.80+504917.3	227.45754	50.8215	4.031	3.592	3.981			
SDSS J150954.06+585129.2	227.47528	58.8582	2.353	2.307	2.319			
SDSS J151002.92+570243.3	227.51218	57.0454	4.304	3.217	4.251			
SDSS J151017.78+452127.8	227.57411	45.3577	3.739	2.965	3.691			
SDSS J151018.74+444527.8	227.57816	44.7577	3.482	2.555	3.437			
SDSS J151022.26+361755.0	227.59280	36.2986	3.030	2.618	2.990			
SDSS J151037.17+340220.6	227.65495	34.0390	2.675	2.307	2.638	2.3226	21.00	0.20
SDSS J151040.11+500912.0	227.66717	50.1534	3.136	2.713	3.095			
SDSS J151041.79+031810.5	227.67414	3.3029	4.280	3.551	4.228			
SDSS J151044.66+321712.9	227.68611	32.2869	3.475	2.730	3.430			
SDSS J151116.39-010524.8	227.81833	-1.0902	3.248	2.828	3.166			
SDSS J151129.54+491637.5	227.87312	49.2771	2.400	2.347	2.366			
SDSS J151130.47+323445.7	227.87697	32.5794	3.008	2.389	2.968			
SDSS J151134.51+330550.0	227.89380	33.0972	2.350	2.307	2.316			
SDSS J151154.13+334129.2	227.97558	33.6915	3.376	2.943	3.294			
SDSS J151155.98+040802.9	227.98327	4.1342	4.679	3.792	4.584	4.0890	21.45	0.20
SDSS J151211.07+350519.2	228.04613	35.0887	3.382	3.203	3.338	3.2907	20.60	0.15
SDSS J151214.09+540816.8	228.05882	54.1380	2.664	2.313	2.581			
SDSS J151224.17+465233.4	228.10075	46.8760	3.360	2.307	3.316	3.0844	20.30	0.15
SDSS J151254.37+371831.1	228.22656	37.3087	2.748	2.377	2.666			
SDSS J151300.36+323658.3	228.25153	32.6162	2.473	2.307	2.438			
SDSS J151304.13-013100.1	228.26721	-1.5167	3.194	2.901	3.152			
SDSS J151307.20+603758.4	228.28004	60.6329	2.761	2.376	2.723			
SDSS J151318.44+545829.6	228.32686	54.9749	3.659	2.654	3.613			
SDSS J151320.89+105807.3	228.33707	10.9687	4.625	3.746	4.531			
SDSS J151336.70+430708.3	228.40297	43.1190	3.293	2.307	3.250			
SDSS J151346.93+425328.8	228.44557	42.8914	3.098	2.383	3.057			
SDSS J151348.32+362105.5	228.45136	36.3515	2.523	2.307	2.488			
SDSS J151401.51+461246.8	228.50631	46.2130	3.353	3.039	3.310	3.2952	21.10	0.20
SDSS J151426.51+452322.9	228.61051	45.3897	3.971	3.139	3.922			
SDSS J151426.98+340221.0	228.61242	34.0392	3.179	2.307	3.137			
SDSS J151441.12+505537.9	228.67136	50.9272	2.786	2.605	2.748			
SDSS J151442.73+532412.0	228.67812	53.4033	3.565	2.713	3.519			
SDSS J151447.29+492121.1	228.69705	49.3559	3.142	2.512	3.100			
SDSS J151456.84+042202.1	228.73685	4.3673	2.909	2.352	2.870			
SDSS J151503.21+613520.2	228.76340	61.5889	2.404	2.307	2.370			
SDSS J151513.83+351927.9	228.80765	35.3244	2.481	2.416	2.447			
SDSS J151537.83+602202.4	228.90764	60.3673	3.030	2.307	2.990			
SDSS J151545.22+542734.0	228.93844	54.4594	3.187	2.773	3.105			
SDSS J151545.44+441150.4	228.93936	44.1973	3.762	3.553	3.715			
SDSS J151602.33+443233.3	229.00974	44.5426	4.100	3.186	4.049	3.6152	20.45	0.25
						3.9436	20.65	0.20
SDSS J151603.79+450620.0	229.01582	45.1056	2.798	2.427	2.760			
SDSS J151616.33+523125.5	229.06807	52.5238	3.226	2.793	3.183			
SDSS J151616.52+320305.1	229.06885	32.0514	3.318	2.310	3.275	2.6308	20.55	0.15
						2.8149	20.80	0.15
SDSS J151625.68+325207.9	229.10703	32.8689	3.392	2.398	3.348			
SDSS J151631.93+442739.5	229.13310	44.4610	3.173	2.746	3.132			
SDSS J151639.89+412224.0	229.16627	41.3733	2.484	2.307	2.449			
SDSS J151652.04+534158.2	229.21688	53.6995	3.302	2.592	3.259			
SDSS J151658.64+032849.6	229.24435	3.4805	2.851	2.490	2.769			
SDSS J151708.07+330132.4	229.28365	33.0257	3.428	2.501	3.384			
SDSS J151715.86+520933.3	229.31615	52.1593	3.800	3.037	3.752	3.5048	21.45	0.15
SDSS J151717.25+035055.8	229.32191	3.8489	3.049	2.323	3.008			
SDSS J151719.09+490003.2	229.32952	49.0009	4.660	3.776	4.566			
SDSS J151752.78+535010.5	229.46992	53.8363	2.934	2.307	2.894			
SDSS J151756.18+051103.5	229.48410	5.1843	3.555	2.249	3.510	2.6885	21.40	0.10
SDSS J151815.06+330523.1	229.56279	33.0898	3.550	2.541	3.505			
SDSS J151816.57+533907.4	229.56908	53.6521	3.081	2.442	3.041	2.8948	20.60	0.15
						3.0147	20.65	0.20
SDSS J151824.37-010149.8	229.60157	-1.0305	2.586	2.307	2.550			
SDSS J151824.51+403218.4	229.60215	40.5385	3.084	2.666	3.043			
SDSS J151836.69+542056.3	229.65294	54.3490	3.701	2.677	3.654			
SDSS J151842.01+444511.0	229.67506	44.7531	2.507	2.338	2.472			
SDSS J151846.09+482245.7	229.69205	48.3794	3.254	2.307	3.212	2.9854	20.95	0.15
SDSS J151909.09+030633.7	229.78788	3.1094	4.355	3.825	4.273			

Continued on Next Page...

Table I.1 – Continued

Name	RA	Dec	z_{em}	z_{min}	z_{max}	z_{abs}	$\log N(\mathrm{H\,I})$	$\epsilon[\log N(\mathrm{H\,I})]$
SDSS J151909.17+371615.5	229.78826	37.2710	3.333	2.890	3.290			
SDSS J151910.37+360940.4	229.79321	36.1613	2.818	2.307	2.780			
SDSS J151915.50+315359.1	229.81461	31.8998	3.126	2.794	3.085			
SDSS J151924.49+034641.5	229.85205	3.7782	3.712	2.972	3.665			
SDSS J151925.71+453432.0	229.85716	45.5756	2.345	2.307	2.311			
SDSS J151936.98+420105.0	229.90413	42.0181	3.122	2.525	3.081			
SDSS J151949.30+361126.6	229.95544	36.1907	3.404	3.031	3.360			
SDSS J151951.41+303011.5	229.96425	30.5032	3.097	2.691	3.014			
SDSS J152005.93+233953.0	230.02472	23.6647	4.487	3.630	4.395			
SDSS J152008.42+442428.8	230.03512	44.4080	2.695	2.317	2.658			
SDSS J152014.32+415907.4	230.05975	41.9854	3.794	3.303	3.746			
SDSS J152034.53+383906.4	230.14390	38.6518	3.397	2.399	3.353			
SDSS J152043.59+473249.3	230.18167	47.5470	2.811	2.307	2.773			
SDSS J152046.08+584715.4	230.19207	58.7876	2.669	2.390	2.633			
SDSS J152046.45+525923.2	230.19360	52.9898	3.374	2.568	3.331	2.7646	20.55	0.15
						3.1792	20.65	0.15
SDSS J152057.27+574139.2	230.23868	57.6943	2.902	2.823	2.863			
SDSS J152058.75+460908.1	230.24483	46.1523	2.375	2.307	2.341			
SDSS J152115.69+294715.8	230.31540	29.7877	2.415	2.307	2.381			
SDSS J152117.57+175601.0	230.32326	17.9336	3.060	1.955	3.019			
SDSS J152119.68-004818.6	230.33200	-0.8052	2.934	2.307	2.895			
SDSS J152145.85+375242.3	230.44106	37.8784	3.063	2.418	3.023			
B3 1520+437	230.45672	43.6109	2.180	1.775	2.148			
SDSS J152200.54+512512.5	230.50229	51.4202	2.614	2.463	2.578			
SDSS J152209.65+454625.6	230.54025	45.7738	4.329	3.310	4.276			
SDSS J152222.52+373743.1	230.59385	37.6286	3.092	2.356	3.051			
SDSS J152226.92+480153.4	230.61220	48.0315	3.320	2.949	3.277			
SDSS J152229.75+034215.4	230.62397	3.7043	2.349	2.307	2.316			
SDSS J152245.19+024543.8	230.68830	2.7622	4.074	3.099	4.023			
SDSS J152308.47+500246.2	230.78534	50.0462	3.651	3.280	3.604			
SDSS J152310.14+573048.6	230.79234	57.5134	2.980	2.307	2.941			
SDSS J152314.87+381402.0	230.81196	38.2339	3.159	2.307	3.117			
SDSS J152326.02+412344.3	230.85846	41.3957	3.197	2.855	3.155			
SDSS J152327.74+474626.9	230.86561	47.7742	2.895	2.307	2.856			
SDSS J152347.62+494138.5	230.94847	49.6940	3.749	2.984	3.702			
SDSS J152348.83+434909.0	230.95354	43.8192	3.765	2.961	3.717	3.5611	20.80	0.15
SDSS J152403.62+311455.8	231.01511	31.2488	3.430	3.018	3.386			
SDSS J152404.23+134417.5	231.01763	13.7382	4.788	3.884	4.691	4.3050	21.05	0.20
SDSS J152413.09+341953.7	231.05456	34.3316	2.357	2.307	2.324			
SDSS J152413.34+430537.3	231.05563	43.0937	3.920	2.862	3.870	2.8706	20.40	0.20
SDSS J152418.29+002426.9	231.07627	0.4074	2.490	2.307	2.455			
SDSS J152421.62+492559.1	231.09010	49.4331	2.553	2.374	2.517			
SDSS J152436.08+212309.1	231.15035	21.3859	3.600	2.052	3.554			
SDSS J152436.19+454744.6	231.15081	45.7957	3.065	2.411	3.024			
SDSS J152459.95+363755.8	231.24981	36.6322	3.185	2.605	3.143			
SDSS J152502.17+401251.8	231.25905	40.2144	2.685	2.320	2.603			
SDSS J152529.17+292813.2	231.37160	29.4703	2.355	2.307	2.322			
SBS 1524+517	231.47455	51.6137	2.883	2.307	2.844			
SDSS J152559.49+485848.1	231.49794	48.9800	3.362	3.010	3.318			
SDSS J152604.77+522920.1	231.51990	52.4889	3.859	2.942	3.810			
SDSS J152626.60+412939.3	231.61087	41.4943	2.684	2.356	2.647			
SDSS J152629.27+585524.2	231.62200	58.9234	2.479	2.307	2.444			
SDSS J152630.34+412021.8	231.62643	41.3394	3.229	2.637	3.187			
SDSS J152636.88+572715.9	231.65374	57.4544	3.187	2.839	3.145			
SDSS J152642.86+665054.7	231.67864	66.8485	3.020	1.955	2.980			
SDSS J152646.13+565348.2	231.69222	56.8967	2.422	2.307	2.388	2.3096	20.60	0.15
SDSS J152652.76+405126.5	231.71987	40.8574	3.712	2.717	3.665			
SDSS J152720.03+543233.9	231.83347	54.5428	2.932	2.530	2.893			
SDSS J152747.70+322215.7	231.94879	32.3710	3.402	2.675	3.358			
SDSS J152807.19+325456.1	232.02998	32.9156	3.651	2.596	3.604	3.4750	21.05	0.15
SDSS J152824.88+344204.1	232.10371	34.7011	2.685	2.352	2.357			
SDSS J152830.41+440216.2	232.12674	44.0378	3.062	2.677	3.021			
SDSS J152834.25+363538.4	232.14274	36.5940	3.233	2.901	3.190			
SDSS J152838.78-001439.0	232.16162	-0.2442	3.244	2.525	3.202			
SDSS J152847.72+315118.6	232.19887	31.8552	3.034	2.387	2.994			
SDSS J152852.86+460408.6	232.22025	46.0691	3.042	2.354	3.001			
SDSS J152917.51+473838.7	232.32298	47.6441	3.079	2.318	3.039	2.6739	20.35	0.15
SDSS J152922.04+570817.3	232.34191	57.1382	2.654	2.352	2.617			
SDSS J152928.24+490651.5	232.36770	49.1144	3.070	2.307	3.029			
SDSS J152949.16+452752.9	232.45485	45.4647	2.373	2.307	2.339			
SDSS J152954.86+353822.3	232.47862	35.6395	3.137	2.494	3.095			
SDSS J153024.15+481416.3	232.60063	48.2379	2.386	2.309	2.352	2.3226	20.40	0.20

Continued on Next Page...

Table I.1 – Continued

Name	RA	Dec	z_{em}	z_{min}	z_{max}	z_{abs}	$\log N(\mathrm{H\,I})$	$\epsilon[\log N(\mathrm{H\,I})]$
SDSS J153047.70+033120.8	232.69877	3.5225	2.597	2.307	2.561			
SDSS J153048.55+353808.9	232.70230	35.6358	3.153	2.742	3.071			
SDSS J153053.14+394101.4	232.72146	39.6838	3.852	3.412	3.803			
SDSS J153111.07+331301.1	232.79615	33.2170	2.479	2.351	2.444			
SDSS J153129.90+451707.6	232.87462	45.2854	4.200	2.868	4.148			
SDSS J153146.20+380835.6	232.94251	38.1432	2.500	2.307	2.465			
SDSS J153201.60+370002.3	233.00667	37.0007	3.098	2.307	3.057			
SDSS J153203.97+312011.9	233.01656	31.3366	3.435	2.532	3.390	3.3390	20.65	0.15
SDSS J153206.35+431255.5	233.02650	43.2155	2.492	2.307	2.457			
SDSS J153226.22+313138.1	233.10926	31.5273	2.875	2.492	2.792			
SDSS J153229.97+323658.4	233.12488	32.6162	3.048	2.647	2.965			
SDSS J153233.35+584238.1	233.13901	58.7106	2.436	2.307	2.402			
SDSS J153247.41+223704.1	233.19759	22.6178	4.434	3.585	4.343	3.8170	20.45	0.20
SDSS J153258.24+305906.6	233.24270	30.9852	2.581	2.307	2.545			
SDSS J153302.47+522928.7	233.26033	52.4913	2.940	2.307	2.901			
SDSS J153302.51+430118.1	233.26048	43.0217	3.409	2.668	3.364			
SDSS J153306.31+525849.4	233.27631	52.9804	3.185	2.756	3.143			
SDSS J153314.35+402756.9	233.30982	40.4658	3.079	2.675	2.996			
SDSS J153335.81+384301.1	233.39927	38.7170	2.533	2.307	2.498			
SDSS J153343.77+363556.4	233.43241	36.5990	2.421	2.307	2.387			
SDSS J153349.49+374048.2	233.45614	37.6801	2.877	2.307	2.838			
SDSS J153417.94+541252.4	233.57479	54.2146	3.136	2.440	3.094			
SDSS J153418.96+351924.1	233.57900	35.3234	2.357	2.307	2.323			
SDSS J153454.86+410003.2	233.72861	41.0009	2.343	2.307	2.310			
SDSS J153459.75+132701.4	233.74901	13.4504	5.043	4.099	4.942			
SDSS J153508.74+395653.2	233.78646	39.9481	2.962	2.557	2.923	2.8601	20.55	0.15
SDSS J153514.65+483659.7	233.81106	48.6166	2.562	2.307	2.527			
SDSS J153517.83+554426.4	233.82431	55.7407	2.891	2.767	2.852			
SDSS J153539.15+335830.8	233.91317	33.9752	4.189	3.206	4.137			
SDSS J153553.80+294313.7	233.97418	29.7205	3.972	2.797	3.922	3.2020	20.60	0.10
						3.7620	20.55	0.15
SDSS J153553.80+294313.7	233.97418	29.7205	3.990	2.769	3.940			
SDSS J153638.69+422825.5	234.16126	42.4738	3.046	2.307	3.005			
SDSS J153648.71+432154.1	234.20301	43.3650	2.775	2.434	2.737			
SDSS J153650.25+500810.3	234.20941	50.1362	4.929	4.003	4.830			
SDSS J153703.94+533219.9	234.26642	53.5389	2.404	2.307	2.321			
SDSS J153725.35-014650.3	234.35565	-1.7807	3.452	2.695	3.407			
SDSS J153809.19+431155.4	234.53831	43.1987	2.343	2.307	2.310			
SDSS J153825.74+420933.3	234.60727	42.1593	3.752	3.281	3.669			
SDSS J153845.34+420106.4	234.68896	42.0185	2.434	2.307	2.400			
SDSS J153907.53+582323.4	234.78151	58.3899	2.531	2.307	2.496			
SDSS J153930.24+285035.2	234.87602	28.8432	3.654	2.726	3.607			
SDSS J153958.04+503840.1	234.99185	50.6445	3.681	3.281	3.599	3.2863	20.35	0.20
SDSS J154019.47+295059.6	235.08114	29.8499	3.680	3.224	3.633			
SDSS J154025.33+562332.1	235.10557	56.3923	2.896	2.829	2.857			
SDSS J154027.45+381920.0	235.11443	38.3222	2.419	2.341	2.385			
FBQS J1540+4138	235.17910	41.6380	2.517	2.307	2.482			
SDSS J154058.70+473827.6	235.24463	47.6410	2.566	2.307	2.530			
SDSS J154059.19+473643.7	235.24663	47.6121	3.134	2.324	3.092			
SDSS J154102.52+530048.1	235.26052	53.0134	2.565	2.307	2.529			
SDSS J154114.41+473138.1	235.31005	47.5273	3.044	2.427	3.004			
SDSS J154116.39+411953.2	235.31831	41.3315	2.954	2.610	2.914			
SDSS J154118.55+390547.4	235.32731	39.0965	3.773	3.284	3.725			
SDSS J154124.47+352907.6	235.35200	35.4855	3.212	2.400	3.170			
SDSS J154125.46+534812.9	235.35610	53.8036	2.543	2.307	2.508			
SDSS J154150.83+054846.2	235.46183	5.8129	2.936	2.546	2.853			
SDSS J154153.46+315329.4	235.47279	31.8915	2.553	2.307	2.517	2.4435	20.85	0.15
SDSS J154201.13+381048.1	235.50476	38.1800	2.509	2.307	2.474			
SDSS J154207.66+555844.6	235.53192	55.9791	2.670	2.307	2.633			
SDSS J154212.17+552925.3	235.55073	55.4904	2.361	2.307	2.327			
SDSS J154219.13+452313.2	235.57977	45.3870	2.522	2.316	2.486			
SDSS J154231.76+432251.6	235.63234	43.3810	2.623	2.307	2.587			
SDSS J154231.95+390854.8	235.63320	39.1486	2.354	2.307	2.320			
SDSS J154236.83-020536.5	235.65351	-2.0935	3.098	2.932	3.057			
SDSS J154237.71+095558.8	235.65713	9.9330	3.986	2.257	3.937			
SDSS J154243.21+452949.1	235.68007	45.4970	2.585	2.334	2.549			
SDSS J154247.57+285607.4	235.69822	28.9354	3.024	2.437	2.983			
SDSS J154257.46+392004.8	235.73946	39.3347	3.204	2.787	3.122			
SDSS J154322.60+360243.9	235.84419	36.0455	2.796	2.408	2.758			
SDSS J154338.10+381631.7	235.90876	38.2755	3.616	3.187	3.570			
SDSS J154340.37+341744.4	235.91827	34.2957	4.407	3.071	4.353			
SDSS J154352.92+333759.5	235.97053	33.6332	4.604	3.728	4.511			

Continued on Next Page...

Table I.1 – Continued

Name	RA	Dec	z_{em}	z_{min}	z_{max}	z_{abs}	$\log N(\mathrm{H\,I})$	$\epsilon[\log N(\mathrm{H\,I})]$
SDSS J154356.31+055145.3	235.98467	5.8626	2.532	2.319	2.497			
SDSS J154358.42+473533.1	235.99345	47.5925	3.341	2.897	3.298			
SBS 1542+541	235.99771	53.9843	2.370	2.307	2.337			
SDSS J154400.16+531903.3	236.00069	53.3176	2.975	2.307	2.935			
SDSS J154405.35+284516.6	236.02231	28.7546	2.897	2.508	2.858			
SDSS J154409.31+023742.3	236.03881	2.6285	2.689	2.311	2.652			
SDSS J154430.77+295047.6	236.12822	29.8466	3.195	3.059	3.153			
SDSS J154431.24+070319.7	236.13021	7.0555	2.374	2.307	2.340			
SDSS J154433.11-010957.7	236.13796	-1.1660	3.027	2.615	2.987			
SDSS J154444.98+433332.8	236.18747	43.5591	3.524	2.522	3.478	3.2087	20.90	0.15
SDSS J154446.33+412035.7	236.19307	41.3433	3.548	2.893	3.502	3.0229	20.90	0.15
						3.0616	20.90	0.15
SDSS J154528.41+500323.1	236.36843	50.0564	3.133	2.422	3.092			
SDSS J154529.52+365304.2	236.37302	36.8845	2.388	2.307	2.354			
SDSS J154534.59+511228.9	236.39414	51.2081	2.453	2.313	2.418			
SDSS J154559.70+065652.4	236.49878	6.9479	3.134	2.725	3.052			
SDSS J154606.79+465614.5	236.52831	46.9374	4.150	3.161	4.099			
SDSS J154611.88+364510.1	236.54952	36.7528	2.854	2.307	2.815			
SDSS J154636.34+262839.6	236.65145	26.4777	2.516	2.394	2.481			
SDSS J154650.55+390315.6	236.71066	39.0543	3.131	2.406	3.090			
SDSS J154723.06+323427.4	236.84610	32.5743	2.448	2.307	2.414			
SDSS J154734.98+412840.2	236.89578	41.4778	2.739	2.356	2.702			
SDSS J154739.17+311922.7	236.91323	31.3230	3.182	2.457	3.140			
SDSS J154749.11+322452.4	236.95467	32.4146	2.971	2.319	2.931			
SDSS J154758.78+362705.3	236.99493	36.4515	3.880	3.385	3.831	3.6473	20.80	0.25
B3 1546+406	237.04736	40.5241	2.832	2.443	2.793	2.7768	20.40	0.15
SDSS J154821.85+310530.6	237.09108	31.0918	2.545	2.410	2.509			
SDSS J154827.08-004343.7	237.11285	-0.7288	3.394	2.678	3.350			
SDSS J154836.99+284025.1	237.15413	28.6736	2.949	2.594	2.910			
SDSS J154841.76+352141.9	237.17402	35.3617	4.956	4.576	4.896			
SDSS J154902.42+321802.0	237.26012	32.3006	2.633	2.307	2.597			
SDSS J154903.86+510320.1	237.26612	51.0556	2.439	2.307	2.405			
SDSS J154905.84+352020.4	237.27434	35.3390	3.044	2.650	3.003			
SDSS J154914.45+364822.0	237.31023	36.8061	3.585	2.677	3.539			
SDSS J154925.97+472345.7	237.35822	47.3960	2.603	2.307	2.567	2.5551	20.70	0.15
SDSS J154941.53+335027.4	237.42306	33.8410	3.068	2.665	2.986			
SBS 1548+505	237.45012	50.3718	2.523	2.307	2.488			
SDSS J154952.63+502048.9	237.46932	50.3469	3.809	2.906	3.761			
SDSS J154955.03+275358.4	237.47933	27.8996	2.433	2.307	2.399			
SDSS J155007.59+462855.6	237.53165	46.4821	3.544	2.607	3.499			
SDSS J155030.82+325614.0	237.62845	32.9372	2.618	2.307	2.582			
SDSS J155036.80+053749.9	237.65337	5.6306	3.152	2.307	3.110	2.4165	20.85	0.20
SDSS J155037.82+271610.5	237.65761	27.2696	3.257	2.338	3.214			
SDSS J155044.47+350943.4	237.68531	35.1621	3.284	2.851	3.242			
[HB89] 1548+092	237.76414	9.1470	2.739	2.356	2.702			
SDSS J155120.79+320155.1	237.83665	32.0320	3.194	2.767	3.152			
SDSS J155140.62+094943.1	237.91927	9.8287	3.114	2.955	3.073			
SDSS J155142.02+335351.0	237.92511	33.8975	3.018	2.328	2.977			
SDSS J155150.55+471331.4	237.96068	47.2254	3.837	2.791	3.789	3.7281	20.30	0.15
SDSS J155201.68+485045.8	238.00706	48.8460	2.522	2.307	2.487			
SDSS J155203.30+352440.3	238.01378	35.4112	3.041	2.627	3.001			
SDSS J155239.97+380023.2	238.16656	38.0064	2.665	2.307	2.628			
SDSS J155243.04+255229.2	238.17934	25.8748	4.645	3.763	4.551			
SDSS J155255.03+100538.3	238.22935	10.0940	3.722	2.529	3.675	3.6010	21.10	0.10
						3.6665	20.70	0.10
SDSS J155255.73+060113.1	238.23223	6.0203	3.644	2.892	3.598			
SDSS J155307.22+310632.7	238.28011	31.1091	3.064	2.706	3.023			
SDSS J155312.70+054644.7	238.30297	5.7791	2.387	2.307	2.353			
B3 1551+408	238.31569	40.6574	2.753	2.368	2.715	2.3767	20.80	0.20
SDSS J155323.89+433704.5	238.34959	43.6179	3.109	2.394	3.068			
SDSS J155344.42+430615.2	238.43513	43.1042	2.651	2.307	2.615			
SDSS J155353.23+363335.8	238.47184	36.5599	3.147	2.725	3.106			
SDSS J155353.74+411208.7	238.47398	41.2024	3.917	2.949	3.867			
SDSS J155353.77+271915.0	238.47407	27.3209	3.664	2.567	3.617	2.9745	20.45	0.15
SDSS J155355.10+375844.1	238.47960	37.9789	2.356	2.307	2.322			
SDSS J155400.89+335957.0	238.50374	33.9992	3.629	2.823	3.583			
SDSS J155415.84+533431.7	238.56605	53.5755	2.404	2.307	2.370			
SDSS J155426.16+193703.0	238.60902	19.6175	4.632	3.752	4.538			
FBQS J1554+3001	238.62251	30.0220	2.692	2.314	2.656			
SDSS J155442.52+045520.6	238.67720	4.9224	4.017	3.196	3.967			
SDSS J155502.54+200325.0	238.76061	20.0570	4.228	2.824	4.176			
SDSS J155506.40+365356.1	238.77673	36.8989	2.534	2.307	2.499			

Continued on Next Page...

Table I.1 – Continued

Name	RA	Dec	z_{em}	z_{min}	z_{max}	z_{abs}	$\log N(\mathrm{H\,I})$	$\epsilon[\log N(\mathrm{H\,I})]$
SDSS J155528.01+431446.8	238.86672	43.2463	2.442	2.307	2.408			
SDSS J155531.64+384924.8	238.88185	38.8236	3.497	3.367	3.452			
SDSS J155538.27+264843.4	238.90948	26.8121	3.584	2.398	3.538			
SDSS J155556.89+480015.0	238.98707	48.0042	3.297	2.703	3.254			
SDSS J155559.07+293436.5	238.99614	29.5768	3.307	2.526	3.264			
SDSS J155600.10+401645.4	239.00044	40.2793	3.573	2.452	3.527			
SDSS J155612.40+335412.4	239.05174	33.9035	2.447	2.357	2.413			
SDSS J155626.33+263100.8	239.10976	26.5169	3.237	2.481	3.194	3.0560	20.60	0.15
SDSS J155635.29+450306.3	239.14707	45.0518	3.691	3.213	3.644	3.3963	20.40	0.15
SDSS J155702.21+482117.8	239.25923	48.3550	2.984	2.401	2.945			
SDSS J155713.06+263621.5	239.30445	26.6060	3.627	3.209	3.581			
SDSS J155731.19+241250.2	239.37997	24.2140	2.369	2.307	2.336			
SDSS J155732.18+442920.3	239.38415	44.4890	2.510	2.307	2.475			
SDSS J155735.83+061237.6	239.39931	6.2105	3.894	2.522	3.845			
SDSS J155738.39+232057.5	239.40999	23.3493	4.130	3.091	4.079	3.5377	20.50	0.20
SDSS J155743.98+432501.0	239.43330	43.4169	2.804	2.307	2.765			
SDSS J155744.01+330231.0	239.43340	33.0420	3.140	2.307	3.099			
SDSS J155800.09+311438.2	239.50044	31.2440	3.301	2.941	3.258			
SDSS J155805.61+265419.0	239.52339	26.9053	2.589	2.307	2.553			
SDSS J155806.99+320238.4	239.52917	32.0440	3.673	2.994	3.627	3.4818	20.45	0.15
SDSS J155814.50+405336.9	239.56046	40.8936	2.640	2.307	2.604	2.5521	20.30	0.15
SDSS J155821.99+354815.4	239.59164	35.8043	3.542	2.788	3.496	2.8134	20.95	0.25
SDSS J155823.21+353252.2	239.59676	35.5478	3.198	2.782	3.116			
SDSS J155834.26+264634.9	239.64279	26.7764	3.878	3.023	3.829	3.4325	20.65	0.20
SDSS J155843.11+055217.1	239.67964	5.8714	3.064	2.649	3.024			
SDSS J155912.14+245046.3	239.80062	24.8462	2.788	2.400	2.750			
SDSS J155912.34+482819.9	239.80142	48.4722	3.424	2.307	3.379			
SDSS J155916.59+540650.7	239.81915	54.1141	3.133	3.061	3.091			
SDSS J155917.35+520244.9	239.82233	52.0459	3.042	2.308	3.001			
SDSS J155923.33+333851.9	239.84722	33.6478	2.895	2.307	2.856			
SDSS J155924.01+280651.2	239.85006	28.1142	2.926	2.842	2.887			
SDSS J155927.51+244100.0	239.86464	24.6833	2.627	2.307	2.590			
PKS 1557+032	239.87905	3.0801	3.891	2.660	3.842			
SDSS J155936.89+163101.5	239.90375	16.5171	3.067	2.674	3.026			
SDSS J155940.01+481657.8	239.91673	48.2827	3.029	2.985	2.989			
SDSS J155941.25+383656.3	239.92191	38.6156	3.035	2.639	2.995			
SDSS J160007.83+351341.5	240.03266	35.2282	3.600	2.584	3.554			
SDSS J160011.74+305712.4	240.04896	30.9534	2.582	2.434	2.546			
SDSS J160033.09+403343.9	240.13791	40.5622	2.761	2.430	2.723			
SDSS J160056.02+235654.4	240.23343	23.9485	3.572	2.871	3.526			
SDSS J160059.97+334022.4	240.24990	33.6729	3.809	3.355	3.727			
SDSS J160103.85+341025.0	240.26606	34.1736	2.972	2.307	2.933			
SDSS J160106.58+043534.4	240.27744	4.5929	3.855	2.809	3.806			
SDSS J160108.39+060036.2	240.28497	6.0101	2.365	2.307	2.331			
SDSS J160108.48+462621.8	240.28538	46.4394	2.594	2.307	2.558			
SDSS J160117.99+420414.4	240.32498	42.0707	3.209	2.384	3.167			
SDSS J160146.51+035612.5	240.44382	3.9368	3.104	2.693	3.063			
[HB89] 1600+284	240.54294	28.2956	3.164	2.759	3.082			
B2 1600+24	240.55252	24.1696	2.531	2.307	2.496			
SDSS J160214.26+354516.8	240.55946	35.7547	3.033	2.351	2.993			
SDSS J160223.34+451950.1	240.59729	45.3306	2.807	2.307	2.769			
SDSS J160232.31+334331.3	240.63464	33.7254	3.012	2.616	2.930			
SDSS J160240.64+474256.0	240.66937	47.7156	2.421	2.307	2.387			
SDSS J160244.75+324036.6	240.68650	32.6769	3.004	2.404	2.964			
SDSS J160303.75+353227.3	240.76567	35.5409	2.435	2.307	2.400			
SDSS J160306.19+380228.5	240.77583	38.0413	3.320	2.425	3.276			
SDSS J160315.72+161406.3	240.81552	16.2351	3.063	2.672	3.022			
SDSS J160320.88+072104.4	240.83703	7.3512	4.385	3.062	4.331			
SDSS J160321.37+154716.9	240.83905	15.7880	2.476	2.307	2.354			
SDSS J160321.89+342516.5	240.84121	34.4213	2.546	2.307	2.511			
SDSS J160329.14+090218.1	240.87143	9.0384	4.742	4.539	4.684			
SDSS J160335.78+453656.3	240.89909	45.6157	3.036	2.638	2.996	2.9436	20.65	0.15
SDSS J160336.64+350824.3	240.90269	35.1401	4.485	3.628	4.394			
SDSS J160337.79+481603.5	240.90749	48.2677	2.405	2.307	2.323			
SDSS J160407.06+523428.1	241.02943	52.5745	2.376	2.307	2.342			
SDSS J160409.03+375942.3	241.03767	37.9951	2.488	2.307	2.453			
SDSS J160413.97+395121.8	241.05822	39.8561	3.154	2.314	3.113			
SDSS J160417.80+292802.1	241.07418	29.4673	2.621	2.307	2.584			
SDSS J160426.17+454416.7	241.10910	45.7380	2.460	2.307	2.425			
SDSS J160439.80+392420.4	241.16586	39.4057	2.817	2.307	2.779			
SDSS J160441.68+310141.3	241.17367	31.0281	2.382	2.307	2.348			
SDSS J160515.70+470551.8	241.31547	47.0977	3.039	2.401	2.999			

Continued on Next Page...

Table I.1 – Continued

Name	RA	Dec	z_{em}	z_{min}	z_{max}	z_{abs}	$\log N(\mathrm{H\,I})$	$\epsilon[\log N(\mathrm{H\,I})]$
SDSS J160516.16+210638.5	241.31734	21.1107	4.495	3.636	4.403			
SDSS J160527.04+395812.4	241.36270	39.9701	2.906	2.513	2.867			
SDSS J160529.53+155903.1	241.37307	15.9842	3.623	3.185	3.577			
SDSS J160552.81+424132.9	241.47011	42.6924	3.002	2.806	2.962	2.8610	20.90	0.15
SDSS J160556.62+234709.9	241.48593	23.7861	3.509	3.069	3.464	3.4626	20.65	0.25
SDSS J160601.25+370046.5	241.50523	37.0129	3.759	2.849	3.712			
SDSS J160612.74+220817.8	241.55311	22.1383	2.969	2.922	2.930			
SDSS J160620.30+321422.7	241.58462	32.2397	3.637	2.659	3.590			
SDSS J160641.00+291919.3	241.67085	29.3220	4.149	3.330	4.098			
SDSS J160649.23+451051.6	241.70519	45.1810	2.826	2.447	2.743			
SDSS J160652.26+072109.5	241.71776	7.3526	2.479	2.335	2.444	2.3976	21.55	0.15
SDSS J160659.85+291217.8	241.74939	29.2050	3.658	2.729	3.611			
SDSS J160705.16+533558.5	241.77151	53.5996	3.653	2.497	3.606			
SDSS J160709.84+084031.8	241.79101	8.6755	2.630	2.307	2.593			
SDSS J160734.22+160417.4	241.89262	16.0715	4.786	3.882	4.689			
SDSS J160734.28+291841.9	241.89286	29.3117	2.884	2.307	2.845			
SDSS J160754.46+465804.8	241.97693	46.9680	3.117	3.019	3.035			
SDSS J160835.63+351257.5	242.14848	35.2160	2.963	2.583	2.923	2.9020	20.55	0.20
SDSS J160843.90+071508.6	242.18294	7.2524	2.880	2.307	2.841			
SDSS J160932.88+462613.2	242.38731	46.4371	2.361	2.307	2.327			
SDSS J160943.33+522550.8	242.43064	52.4308	2.723	2.354	2.641			
SDSS J160944.06+325158.4	242.43361	32.8662	3.047	2.633	3.007			
SDSS J161001.03+305402.7	242.50434	30.9008	3.980	3.583	3.930			
SDSS J161003.53+442353.7	242.51476	44.3983	2.600	2.307	2.564			
[HB89] 1607+183	242.52202	18.1954	3.123	1.814	3.092			
SDSS J161009.42+472444.4	242.53928	47.4124	3.216	2.406	3.174	2.5074	20.90	0.15
SDSS J161100.56+223109.1	242.75237	22.5192	3.781	2.892	3.733	3.2962	21.35	0.15
SDSS J161103.93+264621.0	242.76641	26.7725	2.802	2.418	2.764			
SDSS J161105.64+084435.4	242.77353	8.7432	4.545	3.679	4.453			
SDSS J161122.44+414409.6	242.84353	41.7360	3.153	2.476	3.112			
SDSS J161123.05+074535.3	242.84606	7.7598	3.257	2.406	3.214			
SDSS J161134.83+294131.8	242.89513	29.6922	3.780	2.946	3.733	3.6858	20.40	0.20
SDSS J161140.13+273029.6	242.91724	27.5083	3.333	2.438	3.290			
SDSS J161212.56+432230.0	243.05234	43.3750	2.382	2.307	2.348			
SDSS J161215.84+514500.4	243.06605	51.7501	3.201	2.409	3.159			
SDSS J161228.50+332913.5	243.11876	33.4871	2.459	2.307	2.424			
SDSS J161231.71+250323.6	243.13215	25.0566	3.772	3.302	3.690			
SDSS J161248.73+340219.5	243.20309	34.0388	3.172	2.759	3.090			
SDSS J161250.24+384030.8	243.20937	38.6752	2.926	2.307	2.887			
SDSS J161251.67+311729.9	243.21530	31.2917	3.450	2.473	3.405			
SDSS J161253.41+275842.5	243.22257	27.9785	3.535	2.566	3.489	2.5979	20.75	0.15
SDSS J161302.02+080814.3	243.25846	8.1373	2.346	2.307	2.312			
SDSS J161311.73+070557.2	243.29890	7.0992	2.410	2.307	2.376			
SDSS J161354.47+445245.6	243.47700	44.8794	2.681	2.307	2.644			
SDSS J161407.53+251058.9	243.53141	25.1831	3.033	2.674	2.992			
SDSS J161425.13+464028.9	243.60474	46.6747	5.313	4.327	5.208	4.9120	20.90	0.20
SDSS J161426.81+485958.7	243.61173	48.9997	3.800	2.881	3.752			
SDSS J161443.96+244742.9	243.68318	24.7953	2.882	2.498	2.800			
SDSS J161444.84+253621.7	243.68686	25.6060	2.451	2.307	2.417			
SDSS J161445.81+443944.3	243.69092	44.6623	3.062	2.307	3.021			
SDSS J161447.03+205902.9	243.69599	20.9842	5.081	4.131	4.980			
SDSS J161454.36+300029.7	243.72653	30.0083	3.251	2.840	3.209			
SDSS J161505.88+472308.6	243.77454	47.3857	2.418	2.307	2.384			
SDSS J161522.85+180356.3	243.84524	18.0657	4.010	2.783	3.960			
SDSS J161545.16+453324.9	243.93819	45.5569	2.890	2.307	2.851			
SDSS J161557.84+393913.2	243.99103	39.6537	3.366	2.603	3.322			
FBQS J161602.5+302339	244.01074	30.3944	2.452	2.307	2.418			
SDSS J161602.87+263211.0	244.01198	26.5364	3.786	3.297	3.738			
SDSS J161605.20+413802.1	244.02168	41.6339	2.367	2.307	2.333			
SDSS J161606.25+311811.9	244.02608	31.3033	3.886	3.004	3.837	3.3843	20.65	0.20
SDSS J161616.26+513336.9	244.06775	51.5603	4.528	3.664	4.436			
SDSS J161620.24+410047.7	244.08435	41.0133	3.081	2.879	3.040			
SDSS J161622.10+050127.7	244.09211	5.0244	4.876	3.958	4.778			
SDSS J161635.73+294011.6	244.14890	29.6699	2.558	2.405	2.523			
SDSS J161636.84+471800.7	244.15353	47.3002	2.921	2.316	2.882			
[HB89] 1614+051	244.15649	4.9924	3.210	1.984	3.168	2.5200	20.40	0.20
SDSS J161721.77+232559.3	244.34074	23.4332	3.151	2.307	3.109			
SDSS J161723.47+290421.2	244.34780	29.0726	3.091	2.307	3.050			
SDSS J161723.59+240138.0	244.34832	24.0272	2.370	2.307	2.336			
SDSS J161724.28+240458.3	244.35119	24.0829	3.633	2.913	3.586			
SDSS J161759.31+244917.8	244.49713	24.8216	3.724	2.652	3.676			
SDSS J161813.04+304807.3	244.55438	30.8020	3.201	2.307	3.159			

Continued on Next Page...

Table I.1 – Continued

Name	RA	Dec	z_{em}	z_{min}	z_{max}	z_{abs}	log N(H I)	ϵ[log N(H I)]
2MASSi J1618155+370103	244.56472	37.0178	2.496	2.307	2.461			
SDSS J161822.76+412558.3	244.59485	41.4329	4.216	3.734	4.164			
SDSS J161833.18+312728.5	244.63827	31.4579	2.878	2.307	2.839			
SDSS J161833.54+335826.0	244.63977	33.9739	2.935	2.314	2.895			
SDSS J161859.06+263000.3	244.74611	26.5001	4.544	3.694	4.489	4.0896	20.95	0.20
SDSS J161920.20+375502.7	244.83420	37.9174	2.966	2.588	2.926			
SDSS J161928.49+250241.4	244.86872	25.0449	3.165	2.991	3.123			
SDSS J161933.65+302115.0	244.89022	30.3542	3.794	3.077	3.746			
SDSS J162001.91+254544.7	245.00798	25.7624	2.871	2.316	2.832			
SDSS J162002.86+244131.2	245.01194	24.6920	2.531	2.374	2.496			
SDSS J162004.73+351554.4	245.01956	35.2653	2.960	2.307	2.921			
SDSS J162102.73+491921.5	245.26141	49.3227	3.153	2.784	3.070			
SDSS J1621-0042	245.32046	-0.7142	3.711	2.101	3.664			
SDSS J162145.18+223203.7	245.43830	22.5344	3.299	2.631	3.256			
SDSS J162151.65+335955.9	245.46524	33.9989	3.116	2.402	3.075			
SDSS J162159.09+311005.7	245.49624	31.1683	4.604	3.650	4.548			
SDSS J162249.70+351405.5	245.70712	35.2349	3.028	2.653	2.987			
SDSS J162323.67+331232.6	245.84865	33.2091	2.411	2.307	2.377			
SDSS J162324.75+331049.7	245.85315	33.1805	2.585	2.307	2.549			
SDSS J162331.14+481842.1	245.87979	48.3117	2.843	2.307	2.805			
SDSS J162343.30+070622.8	245.93042	7.1063	2.370	2.307	2.336			
SDSS J162408.60+263031.4	246.03586	26.5087	3.694	3.323	3.647	3.3236	20.80	0.20
SDSS J162445.03+271418.7	246.18767	27.2386	4.498	3.639	4.406			
SDSS J162445.31+445908.9	246.18880	44.9858	3.352	2.635	3.308			
SDSS J162445.66+320722.3	246.19027	32.1229	3.862	2.959	3.813			
SDSS J162453.47+375806.6	246.22280	37.9685	3.381	2.947	3.298			
SDSS J162502.15+432734.9	246.25900	43.4597	3.281	2.605	3.238			
SDSS J162508.09+265052.2	246.28374	26.8478	3.446	2.576	3.402			
SDSS J162516.41+294318.3	246.31842	29.7218	2.358	2.307	2.324			
SDSS J162520.31+225832.9	246.33466	22.9758	3.768	2.308	3.720	2.5844	20.70	0.15
SDSS J162525.64+425157.7	246.35687	42.8661	2.355	2.307	2.322			
SDSS J162530.70+452522.7	246.37795	45.4230	2.396	2.307	2.362			
SDSS J162539.84+251558.8	246.41604	25.2663	4.147	3.103	4.096			
SDSS J162540.93+301059.2	246.42059	30.1831	3.438	2.744	3.394			
[HB89] 1623+268 NED01	246.45036	26.7424	2.470	1.644	2.433			
[HB89] 1623+268 NED02	246.45333	26.7830	2.518	2.307	2.483			
SDSS J162549.16+304106.9	246.45484	30.6852	3.486	2.684	3.442			
[HB89] 1623+268 NED03	246.48911	26.7467	2.602	2.421	2.566			
SDSS J162604.87+471158.7	246.52031	47.1997	2.450	2.307	2.416			
SDSS J162612.98+385627.2	246.55412	38.9409	2.882	2.307	2.843			
SDSS J162622.84+430514.2	246.59518	43.0873	3.193	2.489	3.151			
SDSS J162623.38+484136.4	246.59744	48.6935	4.891	3.747	4.385			
SDSS J162623.99+240611.4	246.59997	24.1032	3.105	2.413	3.064			
SDSS J162625.43+432920.1	246.60601	43.4889	3.717	2.637	3.670			
SDSS J162626.50+275132.4	246.61043	27.8590	5.265	4.286	5.161	4.3130	21.20	0.20
						4.4620	20.70	0.20
						4.4980	20.95	0.20
SDSS J162629.19+285857.5	246.62164	28.9827	5.035	4.092	4.934			
SDSS J162629.76+230253.9	246.62403	23.0483	3.063	2.307	3.022			
SDSS J162651.95+403537.8	246.71648	40.5938	2.542	2.307	2.507			
SDSS J162653.19+351652.6	246.72163	35.2813	2.752	2.380	2.669			
SDSS J162700.40+495240.8	246.75168	49.8780	2.790	2.523	2.752	2.5810	20.30	0.20
SDSS J162722.59+290309.2	246.84416	29.0526	3.669	3.191	3.622			
SDSS J162725.03+290022.1	246.85433	29.0061	2.475	2.307	2.440			
SDSS J162737.90+221509.2	246.90796	22.2526	3.705	2.851	3.658			
SDSS J162738.14+411916.5	246.90895	41.3212	2.551	2.307	2.515			
SDSS J162738.63+460538.4	246.91097	46.0940	3.807	3.137	3.759			
SDSS J162746.40+370710.3	246.94333	37.1196	2.662	2.307	2.580			
SDSS J162802.82+301219.1	247.01177	30.2053	2.445	2.307	2.410			
SDSS J162812.19+235431.5	247.05080	23.9088	2.908	2.508	2.869			
SDSS J162816.24+251340.6	247.06771	25.2280	3.386	2.307	3.342			
SDSS J162828.60+340451.5	247.11918	34.0810	3.873	3.552	3.791			
SDSS J162840.47+375157.5	247.16865	37.8660	3.745	3.013	3.697			
SDSS J162900.82+245927.5	247.25343	24.9910	3.429	2.991	3.347			
SDSS J162916.16+333714.5	247.31739	33.6207	4.392	3.892	4.339			
SDSS J162921.90+300724.7	247.34128	30.1235	2.405	2.307	2.370			
SDSS J162943.43+391211.4	247.43099	39.2032	3.911	3.064	3.862			
SDSS J162951.59+325102.3	247.46498	32.8507	3.023	2.411	2.983			
SDSS J162954.68+370222.4	247.47787	37.0396	3.217	2.378	3.174			
SDSS J162955.14+311317.5	247.47981	31.2216	2.966	2.799	2.883			
SDSS J163042.21+330434.2	247.67591	33.0762	3.236	2.385	3.194			
SDSS J163106.55+453917.3	247.77733	45.6548	3.896	2.935	3.847			

Continued on Next Page...

Table I.1 – Continued

Name	RA	Dec	z_{em}	z_{min}	z_{max}	z_{abs}	$\log N(\mathrm{H\,I})$	$\epsilon[\log N(\mathrm{H\,I})]$
SDSS J163112.05+273141.1	247.80025	27.5281	3.266	2.482	3.224	2.7699	21.00	0.15
SDSS J163121.62+233201.9	247.84011	23.5339	3.022	2.626	2.982	2.9550	20.30	0.15
SDSS J163138.86+211705.1	247.91196	21.2848	2.482	2.312	2.447			
SDSS J163142.72+223448.1	247.92802	22.5800	3.332	2.573	3.289			
SDSS J163148.29+445935.0	247.95128	44.9930	3.042	2.415	3.001			
SDSS J163201.45+424018.1	248.00609	42.6717	2.674	2.307	2.638			
SDSS J163221.04+375507.2	248.08771	37.9187	3.773	2.940	3.725			
FBQS J163221.0+264353	248.08773	26.7315	2.678	2.307	2.642			
[HB89] 1631+373	248.20692	37.2754	2.947	2.307	2.907			
SDSS J163257.06+441110.2	248.23779	44.1862	4.093	2.966	4.042			
SDSS J163259.67+390423.0	248.24868	39.0731	3.106	2.466	3.065			
SDSS J163300.13+362904.8	248.25056	36.4847	3.576	2.567	3.530			
SDSS J163314.34+244629.2	248.30979	24.7748	3.278	2.867	3.235			
SDSS J163314.82+471856.7	248.31179	47.3158	3.861	3.130	3.813			
SDSS J163319.63+141142.0	248.33180	14.1950	4.365	2.439	4.312	2.8820	20.30	0.15
SDSS J163345.88+361211.8	248.44119	36.2033	2.638	2.307	2.602			
SDSS J163352.42+230816.3	248.46844	23.1379	3.229	2.810	3.187			
SDSS J163401.66+235014.7	248.50693	23.8374	2.352	2.307	2.318			
SDSS J163411.82+215325.0	248.54927	21.8903	4.587	3.714	4.494	4.0820	20.60	0.20
FBQS J1634+3203	248.55329	32.0598	2.344	2.307	2.311			
SDSS J163416.17+355812.9	248.56742	35.9703	3.066	2.307	3.026	2.5671	21.25	0.15
[HB89] 1632+338	248.61953	33.7514	2.988	2.342	2.948	2.9426	20.50	0.15
SDSS J163444.13+300759.0	248.68388	30.1331	3.344	2.528	3.301			
SDSS J163456.15+301437.8	248.73398	30.2438	2.504	2.307	2.469			
SDSS J163500.06+301321.7	248.75028	30.2227	2.935	2.355	2.895			
SDSS J163510.84+291540.3	248.79521	29.2612	3.049	2.635	3.009	2.8887	20.70	0.20
SDSS J163533.99+333625.0	248.89165	33.6070	3.648	3.176	3.601			
SDSS J163549.99+231018.1	248.95833	23.1717	3.095	2.677	3.054	2.9691	20.35	0.15
SDSS J163603.23+283908.7	249.01346	28.6524	3.125	2.409	3.084			
SDSS J163609.34+461954.8	249.03895	46.3319	3.204	2.394	3.162			
SDSS J163609.72+313827.9	249.04053	31.6411	3.575	2.794	3.529	3.4193	20.30	0.20
SDSS J163623.82+323519.0	249.09926	32.5886	3.529	2.829	3.484			
SDSS J163630.80+322407.2	249.12836	32.4020	3.101	2.307	3.060	2.5709	20.60	0.15
SDSS J163636.93+315717.1	249.15387	31.9547	4.590	3.717	4.497			
SDSS J163640.55+464707.1	249.16897	46.7853	2.526	2.307	2.491			
SDSS J163647.18+382031.3	249.19662	38.3421	4.180	3.335	4.040			
SDSS J163654.30+323853.0	249.22628	32.6481	2.415	2.307	2.381			
SDSS J163700.18+314224.6	249.25076	31.7068	2.952	2.356	2.912			
SDSS J163705.37+123321.9	249.27241	12.5561	2.503	2.307	2.468			
SDSS J163712.01+381135.2	249.30005	38.1931	3.897	2.811	3.848			
SDSS J163714.68+395706.7	249.31121	39.9519	3.409	2.672	3.365			
SDSS J163726.44+402131.3	249.36017	40.3587	3.699	2.893	3.652	3.3736	20.65	0.15
SDSS J163747.57+290135.2	249.44826	29.0265	3.641	3.237	3.595	3.5035	20.35	0.20
SDSS J163750.36+322313.8	249.45989	32.3872	2.993	2.598	2.911			
SDSS J163809.01+323955.2	249.53758	32.6654	2.933	2.614	2.851			
SDSS J163814.20+120437.7	249.55918	12.0772	2.493	2.307	2.458			
SDSS J163820.04+220620.5	249.58352	22.1057	3.083	2.307	3.042			
SDSS J163851.59+342158.6	249.71498	34.3663	2.656	2.307	2.620			
SDSS J163854.46+211609.4	249.72693	21.2693	2.483	2.338	2.448			
2MASX J16390909+2824468	249.78797	28.4131	3.819	2.750	3.771			
SDSS J163912.86+440813.5	249.80364	44.1371	3.759	3.277	3.712	3.6418	20.50	0.15
SDSS J163936.09+341453.0	249.90042	34.2481	2.560	2.307	2.525			
SDSS J163950.51+434003.7	249.96051	43.6677	3.990	2.769	3.940			
SDSS J163953.84+385449.1	249.97436	38.9137	2.384	2.307	2.350			
SDSS J164010.92+451524.9	250.04554	45.2569	3.038	2.648	2.997			
SDSS J164021.28+243939.7	250.08868	24.6611	3.265	2.831	3.222			
SDSS J164022.78+411548.1	250.09495	41.2634	3.089	2.398	3.048	2.6969	20.55	0.15
						3.0174	20.65	0.15
SDSS J164039.84+325812.9	250.16601	32.9703	2.765	2.380	2.728			
SDSS J164051.91+233633.8	250.21630	23.6094	3.075	2.387	3.035			
SDSS J164052.87+364114.6	250.22031	36.6874	2.644	2.307	2.608			
SDSS J164100.90+425457.6	250.25375	42.9160	2.694	2.316	2.657			
[HB89] 1639+407	250.27231	40.6144	2.445	2.307	2.410			
SDSS J164113.48+330247.4	250.30618	33.0465	3.543	2.410	3.498			
SDSS J164113.75+134158.8	250.30731	13.6997	4.092	3.258	4.041			
SDSS J164130.57+393434.2	250.37741	39.5762	2.612	2.307	2.576			
SDSS J164136.62+344359.3	250.40259	34.7332	2.762	2.377	2.724	2.6358	20.75	0.15
SDSS J164143.39+421648.5	250.43080	42.2802	3.680	2.829	3.633			
SDSS J164146.27+290148.6	250.44282	29.0302	4.111	3.371	4.060	3.9411	20.90	0.20
SDSS J164148.07+334512.1	250.45033	33.7534	2.750	2.366	2.712			
SDSS J164148.19+223225.2	250.45082	22.5403	2.506	2.307	2.471			
SDSS J164154.89+223745.5	250.47872	22.6293	3.617	3.145	3.571			

Continued on Next Page...

Table I.1 – Continued

Name	RA	Dec	z_{em}	z_{min}	z_{max}	z_{abs}	log N(H I)	ϵ[log N(H I)]
SDSS J164205.14+462226.0	250.52145	46.3739	3.700	2.604	3.653			
SDSS J164219.88+445124.0	250.58286	44.8567	2.882	2.498	2.800			
SDSS J164222.94+321710.3	250.59561	32.2862	3.964	3.090	3.915			
SDSS J164238.08+412104.7	250.65869	41.3513	3.123	2.756	3.082			
SDSS J164248.71+240303.3	250.70296	24.0509	3.480	2.511	3.436	3.2652	20.50	0.15
SDSS J164250.77+360531.7	250.71158	36.0922	3.166	2.581	3.124			
SDSS J164251.06+392408.8	250.71277	39.4025	2.384	2.307	2.350			
SDSS J164304.41+344745.4	250.76839	34.7960	3.049	2.322	3.009			
SDSS J164314.75+282812.6	250.81146	28.4702	2.585	2.307	2.354			
SDSS J164330.13+305541.7	250.87555	30.9283	2.703	2.407	2.666			
SDSS J164330.98+365037.9	250.87911	36.8439	2.601	2.307	2.565			
SDSS J164341.27+305859.6	250.92199	30.9833	2.559	2.307	2.523			
SDSS J164417.10+124559.2	251.07125	12.7665	3.500	2.748	3.455			
SDSS J164417.36+342254.2	251.07236	34.3818	2.859	2.581	2.820			
SDSS J164424.98+274136.5	251.10409	27.6935	3.893	2.540	3.844			
SDSS J164431.02+254246.4	251.12929	25.7129	2.437	2.307	2.403			
SDSS J164439.86+214311.5	251.16612	21.7199	3.111	2.307	3.070			
SDSS J164446.39+211039.5	251.19332	21.1776	3.147	2.341	3.106			
SDSS J164452.82+374058.1	251.22013	37.6828	3.275	2.906	3.193			
SDSS J164535.94+230008.4	251.39979	23.0024	2.844	2.510	2.761			
SDSS J164545.31+263732.1	251.43884	26.6256	3.307	2.307	3.264	3.0889	20.45	0.15
FBQS J1645+2244	251.46712	22.7472	2.727	2.346	2.690			
SDSS J164554.26+331717.0	251.47611	33.2881	2.464	2.307	2.429			
SDSS J164602.01+274348.0	251.50842	27.7300	3.722	3.255	3.640			
SDSS J164612.60+641608.2	251.55255	64.2690	3.133	2.430	3.091			
SDSS J164653.72+243942.2	251.72388	24.6617	3.029	2.378	2.989			
2MASSi J1646563+551445	251.73458	55.2458	4.084	2.800	4.033			
SDSS J164704.76+254923.2	251.76987	25.8231	2.416	2.363	2.382			
SDSS J164708.03+255908.3	251.78351	25.9856	3.037	2.664	2.996			
SDSS J164709.20+314437.0	251.78836	31.7436	2.976	2.370	2.936			
SDSS J164716.44+232818.4	251.81855	23.4718	3.215	2.556	3.173			
SDSS J164716.62+313254.4	251.81929	31.5485	2.517	2.307	2.482			
SDSS J164729.55+214113.7	251.87314	21.6871	2.663	2.307	2.627			
SDSS J164739.64+343608.5	251.91518	34.6024	4.010	2.945	3.960			
SDSS J164808.70+391153.5	252.03632	39.1982	2.994	2.325	2.954			
SDSS J164810.07+260211.2	252.04199	26.0365	3.350	2.951	3.306	2.9525	20.45	0.20
						3.2544	21.05	0.15
SDSS J164818.07+415550.2	252.07534	41.9306	2.408	2.307	2.374			
SDSS J164826.98+350017.3	252.11244	35.0048	2.936	2.534	2.897			
SDSS J164843.16+283906.8	252.17986	28.6519	3.321	2.489	3.278			
SDSS J164934.13+203139.8	252.39224	20.5277	2.541	2.307	2.505			
SDSS J164948.09+210636.4	252.45039	21.1101	3.280	2.603	3.238			
SDSS J165001.22+343003.6	252.50512	34.5010	3.871	3.372	3.822			
SDSS J165044.78+390045.6	252.68660	39.0127	3.167	2.307	3.125			
SDSS J165053.86+185031.5	252.72445	18.8421	3.106	2.686	3.065			
SDSS J165112.94+295158.5	252.80393	29.8663	3.211	2.794	3.129			
FBQS J1651+4002	252.90651	40.0385	2.343	2.307	2.310			
SDSS J165142.73+295149.2	252.92808	29.8637	3.910	2.727	3.861			
SDSS J165152.85+333541.0	252.97024	33.5948	3.723	2.784	3.676			
SDSS J165154.06+313305.0	252.97529	31.5514	2.706	2.352	2.623			
SDSS J165215.12+271841.7	253.06301	27.3116	3.342	2.666	3.298			
SDSS J165233.66+184003.2	253.14026	18.6676	3.470	2.563	3.425			
SDSS J165249.81+294059.0	253.20756	29.6831	2.465	2.351	2.431			
SDSS J165255.52+423541.5	253.23138	42.5948	3.685	3.273	3.638			
SDSS J165331.60+362416.1	253.38172	36.4045	3.031	2.654	2.991			
SDSS J165334.39+344413.5	253.39333	34.7371	3.236	2.308	3.194			
SDSS J165354.61+405402.1	253.47758	40.9006	4.977	4.365	4.917	4.5742	20.35	0.20
SDSS J165356.74+283332.7	253.48646	28.5591	3.144	2.960	3.102			
SDSS J165408.17+350954.9	253.53408	35.1653	2.837	2.443	2.798			
SDSS J165411.62+284036.3	253.54843	28.6768	2.880	2.551	2.841			
SDSS J165412.91+373504.0	253.55380	37.5845	2.641	2.307	2.604			
SDSS J165433.32+422053.7	253.63884	42.3483	2.519	2.307	2.484			
SDSS J165436.85+222733.7	253.65356	22.4594	4.678	3.517	4.622	4.0065	20.35	0.20
						4.1005	20.35	0.20
SDSS J165515.56+215417.7	253.81486	21.9049	3.779	2.627	3.732	2.6778	20.40	0.20
B2 1653+32A	253.83011	32.7114	3.186	2.483	3.144			
SDSS J165523.09+184708.4	253.84621	18.7857	3.323	2.307	3.280			
SDSS J165543.86+395322.2	253.93280	39.8895	2.422	2.319	2.388			
SDSS J165559.52+320105.2	253.99803	32.0181	3.257	2.522	3.214			
SDSS J165609.53+312847.6	254.03972	31.4799	3.224	2.551	3.182			
SDSS J165621.65+415524.5	254.09022	41.9235	2.881	2.307	2.842			
SDSS J165647.22+345127.7	254.19678	34.8577	2.748	2.365	2.711			

Continued on Next Page...

Table I.1 – Continued

Name	RA	Dec	z_{em}	z_{min}	z_{max}	z_{abs}	$\log N(\mathrm{H\,I})$	$\epsilon[\log N(\mathrm{H\,I})]$
SDSS J165648.52+635838.3	254.20220	63.9773	2.369	2.307	2.336			
SDSS J165653.31+255944.3	254.22214	25.9957	2.416	2.328	2.382			
SDSS J165655.56+201139.6	254.23151	20.1944	3.110	2.424	3.069			
SDSS J165722.24+333540.2	254.34269	33.5945	2.947	2.344	2.907			
SDSS J165722.77+260702.3	254.34491	26.1173	2.887	2.348	2.849			
SDSS J165742.37+223859.8	254.42656	22.6500	3.250	2.579	3.208			
SDSS J165751.68+355318.0	254.46537	35.8884	3.005	2.307	2.965			
SDSS J165755.53+604002.5	254.48140	60.6674	2.355	2.307	2.321			
SDSS J165801.94+233651.3	254.50813	23.6143	3.785	3.329	3.737	3.4648	20.60	0.20
SDSS J165829.47+332604.8	254.62283	33.4347	3.080	2.382	3.040			
SDSS J165830.66+220727.1	254.62777	22.1242	3.286	2.669	3.243			
CGRaBS J1658-0739	254.68359	-7.6549	3.749	2.537	3.702			
SDSS J165855.19+375853.6	254.72998	37.9816	3.641	2.847	3.594	3.3479	20.95	0.15
SDSS J165902.12+270935.1	254.75881	27.1597	5.316	4.329	5.211			
SDSS J165912.97+185001.5	254.80405	18.8338	3.779	3.042	3.731			
SDSS J165914.54+380900.7	254.81061	38.1502	2.343	2.307	2.309			
SDSS J165918.88+265102.0	254.82868	26.8506	2.947	2.543	2.908			
SDSS J170040.25+331257.8	255.16773	33.2161	3.181	2.833	3.098			
SDSS J170100.60+641209.3	255.25259	64.2025	2.736	2.353	2.698			
SDSS J170102.95+205802.6	255.26234	20.9674	2.555	2.373	2.520			
SDSS J170104.79+241150.0	255.26999	24.1972	3.086	2.323	3.046			
SDSS J170109.25+231509.1	255.28856	23.2525	3.048	2.639	3.007			
SDSS J170118.01+404534.9	255.32509	40.7597	2.515	2.307	2.480			
SDSS J170207.20+250913.0	255.53000	25.1536	2.776	2.389	2.738			
SDSS J170248.55+314047.9	255.70233	31.6800	4.377	3.213	4.323			
SDSS J170306.73+312809.4	255.77804	31.4693	2.990	2.600	2.950			
SDSS J170335.34+612607.4	255.89728	61.4354	3.575	2.856	3.529	3.1316	20.55	0.15
SDSS J170353.98+362439.6	255.97496	36.4110	2.476	2.307	2.442			
SDSS J170415.85+345218.9	256.06606	34.8720	2.441	2.307	2.407			
SDSS J170423.42+212555.8	256.09759	21.4322	2.962	2.557	2.923			
SDSS J170423.43+321313.8	256.09768	32.2205	2.978	2.388	2.939			
SDSS J170500.97+310808.5	256.25407	31.1357	2.964	2.307	2.925			
SDSS J170606.07+350102.0	256.52533	35.0172	2.664	2.307	2.627			
SDSS J1707+6443	256.77031	64.7176	3.163	2.307	3.122			
SDSS J170708.74+330206.8	256.78645	33.0352	2.441	2.370	2.406			
[HB89] 1705+018	256.89340	1.8127	2.576	1.669	2.537			
SDSS J170808.73+334641.2	257.03640	33.7781	3.149	2.452	3.108			
SDSS J170809.45+211712.6	257.03940	21.2869	3.796	3.025	3.748			
SDSS J170839.73+300116.0	257.16560	30.0211	3.898	3.413	3.816	3.4749	20.65	0.20
SDSS J170846.60+214335.1	257.19421	21.7264	2.456	2.307	2.422			
SDSS J170930.99+630357.1	257.37917	63.0659	2.395	2.307	2.312			
SDSS J170931.01+341731.2	257.37925	34.2920	3.309	2.604	3.266	3.0131	20.45	0.15
SDSS J170952.20+332905.9	257.46755	33.4850	4.263	3.113	4.210			
SDSS J171014.51+592326.4	257.56048	59.3907	4.494	3.454	4.440			
SDSS J171040.50+311839.1	257.66877	31.3109	2.526	2.362	2.491			
SDSS J171123.36+332541.2	257.84737	33.4281	2.473	2.307	2.439			
SDSS J1711+6052	257.89338	60.8779	3.826	2.797	3.778			
SBS 1711+579	258.11563	57.9186	3.007	2.307	2.967			
SDSS J171246.14+283657.4	258.19229	28.6160	3.200	2.620	3.158	2.9323	21.05	0.15
SDSS J171304.85+612249.3	258.27030	61.3804	3.153	2.507	3.111			
SDSS J171327.25+222608.1	258.36359	22.4356	3.925	2.913	3.876			
SDSS J171341.05+325045.3	258.42107	32.8459	2.966	2.779	2.926			
SDSS J171421.72+314802.1	258.59051	31.8006	3.507	2.430	3.462			
SDSS J171509.96+294555.0	258.79154	29.7653	4.531	3.390	4.475			
SDSS J171530.49+645319.2	258.87706	64.8887	3.980	3.188	3.930			
SDSS J171539.45+380909.9	258.91441	38.1528	4.520	3.004	4.465	3.3410	21.05	0.20
SDSS J171545.61+264846.9	258.94009	26.8131	2.465	2.317	2.430			
SDSS J171628.32+273450.7	259.11802	27.5808	3.680	2.921	3.633			
SDSS J171652.34+590200.1	259.21811	59.0334	2.368	2.307	2.335			
SDSS J171656.30+551753.0	259.23462	55.2981	2.930	2.536	2.891	2.6033	21.45	0.15
						2.8734	20.30	0.20
SDSS J171704.65+303931.2	259.26940	30.6587	3.581	2.570	3.535			
SDSS J171719.45+580218.0	259.33108	58.0383	3.157	2.496	3.116	3.0463	20.40	0.20
SDSS J171749.21+533123.2	259.45505	53.5231	2.600	2.426	2.564			
SDSS J171800.19+621325.6	259.50082	62.2238	3.672	2.925	3.625			
SDSS J171808.65+551511.1	259.53607	55.2531	4.620	3.640	4.564			
SDSS J171932.93+291929.7	259.88723	29.3249	3.294	2.961	3.251			
SDSS J171936.11+275704.9	259.90049	27.9514	2.342	2.307	2.309			
SDSS J171944.75+554408.4	259.93650	55.7357	3.879	3.396	3.797			
SDSS J171953.26+260212.4	259.97195	26.0368	3.107	2.331	3.066			
SDSS J171954.26+563103.1	259.97611	56.5176	3.211	2.340	3.169			
SDSS J172007.83+523544.1	260.03272	52.5956	2.718	2.610	2.681			

Continued on Next Page...

Table I.1 – Continued

Name	RA	Dec	z_{em}	z_{min}	z_{max}	z_{abs}	$\log N(\mathrm{H\,I})$	$\epsilon[\log N(\mathrm{H\,I})]$
SDSS J172106.64+325636.2	260.27767	32.9434	4.040	2.802	3.990			
SDSS J172141.55+573318.9	260.42317	57.5553	2.518	2.307	2.483			
SDSS J172235.31+290636.3	260.64713	29.1101	2.429	2.307	2.395			
PSS J1723+2243	260.84667	22.7328	4.531	3.056	4.476	3.6980	20.50	0.10
SDSS J172409.19+531405.4	261.03835	53.2349	2.547	2.307	2.511			
[HB89] 1726+344	261.95788	34.3777	2.429	1.669	2.393			
SDSS J173038.68+585847.1	262.66126	58.9798	3.222	2.569	3.179			
SDSS J173100.43+572212.3	262.75180	57.3701	2.800	2.307	2.762			
SDSS J173352.22+540030.5	263.46771	54.0085	3.425	2.307	3.381			
SDSS J173612.69+542009.2	264.05295	54.3359	2.625	2.307	2.588			
SDSS J1737+5828	264.43702	58.4749	4.940	3.383	4.881	4.7410	20.65	0.15
SDSS J173909.10+561317.1	264.78793	56.2214	3.142	2.564	3.101			
SDSS J173935.27+575201.7	264.89699	57.8672	3.208	2.522	3.166	3.1352	20.35	0.15
[HB89] 1738+350	265.08429	35.0132	3.240	2.093	3.197			
SDSS J174405.65+540413.3	266.02361	54.0704	2.931	2.315	2.891			
PSS J1745+6846	266.46000	68.7724	4.130	2.860	4.079			
4C +62.29	266.55848	62.4485	3.901	2.470	3.852			
NVSS J175746+753917	269.44316	75.6545	3.050	1.955	3.010	2.6240	20.77	0.20
AKARI J175928.07+663852.5	269.86679	66.6480	4.320	2.804	4.267	3.4000	20.40	0.20
PSS J1802+5616	270.70375	56.2808	4.158	2.821	4.106	3.5540	20.40	0.10
						3.7620	20.65	0.15
						3.8110	20.35	0.15
[HB89] 1836+511	279.33018	51.1928	2.827	1.920	2.789			
PKS 1937-101	294.98857	-10.0449	3.787	2.442	3.739			
[HB89] 2000-330	300.85048	-32.8625	3.783	2.521	3.729			
SDSS J203642.29-055300.2	309.17622	-5.8834	2.569	2.307	2.533			
SDSS J203724.05-002053.1	309.35023	-0.3481	2.992	2.307	2.953			
SDSS J203814.55-002538.9	309.56063	-0.4275	2.706	2.327	2.669			
SDSS J203906.09-004736.6	309.77540	-0.7935	2.966	2.573	2.884			
[HB89] 2038-012	310.21451	-1.0941	2.783	1.887	2.745			
SDSS J204150.68-065513.5	310.46120	-6.9204	2.609	2.307	2.573			
SDSS J204234.95-003144.1	310.64564	-0.5289	2.479	2.351	2.444			
SDSS J204413.19-003523.8	311.05530	-0.5900	2.589	2.528	2.553			
SDSS J204421.50-052521.8	311.08962	-5.4227	4.322	4.154	4.239			
SDSS J204443.44+011110.1	311.18128	1.1862	2.611	2.307	2.575			
SDSS J204505.32-050157.2	311.27218	-5.0326	2.571	2.415	2.535			
SDSS J204646.07+002813.2	311.69228	0.4703	3.018	2.323	2.978			
SDSS J204941.52-004051.3	312.42328	-0.6809	4.192	3.320	4.140			
SDSS J204946.35-055453.4	312.44315	-5.9149	3.198	2.307	3.156	2.6824	20.30	0.15
PC 2047+0123	312.59663	1.5862	3.799	2.620	3.751	2.7299	20.40	0.20
[HB89] 2048+312	312.71305	31.4576	3.198	1.830	3.143			
SDSS J205141.73-071906.2	312.92388	-7.3184	3.845	3.413	3.796			
SDSS J205214.14-051558.0	313.05895	-5.2661	3.275	2.540	3.232			
SDSS J205316.76+005920.9	313.31987	0.9892	4.299	3.279	4.246			
[WHO91] 2050-359	313.43603	-35.7819	3.490	2.605	3.445			
SDSS J205429.04-011013.2	313.62104	-1.1704	2.548	2.331	2.513			
SDSS J205509.48-071748.6	313.78954	-7.2968	4.006	3.200	3.956			
SDSS J205516.83-051111.0	313.82017	-5.1864	3.005	2.325	2.965			
SDSS J205659.14+004907.7	314.24643	0.8188	2.499	2.310	2.464			
SDSS J205724.14-003018.7	314.35062	-0.5052	4.686	3.798	4.591			
SDSS J205821.27+000731.8	314.58865	0.1255	3.125	2.496	3.084			
SDSS J205922.42-052842.7	314.84344	-5.4786	2.539	2.307	2.504			
SDSS J210018.23-051235.8	315.07599	-5.2100	3.311	2.393	3.268			
SDSS J210025.02-064145.9	315.10429	-6.6961	3.129	2.307	3.088			
SDSS J210054.58-004842.9	315.22745	-0.8119	3.513	3.075	3.468			
FBQS J2102-0733	315.53397	-7.5598	2.660	2.307	2.623			
SDSS J210216.52+104906.5	315.56885	10.8185	4.182	3.209	4.131			
SDSS J210311.68-060059.4	315.79869	-6.0165	3.336	2.614	3.293			
SDSS J210455.43-002352.2	316.23106	-0.3978	2.572	2.307	2.536			
SDSS J210605.15+102434.4	316.52150	10.4096	3.290	2.973	3.247			
SDSS J210831.56-063022.5	317.13152	-6.5063	2.345	2.307	2.311			
SDSS J210935.41+100632.6	317.39756	10.1091	3.028	2.335	2.988			
SDSS J211027.39+111813.7	317.61414	11.3038	3.199	2.441	3.157			
SDSS J211036.79+103529.4	317.65330	10.5915	3.021	2.446	2.981			
SDSS J211313.74+091041.1	318.30729	9.1781	3.892	3.066	3.844			
SDSS J211417.99-011146.3	318.57498	-1.1962	2.948	2.568	2.909			
SDSS J211443.92-005532.7	318.68312	-0.9258	3.424	2.518	3.380			
SDSS J211450.33-063257.0	318.70974	-6.5492	4.257	3.785	4.204	3.9339	21.15	0.15
						4.1268	20.85	0.15
SDSS J211617.26-073410.6	319.07193	-7.5696	2.872	2.489	2.790			
SDSS J211638.79+104149.7	319.16168	10.6971	3.930	3.163	3.881			
LBQS 2113-4345	319.22606	-43.5428	2.050	1.664	2.023			

Continued on Next Page...

Table I.1 – Continued

Name	RA	Dec	z_{em}	z_{min}	z_{max}	z_{abs}	$\log N(\mathrm{H\,I})$	$\epsilon[\log N(\mathrm{H\,I})]$
[MWA91] 2113-4534	319.26033	-45.3617	2.540	1.969	2.506			
SDSS J211704.77+010642.9	319.26988	1.1119	3.858	3.428	3.809			
LBQS 2114-4347	319.33059	-43.5734	2.040	1.606	2.011			
SDSS J211805.15+010758.0	319.52150	1.1328	3.865	2.932	3.816			
GALEXASC J211834.87-44221	319.64469	-44.3708	2.160	1.755	2.128			
SDSS J211936.76+104623.8	319.90322	10.7733	3.249	2.522	3.206			
SDSS J212025.78-001948.0	320.10745	-0.3300	2.581	2.307	2.545			
GALEXASC J212041.88-46510	320.17382	-46.8510	2.260	1.849	2.223			
SDSS J212112.21+115110.5	320.30090	11.8529	2.354	2.320	2.321			
SDSS J212159.03+005224.1	320.49600	0.8734	2.369	2.307	2.335			
SDSS J212207.36-001445.6	320.53067	-0.2460	4.114	2.903	4.063			
LBQS 2122-4231	321.30214	-42.3130	2.270	1.550	2.233			
SDSS J212811.62-010704.8	322.04843	-1.1180	3.273	2.971	3.230	3.2176	20.45	0.20
[HB89] 2126-158	322.30073	-15.6447	3.266	2.011	3.218			
FBQS J2129+0037	322.31918	0.6324	2.959	2.307	2.919			
SDSS J212954.33+002542.6	322.47638	0.4285	3.298	2.602	3.255			
[MWA91] 2126-4618	322.53958	-46.0971	1.890	1.715	1.859			
SDSS J213023.61+122252.2	322.59841	12.3812	3.263	2.307	3.220			
CGRaBS J2130-4515	322.71833	-45.2622	2.710	2.018	2.676			
SDSS J213145.70-082745.2	322.94046	-8.4626	2.414	2.307	2.380			
SDSS J213235.95-001350.6	323.14983	-0.2307	2.493	2.307	2.459			
SDSS J213303.90-082222.8	323.26626	-8.3730	2.388	2.353	2.354			
SDSS J213335.15+111522.4	323.39648	11.2562	3.883	3.062	3.834			
PMN J2134-0419	323.55008	-4.3194	4.334	2.903	4.281			
SDSS J213429.47+003118.3	323.62280	0.5218	4.127	3.603	4.076			
SDSS J213434.97+104548.7	323.64575	10.7636	3.146	2.492	3.105			
LBQS 2131-4257	323.68456	-42.7410	2.100	1.590	2.065			
SDSS J213518.47-010645.1	323.82701	-1.1125	3.186	2.369	3.144			
LBQS 2132-4321	324.02576	-43.1381	2.420	1.595	2.386	1.9160	20.70	0.20
SDSS J213615.34+102754.4	324.06395	10.4651	2.966	2.566	2.926			
SDSS J213629.44+102952.2	324.12268	10.4978	2.555	2.307	2.520			
LBQS 2134-4239	324.44938	-42.4368	1.800	1.590	1.776			
CTS 0559	324.58948	-46.3154	2.210	1.879	2.182			
SDSS J213848.96+002153.2	324.70415	0.3648	2.436	2.307	2.402			
[HB89] 2136+141	324.75545	14.3933	2.430	1.784	2.390			
SDSS J214049.84+103831.7	325.20769	10.6422	3.916	2.945	3.866			
SDSS J214129.38+111958.3	325.37245	11.3329	2.507	2.307	2.472	2.4260	20.30	0.20
SDSS J214132.88-074241.8	325.38702	-7.7116	3.129	2.307	3.088			
[MWA91] 2138-4427	325.49913	-44.2238	3.170	2.107	3.128	2.8510	20.90	0.20
[MWA91] 2139-4434	325.60753	-44.3381	3.230	2.373	3.188			
SDSS J214711.51+122116.1	326.79797	12.3545	2.409	2.359	2.375			
SDSS J214717.88-082926.9	326.82453	-8.4909	2.589	2.307	2.553			
SDSS J214725.71-083834.6	326.85713	-8.6430	4.597	3.722	4.504			
SDSS J214753.29-073031.3	326.97206	-7.5087	3.153	2.427	3.111			
SDSS J215117.00-070753.3	327.82084	-7.1315	2.522	2.307	2.486	2.3274	20.45	0.15
SDSS J215352.98+110907.3	328.47077	11.1520	3.308	2.995	3.265			
PSS J2154+0335	328.52875	3.5944	4.359	3.400	4.305			
SDSS J215436.97+110219.3	328.65408	11.0387	3.196	2.363	3.154	2.4829	20.70	0.20
GALEXASC J215500.37+14344	328.75179	14.5789	2.560	1.800	2.524			
PSS J2155+1358	328.75875	13.9739	4.256	3.064	4.203	3.3180	20.75	0.20
SDSS J215521.12-073217.8	328.83803	-7.5383	3.128	2.726	3.087	2.9389	21.45	0.15
SDSS J215521.37-080532.0	328.83904	-8.0922	3.321	2.700	3.278			
LBQS 2153-2056	328.97208	-20.6946	1.850	1.634	1.821			
SDSS J215601.64-081824.1	329.00687	-8.3067	3.161	2.749	3.120			
SDSS J215604.17+003742.5	329.01742	0.6284	2.844	2.449	2.805			
SDSS J215725.53+124134.7	329.35639	12.6930	2.703	2.324	2.666			
SDSS J215817.60-010555.1	329.57340	-1.0986	4.115	3.313	4.064			
SDSS J215944.01-081634.3	329.93340	-8.2762	3.755	3.357	3.708			
SDSS J220008.66+001744.9	330.03610	0.2958	4.782	3.879	4.686			
SDSS J220116.75+125636.4	330.31983	12.9435	2.922	2.521	2.883			
SDSS J220151.45+130719.9	330.46440	13.1222	2.519	2.307	2.436			
SDSS J220212.82-085221.7	330.55343	-8.8727	3.527	2.549	3.482			
LBQS 2159-2058	330.64583	-20.7394	2.120	1.634	2.089			
SDSS J220307.38-004612.0	330.78078	-0.7701	4.120	3.002	4.069			
PSS J2203+1824	330.93083	18.4703	4.375	2.850	4.321			
SDSS J220402.13-084943.5	331.00890	-8.8288	4.449	4.218	4.394			
LBQS 2203-2145	331.46397	-21.5095	2.270	1.692	2.240			
LBQS 2203-1833	331.66506	-18.3128	2.730	1.849	2.691			
FBQS J2207+0101	331.78467	1.0237	2.911	2.311	2.872			
SDSS J220742.56+134110.9	331.92737	13.6864	3.044	2.487	3.003			
SDSS J220754.00+003220.7	331.97508	0.5391	2.918	2.368	2.878			
LBQS 2205-2014	332.01647	-19.9987	2.640	1.652	2.599			

Continued on Next Page...

Table I.1 – Continued

Name	RA	Dec	z_{em}	z_{min}	z_{max}	z_{abs}	log N(H I)	ϵ[log N(H I)]
GALEXASC J220824.22+18082	332.10080	18.1407	3.140	1.769	3.099			
SDSS J220844.32+122343.7	332.18471	12.3955	3.228	2.503	3.186			
LBQS 2206-1958	332.21667	-19.7331	2.560	1.850	2.525	1.9205	20.50	0.20
						2.0763	20.70	0.20
SDSS J221003.54+120547.6	332.51480	12.0966	2.697	2.492	2.660			
SDSS J221158.07+131036.9	332.99197	13.1769	2.591	2.347	2.555			
SDSS J221202.60+134609.3	333.01085	13.7692	3.883	2.838	3.876			
LBQS 2209-1842	333.04350	-18.4604	2.090	1.634	2.061			
SDSS J221319.99+134832.5	333.33335	13.8090	4.127	3.282	4.075			
LBQS 2211-1915	333.65871	-19.0154	1.950	1.634	1.923			
SDSS J221458.45+135344.7	333.74355	13.8958	3.673	3.592	3.626			
BR 2212-1626	333.86372	-16.1925	3.994	2.529	3.945			
SDSS J221553.42+125625.9	333.97260	12.9405	2.519	2.307	2.483			
FBQS J2216-0057	334.03704	-0.9524	2.396	2.307	2.362			
BR 2213-6729	334.21658	-67.2454	4.479	2.768	4.425			
SDSS J221838.21-083450.0	334.65924	-8.5806	2.540	2.307	2.457			
SDSS J221855.11+134708.6	334.72964	13.7857	4.253	3.439	4.200			
SDSS J221902.26+140232.0	334.75947	14.0422	3.170	2.535	3.129			
SDSS J222116.99+131633.4	335.32082	13.2760	3.350	2.634	3.307			
SDSS J222254.82+130444.3	335.72846	13.0790	4.158	3.242	4.106			
SDSS J222256.11-094636.2	335.73380	-9.7767	2.927	2.307	2.888	2.3542	20.50	0.15
SDSS J222339.21+003942.1	335.91341	0.6617	2.964	2.307	2.924			
SDSS J222408.61-090545.0	336.03588	-9.0959	2.620	2.307	2.584			
FBQS J2224-0846	336.19163	-8.7823	2.603	2.307	2.567			
SDSS J222509.19-001406.9	336.28831	-0.2352	4.882	3.963	4.784			
[HB89] 2222+051	336.31107	5.4526	2.320	1.800	2.287			
MG3 J222537+2040	336.40383	20.6709	3.560	2.101	3.514			
SDSS J222559.51-004157.4	336.49800	-0.6993	2.761	2.376	2.724			
SDSS J222644.78+005019.8	336.68661	0.8389	3.044	2.350	3.003			
SDSS J222737.67-081222.1	336.90699	-8.2061	3.018	2.312	2.977			
SDSS J222824.19+134154.9	337.10082	13.6986	3.987	3.121	3.938			
SDSS J222845.14-075755.3	337.18812	-7.9654	5.150	4.189	5.047			
SDSS J223022.76-081545.5	337.59483	-8.2627	2.504	2.307	2.469			
SDSS J223044.68+121618.3	337.68618	12.2718	3.339	2.649	3.295			
SDSS J223144.19+142107.2	337.93413	14.3520	2.843	2.449	2.804	2.7574	20.30	0.15
SDSS J223157.54-085212.3	337.98975	-8.8701	2.557	2.307	2.522	2.5160	20.70	0.15
LBQS 2230+0232	338.14694	2.7986	2.150	1.634	2.119	1.8642	20.80	0.20
FBQS J2233-0838	338.41117	-8.6481	2.340	2.307	2.307			
LBQS 2231-0015	338.53749	0.0005	3.015	1.749	2.980	2.0657	20.60	0.20
LBQS 2231+0125	338.56324	1.6866	1.900	1.634	1.871			
LBQS 2231-0212	338.61378	-1.9439	1.900	1.634	1.871			
SDSS J223447.03-093759.5	338.69596	-9.6332	3.069	2.405	3.028			
SDSS J223500.04+144556.6	338.75020	14.7657	2.361	2.307	2.327			
SDSS J223521.22-082127.2	338.83844	-8.3576	4.425	3.888	4.342			
[HB89] 2233+131	339.07998	13.4390	3.296	2.312	3.253			
[HB89] 2233+136	339.11284	13.9539	3.216	2.328	3.174			
SDSS J223808.07-080842.1	339.53365	-8.1450	3.172	2.759	3.090			
SDSS J223819.76-092106.0	339.58236	-9.3517	3.259	2.307	3.217	2.8691	20.65	0.15
SDSS J223827.17+135432.6	339.61324	13.9091	3.553	2.803	3.507	3.2587	20.55	0.15
PSS J2238+2603	339.67333	26.0626	4.031	2.816	3.981	3.8570	20.45	0.15
FBQS J2238+0016	339.68153	0.2800	3.450	2.635	3.405	3.3654	20.40	0.15
2MASSi J2239536-055219	339.97333	-5.8719	4.556	2.949	4.501	4.0805	20.60	0.10
SDSS J224115.61+124531.1	340.31507	12.7587	2.965	2.585	2.925			
SDSS J224145.11+122557.1	340.43796	12.4326	2.630	2.307	2.594	2.4180	21.15	0.15
SDSS J224147.75+135202.7	340.44898	13.8674	4.441	3.106	4.387	4.2810	20.75	0.15
[HB93a] 2239-386	340.46601	-38.3381	3.550	2.389	3.508	3.2810	20.80	0.20
SDSS J224212.03-075817.8	340.55015	-7.9716	2.638	2.307	2.601			
SDSS J224246.53+140346.3	340.69388	14.0629	3.161	2.426	3.119			
SDSS J224248.92-085822.8	340.70387	-8.9730	2.389	2.307	2.307			
SDSS J224255.52+124225.6	340.73136	12.7071	4.433	3.895	4.351			
SDSS J224310.01-081307.3	340.79175	-8.2187	3.870	3.389	3.788			
SDSS J224349.90-003629.9	340.95794	-0.6083	3.085	2.688	3.044			
LBQS 2241+0014	340.97807	0.5011	2.140	1.657	2.099			
PSS J2244+1005	341.02250	10.7941	4.040	2.810	3.990			
SDSS J224459.44+000033.4	341.24768	0.0093	2.948	2.544	2.909			
SDSS J224527.04+124537.9	341.36268	12.7605	3.220	2.788	3.178			
SDSS J224531.44-085944.7	341.38101	-8.9958	3.566	2.658	3.520			
SDSS J224553.29-085343.1	341.47207	-8.8953	3.144	2.453	3.103			
SDSS J224621.13+132821.2	341.58807	13.4726	2.492	2.410	2.457			
LBQS 2243+0141	341.61978	1.9580	2.300	1.663	2.267			
SDSS J224630.86+131706.6	341.62861	13.2852	4.089	3.258	4.038	3.6056	21.25	0.25
LBQS 2244-0234	341.68875	-2.3044	1.970	1.787	1.940			

Continued on Next Page...

Table I.1 – Continued

Name	RA	Dec	z_{em}	z_{min}	z_{max}	z_{abs}	$\log N(\mathrm{H\,I})$	$\epsilon[\log N(\mathrm{H\,I})]$
LBQS 2244-0105	341.70540	-0.8318	2.040	1.634	2.010			
LBQS 2246-0006	342.37919	0.1487	2.050	1.651	2.019			
LBQS 2248+0127	342.66644	1.7291	2.560	1.634	2.524	1.9080	20.60	0.20
SDSS J225043.96+125308.0	342.68320	12.8856	2.388	2.307	2.354			
SDSS J225045.58-083411.4	342.68995	-8.5698	3.124	2.475	3.083			
SDSS J225052.66-084600.2	342.71942	-8.7667	3.870	2.986	3.821			
SDSS J225109.09-083137.5	342.78789	-8.5271	3.883	3.400	3.801			
SDSS J225117.79-085722.7	342.82415	-8.9563	3.115	2.307	3.074			
BR 2248-1242	342.82525	-12.4509	4.157	2.940	4.106			
SDSS J225149.94-100357.9	342.95809	-10.0661	2.349	2.307	2.315			
SDSS J225214.31-092730.9	343.05964	-9.4586	2.502	2.323	2.467			
SDSS J225228.56+142608.4	343.11903	14.4357	2.966	2.563	2.926	2.9026	20.80	0.15
SDSS J225238.64+135235.7	343.16105	13.8766	3.228	2.332	3.185			
SDSS J225246.43+142525.8	343.19349	14.4239	4.881	3.962	4.783			
[HB89] 2251+244	343.53892	24.7565	2.330	2.019	2.297			
SDSS J225424.64-103230.4	343.60267	-10.5418	2.742	2.570	2.705			
SDSS J225441.16-095322.7	343.67153	-9.8897	2.350	2.307	2.316			
SDSS J225547.39-081323.0	343.94747	-8.2231	3.061	2.700	2.979			
SDSS J225617.16-091618.7	344.07154	-9.2719	2.401	2.307	2.367			
SDSS J225635.84+143243.5	344.14936	14.5454	2.632	2.307	2.596			
SDSS J225759.66+001645.6	344.49862	0.2793	3.771	2.800	3.724			
SDSS J225827.96+145058.7	344.61651	14.8497	3.116	2.695	3.075			
SDSS J225843.27-092710.5	344.68032	-9.4529	4.065	3.563	3.982			
[HB89] 2256+017	344.74064	2.0617	2.670	1.786	2.629			
SDSS J230019.92+003428.4	345.08317	0.5746	2.525	2.307	2.490			
SDSS J230022.18+125354.0	345.09244	12.8984	3.681	3.230	3.634			
SDSS J230056.88-005134.6	345.23707	-0.8596	3.178	2.439	3.136			
SDSS J230301.45-093930.6	345.75605	-9.6585	3.454	2.374	3.410			
SDSS J230549.75-083102.1	346.45734	-8.5173	2.471	2.307	2.437			
SDSS J230623.69-004611.2	346.59873	-0.7698	3.584	2.763	3.538	3.1187	20.65	0.15
SDSS J230708.31+142635.6	346.78463	14.4433	3.081	2.700	3.041			
SDSS J230716.15+003124.4	346.81735	0.5234	2.551	2.307	2.515			
FBQS J2307-1003	346.96879	-10.0540	2.632	2.307	2.596			
SDSS J230845.84+011201.2	347.19107	1.2004	3.056	2.641	3.015			
SDSS J230959.51+005537.4	347.49805	0.9271	2.414	2.307	2.380			
SDSS J231025.44+141426.9	347.60600	14.2408	3.849	3.067	3.800			
SDSS J231049.67+140901.4	347.70699	14.1504	3.877	3.453	3.828			
SDSS J231055.32+004817.1	347.73050	0.8048	2.993	2.307	2.953			
SDSS J231105.54-102837.5	347.77309	-10.4771	3.194	2.779	3.112			
SDSS J231113.85-085843.7	347.80772	-8.9788	2.671	2.307	2.635			
SDSS J231126.84-092818.2	347.86184	-9.4718	2.961	2.558	2.922			
SDSS J231137.05-084409.5	347.90438	-8.7360	3.745	3.091	3.698	3.5252	20.30	0.15
SDSS J231138.54+144436.7	347.91062	14.7435	3.309	2.457	3.266			
SDSS J231202.40+001930.2	348.01034	0.3251	2.595	2.346	2.559			
SDSS J231332.22+144122.3	348.38427	14.6896	3.337	2.949	3.294			
SDSS J231334.86-101947.0	348.39526	-10.3297	2.798	2.409	2.760			
SDSS J231404.93+150029.0	348.52057	15.0081	2.515	2.307	2.480			
[HB89] 2311-036	348.53004	-3.4244	3.048	1.714	3.001			
SDSS J231543.56+145606.3	348.93152	14.9351	3.377	2.404	3.333	3.2738	20.30	0.15
PSS J2315+0921	348.99667	9.3622	4.412	2.863	4.358	3.2200	21.25	0.15
						3.4250	21.00	0.20
FBQS J2316+0100	349.03021	1.0036	2.629	2.307	2.593			
SDSS J231621.50-091621.1	349.08960	-9.2725	2.610	2.307	2.574			
SDSS J231652.03+005125.8	349.21687	0.8572	3.226	2.403	3.184			
BR J2317-4345	349.36183	-43.7576	3.943	2.448	3.894	3.4900	20.90	0.20
SDSS J231934.76-104037.0	349.89484	-10.6769	3.172	2.307	3.130			
SDSS J232018.34-091029.6	350.07649	-9.1749	2.458	2.307	2.423			
SDSS J232115.48+142131.4	350.31453	14.3587	2.554	2.307	2.518			
SDSS J232133.25+132821.7	350.38855	13.4727	2.623	2.472	2.587			
PSS J2322+1944	350.52984	19.7397	4.170	2.754	4.118			
[HB89] 2320+079	350.65037	8.2004	2.090	1.780	2.059			
SDSS J232329.90-090155.1	350.87463	-9.0320	2.882	2.496	2.844			
PSS J2323+2758	350.92042	27.9668	4.180	2.823	4.128	3.6840	20.60	0.15
SDSS J232424.75+144254.5	351.10315	14.7151	2.467	2.307	2.432			
SDSS J232437.39+001225.6	351.15583	0.2071	2.414	2.353	2.380			
SDSS J232717.95+000545.6	351.82480	0.0960	3.669	2.766	3.623			
SDSS J232732.80-092610.0	351.88670	-9.4361	2.389	2.307	2.307			
SDSS J232735.67-091625.6	351.89865	-9.2738	3.269	2.359	3.227			
BR J2328-4513	352.20250	-45.2293	4.359	2.926	4.305			
SDSS J233120.41+133939.0	352.83506	13.6608	3.162	2.564	3.121			
FBQS J2331+0106	352.88683	1.1058	2.641	2.307	2.605			
SDSS J233133.03-090246.6	352.88766	-9.0463	2.456	2.307	2.421			

Continued on Next Page...

Table I.1 – Continued

Name	RA	Dec	z_{em}	z_{min}	z_{max}	z_{abs}	$\log N(\mathrm{H\,I})$	$\epsilon[\log N(\mathrm{H\,I})]$
SDSS J233156.47-090802.0	352.98533	-9.1339	2.661	2.622	2.624			
SDSS J233330.16+152538.7	353.37571	15.4274	3.680	2.722	3.633			
PC 2331+0216	353.63325	2.5561	4.093	3.115	4.042			
FBQS J2334-0908	353.69333	-9.1367	3.317	2.332	3.274	3.0569	20.35	0.15
SDSS J233532.66+154534.2	353.88614	15.7595	3.132	2.955	3.091			
SDSS J233534.53-085939.3	353.89389	-8.9943	3.683	3.228	3.636			
SDSS J233634.41+133042.8	354.14341	13.5119	3.336	2.615	3.292			
SDSS J233642.61+001653.3	354.17756	0.2815	2.606	2.307	2.570			
[VCV96] Q 2334+10	354.26017	10.7768	2.243	1.634	2.211			
SDSS J233756.58-102000.1	354.48577	-10.3334	2.436	2.307	2.402			
SDSS J233823.15+150445.2	354.59650	15.0792	2.420	2.307	.386			
FBQS J2338-0035	354.65923	-0.5872	2.678	2.349	2.641			
SDSS J233900.26+141418.9	354.75113	14.2386	2.417	2.307	2.382			
FBQS J2339+0030	354.87504	0.5048	3.051	2.307	3.011			
SDSS J233939.48-103539.3	354.91453	-10.5943	2.757	2.373	2.720			
SDSS J234003.51+140257.1	355.01465	14.0492	4.548	3.681	4.455			
SDSS J234033.70-005636.9	355.14045	-0.9436	3.650	2.652	3.604			
SDSS J234128.92-091610.5	355.37051	-9.2696	4.125	3.638	4.041			
SDSS J234147.26+001551.9	355.44695	0.2644	3.954	3.076	3.904			
SDSS J234238.78+141551.6	355.66162	14.2644	2.466	2.375	2.431			
SDSS J234315.84+004659.6	355.81621	0.7832	2.776	2.403	2.694			
SDSS J234349.41-104742.0	355.95588	-10.7950	3.616	3.186	3.570			
SDSS J234352.62+141014.6	355.96929	14.1707	2.913	2.307	2.874	2.6770	20.50	0.15
PSS J2344+0342	356.01333	3.7072	4.248	2.693	4.196	3.2200	21.30	0.10
SDSS J234407.60-005852.7	356.03169	-0.9813	3.208	2.791	3.125			
SDSS J234603.19+151032.0	356.51332	15.1756	3.136	2.362	3.095			
SDSS J234614.26+142022.2	356.55943	14.3395	3.008	2.328	2.968			
SDSS J234623.71+004300.9	356.59884	0.7170	2.861	2.488	2.822			
SDSS J2346-0016	356.60693	-0.2668	3.489	2.307	3.444			
SDSS J234747.00+135405.0	356.94586	13.9014	3.152	2.515	3.111			
SDSS J234806.22+152229.2	357.02595	15.3748	3.312	2.885	3.230			
SDSS J234856.48-104131.1	357.23536	-10.6920	3.172	2.307	3.131	2.9979	20.55	0.15
BR J2349-3712	357.30733	-37.2164	4.219	2.850	4.167			
SDSS J234942.25+154708.1	357.42607	15.7856	2.454	2.307	2.420			
UM 184	357.74115	-0.8694	3.024	2.327	2.983	2.4261	20.55	0.15
						2.6146	21.20	0.15
SDSS J235224.13-000951.0	358.10057	-0.1642	2.744	2.605	2.662			
SDSS J235302.55-100816.2	358.26076	-10.1379	2.612	2.307	2.576			
[LWT91] 2351-1154	358.39265	-11.6217	2.670	1.632	2.633			
SDSS J235344.25+143525.2	358.43440	14.5904	4.242	3.350	4.190			
[VCV96] Q 2351+10	358.51403	10.7782	2.379	1.632	2.345			
LBQS 2351+0217	358.62659	2.5695	2.030	1.634	2.000	1.7660	20.90	0.20
LBQS 2351+0120	358.63515	1.6151	2.070	1.634	2.039			
LBQS 2352+0205	358.88317	2.3717	2.190	1.634	2.158			
SDSS J235546.07-002342.8	358.94228	-0.3953	3.252	2.581	3.209			
SDSS J235628.96-003601.8	359.12068	-0.6006	2.937	2.548	2.855			
LBQS 2354-0134	359.19333	-1.3025	2.210	1.665	2.178			
SDSS J235854.52+144623.7	359.72718	14.7733	3.390	2.956	3.308			
LBQS 2356+0139	359.79873	1.9449	2.070	1.661	2.039			
LBQS 2356+0237	359.84670	2.9108	2.500	1.634	2.465			

Table I.1: Combined Sample

BIBLIOGRAPHY

Thesis Refereed Publications

Z. Cano, A. de Ugarte Postigo, A. Pozanenko, N. Butler, C. C. Thöne, C. Guidorzi, T. Krühler, J. Gorosabel, P. Jakobsson, G. Leloudas, D. Malesani, J. Hjorth, A. Melandri, C. Mundell, K. Wiersema, P. D'Avanzo, S. Schulze, A. Gomboc, A. Johansson, W. Zheng, D. A. Kann, F. Knust, K. Varela, C. W. Akerlof, J. Bloom, O. Burkhonov, E. Cooke, J. A. de Diego, G. Dhungana, C. Farina, F. V. Ferrante, H. A. Flewelling, O. D. Fox, J. Fynbo, N. Gehrels, L. Georgiev, J. J. González, J. Greiner, T. Güver, O. Hartoog, N. Hatch, M. Jelinek, R. Kehoe, S. Klose, E. Klunko, D. Kopač, A. Kutyrev, Y. Krugly, W. H. Lee, A. Levan, V. Linkov, A. Matkin, N. Minikulov, I. Molotov, J. X. Prochaska, M. G. Richer, C. G. Román-Zúñiga, V. Rumyantsev, R. **Sánchez-Ramírez**, I. Steele, N. R. Tanvir, A. Volnova, A. M. Watson, D. Xu, and F. Yuan. A trio of gamma-ray burst supernovae:. GRB 120729A, GRB 130215A/SN 2013ez, and GRB 130831A/SN 2013fu. *A&A*, 568:A19, August 2014.

Z. Cano, A. de Ugarte Postigo, D. Perley, T. Krühler, R. Margutti, M. Friis, D. Malesani, P. Jakobsson, J. P. U. Fynbo, J. Gorosabel, J. Hjorth, R. **Sánchez-Ramírez**, S. Schulze, N. R. Tanvir, C. C. Thöne, and D. Xu. GRB 140606B/iPTF14bfu: detection of shock-breakout emission from a cosmological γ-ray burst? *MNRAS*, 452: 1535–1552, September 2015. doi: 10.1093/mnras/stv1327.

A. de Ugarte Postigo, J. P. U. Fynbo, C. C. Thöne, L. Christensen, J. Gorosabel, B. Milvang-Jensen, S. Schulze, P. Jakobsson, K. Wiersema, R. **Sánchez-Ramírez**, G. Leloudas, T. Zafar, D. Malesani, and J. Hjorth. The distribution of equivalent widths in long GRB afterglow spectra. *A&A*, 548:A11, December 2012a. doi: 10.1051/0004-6361/201219894. 130, 131, 178, 180, 184, 185, 212, 215, 276, 278

A. de Ugarte Postigo, A. Lundgren, S. Martín, D. Garcia-Appadoo, I. de Gregorio Monsalvo, A. Peck, M. J. Michałowski, C. C. Thöne, S. Campana, J. Gorosabel, N. R. Tanvir, K. Wiersema, A. J. Castro-Tirado, S. Schulze, C. De Breuck, G. Petitpas, J. Hjorth, P. Jakobsson, S. Covino, J. P. U. Fynbo, J. M. Winters, M. Bremer, A. J. Levan, A. Llorente, R. **Sánchez-Ramírez**, J. C. Tello, and R. Salvaterra. Pre-ALMA

observations of GRBs in the mm/submm range. *A&A*, 538:A44, February 2012b. doi: 10.1051/0004-6361/201117848. 120, 124, 125, 128, 130

A. de Ugarte Postigo, S. Campana, C. C. Thöne, P. D'Avanzo, R. **Sánchez-Ramírez**, A. Melandri, J. Gorosabel, G. Ghirlanda, P. Veres, S. Martín, G. Petitpas, S. Covino, J. P. U. Fynbo, and A. J. Levan. The obscured hyper-energetic GRB 120624B hosted by a luminous compact galaxy at z = 2.20. *A&A*, 557:L18, September 2013. doi: 10.1051/0004-6361/201322065.

A. de Ugarte Postigo, C. C. Thöne, A. Rowlinson, R. García-Benito, A. J. Levan, J. Gorosabel, P. Goldoni, S. Schulze, T. Zafar, K. Wiersema, R. **Sánchez-Ramírez**, A. Melandri, P. D'Avanzo, S. Oates, V. D'Elia, M. De Pasquale, T. Krühler, A. J. van der Horst, D. Xu, D. Watson, S. Piranomonte, S. D. Vergani, B. Milvang-Jensen, L. Kaper, D. Malesani, J. P. U. Fynbo, Z. Cano, S. Covino, H. Flores, S. Greiss, F. Hammer, O. E. Hartoog, S. Hellmich, C. Heuser, J. Hjorth, P. Jakobsson, S. Mottola, M. Sparre, J. Sollerman, G. Tagliaferri, N. R. Tanvir, M. Vestergaard, and R. A. M. J. Wijers. Spectroscopy of the short-hard GRB 130603B. The host galaxy and environment of a compact object merger. *A&A*, 563:A62, March 2014. doi: 10.1051/0004-6361/201322985.

V. D'Elia, J. P. U. Fynbo, P. Goldoni, S. Covino, A. de Ugarte Postigo, C. Ledoux, F. Calura, J. Gorosabel, D. Malesani, F. Matteucci, R. **Sánchez-Ramírez**, S. Savaglio, A. J. Castro-Tirado, O. E. Hartoog, L. Kaper, T. Muñoz-Darias, E. Pian, S. Piranomonte, G. Tagliaferri, N. Tanvir, S. D. Vergani, D. J. Watson, and D. Xu. VLT/X-shooter spectroscopy of the GRB 120327A afterglow. *A&A*, 564:A38, April 2014. doi: 10.1051/0004-6361/201323057. 51, 120

J. Elliott, T. Krühler, J. Greiner, S. Savaglio, F. Olivares, E. A. Rau, A. de Ugarte Postigo, R. **Sánchez-Ramírez**, K. Wiersema, P. Schady, D. A. Kann, R. Filgas, M. Nardini, E. Berger, D. Fox, J. Gorosabel, S. Klose, A. Levan, A. Nicuesa Guelbenzu, A. Rossi, S. Schmidl, V. Sudilovsky, N. R. Tanvir, and C. C. Thöne. The low-extinction afterglow in the solar-metallicity host galaxy of γ-ray burst 110918A. *A&A*, 556:A23, August 2013. doi: 10.1051/0004-6361/201220968.

P. A. Evans, R. Willingale, J. P. Osborne, P. T. O'Brien, N. R. Tanvir, D. D. Frederiks, V. D. Pal'shin, D. S. Svinkin, A. Lien, J. Cummings, S. Xiong, B.-B. Zhang, D. Götz, V. Savchenko, H. Negoro, S. Nakahira, K. Suzuki, K. Wiersema, R. L. C. Starling, A. J. Castro-Tirado, A. P. Beardmore, R. **Sánchez-Ramírez**, J. Gorosabel, S. Jeong, J. A. Kennea, D. N. Burrows, and N. Gehrels. GRB 130925A: an ultralong gamma ray burst with a dust-echo afterglow, and implications for the origin of the ultralong GRBs. *MNRAS*, 444:250–267, October 2014. 212

E. S. Gorbovskoy, G. V. Lipunova, V. M. Lipunov, V. G. Kornilov, A. A. Belinski, N. I. Shatskiy, N. V. Tyurina, D. A. Kuvshinov, P. V. Balanutsa, V. V. Chazov, A. Kuznetsov, D. S. Zimnukhov, M. V. Kornilov, A. V. Sankovich, A. Krylov, K. I. Ivanov, O. Chvalaev, V. A. Poleschuk, E. N. Konstantinov, O. A. Gress, S. A. Yazev, N. M. Budnev, V. V. Krushinski, I. S. Zalozhnich, A. A. Popov, A. G. Tlatov, A. V. Parhomenko, D. V. Dormidontov, V. Senik, V. V. Yurkov, Y. P. Sergienko, D. Varda, I. P. Kudelina, A. J. Castro-Tirado, J. Gorosabel, R. **Sánchez-Ramírez**, M. Jelinek, and J. C. Tello. Prompt, early and afterglow optical observations of five γ-ray bursts: GRB 100901A, GRB 100902A, GRB 100905A, GRB 100906A and GRB 101020A. *MNRAS*, 421:1874–1890, April 2012. doi: 10.1111/j.1365-2966.2012.20195.x.

E. S. Gorbovskoy, V. M. Lipunov, D. A. H. Buckley, V. G. Kornilov, P. V. Balanutsa, N. V. Tyurina, A. S. Kuznetsov, D. A. Kuvshinov, I. A. Gorbunov, D. Vlasenko, E. Popova, V. V. Chazov, S. Potter, M. Kotze, A. Y. Kniazev, O. A. Gress, N. M. Budnev, K. I. Ivanov, S. A. Yazev, A. G. Tlatov, V. A. Senik, D. V. Dormidontov, A. V. Parhomenko, V. V. Krushinski, I. S. Zalozhnich, R. A. Castro-Tirado, R. Sánchez-Ramírez, Y. P. Sergienko, A. Gabovich, V. V. Yurkov, H. Levato, C. Saffe, C. Mallamaci, C. Lopez, F. Podest, and V. V. Vladimirov. Early polarization observations of the optical emission of gamma-ray bursts: GRB 150301B and GRB 150413A. *MNRAS*, 455:3312–3318, January 2016. doi: 10.1093/mnras/stv2515.

J. Japelj, S. Covino, A. Gomboc, S. D. Vergani, P. Goldoni, J. Selsing, Z. Cano, V. D'Elia, H. Flores, J. P. U. Fynbo, F. Hammer, J. Hjorth, P. Jakobsson, L. Kaper, D. Kopač, T. Krühler, A. Melandri, S. Piranomonte, R. **Sánchez-Ramírez**, G. Tagliaferri, N. R. Tanvir, A. de Ugarte Postigo, D. Watson, and R. A. M. J. Wijers. Spectrophotometric analysis of gamma-ray burst afterglow extinction curves with X-Shooter. *A&A*, 579: A74, July 2015. doi: 10.1051/0004-6361/201525665. 47

S. Jeong, A. J. Castro-Tirado, M. Bremer, J. M. Winters, J. Gorosabel, S. Guziy, S. B. Pandey, M. Jelínek, R. **Sánchez-Ramírez**, I. V. Sokolov, N. V. Orekhova, A. S. Moskvitin, J. C. Tello, R. Cunniffe, O. Lara-Gil, S. R. Oates, D. Pérez-Ramírez, J. Bai, Y. Fan, C. Wang, and I. H. Park. The dark nature of GRB 130528A and its host galaxy. *A&A*, 569:A93, September 2014.

Z.-P. Jin, S. Covino, M. Della Valle, P. Ferrero, D. Fugazza, D. Malesani, A. Melandri, E. Pian, R. Salvaterra, D. Bersier, S. Campana, Z. Cano, A. J. Castro-Tirado, P. D'Avanzo, J. P. U. Fynbo, A. Gomboc, J. Gorosabel, C. Guidorzi, J. B. Haislip, J. Hjorth, S. Kobayashi, A. P. LaCluyze, G. Marconi, P. A. Mazzali, C. G. Mundell, S. Piranomonte, D. E. Reichart, R. **Sánchez-Ramírez**, R. J. Smith, I. A. Steele,

G. Tagliaferri, N. R. Tanvir, S. Valenti, S. D. Vergani, T. Vestrand, E. S. Walker, and P. Woźniak. GRB 081007 and GRB 090424: The Surrounding Medium, Outflows, and Supernovae. *ApJ*, 774:114, September 2013. doi: 10.1088/0004-637X/774/2/114.

D. Kopač, C. G. Mundell, J. Japelj, D. M. Arnold, I. A. Steele, C. Guidorzi, S. Dichiara, S. Kobayashi, A. Gomboc, R. M. Harrison, G. P. Lamb, A. Melandri, R. J. Smith, F. J. Virgili, A. J. Castro-Tirado, J. Gorosabel, A. Järvinen, R. Sánchez-Ramírez, S. R. Oates, and M. Jelínek. Limits on Optical Polarization during the Prompt Phase of GRB 140430A. *ApJ*, 813:1, November 2015. doi: 10.1088/0004-637X/813/1/1. 119

T. Krühler, C. Ledoux, J. P. U. Fynbo, P. M. Vreeswijk, S. Schmidl, D. Malesani, L. Christensen, A. De Cia, J. Hjorth, P. Jakobsson, D. A. Kann, L. Kaper, S. D. Vergani, P. M. J. Afonso, S. Covino, A. de Ugarte Postigo, V. D'Elia, R. Filgas, P. Goldoni, J. Greiner, O. E. Hartoog, B. Milvang-Jensen, M. Nardini, S. Piranomonte, A. Rossi, R. **Sánchez-Ramírez**, P. Schady, S. Schulze, V. Sudilovsky, N. R. Tanvir, G. Tagliaferri, D. J. Watson, K. Wiersema, R. A. M. J. Wijers, and D. Xu. Molecular hydrogen in the damped Lyman α system towards GRB 120815A at z = 2.36. *A&A*, 557:A18, September 2013. doi: 10.1051/0004-6361/201321772. 50, 51

T. Krühler, D. Malesani, J. P. U. Fynbo, O. E. Hartoog, J. Hjorth, P. Jakobsson, D. A. Perley, A. Rossi, P. Schady, S. Schulze, N. R. Tanvir, S. D. Vergani, K. Wiersema, P. M. J. Afonso, J. Bolmer, Z. Cano, S. Covino, V. D'Elia, A. de Ugarte Postigo, R. Filgas, M. Friis, J. F. Graham, J. Greiner, P. Goldoni, A. Gomboc, F. Hammer, J. Japelj, D. A. Kann, L. Kaper, S. Klose, A. J. Levan, G. Leloudas, B. Milvang-Jensen, A. Nicuesa Guelbenzu, E. Palazzi, E. Pian, S. Piranomonte, R. Sánchez-Ramírez, S. Savaglio, J. Selsing, G. Tagliaferri, P. M. Vreeswijk, D. J. Watson, and D. Xu. GRB hosts through cosmic time. VLT/X-Shooter emission-line spectroscopy of 96 γ-ray-burst-selected galaxies at $0.1 < z < 3.6$. *A&A*, 581:A125, September 2015. doi: 10.1051/0004-6361/201425561. 81, 120

A. J. Levan, N. R. Tanvir, S. B. Cenko, D. A. Perley, K. Wiersema, J. S. Bloom, A. S. Fruchter, A. d. U. Postigo, P. T. O'Brien, N. Butler, A. J. van der Horst, G. Leloudas, A. N. Morgan, K. Misra, G. C. Bower, J. Farihi, R. L. Tunnicliffe, M. Modjaz, J. M. Silverman, J. Hjorth, C. Thöne, A. Cucchiara, J. M. C. Cerón, A. J. Castro-Tirado, J. A. Arnold, M. Bremer, J. P. Brodie, T. Carroll, M. C. Cooper, P. A. Curran, R. M. Cutri, J. Ehle, D. Forbes, J. Fynbo, J. Gorosabel, J. Graham, D. I. Hoffman, S. Guziy, P. Jakobsson, A. Kamble, T. Kerr, M. M. Kasliwal, C. Kouveliotou, D. Kocevski, N. M. Law, P. E. Nugent, E. O. Ofek, D. Poznanski, R. M. Quimby, E. Rol, A. J. Romanowsky, R. **Sánchez-Ramírez**, S. Schulze, N. Singh, L. van Spaandonk, R. L. C. Starling, R. G.

Strom, J. C. Tello, O. Vaduvescu, P. J. Wheatley, R. A. M. J. Wijers, J. M. Winters, and D. Xu. An Extremely Luminous Panchromatic Outburst from the Nucleus of a Distant Galaxy. *Science*, 333:199–, July 2011. doi: 10.1126/science.1207143.

A. J. Levan, N. R. Tanvir, R. L. C. Starling, K. Wiersema, K. L. Page, D. A. Perley, S. Schulze, G. A. Wynn, R. Chornock, J. Hjorth, S. B. Cenko, A. S. Fruchter, P. T. O'Brien, G. C. Brown, R. L. Tunnicliffe, D. Malesani, P. Jakobsson, D. Watson, E. Berger, D. Bersier, B. E. Cobb, S. Covino, A. Cucchiara, A. de Ugarte Postigo, D. B. Fox, A. Gal-Yam, P. Goldoni, J. Gorosabel, L. Kaper, T. Krühler, R. Karjalainen, J. P. Osborne, E. Pian, R. **Sánchez-Ramírez**, B. Schmidt, I. Skillen, G. Tagliaferri, C. Thöne, O. Vaduvescu, R. A. M. J. Wijers, and B. A. Zauderer. A New Population of Ultra-long Duration Gamma-Ray Bursts. *ApJ*, 781:13, January 2014. doi: 10.1088/0004-637X/781/1/13.

A. Melandri, M. G. Bernardini, P. D'Avanzo, R. **Sánchez-Ramírez**, F. Nappo, L. Nava, J. Japelj, A. de Ugarte Postigo, S. Oates, S. Campana, S. Covino, V. D'Elia, G. Ghirlanda, E. Gafton, G. Ghisellini, N. Gnedin, P. Goldoni, J. Gorosabel, T. Libbrecht, D. Malesani, R. Salvaterra, C. C. Thöne, S. D. Vergani, D. Xu, and G. Tagliaferri. The high-redshift gamma-ray burst GRB 140515A. A comprehensive X-ray and optical study. *A&A*, 581:A86, September 2015. doi: 10.1051/0004-6361/201526660.

T. Muñoz-Darias, A. de Ugarte Postigo, D. M. Russell, S. Guziy, J. Gorosabel, J. Casares, M. Armas Padilla, P. A. Charles, R. P. Fender, T. M. Belloni, F. Lewis, S. Motta, A. Castro-Tirado, C. G. Mundell, R. **Sánchez-Ramírez**, and C. C. Thöne. The optical counterpart of the bright X-ray transient Swift J1745-26. *MNRAS*, 432:1133–1137, June 2013. doi: 10.1093/mnras/stt532.

L. Resmi, K. Misra, G. Jóhannesson, A. J. Castro Tirado, J. Gorosabel, M. Jelínek, D. Bhattacharya, P. Kubánek, G. C. Anupama, A. Sota, D. K. Sahu, A. de Ugarte Postigo, S. B. Pandey, R. **Sánchez Ramírez**, M. Bremer, and R. Sagar. Comprehensive multiwavelength modelling of the afterglow of GRB 050525A. *MNRAS*, 427: 288–297, November 2012. doi: 10.1111/j.1365-2966.2012.21713.x. 132

T. Sakamoto, E. Troja, K. Aoki, S. Guiriec, M. Im, G. Leloudas, D. Malesani, A. Melandri, A. de Ugarte Postigo, Y. Urata, D. Xu, P. D'Avanzo, J. Gorosabel, Y. Jeon, R. **Sánchez-Ramírez**, M. I. Andersen, J. Bai, S. D. Barthelmy, M. S. Briggs, S. Foley, A. S. Fruchter, J. P. U. Fynbo, N. Gehrels, K. Huang, M. Jang, N. Kawai, H. Korhonen, J. Mao, J. P. Norris, R. D. Preece, J. L. Racusin, C. C. Thöne, K. Vida, and X. Zhao. Identifying the Location in the Host Galaxy of the Short

GRB 111117A with the Chandra Subarcsecond Position. *ApJ*, 766:41, March 2013. doi: 10.1088/0004-637X/766/1/41.

R. Sánchez-Ramírez, S. L. Ellison, J. X. Prochaska, T. A. M. Berg, S. López, V. D'Odorico, G. D. Becker, L. Christensen, G. Cupani, K. D. Denney, I. Pâris, G. Worseck, and J. Gorosabel. The evolution of neutral gas in damped Lyman α systems from the XQ-100 survey. *MNRAS*, 456:4488–4505, March 2016. doi: 10.1093/mnras/stv2732. 176, 177, 178, 196

S. Schulze, D. Malesani, A. Cucchiara, N. R. Tanvir, T. Krühler, A. de Ugarte Postigo, G. Leloudas, J. Lyman, D. Bersier, K. Wiersema, D. A. Perley, P. Schady, J. Gorosabel, J. P. Anderson, A. J. Castro-Tirado, S. B. Cenko, A. De Cia, L. E. Ellerbroek, J. P. U. Fynbo, J. Greiner, J. Hjorth, D. A. Kann, L. Kaper, S. Klose, A. J. Levan, S. Martín, P. T. O'Brien, K. L. Page, G. Pignata, S. Rapaport, R. **Sánchez-Ramírez**, J. Sollerman, I. A. Smith, M. Sparre, C. C. Thöne, D. J. Watson, D. Xu, F. E. Bauer, M. Bayliss, G. Björnsson, M. Bremer, Z. Cano, S. Covino, V. D'Elia, D. A. Frail, S. Geier, P. Goldoni, O. E. Hartoog, P. Jakobsson, H. Korhonen, K. Y. Lee, B. Milvang-Jensen, M. Nardini, A. Nicuesa Guelbenzu, M. Oguri, S. B. Pandey, G. Petitpas, A. Rossi, A. Sandberg, S. Schmidl, G. Tagliaferri, R. P. J. Tilanus, J. M. Winters, D. Wright, and E. Wuyts. GRB 120422A/SN 2012bz: Bridging the gap between low- and high-luminosity gamma-ray bursts. *A&A*, 566:A102, June 2014.

B. Sicardy, J. L. Ortiz, M. Assafin, E. Jehin, A. Maury, E. Lellouch, R. G. Hutton, F. Braga-Ribas, F. Colas, D. Hestroffer, J. Lecacheux, F. Roques, P. Santos-Sanz, T. Widemann, N. Morales, R. Duffard, A. Thirouin, A. J. Castro-Tirado, M. Jelínek, P. Kubánek, A. Sota, R. **Sánchez-Ramírez**, A. H. Andrei, J. I. B. Camargo, D. N. da Silva Neto, A. R. Gomes, R. V. Martins, M. Gillon, J. Manfroid, G. P. Tozzi, C. Harlingten, S. Saravia, R. Behrend, S. Mottola, E. G. Melendo, V. Peris, J. Fabregat, J. M. Madiedo, L. Cuesta, M. T. Eibe, A. Ullán, F. Organero, S. Pastor, J. A. de Los Reyes, S. Pedraz, A. Castro, I. de La Cueva, G. Muler, I. A. Steele, M. Cebrián, P. Montañés-Rodríguez, A. Oscoz, D. Weaver, C. Jacques, W. J. B. Corradi, F. P. Santos, W. Reis, A. Milone, M. Emilio, L. Gutiérrez, R. Vázquez, and H. Hernández-Toledo. A Pluto-like radius and a high albedo for the dwarf planet Eris from an occultation. *Nature*, 478:493–496, October 2011. doi: 10.1038/nature10550.

M. Sparre, O. E. Hartoog, T. Krühler, J. P. U. Fynbo, D. J. Watson, K. Wiersema, V. D'Elia, T. Zafar, P. M. J. Afonso, S. Covino, A. de Ugarte Postigo, H. Flores, P. Goldoni, J. Greiner, J. Hjorth, P. Jakobsson, L. Kaper, S. Klose, A. J. Levan, D. Malesani, B. Milvang-Jensen, M. Nardini, S. Piranomonte, J. Sollerman,

R. **Sánchez-Ramírez**, S. Schulze, N. R. Tanvir, S. D. Vergani, and R. A. M. J. Wijers. The Metallicity and Dust Content of a Redshift 5 Gamma-Ray Burst Host Galaxy. *ApJ*, 785:150, April 2014. doi: 10.1088/0004-637X/785/2/150. 120

J. C. Tello, A. J. Castro-Tirado, J. Gorosabel, D. Pérez-Ramírez, S. Guziy, R. **Sánchez-Ramírez**, M. Jelínek, P. Veres, and Z. Bagoly. Searching for Galactic sources in the Swift GRB catalog. Statistical analyses of the angular distributions of FREDs. *A&A*, 548:L7, December 2012. doi: 10.1051/0004-6361/201220527.

S. D. Vergani, H. Flores, S. Covino, D. Fugazza, J. Gorosabel, A. J. Levan, M. Puech, R. Salvaterra, J. C. Tello, A. de Ugarte Postigo, P. D'Avanzo, V. D'Elia, M. Fernández, J. P. U. Fynbo, G. Ghirlanda, M. Jelínek, A. Lundgren, D. Malesani, E. Palazzi, S. Piranomonte, M. Rodrigues, R. **Sánchez-Ramírez**, V. Terrón, C. C. Thöne, L. A. Antonelli, S. Campana, A. J. Castro-Tirado, P. Goldoni, F. Hammer, J. Hjorth, P. Jakobsson, L. Kaper, A. Melandri, B. Milvang-Jensen, J. Sollerman, G. Tagliaferri, N. R. Tanvir, K. Wiersema, and R. A. M. J. Wijers. GRB 091127/SN 2009nz and the VLT/X-shooter spectroscopy of its host galaxy: probing the faint end of the mass-metallicity relation. *A&A*, 535:A127, November 2011. doi: 10.1051/0004-6361/201117726.

L. P. Xin, A. Pozanenko, D. A. Kann, D. Xu, J. Gorosabel, G. Leloudas, J. Y. Wei, M. Andreev, S. F. Qin, M. Ibrahimov, X. H. Han, A. de Ugarte Postigo, Y. L. Qiu, J. S. Deng, A. Volnova, P. Jakobsson, A. J. Castro-Tirado, F. Aceituno, J. P. U. Fynbo, J. Wang, R. **Sanchez-Ramirez**, V. Kouprianov, W. K. Zheng, J. C. Tello, and C. Wu. The shallow-decay phase in both the optical and X-ray afterglows of Swift GRB 090529A: energy injection into a wind-type medium? *MNRAS*, 422:2044–2050, May 2012. doi: 10.1111/j.1365-2966.2012.20681.x.

D. Xu, A. de Ugarte Postigo, G. Leloudas, T. Krühler, Z. Cano, J. Hjorth, D. Malesani, J. P. U. Fynbo, C. C. Thöne, R. **Sánchez-Ramírez**, S. Schulze, P. Jakobsson, L. Kaper, J. Sollerman, D. J. Watson, A. Cabrera-Lavers, C. Cao, S. Covino, H. Flores, S. Geier, J. Gorosabel, S. M. Hu, B. Milvang-Jensen, M. Sparre, L. P. Xin, T. M. Zhang, W. K. Zheng, and Y. C. Zou. Discovery of the Broad-lined Type Ic SN 2013cq Associated with the Very Energetic GRB 130427A. *ApJ*, 776:98, October 2013. doi: 10.1088/0004-637X/776/2/98.

W. Zheng, R. F. Shen, T. Sakamoto, A. P. Beardmore, M. De Pasquale, X. F. Wu, J. Gorosabel, Y. Urata, S. Sugita, B. Zhang, A. Pozanenko, M. Nissinen, D. K. Sahu, M. Im, T. N. Ukwatta, M. Andreev, E. Klunko, A. Volnova, C. W. Akerlof, P. Anto, S. D. Barthelmy, A. Breeveld, U. Carsenty, S. Castillo-Carrión, A. J. Castro-Tirado, M. M. Chester, C. J. Chuang, R. Cunniffe, A. De Ugarte Postigo, R. Duffard,

H. Flewelling, N. Gehrels, T. Güver, S. Guziy, V. P. Hentunen, K. Y. Huang, M. Jelínek, T. S. Koch, P. Kubánek, P. Kuin, T. A. McKay, S. Mottola, S. R. Oates, P. O'Brien, M. Ohno, M. J. Page, S. B. Pandey, C. Pérez del Pulgar, W. Rujopakarn, E. Rykoff, T. Salmi, R. **Sánchez-Ramírez**, B. E. Schaefer, A. Sergeev, E. Sonbas, A. Sota, J. C. Tello, K. Yamaoka, S. A. Yost, and F. Yuan. Panchromatic Observations of the Textbook GRB 110205A: Constraining Physical Mechanisms of Prompt Emission and Afterglow. *ApJ*, 751:90, June 2012. doi: 10.1088/0004-637X/751/2/90. 119

Thesis Proceedings

A. J. Castro-Tirado, M. Bremer, J.-M. Winters, A. de Ugarte Postigo, J. Gorosabel, S. Guziy, D. Pérez-Ramírez, J. M. C. Cerón, C. Thöne, M. Jelínek, R. **Sánchez-Ramírez**, J. C. Tello, S. B. Pandey, and D. Bhattacharya. Millimetre Observations of Gamma-ray Bursts. In J. E. McEnery, J. L. Racusin, and N. Gehrels, editors, *American Institute of Physics Conference Series*, volume 1358 of *American Institute of Physics Conference Series*, pages 109–112, August 2011. doi: 10.1063/1.3621749.

A. J. Castro-Tirado, J. L. Gómez, I. Agudo, M. A. Guerrero, M. Bremer, J. M. Winters, J. Gorosabel, S. Guziy, M. Jelinek, J. C. Tello, R. **Sánchez-Ramírez**, D. Pérez-Ramírez, J. Reyes-Iturbide, I. H. Park, S. Jeong, and A. S. Pozanenko. The first months in the lifetime of the newly born jet associated to Swift J1644+57. In *European Physical Journal Web of Conferences*, volume 39 of *European Physical Journal Web of Conferences*, page 4002, December 2012a. doi: 10.1051/epjconf/20123904002.

A. J. Castro-Tirado, M. Jelínek, J. Gorosabel, P. Kubánek, R. Cunniffe, S. Guziy, O. Lara-Gil, O. Rabaza-Castillo, A. de Ugarte Postigo, R. **Sánchez-Ramírez**, J. C. Tello, V. Muñoz-Martínez, C. Pérez del Pulgar, S. Castillo-Carrión, J. M. Castro Cerón, T. d. J. Mateo Sanguino, R. Hudec, S. Vitek, B. A. de la Morena Carretero, J. A. Díaz Andreu, R. Fernández-Muñoz, D. Pérez-Ramírez, P. A. Yock, W. H. Allen, I. Bond, G. Christie, L. Sabau-Graziati, A. Castro, A. Pozanenko, J. Bai, Y. Fan, and C. Cui. Building the BOOTES world-wide Network of Robotic telescopes. In *Astronomical Society of India Conference Series*, volume 7 of *Astronomical Society of India Conference Series*, pages 313–320, 2012b.

A. J. Castro-Tirado, M. Bremer, J. M. Winters, J. C. Tello, S. B. Pandey, A. de Ugarte Postigo, J. Gorosabel, S. Guziy, M. Jelinek, R. **Sánchez-Ramírez**, D. Pérez-Ramírez, and J. M. Castro Cerón. Millimetre Observations of Gamma-ray Bursts at IRAM. In A. J. Castro-Tirado, J. Gorosabel, and I. H. Park, editors, *EAS Publications Series*, volume 61 of *EAS Publications Series*, pages 279–281, July 2013a. doi: 10.1051/eas/1361045.

A. J. Castro-Tirado, J. L. Gómez, I. Agudo, M. A. Guerrero, M. Bremer, J. M. Winters, J. Gorosabel, S. Guziy, A. de Ugarte Postigo, M. Jelínek, J. C. Tello, R. **Sánchez-Ramírez**, D. Pérez-Ramírez, J. Reyes-Iturbide, I. H. Park, S. Jeong, A. S. Pozanenko, and J. Acosta-Pulido. The first two months in the lifetime of the newly born jet associated to Swift J1644+57. In *Revista Mexicana de Astronomia y Astrofisica Conference Series*, volume 42 of *Revista Mexicana de Astronomia y Astrofisica Conference Series*, pages 36–37, May 2013b.

A. J. Castro-Tirado, J. L. Gómez, I. Agudo, M. A. Guerrero, M. Bremer, J. M. Winters, J. Gorosabel, R. **Sánchez-Ramírez**, S. Guziy, M. Jelinek, J. C. Tello, D. Pérez-Ramírez, J. Reyes-Iturbide, I. H. Park, S. Jeong, U. Bach, A. Kraussh, T. P. Krichbaumh, and A. S. Pozanenko. The first two years in the lifetime of the newly born jet associated to Sw J1644+57. In *European Physical Journal Web of Conferences*, volume 61 of *European Physical Journal Web of Conferences*, page 1003, December 2013c. doi: 10.1051/epjconf/20136101003.

A. J. Castro-Tirado, J. L. Gómez, I. Agudo, M. A. Guerrero, M. Bremer, J. M. Winters, J. Gorosabel, R. **Sánchez-Ramírez**, S. Guziy, M. Jelinek, J. C. Tello, D. Pérez-Ramírez, J. Reyes-Iturbide, I. H. Park, S. Jeong, and A. S. Pozanenko. The first months in the lifetime of the newly born jet associated to Swift J1644+57. In J. C. Guirado, L. M. Lara, V. Quilis, and J. Gorgas, editors, *Highlights of Spanish Astrophysics VII*, pages 185–189, May 2013d.

A. de Ugarte Postigo, A. Lundgren, S. Martín, D. García-Appadoo, I. de Gregorio Monsalvo, C. C. Thöne, J. Gorosabel, A. J. Castro-Tirado, R. **Sánchez-Ramírez**, and J. C. Tello. Observations of GRBs in the mm/submm range at the dawn of the ALMA era. In *Death of Massive Stars: Supernovae and Gamma-Ray Bursts*, volume 279 of *IAU Symposium*, pages 380–382, September 2012. doi: 10.1017/S1743921312013440.

A. de Ugarte Postigo, J. Gorosabel, C. C. Thöne, and R. **Sánchez-Ramírez**. The role of GTC in gamma-ray burst science. In *Revista Mexicana de Astronomia y Astrofisica Conference Series*, volume 42 of *Revista Mexicana de Astronomia y Astrofisica Conference Series*, pages 73–74, May 2013.

A. de Ugarte Postigo, M. Blazek, P. Janout, P. Sprimont, C. C. Thöne, J. Gorosabel, and R. **Sánchez-Ramírez**. GRBSpec: a multi-observatory database for gamma-ray burst spectroscopy. In *Society of Photo-Optical Instrumentation Engineers (SPIE) Conference Series*, volume 9152 of *Society of Photo-Optical Instrumentation Engineers (SPIE) Conference Series*, page 0, July 2014.

A. de Ugarte Postigo, J. P. U. Fynbo, C. C. Thöne, L. Christensen, J. Gorosabel, and R. **Sánchez-Ramírez**. Statistical study of the ISM of GRB hosts. *Highlights of Astronomy*, 16:620–620, March 2015. doi: 10.1017/S1743921314012496.

J. Gorosabel, P. Kubánek, O. Lara-Gil, M. Jelínek, S. Guziy, N. Morales, A. J. Castro-Tirado, A. de Ugarte Postigo, C. C. Thöne, J. C. Tello, R. **Sanchéz-Ramírez**, S. Castillo-Carrión, N. Huélamo, V. Terrón, J. L. Ortiz, M. Fernández, S. Mottola, S. Hellmich, G. Hahn, R. Cunniffe, V. Peris, and U. Carsenty. The 1.23m CAHA telescope: combining upgrades and scientific observations. In *Astronomical Society of India Conference Series*, volume 7 of *Astronomical Society of India Conference Series*, page 303, 2012.

J. Gorosabel, A. J. Castro-Tirado, A. de Ugarte Postigo, C. C. Thöne, R. **Sánchez-Ramírez**, D. Peréz-Ramírez, J. C. Tello, M. Jelínek, and S. Guziy. Observing GRB afterglows, SNe and their host galaxies with the 10.4 m Gran Telescopio Canarias (GTC). In A. J. Castro-Tirado, J. Gorosabel, and I. H. Park, editors, *EAS Publications Series*, volume 61 of *EAS Publications Series*, pages 235–239, July 2013a. doi: 10.1051/eas/1361035.

J. Gorosabel, A. de Ugarte Postigo, J. P. U. Fynbo, L. Christensen, C. C. Thöne, B. Milvang-Jensen, S. Schulze, P. Jakobsson, K. Wiersema, R. **Sánchez-Ramírez**, G. Leloudas, T. Zafar, D. Malesani, and Hjorth. The distribution of equivalent widths in GRB spectra. In J. C. Guirado, L. M. Lara, V. Quilis, and J. Gorgas, editors, *Highlights of Spanish Astrophysics VII*, pages 230–234, May 2013b.

S. Guziy, A. Castro-Tirado, M. Jelínek, J. Gorosabel, P. Kubánek, R. Cunniffe, O. Lara-Gil, O. Rabaza-Castillo, A. de Ugarte Postigo, R. **Sánchez-Ramírez**, J. Tello, C. Pérez del Pulgar, S. Castillo-Carrión, J. Castro Cerón, T. d. J. Mateo Sanguino, R. Hudec, S. Vitek, B. de la Morena Carretero, J. Díaz Andreu, R. Fernández-Muñoz, D. Pérez-Ramírez, P. Yock, W. Allen, I. Bond, I. Kheyfets, G. Christie, L. Sabau-Graziati, C. Cui, Y. Fan, and I. H. Park. GRBS Followed-up by the bootes network. In A. J. Castro-Tirado, J. Gorosabel, and I. H. Park, editors, *EAS Publications Series*, volume 61 of *EAS Publications Series*, pages 251–254, July 2013. doi: 10.1051/eas/1361038.

O. Lara-Gil, P. Kubanek, A. J. Castro-Tirado, J. Gorosabel, M. Jelinek, R. Cunniffe, S. Guziy, A. D. U. Postigo, R. **Sanchez-Ramirez**, and J. C. Tello. The RTS2 Web Interface. In S. Gajadhar, J. Walawender, R. Genet, C. Veillet, A. Adamson, J. Martinez, J. Melnik, T. Jenness, and N. Manset, editors, *Telescopes from Afar*, March 2011.

D. Pérez-Ramírez, J. P. Norris, J. Gorosabel, A. J. Castro-Tirado, L. Hernández-García, A. de Ugarte Postigo, S. Guziy, J. C. Tello, R. **Sánchez-Ramírez**, and P. Ferrero. A

GTC study of the afterglow and host galaxy of the short-duration GRB 100816A. In A. J. Castro-Tirado, J. Gorosabel, and I. H. Park, editors, *EAS Publications Series*, volume 61 of *EAS Publications Series*, pages 345–349, July 2013. doi: 10.1051/eas/1361055.

J. C. Tello, A. de Ugarte Postigo, R. **Sánchez-Ramírez**, M. Jelínek, J. Gorosabel, P. Kubánek, R. Cunniffe, S. Guziy, W. Allen, P. Yock, K.-Y. Lin, A. J. Castro-Tirado, R. Fernández, and C. Pérez del Pulgar. Bootes 3: first two years of GRB follow-ups in New Zealand. In *Astronomical Society of India Conference Series*, volume 7 of *Astronomical Society of India Conference Series*, page 79, 2012.

J. C. Tello, W. Allen, P. Yock, N. Rattenbury, J., M. Jelinek, J. Gorosabel, R. **Sánchez-Ramírez**, K.-Y. Lin, A. J. Castro-Tirado, and C. Pérez del Pulgar. BOOTES-3 Status. In *Revista Mexicana de Astronomia y Astrofisica Conference Series*, volume 45 of *Revista Mexicana de Astronomia y Astrofisica, vol. 27*, pages 12–, December 2014.

R. **Sánchez-Ramírez**, A. de Ugarte Postigo, J. Gorosabel, P. Hankcock, T. Murphy, A. Lundgren, D. A. Kann, I. de Gregorio Monsalvo, J. P. U. Fynbo, D. Garcia-Appadoo, S. Martín, A. Kamble, M. P. M. Kuin, S. R. Oates, A. J. Castro-Tirado, and J. Greiner. GRB110715A: Multifrequency study of the first gamma-ray burst observed with ALMA. In J. C. Guirado, L. M. Lara, V. Quilis, and J. Gorgas, editors, *Highlights of Spanish Astrophysics VII*, pages 399–404, May 2013a.

R. **Sánchez-Ramírez**, J. Gorosabel, A. de Ugarte Postigo, A. J. Castro-Tirado, C. C. Thöne, J. P. U. Fynbo, A. Cabrera-Lavers, S. Guziy, M. Jelínek, J. C. Tello, V. Peris, and D. Galadí-Enríquez. GRB 100316A: A Burst from a High Redshift Galaxy. In *Revista Mexicana de Astronomia y Astrofisica Conference Series*, volume 42 of *Revista Mexicana de Astronomia y Astrofisica Conference Series*, pages 113–113, May 2013b.

R. **Sánchez-Ramírez**, J. Gorosabel, A. de Ugarte Postigo, A. J. Castro-Tirado, C. C. Thöne, J. P. U. Fynbo, S. Guziy, M. Jelínek, J. C. Tello, V. Peris, and D. Galadí-Enríquez. GRB 100316A: an explosion at a high redshift galaxy. In J. C. Guirado, L. M. Lara, V. Quilis, and J. Gorgas, editors, *Highlights of Spanish Astrophysics VII*, pages 463–463, May 2013c.

R. **Sánchez-Ramírez**, P. Hancock, T. Murphy, A. de Ugarte Postigo, J. Gorosabel, D. A. Kann, C. C. Thöne, A. Lundgren, A. Kamble, S. R. Oates, J. P. U. Fynbo, I. de Gregorio Monsalvo, D. Garcia-Appadoo, S. Martín, N. P. M. Kuin, J. Greiner, and A. J. Castro-Tirado. GRB 110715A: Multiwavelength study of the first gamma-ray burst observed with ALMA. In A. J. Castro-Tirado, J. Gorosabel, and I. H. Park,

editors, *EAS Publications Series*, volume 61 of *EAS Publications Series*, pages 267–269, July 2013d. doi: 10.1051/eas/1361042.

Thesis Circulars

F. Aceituno, R. **Sanchez-Ramirez**, A. de Ugarte Postigo, J. Gorosabel, and A. J. Castro-Tirado. GRB 120722A: 1.5m OSN i-band observations. *GRB Coordinates Network*, 13505:1, 2012.

F. J. Aceituno, A. J. Castro-Tirado, R. **Sanchez-Ramirez**, and J. Gorosabel. GRB 140428A: 1.5m OSN I-band detection. *GRB Coordinates Network*, 16182:1, 2014.

A. J. Castro-Tirado, R. **Sanchez-Ramirez**, J. Gorosabel, M. Jelinek, J. C. Tello, P. Ferrero, O. Lara-Gil, R. Cunniffe, D. Perez-Ramirez, P. Kubanek, J. M. Castro Ceron, S. Mottola, S. Hellmich, R. Fernandez-Munoz, V. F. Munoz-Martinez, L. Sabau-Graziati, A. Martin-Carrillo, J. Cepa, A. Tejero, and C. Alvarez-Iglesias. GRB 130606A: 10.4m GTC refined redshift z = 5.91. *GRB Coordinates Network*, 14796:1, 2013a. 189

A. J. Castro-Tirado, R. **Sanchez-Ramirez**, M. Jelinek, J. Gorosabel, J. C. Tello, P. Ferrero, O. Lara-Gil, R. Cunniffe, D. Perez-Ramirez, P. Kubanek, J. M. Castro Ceron, A. Fernandez-Soto, S. Mottola, S. Hellmich, R. Fernandez-Munoz, V. F. Munoz-Martinez, J. Cepa, and C. Alvarez-Iglesias. GRB 130606A: 10.4m GTC spectroscopy indicates z = 6.1. *GRB Coordinates Network*, 14790:1, 2013b. 189

A. J. Castro-Tirado, R. Cunniffe, R. **Sanchez-Ramirez**, J. Gorosabel, M. Jelinek, S. R. Oates, S. Jeong, J. R. Tello, and S. Pandey. GRB140703A: 10.4m GTC redshift. *GRB Coordinates Network*, 16505:1, 2014a.

A. J. Castro-Tirado, J. Gorosabel, S. Guziy, O. Rabaza, I. Syniavskyi, Y. Ivanov, R. Cunniffe, A. Gonzalez-Rodriguez, M. Jelinek, S. Jeong, O. Lara-Gil, S. R. Oates, R. **Sanchez-Ramirez**, and J. C. Tello. GRB 140614C: 1.23m CAHA (+EDIPO) observations. *GRB Coordinates Network*, 16410:1, 2014b.

A. J. Castro-Tirado, J. Gorosabel, J. C. Tello, R. Cunniffe, A. Gonzalez-Rodriguez, A. Sota, M. Jelinek, S. Jeong, O. Lara-Gil, S. R. Oates, R. **Sanchez-Ramirez**, P. Kubanek, and S. Pandey. GRB 140709A: BOOTES-2 and OSN optical observations. *GRB Coordinates Network*, 16554:1, 2014d.

A. J. Castro-Tirado, J. Gorosabel, J. C. Tello, R. Cunniffe, A. Gonzalez-Rodriguez, A. Sota, M. Jelinek, S. Jeong, O. Lara-Gil, S. R. Oates, R. **Sanchez-Ramirez**, P. Kubanek, and S. Pandey. GRB 140709A: 10.4m GTC optical decay. *GRB Coordinates Network*, 16564:1, 2014c.

A. J. Castro-Tirado, D. Galadí-Enríquez, F. Hoyos, A. Guijarro, R. **Sánchez-Ramírez**, M. Fernández, J. C. Tello, S. Jeong, and J. Maíz-Apellániz. ANTARES neutrino detection: CAHA photometry and spectroscopy of the Swift source. *The Astronomer's Telegram*, 7998:1, September 2015a.

A. J. Castro-Tirado, R. **Sanchez-Ramirez**, J. Gorosabel, and R. Scarpa. GRB 150101B: potential host galaxy redshift by GTC. *GRB Coordinates Network*, 17278:1, 2015b.

A. J. Castro-Tirado, R. **Sanchez-Ramirez**, G. Lombardi, and M. A. Rivero. GRB 150424A: 10.4m GTC spectroscopy. *GRB Coordinates Network*, 17758:1, 2015c.

R. Cunniffe, A. Gonzalez-Rodriguez, V. Casanova, M. Jelinek, S. Jeong, O. Lara-Gil, S. R. Oates, R. **Sanchez-Ramirez**, J. C. Tello, P. Kubanek, J. Gorosabel, and A. J. Castro-Tirado. GRB 140703A: BOOTES-2 and OSN optical observations. *GRB Coordinates Network*, 16504:1, 2014.

A. de Ugarte Postigo, P. Kubanek, J. C. Tello, R. **Sanchez-Ramirez**, M. Jelinek, R. Cunniffe, S. Guziy, J. Gorosabel, R. Fernandez-Munoz, S. Castillo-Carrion, L. Sabau-Graziati, C. Perez Del Pulgar, L. Sabau-Graziati, and A. J. Castro-Tirado. GRB 101112A: BOOTES-2/TELMA optical afterglow candidate. *GRB Coordinates Network*, 11398:1, 2010.

A. de Ugarte Postigo, J. C. Tello, V. Casanova, A. J. Castro-Tirado, R. **Sanchez-Ramirez**, J. Gorosabel, S. Guziy, and D. Malesani. GRB 110915B: afterglow candidate from OSN. *GRB Coordinates Network*, 12350:1, 2011.

A. de Ugarte Postigo, C. De Breuck, T. Stanke, C. Agurto, M. Valencia-S., A. Remy, F. Montenegro, J. Gorosabel, R. **Sanchez-Ramirez**, and J. P. U. Fynbo. GRB 120514A: APEX observations of the submm counterpart. *GRB Coordinates Network*, 13293:1, 2012a.

A. de Ugarte Postigo, R. **Sanchez-Ramirez**, T. Munoz-Darias, J. Gorosabel, C. C. Thoene, and A. Cabrera-Lavers. Swift J1745-26: Spectroscopy and imaging from GTC. *The Astronomer's Telegram*, 4388:1, September 2012b.

A. de Ugarte Postigo, Z. Cano, C. C. Thoene, J. Gorosabel, R. **Sanchez-Ramirez**, G. Leloudas, D. Xu, K. Wiersema, J. P. U. Fynbo, D. Malesani, J. Hjorth, P. Jakobsson,

and O. E. Hartoog. Supernova 2013ez = GRB 130215A. *Central Bureau Electronic Telegrams*, 3637:1, August 2013a.

A. de Ugarte Postigo, N. Tanvir, R. **Sanchez-Ramirez**, C. C. Thoene, J. Gorosabel, and J. P. U. Fynbo. GRB 130420A: redshift from 10.4m GTC. *GRB Coordinates Network*, 14437:1, 2013b.

A. de Ugarte Postigo, C. C. Thoene, J. Gorosabel, R. **Sanchez-Ramirez**, J. P. U. Fynbo, and N. Tanvir. GRB130313A: optical observations from GTC. *GRB Coordinates Network*, 14302:1, 2013c.

A. de Ugarte Postigo, C. C. Thoene, J. Gorosabel, R. **Sanchez-Ramirez**, J. P. U. Fynbo, N. Tanvir, and C. A. Alvarez Iglesias. GRB 130418A: redshift from 10.4m GTC. *GRB Coordinates Network*, 14380:1, 2013d.

A. de Ugarte Postigo, C. C. Thoene, J. Gorosabel, R. **Sanchez-Ramirez**, J. P. U. Fynbo, N. R. Tanvir, A. Cabrera-Lavers, and A. Garcia. GRB 131108A: redshift from 10.4m GTC. *GRB Coordinates Network*, 15470:1, 2013e.

A. de Ugarte Postigo, C. C. Thoene, J. Gorosabel, R. **Sanchez-Ramirez**, G. Leloudas, Z. Cano, D. Xu, K. Wiersema, J. P. U. Fynbo, D. Malesani, J. Hjorth, P. Jakobsson, and O. E. Hartoog. GRB 130215A: detection of the SN with the 10.4m GTC. *GRB Coordinates Network*, 14303:1, 2013f.

A. de Ugarte Postigo, C. C. Thoene, R. **Sanchez-Ramirez**, J. Gorosabel, J. P. U. Fynbo, N. R. Tanvir, and C. A. Alvarez Iglesias. GRB 131030A: spectroscopy from 10.4m GTC. *GRB Coordinates Network*, 15408:1, 2013g.

A. de Ugarte Postigo, D. Xu, G. Leloudas, T. Kruehler, D. Malesani, J. Gorosabel, C. C. Thoene, R. **Sanchez-Ramirez**, S. Schulze, J. P. U. Fynbo, J. Hjorth, Z. Cano, P. Jakobsson, and A. Cabrera-Lavers. Supernova 2013cq = GRB 130427A. *Central Bureau Electronic Telegrams*, 3529:1, May 2013i.

A. de Ugarte Postigo, D. Xu, G. Leloudas, T. Kruehler, D. Malesani, J. Gorosabel, C. C. Thoene, R. **Sanchez-Ramirez**, S. Schulze, J. P. U. Fynbo, J. Hjorth, Z. Cano, P. Jakobsson, and A. Cabrera-Lavers. Supernova 2013cq = GRB 130427A. *Central Bureau Electronic Telegrams*, 3531:1, May 2013h.

A. de Ugarte Postigo, D. Xu, G. Leloudas, T. Kruehler, D. Malesani, J. Gorosabel, C. C. Thoene, R. **Sanchez-Ramirez**, S. Schulze, J. P. U. Fynbo, J. Hjorth, P. Jakobsson, and A. Cabrera-Lavers. GRB 130427A: spectroscopic detection of the SN from the 10.4m GTC. *GRB Coordinates Network*, 14646:1, 2013j.

A. de Ugarte Postigo, C. C. Thoene, D. Malesani, S. Schulze, R. **Sanchez-Ramirez**, J. Gorosabel, C. A. Alvarez Iglesias, J. Molgo, and M. Rivero. GRB141004A: Host galaxy redshift form GTC. *GRB Coordinates Network*, 16902:1, 2014.

A. de Ugarte Postigo, J. P. U. Fynbo, C. Thoene, N. R. Tanvir, R. **Sanchez-Ramirez**, J. Gorosabel, P. Pessev, C. Alvarez-Iglesias, and M. A. Rivero. GRB 150314A: Redshift from OSIRIS/GTC. *GRB Coordinates Network*, 17583:1, 2015.

J. Gorosabel, A. de Ugarte Postigo, S. Mottola, S. Hellmich, P. Ferrero, R. **Sanchez-Ramirez**, J. C. Tello, V. Casanova, R. Marti, and A. J. Castro-Tirado. Swift J1822.3-1606: Optical/NIR counterpart candidate. *The Astronomer's Telegram*, 3496:1, July 2011a.

J. Gorosabel, A. C. Lavers, R. **Sanchez-Ramirez**, A. de Ugarte Postigo, A. J. Levan, C. C. Thoene, N. R. Tanvir, A. J. Castro-Tirado, and P. Kubanek. GRB 111022B: 10.4m GTC z'-band observations. *GRB Coordinates Network*, 12494:1, 2011b.

J. Gorosabel, R. **Sanchez-Ramirez**, R. Gimeno, P. Montañes, and A. D. U. Postigo. MAXIJ1836-194: 1.23m CAHA I-band observations. *The Astronomer's Telegram*, 3673: 1, October 2011c.

J. Gorosabel, N. Huelamo, R. **Sanchez-Ramirez**, A. de Ugarte Postigo, T. Kruehler, A. J. Castro-Tirado, J. C. Tello, and M. Jelinek. GRB 120805A: 1.23m CAHA observations. *GRB Coordinates Network*, 13591:1, 2012a.

J. Gorosabel, M. Jelinek, C. Wang, C. Zurita, A. Sota, J. C. Tello, R. **Sanchez-Ramirez**, and A. J. Castro-Tirado. GRB 120729A: optical observations from OSN, BOOTES1/2 and IAC80. *GRB Coordinates Network*, 13550:1, 2012b.

J. Gorosabel, P. Kubanek, and R. **Sanchez-Ramirez**. GRB 120219A: 1.23m CAHA optical observations. *GRB Coordinates Network*, 12976:1, 2012c.

J. Gorosabel, A. de Ugarte Postigo, J. C. Tello, A. J. Castro-Tirado, J. Cepa, D. Jimenez-Mejias, R. Alonso, R. **Sanchez-Ramirez**, and V. Casanova. GRB 130502A: OSN and IAC80 i-band observations. *GRB Coordinates Network*, 14535:1, 2013a.

J. Gorosabel, A. de Ugarte Postigo, J. C. Tello, A. J. Castro-Tirado, J. Cepa, D. Jimenez-Mejias, J. L. D. Caballero, D. H. Ojados, and R. **Sanchez-Ramirez**. GRB 130504A: IAC80 optical candidate. *GRB Coordinates Network*, 14564:1, 2013b.

J. Gorosabel, J. C. Tello, M. Sanchez-Ramirez, M. Jelinek, and A. J. Castro-Tirado. GRB130313A: GTC early optical limits. *GRB Coordinates Network*, 14319:1, 2013c.

J. Gorosabel, A. de Ugarte Postigo, C. Thone, T. Munoz-Darias, R. **Sanchez-Ramirez**, and R. Scarpa. Swift Trigger 600114: Optical spectroscopy from GTC. *GRB Coordinates Network*, 16335:1, 2014a.

J. Gorosabel, R. **Sanchez-Ramirez**, S. Hellmich, and S. Mottola. GRB 141212A: 1.23m CAHA I-band observations. *GRB Coordinates Network*, 17167:1, 2014b.

S. Guziy, R. **Sanchez-Ramirez**, L. Monteagudo Narvion, O. Lara, M. Jelinek, P. Kubanek, Y. Fan, X. Zhao, J. Bai, C. Wang, Y. Xin, C. Cui, R. Cunniffe, A. J. Castro-Tirado, J. C. Tello, and J. Gorosabel. GRB 121123A: BOOTES-4 and IAC80 optical observations. *GRB Coordinates Network*, 13987:1, 2012b.

S. Guziy, R. **Sanchez-Ramirez**, L. Monteagudo Narvion, O. Lara, M. Jelinek, P. Kubanek, Y. Fan, X. Zhao, J. Bai, C. Wang, Y. Xin, C. Cui, R. Cunniffe, A. J. Castro-Tirado, J. C. Tello, and J. Gorosabel. GRB 121123A: BOOTES-4 optical observations. *GRB Coordinates Network*, 14026:1, 2012a.

S. Guziy, J. Gorosabel, A. J. Castro-Tirado, R. Cunniffe, M. Jelinek, S. Jeong, O. Lara-Gil, R. **Sanchez-Ramirez**, J. C. Tello, P. Kubanek, S. B. Pandey, Y. Fan, X. Zhao, J. Bai, C. Wang, Y. Xin, and C. Cui. GRB 140102A: BOOTES-4 early optical observations. *GRB Coordinates Network*, 15685:1, 2014.

O. E. Hartoog, D. Malesani, R. **Sanchez-Ramirez**, A. de Ugarte Postigo, A. J. Levan, J. P. U. Fynbo, P. M. Vreeswijk, and L. Kaper. GRB 140622A: VLT/X-shooter redshift. *GRB Coordinates Network*, 16437:1, 2014.

S. Jeong, R. **Sanchez-Ramirez**, A. J. Castro-Tirado, J. Gorosabel, M. Jelinek, J. C. Tello, P. Ferrero, O. Lara-Gil, R. Cunniffe, D. Perez-Ramirez, S. Guziy, J. M. Castro Ceron, A. Fernandez-Soto, J. Cepa, M. A. Rivero, and G. Gomez-Velarde. GRB 140304A: 10.4m GTC redshift z = 5.39. *GRB Coordinates Network*, 15922:1, 2014a.

S. Jeong, R. **Sanchez-Ramirez**, J. Gorosabel, and A. J. Castro-Tirado. GRB 140304A: 10.4m GTC refined redshift z = 5.283. *GRB Coordinates Network*, 15936:1, 2014b. 176

T. Kruehler, D. Xu, R. **Sanchez-Ramirez**, D. Malesani, J. Fynbo, and H. Flores. GRB130418A: VLT/X-shooter redshift confirmation. *GRB Coordinates Network*, 14390:1, 2013.

D. Malesani, A. de Ugarte Postigo, R. **Sanchez-Ramirez**, and J. P. U. Fynbo. GRB 120612A: optical observations. *GRB Coordinates Network*, 13363:1, 2012.

A. Moskvitin, R. Burenin, R. Uklein, V. Sokolov, R. **Sanchez-Ramirez**, J. Gorosabel, and A. J. Castro-Tirado. GRB 140629A: BTA redshift. *GRB Coordinates Network*, 16489:1, 2014.

A. d. U. Postigo, J. Gorosabel, C. C. Thoene, R. **Sanchez-Ramirez**, and D. Garcia-Alvarez. MLS121106:014420+082311: 10.4m GTC r-band observations. *The Astronomer's Telegram*, 4589:1, November 2012.

J. C. Tello, R. **Sanchez-Ramirez**, A. Sota, J. Gorosabel, and A. J. Castro-Tirado. GRB 100902A: 1.5m OSN i-band upper limits. *GRB Coordinates Network*, 11196:1, 2010.

J. C. Tello, R. Gimeno, J. Gorosabel, M. Jelinek, R. **Sanchez-Ramirez**, and A. J. Castro-Tirado. Swift trigger 535026: optical decay confirmation with IAC80 and BOOTES-2/TELMA. *GRB Coordinates Network*, 13835:1, 2012a.

J. C. Tello, R. **Sanchez-Ramirez**, J. Gorosabel, A. J. Castro-Tirado, P. Kubanek, W. Allen, P. Yock, and K.-Y. Lin. XRF 120118A: optical candidate. *GRB Coordinates Network*, 12851:1, 2012b.

J. C. Tello, R. **Sanchez-Ramirez**, J. Gorosabel, A. J. Castro-Tirado, M. A. Rivero, G. Gomez-Velarde, and A. Klotz. GRB 120326A: GTC redshift. *GRB Coordinates Network*, 13118:1, 2012c.

J. C. Tello, V. Casanova, J. Gorosabel, R. **Sanchez-Ramirez**, and M. Jelinek. GRB130612A OSN i-band observations. *GRB Coordinates Network*, 14881:1, 2013a.

J. C. Tello, M. Jelinek, J. Gorosabel, A. J. Castro-Tirado, and R. **Sanchez-Ramirez**. GRB130608A: BOOTES-2/TELMA upper limits. *GRB Coordinates Network*, 14829:1, 2013b.

J. C. Tello, R. **Sanchez-Ramirez**, J. Gorosabel, F. Aceituno, and A. Castro-Tirado. GRB130418A: OSN 1.5m fading afterglow detection. *GRB Coordinates Network*, 14385: 1, 2013c.

J. C. Tello, R. **Sanchez-Ramirez**, M. Jelinek, J. Gorosabel, W. Allen, P. Yock, P. Kubanek, and A. J. Castro-Tirado. GRB130315A BOOTES-3 optical limit. *GRB Coordinates Network*, 14312:1, 2013d.

J. C. Tello, R. **Sanchez-Ramirez**, M. Jelinek, J. Gorosabel, W. Allen, P. Yock, P. Kubanek, and A. J. Castro-Tirado. GRB130508A: BOOTES-3 optical limit. *GRB Coordinates Network*, 14609:1, 2013e.

R. **Sanchez-Ramirez**, J. C. Tello, A. Sota, J. Gorosabel, and A. J. Castro-Tirado. GRB 100901A: 1.5m OSN BVRI-band observations. *GRB Coordinates Network*, 11180:1, 2010.

R. **Sanchez-Ramirez**, J. Gorosabel, M. Cebrian, A. de Ugarte Postigo, P. Montanes, and A. R. Anton. GRB 111008A: IAC80 i-band observations. *GRB Coordinates Network*, 12432:1, 2011a.

R. **Sanchez-Ramirez**, N. Morales, J. Gorosabel, J. L. Ortiz, P. Kubanek, A. de Ugarte Postigo, and A. J. Castro-Tirado. GRB 110915A: 1.23m CAHA i-band observations. *GRB Coordinates Network*, 12342:1, 2011b.

R. **Sanchez-Ramirez**, A. de Ugarte Postigo, T. Kruehler, B. Milvang-Jensen, J. P. U. Fynbo, N. Tanvir, D. Malesani, S. Schulze, L. Kaper, and H. Flores. GRB 121201A: x-shooter redshift. *GRB Coordinates Network*, 14035:1, 2012a.

R. **Sanchez-Ramirez**, J. Gorosabel, A. J. Castro-Tirado, M. A. Rivero, and G. Gomez-Velarde. GRB 120327A: GTC redshift confirmation. *GRB Coordinates Network*, 13146: 1, 2012b.

R. **Sanchez-Ramirez**, J. Gorosabel, A. de Ugarte Postigo, and J. M. Gonzalez Perez. GRB 120907A: spectroscopy from OSIRIS/GTC. *GRB Coordinates Network*, 13723:1, 2012c.

R. **Sanchez-Ramirez**, D. Jimenez Mejias, J. C. Tello, A. de Ugarte Postigo, and J. Gorosabel. GRB 120116A: IAC80 i-band observations. *GRB Coordinates Network*, 12837:1, 2012d.

R. **Sanchez-Ramirez**, G. Leloudas, A. de Ugarte Postigo, C. C. Thoene, J. Gorosabel, D. Malesani, S. Schulze, J. P. U. Fynbo, N. R. Tanvir, J. Hjorth, and D. Xu. GRB 120422A: SN identification from GTC. *GRB Coordinates Network*, 13281:1, 2012e.

R. **Sanchez-Ramirez**, A. J. Castro-Tirado, J. Gorosabel, F. J. Aceituno, E. Sonbas, E. Gogus, T. Guver, H. Kirbiyik, and D. Garcia-Alvarez. GRB 130603B: optical follow-up and independent GTC redshift determination and afterglow spectrum. *GRB Coordinates Network*, 14747:1, 2013a.

R. **Sanchez-Ramirez**, J. Gorosabel, A. J. Castro-Tirado, J. Cepa, and G. Gomez-Velarde. GRB 130518A: 10.4m GTC/OSIRIS redshift. *GRB Coordinates Network*, 14685:1, 2013b.

R. **Sanchez-Ramirez**, A. J. Castro-Tirado, F. Hoyos, and J. Aceituno. GRB 150413A: redshift determination with the 2.2m CAHA. *GRB Coordinates Network*, 17697:1, 2015.

C. C. Thoene, J. Gorosabel, A. de Ugarte Postigo, R. **Sanchez-Ramirez**, T. Munoz-Darias, S. Guziy, and A. J. Castro-Tirado. GRB 110328A / Swift J164449.3+573451: optical spectroscopy from GTC. *GRB Coordinates Network*, 11834:1, March 2011.

C. C. Thoene, A. de Ugarte Postigo, J. Gorosabel, R. **Sanchez-Ramirez**, J. P. U. Fynbo, and G. Gomez Velarde. GRB 120811C: redshift from OSIRIS/GTC. *GRB Coordinates Network*, 13628:1, 2012.

References

M. Aaronson, J. H. Black, and C. F. McKee (1974). A Search for Molecular Hydrogen in Quasar Absorption Spectra. *Astrophysical Journal*, **191**, L53–.

B. P. Abbott, R. Abbott, T. D. Abbott, M. R. Abernathy, F. Acernese, K. Ackley, C. Adams, T. Adams, P. Addesso, R. X. Adhikari, et al. (2016a). Observation of Gravitational Waves from a Binary Black Hole Merger. *Physical Review Letters*, **116**, 061102.

B. P. Abbott, R. Abbott, T. D. Abbott, M. R. Abernathy, F. Acernese, K. Ackley, C. Adams, T. Adams, P. Addesso, R. X. Adhikari, et al. (2016b). Localization and broadband follow-up of the gravitational-wave transient GW150914. *arXiv.org*, arXiv:1602.08492.

T. Abel, G. L. Bryan, and M. L. Norman (2002). The Formation of the First Star in the Universe. *Science*, **295**, 93–98.

A. Achterberg, Y. A. Gallant, J. G. Kirk, and A. W. Guthmann (2001). Particle acceleration by ultrarelativistic shocks: theory and simulations. *Monthly Notices of the Royal Astronomical Society*, **328**, 393–408.

P. M. J. Afonso, D. A. Kann, A. Nicuesa Guelbenzu, T. Krühler, J. Elliott, and J. Greiner (2013). GRB 130606A: GROND detection of the Optical/NIR afterglow. *GRB Coordinates Network*, **1480**, 1.

H. Aihara, C. Allende Prieto, D. An, S. F. Anderson, É. Aubourg, E. Balbinot, T. C. Beers, A. A. Berlind, S. J. Bickerton, D. Bizyaev, et al. (2011). The Eighth Data Release of the Sloan Digital Sky Survey: First Data from SDSS-III. *The Astrophysical Journal Supplement Series*, **193**, 29.

L. Amati, F. Frontera, M. Tavani, J. J. M. in't Zand, L. A. Antonelli, E. Costa, M. Feroci, C. Guidorzi, J. Heise, N. Masetti, et al. (2002).

Intrinsic spectra and energetics of BeppoSAX Gamma-Ray Bursts with known redshifts. *Astronomy and Astrophysics*, **390**, 81–89.

M. Arabsalmani, P. Møller, J. P. U. Fynbo, L. Christensen, W. Freudling, S. Savaglio, and T. Zafar (2015). On the mass-metallicity relation, velocity dispersion, and gravitational well depth of GRB host galaxies. *Monthly Notices of the Royal Astronomical Society*, **446**, 990–999.

M. Asplund, N. Grevesse, A. J. Sauval, and P. Scott (2009). The Chemical Composition of the Sun. *Annual Review of Astronomy and Astrophysics*, **47**, 481–522.

D. Band, J. Matteson, L. Ford, B. Schaefer, D. Palmer, B. Teegarden, T. Cline, M. S. Briggs, W. Paciesas, G. N. Pendleton, et al. (1993). BATSE observations of gamma-ray burst spectra. I - Spectral diversity. *The Astrophysical Journal*, **413**, 281–292.

R. Barkana and A. Loeb (2001). In the beginning: the first sources of light and the reionization of the universe. *Physics Reports*, **349**, 125–238.

S. D. Barthelmy, L. M. Barbier, J. R. Cummings, E. E. Fenimore, N. Gehrels, D. Hullinger, H. A. Krimm, C. B. Markwardt, D. M. Palmer, A. Parsons, et al. (2005). The Burst Alert Telescope (BAT) on the SWIFT Midex Mission. *Space Science Reviews*, **120**, 143–164.

S. D. Barthelmy, W. H. Baumgartner, J. R. Cummings, E. E. Fenimore, N. Gehrels, H. A. Krimm, A. Y. Lien, C. B. Markwardt, D. M. Palmer, T. Sakamoto, et al. (2013). GRB 130606A, Swift-BAT refined analysis. *GRB Coordinates Network*, **1481**, 1.

W. A. Baum (1962). Photoelectric Magnitudes and Red-Shifts. *Problems of Extra-Galactic Research*, **15**, 390–.

G. Bazin, V. Ruhlmann-Kleider, N. Palanque-Delabrouille, J. Rich, É. Aubourg, P. Astier, C. Balland, S. Basa, R. G. Carlberg, A. Conley, et al. (2011). Photometric selection of Type Ia supernovae in the Supernova Legacy Survey. *Astronomy and Astrophysics*, **534**, A43.

E. A. Beaver, E. M. Burbidge, C. E. McIlwain, H. W. Epps, and P. A. Strittmatter (1972). Digicon Spectrophotometry of the Quasi-Stellar Object PHL 957. *The Astrophysical Journal*, **178**, 95–104.

G. D. Becker, J. S. Bolton, and A. Lidz (2015a). Reionisation and High-Redshift Galaxies: The View from Quasar Absorption Lines. *Publications of the Astronomical Society of Australia*, **32**, e045.

G. D. Becker, J. S. Bolton, P. Madau, M. Pettini, E. V. Ryan-Weber, and B. P. Venemans (2015b). Evidence of patchy hydrogen reionization from an extreme Lyα trough below redshift six. *Monthly Notices of the Royal Astronomical Society*, **447**, 3402–3419.

R. H. Becker, X. Fan, R. L. White, M. A. Strauss, V. K. Narayanan, R. H. Lupton, J. E. Gunn, J. Annis, N. A. Bahcall, J. Brinkmann, et al. (2001). Evidence for Reionization at z˜6: Detection of a Gunn-Peterson Trough in a z=6.28 Quasar. *The Astronomical Journal*, **122**, 2850–2857.

S. V. W. Beckwith, M. Stiavelli, A. M. Koekemoer, J. A. R. Caldwell, H. C. Ferguson, R. Hook, R. A. Lucas, L. E. Bergeron, M. Corbin, S. Jogee, et al. (2006). The Hubble Ultra Deep Field. *The Astronomical Journal*, **132**, 1729–1755.

K. Belczynski, T. Bulik, A. Heger, and C. Fryer (2007). The Lack of Gamma-Ray Bursts from Population III Binaries. *The Astrophysical Journal*, **664**, 986–999.

T. A. M. Berg, S. L. Ellison, J. X. Prochaska, K. A. Venn, and M. Dessauges-Zavadsky (2015a). The chemistry of the most metal-rich damped Lyman α systems at z ˜ 2 - II. Context with the Local Group. *Monthly Notices of the Royal Astronomical Society*, **452**, 4326–4346.

T. A. M. Berg, M. Neeleman, J. X. Prochaska, S. L. Ellison, and A. M. Wolfe (2015b). The Most Metal-rich Damped Lyα Systems at z gsim 1.5 I: The Data. *The Publications of the Astronomical Society of the Pacific*, **127**, 167–210.

E. Berger, P. A. Price, S. B. Cenko, A. Gal-Yam, A. M. Soderberg, M. Kasliwal, D. C. Leonard, P. B. Cameron, D. A. Frail, S. R. Kulkarni, et al. (2005). The afterglow and elliptical host galaxy of the short γ-ray burst GRB 050724. *Nature*, **438**, 988–990.

M. G. Bernardini, G. Ghirlanda, S. Campana, S. Covino, R. Salvaterra, J. L. Atteia, D. Burlon, G. Calderone, P. D'Avanzo, V. D'Elia, et al. (2015). Comparing the spectral lag of short and long gamma-ray bursts and its relation with the luminosity. *Monthly Notices of the Royal Astronomical Society*, **446**, 1129–1138.

E. Bertin and S. Arnouts (1996). SExtractor: Software for source extraction. *Astronomy and Astrophysics Supplement*, **117**, 393–404.

S. Bird, M. Haehnelt, M. Neeleman, S. Genel, M. Vogelsberger, and L. Hernquist (2015). Reproducing the kinematics of damped Lyman α systems. *Monthly Notices of the Royal Astronomical Society*, **447**, 1834–1846.

A. W. Blain, D. T. Frayer, J. J. Bock, and N. Z. Scoville (2000). Millimetre/submillimetre-wave emission-line searches for high-redshift galaxies. *Monthly Notices of the Royal Astronomical Society*, **313**, 559–570.

J. S. Bloom, S. R. Kulkarni, S. G. Djorgovski, A. C. Eichelberger, P. Côté, J. P. Blakeslee, S. C. Odewahn, F. A. Harrison, D. A. Frail, A. V. Filippenko, et al. (1999). The unusual afterglow of the γ-ray burst of 26 March 1998 as evidence for a supernova connection. *Nature*, **401**, 453–456.

M. Boër, J. L. Atteia, Y. Damerdji, B. Gendre, A. Klotz, and G. Stratta (2006). Detection of a Very Bright Optical Flare from the Gamma-Ray Burst GRB 050904 at Redshift 6.29. *The Astrophysical Journal*, **638**, L71–L74.

J. S. Bolton, M. Haehnelt, S. J. Warren, P. C. Hewett, D. J. Mortlock, B. P. Venemans, R. G. McMahon, and C. Simpson (2011). How neutral is the intergalactic medium surrounding the redshift z = 7.085 quasar ULAS J1120+0641? *Monthly Notices of the Royal Astronomical Society*, **416**, L70–L74.

R. Bouwens, G. D. Illingworth, I. Labbé, P. A. Oesch, M. Trenti, C. M. Carollo, P. G. van Dokkum, M. Franx, M. Stiavelli, V. González, et al. (2011). A candidate redshift z˜10 galaxy and rapid changes in that population at an age of 500Myr. *Nature*, **469**, 504–507.

R. Bouwens, L. Bradley, A. Zitrin, D. Coe, M. Franx, W. Zheng, R. Smit, O. Host, M. Postman, L. Moustakas, et al. (2014). A Census of Star-forming Galaxies in the Z ˜ 9-10 Universe based on HST+Spitzer Observations over 19 Clash Clusters: Three Candidate Z ˜ 9-10 Galaxies and Improved Constraints on the Star Formation Rate Density at Z ˜ 9.2. *The Astrophysical Journal*, **795**, 126.

R. A. A. Bowler, J. S. Dunlop, R. J. McLure, H. J. McCracken, B. Milvang-Jensen, H. Furusawa, J. P. U. Fynbo, O. Le Fèvre, J. Holt, Y. Ideue, et al. (2012). Discovery of bright z $\simeq$ 7 galaxies in the UltraVISTA survey. *Monthly Notices of the Royal Astronomical Society*, **426**, 2772–2788.

B. J. Boyle, T. Shanks, S. M. Croom, R. J. Smith, L. Miller, N. Loaring, and C. Heymans (2000). The 2dF QSO Redshift Survey - I. The optical luminosity function of quasi-stellar objects. *Monthly Notices of the Royal Astronomical Society*, **317**, 1014–1022.

R. Braun (2012). Cosmological Evolution of Atomic Gas and Implications for 21 cm H I Absorption. *The Astrophysical Journal*, **749**, 87.

A. A. Breeveld, W. Landsman, S. T. Holland, P. Roming, N. P. M. Kuin, and M. J. Page (2011). An Updated Ultraviolet Calibration for the Swift/UVOT. In *GAMMA RAY BURSTS 2010. AIP Conference Proceedings*, 373–376, Mullard Space Science Laboratory, University College London, Holmbury St. Mary, Dorking, Surrey RH5 6NT, UK, AIP.

O. Bromberg, E. Nakar, and T. Piran (2011). Are Low-luminosity Gamma-Ray Bursts Generated by Relativistic Jets? *The Astrophysical Journal*, **739**, L55.

V. Bromm (2013). Formation of the first stars. *Reports on Progress in Physics*, **76**, 112901.

V. Bromm and R. B. Larson (2004). The First Stars. *Annual Review of Astronomy and Astrophysics*, **42**, 79–118.

V. Bromm and A. Loeb (2003). The formation of the first low-mass stars from gas with low carbon and oxygen abundances. *Nature*, **425**, 812–814.

V. Bromm and A. Loeb (2006). High-Redshift Gamma-Ray Bursts from Population III Progenitors. *The Astrophysical Journal*, **642**, 382–388.

V. Bromm and N. Yoshida (2011). The First Galaxies. *Annual Review of Astronomy and Astrophysics*, **49**, 373–407.

V. Bromm, P. S. Coppi, and R. B. Larson (2002). The Formation of the First Stars. I. The Primordial Star-forming Cloud. *The Astrophysical Journal*, **564**, 23–51.

V. Bromm, N. Yoshida, L. Hernquist, and C. F. McKee (2009). The formation of the first stars and galaxies. *Nature*, **459**, 49–54.

E. M. Burbidge, C. R. Lynds, and G. R. Burbidge (1966). On the Measurement and Interpretation of Absorption Features in the Spectrum of the Quasi-Stellar Object 3c 191. *The Astrophysical Journal*, **144**, 447.

D. N. Burrows, J. E. Hill, J. A. Nousek, J. A. Kennea, A. A. Wells, J. P. Osborne, A. F. Abbey, A. P. Beardmore, K. Mukerjee, A. D. T. Short, et al. (2005). The Swift X-Ray Telescope. *Space Science Reviews*, **120**, 165–195.

N. R. Butler, A. M. Watson, A. Kutyrev, W. H. Lee, M. G. Richer, C. Klein, O. Fox, J. X. Prochaska, J. S. Bloom, A. Cucchiara, et al. (2013a). GRB 130606B: RATIR optical and NIR observations. *GRB Coordinates Network*, **1482**, 1.

N. R. Butler, A. M. Watson, A. Kutyrev, W. H. Lee, M. G. Richer, C. Klein, O. Fox, J. X. Prochaska, J. S. Bloom, A. Cucchiara, et al. (2013b). GRB 130606A: continued RATIR optical and NIR monitoring. *GRB Coordinates Network*, **1482**, 1.

S. Campana, R. Salvaterra, A. Ferrara, and A. Pallottini (2015). Missing cosmic metals revealed by X-ray absorption towards distant sources. *Astronomy and Astrophysics*, **575**, A43.

M. A. Campisi, U. Maio, R. Salvaterra, and B. Ciardi (2011). Population III stars and the long gamma-ray burst rate. *Monthly Notices of the Royal Astronomical Society*, **416**, 2760–2767.

Z. Cano, D. Bersier, C. Guidorzi, R. Margutti, K. M. Svensson, S. Kobayashi, A. Melandri, K. Wiersema, A. Pozanenko, A. J. van der Horst, et al. (2011). A tale of two GRB-SNe at a common redshift of z=0.54. *Monthly Notices of the Royal Astronomical Society*, **413**, 669–685.

Z. Cano, S.-Q. Wang, Z.-G. Dai, and X.-F. Wu (2016). The Observer's Guide to the Gamma-Ray Burst-Supernova Connection. *arXiv.org*, arXiv:1604.03549.

J. A. Cardelli, G. C. Clayton, and J. S. Mathis (1989). The relationship between infrared, optical, and ultraviolet extinction. *The Astrophysical Journal*, **345**, 245–256.

C. L. Carilli, R. Wang, X. Fan, F. Walter, J. Kurk, D. Riechers, J. Wagg, J. Hennawi, L. Jiang, K. M. Menten, et al. (2010). Ionization Near Zones Associated with Quasars at z ˜ 6. *The Astrophysical Journal*, **714**, 834–839.

R. W. Carlson (1974). Molecular-Hydrogen Absorption Features in the Spectrum of Quasi-Stellar Object 4c 05.34. *Astrophysical Journal*, **190**, L99–.

C. M. Casey, N. Z. Scoville, D. B. Sanders, N. Lee, A. Cooray, S. L. Finkelstein, P. Capak, A. Conley, G. de Zotti, D. Farrah, et al. (2014). Are Dusty Galaxies Blue? Insights on UV Attenuation from Dust-selected Galaxies. *The Astrophysical Journal*, **796**, 95.

A. J. Castro-Tirado and J. Gorosabel (1999). Optical observations of GRB afterglows: GRB 970508 and GRB 980326 revisited. *Astronomy and Astrophysics Supplement*, **138**, 449–450.

A. J. Castro-Tirado, J. Gorosabel, J. Heidt, T. Seitz, E. Thommes, C. Wolf, N. Lund, H. Pedersen, E. Costa, F. Frontera, et al. (1997). GRB 970111 and GRB 970228. *Circulars of the International Astronomical Union*, **6598**, 2.

A. J. Castro-Tirado, J. Gorosabel, N. Benitez, C. Wolf, R. Fockenbrock, E. Martinez-Gonzalez, H. Kristen, A. Broeils, H. Pedersen, J. Greiner, et al. (1998). Photometry and Spectroscopy of the GRB 970508 Optical Counterpart. *Science*, **279**, 1011–.

A. J. Castro-Tirado, M. R. Zapatero-Osorio, N. Caon, L. M. Cairos, J. Hjorth, H. Pedersen, M. I. Andersen, J. Gorosabel, C. Bartolini, A. Guarnieri, et al. (1999). Decay of the GRB 990123 Optical Afterglow: Implications for the Fireball Model. *Science*, **283**, 2069–.

A. J. Castro-Tirado, V. V. Sokolov, J. Gorosabel, J. M. Castro Cerón, J. Greiner, R. A. M. J. Wijers, B. L. Jensen, J. Hjorth, S. Toft, H. Pedersen, et al. (2001). The extraordinarily bright optical afterglow of GRB 991208 and its host galaxy. *Astronomy and Astrophysics*, **370**, 398–406.

A. J. Castro-Tirado, P. Møller, G. García-Segura, J. Gorosabel, E. Pérez, E. Solano, D. Barrado, C. Kouveliotou, H. Pedersen, E. Pian, et al. (2010). GRB 021004: Tomography of a gamma-ray burst progenitor and its host galaxy. *Astronomy and Astrophysics*, **517**, A61.

A. J. Castro-Tirado, R. Sánchez-Ramírez, S. L. Ellison, M. Jelínek, A. Martín-Carrillo, V. Bromm, J. Gorosabel, M. Bremer, J. M. Winters, L. Hanlon, et al. (2013a). GRB 130606A within a sub-DLA at redshift 5.91. *arXiv.org*, 5631.

A. J. Castro-Tirado, R. Sánchez-Ramírez, J. Gorosabel, M. Jelínek, J. C. Tello, P. Ferrero, O. Lara-Gil, R. Cunniffe, D. Pérez-Ramírez, P. Kubánek, et al. (2013b). GRB 130606A: 10.4m GTC refined redshift z = 5.91. *GRB Coordinates Network*, **1479**, 1. 189

A. J. Castro-Tirado, R. Sánchez-Ramírez, M. Jelínek, J. Gorosabel, J. C. Tello, P. Ferrero, O. Lara-Gil, R. Cunniffe, D. Pérez-Ramírez,

P. Kubánek, et al. (2013c). GRB 130606A: 10.4m GTC spectroscopy indicates z = 6.1. *GRB Coordinates Network*, **1479**, 1. 189

B. Catinella and L. Cortese (2015). HIGHz: a survey of the most H I-massive galaxies at z ˜ 0.2. *Monthly Notices of the Royal Astronomical Society*, **446**, 3526–3544.

G. Cavallo and M. J. Rees (1978). A qualitative study of cosmic fireballs and gamma-ray bursts. *Monthly Notices of the Royal Astronomical Society*, **183**, 359–365.

R. Cen, J. Miralda-Escudé, J. P. Ostriker, and M. Rauch (1994). Gravitational collapse of small-scale structure as the origin of the Lyman-alpha forest. *The Astrophysical Journal*, **437**, L9–L12.

J. Cepa, M. Aguiar, V. G. Escalera, I. Gonzalez-Serrano, E. Joven-Alvarez, L. Peraza, J. L. Rasilla, L. F. Rodriguez-Ramos, J. J. Gonzalez, F. J. Cobos Duenas, et al. (2000). OSIRIS tunable imager and spectrograph. *Proc. SPIE Vol. 4008*, **4008**, 623–631.

P. Chandra and D. A. Frail (2012). A Radio-selected Sample of Gamma-Ray Burst Afterglows. *The Astrophysical Journal*, **746**, 156.

H.-W. Chen, J. X. Prochaska, and N. Y. Gnedin (2007). A New Constraint on the Escape Fraction in Distant Galaxies Using γ-Ray Burst Afterglow Spectroscopy. *The Astrophysical Journal*, **667**, L125–L128.

R. A. Chevalier and Z.-Y. Li (1999). Gamma-Ray Burst Environments and Progenitors. *The Astrophysical Journal*, **520**, L29–L32.

R. A. Chevalier and Z.-Y. Li (2000). Wind Interaction Models for Gamma-Ray Burst Afterglows: The Case for Two Types of Progenitors. *The Astrophysical Journal*, **536**, 195–212.

R. Chornock, E. Berger, D. B. Fox, R. Lunnan, M. R. Drout, W.-f. Fong, T. Laskar, and K. C. Roth (2013). GRB 130606A as a Probe of the Intergalactic Medium and the Interstellar Medium in a Star-forming Galaxy in the First Gyr after the Big Bang. *The Astrophysical Journal*, **774**, 26.

R. Chornock, E. Berger, D. B. Fox, W. Fong, T. Laskar, and K. C. Roth (2014). GRB 140515A at z=6.33: Constraints on the End of Reionization From a Gamma-ray Burst in a Low Hydrogen Column Density Environment. *arXiv.org*, 7400.

L. Christensen, J. P. U. Fynbo, J. X. Prochaska, C. C. Thöne, A. de Ugarte Postigo, and P. Jakobsson (2011). A High Signal-to-noise Ratio Composite Spectrum of Gamma-ray Burst Afterglows. *The Astrophysical Journal*, **727**, 73.

L. Christensen, P. Møller, J. P. U. Fynbo, and T. Zafar (2014). Verifying the mass-metallicity relation in damped Lyman α selected galaxies at 0.1 ¡ z ¡ 3.2. *Monthly Notices of the Royal Astronomical Society*, **445**, 225–238.

B. Ciardi and A. Loeb (2000). Expected Number and Flux Distribution of Gamma-Ray Burst Afterglows with High Redshifts. *The Astrophysical Journal*, **540**, 687–696.

B. Ciardi, S. Inoue, F. B. Abdalla, K. Asad, G. Bernardi, J. S. Bolton, M. Brentjens, A. G. de Bruyn, E. Chapman, S. Daiboo, et al. (2015). Simulating the 21 cm forest detectable with LOFAR and SKA in the spectra of high-z GRBs. *Monthly Notices of the Royal Astronomical Society*, **453**, 101–105.

T. L. Cline, U. D. Desai, B. J. Teegarden, W. D. Evans, R. W. Klebesadel, J. G. Laros, C. Barat, K. Hurley, M. Niel, and M. C. Weisskopf (1982). Precise source location of the anomalous 1979 March 5 gamma-ray transient. *The Astrophysical Journal*, **255**, L45–L48.

D. Coe, A. Zitrin, M. Carrasco, X. Shu, W. Zheng, M. Postman, L. Bradley, A. Koekemoer, R. Bouwens, T. Broadhurst, et al. (2013). CLASH: Three Strongly Lensed Images of a Candidate z $\approx$ 11 Galaxy. *The Astrophysical Journal*, **762**, 32.

R. J. Cooke, M. Pettini, C. C. Steidel, G. C. Rudie, and R. A. Jorgenson (2011a). A carbon-enhanced metal-poor damped Lyα system: probing gas from Population III nucleosynthesis? *Monthly Notices of the Royal Astronomical Society*, **412**, 1047–1058.

R. J. Cooke, M. Pettini, C. C. Steidel, G. C. Rudie, and P. E. Nissen (2011b). The most metal-poor damped Lyα systems: insights into chemical evolution in the very metal-poor regime. *Monthly Notices of the Royal Astronomical Society*, **417**, 1534–1558.

S. Covino, E. Rossi, D. Lazzati, D. Malesani, and G. Ghisellini (2005). Gamma-Ray Bursts and Afterglow Polarisation. *INTERACTING BINARIES: Accretion*, **797**, 144–149.

S. Covino, A. Melandri, R. Salvaterra, S. Campana, S. D. Vergani, M. G. Bernardini, P. D'Avanzo, V. D'Elia, D. Fugazza, G. Ghirlanda, et al. (2013). Dust extinctions for an unbiased sample of gamma-ray burst afterglows. *Monthly Notices of the Royal Astronomical Society*, **432**, 1231–1244.

N. H. M. Crighton, M. T. Murphy, J. X. Prochaska, G. Worseck, M. Rafelski, G. D. Becker, S. L. Ellison, M. Fumagalli, S. Lopez, A. Meiksin, et al. (2015). The neutral hydrogen cosmological mass density at z = 5. *Monthly Notices of the Royal Astronomical Society*, **452**, 217–234.

P. A. Crowther (2007). Physical Properties of Wolf-Rayet Stars. *Annual Review of Astronomy and Astrophysics*, **45**, 177–219.

A. Cucchiara, A. J. Levan, D. B. Fox, N. R. Tanvir, T. N. Ukwatta, E. Berger, T. Krühler, A. Küpcü Yoldaş, X. F. Wu, K. Toma, et al. (2011). A Photometric Redshift of z ˜ 9.4 for GRB 090429B. *The Astrophysical Journal*, **736**, 7.

A. Cucchiara, M. Fumagalli, M. Rafelski, D. Kocevski, J. X. Prochaska, R. J. Cooke, and G. D. Becker (2015). Unveiling the Secrets of Metallicity and Massive Star Formation Using DLAs along Gamma-Ray Bursts. *The Astrophysical Journal*, **804**, 51.

F. Daigne and R. Mochkovitch (1998). Gamma-ray bursts from internal shocks in a relativistic wind: temporal and spectral properties. *Monthly Notices of the Royal Astronomical Society*, **296**, 275–286.

R. Davé, N. Katz, B. D. Oppenheimer, J. A. Kollmeier, and D. H. Weinberg (2013). The neutral hydrogen content of galaxies in cosmological hydrodynamic simulations. *Monthly Notices of the Royal Astronomical Society*, **434**, 2645–2663.

A. De Cia, C. Ledoux, A. J. Fox, A. Smette, P. Petitjean, and G. Björnsson (2012). Rapid-response mode VLT/UVES spectroscopy of super iron-rich gas exposed to GRB 080310. Evidence of ionization in action and episodic star formation in the host. *Astronomy and Astrophysics*, **545**, A64.

A. De Cia, C. Ledoux, S. Savaglio, P. Schady, and P. M. Vreeswijk (2013). Dust-to-metal ratios in damped Lyman-α absorbers. Fresh clues to the origins of dust and optical extinction towards γ-ray bursts. *Astronomy and Astrophysics*, **560**, A88.

G. De Rosa, R. Decarli, F. Walter, X. Fan, L. Jiang, J. Kurk, A. Pasquali, and H. W. Rix (2011). Evidence for Non-evolving Fe II/Mg II Ratios in Rapidly Accreting z ˜ 6 QSOs. *The Astrophysical Journal*, **739**, 56.

R. S. de Souza, B. Ciardi, U. Maio, and A. Ferrara (2013a). Dark matter halo environment for primordial star formation. *Monthly Notices of the Royal Astronomical Society*, **428**, 2109–2117.

R. S. de Souza, E. E. O. Ishida, J. L. Johnson, D. J. Whalen, and A. Mesinger (2013b). Detectability of the first cosmic explosions. *Monthly Notices of the Royal Astronomical Society*, **436**, 1555–1563.

A. de Ugarte Postigo, A. J. Castro-Tirado, S. Guziy, J. Gorosabel, G. Jóhannesson, M. A. Aloy, S. McBreen, D. Q. Lamb, N. Benitez, M. Jelínek, et al. (2006). GRB 060121: Implications of a Short-/Intermediate-Duration γ-Ray Burst at High Redshift. *The Astrophysical Journal*, **648**, L83–L87.

A. de Ugarte Postigo, T. A. Fatkhullin, G. Jóhannesson, J. Gorosabel, V. V. Sokolov, A. J. Castro-Tirado, Y. Y. Balega, O. I. Spiridonova, M. Jelínek, S. Guziy, et al. (2007). Extensive multiband study of the X-ray rich GRB 050408. A likely off-axis event with an intense energy injection. *Astronomy and Astrophysics*, **462**, L57–L60.

A. de Ugarte Postigo, I. Horváth, P. Veres, Z. Bagoly, D. A. Kann, C. C. Thöne, L. G. Balazs, P. D'Avanzo, M. A. Aloy, S. Foley, et al. (2011a). Searching for differences in Swift's intermediate GRBs. *Astronomy and Astrophysics*, **525**, A109.

A. de Ugarte Postigo, A. Lundgren, F. Mac-Auliffe, F. M. Montenegro, D. Garcia-Appadoo, I. de Gregorio Monsalvo, S. Martín, C. de Breuk, P. Bergman, M. Hajigholi, et al. (2011b). GRB 110715A: APEX detection of the submm counterpart. *GRB Coordinates Network*, **1216**, 1.

A. de Ugarte Postigo, J. P. U. Fynbo, C. C. Thöne, L. Christensen, J. Gorosabel, B. Milvang-Jensen, S. Schulze, P. Jakobsson, K. Wiersema, R. Sánchez-Ramírez, et al. (2012a). The distribution of equivalent widths in long GRB afterglow spectra. *Astronomy and Astrophysics*, **548**, A11. 130, 131, 178, 180, 184, 185, 212, 215, 276, 278

A. de Ugarte Postigo, A. Lundgren, S. Martín, D. Garcia-Appadoo, I. de Gregorio Monsalvo, A. Peck, M. J. Michałowski, C. C. Thöne,

S. Campana, J. Gorosabel, et al. (2012b). Pre-ALMA observations of GRBs in the mm/submm range. *Astronomy and Astrophysics*, **538**, A44. 120, 124, 125, 128, 130

A. de Ugarte Postigo, J. Gorosabel, C. C. Thöne, A. Cabrera-Lavers, D. Reverte, and C. Álvarez-Iglesias (2014). GRB 140515A: Spectroscopy from the 10.4m GTC. *GRB Coordinates Network*, **1627**.

J. Delhaize, M. Meyer, L. Staveley-Smith, and B. J. Boyle (2013). Detection of H I in distant galaxies using spectral stacking. *Monthly Notices of the Royal Astronomical Society*, **433**, 1398–1410.

V. D'Elia, J. P. U. Fynbo, P. Goldoni, S. Covino, A. de Ugarte Postigo, C. Ledoux, F. Calura, J. Gorosabel, D. Malesani, F. Matteucci, et al. (2014). VLT/X-shooter spectroscopy of the GRB 120327A afterglow. *Astronomy and Astrophysics*, **564**, A38. 51, 120

V. D'Odorico, S. Cristiani, D. Romano, G. L. Granato, and L. Danese (2004). Chemical abundances in QSO host galaxies and environments from narrow absorption line systems. *Monthly Notices of the Royal Astronomical Society*, **351**, 976–988.

B. T. Draine and L. Hao (2002). Gamma-Ray Burst in a Molecular Cloud: Destruction of Dust and H2 and the Emergent Spectrum. *The Astrophysical Journal*, **569**, 780–791.

R. C. Duncan and C. Thompson (1992). Formation of very strongly magnetized neutron stars - Implications for gamma-ray bursts. *The Astrophysical Journal*, **392**, L9–L13.

J. Dunkley, D. N. Spergel, E. Komatsu, G. Hinshaw, D. Larson, M. R. Nolta, N. Odegard, L. Page, C. L. Bennett, B. Gold, et al. (2009). Five-Year Wilkinson Microwave Anisotropy Probe (WMAP) Observations: Bayesian Estimation of Cosmic Microwave Background Polarization Maps. *The Astrophysical Journal*, **701**, 1804–1813.

B. Efron (1987). Better Bootstrap Confidence Intervals. *Journal of the American Statistical Association*, **82**, 171–185.

B. Efron and V. Petrosian (1992). A simple test of independence for truncated data with applications to redshift surveys. *The Astrophysical Journal*, **399**, 345–352.

J. Elliott, S. Khochfar, J. Greiner, and C. Dalla Vecchia (2015). The First Billion Years project: gamma-ray bursts at z ¿ 5. *Monthly Notices of the Royal Astronomical Society*, **446**, 4239–4249.

R. S. Ellis, M. Colless, T. Broadhurst, J. Heyl, and K. Glazebrook (1996). Autofib Redshift Survey - I. Evolution of the galaxy luminosity function. *Monthly Notices of the Royal Astronomical Society*, **280**, 235–251.

S. L. Ellison and S. Lopez (2001). Unusual metal abundances in a pair of damped Lyman alpha systems at z ˜ 2. *Astronomy and Astrophysics*, **380**, 117–122.

S. L. Ellison, L. Yan, I. M. Hook, M. Pettini, J. V. Wall, and P. Shaver (2001). The CORALS survey I: New estimates of the number density and gas content of damped Lyman alpha systems free from dust bias. *Astronomy and Astrophysics*, **379**, 393–406.

S. L. Ellison, L. Yan, I. M. Hook, M. Pettini, J. V. Wall, and P. Shaver (2002). The CORALS survey. II. Clues to galaxy clustering around QSOs from zabs ˜ zem damped Lyman alpha systems. *Astronomy and Astrophysics*, **383**, 91–97.

S. L. Ellison, J. X. Prochaska, J. F. Hennawi, S. Lopez, C. Usher, A. M. Wolfe, D. M. Russell, and C. R. Benn (2010). The nature of proximate damped Lyman α systems. *Monthly Notices of the Royal Astronomical Society*, **406**, 1435–1459.

S. L. Ellison, J. X. Prochaska, and J. T. Mendel (2011). Metallicities and dust content of proximate damped Lyman α systems in the Sloan Digital Sky Survey. *Monthly Notices of the Royal Astronomical Society*, **412**, 448–468.

P. A. Evans, R. Willingale, J. P. Osborne, P. T. O'Brien, K. L. Page, C. B. Markwardt, S. D. Barthelmy, A. P. Beardmore, D. N. Burrows, C. Pagani, et al. (2010). The Swift Burst Analyser. I. BAT and XRT spectral and flux evolution of gamma ray bursts. *Astronomy and Astrophysics*, **519**, A102.

P. A. Evans, M. R. Goad, J. P. Osborne, and A. P. Beardmore (2011). GRB 110715A: enhanced Swift-XRT position. *GRB Coordinates Network*, **1216**.

H. I. Ewen and E. M. Purcell (1951). Observation of a Line in the Galactic Radio Spectrum: Radiation from Galactic Hydrogen at 1,420 Mc./sec. *Nature*, **168**, 356–.

D. Fabbian, P. E. Nissen, M. Asplund, M. Pettini, and C. Akerman (2009). The C/O ratio at low metallicity: constraints on early chemical evolution from observations of Galactic halo stars. *Astronomy and Astrophysics*, **500**, 1143–1155.

X. Fan (2012). Observations of the first light and the epoch of reionization. *Research in Astronomy and Astrophysics*, **12**, 865–890.

X. Fan, J. F. Hennawi, G. T. Richards, M. A. Strauss, D. P. Schneider, J. L. Donley, J. E. Young, J. Annis, H. Lin, H. Lampeitl, et al. (2004). A Survey of z¿5.7 Quasars in the Sloan Digital Sky Survey. III. Discovery of Five Additional Quasars. *The Astronomical Journal*, **128**, 515–522.

X. Fan, M. A. Strauss, R. H. Becker, R. L. White, J. E. Gunn, G. R. Knapp, G. T. Richards, D. P. Schneider, J. Brinkmann, and M. Fukugita (2006). Constraining the Evolution of the Ionizing Background and the Epoch of Reionization with z˜6 Quasars. II. A Sample of 19 Quasars. *The Astronomical Journal*, **132**, 117–136.

E. E. Fenimore, J. P. Conner, R. I. Epstein, R. W. Klebesadel, J. G. Laros, A. Yoshida, M. Fujii, K. Hayashida, M. Itoh, T. Murakami, et al. (1988). Interpretations of multiple absorption features in a gamma-ray burst spectrum. *The Astrophysical Journal*, **335**, L71–L74.

X. Fernández, J. H. van Gorkom, K. M. Hess, D. J. Pisano, K. Kreckel, E. Momjian, A. Popping, T. Oosterloo, L. Chomiuk, M. A. W. Verheijen, et al. (2013). A Pilot for a Very Large Array H I Deep Field. *The Astrophysical Journal*, **770**, L29.

F. Feroz, M. P. Hobson, and M. Bridges (2009). MULTINEST: an efficient and robust Bayesian inference tool for cosmology and particle physics. *Monthly Notices of the Royal Astronomical Society*, **398**, 1601–1614.

R. Filgas, T. Krühler, J. Greiner, A. Rau, E. Palazzi, S. Klose, P. Schady, A. Rossi, P. M. J. Afonso, L. A. Antonelli, et al. (2011). The two-component jet of GRB 080413B. *Astronomy and Astrophysics*, **526**, A113.

G. J. Fishman (1981). The NASA/Marshall Space Flight Center program in gamma-ray burst astronomy. *Symposium on Cosmic Gamma-Ray Bursts*, **75**, 125–133.

G. J. Fishman and C. A. Meegan (1995). Gamma-Ray Bursts. *Annual Review of Astronomy and Astrophysics*, **33**, 415–458.

E. L. Fitzpatrick and D. Massa (2007). An Analysis of the Shapes of Interstellar Extinction Curves. V. The IR-through-UV Curve Morphology. *The Astrophysical Journal*, **663**, 320–341.

C. B. Foltz, F. H. J. Chaffee, and J. H. Black (1988). Molecules at early epochs. IV - Confirmation of the detection of H2 toward PKS 0528 - 250. *Astrophysical Journal*, **324**, 267–278.

A. J. Fox, C. Ledoux, P. Petitjean, and R. Srianand (2007a). C IV absorption in damped and sub-damped Lyman-α systems. Correlations with metallicity and implications for galactic winds at z $\approx$ 2-3. *Astronomy and Astrophysics*, **473**, 791–803.

A. J. Fox, P. Petitjean, C. Ledoux, and R. Srianand (2007b). Hot halos around high redshift protogalaxies. Observations of O VI and N V absorption in damped Lyman-α systems. *Astronomy and Astrophysics*, **465**, 171–184.

A. J. Fox, C. Ledoux, P. M. Vreeswijk, A. Smette, and A. O. Jaunsen (2008). High-ion absorption in seven GRB host galaxies at z = 2-4. Evidence for both circumburst plasma and outflowing interstellar gas. *Astronomy and Astrophysics*, **491**, 189–207.

D. A. Frail, S. R. Kulkarni, L. Nicastro, M. Feroci, and G. B. Taylor (1997). The radio afterglow from the γ-ray burst of 8 May 1997. *Nature*, **389**, 261–263.

D. A. Frail, E. Berger, T. J. Galama, S. R. Kulkarni, G. H. Moriarty-Schieven, G. G. Pooley, R. Sari, D. S. Shepherd, G. B. Taylor, and F. Walter (2000). The Enigmatic Radio Afterglow of GRB 991216. *The Astrophysical Journal*, **538**, L129–L132.

M. Friis, A. De Cia, T. Krühler, J. P. U. Fynbo, C. Ledoux, P. M. Vreeswijk, D. J. Watson, D. Malesani, J. Gorosabel, R. L. C. Starling, et al. (2015). The warm, the excited, and the molecular gas: GRB 121024A shining through its star-forming galaxy. *Monthly Notices of the Royal Astronomical Society*, **451**, 167–183.

S. R. Furlanetto and S. P. Oh (2005). Taxing the rich: recombinations and bubble growth during reionization. *Monthly Notices of the Royal Astronomical Society*, **363**, 1031–1048.

J. P. U. Fynbo, P. Møller, and S. J. Warren (1999). Extended LY alpha emission from a damped LY alpha absorber at z=1.93, and the relation between damped LY alpha absorbers and Lyman-break galaxies. *Monthly Notices of the Royal Astronomical Society*, **305**, 849–858.

J. P. U. Fynbo, S. Holland, M. I. Andersen, B. Thomsen, J. Hjorth, G. Björnsson, A. O. Jaunsen, P. Natarajan, and N. R. Tanvir (2000). Hubble Space Telescope Space Telescope Imaging Spectrograph Imaging of the Host Galaxy of GRB 980425/SN 1998BW. *The Astrophysical Journal*, **542**, L89–L93.

J. P. U. Fynbo, P. Jakobsson, P. Møller, J. Hjorth, B. Thomsen, M. I. Andersen, A. S. Fruchter, J. Gorosabel, S. T. Holland, C. Ledoux, et al. (2003). On the Lyalpha emission from gamma-ray burst host galaxies: Evidence for low metallicities. *Astronomy and Astrophysics*, **406**, L63–L66.

J. P. U. Fynbo, R. L. C. Starling, C. Ledoux, K. Wiersema, C. C. Thöne, J. Sollerman, P. Jakobsson, J. Hjorth, D. J. Watson, P. M. Vreeswijk, et al. (2006). Probing cosmic chemical evolution with gamma-ray bursts: GRB 060206 at z = 4.048. *Astronomy and Astrophysics*, **451**, L47–L50.

J. P. U. Fynbo, J. X. Prochaska, J. Sommer-Larsen, M. Dessauges-Zavadsky, and P. Møller (2008). Reconciling the Metallicity Distributions of Gamma-Ray Burst, Damped Lyα, and Lyman Break Galaxies at z ˜ 3. *The Astrophysical Journal*, **683**, 321–328.

J. P. U. Fynbo, P. Jakobsson, J. X. Prochaska, D. Malesani, C. Ledoux, A. de Ugarte Postigo, M. Nardini, P. M. Vreeswijk, K. Wiersema, J. Hjorth, et al. (2009). Low-resolution Spectroscopy of Gamma-ray Burst Optical Afterglows: Biases in the Swift Sample and Characterization of the Absorbers. *The Astrophysical Journal Supplement Series*, **185**, 526–573.

J. P. U. Fynbo, T. Krühler, K. Leighly, C. Ledoux, P. M. Vreeswijk, S. Schulze, P. Noterdaeme, D. J. Watson, R. A. M. J. Wijers, J. Bolmer, et al. (2014). The mysterious optical afterglow spectrum of GRB 140506A at z = 0.889. *Astronomy and Astrophysics*, **572**, A12.

T. J. Galama, P. M. Vreeswijk, J. van Paradijs, C. Kouveliotou, T. Augusteijn, H. Böhnhardt, J. P. Brewer, V. Doublier, J. F. Gonzalez, B. Leibundgut, et al. (1998). An unusual supernova in the error box of the γ-ray burst of 25 April 1998. *Nature*, **395**, 670–672.

S. Gallerani, R. Salvaterra, A. Ferrara, and T. R. Choudhury (2008). Testing reionization with gamma-ray burst absorption spectra. *Monthly Notices of the Royal Astronomical Society*, **388**, L84–L88.

N. Gehrels, G. Chincarini, P. Giommi, K. O. Mason, J. A. Nousek, A. A. Wells, N. E. White, S. D. Barthelmy, D. N. Burrows, L. R. Cominsky,

ET AL. (2004). The Swift Gamma-Ray Burst Mission. *The Astrophysical Journal*, **611**, 1005–1020.

N. GEHRELS, C. L. SARAZIN, P. T. O'BRIEN, B. ZHANG, L. M. BARBIER, S. D. BARTHELMY, A. BLUSTIN, D. N. BURROWS, J. CANNIZZO, J. R. CUMMINGS, ET AL. (2005). A short γ-ray burst apparently associated with an elliptical galaxy at redshift z = 0.225. *Nature*, **437**, 851–854.

B. GENDRE, G. STRATTA, J. L. ATTEIA, S. BASA, M. BOËR, D. M. COWARD, S. CUTINI, V. D'ELIA, E. J. HOWELL, A. KLOTZ, ET AL. (2013). The Ultra-long Gamma-Ray Burst 111209A: The Collapse of a Blue Supergiant? *The Astrophysical Journal*, **766**, 30.

F. GENET, F. DAIGNE, AND R. MOCHKOVITCH (2007). Can the early X-ray afterglow of gamma-ray bursts be explained by a contribution from the reverse shock? *Monthly Notices of the Royal Astronomical Society*, **381**, 732–740.

G. GHIRLANDA, A. CELOTTI, AND G. GHISELLINI (2002). Time resolved spectral analysis of bright gamma ray bursts. *Astronomy and Astrophysics*, **393**, 409–423.

G. GHIRLANDA, G. GHISELLINI, AND D. LAZZATI (2004a). The Collimation-corrected Gamma-Ray Burst Energies Correlate with the Peak Energy of Their νFν Spectrum. *The Astrophysical Journal*, **616**, 331–338.

G. GHIRLANDA, G. GHISELLINI, D. LAZZATI, AND C. FIRMANI (2004b). Gamma-Ray Bursts: New Rulers to Measure the Universe. *The Astrophysical Journal*, **613**, L13–L16.

G. GHIRLANDA, L. NAVA, G. GHISELLINI, AND C. FIRMANI (2007). Confirming the γ-ray burst spectral-energy correlations in the era of multiple time breaks. *Astronomy and Astrophysics*, **466**, 127–136.

G. GHIRLANDA, L. NAVA, G. GHISELLINI, A. CELOTTI, AND C. FIRMANI (2009). Short versus long gamma-ray bursts: spectra, energetics, and luminosities. *Astronomy and Astrophysics*, **496**, 585–595.

R. GIOVANELLI, M. P. HAYNES, B. R. KENT, P. PERILLAT, A. SAINTONGE, N. BROSCH, B. CATINELLA, G. L. HOFFMAN, S. STIERWALT, K. SPEKKENS, ET AL. (2005). The Arecibo Legacy Fast ALFA Survey. I. Science Goals, Survey Design, and Strategy. *The Astronomical Journal*, **130**, 2598–2612.

N. Y. Gnedin and A. A. Kaurov (2014). Cosmic Reionization on Computers. II. Reionization History and Its Back-reaction on Early Galaxies. *The Astrophysical Journal*, **793**, 30.

P. Goldoni, F. Royer, P. François, M. Horrobin, G. Blanc, J. Vernet, A. Modigliani, and J. Larsen (2006). Data reduction software of the X-shooter spectrograph. *Ground-based and Airborne Instrumentation for Astronomy. Edited by McLean*, **6269**, 62692K–62692K–11.

S. Golenetskii, R. Aptekar, E. Mazets, V. Pal'Shin, D. Frederiks, P. Oleynik, M. Ulanov, D. Svinkin, and T. Cline (2013). Konus-wind observation of GRB 130606A. *GRB Coordinates Network*, **1480**, 1.

J. Gorosabel, E. Rol, S. Covino, A. J. Castro-Tirado, J. M. Castro Cerón, D. Lazzati, J. Hjorth, D. Malesani, M. Della Valle, S. di Serego Alighieri, et al. (2004). GRB 020813: Polarization in the case of a smooth optical decay. *Astronomy and Astrophysics*, **422**, 113–119.

J. Granot and R. Sari (2002). The Shape of Spectral Breaks in Gamma-Ray Burst Afterglows. *The Astrophysical Journal*, **568**, 820–829.

R. F. Green, M. Schmidt, and J. Liebert (1986). The Palomar-Green catalog of ultraviolet-excess stellar objects. *The Astrophysical Journal Supplement Series*, **61**, 305–352.

J. L. Greenstein (1963). Red-Shift of the Unusual Radio Source: 3C 48. *Nature*, **197**, 1041–1042.

J. Greiner, W. Bornemann, C. Clemens, M. Deuter, G. Hasinger, M. Honsberg, H. Huber, S. Huber, M. Krauss, T. Krühler, et al. (2008). GROND—a 7-Channel Imager. *The Publications of the Astronomical Society of the Pacific*, **120**, 405–424.

J. Greiner, T. Krühler, J. P. U. Fynbo, A. Rossi, R. Schwarz, S. Klose, S. Savaglio, N. R. Tanvir, S. McBreen, T. Totani, et al. (2009). GRB 080913 at Redshift 6.7. *The Astrophysical Journal*, **693**, 1610–1620.

D. Guetta, T. Piran, and E. Waxman (2005). The Luminosity and Angular Distributions of Long-Duration Gamma-Ray Bursts. *The Astrophysical Journal*, **619**, 412–419.

C. Guidorzi, C. G. Mundell, R. Harrison, R. Margutti, V. Sudilovsky, B. A. Zauderer, S. Kobayashi, A. Cucchiara, A. Melandri, S. B. Pandey,

et al. (2014). New constraints on gamma-ray burst jet geometry and relativistic shock physics. *Monthly Notices of the Royal Astronomical Society*, **438**, 752–767.

S. Guilloteau, J. Delannoy, D. Downes, A. Greve, M. Guélin, R. Lucas, D. Morris, S. J. E. Radford, J. Wink, J. Cernicharo, et al. (1992). The IRAM interferometer on Plateau de Bure. *Astronomy and Astrophysics*, **262**, 624–633.

R. Guimarães, P. Petitjean, R. R. de Carvalho, S. G. Djorgovski, P. Noterdaeme, S. Castro, Poppe, P. C. Da R., and A. Aghaee (2009). Damped and sub-damped Lyman-α absorbers in z ¿ 4 QSOs. *Astronomy and Astrophysics*, **508**, 133–140.

J. E. Gunn and B. A. Peterson (1965). On the Density of Neutral Hydrogen in Intergalactic Space. *The Astrophysical Journal*, **142**, 1633–1641.

M. G. Haehnelt, M. Steinmetz, and M. Rauch (1998). Damped Lyα Absorber at High Redshift: Large Disks or Galactic Building Blocks? *The Astrophysical Journal*, **495**, 647–658.

X. H. Han, F. Hammer, Y. C. Liang, H. Flores, M. Rodrigues, J. L. Hou, and J. Wei (2010). The Wolf-Rayet features and mass-metallicity relation of long-duration gamma-ray burst host galaxies. *Astronomy and Astrophysics*, **514**, A24.

P. J. Hancock, T. Murphy, and B. P. Schmidt (2011). GRB 110715A: ATCA detection of the radio counterpart. *GRB Coordinates Network*, **1217**.

O. E. Hartoog, D. Malesani, J. P. U. Fynbo, T. Goto, T. Krühler, P. M. Vreeswijk, A. De Cia, D. Xu, P. Møller, S. Covino, et al. (2015). VLT/X-Shooter spectroscopy of the afterglow of the Swift GRB 130606A. Chemical abundances and reionisation at z ˜ 6. *Astronomy and Astrophysics*, **580**, A139.

C. Hazard, M. B. Mackey, and A. J. Shimmins (1963). Investigation of the Radio Source 3C 273 By The Method of Lunar Occultations. *Nature*, **197**, 1037–1039.

P. C. Hewett and V. Wild (2010). Improved redshifts for SDSS quasar spectra. *Monthly Notices of the Royal Astronomical Society*, **405**, 2302–2316.

J. Hjorth and J. S. Bloom (2012). The Gamma-Ray Burst - Supernova Connection. *Chapter 9 in "Gamma-Ray Bursts"*, 169–190.

J. Hjorth, J. Sollerman, P. Møller, J. P. U. Fynbo, S. E. Woosley, C. Kouveliotou, N. R. Tanvir, J. Greiner, M. I. Andersen, A. J. Castro-Tirado,

ET AL. (2003). A very energetic supernova associated with the γ-ray burst of 29 March 2003. *Nature*, **423**, 847–850.

J. HJORTH, D. J. WATSON, J. P. U. FYNBO, P. A. PRICE, B. L. JENSEN, U. G. JØRGENSEN, D. KUBAS, J. GOROSABEL, P. JAKOBSSON, J. SOLLERMAN, ET AL. (2005). The optical afterglow of the short γ-ray burst GRB 050709. *Nature*, **437**, 859–861.

J. HJORTH, D. MALESANI, P. JAKOBSSON, A. O. JAUNSEN, J. P. U. FYNBO, J. GOROSABEL, T. KRÜHLER, A. J. LEVAN, M. J. MICHAŁOWSKI, B. MILVANG-JENSEN, ET AL. (2012). The Optically Unbiased Gamma-Ray Burst Host (TOUGH) Survey. I. Survey Design and Catalogs. *The Astrophysical Journal*, **756**, 187.

K. HORNE (1986). An optimal extraction algorithm for CCD spectroscopy. *The Publications of the Astronomical Society of the Pacific*, **98**, 609–617.

I. HORVÁTH (1998). A Third Class of Gamma-Ray Bursts? *The Astrophysical Journal*, **508**, 757–759.

I. HORVÁTH AND B. G. TÓTH (2016). The duration distribution of Swift Gamma-Ray Bursts. *Astrophysics and Space Science*, **361**, 155.

I. HORVÁTH, J. HAKKILA, AND Z. BAGOLY (2014). Possible structure in the GRB sky distribution at redshift two. *Astronomy and Astrophysics*, **561**, L12.

T. HOSOKAWA, K. OMUKAI, N. YOSHIDA, AND H. W. YORKE (2011). Protostellar Feedback Halts the Growth of the First Stars in the Universe. *Science*, **334**, 1250–1253.

S.-J. HOU, H. GAO, T. LIU, W.-M. GU, D.-B. LIN, Y.-P. LI, Y.-P. MEN, X.-F. WU, W.-H. LEI, AND J.-F. LU (2014). Variability of the giant X-ray bump in GRB 121027A and its possible origin. *Monthly Notices of the Royal Astronomical Society*, **441**, 2375–2379.

S. INOUE, R. SALVATERRA, T. R. CHOUDHURY, A. FERRARA, B. CIARDI, AND R. SCHNEIDER (2010). Probing intergalactic radiation fields during cosmic reionization through gamma-ray absorption. *Monthly Notices of the Royal Astronomical Society*, **404**, 1938–1943.

E. E. O. ISHIDA, R. S. DE SOUZA, AND A. FERRARA (2011). Probing cosmic star formation up to z= 9.4 with gamma-ray bursts. *Monthly Notices of the Royal Astronomical Society*, **418**, 500–504.

K. Iwamoto, P. A. Mazzali, K. Nomoto, H. Umeda, T. Nakamura, F. Patat, I. J. Danziger, T. R. Young, T. Suzuki, T. Shigeyama, et al. (1998). A hypernova model for the supernova associated with the γ-ray burst of 25 April 1998. *Nature*, **395**, 672–674.

M. Iye, K. Ota, N. Kashikawa, H. Furusawa, T. Hashimoto, T. Hattori, Y. Matsuda, T. Morokuma, M. Ouchi, and K. Shimasaku (2006). A galaxy at a redshift z = 6.96. *Nature*, **443**, 186–188.

P. Jakobsson, J. P. U. Fynbo, C. Ledoux, P. M. Vreeswijk, D. A. Kann, J. Hjorth, R. S. Priddey, N. R. Tanvir, D. Reichart, J. Gorosabel, et al. (2006). H I column densities of z ¿ 2 Swift gamma-ray bursts. *Astronomy and Astrophysics*, **460**, L13–L17.

J. Japelj, S. Covino, A. Gomboc, S. D. Vergani, P. Goldoni, J. Selsing, Z. Cano, V. D'Elia, H. Flores, J. P. U. Fynbo, et al. (2015). Spectrophotometric analysis of gamma-ray burst afterglow extinction curves with X-Shooter. *Astronomy and Astrophysics*, **579**, A74. 47

M. Jelínek, M. Prouza, P. Kubánek, R. Hudec, M. Nekola, J. Řídký, J. Grygar, M. Boháčová, A. J. Castro-Tirado, J. Gorosabel, et al. (2006). The bright optical flash from GRB 060117. *Astronomy and Astrophysics*, **454**, L119–L122.

M. Jelínek, J. Gorosabel, A. J. Castro-Tirado, S. Mottola, S. Hellmich, R. Fernández-Muñoz, and V. F. Muñoz-Martínez (2013). GRB 130606A: optical afterglow with BOOTES-2/TELMA and 1.23m CAHA. *GRB Coordinates Network*, **1478**, 1.

E. B. Jenkins and J. P. Ostriker (1991). Lyman-alpha depression of the continuum from high-redshift quasars - A new technique applied in search of the Gunn-Peterson effect. *The Astrophysical Journal*, **376**, 33–42.

S. Jeong, R. Sánchez-Ramírez, J. Gorosabel, and A. J. Castro-Tirado (2014). GRB 140304A: 10.4m GTC refined redshift z = 5.283. *GRB Coordinates Network*, **1593**, 1. 176

L. Jiang, X. Fan, W. N. Brandt, C. L. Carilli, E. Egami, D. C. Hines, J. D. Kurk, G. T. Richards, Y. Shen, M. A. Strauss, et al. (2010). Dust-free quasars in the early Universe. *Nature*, **464**, 380–383.

G. Jóhannesson, G. Björnsson, and E. H. Gudmundsson (2006). Energy Injection in Gamma-Ray Burst Afterglow Models. *The Astrophysical Journal*, **647**, 1238–1249.

M. Kajisawa, T. Ichikawa, I. Tanaka, T. Yamada, M. Akiyama, R. Suzuki, C. Tokoku, Y. Katsuno Uchimoto, M. Konishi, T. Yoshikawa, et al. (2011). MOIRCS Deep Survey. IX. Deep Near-Infrared Imaging Data and Source Catalog. *Publications of the Astronomical Society of Japan*, **63**, 379–401.

Y. Kaneko, E. Ramirez-Ruiz, J. Granot, C. Kouveliotou, S. E. Woosley, S. K. Patel, E. Rol, J. J. M. in 't Zand, A. J. van der Horst, R. A. M. J. Wijers, et al. (2007). Prompt and Afterglow Emission Properties of Gamma-Ray Bursts with Spectroscopically Identified Supernovae. *The Astrophysical Journal*, **654**, 385–402.

D. A. Kann, S. Klose, and A. Zeh (2006). Signatures of Extragalactic Dust in Pre-Swift GRB Afterglows. *The Astrophysical Journal*, **641**, 993–1009.

D. A. Kann, S. Klose, B. Zhang, D. Malesani, E. Nakar, A. Pozanenko, A. C. Wilson, N. R. Butler, P. Jakobsson, S. Schulze, et al. (2010). The Afterglows of Swift-era Gamma-ray Bursts. I. Comparing pre-Swift and Swift-era Long/Soft (Type II) GRB Optical Afterglows. *The Astrophysical Journal*, **720**, 1513–1558.

D. A. Kann, S. Klose, B. Zhang, S. Covino, N. R. Butler, D. Malesani, E. Nakar, A. C. Wilson, L. A. Antonelli, G. Chincarini, et al. (2011). The Afterglows of Swift-era Gamma-Ray Bursts. II. Type I GRB versus Type II GRB Optical Afterglows. *The Astrophysical Journal*, **734**, 96.

T. Karlsson, V. Bromm, and J. Bland-Hawthorn (2013). Pregalactic metal enrichment: The chemical signatures of the first stars. *Reviews of Modern Physics*, **85**, 809–848.

G. Kauffmann (1996). Disc galaxies at z=0 and at high redshift: an explanation of the observed evolution of damped Lyalpha absorption systems. *Monthly Notices of the Royal Astronomical Society*, **281**, 475–486.

N. Kawai, G. Kosugi, K. Aoki, T. Yamada, T. Totani, K. Ohta, M. Iye, T. Hattori, W. Aoki, H. Furusawa, et al. (2006). An optical spectrum of the afterglow of a γ-ray burst at a redshift of z = 6.295. *Nature*, **440**, 184–186.

D. D. Kelson (2003). Optimal Techniques in Two-dimensional Spectroscopy: Background Subtraction for the 21st Century. *The Publications of the Astronomical Society of the Pacific*, **115**, 688–699.

D. Kereš, M. Vogelsberger, D. Sijacki, V. Springel, and L. Hernquist (2012). Moving-mesh cosmology: characteristics of galaxies and haloes. *Monthly Notices of the Royal Astronomical Society*, **425**, 2027–2048.

R. P. Kirshner (2002). The extravagant universe : exploding stars, dark energy and the accelerating cosmos. *The extravagant universe : exploding stars*.

M. D. Kistler, H. Yüksel, J. F. Beacom, A. M. Hopkins, and J. S. B. Wyithe (2009). The Star Formation Rate in the Reionization Era as Indicated by Gamma-Ray Bursts. *The Astrophysical Journal*, **705**, L104–L108.

R. W. Klebesadel, I. B. Strong, and R. A. Olson (1973). Observations of Gamma-Ray Bursts of Cosmic Origin. *The Astrophysical Journal*, **182**, L85.

S. Kobayashi, T. Piran, and R. Sari (1997). Can Internal Shocks Produce the Variability in Gamma-Ray Bursts? *The Astrophysical Journal*, **490**, 92–.

E. Komatsu, K. M. Smith, J. Dunkley, C. L. Bennett, B. Gold, G. Hinshaw, N. Jarosik, D. Larson, M. R. Nolta, L. Page, et al. (2011). Seven-year Wilkinson Microwave Anisotropy Probe (WMAP) Observations: Cosmological Interpretation. *The Astrophysical Journal Supplement Series*, **192**, 18.

D. Kopač, C. G. Mundell, J. Japelj, D. M. Arnold, I. A. Steele, C. Guidorzi, S. Dichiara, S. Kobayashi, A. Gomboc, R. M. Harrison, et al. (2015). Limits on Optical Polarization during the Prompt Phase of GRB 140430A. *The Astrophysical Journal*, **813**, 1. 119

C. Kouveliotou, C. A. Meegan, G. J. Fishman, N. P. Bhat, M. S. Briggs, T. M. Koshut, W. S. Paciesas, and G. N. Pendleton (1993). Identification of two classes of gamma-ray bursts. *The Astrophysical Journal*, **413**, L101–L104.

C. Kouveliotou, S. Dieters, T. Strohmayer, J. van Paradijs, G. J. Fishman, C. A. Meegan, K. Hurley, J. Kommers, I. Smith, D. Frail, et al. (1998). An X-ray pulsar with a superstrong magnetic field in the soft γ-ray repeater SGR1806 - 20. *Nature*, **393**, 235–237.

A. Kovács (2008). CRUSH: fast and scalable data reduction for imaging arrays. *Millimeter and Submillimeter Detectors and Instrumentation for Astronomy IV. Edited by Duncan*, **7020**, 70201S–70201S–15.

T. Krühler, A. Küpcü Yoldaş, J. Greiner, C. Clemens, S. McBreen, N. Primak, S. Savaglio, A. Yoldaş, G. P. Szokoly, and S. Klose (2008). The 2175

Å Dust Feature in a Gamma-Ray Burst Afterglow at Redshift 2.45. *The Astrophysical Journal*, **685**, 376–383.

T. Krühler, C. Ledoux, J. P. U. Fynbo, P. M. Vreeswijk, S. Schmidl, D. Malesani, L. Christensen, A. De Cia, J. Hjorth, P. Jakobsson, et al. (2013). Molecular hydrogen in the damped Lyman α system towards GRB 120815A at z = 2.36. *Astronomy and Astrophysics*, **557**, A18. 50, 51

T. Krühler, D. Malesani, J. P. U. Fynbo, O. E. Hartoog, J. Hjorth, P. Jakobsson, D. A. Perley, A. Rossi, P. Schady, S. Schulze, et al. (2015). GRB hosts through cosmic time. VLT/X-Shooter emission-line spectroscopy of 96 γ-ray-burst-selected galaxies at 0.1 ¡z ¡ 3.6. *Astronomy and Astrophysics*, **581**, A125. 81, 120

S. R. Kulkarni, D. A. Frail, M. H. Wieringa, R. D. Ekers, E. M. Sadler, R. M. Wark, J. L. Higdon, E. S. Phinney, and J. S. Bloom (1998). Radio emission from the unusual supernova 1998bw and its association with the γ-ray burst of 25 April 1998. *Nature*, **395**, 663–669.

S. R. Kulkarni, S. G. Djorgovski, S. C. Odewahn, J. S. Bloom, R. R. Gal, C. D. Koresko, F. A. Harrison, L. M. Lubin, L. Armus, R. Sari, et al. (1999). The afterglow, redshift and extreme energetics of the γ-ray burst of 23 January 1999. *Nature*, **398**, 389–394.

V. P. Kulkarni, P. Khare, D. Som, J. Meiring, D. G. York, C. Péroux, and J. T. Lauroesch (2010). Do damped and sub-damped Lyman-alpha absorbers arise in galaxies of different masses? *New Astronomy Reviews*, **15**, 735–743.

P. Kumar and B. Zhang (2015). The physics of gamma-ray bursts & relativistic jets. *Physics Reports*, **561**, 1–109.

P. Lah, J. N. Chengalur, F. H. Briggs, M. Colless, R. de Propris, M. B. Pracy, W. J. G. de Blok, S. S. Fujita, M. Ajiki, Y. Shioya, et al. (2007). The H I content of star-forming galaxies at z= 0.24. *Monthly Notices of the Royal Astronomical Society*, **376**, 1357–1366.

D. Q. Lamb (1995). The Distance Scale to Gamma-Ray Bursts. *The Publications of the Astronomical Society of the Pacific*, **107**, 1152–.

D. Q. Lamb and D. E. Reichart (2000). Gamma-Ray Bursts as a Probe of the Very High Redshift Universe. *The Astrophysical Journal*, **536**, 1–18.

K. M. Lanzetta, A. M. Wolfe, D. A. Turnshek, L. Lu, R. G. McMahon, and C. Hazard (1991). A new spectroscopic survey for damped Ly-alpha absorption lines from high-redshift galaxies. *The Astrophysical Journal Supplement Series*, **77**, 1–57.

T. Laskar, E. Berger, B. A. Zauderer, R. Margutti, A. M. Soderberg, S. Chakraborti, R. Lunnan, R. Chornock, P. Chandra, and A. Ray (2013a). A Reverse Shock in GRB 130427A. *The Astrophysical Journal*, **776**, 119.

T. Laskar, A. Zauderer, and E. Berger (2013b). GRB 130606A: EVLA detection. *GRB Coordinates Network*, **1481**, 1.

E. Le Floc'h, P. A. Duc, F. Mirabel, D. B. Sanders, G. Bosch, R. J. Diaz, C. J. Donzelli, I. Rodrigues, T. J. L. Courvoisier, J. Greiner, et al. (2003). Are the hosts of gamma-ray bursts sub-luminous and blue galaxies? *Astronomy and Astrophysics*, **400**, 499–510.

C. Ledoux, P. Petitjean, J. Bergeron, E. J. Wampler, and R. Srianand (1998). On the kinematics of damped Lyman-alpha systems. *Astronomy and Astrophysics*, **337**, 51–63.

C. Ledoux, P. Petitjean, and R. Srianand (2003). The Very Large Telescope Ultraviolet and Visible Echelle Spectrograph survey for molecular hydrogen in high-redshift damped Lyman α systems. *Monthly Notices of the Royal Astronomical Society*, **346**, 209–228.

S. A. Levshakov and W. H. Kegel (1998). The Gunn-Peterson effect and the Lyman alpha forest. *Monthly Notices of the Royal Astronomical Society*, **301**, 323–327.

S. A. Levshakov and D. A. Varshalovich (1985). Molecular hydrogen in the Z = 2.811 absorbing material toward the quasar PKS 0528-250. *Monthly Notices of the Royal Astronomical Society (ISSN 0035-8711)*, **212**, 517–521.

L.-X. Li and B. Paczynski (1998). Transient Events from Neutron Star Mergers. *The Astrophysical Journal*, **507**, L59–L62.

Z.-Y. Li and R. A. Chevalier (1999). Radio Supernova SN 1998bw and Its Relation to GRB 980425. *The Astrophysical Journal*, **526**, 716–726.

S. J. Lilly, C. M. Carollo, A. Pipino, A. Renzini, and Y. Peng (2013). Gas Regulation of Galaxies: The Evolution of the Cosmic Specific Star Formation Rate, the Metallicity-Mass-Star-formation Rate Relation, and the Stellar Content of Halos. *The Astrophysical Journal*, **772**, 119.

S. Lopez and S. L. Ellison (2003). Distinct abundance patterns in multiple damped Ly alpha galaxies: Evidence for truncated star formation? *Astronomy and Astrophysics*, **403**, 573–584.

J. L. Lowrance, D. C. Morton, P. Zucchino, J. B. Oke, and M. Schmidt (1972). The Spectrum of the Quasi-Stellar Object PHL 957. *The Astrophysical Journal*, **171**, 233–.

D. Lynden-Bell (1971). Note on N Galaxies and mini-quasars. *Monthly Notices of the Royal Astronomical Society*, **155**, 119.

R. Lynds (1971). The Absorption-Line Spectrum of 4c 05.34. *The Astrophysical Journal*, **164**, L73.

Q. Ma, U. Maio, B. Ciardi, and R. Salvaterra (2015). PopIII signatures in the spectra of PopII/I GRBs. *Monthly Notices of the Royal Astronomical Society*, **449**, 3006–3014.

J. Mackey, V. Bromm, and L. Hernquist (2003). Three Epochs of Star Formation in the High-Redshift Universe. *The Astrophysical Journal*, **586**, 1–11.

P. Madau, F. Haardt, and M. J. Rees (1999). Radiative Transfer in a Clumpy Universe. III. The Nature of Cosmological Ionizing Sources. *The Astrophysical Journal*, **514**, 648–659.

U. Maio, R. Salvaterra, L. Moscardini, and B. Ciardi (2012). Counts of high-redshift GRBs as probes of primordial non-Gaussianities. *Monthly Notices of the Royal Astronomical Society*, **426**, 2078–2088.

A. M. Martin, E. Papastergis, R. Giovanelli, M. P. Haynes, C. M. Springob, and S. Stierwalt (2010). The Arecibo Legacy Fast ALFA Survey. X. The H I Mass Function and Ω(H I) from the 40% ALFALFA Survey. *The Astrophysical Journal*, **723**, 1359–1374.

K. Mawatari, A. K. Inoue, K. Kousai, T. Hayashino, R. J. Cooke, J. X. Prochaska, T. Yamada, and Y. Matsuda (2016). Discovery of a Damped Lyα Absorber at z = 3.3 along a Galaxy Sight-line in the SSA22 Field. *The Astrophysical Journal*, **817**, 161.

E. P. Mazets, S. V. Golenetskii, R. L. Aptekar, I. A. Gurian, and V. N. Ilinskii (1981). Cyclotron and annihilation lines in gamma-ray burst. *Nature*, **290**, 378–382.

I. D. McGreer, A. Mesinger, and X. Fan (2011). The first (nearly) model-independent constraint on the neutral hydrogen fraction at z ˜ 6. *Monthly Notices of the Royal Astronomical Society*, **415**, 3237–3246.

I. D. McGreer, A. Mesinger, and V. D'Odorico (2015). Model-independent evidence in favour of an end to reionization by z ≈ 6. *Monthly Notices of the Royal Astronomical Society*, **447**, 499–505.

J. T. W. McGuire, N. R. Tanvir, A. J. Levan, M. Trenti, E. R. Stanway, J. M. Shull, K. Wiersema, D. A. Perley, R. L. C. Starling, M. Bremer, et al. (2015). Detection of three Gamma-Ray Burst host galaxies at $z \sim 6$. *arXiv.org*, arXiv:1512.07808.

C. F. McKee and J. C. Tan (2008). The Formation of the First Stars. II. Radiative Feedback Processes and Implications for the Initial Mass Function. *The Astrophysical Journal*, **681**, 771–797.

M. McQuinn, A. Lidz, O. Zahn, S. Dutta, L. Hernquist, and M. Zaldarriaga (2007). The morphology of HII regions during reionization. *Monthly Notices of the Royal Astronomical Society*, **377**, 1043–1063.

M. McQuinn, A. Lidz, M. Zaldarriaga, L. Hernquist, and S. Dutta (2008). Probing the neutral fraction of the IGM with GRBs during the epoch of reionization. *Monthly Notices of the Royal Astronomical Society*, **388**, 1101–1110.

C. A. Meegan, G. J. Fishman, R. B. Wilson, J. M. Horack, M. N. Brock, W. S. Paciesas, G. N. Pendleton, and C. Kouveliotou (1992). Spatial distribution of gamma-ray bursts observed by BATSE. *Nature*, **355**, 143–145.

B. Ménard, D. Nestor, D. Turnshek, A. Quider, G. Richards, D. Chelouche, and S. Rao (2008). Lensing, reddening and extinction effects of MgII absorbers from z = 0.4 to 2. *Monthly Notices of the Royal Astronomical Society*, **385**, 1053–1066.

P. Mészáros (2002). Theories of Gamma-Ray Bursts. *Annual Review of Astronomy and Astrophysics*, **40**, 137–169.

P. Mészáros (2006). Gamma-ray bursts. *Reports on Progress in Physics*, **69**, 2259–2321.

P. Mészáros and M. J. Rees (1992a). High-entropy fireballs and jets in gamma-ray burst sources. *Monthly Notices of the Royal Astronomical Society*, **257**, 29P–31P.

P. Mészáros and M. J. Rees (1992b). Tidal heating and mass loss in neutron star binaries - Implications for gamma-ray burst models. *The Astrophysical Journal*, **397**, 570–575.

P. Mészáros and M. J. Rees (1993). Relativistic fireballs and their impact on external matter - Models for cosmological gamma-ray bursts. *The Astrophysical Journal*, **405**, 278–284.

P. Mészáros and M. J. Rees (1997). Optical and Long-Wavelength Afterglow from Gamma-Ray Bursts. *The Astrophysical Journal*, **476**, 232–237.

P. Mészáros and M. J. Rees (2010). Population III Gamma-ray Bursts. *The Astrophysical Journal*, **715**, 967–971.

P. Mészáros, K. Asano, K. Murase, D. Fox, H. Gao, and N. Senno (2015). Gamma Ray Bursts in the HAWC Era. *arXiv.org*, arXiv:1506.02707.

M. R. Metzger, J. G. Cohen, F. H. Chaffee, and R. D. Blandford (1997a). GRB 970508. *Circulars of the International Astronomical Union*, **6676**, 3.

M. R. Metzger, S. G. Djorgovski, S. R. Kulkarni, C. C. Steidel, K. L. Adelberger, D. A. Frail, E. Costa, and F. Frontera (1997b). Spectral constraints on the redshift of the optical counterpart to the γ-ray burst of 8 May 1997. *Nature*, **387**, 878–880.

B. Milvang-Jensen, J. P. U. Fynbo, D. Malesani, J. Hjorth, P. Jakobsson, and P. Møller (2012). The Optically Unbiased GRB Host (TOUGH) Survey. IV. Lyα Emitters. *The Astrophysical Journal*, **756**, 25.

J. Miralda-Escudé (1998). Reionization of the Intergalactic Medium and the Damping Wing of the Gunn-Peterson Trough. *The Astrophysical Journal*, **501**, 15–22.

J. Miralda-Escudé, M. Haehnelt, and M. J. Rees (2000). Reionization of the Inhomogeneous Universe. *The Astrophysical Journal*, **530**, 1–16.

A. Modigliani, P. Goldoni, F. Royer, R. Haigron, L. Guglielmi, P. François, M. Horrobin, P. Bristow, J. Vernet, S. Moehler, et al. (2010). The X-shooter pipeline. In D.R. Silva, A.B. Peck & B.T. Soifer, eds., *Proceedings of the SPIE*, 773728–773728–12, European Southern Observatory, Germany, SPIE.

P. Møller, J. P. U. Fynbo, C. Ledoux, and K. K. Nilsson (2013). Mass-metallicity relation from z = 5 to the present: evidence for a transition in the mode

of galaxy growth at z = 2.6 due to the end of sustained primordial gas infall. *Monthly Notices of the Royal Astronomical Society*, **430**, 2680–2687.

D. J. Mortlock, M. Patel, S. J. Warren, B. P. Venemans, R. G. McMahon, P. C. Hewett, C. Simpson, R. G. Sharp, B. Burningham, S. Dye, et al. (2009). Discovery of a redshift 6.13 quasar in the UKIRT infrared deep sky survey. *Astronomy and Astrophysics*, **505**, 97–104.

D. J. Mortlock, S. J. Warren, B. P. Venemans, M. Patel, P. C. Hewett, R. G. McMahon, C. Simpson, T. Theuns, E. A. Gonzáles-Solares, A. Adamson, et al. (2011). A luminous quasar at a redshift of z = 7.085. *Nature*, **474**, 616–619.

S. Mukherjee, E. D. Feigelson, G. Jogesh Babu, F. Murtagh, C. Fraley, and A. Raftery (1998). Three Types of Gamma-Ray Bursts. *The Astrophysical Journal*, **508**, 314–327.

C. G. Mundell, D. Kopač, D. M. Arnold, I. A. Steele, A. Gomboc, S. Kobayashi, R. M. Harrison, R. J. Smith, C. Guidorzi, F. J. Virgili, et al. (2013). Highly polarized light from stable ordered magnetic fields in GRB 120308A. *Nature*, **504**, 119–121.

T. Murakami, M. Fujii, K. Hayashida, M. Itoh, and J. Nishimura (1988). Evidence for cyclotron absorption from spectral features in gamma-ray bursts seen with Ginga. *Nature*, **335**, 234–.

H. S. Murdoch, R. W. Hunstead, M. Pettini, and J. C. Blades (1986). Absorption spectrum of the Z = 3.78 QSO 2000-330. II - The redshift and equivalent width distributions of primordial hydrogen clouds. *Astrophysical Journal*, **309**, 19–32.

K. Nagamine, V. Springel, and L. Hernquist (2004a). Abundance of damped Lyman α absorbers in cosmological smoothed particle hydrodynamics simulations. *Monthly Notices of the Royal Astronomical Society*, **348**, 421–434.

K. Nagamine, V. Springel, and L. Hernquist (2004b). Star formation rate and metallicity of damped Lyman α absorbers in cosmological smoothed particle hydrodynamics simulations. *Monthly Notices of the Royal Astronomical Society*, **348**, 435–450.

D. Nakauchi, Y. Suwa, T. Sakamoto, K. Kashiyama, and T. Nakamura (2012). Long-duration X-Ray Flash and X-Ray-rich Gamma-Ray Bursts from Low-mass Population III Stars. *The Astrophysical Journal*, **759**, 128.

R. Narayan, B. Paczynski, and T. Piran (1992). Gamma-ray bursts as the death throes of massive binary stars. *The Astrophysical Journal*, **395**, L83–L86.

L. Nava, G. Ghirlanda, G. Ghisellini, and A. Celotti (2011a). Fermi/GBM and BATSE gamma-ray bursts: comparison of the spectral properties. *Monthly Notices of the Royal Astronomical Society*, **415**, 3153–3162.

L. Nava, G. Ghirlanda, G. Ghisellini, and A. Celotti (2011b). Spectral properties of 438 GRBs detected by Fermi/GBM. *Astronomy and Astrophysics*, **530**, A21.

M. Neeleman, J. X. Prochaska, J. Ribaudo, N. Lehner, J. C. Howk, M. Rafelski, and N. Kanekar (2016). The H I Content of the Universe Over the Past 10 GYRS. *The Astrophysical Journal*, **818**, 113.

P. Nelson (2011). GRB 110715A optical observations. *GRB Coordinates Network*, **1217**.

R. J. Nemiroff (1994). A Century of Gamma-Ray Burst Models. *Gamma-Ray Bursts*, **307**, 730–.

Y. Niino (2011). Revisiting the metallicity of long-duration gamma-ray burst host galaxies: the role of chemical inhomogeneity within galaxies. *Monthly Notices of the Royal Astronomical Society*, **417**, 567–572.

J. P. Norris, G. F. Marani, and J. T. Bonnell (2000). Connection between Energy-dependent Lags and Peak Luminosity in Gamma-Ray Bursts. *The Astrophysical Journal*, **534**, 248–257.

P. Noterdaeme, P. Petitjean, C. Ledoux, and R. Srianand (2009). Evolution of the cosmological mass density of neutral gas from Sloan Digital Sky Survey II - Data Release 7. *Astronomy and Astrophysics*, **505**, 1087–1098.

P. Noterdaeme, P. Petitjean, W. Carithers, I. Pâris, A. Font-Ribera, S. Bailey, É. Aubourg, D. Bizyaev, G. Ebelke, H. Finley, et al. (2012). Column density distribution and cosmological mass density of neutral gas: Sloan Digital Sky Survey-III Data Release 9. *Astronomy and Astrophysics*, **547**, L1.

P. Noterdaeme, P. Petitjean, and R. Srianand (2015a). The elusive HI to H_2 transition in high-z damped Lyman-α systems. *Astronomy and Astrophysics*, **578**, L5.

P. Noterdaeme, R. Srianand, H. Rahmani, P. Petitjean, I. Pâris, C. Ledoux, N. Gupta, and S. Lopez (2015b). VLT/UVES observations of extremely strong intervening damped Lyman-α systems. Molecular hydrogen and excited carbon, oxygen, and silicon at log N(H i) = 22.4. *Astronomy and Astrophysics*, **577**, A24.

S. R. Oates, M. J. Page, P. Schady, M. De Pasquale, T. S. Koch, A. A. Breeveld, P. J. Brown, M. M. Chester, S. T. Holland, E. A. Hoversten, et al. (2009). A statistical study of gamma-ray burst afterglows measured by the Swift Ultraviolet Optical Telescope. *Monthly Notices of the Royal Astronomical Society*, **395**, 490–503.

P. A. Oesch, G. Brammer, P. G. van Dokkum, G. D. Illingworth, R. Bouwens, I. Labbé, M. Franx, I. Momcheva, M. L. N. Ashby, G. G. Fazio, et al. (2016). A Remarkably Luminous Galaxy at z=11.1 Measured with Hubble Space Telescope Grism Spectroscopy. *The Astrophysical Journal*, **819**, 129.

J. M. O'Meara, J. X. Prochaska, S. M. Burles, G. Prochter, R. A. Bernstein, and K. M. Burgess (2007). The Keck+Magellan Survey for Lyman Limit Absorption. I. The Frequency Distribution of Super Lyman Limit Systems. *The Astrophysical Journal*, **656**, 666–679.

A. Omont (2007). Molecules in galaxies. *Reports on Progress in Physics*, **70**, 1099–1176.

K. Omukai and R. Nishi (1999). Photodissociative Regulation of Star Formation in Metal-free Pregalactic Clouds. *The Astrophysical Journal*, **518**, 64–68.

B. Paczynski (1995). How Far Away Are Gamma-Ray Bursters? *The Publications of the Astronomical Society of the Pacific*, **107**, 1167–.

H. Padmanabhan, T. R. Choudhury, and R. Srianand (2014). Probing reionization using quasar near-zones at redshift z ˜ 6. *Monthly Notices of the Royal Astronomical Society*, **443**, 3761–3779.

A. Panaitescu and P. Kumar (2001). Jet Energy and Other Parameters for the Afterglows of GRB 980703, GRB 990123, GRB 990510, and GRB 991216 Determined from Modeling of Multifrequency Data. *The Astrophysical Journal*, **554**, 667–677.

A. Panaitescu and P. Kumar (2002). Properties of Relativistic Jets in Gamma-Ray Burst Afterglows. *The Astrophysical Journal*, **571**, 779–789.

M. Patel, S. J. Warren, D. J. Mortlock, and J. P. U. Fynbo (2010). The reanalysis of spectra of GRB 080913 to estimate the neutral fraction of the IGM at a redshift of 6.7. *Astronomy and Astrophysics*, **512**, L3.

A. Pe'er and F. Ryde (2016). Photospheric Emission in Gamma-Ray Bursts. *arXiv.org*, arXiv:1603.05058.

A. Pe'er, P. Mészáros, and M. J. Rees (2006). Radiation from an Expanding Cocoon as an Explanation of the Steep Decay Observed in GRB Early Afterglow Light Curves. *The Astrophysical Journal*, **652**, 482–489.

Y. C. Pei and S. M. Fall (1995). Cosmic Chemical Evolution. *The Astrophysical Journal*, **454**, 69–.

D. A. Perley, S. B. Cenko, J. S. Bloom, T. Krühler, A. V. Filippenko, A. Fruchter, J. Kalirai, A. N. Morgan, J. X. Prochaska, and J. M. Silverman (2013). A Population of Massive, Luminous Galaxies Hosting Heavily Dust-obscured Gamma-Ray Bursts: Implications for the Use of GRBs as Tracers of Cosmic Star Formation. *The Astrophysical Journal*, **778**, 128.

D. A. Perley, T. Krühler, S. Schulze, A. de Ugarte Postigo, J. Hjorth, E. Berger, S. B. Cenko, R. Chary, A. Cucchiara, R. Ellis, et al. (2016a). The Swift Gamma-Ray Burst Host Galaxy Legacy Survey. I. Sample Selection and Redshift Distribution. *The Astrophysical Journal*, **817**, 7.

D. A. Perley, Y. Niino, N. R. Tanvir, S. D. Vergani, and J. P. U. Fynbo (2016b). Long-Duration Gamma-Ray Burst Host Galaxies in Emission and Absorption. *Space Science Reviews*, 1–32.

D. A. Perley, N. R. Tanvir, J. Hjorth, T. Laskar, E. Berger, R. Chary, A. de Ugarte Postigo, J. P. U. Fynbo, T. Krühler, A. J. Levan, et al. (2016c). The Swift GRB Host Galaxy Legacy Survey. II. Rest-frame Near-IR Luminosity Distribution and Evidence for a Near-solar Metallicity Threshold. *The Astrophysical Journal*, **817**, 8.

R. Perna and D. Lazzati (2002). Time-dependent Photoionization in a Dusty Medium. I. Code Description and General Results. *The Astrophysical Journal*, **580**, 261–277.

C. Péroux, L. J. Storrie-Lombardi, R. G. McMahon, M. Irwin, and I. M. Hook (2001). Absorption Systems in the Spectra of 66 Z¿˜4 Quasars. *The Astronomical Journal*, **121**, 1799–1820.

C. Péroux, R. G. McMahon, L. J. Storrie-Lombardi, and M. J. Irwin (2003). The evolution of ΩHI and the epoch of formation of damped Lyman α absorbers. *Monthly Notices of the Royal Astronomical Society*, **346**, 1103–1115.

C. Péroux, M. Dessauges-Zavadsky, S. D'Odorico, T. Sun Kim, and R. G. McMahon (2005). A homogeneous sample of sub-damped Lyman α systems - III. Total

gas mass ΩHI+HeII at z ¿ 2*. *Monthly Notices of the Royal Astronomical Society*, **363**, 479–495.

C. Péroux, M. Dessauges-Zavadsky, S. D'Odorico, T. S. Kim, and R. G. McMahon (2007). A homogeneous sample of sub-damped Lyman systems - IV. Global metallicity evolution. *Monthly Notices of the Royal Astronomical Society*, **382**, 177–193.

S. E. Persson, D. C. Murphy, W. Krzeminski, M. Roth, and M. J. Rieke (1998). A New System of Faint Near-Infrared Standard Stars. *The Astronomical Journal*, **116**, 2475–2488.

P. Petitjean, C. Ledoux, P. Noterdaeme, and R. Srianand (2006). Metallicity as a criterion to select H_2-bearing damped Lyman-α systems. *Astronomy and Astrophysics*, **456**, L9–L12.

P. Petitjean, F. Y. Wang, X. F. Wu, and J. J. Wei (2016). GRBs and Fundamental Physics. *Space Science Reviews*, 1–40.

V. Petrosian, E. Kitanidis, and D. Kocevski (2015). Cosmological Evolution of Long Gamma-Ray Bursts and the Star Formation Rate. *The Astrophysical Journal*, **806**, 44.

M. Pettini, L. J. Smith, R. W. Hunstead, and D. L. King (1994). Metal enrichment, dust, and star formation in galaxies at high redshifts. 3: Zn and CR abundances for 17 damped Lyman-alpha systems. *The Astrophysical Journal*, **426**, 79–96.

M. Pettini, S. L. Ellison, C. C. Steidel, and D. V. Bowen (1999). Metal Abundances at z¡1.5: Fresh Clues to the Chemical Enrichment History of Damped Lyα Systems. *The Astrophysical Journal*, **510**, 576–589.

M. Pettini, S. A. Rix, C. C. Steidel, M. P. Hunt, A. E. Shapley, and K. L. Adelberger (2002). MS 1512 cB58: A case study of star formation, metal enrichment and superwinds in Lyman break galaxies. *Astrophysics and Space Science*, **281**, 461–466.

S. Piranomonte, S. D. Vergani, D. Malesani, J. P. U. Fynbo, K. Wiersema, and L. Kaper (2011). GRB110715A: VLT redshift. *GRB Coordinates Network*, **1216**.

L. Piro, E. Costa, M. Feroci, M. Cinti, F. Frontera, D. dal Fiume, M. Orlandini, G. Pizzichini, J. Heise, R. Jager, et al. (1996). Gamma-Ray Burst. *Circulars of the International Astronomical Union*, **6467**, 1.

L. Piro, E. Troja, B. Gendre, G. Ghisellini, R. Ricci, K. Bannister, F. Fiore, L. A. Kidd, S. Piranomonte, and M. H. Wieringa (2014). A Hot Cocoon in the Ultralong GRB 130925A: Hints of a POPIII-like Progenitor in a Low-Density Wind Environment. *The Astrophysical Journal*, **790**, L15.

C. Planck, P. A. R. Ade, N. Aghanim, C. Armitage-Caplan, M. Arnaud, M. Ashdown, F. Atrio-Barandela, J. Aumont, C. Baccigalupi, A. J. Banday, et al. (2014). Planck 2013 results. XVI. Cosmological parameters. *Astronomy and Astrophysics*, **571**, A16.

A. Pontzen, F. Governato, M. Pettini, C. M. Booth, G. Stinson, J. Wadsley, A. Brooks, T. Quinn, and M. Haehnelt (2008). Damped Lyman α systems in galaxy formation simulations. *Monthly Notices of the Royal Astronomical Society*, **390**, 1349–1371.

M. Postman, D. Coe, N. Benitez, L. Bradley, T. Broadhurst, M. Donahue, H. Ford, O. Graur, G. Graves, S. Jouvel, et al. (2012). The Cluster Lensing and Supernova Survey with Hubble: An Overview. *The Astrophysical Journal Supplement Series*, **199**, 25.

J. X. Prochaska (1999). The Physical Nature of the Lyman-Limit Systems. *The Astrophysical Journal*, **511**, L71–L74.

J. X. Prochaska (2006). On the Perils of Curve-of-Growth Analysis: Systematic Abundance Underestimates for the Gas in Gamma-Ray Burst Host Galaxies. *The Astrophysical Journal*, **650**, 272–280.

J. X. Prochaska and S. Herbert-Fort (2004). The Sloan Digital Sky Survey Damped Lyα Survey: Data Release 1. *The Publications of the Astronomical Society of the Pacific*, **116**, 622–633.

J. X. Prochaska and A. M. Wolfe (1997). On the Kinematics of the Damped Lyman-α Protogalaxies. *The Astrophysical Journal*, **487**, 73–95.

J. X. Prochaska and A. M. Wolfe (2001). Are Simulations of Cold Dark Matter Consistent with Galactic-Scale Observations at High Redshift? *The Astrophysical Journal*, **560**, L33–L36.

J. X. Prochaska and A. M. Wolfe (2009). On the (Non)Evolution of H I Gas in Galaxies Over Cosmic Time. *The Astrophysical Journal*, **696**, 1543–1547.

J. X. Prochaska, E. Gawiser, A. M. Wolfe, J. Cooke, and D. Gelino (2003). The ESI/Keck II Damped Lyα Abundance Database. *The Astrophysical Journal Supplement Series*, **147**, 227–264.

J. X. Prochaska, S. Herbert-Fort, and A. M. Wolfe (2005). The SDSS Damped Lyα Survey: Data Release 3. *The Astrophysical Journal*, **635**, 123–142.

J. X. Prochaska, H.-W. Chen, M. Dessauges-Zavadsky, and J. S. Bloom (2007). Probing the Interstellar Medium near Star-forming Regions with Gamma-Ray Burst Afterglow Spectroscopy: Gas, Metals, and Dust. *The Astrophysical Journal*, **666**, 267–280.

J. X. Prochaska, H.-W. Chen, A. M. Wolfe, M. Dessauges-Zavadsky, and J. S. Bloom (2008a). On the Nature of Velocity Fields in High-z Galaxies. *The Astrophysical Journal*, **672**, 59–71.

J. X. Prochaska, J. F. Hennawi, and S. Herbert-Fort (2008b). The SDSS-DR5 Survey for Proximate Damped Lyα Systems. *The Astrophysical Journal*, **675**, 1002–1013.

J. X. Prochaska, G. Worseck, and J. M. O'Meara (2009). A Direct Measurement of the Intergalactic Medium Opacity to H I Ionizing Photons. *The Astrophysical Journal*, **705**, L113–L117.

J. X. Prochaska, J. M. O'Meara, and G. Worseck (2010). A Definitive Survey for Lyman Limit Systems at z ˜ 3.5 with the Sloan Digital Sky Survey. *The Astrophysical Journal*, **718**, 392–416.

S. Quiret, C. Péroux, T. Zafar, V. P. Kulkarni, E. D. Jenkins, B. Milliard, H. Rahmani, A. Popping, R. M. Sandhya, D. A. Turnshek, et al. (2016). The ESO UVES Advanced Data Products Quasar Sample - VI. Sub-Damped Lyman-α Metallicity Measurements and the Circum-Galactic Medium. *arXiv.org*, arXiv:1602.02564.

J. L. Racusin, S. V. Karpov, M. Sokolowski, J. Granot, X. F. Wu, V. Pal'Shin, S. Covino, A. J. van der Horst, S. R. Oates, P. Schady, et al. (2008). Broadband observations of the naked-eye γ-ray burst GRB080319B. *Nature*, **455**, 183–188.

M. Rafelski, A. M. Wolfe, J. X. Prochaska, M. Neeleman, and A. J. Mendez (2012). Metallicity Evolution of Damped Lyα Systems Out to z ˜ 5. *The Astrophysical Journal*, **755**, 89.

M. Rafelski, M. Neeleman, M. Fumagalli, A. M. Wolfe, and J. X. Prochaska (2014). The Rapid Decline in Metallicity of Damped Lyα Systems at z ˜ 5. *The Astrophysical Journal*, **782**, L29.

E. Ramirez-Ruiz, A. Celotti, and M. J. Rees (2002). Events in the life of a cocoon surrounding a light, collapsar jet. *Monthly Notices of the Royal Astronomical Society*, **337**, 1349–1356.

S. M. Rao and D. A. Turnshek (2000). Discovery of DampedLyα Systems at Redshifts Less than 1.65 and Results on Their Incidence and Cosmological Mass Density. *The Astrophysical Journal Supplement Series*, **130**, 1–35.

S. M. Rao, D. A. Turnshek, and D. B. Nestor (2006). Damped Lyα Systems at z¡1.65: The Expanded Sloan Digital Sky Survey Hubble Space Telescope Sample. *The Astrophysical Journal*, **636**, 610–630.

S. Raskutti, J. S. Bolton, J. S. B. Wyithe, and G. D. Becker (2012). Thermal constraints on the reionization of hydrogen by Population II stellar sources. *Monthly Notices of the Royal Astronomical Society*, **421**, 1969–1981.

M. Rauch, J. Miralda-Escudé, W. L. W. Sargent, T. A. Barlow, D. H. Weinberg, L. Hernquist, N. Katz, R. Cen, and J. P. Ostriker (1997). The Opacity of the Lyα Forest and Implications for Ωb and the Ionizing Background. *The Astrophysical Journal*, **489**, 7–20.

M. J. Rees (1998). The Universe at z ¿ 5: When and How did the "Dark Age" End? In *Proceedings of the National Academy of Sciences of the United States of America*, 47–52, Institute of Astronomy, Madingley Road, Cambridge, CB3 OHA, United Kingdom., National Acad Sciences.

M. J. Rees and P. Mészáros (1992). Relativistic fireballs - Energy conversion and time-scales. *Monthly Notices of the Royal Astronomical Society*, **258**, 41P–43P.

M. J. Rees and P. Mészáros (1994). Unsteady outflow models for cosmological gamma-ray bursts. *The Astrophysical Journal*, **430**, L93–L96.

M. J. Rees and P. Mészáros (1998). Refreshed Shocks and Afterglow Longevity in Gamma-Ray Bursts. *The Astrophysical Journal*, **496**, L1–L4.

L. Resmi, K. Misra, G. Jóhannesson, A. J. Castro-Tirado, J. Gorosabel, D. Bhattacharya, G. C. Anupama, D. K. Sahu, S. B. Pandey, M. Bremer, et al. (2012). Comprehensive multiwavelength modelling of the afterglow of GRB 050525A. *Monthly Notices of the Royal Astronomical Society*, **427**, 288–297. 132

J. Rhee, M. A. Zwaan, F. H. Briggs, J. N. Chengalur, P. Lah, T. Oosterloo, and T. van der Hulst (2013). Neutral atomic hydrogen (H I) gas evolution in field galaxies at z ˜ 0.1 and ˜0.2. *Monthly Notices of the Royal Astronomical Society*, **435**, 2693–2706.

J. E. Rhoads (1997). How to Tell a Jet from a Balloon: A Proposed Test for Beaming in Gamma-Ray Bursts. *The Astrophysical Journal*, **487**, L1–L4.

J. E. Rhoads (1999). The Dynamics and Light Curves of Beamed Gamma-Ray Burst Afterglows. *The Astrophysical Journal*, **525**, 737–749.

B. E. Robertson and R. S. Ellis (2012). Connecting the Gamma Ray Burst Rate and the Cosmic Star Formation History: Implications for Reionization and Galaxy Evolution. *The Astrophysical Journal*, **744**, 95.

B. E. Robertson, S. R. Furlanetto, E. Schneider, S. Charlot, R. S. Ellis, D. P. Stark, R. J. McLure, J. S. Dunlop, A. Koekemoer, M. A. Schenker, et al. (2013). New Constraints on Cosmic Reionization from the 2012 Hubble Ultra Deep Field Campaign. *The Astrophysical Journal*, **768**, 71.

B. E. Robertson, R. S. Ellis, S. R. Furlanetto, and J. S. Dunlop (2015). Cosmic Reionization and Early Star-forming Galaxies: A Joint Analysis of New Constraints from Planck and the Hubble Space Telescope. *The Astrophysical Journal*, **802**, L19.

E. Rodríguez, P. Petitjean, B. Aracil, C. Ledoux, and R. Srianand (2006). Relative abundance pattern along the profile of high redshift Damped Lyman-α systems. *Astronomy and Astrophysics*, **446**, 791–804.

P. W. A. Roming, T. E. Kennedy, K. O. Mason, J. A. Nousek, L. Ahr, R. E. Bingham, P. S. Broos, M. J. Carter, B. K. Hancock, H. E. Huckle, et al. (2005). The Swift Ultra-Violet/Optical Telescope. *Space Science Reviews*, **120**, 95–142.

J. L. Rosenberg and S. E. Schneider (2002). The Arecibo Dual-Beam Survey: The H I Mass Function of Galaxies. *The Astrophysical Journal*, **567**, 247–257.

D. M. Russell, S. L. Ellison, and C. R. Benn (2006). An excess of damped Lyman α galaxies near quasi-stellar objects. *Monthly Notices of the Royal Astronomical Society*, **367**, 412–422.

G. Ryan, H. van Eerten, A. MacFadyen, and B.-B. Zhang (2015). Gamma-Ray Bursts are Observed Off-axis. *The Astrophysical Journal*, **799**, 3.

E. E. Salpeter (1964). Accretion of Interstellar Matter by Massive Objects. *The Astrophysical Journal*, **140**, 796–800.

R. Salvaterra (2015). High redshift Gamma-Ray Bursts. *Journal of High Energy Astrophysics*, **7**, 35–43.

R. Salvaterra, M. Della Valle, S. Campana, G. Chincarini, S. Covino, P. D'Avanzo, A. Fernandez-Soto, C. Guidorzi, F. Mannucci, R. Margutti, et al. (2009). GRB090423 at a redshift of z˜8.1. *Nature*, **461**, 1258–1260.

R. Salvaterra, S. Campana, S. D. Vergani, S. Covino, P. D'Avanzo, D. Fugazza, G. Ghirlanda, G. Ghisellini, A. Melandri, L. Nava, et al. (2012). A Complete Sample of Bright Swift Long Gamma-Ray Bursts. I. Sample Presentation, Luminosity Function and Evolution. *The Astrophysical Journal*, **749**, 68.

R. Salvaterra, U. Maio, B. Ciardi, and M. A. Campisi (2013). Simulating high-z gamma-ray burst host galaxies. *Monthly Notices of the Royal Astronomical Society*, **429**, 2718–2726.

R. Sánchez-Ramírez, S. L. Ellison, J. X. Prochaska, T. A. M. Berg, S. Lopez, V. D'Odorico, G. D. Becker, L. Christensen, G. Cupani, K. D. Denney, et al. (2016). The evolution of neutral gas in damped Lyman α systems from the XQ-100 survey. *Monthly Notices of the Royal Astronomical Society*, **456**, 4488–4505. 176, 177, 178, 196

W. L. W. Sargent, P. J. Young, A. Boksenberg, and D. Tytler (1980). The distribution of Lyman-alpha absorption lines in the spectra of six QSOs - Evidence for an intergalactic origin. *The Astrophysical Journal Supplement Series*, **42**, 41–81.

R. Sari and T. Piran (1995). Hydrodynamic Timescales and Temporal Structure of Gamma-Ray Bursts. *The Astrophysical Journal*, **455**, L143–.

R. Sari and T. Piran (1999). Predictions for the Very Early Afterglow and the Optical Flash. *The Astrophysical Journal*, **520**, 641–649.

R. Sari, T. Piran, and R. Narayan (1998). Spectra and Light Curves of Gamma-Ray Burst Afterglows. *The Astrophysical Journal*, **497**, L17–L20.

R. Sari, T. Piran, and J. P. Halpern (1999). Jets in Gamma-Ray Bursts. *The Astrophysical Journal*, **519**, L17–L20.

R. J. Sault, P. J. Teuben, and M. C. H. Wright (1995). A Retrospective View of MIRIAD. In *Astronomical Data Analysis Software and Systems IV*, 433, Australia Telescope National Facility, CSIRO, P.O. Box 76, Epping, N.S.W., 2121, Australia.

B. D. Savage and K. R. Sembach (1991). The analysis of apparent optical depth profiles for interstellar absorption lines. *The Astrophysical Journal*, **379**, 245–259.

B. D. Savage and K. R. Sembach (1996). Interstellar Abundances from Absorption-Line Observations with the Hubble Space Telescope. *Annual Review of Astronomy and Astrophysics*, **34**, 279–330.

S. Savaglio (2006). GRBs as cosmological probes—cosmic chemical evolution. *New Journal of Physics*, **8**, 195–.

S. Savaglio, K. G. Collaboration, and D. Le Borgne Collaboration (2006). Stellar Masses and Metallicities of GRB Host Galaxies. *American Astronomical Society Meeting 207*, **207**, 16.18.

E. Scannapieco, P. Madau, S. Woosley, A. Heger, and A. Ferrara (2005). The Detectability of Pair-Production Supernovae at z ¡˜ 6. *The Astrophysical Journal*, **633**, 1031–1041.

P. Schady, M. J. Page, S. R. Oates, M. Still, M. De Pasquale, T. Dwelly, N. P. M. Kuin, S. T. Holland, F. E. Marshall, and P. W. A. Roming (2010). Dust and metal column densities in gamma-ray burst host galaxies. *Monthly Notices of the Royal Astronomical Society*, **401**, 2773–2792.

P. Schady, S. Savaglio, T. Krühler, J. Greiner, and A. Rau (2011). The missing gas problem in GRB host galaxies: evidence for a highly ionised component. *Astronomy and Astrophysics*, **525**, A113.

P. Schady, T. Dwelly, M. J. Page, T. Krühler, J. Greiner, S. R. Oates, M. De Pasquale, M. Nardini, P. W. A. Roming, A. Rossi, et al. (2012). The dust extinction curves of gamma-ray burst host galaxies. *Astronomy and Astrophysics*, **537**, A15.

E. F. Schlafly and D. P. Finkbeiner (2011). Measuring Reddening with Sloan Digital Sky Survey Stellar Spectra and Recalibrating SFD. *The Astrophysical Journal*, **737**, 103.

D. J. Schlegel, D. P. Finkbeiner, and M. Davis (1998). Maps of Dust Infrared Emission for Use in Estimation of Reddening and Cosmic Microwave Background Radiation Foregrounds. *The Astrophysical Journal*, **500**, 525–553.

M. Schmidt (1963). 3C 273 : A Star-Like Object with Large Red-Shift. *Nature*, **197**, 1040–1040.

M. Schmidt and R. F. Green (1983). Quasar evolution derived from the Palomar bright quasar survey and other complete quasar surveys. *The Astrophysical Journal*, **269**, 352–374.

R. Schneider, K. Omukai, A. K. Inoue, and A. Ferrara (2006). Fragmentation of star-forming clouds enriched with the first dust. *Monthly Notices of the Royal Astronomical Society*, **369**, 1437–1444.

S. Schulze, R. Chapman, J. Hjorth, A. J. Levan, P. Jakobsson, G. Björnsson, D. A. Perley, T. Krühler, J. Gorosabel, N. R. Tanvir, et al. (2015). The Optically Unbiased GRB Host (TOUGH) Survey. VII. The Host Galaxy Luminosity Function: Probing the Relationship between GRBs and Star Formation to Redshift $\sim$ 6. *The Astrophysical Journal*, **808**, 73.

A. Shahmoradi (2013). Gamma-Ray bursts: Energetics and Prompt Correlations. *arXiv.org*, arXiv:1308.1097.

A. Shahmoradi and R. J. Nemiroff (2011). The possible impact of gamma-ray burst detector thresholds on cosmological standard candles. *Monthly Notices of the Royal Astronomical Society*, **411**, 1843–1856.

N. J. Shaviv and A. Dar (1995). Gamma-Ray Bursts from Minijets. *Astrophysical Journal v.447*, **447**, 863–.

A. I. Sheinis, M. Bolte, H. W. Epps, R. I. Kibrick, J. S. Miller, M. V. Radovan, B. C. Bigelow, and B. M. Sutin (2002). ESI, a New Keck Observatory Echellette Spectrograph and Imager. *The Publications of the Astronomical Society of the Pacific*, **114**, 851–865.

R. Shen, P. Kumar, and E. L. Robinson (2006). No universality for the electron power-law index (p) in gamma-ray bursts and other relativistic sources. *Monthly Notices of the Royal Astronomical Society*, **371**, 1441–1447.

L. Silva, G. L. Granato, A. Bressan, and L. Danese (1998). Modeling the Effects of Dust on Galactic Spectral Energy Distributions from the Ultraviolet to the Millimeter Band. *The Astrophysical Journal*, **509**, 103–117.

R. A. Simcoe, P. W. Sullivan, K. L. Cooksey, M. M. Kao, M. S. Matejek, and A. J. Burgasser (2012). Extremely metal-poor gas at a redshift of 7. *Nature*, **492**, 79–82.

G. Siringo, E. Kreysa, A. Kovács, F. Schuller, A. Weiss, W. Esch, H. P. Gemünd, N. Jethava, G. Lundershausen, A. Colin, et al. (2009). The Large APEX BOlometer CAmera LABOCA. *Astronomy and Astrophysics*, **497**, 945–962.

M. F. Skrutskie, R. M. Cutri, R. Stiening, M. D. Weinberg, S. Schneider, J. M. Carpenter, C. Beichman, R. Capps, T. Chester, J. Elias, et al. (2006). The Two Micron All Sky Survey (2MASS). *The Astronomical Journal*, **131**, 1163–1183.

H. E. Smith, B. Margon, and M. Jura (1979). On the abundances in the Z = 2.81 absorbing material toward the quasi-stellar object PKS 0528-250. *The Astrophysical Journal*, **228**, 369–374.

R. S. Somerville and R. Davé (2015). Physical Models of Galaxy Formation in a Cosmological Framework. *Annual Review of Astronomy and Astrophysics*, **53**, 51–113.

E. Sonbas, S. D. Barthelmy, W. H. Baumgartner, A. P. Beardmore, D. N. Burrows, V. D'Elia, M. De Pasquale, P. A. Evans, N. Gehrels, C. Guidorzi, et al. (2011). GRB 110715A: Swift detection of a bright burst with an optical counterpart. *GRB Coordinates Network*, **1215**.

A. Songaila (2004). The Evolution of the Intergalactic Medium Transmission to Redshift 6. *The Astronomical Journal*, **127**, 2598–2603.

A. Songaila and L. L. Cowie (2002). Approaching Reionization: The Evolution of the Ly α Forest from z=4 to z=6. *The Astronomical Journal*, **123**, 2183–2196.

A. Songaila and L. L. Cowie (2010). The Evolution of Lyman Limit Absorption Systems to Redshift Six. *The Astrophysical Journal*, **721**, 1448–1466.

A. Songaila, E. M. Hu, L. L. Cowie, and R. G. McMahon (1999). Limits on the Gunn-Peterson Effect at Z = 5. *The Astrophysical Journal*, **525**, L5–L8.

M. Sparre, O. E. Hartoog, T. Krühler, J. P. U. Fynbo, D. J. Watson, K. Wiersema, V. D'Elia, T. Zafar, P. M. J. Afonso, S. Covino, et al. (2014). The Metallicity and Dust Content of a Redshift 5 Gamma-Ray Burst Host Galaxy. *The Astrophysical Journal*, **785**, 150. 120

A. Stacy, V. Bromm, and A. Loeb (2011). Rotation speed of the first stars. *Monthly Notices of the Royal Astronomical Society*, **413**, 543–553.

A. Stacy, A. H. Pawlik, V. Bromm, and A. Loeb (2012). Effect of Population III multiplicity on dark star formation. *Monthly Notices of the Royal Astronomical Society*, **421**, 894–907.

A. Stacy, T. H. Greif, R. S. Klessen, V. Bromm, and A. Loeb (2013). Rotation and internal structure of Population III protostars. *Monthly Notices of the Royal Astronomical Society*, **431**, 1470–1486.

M. Stamatikos (2009). The Cross-Calibration of Swift-BAT and Fermi-GBM via Correlative Spectral Analysis of GRBs. *arXiv.org*, arXiv:0907.3190.

K. Z. Stanek, T. Matheson, P. M. Garnavich, P. Martini, P. Berlind, N. Caldwell, P. Challis, W. R. Brown, R. Schild, K. Krisciunas, et al. (2003). Spectroscopic Discovery of the Supernova 2003dh Associated with GRB 030329. *The Astrophysical Journal*, **591**, L17–L20.

R. L. C. Starling, R. A. M. J. Wijers, M. A. Hughes, N. R. Tanvir, P. M. Vreeswijk, E. Rol, and I. Salamanca (2005). Spectroscopy of the γ-ray burst GRB 021004: a structured jet ploughing through a massive stellar wind. *Monthly Notices of the Royal Astronomical Society*, **360**, 305–313.

R. L. C. Starling, R. A. M. J. Wijers, K. Wiersema, E. Rol, P. A. Curran, C. Kouveliotou, A. J. van der Horst, and M. H. M. Heemskerk (2007). Gamma-Ray Burst Afterglows as Probes of Environment and Blast Wave Physics. I. Absorption by Host-Galaxy Gas and Dust. *The Astrophysical Journal*, **661**, 787–800.

L. Staveley-Smith and T. Oosterloo (2015). HI Science with the Square Kilometre Array. In *Proceedings of Advancing Astrophysics with the Square Kilometre Array (AASKA14). 9 -13 June*, 167.

C. C. Steidel, M. Giavalisco, M. Dickinson, and K. L. Adelberger (1996). Spectroscopy of Lyman Break Galaxies in the Hubble Deep Field. *The Astronomical Journal*, **112**, 352.

A. N. Stockton and C. R. Lynds (1966). The Remarkable Absorption Spectrum of 3c 191. *The Astrophysical Journal*, **144**, 451.

L. J. Storrie-Lombardi and A. M. Wolfe (2000). Surveys for z¿3 Damped Lyα Absorption Systems: The Evolution of Neutral Gas. *The Astrophysical Journal*, **543**, 552–576.

L. J. Storrie-Lombardi, M. J. Irwin, and R. G. McMahon (1996a). APM z¿˜4 survey: distribution and evolution of high column density HI absorbers. *Monthly Notices of the Royal Astronomical Society*, **282**, 1330–1342.

L. J. Storrie-Lombardi, R. G. McMahon, and M. J. Irwin (1996b). Evolution of neutral gas at high redshift: implications for the epoch of galaxy formation. *Monthly Notices of the Royal Astronomical Society*, **283**, L79–L83.

L. J. Storrie-Lombardi, R. G. McMahon, M. J. Irwin, and C. Hazard (1996c). APM Z ¿=4 QSO Survey: Spectra and Intervening Absorption Systems. *The Astrophysical Journal*, **468**, 121.

I. B. Strong and R. W. Klebesadel (1976). Cosmic gamma-ray bursts. *Scientific American*, **235**, 66–70.

G. Tagliaferri, L. A. Antonelli, G. Chincarini, A. Fernandez-Soto, D. Malesani, M. Della Valle, P. D'Avanzo, A. Grazian, V. Testa, S. Campana, et al. (2005). GRB 050904 at redshift 6.3: observations of the oldest cosmic explosion after the Big Bang. *Astronomy and Astrophysics*, **443**, L1–L5.

Y. Taniguchi, Y. Shioya, and J. R. Trump (2010). Low-metallicity Star Formation in High-redshift Galaxies at z ˜ 8. *The Astrophysical Journal*, **724**, 1480–1490.

N. R. Tanvir, D. B. Fox, A. J. Levan, E. Berger, K. Wiersema, J. P. U. Fynbo, A. Cucchiara, T. Krühler, N. Gehrels, J. S. Bloom, et al. (2009). A γ-ray burst at a redshift of z˜8.2. *Nature*, **461**, 1254–1257.

N. R. Tanvir, A. J. Levan, A. S. Fruchter, J. P. U. Fynbo, J. Hjorth, K. Wiersema, M. Bremer, J. Rhoads, P. Jakobsson, P. T. O'Brien, et al. (2012). Star Formation in the Early Universe: Beyond the Tip of the Iceberg. *The Astrophysical Journal*, **754**, 46.

N. R. Tanvir, A. J. Levan, A. S. Fruchter, J. Hjorth, R. A. Hounsell, K. Wiersema, and R. L. Tunnicliffe (2013). A 'kilonova' associated with the short-duration γ-ray burst GRB 130603B. *Nature*, **500**, 547–549.

O. V. Terekhov, V. A. Lobachev, D. V. Denisenko, I. Y. Lapshov, R. A. Syunyaev, N. Lund, A. J. Castro-Tirado, and S. Brandt (1993). Observations of the cosmic gamma-ray burst by the WATCH instrument of the GRANAT observatory on July 23, 1992. *Astronomy Letters*, **19**, 276–279.

C. C. Thöne, D. A. Kann, G. Jóhannesson, J. H. Selj, A. O. Jaunsen, J. P. U. Fynbo, C. W. Akerlof, K. S. Baliyan, C. Bartolini, I. F. Bikmaev, et al. (2010). Photometry and spectroscopy of GRB 060526: a detailed study of the afterglow and host galaxy of a z = 3.2 gamma-ray burst. *Astronomy and Astrophysics*, **523**, A70.

C. C. Thöne, P. Goldoni, A. de Ugarte Postigo, S. Campana, S. D. Vergani, T. Krühler, T. Zafar, J. Gorosabel, P. Groot, F. Hammer, et al. (2013). GRB 100219A with X-shooter - abundances in a galaxy at z =4.7. *Monthly Notices of the Royal Astronomical Society*, **428**, 3590–3606.

C. Tinney, R. Stathakis, R. Cannon, T. J. Galama, M. Wieringa, D. A. Frail, S. R. Kulkarni, J. L. Higdon, R. Wark, J. S. Bloom, et al. (1998). GRB 980425. *Circulars of the International Astronomical Union*, **6896**, 1.

D. Tody (1993). IRAF in the Nineties. *Astronomical Data Analysis Software and Systems II*, **52**, 173.

K. Toma, T. Sakamoto, and P. Mészáros (2011). Population III Gamma-ray Burst Afterglows: Constraints on Stellar Masses and External Medium Densities. *The Astrophysical Journal*, **731**, 127.

K. Toma, S.-C. Yoon, and V. Bromm (2016). Gamma-Ray Bursts and Population III Stars. *Space Science Reviews*, 1–22.

T. Totani, N. Kawai, G. Kosugi, K. Aoki, T. Yamada, M. Iye, K. Ohta, and T. Hattori (2006). Implications for Cosmic Reionization from the Optical Afterglow Spectrum of the Gamma-Ray Burst 050904 at z = 6.3. *Publications of the Astronomical Society of Japan*, **58**, 485–498.

T. Totani, K. Aoki, T. Hattori, G. Kosugi, Y. Niino, T. Hashimoto, N. Kawai, K. Ohta, T. Sakamoto, and T. Yamada (2014). Probing intergalactic neutral hydrogen by the Lyman alpha red damping wing of gamma-ray burst 130606A afterglow spectrum at z = 5.913. *Publications of the Astronomical Society of Japan*, **66**, 63–63.

T. Totani, K. Aoki, T. Hattori, and N. Kawai (2016). High-precision analyses of Lyα damping wing of gamma-ray bursts in the reionization era: On the controversial results from GRB 130606A at z = 5.91. *Publications of the Astronomical Society of Japan*, **68**, 15.

M. Trenti, R. Perna, and R. Jimenez (2015). The Luminosity and Stellar Mass Functions of GRB Host Galaxies: Insight Into the Metallicity Bias. *The Astrophysical Journal*, **802**, 103.

T. N. Ukwatta, S. D. Barthelmy, N. Gehrels, H. A. Krimm, D. Malesani, F. E. Marshall, A. Maselli, A. Melandri, D. M. Palmer, and M. Stamatikos (2013). GRB 130606A: Swift detection of a burst. *GRB Coordinates Network*, **1478**, 1.

A. C. Updike, P. Schady, J. Greiner, T. Krühler, D. A. Kann, S. Klose, and A. Rossi (2011). GRB110715A: GROND detection of the Optical/NIR afterglow. *GRB Coordinates Network*, **1216**.

A. J. van der Horst, Z. Paragi, A. G. de Bruyn, J. Granot, C. Kouveliotou, K. Wiersema, R. L. C. Starling, P. A. Curran, R. A. M. J. Wijers, A. Rowlinson, et al. (2014). A comprehensive radio view of the extremely bright gamma-ray burst 130427A. *Monthly Notices of the Royal Astronomical Society*, **444**, 3151–3163.

P. G. van Dokkum (2001). Cosmic-Ray Rejection by Laplacian Edge Detection. *The Publications of the Astronomical Society of the Pacific*, **113**, 1420–1427.

H. van Eerten, A. van der Horst, and A. MacFadyen (2012). Gamma-Ray Burst Afterglow Broadband Fitting Based Directly on Hydrodynamics Simulations. *The Astrophysical Journal*, **749**, 44.

J. van Paradijs, P. J. Groot, T. J. Galama, C. Kouveliotou, R. G. Strom, J. Telting, R. G. M. Rutten, G. J. Fishman, C. A. Meegan, M. Pettini, et al. (1997). Transient optical emission from the error box of the γ-ray burst of 28 February 1997. *Nature*, **386**, 686–689.

S. D. Vergani, R. Salvaterra, J. Japelj, E. Le Floc'h, P. D'Avanzo, A. Fernandez-Soto, T. Krühler, A. Melandri, S. Boissier, S. Covino, et al. (2015). Are long gamma-ray bursts biased tracers of star formation? Clues from the host galaxies of the Swift/BAT6 complete sample of LGRBs . I. Stellar mass at z ¡ 1. *Astronomy and Astrophysics*, **581**, A102.

J. Vernet, H. Dekker, S. D'Odorico, P. Kjaergaard, F. Hammer, S. Randich, F. Zerbi, P. J. Groot, I. Guinouard, R. Navarro, et al. (2011). X-shooter, the new wide band intermediate resolution spectrograph at the ESO Very Large Telescope. *Astronomy and Astrophysics*, **536**, A105.

S. M. Viegas (1995). Abundances at high redshift: ionization correction factors. *Monthly Notices of the Royal Astronomical Society*, **276**, 268–272.

F. J. Virgili, B. Zhang, K. Nagamine, and J.-H. Choi (2011). Gamma-ray burst rate: high-redshift excess and its possible origins. *Monthly Notices of the Royal Astronomical Society*, **417**, 3025–3034.

F. J. Virgili, C. G. Mundell, and A. Melandri (2013a). GRB 130606A - Liverpool telescope optical afterglow confirmation. *GRB Coordinates Network*, **1478**, 1.

F. J. Virgili, C. G. Mundell, A. Melandri, and A. Gomboc (2013b). GRB 130606A - Liverpool telescope and Faulkes telescope north optical observations. *GRB Coordinates Network*, **1484**, 1.

G. Vladilo (1998). Dust and Elemental Abundances in Damped Lyα Absorbers. *The Astrophysical Journal*, **493**, 583–594.

G. Vladilo (2002a). A Scaling Law for Interstellar Depletions. *The Astrophysical Journal*, **569**, 295–303.

G. Vladilo (2002b). Chemical abundances of damped Ly alpha systems:. A new method for estimating dust depletion effects. *Astronomy and Astrophysics*, **391**, 407–415.

G. Vladilo, M. Centurión, P. Bonifacio, and J. C. Howk (2001). Ionization Properties and Elemental Abundances in Damped Lyα Systems. *The Astrophysical Journal*, **557**, 1007–1020.

G. Vladilo, M. Centurión, S. A. Levshakov, C. Péroux, P. Khare, V. P. Kulkarni, and D. G. York (2006). Extinction and metal column density of HI regions up to redshift z $\simeq$ 2. *Astronomy and Astrophysics*, **454**, 151–164.

N. Vlahakis, F. Peng, and A. Königl (2003). Neutron-rich Hydromagnetic Outflows in Gamma-Ray Burst Sources. *The Astrophysical Journal*, **594**, L23–L26.

P. M. Vreeswijk, P. Møller, and J. P. U. Fynbo (2003). New search strategy for high z intervening absorbers: GRB 021004, a pilot study. *Astronomy and Astrophysics*, **409**, L5–L8.

P. M. Vreeswijk, C. Ledoux, A. Smette, S. L. Ellison, A. O. Jaunsen, M. I. Andersen, A. S. Fruchter, J. P. U. Fynbo, J. Hjorth, A. Kaufer, et al. (2007). Rapid-response mode VLT/UVES spectroscopy of GRB 060418. Conclusive evidence for UV pumping from the time evolution of Fe II and Ni II excited- and metastable-level populations. *Astronomy and Astrophysics*, **468**, 83–96.

F. Y. Wang (2013). The high-redshift star formation rate derived from gamma-ray bursts: possible origin and cosmic reionization. *Astronomy and Astrophysics*, **556**, A90.

F. Y. Wang and Z. G. Dai (2011a). An Evolving Stellar Initial Mass Function and the Gamma-ray Burst Redshift Distribution. *The Astrophysical Journal*, **727**, L34.

F. Y. Wang and Z. G. Dai (2011b). Weak gravitational lensing effects on cosmological parameters and dark energy from gamma-ray bursts. *Astronomy and Astrophysics*, **536**, A96.

F. Y. Wang, V. Bromm, T. H. Greif, A. Stacy, Z. G. Dai, A. Loeb, and K. S. Cheng (2012). Probing Pre-galactic Metal Enrichment with High-redshift Gamma-Ray Bursts. *The Astrophysical Journal*, **760**, 27.

F. Y. Wang, Z. G. Dai, and E. W. Liang (2015). Gamma-ray burst cosmology. *New Astronomy Reviews*, **67**, 1–17.

R. Wang, C. L. Carilli, J. Wagg, F. Bertoldi, F. Walter, K. M. Menten, A. Omont, P. Cox, M. A. Strauss, X. Fan, et al. (2008). Thermal Emission from Warm Dust in the Most Distant Quasars. *The Astrophysical Journal*, **687**, 848–858.

R. Wang, C. L. Carilli, R. Neri, D. A. Riechers, J. Wagg, F. Walter, F. Bertoldi, K. M. Menten, A. Omont, P. Cox, et al. (2010). Molecular Gas in z ˜ 6 Quasar Host Galaxies. *The Astrophysical Journal*, **714**, 699–712.

S. J. Warren, P. C. Hewett, M. J. Irwin, R. G. McMahon, and M. T. Bridgeland (1987). First observation of a quasar with a redshift of 4. *Nature*, **325**, 131–133.

E. Waxman, S. R. Kulkarni, and D. A. Frail (1998). Implications of the Radio Afterglow from the Gamma-Ray Burst of 1997 May 8. *The Astrophysical Journal*, **497**, 288–293.

J. C. Weisheit (1978). On the use of line shapes in the analysis of QSO absorption spectra. *Astrophysical Journal*, **219**, 829–835.

R. J. Weymann, R. E. Williams, B. M. Peterson, and D. A. Turnshek (1979). Results of a homogeneous survey of absorption lines in QSOs of small and intermediate emission redshift. *The Astrophysical Journal*, **234**, 33–46.

R. J. Weymann, R. F. Carswell, and M. G. Smith (1981). Absorption lines in the spectra of quasistellar objects. *In: Annual review of astronomy and astrophysics. Volume 19. (A82-11551 02-90) Palo Alto*, **19**, 41–76.

R. A. M. J. Wijers and T. J. Galama (1999). Physical Parameters of GRB 970508 and GRB 971214 from Their Afterglow Synchrotron Emission. *The Astrophysical Journal*, **523**, 177–186.

R. E. Williams, B. Blacker, M. Dickinson, W. V. D. Dixon, H. C. Ferguson, A. S. Fruchter, M. Giavalisco, R. L. Gilliland, I. Heyer, R. Katsanis, et al. (1996). The Hubble Deep Field: Observations, Data Reduction, and Galaxy Photometry. *The Astronomical Journal*, **112**, 1335–.

R. E. Williams, S. Baum, L. E. Bergeron, N. Bernstein, B. S. Blacker, B. J. Boyle, T. M. Brown, C. M. Carollo, S. Casertano, R. Covarrubias, et al. (2000). The Hubble Deep Field South: Formulation of the Observing Campaign. *The Astronomical Journal*, **120**, 2735–2746.

R. Willingale, D. D. Frederiks, V. D. Pal'shin, D. S. Svinkin, A. Lien, J. Cummings, S. Xiong, B.-B. Zhang, D. Götz, V. Savchenko, et al. (2014). GRB 130925A: an ultralong gamma ray burst with a dust-echo afterglow, and implications for the origin of the ultralong GRBs. *Monthly Notices of the Royal Astronomical Society*, **444**, 250–267. 212

C. J. Willott, P. Delorme, C. Reylé, L. Albert, J. Bergeron, D. Crampton, X. Delfosse, T. Forveille, J. B. Hutchings, R. J. McLure, et al. (2010). The Canada-France High-z Quasar Survey: Nine New Quasars and the Luminosity Function at Redshift 6. *The Astronomical Journal*, **139**, 906–918.

W. E. Wilson, R. H. Ferris, P. Axtens, A. Brown, E. Davis, G. Hampson, M. Leach, P. Roberts, S. Saunders, B. S. Koribalski, et al. (2011). The Australia Telescope Compact Array Broad-band Backend: description and first results. *Monthly Notices of the Royal Astronomical Society*, **416**, 832–856.

M. J. Wolf and A. I. Sheinis (2008). Host Galaxies of Luminous Quasars: Structural Properties and the Fundamental Plane. *The Astronomical Journal*, **136**, 1587–1606.

A. M. Wolfe, D. A. Turnshek, H. E. Smith, and R. D. Cohen (1986). Damped Lyman-alpha absorption by disk galaxies with large redshifts. I - The Lick survey. *The Astrophysical Journal Supplement Series*, **61**, 249–304.

A. M. Wolfe, X.-M. Fan, D. Tytler, S. S. Vogt, M. J. Keane, and K. M. Lanzetta (1994). Metal abundances and kinematics of a high-redshift galaxy obtained with the Kech telescope. *Astrophysical Journal*, **435**, L101–L104.

A. M. Wolfe, K. M. Lanzetta, C. B. Foltz, and F. H. Chaffee (1995). The Large Bright QSO Survey for Damped LY alpha Absorption Systems. *The Astrophysical Journal*, **454**, 698.

A. M. Wolfe, E. Gawiser, and J. X. Prochaska (2005). Damped Ly α Systems. *Annual Review of Astronomy and Astrophysics*, **43**, 861–918.

M. G. Wolfire, C. F. McKee, D. Hollenbach, and A. G. G. M. Tielens (2003). Neutral Atomic Phases of the Interstellar Medium in the Galaxy. *The Astrophysical Journal*, **587**, 278–311.

S. E. Woosley (1993). Gamma-ray bursts from stellar mass accretion disks around black holes. *The Astrophysical Journal*, **405**, 273–277.

S. E. Woosley and J. S. Bloom (2006). The Supernova Gamma-Ray Burst Connection. *Annual Review of Astronomy and Astrophysics*, **44**, 507–556.

G. Worseck and J. X. Prochaska (2011). GALEX Far-ultraviolet Color Selection of UV-bright High-redshift Quasars. *The Astrophysical Journal*, **728**, 23.

G. Worseck, J. X. Prochaska, J. M. O'Meara, G. D. Becker, S. L. Ellison, S. Lopez, A. Meiksin, B. Ménard, M. T. Murphy, and M. Fumagalli (2014). The Giant Gemini GMOS survey of zem ¿ 4.4 quasars - I. Measuring the mean free path across cosmic time. *Monthly Notices of the Royal Astronomical Society*, **445**, 1745–1760.

S.-W. Wu, D. Xu, F.-W. Zhang, and D.-M. Wei (2012). Gamma-ray bursts: the isotropic-equivalent-energy function and the cosmic formation rate. *Monthly Notices of the Royal Astronomical Society*, **423**, 2627–2632.

X.-B. Wu, F. Y. Wang, X. Fan, W. Yi, W. Zuo, F. Bian, L. Jiang, I. D. McGreer, R. Wang, J. Yang, et al. (2015). An ultraluminous quasar with a twelve-billion-solar-mass black hole at redshift 6.30. *Nature*, **518**, 512–515.

X. F. Wu, Z. G. Dai, Y. F. Huang, and H. T. Ma (2004). Afterglow light curves of jetted gamma-ray burst ejecta in stellar winds. *Chinese J. Astron. Astrophys.*, **4**, 455–472.

A. K. Yoldaş, T. Krühler, J. Greiner, A. Yoldaş, C. Clemens, G. Szokoly, N. Primak, and S. Klose (2008). First Results of GROND. In *GAMMA-RAY BURSTS 2007: Proceedings of the Santa Fe Conference. AIP Conference Proceedings*, 227–231, Max-Planck-Institut für extraterrestrische Physik, Giessenbachstr. 1 85741 Garching bei München, Germany, AIP.

S. C. Yoon, A. Dierks, and N. Langer (2012). Evolution of massive Population III stars with rotation and magnetic fields. *Astronomy and Astrophysics*, **542**, A113.

D. G. York, J. Adelman, J. E. J. Anderson, S. F. Anderson, J. Annis, N. A. Bahcall, J. A. Bakken, R. Barkhouser, S. Bastian, E. Berman, et al. (2000). The Sloan Digital Sky Survey: Technical Summary. *The Astronomical Journal*, **120**, 1579–1587.

N. Yoshida, K. Omukai, L. Hernquist, and T. Abel (2006). Formation of Primordial Stars in a ΛCDM Universe. *The Astrophysical Journal*, **652**, 6–25.

H. Yu, F. Y. Wang, Z. G. Dai, and K. S. Cheng (2015). An Unexpectedly Low-redshift Excess of Swift Gamma-ray Burst Rate. *The Astrophysical Journal Supplement Series*, **218**, 13.

T. Zafar, D. J. Watson, J. P. U. Fynbo, D. Malesani, P. Jakobsson, and A. de Ugarte Postigo (2011). The extinction curves of star-forming regions from z = 0.1 to 6.7 using GRB afterglow spectroscopy. *Astronomy and Astrophysics*, **532**, A143.

T. Zafar, C. Péroux, A. Popping, B. Milliard, J. M. Deharveng, and S. Frank (2013). The ESO UVES advanced data products quasar sample. II. Cosmological evolution of the neutral gas mass density. *Astronomy and Astrophysics*, **556**, A141.

Y. B. Zel'dovich and I. D. Novikov (1964). The Radiation of Gravity Waves by Bodies Moving in the Field of a Collapsing Star. *Soviet Physics Doklady*, **9**, 246–.

B. Zhang and H. Yan (2011). The Internal-collision-induced Magnetic Reconnection and Turbulence (ICMART) Model of Gamma-ray Bursts. *The Astrophysical Journal*, **726**, 90.

B. Zhang, Y.-Z. Fan, J. Dyks, S. Kobayashi, P. Mészáros, D. N. Burrows, J. A. Nousek, and N. Gehrels (2006). Physical Processes Shaping Gamma-Ray Burst X-Ray Afterglow Light Curves: Theoretical Implications from the Swift X-Ray Telescope Observations. *The Astrophysical Journal*, **642**, 354–370.

B.-B. Zhang, B. Zhang, E.-W. Liang, and X.-Y. Wang (2009). Curvature Effect of a Non-Power-Law Spectrum and Spectral Evolution of GRB X-Ray Tails. *The Astrophysical Journal Letters*, **690**, L10–L13.

B.-B. Zhang, B. Zhang, E.-W. Liang, Y.-Z. Fan, X.-F. Wu, A. Pe'er, A. Maxham, H. Gao, and Y.-M. Dong (2011). A Comprehensive Analysis of Fermi Gamma-ray Burst Data. I. Spectral Components and the Possible Physical Origins of LAT/GBM GRBs. *The Astrophysical Journal*, **730**, 141.

B.-B. Zhang, B. Zhang, K. Murase, V. Connaughton, and M. S. Briggs (2014). How Long does a Burst Burst? *The Astrophysical Journal*, **787**, 66.

B.-B. Zhang, H. van Eerten, D. N. Burrows, G. S. Ryan, P. A. Evans, J. L. Racusin, E. Troja, and A. MacFadyen (2015). An Analysis of Chandra Deep Follow-up Gamma-Ray Bursts: Implications for Off-axis Jets. *The Astrophysical Journal*, **806**, 15.

W. Zheng, R. F. Shen, T. Sakamoto, A. P. Beardmore, M. De Pasquale, X. F. Wu, J. Gorosabel, Y. Urata, S. Sugita, B. Zhang, et al. (2012). Panchromatic Observations of the Textbook GRB 110205A: Constraining Physical Mechanisms of Prompt Emission and Afterglow. *The Astrophysical Journal*, **751**, 90. 119

A. Zitrin, I. Labbé, S. Belli, R. Bouwens, R. S. Ellis, G. Roberts-Borsani, D. P. Stark, P. A. Oesch, and R. Smit (2015). Lymanα Emission from a Luminous z = 8.68 Galaxy: Implications for Galaxies as Tracers of Cosmic Reionization. *The Astrophysical Journal*, **810**, L12.

E. Zucca, S. Bardelli, M. Bolzonella, G. Zamorani, O. Ilbert, L. Pozzetti, M. Mignoli, K. Kovač, S. Lilly, L. Tresse, et al. (2009). The zCOSMOS survey: the role of the environment in the evolution of the luminosity function of different galaxy types. *Astronomy and Astrophysics*, **508**, 1217–1234.

M. A. Zwaan, L. Staveley-Smith, B. S. Koribalski, P. A. Henning, V. A. Kilborn, S. D. Ryder, D. G. Barnes, R. Bhathal, P. J. Boyce, W. J. G. de Blok, et al. (2003). The 1000 Brightest HIPASS Galaxies: The H I Mass Function and ΩHI. *The Astronomical Journal*, **125**, 2842–2858.

M. A. Zwaan, J. M. van der Hulst, F. H. Briggs, M. A. W. Verheijen, and E. V. Ryan-Weber (2005). Reconciling the local galaxy population with damped Lyman α cross-sections and metal abundances. *Monthly Notices of the Royal Astronomical Society*, **364**, 1467–1487.